Journal of ASTM International
Selected Technical Papers

INTERNATIONAL
Standards Worldwide

STP 1526

Fatigue and Fracture Mechanics
37th Volume

European Structural Integrity Society

JAI Guest Editors:
Sreeramesh Kalluri
Michael A. McGaw
Andrzej Neimitz

Journal of ASTM International Selected Technical Papers STP1526

Fatigue and Fracture Mechanics: 37th Volume

JAI Guest Editors:
Sreeramesh Kalluri
Michael A. McGaw
Andrzej Neimitz

ASTM International
100 Barr Harbor Drive
PO Box C700
West Conshohocken, PA 19428-2959

INTERNATIONAL
Standards Worldwide

Printed in the U.S.A.

ASTM Stock #: STP1526

Library of Congress Cataloging-in-Publication Data

ISBN: 978-0-8031-7512-9

ISSN: 1040-3094

Journal of ASTM International (JAI) Scope

The JAI is a multi-disciplinary forum to serve the international scientific and engineering community through the timely publication of the results of original research and critical review articles in the physical and life sciences and engineering technologies. These peer-reviewed papers cover diverse topics relevant to the science and research that establish the foundation for standards development within ASTM International.

Photocopy Rights

The Society is not responsible, as a body, for the statements and opinions expressed in this publication. ASTM International does not endorse any products represented in this publication.

Peer Review Policy

Each paper published in this volume was evaluated by two peer reviewers and at least one editor. The authors addressed all of the reviewers' comments to the satisfaction of both the technical editor(s) and the ASTM International Committee on Publications.

The quality of the papers in this publication reflects not only the obvious efforts of the authors and the technical editor(s), but also the work of the peer reviewers. In keeping with long-standing publication practices, ASTM International maintains the anonymity of the peer reviewers. The ASTM International Committee on Publications acknowledges with appreciation their dedication and contribution of time and effort on behalf of ASTM International.

Citation of Papers

When citing papers from this publication, the appropriate citation includes the paper authors, "paper title", J. ASTM Intl., volume and number, Paper doi, ASTM International, West Conshohocken, PA, Paper, year listed in the footnote of the paper. A citation is provided as a footnote on page one of each paper.

Printed in Baltimore, MD
February, 2011

Foreword

THIS COMPILATION OF THE *JOURNAL OF ASTM INTERNATIONAL (JAI)*, STP1526, on *Fatigue and Fracture Mechanics: 37th Volume*, contains only the papers published in JAI that were presented at the Ninth International ASTM/ESIS Symposium on Fatigue and Fracture Mechanics (37th National Symposium on Fatigue and Fracture Mechanics) held during May 20–22, 2009 in Vancouver, BC, Canada. The Symposium was jointly sponsored by ASTM International Committee E08 on Fatigue and Fracture and the European Structural Integrity Society (ESIS).

Dr. Sreeramesh Kalluri, Ohio Aerospace Institute, Brook Park, OH, USA, Dr. Michael A. McGaw, McGaw Technology, Fairview Park, OH, USA, and Prof. Andrzej Neimitz, Kielce University of Technology, Kielce, Poland co-chaired the Symposium and served as JAI Guest Editors.

Contents

Multiaxial Fatigue and Fracture

Residual Stress Effects on Fatigue and Fracture

Fatigue and Fracture Under Thermomechanical Conditions

Overview

This special technical publication (STP1526) is a compilation of papers presented by several authors at the Ninth International ASTM/ESIS Symposium on Fatigue and Fracture Mechanics (37th National Symposium on Fatigue and Fracture Mechanics) and published in the Journal of ASTM International (JAI) after successful peer reviews. The International Symposium was jointly sponsored by ASTM Committee E08 on Fatigue and Fracture and the European Structural Integrity Society. The Symposium was held during May 20–22, 2009 in Vancouver, British Columbia, Canada, in conjunction with the May 18–19, 2009 standards development meetings of ASTM Committee E08.

The opening Jerold L. Swedlow memorial lecture was delivered at the Symposium by Professor Dr.-Ing. Karl-Heinz Schwalbe on analytical models for fatigue crack propagation and fracture. The symposium focused on three major tracks of fatigue and fracture of structures and materials under 1) thermomechanical conditions, 2) multiaxial loading conditions, and 3) application of cohesive zone models to fracture problems. In addition, several papers were presented at the Symposium in the traditional areas of fatigue behavior, fracture mechanics and mechanisms, fatigue crack propagation, and effects of residual stresses on fatigue and fracture.

In the last decade, physics- and mechanics-based approaches gained prominence in assessing fatigue and fracture related design lives of structures used in aerospace, surface transportation, power generation, biomedical, and petroleum industries. Advanced structures in these industries utilize specially engineered materials with heterogeneous properties (for example, materials with coatings as thermal barriers or to resist wear and corrosion) that serve multiple purposes and require application of mechanics at both micro- and macro-scales to estimate the damages associated with fatigue and fracture. In particular, estimating the remaining lives of such structures under prototypical loading conditions poses significant challenges during the operation of those structures. Complexities associated with the challenges increase significantly when the advanced structures are subjected to loads in multiple directions and nonisothermal loading conditions. Papers presented at the Symposium and compiled in this STP (after publication in JAI) address some of these challenging areas.

A total of 33 papers, including the Jerold L. Swedlow memorial lecture paper, are compiled in this STP. The remaining 32 papers are grouped into the following categories: 1) elastic—plastic fracture mechanics and fracture mechanisms, 2) fatigue behavior and life estimation, 3) fatigue crack growth, 4) multiaxial fatigue and fracture, 5) residual stress effects on fatigue and fracture, 6) fatigue and fracture under thermomechanical conditions, and 7) application of fracture mechanics and cohesive zone models. It is our sincere hope that papers compiled in this STP advance the state-of-the-art in analytical methods and testing techniques for fatigue and fracture mechanics. In addition, some of the papers documented in this STP are expected to promote the development of fatigue and fracture related standards within ASTM Committee E08.

We would like to thank all the authors for their valuable contributions to the STP and all the reviewers for their thorough reviews, which substantially improved the quality of published papers. We are grateful to Ms. Dorothy Fitzpatrick and Ms. Hannah Sparks at ASTM International for their meticulous organization of the Symposium, Ms. Susan Reilly at ASTM International for her help with the STP, and Ms. Linda Boniello at the American Institute of Physics (AIP) for her excellent coordination of peer reviews for all the papers and publication of the manuscripts in JAI.

Dr. Sreeramesh Kalluri
Ohio Aerospace Institute
NASA Glenn Research Center
Brook Park, Ohio, USA
Symposium Co-Chairman and JAI Guest Editor

Dr. Michael A. McGaw
McGaw Technology, Inc.
Fairview Park, Ohio, USA
Symposium Co-Chairman and JAI Guest Editor

Prof. Andrzej Neimitz
Kielce University of Technology
Kielce, Poland
Symposium Co-Chairman and JAI Guest Editor

THE JEROLD L. SWEDLOW MEMORIAL LECTURE

Reprinted from JAI, Vol. 7, No. 8
doi:10.1520/JAI102713
Available online at www.astm.org/JAI

Karl-Heinz Schwalbe[1]

On the Beauty of Analytical Models for Fatigue Crack Propagation and Fracture—A Personal Historical Review

ABSTRACT: Starting from James Rice's classical work on cyclic plastic stresses and deformations in the plastic zone of a Mode III loaded crack, it will be shown that the crack tip opening displacement of a Mode I crack in a work hardening material can be written in analytical form. This result was then used to formulate the blunting line for *J*-integral testing and to estimate the fatigue crack propagation rate of a number of materials. In a similar manner—based on the strain distribution within the plastic zone of a work hardening material—the initiation of crack extension under static loading was estimated. The stress distribution ahead of a crack and the Ritchie, Knott. and Rice model were applied to the ductile-to-brittle transition of ferritic steels as well as the transition temperature shift due to neutron irradiation. Inspired by Fong Shih's contribution to the Electric Power Research Institute Handbook, a simple but straightforward method for expressing the δ_5 crack opening displacement as a crack driving force for fully plastic conditions was developed, finally ending up in a comprehensive assessment method for cracked components. The application to mismatched welded joints was demonstrated to be possible if the yield load for mismatch is available; this latter task was performed using both slip line theory and finite element (FE) analyses. Application examples of these models will be shown, and it will be seen that estimates using these models are in reasonable agreement with experimental results and FE analyses. Several elements of these models have made their way to international codes and standards.

Manuscript received September 2, 2009; accepted for publication June 21, 2010; published online August 2010.
[1] Consultant, Technische Universität Hamburg-Harburg; Ruhr-Universität Bochum; and Anemonenweg 32, 21360 Vögelsen (Lüneburg), Germany.

Cite as: Schwalbe, K.-H., "On the Beauty of Analytical Models for Fatigue Crack Propagation and Fracture—A Personal Historical Review," *J. ASTM Intl.*, Vol. 7, No. 8. doi:10.1520/JAI102713.

KEYWORDS: fatigue crack propagation, crack tip blunting, structural assessment, ductile-to-brittle transition, crack opening displacement, ductile tearing

Nomenclature

Roman Symbols

a = crack size
B = thickness of test piece or component
d = distance between inclusions
d_N = factor quantifying the effect of strain hardening on crack tip opening displacement; see Eq 31
E = Young's modulus
F = force
J = J-integral
K = stress intensity factor
K_c = fracture toughness in terms of stress intensity factor
K_i = stress intensity factor at initiation of ductile tearing
$K_{\max}$ = maximum stress intensity facture during cyclic loading
ΔK_{th} = threshold value of cyclic stress intensity factor
M = mismatch factor; see Eq 58
N = number of load cycles
N = strain hardening exponent as defined in Eq 4
n = strain hardening exponent used in the Ramberg-Osgood formulation of a stress-strain curve
r = radius from crack tip to point under consideration
R = stress ratio under cyclic loading
R = radius as defined in Figs. 2 and 3
R_m = fracture strength
$R_{p0.2}$ = yield strength defined at 0.2% plastic strain
s = load point displacement
u = crack displacement in x direction
W = width of test piece

Greek Symbols

γ = shear strain
δ = crack tip opening displacement
δ_{45} = crack tip opening displacement defined in Fig. 1(c)
δ_x = crack tip advance displacement defined in Fig. 1(a)
δ_5 = crack tip opening displacement defined in Fig. 28

δ_i = δ at initiation of ductile tearing
$\varepsilon_{0.2}$ = strain related to $R_{p0.2}$
ε_f = true fracture strain
ε_Y = yield strain
ν = Poisson constant
σ_{cl} = cleavage strength
σ_{yy} = stress in y-direction
τ = shear stress
ω = plastic zone size
Ω = size of intense plastic zone as defined in Fig. 15

Subscripts

Y = values at yield point
W = weld metal
B = base plate
M = mismatch

Acronyms

BM = base material
CTOD = crack tip opening displacement
ETM = Engineering Treatment Model
HAZ = heat affected zone
SZW = stretch zone width
WM = weld metal

Comment on the Term "Crack Tip Advance Displacement"

In this paper, three symbols will be seen for the motion of the crack tip in x-direction.

- u denotes the displacement of the crack tip in x-direction as determined based on Rice's model for crack loading mode III
- δ_x denotes the displacement—the crack tip advance displacement—after conversion of the solution for u to crack loading mode I; this symbols is also used for the experimentally observed crack tip advance displacement
- SZW: Stretch zone width, which is the observed crack tip advance displacement observed when ductile tearing has initiated; it is the critical value of δ_x

Introduction

Analytical formulations of mechanical problems are always very useful even in the era of ever faster growing computer capabilities. They are handy, allow quick estimates and sensitivity studies, show immediately how the various parameters affect the problem under consideration, and possess (usually) some elegance and beauty. Furthermore, in the early days of fracture mechanics, numerical techniques in the literature today were not available to the ordinary engineer. Last but not least, codes and standards use equations for testing and structural assessment purposes.

The present paper presents a historical technical review of the author's activities during his tenure at the University of Karlsruhe, at the German Aerospace Research Centre, and later with his research group at GKSS Research Centre performed in the area of practical fracture mechanics, combining experiments with engineering analytical models in order to obtain tools for quantitative representation of experimental findings in the form of easy to use equations. The term "analytical models" refers to mechanical models, which can be formulated in a pragmatic way with analytical expressions rather than rigorous analytical solutions of the mechanical problems under consideration. Later on, extensive finite element work was added, in many cases to extend the analytical formulas to regions not accessible without numerical contributions.

Being an experimentalist, the author tried to describe his experimental findings with easy to use formulas, and it all began in the late 1960s during the author's Ph.D. work on experimental fatigue crack propagation in aluminum. Fate led him to the early publications of Rice that gave rise to an attempt to finding an analytical expression for the rate of crack propagation. Further on, it was work emerging from creating the Electric Power Research Institute (EPRI) Handbook—mainly influenced by Shih—which motivated further developments, such as the structural assessment method Engineering Treatment Model (ETM).

In the following, some selected models and their applications will be described.

- Fatigue crack propagation
- Crack tip blunting
- Initiation of ductile tearing
- Ductile-to-brittle transition using the Ritchie–Knott–Rice model
- Crack tip opening displacement for finite width using the Dugdale model
- ETM for structural assessment

When reporting this work, a number of items will be included, which are now standard knowledge. It is believed that this is needed to show the flow of development of the various models. And also the readership will see that today, much would be done in a different way.

As this is a personal review, the vast majority of references are those of the author. However, full credit will be given to those authors in the field whose work was essential to the present paper.

Fatigue Crack Propagation

In this section, the derivation of two models for estimating the fatigue crack propagation rate will be summarized, and in spite of the different assumptions

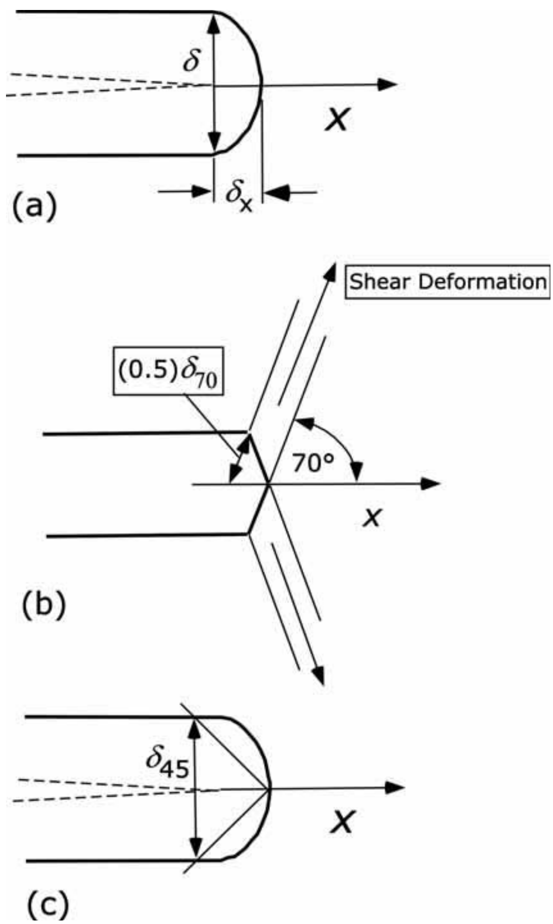

FIG. 1—*Three types of idealised plane strain crack tip deformation after, Ref 2:* (*a*) *Blunted crack tip;* (*b*) *shearing along slip lines inclined at 70° to the x-axis; and* (*c*) *definition of* δ_{45} *according to Refs 4 and 5.*

underlying these models, it will be seen that the results are quite close to each other.

Model A

The idea that the propagation of a crack under cyclic loading is a function of plastic deformations, represented by the cyclic crack tip opening displacement [1], was the starting point of the development of the fatigue crack propagation model. As no closed form solutions were available for crack opening Mode I cracks and work hardening materials, the model [2,3] makes a certain detour.

(a) First, let us look at the actual crack tip deformation for which plane strain conditions are assumed. Figure 1(*a*) shows a simplifying sketch

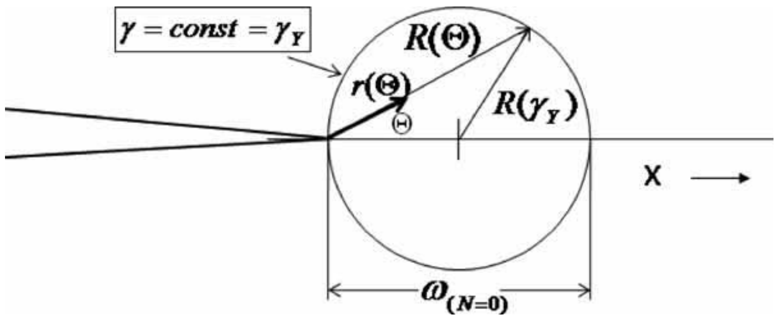

FIG. 2—*Plastic zone at a crack in a non-hardening material under Mode III loading* [*1*].

of a crack tip deformed under an applied Mode I load. (Fig. 1(*b*) and 1(*c*) will be referred to later). Due to the blunting process in Mode I loading, the crack opens by the amount δ and extends by the crack advance displacement, δ_x. The latter quantity will be determined because its cyclic value is set equal to the amount of crack propagation during each load cycle.

(b) Due to the coordinate system having its origin in the physical crack tip, the displacement at the very crack tip is zero for hardening materials, and the model determines the displacement at that distance ahead of the crack tip (with the origin of the coordinate system remaining stationary), x^*, which is equal to δ_x. In other words, the displacement of the material point at $x = x^*$ relative to the point $x = 0$ reduces its distance to the tip to zero. (Later finite element analyses, e.g., Refs 4 and 5, provided an elegant solution to this case: The near-tip contour of a crack was calculated, and the interception points between the contour and two straight lines including the angles of $\Theta = \pm 135°$ define a crack tip opening displacement, δ_{45}, which will be used later.)

(c) The actual analysis was performed for work hardening materials with a Mode III crack.

(d) Finally, the result was transferred to Mode I.

Although the analysis was carried out for a piece-wise power law hardening material, it is useful to recall the conditions of a crack in an elastic-perfectly plastic, i.e., non-hardening material under Mode III loading (Fig. 2). The shear strain distribution reads [6]

$$\gamma = \frac{\partial u}{r\,\partial \Theta} = \gamma_Y \frac{R(\Theta)}{r} = \gamma_Y \frac{\omega_{N=0} \cos \Theta}{r} \tag{1}$$

where:

$\gamma_Y = \tau_Y / G$ denotes the shear strain at incipient yielding,

u = crack tip shear displacement of one crack half, which is obtained by integrating Eq 1

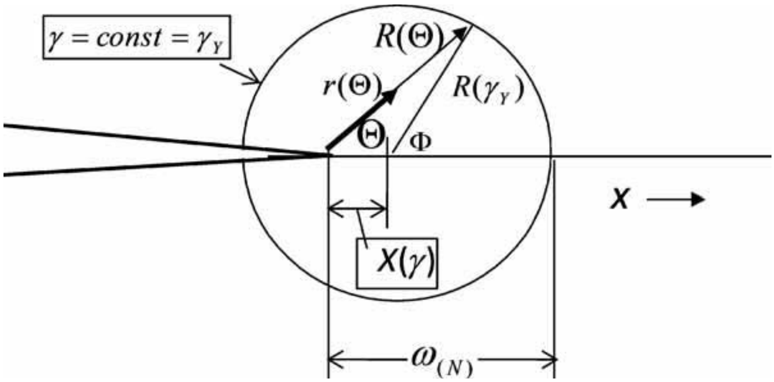

FIG. 3—*Plastic zone for a crack under Mode III loading, after Ref 1.*

$$u_{N=0} = \gamma_Y \int_0^{\pi/2} R(\Theta) d\Theta = \gamma_Y \omega_{N=0} \tag{2}$$

and

$$\omega_{N=0} = \frac{K^2}{\pi \tau_Y^{\,2}} \tag{3}$$

being the length of the plastic zone.

The formulation in Eq 2: Shear strain times length of plastic zone for the crack tip displacement will be used later; see, e.g., Eq 13.

Rice [1,7] studied the conditions within a plastic zone under Mode III loading for a piece-wise power law hardening material given by

$$\frac{\tau}{\tau_Y} = \left[\frac{\gamma}{\gamma_Y}\right]^N \tag{4}$$

for $\tau > \tau_Y$ and $0 < N < 1$ and derived exact solutions for stress and strain fields. The plastic zone for a work hardening material is shown in Fig. 3. The solutions for the *von Mises* equivalent shear strain within that zone was derived as

$$\frac{\gamma}{\gamma_Y} = \left[\frac{R(\Theta}{r(\Theta)}\right]^{1/(1+N)} \tag{5}$$

with

$$R(\Theta) = \omega_N \frac{1}{\sqrt{2}} [1 + N^2 + (1 - N^2)\cos(2\Phi)]^{-1/2} \tag{6a}$$

and

$$r(\Theta) = \omega_N \left[\frac{\gamma_Y}{\gamma} \right]^{1+N} \left[\left(\frac{1-N}{1+N} + \cos 2\Phi \right)^2 + \sin^2 2\Phi \right]^{1/2} \quad (6b)$$

being the radius where the shear strain γ is determined. The length of the plastic zone amounts to

$$\omega_N = \frac{K^2}{\pi \tau_Y{}^2 (1+N)}, \quad (7)$$

where the term $(1+N)$ stands for the effect of hardening on the size of the plastic zone.

For the equivalent shear stress distribution, the relation

$$\frac{\tau}{\tau_Y} = \left[\frac{R(\Theta)}{r(\Theta)} \right]^{N(1+N)} \quad (8)$$

holds.

In contrast to the non-hardening solution, the displacement for hardening materials is dependent on the radius r

$$du_N = \gamma \cdot dr \quad (9)$$

Model A uses these derivations and takes the displacement, u, at a point on the crack flanks within the plastic zone, and this point is located at [8]

$$r = R(\gamma) - X(\gamma) = \omega_N/2 - R(\gamma)\frac{1-N}{1+N} = \frac{K^2}{2\pi\tau_Y{}^2}\frac{2N}{1+N}\left(\frac{\gamma_Y}{\gamma}\right)^{1+N} \quad (10)$$

and the solution for the displacement reads

$$u_N = \frac{K^2 \gamma_Y}{\pi \tau_Y^2} \left[\frac{\gamma_Y}{\gamma} \right]^N \quad (11)$$

The assumption of the model developed in Refs 2 and 3 requires that the displacement has to be equal to the distance from the crack tip, i.e., $u_N = r$, and according to Eqs 10 and 11, at that point the shear strain is

$$\gamma = \frac{N}{1+N} \quad (12)$$

Finally, the displacement of one crack flank at $u_N = r$ is given by

$$u_{N,r} = \left[\gamma_Y \frac{(1+N)}{N^{N/(1+N)}} \right]^{1+N} \omega_N \quad (13)$$

which is hardening modified shear strain times length of the plastic zone; see Eq 2.

The transfer of Eq 13 to cyclic deformation can easily be done using Rice's [1] suggestion to double the material's yield strength to take account of the unloading process, ignoring the *Bauschinger* effect, i.e., the yield strength in compression after unloading from tension is identical to that of the original tensile load. This way the cyclic displacement is obtained

$$\Delta u_{N,r} = \left[2\gamma \frac{(1+N)}{N^{N/(1+N)}} \right]^{1+N} \Delta\omega \tag{14}$$

where $\Delta\omega = \omega/4$ represents the cyclic plastic zone size, with ω being the plastic zone under monotonic loading, more precisely, for the maximum load occurring during cyclic loading.

It should be noted that the derivations for cyclic loading were done for a stress ratio, R, equal to zero.

Turning now to crack opening Mode I, the solution just obtained for Mode III is formally converted using

$$\gamma_Y = \frac{\tau_Y}{G} = \frac{\sigma_Y(1+\nu)}{E} \tag{15}$$

and the general relationship between the crack tip opening displacements for Modes I and III (dropping the subscript N, which is now no longer needed)

$$\delta/2 \approx \frac{4(1-\nu)}{\pi} u = \frac{4(1-\nu)}{\pi} \left[\gamma_Y \frac{(1+N)}{N^{N/(1+N)}} \right]^{1+N} \omega \tag{16a}$$

where:

δ= displacement shown in Fig. 1(*a*) and

the stress-strain curve in tensile loading can be approximated by the power law

$$\frac{\sigma}{\sigma_Y} = \left[\frac{\varepsilon}{\varepsilon_Y} \right]^N \tag{16b}$$

for $\sigma > \sigma_Y$, where $0 < N < 1$.

For further processing, it has to be decided which extension of the plastic zone has to be taken. Since plane strain conditions are realistic for low-stress fatigue crack propagation, plane strain is assumed. Furthermore, as mentioned in the beginning, the crack advance displacement—i.e., the displacement in x-direction, δ_x (see Fig. 1(*a*))—is sought for, the plastic zone in x direction, i.e., for $\Theta = 0$ is relevant

$$\omega_0 = \frac{K^2}{\pi {\sigma_Y}^2 (1+N)} (1-2\nu)^2 \tag{17}$$

Using Eqs 11 and 12, the model assumption

$$r \equiv x = x^* \tag{18}$$

is fulfilled, and with Eq 16a, δ_x reads now

$$\delta_x = 2 \frac{4(1-\nu)(1-2\nu)^2}{\pi^2 \sigma_Y^2 (1+N)} \left[\frac{\sigma_Y(1+\nu)}{E} \frac{(1+N)}{N^{N/(1+N)}} \right]^{1+N} K^2. \tag{19}$$

Transferring Eq 19 to cyclic loading, an expression for the cyclic crack advance displacement and hence for the crack propagation per load cycle, da/dN is obtained

$$\Delta\delta_x = 2\frac{(1-\nu)(1-2\nu)^2}{\pi^2(1+N)\sigma_Y{}^2}\left[\frac{2\sigma_Y(1+\nu)}{E}\frac{(1+N)}{N^{N/(1+N)}}\right]^{1+N}\Delta K^2 \equiv da/dN$$
$$= \frac{0.022}{(1+N)\sigma_Y{}^2}\left[\frac{2\sigma_Y(1+\nu)}{E}\frac{(1+N)}{N^{N/(1+N)}}\right]^{1+N}\Delta K^2 \qquad (20)$$

with $\nu=0.3$ in the first term of the second line. This formulation is assumed to be valid for stress ratios $R \geq 0$.

It should be noted that the combined N-terms on the right hand side in the large bracket are close to unity for small values of N, which are typical of most metallic alloys. For higher values, e.g., $N \approx 0.3$, the N terms rise to about 1.5. (The original version derived in Ref 3 had an integral instead of these N terms, which was graphically evaluated. Its value varies only slightly with N, it lies always below unity. For $N \approx 0.3$, this integral is about 0.95. Thus, both variants are numerically close to each other.)

Model B

The second model [9] uses the strain distribution ahead of the crack tip following the formulation in Eq 5 and again assuming plane strain conditions

$$\frac{\varepsilon}{\varepsilon_Y} = \left[\frac{\omega_0}{x}\right]^{1/(1+N)} \qquad (21)$$

where ω_0 is given by Eq 17. (Interestingly, Rice and Rosengren made a similar proposal in Ref 10).

A fracture criterion was suggested, which assumes that the crack propagates per load cycle by the distance x^*, where ε exceeds the logarithmic fracture strain

$$\varepsilon_f = \ln\frac{1}{1-\psi} \quad \text{with} \quad \psi = (A_0 - A_f)/A_0 \qquad (22)$$

where:

A_0 denotes the cross section of the tensile specimen prior to deformation and

A_f= cross section after the test.

Conversion to cyclic load as above yields

$$da/dN = \frac{(1-2\nu)^2}{4\pi\sigma_Y{}^2(1+N)}\left[\frac{2\sigma_Y}{E\varepsilon_f}\right]^{1+N}\Delta K^2 \qquad (23)$$

It is somehow disturbing that these models end up with a ΔK power of 2, whereas experimental results are characterized with exponents that frequently greater than 2. This point will be discussed later.

Validation

For validating any model, the determination of the model parameters has to be clarified. In our case, the yield strength, the hardening exponent, N, and the fracture strain, ε_f, are relevant. The fracture strain in Eq 23 was already defined by Eq 22.

The yield strength is set equal to the standard value, $R_{p0.2}$, if a continuously hardening material is to be analyzed. In case of a material with a yield plateau, the lower yield strength, R_{el}, has to be taken.

For the determination of the hardening exponent, the method outlined in Fig. 4 has been suggested: The graphical determination uses a double logarithmic plot of the stress-strain curve, and an averaging straight line is drawn from the yield point to the fracture point as shown in Fig. 4(*a*). Materials exhibiting a yield plateau are treated using the method in Fig. 4(*b*): The yield point is defined at a strain $\varepsilon_{0.2} = \varepsilon(R_{\mathrm{el}})/E + 0.002$. Alternatively, the exponent may be calculated from

$$N = \frac{\lg R_m - \lg R_{p0.2}}{\lg \ln \frac{1}{1-\psi} - \lg \varepsilon_{0.2}} \tag{24}$$

For a quick estimate, the graph in Fig. 4(*c*) may be consulted.

Under the conditions of cyclic loading, the material within the plastic zone undergoes cyclic hardening or softening. Therefore, inserting data obtained from standard tensile tests may be questionable. Consequently, tensile tests were done on specimens made of cyclically pre-deformed pure aluminum and pure copper [2,9,11]. These materials exhibit cyclic hardening; the increase in yield strength comes along with a reduction in the hardening exponent. Thus, the determined values of yield strength and hardening exponent [2,3] were then used to check the effect on the estimated fatigue crack propagation by means of the same materials. Figure 5 shows that within the parameters studied, the effect is small. Furthermore, both models A and B provide results for copper very close to each other and can be regarded as equivalent. Therefore, the two models can be regarded as equivalent.

The diagram in Fig. 5 also compares the estimates with measured values. The aluminum experiments are very well matched by *Model A*. For copper, the two models over predict substantially the crack propagation rate at low rates because here the stress intensity factor was close to the threshold value. At the time of the analysis, no threshold values were available.

Apart from the exercise shown in Fig. 5, a number of experimental data from the literature were compared with Model A [12]. These data were obtained on a titanium alloy, pure aluminum (see Fig. 5), pure copper, again from Fig. 5, four aluminum alloys, and seven steels. The data extracted from the papers referred to in Ref 14 are represented in Fig. 6(*a*) by straight lines through the da/dN points. In the two estimation models the term E^{1+N} has a dominant influence and was therefore used to normalize the data of Fig. 6(*a*), and Fig. 6(*b*) shows that a certain compression of the data was achieved; at $\Delta K = 100\ \mathrm{kp/mm^{1.5}}$, the compression amounts to about an order of magnitude in crack rate. Thus, the obtained data band was then compared with the estimates

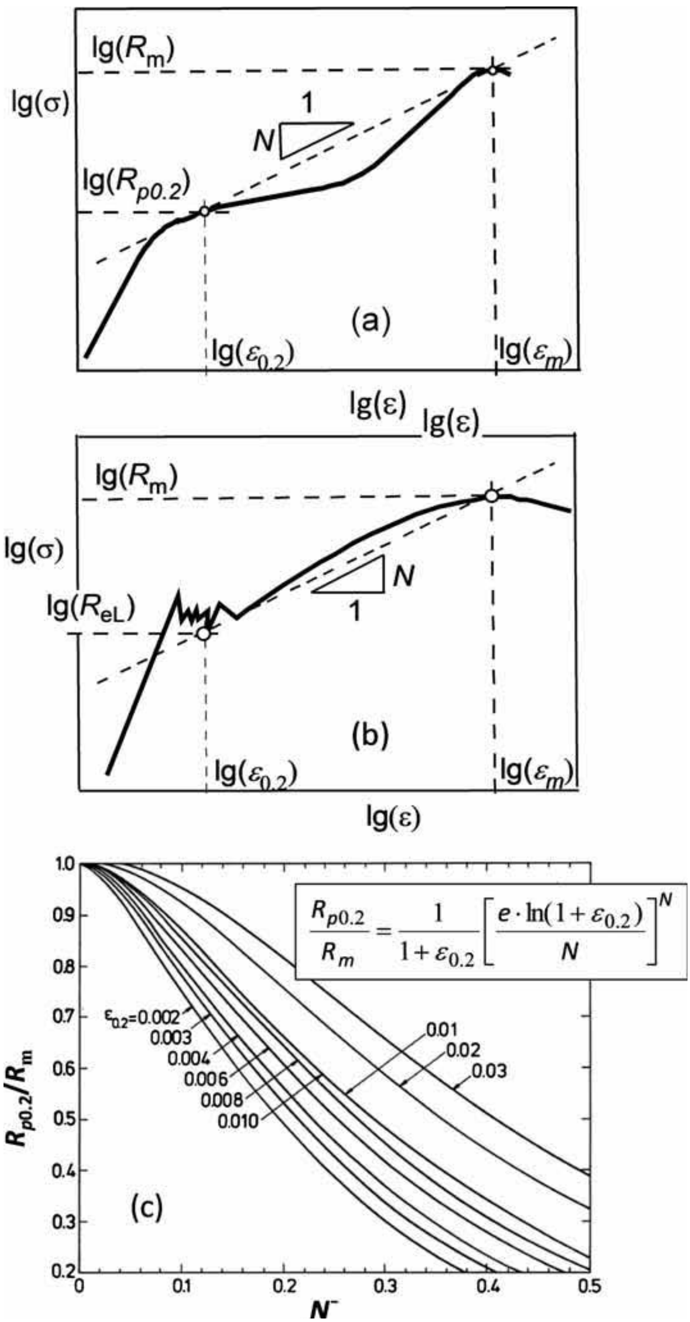

FIG. 4—*Determination of the strain hardening exponent, N: (a) For continuously hardening materials; (b) for materials with a yield plateau; and (c) estimation scheme.*

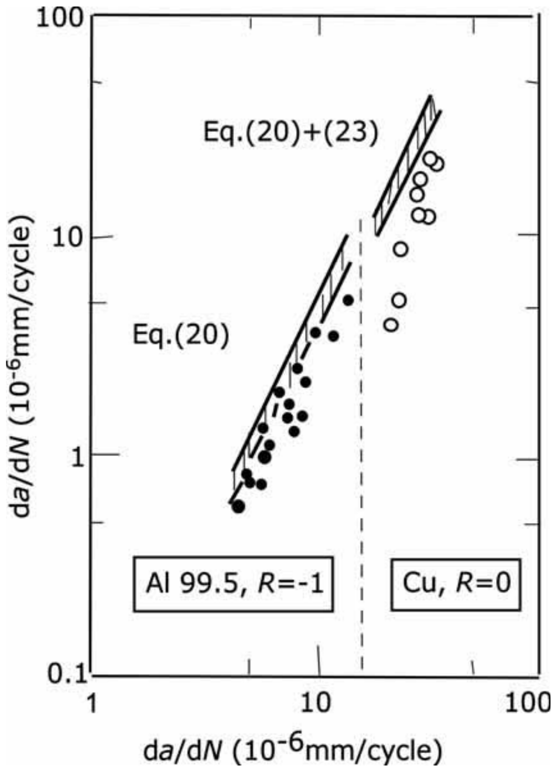

FIG. 5—*Fatigue crack propagation rates as measured on pure aluminum and pure copper in comparison with estimated values using Eqs 20 and 23* [2,9].

of Models A and B. Both experiments and estimates are represented in Fig. 7 again as data bands, and the diagrams show that a reasonable coincidence between the trends of experiments and estimates was obtained.

Now, in the light of experimental evidence showing a sigmoidal shape of a fatigue crack propagation curve, some fine tuning was needed. When ΔK approaches the threshold value, ΔK_{th}, the crack propagation rate vanishes, and when ΔK approaches the fracture condition at $K_{\max} = K_c$, the crack propagation rate approaches infinity. These effects can be accounted for by adjustments of equations like those representing the two models. For this purpose, a number of suggestions have been reported in the relevant literature.

In the studies reported here [11–15], the following modification was adopted:

$$da/dN = \frac{(1-2\nu)^2}{4\pi\sigma_Y^{\,2}(1+N)}\left[\frac{2\sigma_Y}{E\varepsilon_f}\right]^{1+N}(\Delta K - \Delta K_{\mathrm{th}})^2\frac{K_c}{K_c - K_{\max}} \tag{25}$$

where: ΔK_{th} denotes the threshold value for fatigue crack propagation,

K_c = fracture toughness, and

$K_{\max}$ = maximum stress intensity factor occurring during cyclic loading.

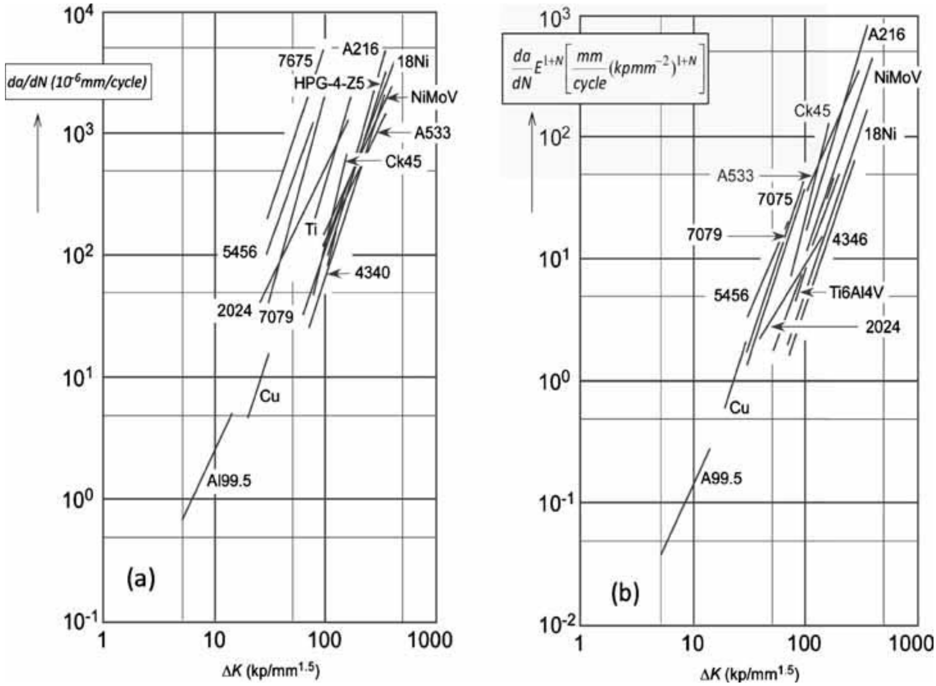

FIG. 6—*Fatigue propagation data* [*12*]: (*a*) *As taken from literature;* (*b*) *normalized with* E^{1+N}.

This modification is also able to approximately describe the effect of the stress ratio, R, on the crack propagation rate.

Equation 25 was applied to two experiments, of which the data for ΔK_{th} and K_c had been determined. These comprised an aluminum alloy and the heat affected zone (HAZ) of a welded high strength steel (Fig. 8). The properties needed for evaluating Eq 25 are compiled in Table 1.

It is seen in Fig. 8 that the modification of the models according to Eq 29 provides very good approximations. In particular the second power dependence of da/dN on ΔK has disappeared. The point is that pinning the equations down to the end points given by ΔK_{th} and K_c provides a quasi automatic rectification of the original model formulations; for the same reason, the effect of the stress ratio is well captured in Fig. 8(*b*). Further validations are reported in Ref 16 by means of the steel StE 960, a weld of this steel and other steels.

It is, however, interesting to note that the second power dependence of crack tip deformations remains when one looks at the fatigue striations on the fracture surface (Fig. 9). Furthermore, Eq 23 provides a very good estimate of the striation size. A detailed discussion of the question why the rate of crack propagation deviates from the expected ΔK^2 dependence was given in Ref 17: At low ΔK values, the crack front does propagate by a striation width every cycle, however, not along the whole length of the front. Therefore, the average amount of crack front propagation is less than the striation width. When ΔK

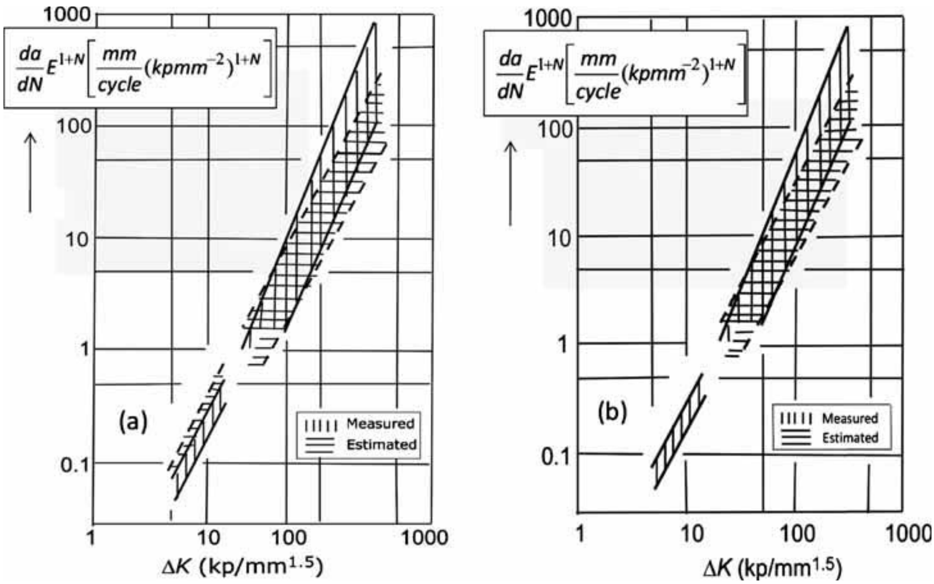

FIG. 7—*Experimental data from Fig. 6(a): (a) Compared with Model A; (b) compared with Model B.*

approaches the critical value for static failure, elements of static fracture take progressively over, thus leading to accelerated crack propagation. This item will be dealt with in the section Initiation of Ductile Tearing.

Crack Tip Blunting

In this section, the blunting process at the crack tip will again be looked at but now for static loading. Using Eq 13, the crack tip opening displacement was formulated as

$$\delta = 2\left[\gamma_Y \frac{(1+N)}{N^{N/(1+N)}}\right]^{1+N}\omega \tag{26}$$

and in the fashion proposed in Ref 18

$$\delta = d_N \frac{J}{\sigma_Y} = d_N \frac{K^2}{\sigma_Y E} \tag{27}$$

in order to compare it with the graphs in Ref 18. It should be noted that the definition of δ in Ref 18 is depicted in Fig. 1(*c*).

The model was derived from the sketch in Fig. 1(*b*) where the plastic deformation in plane strain is supposed to be concentrated along slip planes inclined under 70° to the x-axis. For this case, the length of the plastic zone, which has its maximum at $\Theta = 70°$, is

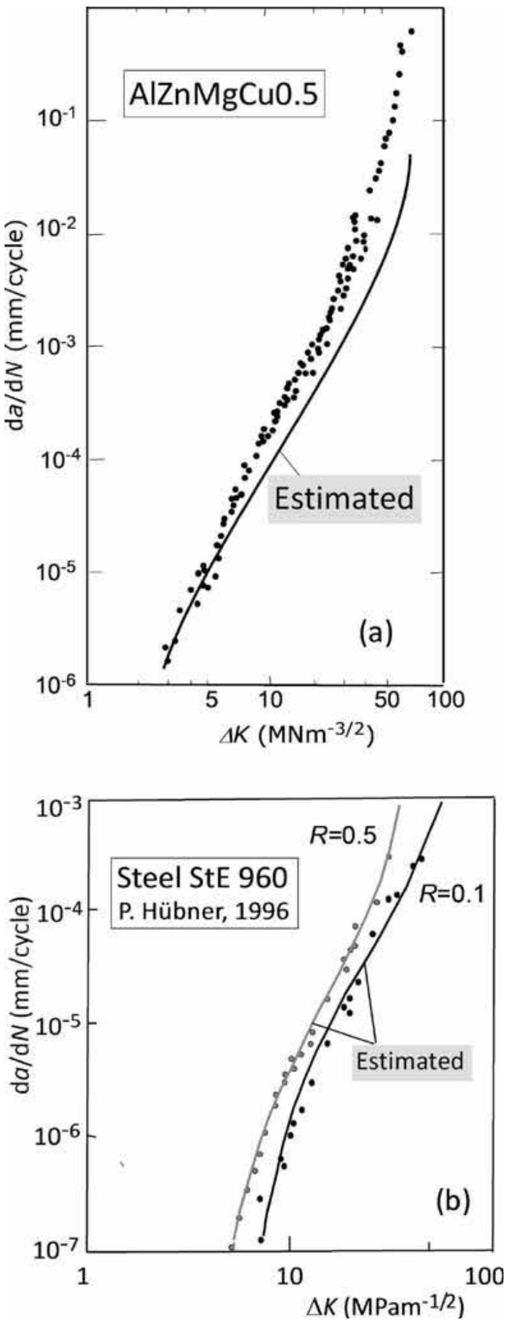

FIG. 8—*Experimental fatigue crack propagation rates compared with Eq 25:* (*a*) *AlZn-MgCu 0.5* [*14*]*;* (*b*) *HAZ in a weld of the steel StE 960, after Ref 16.*

TABLE 1—*Tensile properties of the materials shown in Fig. 8, from Refs 14 and 16. The tensile properties are in MPa, fracture mechanics properties in MPam$^{-1/2}$. (For StE 960, HAZ, the threshold values are for R=0.1 and 0.5, respectively.)*

Material	$R_{p0.2}$	R_m	E	ΔK_{th}	K_c	N	ε_f
AlZnMgCu0.5	397	481	68 700	1.9	54.5	0.114	0.32
StE 960, HAZ	787	1000	206 010	7.3,5.3	83.3	0.057	0.62

$$\omega_{70} = \frac{K^2}{\pi\sigma_Y{}^2(1+N)}\sin^2 70 \cos^2 35 = 0.59\frac{K^2}{\pi\sigma_Y^2(1+N)} \tag{28}$$

Using the expression for the plastic zone in Eq 28, the crack tip opening displacement for plane strain was derived as follows:

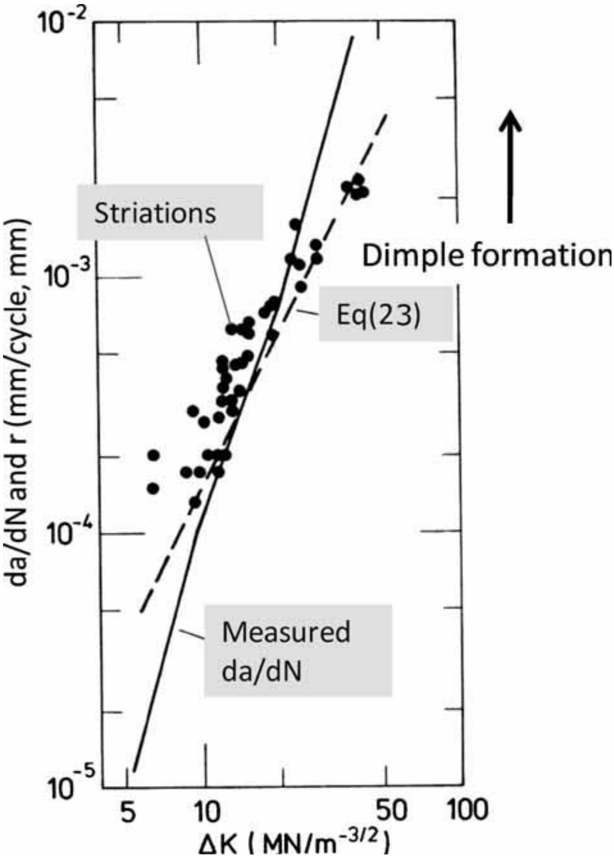

FIG. 9—*Striation size of AlZnMgCu 0.5 in comparison with the measured fatigue propagation rate and Eq 23 [14].*

$$\delta = \frac{0.38}{\sigma_Y{}^2(1+N)}\left[\frac{2}{\sqrt{3}}\frac{\sigma_Y(1+\nu)}{E}\frac{(1+N)}{N^{N/(1+N)}}\right]^{1+N} JE \tag{29}$$

For $\nu=0.3$ the non-hardening case yields $d_N=0.57$. Similarly, plane stress can be represented by inserting the plane stress plastic zone

$$\omega = \frac{K^2}{(1+N)\pi\sigma_Y{}^2} \tag{30}$$

hence

$$\delta = \frac{0.57}{\sigma_Y{}^2(1+N)}\left[\frac{2}{\sqrt{3}}\frac{\sigma_Y(1+\nu)}{E}\frac{(1+N)}{N^{N/(1+N)}}\right]^{1+N} JE \tag{31}$$

Again, for $\nu=0.3$ the non-hardening case yields $d_N=0.95$. Note that in the original work [3], the conversion from Mode III to Mode I was done as shown in Eq 16a, with the factor $4(1-\nu)/\pi$, which amounts to 0.89. In Ref 19, this factor was taken as 1.

The results displayed in Fig. 10 show that for plane stress there is excellent agreement with Shih's analysis based on the Hutchinson, Rice, Rosenfield (HRR) field (represented by the shaded area), whereas for vanishing hardening, there is some discrepancy in the plane strain results. In the present analysis, d_N approaches 0.6 for vanishing hardening, in comparison to 0.8 in Ref 18. The reason is, as discussed by Shih [18], for vanishing hardening, the HRR field loses its dominance. Finite element analyses carried out for the same problem shown in Ref 18 are in the range of 0.62–0.66.

In a comprehensive series of experiments on a number of materials [20,13,14,21,22], fatigue pre-cracked specimens were statically loaded to various levels, unloaded, and subsequently re-fatigued. In these experiments, the intermediate static loading created a step on the fracture surface, which was quantitatively evaluated by measurements in a scanning electron microscope (Figs. 11 and 12).

It was shown that the step sizes increased with an exponent greater than 2, the reason being that unloading resulted in reverse deformations, an effect that gradually disappears at higher K values because the small amounts of ductile tearing start to occur, plus the elastic unloading becomes progressively smaller compared to the total displacement, thus minimizing the unloading effects [20].

Other fatigue pre-cracked specimens were just loaded to final fracture, and the transition from fatigue to final fracture—known as the stretched zone—was also quantitatively analyzed in the scanning electron microscope. Figure 12 demonstrates how the height of such a step was measured; this height represents one half of the crack tip opening displacement at initiation of ductile tearing. The determination of the crack advance displacement, δ_x, is demonstrated in Fig. 13, which shows that due to the large variability of blunting, a number of measurements along the crack front are needed. This method has been introduced into the test methods EFAM GTP 02 [23], ESIS P2-92 [24], and ISO 12135:2002(E) [25]. It is needed for the determination of the values of the

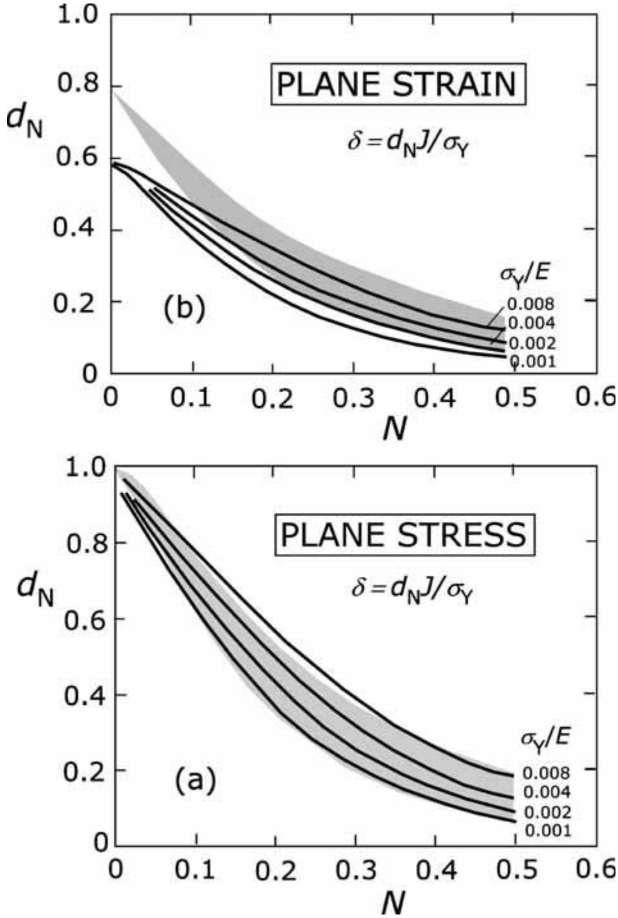

FIG. 10—*Graphical representation of Eqs 29 and 31 for plane strain and plane stress* [*19*]. *The shaded areas represent Shih's results of a HRR-field analysis* [*18*] *for the range of* $\sigma_Y/E = 0.001-0.008$.

crack resistance at initiation of ductile tearing, and it has been verified by a large round robin exercise on eight materials as part of a European project [22,26].

The resulting data were used for calibrating a theoretical blunting line, which is needed for determining initiation of ductile tearing [23–25]. The theoretical blunting line was determined using the crack tip blunting model depicted in Fig. 1(*a*), which assumes a near semicircular profile. Various finite element analyses, e.g., Refs 5, 10, 18, and 27, and slip line theory analyses [28] confirm this model. Since standard crack initiation tests are usually done on high constraint specimens crack tip blunting occurs under conditions characteristic of plane strain. Therefore, the experimental data were compared with

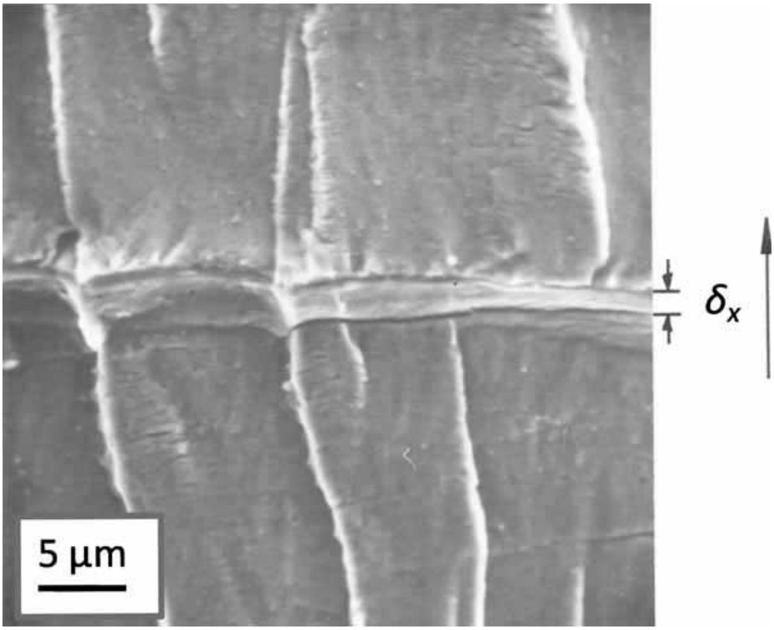

FIG. 11—*Step formed on the fracture surface of the aluminum alloy AlZnMgCu 0.5 during static loading, followed by subsequent fatigue loading* [*20*]. *The electron beam is perpendicular to the fracture surface for measuring the crack advance displacement,* δ_x.

Eq 28. It was found that the crack advance displacement follows the relationship

$$\delta_x = 0.4 d_N \frac{J}{\sigma_Y} \tag{32}$$

Here the factor 0.4 was taken as the average of all experimental results. As soon as ductile tearing has started, the development of blunting ceases, and the crack advance displacement attains the constant value SZW (see Fig. 13).

According to Fig. 14, the δ_x values of the six materials tested are well represented by Eq 32, which has become the blunting line as proposed in Ref 29. This blunting line is used in the test methods [23–25] for determining the values of the J-integral and crack tip opening displacement at 0.2 mm of ductile tearing, $J_{0.2/\mathrm{BL}}$ and $\delta_{0.2/\mathrm{BL}}$. (Note that the equation used in Ref 25 is a simplified version of Eq 32.)

Interestingly, the experimental findings formulated by Eq 32 are in line with findings using slip line theory: The sketch in Fig. 6 in Ref 7 shows a crack tip contour with a crack tip advance displacement close to Eq 32.

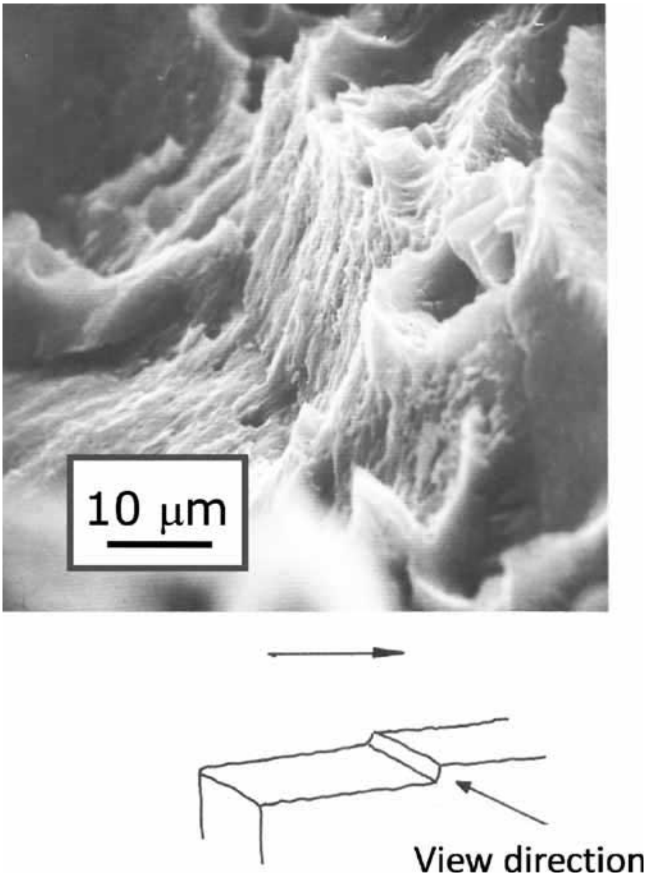

FIG. 12—*Step on the fracture surface of AlZnMgCu 0.5 prior to final fracture* [*20*]. *The specimen is oriented such that the electron beam is almost parallel to the step to enable measurement of the step height.*

Initiation of Ductile Tearing

Model A

Experiments with interrupted loading of fatigue cracked specimens of the aluminum alloy AlZnMgCu0.5 [20] revealed broken inclusions ahead of the crack front as nuclei for void formation (Fig. 15(*a*)). At a stress intensity factor of $K = 15.5\ \mathrm{MNm}^{-3/2}$, the first isolated events of this kind along the crack front were observed. At $K = 25\ \mathrm{MNm}^{-3/2}$, dimples were visible along the complete crack front; this represents the physical background of the determination of initiation of ductile tearing (J_i and δ_i) in the three test methods [23–25].

The slip line theory study [28] mentioned above was then used to estimate the onset of void formation [14,17,20]. This theory predicts a zone of intense

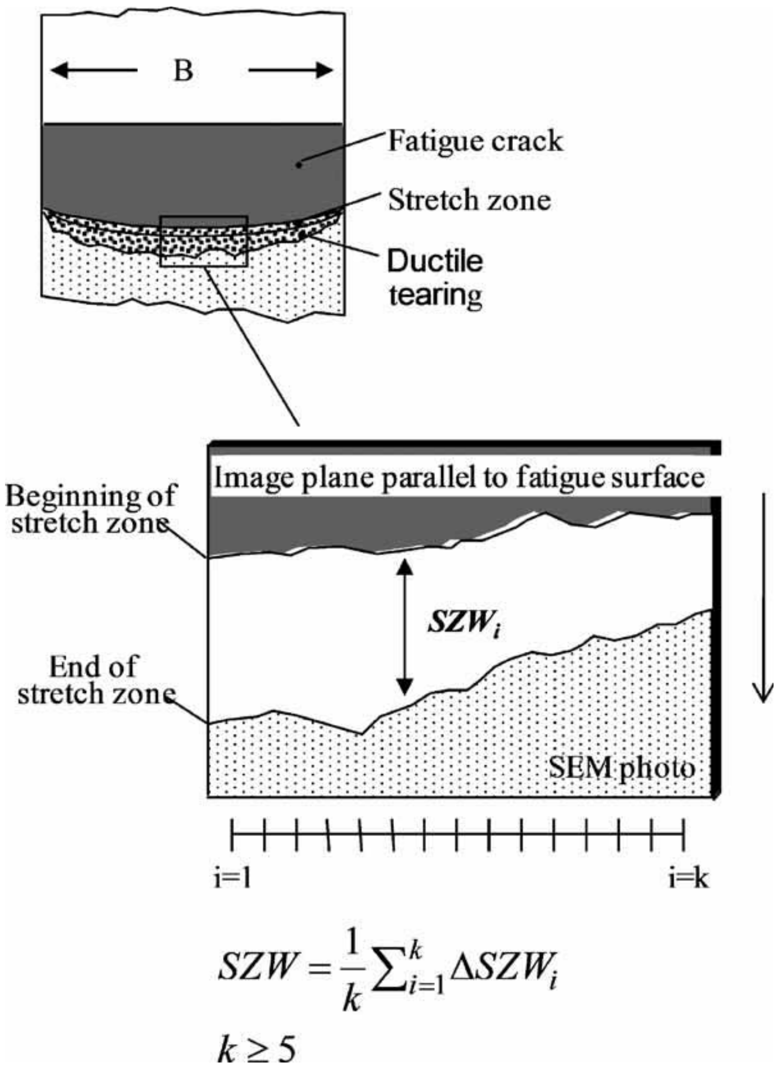

FIG. 13—*Principle of measurement of small amounts of crack extension in the scanning electron microscope, after Refs 21–25.*

plastic deformation ahead of a crack tip, Ω, whose length is about two times the crack tip opening displacement. It is assumed that the first stage of local void formation occurs when this plastic zone reaches an inclusion (Fig. 15(*b*)). With d for the inclusion spacing, one may set

$$\Omega \approx 2\delta = d \tag{33}$$

In this context, the spacing of the inclusions, d, is a critical parameter since the inclusion spacing is not constant; in this material it was found to vary between

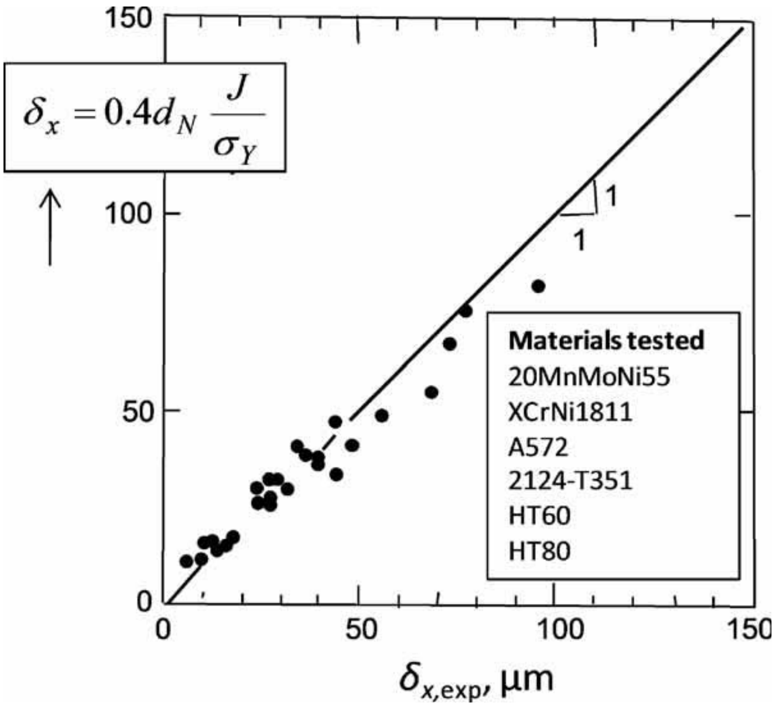

FIG. 14—*SZW width data obtained on six materials in comparison with the blunting line in Eq 32, after Ref 21.*

5 and 15 μm. Hence, the analysis was done with the observed minimum and maximum values of d, and with Eqs 31 and 35, a range of $12.5 < K < 22$ MNm$^{-3/2}$ was estimated [30], which is very close to the observed values, first line in Table 2. The upper bound values of the stress intensity factors (25 MNm$^{-3/2}$ from the experiments and 22 MNm$^{-3/2}$) from the estimate correspond to the fracture resistance at crack initiation, K_i.

Coming back to the Rice and Johnson analysis [28], using a void growth model, these authors estimate δ_i as a function of the distance of a pre-existing void from the crack tip, d, normalized by the original void radius, R_0. The graph in Fig. 16 implies that for relatively large initial voids—realized in an engineering alloy by large second phase particles (as were present in the aluminum alloy investigated here) the crack tip opening displacement at initiation of ductile tearing is roughly equal to the void's distance from the crack tip

$$\delta_i \approx d \tag{34}$$

Summarizing the experimental and analytical findings, the following statements can be made.

The model in Fig. 15(*b*) knows only one value of d. However, as Fig. 15(*c*) shows, the particles present in an alloy have varying distances from the crack tip. Those particles that are closest to the crack front feel the edge of the zone

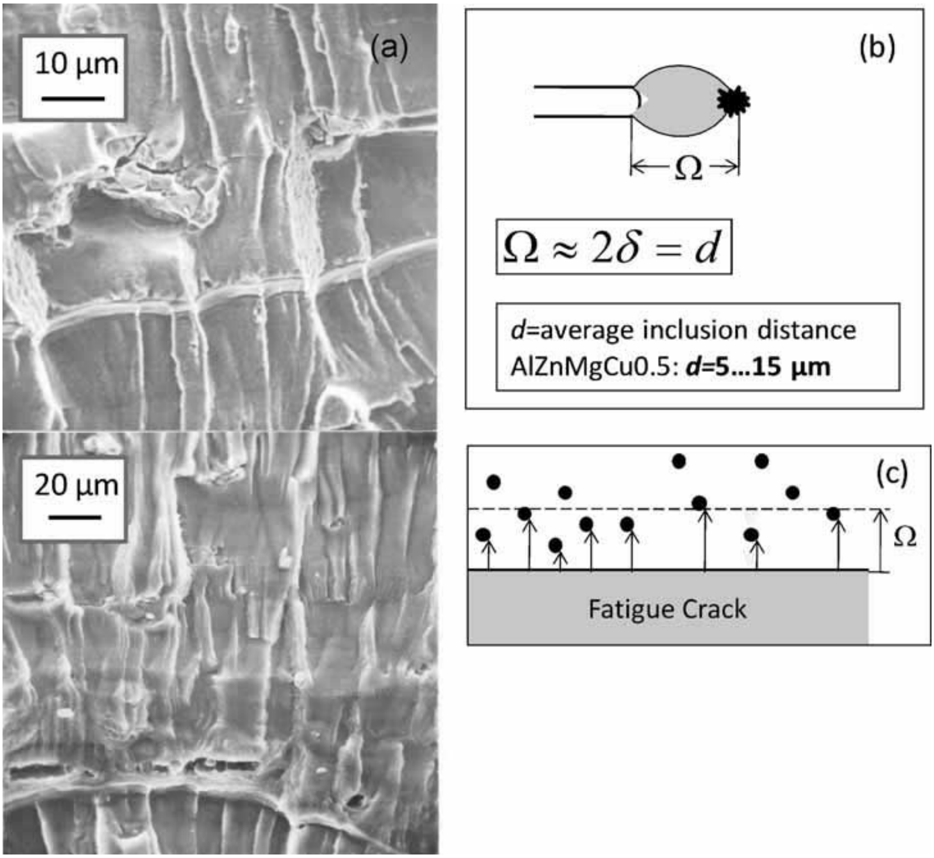

FIG. 15—(*a*) *Occurrence of broken inclusions ahead of the crack front during static loading, AlZnMgCu0.5* [*20*]. (*b*) *Rice–Johnson model for intense plastic zone* [*28*] *applied to void formation.* (*c*) *Application of the model to a distribution of inclusions.*

characterized by Ω under low applied loads, as represented by the lower *K*-values in Table 2. At this stage, only isolated dimples can be detected along the crack front. A fully developed dimple structure along the crack front is achieved when Ω reaches also those particles having the largest distance from the crack front and no other particle between them and the crack front. This

TABLE 2—*Observed and, by Eq 33, estimated first occurrence of dimples on the fracture surfaces created by static and cyclic loadings* [*20,31*].

	Observed	Estimated
Static	$12.5<K<22$ MNm$^{-3/2}$	$15.5<K<25$ MNm$^{-3/2}$
Cyclic, $R=0$	$14<K_{max<}19$ MNm$^{-3/2}$	$15.5<K<25$ MNm$^{-3/2}$
Cyclic, $R=0.5$	$K_{max}\sim 20$ MNm$^{-3/2}$	$15.5<K<25$ MNm$^{-3/2}$

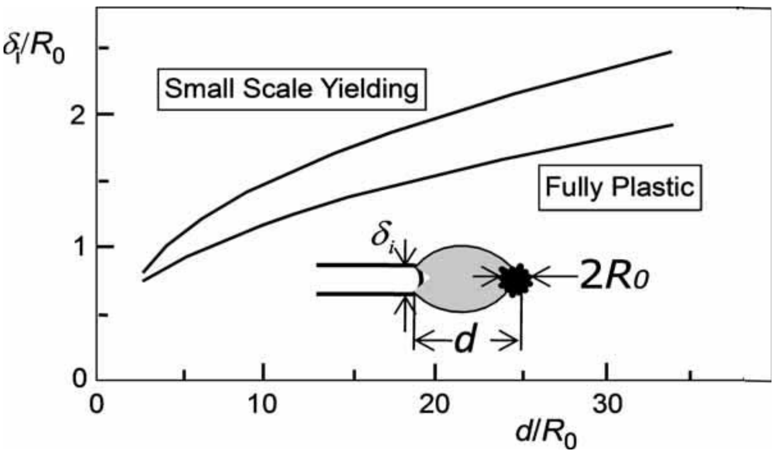

FIG. 16—*Crack tip opening displacement at initiation of ductile tearing, after Ref 28.*

condition can be quantified by Eq 34. Thus, the quantity d is a micro structural length parameter relevant to the fracture condition defined by initiation of ductile tearing.

The high ends of the curves shown in the graph seem realistic for materials with small particles requiring much larger deformations for void formation, growth, and coalescence.

It may be interesting to note that at high propagation rates of a fatigue crack, first dimples occur at K_{max} values that are similar to the K values of static fracture [14,31]; obviously, dimple formation on fatigue fracture surfaces is K_{max} controlled as one may have expected (see Fig. 17 and Table 2).

Model B

Similar to *Model C* for fatigue crack propagation, the initiation of ductile tearing was estimated under the assumption that the crack tip propagates by that distance over which the fracture strain is reached [32] (Fig. 18(*a*)). A combination of Eq 21, representing the strain distribution, with Eq 17 and representing the plastic zone size, ω_0, can be solved for the stress intensity factor at initiation of ductile tearing and yields

$$K_i = \frac{\sigma_Y}{(1-2\nu)(1+N)}\sqrt{d\pi(1+N)\left[\frac{\varepsilon_f E}{\sigma_Y}\frac{\sqrt{3}}{2}\right]^{1+N}} \tag{35}$$

In this case, the fracture strain was measured on Hill specimens [33] (see Fig. 18(*b*)). This specimen represents a stress state close to plane strain since strains in width direction of the specimen are suppressed. Figure 18(*c*) depicts a somewhat different way of determining the fracture strain, which will be used later in Model B. Equation 35 was applied to a high strength steel, which was given a number of different heat treatments (quench and temper) to achieve a range of strengths. An important finding is that the various heat treatments had ef-

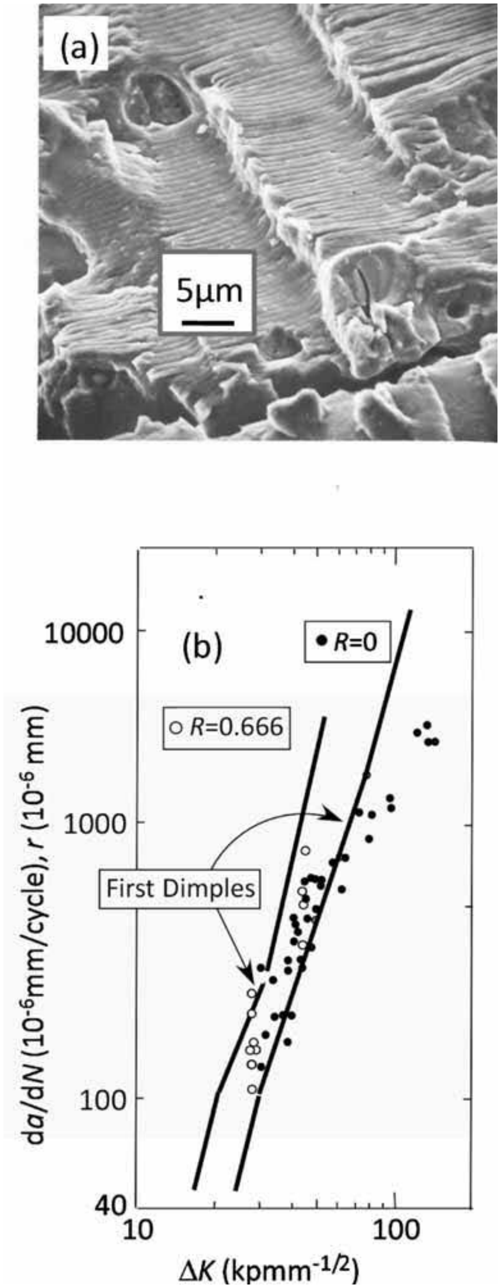

FIG. 17—*Occurrence of broken inclusions on the fatigue fracture surface of AlZn-MgCu0.5:* (*a*) *Fractograph showing striations and initial dimples* [*30*]*;* (*b*) *striations observed for two R ratios and related crack propagation rates* [*17*].

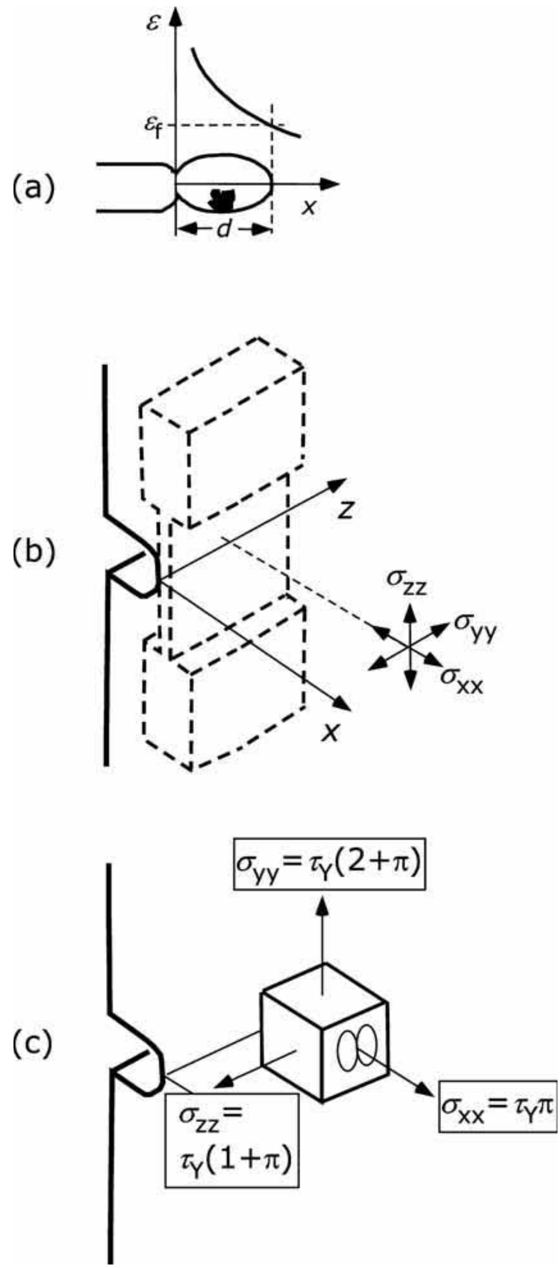

FIG. 18—*Model B for the determination of initiation of ductile tearing:* (*a*) *Strain distribution near crack tip;* (*b*) *Hill specimen at crack tip and stress state near crack tip;* (*c*) *McClintocks void growth model, after Ref 34.*

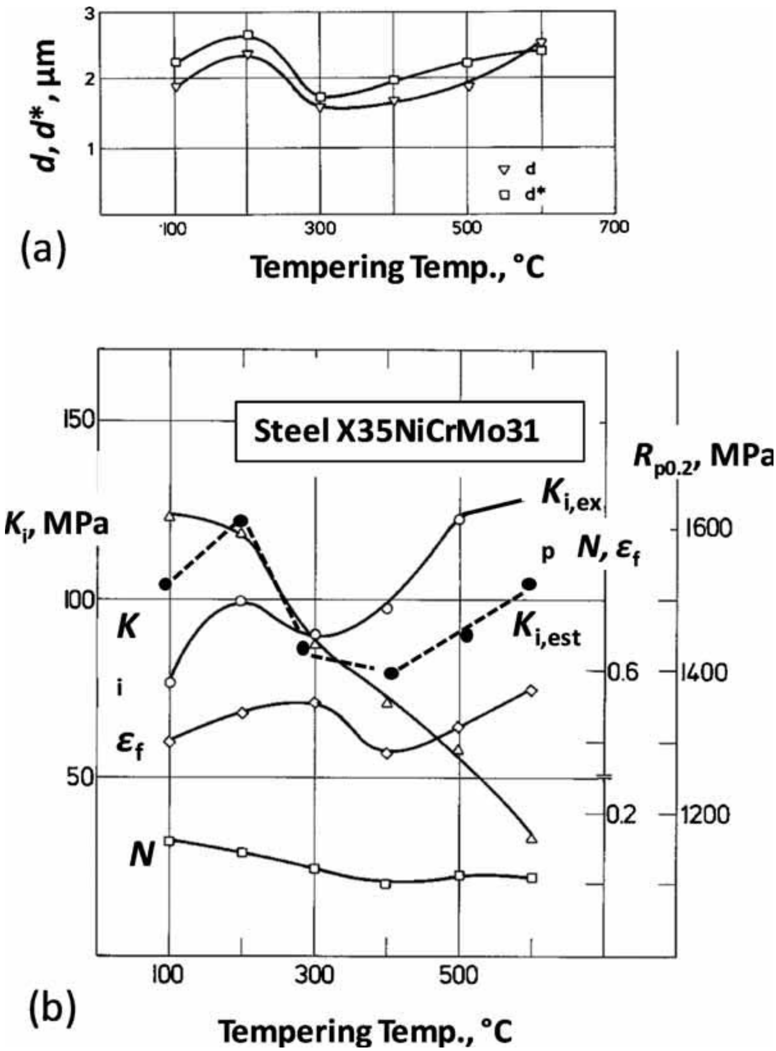

FIG. 19—*Fracture experiments on a high strength steel in various tempering conditions [32]: (a) Fractographic features; (b) tensile data and measured and estimated fracture toughness.*

fects on all material parameters entering Eq 35. This is demonstrated in Fig. 19(*a*) and 19(*b*) and shows that it is impossible to vary just a single material property by thermo mechanical treatment. The micro structural size, d, to be used for evaluating Eq 35 was set equal to the average dimple size on the fracture surface. It may be interesting to note that for the material investigated, the dimple size correlates very well with micro structural features observed on metallographic sections. These features can be identified as the sizes, d^*, of martensite plates at low tempering temperatures and ferrite zones between carbide stringers at high tempering temperatures (Fig. 19(*a*)).

As already mentioned, for the determination of the fracture strain, the Hill specimen, a plane strain tensile specimen described in Ref 35 was used. It is supposed that this specimen configuration models the conditions of the matrix bridge between the actual crack tip and the void forming at an inclusion (Fig. 18(*b*)). The experimental data that were available to be compared with Eq 35 were K_i values determined using the electrical potential method. The validation in Fig. 19(*b*) shows that the estimation procedure models the general trend of the experimental toughness values with tempering temperature reasonably well.

What the diagrams in Fig. 19 also demonstrate is that in contrast to common belief, the fracture toughness does not steadily increase with decreasing yield strength. Furthermore, the way fracture toughness varies with tempering temperature is almost the same as that of the dimple size. Inspecting Eq 35 shows also that seemingly toughness increases roughly with the square root of yield strength. However, this shows also that focusing on a single parameter is not the way to make judgments on the basis of just one parameter. It is the combined effect of all essential parameters that matters.

Model C

This model is different from Model B in that it determines the fracture strain in the neighborhood of the crack tip in a slightly different manner [34,35]. Two regions ahead of the crack tip are considered. The region at the very tip of the crack where the fracture strain is again supposed to be represented by the fracture strain, ε_f, as measured on the Hill specimen, and the region at that spot where the first void ahead of the crack is formed, i.e., at a distance from the crack tip equal to the average inclusion distance, d, being represented by the average dimple diameter.

The fracture strain thus determined was then converted to the stress state shown in Fig. 18(*c*) using McClintock's growth model for cylindrical voids [34]. At the location of the inclusion, the constraint conditions are more severe than at the crack tip; they are supposed to be given by Fig. 18(*c*) taken from Ref 34. There the fracture strain, ε_f^*, is determined using the growth model for cylindrical voids, Fig. 18(*c*), which is given by

$$\varepsilon_f^* = \frac{\ln Q}{\dfrac{\sqrt{3}}{2(1-N)}\sinh\left[\dfrac{\sqrt{3}(1-N)}{2}\dfrac{\sigma_a+\sigma_b}{\bar{\sigma}}\right]+\dfrac{3}{4}\dfrac{\sigma_a-\sigma_b}{\bar{\sigma}}} \tag{36}$$

The growth function, Q, was calibrated by using the fracture strain from a tensile specimen with a known stress state at fracture. Then ε_f^* can be calculated for the stress state at the void nucleation site, which is certainly a bit simplistic from the contemporary point of view; however, it is useful for the present model. Finally, from both fracture strains, the average value was taken as the relevant quantity for the failure condition.

The validation of this model was performed on four alloys (one of which is the material investigated for Model B above) and is depicted in Fig. 20. It is

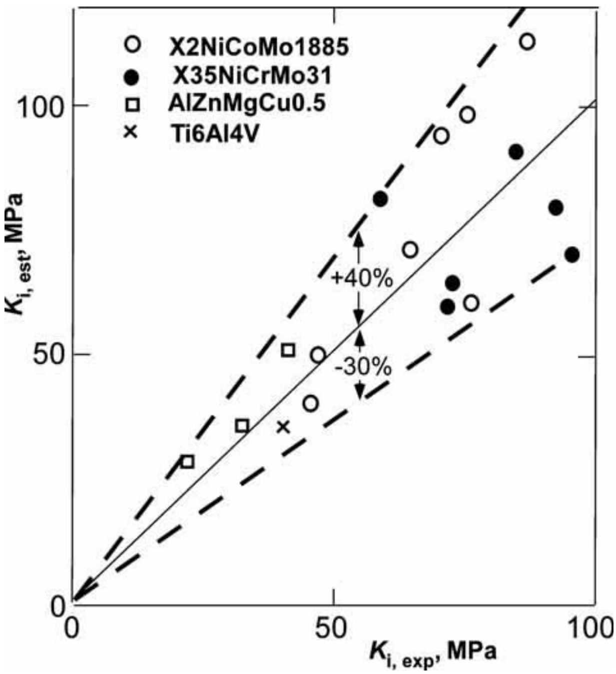

FIG. 20—*Experimental and, with Eqs 35 and 36, estimated initiation values of K for ductile tearing, data from Ref 36.*

clear that such models can never be used to "predict" fracture toughness; however, they show how the various basic material parameters affect the result, and what could be done to improve the toughness of a specific material. Material data for validation of the three models can be found in Ref 36.

It should be noted that the above derivations done in the framework of linear elastic fracture mechanics could be easily converted to elastic-plastic parameters such as the J-integral. However, at the time of the investigations reported here, there were no appropriate experiments available to the author.

Ductile-to-Brittle Transition of Steel Using the Ritchie–Knott–Rice Model

Brittle fracture of steels exhibits large scatter and needs statistical treatment using weakest link models. However, statistics do not tell what is going on in the material, i.e., the physical mechanisms of the origin of scatter remain unclear. This motivated a research program dedicated to clarify qualitatively and quantitatively the micro mechanisms responsible for the immense variability of fracture toughness of ferritic steels, which is observed when cleavage fracture is the cause of failure.

The pressure vessel steel DIN 20 MnMoNi 55 (similar to the steel ASTM A533B) was mechanically tested by means of side-grooved $C(T)$, tensile and

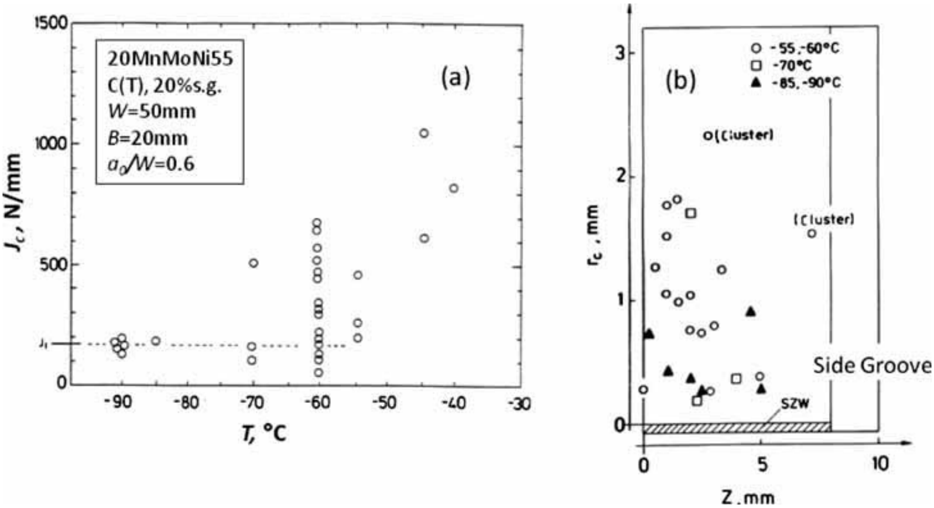

FIG. 21—*Scatter of fracture toughness of the pressure vessel steel DIN 20 MnMoNi 55 in the ductile-to-brittle transition regime* [37,38]: (*a*) *Fracture toughness at various temperatures;* (*b*) *Brittle fracture initiation points on the fracture surfaces of side-grooved* (*CT*) *specimens.*

blunt notched bend bar specimens [37–39]. Tests were performed on neutron-irradiated and non-irradiated specimens. Fracture toughness in terms of J_c is shown in Fig. 21(*a*) for the non-irradiated material.

Since cleavage fracture is known to originate at a single point in the material, intensive fractography was carried out, which revealed indeed the existence of isolated locations on the fracture surface from where cleavage fracture spread all over the fracture surface. These locations observed on 25 $C(T)$ specimens tested between −55 and −90°C are compiled in Fig. 21(*b*). It is clearly seen that their positions, r_c, ahead of the crack front vary within a wide range, which indicates that also several amounts of ductile tearing are needed to reach the weak points further ahead of the crack front. This in turn shows that the J integral at fracture varies also. From this the conclusion was drawn that the distribution of weak micro structural features leading to cleavage fracture contributes to the observed scatter in fracture toughness.

In addition to this qualitative part of the work, an attempt was made to quantify the transition from ductile tearing to cleavage fracture. The governing basic material properties are the yield strength and the cleavage strength of the steel [40]. The former property was measured on tensile specimens; the latter property was determined on blunt notched bend bars, with the aid of a finite element stress analysis from the literature. The Ritchie, Knott, and Rice model [41] states that cleavage fracture occurs when the local stress equals or exceeds a material specific critical stress—the cleavage stress, σ_{cl}—over a critical distance, which is supposed to be twice the grain size. Our experiments do not speak against the possibility that a material may have an average value characteristic of that material, but the actual failure of an individual specimen is

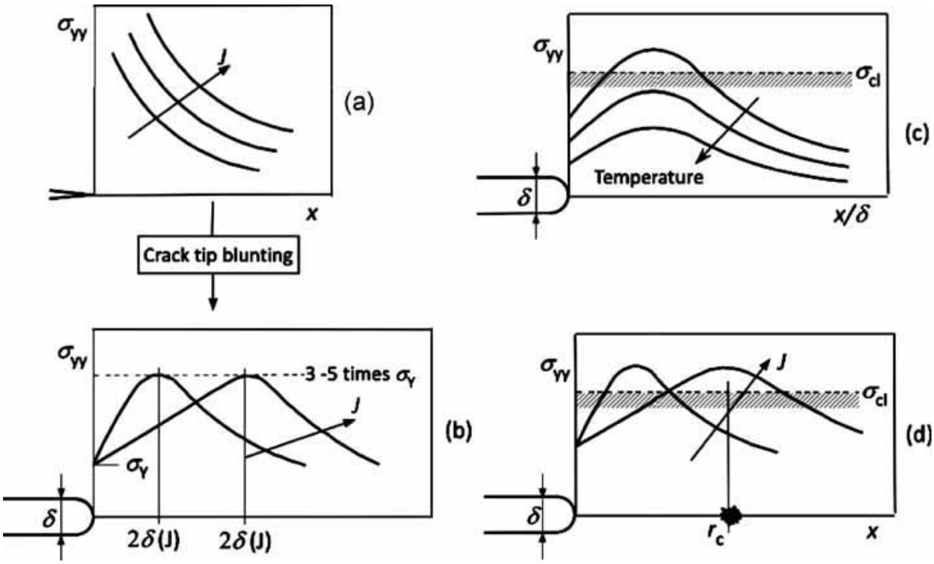

FIG. 22—*Distribution of the normal stress σ_{yy} at a blunted crack: (a) Initially sharp crack; (b) effect of applied load; (c) effect of temperature; (d) combined effect of applied load and cleavage stress, stress peak reaching a weak spot at $x = r_c$.*

controlled by the distance of the weak spot nearest to the crack front.

It has been shown [4,27,28] that at a blunted crack tip, the stress does not approach infinity; from the tip, it starts with a finite value, the magnitude of which increases with the yield strength and increases with decreasing distance from the tip until it reaches a maximum. The magnitude of this maximum is an increasing function of the yield strength and the hardening exponent (Fig. 22). The location of the stress peak ahead of the crack tip is roughly two times the crack tip opening displacement [27].

The present model says that with decreasing temperature the stress peak eventually reaches the material's cleavage stress, σ_{cl} (Fig. 22(*c*)). This is the moment when cleavage failure may occur, i.e., the transition from ductile-to-brittle failure is likely to occur. This is a necessary but not a sufficient condition; the stress peak moving along the x-axis with increasing applied load has to hit a weak spot that may cause cleavage (Fig. 22(*d*)). This latter effect is one of the origins of scatter. Further scatter is caused by variability of cleavage strength and yield strength. With the values of σ_Y and σ_{cl}, as well as the stress distribution, the onset of cleavage fracture can be estimated. The stress distribution was taken from Ref 42, which is an analytical formulation of the result from a finite element study [43]

$$\frac{\sigma_{yy}}{\sigma_Y} = \frac{0.3}{\dfrac{x}{(K/\sigma_Y)^2} + 0.1}\left[\frac{0.051}{(1+N)\left(\dfrac{K}{\sigma_Y}\right)^2}\right]^{N/(1+N)} \tag{37}$$

The cleavage strength as obtained from the bend bars at −196 °C exhibits substantial variability (Fig. 23(*a*)). The lowest value indicates the lowest probability of the stress peak to hit the cleavage value. Figure 23(*b*) shows similar measurements at higher temperatures, indicating that the cleavage stress decreases with temperature. Since Eq 37 does not exhibit a peak, the stress at $x = 2\delta$ was taken as the peak stress, according to Refs 4, 27, and 28. Figure 24 provides support of the validity of the model: It shows the location of the cleavage initiation points along with the location of the stress peak at fracture. Both compare reasonably well.

With the distributions of r_c and σ_{cl}, a range of ductile-to-brittle transition temperatures was estimated using Eq 37. The compilation of experimental toughness data and estimated transition temperatures in Fig. 25 shows the increase in transition temperature with neutron irradiation and that the model applied provides a realistic picture of the transition behavior.

It may be interesting to note that the Ritchie–Knott–Rice model has been recently extended for variable in-plane constraint [45].

Crack Tip Opening Displacement for Finite Width Using the Dugdale Model

The Dugdale model for the plastic zone size [46], modified in Ref 47, provides a closed form solution for a linear array of cracks, which was supposed to represent a crack in a finite width sheet [48]

$$\omega = a\left[\frac{2W}{\pi a}\arcsin\left(\sin\frac{\pi a}{2W}\sec\frac{\pi\sigma}{2\sigma_Y}\right) - 1\right] \tag{38}$$

where:

σ = applied stress perpendicular to the crack and

W = designates the half width of a sheet containing a central crack (Fig. 26).

Starting from the relationship

$$\delta = \frac{8\sigma_Y a}{\pi E}\ln\left[\frac{\omega}{a} + 1\right] \tag{39}$$

for the infinitely wide sheet, it is assumed that this relationship holds also for finite width, an expression for the crack tip opening displacement was derived as follows [48]:

$$\delta = \frac{8\sigma_Y a}{\pi E}\ln\left[\frac{2W}{\pi a}\arcsin\left(\sin\frac{\pi a}{2W}\sec\frac{\pi\sigma}{2\sigma_Y}\right)\right] \tag{40}$$

From the plot of the normalized δ in Fig. 26, two effects are obvious: The finite width has a large effect on the crack tip opening displacement, and δ takes finite values when the condition of net section yielding is approached, unlike

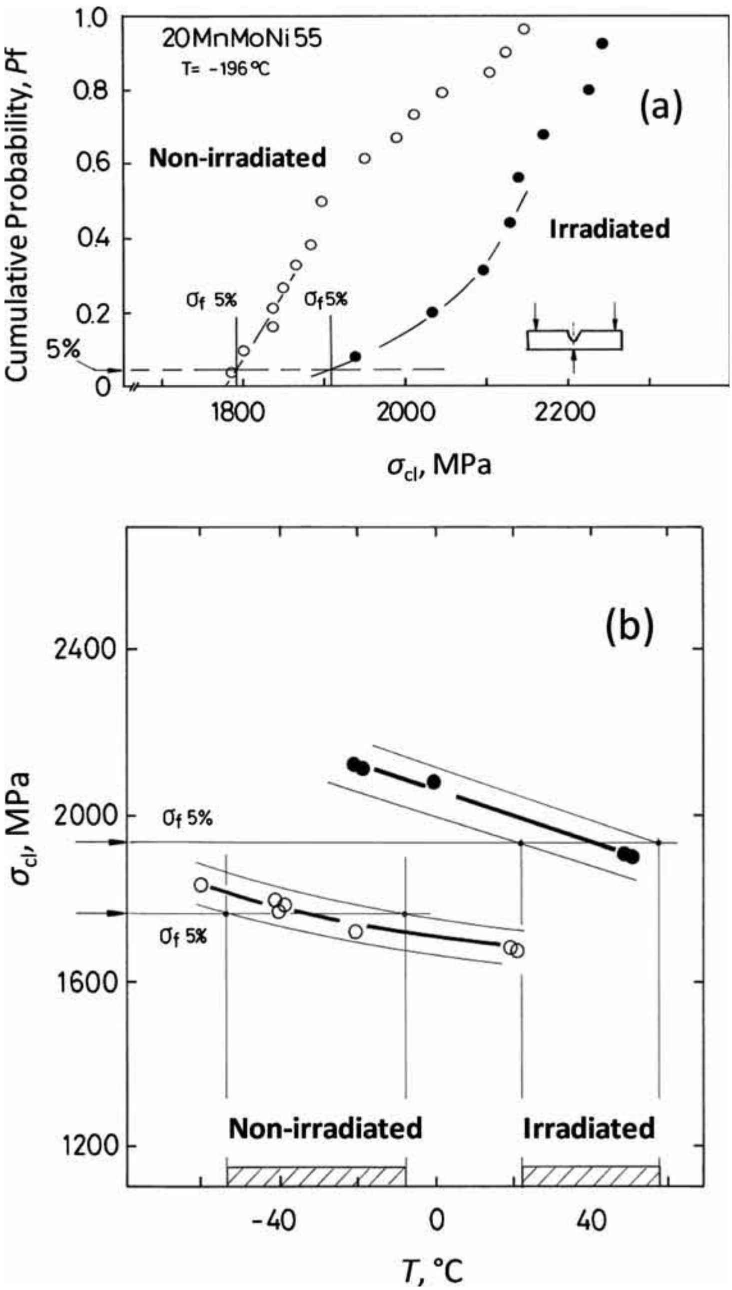

FIG. 23—*Cleavage fracture stress of the steel 20MnMoNi55 in unirradiated and neutron irradiated conditions* [*37–39*]*:* (*a*) *Determined at −196°C, showing scatter;* (*b*) *at higher temperatures.*

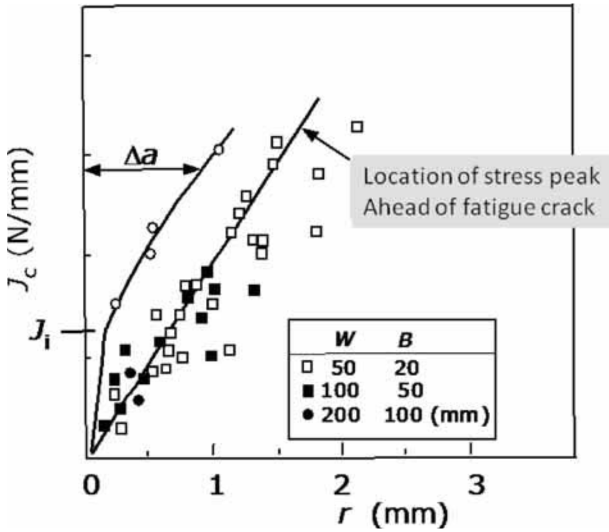

FIG. 24—*Experimentally determined locations,* r_c*, of the cleavage initiation points compared with the location of the stress peak* [*44*].

the case of infinite width. These results are in excellent agreement with a finite element analysis in Ref 49.

Equation 40 can be used for the assessment of structural components loaded in tension if a critical crack tip opening displacement (CTOD) for the material is available; solving for the applied stress, the critical condition in

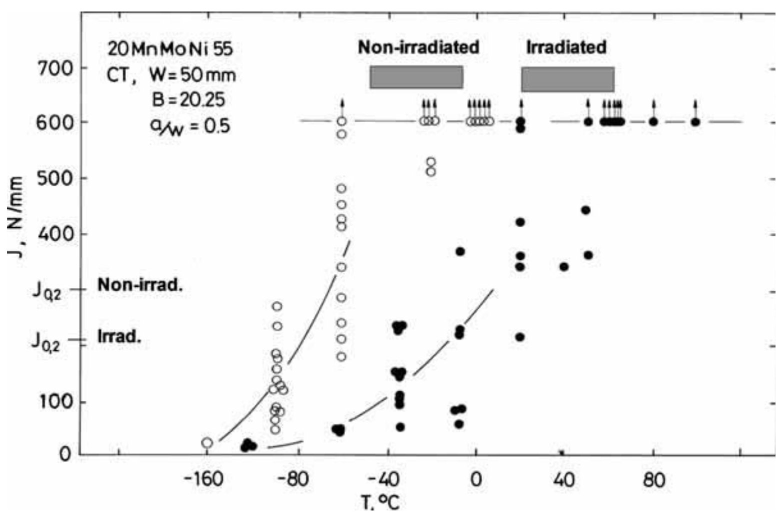

FIG. 25—*Cleavage ductile-to-brittle transition of the steel 20MnMoNi55, experimental and estimated* (*gray bars*) [*44*]. *The arrows indicate failure by ductile tearing.*

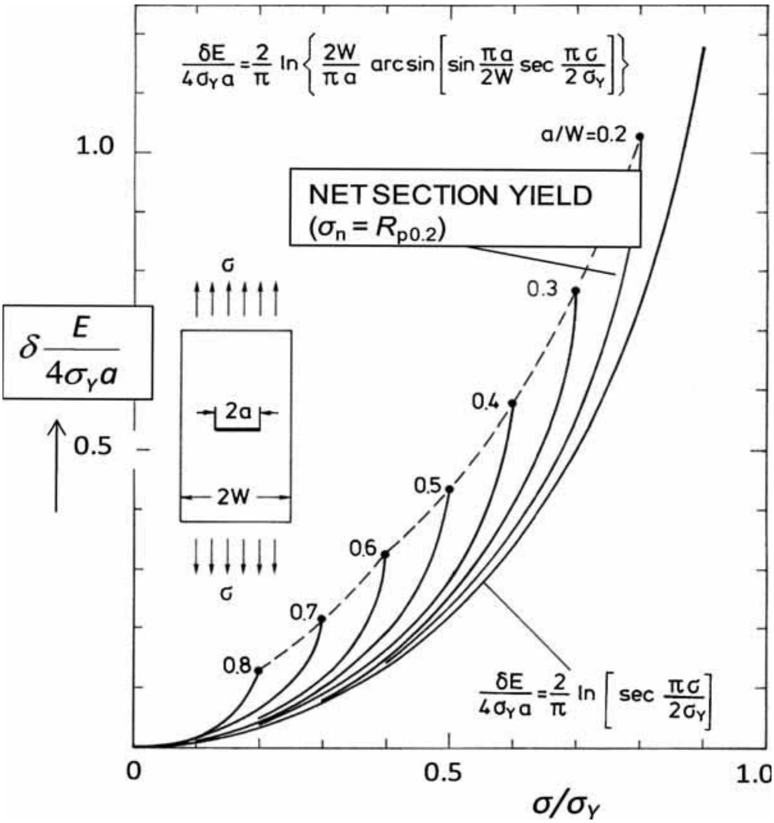

FIG. 26—*Equation 40 plotted in a normalized manner as a function of the degree of plasticity* [*48*].

terms of the critical stress, σ_c, of the component can be easily estimated. As no such configuration was available for validation, experimental results obtained on $M(T)$ specimens of different sizes and made from thin sheet of four aluminum alloys were tentatively used. The problem was that the critical stress, in these cases equal to the maximum stress of the individual specimens, varies with width and a/W due to the R-curve effect. For a first trial, the maximum stress at $a/W=0.6$ for each specimen width was taken as representative of the given width, and the critical situations for other a/W ratios were predicted. Work hardening was accounted for by using $\sigma_Y=0.5(R_{p0.2}+R_m)$ as a flow stress. Figure 27(a) depicts an example, and Fig. 27(b) compiles all results.

Figure 27(a) shows also that for vanishing crack size, the failure stress approaches the flow stress. This property of the model shows that it works from linear elastic to fully plastic (i.e., net section yielding) behavior with a single parameter, namely, a critical crack tip opening displacement, provided an expression for the net section yield load is available; not every case can be dealt with using the term σ/σ_Y as a measure of the degree of plasticity. In more

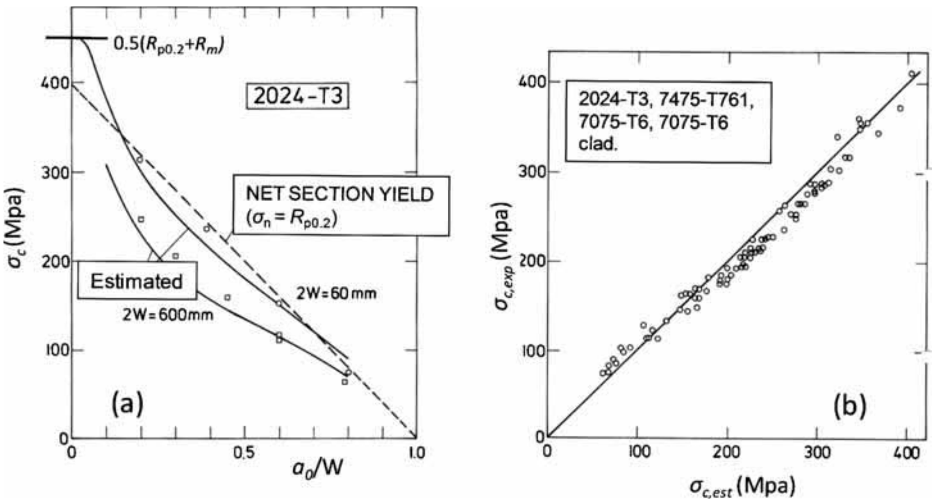

FIG. 27—*Prediction of critical conditions of M(t) specimens using Eq 40 solved for the applied stress* [48]*:* (*a*) *Aluminum alloy 2024-T3;* (*b*) *compilation of data obtained on 2024-T3, 7475-T761, 7075-T6, and 7075-T6 clads.*

general cases, this has to be replaced with F/F_Y (where F_Y is the net section yield load) as is done in the ETM (see next chapter).

In a similar manner, a solution for the crack mouth opening displacement (CMOD) in middle cracked tensile structures was derived [50]. A relationship of the resulting equation with the crack tip opening displacement was also developed so that the CTOD can be easily determined in experiments by measuring the CMOD.

Engineering Treatment Model for Structural Assessment

The stress intensity factor of an actual component can be determined using the infinite width solution times a dimensionless calibration function

$$K = \sigma\sqrt{\pi a}Y(a/W)$$

where:

$Y(a/W)$ = function of geometry only, that is to say of the geometry of component, crack (e.g., straight or curved), and loading configuration (e.g., bending and tension). However, in the case of global elastic-plastic behavior, a single parameter characterization of stresses and strains near a crack tip is no longer possible. In that case, the elastic-plastic deformation properties of the material used enters the problem of determining a crack driving force parameter, such as the J-integral and the crack tip opening displacement. This fact requires extensive finite element work for even a limited number of cases; such a task was performed for creating the Elastic Plastic Handbook by EPRI [51]. Therefore, a simple to use formulation for J and CTOD was sought for.

The basic idea was found in Ref 51 where the J-integral is formulated as the sum of elastic and plastic contributions, where the latter uses the term

$$J_{\mathrm{pl}} = \alpha g_1\left[\frac{a}{W},n\right]\left[\frac{F}{F_Y}\right]^{(1+n)/n} \tag{41}$$

In this equation, α is the material coefficient, n the hardening exponent in the Ramberg–Osgood formulation of the stress-strain curve, and g_1 is a function accounting for effects of geometry and strain hardening on J. It was the last term in Eq 41 that was going to be used in the formulation of the ETM.

The ETM is a comprehensive method for assessing structural integrity under static loading conditions [52,53]. It provides detailed guidance on performing structural assessment using one of the following four modules:

- Basic module
- Strain module
- Notch module
- Module for load point displacement

This document provides detailed formulations for determining the crack driving force in terms of the crack opening displacement, δ_5, and the J-integral. Guidance is also given for assessing acceptable or critical conditions. Several appendices provide further information needed for assessing structural integrity.

A separate document for mismatched welded joints has also been developed (see below).

Basic Module

The basic idea is to directly transfer the material's stress-strain curve given by Eq 16b to the yielding net section of a component as a basis for estimating J or δ in the fully plastic regime. The principle is depicted in Fig. 28. The idea is that under contained yielding conditions, either J or δ, the latter here in terms of δ_5 [54] can be formulated using the plasticity corrected expressions of linear elastic fracture mechanics up to net section yielding, which is characterized by the net section yield load, F_Y; beyond F_Y, the values of J or δ_5 are extrapolated into the fully plastic regime using the strain hardening exponent of the material. The formulations for the regime below yield load are taken from standard solutions for small scale yielding$F < F_Y$:

$$J = (K_{\mathrm{eff}})^2/E \tag{42a}$$

$$\delta_5 = \frac{\beta_1}{E}K + \frac{(K_{\mathrm{eff}})^2}{mE\sigma_Y}\left[\frac{F}{F_Y}\right] \tag{42b}$$

where

$$K_{\mathrm{eff}} = \sigma\sqrt{\pi a_{\mathrm{eff}}}Y(a_{\mathrm{eff}}W) \tag{42c}$$

is the stress intensity factor calculated with the effective crack size

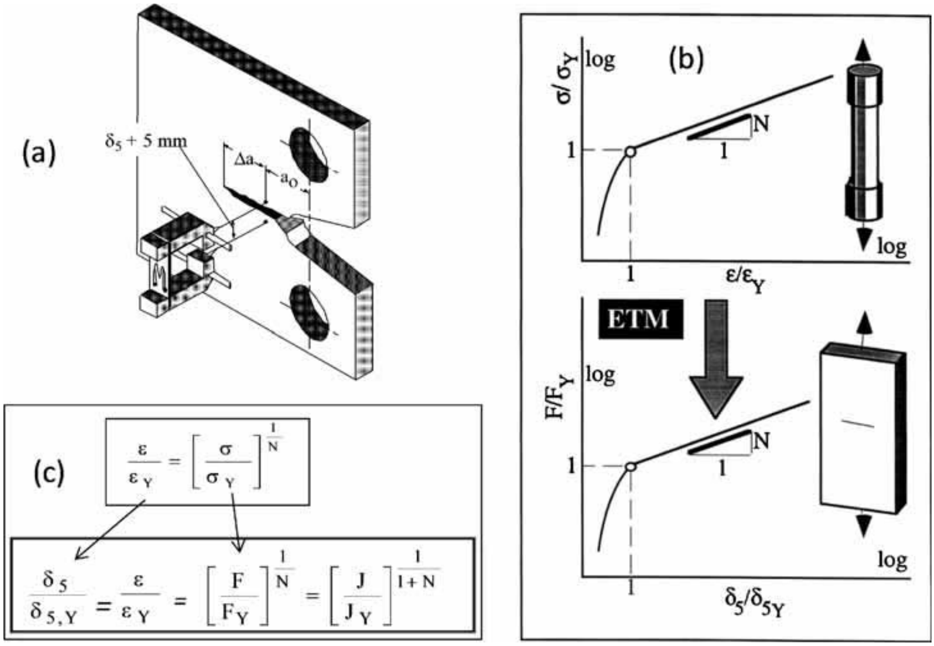

FIG. 28—*Schematic of the ETM* [52]*:* (*a*) *The* δ_5 *crack opening parameter;* (*b*) *stress-strain curve and load-*δ_5 *curve of a component; and* (*c*) *formulation of the ETM.*

$$a_{\mathrm{eff}} = a + \frac{1}{2\pi}\left[\frac{K}{\sigma_Y}\right]^2 \tag{42d}$$

The first term in Eq 42b represents the sum of the elastic strains picked up by the clip gage with its 5 mm gage length; m equals unity for plane stress and 2 for plane strain

$$\beta_1 = 2.41 \text{ and } m = 1 \text{ for plane stress} \tag{42e}$$

$$\beta_1 = 2.09 \text{ and } m = 2 \text{ for plane strain} \tag{42f}$$

The bracket term in Eq 42b was added to obtain a smoother transition from the yield point to the fully plastic region. The values that occur just at yield load, J_Y and $\delta_{5,Y}$, respectively, are evaluated using Eqs 42 and are then taken as hinge points for extrapolation (see Fig. 28(*b*)). Hence, for fully plastic conditions, the two parameters can be related to the applied force or strain as$F > F_Y$:

$$\frac{\delta_5}{\delta_{5,Y}} = \frac{\varepsilon}{\varepsilon_Y} = \left[\frac{F}{F_Y}\right]^{1/N} = \left[\frac{J}{J_Y}\right]^{1/(1+N)} \tag{43}$$

This equation is regarded as a master curve since it provides a size and geometry independent formulation of J and δ_5, which is due to the normalization by the yield values of the parameters in the equation. The second term, referring to

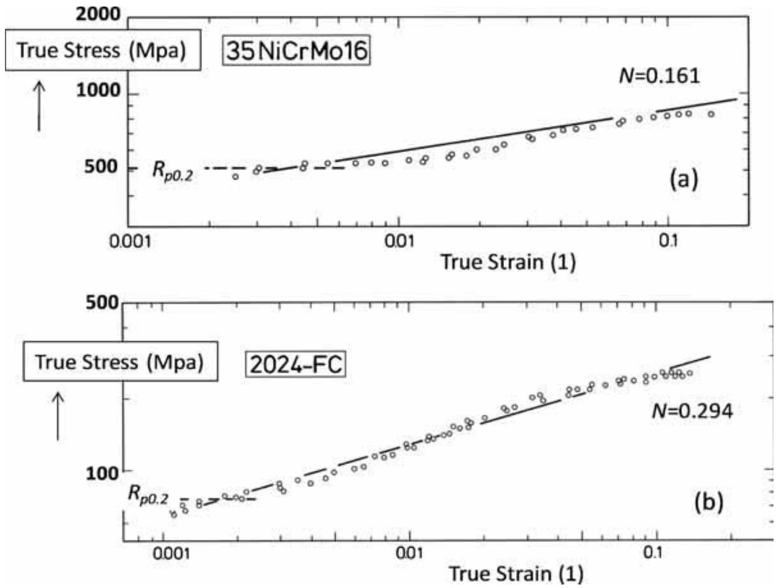

FIG. 29—*Stress-strain curves of* (*a*) *alloy steel 35NiCrMo16 and* (*b*) *Al alloy 20245-FC* [*50*].

the applied strain, can be related to J or δ_5 in the form of Eq 43 for short cracks only, i.e., for $a/W < 0.15$.

It should be noted that in plane stress the driving force is higher than in plane strain. This means that using the plane stress formulations, the user is on the safe side.

It should be noted that the δ_5 parameter is the preferred parameter for R-curve measurements since δ_5 is an ideal parameter for correlating relatively large amounts of crack extension. Therefore, this parameter has recently been included in three test standards, ASTM E2472-06 [55], ISO 22889:2007(E) [56], and ESIS P3-09 [57].

The ETM was first introduced by a GKSS report [50], whereas the GKSS report [52] contains the method in complete procedural form. In addition, the core modules are described in detail in various international publications, e.g., Refs 55 and 58–62.

The input information required for applying the ETM is the same as in other assessment methods, one additional parameter is the strain hardening exponent, which is determined as shown in Fig. 4; two examples are given in Fig. 29.

The ETM equation can be used for estimating critical loads in terms of force or strain when toughness is given or for determining required minimum toughness for given operating conditions. A particularly appealing property of analytical expressions is the ability to perform quick sensitivity studies. Alternatively, a graphical representation of Eq 42 can be used (Fig. 30). It is obvious that sensitivity studies can be very easily performed using either the equation

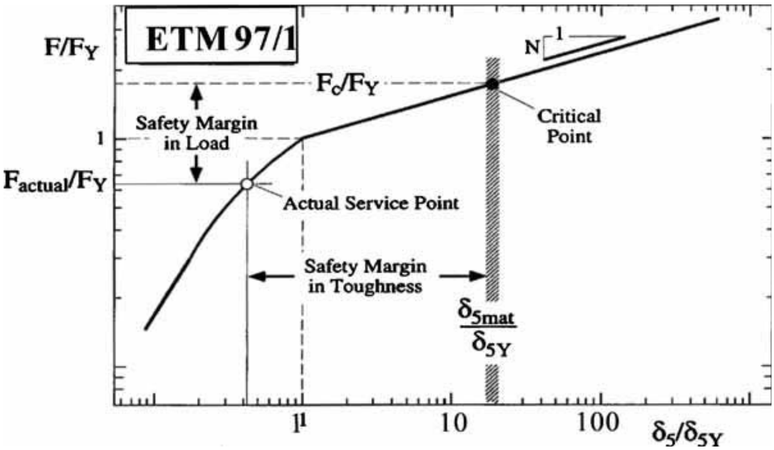

FIG. 30—*Graphical representation of Eq 43 for CTOD* [52].

or the diagram. For example, the state of stress is usually categorized in terms of plane stress or plane strain. These conditions have inverse effects on crack resistance and on the yield load, whereas plane strain reduces the crack resistance as compared to plane stress; the yield load is increased, thus decreasing the crack driving force, a fact which is seldom acknowledged.

The considerations so far have been dealing with the case of single valued crack resistance (fracture toughness). However, the ETM can as well be used for R-curve analyses; again, sensitivity analyses are easy to be performed. An example will be given later.

Validation

Validation has been performed by means of numerous experiments and FE analyses. Figure 31(a) shows that the increase of δ_5, experimentally measured on an $M(T)$ specimen of Al 2024-FC, with the applied stress follows exactly as predicted by the material's strain hardening exponent (see Fig. 29(b)). For the same material, three-hole specimens were fabricated, tested, and also analyzed using FE technique; in Fig. 31(b), numerical values of δ_5 and J are plotted against each other [62], and also in this case, the correlation follows precisely that predicted by Eq 42. A further example shows the alloy steel 35NiCrMo16, the deformation behavior was already depicted in Fig. 29(a), with δ_5 again as a function of the applied load, but now unlike standard ETM plots using double logarithmic plots, in linear coordinates (Fig. 32). The diagram is partitioned into two parts, the small scale yielding and the fully plastic sections. It is seen that the standard small scale yielding solution, i.e., $\delta_5 = K_{\mathrm{eff}}{}^2/(E\sigma_Y)$ works well up to about $0.9F/F_Y$, whereas Eq 40 based on the Dugdale model is very close to the experiment at the net section yield point.

The δ_5 R-curve analysis in Fig. 33 shows that under the conditions of net section yielding, the sensitivity of the instability stress to errors in finding the correct tangency condition is quite low [64]. Linear interpolation between the

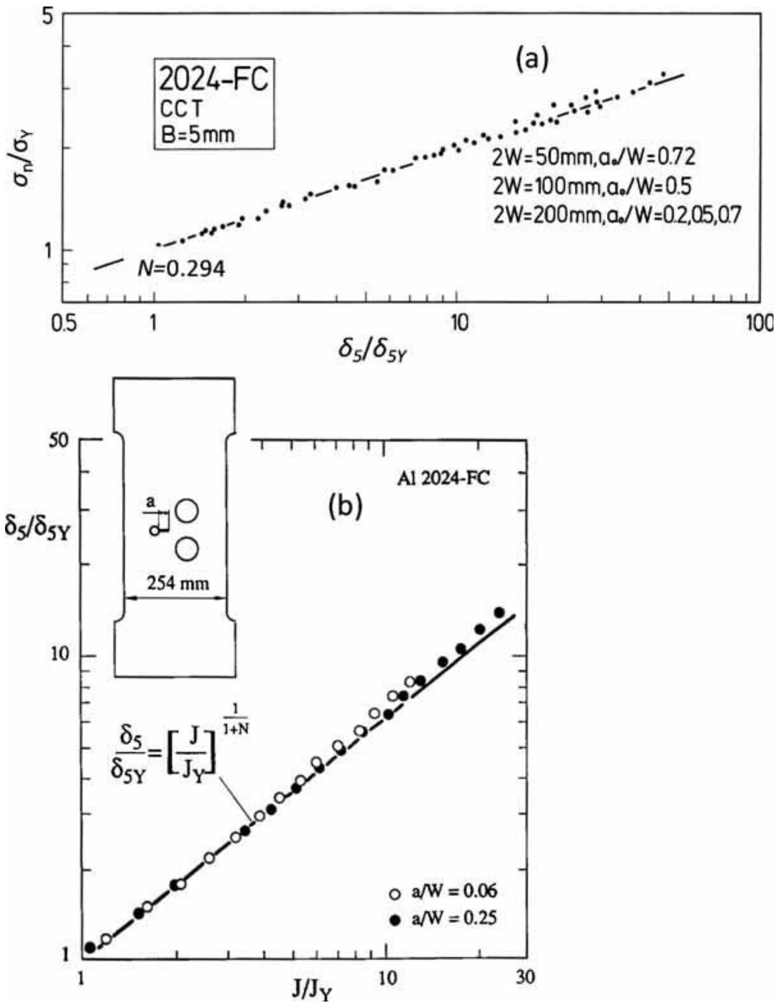

FIG. 31—*Validation of the basic ETM equation for Al 2024-FC:* (*a*) *Crack tip opening displacement as a function of the applied stress, experiments on M*(*T*) *specimens from Ref 50;* (*b*) *correlation between J and* δ_5 [54], *after an FE analysis in Ref 63.*

crack driving force curves below and above the expected point of tangency provides accurate results; this is also depicted in Fig. 34, demonstrating high accuracy of the method even at net section stresses close to the tensile strength.

It may be interesting to note that the ETM has also been applied to mixed-mode fracture [65,66]. The authors define a crack tip displacement vector, δ_v, consisting of an opening (δ_I) and sliding (δ_{II}) component

$$\delta_v = \sqrt{\delta_I^2 + \delta_{II}^2} \tag{44}$$

which for the small scale yielding regime reads

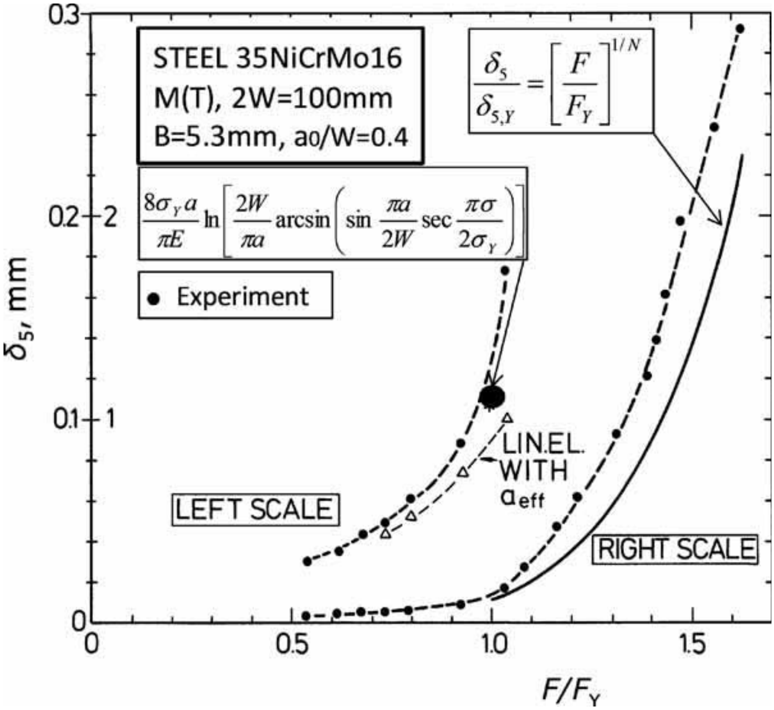

FIG. 32—δ_5 *of an alloy steel as a function of the applied load* [*50*].

$$\delta_v = \frac{\sqrt{K_{\mathrm{I,eff}}^2 + K_{\mathrm{II,eff}}^2}\sqrt{K_{\mathrm{I,eff}}^2 + 3K_{\mathrm{II,eff}}^2}}{E\sigma_Y} \tag{45}$$

A number of validations demonstrate the usefulness of this concept; for an example, see Fig. 35.

The basic module has also been applied to experiments on large austenitic steel pipes, which were performed within a program for a breeder reactor [68]. Six pipes with a nominal diameter of 700 mm and a nominal wall thickness of 11 mm contained circumferential through-cracks of different sizes and were tested by INTERATOM in a bending rig. Table 3 compiles the relevant test data. It is seen in the table that the actual dimensions deviated to some extent from the nominal ones. The table shows also that the pre-cracks were located in the base metal (BM), in the HAZ, and in the weld deposit (WD). During loading, the crack opening displacement δ_5 was measured on the pipes, and it could be demonstrated that within the range of validity, these R-curves coincided with those measured on $C(T)$ specimens. The maximum bending moments were determined graphically using the ETM R-curve method and compared with the experimental ones. The plot in Fig. 36 shows that for each test several estimates were performed, the reason being that actual and nominal input data exhibited some deviations. In the evaluation, the following parameters were varied: Nominal yield strength versus actual yield strength determined on specimens

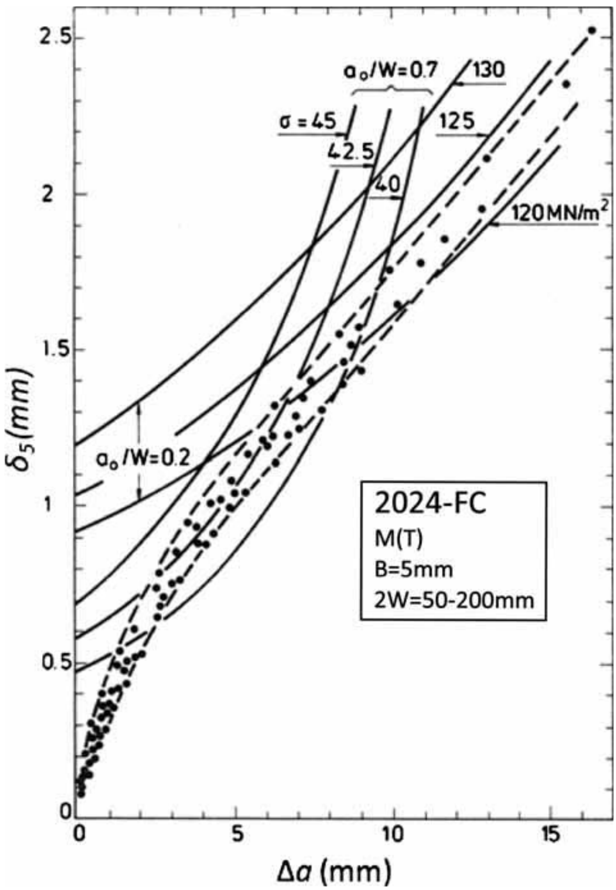

FIG. 33—*Determination of instability using R-curve analysis* [*64*]. *The* δ_5 *R-curve of a low strength aluminum alloy is the result of measurements on specimens with widths from 50 to 200 mm. The crack driving force curves are drawn* δ_5 *for 2W=200 mm and for two a/W ratios.*

extracted from pipe material; nominal wall thickness versus actual thickness; and stress intensity factor experimentally determined on actual pipes using the compliance method versus a polynomial formula. However, not every test was evaluated by varying all parameters.

This way a sensitivity study could be done, and it is seen from the graph that in some cases substantially different magnitudes of the estimated maximum moment resulted. The solid symbols indicate those analyses that were done using the dimensions and tensile properties directly measured on the respective pipes; they are closest to the experimental values. This and other similar studies concluded in the recommendation that much attention should be paid to the quality of input information.

It should be noted that the *R*-curves used for the analyses were determined

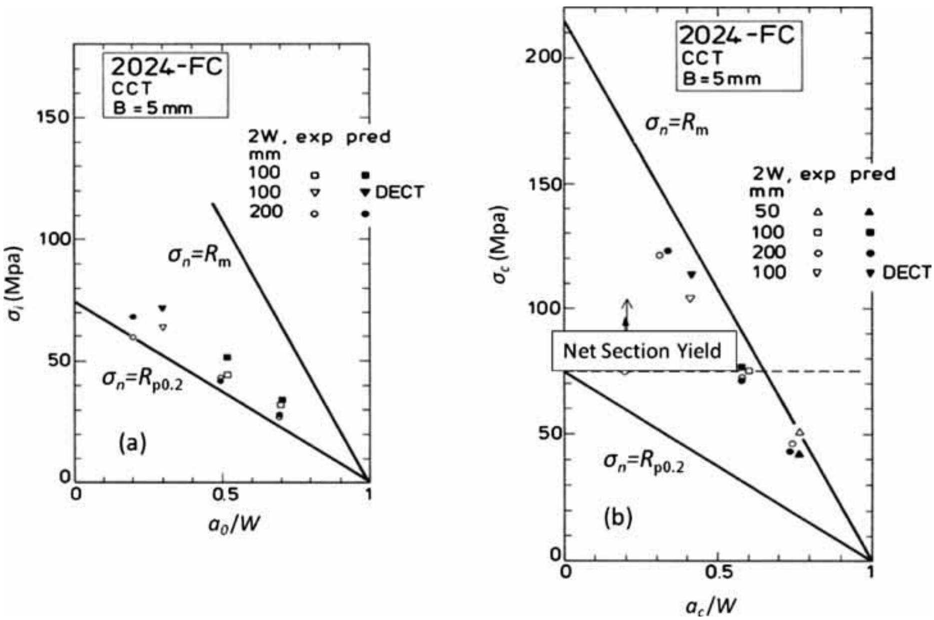

FIG. 34—*Experimental and predicted critical situations* [*64*]*:* (*a*) *Stress at initiation of crack extension,* σ_i*;* (*b*) *maximum stress,* σ_c*, obtained from the R-curve analysis in Fig. 33.*

directly on the component. The aim of the investigation was not to determine the transferability of an *R*-curve from specimen to component; the aim was rather to check the ability of the ETM to estimate the deformation and fracture behavior of the large scale pipes.

A study on internally pressurized cylinders [69] yielded also promising results. A thin-walled cylinder with a through-crack tested at TWI, Cambridge [70], was equipped with CTOD gages at both crack tips. The ETM estimates (Fig. 37) compare reasonably well with the pressure-CTOD record as averaged for both crack tips.

A further validation exercise was performed on four welded tubular T-joints, in a post weld heat treatment condition, made of a TMCP steel [71]. Although the test pieces were welded, the weld was not modelled since the crack front was in the base material. Figure 38(*a*) shows the test set up. The input information was obtained as follows.

- The stress distribution in the cross section containing the crack was determined using a parametric formula obtained from the literature [72].
- From this, the stress intensity factor was calculated using weight function solutions, again from the literature [73].
- The yield load was obtained by determining the intersection of the linear elastic with the fully plastic sections of the deformation curve. These sections were obtained in three different ways: From an elastic-plastic

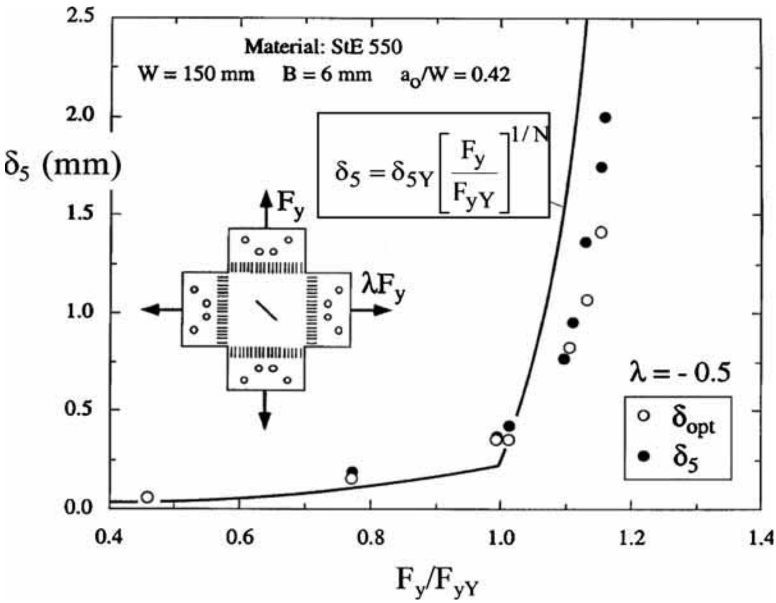

FIG. 35—*Application of the ETM concept to mixed mode loading* [*67*].

finite element deformation analysis, from an experiment, and using a parametric formula [73] (Fig. 38(*b*)). These methods were applied to the four joints tested and yielded values for F_Y between 1.64 and 1.73 MN.

- The fracture resistance properties of the material were determined as *R*-curves in terms of the CTOD according to the test methods ASTM E1290-07 [74] and ESIS P2-92 [24], delivering almost identical results [75]. Furthermore, on one joint the CTOD was measured using an infiltration technique, which gave values very close to those from the standard methods.

As the compilation of the deformation behavior of the four joints tested in Fig. 38(*c*) demonstrates that the data of the individual test pieces coincide very well. All joints were loaded to a specific deformation and then unloaded. The

TABLE 3—*Parameters of tested pipes* [*68*].

Experiment Number	Crack Location	Actual t (mm)	Actual Diameter (mm)	Pre-Crack Angle, φ (°)
1	BM	12.19	701.2	61.6
2	HAZ	11.47	697.9	124.2
3	WD	14.25	694.7	120.9
4	WD	13.37	697.4	175.4
5	BM	11.57	700.3	120
6	BM	10.43	696.7	120.7

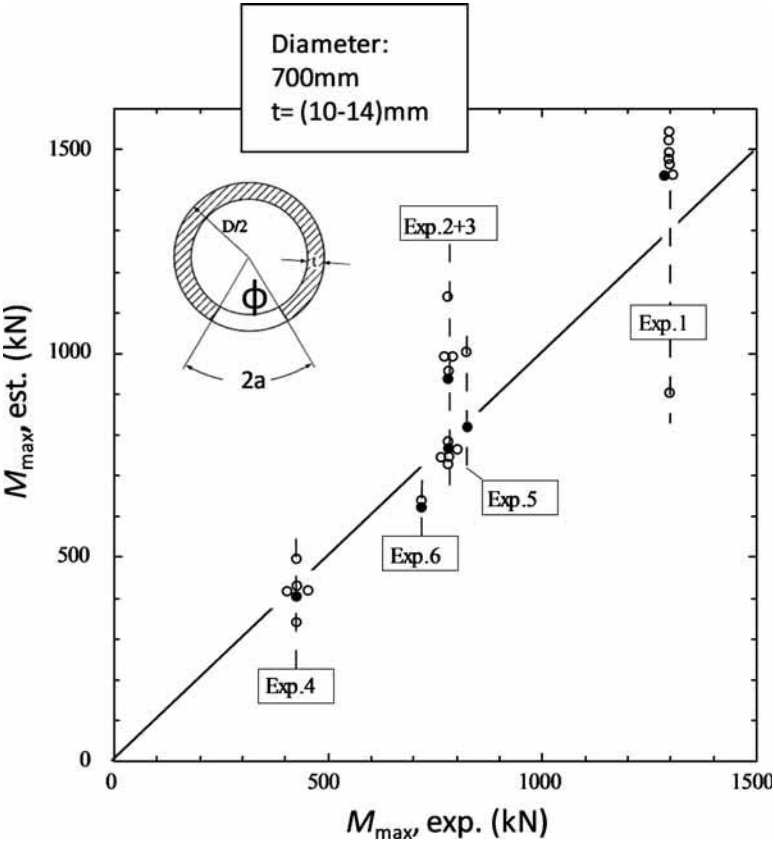

FIG. 36—*Estimated and experimental maximum bending moments obtained from bend tests on pipes made of the austenitic steel AISI-316L mod* [*68*].

fully plastic ETM estimate underestimates the applied force to some extent. For this estimate, the lower of two yield load values was chosen in order to stay on the safe side.

Strain Module

The ETM document [52] provides guidance on determining the crack driving force for strain controlled loading when the applied strain is greater than the yield strain. For tension loaded parts with short through cracks ($a/W \ll 1$), a very simple expression for δ_5 as a function of the applied strain can be derived from Eq 44

$$\delta_5 = 1.5\pi\varepsilon \tag{46}$$

The factor of 1.5 is obtained when the yield load F_Y is determined with the actual values of either $R_{p0.2}$ or R_{el}. For tensile loaded members, these are quite high values since substantial plasticity occurs already at lower applied stresses.

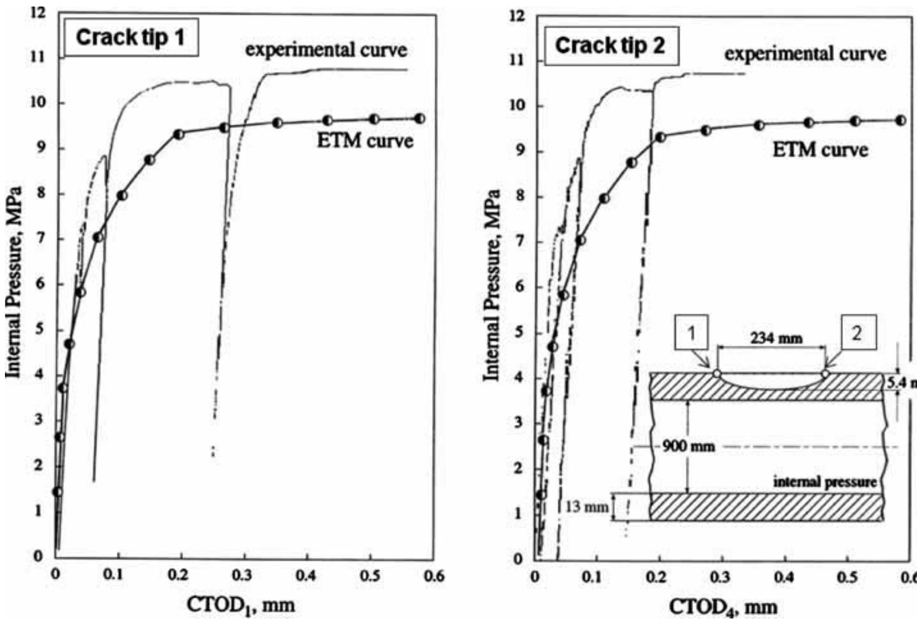

FIG. 37—*Estimated and measured pressure—CTOD behavior of an internally pressurized cylinder with a through-crack* [69], *test from Ref 70.*

For this case only 0.9 times $R_{p0.2}$ or R_{el} would be more appropriate; hence

$$\delta_5 = 1.14\pi\varepsilon \tag{47}$$

Part-through cracks can be characterized using

$$\delta_5 = 1.34\pi\varepsilon \tag{48}$$

with the actual values of $R_{p0.2}$ or R_{el} and using

$$\delta_5 = 1.085\pi\varepsilon \tag{49}$$

for 0.9 times $R_{p0.2}$ or R_{el}. However, it was decided in the document [52] to use the former alternative to obtain conservative estimates of the crack driving force. A validation for an $M(T)$ specimen is illustrated in Fig. 39, demonstrating that the second alternative provides indeed quite accurate estimates, whereas the former one—the one chosen for the ETM document—is on the conservative side [76].

Notch Module

For cracks within the stress field of a notch, the problem of determining the crack driving force becomes somewhat more complex. Figure 40 shows the situation of a crack emanating from a stress concentration. Due to the space limitations, not all relevant equations will be shown here. It should suffice to

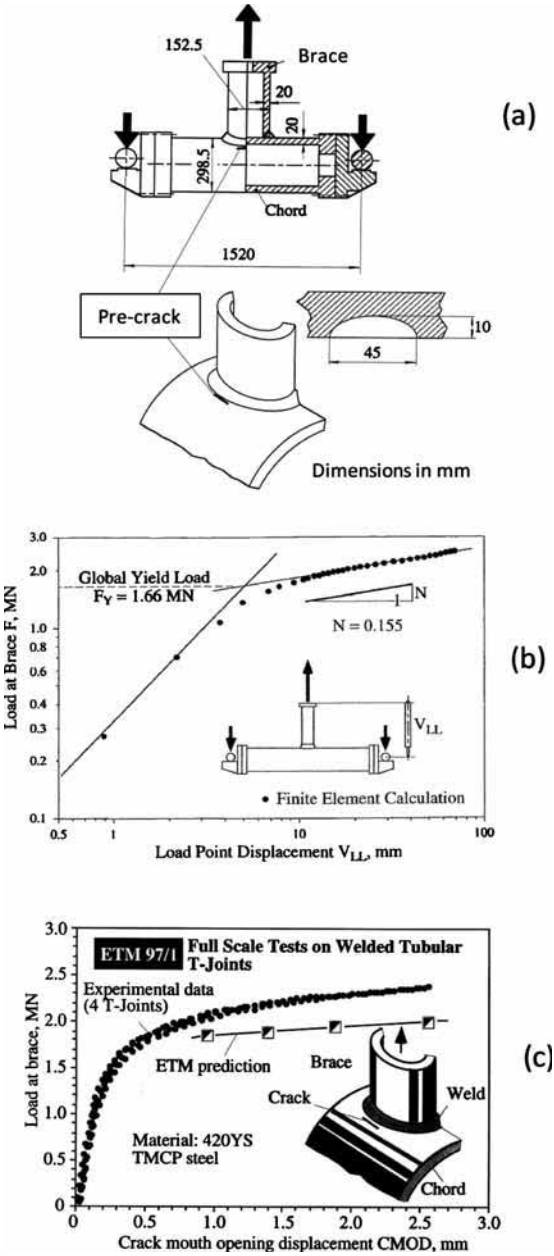

FIG. 38—*Test and assessment of four tubular T-joints* [*71*]*:* (*a*) *Test set up for and dimension of the T-joint;* (*b*) *deformation characteristics from FE analysis; and* (*c*) *applied tensile force versus CMOD experimentally determined on four test pieces, along with the ETM estimate.*

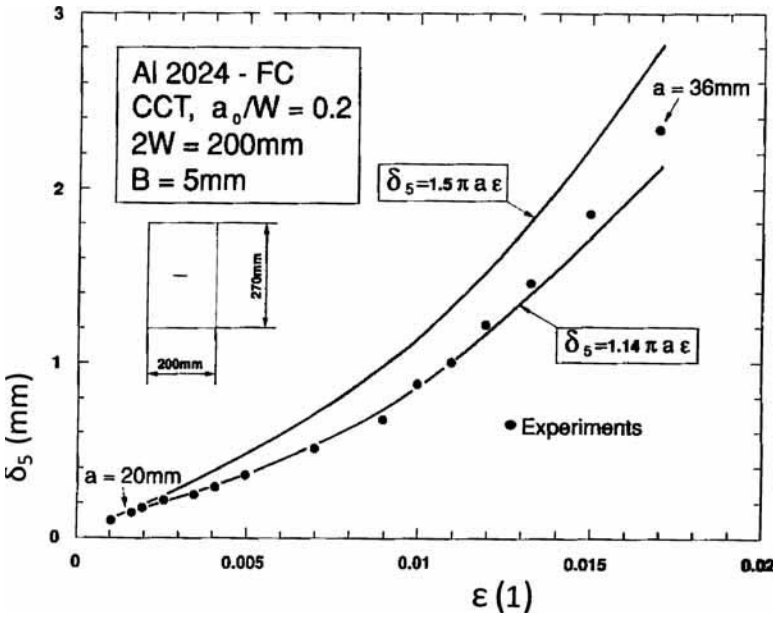

FIG. 39—*Measured and with ETM-strain estimated δ_5 for an M(T) specimen, after Ref 76.*

mention that for analyzing a crack within the notch field, an additional yield load is needed, namely, the local yield load at the notch tip

$$F_{YL} = \frac{F_Y}{K_t} = \frac{2\sigma_Y AB}{K_t} \tag{50}$$

with K_t denoting the linear elastic stress concentration factor. The global yield load is determined as that load, F_Y, which leads to net section yielding. From the relationship between δ_5 or J and the applied load (Fig. 41), two regimes of elastic-plastic behavior of a crack whose length is smaller than the notch radius can be distinguished. The first one is related to a crack whose length, l, meets the conditions

$$l \leq \rho \text{ and } l/A \leq 0.15 \tag{51}$$

These conditions mean that the crack is still within the stress field of the notch and much smaller than the width of the test piece or component. The second one represents the behavior given by Eq 43.

This module was applied to a pressure vessel with a crack in a nozzle as shown in Fig. 42. During the test, the crack tip opening displacement had been measured [77]. The analysis [78] was based on the average hoop stress in the vessel as determined by the standard formula for thin-walled pressure vessels and an empirical formula for the stress concentration factor [77]

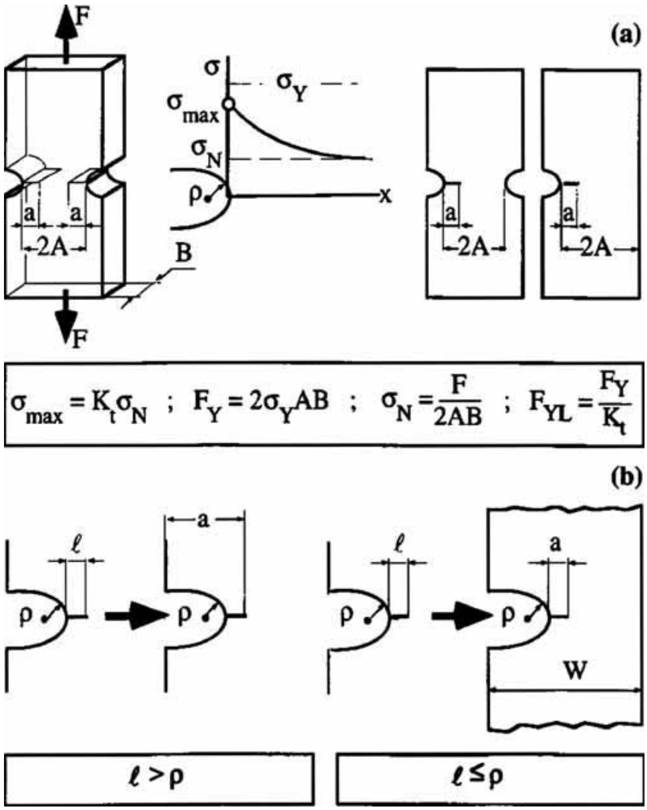

FIG. 40—*Notch module of the ETM* [52]*:* (*a*) *Cracks emanating from a stress concentration;* (*b*) *definition of crack length to be used in the analysis.*

$$K_t = \max\left\{2.5 \text{ or } 2.5\left[1 + 1.6\left(\frac{r^2}{Rt}\right)^{1/3} - 1.2\left(\frac{R}{t}\right)^{1/4}\right]\right. \qquad (52)$$

where r and R denote the inner radius of vessel and nozzle, respectively.

The resulting estimates model the test remarkably well, Fig. 42, although the crack configuration looks quite complicated.

Engineering Treatment Model for Mismatched Welded Joints

This work was motivated by the unexpected observation that in certain experiments on welded joints, a fatigue pre-crack located in a relatively low toughness area in a fracture mechanics test deviated into an area with higher toughness [79].

Welded joints with yield strength mismatched weld metal can be regarded as a model of a compound material, presenting very interesting scientific problems. These are due to the presence of the interfaces between the base plate and

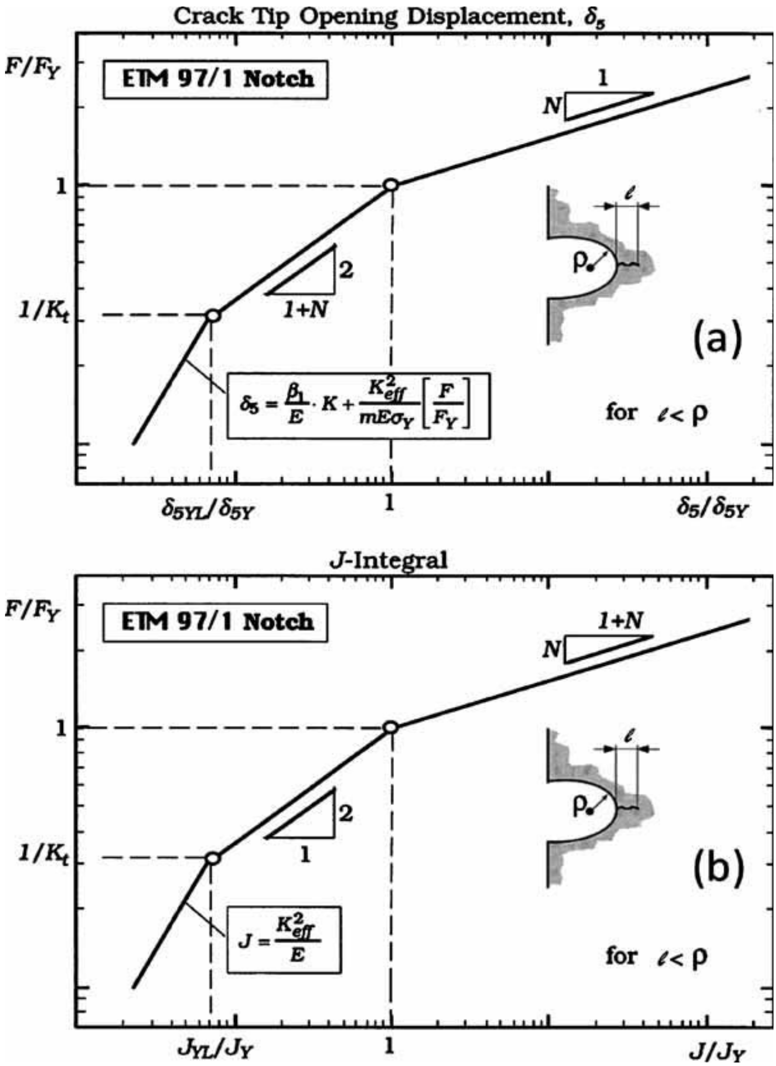

FIG. 41—*Notch module of the ETM* [52], *driving force diagrams:* (*a*) *For CTOD;* (*b*) *for J.*

weld metal, causing inhomogeneous deformation and constraint conditions. For simplicity, a weld can be regarded as consisting of the base plate, B, and an embedded strip having the width, $2H$, representing the weld metal, W (Fig. 43(*a*)). As a consequence of the different plastic properties of the two constituents, a strongly discontinuous strain distribution across the weld is observed; this, of course, is only the case when at least one of the two partners exceeds its yield strength.

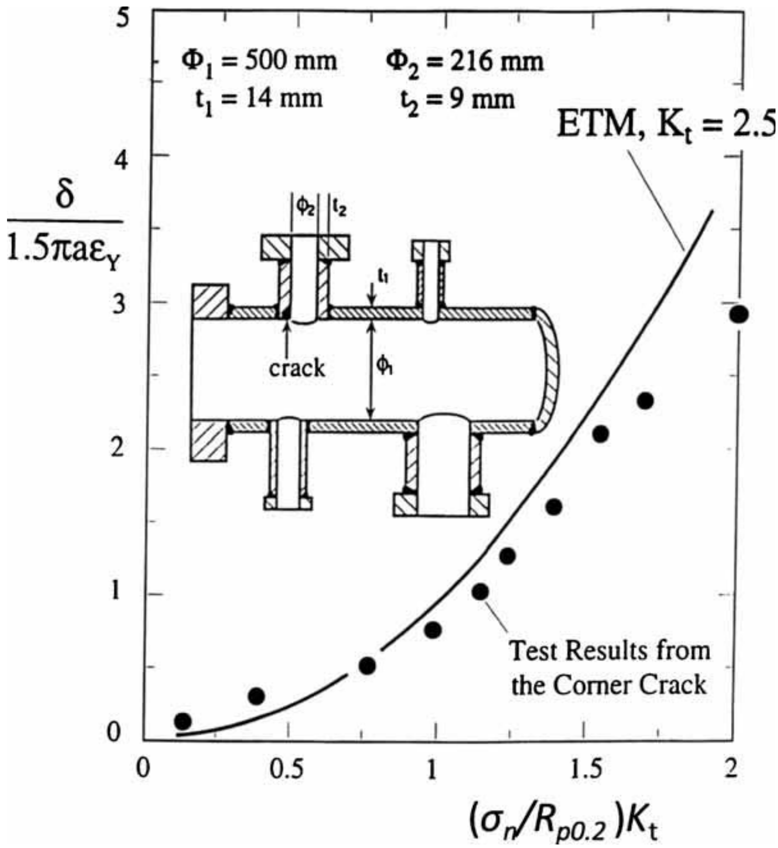

FIG. 42—*Pressure vessel with a cracked nozzle, test results, and ETM estimate* [77,78]. *The symbol σ_n designates the nominal stress as calculated for a pressure vessel.*

The yield strength mismatch is quantified by the mismatch factor, M, defined as

$$M = \frac{\sigma_{YW}}{\sigma_{YM}} \tag{53}$$

$M > 1$ is designating overmatch, $M < 1$ stands for under match, and $M = 1$ is even match. Overmatch is the condition where welding procedures are usually aimed at to avoid the detrimental strain concentration in an under-matched weld metal (Fig. 43(*a*)). The consequences for the crack driving force of the weld—loaded transverse to the weld—are depicted in Fig. 43(*b*), where the three force versus δ_5 diagrams represent the three kinds of weld metal yield strength matching; the under match and overmatch curves are valid when the base plate properties are kept constant, whereas the weld metal properties vary. The under match and overmatch curves change their order when the weld metal properties are used as reference. The slope, N_M, is the hardening expo-

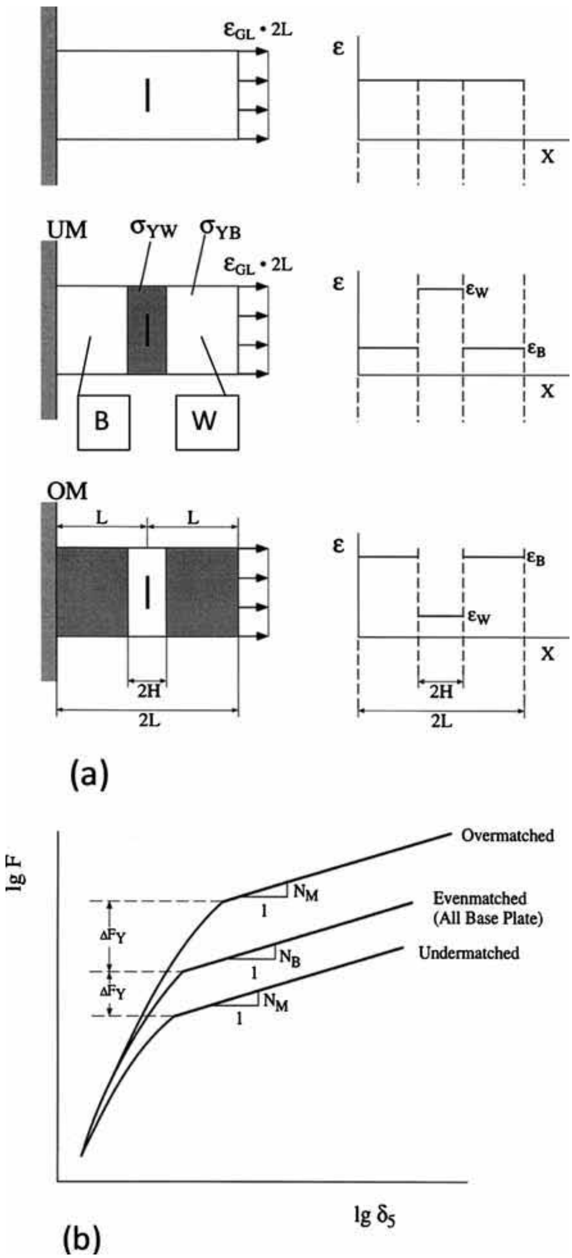

FIG. 43—*Mismatched welded joint under tension* [*80*]*:* (*a*) *Strain distribution;* (*b*) *resulting crack driving force with base plate used as reference.*

nent for fully plastic behavior of the compound (see below).

The document [80] offers the following four assessment levels:

- Exclusion level
- Screening level
- Baseline solution
- General solution

Appendices provide yield load solutions and information about local stress and constraint conditions.

Exclusion Level

The crack driving force in slender configurations where crack and remaining ligament are much greater than the weld metal width, $2H$, does not sense mismatch effects. The driving force can then be determined via the original ETM document [52] using the base plate properties.

Range of Applicability:

- $a > H$
- $(W - a) > 10H$
- Plane strain: Over and under match
- Plane stress: Over match

Screening Level

This is the level for conservative assessment that can be accomplished by using Eqs 42 and 43, with the lowest values of the deformation properties of base plate and weld metal, respectively

$$\sigma_Y = \min(\sigma_{YB}, \sigma_{YW}) \tag{54a}$$

$$N = \min(N_B, N_W) \tag{54b}$$

Although the screening level can be applied to all values of a/H and $(W - a)/H$, it is recommended to use it only outside the range specified for the exclusion level. Otherwise, the degree of conservatism could be unduly high. If the result turns out to be unsatisfactory, then one of the following levels should be used.

Baseline Solution

Comprehensive analytical derivations have been reported in Refs 81 and 82. The power laws of both base plate and weld metal

$$\frac{\sigma}{\sigma_{YB}} = \left[\frac{\varepsilon}{\varepsilon_{YB}}\right]^{1/N_B} \tag{55a}$$

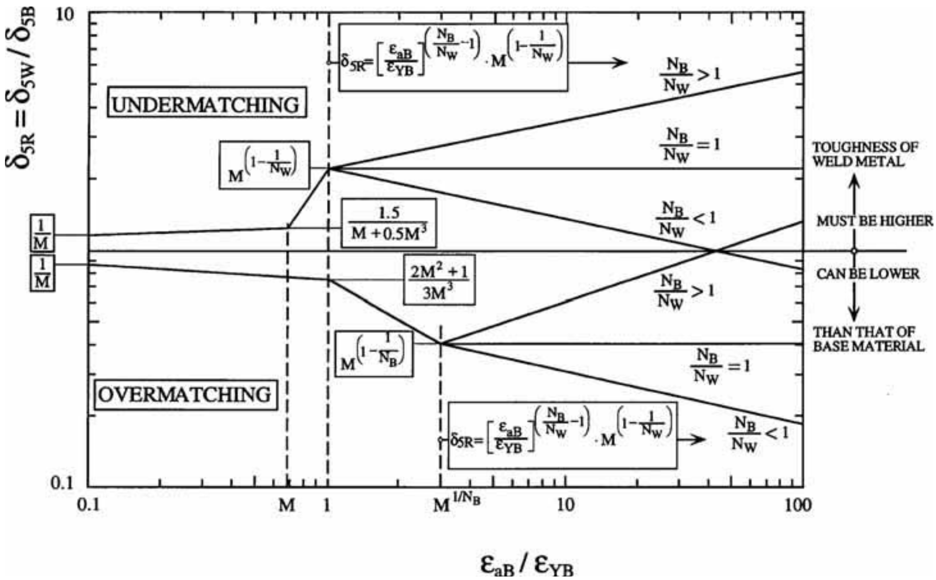

FIG. 44—*Schematic of ETM-MM Base Line Solution, showing the development of δ_{5R} as functions of the applied strain in the base plate* [*81*].

$$\frac{\sigma}{\sigma_{YW}} = \left[\frac{\varepsilon}{\varepsilon_{YW}}\right]^{1/N_W} \tag{55b}$$

are stacked at the interface between both materials. By equating both stresses, the CTOD, e.g., in terms of δ_5, can be calculated either as a function of the applied force or of the applied strain, ε_{aB}. The result depends on whether only the base plate (happens in under match), only the weld metal (happens in over match), or both components are plastic, i.e., the stress exceeds the yield strength in both base plate and weld metal. Normalization helps also here to ease judging the effect of mismatch on the crack driving force: The CTOD in the weld metal, δ_{5W}, is normalized by the CTOD in the base plate, δ_{5B}, to determine the driving force ratio

$$\delta_{5R} = \delta_{5W} / \delta_{5B} \tag{56}$$

This way it can be easily seen how effectively the undermatch increases the driving force or how the overmatch is able to shield a weld metal crack from plastic deformation. A host of analytical expressions has been derived in Refs 81 and 82, which is impossible to show here. It may suffice to display the equation for full plasticity, i.e., for the case when both base plate and weld metal yield

$$\delta_R = M^{(1-1/N_W)} \left[\frac{\varepsilon_{aB}}{\varepsilon_{YB}}\right]^{(N_B/N_W-1)} \tag{57}$$

Figure 44 provides a schematic overview on how the driving force develops

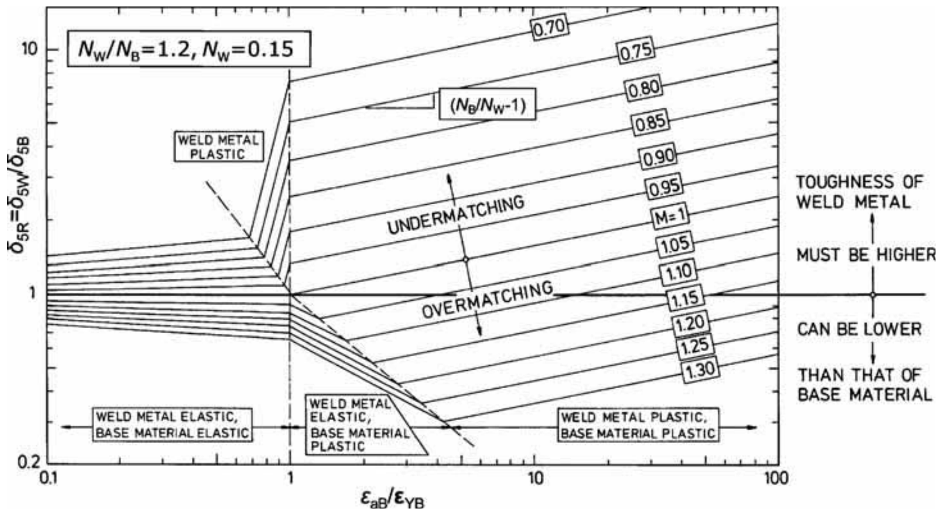

FIG. 45—*Driving force ratio for NB/NW=1.2 and NW=0.15* [*81*].

under various mismatch conditions and shows how the driving force can be constructed when the plastic properties of both materials are known. The concrete examples shown in Fig. 45 demonstrate how strongly the driving force reacts to even moderate mismatch values; it takes an under match of just a bit more than 30 % to let the CTOD of a weld metal crack exceed that of a crack with the same size in the base plate by an order of magnitude. Here it becomes clear why welding procedures are usually aimed at yield strength over matched weld metal. However, the previous diagram (Fig. 44) shows also that yield strength mismatch is not the only one, albeit the most important, parameter. Differences in hardening behavior do also play a role: For example, the beneficial effect of overmatch can be overridden by lower weld metal hardening, i.e., when $N_W < N_B$. This can be easily seen from Eq 57 and also from Fig. 45, where the slope in the fully plastic range is given by $(N_B/N_W - 1)$.

The magnitude of δ_{5R} provides also a toughness requirement for the weld metal, which can also be deduced from Figs. 44 and 45.

The equations derived for δ_{5R} were also reformulated in design curve style [82] following PD6493 [83]. For this purpose, the CTOD for a weld metal crack was normalized as follows:

$$\delta^*_5 = \frac{\delta_{5W} E}{\pi a M \sigma_{YB}} \tag{58}$$

In analogy to Fig. 44, a schematic representation of Eq 58 for all loading ranges is depicted in Fig. 46. Critical crack sizes can be immediately derived by solving Eq 58 either for the normalized critical crack size a_c^*

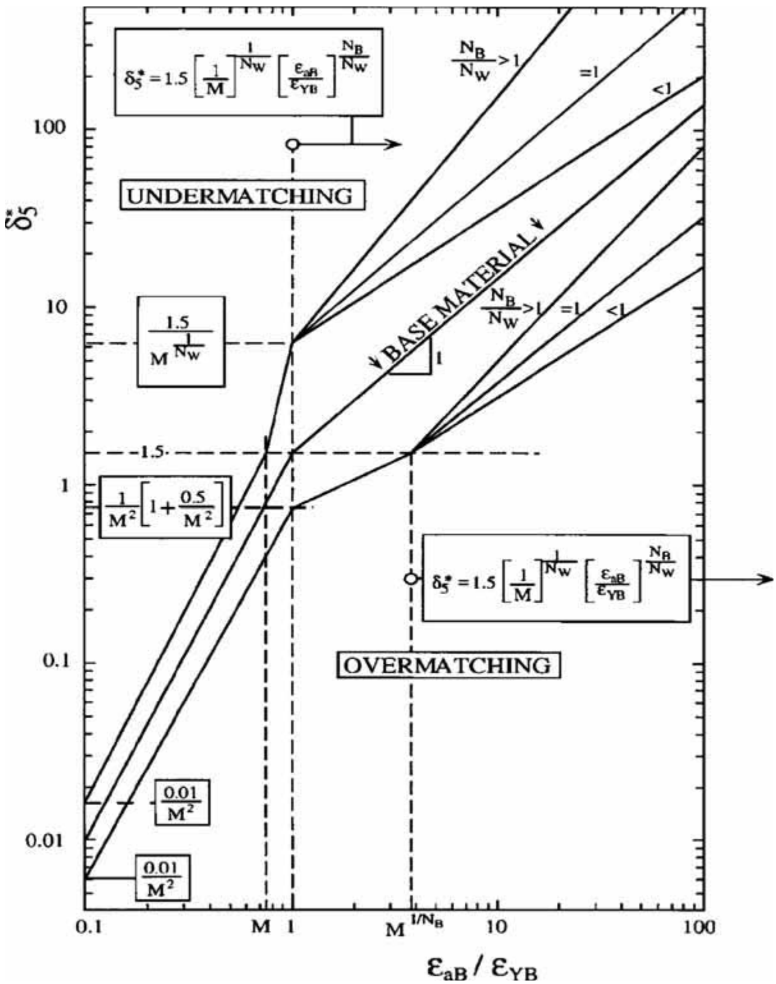

FIG. 46—*Schematic showing the design curve formulation of the Base Line Solution* [*82*].

$$a^*_c = 1/\delta^*_{5matW} \tag{59}$$

where the term in the denominator is δ^*_5 from Eq 58, however, with δ_{5W} replaced with its critical value, δ_{5matW}. Alternatively, the absolute critical crack size is

$$a_c = \frac{\delta_{5matW}E}{\pi\sigma_{YW}}\frac{1}{\delta^*_{5matW}} \tag{60}$$

The quantities δ^*_5 and the critical crack size are also given as functions of the applied force; for details, see Refs 80 and 82.

The formulations of the Base Line Solution have been derived for tensile plates with small cracks, $a/W<0.1$. The latter limitation can be easily extended to finite a/W ratios by accounting for the proper yield load solution. As far as configurations other than tensile plates are concerned, the findings presented here provide nevertheless quick information about the effect of yield strength mismatch on the crack driving force, even when accurate quantitative solutions are not available.

General Solution

This module is valid for all values of a/H and a/W; however, due to its greater efforts needed for evaluation, it only makes sense to use it outside the ranges specified for the three previous levels. It makes use of Eqs 42a and 43, however, with some modifications. The yield load has to be determined considering the peculiarities of the actual weld, i.e., a mismatch yield load, F_{YM}, is required for which solutions are provided in an appendix to the document [80]. These solutions are based on finite element analyses; however, many of them could be well reproduced using the slip line analysis method; see, e.g., Ref 84. It should be noted that the document provides also solutions for interface cracks, i.e., those cracks that are located between base plate and weld metal.

When deriving yield load solutions, it was found that for a given geometry, the result is independent of absolute dimensions when the normalized mismatch yield load, F_{YM}/F_{YB}, is regarded as a function of the geometric parameter $(W-a)/H$. An example is depicted in Fig. 47 for a plate under tensile load. F_{YB} is the yield load for the base plate. It is seen from the diagram that for short ligaments, i.e., low values of the parameter $(W-a)/H$, the mismatch yield load is entirely given by the weld metal properties. This mismatch effect decays for longer ligaments and eventually disappears. In other words, cracked components with very long ligaments do not sense mismatch effects at all; here we refer to plasticity and hence to the crack driving force, not to fracture, which needs the toughness properties of the weld metal. It should be noted that for configurations other than that shown in Fig. 47, different patterns may be obtained. In particular, plane stress tends to retain the mismatch effect for all values of the parameter $(W-a)/H$.

The construction of the force-δ_5 diagram is different for over and under match.

Over Match:

$F<F_{YM}$

$$\delta_5 = \frac{\beta_1}{E}K + \frac{(K_{\mathrm{eff}})^2}{mE\sigma_{YW}}\left[\frac{F}{F_{YM}}\right] \tag{61}$$

with K_{eff} determined using

$$a_{\mathrm{eff}} = a + \frac{1}{2\pi}\left[\frac{K}{\sigma_{YW}}\right]^2, \tag{62}$$

and β_1 and m from Eqs 42e and 42f.In this range, the original ETM expression, Eq 42, is adapted to mismatch conditions and reads$F\geqslant F_{YM}$

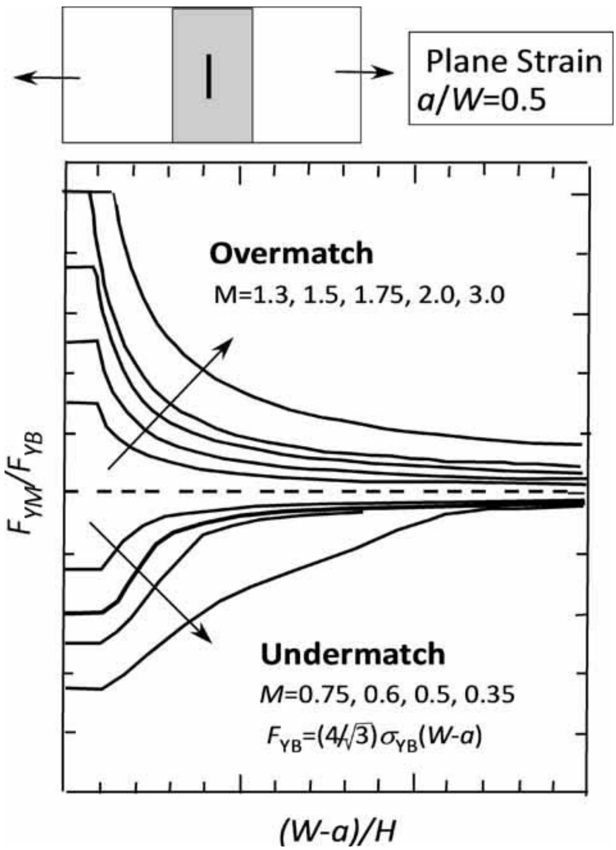

FIG. 47—*Mismatch yield load for a middle cracked tensile panel* [*80*].

$$\frac{\delta_5}{\delta_{5YM}} = \left[\frac{F}{F_{YM}}\right]^{1/N_M} \tag{63}$$

where:

$\delta_{5YM} = \delta_5$ calculated with Eq 61 at the mismatch yield load, F_{YM}, and the hardening exponent is estimated by

$$N_M = N_W \quad \text{plane stress,} \quad \text{for } (W-a) \le H \tag{64a}$$

$$N_M = \frac{(W-a)}{H/N_W + (W-a-H)/N_B} \quad \text{plane strain,} \quad \text{for } (W-a) \ge H \tag{64b}$$

These expressions were derived for middle cracked panels under plane strain conditions using slip line theory [85], under consideration of finite element work in [86]. For plane stress conditions, plasticity is mainly concentrated in shear planes inclined to the wall surface under 45° and parallel to the crack,

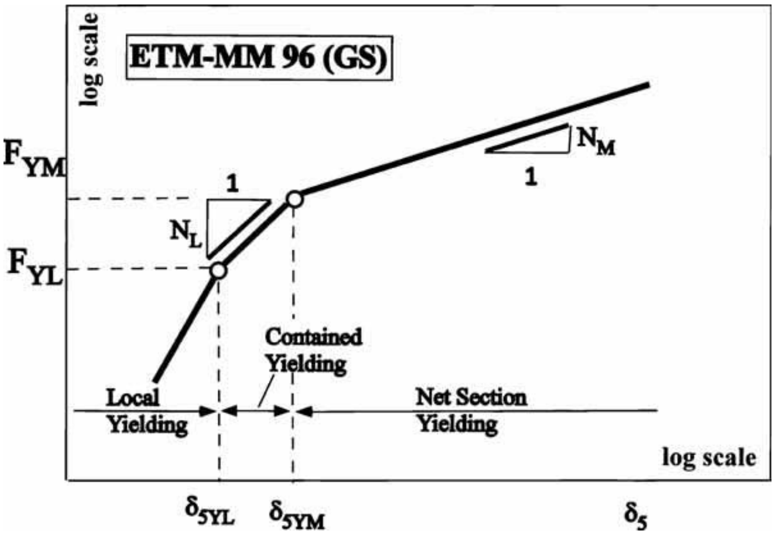

FIG. 48—*Schematical shape of the force-δ_5 curve for under match condition* [*80*].

which means that it is the weld metal strip that attracts the plastic deformation. Hence, the hardening exponent can be approximated by

$$N_M = N_W \text{ plane stress,} \quad \text{for all } (W - a) \tag{64c}$$

Under Match—Finite element work [85] suggests displaying the ETM-MM diagram for under match in the three sections shown in Fig. 48 (similar to the pattern shown in Fig. 41), where two kinds of yield loads are defined

- *Local yield load*, where the plastic zone touches the interface between weld metal and base plate (as represented by the HAZ)

$$F_{YL} = 0.7F_{YW} \quad \text{for } M < 1 \tag{65}$$

  where: F_{YW} = yield load for the component under consideration as if it would consist of weld metal only.
- *Mismatch yield load, F_{YM}*, as introduced above. The diagram is thus given by the following expressions:
- *Local yielding, $F < F_{YL}$*, uses Eqs 42b–42d with σ_{YW} as the relevant yield strength,
- *Contained yielding, $F_{YL} < F < F_{YM}$*, uses

$$\frac{\delta_5}{\delta_{5YL}} = \left[\frac{F}{F_{YL}}\right]^{1/N_L} \tag{66}$$

  with N_L being

$$N_L = \frac{1 + N_W}{4N_W} \tag{67}$$

  and

$$\delta_5 = \frac{\beta_1}{E}K + \frac{(K_{\text{eff}})^2}{mE\sigma_{YW}}\left[\frac{F}{F_{YM}}\right] \quad \text{at } F = F_{YL} \tag{68}$$

- *Net section yielding*, $F > F_{YM}$, uses Eq 63 with

$$\delta_{5YM} = \delta_{5YL}\left[\frac{F_{YM}}{F_{YL}}\right]^{1/N_L} \tag{69}$$

It should be noted that formulations in the document ETM-MM were not derived for elastic mismatch, i.e., they are valid for the case that the elastic moduli in base plate and weld metal are the same. The determination of the J-integral is outlined in Ref 92.

Constraint Conditions

The yield strength mismatch between the two constituents of the compound base plate/weld metal does not only affect the commonly used crack driving force CTOD (and J integral, which is not included in the ETM-MM document); an equally important effect is the alteration of the stress state. This effect was studied in a number of papers [84,85,87–91] using the slip-line method. For a given geometry, the slip-line fields in such a configuration are a strong function of the parameter $(W-a)/H$ [84,88,90], which has already been introduced above in the context of mismatch yield loads.

A particularly intriguing case is given by a soft strip between two hard materials, representing a strongly under matched weld. Figure 49 shows a middle cracked tensile panel with a relatively long ligament. At the node of the slip lines, a stress peak is created ahead of the crack tip which can be substantially higher than the maximum stress at the crack tip. This peak increases with increasing $(W-a)/H$ and may attain very high values. As a consequence, failure may occur ahead of the tip of a crack, albeit driven by the presence of the crack. Such kind of failure can be generalized for all kinds of material combinations similar to the geometry treated here; if the interface between the strip and the surrounding material is weak, then interface failure is likely to occur, even when the crack is in the middle of the strip. A similar problem was studied in [94] for small scale yielding conditions: A metal foil was placed between two ceramic blocks. Although this work was performed using a finite element procedure, it is cited here since it reports findings similar to those obtained by our slip-line analysis in Ref 84.

Finally, the constraint conditions near an interface crack are shown here: Fig. 50 displays the dependence of the near-tip constraint as functions of the yield strength mismatch [89,91]. On the lower strength side, the stress triaxiality increases with the degree of mismatch beyond that a crack would sense as if it were located in a specimen (or component) made of the low strength material only. The reverse is true for the harder material side.

The basic effects of mismatch on crack driving force and stress state have been obtained using analytical methods and extended and refined by numerous finite element studies, e.g., Refs 82, 84, 85, and 88–93, a study using the slip-line theory in combination with a modified boundary layer method [93], as well as experimental work combined with numerical analysis, e.g. Refs 94–96. These

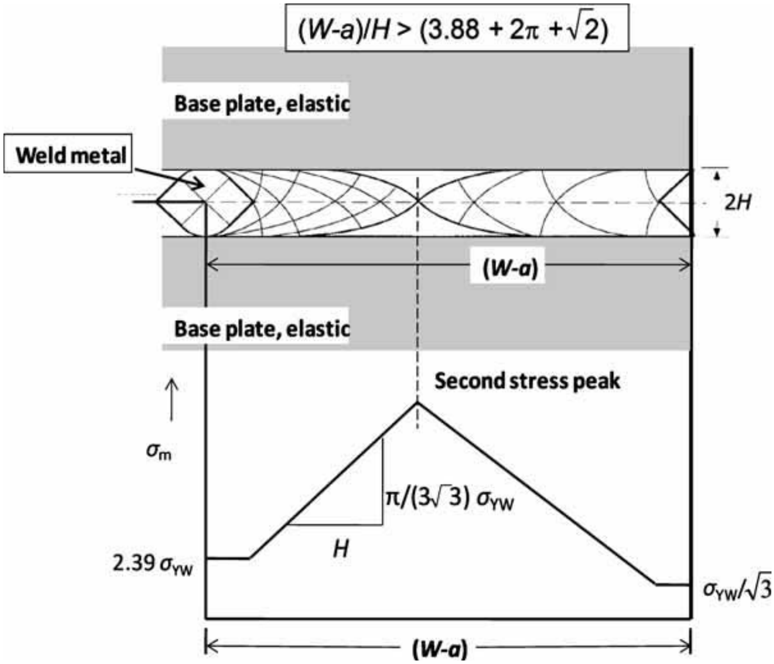

FIG. 49—*Slip-line field in extremely under matched tensile plate, showing second stress peak ahead of crack, after Ref 87.*

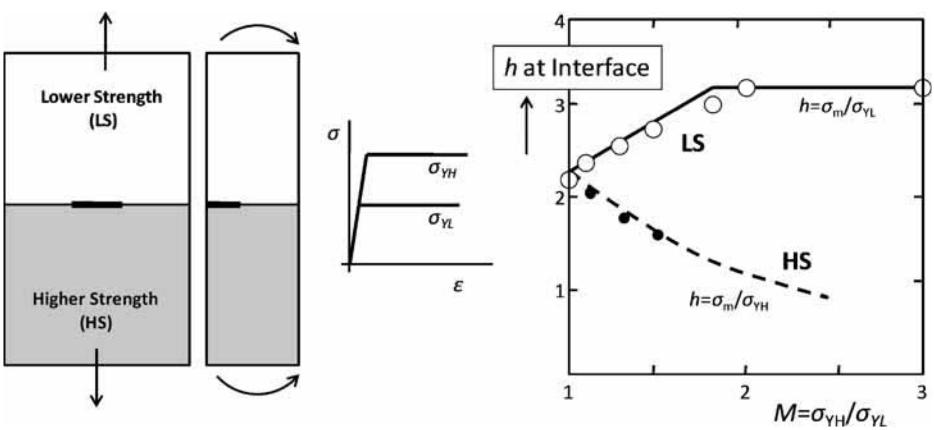

FIG. 50—*Triaxiality at interface cracks, small scale yielding analysis, after [89]; σ_m is the hydrostatic stress. The symbols were obtained by FE analysis; the curves represent results obtained from a slip line analysis.*

findings show that the constraint conditions can be substantially different from those of the homogenous case. They can be summarized and generalized as follows:

- *Soft strip* in a hard environment with a crack in the center of the strip, representing an under matched weld, but also metal foil between hard materials such as ceramics, and adhesive layers: The local stresses and hence constraint are elevated above those present near a crack in a body consisting of the soft material only (see Fig. 49). This is accompanied by a higher driving force as compared to the homogeneous case (see Figs. 44 and 45).
- *Hard strip* in a soft environment, representing an overmatched weld: The local stresses and hence constraint are lower than those present near a crack in a body consisting of the hard material only. This is accompanied by a lower driving force (see Figs. 44 and 45).
- *Crack in an interface:* The stress triaxiality is higher on the softer side and lower on the harder side than in the homogeneous case (see Fig. 50). This means that there is a fair chance that an interface crack may deviate into the softer material, although its toughness may be much higher than that of the harder material.

These effects depend on geometrical parameters, such as tension versus bending and the parameter $(W-a)/H$, and may thus have consequences for structural assessment: The test piece configuration must be carefully selected to model the constraint conditions in the component to be assessed as closely as possible.

Concluding Remarks

It has been shown that it is possible to describe important characteristics of fracture problems using analytical expressions. The validation examples demonstrate that reasonable estimates can be achieved and sensitivity studies can be easily performed.

The various events occurring in a material during a failure process can be described by models presented in this paper: Fatigue propagation under constant amplitude loading as well as ductile tearing from the formation of the first voids ahead of the crack front until final instability after substantial crack extension.

Some of the methods presented have substantially influenced several standards/codes.

- ESIS P3-09, a comprehensive procedure describing the fracture resistance of materials from linear elastic to fully plastic conditions and under various constraint conditions [57]
- ISO 12135:2002(E), dealing with a unified method for determining fracture toughness [25]
- ISO 22889:2007(E), describing tests on specimens with low constraint [56]
- ASTM E2472-06, describing tests on specimens with low constraint [55]

- SINTAP, a European structural assessment method for static loading [97–99]
- FITNET, extension of the SINTAP procedure to include fatigue, creep, and corrosion [98]

Acknowledgments

The writer is deeply indebted to his colleagues at the laboratories of the University of Karlsruhe, the German Aerospace Research Establishment, and the GKSS Research Center for their contributions by performing tests and numerical simulations as well as stimulating discussions in a friendly and stimulating atmosphere. The writer had been blessed with wonderful people he had the pleasure to work with, and the writer thanks all of them for what he owes them. Thanks are also due to financing bodies such as the German Science Foundation (DFG) and the European Commission. Last but not least, the writer enjoyed a great deal of freedom for his activities, which is one of the most important ingredients for every kind of work. Unfortunately, this seems to be going the wrong way because of the increasing formalization and bureaucratization of scientific work.

References

[1] Rice, J. R., "Mechanics of Crack Tip Deformation and Extension by Fatigue," *Fatigue Crack Propagation, ASTM STP 415*, ASTM International, West Conshohocken, PA, 1966.

[2] Schwalbe, K.-H., 1969, "Die Ausbreitung von Ermüdungsrissen in reinem Aluminium [Fatigue Crack Propagation in Pure Aluminium]," Ph.D. thesis, University of Karlsruhe, Karlsruhe, Germany.

[3] Schwalbe, K.-H., "Approximate Calculation of Fatigue Crack Growth," *Int. J. Fract.*, Vol. 9, 1973, pp. 381–395.

[4] Shih, C. F. and Hutchinson, J. W., "Fully Plastic Solutions and Large Scale Yielding Estimates for Plane Stress Crack Problems," *J. Eng. Mater. Technol.*, Vol. 98, 1976, pp. 289–295.

[5] Aravas, N. and McMeeking, R. M., "Finite Element Analysis of Void Growth near a Blunting Crack Tip," *J. Mech. Phys. Solids*, Vol. 33, 1985, pp. 25–49.

[6] McClintock, F. A. and Irwin, G. R., "Plasticity Aspects of Fracture Mechanics," *Fracture Toughness Testing and Its Applications, 67th Annual Meeting of the ASTM, ASTM STP 381*, West Conshohocken, PA, 1964, ASTM International, West Conshohocken, PA.

[7] Rice, J. R., "Stresses Due to a Sharp Notch in a Work-Hardening Elastic-Plastic Material Loaded by Longitudinal Shear," *J. Appl. Phys.* (*Trans. ASME*), 1967, pp. 287–298.

[8] Rice, J. R., private communication, February 1972.

[9] Schwalbe, K.-H., "Zur Abschätzung der Ausbreitungs-Geschwindigkeit von Ermüdungsrissen [On the Estimation of the Fatigue Crack Propagation Rate]," *Z. Metallkd.*, Vol. 64, 1973, pp. 453–457.

[10] Rice, J. R. and Rosengren, G. F., "Plane Strain Deformation near a Crack Tip in a Power-Law Hardening Material," *J. Mech. Phys. Solids*, Vol. 16, 1968, pp. 1–12.

[11] Schwalbe, K.-H., "Anwendung der Bruchmechanik auf das Verhalten bei Schwingender Beanspruchung [Application of Fracture Mechanics to the Behavior under Cyclic Loading]," *Verhalten von Stahl unter Schwingender Beanspruchung*, Verlag Stahleisen, Düsseldorf, 1979, pp. 180–189.

[12] Schwalbe, K.-H., "Comparison of Several Fatigue Crack Propagation Laws with Experimental Results," *Eng. Fract. Mech.*, Vol. 6, 1974, pp. 325–341.

[13] Schwalbe, K.-H., "Rissausbreitung bei Statischer und Schwingender Beanspruchung in AlZnMgCu 0.5 [Crack Propagation under Static and Cyclic Loads in AlZnMgCu0.5]," *Oral Presentation at the Meeting of the German Fracture Group*, Aachen, May 20, 1974.

[14] Schwalbe, K.-H., 1977, "Mechanik und Mechanismen des stabilen Risswachstums in Metallischen Werkstoffen [Mechanics and Mechanisms of Stable Crack Propagation in Metallic Materials]," Thesis for Habilitation, Ruhr University Bochum, Bochum, Germany.

[15] Schwalbe, K.-H., *Bruchmechanik Metallischer Werkstoffe*, Hanser, Munich, Vienna, 1980.

[16] Hübner, P., 1996, "Schwingfestigkeit der Hochfesten Schweißbaren Baustähle StE 885 und StE 960 [Fatigue Strength of the High Strength Weldable Steels StE 885 and StE 960]," Ph.D. thesis, School of Mining Freiberg, Freiberg, Germany.

[17] Schwalbe, K.-H., "Bruchflächenuntersuchungen bei der Ausbreitung von Ermüdungsrissen in AlZnMgCu 0,5 F46," *Z. Metallkd.*, Vol. 66, 1975, pp. 408–416.

[18] Shih, C. F., "Relationships Between the *J*-Integral and the Crack Opening Displacement for Stationary and Extending Cracks," *J. Mech. Phys. Solids*, Vol. 29, 1981, pp. 305–326.

[19] Schwalbe, K.-H., "Crack Tip Opening Displacement for Work Hardening Materials," *Int. J. Fract.*, Vol. 25, No. 2, 1984.

[20] Schwalbe, K.-H., "Crack Propagation in AlZnMgCu 0.5 During Static Loading," *Eng. Fract. Mech.*, Vol. 6, 1974, pp. 415–434.

[21] Cornec, A., Heerens, J., and Schwalbe, K.-H., "Bestimmung der Rissspitzenaufweitung CTOD und Rissabstumpfung SZW aus dem J-Integral," *German Fracture Group, Proceedings of the18th Meeting*, Berlin, 1986, Deutscher Verband für Materialprüfung (DVM), Berlin.

[22] Heerens, J., Cornec, A., and Schwalbe, K.-H., "Results of a Round Robin on Stretch Zone Width Determination," *Fatigue Fract. Eng. Mater. Struct.*, Vol. 11, 1988, pp. 19–29.

[23] Schwalbe, K. H., Heerens, J., Zerbst, U., Pisarski, H., and Kocak, M., "EFAM GTP 02—the GKSS Test Procedure for Determining the Fracture Behavior of Materials," *Report* GKSS 2002/24, GKSS Research Centre Geesthacht, Geesthacht, Germany, 2002.

[24] ESIS P2-92, 1992, "ESIS Procedure for Determining the Fracture Behavior of Materials," European Structural Integrity Society, Delft (copies available from K.-H. Schwalbe).

[25] ISO 12135:2002(E), 2002, "Metallic Materials—Unified Method of Test for the Determination of Quasistatic Fracture Toughness," International Standards Organization, Geneva, Switzerland.

[26] Schwalbe, K.-H., Hayes, B., Baustian, K., Cornec, A., Gordon, R., Homayun, M., and Voss, B., "Validation of the Fracture Mechanics Test Method EGF P1-87D (ESIS P1-90/ESIS P1-92)," *Fatigue Fract. Eng. Mater. Struct.*, Vol. 16, 1993, pp. 1231–1284.

[27] Rice, J. R., McMeeking, R. M., Parks, D. M., and Sorensen, E. P., "Recent Finite Element Studies in Plasticity and Fracture Mechanics," *Comput. Methods Appl.*

Mech. Eng., Vol. 17–18, 1979, pp. 411–442.

[28] Rice, J. R. and Johnson, M. A., "The Role of Large Crack Tip Geometry Changes in Plane Strain Fracture," *Inelastic Behavior of Solids*, M. F. Kanninen et al., Eds., Mc.Graw Hill, New York, 1970.

[29] Schwalbe, K.-H. and Heerens, J., "Proposed Modifications of ASTM E813-81 Standard Test Method for J_{Ic}," *Nucl. Eng. Des.*, Vol. 87, 1985, pp. 101–107.

[30] Schwalbe, K.-H., "Some Aspects of Crack Propagation Under Monotonic and Cyclic Load," *Eng. Fract. Mech.*, Vol. 9, 1977, pp. 547–556.

[31] Schwalbe, K.-H., "Ausbreitung von Ermüdungsrissen in AlZnMgCu 0.5 F46 [Fatigue Crack Propagation in AlZnMgCu0.5F46]," *Oral Presentation at the Annual Meeting of DGM* (*Deutsche Gesellschaft für Metallkunde*), Villach, Austria, June 1973.

[32] Schwalbe, K.-H. and Backfisch, W., "Correlation Between Fracture Toughness, Tensile Properties, Fracture Morphology, and Microstructure of a High-Strength Steel," *Fracture 1977, Proceedings of ICF4*, Vol. 3, Waterloo, Canada, 1977, University of Waterloo, Waterloo, Canada.

[33] Clausing, D. P., "Effect of Plane Strain State on Ductility and Toughness," *Int. J. Fract. Mech.*, Vol. 6, 1970, pp. 71–85.

[34] McClintock, F. A., "A Criterion for Ductile Fracture by Internal Necking of Cavities," *J. Inst. Met.*, Vol. 96, 1968, p. 360.

[35] Schwalbe, K.-H., "Einige Eigenschaften des Stabilen Risswachstums und ihre Näherungsweise Berechnung [Some properties of Stable Crack Propagation and Their Approximate Estimation]," *Oral Presentation at the Ninth Meeting of the German Fracture Group*, Aachen, 1977.

[36] Schwalbe, K.-H., "On the Influence of Microstructure on Crack Propagation Mechanisms and Fracture Toughness of Metallic Materials," *Eng. Fract. Mech.*, Vol. 9, 1977, pp. 795–832.

[37] Heerens, J. and Read, D. T., "Fracture Behavior of a Pressure Vessel Steel in the Ductile-to-brittle Transition Regime," *NISTIR* 88-3099, National Institute of Standards and Technology, Boulder, CO, 1988.

[38] Heerens, J., Read, D. T., Cornec, A., and Schwalbe, K.-H., "Interpretation of Fracture Toughness in the Ductile-to-Brittle Transition Region by Fractographical Observations," *Defect Assessment in Components—Fundamentals and Applications, ESIS/EGF Publication 9*, J. G. Blauel and K. H. Schwalbe, Eds., Mechanical Engineering Publications Limited, London, 1991, pp. 659–678.

[39] Heerens, J., Anantharaman, S., Hebenbrock, D., and Schwalbe, K.-H., "Einfluss von Neutronenbestrahlung auf das Sprödbruchverhalten des Druckbehälterstahls 20MnMoNi55 [Effect of Neutron Radiation on the Brittle Fracture Behaviour of the Pressure Vessel Steel 20MnMoNi55]," *Proceedings of the 25th meeting of the German Fracture Group*, Deutscher Verband für Materialforschung und Prüfung, Berlin, 1977, pp. 223–228.

[40] Hahn, G. T. and Rosenfield, A. R., "The Variation of K_{Ic} with Temperature and Loading Rate," *Metall. Trans.*, Vol. 2, 1971, pp. 537.

[41] Ritchie, R. O., Knott, J. F., and Rice, J. R., "On the Relationship Between Critical Tensile Stress and Fracture Toughness in Mild Steel," *J. Mech. Phys. Solids*, Vol. 21, 1973, pp. 395–410.

[42] Schwalbe, K.-H., "Finite Element Solutions for Crack-Tip Behavior in Small Scale Yielding," *Trans. ASME, Ser. B*, 1977, pp. 186–188.

[43] Tracey, D. M., "Finite Element Solutions for Crack-Tip Behavior in Small Scale Yielding," *Trans. ASME, Ser. B*, 1976, pp. 146–151.

[44] Heerens, J., Zerbst, U., and Schwalbe, K.-H., "Strategy for Characterizing Fracture

Toughness in the Ductile to Brittle Transition Regime," *Fatigue Fract. Mater. Struct.*, Vol. 16, 1993, pp. 1213–1230.

[45] Neimitz, A., Graba, M., and Galkiewicz, J., "An Alternative Formulation of the Ritchie–Knott–Rice Local Fracture Criterion," *Eng. Fract. Mech.*, Vol. 74, 2007, pp. 1308–1322.

[46] Dugdale, D. S., "Yielding of Steel Containing Slits," *J. Mech. Phys. Solids*, Vol. 8, 1960, pp. 100.

[47] Bilby, B. A., Cottrell, A. H., and Swinden, K. H., *Proc. R. Soc. London, Ser. A*, No. 297, 1964, p. 1.

[48] Schwalbe, K.-H., "A Modification of the COD Concept and Its Tentative Application to the Residual Strength of Center Cracked Panels," *Fracture Mechanics: 12th Conference, ASTM STP 700*, West Conshohocken, PA, 1980, P. C. Paris, Ed., ASTM International, West Conshohocken, PA, pp. 500–512.

[49] Erdogan, F. and Bakioglu, M., "Crack Opening Stretch in a Plate of Finite Width," *Int. J. Fract.*, Vol. 8, 1975, pp. 1031–1039.

[50] Schwalbe, K.-H., "A Simple Engineering Treatment of Center Cracked Tension Panels in the Regime of Non-Linear Fracture Mechanics Under Plane Stress Conditions," *Report* GKSS 84/E/38, GKSS Research Centre Geesthacht, Geesthacht, Germany, 1984.

[51] Kumar, V., German, M. D., and Shih, C. F., "An Engineering Approach for Elastic-Plastic Fracture Analysis," *EPRI Report* NP 1931, Electric Power Research Institute, Palo Alto, 1981.

[52] Schwalbe, K.-H., Zerbst, U., Kim, Y.-J., Brocks, W., Cornec, A., Heerens, J., and Amstutz, H., "EFAM ETM 97—the ETM Method for Assessing the Significance of Crack-Like Defects in Engineering Structures, Comprising the Versions ETM 97/1 and ETM 97/2," *Report* GKSS 98/E/6, GKSS Research Centre Geesthacht, Geesthacht, Germany, 1998.

[53] Schwalbe, K.-H., Zerbst, U., Brocks, W., Cornec, A., Heerens, J., and Amstutz, H., "The ETM Method for Assessing the Significance of Crack-Like Defects in Engineering Structures," *Fatigue Fract. Eng. Mater. Struct.*, Vol. 21, 1998, pp. 1215–1231.

[54] Schwalbe, K.-H., "Introduction of δ_5 as an Operational Definition of the CTOD and Its Practical Application," *Fracture Mechanics: 26th Volume, ASTM STP 1256*, W. G. Reuter, J. H. Underwood, and J. C. Newman, Eds., ASTM International, West Conshohocken, PA, 1997, pp. 763–778.

[55] ASTM E2472-06, 2008, "Standard Test Method for Determination of Resistance to Stable Crack Extension Under Low-Constraint Conditions," *Annual Book of ASTM Standards*, Vol. 03.01, ASTM International, West Conshohocken, PA, pp. 1397–1422.

[56] ISO 22889:2007(E), 2007, "Metallic Materials—Method of Test for the Determination of Resistance to Stable Crack Extension Using Specimens of Low Constraint," ISO, Geneva, Switzerland.

[57] ESIS P3-09, "Unified Procedure for Determining the Fracture Resistance of Materials," European Structural Integrity Society, Milano, Italy (being prepared for submission to Engineering Fracture Mechanics).

[58] Su, H., Cornec, A., and Schwalbe, K.-H., "Engineering Treatment Model (ETM) for Crack Driving Force Estimation of Structures with Stress Concentration," *J. Pressure Vessel Technol.*, Vol. 115, 1993, pp. 164–170.

[59] Schwalbe, K.-H., "Prediction of Load Point Displacement and J-Integral Using ETM—Progress Report on Elastic-Plastic Flaw Assessment Methods," *Report* GKSS 89/E/3, GKSS Research Centre Geesthacht, Geesthacht, Germany, 1989.

[60] Schwalbe, K.-H., Cornec, A. and Baustian, K. "Application of Fracture Mechanics Principles to Austenitic Steels," *Int. J. Pressure Vessels Piping*, Vol. 65, 1996, pp. 193–207.

[61] Zerbst, U., Ainsworth, R. A., and Schwalbe, K.-H., "Basic Principles of Analytical Flaw Assessment Methods," *Int. J. Pressure Vessels Piping*, Vol. 77, 2000, pp. 855–867.

[62] Ainsworth, R. A., Schwalbe, K.-K., and Zerbst, U., "Crack Driving Force Estimation Methods," *Comprehensive Structural Integrity*, Vol. 7, R. A. Ainsworth and K.-H. Schwalbe, Eds., Elsevier, Oxford, United Kingdom, 2003, pp. 133–176.

[63] Amstutz., H. and Seeger, T., "Spannungs und Verformungszustände einer Dreilochprobe," *Report* Fl-18/1986, Technische Hochschule Darmstadt, Darmstadt, Germany, 1986.

[64] Schwalbe, K.-H., "Some Aspects of the Crack Tip Opening Displacement Concept," *J. Aeronaut. Soc. India*, 1986, pp. 271–285 (Special Issue dedicated to G. R. Irwin).

[65] Dalle Donne, C., "The Crack Tip Displacement Vector Approach to Mixed-Mode Fracture," *Mixed-Mode Crack Behavior, ASTM STP 1359*, K. J. Miller and D. L. McDowell, Eds., ASTM International, West Conshohocken, PA, 1999, pp. 21–40.

[66] Pirondi, A. and Dalle Donne, C., "Characterization of Ductile Mixed-Mode Fracture with the Crack-Tip Displacement Vector," *Eng. Fract. Mech.*, Vol. 68, 2001, pp. 1385–1402.

[67] Pirondi, A. and Dalle Donne, C., "Mixed Mode Fracture of a Ferritic Steel," *Proc. Fifth International Conference on Biaxial/Multiaxial Fatigue and Fracture*, Vol. 2, Technical University of Opole, Poland, 1997, E. Macha and Z. Mroz, Eds., Technical University of Opole, Opole, Polandpp. 559–576.

[68] Schwalbe, K.-H. and Grüter, L., "Ductile Crack Growth Under Plane Stress Conditions: Size Effects and Structural Assessment—II. Assessment of Circumferential Through-Cracks in Austenitic Steel Pipes Using the δ_5 Technique and the Engineering Treatment Model," *Eng. Fract. Mech.*, Vol. 42, 1992, pp. 221–235.

[69] Hamann, R., Zerbst, U., and Beeck, F., "Vergleich Unterschiedlicher Bruchmechanischer Bewertungsverfahren am Beispiel Zweier Innendruckbelasteter Hohlzylinder [Comparison of Several Fracture Mechanics Assessment Methods by Means of Two Internally Pressurized Cylinders]," *Proceedings of the 25th Meeting of the German Fracture Group*, Berlin, 1977, Deutscher Verband für Materialforschung und Prüfung, Berlin, pp. 223–228.

[70] Willoughby, A. A. and Garwood, S. J., "Ductile Fracture in Thin Section Pipeline Material," *TWI Contract Report* 3591/2/81, The Welding Institute, Cambridge, United Kingdom, 1981.

[71] Zerbst, U., Primas, R., Schindler, H.-J., Heerens, J., and Schwalbe, K.-H., "The Fracture Behaviour of a Welded Tubular Joint—an ESIS TC1-3 Round Robin on Failure Assessment Methods, Part IV: Application of the ETM 97/1," *Eng. Fract. Mech.*, Vol. 69, 2002, pp. 1129–1148.

[72] Connolly, M. P., Hellier, A. K., Dover, W. D., and Sutomo, J., "A Parametric Study of the Ratio of Bending to Membrane Stress in Tubular Y- and T-Joints," *Int. J. Fatigue*, Vol. 12, 1990, pp. 3–11.

[73] Alexandrov, S., Zerbst, U., and Schwalbe, K.-H., "Limit Load Solution for Cracked Tubular T-Joints Loaded in Tension," *Fatigue Fract. Eng. Mater. Struct.*, Vol. 21, 1998, pp. 1249–1257.

[74] ASTM E1290-07, 2008, "Standard Test Method for Crack-Tip Opening Displacement (CTOD) Fracture Toughness Measurement," *Annual Book of ASTM Standards*, Vol. 03.01, ASTM International, West Conshohocken, PA, pp. 923–835.

[75] Zerbst, U., Heerens, J., and Schwalbe, K.-H., "The Fracture Behavior of a Welded

Tubular Joint—an ESIS TC1.3 Round Robin on Failure Assessment Methods, Part I: Experimental Data Base and Brief Summary of the Results," *Eng. Fract. Mech.*, Vol. 69, 2002, pp. 1093–1110.
[76] Schwalbe, K.-H., "The Crack Tip Opening Displacement and J Integral Under Strain Control and Fully Plastic Conditions Estimated by the Engineering Treatment Model for Plane Stress Tension," *Fracture Mechanics: Twenty-Fourth Volume, ASTM STP 1207*, J. D. Landes, D. E. McCabe, and J. A. M. Boulet, Eds., ASTM International, West Conshohocken, PA, 1994, pp. 636–651.
[77] Hao, S., 1986, "Crack Tip Large Deformation Field Solution and Applications to Safety Assessment of Pressure Vessel with Defects in HIgh-Strain Zone," Ph.D. thesis, Zhejang University, P.R. China.
[78] Hao, S., Cornec, A., and Schwalbe, K.-H., "Engineering Treatment Model (ETM) for Crack Driving Force Estimation of Structures with Stress Concentration," *Trans. ASME, Ser. B*, Vol. 115, 1993, pp. 164–170.
[79] Kocak, M., Knaack, J., and Schwalbe, K.-H. "Fracture Behaviour of Undermatched Weld Joints," *Proceedings of the Ninth International Conference of Offshore Mechanics and Arctic Engineering*, M. M. Salama, H. C. Rhee, J. G. Williams, and S. Liu, Eds., Offshore Mechanics and Arctic Engineering (OMAE), Houston, TX, 1990, pp. 453–459.
[80] Schwalbe, K.-H., Kim, Y.-J., Cornec, A., and Kocak, M., "EFAM ETM-MM 96—the ETM Method for Assessing the Significance of Crack-Like Defects in Joints with Mechanical Heterogeneity (Strength Mis-Match)," *Report* GKSS 97/E/9, GKSS Research Centre, Geesthacht, Germany, 1997.
[81] Schwalbe, K.-H., "Effect of Weld Metal Mis-Match on Toughness Requirements: Some Simple Analytical Considerations Using the Engineering Treatment Model (ETM)," *Int. J. Fract.*, Vol. 56, 1992, pp. 257–277.
[82] Schwalbe, K.-H., "Welded Joints with Non-Matching Weld Metal—Crack Driving Force Considerations on the Basis of the Engineering Treatment Model (ETM)," *Int. J. Fract.*, Vol. 62, 1993, pp. 1–24.
[83] PD6493, 1980, "Guidance on Some Methods for the Derivation of Acceptance Levels for Defects in Fusion Welded Joints," British Standards Institution, London.
[84] Hao, S., Cornec, A., and Schwalbe, K.-H., "Plastic Stress-Strain Fields and Limit Loads of a Plane Strain Cracked Tensile Panel with a Mismatched Welded Joint," *Int. J. Solids Struct.*, Vol. 34, 1997, pp. 297–311.
[85] Schwalbe, K.-H., Hao, S., and Cornec, A., "ETM-MM—The Engineering Treatment Model for Mis-Matched Welded Joints," *Mis-Matching of Welds*, K.-H. Schwalbe and M. Kocak, Ed., Mechanical Engineering Publications, London, 1994, pp. 539–560.
[86] Zhang, J. X., Shi, Y. W., and Tu, M. J., "Studies on the Fracture Mechanics Parameters of Weldment with Mechanical Heterogeneity," *Eng. Fract. Mech.*, Vol. 34, 1989, pp. 1041–1050.
[87] Hao, S., Cornec, A., and Schwalbe, K.-H., "On the Crack Driving Force and Constraint State in a Mis-Matched Welded Plate Under Tension," *Mis-Matching of Welds*, K.-H. Schwalbe and M. Kocak, Ed., Mechanical Engineering Publications, 1994, pp. 561–571.
[88] Hao, S., Schwalbe, K.-H., and Cornec, A., "The Effect of Yield Strength Mis-Match on The Fracture Analysis of Welded Joints: Slip-Line Field Solutions for Pure Bending," *Int. J. Solids Struct.*, Vol. 37, 2000, pp. 5385–5411.
[89] Kim, Y.-J. and Schwalbe, K.-H., "Numerical Analyses of Strength Mis-Match Effect on Local Stresses for Ideally Plastic Materials," *Eng. Fract. Mech.*, Vol. 71, 2004, pp. 1177–1199.

[90] Varias, A. G., Suo, R. J., and Shih, F. C., "Ductile Failure of a Constrained Metal Foil," *J. Mech. Phys. Solids*, Vol. 39, 1991, pp. 963–986.

[91] Lin, G., Kim, Y.-J., Cornec, A., and Schwalbe, K.-H., "Fracture Toughness of a Constrained Metal Layer," *Comput. Mater. Sci.*, Vol. 9, 1997, pp. 36–47.

[92] Kim, Y.-J., Schwalbe, K.-H., and Ainsworth, R. A., "Simplified J Estimations Based on the Engineering Treatment Model for Homogeneous and Mismatched Structures," *Eng. Fract. Mech.*, Vol. 68, 2001, pp. 9–27.

[93] Ganti, S., Parks, D. M., and McClintock, F. A., "Analysis of Strength Mis-Matched Interfacial Cracks in SSY," *Mis-Matching of Interfaces and Welds*, K.-H. Schwalbe and M. Kocak, Ed., GKSS Research Centre, Geesthacht, Germany, 1997, pp. 3–16.

[94] Dexter, R. J., "Significance of Strength Undermatching of Welds in Structural Behavior," *Mis-Matching of Interfaces and Welds*, K.-H. Schwalbe and Kocak, M., Eds., GKSS Research Centre, Geesthacht, Germany, 1997, pp. 55–73.

[95] Chiesa, M., Skallerud, B., and Thaulow, C., "Fracture Analysis of Strength Mis Matched Welded Wide Plates by Line Spring Elements," *Eng. Fract. Mech.*, Vol. 68, 2001, pp. 987–1001.

[96] Betegón, C. and Penuelas, I., "A Constraint Based Parameter for Quantifying the Crack Tip Stress Fields in Welded Joints," *Eng. Fract. Mech.*, Vol. 73, 2006, pp. 1865–1877.

[97] Webster, S., ed., "Structural Integrity Assessment Procedures for European Industry (SINTAP)," *Eng. Fract. Mech.*, Vol. 67, 2000 (Special Issue).

[98] Zerbst, U., Schödel, M., Webster, S., and Ainsworth, R. A., *Fitness-for-Service Fracture Assessment of Structures Containing Cracks*, Elsevier, Oxford, 2007.

[99] Kim, Y.-J., Kocak, M., Ainsworth, R. A., and Zerbst, U., "SINTAP Defect Assessment Procedures for Strength Mismatch Structures," *Eng. Fract. Mech.*, Vol. 67, 2000, pp. 529–546.

ELASTIC-PLASTIC FRACTURE MECHANICS AND FRACTURE MECHANISMS

Reprinted from JAI, Vol. 7, No. 1
doi:10.1520/JAI102431
Available online at www.astm.org/JAI

Enrico Lucon,[1] *Ann Leenaers,*[1] *Willy Vandermeulen,*[1] *and Marc Scibetta*[1]

Investigation of Transition Fracture Toughness Variation within the Thickness of Reactor Pressure Vessel Forgings

ABSTRACT: An investigation has been conducted on the influence of the through-thickness sampling position on the tensile and fracture toughness properties of reactor pressure vessel forgings, using material from two actual pressurized water reactor vessels. The aim was to quantify the safety margins entailed by extracting surveillance samples from the 1/4T and 3/4T positions, as recommended by the current legislation. For each forging, seven layers have been considered: Inner surface, 1/8T, 1/4T, 1/2T, 3/4T, 7/8T, and outer surface; for each position, two tensile tests at room temperature and 16 fracture toughness tests in the ductile-to-brittle transition region have been performed. In terms of tensile properties, for both forgings the strength is higher at the surfaces than in the centre, while ductility (elongations and reduction of area) is substantially unaffected. For both materials, fracture toughness is better at the surfaces than in the central portion, although differences in terms of Master Curve reference temperatures are statistically not relevant at the 95 % confidence level. This effect is more pronounced for one of the materials, due to the larger amount of material removed with respect to the original heat-treated forging, and is qualitatively confirmed by metallographic observations. The results obtained from this study are in substantial agreement with similar studies found in the literature, although most authors have reported larger differences between surface and central layers.

KEYWORDS: sampling position, fracture toughness, RPV forgings, PWR pressure vessel, Master Curve

---

Manuscript received March 19, 2009; accepted for publication September 14, 2009; published online October 2009.

[1] Institute for Nuclear Material Science, SCK•CEN, Boeretang 200, B-2400, Mol, Belgium.

Cite as: Lucon, E., Leenaers, A., Vandermeulen, W. and Scibetta, M., "Investigation of Transition Fracture Toughness Variation within the Thickness of Reactor Pressure Vessel Forgings," *J. ASTM Intl.*, Vol. 7, No. 1. doi:10.1520/JAI102431.

Introduction

In the construction of the pressure vessels of nuclear power plants, the increase in reactor power has lead to the increase in the dimensions of the vessels, and particularly the thickness. This has in turn guided the choice of the structural material (reactor pressure vessel (RPV) steel) from C-Mn to Mn-Mo and finally to Mn-Ni-Mo steels, in an effort to improve the quenchability and the core toughness of the component, without impairing the material weldability.

The typical heat treatment of RPV forgings consists of quenching, tempering and post-weld heat treatment; methods and conditions are given in American Society of Mechanical Engineers (ASME) and ASTM specifications [1,2].

Quenching consists of cooling the material in water after austenitizing at high temperatures. Indeed, the practice of double austenitization has been recommended: the first austenitization is performed at a sufficiently high temperature to achieve dissolution of the carbides precipitated during the slow post-forging cooling; the second low temperature austenitization, followed by water quenching, produces the definitive grain size [3].

A finer microstructure and hence a better toughness for the final product can be obtained by increasing the cooling rate and by optimizing the tempering conditions. However, in the case of extremely heavy and thick components such as RPVs, it is substantially impossible to increase the cooling rate above $30^{\circ}\mathrm{C/min}$ [3]. As far as tempering is concerned, ASME/ASTM specifications prescribe that tempering be performed above $650^{\circ}\mathrm{C}$ for at least 30 min per inch thickness of the vessel wall; this corresponds to more than 5 h for vessels of 10 in. thickness (250 mm). If post-weld heat treatment is performed in order to relieve residual stresses, ASME/ASTM specifications allow tempering at $635^{\circ}\mathrm{C}$ or above. The fracture toughness of low-alloy steels is very strongly dependent on microstructural features such as the grain size and the post-quenching microstructure; generally, a decrease in grain size corresponds to an increase of toughness [3].

Besides the grain size, the role of microstructure is essential. Typical cooling rates during water quenching of thick components range from $10{,}000^{\circ}\mathrm{C/h}$ at the surface (corresponding to a fully bainitic structure) to $400^{\circ}\mathrm{C/h}$ in the core region (corresponding to 40 % ferrite). It has been reported [3] that an increase in the ferrite content yields a clear increase of toughness (represented by the 50 % shear fracture appearance temperature measured from Charpy tests), whereas the nil ductility temperature (NDT) measured by means of Pellini/drop weight tests is substantially unaffected.

The different microstructures/grain sizes produced by quenching cause a significant heterogeneity in the fracture toughness of a pressure vessel through the wall thickness, where significantly higher toughness is expected for the surface layers (inner surface (IS); outer surface (OS)) with respect to the central portion (i.e., between 1/4T and 3/4T, where T = thickness). This is confirmed by several literature studies, as will be reported next. It must however be noted that, after manufacture and heat treatment, the forged rings are machined down to the final size (thickness). Therefore, the IS and OS of the vessel wall do not actually correspond to the surfaces of the original heat-treated forging.

The main objective of this study was to investigate the variation of the fracture toughness in the ductile-to-brittle transition regime for two typical SA 508 Cl. 3 RPV forgings. In particular, the aim was to quantify the margins of conservatism in terms of Master Curve reference temperature T_0, when using surveillance samples extracted from the 1/4T or 3/4T position, with respect to the fracture toughness of the vessel at the surface position.

Short Literature Review

Four studies have been reviewed, covering the period 1970–2006. Depending on the era in which results were produced, toughness was characterized in terms of Charpy impact properties or Master Curve reference temperature; in some cases, tensile properties were also reported.

Heavy Section Steel Technology Plates

This program [4,5] was executed around 1970, in order to determine the effect of flaws, material inhomogeneities and discontinuities on the behavior of pressure vessels under normal and accident conditions, using several ASTM A533 Type B Class 1 steel plates with a thickness of 30.5 cm (12 in.). During quenching, the temperature was measured by means of thermocouples located at different depths; it was reported in Ref 4 that the cooling rate at the surface was more than ten times higher than in the central region.

Mechanical properties such as tensile strength, hardness, and NDT, show a variation from the surface to about 50 mm below the surface. In the central region, most properties remain constant except for hardness, which shows a depression in the middle position. NDT results are confirmed by the transition curves of the Charpy absorbed energy: the 30 ft lb (40.7 J) transition temperature at the 1/4T and 1/2T positions is about 0°C while at the surface it is −80°C. A similar behavior is shown from dynamic tear tests: in lower shelf conditions the more external layers have a considerably more brittle behavior compared to the central layers, which all show approximately the same characteristics. In upper shelf (fully ductile) conditions, more difference is observed between the central layers.

HEW A533B Steel Plate

HEW designates material from the decommissioned Shoreham, NY boiling water RPV [6,7].

Tensile tests were performed on specimens machined in the L direction at various depths in the plate (thickness of 150 mm, with a 6-mm cladding). Similarly, the Master Curve reference temperature T_0 was measured throughout the plate thickness using precracked Charpy (PCC, C(T) and SE(B)) specimens, all in L-S orientation.

It was observed that in the depth range of 12–138 mm, position has very little effect on the tensile properties. As far as fracture toughness is concerned, Fig. 1 shows the T_0 temperature measured at different positions and obtained using the three types of specimens. The letters indicate the layer from which the specimens were cut. Each layer is approximately 16 mm, meaning that the

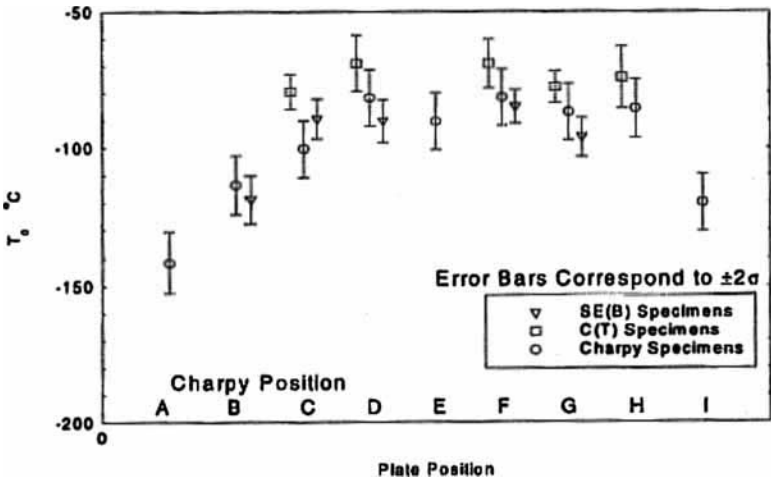

FIG. 1—*HEW A533B steel plate: Master Curve reference temperature versus crack position for three specimen geometries.*

crack tips of Layer A are at about 8 mm from the surface. The crack tip of Layer I (cladding side) is reported to extend 0.25 mm into the base material. From Fig. 1 it can be seen that between Positions C to H, T_0 values remain almost constant. Positions A (8 mm below the surface), B (40 mm below the surface), and I (8 mm below the surface on cladding side) show a lower T_0 (higher fracture toughness) instead.

IAEA JRQ Correlation Monitor Steel

Two plates (A and B) of ASTM A533 Grade B Class 1 steel, with thickness of 225 mm, were manufactured to serve as a reference material in International Atomic Energy Agency (IAEA) irradiation programs [8].

Acceptance tests were performed on both plates, as well as more extensive testing on two parts of Plate A (tensile, Charpy impact, and Master Curve fracture toughness).

In terms of tensile properties variation from a depth of 35 mm to the plate centre, test results do not vary systematically, although data reported by one laboratory show that specimens extracted next to the surface (5 mm depth) have a significantly higher strength.

The through-thickness variation of the Charpy transition temperature at 41 J (T_{41J}) is shown in Fig. 2. In the range of 50–175 mm the transition temperature is rather constant, whereas closer to the surfaces, T_{41J} shows a substantial decrease. In terms of upper shelf energy, the observed scatter was such that no clear trend with plate position was apparent.

The reference temperature was measured through the thickness using PCC specimens in accordance with ASTM E1921-97. The results are shown in Fig. 3: The trend of T_0 with thickness is similar to the trend shown by T_{41J}.

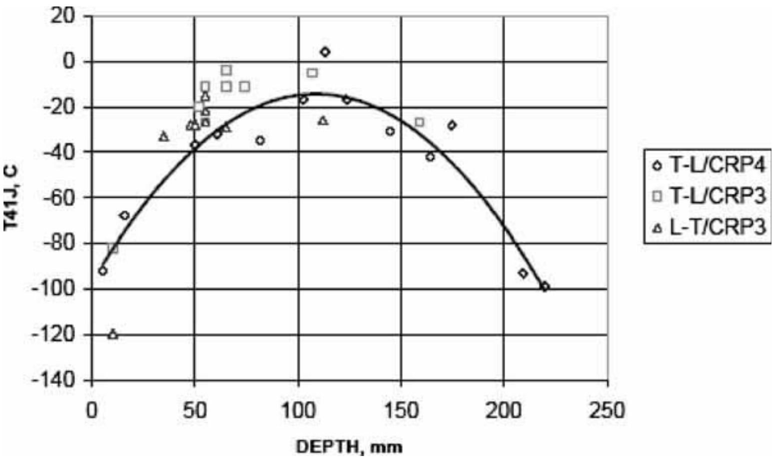

FIG. 2—*JRQ plate: Through-thickness variation of T_{41J}.*

WWER-440 Reactor Pressure Vessel Steel

Two forgings (0.3.1 and 0.3.2), each one 150 mm thick, were cut along the thickness in 13 equally thick slices. PCC specimens, fatigue precracked to $a/W = 0.5$, were extracted from each slice and used to determine the T_0 reference temperature according to the Master Curve procedure [9].

The through-thickness variation of the reference temperature is shown in Fig. 4: for both forgings, T_0 is almost constant in the two central quarters, while

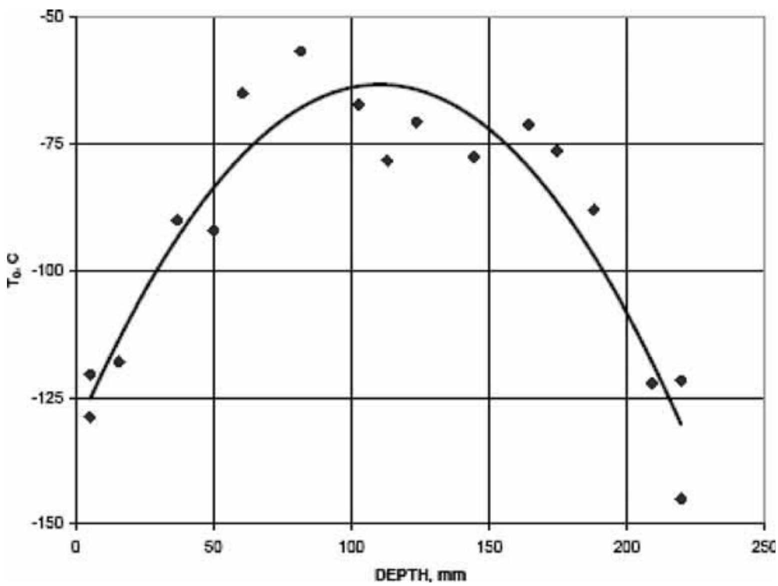

FIG. 3—*JRQ plate: Through-thickness variation of T_0.*

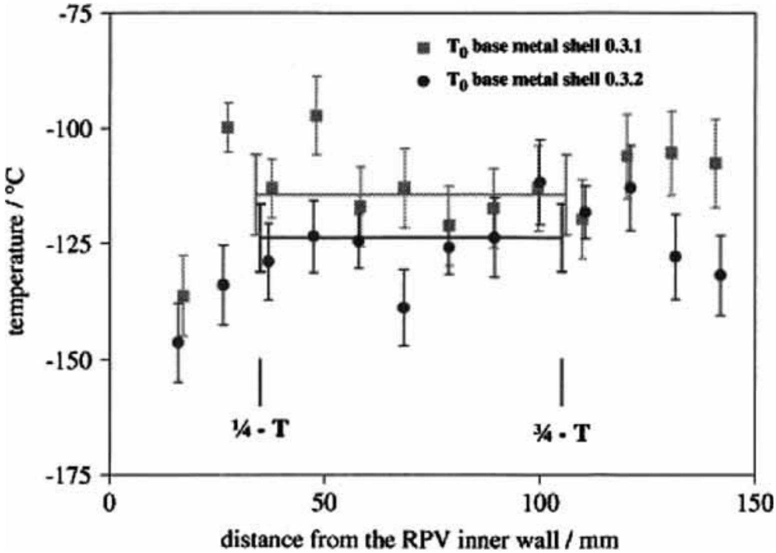

FIG. 4—*Water-Water Energetic Reactor (WWER) 440 plates: Reference temperature T_0 versus distance from the inner RPV wall.*

in the two outer quarters, it decreases towards the surface with the exception of one case where it rises. Since no information is given in Ref 9 on the heat treatment procedure, it is difficult to explain this atypical behavior.

General Observations

- During quenching of thick plates, the cooling rate in the first 50 mm has been reported to be over ten times higher than in the centre;
- The higher cooling rate leads to an increase of the yield and tensile strength and of the reduction of area by about 10 %, with the highest values occurring near the surfaces. Total elongation remains unaffected;
- Charpy transition temperatures or Master Curve reference temperatures at the surface are 35–70°C lower than in the central regions. The thickness of the layer in which the fracture toughness varies significantly is about 50 mm; and
- In the central region, transition or reference temperatures do not seem to change systematically with position. However, actual property variations may be less significant than data scatter.

Significant variations in the microstructure through the thickness have also been reported [10], with grain size ranging from fine near the surfaces to quite coarse in the central section.

Materials and Experimental

Both RPV forgings, here identified as FG1 and FG2, are ASME SA508, Class 3 (FG1) and Class 2 (FG2) materials. Their chemical composition and main mechanical properties are given in Tables 1 and 2.

TABLE 1—*Chemical composition of the two investigated RPV forgings (weight %).*

	C	Si	Mn	P	S	Ni	Mo	Cu	Co
FG1	0.20	0.28	1.43	0.008	0.008	0.75	0.53	0.05	0.013
FG2	0.21	0.26	0.62	0.008	0.007	0.66	0.58	0.05	0.015

Seven positions were investigated through the thickness of each forging: IS, 1/8T, 1/4T, 1/2T, 3/4T, 7/8T, and OS. From each position, two tensile and 16 Charpy specimens were extracted in T and T-L orientation, respectively. Tensile specimens had the following nominal dimensions: total length $L=55$ mm, diameter of the reduced section $D=4$ mm, length of the reduced section $A=20$ mm, heads M8. They were tested at room temperature in accordance with the ASTM E8/E8M-08 Standard. The Charpy specimens were fatigue precracked, side-grooved, and tested in accordance with the ASTM E1921-08 standard for the establishment of the Master Curve reference temperature, T_0, corresponding to each sampling position. Fracture toughness tests were executed at several temperatures within the ductile-to-brittle transition region and analyzed using the multi-temperature approach.

Tensile Test Results

The influence of sampling position on tensile strength is depicted in Figs. 5 and 6 for FG1 and FG2, respectively. The expected trend is observed, in that strength increases closer to the block surfaces with respect to the centre. It is also remarked that the influence of sampling position is more pronounced for FG2 than for FG1; this can be explained by the fact that for FG1 the thickness reduction from the original forging was larger (from 238 to 200 mm, by removing 19 mm from each side) and therefore the difference in cooling rates during water quenching between surface and center of the block is less significant.

Fracture Toughness Test Results

The evolution of the Master Curve reference temperature through the thickness of the two investigated forgings is illustrated in Fig. 7 (FG1) and Fig. 8 (FG2). T_0

TABLE 2—*Main mechanical properties of the two investigated RPV forgings.*

	$R_{p0.2}$ (MPa)	R_m (MPa)	ε_t (%)	RA (%)	T_{41J} (°C)	USE (J)	NDT (°C)
FG1	462	615	27	72	−41	197	−37
FG2	459	607	27	70	−19	204	−18

Note: $R_{p0.2}$ = yield strength; R_m = tensile strength; ε_t = total elongation; RA = reduction of area; T_{41J} = temperature corresponding to a Charpy absorbed energy of 41 J; USE = upper shelf energy from Charpy tests; NDT = nil ductility temperature from drop weight tests.

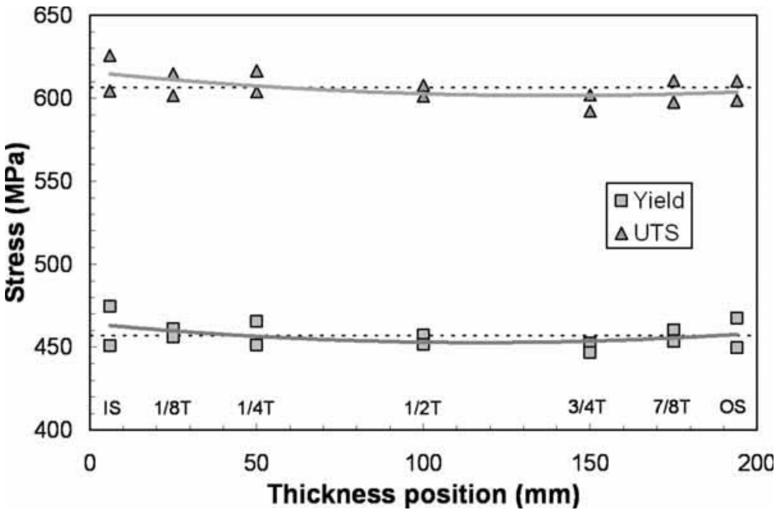

FIG. 5—*Yield and ultimate tensile strengths through the thickness of FG1. Mean values are indicated by dotted lines.*

values are shown with ±2σ error bands. Note that, in accordance with ASTM E1921-08, standard deviations include a 4°C contribution related to experimental uncertainties.

For both forgings, the influence of sampling position on the reference temperature is similar to what has been reported in the literature, i.e., T_0 increasing (toughness decreasing) from the block surfaces to the center. The fact that

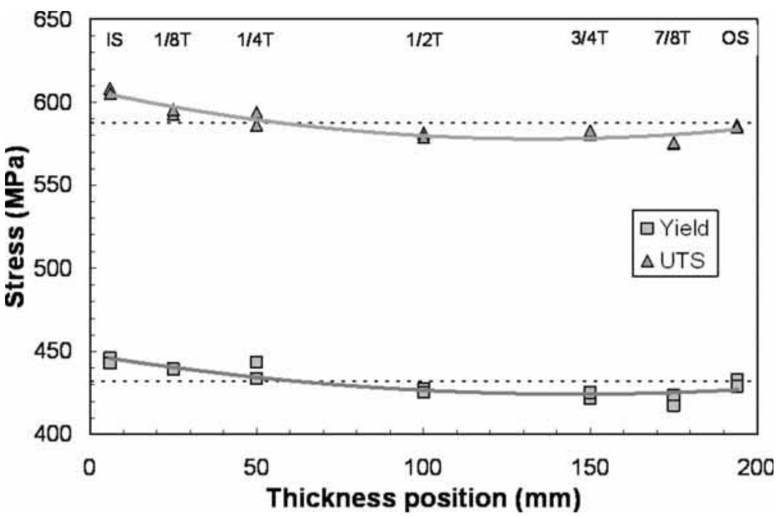

FIG. 6—*Yield and ultimate tensile strengths through the thickness of FG2. Mean values are indicated by dotted lines.*

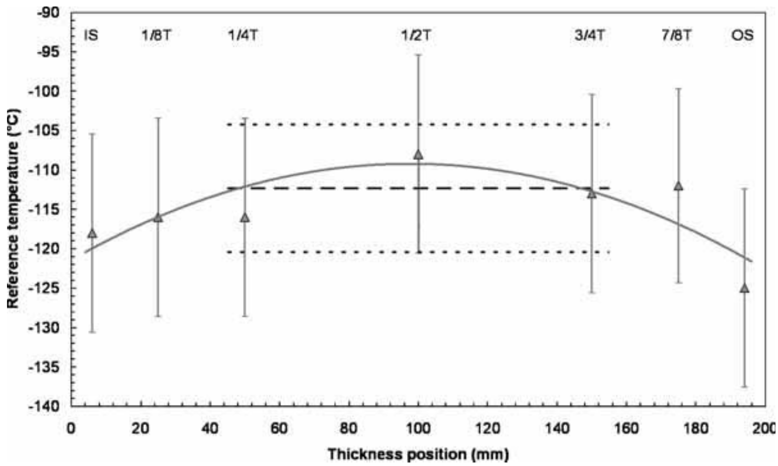

FIG. 7—*Values of reference temperature, with ±2σ error bands, calculated for different positions through the thickness of FG1. The dashed and dotted lines represent the average value of* $T_0 \pm 2\sigma$ *between 1/4T and 3/4T.*

the central position (1/2T) has respectively a higher (Fig. 7) or lower (Fig. 8) value of T_0 than the 1/4T and 3/4T positions does not reflect an actual difference in fracture toughness, but it is only a consequence of material inhomogeneity and experimental uncertainties. Indeed, we observe that, when ±95 % confidence bounds are used, for both materials none of the seven calculated reference temperatures is statistically different from the others.

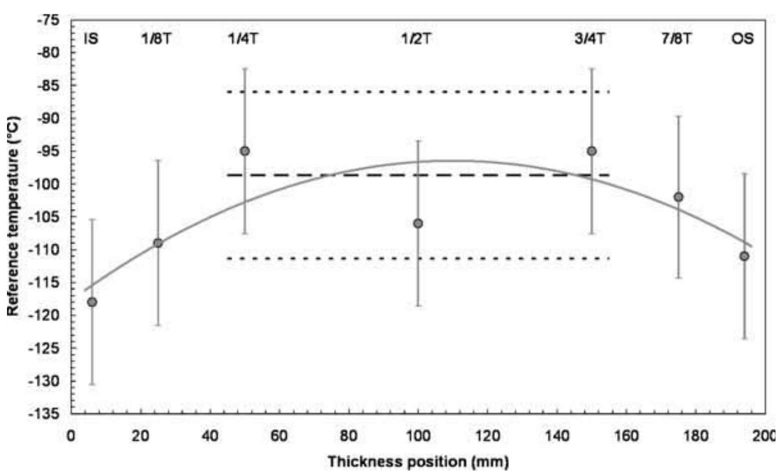

FIG. 8—*Values of reference temperature, with ±2σ error bands, calculated for different positions through the thickness of FG2. The dashed and dotted lines represent the average value of* $T_0 \pm 2\sigma$ *between 1/4T and 3/4T.*

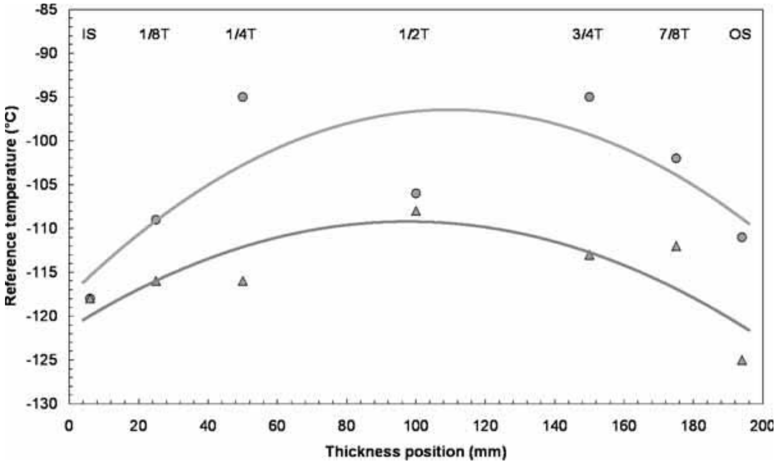

FIG. 9—*Variation of the Master Curve reference temperature through the thickness of the two investigated RPV forgings.*

Moreover, as in the case of tensile properties, a more pronounced position dependence is observed for FG2 than for FG1 (Fig. 9), possibly caused by the more significant material removal with respect to the original forging.

For the materials under investigation and for the test program described, we can quantify the margin of conservatism obtained by extracting surveillance specimens at the 1/4T or 3/4T positions, with respect to the surface positions, as

- FG1: 2–12°C in terms of reference temperature or 2.5–15.7 $\mathrm{MPa}\sqrt{\mathrm{m}}$ in terms of median toughness;
- FG2: 16–23°C in terms of reference temperature or 20.3–31.4 $\mathrm{MPa}\sqrt{\mathrm{m}}$ in terms of median toughness.

These values are still considerably lower than what typically reported in the literature studies previously reviewed: For example, in Ref 11 differences up to 75°C were observed between E1921 valid data sets obtained from the EURO forging.

For both forgings, some asymmetry in the distribution of T_0 through the thickness is noticeable in Fig. 9, pointing at the fact that the cooling rates were probably different between the two surface layers. Whether this is related to an asymmetrical removal of material from the original forging, it is impossible to ascertain.

Metallographic Observations

In order to confirm the observations resulting from the mechanical tests, selected fracture toughness samples from both forgings were subjected to metallographic analyses. The aim was to detect microstructural differences between surface and center layers, which could result from different post-quenching cooling rates and justify the different toughness levels measured.

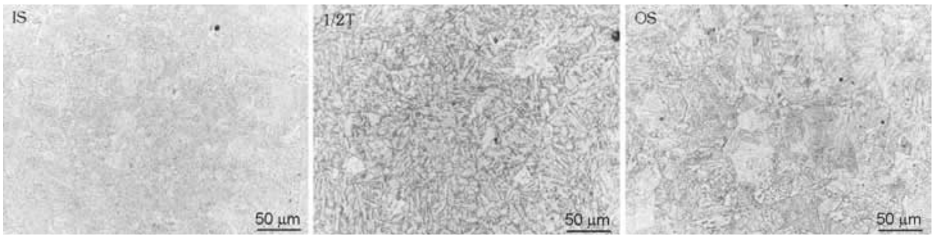

FIG. 10—*Microscopic observations of FG1 samples from positions IS, 1/2T, and OS.*

The micrographs of FG1 (IS, 1/2T, and OS in Fig. 10) show a bainitic structure, with slightly smaller grain size for positions IS and 1/2T. The fact that this finer grain structure is not observed at the OS is likely related either to the fact that more material was removed from this side than from the IS or to processing differences.

In the case of FG2 (Fig. 11), the IS and OS have a typical bainitic structure, while moving towards the center of the forging, some of the prior austenite grain boundaries can be observed and in the central part (1/2T), grains of different size are noticeable. As expected, quenching has not been fully effective in this central part as not all of the austenite is transformed into bainite, and this explains the lower toughness measured in the central portion of the forging (as shown by the general trend in Fig. 8).

Conclusions

Tensile and fracture toughness tests have been conducted at seven different levels within the thickness of two blocks extracted from SA508 RPV forgings.

During the heat treatment of vessel materials, the cooling rate at the surfaces has been reported to be more than ten times higher than in the central portion. As a consequence, tensile strength is expected to be higher at the surfaces and ductile-to-brittle transition temperatures lower.

The main observations which have emerged from the investigation are summarized as follows:

- Consistent with expectations, tensile strengths for both forgings are

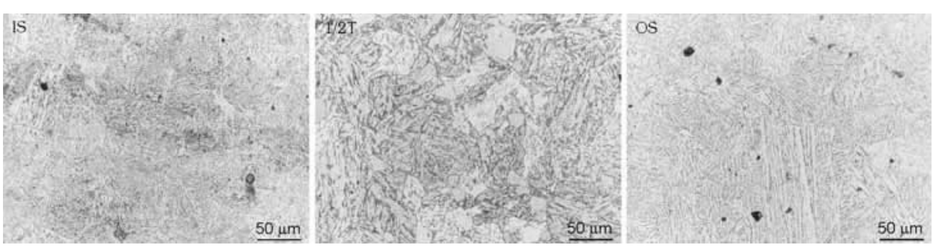

FIG. 11—*Microscopic observations of FG2 samples from positions IS, 1/2T, and OS.*

higher at the surfaces than in the centre. Ductility is practically unaffected;

- For both materials investigated, the values of reference temperature obtained from the Master Curve analyses show that fracture toughness is higher (i.e., T_0 lower) at the block surfaces. The observed differences are lower than what other investigators have previously reported. In all cases, the measured T_0 are not statistically different from each other at the 95 % confidence level;
- The more pronounced effects of sampling location which have been observed on one of the two forgings might be attributed to the larger amount of material which was removed during its final machining, or to processing (cooling rate) differences;
- Metallographic investigations have qualitatively confirmed the observed differences between the outer and central portion of the forgings, as well as the more significant effect of sampling location for the forging denominated FG2; and
- The main implication of this investigation is that, if small underclad cracks have to be assessed in the framework of a pressurized thermal shock study, using the fracture toughness properties measured at 1/4T–3/4T provides a conservative approach. Margins of conservatism are of the order of 7°C for FG1 and 20°C for FG2 in terms of Master Curve reference temperature.

Acknowledgments

This work was partially sponsored by Suez/Tractebel Energy Engineering, whose support is kindly appreciated.

References

[1] ASME SA-508/SA-508M, 1995, "Specification for Quenched and Tempered Vacuum-Treated Carbon and Alloy Steel Forgings for Pressure Vessels," American Society of Mechanical Engineers (ASME), New York, pp. 785–792.

[2] ASTM A508/A508M-05, 1995, "Standard Specification for Quenched and Tempered Vacuum-Treated Carbon and Alloy Steel Forgings for Pressure Vessels," *Annual Book of ASTM Standards*, Vol. 01.05, ASTM International, West Conshohocken, PA, pp. 1–6.

[3] Bocquet, P., Buisine, D., and Dunand-Roux, L., "Les Facteurs Métallurgiques de la Ténacité de l'Acier de Cuve," *Endommagement des matériaux dans les centrales nucléaires à eau pressurisée*, P. Berge and G. Zacharie, Eds., Editions Eyrolles, Paris, 1997.

[4] Canonico, D. A. and Berggren, R. G., "Tensile and Impact Properties of Thick-Section Plate and Weldments," *Technical Report No.* ORNL-TM-3211/CONF-700935-2, Oak Ridge National Laboratory, January 1971, pp. 4–15.

[5] Loss, F. J., "Effect of Mechanical Constraint on the Fracture Characteristics of Thick-Section Steel," *Nucl. Eng. Des.*, Vol. 17, 1971, pp. 16–31.

[6] Joyce, J. A. and Tregoning, R. L., "Development of the T_0 Reference Temperature

from Precracked Charpy Specimens," *Eng. Fract. Mech.*, Vol. 68, 2001, pp. 861–894.

[7] Joyce, J. A. and Tregoning, R. L., "Investigation of Specimen Geometry Effects and Material Inhomogeneity Effects in A533B Steel," *Proceedings ECF14, Fracture Mechanics Beyond 2000*, Vol. II/III, A. Neimitz, I. V. Rokach, D. Kocanda, and K. Golos, Eds., Krakow, September 13–18, 2002, p. 55.

[8] IAEA-TECDOC-1230, 2001, "Reference Manual on the IAEA JRQ Correlation Monitor Steel for Irradiation Damage Studies," IAEA, Vienna.

[9] Viehrig, H.-W., Scibetta, M., and Wallin, K., "Application of Advanced Master Curve Approaches on WWER-440 Reactor Pressure Vessel Steels," *Int. J. Pressure Vessels Piping*, Vol. 83, 2006, pp. 584–592.

[10] Marini, B., "Fracture Toughness Module, FT2—Fracture Properties, Irradiation Effects," *ISMID, International School on Modelling of Irradiation Damage*, October 1–5, 2007, Rochehaut s/Semois, Belgium.

[11] Joyce, J. A. and Gao, X., "Analysis of Material Inhomogeneity in the European Round Robin Fracture Toughness Data Set," *J. ASTM Int.*, Vol. 5, No. 9, 2008.

Reprinted from JAI, Vol. 7, No. 1
doi:10.1520/JAI102505
Available online at www.astm.org/JAI

Xian-Kui Zhu[1] *and James A. Joyce*[2]

More Accurate Approximation of *J*-Integral Equation for Evaluating Fracture Resistance Curves

ABSTRACT: Accurate estimate of the *J* integral is required in a valid experimental evaluation of *J*-based fracture resistance curves for ductile materials. The fracture toughness test standard ASTM E1820 allows a basic method and a resistance curve method to be used experimentally to evaluate the *J* values via standard specimens. The basic method obtains *J* estimates using the η factor method that was developed for a stationary crack. The resistance curve method obtains crack growth corrected *J* estimates using an incremental equation that was proposed by Ernst et al. ("Estimation on *J*-Integral and Tearing Modulus *T* from a Single Specimen Test Record," Fracture Mechanics: Thirteenth Conference, ASTM STP 743, 1981, pp. 476–502) for a growing crack and has been accepted as the most accurate equation available for about three decades. Recently, Neimitz ("The Jump-Like Crack Growth Model, the Estimation of Fracture Energy and J_R Curve," *Eng. Fract. Mech.*, Vol. 75, 2008, pp. 236–252), and Kroon et al. ("A Probabilistic Model for Cleavage Fracture with a Length Scale-Parameter Estimation and Predictions of Growing Crack Experiments," *Eng. Fract. Mech.*, Vol. 75, 2008, pp. 2398–2417) presented two different approximate equations for the *J*-integral, which they proposed as more accurate than the Ernst equation. Therefore, further investigation is needed to determine a truly accurate approximation for the *J*-integral equation. With this objective, the present paper proposes different mathematical and physical models to approximate the *J*-integral equation. The physical models are developed in terms of the deformation theory and the jump-like crack growth assumption. Relations between the proposed models and the existing equations are identified. Systematic evaluations of the proposed models are then made using a theoretical procedure of *J-R* curves for both low and high strain hardening

Manuscript received May 12, 2009; accepted for publication September 17, 2009; published online October 2009.

[1] Battelle Memorial Institute, Columbus, OH, 43201.
[2] Mechanical Engineering Dept., U.S. Naval Academy, Annapolis, MD, 21402.

Cite as: Zhu, X.-K. and Joyce, J. A., "More Accurate Approximation of *J*-Integral Equation for Evaluating Fracture Resistance Curves," *J. ASTM Intl.*, Vol. 7, No. 1. doi:10.1520/JAI102505.

materials, and using experimental data from an actual single edge-notched bend specimen made of HY80 steel. Accuracy of the proposed models is determined, and a more accurate approximation of *J*-integral equation is thus suggested for *J-R* curve testing.

KEYWORDS: *J*-integral, *J-R* curve, incremental *J*-integral equation, crack growth, fracture test

Introduction

Fracture resistance is often characterized by a *J-R* curve, i.e., the *J*-integral plotted against crack extension for ductile materials. As an effective measure of fracture toughness, the *J-R* curve is the most important material property in elastic-plastic fracture mechanics, and has been extensively applied to flaw assessment, material selection, material performance evaluation, fitness-for-service analysis, and structural integrity management for various engineering structures. Examples include nuclear pressure vessels and piping, oil and gas pipelines, petrochemical storage tanks, and aircraft structures.

The *J*-integral concept was proposed by Rice [1] in the late 1960s and used as a measure of the intensity of singularity of elastic-plastic crack-tip fields. The pioneering experimental work of Begley and Landes [2,3] in the early 1970s made the *J*-integral become a measurable material parameter. Since then, broad analytical and experimental investigations have been done in order to develop effective methodologies for estimating the *J*-integral for stationary cracks and *J-R* curves for growing cracks. The early reviews of this topic can be found in Turner [4] and Etemad and Turner [5], and a recent review was given by Zhu et al. [6]. A further technical review of *J* evaluation is given later in this work. Detailed experimental techniques and developments for *J-R* curve testing were documented in an ASTM manual by Joyce [7]. In the earliest *J* test standard ASTM E813 [8], only experimental measurement of the critical *J*-integral at the onset of ductile tearing, J_{Ic}, was accepted as the fracture toughness of the material. The later versions, including ASTM E1152 [9], E1737 [10], and E1820 [11], provided the standard procedures and methods for both J_{Ic} and *J-R* curve testing.

ASTM E1820 is presently used worldwide for measuring the critical *J*-integral and *J-R* curves. The standard specimens include single edge-notched bend [SE(B)], compact tension [C(T)], and disk-shaped C(T) specimens. The recommended test procedure is the elastic unloading compliance method where multiple data points are determined from a single specimen. This test procedure requires continuous measurements of applied load, load-line displacement (LLD), and crack mouth opening displacement (CMOD). The load-CMOD records are used to determine the crack extension, and the load-LLD records in conjunction with the crack extension are used to determine the *J*-integral. For a stationary crack, the *J*-integral for a standard specimen is obtained using the η factor equation and the area under the measured load versus LLD curve. For a growing crack, the *J* integral is determined using an incremental equation proposed by Ernst et al. [12], in which the crack growth correction was considered. This incremental equation has been widely accepted as the most accurate formulation available to obtain crack growth corrected J in a J-R curve test for about three decades. Recently, Neimitz [13] and Kroon et al. [14] presented two different but "better" approximate equations for the J-integral. Therefore, the accuracy of existing approximate equations needs to be justified and a truly accurate J-integral approximation equation needs to be developed.

So motivated, this paper proposes different mathematical and physical models in order to determine a more accurate J-integral approximation equation. The physical models are developed in terms of the deformation theory and the jump-like crack growth assumption. Relations between the proposed models and the existing approximate equations are established, and three representative equations are identified. These representative equations are then evaluated systematically using a theoretical procedure of J-R curves for both low and high strain hardening material models, and using experimental data for an actual SE(B) specimen made of HY80 steel. Detailed comparisons and discussions are given, accuracies of proposed models are determined, and a more accurate approximation of J-integral equation is thus suggested for J-R curve testing.

Brief Review of *J*-Integral Evaluations

J-Integral Estimates for Stationary Cracks

Since the late 1960s when the J integral [1] was proposed, extensive efforts have been devoted to developing experimental methods to evaluate its critical value, J_{Ic}. Begley and Landes [2,3] were the pioneers who first successfully measured J and its critical value, J_{Ic}, using multiple specimens from the interpretation of J as an energy release rate given by

$$J = -\frac{dU}{Bda} \tag{1}$$

where:

U = strain energy,
a = crack length, and
B = specimen thickness.

They tested a series of specimens made of the same geometry but different crack sizes, and measured load-displacement data. From the test data, the energy absorbed by each specimen was obtained, and the J integral was estimated from Eq 1. This approach has obvious disadvantages; principle among them was the need to test multiple specimens and the complicated analysis needed to obtain a single experimental result.

Rice et al. [15] showed that it was possible to determine J directly from the load-displacement curve of a single specimen. For convenience, they introduced two alternative, but equivalent expressions of J as

$$J = \frac{1}{B}\int_0^P \frac{\partial \Delta}{\partial a} dP \tag{2a}$$

or

$$J = -\frac{1}{B}\int_0^\Delta \frac{\partial P}{\partial a} d\Delta \tag{2b}$$

where:

P = total generalized load, and

Δ = associated load-point or LLD.

For deeply cracked SE(B) specimens, Eq 2 was simplified as

$$J = \frac{2}{Bb}\int_0^\Delta P d\Delta = \frac{2A}{Bb} \tag{3}$$

where:

$b = W - a$ = remaining ligament size,

W = specimen width, and

A = area under a P-Δ record.

This simple relationship marks a major step in the development of a practical test method for the J-integral. It is noted that Eq 3 was developed initially for deeply cracked SE(B) specimens in pure bending, where the generalized load was an applied moment M, and the load-point displacement was a relative rotation θ at the beam ends. Equation 3 was also considered to be applicable to three-point bend and C(T) specimens with deep cracks because their remaining ligaments primarily support a bending moment due to an applied load P. A more general relationship of Eq 3 was obtained by Sumpter and Turner [16] as

$$J = \frac{\eta}{Bb}\int_0^\Delta P d\Delta = \frac{\eta A}{Bb} \tag{4}$$

where:

η = LLD-based geometry factor that is a function of a/W only.

The use of the η factor method considerably simplifies the task of determining J, and Eq 4 gives a very convenient way for experimentally evaluating J for any specimen from a single load-displacement record, provided that the η factor is determined for that specimen.

For analytical convenience, a total LLD is often separated into an elastic and a plastic component [17], i.e., $\Delta = \Delta_{el} + \Delta_{pl}$. From this relationship and using Eq 2b, the total J can be similarly split into elastic and plastic components [15,16]

$$J = J_{el} + J_{pl} \tag{5}$$

in which the elastic J can be calculated directly and accurately from the stress intensity factor K, as used in ASTM E1820 for a plane strain crack

$$J_{el} = \frac{K^2(1-\nu^2)}{E} \tag{6}$$

where:

E = Young's modulus, and

ν = Poisson's ratio.

The plastic J is determined from Eqs 2a, 2b, and 4 as

$$J_{pl} = \frac{1}{B}\int_0^P \frac{\partial \Delta_{pl}}{\partial a} dP = -\frac{1}{B}\int_0^{\Delta_{pl}} \frac{\partial P}{\partial a} d\Delta_{pl} = \frac{\eta A_{pl}}{Bb} \tag{7}$$

where η denotes a plastic geometry factor and A_{pl} is the plastic area under the P-Δ_{pl} curve. Equations 5–7 are used as the basic procedure in ASTM E1820 to estimate J_{Ic}, when a crack growth resistance is not desired.

J-Integral Estimates for Growing Cracks

All equations introduced earlier are valid only for determining J and its critical value at fracture initiation for stationary cracks. However, the early J-R curves were obtained directly from Eq 4, with the use of crack extension measured by an unloading compliance technology proposed first by Clark et al. [18]. This result tends to overestimate J for a growing crack because the crack growth correction was not taken into account. Since the J-integral is a non-linear elastic quantity, the J desired at each point during the J-R curve test is the J-integral that would be present at that point if the current crack length had existed from the start of the test. To obtain this value using an R-curve based procedure the user needs to correct the plastic area under the P-Δ_{pl} curve to approximate what it would have if the current crack length had been in the sample from the start of the test. Not correcting the J-integral results in J values that are unconservative.

Different approaches were then developed in order to estimate a crack growth corrected J as needed in an accurate J-R curve evaluation. Two representatives are incremental equations, in which test data are spaced at small intervals of the crack extension and J is evaluated always from the previous step. The first incremental J-integral equation was proposed by Garwood et al. [19] in 1975 for a single edge bending specimen with a deep crack. At the nth step of crack growth, the total J was determined as

$$J_n = J_{n-1}\left(\frac{W-a_n}{W-a_{n-1}}\right) + \frac{2U_4}{B(W-a_{n-1})} \tag{8}$$

where the term U_4 refers to the increment of the area under an actual load-displacement record from step $n-1$ to n. About 10 years later, Eq 8 was generalized by Etemad and Turner and Etemad et al. [5,20] as

$$J_n = J_{n-1}\left(1 + \frac{g(\eta)_n}{(W-a_n)}(a_n - a_{n-1})\right) + \frac{\eta_n \Delta U_{n,(n-1)}}{B(W-a_n)} \tag{9a}$$

where $g(\eta)$ is a geometry factor given by

$$g(\eta) = 1 + \frac{b}{\eta}\frac{d\eta}{da} - \eta \tag{9b}$$

The second incremental J-integral equation was obtained by Ernst et al. [12] in 1981 in reference to the principle of variable separation that determines the condition for the existence of the η-factor method [17]. At the ith step of crack growth, the total J was determined as

$$J_i = \left[J_{i-1} + \frac{\eta_{i-1}}{Bb_{i-1}}A_{i-1,i}\right]\left(1 - \frac{\gamma_{i-1}}{b_{i-1}}(a_i - a_{i-1})\right) \tag{10a}$$

where γ is a geometry factor given by

$$\gamma = \eta - 1 - \frac{b}{W\eta}\frac{d\eta}{d(a/W)} \tag{10b}$$

where:

$A_{i-1,i}$ = incremental area under an actual load-displacement record from step $i-1$ to i.

It is seen from Eqs 9b and 10b that $g(\eta) = -\gamma$. These two types of incremental equations both correct the last step J, but Eq 10a also corrects all that comes before as well. This results in a larger crack growth correction on J from Eq 10a and hence a smaller J estimate is obtained from Eq 10a than from Eq 9a, as shown in an application to test data presented in Ref 12 in Figs. 5–7. In general, these two types of incremental formulation of the J-integral are similarly applicable to any specimen, provided that the two geometry factors, η and γ, are known for that specimen.

In ASTM E1820, the total J is split into elastic and plastic parts, as shown in Eq 5, and determined separately. The objective is to improve the accuracy of J estimates, and to obtain the consistency of J when near linear elastic conditions applied. For a set of discrete experimental data, at each step of crack growth, the elastic component of J is obtained directly from the stress intensity factor using Eq 6, and only the plastic component of J needs to be determined from the η factor method. The incremental J-integral equation developed by Ernst et al. [12] was adopted in ASTM E1152 and its later versions to calculate the plastic J

$$J_{\mathrm{pl}(i)} = \left[J_{\mathrm{pl}(i-1)} + \frac{\eta_{i-1}}{Bb_{i-1}}A_{\mathrm{pl}}^{i-1,i}\right]\left(1 - \frac{\gamma_{i-1}}{b_{i-1}}(a_i - a_{i-1})\right) \tag{11}$$

where $A_{\mathrm{pl}}^{i-1,i}$ is the increment of plastic area under a load-displacement record from step $i-1$ to i

$$A_{\mathrm{pl}}^{i-1,i} = \frac{1}{2}(P_i + P_{i-1})(\Delta_{\mathrm{pl}(i)} - \Delta_{\mathrm{pl}(i-1)}) \tag{12}$$

These two equations are used by ASTM E1820, with a net thickness B_N being used for specimens with side grooves in place of the full thickness B. Small and uniform crack growth increments are required in Eq 11 for accurate estimates of $J_{\mathrm{pl}(i)}$. With the calculated J and measured crack extension of $(a_i - a_0)$, where

a_0 is an original crack length, a *J-R* curve is obtained by applying Eqs 5, 6, and 11 to successive increments of crack growth from a single test.

Note that Anderson [21] proposed another incremental equation equivalent to Eq 9a for the plastic J in a different derivation. Recently, Neimitz [13] obtained a new incremental J equation for SE(B) specimens that is similar to Eq 8, and Kroon et al. [14] gave another J estimate equation that is similar to Anderson's result. Accordingly, these "new" estimate equations may determine an elevated *J-R* curve as compared to the result from Eq 11. Thus, a question arises: Which approximation of the J-integral equation discussed earlier is more accurate? To answer this question, different mathematical and physical models are developed next for estimating J values, and their accuracies are then discussed using theoretical and experimental results.

Mathematical Models

This section deals with pure mathematical models for estimating the J-integral without consideration of its physical meaning. Since the elastic J is directly obtained from the stress intensity factor, only plastic J estimates are discussed herein. Recall the J-integral was developed using the deformation theory of plasticity, and the deformation J_{pl} can be expressed as a unique function of two independent variables: Δ_{pl} and a. As done by Ernst et al. [12], an exact differential of the deformation J_{pl} is expressed for a growing crack as

$$dJ_{\text{pl}} = \frac{\eta}{Bb} P d\Delta_{\text{pl}} - \frac{\gamma}{b} J_{\text{pl}} da \tag{13}$$

Using the single specimen technique, a fracture test obtains multiple discrete experimental data of load, displacement, and crack size. To obtain J_{pl}, a numerical integration technique is needed to integrate the differential Eq 13. The most commonly used numerical integration schemes are Newton-Cotes formulas based on the strategy of replacing a complicated integrand or discrete data with an approximate polynomial, because polynomial functions are easily integrated and can capture a fair amount of curvature of the integrand. The often used versions are rectangular rule, trapezoidal rule, Simpson's 1/3 rule, and Simpson's 3/8 rule that use a zeroth-, first-, second-, and third-order polynomial approximation, respectively. Since the size of crack growth increments varies typically in a fracture test, it is convenient to use the one-step integration rules: The rectangular rule and trapezoidal rule to integrate Eq 13 step by step.

For two adjacent discrete points $i-1$ and i, integrating Eq 13 obtains

$$J_{\text{pl}(i)} = J_{\text{pl}(i-1)} + \frac{1}{B}\int_{\Delta_{\text{pl}(i-1)}}^{\Delta_{\text{pl}(i)}} \frac{\eta}{b} P d\Delta_{\text{pl}} - \int_{a_{i-1}}^{a_i} \frac{\gamma}{b} J_{\text{pl}} da \tag{14}$$

The use of the left rectangular rule, right rectangular rule, and trapezoidal rule for integrating the two integrals in Eq 14 gives three different mathematical solutions described in the following three subsections.

Left Rectangular Rule

The left rectangular rule is used here to perform numerical integration for the two integrals in Eq 14, and one obtains

$$J_{\text{pl}(i)} = J_{\text{pl}(i-1)}\left(1 - \frac{\gamma_{i-1}}{b_{i-1}}(a_i - a_{i-1})\right) + \frac{\eta_{i-1}}{Bb_{i-1}}P_{i-1}(\Delta_{\text{pl}(i)} - \Delta_{\text{pl}(i-1)}) + O((da)^2) \quad (15)$$

where $O((da)^2)$ denotes the second- and higher-order term of crack growth incremental step size, $da = a_i - a_{i-1}$. In other words, $J_{\text{pl}(i)}$ in Eq 15 has an error in the second-order of crack growth increment. When crack growth increments are very small, the error is negligible. Note that plastic displacement increments applied during a fracture test are assumed in this work to have the same order of magnitude as crack growth increments.

Right Rectangular Rule

The right rectangular rule is used in this subsection to do numerical integration for the two integrals in Eq 14, and another incremental J-integral equation is obtained

$$J_{\text{pl}(i)} = \left[J_{\text{pl}(i-1)} + \frac{\eta_i}{Bb_i}P_i(\Delta_{\text{pl}(i)} - \Delta_{\text{pl}(i-1)})\right]\left(1 - \frac{\gamma_i}{b_i}(a_i - a_{i-1})\right) + O((da)^2) \quad (16)$$

This approximate equation has an error of the second-order of crack growth increment, and the following first approximation relationship is used in the deviation of Eq 16:

$$\left(1 + \frac{\gamma_i}{b_i}(a_i - a_{i-1})\right)^{-1} = 1 - \frac{\gamma_i}{b_i}(a_i - a_{i-1}) + O((da)^2) \quad (17)$$

Trapezoidal Rule

In numerical integrations, the trapezoidal rule is considered more accurate than the two rectangular rules because a first-order polynomial approximation is used in lieu of the zeroth-order approximation. Using the trapezoidal rule, Eq 14 becomes

$$J_{\text{pl}(i)} = J_{\text{pl}(i-1)}\left(1 - \frac{1}{2}\left(\frac{\gamma_{i-1}}{b_{i-1}} + \frac{\gamma_i}{b_i}\right)(a_i - a_{i-1})\right) + \left[\frac{1}{2B}\left(\frac{\eta_{i-1}}{b_{i-1}}p_{i-1} + \frac{\eta_i}{b_i}p_i\right)(\Delta_{\text{pl}(i)} - \Delta_{\text{pl}(i-1)})\right]$$
$$\times\left(1 - \frac{\gamma_i}{2b_i}(a_i - a_{i-1})\right) + O((da)^2) \quad (18)$$

To be consistent with Eqs 15 and 16, Eq 18 also keeps the first-order of accuracy with respect to crack growth increment and the approximate relationship in Eq 17 is used. Obviously, Eq 18 is the average of Eqs 15 and 16, and thus Eq 18 would give a better estimate of J-integral than Eq 15 or Eq 16. The first J-R curve test standard, ASTM E1152, included Eq 11 as well as Eq 18, which was considered to be a more accurate estimate of the J-integral. When later standards limited the size of the crack increments allowed, this more complex relationship was felt to be unnecessary and was not included in the later revisions, ASTM E1737 and ASTM E1820.

Physical Models

This section considers physical models of the J-integral estimation in order to determine physically meaningful solutions. Since a continuous crack growth process is often assumed as a jump-like crack growth process [13], an actual loading path can be thus approximated by different segments of deformation paths in a load-displacement space. Accordingly, an integration along the actual loading path can be simplified considerably. For instance, integration of Eq 13 gives a general expression of J_{pl} for a growing crack

$$J_{pl} = \int_0^{\Delta_{pl}} \frac{\eta}{Bb} P d\Delta_{pl} - \int_{a_0}^{a} \frac{\gamma}{b} J_{pl} da \tag{19}$$

This equation holds true for any loading path leading to the current values of a and Δ_{pl}, including the actual loading path for a growing crack, provided that the J-controlled crack growth conditions [22] are satisfied. Based on the jump-like crack growth assumption, the two integrations in Eq 19, along an actual loading path, can be approximated by various step lines consisting of multiple segments of deformation paths, as shown in Fig. 1.

Upper Step Line Approximation

Figure 1(a) illustrates an actual P-Δ_{pl} curve for a growing crack, and three "deformation" paths for an original crack of a_0 and for two arbitrarily stationary cracks of a_{i-1} and a_i that represent two adjacent discrete experimental points. The multiple upper step lines shown in this figure are used to approximate the actual loading path. In particular, an actual loading segment AC for one crack growth step from point $i-1$ to i is approximated by two step lines AB and BC. At points A and C, $J_{pl(i-1)} = J_{pl}^A$ and $J_{pl(i)} = J_{pl}^C$. Integrating Eq 19 along segment AB, one obtains J_{pl} at point B as

$$J_{pl}^B = J_{pl}^A + \frac{\eta_{i-1}}{Bb_{i-1}} A_{pl}^{i-1,i} \tag{20}$$

where $A_{pl}^{i-1,i}$ is the increment of the plastic area under the P-Δ_{pl} curve between $\Delta_{pl(i)}$ and $\Delta_{pl(i-1)}$, as defined in Eq 12, and represents the actual incremental work input done by the applied load. The integration of Eq 19 along segment BC, where the displacement is constant, gives

$$J_{pl}^C = J_{pl}^B - \int_{B(a_{i-1})}^{C(a_i)} \frac{\gamma}{b} J da \tag{21}$$

Applying the three numerical integration rules used in the previous section to integrate the integral in Eq 21, and combining the result with Eq 20, results in three solutions as follows:

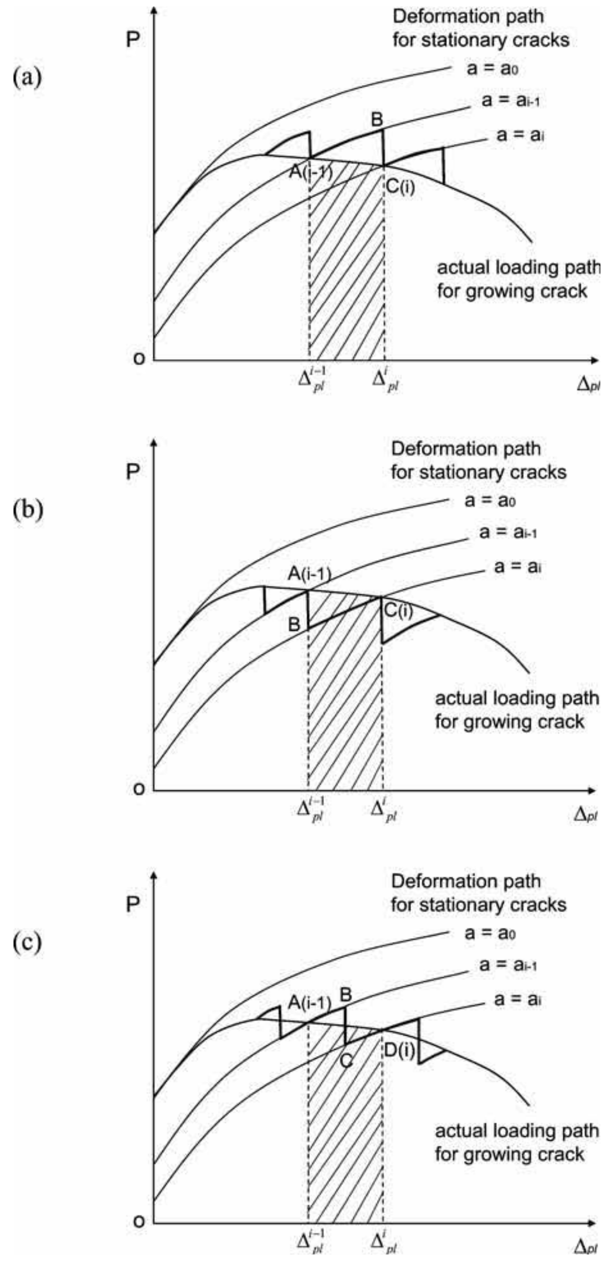

FIG. 1—*Schematic load-plastic displacement curves for stationary and growing cracks:* (*a*) *USLA;* (*b*) *LSLA; and* (*c*) *MSLA.*

(1) Left rectangular rule

$$J_{\mathrm{pl}(i)} = \left[J_{\mathrm{pl}(i-1)} + \frac{\eta_{i-1}}{Bb_{i-1}} A_{\mathrm{pl}}^{i-1,i} \right] \left(1 - \frac{\gamma_{i-1}}{b_{i-1}} (a_i - a_{i-1}) \right) \tag{22}$$

(2) Right rectangular rule

$$J_{\mathrm{pl}(i)} = \left[J_{\mathrm{pl}(i-1)} + \frac{\eta_{i-1}}{Bb_{i-1}} A_{\mathrm{pl}}^{i-1,i} \right] \left(1 - \frac{\gamma_i}{b_i} (a_i - a_{i-1}) \right) \tag{23}$$

(3) Trapezoidal rule

$$J_{\mathrm{pl}(i)} = \left[J_{\mathrm{pl}(i-1)} + \frac{\eta_{i-1}}{Bb_{i-1}} A_{\mathrm{pl}}^{i-1,i} \right] \left(1 - \frac{1}{2} \left(\frac{\gamma_{i-1}}{b_{i-1}} + \frac{\gamma_i}{b_i} \right) (a_i - a_{i-1}) \right) \tag{24}$$

The approximate relationship (Eq 17) is used in the derivation of Eqs 23 and 24. These three incremental equations have ignored the higher-order terms other than $(a_i - a_{i-1})$, and their differences are negligible if crack growth increments are sufficiently small.

Lower Step Line Approximation

Figure 1(*b*) duplicates Fig. 1(*a*), except that the actual loading path is approximated by multiple lower step lines on deformation paths. In particular, an actual loading segment AC for one crack growth step from point $i-1$ to i is approximated by another two step lines AB and BC. At points A and C, $J_{\mathrm{pl}(i-1)} = J_{\mathrm{pl}}^A$ and $J_{\mathrm{pl}(i)} = J_{\mathrm{pl}}^C$. Integrating Eq 19 along segment AB, where the displacement is constant, gives

$$J_{\mathrm{pl}}^B = J_{\mathrm{pl}}^A - \int_{A(a_{i-1})}^{B(a_i)} \frac{\gamma}{b} J da \tag{25}$$

and integrating Eq 19 along segment BC, where the crack size remains constant, gives

$$J_{\mathrm{pl}}^C = J_{\mathrm{pl}}^B + \frac{\eta_i}{Bb_i} A_{\mathrm{pl}}^{i-1,i} \tag{26}$$

Likewise, applying the three numerical integration rules to integrate the integral in Eq 25 and combining the result with Eq 26, another three solutions are obtained as follows:

(1) Left rectangular rule

$$J_{\mathrm{pl}(i)} = J_{\mathrm{pl}(i-1)} \left(1 - \frac{\gamma_{i-1}}{b_{i-1}} (a_i - a_{i-1}) \right) + \frac{\eta_i}{Bb_i} A_{\mathrm{pl}}^{i-1,i} \tag{27}$$

(2) Right rectangular rule

$$J_{\mathrm{pl}(i)} = J_{\mathrm{pl}(i-1)} \left(1 - \frac{\gamma_i}{b_i} (a_i - a_{i-1}) \right) + \frac{\eta_i}{Bb_i} A_{\mathrm{pl}}^{i-1,i} \tag{28}$$

(3) Trapezoidal rule

$$J_{\mathrm{pl}(i)} = J_{\mathrm{pl}(i-1)}\left(1 - \frac{1}{2}\left(\frac{\gamma_{i-1}}{b_{i-1}} + \frac{\gamma_i}{b_i}\right)(a_i - a_{i-1})\right) + \frac{\eta_i}{Bb_i}A_{\mathrm{pl}}^{i-1,i} \tag{29}$$

In the derivation of Eqs 28 and 29, the approximate relationship (Eq 17) is used. The incremental equations 27–29 have ignored the higher-order terms, other than $(a_i - a_{i-1})$, and their differences are negligible if crack growth increments are sufficiently small.

Median Step Line Approximation

Figure 1(c) is also a duplicate of Fig. 1(a), except that the actual loading path is approximated by multiple median or midpoint step lines. In particular, an actual loading segment AD for one crack growth step from point $i-1$ to i is approximated by three step lines AB, BC, and CD. At points A and D, $J_{\mathrm{pl}(i-1)} = J_{\mathrm{pl}}^{A}$ and $J_{\mathrm{pl}(i)} = J_{\mathrm{pl}}^{D}$. Integrating Eq 19 along segments AB, BC, and CD, respectively, one has

$$J_{\mathrm{pl}}^{B} = J_{\mathrm{pl}}^{A} + \frac{\eta_{i-1}}{2Bb_{i-1}}A_{\mathrm{pl}}^{i-1,i} \tag{30}$$

$$J_{\mathrm{pl}}^{C} = J_{\mathrm{pl}}^{B} - \int_{B(a_{i-1})}^{C(a_i)} \frac{\gamma}{b} J da \tag{31}$$

$$J_{\mathrm{pl}}^{D} = J_{\mathrm{pl}}^{C} + \frac{\eta_i}{2Bb_i}A_{\mathrm{pl}}^{i-1,i} \tag{32}$$

Once again, applying the three numerical integration rules to integrate Eq 31 and combining the result with Eqs 30 and 32, three more solutions are obtained as follows:

(1) Left rectangular rule

$$J_{\mathrm{pl}(i)} = J_{\mathrm{pl}(i-1)}\left(1 - \frac{\gamma_{i-1}}{b_{i-1}}(a_i - a_{i-1})\right) + \left[\frac{1}{2B}\left(\frac{\eta_{i-1}}{b_{i-1}} + \frac{\eta_i}{b_i}\right)A_{\mathrm{pl}}^{i-1,i}\right]\left(1 - \frac{\gamma_{i-1}}{2b_{i-1}}(a_i - a_{i-1})\right) \tag{33}$$

(2) Right rectangular rule

$$J_{\mathrm{pl}(i)} = J_{\mathrm{pl}(i-1)}\left(1 - \frac{\gamma_i}{b_i}(a_i - a_{i-1})\right) + \left[\frac{1}{2B}\left(\frac{\eta_{i-1}}{b_{i-1}} + \frac{\eta_i}{b_i}\right)A_{\mathrm{pl}}^{i-1,i}\right]\left(1 - \frac{\gamma_i}{2b_i}(a_i - a_{i-1})\right) \tag{34}$$

(3) Trapezoidal rule

$$J_{\mathrm{pl}(i)} = J_{\mathrm{pl}(i-1)}\left(1 - \frac{1}{2}\left(\frac{\gamma_{i-1}}{b_{i-1}} + \frac{\gamma_i}{b_i}\right)(a_i - a_{i-1})\right) + \left[\frac{1}{2B}\left(\frac{\eta_{i-1}}{b_{i-1}} + \frac{\eta_i}{b_i}\right)A_{\mathrm{pl}}^{i-1,i}\right] \times\left(1 - \frac{1}{4}\left(\frac{\gamma_{i-1}}{b_{i-1}} + \frac{\gamma_i}{b_i}\right)(a_i - a_{i-1})\right) \quad (35)$$

The derivation of Eqs 34 and 35 uses the approximate relationship (Eq 17). The incremental Eqs 33–35 have ignored the higher-order terms other than $(a_i - a_{i-1})$, and their differences are negligible if crack growth increments are sufficiently small.

Preliminary Discussions on the Proposed Models

Nine incremental equations for three physical models were developed earlier for estimating the J-integral. For each model [upper step line approximation (USLA), lower step line approximation (LSLA), and median step line approximation (MSLA)], the equation obtained with the trapezoidal rule is the average of the equations obtained using the right and left rectangular rules. Moreover, further examination indicates that each equation in the MSLA model is equivalent to the average of the other two corresponding equations in the ULSA and LSLA models. Although the trapezoidal rule obtains more accurate results, it is also considerably more complicated and all of the proposed J estimate equations may determine results that are sufficiently accurate for engineering applications if crack growth increments are small enough.

In the following analysis the set of nine equations is reduced to three, namely Eqs 22, 28, and 35. Equation 22 is chosen since it is the present equation used in ASTM E1820, Eq 28 is chosen since it has the form proposed recently by Neimitz [12] and Kroon et al. [10]; and Eq 35 is chosen since it is considered to be the most accurate model considered in this work. These three choices also represent one each of the USLA, LSLA, and MSLA analysis procedures.

A common feature of the proposed models is that a current plastic $J_{\mathrm{pl}(i)}$ is obtained in two steps by first modifying the existing $J_{\mathrm{pl}(i-1)}$ to account for a full crack growth correction as defined in ASTM E1820, and then accumulating the incremental work done on the specimen. Another common feature is that these physical models are subjected to three major sources of errors, namely, the degree of polynomial order used in the approximation of the integrand, the magnitude of crack growth increment, and the difference between the approximate and measured incremental work determined by the area under a load-displacement curve. Except for these, an additional error may be generated due to the different crack growth corrections used for modifying the incremental work input done on the specimen. For instance, the USLA, LSLA, and MSLA models use a full, zero, and half-crack increment correction, respectively, for modifying the incremental work. An accumulation of all errors determines the final accuracy of the proposed models, as discussed next.

Evaluation of Accuracy of *J*-Integral Approximations

Theoretical Evaluation

A theoretical procedure is developed in this section to evaluate the accuracy of the proposed models for *J*-integral approximation. Wallin and Laukkanen [23] showed that it is possible to construct an assumed "true" *J-R* curve for ductile materials. According to the principle of load separation [12,24], a load can be expressed as a product of a crack length dependent function and a plastic displacement dependent function, as used by the normalization method [25,26]. For materials exhibiting a power-law relationship for the plastic displacement function [25], a crack size dependent load versus displacement curve can be expressed analytically as

$$P = WB\left(1 - \frac{a}{W}\right)^{\eta} \cdot k\left(\frac{\Delta_{pl}}{W}\right)^{n} \tag{36}$$

where:

n = strain hardening exponent, and

k = material constant having the dimensions of stress.

Recall that ASTM E1820 suggests a power-law function to be used for curve fitting a valid *J-R* curve. Likewise, for a material whose crack extension is controlled by plastic deformation, the plastic part of the *J-R* curve is adequately assumed to follow a power-law relationship

$$J_{pl} = J_{pl(1\ mm)}(\Delta a)^{m} \tag{37}$$

where:

$\Delta a = a - a_0$ = crack extension,

m = *J-R* curve exponent, and

$J_{pl(1\ mm)}$ = plastic *J* value at 1 mm in crack extension.

At the ith step of crack extension, the deformation *J* can be determined from a stationary crack with a crack length of a_i. From Eq 4, one has

$$J_{pl}(a_i) = \frac{\eta(a_i)\int_0^{\Delta_{pl(i)}} P|_{ai} d\Delta_{pl}}{B(W - a_i)} \tag{38}$$

From Eqs 36–38, the plastic displacement is determined as a function of crack extension in the form of

$$\frac{\Delta_{pl(i)}}{W} = \left[\frac{(n+1)J_{pl(1\ mm)}(\Delta a_i)^{m}}{kW\eta(a_i)(1 - a_0/W - \Delta a_i/W)^{\eta-1}}\right]^{1/(n+1)} \tag{39}$$

For a theoretical function of the *J-R* curve in the power-law form of Eq 37 with known parameters of $J_{pl(1\ mm)}$ and m for a material, load and plastic displacement data can be analytically obtained as a function of crack extension from Eqs 36 and 39, respectively. In this manner, from a given *J-R* curve, the load-displacement curve and the load-crack extension curve can be constructed analytically for a specific specimen. Conversely, using the analytic load-

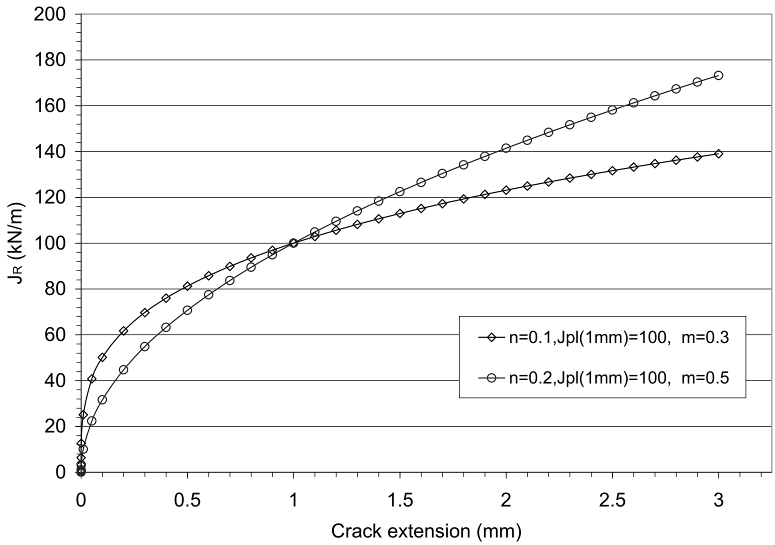

FIG. 2—*Two given J-R curves in power-law functions.*

displacement curve and the load-crack extension curve, a theoretical or true *J-R* curve can be obtained if an appropriate method is used.

Figure 2 plots *J-R* curves in power-law functions suggested by Wallin and Laukkanen [23] for two different material assumptions. The one material has a moderate strain hardening ($n=0.1$) and a shallow *J-R* curve ($m=0.3$), whereas the other has a higher strain hardening ($n=0.2$) and a steeper *J-R* curve ($m=0.5$). Figure 3(*a*) and 3(*b*) shows the analytic load-displacement curves and the analytic load-crack extension curves determined from Eqs 36 and 39 for SE(B) specimens made of the two model materials with known *J-R* curves. In these figures, the SE(B) specimen sizes used are $W=20$ mm, $B=10$ mm, and $a_0/W=0.5$; the plastic geometry factors $\eta=1.9$ and $\gamma=0.9$ as prescribed in ASTM E1820-08; the material parameters used are $k=300$ MPa, $J_{\mathrm{pl(1\ mm)}}=100$ kN/m, and $m=0.3$ for $n=0.1$, and $k=280$ MPa, $J_{\mathrm{pl(1\ mm)}}=100$ kN/m, and $m=0.5$ for $n=0.2$. Using the analytical results of load, displacement and crack extension illustrated in Fig. 3, *J-R* curves can be calculated for the two SE(B) specimens using the three physical models developed previously. The accuracy of calculated *J-R* curves can be thus evaluated through comparison with the given *J-R* curve functions.

Three typical sizes of crack growth increments, i.e., $da=a_i-a_{i-1}=0.005b_0$, $0.01b_0$, and $0.02b_0$ or with the original ligament size b_0 assumed here to be 10 mm, $da=0.05$, 0.1, and 0.2 mm, are considered. For consistency, the first point of crack extension for all cases analyzed is set at 0.05 mm, as marked with the solid points on the load-displacement curves in Fig. 3(*a*). Before this assumed initiation point, five points representing crack blunting of 0.000001, 0.00001, 0.0001, 0.001, and 0.01 mm are inserted on each of the load-displacement curves to ensure its continuity for the two SE(B) specimens. After this initiation

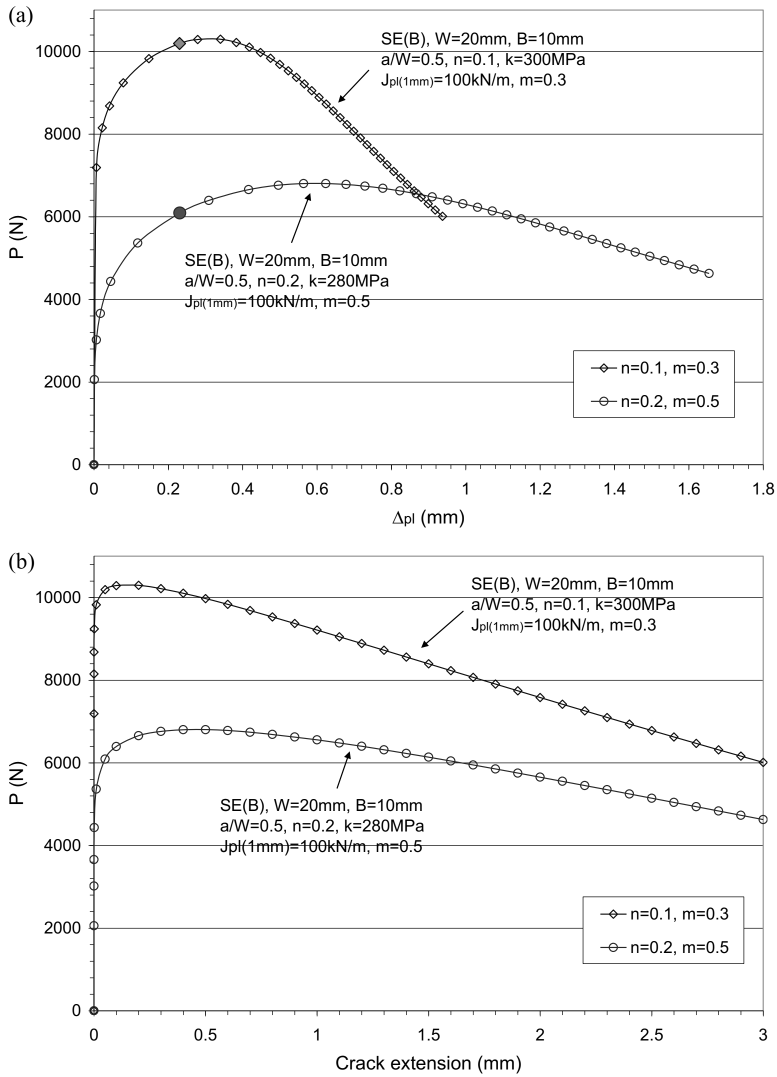

FIG. 3—*Analytical data of load, displacement, and crack extension for two material models:* (*a*) *load-displacement curves;* (*b*) *load-crack extension curves.*

point, crack growth is assumed to be uniform for a given increment size. Figure 4(*a*)–4(*c*) compares the *J-R* curves obtained by the USLA (Eq 22), LSLA (Eq 28) and MSLA (Eq 35) models, respectively, for the crack growth incremental steps of $0.005b_0$, $0.01b_0$, and $0.02b_0$ with the given *J-R* curve for the moderate hardening material ($n=0.1$). Figure 5(*a*)–5(*c*) compares those obtained by the USLA, LSLA, and MSLA models, respectively, for the crack growth incremental sizes of $0.005b_0$, $0.01b_0$, and $0.02b_0$ with the given *J-R* curve for the high hardening material ($n=0.2$). Figures 4 and 5 show that for both materials

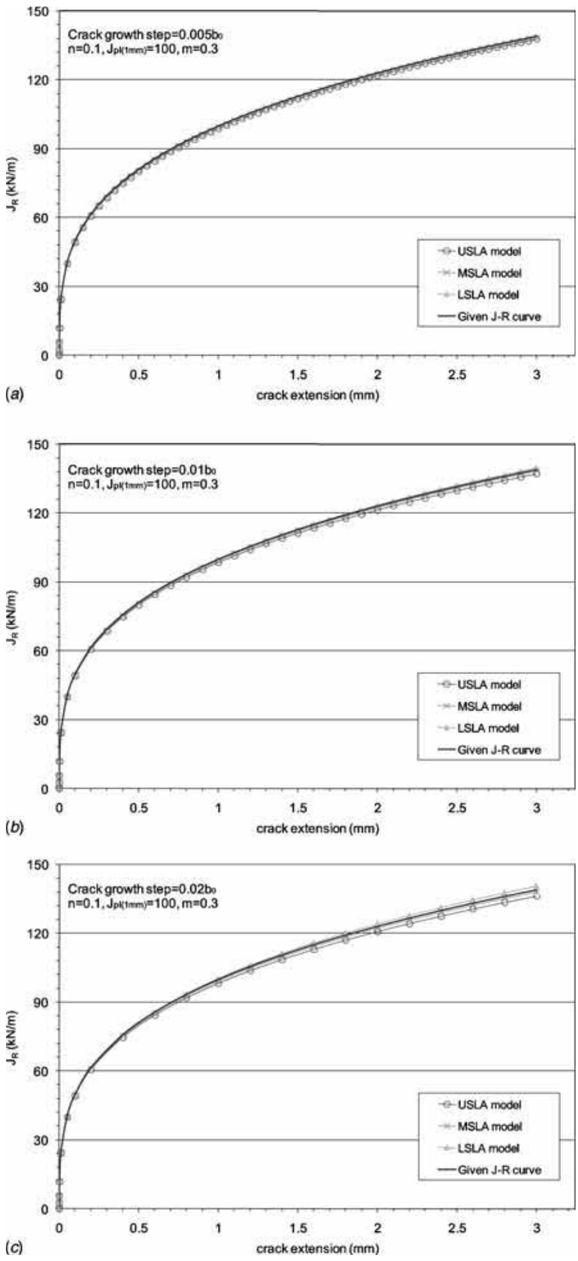

FIG. 4—*J-R curves determined by three proposed models for a moderate hardening material* ($n = 0.1$) *and three crack growth step sizes:* (*a*) $da = 0.005b_0$; (*b*) $da = 0.01b_0$; *and* (*c*) $da = 0.02b_0$.

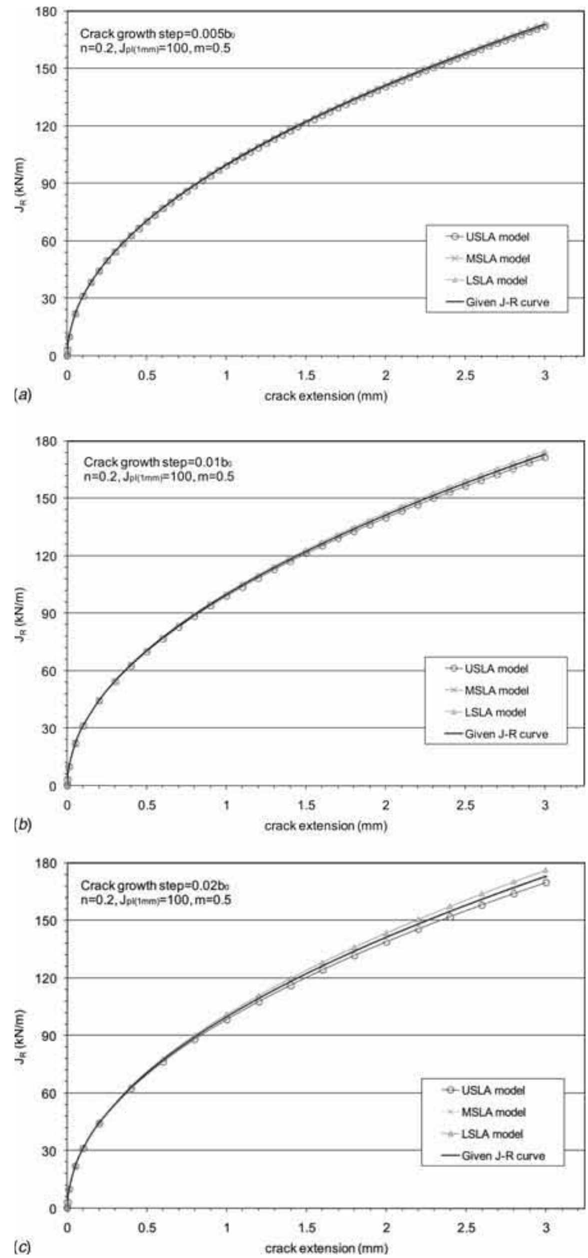

FIG. 5—*J-R curves determined by three proposed models for a high hardening material* ($n = 0.2$) *and three crack growth step sizes:* (*a*) $da = 0.005b_0$; (*b*) $da = 0.01b_0$; *and* (*c*) $da = 0.02b_0$.

TABLE 1—*Relative errors (%) for three proposed physical models.*

	$n=0.1$			$n=0.2$		
	$\Delta a=0.05b_0$	$\Delta a=0.1b_0$	$\Delta a=0.2b_0$	$\Delta a=0.05b_0$	$\Delta a=0.1b_0$	$\Delta a=0.2b_0$
USLA	−0.89	−1.28	−2.01	−0.63	−1.11	−2.01
MSLA	−0.48	−0.54	−0.66	−0.16	−0.22	−0.34
LSLA	0.06	0.47	1.26	0.43	0.91	1.85

(1) For the smallest crack growth increment step, i.e., $da=0.005b_0$, the *J-R* curves calculated by three proposed relationships are nearly coincident with the given *J-R* curve;
(2) For the two larger crack growth increment sizes, the differences between the calculated and given *J-R* curves become larger for USLA and LSLA models, but not for MSLA model; and
(3) As crack growth step size increases, the USLA and LSLA results deviate gradually from the given *J-R* curve with the USLA results being conservative and the LSLA results becoming unconservative, and the MSLA results remaining almost unchanged.

As noted from Figs. 4 and 5, a maximum crack extension is set as 3 mm for all cases so that the crack growth limit criterion required by ASTM E1820 is met. The relative errors between the calculated results and the given *J-R* curve for the two hardening material models are determined at the maximum extent of crack growth, and are shown in Table 1 and Fig. 6. The following observations can be made from these results:

(1) The errors for three models vary linearly with the crack growth step

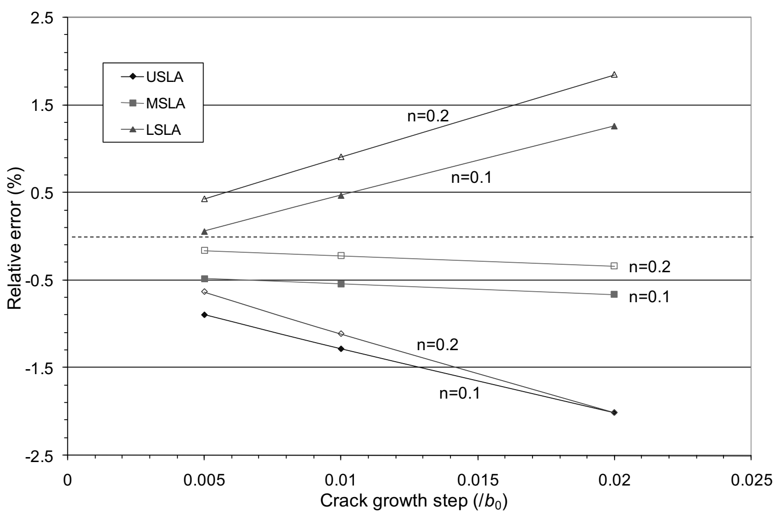

FIG. 6—*Error comparisons for three proposed models and two hardening materials.*

size, and all errors are less than 1 % for crack growth increments less than 0.5 % of the original ligament size;

(2) For the LSLA model, the error is positive and increases with increasing crack growth step size and strain hardening exponent;

(3) For the USLA model, the error is negative and decreases with increasing crack growth step size, and is less sensitive to the strain hardening exponent than the LSLA model; and

(4) For the MSLA model, the error is very small and depends only slightly on the crack growth step size for both material models.

From these theoretical evaluations, it is concluded that if a crack growth increment is less than 0.5 % of the original ligament size, all three models can determine very accurate J-integral values. Otherwise,

(1) The LSLA model, in which the crack growth correction is not considered for modifying the incremental work input, overestimates J and the error becomes larger as crack growth step size increases;

(2) The USLA model, in which a full ASTM E1820 crack growth correction is considered for modifying the incremental work input, underestimates J and the error becomes larger as crack growth step size increases;

(3) The MSLA model, in which a half ASTM E1820 crack growth correction is considered for modifying the incremental work input, gives the most accurate J estimate with slight conservatism for all crack growth step sizes considered; and

(4) In all cases considered in this study, the error in J is less than 2 %.

Experimental Evaluation

For a real material, the J-R curve may not follow a simple power-law relationship, as shown in Ref 27, and thus actual experimental data should also be considered to evaluate the proposed models. Joyce and his co-workers [28,29] tested a series of HY80 steel 1T SE(B) specimens with a wide range of crack lengths at room temperature. All specimens were side-grooved with a total 20 % reduction of specimen thickness in order to obtain straight crack fronts over relatively large crack extensions. The unloading compliance method was employed for measuring crack extension and developing J-R curves. Recently, Zhu and Joyce [26] reanalyzed the experimental data and obtained J-R curves for the HY80 steel using the standard normalization method in the guidance of ASTM E1820 A15. Their results indicated that the normalization method can determine a J-R curve equivalent to the unloading compliance method. A real analytical result of crack size dependent load-displacement curve can be thus extracted from Ref 26, and used here experimentally to evaluate the proposed models. For example, for the deep crack case of $a_0/W = 0.549$, the crack size dependent load-displacement curve obtained by the normalization method is expressed as

$$P = WB\left(1 - \frac{a}{W}\right)^2 \left[\frac{-0.012 + 199.5\left(\frac{\Delta_{pl}}{W}\right) + 665\left(\frac{\Delta_{pl}}{W}\right)^2}{0.000187 + \left(\frac{\Delta_{pl}}{W}\right)} \right] \tag{40}$$

and crack extension is approximated as a function of plastic displacement

$$\Delta a = 0.4688\Delta_{pl} + 0.8361(\Delta_{pl})^2 \tag{41}$$

where the load P has units in Newtons and the displacement and dimensions are in units of millimeters. $W = 50.8$ mm, $B = 25.4$ mm, $B_N = 20.32$ mm, $a_0 = 27.86$ mm, and $b_0 = 22.94$ mm.

Figure 7(*a*) shows the analytical load versus plastic displacement curve determined from Eq 40 and the comparison with the test data, and Fig. 7(*b*) compares the analytic crack extension versus plastic displacement determined from Eq 41 with the test data for the HY80 SE(B) specimen. Using these analytical results of load, displacement and crack extension obtained from experimental data, *J-R* curves are determined by the three proposed models using uniform crack growth incremental steps of $0.01b_0$ and $0.02b_0$ or 0.23 mm and 0.46 mm, and shown in Fig. 8. Similarly using the test data of load, displacement and crack extension obtained using the unloading compliance method, the *J-R* curves are obtained for all three proposed models and are included in Fig. 8. It should be noted that all *J-R* curves shown in these two figures are expressed in the total value of *J*-integral, which means that the elastic component of *J* has been added to the plastic component of *J*. For a small crack growth increment of $0.005b_0$ or 0.115 mm, the results for the normalization method are not shown here, because all models produce equivalent *J-R* curves.

The results obtained here from Fig. 8(*a*) and 8(*b*) are identical to the observations made in the previous section, namely:

(1) For the smallest crack growth increment, i.e., $da = 0.005b_0$, the *J-R* curves calculated by all three proposed models are equivalent;
(2) For the two larger crack growth step sizes, the USLA and LSLA model results deviate from the results of the $da = 0.005b_0$ case and the differences gradually become larger as crack extension increases; and
(3) For all three crack growth step sizes the MSLA results remain almost identical.

For the unloading compliance method, the measured crack growth increments are less than $0.01b_0$ for crack extensions less than 2.2 mm, and fall between $0.01b_0$ and $0.02b_0$ for crack extensions beyond 2.2 mm. As a result, the *J-R* curves determined using the three models are similar, with *J* being slightly larger for the LSLA model and slightly lower for the USLA model in comparison with the MSLA model. Again, these experimental evaluations confirm the same conclusions obtained using the assumed analytical results:

(1) The three models determine equivalent *J-R* curves if a crack growth incremental step is less than 0.5 % of the original ligament size;
(2) The LSLA model may overestimate *J* for large crack growth step sizes;
(3) The USLA model may underestimate *J* for large crack growth step sizes; and

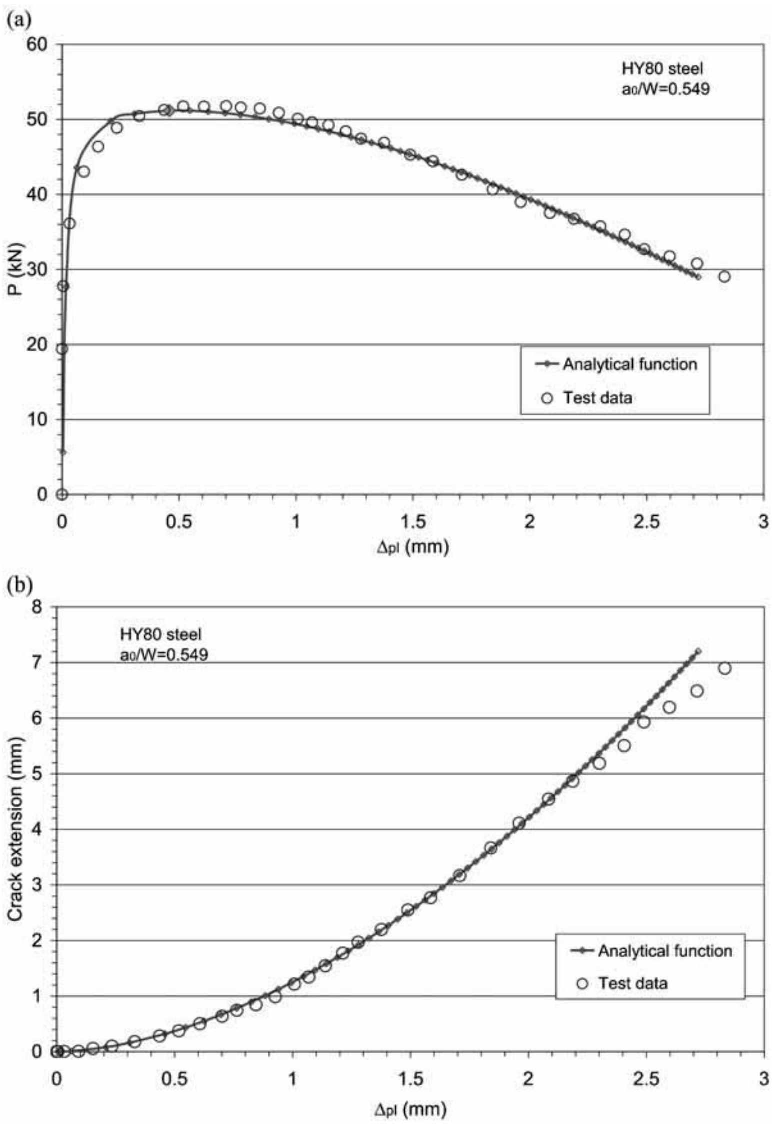

FIG. 7—*Experimental data of load, displacement, and crack extension for HY80 steel:* (*a*) *Load-displacement curve;* (*b*) *crack extension-displacement curve.*

(4) The MSLA model can determine J nearly independent of crack growth increments.

ASTM E1820 recommends that the elastic unloading compliance technique be used as a standard procedure to monitor instantaneous crack lengths through loading and partially unloading cycles during a fracture test. If the maximum crack extension for a specimen is $0.3b_0$ and the uniform sizes of

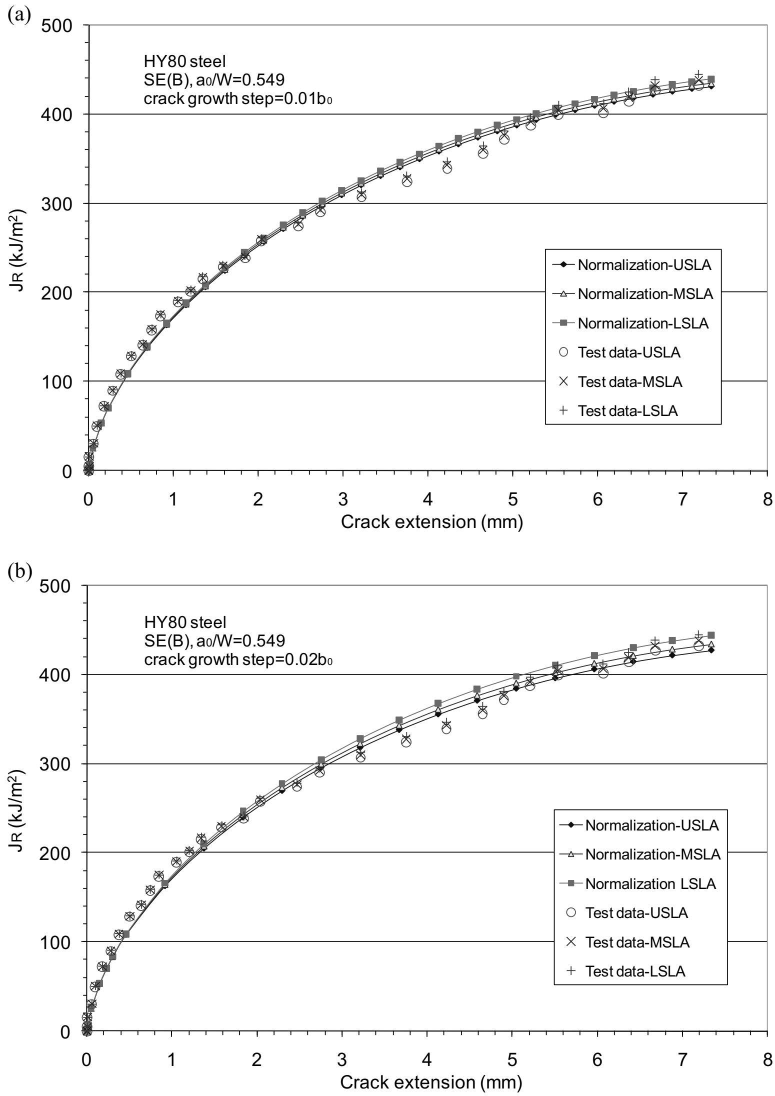

FIG. 8—*J-R curves determined from three proposed models for HY80 steel and two crack growth step sizes:* (*a*) *da* = *0.01*b_0; (*b*) *da* = *0.02*b_0.

crack growth increments are $0.005b_0$, $0.01b_0$, and $0.02b_0$, the corresponding number of unloading cycles are 60, 30, and 15, respectively. Since the initial ductile crack growth is slow and the crack increment sizes allowed in the standard are small, actual unloading cycles would be much larger than these predictions. As a result, the USLA model used by the present ASTM E1820 can be very accurate and the complicated MSLA model may not be necessary to use. However, for some materials exhibiting low toughness and large crack increments, the MSLA model can be used effectively to determine crack growth corrected J-integral values and then to construct a J-R curve.

Remarks and Conclusions

In order to determine an accurate approximation of the J-integral equation, this paper proposed different mathematical and physical models based on the deformation theory of plasticity. Three physical models each of USLA, LSLA, and MSLA were developed for estimating J in terms of the jump-like crack growth assumption. The relations between the mathematical and physical models and the relations between the proposed models and existing equations were identified. Among them, three typical equations in the physical models were selected as representative, and then were used for the accuracy evaluation. The evaluation was made systematically using a theoretical procedure of J-R curves for two assumed strain hardening materials and using experimental data for an HY80 steel.

A common feature for all proposed models and existing incremental equations is that a current plastic $J_{pl(i)}$ is obtained in two steps by first modifying the existing $J_{pl(i\text{-}1)}$ obtained at the previous step to account for a full crack growth correction as defined in ASTM E1820, and then accumulating an incremental work obtained during the fracture test. However, different crack growth corrections were used in the three models for modifying the incremental work input. The USLA, LSLA, and MSLA models used a full, zero, and half-crack growth correction, respectively for modifying the incremental work done on the specimen. It was found the Ernst-type [12] incremental J-integral equation, as used in ASTM E1820, is the same as the USLA model; the Garwood-type [19] incremental equations, as presented recently by Neimitz [13] and Kroon et al. [14], are similar to the LSLA model; and the MSLA model is a new approximation for the J-integral equation.

Both theoretical and experimental evaluations showed that (1) the three proposed models can determine equivalent, accurate J-R curves if a crack growth incremental step size is less than 0.5 % of the original ligament size, (2) the LSLA model overestimates J for larger crack growth increments, and hence is unconservative, (3) the USLA model underestimates J for larger crack growth increments and is thus conservative, while (4) the MSLA model can accurately determine a consistent J nearly independent of the crack growth increment size. Since the ASTM E1820 equation is equivalent to the USLA model, it can continue to be used conservatively and accurately if the crack growth increment is sufficiently small. The incremental equations presented by Neimitz [13] and Kroon et al. [14] should not be substituted due to their non-conservative nature. The proposed MSLA model is the most accurate and remains accurate even for large crack growth increments. If the MSLA model is used, the unloading cycles can be significantly reduced in the measurement of instantaneous crack sizes using the elastic unloading compliance technique. Therefore, in addition to using the present ASTM E1820 incremental equation, it is recommended that one use the MSLA model for accurately evaluating J-R curves in instances where one or more relatively large crack extension increments are present in the resistance curve data.

Note that all evaluations of the proposed models presented in this work were based on SE(B) specimens only. Similar results and conclusions were also obtained using C(T) specimens, but not presented here due to space limitations. In addition, this paper only dealt with LLD-based incremental J-integral equations. The same methodology can be used to determine similar, incremental J-integral equations when only CMOD data are available as discussed recently by Zhu et al. [6] and Zhu and Joyce [30] for SE(B) specimens and by Cravero and Ruggieri [31] for single edge-notched tension specimens.

References

[1] Rice, J. R., "A Path Independent Integral and the Approximate Analysis of Strain Concentration by Notches and Cracks," *ASME J. Appl. Mech.*, Vol. 35, 1968, pp. 379–386.

[2] Begley, J. A. and Landes, J. D., "The J-Integral as a Fracture Criterion," *Fracture Mechanics, ASTM STP 515*, ASTM International, West Conshohocken, PA, 1972, pp. 1–23.

[3] Landes, J. D. and Begley, J. A., "The Effect of Specimen Geometry on J_{IC}," *Fracture Mechanics, ASTM STP 515*, ASTM International, West Conshohocken, PA, 1972, pp. 24–39.

[4] Turner, C. E., "Fracture Mechanics Assessment and Design," *Philos. Trans. R. Soc. London, Ser. A*, Vol. 299, 1981, pp. 73–92.

[5] Etemad, M. R. and Turner, C. E., "An Experimental Investigation of Slow Stable Crack Growth Using HY130 Steel," *J. Strain Anal.*, Vol. 20, 1985, pp. 201–208.

[6] Zhu, X. K., Leis, B. N., and Joyce, J. A., "Experimental Evaluation of J-R Curves from Load-CMOD Record for SE(B) Specimens," *J. ASTM Int.*, Vol. 5, 2008, paper ID JAI101532.

[7] Joyce, J.A., *Manual on Elastic-Plastic Fracture: Laboratory Test Procedures*, ASTM International, West Conshohocken, PA, 1996.

[8] ASTM E813-81, 1982, "Standard Test Method for J_{Ic}, a Measure of Fracture Toughness," *Annual Book of ASTM Standards*, Vol. 03.01, ASTM International, West Conshohocken, PA.

[9] ASTM E1152-87, 1987, "Standard Test Method for Determining J-R Curves," *Annual Book of ASTM Standards*, Vol. 03.01, ASTM International, West Conshohocken, PA.

[10] ASTM E1737-96, 1996, "Standard Test Method for J-integral Characterization of Fracture Toughness," *Annual Book of ASTM Standards*, Vol. 03.01, ASTM International, West Conshohocken, PA.

[11] ASTM E1820-08, 2008, "Standard Test Method for Measurement of Fracture Toughness," *Annual Book of ASTM Standards*, Vol. 03.01, ASTM International, West Conshohocken, PA.

[12] Ernst, H. A., Paris, P. C., and Landes, J. D., "Estimations on J-Integral and Tearing Modulus T from a Single Specimen Test Record," *Fracture Mechanics: Thirteenth Conference, ASTM STP 743*, 1981, pp. 476–502.

[13] Neimitz, A., "The Jump-Like Crack Growth Model, the Estimation of Fracture Energy and J_R Curve," *Eng. Fract. Mech.*, Vol. 75, 2008, pp. 236–252.

[14] Kroon, M., Faleskog, J., and Oberg, H., "A Probabilistic Model for Cleavage Frac-

ture with a Length Scale-Parameter Estimation and Predictions of Growing Crack Experiments," *Eng. Fract. Mech.*, Vol. 75, 2008, pp. 2398–2417.

[15] Rice, J. R., Paris, P. C., and Merkle, J. G., "Some Further Results of *J*-Integral Analysis and Estimates," *Progress in Flaw Growth and Fracture Toughness Testing, ASTM STP 536*, ASTM International, West Conshohocken, PA, 1973, pp. 231–245.

[16] Sumpter, J. D. G. and Turner, C. E., "Method for Laboratory Determination of J_C (Contour Integral for Fracture Analysis)," *Cracks and Fracture, ASTM STP 601*, ASTM International, West Conshohocken, PA, 1976, pp. 3–18.

[17] Paris, P. C., Ernst, H., and Turner, C. E., "A *J*-Integral Approach to Development of η-Factors," *Fracture Mechanics: Twelfth Conference, ASTM STP 700*, 1980, pp. 338–351.

[18] Clarke, G. A., Andrews, W. R., Paris, P. C., and Schmidt, D. W., "Single Specimen Tests for J_{IC} Determination," *Mechanics of Crack Growth, ASTM STP 590*, ASTM International, West Conshohocken, PA, 1976, pp. 27–42.

[19] Garwood, S. J., Robinson, J. N., and Turner, C. E., "The Measurement of Crack Growth Resistance Curves (R-Curves) Using the *J* Integral," *Int. J. Fract.*, Vol. 11, 1975, pp. 528–530.

[20] Etemad, M. R., John, S. J., and Turner, C. E., "Elastic-Plastic R-Curves for Large Amounts of Crack Growth," *Fracture Mechanics: Eighteenth Symposium, ASTM STP 945*, 1988, pp. 986–1004.

[21] Anderson, T. L., 1995, *Fracture Mechanics—Fundamentals and Applications*, 2nd ed., CRC Press, Boca Raton, FL.

[22] Hutchinson, J. W. and Paris, P. C., "Stability Analysis of *J*-Controlled Crack Growth," *Elastic-Plastic Fracture, ASTM STP 668*, ASTM International, West Conshohocken, PA, 1979, pp. 37–64.

[23] Wallin, K. and Laukkanen, A., "Improved Crack Growth Corrections for *J-R* Curve Testing," *Eng. Fract. Mech.*, Vol. 71, 2004, pp. 1601–1614.

[24] Sharobeam, M. H. and Landes, J. D., "The Load Separation Criterion and Methodology in Ductile Fracture Mechanics," *Int. J. Fract.*, Vol. 47, 1991, pp. 81–104.

[25] Herrera, R. and Landes, J. D., "Direct *J-R* Curve Analysis of Fracture Toughness Test," *J. Test. Eval.*, Vol. 16, 1988, pp. 427–449.

[26] Zhu, X. K. and Joyce, J. A., "*J*-Resistance Curve Testing of HY80 Steel Using SE(B) Specimens and Normalization Method," *Eng. Fract. Mech.*, Vol. 74, 2007, pp. 2263–2281.

[27] Orange, T. W., "Methods and Models for R-Curve Instability Calculations," *Fracture Mechanics: Twenty-First Symposium, ASTM STP 1074*, 1990, pp. 545–559.

[28] Joyce, J. A. "*J*-Resistance Curve Testing of Short Crack Bend Specimens Using Unloading Compliance," *Fracture Mechanics: Twenty-Second Symposium, ASTM STP 1131*, Vol. I, 1992, pp. 904–924.

[29] Joyce, J. A., Hackett, E. M., and Roe, C., "Effect of Crack Depth and Mode of Loading on the *J-R* Curve Behavior of a High-Strength Steel," *Constraint Effects in Fracture, ASTM STP 1171*, ASTM International, West Conshohocken, PA, 1993, pp. 239–263.

[30] Zhu, X. K. and Joyce, J. A., "Revised Incremental *J*-Integral Equations for ASTM E1820 Using Crack Mouth Opening Displacement," *J. Test. Eval.*, Vol. 37, 2009, pp. 205–214.

[31] Cravero, S. and Ruggieri, C., "Further Developments in *J* Evaluation Procedure for Growing Cracks Based on LLD and CMOD Data," *Int. J. Fract.*, Vol. 148, 2007, pp. 387–400.

Reprinted from JAI, Vol. 7, No. 1
doi:10.1520/JAI102403
Available online at www.astm.org/JAI

Enrico Lucon[1] *and Marc Scibetta*[1]

Application of Advanced Master Curve Approaches to the EURO Fracture Toughness Data Set

ABSTRACT: The so-called EURO data set is the largest set ever assembled, consisting of fracture toughness results obtained in the ductile-to-brittle transition region. It was the outcome of a large project, sponsored by the European Union, which involved ten European laboratories in the second half of the 1990s. Several post-project investigations have identified one of the blocks from which specimens were extracted (block SX9) as macroscopically inhomogeneous and significantly tougher than the remaining blocks. In this paper, the variability of block SX9 has been investigated using the conventional master curve (MC) methodology and some recent MC extensions, namely, the SINTAP (structural integrity assessment procedure) lower tail, the single point estimation, the bi-modal MC, and the multi-modal MC. The basic MC method is intended for macroscopically homogeneous ferritic steels only, and the alternative approaches have been developed for the investigation of inhomogeneous materials. Therefore, these methods can be used to study the behavior of block SX9 within the EURO data set. It has been found that the bi-modal and multi-modal MC approaches are quite effective in detecting the "anomaly" represented by block SX9 but only when analyses are performed on data sets of comparable size.

KEYWORDS: EURO data set, ductile-to-brittle transition region, macroscopic inhomogeneity, master curve extensions, SINTAP lower tail, single point estimation, bi-modal master curve, multi-modal master curve

Manuscript received March 3, 2009; accepted for publication October 2, 2009; published online December 2009.

[1] Institute for Nuclear Materials Science, SCK•CEN, Boeretang 200, B-2400 Mol, Belgium.

Cite as: Lucon, E. and Scibetta, M., "Application of Advanced Master Curve Approaches to the EURO Fracture Toughness Data Set," *J. ASTM Intl.*, Vol. 7, No. 1. doi:10.1520/JAI102403.

Introduction

The so-called EURO fracture toughness data set is definitely the largest and most comprehensive set of fracture toughness data obtained in the ductile-to-brittle transition region on a typical reactor pressure vessel steel (Deutsches Institut fur Normung (DIN) 22NiMoCr37).

It was generated during the second half of the 1990s when ten European laboratories took part in a EU-sponsored project called “Fracture Toughness of Steel in the Ductile-to-Brittle Transition Regime” [1]. Within the project, more than 700 compact tension specimens of different thickness (0.5T, 1T, 2T, and 4T) were tested at different temperatures in order to produce a sufficiently large data set to be used for the validation of various statistical methods, in primis the master curve (MC) methodology, which in the mid-1990s was not yet standardized by ASTM (the first edition of ASTM E1921 [2] came out in 1997).

The development and the statistical analysis of the EURO data set were the subject of several publications [1,3–7]. Besides the straightforward MC analysis [5], other approaches were used [1], such as the analysis of data at the onset of ductile tearing (Neale), a lower bound fracture toughness procedure (Heerens, Pfaff, Hellmann, and Zerbst) and modelling by statistical analysis for the quantification of the probability of cleavage fracture (Moskovic).

Moreover, Wallin [6] examined the data set for possible inhomogeneities using two of the advanced MC approaches considered in this work (the BMMC and the MMMCs).

Although the material had been found to be “homogeneous” during preliminary investigations, the examination of test results showed that at −60°C the expected size effect was not observed: 2TC(T) specimens exhibited a clearly higher toughness and larger scatter than the smaller 0.5TC(T) and 1TC(T) specimens. To investigate this discrepancy, an additional set of 0.5TC(T) specimens was machined from the broken 2TC(T) samples and tested at −60°C. The results confirmed the existence of a macroscopic material variability for block SX9 from which the original 2TC(T) specimens were extracted. A clear inhomogeneity problem for this block was confirmed by Wallin’s analyses [6], while for other neighbouring blocks (SX8 and SX10) only a moderate inhomogeneity was observed.

It is to note that in a recent paper [7], Joyce and Gao showed through the use of some of the same advanced MC approaches used in this work that other data subsets could be classified as significantly inhomogeneous. However, in this paper attention will be focused on block SX9, as compared to the remaining data set. The following MC approaches will be used:

- The conventional MC analysis in accordance with ASTM E1921-09c [2] (which is only applicable to homogeneous data sets);
- The structural integrity assessment procedure (SINTAP) lower tail (SLT) procedure;
- The single point estimation (SPE) procedure;
- The bi-modal MC (BMMC); and
- The multi-modal MC (MMMC).

More details on the last four approaches are provided in the next section. For all the methods considered, the objective is to assess their reliability in recognizing the "anomaly" represented by block SX9 according to published analyses [1,6].

After individually examining block SX9 for possible influences of specimen size (2TC(T) versus 0.5TC(T)) or testing laboratory (GKSS versus Technische Hochschule Aachen (THA)), the whole EURO data set will be considered, both including and excluding data from SX9. Subsequently, in order to have more "comparable" numbers, the same analyses will be performed on the tests performed at $-60°C$ (all specimens from SX9 were tested at $-60°C$). Finally, a "one-to-one" comparison will be presented between blocks SX9 and SX12, with the latter taken as representative of the "average" behavior of the EURO material in accordance with Wallin's analysis [6].

Alternative Master Curve Approaches

All the methodologies addressed in this section are described in more detail in Ref 8. A recent application of two of them (SLT and MMMC) to VVER-440 pressure vessel steels can be found in Ref 9.

SINTAP Lower Tail

The SINTAP [10] contains a lower tail modification of the MC analysis [11]. This allows conservative lower bound-type fracture toughness estimates, which are then governed by the toughness of the more brittle constituent.

However, the method does not provide information about the tougher material, and a probabilistic description of the whole material is not possible.

The SLT procedure guides the user to an estimate of the reference temperature, which describes the population having the lowest toughness. It consists of three steps.

- *Step 1* is a standard estimation of the median fracture toughness in accordance with ASTM E1921-09c [2].
- *Step 2* performs a lower tail estimation by censoring all K_{Jc} values above the 50 % failure probability, $K_{Jc(\mathrm{med})}$, and determining the corresponding reference temperature $T_{o,i}$. The process is iterated until a constant value of T_o (or K_o) is reached.
- *Step 3*, which performs a minimum value estimation, is only required for small data sets (less than ten values). It allows calculating the maximum value of T_o, $T_{o(\mathrm{max})}$, using all non-censored data. If $T_{o(\mathrm{max})} - 8°C > T_{o(\mathrm{step\ 2})}$, there is indication that the data is inhomogeneous and $T_{o(\mathrm{max})}$ should be taken as the representative value of T_o.

Single Point Estimation

This simple method provides a quick and rather crude engineering assessment in cases where the inhomogeneity is so large that it becomes a random variable.

After size adjustment, all non-censored values are used to derive individual estimates of T_o, which are then averaged over the number of valid (non-censored) data to obtain the single point value $T_{o,\mathrm{SP}}$. This includes a 4°C bias correction to account for the non-symmetry of the MC distribution.

The standard deviation for T_o can be calculated through a simple formula which accounts for the average inherent scatter of the MC distribution, taken conservatively as 21°C. No specific criterion is indicated for identifying a data set as inhomogeneous.

Bi-Modal Master Curve

When the data population of a material consists of two combined MC distributions (as in the case of a heat affected zone), the total cumulative probability can be expressed as a bi-modal distribution and two characteristic toughness values (K_{o1} and K_{o2}) can be defined. In contrast to the standard MC analysis, the bi-modal distribution contains three parameters (the two characteristic toughness values and the probability p_a of belonging to distribution a; the probability p_b of belonging to distribution b is obviously given by $1-p_a$). In order to be able to handle randomly censored multi-temperature data sets, the estimation must be based on the maximum likelihood (MML) procedure.

The minimum number of data points that can be handled by the BMMC is around 12–15, but preferably the size should be in excess of 20. A simple criterion to judge the likelihood that the data set represents an inhomogeneous material is

$$|T_{o1} - T_{o2}| > 2\sqrt{\sigma_{T_o1}^2 + \sigma_{T_o2}^2} \tag{1}$$

where:

T_{o1} and T_{o2} = reference temperatures of the two populations and

σ_{T_o1} and σ_{T_o2} = their respective standard deviations calculated from Ref 2.

In order to judge the reliability of the statement "homogeneous versus non-homogeneous" provided by the BMMC analysis, we will also evaluate the terms at the left and right hand side of Eq 1, and based on their ratio R_σ

$$R_\sigma = \frac{|T_{o1} - T_{o2}|}{2\sqrt{\sigma_{T_o1}^2 + \sigma_{T_o2}^2}} \tag{2}$$

we will establish the "degree of non-homogeneity" of each data set according to the following (purely subjective) criteria:

if $R_\sigma \le 1 \rightarrow$ **homogeneous**

if $1 < R_\sigma \le 1.5 \rightarrow$ **moderately inhomogeneous**

if $1.5 < R_\sigma \le 2 \rightarrow$ **inhomogeneous**

if $R_\sigma > 2 \rightarrow$ **highly inhomogeneous**

TABLE 1—*Chemical composition of 22NiMoCr37 steel (wt %).*

C	Si	P	S	Cr	Mn	Ni	Cu	Mo
0.21	0.24	0.003	0.004	0.003	0.82	0.79	0.049	0.56

Multi-Modal Master Curve

Based on the MML principle, this method was developed for the analysis of data sets consisting of multiple populations, each characterized by a random variable T_o that is assumed to follow a Gaussian distribution. It is especially suited to data sets including several heats of a single material or inherently macroscopically inhomogeneous materials. The minimum size of the data set for a reliable analysis is around 20.

A simple criterion to judge the likelihood that the data represent an inhomogeneous material is given by

$$\sigma_{T_o,\mathrm{MMMC}} > 2\sigma_{T_o,\mathrm{ASTM\ E1921}} \tag{3}$$

i.e., the steel is likely to be inhomogeneous if the standard deviation from the MML estimate ($\sigma_{T_o,\mathrm{MMMC}}$) [6] is bigger than twice the theoretical uncertainty for a nominally homogeneous steel ($\sigma_{T_o,\mathrm{ASTM\ E1921}}$). Similar to the BMMC method, the ratio between the two members of Eq 3,

$$R_\sigma = \frac{\sigma_{T_o,\mathrm{MMMC}}}{2\sigma_{T_o,\mathrm{ASTM\ E1921}}} \tag{4}$$

will be used following the same (subjectively established) criteria described above.

Material and Characteristics of the EURO Data Set

The material used to build the EURO data set was a large forged, quenched, and tempered ring segment of the reactor pressure vessel steel DIN 22NiMoCr37, similar to A508 Cl.3, supplied by Siemens to the project coordinator, GKSS (Geesthacht, Germany). The chemical composition of the material is given in Table 1.

The cutting scheme of the various blocks extracted from the steel segment is shown in Fig. 1. All samples were prepared so that the crack front was located in the region 1/4T-1/2T, which had been found to be homogeneous in the preliminary investigations conducted by GKSS [1].

The experimental work was shared among ten different laboratories belonging to six European countries. The test matrix included tests performed at eight different temperatures from -154 to $20°C$, covering the whole range among lower and upper shelf. Fracture toughness specimens were standard C(T) with thickness ranging from 0.5T (12.5 mm) to 4T (100 mm) and initial crack size to width ratio of $0.52 \leq a_o/W \leq 0.6$. All specimens were plain sided, except for a set of 20 % side-grooved 1TC(T) samples tested at $-20°C$.

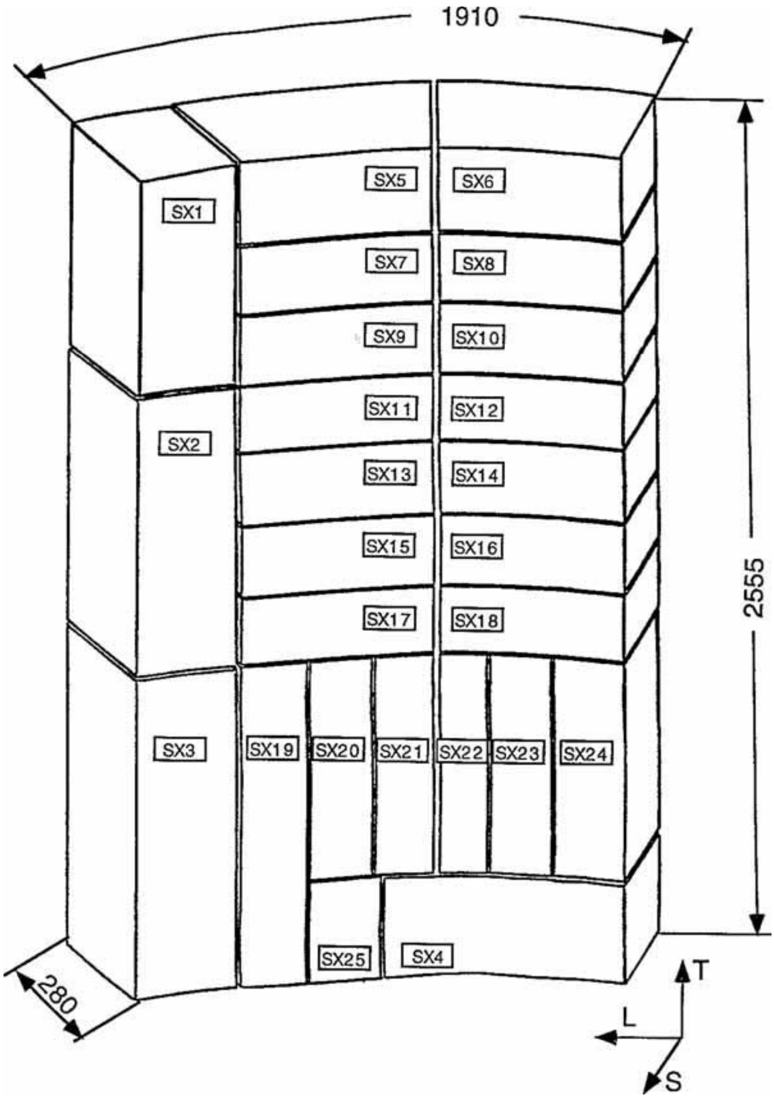

FIG. 1—*Cutting scheme of the 22NiMoCr37 ring segment.*

The overall data set consists of 734 K_{Jc} test results, for which nominal values of specimen width and thickness as well as measured values of initial crack size and ductile crack extension are available from a database distributed by GKSS to the participants after the conclusion of the project.

TABLE 2—*Reference temperatures measured from ASTM E1921-09c and SLT and SPE analyses.*

Method	All Tests	All Except SX9	Only SX9
ASTM E1921-09c	−91.3	−86.4	−107.3
SLT	−96.1	−90.8	−99.5
SPE	−87.3	−85.3	−102.3

Analyses Performed

Complete EURO Data Set

The conventional MC analysis of the complete EURO data set (734 tests and 278 valid data) yields $T_o = -91.3°C$ with a standard deviation $\sigma_{T_o} = 4.1°C$.

If data from block SX9 are excluded, the reference temperature becomes $T_o = -86.4°C$ associated to the same standard deviation. The difference $\Delta T_o = 4.9°C$ is small enough to render the two temperatures statistically not different at the 95 % confidence level (i.e., considering $\pm 2\sigma$ intervals).

A similar increase of T_o is observed when applying the SLT approach (from −96.1 to −90.8°C after excluding SX9). The variation is only 2°C for the SPE method (−87.3 and −85.3°C, respectively).

The reference temperatures obtained from ASTM E1921-09c, SLT, and SPE analyses are summarized in Table 2.

Since test results from SX9 represent only less than 5 % of the entire EURO data set, the applicability of the BMMC and MMMC analyses might be questionable. Indeed, $R_\sigma > 1.4$ is obtained both before and after excluding SX9. Moreover, the value of p_a returned by BMMC for the complete data (0.91) set is quite close to the fraction of data points not coming from SX9 (0.95). Results from the BMMC and MMMC analyses are summarized in Table 3.

It is interesting to note that the reference temperatures calculated on the abridged EURO data set (i.e., excluding SX9) using MC, SLT, SPE, and MMMC are all within 6°C, while more scatter is observed (13°C) for the complete data set. This indicates that excluding SX9 results significantly decreases the value of R_σ for the MMMC analysis to a value close to the threshold of homogeneity (1.01).

Block SX9

From block SX9, GKSS extracted 24 2TC(T) specimens, which were all tested at −60°C, partly by GKSS and partly by THA. As previously mentioned, 12 additional 0.5TC(T) samples were subsequently machined from the broken 2TC(T) and tested at the same temperature, all by GKSS. The SX9 data set therefore includes 36 data points.

The conventional MC analysis yields $T_o = -107.3°C$ with a standard deviation of 5.2°C and 30 valid data. Both BMMC and MMMC yield $R_\sigma > 1$, and the bi-modal analysis splits the data set approximately in half ($p_a = 0.51$).

If data is partitioned according to specimen size (Fig. 2) or testing labora-

TABLE 3—*Results of the BMMC and MMMC analyses.*

	All Tests				All Except SX9				Only SX9			
Method	$T_{o,A}$ (°C)	p_A	$T_{o,B}$ (°C)	R_σ	$T_{o,A}$ (°C)	p_A	$T_{o,B}$ (°C)	R_σ	$T_{o,A}$ (°C)	p_A	$T_{o,B}$ (°C)	R_σ
BMMC	−81.6	0.91	−110.4	1.52	−79.5	0.88	−99.6	1.43	−93.3	0.51	−115.1	1.13
MMMC	T_o = −83.0°C			1.78	T_o = −85.0°C			1.01	T_o = −104.0°C			1.21

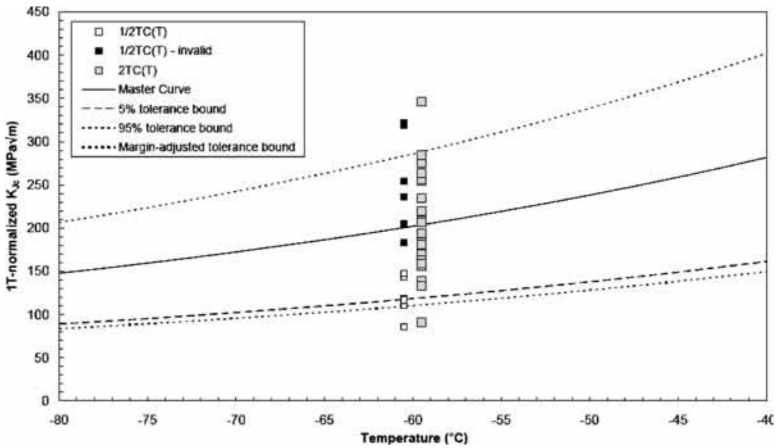

FIG. 2—*Test results from block SX9 separated on account of specimen size. Note: The margin-adjusted tolerance bound is calculated in accordance with X4.2 of ASTM E1921-09c.*

tory (Fig. 3), no obvious influence of either variable can be observed. Nevertheless, individual MC, BMMC, and MMMC analyses have been performed separately on the 0.5TC(T) and 2TC(T) data sets and on the results provided by GKSS and THA.

The value of T_o for 0.5TC(T) is significantly higher than for 2TC(T) (−95.1°C versus −109.4°C); however, for the former data set half of the results are censored and only six valid data is available. BMMC is unable to guarantee that the 2TC(T) data set contains two populations, while for the 0.5TC(T) set the

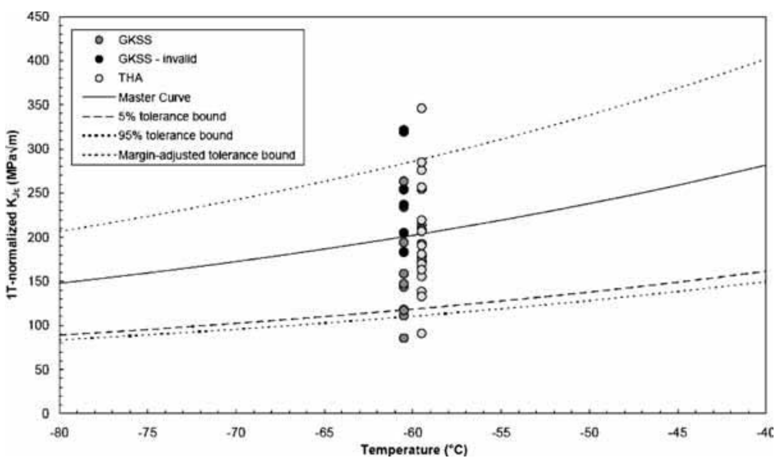

FIG. 3—*Test results from block SX9 separated on account of testing laboratory. Note: The margin-adjusted tolerance bound is calculated in accordance with X4.2 of ASTM E1921-09c.*

TABLE 4—*Results of the analyses performed on block SX9.*

	ASTM E1921-09c	BMMC				MMMC	
Data Set	T_o (°C)	$T_{o,A}$ (°C)	p_A	$T_{o,B}$ (°C)	R_σ	T_o (°C)	R_σ
All tests	−107.3	−93.3	0.51	−115.1	1.13	−104.0	1.21
1/2TC(T) only	−95.1	No convergence				−97.5	1.43
2TC(T) only	−109.4	−98.8	0.64	−118.6	0.85	−106.3	0.93
GKSS only	−101.9	−71.9	0.27	−108.9	1.07	−100.2	1.19
THA only	−109.4	−108.5	0.64	−128.1	0.85	−115.9	0.92

number of valid data is too low and the analysis does not converge. The MMMC analysis yields $R_\sigma = 0.93$. The hypothesis that 2TC(T) specimens have their cracks located in a region of the forging showing different toughness has been sustained in the work of Joyce and Gao [7].

Concerning the two testing laboratories, their respective reference temperatures are rather close (−101.9°C for GKSS and −109.4°C for THA). The BMMC analysis identifies two populations for GKSS ($R_\sigma = 1.07$) but not for THA ($R_\sigma = 0.85$); for the latter data set the MMMC analysis yields $R_\sigma = 0.92$. Note that the GKSS set contains only 10 valid data.

A summary of the results obtained for block SX9 is presented in Table 4.

In summary, the advanced MC approaches are unable to detect an influence of specimen size or testing laboratory on the results measured from block SX9.

Restricted Data Set: Tests Performed at −60°C

In order to work with more comparable numbers and more importantly to eliminate the effect of test temperature and MC shape, a restricted subset of fracture toughness results has been extracted from the complete data set, namely, the tests performed at −60°C (which include all specimens from the SX9 block).

The subset consists of 126 data from 0.5TC(T), 1TC(T), and 2TC(T) specimens; approximately 1/3 (29 %) are from block SX9.

Following the conventional MC analysis, a reference temperature of −94.2°C is calculated for the −60°C data set (113 valid data, $\sigma_{T_o} = 4.3$). After excluding SX9 specimens, T_o increases by almost 12°C to −82.4°C ($\sigma_{T_o} = 4.5$°C).

The increase in T_o caused by the removal of SX9 data is even more pronounced for the SLT analysis (15.1°C), while the variation is smaller for the SPE approach (5.1°C).

In this case, the outcome of the BMMC and MMMC analyses is quite significant.

- When all tests are accounted for, both methods yield $R_\sigma > 1.5$ (1.79 and 1.96, respectively); furthermore, BMMC reports the probability of belonging to population A as 0.81 (the actual share of non-SX9 tests in the set is 71 %);

TABLE 5—*Summary of the analyses performed on the tests performed at –60°C.*

	ASTM E1921-09c	SLT	SPE	BMMC				MMMC	
Data Set	T_o (°C)	T_o (°C)	T_o (°C)	$T_{o,A}$ (°C)	p_A	$T_{o,B}$ (°C)	R_σ	T_o (°C)	R_σ
All –60°C tests	−94.2	−97.1	−87.2	−83.3	0.81	−114.2	1.79	−88.2	1.96
All except SX9	−82.4	−82.0	−82.1	−72.1	0.10	−83.3	0.54	−82.4	0.15
Only SX9	−107.3	−99.5	−102.3	−93.3	0.51	−115.1	1.13	−104.0	1.21

- Once test results from SX9 samples are removed, the criteria expressed by Eqs 1 and 3 are not fulfilled and for both methods the ratio R_σ is significantly lower than 1 (0.54 and 0.15, respectively).

Moreover, we observe that the reference temperatures measured by MC, SLT, SPE, and MMMC for the non-SX9 subset are all within 0.3°C and that MC and MMMC provide exactly the same T_o (–82.4°C).

A summary of the analyses performed is provided in Table 5.

Comparison between Blocks SX9 and SX12

As a final assessment of the variability of block SX9 with respect to the "mean" fracture behavior of the 22NiMoCr37 forged ring, we decided to select another block, which might be considered representative of such mean behavior. According to the analyses performed by Wallin in Ref 6, the block that best represents the average fracture properties of the material is SX12 (Fig. 4).

From block SX12, 0.5TC(T), 1TC(T), 2TC(T), and 4TC(T) specimens were extracted; they were tested at −91, −40, and –20°C (Fig. 1). In total, the SX12 data set consists of 68 tests. In this case, only MC, BMMC, and MMMC analyses were performed.

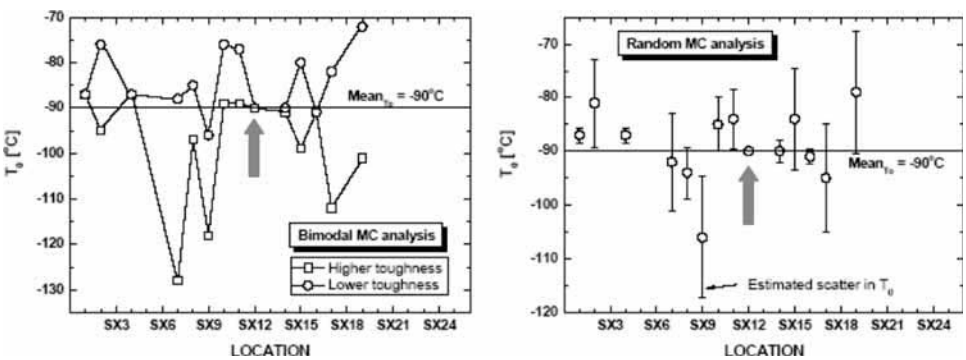

FIG. 4—*Inhomogeneity analyses performed by Wallin* [6] *on the EURO data set. Block SX12 is indicated by the arrows.*

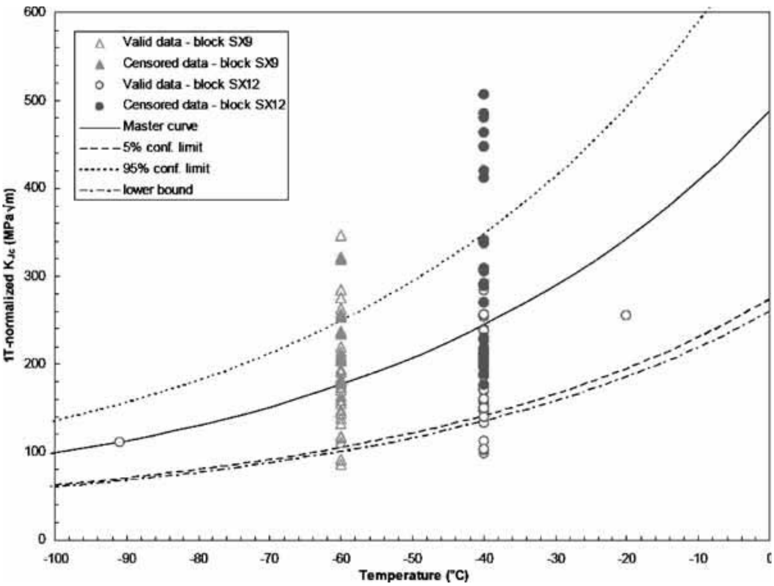

FIG. 5—*MC analysis of data from blocks SX9 and SX12. Note: The lower bound curve is calculated in accordance with X4.2 of ASTM E1921-09c.*

A "modified" MC analysis of the two blocks (SX9+SX12) (Fig. 5) was performed by censoring K_{Jc} values falling above the measuring capacity K_{limit} but without accounting for the temperature validity window of the ASTM E1921-09c standard ($T_o \pm 50°C$). Otherwise, all data from block SX12 (except one) would have been censored and the calculated reference temperature ($-107.1°C$) would have practically coincided with that of block SX9 ($-107.3°C$). In the case of BMMC, the test temperature validity window is defined by $T_L - 50°C \leq T \leq T_H + 50°C$, where T_L and T_H are the lower and the higher between T_{o1} and T_{o2}. For MMMC, the requirement is $T_X - 50°C \leq T \leq T_X + 50°C$, with $T_X = T_{o,\text{MMMC}} + \sigma_{T_o,\text{MMMC}}$.

The reference temperature of block SX12 ($-87.6°C$ and $\sigma_{T_o} = 4.8°C$) is very close to that of the overall EURO data set after excluding SX9 data ($-86.4°C$ and $\sigma_{T_o} = 4.1°C$), and statistically different at the 95 % confidence level from the reference temperature of block SX9 ($-107.3°C$).

The BMMC analysis of the combined data set (SX9+SX12) is unable to detect two populations ($R_\sigma = 0.08$); however, the value obtained for p_a (0.78) is not too far from the percentage of SX12 data (65 %) and the values of T_o for populations A and B (-89.2 and $-115.8°C$) are fairly similar to those calculated for the individual blocks. Therefore, although strictly speaking Eq 3 is not fulfilled and the calculated value of R_σ is very small, the BMMC analysis seems to have identified the two blocks as two substantially different materials. Note also that for the individual block SX12, BMMC provides exactly the same reference temperature as MC and yields $p_a = 1.0$ and $R_\sigma = 0.00$ ($T_{o1} = T_{o2}$).

As far as the MMMC method is concerned, for the combined data set R_σ

TABLE 6—*Results of the analyses conducted on blocks SX9 and SX12.*

	ASTM E1921-09c	BMMC				MMMC	
Data Set	T_o (°C)	$T_{o,A}$ (°C)	p_A	$T_{o,B}$ (°C)	R_σ	T_o (°C)	R_σ
SX9+SX12	−98.8	−89.2	0.78	−115.8	0.08	−95.0	1.61
SX9	−107.3	−93.3	0.51	−115.1	1.13	−104.0	1.21
SX12	−87.6	−87.6	1.00	−88.2	0.00	−87.6	0.00

$=1.61$, while for the individual block SX12 we obtain again $R_\sigma=0.00$ ($\sigma_{T0,MMMC}=0$). In other words, adding SX9 data to the SX12 set introduces a significant inhomogeneity source, which is detected by both the bi-modal and the MMMC analyses.

The results of the analyses conducted in accordance with the different approaches are summarized in Table 6.

Conclusions

Alternative MC approaches (SLT, SPE, BMMC, and MMMC) have been used for the investigation of the largest available fracture toughness data set (the EURO data set). More specifically, the analyses have been aimed at investigating the previously reported macroscopic inhomogeneity corresponding to one of the blocks extracted from the forged ring section of 22NiMoCr37 used for the EURO project (block SX9).

It has been found that the most advanced methodologies (BMMC and MMMC) are quite effective in rationalizing the outlier behavior of the “suspect” block.

However, detecting the anomaly represented by block SX9 is more feasible when the contributions of the two populations are numerically “balanced,” which is not the case when investigations are performed on the complete data set (734 test results, only 5 % coming from SX9). More meaningful results have been obtained by considering the single-temperature −60°C data set (126 data, 29 % from SX9), which avoids considering test temperature as a variable; or by directly comparing SX9 with another block fully representative of the mean behavior of the investigated material (SX12).

Acknowledgments

This work was partially sponsored by Tractebel Energy Engineering, whose support is kindly appreciated.

References

[1] Heerens, J. and Hellmann, D., “Final Report: Fracture Toughness of Steel in the Ductile to Brittle Transition Regime,” *Measurement and Testing Programme Con-*

tract MAT1-CT-940080, February 1999.
[2] ASTM E1921-09c, 2009, "Standard Test Method for Ferritic Steels in the Transition Range," *Annual Book of ASTM Standards*, Vol. 03.01, ASTM International, West Conshohocken, PA.
[3] Chaouadi, R., "Analysis of Fracture Toughness Behavior of 22NiMiCr37 Steel in the Transition Regime (SM&T Round Robin)," *SCK•CEN Report No.* BLG 799 (*unrestricted*), Mol, Belgium, December 1998.
[4] Heerens, J. and Hellmann, D., "Development of the EURO Fracture Toughness Dataset," *Eng. Fract. Mech.*, Vol. 69, 2002, pp. 421–449.
[5] Wallin, K., "Master Curve Analysis of the 'EURO' Fracture Toughness Dataset," *Eng. Fract. Mech.*, Vol. 69, 2002, pp. 451–481.
[6] Wallin, K., "Inhomogeneity Check of the 'EURO' Fracture Toughness Reference Data Set," *Proceedings of ECF15, 15th European Conference on Fracture-Advanced Fracture Mechanics for Life and Safety Assessments*, Stockholm, Sweden, August 11–13, 2004, ESIS, Sweden, available at http://www.ecf15.org/proceedings.html.
[7] Joyce, J. A. and Gao, X., "Analysis of Material Inhomogeneity in the European Round Robin Fracture Toughness Data Set," *J. ASTM Int.*, Vol. 5, No. 9, 2008, Paper ID JAI101512.
[8] Wallin, K., Nevasmaa, P., Laukkanen, A., and Planman, T., "Master Curve analysis of Inhomogeneous Ferritic Steels," *Eng. Fract. Mech.*, Vol. 71, 2004, pp. 2329–2346.
[9] Viehrig, H.-W., Scibetta, M., and Wallin, K., "Application of Advanced Master Curve Approaches on WWER-440 Reactor Pressure Vessel Steels," *Int. J. Pressure Vessels Piping*, Vol. 83, 2006, pp. 584–592.
[10] "SINTAP—Structural Integrity Assessment Procedures for European Industry," *Final Procedure, British Steel Report, Project* BR95-1426, British Steel, Rotherham, United Kingdom, 1999.
[11] Pisarski, H. G. and Wallin, K., "The SINTAP Fracture Toughness Estimation Procedure," *Eng. Fract. Mech.*, Vol. 67, No. 6, 2000, pp. 613–624.

Reprinted from JAI, Vol. 7, No. 1
doi:10.1520/JAI102510
Available online at www.astm.org/JAI

Xian-Kui Zhu[1] *and Brian N. Leis*[2]

Revisit of ASTM Round-Robin Test Data for Determining *R* Curves of Thin-Sheet Materials

ABSTRACT: This paper revisits the ASTM round-robin fracture test data obtained in 1979–1980 by ASTM Task Group E24.06.02 on Application of Fracture Analysis Methods. The fracture tests were conducted using thin-sheet compact tension [C(T)] specimens made of three materials—7075-T561 aluminum alloy, 2024-T351 aluminum alloy, and 304 stainless steel—and different specimen widths were employed in order to take account of in-plane specimen size effect on fracture toughness. Typical experimental data are reanalyzed, and crack growth resistance curves are developed in accordance with fracture test standards, ASTM E561-05 and ASTM E1820-08. Several useful results as well as the conditions under which the two standards can equivalently determine a geometry-independent resistance curve are obtained for the thin-sheet C(T) specimens.

KEYWORDS: fracture toughness, *R* curve, ductile crack growth, thin sheet, ASTM E561-05, ASTM E1820-08

Introduction

Thin-sheet materials or thin-walled structures are used widely in various engineering fields, such as aerospace, shipbuilding, pressure vessels, pipelines, and ground-vehicles. A key property for thin-sheet metals is the plane stress fracture toughness that can be measured with a critical point value or in a resistance (*R*) curve format. Effective and accurate measurement of this fracture property is critical for engineering design, material selection, and structural

Manuscript received May 13, 2009; accepted for publication September 24, 2009; published online November 2009.

[1] Senior Research Scientist, Battelle Memorial Institute, 505 King Ave., Columbus, OH 43201.

[2] Senior Research Leader, Battelle Memorial Institute, 505 King Ave., Columbus, OH 43201.

Cite as: Zhu, X.-K. and Leis, B. N., "Revisit of ASTM Round-Robin Test Data for Determining *R* Curves of Thin-Sheet Materials," *J. ASTM Intl.*, Vol. 7, No. 1. doi:10.1520/JAI102510.

integrity assessment. Two typical R curve test methods have been standardized in fracture test methods ASTM E561-05 [1] and ASTM E1820-08 [2], respectively, in reference to the linear elastic fracture mechanics (LEFM) and elastic-plastic fracture mechanics (EPFM). Recently, a comprehensive review of fracture mechanics testing and methods in application to thin-walled structures was given by Zerbst et al. [3].

Fracture mechanics tests were initially developed to measure crack growth resistance curves for sheet metals using large specimens that were highly constrained to plastic deformation or dominated by elastic deformation. As such, the stress intensity factor (K) theory in terms of LEFM was able to be used to characterize fracture behavior and R curves for thin-sheet materials that exhibit ductile crack extension. ASTM E561-05 [1] outlines a procedure to determine K-R curves from a single test using a middle-cracked tension [M(T)] specimen, a compact tension [C(T)] specimen, and a crack-line-wedge-loaded [C(W)] specimen. In ASTM E561-05, a K-R curve is defined in regard to effective stress intensity factor (K_{eff}) as a function of effective crack extension (Δa_{eff}) under predominantly elastic conditions. Such K-R curves are regarded as being independent of original crack size and the specimen configuration in which they are developed. For example, different experimental results in Ref 4 showed that a K-R curve for a given thickness was independent of crack size and specimen geometry. Schwalbe and co-workers [5,6] drew the same conclusion provided that an upper limit of the extent of plasticity (i.e., 0.9 times the yield stress) is not exceeded. Geometry independence of crack growth resistance curves was later verified theoretically by Yuan and Yang [7] and numerically by Yan and Mai [8] under plane stress elastic and plastic conditions.

The earliest R curve tests were conducted using wide panels or large M(T) specimens [9,10] so as to meet the requirement of linear elastic response. For example, an M(T) specimen made of aluminum alloys typical of airframe structures often requires the specimen width of up to 2 m in order to determine valid K-R curves [11]. As such, a large volume of material is used, and a large test machine with high loading capacity is required. To avoid these requirements, small specimen R-curve test methods were developed to generate R curve data comparable to that generated with wide panels. Under the condition of small-scale yielding or elastic dominance, ASTM E561-05 allows small C(T) and M(T) specimens to be used to determine K-R curves.

A round-robin program [12] organized by ASTM Task Group E24.01.02 on Crack Growth Resistance Curves established the guidelines for K-R curve testing used in the practice ASTM E561-05. Pearson [13] further showed good agreement of the valid R curves obtained using C(T) and M(T) specimens for two materials of 7075-T561 aluminum alloy and 4340 steel. However, when large-scale yielding or large plastic deformation prevails in a small specimen, the LEFM based K theory becomes invalid, and the J-integral theory (EPFM) should be used to characterize ductile crack growth resistance. Different J-R curve test methods have been thus developed. ASTM E1820-08 (or its predecessors ASTM E813 [14], ASTM E1152 [15], and ASTM E1737 [16]) provides standard procedures and methods to determine J-R curves for CT and other specimens. Since ASTM E1820-08 was developed primarily for testing plane strain fracture toughness, a minimum specimen thickness is required. In contrast, ASTM E561-05 does not contain any minimum thickness criteria, which makes it more suitable for thin-sheet fracture testing.

Reynolds [17,18] investigated the *R* curves of 2024-T3 aluminum alloy obtained by five laboratories using small and large sheet specimens for a NASA round-robin program. The crack resistance curves generated with small C(T) and M(T) specimens were compared to those obtained from 1.5 m wide panels. Their results indicated that the effective stress intensity factor K_{eff} determined using secant compliance based crack length as defined in ASTM E561-05 was equivalent to the stress intensity factor K_J calculated using physical crack length and the *J*-integral equation prescribed in ASTM E1152. When *R*-curves were plotted as either K_{eff} or K_J against physical crack extension, the small C(T) and M(T) specimen data matched well with each other and with the initial portion of the wide-panel test data, with a larger specimen providing more data that could be directly related to the wide-panel *R* curve. The excellent correlation between K_{eff} and K_J cast their doubt on the necessity for *J*-integral calculations when producing resistance curves for 2024-T3 aluminum alloy. However, they did not give any limitations for the equivalence between K_{eff} and K_J, except for the observation that the physical and effective crack extensions differed, which became particularly significant at larger crack extensions. Haynes and Gangloff [19] presented experimental results of K_J versus physical crack extension curves for three aluminum alloy sheets—2024-T3, 2519-T87, and 2650-T6, using small C(T) specimens, where crack extension was measured with the potential drop method and the stress intensity factor was calculated from the *J*-integral by following ASTM E1152. Their results from the small specimens were in reasonable agreement with the linear elastic resistance curves determined from wide panels. To date, the conditions for which ASTM E561-05 and ASTM E1820-08 can determine an equivalent *R* curve using the same small specimens remain unclear, which motivates the present study.

Newman [20] presented the detailed results of an experimental and predictive round-robin program conducted in 1979–1980 by ASTM Task Group E24.06.02 on Application of Fracture Analysis Methods, with an aim if determining appropriate fracture analysis methods for predicting failure loads of complex thin-walled structural components containing cracks. Fracture test data on thin-sheet C(T) specimens made of three materials—7075-T652 aluminum alloy, 2024-T351 aluminum alloy, and 304 stainless steel—were used as baseline data for 18 participants to make their predictions. To account for in-plane specimen size effect on the fracture property, different specimen widths were employed in these tests. Since the test data were explained and used in different ways by the participants, it is not surprising that different predictions were developed in this round robin. This paper revisits these fracture tests and reanalyzes the typical experimental data available in Ref 20 with a view to obtain more consistent predictions. Crack growth resistance curves for the three metals are then developed in reference to the two *R*-curve test standards, ASTM E561-05 and ASTM E1820-08. The objective is to determine the conditions for which these two standards can equivalently determine crack growth resistance curves using C(T) specimens.

Fracture Experiments

The experimental fracture tests were conducted by NASA Langley Research Center and Westinghouse Research and Development Laboratory [20,21] to obtain data quantifying load as a function of physical crack extension. These data formed the baseline for the above-noted round robin.

Fracture tests were done using the single specimen technique for thin-sheet C(T) specimens made of three materials with three specimen sizes. Three nominal specimen widths of $W=51$ mm (2 in.), 102 mm (4 in.), and 203 mm (8 in.) were employed for each material in order to take account of specimen size effect on the fracture property. Specimen height was 1.2 times of the width, i.e., $H=1.2W$, and the nominal crack length to width ratio a_0/W was 0.5. The nominal thickness of all specimens was 12.7 mm (0.5 in.), a typical thickness size used in thin-walled structures. All other planar configurations were identical to those specified in ASTM E561-05 for standard C(T) specimens. All specimens with plain sides were fatigue precracked and then tested under the displacement control conditions at room temperature.

Three materials were tested: 7075-T651 aluminum alloy, 2024-T351 aluminum alloy, and 304 stainless steel. These materials were selected because they would exhibit a wide range in fracture toughness behavior from low to high in relative terms. The mechanical properties and engineering stress-strain curves of these materials were measured from the standard tension tests and reported in Ref 20. For 7075-T651 material, the 0.2 % offset yield stress $\sigma_{ys}=530$ MPa, the ultimate tensile strength $\sigma_{uts}=585$ MPa, and the elastic modulus $E=71.7$ GPa. For 2024-T531 material, $\sigma_{ys}=315$ MPa, $\sigma_{uts}=460$ MPa, and $E=71.4$ GPa. For 304 steel, $\sigma_{ys}=265$ MPa, $\sigma_{uts}=630$ MPa, and $E=203$ GPa.

For each material, three duplicate C(T) specimens were tested for a given width, which leads to a total of nine tests for each material or 27 tests for all three materials. The applied load, crack mouth opening displacement (CMOD), and load-line displacement (LLD) were recorded. The effective crack length (a_{eff}) was determined from the secant compliance method, while the physical crack length (a_{phy}) was measured using the elastic unloading compliance method. Effective crack lengths were averages between compliance measurements at the crack mouth and load line. In addition, the visual crack length (a_{vis}) was observed to the nearest 1 mm on each specimen surface. Representative load-displacement records and crack length measurements for nine typical tests were presented in Tables 17–19 in Ref 20. These tables list applied load, CMOD, LLD, a_{eff}/W and a_{phy}/W determined from the compliance data, and a_{vis}/W measured on the surface. Crack growth resistance (K-R or J-R) curves were developed by Newman [20] using the typical fracture data in terms of Δa_{eff} or Δa_{phy}, where the effective stress intensity factor K_{eff} was calculated using the effective crack lengths in accordance with ASTM E561-05, the physical stress intensity factor K_{phy} was similarly determined using the physical crack lengths, and the J-integral was determined either from the physical stress intensity factor K_{phy} or from a J-integral equation different from that used in ASTM E1820-08. As such, direct comparison between K and J resistance curves obtained from these inconsistent methods is difficult. To this end, consistent R-curves are developed and analyzed for these materials in the following sections through reanalyzing the fracture test data in accordance with ASTM E561-05 and ASTM E1820-08.

Determination of *R* Curves

This section reanalyzes all typical fracture test data presented in Ref 20 and then develops crack growth resistance curves in terms of K and J for the three materials. Detailed comparisons and discussions on the results then follow. For convenience, the basic equations for determining R curves specified in ASTM E561-05 and ASTM E1820-08 are outlined first.

Calculation Equations

In ASTM E561-05, the general equation for calculating the stress intensity factor K that is a function of the crack size for a specific $C(T)$ specimen is given by

$$K = \frac{P}{B\sqrt{W}} \frac{\left(2 + \frac{a}{W}\right)}{\left(1 - \frac{a}{W}\right)^{3/2}} f\left(\frac{a}{W}\right) \tag{1}$$

where:

P = applied load,
B = specimen thickness,
W = specimen width measured from the load line,
a = crack size, and

$$f\left(\frac{a}{W}\right) = \left[0.886 + 4.64\left(\frac{a}{W}\right) - 13.32\left(\frac{a}{W}\right)^2 + 14.72\left(\frac{a}{W}\right)^3 - 5.6\left(\frac{a}{W}\right)^4\right] \tag{2}$$

Depending on the calculation methods, the crack size could be the effective crack size a_{eff} or the physical crack size a_{phy}. The a_{eff} denotes a plastic zone corrected crack size and is often determined from specimen secant compliance data. In ASTM E561-05, an R curve is defined as an effective stress intensity factor K_{eff} versus Δa_{eff} curve. In this work, an alternative R curve is also generated as an effective stress intensity factor K_{eff} versus Δa_{phy} curve.

In ASTM E1820-08, the elastic unloading compliance method is suggested for measuring the physical crack length a_{phy}. The total J-integral is separated into an elastic component and a plastic component and is calculated with incremental equations in the resistance curve test procedure. For the plane stress dominant deformation, if the specimen is not side grooved, the net thickness B_N is equal to the full thickness B, and all J-integral equations for the plane strain conditions can be directly used. At the ith loading step, the total J-integral is expressed generally as

$$J_i = \frac{K_i^2}{E} + J_{\text{pl}(i)} \tag{3}$$

where:

K_i is calculated by Eq 1 using the physical crack size $a_{\mathrm{phy}(i)}$ and plastic component $J_{\mathrm{pl}(i)}$ is determined by

$$J_{\mathrm{pl}(i)} = \left[J_{\mathrm{pl}(i-1)} + \frac{\eta_{(i-1)}}{b_{(i-1)}B} \cdot (A_{\mathrm{pl}(i)} - A_{\mathrm{pl}(i-1)})\right]\left[1 - \frac{\gamma_{(i-1)}}{b_{(i-1)}}(a_{(i)} - a_{(i-1)})\right] \tag{4}$$

where:
physical crack size is used,
crack ligament size $b_{(i-1)} = W - a_{(i-1)}$, and
two geometry factors for $C(T)$ specimens are functions of a/W

$$\eta_{(i-1)} = 2.0 + 0.522(1 - a_{(i-1)}/W)$$

$$\gamma_{(i-1)} = 1.0 + 0.76(1 - a_{(i-1)}/W) \tag{5}$$

In Eq 4, the quantity $A_{\mathrm{pl}(i)} - A_{\mathrm{pl}(i-1)}$ is the increment of plastic area under the load versus plastic LLD record between two lines of constant displacement at load points $i-1$ and i.

In order to compare a J-R curve with a K-R curve obtained for a plane stress specimen, the J-integral determined from Eq 3 is converted for this work into a J-based stress intensity factor by

$$K_J = \sqrt{EJ} \tag{6}$$

In this way, a K_J versus physical crack extension curve is equivalent to a J-R curve.

As noted above, two different compliance technologies are used to determine crack sizes in the ASTM E561-05 and ASTM E1820-08. In the secant compliance technology, specimen loading compliance is inferred from the secant slope of a measured load-displacement curve and is calculated as the ratio of specimen displacement to the load carried by the specimen (V/P, where the initial displacement and load are assumed to be zero) during the test, as shown in Fig. 1. The secant compliance value and an appropriate calibration equation are used at each loading point to determine effective crack size that can be used directly in the stress intensity factor solutions to determine K_{eff}. In the elastic unloading compliance technology, specimen unloading compliance is measured through periodically partially unloading (e.g., about 15 % at various load levels) during the test and is calculated from the unloading slope reciprocal or $\Delta V/\Delta P$, as shown in Fig. 1. Specimen elastic unloading compliance values are substituted into the appropriate calibration curve at each unloading point to determine physical crack size that is required in the calculation of crack growth corrected J-integral. As Fig. 1 illustrates, the secant compliance is larger than the unloading compliance. Because unloading cycles are not required, the secant compliance technique is much simpler than the unloading compliance technique.

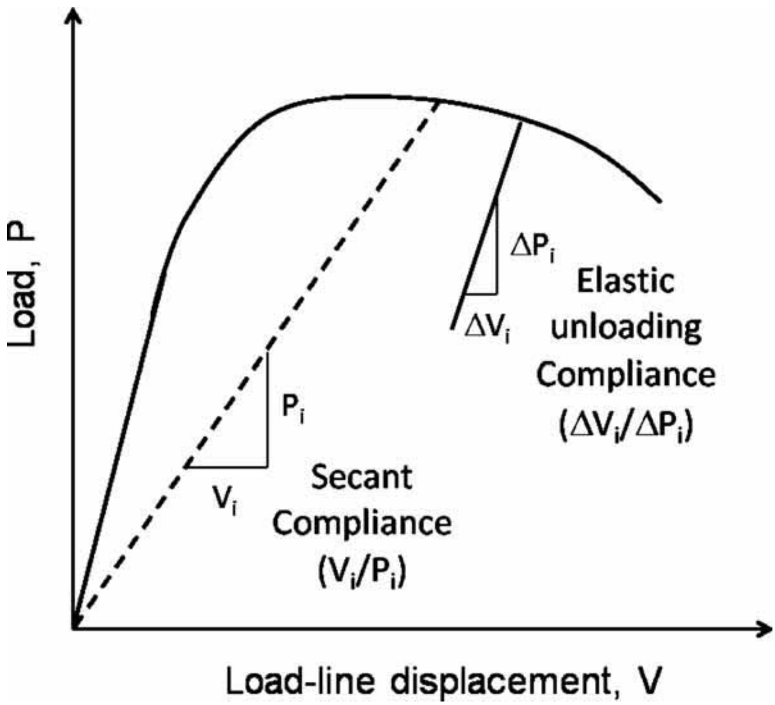

FIG. 1—*Schematic load versus LLD curve and comparison of secant compliance with unloading compliance.*

Test Data Analysis

The fracture data from the nine typical tests using thin-sheet C(T) specimens are available in Tables 17–19 in Ref 20. These tables contain applied load, CMOD, LLD, effective crack length and physical crack length determined from the compliance data, and visual crack length measured on the surface. For every material, three specimen widths of $W = 51$ mm (1T), 102 mm (2T) and 203 mm (4T) were employed in the tests. All C(T) specimens have the nominal crack length to width ratio $a_0/W = 0.5$ and the nominal thickness $B = 12.7$ mm. The test data are reanalyzed here so that adequate data can be identified in order to develop valid crack growth resistance curves.

Aluminum Alloy 7075-T561—Figure 2(*a*) and 2(*b*) shows the test data of load versus LLD and load versus unloading compliance based physical crack extension, respectively, for 7075-T651 C(T) specimens for the three specimen size cases of 1T, 2T, and 4T. It is seen from these figures that the maximum applied load, the maximum LLD, and the maximum crack extension increase as the specimen width increases. Comparing to the specimen thickness, the maximum displacements are very small and equal to about 9 %, 15 %, and 20 % of the thickness, respectively, for the 1T, 2T, and 3T specimens. In contrast, the

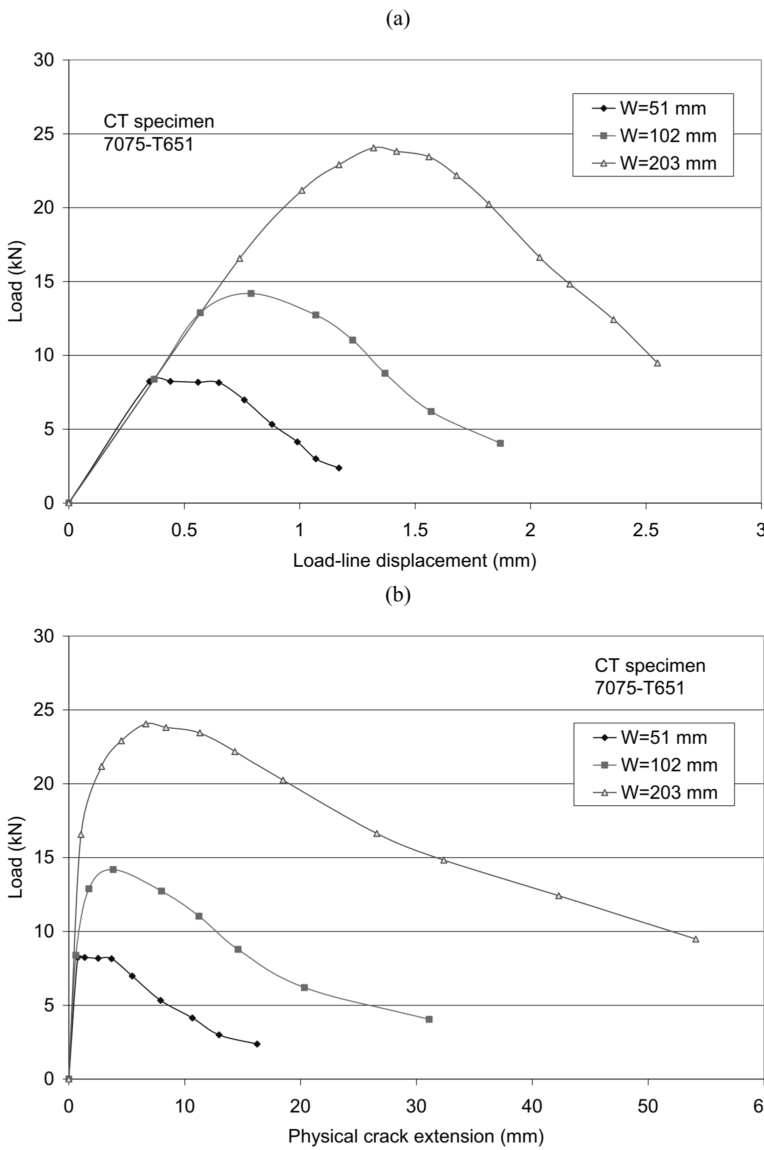

FIG. 2—*Test data for 7075-T651 CT specimens. (a) Load versus LLD. (b) Load versus physical crack extension.*

maximum crack extensions are very large and have a factor of about 14, 17, and 21 of the maximum displacements for the corresponding specimens. This indicates that the 7075-T651 aluminum alloy evaluated has relatively very poor ductility.

Figure 3 compares the crack length to width ratios a/W calculated from

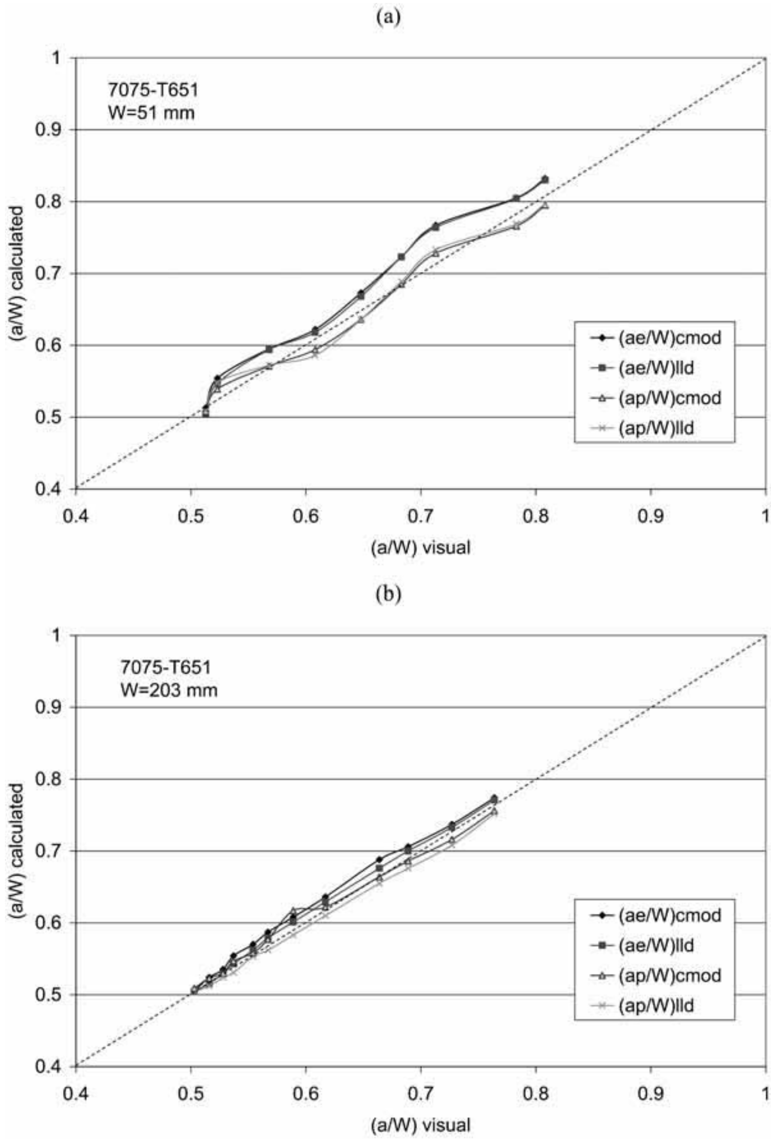

FIG. 3—*Crack length to width ratios calculated from compliance based CMOD and LLD versus visual data for 7075-T651 CT specimens:* (*a*) *W=51 mm and* (*b*) *W=203 mm.*

CMOD and LLD using the secant and unloading compliance data versus visually measured data for 7075-T651 1T and 4T C(T) specimens. In this figure, $(ae)_{CMOD}$ and $(ae)_{LLD}$ denote the effective crack sizes determined from the CMOD and LLD data using the secant compliance approach. $(ap)_{CMOD}$ and

$(ap)_{LLD}$ stand for the physical crack sizes determined from the CMOD and LLD data using the unloading compliance technique. The test results for 2T specimen are not shown here because they are similar to those for the 1T case. From Fig. 3, it is observed that (1) the secant compliance determined effective crack lengths from CMOD and LLD are almost identical, (2) the unloading compliance determined physical crack lengths from CMOD and LLD are equivalent, (3) physical crack lengths are within 5 % of visual crack length measurements on the specimen surface, and (4) the effective crack length estimates are slightly larger than the visual data for 1T and 2T specimens but are good for 4T specimen.

Figure 4 displays the variations in physical crack length to width ratio a/W versus LLD for 7075-T651 1T and 4T C(T) specimens. It is interesting from this figure to note that the physical crack extensions obtained from the unloading compliance and the visual measurements on the surface are closely related to the LLD following a power-law relationship. A power-law function is determined by curve fitting using the least-squares regression method, as included in Fig. 4. The power-law relationship existing between the physical crack extension and the LLD is very important and useful because it can be used to smooth the raw experimental data or to estimate crack extension in case the physical crack length measurements inaccurate.

Aluminum Alloy 2024-T351—Figure 5(*a*) and 5(*b*) shows the experimental data of load versus LLD and load versus physical crack extension, respectively, for three 2024-T351 C(T) specimens. Comparison of Fig. 5 with Fig. 2 indicates that the applied load and LLD for each specimen size for 2024-T351 aluminum alloy are nearly double higher than those for 7075-T561 aluminum alloy and the curve shapes are similar for the same specimen size. Comparing to the 7075-T351 material, Fig. 5 shows that the maximum displacements for the 2024-T351 material increase to about 24 %, 35 %, and 53 % of the thickness, respectively, for the 1T, 2T, and 3T specimens. In contrast, the maximum crack extensions decrease considerably to a factor of 3.2, 3.6, and 4.3 of the maximum displacements for the three corresponding specimens. This indicates that the 2024-T351 material evaluated is relatively tougher than the 7075-T651 material and has good ductility.

Figure 6 compares the crack length to width ratios a/W calculated from CMOD and LLD using the secant and unloading compliance data versus visually measured data for 2024-T351 C(T) specimens for the two specimen size cases of 1T and 4T. Again, the measured results for the 2T specimen are similar to those for the 1T case. From the figure, it is observed that (1) the effective crack lengths determined from the CMOD and LLD secant compliance data are nearly identical but significantly larger than the physical crack lengths and (2) the physical crack lengths determined from the CMOD and LLD unloading compliance data are almost the same and close to or relatively smaller than the visual crack length measurements on the specimen surface.

Figure 7 depicts the variations in physical crack length to width ratio a/W versus LLD for 2024-T351 1T and 4T C(T) specimens. As evident from this figure, the physical crack extensions measured from the unloading compliance fit well the LLDs in a power-law relationship for the specimens. The visual

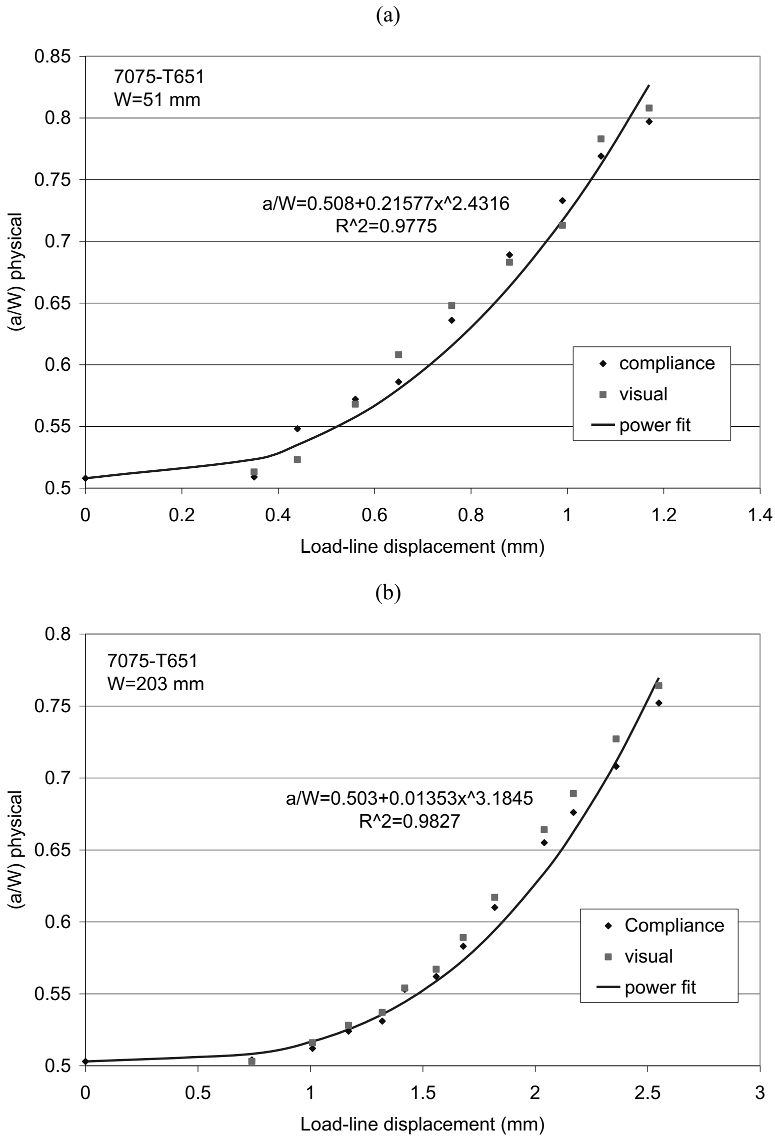

FIG. 4—*Variations in physical crack length to width ratios versus LLD for 7075-T651 CT specimens:* (*a*) *W=51 mm and* (*b*) *W=203 mm.*

crack extensions reasonably follow the power-law relationship for the 1T and 2T specimens but deviate linearly from the power-law curve at a large LLD of 3 mm for the 4T specimen. This indicates that the visual crack length measurements can be imprecise under large deformation due to the plastic zone interface and crack tunneling.

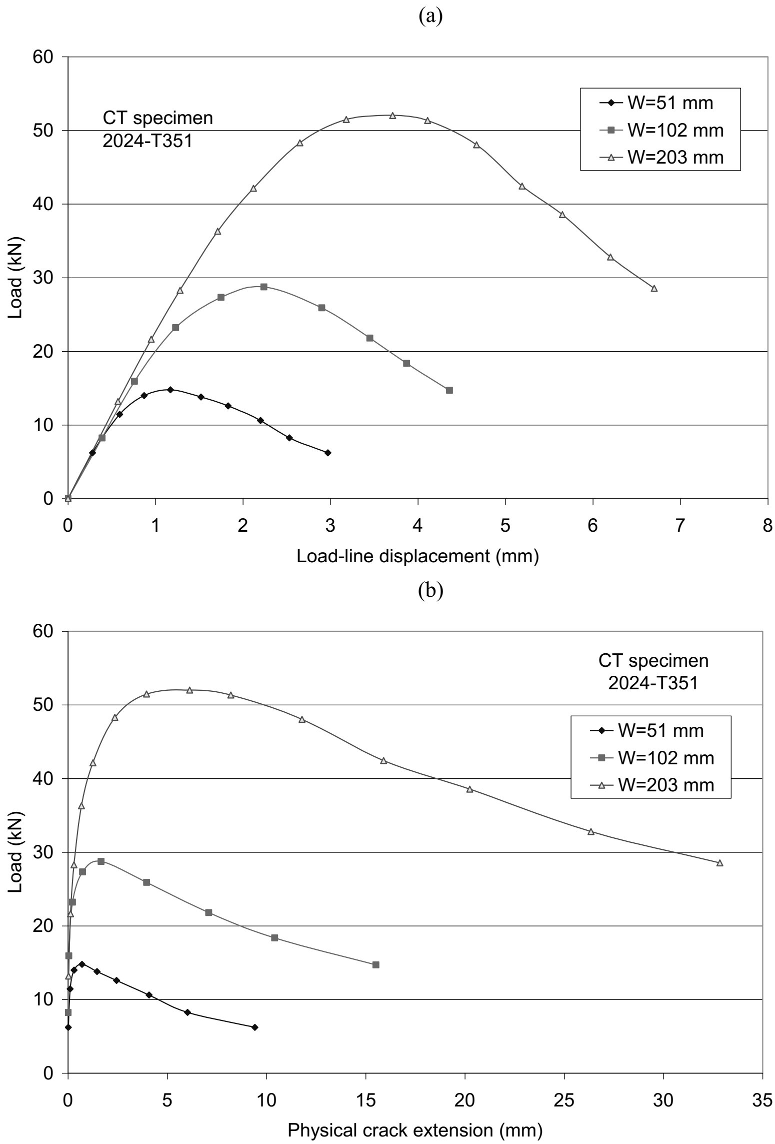

FIG. 5—*Test data for 2024-T351 CT specimens.* (*a*) *Load versus LLD.* (*b*) *Load versus physical crack extension.*

Stainless Steel 304—Figure 8(*a*) and 8(*b*) shows the test data of load versus LLD and load versus physical crack extension, respectively, for three 304 stainless steel C(T) specimens. It is seen that the applied load, LLD, and crack extension for the three specimen sizes for this steel are considerably larger than those for the two aluminum alloys and all curve shapes are totally different. For

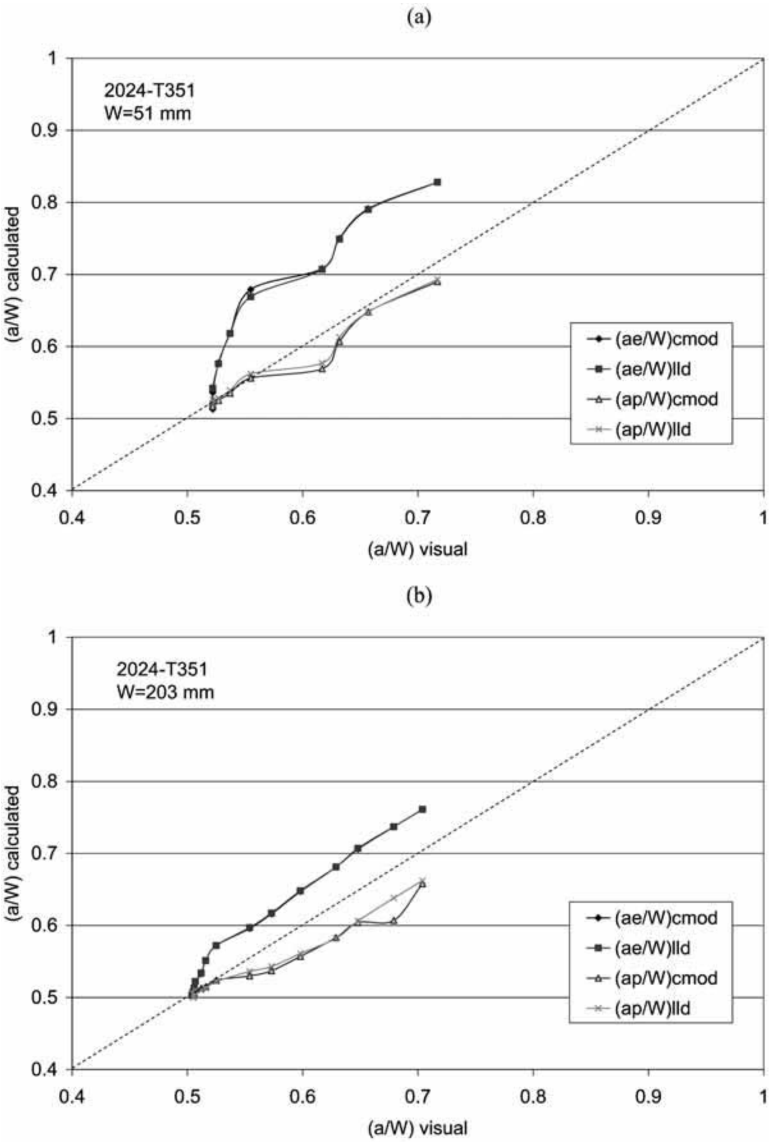

FIG. 6—*Crack length to width ratios calculated from compliance based CMOD and LLD versus visual data for 2024-T351 CT specimens:* (*a*) *W=51 mm and* (*b*) *W=203 mm.*

this steel, the maximum displacements are large and comparable to the thickness and equal to about 65 %, 103 %, and 124 % of the thickness, respectively, for the 1T, 2T, and 3T specimens. However, the maximum crack extensions are very small and only equal to 0.14, 0.33, and 0.33 of the maximum displace-

(a)

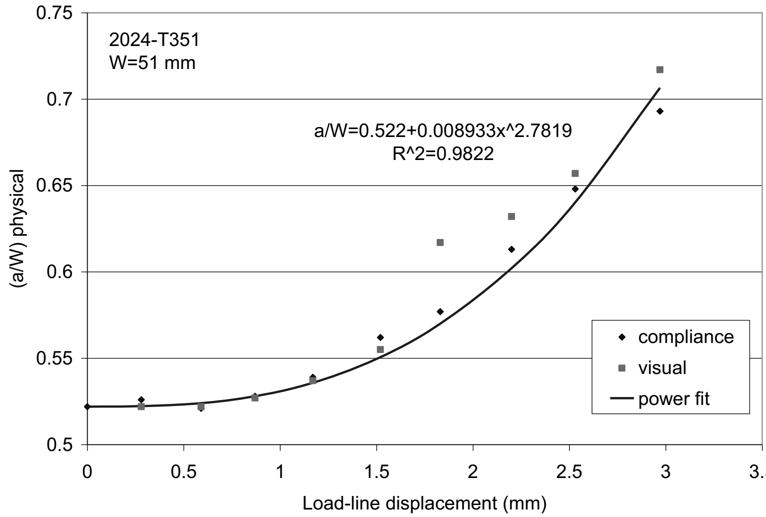

(b)

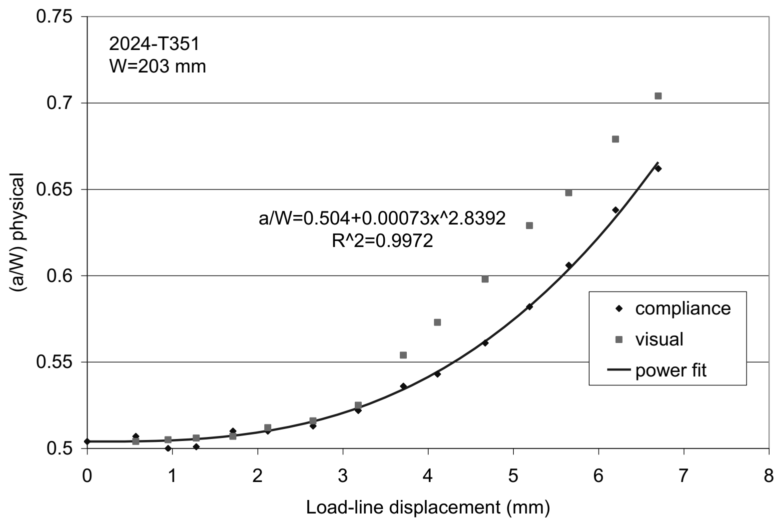

FIG. 7—*Variations in physical crack length to width ratios versus LLD for 2024-T351 CT specimens:* (*a*) *W=51 mm and* (*b*) *W=203 mm.*

ments for the three corresponding specimens. This indicates that the 304 steel evaluated has very good ductility and can exhibit large plastic deformation.

Figure 9 compares crack length to width ratios a/W calculated from CMOD and LLD using the secant and unloading compliance data versus visually measured data for 304 steel 2T and 4T C(T) specimens. Note that visual crack length measurements are not available for 1T case in Ref 20. As shown in Fig. 9, it is

(a)

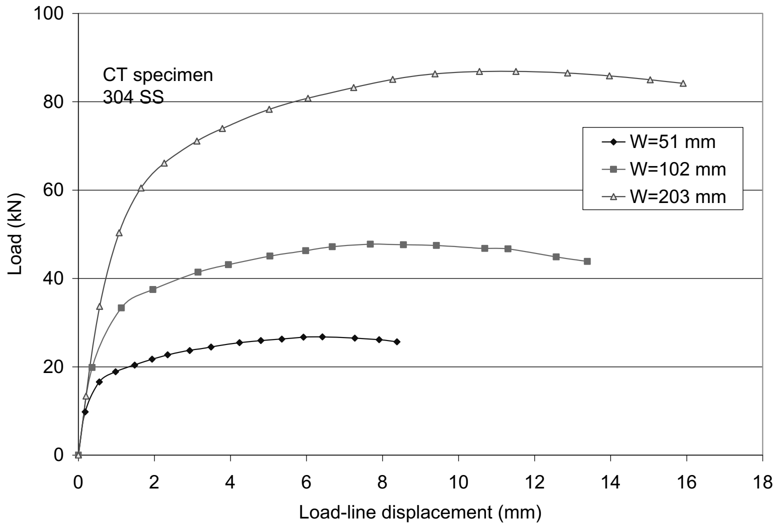

(b)

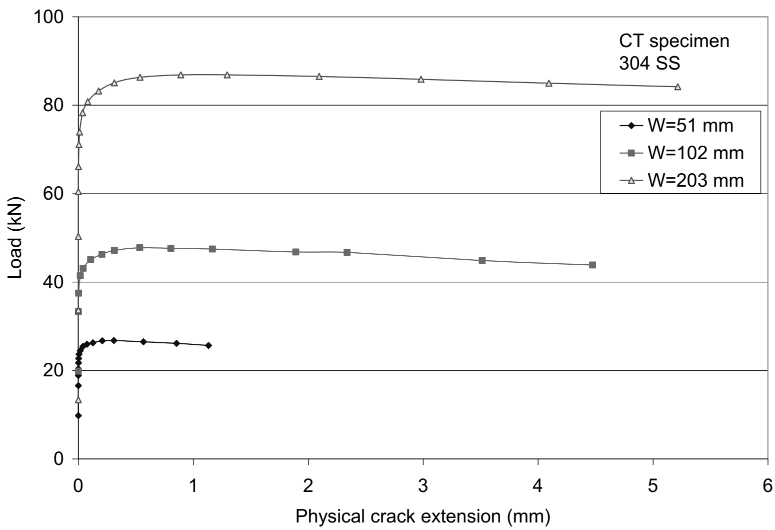

FIG. 8—*Test data for 304 steel CT specimens.* (*a*) *Load versus LLD.* (*b*) *Load versus physical crack extension.*

observed that (1) the CMOD and LLD based effective crack lengths are nearly identical but overly larger than the two physical crack length measurements and (2) the CMOD and LLD based physical crack lengths obtained from the unloading compliance are similar, with the LLD data being more close to the visual crack length measurements on the surface. This may imply that the effective crack length estimates are too unrealistic to be acceptable for this duc-

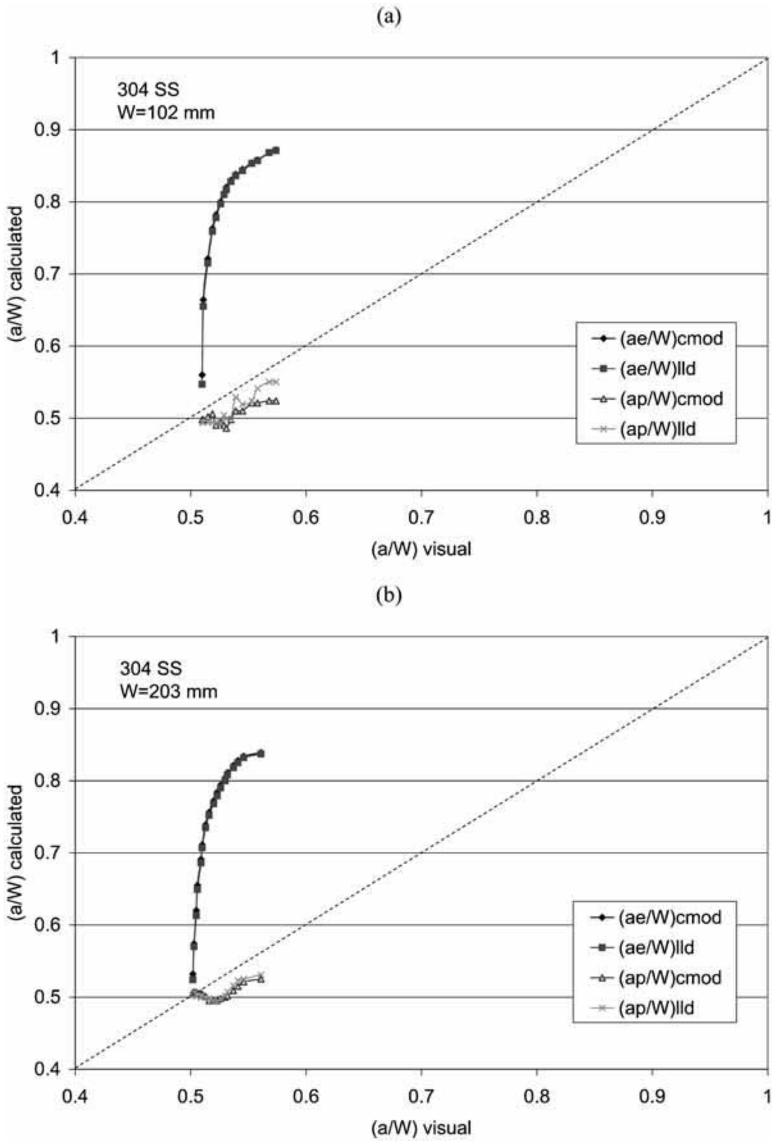

FIG. 9—*Crack length to width ratios calculated from compliance based CMOD and LLD versus visual data for 304 steel CT specimens:* (*a*) *W=102 mm and* (*b*) *W=203 mm.*

tile material exhibiting very large plastic deformation.

Figure 10 presents the variations in physical crack length to width ratios a/W versus LLD for 304 steel 2T and 4T C(T) specimens. From this figure, it is found that (1) the visual crack extension measurements are remarkably larger than the physical crack extension and almost linearly related to LLD for these

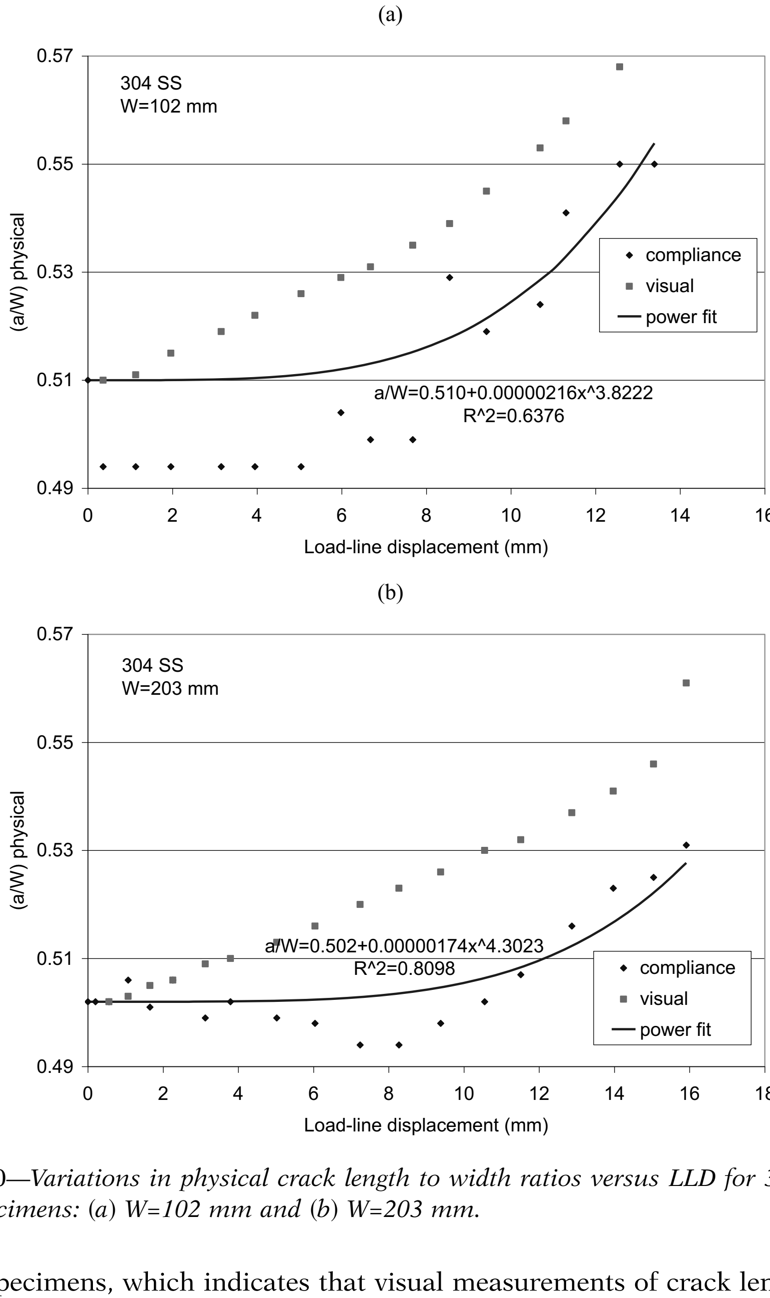

FIG. 10—*Variations in physical crack length to width ratios versus LLD for 304 steel CT specimens:* (a) *W=102 mm and* (b) *W=203 mm.*

C(T) specimens, which indicates that visual measurements of crack length are highly inaccurate for this steel due to very large plastic deformation, and (2) the physical crack extensions measured from the unloading compliance approximately follow a power-law relationship with LLD if the inaccurate measurements of crack lengths after precracking are excluded. The curve-fitted power-law functions as included in Fig. 10 are considered to be more accurate than

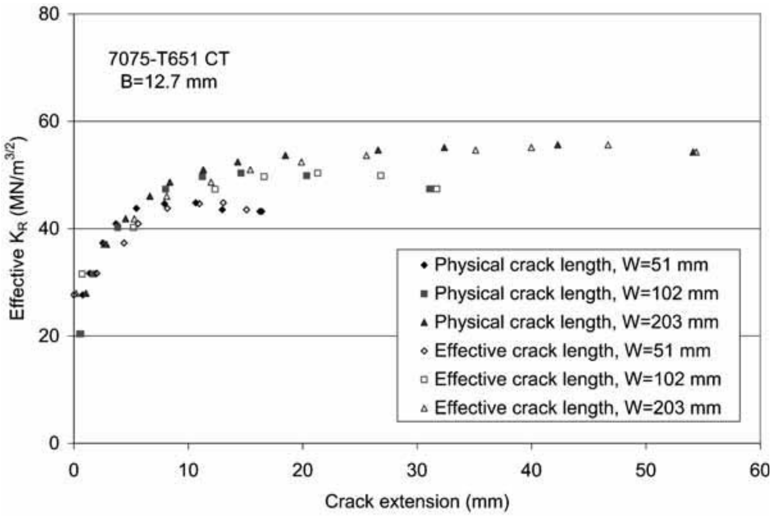

FIG. 11—*Effective K-R curves in terms of effective crack length and physical crack length for three 7075-T651 CT specimens.*

the measurements of physical crack lengths over the full range of deformation for the 304 stainless steel. Therefore, the power-law functions are used in this work to estimate the physical crack extensions and to determine resistance curves for all three 304 steel C(T) specimens.

Comparisons of R Curves

Through the above analyses, the test data of load, LLD, effective crack length a_{eff} determined from the LLD secant compliance, and physical crack length a_{phy} determined from the LLD unloading compliance or the corresponding curve-fitted results are selected here to develop three typical R curves, namely, K_{eff} versus Δa_{eff}, K_{eff} versus Δa_{phy}, and K_J versus Δa_{phy} curves using Eqs 1–6 for all nine typical tests. Among these R curves, the K_{eff}-Δa_{eff} curve is the simplest because it needs load-displacement records only, whereas the other two require both load-displacement records and physical crack length measurements obtained using the elastic unloading compliance technology.

Aluminum Alloy 7075-T561—Figure 11 shows the effective *K-R* curves determined by ASTM E561-05 in terms of effective crack length (i.e., K_{eff} versus a_{eff} curve) and physical crack length (i.e., K_{eff} versus a_{phy} curve) for three 7075-T651 C(T) specimens. It is seen from this figure that (1) the effective *K-R* curves in terms of effective and physical crack extensions are nearly identical for a given specimen; this is because the effective and physical crack length estimates are very close, as observed in Fig. 3. And (2) these two kinds of effective *K-R* curves are approximately independent of specimen size except for large

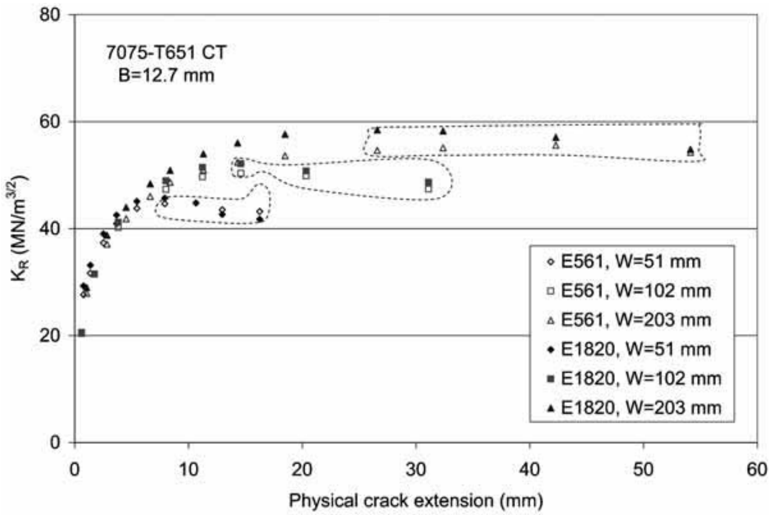

FIG. 12—*R curves determined by ASTM E561-05 and ASTM E1820-08 for three 7075-T651 CT specimens.*

crack extensions, where the *R* curves begin to drop.

Figure 12 compares the effective *K*-*R* curves in terms of physical crack length (i.e., K_{eff} versus Δa_{phy} curve, as shown in Fig. 11) with the *J*-integral based *K*-*R* curves (i.e., K_J versus Δa_{phy} curve determined in accordance with ASTM E1820-08) for the three 7075-T561 C(T) specimens. From this figure, it is apparent that the physical crack size based *R* curves determined using ASTM E561-05 and ASTM E1820-08 closely agree with each other for each specimen size, and these two *R* curves are independent of specimen size if the large crack extensions are not accounted for these specimens.

It can be thus concluded that for 7075-T651 aluminum alloy, (1) ASTM E561-05 and ASTM E1820-08 can determine equivalent *R* curves using C(T) specimens in terms of either effective or physical crack extension and (2) the *R* curves are independent of specimen size except for large values of crack extension, where K_R deviates from the curve trend or drops from its peak value.

Aluminum Alloy 2024-T351—Figure 13 shows the effective *K*-*R* curves determined by using ASTM E561-05 in terms of effective and physical crack extensions for three 2024-T351 C(T) specimens. It is apparent that (1) the effective and physical crack extension based *K*-*R* curves are significantly different for each specimen with the K_{eff} versus Δa_{eff} curve being much lower than the K_{eff} versus Δa_{phy} curve; this is because the effective crack length estimate is significantly larger than the physical crack length estimate, as shown in Fig. 6. And (2) the K_{eff}-Δa_{eff} curves are excellently correlated, which shows the geometry independence over the full range of crack extension, and (3) the K_{eff}-Δa_{phy} curve is independent of specimen size except for few points of large crack extensions.

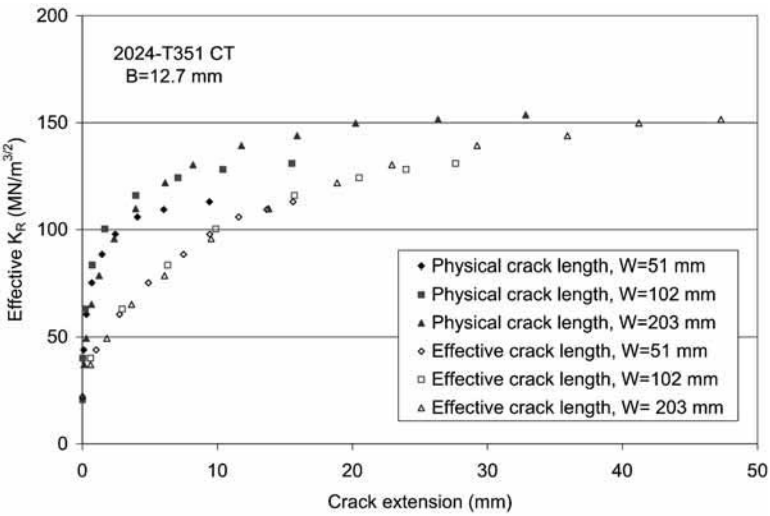

FIG. 13—*Effective K-R curves in terms of effective crack length and physical crack length for three 204-T351 CT specimens.*

Similarly, Pearson and McCabe [12] showed that the scatter of *K-R* curves using the effective crack size is smaller than that using physical crack size for 2024-T351 and 7475-T7351 aluminum alloys.

Figure 14 compares the effective K_{eff} versus Δa_{phy} curves as shown in Fig.

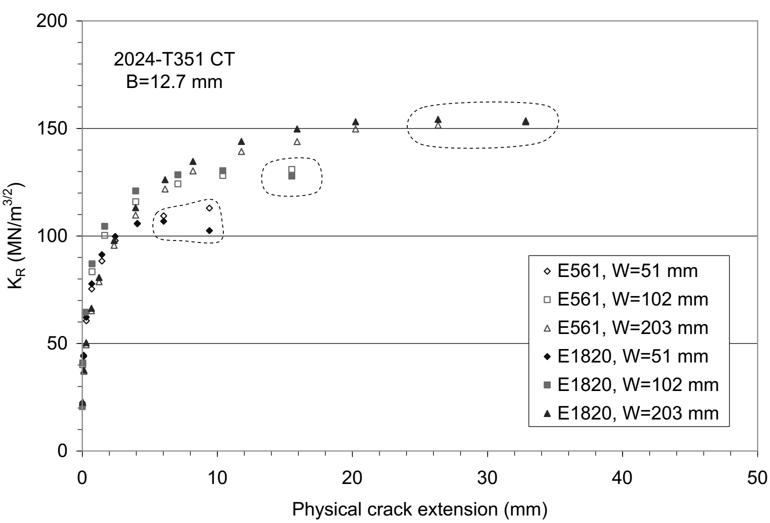

FIG. 14—*R curves determined by ASTM E561-05 and ASTM E1820-08 for three 2024-T351 CT specimens.*

13 with the *J*-integral based K_J-*R* curve (i.e., K_J versus Δa_{phy} curves determined in accordance with ASTM E1820-08) for three 2024-T351 C(T) specimens. Similar observations in Fig. 12 for 7075-T561 aluminum alloy are apparent here.

Thus, one can conclude that for 2024-T351 aluminum alloy, (1) the effective *K*-*R* curves determined using ASTM E561-05 in terms of effective and physical crack extensions are significantly different for a given C(T) specimen, (2) ASTM E561-05 and ASTM E1820-08 can equivalently determine an *R* curve in terms of physical crack extension, and (3) the equivalent *R* curves are independent of specimen sizes except for large crack extension, where the K_R deviates from the curve trend or drops from its peak value.

Stainless Steel 304—Figure 15(*a*) shows the K_{eff} versus Δa_{eff} curves, and Fig. 15(*b*) shows the K_{eff} versus Δa_{phy} curve for three 304 steel C(T) specimens. In Fig. 15(*a*), three completely separate effective *R* curves with largely steep gradients are generated using ASTM E561-05, and no correlation exists between these *R* curves in terms of effective crack extension for this ductile steel. This is not surprising because the effective crack length estimate is much larger than the physical estimate, as shown in Fig. 9. Figure 15(*b*) displays a good correlation between the effective *R* curves in terms of physical crack extension. It means that the secant compliance method suggested in ASTM E561-05 overly estimates the effective crack extension and should not be used to characterize an *R* curve for ductile materials exhibiting very large plastic deformation. In contrast, physical crack extension is viable when used to quantify the crack growth resistance curve for this ductile material.

Figure 16 compares the K_{eff} versus Δa_{phy} curves determined by using ASTM E561-05 with the K_J-*R* curves determined in accordance with ASTM E1820-08 for three 304 steel C(T) specimens. As evident in this figure, (1) the *R* curves determined using E561 are fairly correlated, (2) the *J*-based *R* curves obtained from E1820 are excellently correlated for these C(T) specimens and are independent of specimen size, and (3) an effective K_{eff} value is larger than the corresponding *J*-based K_J value at a given physical crack extension, particularly at large crack extension. Note that similar observations to Figs. 15(*a*) and 16 were found by McCabe and Ernst [22] for A533B steel. They showed that K_{eff} versus Δa_{eff} curves deviate from intrinsic behavior at or near the onset of limit load, but the K_J-*R* curves are generally unaffected by the onset of limit load. Therefore, they suggested to always use *J*-*R* curves with effective *K*-*R* curves plotted as a convention for easy identification.

Note that the physical crack length based stress intensity factor K_{phy} versus Δa_{phy} curves are also obtained for all nine tests but were not presented here due to length limitations. It was found that a K_{phy}-Δa_{phy} curve is geometry dependent for all C(T) specimens and can be much lower than the corresponding K_{eff}-Δa_{eff} curve or K_{eff}-Δa_{phy} curve because K_{phy} is a pure elastic parameter as shown in Eq 3.

Evaluation of Toughness—To quantitatively compare fracture toughness for the three materials, the values of K_R at 1 mm crack extension are determined from Figs. 12, 14, and 16 as $K_{1\ \mathrm{mm}} = 28$, 83, and 510 $\mathrm{MN/m^{3/2}}$, respectively, for

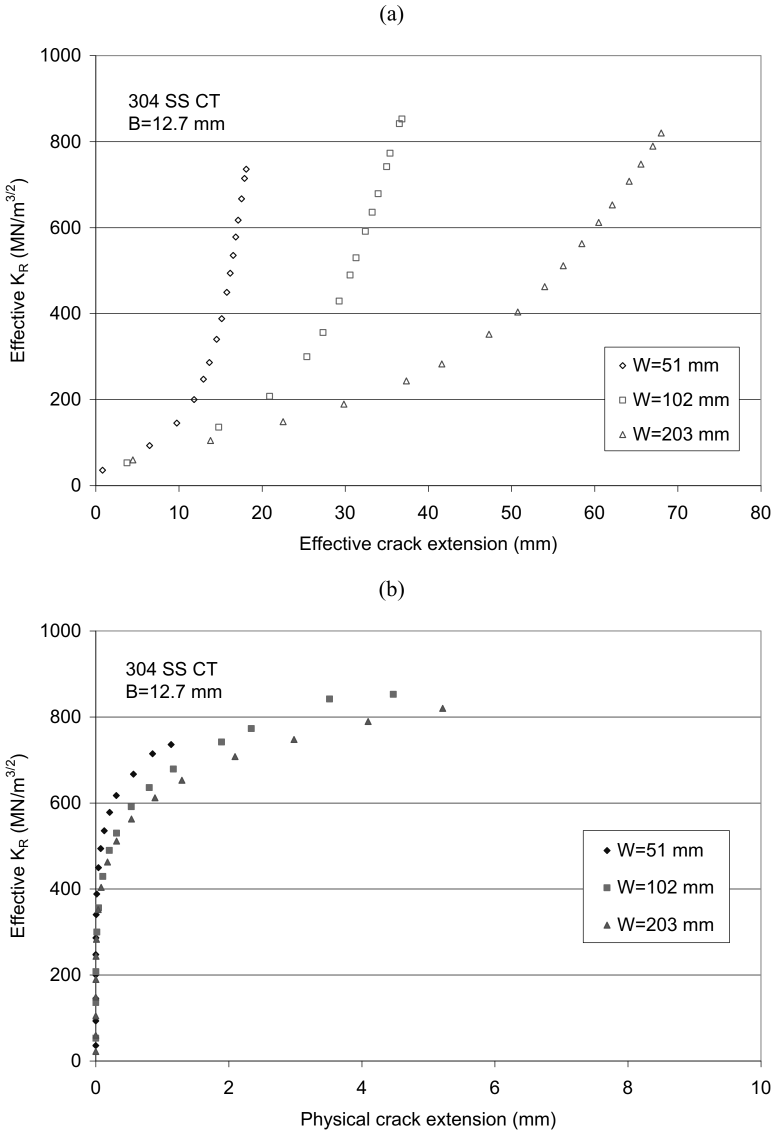

FIG. 15—*Effective K-R curves in terms of* (*a*) *effective crack length and* (*b*) *physical crack length for three 304 stainless steel CT specimens.*

7075-T561, 2024-T351, and 304 steel. Accordingly, 2024-T351 aluminum alloy and 304 stainless steel have considerably higher toughness than 7075-T561 aluminum alloy by a factor of 3 and 18, respectively. On the other hand, the previous analyses indicate that 7075-T561 material evaluated shows relatively poor ductility and 2024-T351 material evaluated shows good ductility, while the 304 steel has very good ductility. Furthermore, the fracture experiments [20] indi-

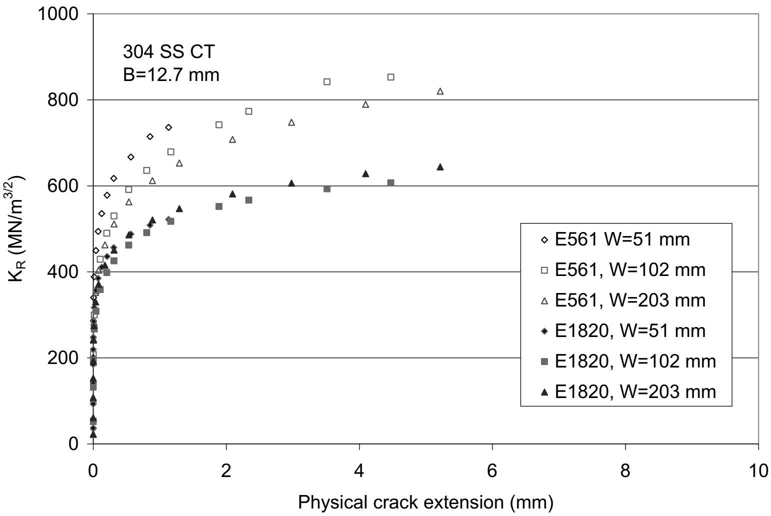

FIG. 16—*R curves determined by ASTM E561-05 and ASTM E1820-08 for three 304 stainless steel CT specimens.*

cated that the 7075-T561 C(T) specimens exhibited a very flat fracture surface appearance, typical of brittle materials, and the fatigue crack front is nearly straight. In contrast, the 2024-T351 C(T) specimens showed the fracture surface has substantial shear-lips during fracture and the fatigue crack front shows a thumbnail shape or tunneling. The 304 steel C(T) specimens exhibited very large deformation along the crack line during fracture, the thickness of the material along the crack line necked and contracted laterally by 65 % of the original thickness, with the fatigue crack front also showing a thumbnail shape.

As expected, therefore, these three metals exhibit a relatively wide range of ductility and fracture toughness. In this regard the 7075-T561 aluminum alloy reflects a high strength low toughness material, the 2024-T351 reflects a medium strength medium toughness material, and 304 stainless steel reflects a high strength high toughness material.

Discussions on Validity Criteria

From the above analyses, one can determine an in-plane geometry-independent *R* curve equivalently using ASTM E561-05 and E1820-08 for the two aluminum alloys except for large crack extension. It remains to determine what crack extensions should be excluded in order to obtain a consistent *R* curve for these materials. To that end the validity of test data is considered in the following paragraphs.

Plastic Deformation Limitation in ASTM E561-05

To ensure that a given calculated value of K_R is valid for a specimen, ASTM E561-05 requires that the remaining ligament in the plane of crack be predomi-

TABLE 1—*Estimated relative sizes of the plastic zone for the three materials.*

	7075-T561 Aluminum			2024-T351 Aluminum			304 Steel		
Material Specimen Size	1T	2T	3T	1T	2T	3T	1T	2T	3T
r_y/B	0.09	0.11	0.13	1.53	2.10	2.92	48	61	73
r_y/b	0.07	0.04	0.02	1.04	0.67	0.50	26	17	10

nantly elastic at the value of applied load corresponding to that value of effective crack extension. This requirement is considered to be met for C(T) specimens in the standard as long as the length of the remaining ligament at the end of the test is greater than or equal to eight plastic zone sizes, which restricts plastic deformation to the crack tip in the specimens. This validity criterion can be mathematically expressed as

$$(W - a_{\mathrm{phy}}) \geq 8r_y = \frac{4}{\pi}\left(\frac{K_{\max}}{\sigma_{\mathrm{ys}}}\right)^2 \tag{7}$$

where:

$K_{\max}$ designates the maximum expected or desired effective K_R level in the test and

$\sigma_{\mathrm{ys}} = 0.2$ % offset yield strength of materials.

Using the validity criterion in Eq 7, the validity of the data comprising the K-R curves has been determined for the nine tests analyzed previously. This indicates that (1) all data points are valid for all three 7075-T561 C(T) specimens, (2) only first two to five data points are valid for the 2024-T351 C(T) specimens, and (3) there are no valid data points for the 304 steel C(T) specimens. Comparing these findings with Figs. 11 and 13, it is seen that the validity criterion of Eq 7 is not conservative for the low toughness 7075-T561 aluminum alloy. This is because the data points at large crack extension where K_R drops from its peak value are invalid, but they were not excluded. In contrast, the criterion of Eq 7 is overly conservative for the medium toughness 2024-T351 aluminum alloy because more "invalid" data points are actually in good agreement with the curve trend from the valid data. This same observation on the validity of C(T) specimen data for 2024-T351 aluminum alloy was also reported by Reynolds [17,18]. Therefore, the validity criterion on R-curve data for C(T) specimens of Eq 7 should be modified.

Table 1 gives the relative sizes (r_y/B and r_y/b) of the plastic zone ahead of the crack tip to the sheet thickness and to the remaining ligament for the three materials that are estimated from Eq 7 using the maximum valid values of the effective K_{eff} for the two aluminum alloys and of the J-based K_J for the steel. Note that the estimated plastic zone sizes are accurate only for small-scale yielding. Accordingly, the results for the 304 steel in Table 1 are nominal values. As shown in this table, for all three materials, the relative size of the plastic zone to the sheet thickness, r_y/B, increases with the increasing specimen size, and the relative size, r_y/b, of the plastic zone to the uncracked ligament decreases with the increasing specimen size. For the 7075-T561 material, all relative plastic zone sizes, r_y/B and r_y/b, are very small, with the maximum plastic zone size being about 13 % of the sheet thickness. This indicates that the plastic deformation is highly confined to the crack tip for the three 7075-T561 specimens such that the validity criterion in Eq 7 is met. For the 2024-T351 material, the plastic zone sizes increase significantly for all three specimen sizes. For the 1T specimen, the entire ligament may be experiencing yield, while for the 4T specimen, the plastic zone size is about 50 % of the uncracked ligament. As such, the validity criterion in Eq 7 that requires the plastic zone size less than 12.5 % of the ligament is not satisfied for large deformation for these C(T) specimens. For the 304 steel, the entire ligament experiences yield for the three C(T) specimens such that the validity criterion in Eq 7 is violated. It follows that the plastic deformation was highly constrained to the crack tip and the elastic deformation dominates in the specimens only for the 7075-T351 aluminum alloy, whereas the plastic deformation was large to very large, respectively, for the 2024-T351 aluminum alloy and the 304 steel.

J-Integral and Crack Growth Limitation in ASTM E1820-08

In ASTM E1820-08, except for the minimum thickness limitation required for the plane strain fracture toughness testing, two separate criteria regarding J-R curve testing are applicable to the plane stress conditions. One is for specifying the maximum value of J (J_{max}) that can be measured with a specific specimen, and the other is for specifying the maximum amount of crack growth (Δa_{max}) that is allowable for a specific specimen. These two limitation requirements are presently set in ASTM E1820-08 as

$$J_{max} = B\sigma_Y/10 \tag{8}$$

$$\Delta a_{max} \leq 0.25 b_0 \tag{9}$$

where:

σ_Y = effective yield strength with the average value of the yield stress and the ultimate tensile stress and

$b_0 = W - a_0$ = initial crack ligament size.

The backgrounds for these limitations have been well described by Joyce and Hackett [23]. Recently, based on a statistical analysis for extensive fracture test data, Wallin [24] concluded that (1) the present crack growth limitation in Eq 9 imposed by ASTM E1820-08 is appropriate and (2) there is no need for a J_{max} criterion in Eq 8 when the crack growth criterion in Eq 9 is fulfilled. Similar suggestions were also given by Landes [25]. Accordingly, the Δa_{max} criterion in Eq 9 is utilized here to define the crack growth limitation for all specimens analyzed. The results show that all test data are valid for 304 steel, and some data are invalid for 7075-T651 and 2024-T351 aluminum alloys, as circled in Figs. 12 and 14. Consequently, the use of valid data leads to specimen size-independent R curves obtained by ASTM E1820-08 or ASTM E561-05 for all three materials. Therefore, Eq 9 is suggested for use as the crack growth limit criterion in the R curve testing for thin-sheet materials. This is consistent with the validity criterion used by Schwalbe et al. [6,26,27] in the δ_5-R curve testing with thin-walled specimens.

In addition, from Eq 8, the values of J_{max} are determined as 708, 492, and 568 kJ/m^2, respectively, for 7075-T561 aluminum, 2024-T351 aluminum, and 304 steel. From Eq 6, the corresponding equivalent $K_{J,max}$ values are calculated as 225, 187, and 340 $MN/m^{3/2}$ for the three materials. Comparison of these values with the experimental data of R curves in Figs. 12, 14, and 16 shows that the J_{max} criterion is satisfied for the two aluminum alloys but not for the steel. Even so, the K_J-R curves are specimen size-independent for the 304 steel. This may imply that the J_{max} criterion is not needed, as suggested by Wallin [24] and Landes [25]. Anyway, for the two aluminum alloys, the two limitation criteria in Eqs 8 and 9 required in ASTM E1820-08 can be used appropriately in ASTM E561-05 for the K-R curve testing.

Once the invalid test data are eliminated from Figs. 11, 12, 14, and 16 by applying the crack growth limit criterion in Eq 8, it is apparent that (1) K_J-R curves are size-independent for all three metals considered, (2) K_{eff}-Δa_{phy} curves are size-independent for the two aluminum alloys, and (3) K_{eff}-Δa_{eff} curves are size-independent only for the 7074-T651 aluminum alloy. In other words, ASTM E1820-08 can determine size-independent J-R curves for all materials, whereas ASTM E561-05 can determine size-independent effective K-R curves only for the lowest toughness material. However, the situation is completely different under plane strain conditions. Detailed discussions and methods of fracture constraint quantification can be found in Refs 28–30.

Conclusions

This paper revisited the ASTM round-robin fracture test data obtained in 1979–1980 by ASTM Task Group E24.06.02 on Application of Fracture Analysis Methods. The fracture toughness tests were conducted using thin-sheet C(T) specimens made of three materials: 7075-T561 aluminum alloy, 2024-T351 aluminum alloy, and 304 stainless steel. Typical experimental data from nine tests were reanalyzed, and specimen size-independent R curves were developed using fracture test standards ASTM E561-05 and ASTM E1820-08. The following conclusions can be drawn.

(1) The secant compliance method suggested in ASTM E561-05 developed acceptable crack extension data only for 7075-T561 aluminum alloy but overly predicted crack extension for other two ductile materials in comparison to the accurate physical crack sizes determined from the elastic unloading compliance technology. Visual measurements of crack length on the specimen surface were good for 7075-T651 material but were inaccurate for the two ductile materials due to large plastic deformation and well-known tunneling effects.

(2) A power-law relationship was found to exist between the physical crack extension obtained from the unloading compliance as suggested in ASTM E1820-08 and the LLD. The power-law relationship proved very useful in smoothing raw experimental data and/or estimating crack extension in case that the physical crack length measurements were inaccurate.

(3) A K-R curve expressed in terms of effective stress intensity factor K_{eff} and effective crack extension Δa_{eff} can correlate the test data for the

two aluminum alloys but had no physical meaning for the 304 stainless steel. The K_{eff}-Δa_{eff} curve was equivalent to the *J*-*R* curve only for the 7075-T561 aluminum alloy.

(4) The effective stress intensity factor K_{eff} obtained using ASTM E561 and the *J*-based K_J determined according to ASTM E1820 correlated very well, such that a K_{eff}-Δa_{phy} curve was equivalent to the K_J-*R* curve for the two aluminum alloys.

(5) The validity criterion specified by ASTM E561-05 for C(T) specimens was not conservative for the 7075-T561 aluminum alloy but was overly conservative for the 2024-T351 aluminum alloy. In contrast, the crack growth limit criterion imposed by ASTM E1820-08 worked well to eliminate invalid test data in the *R* curve testing for all thin-sheet C(T) specimens considered.

(6) The three metals exhibited a wide range of relative fracture toughness from low to high. At the crack extension of 1 mm, the relative toughness $K_{1\ mm}=28$, 83, and 510 $MN/m^{3/2}$ were obtained, respectively, for 7075-T561 aluminum alloy, 2024-T351 aluminum alloy, and 304 steel. Thus, the 2024-T351 material and 304 steel have considerably higher toughness than the 7075-T561 material in a factor of 3 and 18, respectively. As a result, the 7075-T561 aluminum alloy reflects the response of a high strength low toughness material, the 2024-T351 aluminum alloy reflects the response of a medium strength medium toughness material, and the 304 stainless steel reflects the response of a high strength high toughness material.

(7) The three materials evaluated showed much different deformation and fracture characteristics. For the 7075-T561 aluminum alloy, the plastic deformation was very small and confined to the crack tip, but the crack extension was very large, and all three specimen sizes exhibited a very flat fracture surface appearance and straight fatigue crack front, typical of brittle materials. For the 2024-T351 aluminum alloy, both plastic deformation and crack extension were large, the fracture surface showed substantial shear-lips, and the fatigue crack front showed the typical thumbnail shape for all specimens. For the 304 stainless steel, the plastic deformation is very large, but the crack extension is small; the sheet thickness along the crack line contracted to 65 % of the original thickness, and the fatigue crack front showed the thumbnail shape. Thus, the 7075-T651 material has relatively poor ductility, the 2024-T351 material has good ductility, and the 304 steel has excellent ductility.

(8) ASTM E1820-08 can be used generally to determine a specimen independent *R* curve in the form of *J*-Δa_{phy} or K_J-Δa_{phy} curve for thin-sheet C(T) specimens for all metals considered, while ASTM E561-05 works only for the determination of a specimen independent *R* curve in form of K_{eff}-Δa_{eff} curve for thin-sheet C(T) specimens with the lowest toughness material of 7075-T561 aluminum alloy. Therefore, the two standards become equivalent in *R* curve testing only for this lowest toughness material exhibiting poor ductility as characterized by small plastic deformation, large crack extension, and flat fracture surfaces.

In addition, Schwalbe et al. [11] pointed out that a number of drawbacks have been noted for the K_{eff}-Δa_{eff} curve concept since its introduction in the 1970s. The principal drawback is the representation of the crack length by its effective size that is not compatible with the real or physical crack size. They thus argued that the *K*-*R* concept is no longer up to date and should be replaced with a procedure representing the state of the art of EPFM. Nevertheless, the present study indicated that ASTM E561-05 is very simple and cost-effective and can be reasonably used to determine *K*-*R* curves for low toughness materials with $K_{1\ \text{mm}} \approx 30\ \text{MN/m}^{3/2}$ and exhibiting poor ductility. However, for ductile materials exhibiting medium to high toughness with $K_{1\ \text{mm}} > 80\ \text{MN/m}^{3/2}$ and showing good ductility, ASTM E1820-08 methods rather than ASTM E561-05 should be used in experimental evaluation of valid crack growth resistant curves for thin-sheet specimens. Further experimental investigations are needed to identify materials with how low fracture toughness for which ASTM E561-05 still works.

References

[1] ASTM E561-05, "Standard Test Method for *K-R* Curve Determination," *Annual Book of ASTM Standards*, Vol. 03.01, ASTM International, West Conshohocken, PA, 2006.

[2] ASTM E1820-08, "Standard Test Method for Measurement of Fracture Toughness," *Annual Book of ASTM Standards*, Vol. 03.01, ASTM International, West Conshohocken, PA, 2008.

[3] Zerbst, U., Heinimann, M., Donne, C. D., and Steglich, D., "Fracture and Damage Mechanics Modelling of Thin-Walled Structures—An Overview," *Eng. Fract. Mech.*, Vol. 76, 2009, pp. 5–43.

[4] McCabe, D. E., *Fracture Toughness Evaluation by the R-Curve Methods, ASTM STP 527*, ASTM International, West Conshohocken, PA, 1973.

[5] Schwalbe, K. H. and Setz, W., "R Curve and Fracture Toughness of Thin Sheet Materials," *J. Test. Eval.*, Vol. 9, 1981, pp. 182–194.

[6] Hellmann, D. and Schwalbe, K. H., "Geometry and Size Effects on *J-R* and *δ-R* Curves Under Plane Stress Conditions," *Fracture Mechanics: 15th Symposium, ASTM STP 833*, ASTM International, West Conshohocken, PA, 1984, pp. 557–605.

[7] Yuan, F. G. and Yang, S., "Crack-Tip Fields in Elastic-Plastic Material Under Plane Stress Mode I Loading," *Int. J. Fract.*, Vol. 85, 1997, pp. 131–155.

[8] Yan, C. and Mai, Y. W., "Numerical Investigation on Stable Crack Growth in Plane Stress," *Int. J. Fract.*, Vol. 91, 1998, pp. 117–130.

[9] Fedderson, C. E., Simonen, F. A., Hulbert, L. E., and Hyler, W. S., "An Experimental and Theoretical Investigation of Plane-Stress Fracture of 2024-T351 Aluminum Alloy," *NASA* CR-1678, National Aeronautics and Space Administration, Washington, D.C., September 1970.

[10] Orange, T. W., Sullivan, T. L., and Calfo, F. D., "Fracture of Thin Sections Containing Through and Part-Through Cracks," *NASA* TN-6305, National Aeronautics and Space Administration, Washington, D.C., April 1971.

[11] Schwalbe, K. H., Newman, J. C., and Shannon, J. L., "Fracture Mechanics Testing on Specimens with Low Constraint—Standardisation Activities Within ISO and ASTM," *Eng. Fract. Mech.*, Vol. 72, 2005, pp. 557–576.

[12] Pearson, H. S. and McCabe, D. E., "R-Curve Round-Robin Program for ASTM

Recommended Practice for R-Curve Determination (E561)," *J. Test. Eval.*, Vol. 14, 1986, pp. 191–199.
[13] Pearson, H. S., "Evaluation of Plane Stress Fracture Testing Methods," *J. Test. Eval.*, Vol. 14, 1986, pp. 224–226.
[14] ASTM E813, "Standard Test Method for J_{Ic}, a Measure of Fracture Toughness," *Annual Book of ASTM Standards*, Vol. 03.01, ASTM International, West Conshohocken, PA, 1982.
[15] ASTM E1152, "Standard Test Method for Determining *J-R* Curves," *Annual Book of ASTM Standards*, Vol. 03.01, ASTM International, West Conshohocken, PA, 1987.
[16] ASTM E1737, "Standard Test Method for J-integral Characterization of Fracture Toughness," *Annual Book of ASTM Standards*, Vol. 03.01, ASTM International, West Conshohocken, PA, 1996.
[17] Reynolds, A. P., "Multi-Lab Comparison of R-Curve Methodologies: Alloy 2024-T3," *Report No. NASA CR 195004* , National Aeronautics and Space Administration, Washington, D.C., October 1994.
[18] Reynolds, A. P., "Comparison of R-Curve Methodologies for Ranking the Toughness of Aluminum Alloys," *J. Test. Eval.*, Vol. 24, 1996, pp. 406–410.
[19] Haynes, M. J. and Gangloff, R. P., "High Resolution R-Curve Characterization of the Fracture Toughness of Shin Sheet Aluminum Alloys," *J. Test. Eval.*, Vol. 25, 1997, pp. 82–98.
[20] Newman, J. C., "An Evaluation of Fracture Analysis Methods," *Elastic-Plastic Fracture Mechanics Technology, ASTM STP 896*, ASTM International, West Conshohocken, PA, 1985, pp. 5–96.
[21] McCabe, D. E., "Data Development for ASTM E24.06.02 Round Robin Program on Instability Prediction," *NASA* CR-159103, National Aeronautics and Space Administration, Washington, D.C., August 1979.
[22] McCabe, D. E. and Ernst, H. A., "A Perspective on *R*-Curves and Instability Theory," *Fracture Mechanics: 14th Symposium—Volume I: Theory and Analysis, ASTM STP 791*, ASTM International, West Conshohocken, PA, 1983, pp. I-561–I-584.
[23] Joyce, J. A. and Hackett, E. M., "Extension and Extrapolation of *J-R* Curves and Their Application to the Low Upper Shelf Toughness Issue," *Report No.* NUREG/CR-5577, U.S. Nuclear Regulatory Commission, Washington, D.C., 1991.
[24] Wallin, K., "Specimen Size Limitation in *J-R* Curve Testing—Standards Versus Reality," *J. ASTM Int.*, Vol. 4, 2007, Paper no. JAI100978.
[25] Landes, J. D., "Evaluation of the ASTM J Initiation Procedure Using the EURO Fracture Toughness Data Set," *J. Test. Eval.*, Vol. 34, 2006, pp. 200–210.
[26] Schwalbe, K. H., Heerens, J., Zerbst, U., Pisarski, H., and Kocak, M., "EFAM GTP02—The GKSS Test Procedure for Determining the Fracture Behaviour of Materials," *GKSS—Forschungszenrum Geesthacht GmbH*, Geesthacht, Germany, 2002.
[27] Schwalbe, K. H., Cornec, A., and Baustian, K., "Application of Fracture Mechanics Principles to Austenitic Steels," *Int. J. Pressure Vessels Piping*, Vol. 65, 1996, pp. 193–207.
[28] Joyce, J. A. and Link, R. E., "Application of Two Parameter Elastic-Plastic Fracture Mechanics to Analysis of Structures," *Eng. Fract. Mech.*, Vol. 57, 1997, pp. 431–446.
[29] Zhu, X. K. and Jang, S. K., "*J-R* Curves Corrected by Load Independent Parameter in Ductile Crack Growth," *Eng. Fract. Mech.*, Vol. 68, 2001, pp. 285–301.
[30] Zhu, X. K. and Leis, B. N. "Application of Constraint-Corrected *J-R* Curve to Fracture Analysis of Pipelines," *J. Pressure Vessel Technol.*, Vol. 128, 2006, pp. 581–589.

Reprinted from JAI, Vol. 7, No. 5
doi:10.1520/JAI102470
Available online at www.astm.org/JAI

A. Neimitz[1] *and J. Galkiewicz*[2]

The Analysis of Fracture Mechanisms of Ferritic Steel 13HMF at Low Temperatures

ABSTRACT: In this paper, the transition from a ductile fracture mechanism to a cleavage fracture mechanism is analyzed. Microscopic observations of the domains in front of a crack were followed by numerical analysis. The microscopic observations were accompanied by analysis of the fracture surfaces. Both the influences of temperature and an in-plane constraint on the mechanism transition were taken into account. The numerical analyses were carried out using two different models of a crack: Stationary and propagating. The direct, simultaneous influence of the level of the opening stress maximum, the characteristic distance in front of the crack tip, and the level of plastic strain on the ductile-cleavage transition have been confirmed.

KEYWORDS: ductile to cleavage fracture mechanism transition

Introduction

The transition from a ductile to a cleavage fracture mechanism is a well-recognized problem from an engineering point of view as shown in Refs 1–6, which studied transition temperature assessment using a statistical local criterion based on the Beremin model and Weibull stress [7]. This method has been utilized by many authors in the literature and is broadly accepted; therefore, only a few papers [8–10] are referenced.

The fundamental question concerning the ductile to brittle transition is why does it happen. What is the physical explanation for such a transition? To understand this complex problem, one first needs to understand the ductile and cleavage fracture mechanisms separately. In this field, many papers have been published. One of the first and the most well known is the paper by Rice and Thompson [11]. It is difficult to list the most important articles on the subject;

Manuscript received April 15, 2009; accepted for publication April 20, 2010; published online June 2010.
[1] Kielce Univ. of Technology, 25-314 Kielce, Poland, e-mail: neimitz@tu.kielce.pl
[2] Kielce Univ. of Technology, Kielce 25-314, Poland, e-mail: jgalka@tu.kielce.pl

Cite as: Neimitz, A. and Galkiewicz, J., "The Analysis of Fracture Mechanisms of Ferritic Steel 13HMF at Low Temperatures," *J. ASTM Intl.*, Vol. 7, No. 5. doi:10.1520/JAI102470.

TABLE 1—*Chemical composition of 13HMF steel.*

C	Mn	Si	P	S	Cr	V	Ni	Mo	Cu
0.17 %	0.53 %	0.3 %	0.011 %	0.006 %	0.35 %	0.28 %	0.04 %	0.55 %	0.01 %

therefore, we refer to review papers and well known books where numerous papers are analyzed and listed [12–17]. In these articles, the problems of void and micro-crack nucleation, growth, and coalescence are discussed. The authors discussed the questions concerning the controlling quantities in these phenomena: Opening stress level, plastic strain, and stress triaxiality measures.

The transition from a ductile to a cleavage fracture mechanism depends on many factors including the microstructure of the material (the size of grains, the form of inclusions, and precipitates, e.g., carbides—pearlite or bainite coagulated, within a ferrite grain), the temperature (the mobility of dislocations is highly dependent on temperature), the stress field (both hydrostatic and shear components are important), and the strain field (mainly plastic strains). The theories published so far frequently contradict each other. Nevertheless, different theories may be correct but are based on different assumptions due to different experimental conditions. Therefore, the authors decided to reanalyze the problem of the ductile to cleavage transition starting from experimental measurements of the uniaxial tensile and fracture properties of a material, then making fractographic and microscopic structural observations, and applying numerical models to analyze the fracture processes.

13HMF steel, according to Polish standards, has been selected as a popular structural material for many structures including power plants. Four different heat treatments were applied to obtain the desired material structure: From a ferritic through ferritic-pearlitic, ferritic-bainitic, and martensitic. As a result, we were able to observe the ductile to cleavage fracture transition in two materials in a wide range of test temperatures. One material was ductile and one was brittle.

The fracture test temperatures were varied from -20 to $-180°C$, and two in-plane constraints were imposed.

First, the uniaxial tensile and preliminary fracture tests were performed. Next, the fractographic analysis was made in conjunction with the preliminary finite element computations for the stationary cracks. Basing upon the results of the preliminary analysis, the authors selected two temperatures (-20 and $-50°C$), two crack lengths ($a/W=0.5$ and 0.2, where a is the crack length and W is the specimen width), and three materials for more detailed testing. Some results concerning the material after one of the four heat treatments are presented in this paper.

Material

The chemical composition of the tested 13HMF steel is shown in Table 1. Equivalent to 13HMF steel, according to other standards are ^{14}CrMo4-5 (ISO 9328-2 [18]), 13CrMo4-5 (EN 10028-2 [19]), and 12Kh1MF (GOST 5520 [20]).

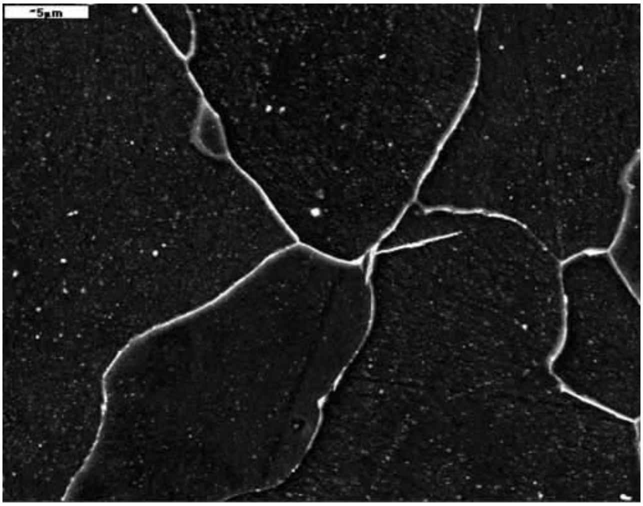

FIG. 1—*The microstructure of the tested 13HMF steel.*

The purpose of the heat treatment was to produce a ferrite structure with a uniform distribution of carbides of different sizes. The steel was austenitized at 1030°C for 40 min and cooled in the oven. Next, it was tempered at 735°C for 90 h and cooled in air. The resultant microstructure is shown in Fig. 1

The average sizes of the small vanadium carbides and Mo_2C carbides were 62 and 152 nm, respectively. The large cementite particles (of the order of 1 μm) in the form of deformed pearlite were evenly distributed within the ferrite grains. The uniaxial tensile properties and fracture toughness are presented in Table 2.

The K_{JC} values were obtained using the formula $K_{JC}=\sqrt{J_{IC}E/(1-\nu^2)}$, and the values of J_{IC} were measured according to ASTM E1820-05 [21] using the potential drop technique and specimens with the following size parameters: Thickness $B=10$ mm, width $(a/W=0.5)$, span $S=80$ mm, and $a/W\cong 0.5$ or 0.2.

TABLE 2—*Tensile and fracture properties of the tested materials.*

Test Temp.	R_{eL} (MPa)	R_m (MPa)	A_5 (%)	n	K_{JC} $(a/W=0.5)$ $(\mathrm{MPa\cdot m^{1/2}})$	T_0 $(a/W=0.5)$ (°C)	K_{JC} $(a/W=0.2)$ $(\mathrm{MPa\cdot m^{1/2}})$	T_0 $(a/W=0.2)$ (°C)
20°C	265	410	32.4	11.2	128.6; 117.5		240	
−20°C	296	440	33.7	11.5	113.7		219	
−50°C	324	475	33.3	12.9	66.3; 105	−17.2	167	−87
−80°C	380	520	35.5	14.1	55		117.2	
−100°C	400	545	33.6	14.9	45		103.7	

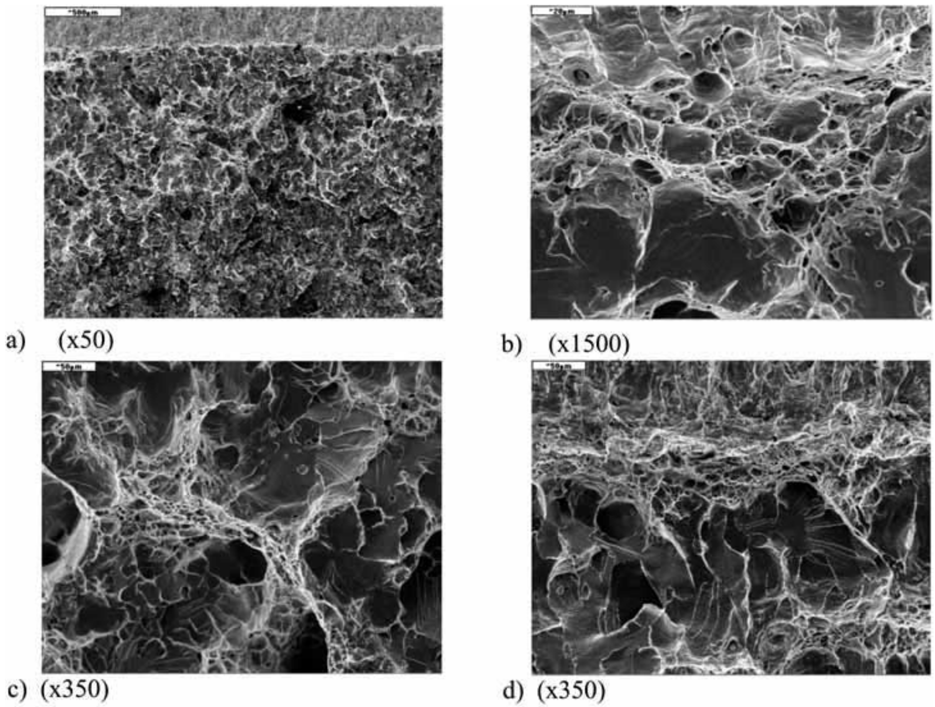

FIG. 2—*The honeycomb-like structure of the fracture surfaces* (*a*) *–50°C a/W=0.2;* (*b*) *–50°C, a/W=0.5;* (*c*) *–20°C, a/W=0.5; and* (*d*) *–20°C, a/W=0.2.*

Fractographic Analysis

At a temperature of −80°C, a typical cleavage fracture was observed for long cracks ($a/W=0.5$). However, for the short cracks ($a/W=0.2$), traces of a ductile fracture mechanism could also be noticed at −80°C.

At −50°C, the fracture mechanism is mixed at the beginning of crack extension both for long and short cracks. We observed the islands of cleavage fracture surrounded by bridges of ductile fracture, resembling a honeycomb (Fig. 2(*a*) and 2(*b*)). At −20°C, the crack began propagating by a ductile mechanism (40–50 μm long domain; Fig. 2(*d*)). Then the honeycomb-like fracture surface was observed (Fig. 2(*c*)) before a cleavage mechanism dominated the fracture process.

For both crack lengths ($a/W=0.2$ and 0.5) and temperatures (−20 and −50°C), the fracture process was similar. After a shorter or longer stable crack growth with a mixed fracture mechanism, we observed a sudden cleavage jump over a distance of several millimetres. Then a short stable growth was observed again. As an example, the deflection versus force and deflection versus potential drop curves were plotted and are shown in Fig. 3.

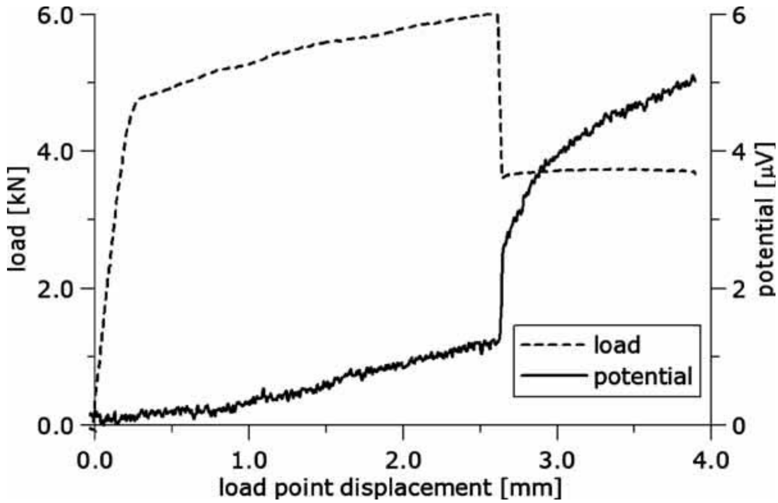

FIG. 3—*Load-point displacement versus force and potential change curves, temp. =−20°C, a/W=0.5.*

Microscopic Observations and Numerical Analysis

After the preliminary fracture tests, the numerical computations of the stress and strain fields, and the microscopic observations, the working hypothesis concerning the ductile to brittle transition was formulated. It was proposed that the cleavage micro-cracks initiate a small distance from the macro-crack tip and then grow to neighbor grains or join together, breaking the bridges between the growing voids and cleavage islands.

The process takes place on two size scales. At the micro-scale, the structure of the honeycomb-like fracture surface is created. At the meso-scale, the cleavage micro-cracks join together and create the cleavage meso-cracks, and these meso-cracks join the tip of the macro-crack.

To initiate the cleavage fracture, the opening stress must be greater than the critical value, which is dependent on the material *and* temperature, and this should happen along the distance characteristic for the material of interest. This hypothesis is not a new one, and the critical or characteristic length concept was previously introduced to elastic-plastic fracture analysis. Among the earliest and the most well known papers on this subject are those by Rice and Johnson [22] and Ritche et al. [23]. This concept was also discussed in a recent paper by Neimitz et al. [24]. The listed authors noticed that if only the magnitude of the opening stress was sufficient for the cleavage crack to grow, every material would break, and the site of the cleavage fracture would be at the tip of the macro-crack even with minimal external loading. This reasoning would apply for both small and finite strains assumptions. In the latter case, the maximum stress level does not change significantly with the external loading; it can even decrease slightly when the external load increases. However, the maximum value of the normal stress components moves away from the crack tip when the external load increases.

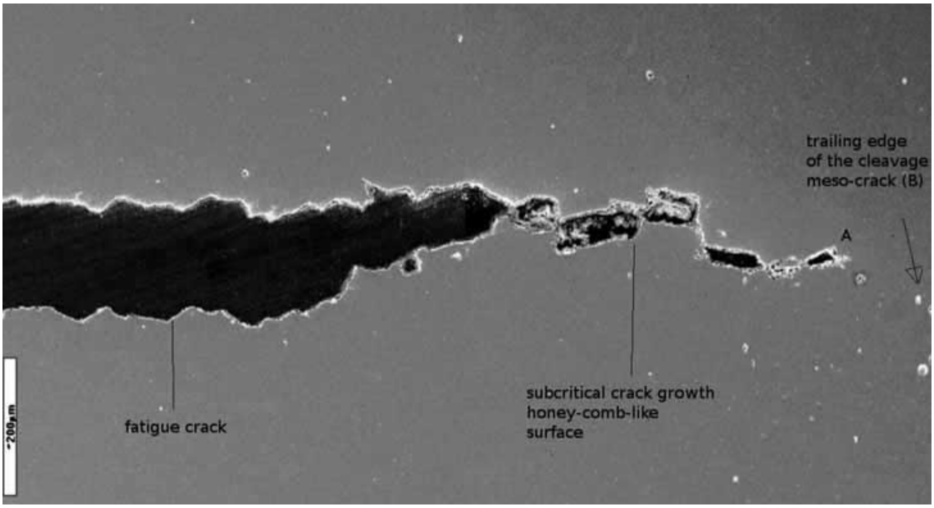

FIG. 4—*General view at the macroscopic crack. Temp.=−20°C, a/W=0.5, Polished surface. Observations were made at the surface located 0.25B from the axis of the specimen.*

In order to trace the evolution of a damage zone, which is expected to deform plastically, and the formation of a micro-crack in front of the main fatigue crack, several tests were interrupted before the presumed onset of a cleavage crack jump and after the jump had been observed. Next, layers of the specimen were removed by careful grinding and polishing to reduce the specimen thickness. After polishing with a diamond paste, the surface was observed with a Jeol JSM 5400 scanning electron microscope. Observations were made before and after the acid etching. In some specimens, we were able to capture pictures of the "frozen" specimens at the moment we believe directly preceded the onset of a macroscopic crack jump. In others, the evolution of the growing cracks was observed in different stages of the crack front extension. Detailed quantitative analysis of the frozen processes is not possible for several reasons. First, we observed the individual cross-sections at different distances from the specimen axes. Second, the crack fronts were not uniform. Third, the crack surfaces were often discontinuous. Thus, we were only able to observe fragments of this geometrically complex situation, and only a three-dimensional picture could lead to a more quantitative image.

Figures 4–7 concern a specimen tested at $-20°C$ with a crack length $a/W = 0.5$. The test was stopped just before the presumed onset of a crack jump. Until that moment, the crack might extend 0.5–0.7 mm. The fracture surface, which was in the stage of stable crack growth, exhibits the mixture of cleavage islands surrounded by ductile bridges (Figs. 2(*c*) and 4).

In front of the main crack, the cleavage meso-crack was created (Figs. 4 and 5). We assume that such cracks grow both toward and away from the main crack edge.

Figure 5 shows the domain between the macro-crack (arrow A) and cleav-

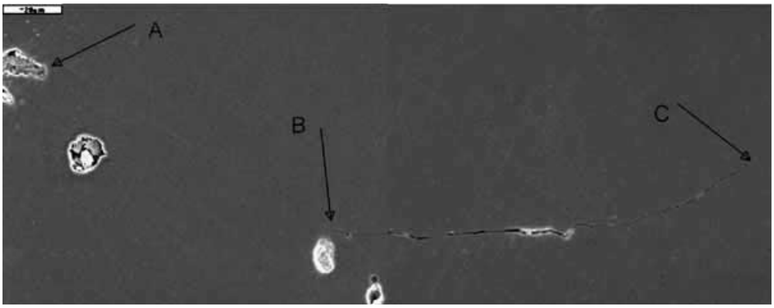

FIG. 5—*General view at the meso-crack. Temp.=–20°C, a/W=0.5. Point A—the macro-crack edge; points B and C show the trailing and leading edges of the meso-crack, respectively.*

age meso-crack (arrow B). The meso-crack is 150 μm long. The distance between the edges of the macro- and meso-cracks is 120 μm. One may notice that the area between the tips of the macro- and meso-cracks is free of any "open" defects.

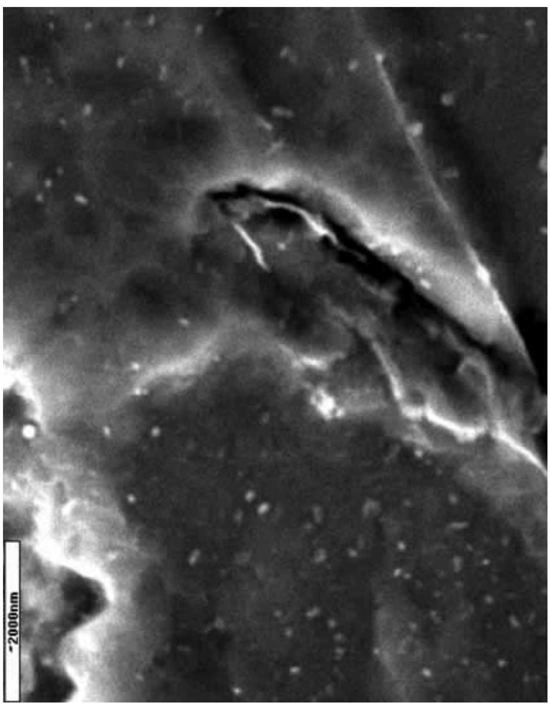

FIG. 6—*The meso-crack trailing edge is located within the zone of extensive plastic deformation.*

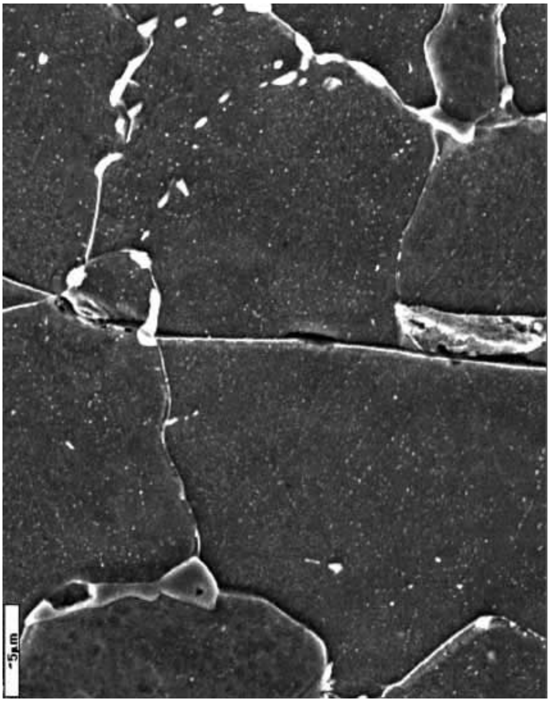

FIG. 7—*Here, the meso-crack propagates through the ferrite grain, passing close to the carbide. Distribution of small carbides can be seen. The surface was acid etched after polishing.*

Figure 6 shows the trailing edge of the cleavage meso-crack, and Fig. 7 demonstrates the profile of the meso-crack along its entire length. One may see kinks, voids, and carbide inclusions close to the meso-crack. It is clear that the meso-crack passed through the material, which yielded little with the exception of the area close to the trailing edge of the meso-crack (Fig. 6). The immediate conclusions from these pictures are that meso-cracks, the candidates to grow and join a macro-crack, must nucleate and grow in the vicinity of large opening stresses and small plastic deformations. However, the area directly in front of a macro-crack is expected to experience large plastic deformations.

The numerical computations were made for the same material, temperature, and crack length as the case shown in Figs. 4–7; however, the specimen could be slightly different (pre-fatigue crack length), and it was loaded until the crack had grown several millimetres. The crack length versus load-point history was based on the recorded experimental signals (Fig. 3) and microscopic measurements along the fracture surface and used to numerically simulate the crack extension.

The numerical analysis was performed using two numerical models of the specimens. The first was a classical model commonly used for stationary cracks in elastic-plastic work-hardening materials. It contained a blunted crack mod-

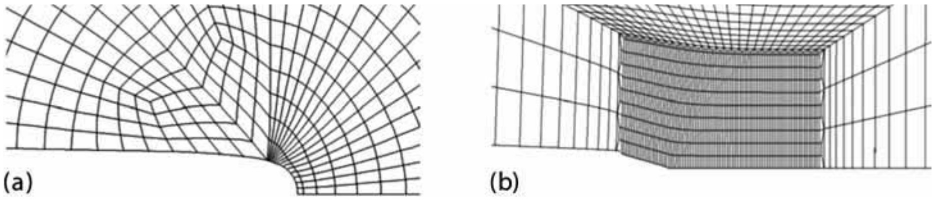

FIG. 8—(*a*) *FE mesh in model 1.* (*b*) *FE mesh in model 2.*

eled as a quarter of a circle (Fig. 8(*a*)). The radius of the crack tip depended on the extent of plastic deformation in each case and was of the order of 1–10 μm. In all cases, the radius of the crack tip was much smaller than $3\delta_T$, where δ_T is a crack tip opening displacement. Due to symmetry, only half of the specimen was modeled. The finite element mesh was filled with nine-node, two-dimensional plane strain elements. The size of the finite elements in the radial direction decreased toward the crack tip.

The second model was used to simulate a growing crack. It had a sharp tip and several layers of rectangular, nine-node, plane strain finite elements in front of the crack tip (Fig. 8(*b*)). The crack growth was modeled using a shift and release procedure applied to nodes in front of the crack. The nodes were released according to the experimental deflection-crack extension curves.

The stress and strain fields were observed and analyzed during the entire loading history recorded in the experiment. Special attention was focused on the onset of stable crack growth, the first steps of stable crack growth, the onset of a cleavage crack jump, and the phenomena that occurred right after this jump. The experimental results of the deflection-force and deflection-potential drop curves, as shown in Figs. 3, 12, and 15, and the measured crack lengths provided sufficient information to identify the moments of interests, the lengths of stable crack extensions, and the lengths of cleavage crack jumps.

Computations were performed using ADINA SYSTEM 8.4. In the FEM simulation, the deformation theory of plasticity and the Huber–von Mises yield criterion were used. In the model, the true stress-strain curves recorded in the experiment were used including the Lüders plateau, which was simplified in such a way that the stresses within the plateau were slowly increasing. Additionally, finite strains were assumed.

The results obtained from the two crack models were similar but not identical. Despite the important differences in the shape of the crack tip and the finite element (FE) mesh at a crack tip for the two models, the stress fields computed before the presumed stable crack extension were similar (Fig. 9). This similarity concerns both the level and location of the opening stress maximum. It is not so after crack had stably grown roughly 0.7 mm (the moment before the cleavage jump). In both models, the opening stress increased up to 1170 MPa for the stationary crack model and up to 1240 MPa for the growing crack model. Another difference is that the stress maximum moves closer to the crack tip in the case of the growing crack model. Finally, the accumulated effective plastic strain increases more rapidly in the direction of the crack tip for a stationary crack than for a growing one; however, the strain starts to

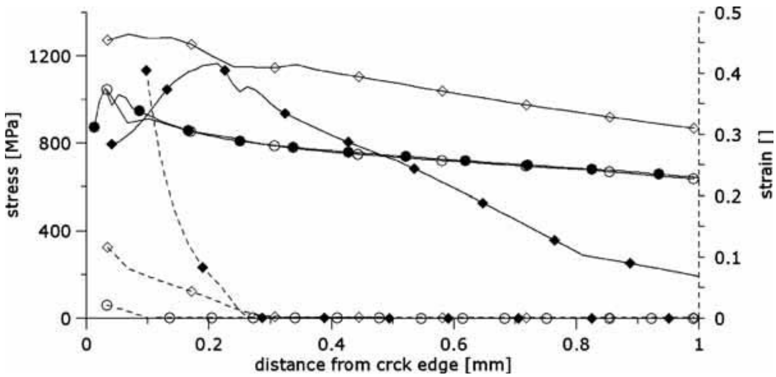

FIG. 9—*The opening stress, σ_{22} (solid lines), and strain (dashed lines) distributions in front of a crack before the onset of stable crack growth (circles) and before the jump (diamonds) according to the first model (filled symbols) and the second model (empty symbols). Temp.=–20°C, a/W=0.5.*

increase from nearly the same location in front of the crack in both cases. These differences do not change the general hypotheses regarding the fracture mechanism change from a ductile to a cleavage one that was formulated after the preliminary investigation.

Assuming that the critical length is of the order of 200–300 μm and is located 150–200 μm from the crack tip, the critical stress is either between 950 and 980 MPa, as predicted by the static crack model, or between 1100 and 1150 MPa, as predicted in the case of the model with the moving crack tip. The assumption above is supported by fractographic observations as well as the pictures of the meso-crack in front of the macro-crack. The yield stress, σ_o, of this material is roughly 300 MPa; thus, the critical stress value may be expected to be in the range of $(3.5–3.8)\sigma_o$.

After the onset of a crack jump, the opening stress rapidly decreased in front of the crack while the crack was growing (Fig. 10). The crack grows due to the elastic energy accumulated within the specimen; however, the stress field rebuilds during the stable crack growth after the cleavage jump (Fig. 10).

In the further analysis, the discussion will concern a specimen with a crack length $a/W=0.2$ and tested at $-50°\mathrm{C}$ (Fig. 11). The fracture surface of such a specimen is shown in Fig. 2(*a*). The stable crack growth is due to the mixed fracture mechanisms, and a honeycomb-like fracture surface characteristic for this steel can be observed. The situation shown in Fig. 11 was captured during stable crack growth but prior to the presumed onset of the cleavage crack jump. The figure shows the specimen at a load-point displacement of $u=1.3$ mm, and the onset of the crack jump is expected at a load-point displacement of $u=1.6$ mm. One may see the honeycomb-like zone formation process with numerous cleavage micro-cracks and ductile bridges. The micro-cracks are of the order of one or two grain sizes and have not grown to larger meso-cracks yet. These micro-cracks become longer when the crack propagates.

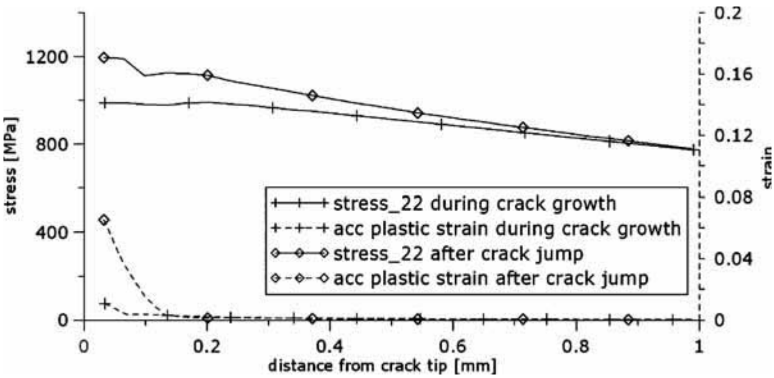

FIG. 10—*The stress, σ_{22} (solid lines), and accumulated plastic strain (dashed lines) distribution in front of a crack before cleavage jump is completed (crosses) and during the stable growth after cleavage jump (diamonds) Temp.=–20°C, a/W=0.5.*

Directly in front of the blunted pre-fatigue crack, no ductile process zone is observed in this cross-section.

The numerical analysis was performed using the data shown in Fig. 12. Again, two numerical models of the crack were used. The results are similar but not identical (Fig. 13). Before the onset of stable crack growth, the opening stress distributions are almost identical for both models. At the onset of a cleavage crack jump, the maximum of the opening stress is roughly 1300 and 1400

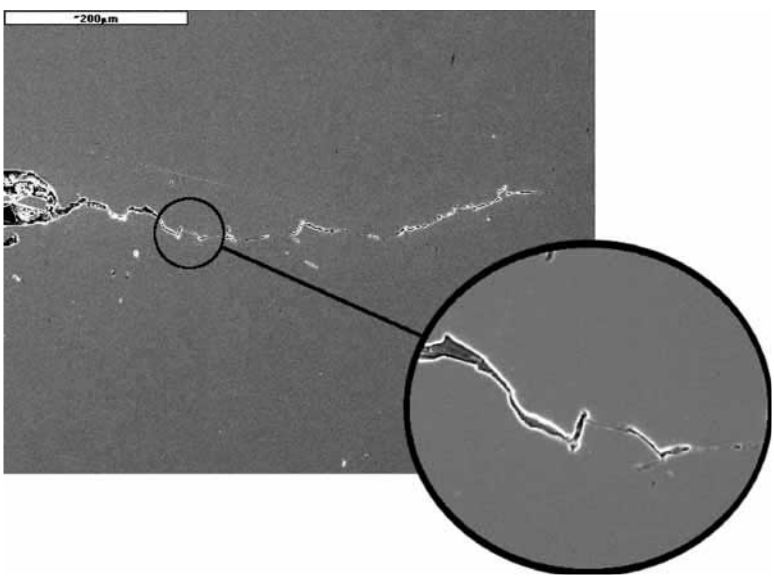

FIG. 11—*The honeycomb-like fracture surface creation during the stable crack extension. Temp.=–50°C, a/W=0.2.*

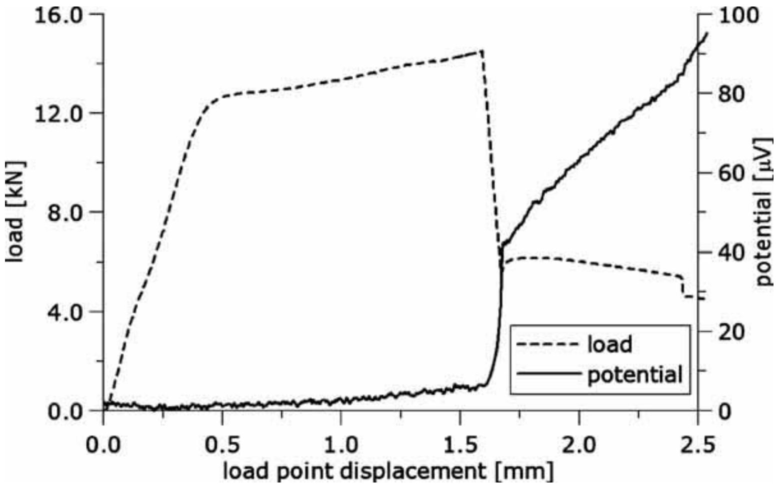

FIG. 12—*External force and potential drop as functions of load-point displacement. Temp.=−50°C, a/W=0.2.*

MPa for the first and second models, respectively. There is a large difference in locations of these maxima with respect to the crack edges. If one chooses the critical value for the opening stress to be 1100 MPa, the characteristic distance would be in the range of 300–400 μm for both models. For the first model, the stresses are higher than the critical value starting at a distance of 250 μm from the crack edge. For a growing crack, when a critical stress is 1100 MPa, the observed distance at which the opening stress exceeds the critical value may vary from the specimen to specimen due to a kink in the stress distribution, following from the discontinuous uniaxial tensile curve. In order to establish

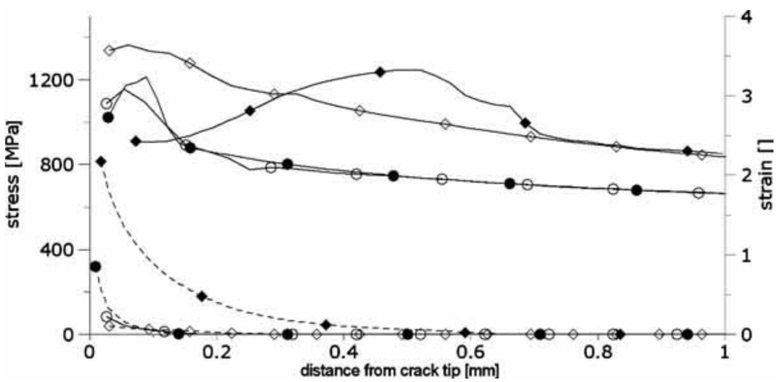

FIG. 13—*The opening stress, σ_{22} (solid lines), and strain (dashed lines) distributions in front of a crack before the onset of stable crack growth (circles) and before the jump (diamonds) according to the first model (filled symbols) and the second model (empty symbols). Temp.=−50°C, a/W=0.2.*

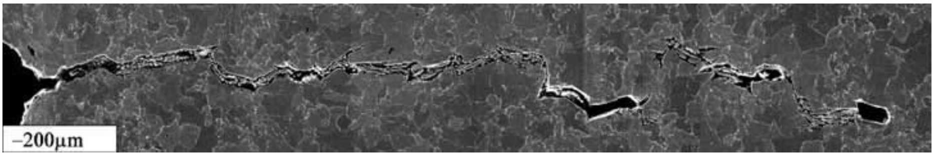

FIG. 14—*Growing crack profile, temp.=−20°C, a/W=0.2. After acid etching.*

the same critical length for both temperatures, the critical stress value at −50°C is likely to be 50 MPa lower than the critical stress value at the higher temperature.

At a critical stress of 1100 MPa, there is also some probability of micro-crack nucleation close to the growing crack edge from the beginning of the crack growth. However, at these small distances, the plastic strains are very high (the low in-plane constraint, $a/W=0.2$), and the excess of potential energy is dissipated by a plastic deformation also. At −50°C, the zone where the large accumulated plastic strains are observed is greater than the distance from the crack tip to the maximum stress location. At the beginning of the stable growth of the crack, the stresses are higher than the critical value but over a distance shorter than the critical length.

The fracture process was analyzed at −20°C again; however, the low in-plane constraint condition was used this time. The strong influence of the in-plane constraint on the fracture process can be seen not only by comparing the load-point displacement versus external load curves and the amounts of energy dissipated before the onset of a crack jump (Figs. 3 and 15) but also by comparing the way the material fractured (compare Figs. 4, 5, and 14). Figure 14 reflects the manner in which the honeycomb-like stable crack was created. In this particular cross-section, no meso-crack was observed in front of the growing crack. The length of the stable crack growth is now much longer than for a longer crack. There are numerous open cavities along the crack profile that were not observed along the profile of a longer crack.

Numerical analysis was performed using the data shown in Fig. 15. One may notice that the opening stress level in front of the crack immediately before the onset of the stable crack growth is not high enough for a cleavage micro-crack to nucleate and grow (Fig. 16). The critical stress level is expected to be equal to 1100 MPa, as it was assumed earlier. The high accumulated effective plastic strains cover a domain of 150 μm long in front of the crack. In Fig. 2(*d*), one may observe a ductile fracture mechanism at the beginning of the stable crack extension, which agrees with the computed stress and strain distribution. When the external load increases, both the opening stress maximum and the length of the domain where the opening stress is higher than the critical value also increase. Finally, when this area reaches a length of 300 μm (the assumed critical length), the cleavage meso-crack is created, and the fracture mechanism changes from ductile (in our case mixed) to cleavage. After the jump, the stresses drop to lower values.

Next, the most brittle test specimen will be analyzed. It had a crack length with $a/W=0.5$ and was loaded at a temperature of −50°C. The crack profile recorded after the test, which was interrupted is shown in Fig. 17. The stable

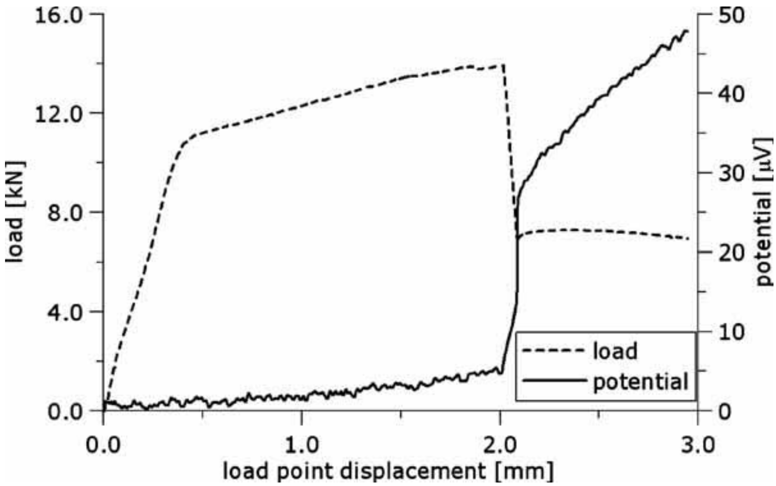

FIG. 15—*External force and potential drop as a function of load-point displacement. Temp.=–20°C, a/W=0.2. This figure is associated with the numerical computations.*

crack growth was predominantly cleavage; however, the fracture surface revealed numerous ductile fragments (Fig. 2(*b*)). The crack profile shows that the fracture took place in a discontinuous manner. However, these discontinuities had a local character, so they are undetectable along the force-deflection curve. These discontinuities indicate the statistical character of the micro-crack nucleation process, which depends on the stress level and the characteristic length. The characteristic length for a tested material was assumed in this paper to be 300 μm. It is worth stressing that the lengths of the segments of the crack profile are roughly equal to this length (Fig. 17). The situation shown in Fig. 17

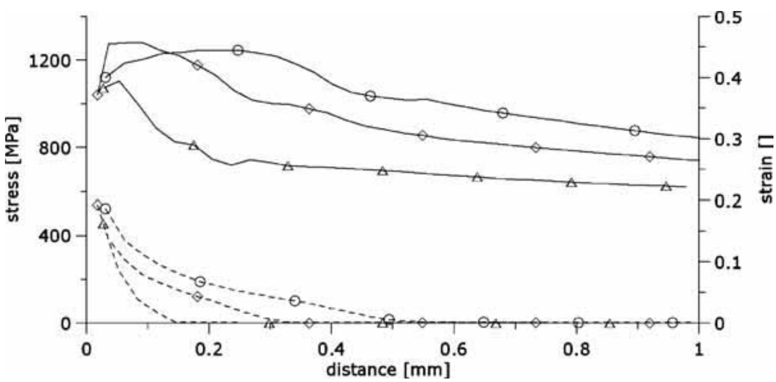

FIG. 16—*The opening stress, σ_{22} (solid lines), and plastic strain (dashed lines) distributions in front of a crack before the onset of stable crack growth (triangles), during the stable crack growth (diamonds), and right before the onset of a cleavage crack jump (circles), according to the second model. Temp.=–20°C, a/W=0.2.*

FIG. 17—*Growing crack profile (shown prior to acid etching). Temp.=–50, a/W=0.5.*

may not reflect the moment right before an unstable cleavage jump. The loading process was interrupted when the deflection was equal to 0.9 mm. The unstable crack growth was observed at a deflection of 1.2 mm for similar specimens. For this loading history, the numerical computations were performed.

As before, the crack extension versus deflection curve was utilized in the numerical computations. The results of the numerical analysis showing the evolution of the stress and strain fields in front of the growing crack are presented in Fig. 18. One may notice that the opening stress level was greater than the critical value from the very beginning of the stable crack growth. Moreover, the opening stress exceeded the critical value over a sufficiently long distance from the crack tip to cause nucleation and the growth of cleavage micro-cracks (Fig. 18), then the formation of a meso-crack, and, finally, a cleavage jump. In the last case, the accumulated effective plastic strain was not sufficient to produce ductile bridges.

Concluding remarks

In the paper, a complete analysis of a stable and jump-like crack extension has been performed in order to study the process of the transition from a ductile to a cleavage fracture mechanism in ferritic steel after a heat treatment producing ferrite grains with evenly distributed carbides of various sizes.

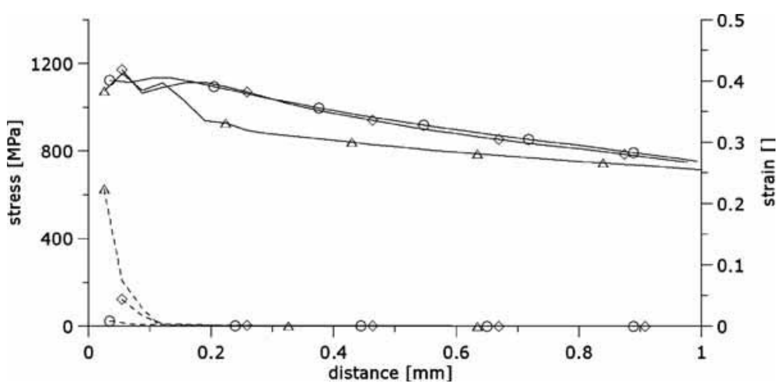

FIG. 18—*The opening stress, σ_{22} (solid line), and accumulative effective plastic strain (dashed lines) distributions according to the second crack model directly before the stable crack growth (triangles), during the stable crack growth (diamonds), and immediately preceding the onset of a cleavage crack jump (circles). Temp.=–50, a/W=0.2.*

The phenomenon of the ductile to cleavage transition is a result of the competition between two processes of energy dissipation: Plastic deformation and new surface creation. The role of a macro-crack, introduced into a specimen before it was loaded, was to localize these processes in time and space. The crack edge elevates the stresses and strains in a well-defined small domain. The levels of stress and strain were controlled by an in-plane constraint through the relative crack length (a/W) and the temperature of the material, which influences the yield strength and the level of work-hardening. Temperature also affects the ductility of the material.

If temperature is high enough, the number of dislocations and their mobility is sufficient to start a failure process in front of the crack due to a ductile mechanism of void nucleation, growth, and coalescence. The strains are maximized at the crack tip, and the maxima of the normal stress components are observed at a very small distance from the crack edge. A higher opening stress is recorded at a lower temperature. It is a feature of the stress distribution in front of cracks in many ferritic steels that when the external loading reaches a level close to the limit load, the opening stress maximum reaches a nearly constant value and this maximum moves out from the crack tip when the external loading further increases. All our specimens had been in a full yielding before a stable crack growth started. The curves representing the stress distribution in front of the crack were often not smooth because of a discontinuity along the stress-strain tensile curves.

The history of the evolution of the subcritical and post-critical crack growth in a ferritic 13HMF steel at the cleavage-ductile transition temperature range is summarized below based on microscopic observation and numerical analysis.

- At low levels of external loading, the accumulated effective plastic strain covers a larger area with respect to the location of the maximum opening stress than at high levels of external loading. Therefore, the stress maximum is surrounded by a large plastic deformation. Near the crack tip, the normal stresses decrease but are still sufficient to aid the plastic deformation in the nucleation and growth of voids around foreign particles. The growth of voids is mainly due to plastic deformation because the normal stresses decrease toward the crack tip.
- When an external load (deflection) increases, the maximum of the opening stress moves out from the crack tip and away from the domain of very high plastic strains. Now, many of the initiation kernels, after they have been broken or delaminated, meet favorable conditions to grow as micro-cracks. The stresses exceed the critical value for cleavage over an area comparable to the grain size. The grains in which the cleavage planes are almost normal to the opening stress break first due to a cleavage fracture mechanism. However, in the neighboring grains that are not favorably oriented, the plastic deformation can still be high enough to create plastic bridges. In such a way, the honeycomb-like fracture surface is formed. The plastic bridges break slightly later when the cleavage micro-crack becomes a meso-crack or much later during the final process of the splitting of the specimen. In our numerical analysis,

we considered the honeycomb-like structure in front of the macro-crack as a part of the crack.

- When the deformation proceeds, the stress maximum increases (second model) while the crack is growing. The domain in which the opening stresses become greater than the critical value spreads over several grains (10–15). The probability of several cleavage planes in the neighboring grains being in a favorable direction for cleavage increases. An increasing number of grains next to the maximum of the opening stress locations are not in the yielding state. The meso-crack can be created in front of the macro-crack. The proper amount of elastic energy is accumulated in the specimen, and the requirements for a sudden cleavage jump are met.

The results of this paper confirm the known hypothesis that an unstable cleavage fracture mechanism may take place when the opening stress in front of a crack is greater than the critical value over a distance greater than the critical length. It was demonstrated that the nucleation kernels are activated at a certain distance from the crack tip, and this distance may be greater than 100 μm.

However, if the stresses are greater than the critical value over a length shorter than the critical value, the cleavage fracture mechanism can still be activated locally with the cleavage facets surrounded by plastic bridges. We observed a subcritical crack growth, and the fracture surface resembled a honeycomb. To create such a mechanism, the opening stresses must be greater than the critical value over a distance comparable to the grain size. If this distance is shorter, we observed a ductile fracture surface.

It was confirmed that the critical stress depends on temperature, and the critical distance does not.

In the paper, the values of the critical stresses and lengths for the tested material were estimated for two temperatures.

If both of the critical values (stress and distance) are known from the experiment and numerical analysis, they can be used to predict the critical moments in real structures using the local approach and numerical analysis.

Acknowledgments

The financial support from the Polish Ministry of Science and Higher Education under Contract No. N504 004 31/0106 is gratefully acknowledged. The writers would also like to acknowledge Dr. I. Dzioba for technical contribution in performing the fracture tests and Professor M. Gajewski for the scanning microscopy observations.

References

[1] Wallin, K., “Master Curve Analysis of the ‘Euro’ Fracture Toughness Dataset,” *Eng. Fract. Mech.*, Vol. 69, 2002, pp. 451–481.

[2] Wallin, K., Nevasmaa, P., Laukkanen, A., and Planman, T., “Master Curve Analysis

of Inhomogeneous Ferritic Steels," *Eng. Fract. Mech.*, Vol. 71, 2004, pp. 2329–2346.

[3] Gao, X. and Dodds, R. H., Jr., "Constraint Effects on the Ductile-to-Brittle Transition Temperature of Ferritic Steels: A Weibull Stress Model," *Int. J. Fract.*, Vol. 102, 2000, pp. 43–69.

[4] Ruggieri, C. and Dodds, R. H., Jr., "A Transferability Model for Brittle Fracture Including Constraint and Ductile Tearing Effects: A Probabilistic Approach," *Int. J. Fract.*, Vol. 79, 1996, pp. 309–340.

[5] Ruggieri, C., Dodds, R. H., Jr., and Wallin, K., "Constraint Effects on Reference Temperature, T_0, for Ferritic Steels in the Transition Region," *Eng. Fract. Mech.*, Vol. 60, 1998, pp. 19–36.

[6] Tanguy, B., Besson, J., Piques, R., and Pineau, A., "Ductile to Brittle Transition of an A508 Steel Characterized by Charpy Impact Test, Part II: Modeling of the Charpy Transition Curve," *Eng. Fract. Mech.*, Vol. 72, 2005, pp. 413–434.

[7] Beremin, N., "A Local Criterion for Cleavage Fracture of a Nuclear Pressure Vessel Steel," *Metall. Trans. A*, Vol. 14A, 1983, pp. 2277–2287.

[8] Bordet, S. R., Karstensen, A. D., Knowles, D. M., and Wiesner, C. S., "A New Statistical Local Criterion for Cleavage Fracture in Steel. Part I: Model Presentation," *Eng. Fract. Mech.*, Vol. 72, 2005, pp. 435–452.

[9] Bordet, S. R., Karstensen, A. D., Knowles, D. M., and Wiesner, C. S., "A New Statistical Local Criterion for Cleavage Fracture in Steel. Part II: Application to an Offshore Structural Steel," *Eng. Fract. Mech.*, Vol. 72, 2005, pp. 453–474.

[10] Xia, L. and Shih, F., "Ductile Crack Growth—III. Transition to Cleavage Fracture Incorporating Statistics," *J. Mech. Phys. Solids*, Vol. 44, 1996, pp. 603–615.

[11] Rice, J. R. and Thomson, R., "Ductile Versus Brittle Behaviour of Crystals," *Philos. Mag.*, Vol. 29, 1974, pp. 73–97.

[12] Broberg, K. B., *Cracks and Fracture*, Academic Press, San Diego, London, New York, Tokyo, Toronto, 1999.

[13] Berdin, C., Besson, J., Bugat, S., Desmorat, R., Feyel, F., Forest, S., Lorenz, E., Maire, E., Pardoen, T., Pineau, A., and Tanguy, B., *Local Approach to Fracture*, J. Besson, Ed., Eccole des Mines de Paris, Les Presses, 2004.

[14] Yu, S. R., Yan, Z. G., Cao, R., and Chen, J. H., "On the Change of Fracture Mechanism with Test Temperature," *Eng. Fract. Mech.*, Vol. 73, 2006, pp. 331–347.

[15] Tanguy, B., Besson, J., Piques, R., and Pineau, A., "Ductile to Brittle Transition of an A508 Steel Characterized by Charpy Impact Test Part I: Experimental Results," *Eng. Fract. Mech.*, Vol. 72, 2005, pp. 49–72.

[16] Pineau, A., "Development of the Local Approach to Fracture over the Past 25 Years: Theory and Applications," *Int. J. Fract.*, Vol. 138, 2006, pp. 139–166.

[17] Knott, J. F. and Met, B., *Fundamentals of Fracture Mechanics*, Buttterworths & Co., Ltd., London, 1973.

[18] ISO 9328-2, 2004, "Steel Flat Products for Pressure Purposes—Technical Delivery Conditions, Part 2: Non Aloy and Alloy Steels with Specified Temperature Properties," International Standards Organization.

[19] EN 10028-2, 1992, "Steel Flat Products for Pressure Purposes, Part 2: Pressure Vessels, Fine Grain Steel Plates," issued by European Committee for Standardization.

[20] GOST 5520, 1979, "Rolled Carbon Low-Alloy Steel Sheets and Plates for Boilers and Pressure Vessels," issued by Russian Natioanl Standardization Committee.

[21] ASTM E1820-05, 2005, "Standard Test Method for Measurement of Fracture Toughness," *Annual Book of ASTM Standards*, Vol. 03.01, ASTM International, West Conshohocken, PA.

[22] Rice, J. R. and Johnson, M. A., "The Role of Large Crack Tip Geometry Changes in Plane Strain Fracture," *Inelastic Behaviour of Solids*, M. F. Kanninen W. F. Adler, A. R. Rosenfield, and R. I. Joffe, Eds., McGraw-Hill, New York, 1970, p. 641–672.

[23] Ritchie, R. O., Knott, J. F., and Rice, J. R., "On the Relationship Between Critical Tensile Stress and Fracture Toughness in Mild Steel," *J. Mech. Phys. Solids*, Vol. 21, 1973, pp. 395–410.

[24] Neimitz, A., Graba, M., and Galkiewicz, J., "An Alternative Formulation of the Ritchie–Knott–Rice Local Fracture Criterion," *Eng. Fract. Mech.*, Vol. 74(8), 2007, pp. 1308–1322.

Reprinted from JAI, Vol. 7, No. 2
doi:10.1520/JAI102508
Available online at www.astm.org/JAI

Claudio Ruggieri[1]

A Weibull Stress Model to Predict Effects of Weld Strength Mismatch on Cleavage Fracture Toughness

ABSTRACT: This work describes the development of a toughness scaling methodology incorporating the effects of weld strength mismatch on crack-tip driving forces. The approach adopts a nondimensional Weibull stress, $\bar{\sigma}_w$, as a the near-tip driving force to correlate cleavage fracture across cracked weld configurations with different mismatch conditions even though the loading parameter (measured by J or crack-tip opening displacement) may vary widely due to mismatch and constraint variations. Application of the procedure to predict the failure strain for an overmatch girth weld made of an API X80 pipeline steel demonstrates the effectiveness of the micromechanics approach. Overall, the results lend strong support to use a Weibull stress based procedure in defect assessments of structural welds.

KEYWORDS: cleavage fracture, weld strength mismatch, Weibull stress, local approach, toughness scaling model

Introduction

Fracture mechanics based approaches for structural components rely on the notion that a single parameter that defines the crack driving force characterizes the fracture resistance of the material [1,2]. These approaches allow the severity of crack-like defects to be related to the operating conditions in terms of a critical applied load or critical crack size. In particular, assessments of cleavage fracture for ferritic steels in the ductile-to-brittle transition (DBT) region are based on the one-parameter elastic-plastic characterization of macroscopic loading, most commonly the J-integral or the crack-tip opening displacement

Manuscript received May 15, 2009; accepted for publication November 25, 2009; published online January 2010.
[1] Dept. of Naval Architecture and Ocean Engineering, Univ. of São Paulo, Av. Prof. Mello Moraes, 2231 (PNV-EPUSP), São Paulo, São Paulo 05508-030, Brazil, e-mail: claudio.ruggieri@usp.br

Cite as: Ruggieri, C., "A Weibull Stress Model to Predict Effects of Weld Strength Mismatch on Cleavage Fracture Toughness," *J. ASTM Intl.*, Vol. 7, No. 2. doi:10.1520/JAI102508.

(CTOD or δ), and their corresponding macroscopic measures of cleavage fracture toughness (J_c or δ_c). Several flaw assessment methods [3–5] make extensive use of these toughness parameters to define simplified and conservative criteria to evaluate cleavage fracture in structural components containing defects, including welded structures. However, while used effectively in integrity analyses of engineering structures made of homogeneous materials, the application (and validation) of these existing methodologies in defect assessments of welded structural components with mismatch in tensile properties (and possibly hardening behavior) between the weld metal and base metal remains a potential open issue.

Experimental observations consistently reveal the occurrence of a variety of crack-like defects in the welded region which are either planar (e.g., hot or cold cracking, lack of penetration, and undercut) or volumetric (e.g., porosity and entrapped slag) [6,7] even if good workmanship and proper selection of the welding procedure and filler-metal composition are employed. To reduce the likelihood of structural failure caused by an undetected weld defect or by a weld flaw formed during operation, many codes and current fabrication practices require the use of weldments with weld metal strength higher than the base plate strength, a condition referred to as overmatching. An evident benefit and primary motivation to use weld overmatching is to promote gross section yielding of the base plate due to the higher yield stress of the weld metal. This has the effect of limiting the higher stresses that would otherwise occur in a homogeneous material thereby shielding the welded region. The overmatch weld also causes the large plastic deformation field to shift into the lower strength base metal where the fracture resistance is presumably higher and fewer defects occur.

However, while the overmatch practice has been used effectively in many structural applications, the level of mismatch between the weld metal and base plate material may strongly alter the relationship between remotely applied loading and crack-tip driving forces. The complex interaction between the local crack-tip fields (most often controlled by the flow properties of the weld metal) and the global plastic regime gives rise to near-tip constraint states, which can differ significantly than the corresponding levels in crack-tip constraint for a homogeneous fracture specimen at the same (macroscopic) loading. Moreover, cleavage fracture is a highly localized failure mechanism, which is strongly dependent on material characteristics at the microlevel. This phenomenon is further magnified by the overmatching condition in steel weldments, thereby contributing to increase the propensity to trigger cleavage before gross yield section. Clearly, the transferability of fracture toughness data measured using small laboratory specimens to large complex structural components still remains one of the key difficulties in developments of predictive procedures for defect assessments of welded structures. Advanced procedures for structural integrity analyses must include the complex interplay between the effects of weld strength mismatch and the variability of cleavage resistance at the microstructural level for the different regions of steel weldments.

This work describes the development of a micromechanics-based methodology incorporating the effects of weld strength mismatch on crack-tip driving forces. One purpose of this investigation is to extend the framework for structural integrity assessments building upon a local fracture parameter, here characterized by the Weibull stress (σ_w), to welded components. Another purpose is to assess the effectiveness of a toughness scaling model (TSM) based on a normalized interpretation of σ_w in integrity analyses of girth welds with varying mismatch conditions. Fracture testing of girth welds obtained from an API X80 pipeline steel provides the data needed to validate the proposed methodology in failure predictions. Such an application serves as a prototype for a wide class of integrity assessment problems involving the effects of weld strength mismatch on fracture toughness values. Overall, the results lend strong support to use a Weibull stress based procedures in defect assessments of structural welds.

The Weibull Stress Model to Mismatched Welds

Overview of Weakest Link Modeling for Cleavage Fracture

Experimental studies consistently reveal large scatter in the measured values of cleavage fracture toughness for ferritic steels tested in the DBT region (see Ref 8 for illustrative data and the experimental results presented next). A continuous probability function derived from weakest link statistics conveniently characterizes the distribution of toughness values in the form [9]

$$F(J_c) = 1 - \exp\left[-\left(\frac{J_c - J_{\text{th}}}{J_0 - J_{\text{th}}}\right)^{\alpha}\right] \tag{1}$$

which is a three-parameter Weibull distribution with parameters ($\alpha, J_0, J_{\text{th}}$). Here, α denotes the Weibull modulus (shape parameter), J_0 defines the characteristic toughness (scale parameter) and J_{th} is the threshold fracture toughness. Often, the threshold fracture toughness is set equal to zero so that the Weibull function given by Eq 1 assumes its more familiar two-parameter form. The above limiting distribution remains applicable for other measures of fracture toughness, such as K_{J_c} or CTOD. A central feature emerging from this model is that under small scale yielding conditions, the scatter in cleavage fracture toughness data is characterized by $\alpha=2$ for J_c-distributions or $\alpha=4$ for K_{J_c}-distributions [10,11].

To extend the previous methodology to multiaxially stressed crack configurations, research efforts have focused on probabilistic models, which couple the micromechanical features of the fracture process (such as the inherent random nature of cleavage fracture) with the inhomogeneous character of the near-tip stress fields. Motivated by the specific micromechanism of transgranular cleavage, a number of such models (most often referred to as *local approaches* [12] employ weakest link arguments to describe the failure event. The overall fracture resistance is thus controlled by the largest fracture-triggering particle that is sampled in the fracture process zone ahead of crack front. In the local approach to cleavage fracture, the probability distribution for the fracture stress of a cracked solid increases with loading (represented by the J-integral) according to the two-parameter Weibull distribution [8,11,13]

$$P(\sigma_w) = 1 - \exp\left[- \int_\Omega \left(\frac{\sigma_1}{\sigma_u} \right)^m d\Omega \right] = 1 - \exp\left[- \left(\frac{\sigma_w}{\sigma_u} \right)^m \right], \quad \sigma_1 \geq 0 \qquad (2)$$

where:

Ω denotes the volume of the (near-tip) fracture process zone and

σ_1 = maximum principal stress acting on material points inside the fracture process zone.

In the present work, the active fracture process zone is defined as the loci where $\sigma_1 \geq \lambda\sigma_{ys}$, with $\lambda \approx 2 \sim 2.5$ and σ_{ys} represents the material's yield stress. Parameters m and σ_u appearing in Eq 2 denote the Weibull modulus and the scale parameter of the Weibull distribution for the fracture stress. The stress integral appearing in Eq 2 defines the Weibull stress, σ_w, a term coined by the Beremin group [13], in the form

$$\sigma_w = \left[\int_\Omega (\sigma_1)^m d\Omega \right]^{1/m}, \quad \sigma_1 \geq 0 \qquad (3)$$

A central feature of this methodology involves the interpretation of σ_w as a macroscopic crack driving force [8,14]. Consequently, it follows that unstable crack propagation (cleavage) occurs at a critical value of the Weibull stress; under increased remote loading (as measured by J), differences in evolution of the Weibull stress reflect the potentially strong variations of near-tip stress fields. Moreover, the nature of the stress integral given by Eq 3 imposes essentially no restrictions on models to describe the material flow properties, including the yield plateau displayed by ferritic steels, as well as strain rate and ductile tearing effects on cleavage fracture.

Toughness Scaling Methodology Incorporating Mismatch Effects

Ruggieri and Dodds [8] proposed a TSM based on the Weibull stress to assess the effects of constraint variations on cleavage fracture toughness data. The present framework adopts the same philosophy to assess effects of weld strength mismatch on toughness measurements but utilizes the concept of a nondimensional Weibull stress, hereafter denoted $\bar{\sigma}_w$, which is defined as σ_w normalized by the yield stress of the material where fracture takes place. The central feature of this methodology lies on the interpretation of $\bar{\sigma}_w$ as the crack-tip driving force coupled with the simple axiom that cleavage fracture occurs when $\bar{\sigma}_w$ reaches a critical value, $\bar{\sigma}_{w,c}$, as illustrated in Fig. 1. For the same material at a fixed temperature, the scaling model requires the attainment of a specified value for $\bar{\sigma}_w$ to trigger cleavage fracture across crack configurations with different mismatch conditions, even though the loading parameter (measured by J in the present work) may vary widely due to the effect of weld strength mismatch. In the probabilistic context adopted here, attainment of equivalent values of normalized Weibull stress in cracked configurations with different mismatch conditions implies the same probability for cleavage fracture. Such an ad hoc assumption for the crack driving force interpretation of $\bar{\sigma}_w$ is motivated by fundamental models based on a critical tensile stress criterion for cleavage microcrack [25–27] coupled with the stress integral definition

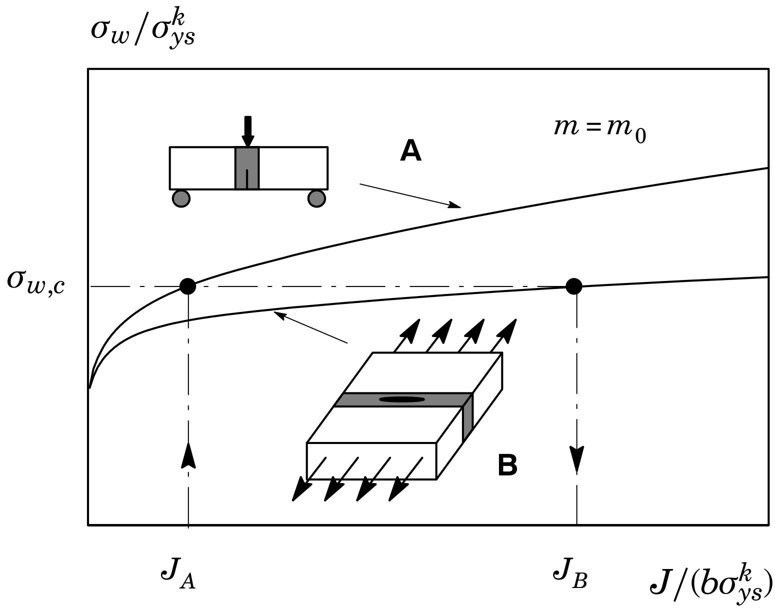

FIG. 1—*Scaling procedure based on the Weibull stress to correct toughness values for different crack configurations and mismatch conditions.*

of σ_w given by Eq 3. Moreover, consideration of the relative size of the highly near-tip stress region (taken here as the fracture process zone) given by $\sigma_1 \geq \lambda\sigma_{ys}$, with $\lambda \approx 2 \sim 2.5$, also aids in providing some justification for the adoption of $\bar{\sigma}_w$. For example, contours of a specified σ_1/σ_{ys}-ratio for an overmatched weld are smaller than the corresponding σ_1/σ_{ys} contours for an evenmatched weld under the same load level as characterized by J. Consequently, the overmatched weld must be loaded to higher J-values to reach crack-tip conditions that trigger cleavage fracture as in the evenmatched weld. Evidence supporting these arguments can be found by examining the experimental results shown in the Experimental Program section for the tested API X80 girth weld employed in this study.

To facilitate the development of the TSM incorporating effects of weld strength mismatch, it proves convenient to first define the mismatch ratio, M_y, as

$$M_y = \frac{\sigma_{ys}^{WM}}{\sigma_{ys}^{BM}} \tag{4}$$

where:

σ_{ys}^{BM} and σ_{ys}^{WM} denote the yield stress for the base metal and weld metal.

Based on the interpretation of σ_w as the crack-tip driving force previously introduced, it follows that the nondimensional Weibull stress for a bimaterial system such as a welded joint can be defined as

$$\bar{\sigma}_w^k = \frac{\sigma_w^k}{\sigma_{ys}^k} \tag{5}$$

where:

$k = 1, 2$ refers to the base metal and weld metal.

Figure 1 illustrates the procedure to assess the effects of mismatch on cleavage fracture behavior needed to scale toughness values for cracked configurations with different mismatch conditions based on the TSM strategy outlined above. The procedure employs J as the measure of macroscopic loading but remains valid for other measures of remote loading, such as CTOD. Very detailed nonlinear finite element analyses provide the functional relationship between $\bar{\sigma}_w$ for a specified value of the Weibull modulus, m_0, with the normalized applied loading, $\bar{J} = J/(b\sigma_{ys}^k)$, for each material. Here, b is the remaining crack ligament. Without loss of generality, Fig. 1 displays $\bar{\sigma}_w$ versus $\bar{J}$ curves for a high constrained welded configuration (such as a deep notch SE(B) specimen with a center-cracked square groove) made with an evenmatched condition ($M_y = 1.0$), denoted as configuration **A**, and a welded structural component (such as a surface crack specimen under tension loading) made with an overmatch condition ($M_y > 1.0$), denoted as configuration **B**. Given a measured toughness values at cleavage (J_A) for the high constraint evenmatch fracture specimen, the lines shown on Fig. 1 readily illustrate the technique used to determine the corresponding J_B-value for the welded component.

Weibull Modulus Calibration

Application of the methodology outlined above requires correct specification of the m-value entering directly into the calculation of σ_w through Eq 3. This parameter thus plays a crucial role in defining the scaling curves displayed in Fig. 1 upon which the toughness correction is derived. The procedure used here to calibrate the Weibull modulus, m, follows the proposed scaling model outlined in previous section for two sets of fracture specimens with different strength mismatch conditions. The notion of the Weibull stress as a crack-tip driving force establishes a function of the applied load and strength mismatch condition (and possibly geometry), which describes the local crack-tip response for cleavage fracture. By postulating a critical value of Weibull stress at fracture, $\bar{\sigma}_{w,c}$ (see Fig. 1), the distribution of measured toughness values for one configuration may then be rationally correlated with the toughness distribution for other configuration. The scaling curves shown in Fig. 1 refer to $\bar{\sigma}_w$ versus $\bar{J}$ trajectories for a welded fracture specimen and a welded structural component but are equally applicable to conventional SE(B) or C(T) specimens with varying degree of weld strength mismatch. Retaining contact with the TSM methodology and using experimental toughness values obtained from these fracture specimens, a pair of $\bar{\sigma}_w$ versus $\bar{J}$ curves corresponding to a fixed value of parameter m is found, which then correlates both toughness distributions.

The following steps summarize the key procedures in the calibration of parameter m, which enters directly into the TSM using $\bar{\sigma}_w$ to correct the loading trajectory for effects of weld strength mismatch. The approach builds upon previous calibration strategy for homogeneous materials introduced by Gao et al. [15] and Ruggieri et al. [16]. The next sections illustrate a validation study of the process for an API X80 girth weld.

- Step 1. Test two sets of specimens with different strength mismatch conditions (**A** and **B**) in the DBT region to generate two distributions of fracture toughness data. Ideally, configuration **A** should correspond to fracture specimens for the evenmatch condition ($M_y = 1$). Determine the mean value for each data set, J_0^A and J_0^B, using, for example, the Master Curve procedure given by ASTM E1921 [17]. Select the specimen geometries and the common test temperature to ensure different evolutions of constraint levels for the two configurations. No ductile tearing should develop prior to cleavage fracture in either set of tests. In case limited ductile tearing does develop in some specimens, the corresponding toughness values can be treated as censored values (see ASTM E1921 [17]).
- Step 2. Perform detailed nonlinear (large strain) finite element analyses for the tested specimen geometries. The mesh refinements must be sufficient to ensure converged σ_w versus J histories for the expected range of m-values and loading levels.
- Step 3

(i) Assume an m-value. Compute the evolution of $\bar{\sigma}_w$ versus $\bar{J}$ for configurations **A** and **B** to construct the TSM relative to both configurations and mismatch conditions.

(ii) Correct J_0^A to its equivalent $J_{0,m}^B$ (i.e., the corrected value of the mean toughness for the assumed m-value) for effects of weld strength mismatch. Define the error of toughness scaling as $R_m = (J_{0,m}^B - J_0^B)/J_0^B$. If $R_m \neq 0$, repeat substeps (i) and (ii) for additional m-values.

(iii) Plot R_m versus m. The calibrated Weibull modulus makes $R_m = 0$ within a small tolerance.

Computational Procedures and Finite Element Models

Calibration of the Weibull modulus for the tested girth weld is conducted by performing detailed finite element analyses on plane-strain models for deep crack SE(B) specimens having a center-cracked groove weld with two mismatch conditions: $M_y = 1.02$ (evenmatch) and $M_y = 1.09$ (overmatch). The specimens have thickness, $B = 25$ mm, a loading span, $S = 100$ mm, and width, $W = 25$ mm. Minami et al. [18] used these specimens to measure the cleavage fracture resistance for steel weldments made of an API X80 pipeline steel as described in Experimental Program section. A conventional mesh configuration having a focused ring of elements surrounding the crack front is used with a small key-hole at the crack tip; the radius of the key-hole, ρ_0, is 0.025 mm. Symmetry conditions permit modeling of only one-half of the specimen with appropriate constraints imposed on the remaining ligament. The half-symmetric model has one thickness layer of approximately 1000 eight-node three-dimensional (3D) elements ($\sim$2100 nodes) with plane-strain constraints

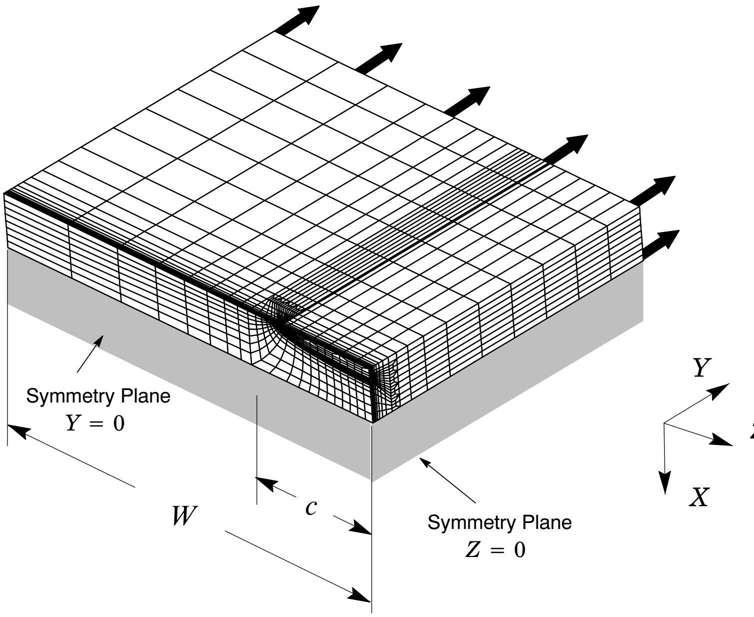

FIG. 2—*Finite element model used in 3D analyses of the wide plate specimen for API X80 girth weld.*

imposed ($w=0$) on each node. These finite element models are loaded by displacement increments imposed on the loading points to enhance numerical convergence.

Predictions of the failure load for the wide plate M(T) specimen based on the proposed Weibull stress model require additional numerical analyses for this crack configuration. Figure 2 shows the 3D finite element model constructed for the wide plate specimen. This crack models has very similar features as other numerical models and also employs a conventional focused mesh surrounding the crack front with a small key-hole at the crack tip ($\rho_0 = 0.025$ mm). The quarter-symmetric model has 18 layers with 9526 eight-node 3D elements (11 233 nodes).

The numerical computations for the cracked configurations reported here are generated using the research code WARP3D [19]. The analyses utilize an elastic-plastic constitutive model with J_2 flow theory and conventional von Mises plasticity in large geometry change setting. The stress-strain response for the tested material follows a power hardening law given by $\varepsilon/\varepsilon_{ys} \propto (\sigma/\sigma_{ys})^n$, where n denotes the strain hardening exponent and σ_{ys} and ε_{ys} are the (reference) yield stress and strain. For the finite element computations reported here, an estimate for the hardening exponent is given by [2,5]

$$\sigma_{uts} = \sigma_{ys}\left[\frac{(500N)^N}{\exp(N)}\right] \tag{6}$$

where:

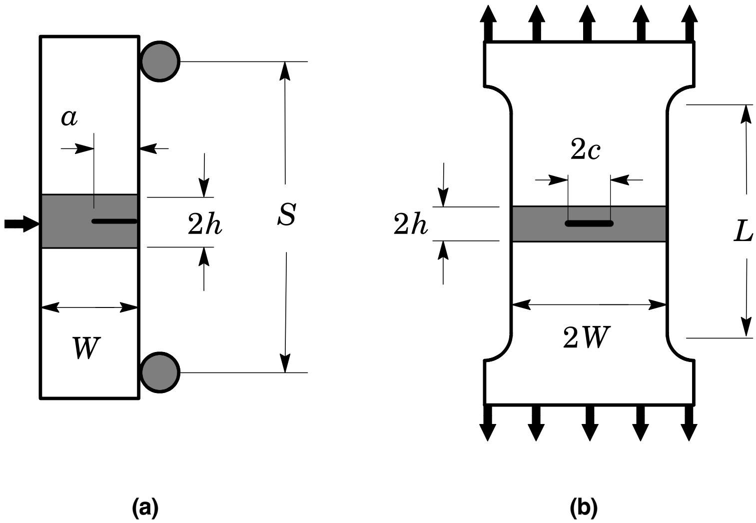

FIG. 3—*Geometries for the welded fracture specimens tested by Minami et al.* [*18*]*:* (*a*) *SE*(*B*) *specimens and* (*b*) *wide plate M*(*T*) *specimen with a surface center crack.*

σ_{uts} = tensile strength and $N = 1/n$. Using the tensile properties described next in Experimental section, Eq 6 then provides $n = 17.7$ for the evenmatch weld and $n = 20.4$ for the overmatch weld.

Application to Predict the Failure Load in Girth Welds

Experimental Program

Minami et al. [18] reported on a series of fracture tests conducted on weld specimens made of an API X80 pipeline steel. The welding procedure and welding conditions follow closely those employed in girth welds made in field conditions. Figure 3 shows the tested weld configurations, which include deep notch SE(B) fracture specimens and a wide plate M(T) specimen with a semi-elliptical surface center crack with three levels of weld strength mismatch: 10 % undermatch ($M_y = 0.88$), evenmatch ($M_y = 1.02$), and 10 % overmatch ($M_y = 1.09$). This validation study focuses on tests of the evenmatch and 10 % overmatch cracked specimens. The SE(B) specimens have $a/W = 0.5$ with thickness $B = 25$ mm, width $W = 25$ mm, and span distance $S = 100$ mm (refer to Fig. 3). The wide plate specimens have thickness $B = 25$ mm, width $2W = 400$ mm, and length $L = 300$ mm; here, the surface crack has length $2c = 100$ mm and depth $a = 6$ mm. In all fracture specimens, the weld groove width, $2h$, is 10 mm.

The material is a high strength low alloy Grade 550 pipeline steel equivalent to API 5L Grade X80 steel [20]. The weld specimens were prepared using standard gas metal arc welding procedure with heat inputs ranging from 0.3 to 0.9 according to the pass sequence (see details in Minami et al. [18]). Mechani-

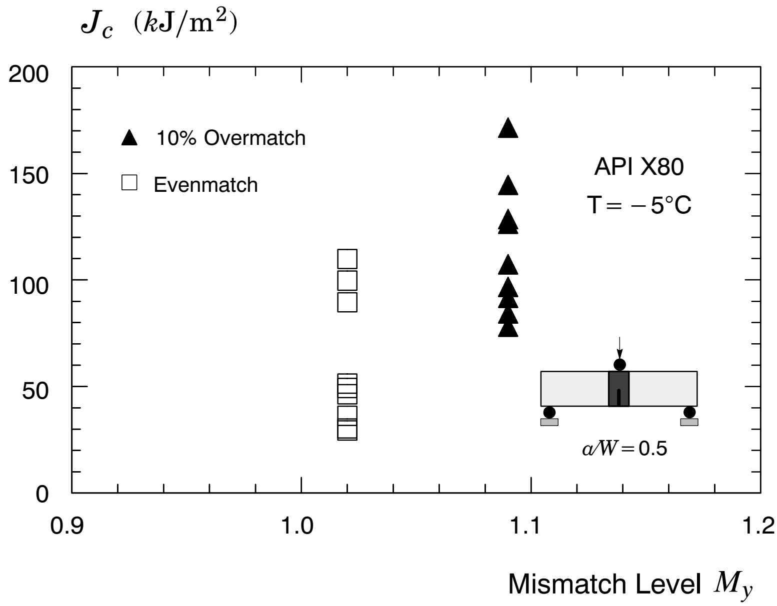

FIG. 4—*Experimental toughness values for welded deep crack SE(B) fracture specimens of API X80 steel with two mismatch levels tested by Minami et al.* [*18*] (*T=–5°C*).

cal tensile tests extracted from the longitudinal weld direction provide the room temperature (20°C) stress-strain data. The evenmatch weld has 581 MPa yield stress (σ_{ys}) and 670 MPa tensile strength (σ_{uts}). The 10 % overmatch weld has yield stress, $\sigma_{ys}=621$ MPa, and tensile strength, $\sigma_{uts}=691$ MPa. Both materials display relatively low strain hardening ($\sigma_{uts}/\sigma_{ys}=1.11\sim 1.15$) so that effects of hardening mismatch are considered negligible. Other mechanical properties for this material include Young's modulus, $E=206$ GPa, and Poisson's ratio, $\nu=0.3$. Minami et al. [18] provided further details on the mechanical tensile test data for this material.

Testing of the SE(B) specimens was performed at $T=-5°$C, which is within the range of the DBT behavior for the material. Records of load versus crack mouth opening displacements (CMODs) were obtained for each specimen using a clip gauge mounted on knife edges attached to the specimen surface. Post-test examinations established the amount of stable crack growth prior to final fracture by cleavage. While Minami et al. [18] report CTOD toughness values derived from the plastic hinge model using the BS 7448 standard [21], the present analyses are conducted based upon J_c-values. Using the measured plastic work defined by the plastic component of the area under the load versus CMOD curve, the experimental fracture toughness values (J_c) are obtained using the *eta* method [2] with the η-factors given by Donato and Ruggieri [22] for welded SE(B) specimens with center crack grooves and varying tensile properties and mismatch levels. Figure 4 reveals the effect of strength mismatch on J_c-values;

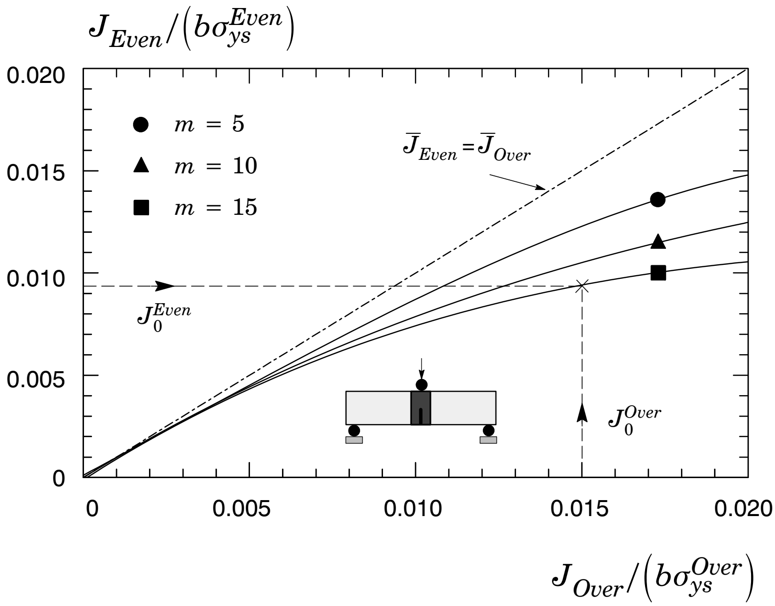

FIG. 5—*Fracture toughness correction using the TSM methodology based on the non-dimensional Weibull stress with varying Weibull moduli for tested API X80 girth weld. The lines on the plot indicate the calibration process to determine parameter m.*

here, for the 10 % overmatch specimens, the toughness values exceed the even-match toughness by a factor of 1.5∼2.0.

Fracture testing was also conducted on the wide plate specimens with a 10 % overmatch girth weld at $T = -5°C$. The specimen failed by cleavage fracture after some amount of ductile tearing with the experimentally measured failure strain given by $\varepsilon_f = 2.25$ % [18].

Calibration of Weibull Modulus for the Tested Girth Weld

The procedure used here to calibrate the Weibull stress parameters for the tested girth weld follows the proposed scheme outlined previously. In the present application, calibration of parameter m is conducted by scaling the mean value of the measured toughness distribution for the evenmatch SE(B) specimen (taken here as the "baseline" value) to an equivalent mean value of the toughness distribution for the 10 % overmatch SE(B) specimen. The calibration process simply becomes one of determining an m-value that corrects J_0^{even} to its equivalent value J_0^{over}. The research code WSTRESS [24] is used to construct J versus J_w trajectories for these fracture specimens needed to perform the calibration of parameter m.

Very detailed finite element computations of these specimens enable construction of the $J_0^{\text{even}} \rightarrow J_0^{\text{over}}$ correction shown in Fig. 5 for varying m-values. These m-values are consistent with previously reported values for structural steels [14–16,23]. Each curve provides pairs of J-values corresponding to the 10 % overmatch and evenmatch SE(B) specimen that produce the same $\bar{\sigma}_w$. A reference line is shown, which defines a unit ratio of mismatch correction, i.e., $\bar{J}_{\text{even}} = \bar{J}_{\text{over}}$, in which the corresponding J-value is normalized by each material's yield stress and the remaining ligament, b, defined by $b = (W - a)$ for the SE(B) specimen and $b = (B - a)$ for the M(T) specimen. The Weibull modulus does affect predictions of mismatch effects; here, the increase in the m-value assigns a greater weight factor to stresses at locations very near to the crack front thereby strongly altering the ratio of mismatch correction.

Now, following the master curve procedure in ASTM E1921 [17] and adopting a Weibull distribution [9] to describe the toughness distribution, the mean values are $J_0^{\text{even}} = 66.9$ kJ/m^2 and $J_0^{\text{over}} = 118.0$ kJ/m^2. Once the mean toughness for each mismatch condition is determined, the calibration procedure then yields $m \approx 15$ for the tested material at $T = -5\,^\circ\text{C}$. To simplify interpretation of the calibrated m-value, Fig. 5 recasts the calibration strategy into a graphical procedure to determine parameter m using the scaling curves displayed in that plot.

Prediction of Failure Load for the Wide Plate Girth Weld

To verify the predictive capability of the Weibull stress methodology adopted in the present work, this section describes application of the TSM based on the nondimensional Weibull stress ($\bar{\sigma}_w$) incorporating effects of weld strength mismatch to predict the failure strain for the wide plate M(T) specimen with 10 % overmatch. Very detailed nonlinear finite element analyses provide crack front stress fields to generate the evolution of $\bar{\sigma}_w = \sigma_w / \sigma_{\text{ys}}^k$ versus $\bar{J} = J/(b\sigma_{\text{ys}}^k)$ for the m-value calibrated in the previous section. Here, the J-value at fracture and corresponding failure strain for the tested wide plate specimen are predicted using the measured deep crack toughness values for the evenmatched SE(B) specimen, J_0^{even}. Numerical calibration of the Weibull parameter m used to construct $\bar{\sigma}_w$ versus $\bar{J}$ trajectories is performed using the research code WSTRESS [24], which implements a finite element form of Beremin's formulation [13].

Figure 6 shows the computed evolution of $\bar{\sigma}_w$ under increasing values of $\bar{J}$ for the SE(B) and M(T) configurations using $m = 15$. Given the normalized J_0-value for the evenmatch SE(B) specimen, the lines shown on this plot illustrate the scaling procedure to determine the corresponding J-value for the welded M(T) specimen. Figure 7 displays the mechanical response of the wide plate specimen characterized in terms of the evolution of remote applied strain, ε_r, with increased crack-tip loading, $\bar{J}$. These curves provide the quantitative basis to predict the failure strain for the wide plate M(T) specimen with 10 % overmatch. Here, the $\bar{\sigma}_w$-values for the plane-strain deep crack SE(B) specimen are scaled to the effective length of the M(T) specimen to guarantee that similar volumes of the (near-tip) fracture process zone are included into the computation of the Weibull stress for each crack configuration (see Eq 3). Using again the TSM procedure outlined previously, the predicted failure strain, $\tilde{\varepsilon}_f$, is evalu-

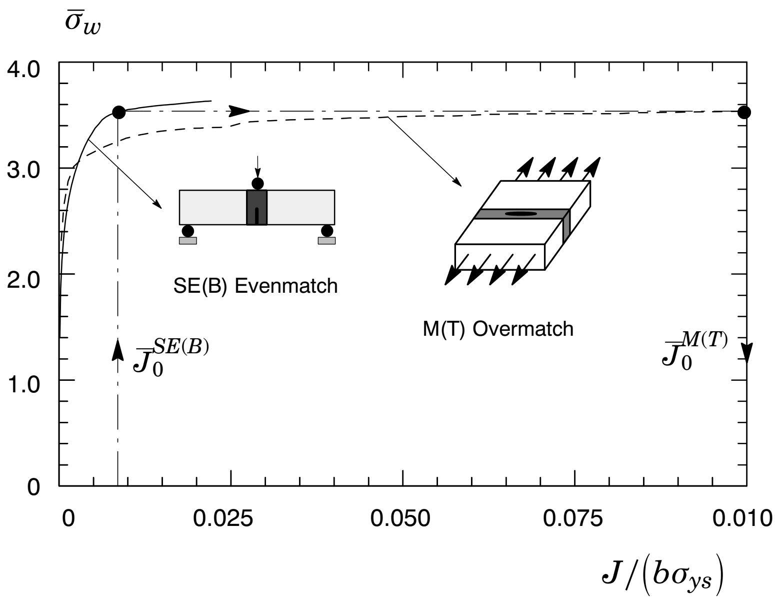

FIG. 6—*Evolution of normalized Weibull stress with normalized J for the evenmatch SE(B) specimen and the overmatched wide plate configuration for m=15.*

ated from first determining the corresponding characteristic J_0-value for the 10 % overmatch M(T) specimen based upon the J_0-value for the evenmatch SE(B) specimen and then computing the failure strain by means of the strain-crack driving force relationship shown in Fig. 7. This procedure yields $\tilde{\varepsilon}_f \approx 2.8$ %, which overestimates the experimentally measured failure strain by 25 %. Such overprediction is most likely caused by the use of plane-strain models to describe the stress fields for the SE(B) specimens, which result in a stiffer mechanical response and higher near-tip stresses (and, consequently, higher Weibull stress versus J trajectories) compared to 3D models. Moreover, because of the strong constraint loss displayed by the M(T) specimen, the evolution of $\bar{\sigma}_w$ versus $\bar{J}$ for this crack configuration rises rather slowly with increased levels of loading as measured by J. Such behavior clearly affects the accuracy of the predicted toughness value for the M(T) specimen and underscores the need of further refinement in the Weibull stress model for very low constraint configurations. Nevertheless, given the strong effect of specimen constraint coupled with a varying degree of weld mismatch on failure behavior, the overall error appears acceptable to support the use of the proposed Weibull stress model to predict effects of weld strength mismatch on cleavage fracture resistance.

Summary and Conclusions

This work describes the development of a toughness scaling methodology incorporating the effects of weld strength mismatch on crack-tip driving forces.

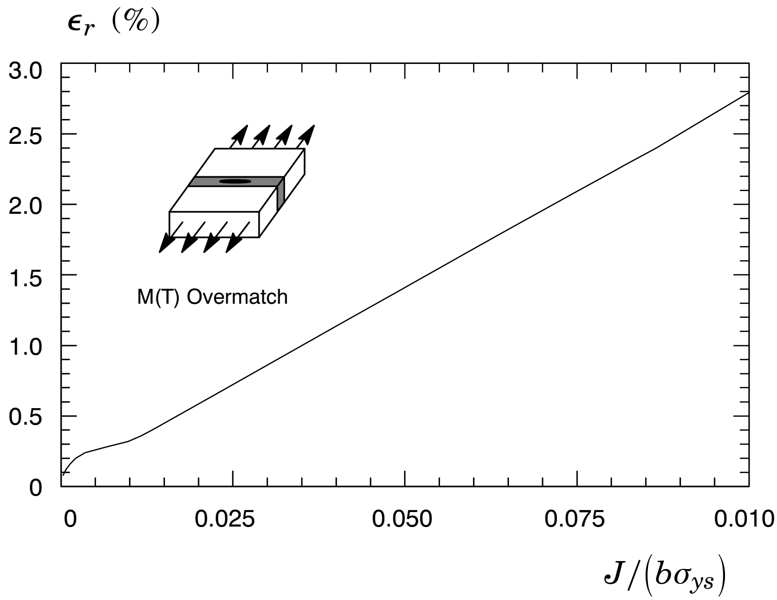

FIG. 7—*Mechanical response of the wide plate specimen characterized in terms of the evolution of remote applied strain,* ε_r*, with increased crack-tip loading,* $\bar{J}$.

The approach builds on a micromechanics description of the cleavage fracture process using a nondimensional Weibull stress, $\bar{\sigma}_w$, as a near-tip driving force coupled to a convenient extension of the TSM. For the same material at a fixed temperature, the scaling model requires the attainment of a specified value for $\bar{\sigma}_w$ to trigger cleavage fracture across cracked weld configurations with different mismatch conditions even though the loading parameter (measured by J or CTOD) may vary widely due to mismatch and constraint variations. Application of the procedure to predict the failure strain for an overmatch girth weld made of an API X80 pipeline steel clearly demonstrates the effectiveness of the micromechanics approach. Overall, the results lend strong support to use a Weibull stress based procedure in defect assessments of structural welds. Current work is in progress to include a full-thickness treatment of the TSM based on 3D SE(B) fracture specimens and a more refined formulation for the Weibull stress incorporating plastic strain effects and different local criteria.

Acknowledgments

This investigation was supported by the Brazilian Council for Scientific and Technological Development (CNPq). The author acknowledges Prof. F. Minami from Osaka University for making the girth weld data for the API X80 steel available.

References

[1] Hutchinson, J. W., "Fundamentals of the Phenomenological Theory of Nonlinear Fracture Mechanics," *J. Appl. Mech.*, Vol. 50, 1983, pp. 1042–1051.

[2] Anderson, T. L., *Fracture Mechanics: Fundaments and Applications*, 3rd ed., CRC Press, Boca Raton, 2005.

[3] BS 7910, 2005, "Guide on Methods for Assessing the Acceptability of Flaws in Metallic Structures," British Standards Institution, London.

[4] SINTAP: Structural Integrity Assessment Procedure for European Industry, Final Procedure, British Steel Report, Rotherham, 1999.

[5] API RP-579-1/ASME FFS-1, 2007, "Fitness-for-Service," American Petroleum Institute, Washington, DC.

[6] Jutla, T., "Fatigue and Fracture Control of Weldments," *ASM Handbook—Volume 19: Fatigue and Fracture*, ASM International, Materials Park, OH, 1996, pp. 434–449.

[7] Glover, A. G., Hauser, D., and Metzbower, E. A., "Failures of Weldments" *Metals Handbook—Volume 11: Failure Analysis and Prevention*, American Society for Metals, Materials Park, OH, 1986, pp. 411–449.

[8] Ruggieri, C. and Dodds, R. H., "A Transferability Model for Brittle Fracture Including Constraint and Ductile Tearing Effects: A Probabilistic Approach," *Int. J. Fract.*, Vol. 79, 1996, pp. 309–340.

[9] Mann, N. R., Schafer, R. E., and Singpurwalla, N. D., *Methods for Statistical Analysis of Reliability and Life Data*, John Wiley & Sons, New York, 1974.

[10] Wallin, K., "The Scatter in KIc Results," *Eng. Fract. Mech.*, Vol. 19, 1984, pp. 1085–1093.

[11] Minami, F., Brückner-Foit, A., Munz, D., and Trolldenier, B., "Estimation Procedure for the Weibull Parameters Used in the Local Approach," *Int. J. Fract.*, Vol. 54, 1992, pp. 197–210.

[12] Pineau, A., "Global and Local Approaches to Fracture-Transferability of Laboratory Test Results to Components," *Topics in Fracture and Fatigue*, A. S. Argon, Ed., Springer Verlag, New York, 1992, pp. 197–234.

[13] Beremin, F. M., "A Local Criterion for Cleavage Fracture of a Nuclear Pressure Vessel Steel," *Metall. Trans. A*, Vol. 14A, 1983, pp. 2277–2287.

[14] Ruggieri, C., "Influence of Threshold Parameters on Cleavage Fracture Predictions Using the Weibull Stress Model," *Int. J. Fract.*, Vol. 110, 2001, pp. 281–304.

[15] Gao, X., Ruggieri, C., and Dodds, R. H., "Calibration of Weibull Stress Parameters Using Fracture Toughness Data," *Int. J. Fract.*, Vol. 92, 1998, pp. 175–200.

[16] Ruggieri, C., Gao, X., and Dodds, R. H., "Transferability of Elastic-Plastic Fracture Toughness Using the Weibull Stress Approach: Significance of Parameter Calibration," *Eng. Fract. Mech.*, Vol. 67, 2000, pp. 101–117.

[17] ASTM E1921, 2008, "Standard Test Methods for Determination of Reference Temperature, T0, for Ferritic Steels in the Transition Range," *Annual Book of ASTM Standards*, ASTM International, West Conshohocken, PA.

[18] Minami, F., Ohata, M., Toyoda, M., Tanaka, T., Arimochi, K., Glover, A. G., and North, T. H., "The Effect of Weld Metal Yield Strength on the Fracture Behavior of Girth Welds in Grade 550 Pipe," *Pipeline Technology*, Vol. 1, 1995, pp. 441–461.

[19] Gullerud, A., Koppenhoefer, K., Roy, A., Chowdhury, S., Walters, M., Bichon, B., Cochran, K., and Dodds, R., "WARP3D: Dynamic Nonlinear Fracture Analysis of Solids Using a Parallel Computers and Workstations," *Structural Research Series* (*SRS*) *607*, UILU-ENG-95-2012, University of Illinois at Urbana-Champaign, Ur-

bana, IL, 2004.

[20] American Petroleum Institute, *API Specification for 5L Line Pipe*, 42nd ed., American Petroleum Institute, Washington, DC, 2000.

[21] BS 7448, 1991, "Fracture Mechanics Toughness Tests," British Standards Institution, London.

[22] Donato, G. H. B. and Ruggieri, C., "Effects of Weld Strength Mismatch on Estimation Procedures for J and CTOD Fracture Parameters Using SE(B) Specimens," *ASME Pressure Vessels and Piping Division Conference* (*PVP*), San Antonio, Texas, 2007, ASME, New York.

[23] Gao, X., Dodds, R. H., Tregoning, R. L., Joyce, J. A., and Link, R. E., "A Weibull Stress Model to Predict Cleavage Fracture in Plates Containing Surface Cracks," *Fatigue Fract. Eng. Mater. Struct.*, Vol. 22, 1999, pp. 481–493.

[24] Ruggieri, C., 2002, "WSTRESS Release 3.0: Numerical Computation of Probabilistic Fracture Parameters for 3D Cracked Solids," *Technical Report No.* BT-PNV-51, EPUSP, University of São Paulo, São Paulo, SP.

[25] Smith, E., "Cleavage Fracture in Mild Steel," *Int. J. Fract. Mech.*, Vol. 4, 1968, pp. 131–145.

[26] Tetelman, A. S., Wilshaw, T. R., and Rau, C. A., "The Critical Tensile Stress Criterion for Cleavage," *Int. J. Fract. Mech.*, Vol. 4, 1968, pp. 147–157.

[27] Ritchie, R. O., Knott, J. F., and Rice, J. R., "On the Relationship Between Critical Tensile Stress and Fracture Toughness in Mild Steel," *J. Mech. Phys. Solids*, Vol. 21, 1973, pp. 395–410.

FATIGUE BEHAVIOR AND LIFE ESTIMATION

Reprinted from JAI, Vol. 7, No. 7
doi:10.1520/JAI102552
Available online at www.astm.org/JAI

Julien Schwartz,[1] *Olivier Fandeur,*[2,3] *and Colette Rey*[1]

Fatigue Initiation Modeling of 316LN Steel Based on Nonlocal Plasticity Theory

ABSTRACT: Nucleation of intragranular cracks during low cycle fatigue is governed by various micro-structural phenomena. Complex dislocation arrangements and rearrangements have been identified in several experimental studies carried out on cyclically loaded steel specimens. Different dislocation structures, such as vein, ladder, and/or cell structures, have been observed. They are related to an inhomogeneous localization of plastic strain, which is mostly accommodated by the ladder structures of dislocations, also named persistent slip bands. These regions of intensive slip generate on the material surface intrusions and extrusions, called persistent slip markings. The emergence of this rough relief leads to the initiation of fatigue cracks and can be considered as the first sign of fatigue damage. For a better comprehension of crack nucleation in 316LN stainless steel, low cycle fatigue tests and numerical simulations were performed. Specimens of 316LN steel with polished shallow notches were cycled with constant loading amplitude. In situ observations with a long distance microscope and scanning electron microscopy and electron back scattered diffraction analyses were used to observe fatigue crack initiation. Persistent slip markings have been identified. In parallel, a three-dimensional finite element model of crystalline plasticity, named Cristal-ECP, has been developed in both ABAQUS™ and CAST3M™ finite element codes. The numerical studies performed on various polycrystalline aggregates of 316LN steel have shown a heterogeneous localization of strain in bands. For a more precise computation and to introduce a grain size effect, geometrically necessary dislocations directly related and computed with the lattice curvature have been introduced in

Manuscript received May 20, 2009; accepted for publication June 8, 2010; published online July 2010.
[1] LMSSMAT, UMR CNRS 8579, Ecole Centrale Paris, F-92295 Châtenay-Malabry, France.
[2] CEA, DEN, DM2S, SEMT, LM2S, F-91191 Gif-sur-Yvette, France.
[3] LaMSID, UMR CNRS-EDF-CEA, F-92141 Clamart, France.

Cite as: Schwartz, J., Fandeur,, O. and Rey, C., "Fatigue Initiation Modeling of 316LN Steel Based on Nonlocal Plasticity Theory," *J. ASTM Intl.*, Vol. 7, No. 7. doi:10.1520/JAI102552.

Cristal-ECP. The first simulations have shown a real influence of the geometrically necessary dislocations on the hardening slope and more heterogeneous mechanical fields.

KEYWORDS: low cycle fatigue, crack initiation, persistent slip bands, persistent slip markings, 316LN stainless steel, crystalline plasticity, geometrically necessary dislocations, lattice curvature

Introduction

Nucleation of fatigue cracks in crystalline materials has been a subject of research for more than a century. One of the first studies that related surface relief evolution during cycling to the first signs of fatigue damage was carried out by Ewing and Humfrey [1]. Their observations of polycrystalline Swedish iron loaded in reverse bending with an optical microscope have revealed a heterogeneous localization of surface damage in bands of intensive slip, later called persistent slip bands (PSBs). Emergence of PSBs at the surface induces intrusions and extrusions, also called persistent slip markings (PSMs). Ewing and Humfrey identified initiated fatigue cracks within this rough relief. The development of transmission electron microscopy observations enabled a good description and understanding of dislocation structures formed during cycling and models of surface relief formation based on these observations were proposed [2–4]. Recent combination of modern techniques, such as electron back scattered diffraction (EBSD) and atomic force microscopy (AFM), yielded precise crystallographic and topographic information about surface relief evolution [5,6]. The localization of plastic cyclic strain in PSBs has been clearly identified, and the emergence of PSMs on an initial flat surface is now considered as the sign of fatigue damage [7–11].

Although the principal mechanisms leading to fatigue crack nucleation have been identified, the effects of microstructure (grain size and grain orientation) are not clear. For a better understanding of strain localization and shear bands formation on the surface of a cycled specimen, simulations have been performed with a model of crystalline plasticity named Cristal-ECP [12,13]. Based on large plastic deformation [14], this model has been implemented in the finite element codes ABAQUS™ and CAST3M™. The activation condition of the flow rule is given by the criterion of Schmid. The viscoplastic law, used in the model, is related to the theory of thermally activated dislocation glide. The hardening is introduced by describing the evolution of dislocation densities and dislocation interactions between the different slip systems. Low cycle fatigue simulations were performed on different three-dimensional (3D) polycrystalline aggregates. These aggregates were made via EBSD mappings and represent the real material texture and grain morphology. In parallel, low cycle fatigue tests were carried out on cylindrical specimens of 316LN stainless steel with polished shallow notches. Observations were realized before, during, and after cycling by means of a long distance microscope and scanning electron microscopy (SEM) and EBSD analyses. Simulation results and experimental data have been compared.

To improve the prediction of this first signs of fatigue damage, geometri-

TABLE 1—*Chemical composition of 316LN austenitic stainless steel (element in wt %).*

Element	C	Mn	Si	P	S	Cr	Ni	Mo	Fe
In wt %	0.024	1.86	0.36	0.026	0.0045	17.2	11.6	2.55	Rest

cally necessary dislocations (GNDs) have been introduced in the model. The density of GNDs is directly characterized and related to the lattice curvature [15–18]. The introduction of GNDs enables a more precise description of the computed mechanical fields and induces a grain size effect that influences the macroscopic hardening slope. Simulations were performed on small test aggregates of 316LN stainless steel.

Low Cycle Fatigue Tests

Experimental Procedure

The austenitic 316LN stainless steel (Creusot Loire Industrie, France) was supplied in form of a 30 mm thick rolled plate. The chemical composition can be seen in Table 1. The heat treatment consists of austenitization between 1050 and 1150 °C and water quenching. EBSD analyses have shown an average grain size of 80 μm (found using the area averaging method of the TSL-OIM™ software), an isotropic texture and about 4 % of residual ferrite δ.

In this work, the results obtained with three cycled specimens are detailed. These specimens are cylindrical specimens with a gauge diameter and a length of 8 and 16 mm, respectively. Specimen 1 was cycled till specimen failure. For specimen 2 and specimen 3, two shallow notches located at both sides of the each specimen gauge were produced by wire electrical discharge machining. These shallow notches consist of a flat area and two fillets that avoid stress concentration during cycling. The flat area has a size of 2 mm in length (gauge length direction) and 3 mm in width. The fillets were machined in the gauge length direction and have a radius of 20 mm. Each notch surface was mechanically and electrochemically polished in order to achieve a smooth surface and facilitate the observation of the surface relief. Specimen 2 was cycled 200 times. For specimen 3, straining was interrupted after 2000 cycles. All specimens were cycled in a symmetrically push-pull cycle in strain control. The strain amplitude $\Delta\varepsilon/2 = 5 \times 10^{-3}$, equal to half of the hysteresis loop width, and the strain rate $\dot{\varepsilon} = 5 \times 10^{-3}\ \mathrm{s}^{-1}$ were kept constant for the whole period of the fatigue test. During cycling, the shallow notches were observed by means of a long distance microscope QUESTAR QM200™. Before and after cycling, the crystallographic orientations of the grains of the notch surface were analyzed by EBSD measurements. After cycling, the notches were investigated by using the high resolution SEM-FEG (field emission gun) Leo™ 1530.

Results

Analysis of Measured Data—The evolution of stress amplitude ($\Delta\sigma/2$) during cycling for the three tested specimens can be seen on Fig. 1(*a*). This curve

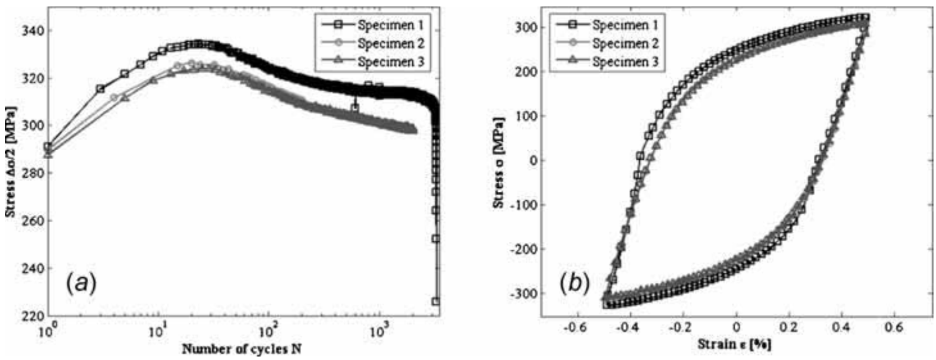

FIG. 1—*Cyclic behavior of 316LN steel:* (*a*) *Evolution of stress amplitude* $\Delta\sigma/2$ *during cycling;* (*b*) *stress/strain curve.*

shows that the stress amplitude of specimen 1 is about 10 MPa higher than the stress amplitude of the other specimens. This can be attributed to the fact that no shallow notches were machined on specimen 1. The study of the evolution of the stress amplitude during cycling has yielded important information about the cyclic behavior of this 316LN steel. Three different phases can be identified. During the first phase (cycle $1 \rightarrow$ cycle 20), the material cyclically hardens. The stress amplitude increases by about 30 MPa. Between 20 and 200 cycles (phase 2), a cyclic softening can be observed for all specimens. The decrease in stress amplitude is about 20 MPa. The second phase is followed by a plateau (phase 3) during which the stress amplitude remains quasi constant.

Hysteresis loops of the three tested specimens for cycle 200 (beginning of the plateau) can be seen on Fig. 1(*b*). The study of the stress/strain curve has led to the identification of a Young modulus of 195 GPa. The analysis of different cycles has shown that the material exhibits Bauschinger effect.

In Situ Observations—Micrographs were collected with the long distance microscope during the whole length of fatigue tests carried out on specimen 2 and 3. The in situ observations enable a good qualitative analysis of the surface relief evolution but the micrographs quality is not sufficient to perform precise measurements. The results of the observations during cycling can be observed on Fig. 2 for specimen 3. The observed areas have a size of $400 \times 550\ \mu m^2$. The straining axis is axis 1.

The micrographs, collected during the cycling of specimen 2, show that PSMs have been formed during the first cycle. They are thin, equidistantly spaced but not present in each grain of the observed surface. Their number and size increase during the whole 200 cycles of the test. In grains presenting PSMs, the orientation of the slip bands is unique. This suggests that only one slip plane is activated per grain during cycling. Observations of PSMs and calculation of Schmid's factors with the crystalline orientations measured by EBSD have shown that only the slip system having the highest Schmid's factor is generally activated during cycling [6].

The micrographs, collected during the cycling of specimen 3, show the

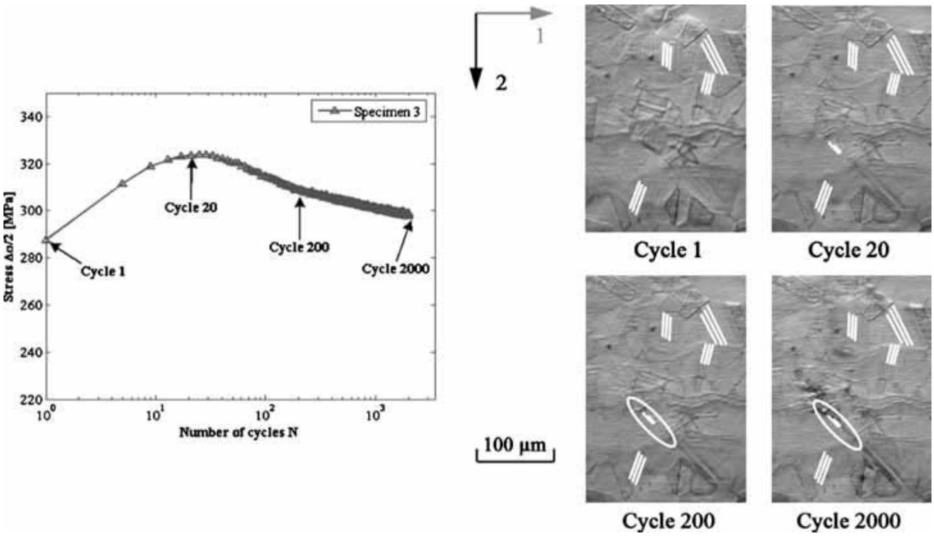

FIG. 2—*Long distance microscope observations: Micrograph of the shallow notch of specimen 3 after 1, 20, 200, and 2000 cycles. Some PSMs are shown in white. An initiated fatigue crack can be seen in the white circle on the micrograph of cycles 200 and 2000.*

same tendencies. PSMs have been formed during the first cycle, their number and size increase during the whole 2000 cycles, and their orientation also suggests that only one slip plane per grain is activated. The analysis of the micrographs has shown for this specimen the development of a marked dark zone in the middle of the observed area. At cycle 200, only PSMs can be identified in this zone. After 2000 cycles, a thin dark zone has developed. This dark zone suggests the appearance of a fatigue crack.

Scanning Electron Microscopy Observations—After cycling, SEM investigations were carried out. The zones observed with the long distance microscope were observed as well as other parts of the polished shallow notches. The straining axis is axis 1.

The SEM observations made on specimen 2 have shown the presence of PSMs. Their presence has not been identified in every grain. Their width varies between 50 and 500 nm. But most of them are 100–200 nm wide. Some of these bands cross the whole grain when others are just present in the middle of the grain or at grain or twin boundaries. The observed PSMs are equidistantly spaced, and when a whole grain is marked by these bands, new PSMs seem to emerge just between the other ones (Fig. 3(*a*)). In most of the grains presenting PSMs, the bands have only one orientation. Only a few grains are marked by bands with two different orientations (Fig. 3(*b*)). So, only one or two slip systems seem to be activated per grain during cycling. Some initiated cracks have

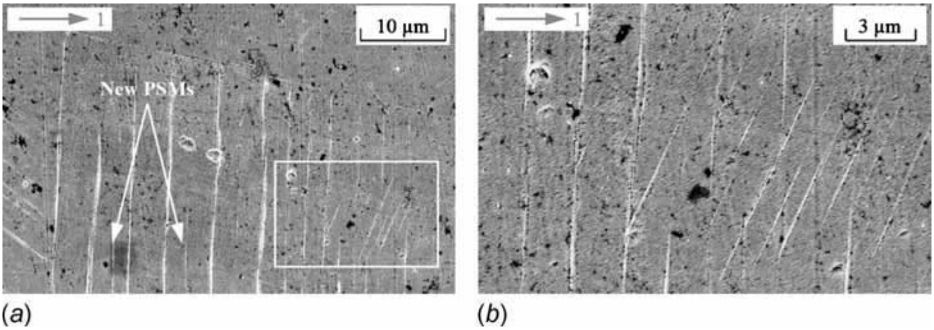

FIG. 3—*SEM observations of the shallow notch of specimen 2:* (*a*) *Equidistantly spaced well developed PSMs with new PSMs emerging between them;* (*b*) *two activated slip planes in the same grain* (*the observed area is marked in* (*a*)) *by a white box*).

been identified within only few PSMs located within a grain or near twin boundaries.

The presence of PSMs can also be observed on the SEM micrographs realized on specimen 3. After 2000 cycles, most of the grains are marked by these regions of intensive slip. Compared to specimen 2 (cycled 200 times), the number of PSMs observed on the surface of specimen 3 is more important, and their width is greater. Their width varies between 100 and 800 nm, and most of them are 200–500 nm wide. When PSMs are present in a grain, most of the time they cross the whole grain. The bands of similar width are equidistantly spaced, and smaller bands have emerged between them. The orientation of the PSMs confirms the fact that only one or two slip systems have been activated in a grain during straining. The SEM micrographs realized in the zone observed by

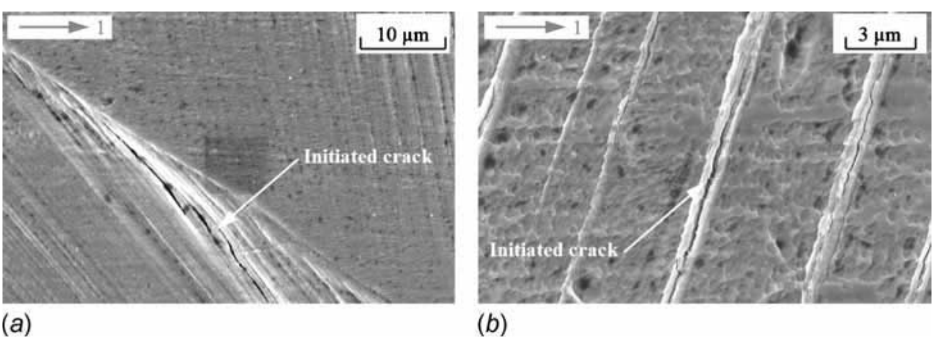

FIG. 4—*SEM observations of initiated fatigue cracks on the shallow notch of specimen 3:* (*a*) *Nucleated crack within PSMs located near a twin boundary in the area monitored with the long distance microscope;* (*b*) *nucleated crack within large and well developed PSMs in the middle of a grain.*

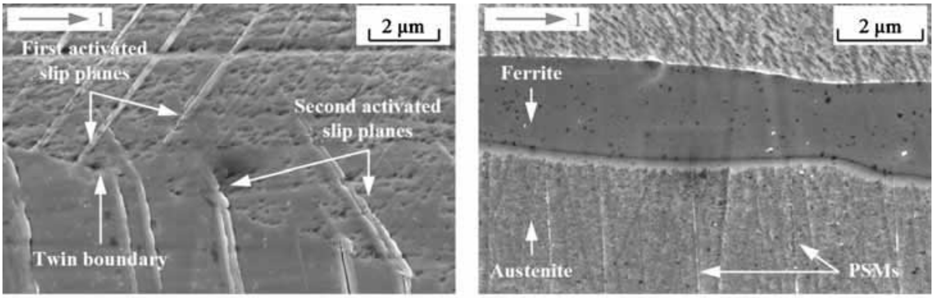

(*a*) (*b*)

FIG. 5—*SEM observations of PSMs on the shallow notch of specimen 3.* (*a*) *shows the influence of the grain on the activation of slip planes.* (*b*) *shows that ferrite grains do not develop PSMs during cycling.*

the QUESTAR™ microscope confirm that a crack initiated. Thin PSMs have developed just near a twin boundary, and a crack has nucleated within these bands (Fig. 4(*a*)). Other fatigue cracks have initiated in the grain within large PSMs (Fig. 4(*b*)). A precise analysis of some twins has pointed out that the activated slip system on one side of the twin boundary can influence the activation of a slip system at the other side of the twin boundary. Figure 5(*a*) illustrates this observation. The PSMs of the grain situated at the bottom of the micrograph have influenced the activation of a new slip system in the grain at the top of the micrograph. Observations were also made on grains of ferrite δ. No PSM has been identified in these grains (Fig. 5(*b*)).

Electron Back Scattered Diffraction Analyses—EBSD analyses were carried out before and after cycling on the zones observed with the QUESTAR™ microscope. Each EBSD map has a size of $1000 \times 1000\ \mu m^2$ and contains more than 500 grains. They were all realized with a step of 1 μm. The straining axis is axis 1. PSMs can be observed via the image quality map. They appear as thin dark bands (Fig. 6(*a*)). The comparisons between the inverse pole figure maps realized before and after straining have shown the same results for both specimens (Fig. 6(*b*)). No rotations of more than 1° can be observed. So the deformation seems to occur during cycling with no apparent lattice rotation.

These observations were completed with a high resolution EBSD analysis carried out on a selected zone from a shallow notch of specimen 3. The EBSD map has a size of $70 \times 70\ \mu m^2$ and contains 13 grains. The analysis step is equal to 0.1 μm. The straining axis is axis 1. The image quality map has shown that the analyzed region contains PSMs and one fatigue crack initiated within thin PSMs situated near a twin boundary (Fig. 7(*a*)). The inverse pole figure map shows lattice rotations of more than 1°. This result was unexpected because the other analyzed zones have not shown any lattice rotation. So lattice rotations seem to appear quite rarely during cycling. An analysis of grain and twin boundaries was also realized. It has shown that some dark bands are in fact very thin twins σ_3 of about 300 nm in width (Fig. 7(*a*) and 7(*b*)).

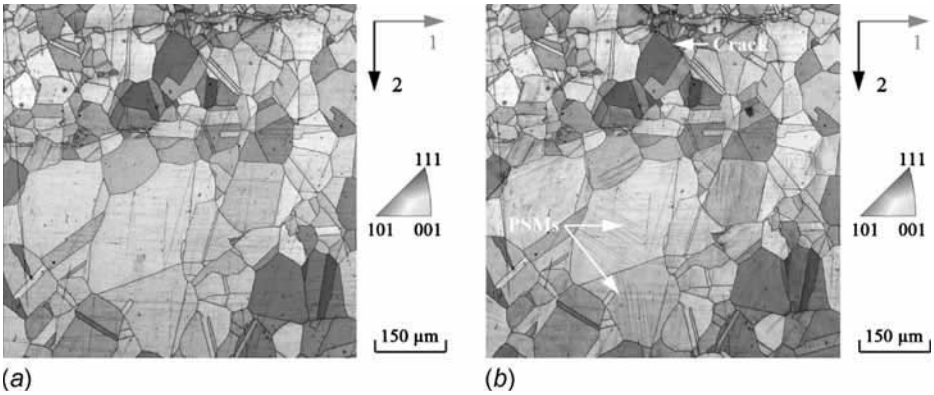

FIG. 6—*EBSD measurements performed on the area of specimen 3 observed the QUESTAR™ microscope:* (*a*) *Image Quality map superposed with the Inverse Pole Figure before the low cycle fatigue test;* (*b*) *Image Quality map superposed with the Inverse Pole Figure after 2000 cycles. The crack observed with the long distance microscope as well as PSMs are shown in* (*b*).

Modeling: Classic Approach (Without Geometrically Necessary Dislocations)

Model Description

The model of crystalline plasticity Cristal-ECP is based on the large deformation theory proposed by Pierce et al. [14] and uses the modified hardening rules proposed by Teodosiu et al. [12]. Implemented in the finite element codes

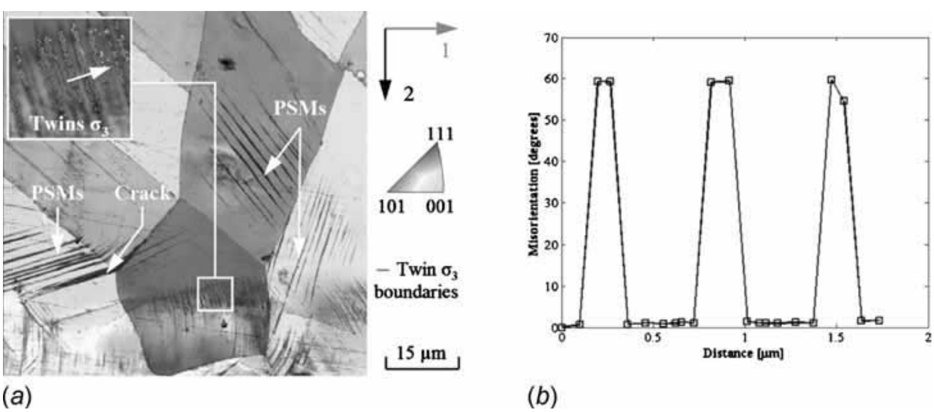

FIG. 7—*High resolution EBSD measurements performed on the shallow notch of specimen 3:* (*a*) *Image Quality map superposed with the Inverse Pole Figure;* (*b*) *misorientation profile along a vector crossing three twins* (*the vector can be seen in the white box in* (*a*)).

ABAQUS™ and CAST3M™, this model has shown great abilities to capture the characteristics of single and polycrystals deformation during monotonic and cyclic loadings with a good agreement between computation and experiments [13]. The numerical scheme used is an explicit forward gradient procedure, which provides a sufficient accuracy and a high integration speed. The model has been implemented for body-centered cubic, face-centered cubic (fcc), and simple cubic lattice structures.

For fcc crystals, which are the crystals of interest, slip occurs respectively on the 12 systems {111} ⟨110⟩. The glide velocity $\dot{\gamma}^s$ for each slip system (s) is expressed with a classic viscoplastic rule based on of the resolved shear stress τ^s and the critical resolved shear stress $\tau_c^{\ s}$

$$\begin{cases} \dot{\gamma}^s = \dot{\gamma}_0^s \left| \dfrac{\tau^s}{\tau_c^s} \right|^n & \text{if } |\tau^s| \geq \tau_c^s \\ \dot{\gamma}^s = 0 & \text{otherwise} \end{cases} \tag{1}$$

where:

$\dot{\gamma}_0^s$ = reference shear rate and

n = rate sensitivity exponent.

The activation condition of this viscoplastic law is given by the criterion of Schmid. As long as slip occurs, hardening is caused by the interaction between different active or latent slip systems. This is modeled by the following phenomenological relationship between the critical shear stress increment on a slip system and all the slip increments weighted by the hardening matrix h^{su}:

$$\dot{\tau}_c^s = \sum_u h^{su} |\dot{\gamma}^u| \tag{2}$$

The h^{su} terms are derived from relationship accounting for physical aspects of plasticity and based on internal variables such as dislocation densities on each slip systems. On a particular slip system, the dislocation density ρ^s is governed by a production term derived from Orowan's relationship and balanced by an annihilation term, which takes into account the dynamic recovery during deformation

$$\begin{cases} \dot{\rho}^s = \dfrac{|\dot{\gamma}^s|}{b} \left(\dfrac{1}{L^s} - g_c \rho^s \right) \\ \rho^s(t = 0) = \rho_0 \end{cases} \tag{3}$$

where:

b = Burgers vector magnitude,

g_c = proportional to the annihilation distance of dislocation dipole, and

L^s = average free path of the mobile dislocation on the system (s).

At the onset of plastic deformation, L^s is close to the grain average size D and then evolves because of interactions between gliding dislocations on system (s) and a density of created point obstacles cutting this system

$$\frac{1}{L^s} = \frac{\sum\limits_{u \neq s} \rho^u}{K} + \frac{1}{D} \tag{4}$$

where:

K = material parameter.

The critical resolved shear stress can be related to the dislocation densities by the following hardening rule:

$$\tau_c^s = \tau_0 + \mu b \sqrt{\sum_t a^{st} \rho^t} \tag{5}$$

where:

τ_0 = lattice friction stress,

μ = isotropic shear modulus, and

a^{st} = hardening matrix whose terms depend on the type of elastic interactions between dislocation families (s) and (t) [19].

Differentiating equation Eq 5 with respect to time and considering equations Eqs 3 and 4, the complete expression of h^{su} can be written as

$$h^{su} = \frac{\mu}{2} \frac{a^{su}}{\sqrt{\sum\limits_q a^{sq} \rho^q}} \left(\frac{1}{K} \sqrt{\sum_{q \neq u} \rho^q} + \frac{1}{D} - g_c \rho^u \right) \tag{6}$$

Simulation Procedure

Simulations were performed on 3D polycrystalline aggregates of 316LN steel. The creation process is based on EBSD measurements. The inverse pole figure map is meshed with linear, eight noded, cubic finite elements with reduced integration. An aggregate can be composed of only one layer of elements, of a piling of same meshed EBSD map, or of a piling of different meshed EBSD maps obtained by a successive polishing of the material. The Euler angles of each grain are then attributed to the corresponding meshed grains. The material parameters are finally defined for the whole aggregate.

The simulation results described in the following section have been obtained with computations performed on a 3D aggregate realized with an EBSD map of $1000 \times 1000\ \mu m^2$ containing 680 grains (Fig. 8(*a*)). This EBSD map corresponds to the EBSD map realized before cycling on the shallow notch of specimen 3. The element size is equal to $4 \times 4 \times 4\ \mu m^3$, and the aggregate is composed of a piling of four same meshed EBSD maps. The material parameters used are given in Table 2 and were identified by Medina Almazán [20]. The boundary conditions were chosen to approximate the boundary conditions of an aggregate contained on the surface of the shallow notch of a specimen (Fig. 8(*b*)). The aggregate was cycled in a symmetrically push-pull cycle ten times along direction 1 (Fig. 8(*b*)). The straining conditions are the same as during the low cycle fatigue. The applied strain amplitude $\Delta\varepsilon/2$ is equal 5×10^{-3} and the strain rate $\dot{\varepsilon}$ to $5 \times 10^{-3}\ s^{-1}$.

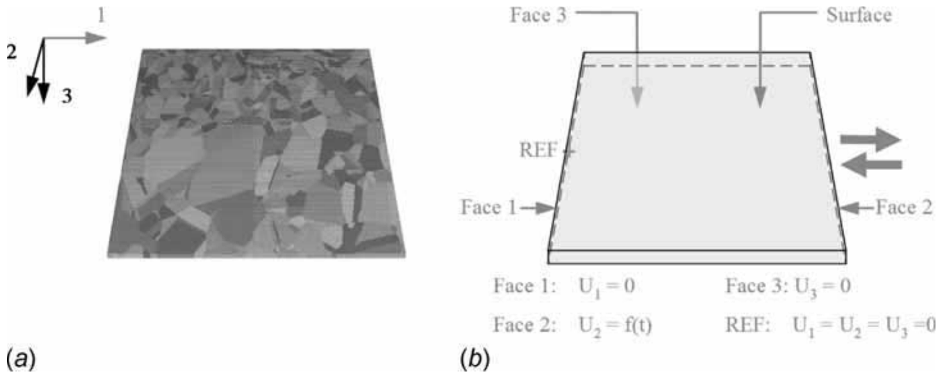

FIG. 8—(*a*) *Aggregate of 316LN steel made with EBSD measurement performed on the area of specimen 3 observed with the QUESTAR™ microscope.* (*b*) *Boundary conditions applied to the aggregate during the simulation.*

Results

Macroscopic Behavior—Figure 9(*a*) represents the evolution of the stress amplitude $\Delta\sigma_{11}/2$ during the ten simulated cycles compared to the experimental data $\Delta\sigma/2$ measured during the ten first cycles of the test performed on specimen 3. The stress/strain curve of the aggregate is compared to the stress/strain curve of specimen 3 on Fig. 9(*b*). During cycling, the aggregate presents a cyclic hardening superior to the cyclic hardening of the specimen. The average stress value σ_{11} at the end of the first cycle for the aggregate is equal to 339.0 MPa and is about 37.6 MPa greater than the stress measured at the end of the first cycle for specimen 3. After ten cycles, σ_{11} for the aggregate is equal to 378.3 MPa where the measured stress is equal to 316.1 MPa. The shape of the hysteresis loop obtained per simulation is globally similar to the experimental one even if the stress is overestimated and the entry in the plastic domain occurs earlier for the specimen than for the aggregate. The aggregate stress/strain curve seems to stabilize progressively. A more precise investigation of this stabilization process requires the simulation of more cycles, but for computation time reasons, it has not been realized. Concerning the cyclic softening, the implemented laws might not be able to describe the cyclic softening observed during the tests.

In a first approximation, the material parameters used fit quite well, but they have to be optimized for a better fit. The simulation of more cycles is

TABLE 2—*Material parameters of 316LN austenitic stainless steel* [*20*].

C_{11} [GPa]	C_{12} [GPa]	C_{44} [GPa]	a_0	a_1	a_2	a_3	$\dot{\gamma}_0$ [s^{-1}]	n	g_c [nm]	K	τ_0 [MPa]	ρ_0 [m^{-2}]	D [μm]	b [nm]
197	122	125	0.02	0.08	0.18	0.30	10^{-11}	80	8.25	7	45	10^{12}	22	0.25

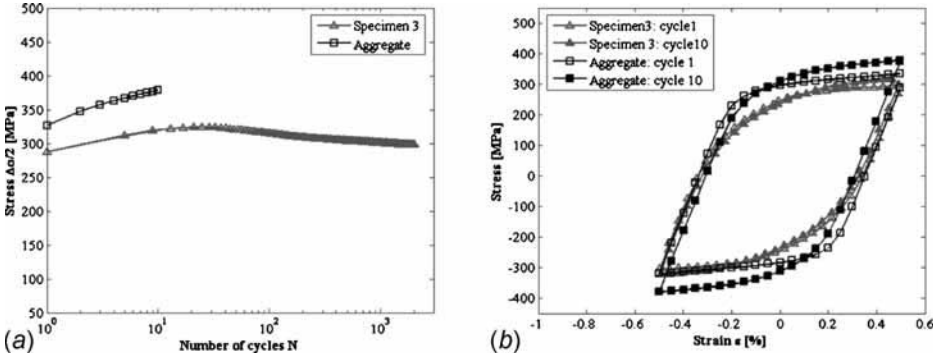

FIG. 9—*Comparison between the cyclic behaviors of specimen 3 and aggregate used for the simulation:* (*a*) *Evolution of the stress amplitude* $\Delta\sigma/2$ *during cycling;* (*b*) *stress/strain curves.*

required for a better understanding of the stabilization process of the hysteresis loop and a modification of the implemented laws may be needed to predict the cyclic softening.

Results after Ten Cycles—After ten cycles, the results of the finite element simulation have shown a strong heterogeneity of the computed mechanical fields. The strain ε_{11}, the stress σ_{11}, the number of active slip systems, and the lattice orientation changes as well as the relief of the aggregate were analyzed.

The strain values ε_{11} of the aggregate surface layer spread between -0.04 % and 1.59 % (Fig. 10(*a*)). A localization of strain field ε_{11} in bands can easily be observed. These bands are not only present in particular grains, but they are quite well distributed on the whole surface of the aggregate. No special effects

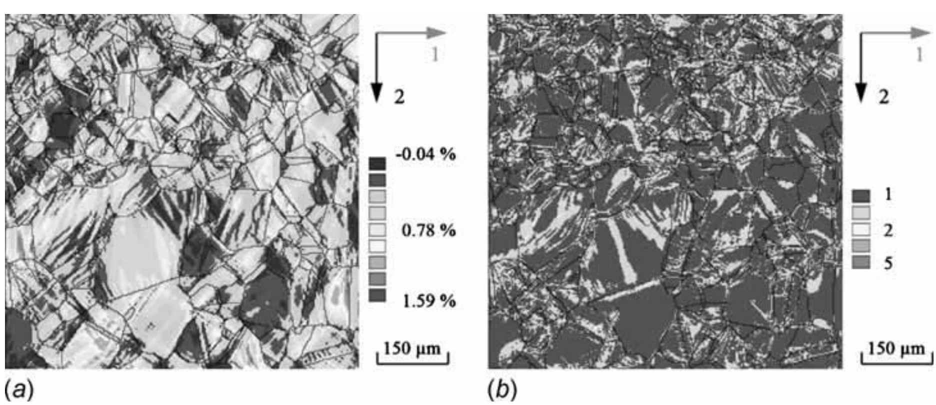

FIG. 10—(*a*) *Strain* ε_{11} *map of the surface element layer of the aggregate after ten cycles.* (*b*) *Activated slip systems map of the surface element layer of the aggregate after ten cycles.*

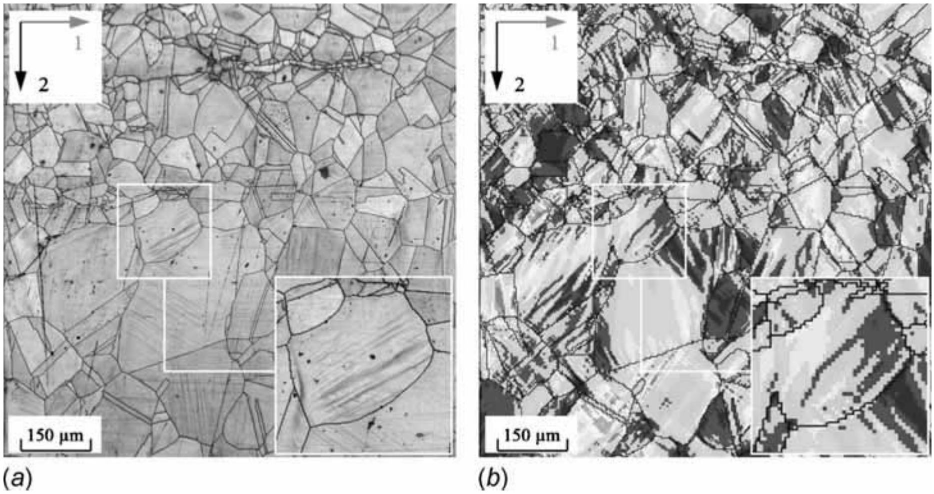

FIG. 11—*Comparison between the observed PSMs and the simulated strain bands:* (*a*) *Image Quality map after 2000 cycles of the area of specimen 3 observed with the long distance microscope;* (*b*) *strain* ε_{11} *map of the surface element layer of the aggregate after ten cycles.*

of grain, sub-grain, and twin boundaries have been identified. The presence of these bands is in concordance with the experimental observations. Although some grains contain bands with two different orientations, most of the aggregate grains present only bands with one unique orientation. The fact that only one and in the worst case two slip systems are activated per grain is confirmed by the map of number of active slip systems (Fig. 10(*b*)). This map shows that in 98.2 % of the aggregate surface layer, only one or two slip systems are active These bands were compared with the EBSD measurement carried out on specimen 3 after 2000 cycles (Fig. 11). The number of the simulated bands is less important than those observed experimentally after 2000 cycles. Their width is greater than the width of those present on the shallow notch of specimen 3. This can be attributed to element size chosen for the simulation. Simulations with elements of smaller size have to be performed to evaluate which element size is more appropriate. The orientation of the strain bands ε_{11} were also compared to the orientation of the PSMs observed on specimen 3. For some grains, the simulated bands are orientated as those of the specimen (Fig. 11). But for others, the orientation of the shear bands obtained per simulation does correspond to the experimental observations. It shows that the correct slip systems are not always activated during the simulation. This difference is particularly remarkable in grains well oriented for multiple slip. It can be attributed to the boundary conditions applied on the aggregate. Other boundary conditions should be evaluated.

After ten cycles, the stress values σ_{11} on the aggregate surface spread between -113.7 and 1166.3 MPa with an average value of 373.3 MPa (Fig. 12). For the third aggregate layer, σ_{11} varies between -153.8 and 1215.5 MPa with

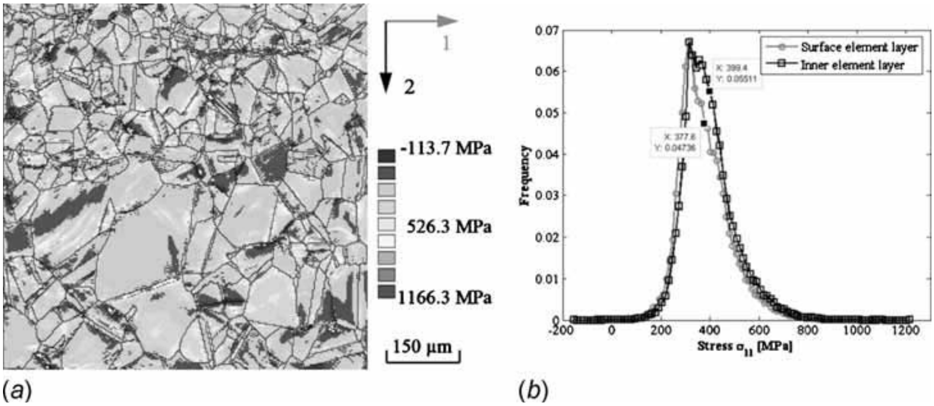

FIG. 12—(*a*) *Stress* σ_{11} *map of the surface element layer of the aggregate after ten cycles.* (*b*) *Distribution of* σ_{11} *in the surface element layer and in the third element layer after ten cycles* (*the mean values are reported in the figure*).

an average value of 396.5 MPa. So the surface layer is less stressed than inner layers. These results are coherent because the boundary conditions are stronger in the middle of the aggregate than at the surface.

The relief of the aggregate surface layer shows the presence of kind of intrusions and extrusions (Fig. 13). Compared to the initial flat surface, the highest extrusion is equal to 165 nm, and the deepest intrusion is equal to −27 nm. These intrusions and extrusions obtained after simulation appear at the same location as the simulated strain bands, and their shape corresponds to them. Man et al. [5,6] observed through AFM measurements PSMs with a height and a width of respectively 19 and 600 nm on the surface of 316L austenitic stainless steel after 50 cycles performed with a plastic strain amplitude of 2×10^{-3}. The height of the simulated extrusions is overestimated compared

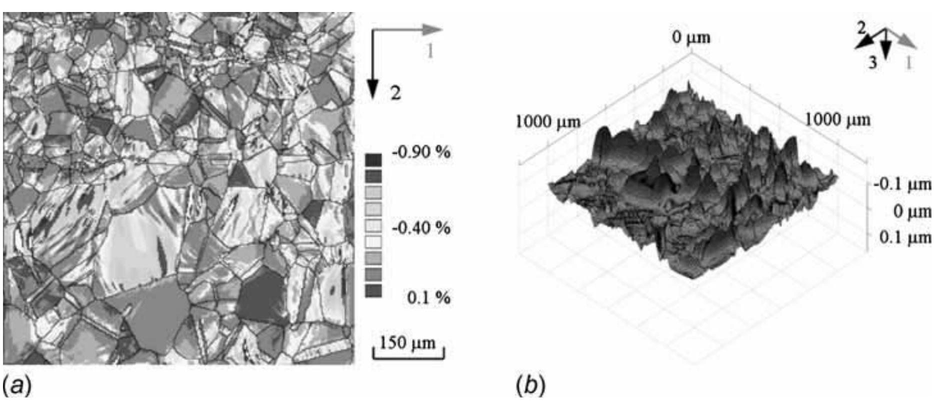

FIG. 13—(*a*) *Strain* ε_{33} *map of the surface element layer of the aggregate after ten cycles.* (*b*) *Relief of the surface element layer of the aggregate after ten cycles.*

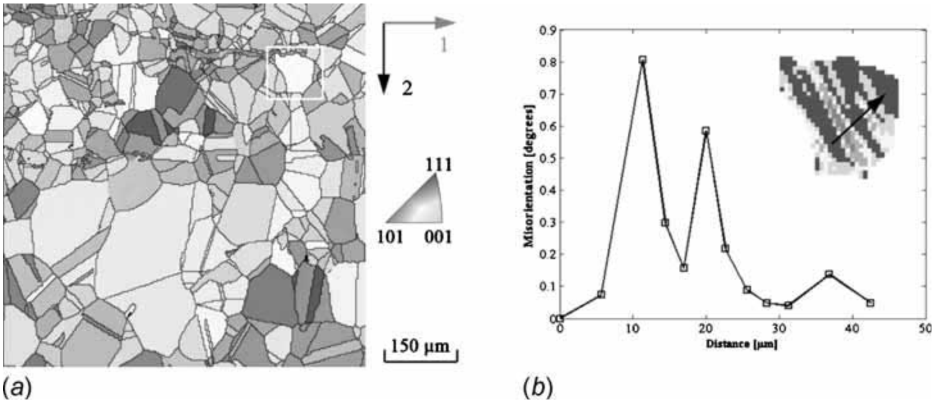

FIG. 14—(*a*) *Inverse Pole Figure of the surface element layer of the aggregate after ten cycles.* (*b*) *Misorientation profile along a vector* (*the grain in which the vector was traced is marked by the white box in* (*a*)).

to these experimental data, but the straining amplitude applied by Man et al. is less than the straining amplitude applied here. With a straining amplitude of 5×10^{-3}, the plastic strain amplitude varies between 3.4 and 3.6×10^{-3} during the low cycle fatigue tests and simulations presented in this paper. As the simulated strain bands, the width of the simulated extrusions and intrusions is overestimated.

The analysis of the inverse pole figure maps of the aggregate surface layer has shown that only very small rotations occur during the ten simulated cycles. An observation of these maps before and after simulation did not enable the identification of any lattice rotations. But a misorientation profile along one vector crossing strain bands revealed small lattice orientation changes, all less than 1° (Fig. 14).

Evolution during Cycling—The evolution of the aggregate during the ten simulated cycles was investigated. The evolution of the strain field ε_{11} and relief during the last cycle is described in the following section and can be observed in Fig. 15.

At the beginning of the tenth cycle, the strain field shows strong heterogeneities localized in bands. The average strain value is equal to 0.50 % (point 1 in Fig. 15). Corresponding intrusions and extrusions are present on the aggregate surface layer. The diminution of the applied strain leads to a decrease not only in the strain field values but also in the strain field heterogeneity (point 2 in Fig. 15). The bands have progressively disappeared as well as the relief. When the controlled strain reaches the value of −0.50 % (point 3 in Fig. 15), new strain bands are formed with the same orientations. But their location differs from the location of the shear bands observed for the applied strain of 0.50 % (point 1 in Fig. 15). The strain field shows strong heterogeneities comparable to those observed at the beginning of the cycle. New intrusions and extrusions have been formed. Their orientation and their width correspond with the new strain

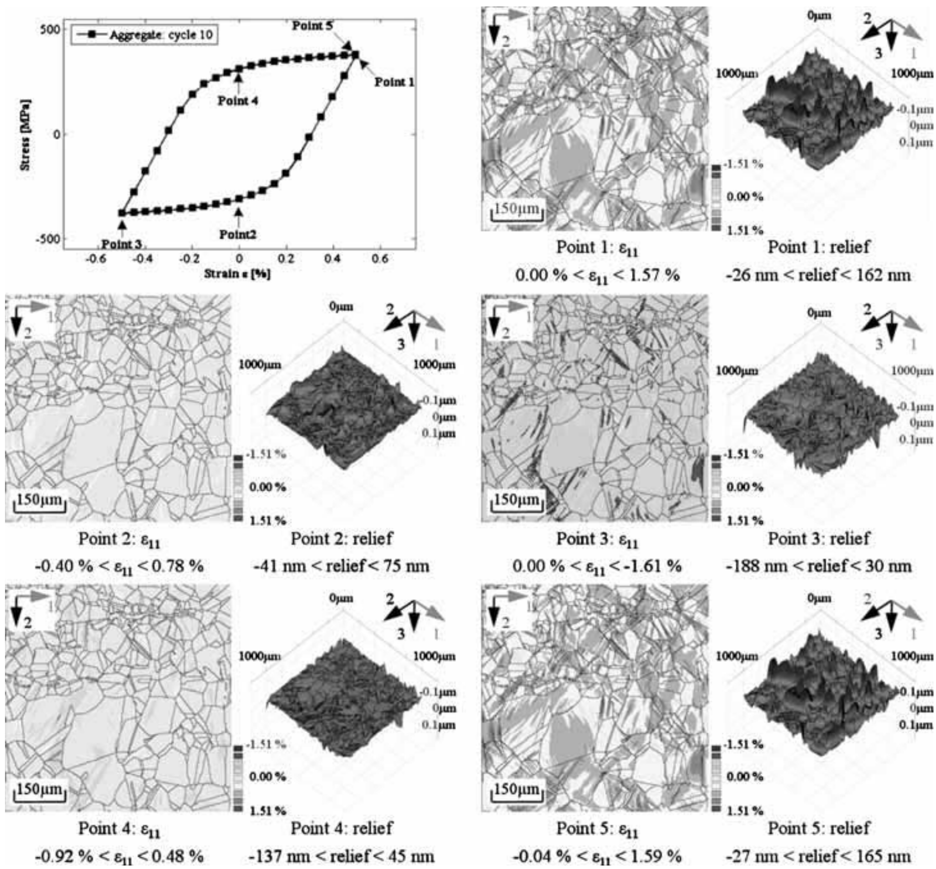

FIG. 15—*Evolution of the strains* ε_{11} *and the relief of the surface element layer of the aggregate during the tenth cycle. The results are only shown for points 1, 2, 3, 4, and 5.*

bands formed. When the imposed strain value reaches 0.00 % again (point 4 in Fig. 15), the strain bands formed during compression have disappeared, and the field heterogeneity has decreased. The rough relief observed at −0.50 % has also disappeared. The increase in controlled strain from 0.00 % to 0.50 % leads the reformation of the strain bands observed at the beginning of the cycle (point 5 in Fig. 15). Compared to the initial bands, their intensity has increased during the cycle, and the field heterogeneity has also risen. The reappearance of the strain bands has led to the reappearance of the initial relief. Compared to the intrusions and extrusions present on the aggregate surface layer at the beginning of the cycle, the height and the depth have increased.

The analysis of the tenth cycle has shown a clear cyclic behavior of the strain bands and of the corresponding relief.

Modeling: Introduction of Geometrically Necessary Dislocations

Model Description

The GNDs implemented in the model are based on the large deformation theory [15–18]. They are directly related to the expression of the Burgers vector b^e

$$b^e = \oint_{\partial S} F^{e-1} dx = \int\int \mathrm{curl}(F^{e-1})^T \vec{n} dS = \int\int \Lambda \vec{n} dS \tag{7}$$

where F^e corresponds to elastic stretching and rotation and Λ corresponds to the tensor of GNDs. By considering that only small deformations are made, Λ can easily be simplified

$$\Lambda = \mathrm{curl}(F^{e-1})^T \approx \mathrm{curl}(R^e) \tag{8}$$

where:

R^e = tensor of elastic rotation.

An explicit procedure computes this tensor at each time increment. Λ is then projected on each slip system. The results of this projection are new sources of dislocation density λ^s for each slip system (s). λ^s is then introduced in the evolution of dislocation density (Eq 3)

$$\begin{cases} \lambda^s = \sqrt{(\Lambda \vec{n}^s):(\Lambda \vec{n}^s)} \\ \dot{\rho}^s = \dfrac{|\dot{\gamma}^s|}{b}\left(k_0 \lambda^s + \dfrac{1}{L^s} - g_c \rho^s\right) \quad \text{with} \quad \rho^s(t=0) = \rho_0 \end{cases} \tag{9}$$

where:

k_0 = material parameter to be determined.

Simulation Procedure

The first simulations with this model were performed on a 3D polycrystalline test aggregate of 316LN steel. A two-dimensional microstructure with dimensions of $100 \times 100\ \mu\mathrm{m}^2$ was generated with Voronoï polyhedrons and extended in the third dimension (Fig. 16(*a*)). The aggregate contains 11 grains and is meshed with the linear, eight noded, cubic finite elements with full integration. The test aggregate is composed of one element layer. The material parameters are those of Table 2, and the boundary conditions used for the previously described simulations were applied (Fig. 16(*b*)). The value of k_0 was arbitrarily fixed to 500. For the first simulations, one tensile test with an applied strain of $\varepsilon = 2 \times 10^{-2}$ and a strain rate of $\dot{\varepsilon} = 5 \times 10^{-3}\ \mathrm{s}^{-1}$ was performed along direction 1 (Fig. 16(*b*)). Simulations with the classic model and with the model including GNDs were carried out.

Results

The analysis results obtained with the model including GNDs have shown an improvement in the description of the computed mechanical fields over the

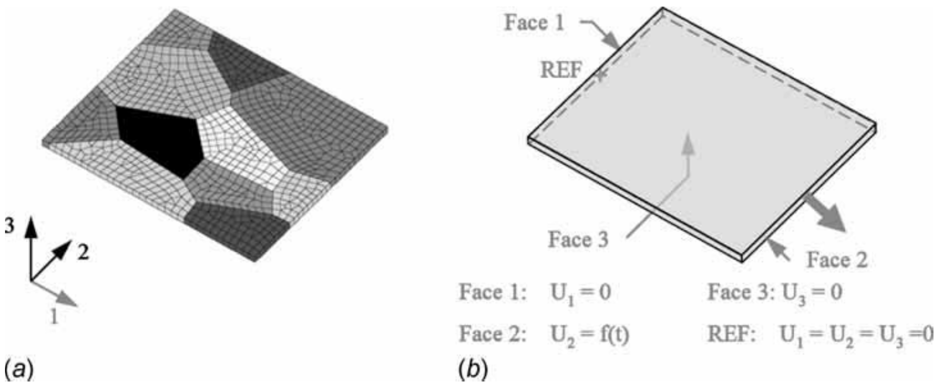

FIG. 16—(*a*) *Test aggregate of 316LN steel.* (*b*) *Boundary conditions applied to the aggregate during the simulation.*

classic model. With GNDs, an increase in heterogeneity of strain field ε_{11} can be clearly identified (Fig. 17). Grain boundaries have more effects on the spatial distribution the strain field ε_{11} (Fig. 17). More generally, these boundaries are less deformed and exhibit more stress concentrations in simulations performed with the model including GNDs.

A homothetic reduction of the aggregate dimensions from 100×100 to $15 \times 15\ \mu m^2$ was made to study if GNDs induce a real grain size effect. Simulations were done on these aggregates with both models. No grain size effect can be observed on these stress/strain curves for the simulations performed with the classic model. But with the model including GNDs, the reduction of the aggregate grain size has led to an increase in the macroscopic hardening slope.

Summary

The analyses of the polished shallow notches of 316LN stainless steel before, during, and after low cycle fatigue tests have put out the formation of PSMs. In

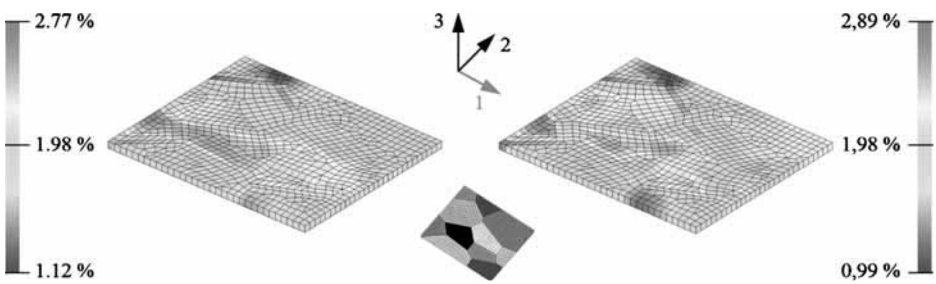

FIG. 17—*Comparison between the approach without GNDs and the model with GNDs: Strain* ε_{11} *map obtained with the classic approach* (*left*) *and strain* ε_{11} *map obtained with the model including GNDs* (*right*).

situ observations have shown that they are formed during the first cycle. Their size as well as their number has increased during the whole test. Initiated fatigue cracks within these regions of intensive slip have been identified by SEM-FEG observations. EBSD measurements have shown that quasi no lattice rotations occur during straining. Twinning has also been observed.

Simulations performed with the classic model Cristal-ECP have shown strong heterogeneities of the computed mechanical fields. Localization of strain in bands has been observed. These strain bands have a clear cyclic behavior. In addition, a rough relief comparable to intrusions and extrusions has developed. The positions of these intrusions and extrusions, their width, and their behavior during a cycle correspond to observable strain bands. Compared to the experimental data, their width is overestimated, and their orientation does not always fit. These results might be improved with a finer mesh and other boundary conditions.

GNDs have been implemented to improve the accuracy of the computed mechanical fields and to introduce a grain size effect in the model. The first simulation results are encouraging. The heterogeneity of computed mechanical fields has been improved, and the grain size affects the macroscopic hardening slope.

Acknowledgments

The writers would like to express their thanks to Dr F. Curtit and Dr. J. M. Stephan from MMC Department of EDF Research Center Les Renardières for supplying the studied material and the specimens used in this work. The assistance of G. Fréville from MMC Department of EDF Research Center Les Renardières and N. Roubier from LMSSMat (École Centrale Paris) during the low cycle fatigue tests is acknowledged. Special thanks goes to F. Garnier from LMSSMat (École Centrale Paris) for her help during the SEM-FEG observations and the EBSD measurements. The writers are also indebted to CEA Research Center of Saclay and EDF Research Center Les Renardières for financial support.

References

[1] Ewing, J. A. and Humfrey, J. C., "The Fracture of Metals Under Rapid Alterations of Stress," *Philos. Trans. R. Soc. London A*, Vol. 200, 1903, pp. 241–250.

[2] Essmann, U., Gösele, U., and Mughrabi, H., "A Model of Extrusions and Intrusions in Fatigued Metals—I. Point-Defect Production and the Growth of Extrusions," *Philos. Mag.*, Vol. A44, 1981, pp. 405–426.

[3] Polák, J., "On the Role of Point Defects in Fatigue Crack Initiation," *Mater. Sci. Eng.*, Vol. 92, 1987, pp. 71–80.

[4] Repetto, E. A. and Ortiz, M., "A Micromechanical Model of Cyclic Deformation and Fatigue Crack Nucleation in FCC Single Crystals," *Acta Mater.*, Vol. 45, 1997, pp. 2577–2595.

[5] Man, J., Obrtlik, K., and Polàk, J., "Study of Surface Relief Evolution in Fatigued 316L Austenitic Stainless Steel by AFM," *Mater. Sci. Eng.*, Vol. A351, 2003, pp.

123–132.
[6] Man, J., Obrtlik, K., Blochwitz, C., and Polàk, J., "Atomic Force Microscopy of Surface Relief in Individual Grains of Fatigued 316L Austenitic Stainless Steel," *Acta Mater.*, Vol. 50, 2002, pp. 3767–3780.
[7] Mughrabi, H., *Dislocations and Properties of Real Materials*, M. H. Loretto, ed., Book No. 323, The Institute of Metals, London, 1985, pp. 244–262.
[8] Polàk, J., *Cyclic Plasticity and Low Cycle Fatigue Life of Metals*, Academia/Elsevier, Prague, 1991.
[9] Suresh, S., *Fatigue of Materials*, 2nd ed., Cambridge University Press, Cambridge, 1998.
[10] Polák, J., Vasek, A., and Obrtlik, K., "Fatigue Damage in Two Steploading of 316L Steel I: Evolution of Persistent Slip Bands," *Fatigue Fract. Eng. Mater. Struct.*, Vol. 19, 1996, pp. 147–155.
[11] Mineur, M., Villechaise, P., and Mendez, J., "Influence of the Crystalline Texture on the Fatigue of 316L Austenitic Stainless Steel," *Mater. Sci. Eng.*, Vol. 286, 2000, pp. 257–268.
[12] Teodosiu, C., Raphanel, J. L., and Tabourot, L., "Finite Implementation of the Large Elastoplastic Deformation of Multicrystals," *Large Plastic Deformation, Proc. Int. Seminar MECAMAT'91* (*Fontainebleau*), 1993, C. Teodosiu, J. L. Raphanel, and F. Sidoroff, Eds., Rotterdam, pp. 153–168.
[13] Erieau, P. and Rey, C., "Modeling of Deformation and Rotation Bands and of Deformation Induced Grain Boundaries in IF Steel Aggregate During Large Plane Strain Compression," *Int. J. Plast.*, Vol. 20, 2004, pp. 1763–1788.
[14] Peirce, D., Asaro, D. J., and Needleman, A., "Material Rate Dependence and Localized Deformation in Crystalline Solids," *Acta Metall.*, Vol. 31, 1983, pp. 1951–1976.
[15] Beaudoin, A. J., Acharya, A., Chen, S. R., Korzekwa, D. A., and Stout, M. G., "Consideration of Grain-Size Effect and Kinetics in the Plastic Deformation of Metal Polycrystals," *Acta Mater.*, Vol. 48, 2000, pp. 3409–3423.
[16] Cermelli, P. and Gurtin, M., "On the Characterisation of Geometrically Necessary Dislocations in Finite Plasticity," *J. Mech. Phys. Solids*, Vol. 49, 2001, pp. 1539–1568.
[17] Schwartz, J., Fandeur, O., and Rey, C., "Modelling of Low Cycle Fatigue Crack Initiation in 316LN Steel Based on Crystalline Plasticity and Geometrically Necessary Dislocations," *Mater. Sci. Forum*, Vol. 636–637, 2009, pp. 1137–1142.
[18] Schwartz, J., Fandeur, O., and Rey, C., "Fatigue Crack Initiation Modelling of 316LN Steel Based on Non Local Plasticity Theory," *Procedia Engineering*, Vol. 2, 2010, pp. 1353–1362.0002-7820
[19] Franciosi, P., Berveiller, M., and Zaoui, A., "Latent Hardening in Copper and Aluminium Single Crystals," *Acta Metall.*, Vol. 28–3, 1980, pp. 273–283.
[20] Medina Almazán, A. L., 2008, "Experimental and Numerical Study of the 316L and T91 Steels Embrittlement Induced by Mercury," Ph.D. thesis, École Centrale Paris, Chantenay Malabry (France).

Reprinted from JAI, Vol. 7, No. 5
doi:10.1520/JAI102547
Available online at www.astm.org/JAI

Jeremy E. Schaffer[1]

Mechanical Conditioning of Superelastic Nitinol Wire for Improved Fatigue Resistance

ABSTRACT: Metallic wire used in medical devices contains small defects that must be accounted for in design to guard against failure. Sites of probable failure are often constituent inclusion particles, pores, or surface defects that behave as crack-like, stress concentrators. The aim of this research is to examine the effects of mechanical overload conditioning applied to medical-grade nitinol wire on fatigue performance. A mechanical overload conditioning treatment comprising a single axial tensile strain cycle of 11.5 % was applied at room temperature (300 K) to nominally Ti 50.9 at. % Ni wires with active A_f 280 K. The conditioning strain cycle was applied to both plain wire samples with only process and melt-intrinsic defects and to samples which were milled by focused ion beam to produce a transverse 10×0.5×3 μm notch. Transmission electron microscopy was used to probe the root of the milled notch before and after overload conditioning in order to ascertain microstructural parameters responsible for property changes. Evidence of a plasticity-locked, mixed-phase, microstructure at the sharp defect root was found after conditioning. Samples were loaded in a rotary beam fatigue apparatus and cycled in air at 60 s^{-1} to a maximum of 10^9 cycles. The fatigue strain limit was increased by more than 20 % at 10^7 cycles in the conditioned versus non-conditioned plain wire.

KEYWORDS: nitinol wire, nanocrystalline, medical wire, fatigue behavior, nitinol properties

---

Manuscript received May 19, 2009; accepted for publication April 16, 2010; published online May 2010.
[1] Fort Wayne Metals Research Products Corporation, 9609 Ardmore Ave. Fort Wayne, IN 46809 and Weldon School of Biomedical Engineering, Purdue Univ., West Lafayette, IN 47906, E-mail: jeremy_schaffer@fwmetals.com

Cite as: Schaffer, J. E., "Mechanical Conditioning of Superelastic Nitinol Wire for Improved Fatigue Resistance," *J. ASTM Intl.*, Vol. 7, No. 5. doi:10.1520/JAI102547.

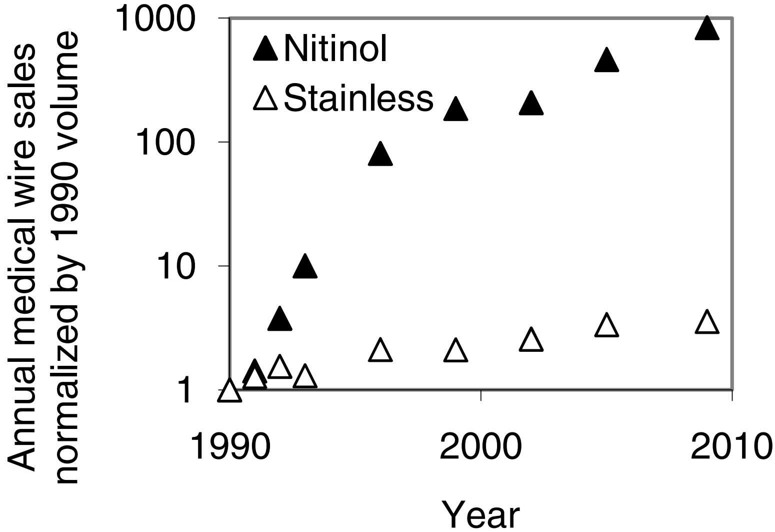

FIG. 1—*Normalized (to 1990 level in pounds) annual medical wire sales at Fort Wayne Metals (Fort Wayne, IN, USA) of NiTi compared to stainless steel for medical device applications.*

Introduction

Nitinol has grown rapidly as an important material in biomedical design. Typified in Fig. 1, the use of nitinol wire in biomedicine has grown exponentially for more than two decades at an annual rate of about 30 % [1]. With the assumption of clinical relevance, these data indicate that the number of nitinol medical appliances has doubled every 2.5 years since 1989, more than twice the rate of stainless steel. Nitinol is seductive for biomedical design largely for its elastic properties and extremely high strain fatigue limit that are attributable to shape memory and superelastic effects [2]. The resilient intermetallic has been used to pioneer new therapies, for example, self-expanding stents, which take advantage of nitinol's unequalled static as well as dynamic strain limits. The properties of nitinol enable aggressive and diverse design which pushes the limits of engineering technique. While contributing substantial therapeutic value, such aggressive design may also contribute to occasional failures, which occur outside the mechanical bounds of other conventional metallic structures. Nitinol's relative biocompatibility [3], magnetic resonance imaging (MRI) compatibility [4], and low stiffness that is similar to many biological materials, such as bone, tendons, and hair, further potentiate its biomedical utility.

The fatigue properties of nitinol are the subject of some consternation in device design as they are not yet well understood. Only recently have thorough fracture mechanics treatments been applied to material forms which are used in implantable medical devices [5,6]. The fatigue crack propagation behavior of the alloy was studied in detail by McKelvey and Ritchie [5]. McKelvey et al. observed that the crack growth propagation rate and ΔK_{th} fatigue threshold were different for equivalent composition nitinol alloy at martensite-stable and austenite-stable temperatures where the crack growth rate was generally lower at martensite-stable temperatures. They also observed that, under plane-strain conditions, the heavily slipped material near the crack tip at superelastic regime temperatures remained austenitic, presumably inhibited from undergoing volume contractile, stress-induced phase transformation by the triaxial stress state while plane-stress conditions generally resulted in stress-induced martensite near the crack tip.

In thin wires, where plane-strain conditions are not approached, it is expected that sufficient loading will result in incipient phase transformation near the largest or shape-conducive crack-like defects. Under sufficient load, complete transformation of the bulk, defect-free material will occur only after plastic damage at the most potent stress concentrators. The goal of this research is to examine the effects of mechanical overload conditioning of superelastic wire and the possibility of increased fatigue damage resistance associated with near-defect, plasticity-locked phase transformation.

Experimental

Nitinol wire with an ingot A_S of 243 K, comprising Ti 50.9 at. % Ni was repetitively drawn and annealed from ∅2 mm to a diameter of 177 μm. At this stage, wires were annealed continuously, reel-to-reel, at 770–800 K while dynamically loaded at nominally 100 MPa tensile stress. Final cold working was completed using diamond dies to draw ∅150 μm round wire prior to continuous, reel-to-reel annealing at 750 to 780 K under constant stress for less than 60 s to effect linear shape setting. The final wire comprised a room-temperature-superelastic nitinol wire with an active A_f of 280 K and an approximately 120 nm thick, dark brown oxide layer similar to material from Ref 7.

Artificial defects were milled into each sample in order to act as high potential sites of incipient fatigue crack formation and to facilitate user-defined damage localization and monitoring. A dual-beam (Nova 200 NanoLab, FEI Co.) focused ion beam (FIB) with in situ scanning electron microscopy (SEM) was used to simultaneously monitor samples by SEM during the FIB milling process. A 30 keV Ga+ ion beam at 500 pA current was used to precisely mill transverse notches into wire specimens. The Ga+ ion beam spot size at this current was about 10 nm. The notches were of consistent dimension measuring 10 μm transverse length by 3 μm radial depth by 0.5 μm axial surface width, an example of which is shown in Fig. 2. Cue lines were milled into the oxide surface at a depth of about 50 nm on either side of each FIB-milled sharp defect (FSD) in order to enhance optical detection for accurate placement in fatigue test gages after removal from the SEM chamber. As shown in Fig. 2, the cue lines were of sufficient depth to create a color gradient associated with the reduced oxide thickness, while shallow enough to minimize undesirable mechanical impact as evidenced by a lack of fatigue crack propagation from any of the cue lines.

Cyclic and monotonic uniaxial tensile properties were measured at an ambient temperature of 295 K at a strain rate of 10^{-3} s^{-1} using an Instron Model

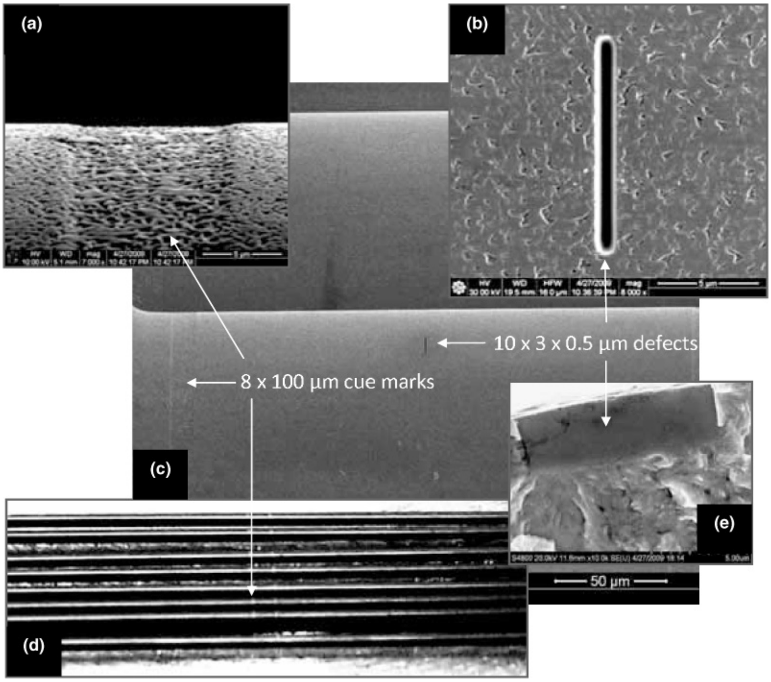

FIG. 2—(*a*) *Secondary electron image of a 50 nm deep cue mark for optical determination of the target defect zone.* (*b*) *Transversely oriented, 10×3×0.5 μm* (*T×R×L*) *FSD.* (*c*) *Overall view of FSD zone.* (*d*) *Optical photograph of ∅150 μm NiTi wires with cue marks evident near centerline.* (*e*) *Transverse SEM micrograph of failed fatigue fracture specimen showing FSD depth.*

5565 Tensile Test Bench equipped with pneumatic, smooth face grips. Six hundred grit emery-cloth was used to reduce grip-specimen interface slip. Strain was measured based on initial gage length and cross-head motion. Elevated temperature testing was completed on an equivalent tensile bench fitted with an environmental chamber capable of maintaining a temperature of 310 ± 0.5 K.

Fatigue behavior was characterized using rotary beam fatigue test equipment manufactured by Positool, Inc. at a test rate of 60 s^{-1} in ambient 298 K air. The test rate was chosen at a rate significantly higher than physiological loading frequencies to promote expediency. Data have recently been presented by Robertson and Ritchie suggesting that high rate testing may well estimate *in vivo* fatigue failure lifetimes [6]. Plain wire specimens from each group, non-conditioned (NC) and conditioned (C), were tested at alternating strain (1/2 peak-to-peak amplitude) levels ranging from 0.8 % to 1.6 %, according to Eq 1, where d is the wire diameter and R is the bend radius. Testing was stopped at 10^9 cycles or 200 days test time. Additional FSD specimens were tested at 1 % strain level before and after conditioning. The FSD zone was located within 1 mm of the bend apex by optical positioning using the cue marks as guides,

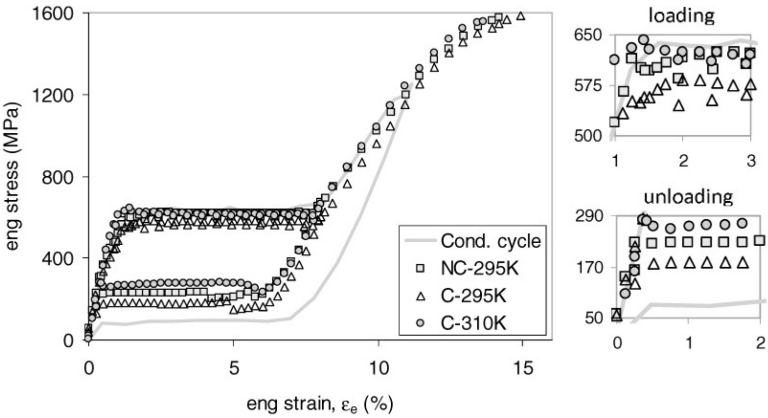

FIG. 3—*Cyclic tensile data for each sample including the high strain rate overload conditioning cycle* (*Cond. Cycle*)*, shown here for information purposes only, NC, and C wire. Test temperature is given for each condition. Insets show zoom of loading and unloading regions.*

$$\varepsilon = d/2R \tag{1}$$

Electron microscopy of fracture surfaces was carried out using a Hitachi S4800 field emission SEM operated at 10 to 20 kV. Transmission electron microscopy (TEM) samples were extracted and prepared using the FIB/SEM dual beam equipment previously mentioned with an in situ tungsten hairpin sample manipulator and platinum deposition system for thin foil removal and transport to TEM grids. Details of this method can be found in Ref 7. TEM imaging and diffraction experiments were carried out on a 200 kV machine equipped with a LaB_6 emitter. (Tecnai 20, FEI Co., Oregon).

Results and Discussion

Conditioning was applied by approaching the martensitic yield point at 295 K using strain-rate-controlled loading in order to induce some dislocation locking of stress-transformed material in the vicinity of stress concentrators. Figure 3 shows the tensile data that were gathered in this experiment. The conditioning cycle comprised a strain-controlled ramp to a stress level of 1240 MPa engineering stress followed by a 3 s hold, finishing with a strain-controlled ramp to zero load. The total engineering strain departure for this cycle, measured by crosshead extension, was 11.5 %. Conditioning initially resulted in 0.3 % residual strain comprising both plastic and pseudo-plastic strain contributions.

The martensite to austenite reversion plateau stress associated with unloading was significantly reduced during unloading from the conditioning cycle, but was observed to elevate in subsequent testing to 8 % strain. Some of this effect can be accounted for by strain rate differences: the conditioning cycle was run at a strain rate of 10^{-2} s^{-1}, compared to 10^{-3} s^{-1} for the 8 % test cycles. High strain rates can cause heating during loading and cooling during

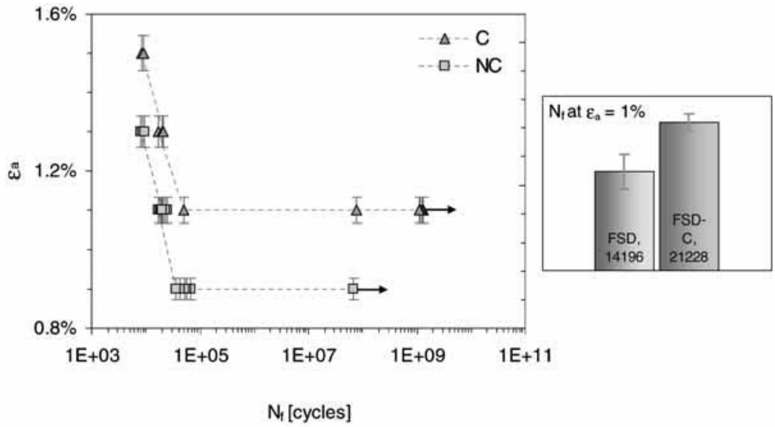

FIG. 4—(*left*) *Rotary bend fatigue data for C and NC plain wire samples. Test parameters: T=300 K, rate=60 s^{-1}, R=−1; max stress error=3 %, max cycle count error=0.5 %;* (*right*) *Single test level* (*1 % alternating strain*) *data for FSD and FSD-C samples. Extension bars represent data spread for n=3 samples.*

unloading resulting in increasing stress hysteresis. Further testing at body temperature (310 K) showed elevation of the unloading plateau stress to levels greater than the NC sample at 295 K. This result was expected based on known test temperature-plateau stress relationships.

The downward shift in the unloading plateau stress of the C sample can be attributed to plastic damage, some of which may be directly beneficial to resistance against subsequent fatigue crack growth. The lack of significant shift in the strain length of the plateaus indicates that plastic damage to the overall microstructure was minimal during overload conditioning.

Figure 4 shows the observed differences in fatigue performance for C versus NC plain wire specimens. Conditioning resulted in an upwards strain shift of greater than 20 % at the 10^7 cycle life (1.1 % versus 0.9 %). Eight out of ten samples of the C plain wire material survived more than 10^9 cycles and are still running at the time of this writing. Three FSD specimens were tested at an alternating strain of 1 % in the NC and C states. In this case, the FSD-C group outperformed the NC samples by 50 %, while all FSD samples failed considerably before the non-FSD samples because of the damage potential associated with the geometry of the FIB-milled defects. They were purposefully milled larger and sharper than the 2–6 μm inclusion particles found at fatigue failure sites in this grade of nitinol wire in order to direct site-specific, locatable failure for study [8].

A microstructurally distinct region was observed within an approximately 500 nm radius of the 10 nm width FSD crack root. Figure 5 shows TEM work that was completed to help elucidate mechanisms giving rise to mechanical property changes associated with the mechanical conditioning. Selected area diffraction patterns within and outside of the distinct FSD concentration zone of wires which were mechanically conditioned but not fatigue tested reveal

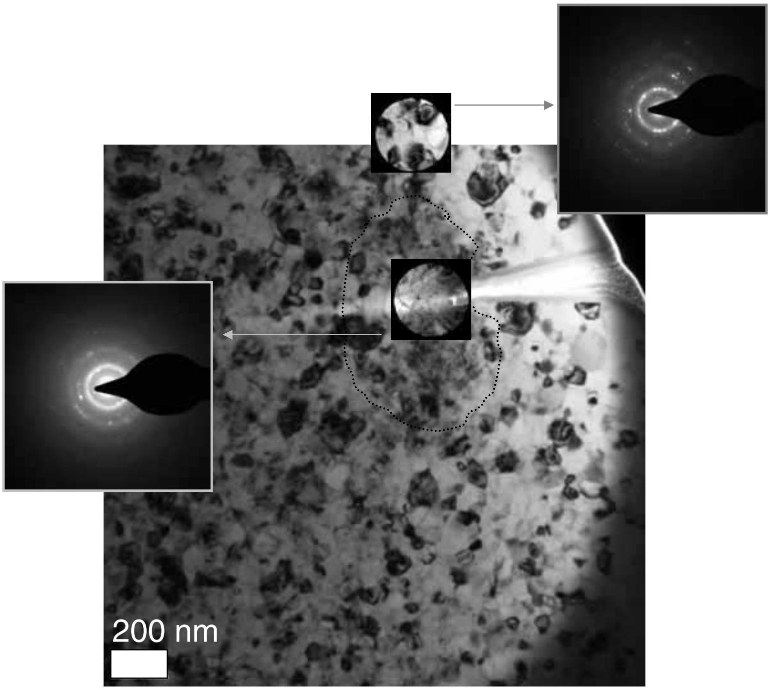

FIG. 5—*Bright field TEM image of FSD crack root after mechanical conditioning. Insets show SADP for regions within (left) and outside of (right) the structurally distinct zone demarcated by a dashed line and extending approximately 0.5 μm from the crack tip.*

significant differences in contributing bright field contrast signal. A typical polycrystalline, B2 pattern was observed at approximately 1 μm from the crack tip while the selected-area diffraction pattern (SADP) adjacent to the root revealed what appears to be superimposed diffuse rings, B2 polycrystalline reflections, as well some evidence of $\frac{1}{2}(110)$ reflections associated with the B19′ martensitic phase. Also evident is a significant increase in dislocation density and associated contrast.

Microstructural amorphization has been shown to occur in nitinol at moderate to high levels of deformation [9]. In the present case, the diffuse (110) rings observed within the FSD zone may be related to partial amorphization and/or due to (110) reflection splitting and the presence of $\frac{1}{2}(110)$ reflections associated with a mixed B2-B19′ structure [10]. Further high resolution TEM is needed to understand the phase composition in the vicinity of these stress concentrators after mechanical conditioning.

The presence of plasticity in the FSD region may also contribute to increased fatigue performance due to residual stresses which offset the effective crack-opening stress intensity range. The reduction in the operating stress intensity range can serve to increase the effective ΔK_{th} fatigue threshold thereby

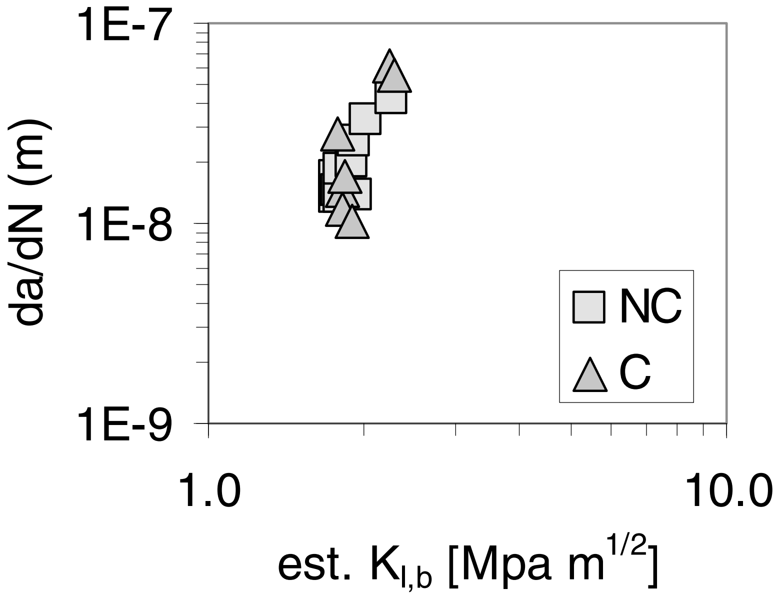

FIG. 6—*Crack growth rate data inferred from high resolution SEM of ductile striation spacing observations and estimated stress intensity at probable crack front location based on a semi-elliptical crack in an infinite rod.*

elevating the strain load level required to initiate or maintain crack growth. The mixed microstructure may also promote crack front tortuosity thereby promoting crack arrest associated with roughness-induced crack closure at near-threshold crack growth conditions [6].

The narrowest ductile striations were observed in C samples near the FSD incipient crack front. High resolution SEM analysis of fatigue failure sites in NC and C specimens was completed and the stress intensity was estimated based on the probable crack front location at the examined site using assumptions of a semi-elliptical crack in an infinite cylinder. Figure 6 shows a crack growth rate plot as a function of the estimated stress intensity factor not taking into account crack closure effects. While slight, the differences may suggest martensitic growth rate inhibition similar to observations by McKelvey and Ritchie in [5].

Conclusions

1. The mechanical conditioning of superelastic NiTi wire for improved fatigue performance, while maintaining desirable superelastic mechanical properties, was demonstrated. Greater than 8 % recoverable strain is observed with zero residual strain and good plateau stresses at body temperature after mechanical conditioning.
2. An increase in the smooth specimen, rotary bend strain fatigue limit of

greater than 20 % at 10^7 cycles, 1.1 % versus 0.9 %, is observed respectively in plain wire conditioned via 11.5 % axial strain overload versus NC plain wire. A 50 % increase in low cycle rotary bend fatigue life is observed for the FIB-notched samples, 21 200 versus 14 200, in C versus NC wire respectively.

3. The tensile overload conditioning treatment results in a mixed-phase microstructure in the vicinity of stress concentrators that comprises increased dislocation density and possible plasticity-induced or roughness-induced crack closure.

In order to be useful in a device application, the gains made through conditioning must be proven to be stable through additional processing such as secondary shape setting, sterilization, and handling prior to final implant or service placement. Device consistency and reliability are paramount in the design of permanent implants and these questions are currently the subject of follow-up research aimed at successful transfer of the observed mechanical benefits to the medical device market. Further experiments are currently underway to illuminate the phase mix in the sharp defect zone after conditioning. Other loading regimes and material conditions are also being explored in order to define the processing domain that is most suitable for material reliability.

Acknowledgments

As with many research projects, submission deadlines often induce a finishing flurry of activity that can tax even the most dutiful of investigators, particularly outside the sheltered realm of academia. In this case, much of the final scrambling fell square on the shoulders of Biomedical Engineering tech., Mr. David Snider, thank you. I would also like to thank the staff of Fort Wayne Metals for the opportunity, and lastly Bob Colby for some last minute training on the Titan.

[1] Myers, R. J., personal communication. 2010.

[2] Duerig, T. W., Pelton, A. R., and Stöckel, D., "The Utility of Superelasticity in Medicine," *Biomed. Mater. Eng.*, Vol. 6, 1996, pp. 255–266.

[3] Shabalovskaya, S. A., "Surface, Corrosion and Biocompatibility Aspects of Nitinol as an Implant Material," *Biomed. Mater. Eng.*, Vol. 12, 2002, pp. 69–109.

[4] Holton, A., Walsh, E., Anayiotos, A., Pohost, G., and Venugopalan, R., "Comparative MRI Compatibility of 316L Stainless Steel Alloy and Nickel–Titanium Alloy Stents," *J. Cardiovasc. Magn. Reson.*, Vol. 4, 2003, pp. 423–430.

[5] McKelvey, A. L. and Ritchie, R. O., "Fatigue-Crack Growth Behavior in the Superelastic and Shape-Memory Alloy Nitinol," *Metall. Mater. Trans. A*, Vol. 32, 2001, pp. 731–743.

[6] Robertson, S. W., and Ritchie, R. O., "In Vitro Fatigue–Crack Growth and Fracture Toughness Behavior of thin-walled superelastic nitinol tube for Endovascular Stents: A Basis for Defining the Effect of Crack-Like Defects," *Biomaterials*, Vol. 28, 2007, pp. 700–709.

[7] Schaffer, J. E., "Structure-Property Relationships in Conventional and Nanocrystalline NiTi Intermetallic Alloy Wire," *J. Mater. Eng. Perform.*, Vol. 18, 2009, pp. 582-587.

[8] Reinoehl, M., Bradley, D., Bouthot, R., and Proft, J., "The Influence of Melt Practice on Final Fatigue Properties of Superelastic NiTi Wires," *Proceedings of the International Conference on SMST 2000*, S. M. Russell and A. R. Pelton, Pacific Gove, CA May2000, ASM, Materials Park, OH, pp. 397–403.

[9] Waitz, T., Kazykhanov, V., and Karnthaler, H. P., "Martensitic Phase Transformations in Nanocrystalline NiTi studied by TEM," *Acta Mater.*, Vol. 52, 2004, pp. 137–147.

[10] Kröger, A., Wernhardt, R., Somsena, Ch., Eggeler, G., and Wieck, A., "In Situ Transmission Electron Microscopy-Investigations on the Strain-Induced B19′-Phase in NiTi Shape Memory Alloys Structured by Focused Ion Beam," *Mater. Sci. Eng., A*, Vol. 438–440, 2006, pp. 513–516.

Reprinted from JAI, Vol. 7, No. 4
doi:10.1520/JAI102521
Available online at www.astm.org/JAI

Aleksandra M. Vinogradov,[1] *Curtis M. Ihlefeld,*[2] *and Isaac Henslee*[1]

Creep-Fatigue Relationships in Electroactive Polymer Systems and Predicted Effects in an Actuator Design

ABSTRACT: The paper concerns the time-dependent behavior of electroactive polymers (EAPs) and their use in advanced intelligent structures for space exploration. Innovative actuator design for low weight and low power valves required in small plants planned for use on the moon for chemical analysis is discussed. It is shown that in-depth understanding of cyclic loading effects observed through accelerated creep rates due to creep-fatigue interaction in polymers is critical in terms of proper functioning of EAP based actuator devices. In the paper, an overview of experimental results concerning the creep properties and cyclic creep response of a thin film piezoelectric polymer polyvinylidene fluoride is presented. The development of a constitutive creep-fatigue interaction model to predict the durability and service life of EAPs is discussed. A novel method is proposed to predict damage accumulation and fatigue life of polymers under cyclic loading conditions in the presence of creep. The study provides a basis for ongoing research initiatives at the National Aeronautics and Space Administration Kennedy Space Center in the pursuit of new technologies using EAP as active elements for lunar exploration systems.

KEYWORDS: electroactive polymers, actuators, creep, fatigue, viscoelasticity, damage

Manuscript received May 15, 2009; accepted for publication March 8, 2010; published online April 2010.

[1] Dept. of Mechanical and Industrial Engineering, Montana State Univ., Bozeman, MT 59717.

[2] Applied Physics Laboratory, Kennedy Space Center, NASA, Orlando, FL 32899.

Cite as: Vinogradov, A. M., Ihlefeld, C. M. and Henslee, I., "Creep-Fatigue Relationships in Electroactive Polymer Systems and Predicted Effects in an Actuator Design," *J. ASTM Intl.*, Vol. 7, No. 4. doi:10.1520/JAI102521.

Introduction

In the past decades electroactive polymers (EAPs) have been increasingly used in many technological fields including aerospace, transportation, telecommunication, photonics, and bioengineering due to their unique ability to sense and react to external stimuli in the form of electrical signals or mechanical deformations. Polymer based transducers, sensors, and actuators have shaped an impressive array of advanced technologies including acoustic microscopy, active vibration control, damage detection in fibrous composites, optoelectronics, and marine fouling prevention. Increasingly, EAP systems have been used for space exploration in weight sensitive applications such as shape and position control of compliant structures, smart skins, solar sails, deployable membrane mirrors, atmospheric balloons, antennae, reflectors, flexible robotic manipulators for grasping and locomotion, pumps, valves, relays, and other applications which have traditionally relied on electromagnetic components. The use of EAPs provides numerous advantages in terms of reduced weight, large motions without gearing, and built in position sensing capabilities [1,2].

The National Aeronautics and Space Administration (NASA) is currently pursuing a lunar exploration program that will benefit from innovations in system components designed to reduce weight and power consumption without sacrificing reliability. For example, low weight and low power fluid handling valves will be required in small chemical plants planned for use on the moon for chemical analysis. Available valves based on solenoids can produce millions of opening and closing cycles so that valve seat design rather than the electromagnets becomes the limiting life design factor. In these applications, EAP actuators are considered to be a logical substitute for current electromagnetic devices.

The effective use of EAPs as active elements in actuator design requires precise understanding of their properties. Many important issues in this regard arise in connection with material nonlinearities, time-dependent effects, and energy losses that characterize the electromechanical response of EAP [3–6]. It is well known that under sustained loading conditions polymers exhibit creep at room temperature with accelerated creep rates at elevated temperatures. The creep behavior of polymers in response to static loads changes dramatically in response to cyclic load histories involving stress reversals or cyclic temperatures. Under such conditions polymers develop much higher creep rates than those observed in static experiments. It is considered that cyclic creep acceleration in polymers is caused by material damage due to fatigue which results in creep-fatigue interaction [7,8].

Enhanced understanding and accurate prediction of creep-fatigue interaction effects on the performance and longevity of EAP devices is critical. Since such devices are designed to operate in dynamic environments, accelerated material degradation processes are likely to impair the functional performance of EAP systems, similarly to the effects of microcracking that tend to decrease the accuracy of piezoelectric sensors and actuators by weakening the electromechanical couplings in material properties [9].

Experimental Results

A representative group of EAP comprises piezoelectric polymer systems including polyvinylidene fluoride (PVDF), PVDF co-polymers, and piezoelectric polymer based composites. At present, this group has reached a greater degree of maturity in terms of technological applications as compared with other EAPs. Essentially, PVDF and PVDF co-polymers represent the principal commercially available high-performance piezoelectric polymers currently in use. These materials are characterized by many attractive properties such as stable response characteristics in a wide frequency range of up to 10^9 Hz, low acoustic impedance, high degree of resistance to impact, resistance to moisture absorption, and marginal sensitivity to ultraviolet and nuclear radiation [3–5].

Strong piezoelectric effects in PVDF are obtained through a technological process that involves stretching and polling of extruded thin sheets of the polymer. Stretching provides an alignment of molecular chains in the stretch direction. An applied electric field of 100 kV/mm at an elevated temperature of about 103 °C causes permanent polarization which is maintained after the material is cooled to room temperature. These processing and fabrication conditions play a decisive role in defining the electromechanical properties of piezoelectric polymers.

The time-dependent mechanical properties of PVDF have been studied based on a series of quasi-static creep tests and dynamic mechanical tests of 28 μm thick commercially produced PVDF thin films. In the experiments, PVDF samples have been tested in two in-plane material directions, i.e., parallel (Direction 1) and perpendicular (Direction 2) to the aligned molecular chains of the polymer. Creep experiments have been performed at 10 different stress levels under sustained loading conditions at room temperature. Strain measurements have been taken by a linear variable differential transformer. The creep behavior of PVDF has been also studied using the method of dynamic mechanical testing and analysis under cyclic loading conditions, see Ref 10 for details. The results of these experiments are illustrated in Figs. 1 and 2 that demonstrate the creep response of PVDF in terms of strain ε (%) as a function of time t [10,11].

It has been determined that at stresses σ below 57 % of the yield stress $\sigma_{Y1} = 45$ MPa in Material Direction 1, and below 76 % of the yield stress $\sigma_{Y2} = 39$ MPa in Direction 2 the creep response of PVDF is linear such that the strain histories $\varepsilon(t)$ obtained at various constant stresses and normalized based on the respective stress can be represented by a single curve known as creep compliance. The creep compliances for PVDF, $C_n(t) = \varepsilon(t)/\sigma$ $(n = 1, 2)$, for Material Directions 1 and 2 are shown in Figs. 3 and 4, respectively.

Cyclic creep response of PVDF has been studied in the stretch direction of the polymer (Direction 1) because of higher creep rates as compared with the Direction 2. The experimental investigation involved a series of tests under the conditions of superimposed static and cyclic loads, i.e., $\sigma(t) = \sigma_m + \sigma_a \sin \omega t$ applied in asymmetric tension-tension mode. The applied cyclic amplitude, σ_a was much smaller than the mean stress σ_m, i.e., $\sigma_a \ll \sigma_m$; ω (rad/s) represents angular frequency. The results were obtained in terms of creep strains $\varepsilon(t)$ and interpreted in terms of normalized creep strain $\varepsilon(t)/\sigma_m$. At least three to five

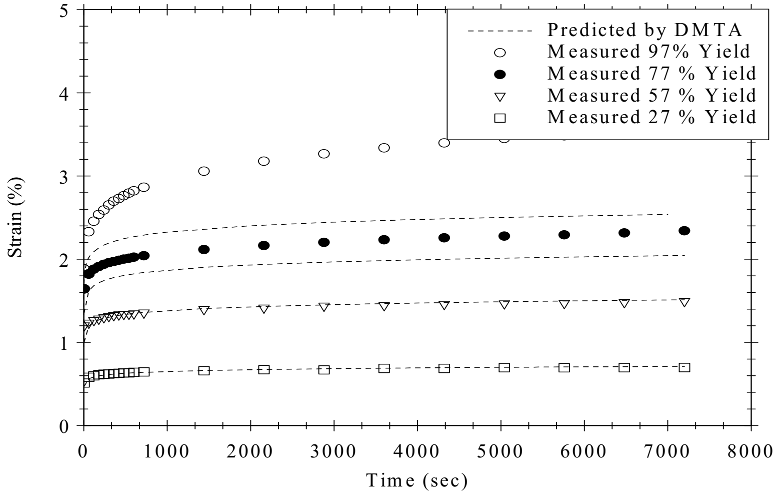

FIG. 1—*Creep strain of PVDF (Direction 1).*

identical experiments were repeated under the same loading conditions to ensure reproducible results [8,12].

This study has demonstrated that under cyclic loading conditions creep rates of PVDF accelerated with an increase of the amplitude and frequency of the cyclic load. These effects are illustrated in Fig. 5 which provides a comparison between cyclic creep strains $\varepsilon(t)$ normalized by the mean stress σ_m and the respective creep compliances obtained under static loading conditions. Cyclic

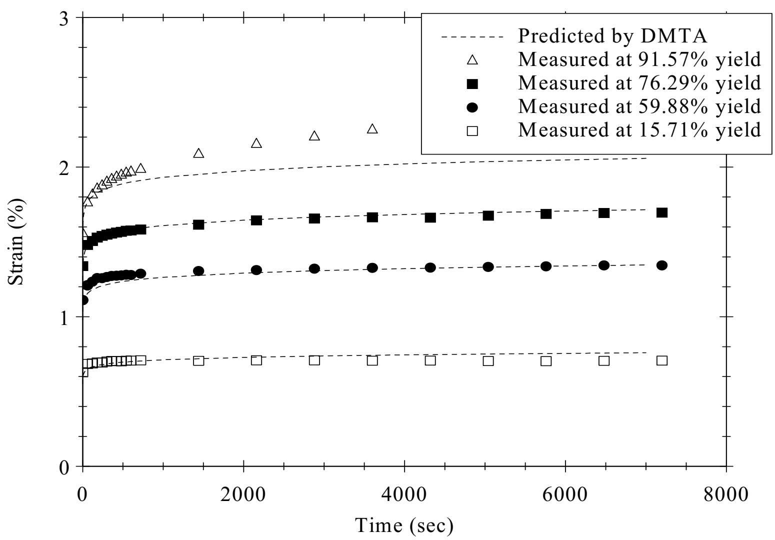

FIG. 2—*Creep strain of PVDF (Direction 2).*

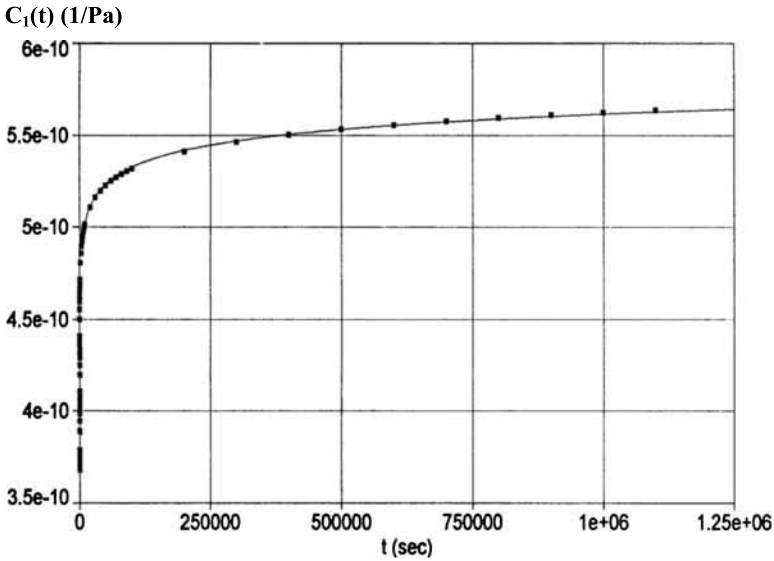

FIG. 3—*Creep compliance of PVDF* (*Direction 1*).

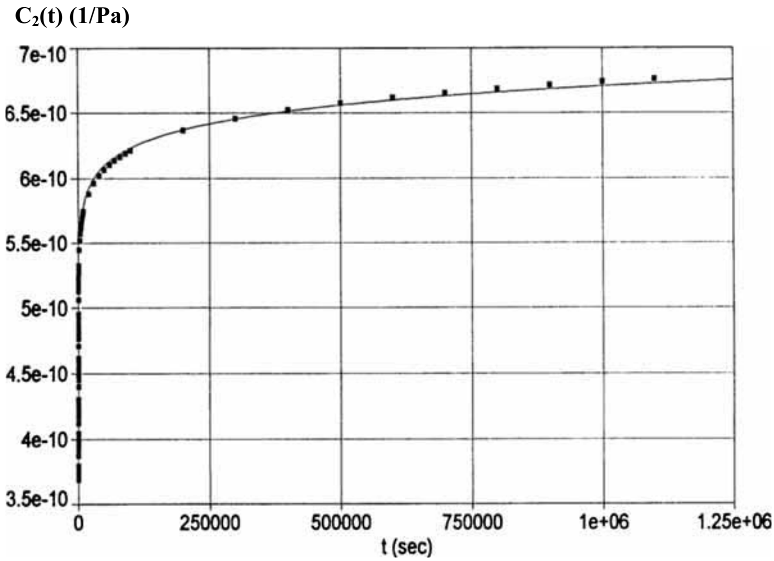

FIG. 4—*Creep compliance of PVDF* (*Direction 2*).

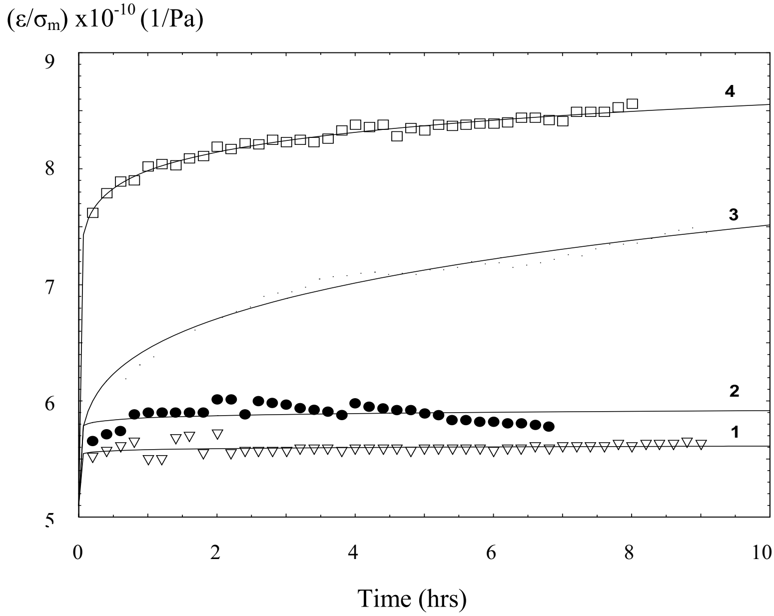

FIG. 5—*Cyclic and static creep responses of PVDF.*

creep of PVDF depicted by Curve 3 has been obtained for the following loading conditions: $\sigma_m = (0.45)\sigma_Y$, $\sigma_a = (0.014)\sigma_Y$, and cyclic frequency $f = \omega/2\pi = 10$ Hz. Curve 4 was obtained for $\sigma_m = (0.34)\sigma_Y$, $\sigma_a = (0.068)\sigma_Y$, and cyclic frequency $f = 5$ Hz. Curves 1 and 2 represent static creep compliances obtained at $\sigma = (0.34)\sigma_Y$ and $\sigma = (0.45)\sigma_Y$, respectively.

These and other results reported in Refs 8 and 12 demonstrate that piezoelectric polymers undergo measurable creep acceleration when subjected to superimposed static and cyclic loads. Consistently, cyclic creep rates tended to increase with an increase of frequencies or amplitudes. This phenomenon can be explained by the presence of several interactive mechanisms including creep, hysteretic heating, and fatigue damage. The contribution of each individual mechanism depends on the loading and temperature conditions. In particular, experiments indicate that fatigue failure of polymers is dominated by hysteretic heating at higher stress levels and frequencies, whereas damage accumulation processes become critical at lower stresses and frequencies [7,13]. In general, cyclic damage evolution in polymers involves several consecutive stages, the formation of crazes, craze growth, crack nucleation, and crack propagation [13]. Even before the appearance of crazes, polymers subjected to cyclic loading regimes tend to undergo measurable changes of their density, shear modulus, and internal damping. The study reported in Ref 14 has shown direct correlation between the sensitivity of polymers to cyclic frequency effects and damage evolution in terms of nucleation and propagation of crazes. These observations, however, have not been consistently characterized or quantified.

To date, the creep-fatigue interaction effects in the behavior of EAPs remain unexplored.

Modeling of Static Creep

As discussed in the foregoing section, within the range of stresses not exceeding 25 MPa the creep properties of PVDF can be represented by creep compliances shown in Figs. 3 and 4. Respectively, the polymer can be characterized by the constitutive equations of linear viscoelasticity based on the Boltzmann superposition principle which states that since strain is a linear function of stress the total effect of applying several stresses is the sum of the effect of applying each one separately. The application of this principle leads to the stress-strain relation in the form [15]

$$\varepsilon(t) = \sigma(0)C_n(t) + \int_0^t C_n(t-\tau)\frac{d\sigma}{d\tau}d\tau \tag{1}$$

where:

stress σ and strain ε = functions of time t, and

C_n $(n = 1, 2)$ denote the creep compliances in the respective material direction of PVDF.

The creep compliances $C_n(t)$ of PVDF can be represented analytically in the form

$$C_n(t) = a_n + b_n(t^{\alpha_n}), \ \ n = 1,2 \tag{2}$$

where the coefficients a_n, b_n, and α_n are defined as follows:

$$\text{Direction } 1{:}a_1 = 3.206 \times 10^{-10}, \ \ b_1 = 5.018 \times 10^{-11}, \ \ \alpha_1 = 0.107 \tag{3}$$

$$\text{Direction } 2{:}a_2 = 3.514 \times 10^{-10}, \ \ b_2 = 0.111 \times 10^{-11}, \ \ \alpha_2 = 0.085 \tag{4}$$

Substitution of Eq 2 into Eq 1 leads to an integral equation which can be solved using the Laplace transformation method in terms of the stress function $\sigma(t)$ in the form

$$\sigma(t) = \frac{\varepsilon(t)}{a_n} - \frac{1}{a_n}\int_0^t \sum_{j=1}^{\infty} \frac{[(b_n\alpha_n/a_n)\Gamma(\alpha_n)(t-\tau)^{\alpha_n}]^j}{(t-\tau)\Gamma(j\alpha_n)}\varepsilon(\tau)d\tau, \ \ n = 1,2 \tag{5}$$

where:

$\Gamma(\alpha_n)$ and $\Gamma(j\alpha_n)$ = gamma functions, and

coefficients a_n, b_n, and α_n $(n = 1, 2)$ are defined by Eqs 3 and 4.

In the case of constant strain $\varepsilon(t) = \varepsilon_o$ = const., Eq 5 is of the form

$$\sigma(t)/\varepsilon_o = \frac{1 - R_n(t)}{a_n}, \ \ n = 1,2 \tag{6}$$

where

$$R_n(t) = \int_0^t \sum_{j=1}^{\infty} \frac{[(b_n\alpha_n/a_n)\Gamma(\alpha_n)(t-\tau)^{\alpha_n}]^j}{(t-\tau)\Gamma(j\alpha_n)} d\tau, \quad n = 1,2 \tag{7}$$

denote the relaxation functions of PVDF in both in-plane material directions. The set of Eqs 1–7 completes the characterization of PVDF in the linear viscoelastic range of creep properties under static loading conditions.

Modeling of Creep-Fatigue Interaction

To characterize creep-fatigue interaction effects in PVDF, a constitutive model has been developed based on the principles of linear viscoelasticity and continuum damage mechanics [15–17]. The concept of a fictitious undamaged continuum with effective material characteristics has been used to represent fatigue damage in the material. Specifically, damage evolution in PVDF has been characterized by a damage function D which depends on the number of cycles N, i.e., $D = D(N)$. The damage function is defined within the limits $0 \leq D \leq D^*$, where the low limit represents undamaged material, $D(0) = 0$, and $D^* < 1$ characterizes the degree of damage at which the response of the material cannot be treated anymore as linearly viscoelastic. The value of D^* must be determined experimentally.

Based on these assumptions, the properties of a fatigue damaged linear viscoelastic material can be defined by the following constitutive equation:

$$\varepsilon_D(t,N) = C_{\text{eff}}(t,N)\sigma(0) + \int_0^t C_{\text{eff}}(t-\tau,N)\frac{d\sigma}{d\tau}d\tau \tag{8}$$

where

$$C_{\text{eff}}(t,N) = C(t)/[1 - D(N)] \tag{9}$$

denotes the effective creep compliance of the material with damage and $C(t)$ is the creep compliance of undamaged material. Note that, at $N = 0$, $C_{\text{eff}}(t,0) = C(t)$. In Eq 8, $\varepsilon_D(t,N)$ denotes the strain in the damaged material produced in response to the stress history $\sigma(t)$.

It follows from Eq 9 that the damage function $D(N)$ can be represented in the form

$$D(N) = 1 - \frac{C(t)}{C_{\text{eff}}(t,N)} \tag{10}$$

Based on this representation an experimental protocol can be developed to characterize the damage function $D(N)$ since the creep compliances $C_{\text{eff}}(t,N)$ and $C(t)$ can be determined experimentally. Specifically, the creep compliance $C(t)$ can be obtained from static creep experiments at a constant stress σ_o by normalizing creep deformations based on the applied stress. The same method can be applied to a damaged material after N number of cycles, providing the effective creep compliance $C_{\text{eff}}(t,N)$. Note that this approach is based on the assumption that the damaged material is linearly viscoelastic.

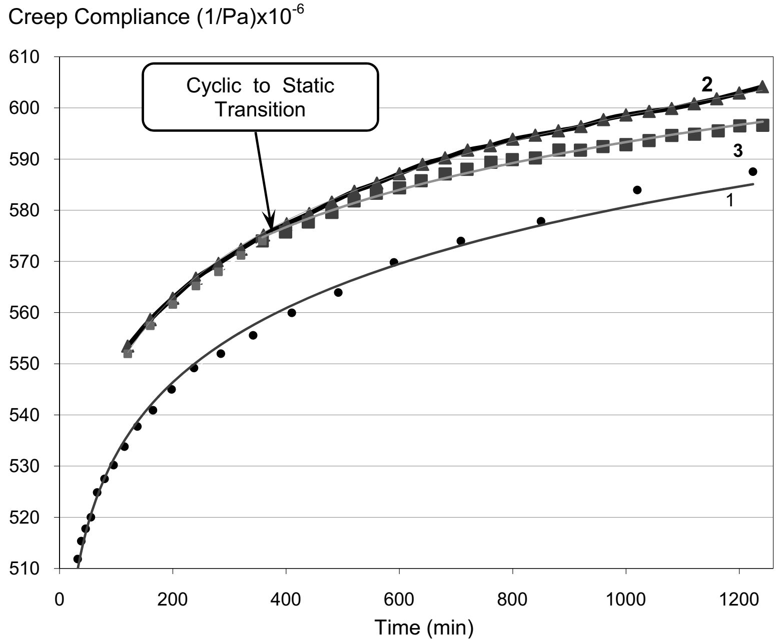

FIG. 6—*Creep of PVDF (1: Static; 2: Cyclic; 3: Two-stage stress history).*

Since the creep compliances $C(t)$ and $C_{\text{eff}}(t,N)$ are obtained by normalizing the experimentally determined strains in the damaged and undamaged materials, $\varepsilon_D(t,N)$ and $\varepsilon(t)$, respectively, such that

$$C_{\text{eff}}(t,N) = \varepsilon_D(t,N)/\sigma_o \quad \text{and} \quad C(t) = \varepsilon(t)/\sigma_o \tag{11}$$

substitution of Eq 11 into Eq 10 provides an alternative equation for computing the damage function

$$D(N) = 1 - \frac{\varepsilon(t)}{\varepsilon_D(t,N)} \tag{12}$$

The proposed creep-fatigue interaction model has been validated experimentally. PVDF samples were prepared from commercially available thin sheets of the material with deposited silver electrode layers on both surfaces of the polymer. The total thickness of the samples including the thickness of silver layers was 46 μm, with the thickness of the PVDF layer of 28 μm. The samples had in-plane dimensions 22 mm$\times$1.5 mm, and were tested in the direction of the aligned molecular chains of the polymer (Direction 1). Tests were performed using a TA Instruments dynamic mechanical analyzer DMA 2980.

As the first step, the creep compliance $C(t) = \varepsilon(t)/\sigma_o$ of undamaged material was determined from creep tests under sustained loading conditions at the stress level $\sigma_o = 10$ MPa, which is below the viscoelastic linearity limit. The results of these tests are shown by the Curve 1 in Fig. 6, in which solid lines

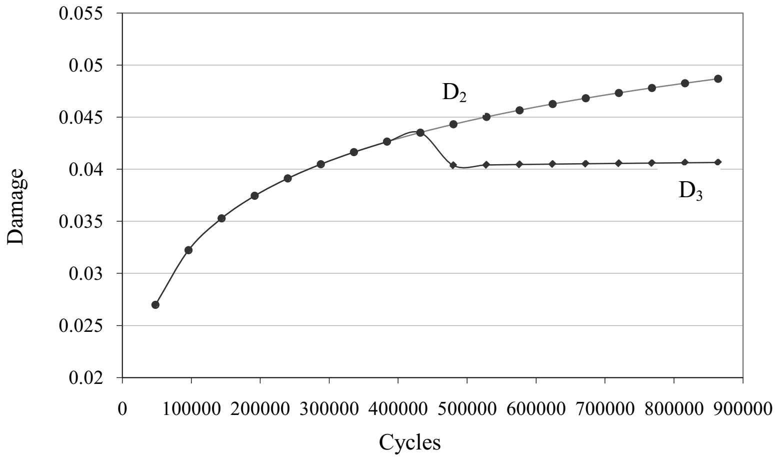

FIG. 7—*Damage characterization of PVDF.*

represent curve fits of test data.

The second series of experiments was conducted under the conditions of superimposed static stress $\sigma_o = 10$ MPa and cyclic stress with the amplitude $\sigma_a = 4.5$ MPa and frequency $f = 20$ Hz. Note that the total maximum stress $\sigma_{\max} = 14.5$ MPa did not exceed the viscoelastic linearity limit of PVDF determined as 25.65 MPa. The respective cyclic strains were measured and normalized with respect to σ_o as represented by the Curve 2 in Fig. 6. As expected, at this stage, the material demonstrated visible creep acceleration as compared with static creep.

The third series of experiments consisted of two types of tests. First, cyclic damage was generated for over 6 h under the same stress conditions as applied at the second stage of the program. After that period only the static load was maintained. The respective effective creep compliances $C_{\text{eff}}(t)$ was determined by normalizing the measured creep strain of the damaged material by the respective static stress. The results of these experiments are illustrated by Curve 3 in Fig. 6.

It is clear that under static loading conditions the damage function $D_1 = 0$. Based on the experimental data obtained from the second and third series of tests, the respective damage functions D_2 and D_3 shown in Fig. 7 were determined using Eq 10. Similarly to Fig. 6, solid lines in Fig. 7 represent curve fits of test data.

It follows from these diagrams that cyclic damage in PVDF initiates immediately upon the load application. Both functions D_2 and D_3 increase with the number of cycles N which characterizes the rate of damage evolution. The damage function D_3 becomes constant, which indicates no further damage development in the material in the absence of the cyclic load.

Challenges

Integration of EAPs into structural design provides the capability of controlling the mechanical characteristics of structures in terms of stiffness or damping, or modify the structural response in terms of position or velocity. This type of built-in structural intelligence has been particularly effective in space applications. In particular, the use of EAP in machine components and devices for lunar exploration has been actively pursued at the NASA Kennedy Space Center. In November of 2008, NASA performed a series of experiments at the lunar analog site on Mauna Kea, Hawaii, chiefly to demonstrate the technologies capable of analyzing and extracting oxygen from lunar soil. Experiments like the Regolith Volatiles Characterization and the Lunar Water Resource Demonstrator were essentially miniaturized chemical plants for detecting soil volatiles and analyzing water [20]. The plants contained rotary valves, solenoid valves, and pumps for routing gases. Ambitious goals have been set for the design of these devices in terms of mass, thermal, and power requirements. In this regard, the existing technologies appear ineffective. It is expected that a promising alternative to traditional design will be provided by EAP systems that will enable new technological developments for lunar exploration.

It is clear that, in practice, successful implementation of EAP systems directly depends on the degree of understanding of their behavior and properties. To date, considerable progress has been made in this subject area [2,4]. However, many aspects of the performance and properties of EAPs remain unexplored. In particular, challenges arise due to the sensitivity of polymers to fabrication and temperature conditions, time-dependent effects, and material nonlinearities. An immediately obvious challenge to fielding EAPs is a lack of understanding of their failure modes, reliability, and the change of electromechanical properties depending on time and temperature. Questions as to the nature of long-term creep and fatigue-fatigue interaction effects in polymers must be understood and quantified before EAP can be widely accepted as viable competitors to the electromagnetic actuator technologies currently in use.

Work-in-Progress

To investigate the potential use of EAP in lunar exploration, the Kennedy Space Center is sponsoring research on the creation of simulation models to assist in the design of EAP based active control systems. To illustrate the importance of understanding long-term creep and fatigue effects in an EAP element, consider the design of a valve currently under investigation at Kennedy Space Center. A simplified valve schematic and the corresponding valve seal free body diagram demonstrating the acting forces are shown in Fig. 8.

In this normally open design, a valve seal moves downward on application of voltage to mate with a seat and cut off the flow of gas. When no voltage is applied, the seal is at $x_1 = 0$, and the spring forces F_s and membrane viscoelastic forces F_v are in equilibrium. As Maxwell force F_m increases with increasing voltage, the seal moves toward the seat to a new equilibrium position. At sufficient voltage the Maxwell force overcomes viscoelastic, frictional, and gas pressure forces so that the seal contacts the seat resulting in a reactive force at the seal-seat interface

$$F_r = F_s + F_m - F_v - F_g - F_f \tag{13}$$

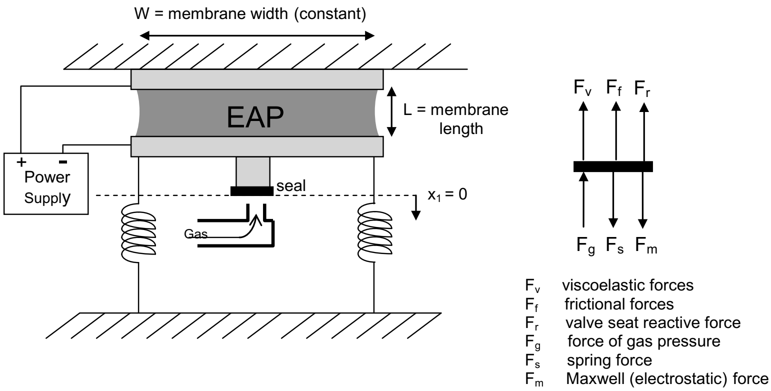

FIG. 8—*Valve schematic and free body diagram.*

The reactive force F_r, equivalent to the blocking force in Ref 18, for a given applied voltage can be increased by designing the seat as close as possible to the seal. However, due to the long-term effects of creep and fatigue the initial zero-voltage equilibrium position of the seal will drift towards the seat so that designing with the initial seal position too close to the seat would cause the valve to fail prematurely. It is clearly important to be able to predict these time-dependent effects under the given loading and temperature conditions in order to accurately design the seal to seat gap to avoid gas leakage and increase the reliability of the valve.

Potentially, an electroactive EAP membrane can be used as a sensor and modeled as a capacitor with the capacitance being a function of the actuator geometry and the dielectric properties of the polymer [19,20]. As the membrane extends, the capacitance will increase in a predictable and repeatable manner. With proper design of circuitry, an EAP valve can exploit this built-in displacement sensor without the need for a separate sensing device. It should be noted that since highly piezoelectric materials like PVDF have the additional property of generating voltages when deformed, this property could also be used to measure actuator position. However for static or very slow frequency measurements, determination of position from measurement of capacitance may prove to be more accurate and will be considered here for the fault detection algorithm.

Long-term drift can be measured and compared to the predicted creep models. Specifically, and estimated damage function, $\hat{D}(n_v)$, can be updated using the empirically determined model and a count of total valve cycles, n_v. When the valve is closed, the constant strain is known, and when the valve is open, the stress is known, based on the known force F_s and the respective position of the valve. Using the material characterization provided by the constitutive Eqs 7 and 8 together with the measured opening and closing times and positions, it will be possible to simulate an estimated strain, $\hat{\varepsilon}(n_v)$ estimate the accumulated damage and compare this estimate to the measured strain giving the rule

$$|\hat{\varepsilon}(n_v) - \varepsilon(n_v)| < K \tag{14}$$

where:

K denotes a certain limit based on the accuracy of the estimates, and violation of the rule signifies a valve fault.

In practice, accurate simulation of $\hat{\varepsilon}(n_v)$ may be computationally intensive. Instead, an approximation consisting of a series of exponential terms will be sought based on the analysis of Eqs 7 and 8. It is hypothesized that this estimator could be designed with a low order digital filter and would not be computationally intensive.

Conclusions

Experimental results show that the mechanical properties of EAPs are time-dependent. Within certain limits creep deformations of EAP measured at room temperature can be accurately predicted using the constitutive equations of linear viscoelasticity. The dynamic response of EAP subjected to superimposed static and cyclic loads is characterized by accelerated creep rates due to the effects of creep-fatigue interaction. Cyclic creep acceleration has been observed even in the range of stresses well below the viscoelastic linearity limit. It is clear that the cyclic response of the EAP is essentially nonlinear, since it does not represent a simple superposition of the responses to static and fully reversed cyclic loads applied separately.

To characterize cyclic damage evolution in PVDF, a constitutive material model has been developed based on the principles of linear viscoelasticity and continuum damage mechanics. The model has been validated experimentally. Fatigue induced material degradation has been characterized by experimentally determined damage function. This approach provides a reliable predictive capability for assessing the long-term integrity and functionality of EAP.

The study presented in this paper provides a basis for ongoing research initiatives at the NASA Kennedy Space Center in the pursuit of new technological developments using EAP as active elements for lunar exploration systems.

References

[1] Ihlefeld, C. M. and Qu, Z., "A Dialectric Electroactive Polymer Generator-Actuator Model: Modeling, Identification, and Dynamic Simulation," *Proceedings of SPIE "Electroactive Polymer Actuators and Devices* (*EAPAD 2008*)", Y. Bar-Cohen, Ed., San Diego, CA, March 10–13, SPIE, Bellingham, WA, 2008.

[2] Vinogradov, A. M., "Accomplishments and Future Trends in the Field of Electroactive Polymers," *Proceedings of SPIE "Electroactive Polymer Actuators and Devices* (*EAPAD*) *2008,"* Y. Bar-Cohen, Ed., San Diego, CA, March 10–13, SPIE, Bellingham, WA, 2008.

[3] Vinogradov, A. M., "Piezoelectricity in Polymers," *Encyclopedia of Smart Materials*, Vol. 2, M. Schwartz, Ed., J. Wiley & Sons, New York, 2002, pp. 780–792.

[4] Zhang, Q. M., Bharti, V., and Kavarnos, G., "Poly(Vinylidene Fluoride) (PVDF) and Its Copolymers," *Encyclopedia of Smart Materials*, Vol. 2, M. Schwartz, Ed., J.

Wiley & Sons, New York, 2002, pp. 807–825.

[5] Harrison, J. S. and Ounaies, Z., "Polymers, Piezoelectric," *Encyclopedia of Smart Materials*, Vol. 2, M. Schwartz, Ed., J. Wiley & Sons, New York, 2002, pp. 860–873.

[6] Vinogradov, A. M., Schmidt, V. H., Tuthill, G. F., and Bohannan, G. W., "Damping and Electromechanical Energy Losses in the Piezoelectric Polymer PVDF," *Mech. Mater.*, Vol. 36, 2004, pp. 1007–1016.

[7] Lesser, A. J., "Changes in Mechanical Behavior During Fatigue of Semicrystalline Thermoplastics," *J. Appl. Polym. Sci.*, Vol. 58, 1995, pp. 869–879.

[8] Vinogradov, A. M. and Schumacher, S. C., "Cyclic Creep of Polymers and Polymer Matrix Composites," *Mech. Compos. Mater.*, Vol. 37, 2001, pp. 29–34.

[9] Sevostianov, I. and Kachanov, M., "Microcracking in Piezoelectrics Weakens the Electro-Mechanical Coupling and Changes Its Directionality," *Int. J. Fract.*, Vol. 101, 2000, pp. 1–8.

[10] Holloway, F., 1997, "Material Characterization of Poly(Vinylidene Fluoride): A Thin Film Piezoelectric Polymer," M.S. dissertation, Montana State University-Bozeman, Bozeman, MT.

[11] Vinogradov, A. M. and Holloway, F., "Electro-Mechanical Properties of the Piezoelectric Polymer PVDF," *Ferroelectrics*, Vol. 226, 1999, pp. 169–181.

[12] Schumacher, S. C., 2000, "Parametric Study of Cyclic Loading Effects on the Creep Behavior of Polymers and Polymer Based Composites," M.S. dissertation, MSU, Bozeman, MT.

[13] Hertzberg, R. W. and Manson, J. A., *Fatigue of Engineering Plastics*, Academic Press, New York, 1980.

[14] Hertzberg, R. W., Manson, J. A., and Skibo, M., "Frequency Sensitivity of Fatigue Processes in Polymeric Solids," *Polym. Eng. Sci.*, Vol. 15, 1975, pp. 252–260.

[15] Wineman, A. S. and Rajagopal, K. R., *Mechanical Response of Polymers*, Cambridge Univ. Press, Cambridge, 2000.

[16] Krajcinovic, D., *Damage Mechanics*, Elsevier, New York, 1996.

[17] Skrzypek, J. and Ganczarski, A., *Modeling of Material Damage and Failure of Structures*, Springer, New York, 1999.

[18] Muscatello, A., Captain, J., Lueck, D., Quinn, J., Gibson, T., and Weis, K., "Lunar Water Resource Demonstrator," *Proceedings of 47th AIAA Aerospace Sciences Meeting*, Orlando, FL, January 5–8, American Institute of Aeronautics and Astronautics (AIAA), Reston, VA, 2009.

[19] Kofod, G., Sommer-Larsen, P., Kornbluh, R., and Pelrine, R., "Actuation Response of Polyacrylate Dielectric Elastomers," *J. Intell. Mater. Syst. Struct.*, Vol. 14, 2003, pp. 787–793.

[20] Pelrine, R., Kornbluh, R., Eckerle, J., Jeuck, P., Oh, S., Pei, Q., and Stanford, S., "Dielectric Elastomers: Generator Mode Fundamentals and Applications," *Proceedings of the SPIE "Smart Structures and Materials 2001: Electroactive Polymer Actuators and Devices"*, Vol. 4329, Y. Bar-Cohen, Ed., San Diego, CA, July 2001, SPIE, Bellingham, WA, 2001, pp. 148–156.

Reprinted from JAI, Vol. 7, No. 4
doi:10.1520/JAI102530
Available online at www.astm.org/JAI

Jessica Delacroix,[1] *Jean-Yves Buffiere,*[2] *Siegfried Fouvry,*[3] *and Armelle Danielou*[4]

Effects of Microstructure on the Incipient Fatigue and Fretting Crack Processes in Al-Cu-Li Alloys

ABSTRACT: The influence of microstructure on the crack nucleation and growth under fatigue and fretting loadings was investigated on two different Al-Cu-Li alloys used for aerospace applications (2050-T8 and 2196-T8) and containing different hardening precipitates (mainly T_1 precipitates for 2050-T8 and $T_1+\delta'$ for 2196-T8). Fatigue tests have been carried out on specimens with a central hole to take into account the stress concentration present in riveted plates. The number of cycles for crack initiation in fatigue is found to be smaller in the plate which contains larger intermetallic particles. Concerning the fretting tests, cracking seems to be essentially controlled by contact conditions and no influence of precipitation microstructure was observed for the experimental conditions investigated.

KEYWORDS: fatigue, fretting, cracks, tomography, Al-Li

Introduction

Weight saving has always been a key issue in aeronautics, and it is getting even more crucial nowadays due the dramatic increase in fuel prices and ecological

Manuscript received May 18, 2009; accepted for publication March 10, 2010; published online April 2010.
[1] Université de Lyon/INSA-Lyon, Laboratoire MATEIS, CNRS UMR 5510, Bât. St Exupéry, 69621 Villeurbanne Cedex, France; École Centrale de Lyon, Laboratoire LTDS, Bât. D4, 36 Avenue Guy de Collongue, 69134 Ecully Cedex, France; and Alcan Centre de Recherches de Voreppe, BP 27, 38341 Voreppe Cedex, France.
[2] Université de Lyon/INSA-Lyon, Laboratoire MATEIS, CNRS UMR 5510, Bât. St Exupéry, 69621 Villeurbanne Cedex, France.
[3] École Centrale de Lyon, Laboratoire LTDS, Bât. D4, 36 Avenue Guy de Collongue, 69134 Ecully Cedex, France.
[4] Alcan Centre de Recherches de Voreppe, BP 27, 38341 Voreppe Cedex, France.

Cite as: Delacroix, J., Buffiere, J.-Y., Fouvry, S. and Danielou, A., "Effects of Microstructure on the Incipient Fatigue and Fretting Crack Processes in Al-Cu-Li Alloys," *J. ASTM Intl.*, Vol. 7, No. 4. doi:10.1520/JAI102530.

TABLE 1—*Chemical compositions of the studied Al-Cu-Li alloys (in wt %).*

Alloy	Cu	Li	Mg	Mn	Ag	Zr	Zn	Si	Fe
AA2196	2.5–3.3	1.4–2.1	0.25–0.8	<0.35	0.25–0.6	0.04–0.18	<0.35	<0.12	<0.15
AA2050	3.2–3.9	0.7–1.3	0.2–0.6	0.2–0.5	0.2–0.7	0.06–0.14	<0.25	<0.08	<0.1

constraints. Confronted by the increasing use of composite materials in aircrafts, aluminum alloys have to be constantly improved. From a weight saving point of view, lithium addition offers interesting perspectives, as it reduces the density while improving at the same time mechanical properties like elastic stiffness and strength-damage tolerance compromise. The first Al-Li alloys developed in the 1960s and 1990s contained more than 2 % Li, and their commercial applications were limited due to some technical problems, such as a low corrosion resistance. New low density alloys currently developed contain a lower fraction of lithium.

A key issue in aircraft design is the use of rivets to join components which highly contribute to the risk of failure by fatigue. Higher fatigue stresses (induced *y* section reduction) can become limiting in the case of riveted or bolted joints. Fundamentally, this problem can be considered from at least two points of view:

- First, through the influence of the rivet hole which acts as a stress raiser and therefore promotes fatigue crack initiation; and
- Second, through the presence of a contact between the rivet and the fuselage material which can generate sub-surface damage through a fretting fatigue phenomenon. It is generally observed that fretting leads to premature crack nucleation compared to classic fatigue loading.

Although considerable research has been carried out on the initiation and growth of fatigue cracks from notches or holes in a vast range of Al alloys including the previous Al-Li alloys, the fatigue properties of the low density Al-Li recently developed has been poorly investigated [1] not to mention the fretting properties. In this paper, both aspects are investigated on two Al-Cu-Li alloys with different Cu/Li ratios.

Method

Materials

Two Al-Cu-Li 15 mm plates of alloys 2050-T8 (plate B) and 2196-T8 (plate A) were supplied by Alcan Centre de Recherches de Voreppe (Alcan CRV). The

TABLE 2—*Mechanical properties of the two studied alloys (15 mm plates) with T8 condition. σ_d is the fatigue limit at 10^6 cycles (R=0.1).*

Plate	Alloy	Temper	$Rp_{0,2}$ (MPa)	E (MPa)	ν	σ_d (MPa)
A	2196	T8	554	79 000	0.305	140–150
B	2050	T8	525	77 000	0.305	150

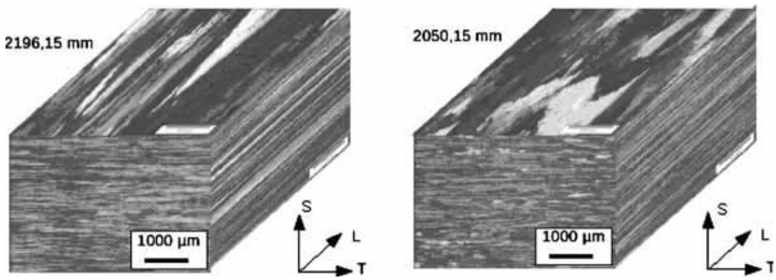

FIG. 1—*Microstructure of studied alloys showing pancake shape grains after anodic oxidation etching.*

chemical compositions of the alloys are detailed in Table 1. The following processing route has been used: Casting, homogenization, hot rolling, solution heat treatment, quenching, stress relieving by controlled tension, and artificial ageing. Both materials have been used in the T8 temper. The mechanical properties of the two materials are given in Table 2.

Microstructural characterization using optical observations after polishing and anodic oxidation reveals pancake shape grains with similar size for both alloys (Fig. 1).

Needle-like specimens with a 1 mm^2 square section were extracted from each plate and analyzed by X-ray microtomography at the European Synchrotron Radiation Facility in Grenoble, France (beamline ID19). This technique reveals in the two plates (Fig. 2) the presence of insoluble intermetallic particles (probably Al_7Cu_2Fe and Mg_2Si), the characteristics of which (size, volume fraction, etc.) are given in Table 3. It can be seen from this table that the 2050-T8 plate contains a slightly higher volume fraction of intermetallic particles with, on average, a smaller size.

The 2050-T8 alloy exhibits mainly T_1 precipitates (Al_2CuLi, platelet shape) as hardening precipitation, whereas a mixture of T_1 and δ' (Al_3Li globular precipitates) is observed in 2196-T8 alloy (Fig. 3) [2,3].

Fatigue Experimental Setup

Constant amplitude uniaxial fatigue tests were carried out on standard fatigue specimens with a central hole (hole diameter = 10 mm) which acts as a stress raiser (Fig. 4) in order to mimic the effect of the hole in the rivet assembly. The stress concentration factor *Kt* is equal to 2.3 for this sample geometry. All specimens were tested in the *L-T* [5] direction. In order to follow in situ the crack nucleation and growth, the sample surface was monitored with a traveling microscope composed of a high focal length (20 mm) lens coupled with a charge-coupled device camera and a X,Y,Z translation stage (Fig. 4). This monitoring

[5]*L-T* sample corresponds to a sample loaded along the L direction (hot rolling direction) in which crack propagation occurs along the LT direction (long transverse direction).

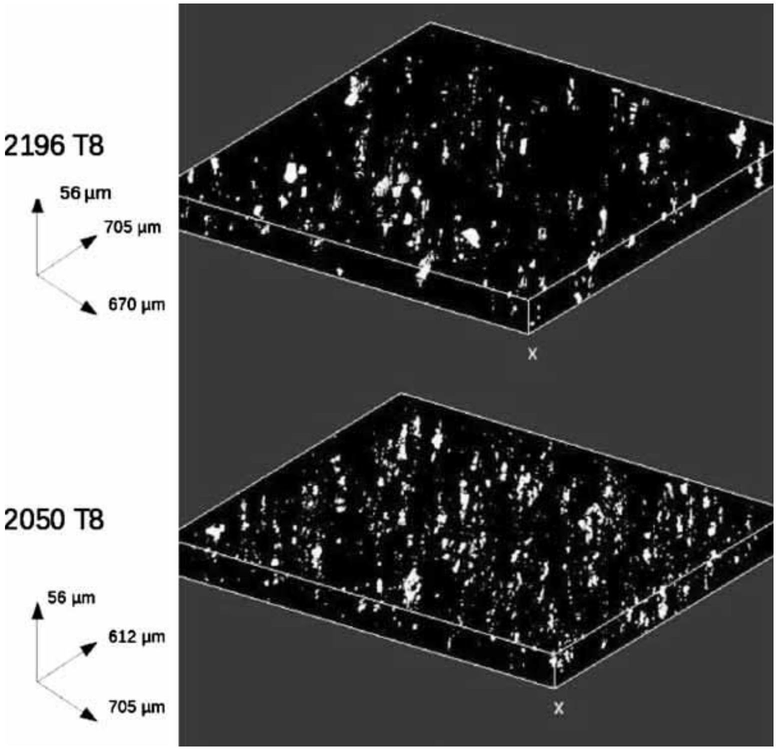

FIG. 2—*3D rendition of intermetallic particles present in the two studied plates. The vertical direction on the figures corresponds to the rolling direction L.*

TABLE 3—*Density, volume ratio, and equivalent radius of the intermetallic particles present in the studied alloys.*

Plate	Alloy	Number/μm^3	Volume Fraction (%)	Mean Radius (μm)
A	2196-T8	1.90×10^{-5}	0.23	3.07
B	2050-T8	4.35×10^{-5}	0.32	2.59

requires mirror polished surfaces and no chamfer on the hole edge.[6] It was checked that the lack of chamfer has no effect on the mean value of fatigue cycles for a nominal stress of 200 MPa which is the value investigated in this work. Fatigue tests have been performed at room temperature using a 8516 INSTRON hydraulic testing device (maximum stress = 200 MPa in the section containing the hole, $R = 0.1$ and $f = 10$ Hz). Fatigue cycling was periodically stopped (every 5000 cycles before crack initiation and every 200 cycles during

[6]On standard specimens, a chamfer is present in order to reduce the notch severity.

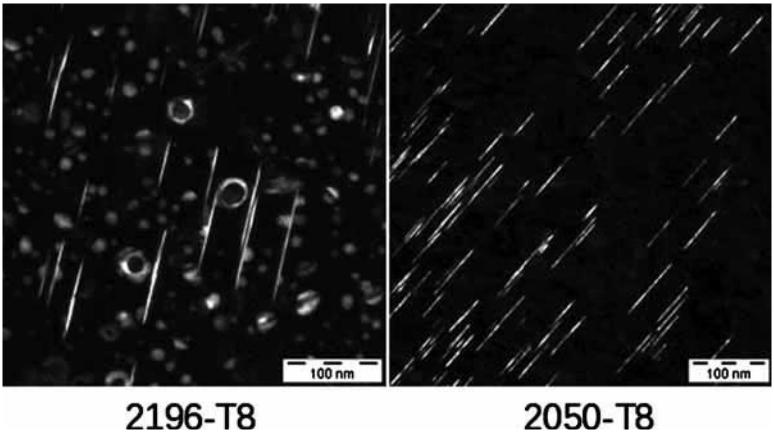

FIG. 3—*Transmission electron microscopy micrograph dark field observations of the hardening precipitates observed in the 2196-T8 alloy (left) and 2050-T8 (right). Platelet precipitates T_1 and globular precipitates δ′ are observed in the 2196 alloy whereas 2050 only contains T_1 precipitates.*

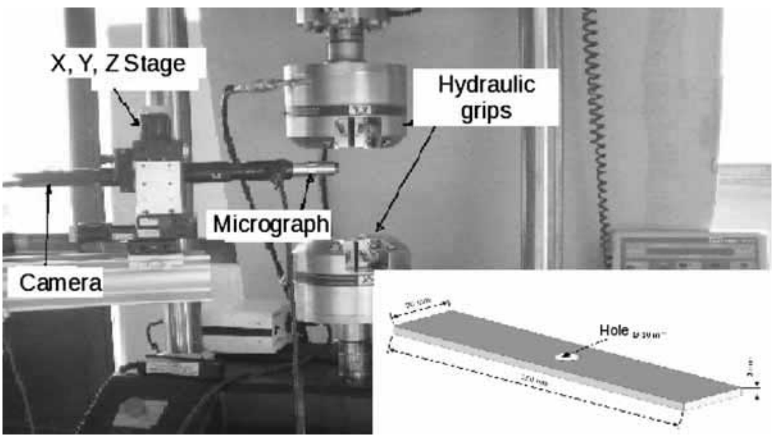

FIG. 4—*Geometrical parameters of fatigue specimen tested and fatigue device used.*

its propagation) to take pictures of the specimen's surface (under load). The numbers of cycles corresponding to crack initiation Ni,[7] and final failure *Nf* were measured for both alloys. The crack length and its projected length along

[7]The crack size at initiation corresponds to the detection of a crack on the polished surface monitored by microscopy. In practice, this size ranges between 10 and 100 μm, see the Results section.

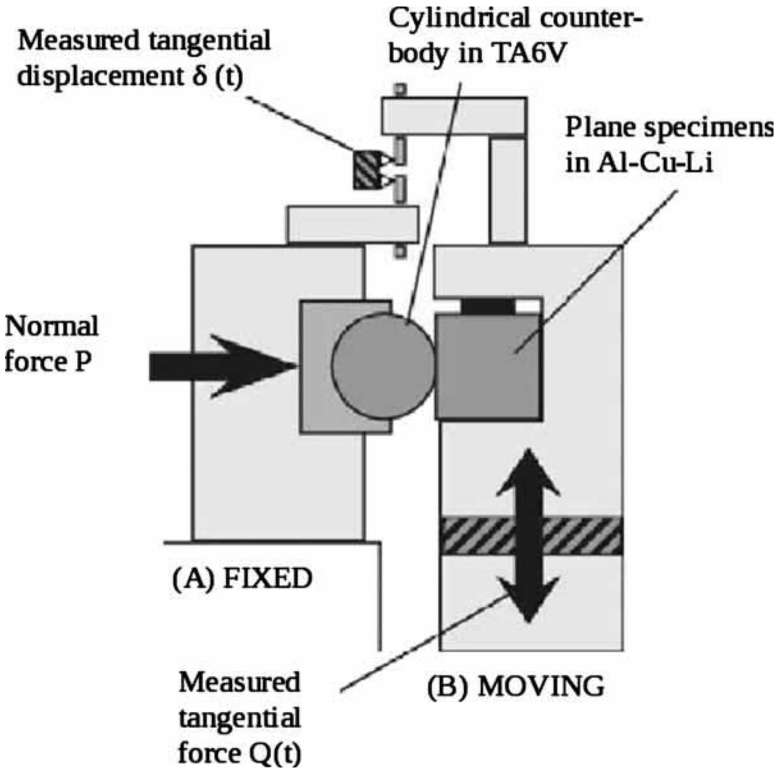

FIG. 5—*Schematic representation of the fretting device for the cylinder/plane configuration.*

the direction perpendicular to the applied stress were measured. The crack paths were also analyzed as a function of the local microstructure at the surface (presence of grain boundaries).

Fretting Experimental Setup

The experimental setup used for the fretting experiments is shown schematically on Fig. 5. The flat Al specimen is maintained in contact with a cylindrical counter-body made of a titanium alloy thanks to the normal force P, which is kept constant during the test. A relative sinusoidal displacement δ is imposed, with a 10 Hz frequency, between the two bodies giving rise to a contact shear force of amplitude Q. Al-Cu-Li specimens have a controlled planar surface with a roughness Ra[8] of 0.2 μm. The pads which form counter-body are machined from bars of a titanium alloy (TIMETAL 6-4 from Timet company: 4.1 wt % of V, 6.5 wt % of Al and $Rp_{0,2}$ of 952 MPa). They have a cylindrical surface with a constant radius of $R = 80$ mm and a roughness Ra of 0.45 μm. The normal

[8]Ra corresponds to the arithmetic average of absolute values of roughness.

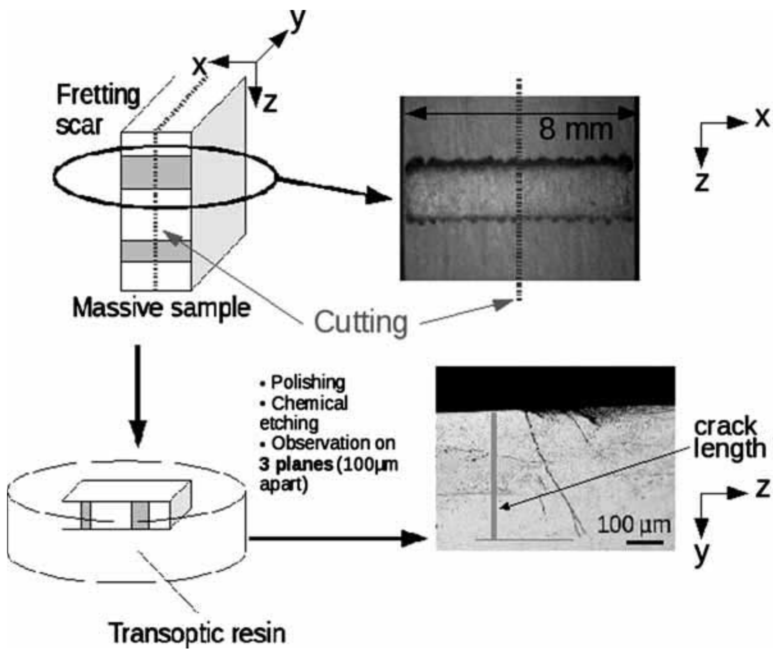

FIG. 6—*Experimental method to investigate cracking after fretting test.*

force P was fixed at 346.5 N/mm along the contact corresponding to a calculated maximum Hertzian contact pressure of 300 MPa (Hertz law). Tests were conducted at different values of the tangential force Q ranging between 75 and 275 N/mm. During the tests, P, Q, and δ were recorded. A given number of cycles N of amplitude δ/tangential force Q is imposed on the sample; in the present case, N was fixed at 100 000 cycles. All the tests are carried out in partial slip conditions which are characterized by no relative movement between the cylinder and the plane at the centre of the contact and, simultaneously, a relative movement (slip) at the edges of the contact area [4]. Depending on the contact loading conditions, cracks may or may not nucleate in these slip zones. This cannot be detected by direct observation of the cycled sample, as cracking occurs below the contact surface. Therefore when the test is stopped ($N = 100\ 000$), the sample is cut in two in the middle of the fretting scars. One of the new surfaces thus created is mechanically polished and the crack length measured by optical observation after Keller etching. The surface is further polished and etched twice (approximately 100 μm of material removed along the X direction between each observation) in order to evaluate the homogeneity of the crack length in volume. The crack length is defined as the projected length along the Y axis (see Fig. 6 for a schematic of the whole process and for a definition of the X, Y, and Z axes).

Fretting crack nucleation is characterized by plotting the evolution of the measured crack length l as a function of Q (Fig. 7). By extrapolating this curve to $l = 0$, the crack nucleation threshold Qc is determined for each alloy studied.

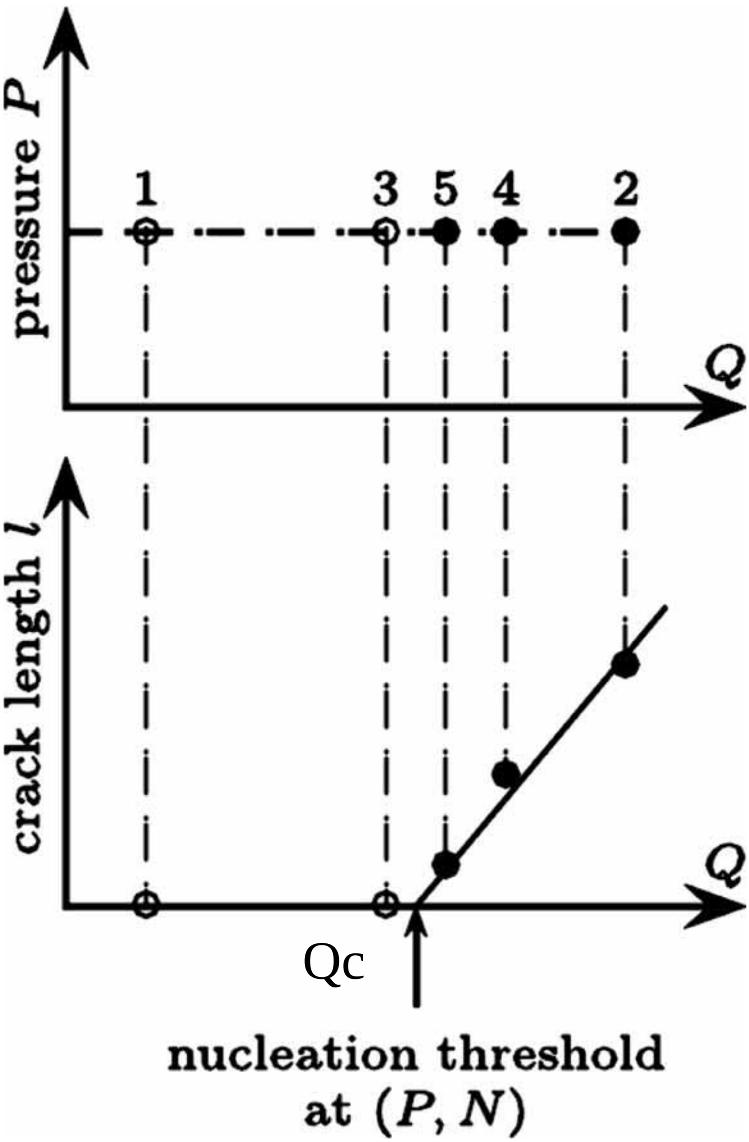

FIG. 7—*Methodology used to determine the crack nucleation threshold. Hollow symbols correspond to samples for which no cracks were observed; full symbols correspond to samples with cracks.*

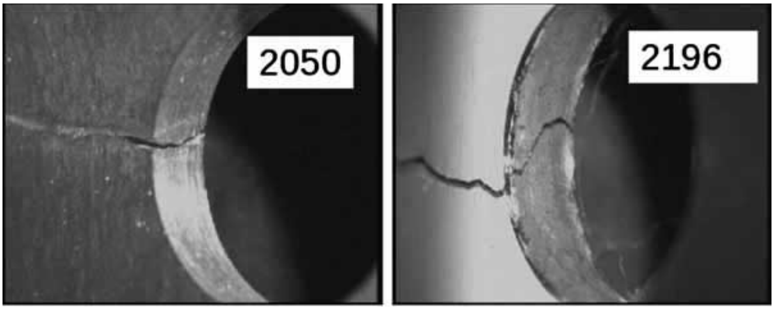

FIG. 8—*Optical micrographs of the crack path through the sample thickness. Open hole fatigue tests. Hole diameter: 10 mm.*

The crack propagation rate corresponds to the slope of the curve $l = f(Q)$. For each material, at least six values of the tangential force were tested and the associated cracks were analyzed.

Results and Analysis

Fatigue Behavior

Crack Paths Morphology—The observed macroscopic crack path through thickness is different in the two alloys: Cracks tend to grow more or less perpendicular to the loading direction for the 2050-T8 alloy whereas large portions of cracks with a 45° orientation are observed in the 2196-T8 alloy (Fig. 8).

The crack paths on the polished surfaces were analyzed at a high magnification. Figure 9 shows that cracks tend to grow with a global direction perpendicular to the loading axis. The crack observed on Fig. 9 initiated from an intermetallic particle intersecting the surface.

From a microscopic point of view, alloy 2050-T8 contains essentially semi-coherent platelet T_1 precipitates which are not easily sheared and should induce deviated slip and/or Orowan by passing. In the 2196-T8 alloy, the presence of coherent globular δ' precipitates is assumed to favor a more planar slip. However, for the experimental conditions investigated, these differences in deformation mechanisms do not produce different macroscopic crack paths on the flat surfaces of the specimens (where plane stress conditions prevail). More detailed observations at higher magnification of the crack paths are currently being carried out to analyze the type of plastic deformation occurring at the crack tip (e.g., planar versus wavy slip bands). It is interesting to note, however, that the tendency of the cracks to propagate at 45° of the loading axis through the thickness of the samples (where plain strain conditions prevail) is observed for the alloy 2196-T8 where planar slip is expected.

Fatigue Lives—Table 4 summarizes the fatigue lives obtained for the two materials. On average, the 2196-T8 alloy exhibits shorter fatigue and less scat-

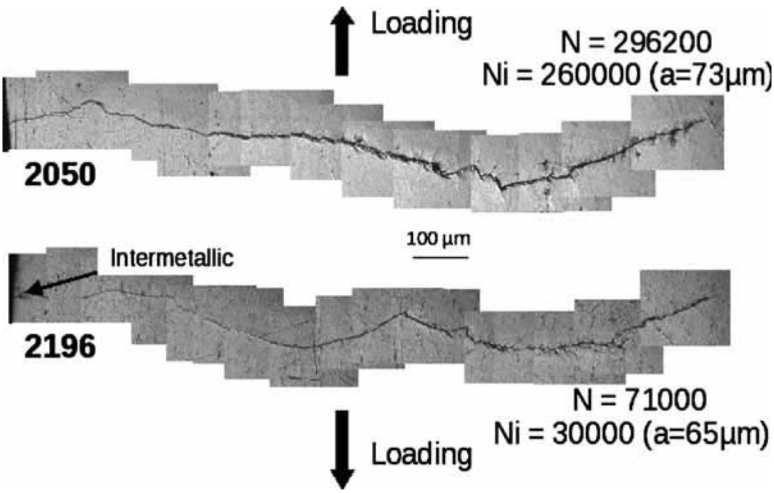

FIG. 9—*Optical micrographs of the crack path in the two alloys studied. The edge of the hole appears in black on the left of the figure. The crack path observed on the polished faces appear quite similar in the two materials with a global direction of propagation perpendicular to the loading axis.*

tered fatigue lives than the 2050-T8 alloy.

The total number of fatigue cycles to failure is classically defined as the sum of the fatigue cycles corresponding to initiation Ni plus the number of fatigue cycles corresponding to propagation Np. In practice, however, it is difficult to determine exactly Ni as the first detected crack can sometimes be a few hundred microns long. To overcome this problem the number of cycles corresponding to a 250 μm long crack is used ($Nf = N250 + Np^*$). Table 5 summarizes the values of $N250$ and Np^* for both materials. Based on this set of parameters, it can be seen that crack initiation tends to occur earlier for plate in alloy 2196-T8 while crack propagation shows no significant differences between the two materials.

This phenomenon can be related to the presence of larger intermetallic particles in the 2196-T8 specimen. These particles have different mechanical properties than the aluminum matrix leading to a stress concentration at the particle/matrix interface during fatigue and to decohesion or crack initiation [5]. According to literature, the size of intermetallics is a predominant factor on crack nucleation, while the stoichiometry of the particles, their volume fraction, and repartition play only a minor role [6,7].

TABLE 4—*Statistics on fatigue failures.* $\langle Nf \rangle$ *is the mean number of cycles to failure.*

Plate	Number of Tests	$\langle Nf \rangle$	Standard Deviation/$\langle Nf \rangle$
2050-T8	10	171 414	0.63
2196-T8	6	124 500	0.45

TABLE 5—*Statistics on fatigue tests results. Nf, N 250, and Np* corresponding, respectively, to the number of cycles for failure, a crack of 250 μm and the propagation of such a crack until failure. STDEV is the standard deviation.*

		Nf	*N*250	*N*250/*Nf*	*Np**
2050-T8 (four tests)	Mean	198 375	173 025	0.82	25 350
	STDEV	131 171	129 257	0.11	5 785
	STDEV/mean	0.66	0.75	0.14	0.23
2196-T8 (four tests)	Mean	124 117	93 167	0.72	30 950
	STDEV	79 984	70 879	0.1	10 739
	STDEV/mean	0.64	0.76	0.13	0.35

Fretting Behavior

The fretting behaviors of the two investigated materials were very similar. First, as seen in Fig. 10, it appears that the threshold tangential force is approximately the same for the two materials: 102 N/mm for 2196-T8 alloy and 96 N/mm for 2050-T8 alloy. Second, the crack propagation rate is also similar for both materials.

No obvious difference was found between both materials in terms of crack paths, as illustrated in Fig. 11. This is coherent with the behavior observed in Fig. 10 for the two alloys and tends to indicate that the very complex (and highly triaxial) stress state which exists below the contact is not very sensitive to a microstructural effect as already shown in Ref 8 for a 2024 Al alloy. The same results have been reported by Giummarra et al. [9] who assumed that the severe contact conditions such as very strong stress gradients at the contact edge smear out any microstructural effect. However such a comparison remains quite qualitative if it is only carried out on a few polished slices such as those shown on Fig. 11. High resolution X-ray tomography experiments are

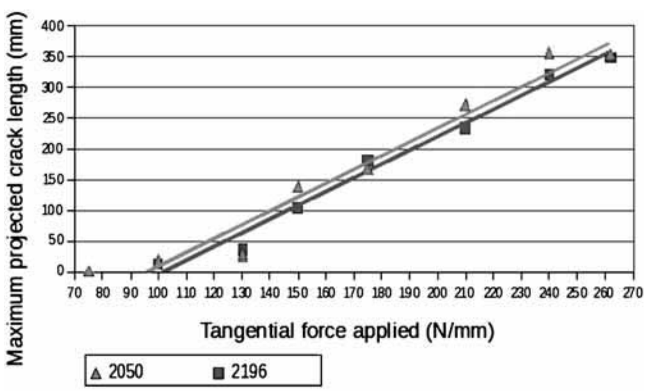

FIG. 10—*Comparison of the crack nucleation and propagation under fretting for the alloys 2050-T8 and 2196-T8.*

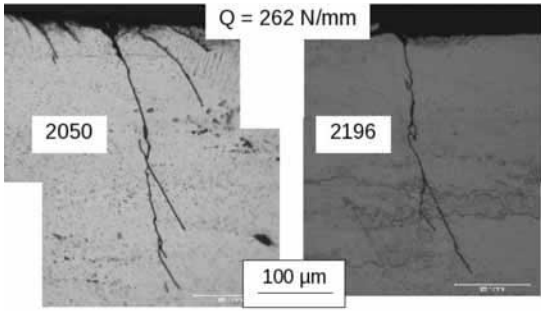

FIG. 11—*Optical observations after Keller etching of fretting cracks for N=100 000 cycles and Q=262 N/mm in specimen in alloy 2050-T8 and 2196-T8. The crack paths observed on the 2D polished sections of the fretting scars appear very similar in the two materials.*

currently being carried out in order to obtain and compare the three-dimensional morphologies of the fretting cracks as shown in Ref 10.

Summary

For the experimental conditions investigated, the 2050-T8 and 2196-T8 alloys exhibit very similar behaviors in fretting: Same threshold tangential force for cracks initiation, same crack propagation rate, and similar crack path morphology. Concerning the fatigue tests on notched specimens, the number of cycles for crack initiation in fatigue is found to be smaller in the plate which contains larger intermetallic particles. No obvious difference is seen for the propagation stage.

Acknowledgments

This research is supported by Alcan Global Aerospace, Transportation, and Industry.

References

[1] Chen, D. L., Chaturvedi, M. C., Goel, N., and Richards, N. L., "Fatigue Crack Growth Behavior of X2095 Al-Li Alloy," *Int. J. Fatigue*, Vol. 21, No. 10, 1999, pp. 1079–1086.

[2] Cassada, W. A., Shiflet, G. J., and Starke, E. A., "Mechanism of Al_2CuLi (T_1) nucleation and growth," *Metall. Trans.*, Vol. 22A, 1991, pp. 287–297.

[3] Lequeu, P., Eberl, F., Jambu, S., Warner, T., Daniélou, A., and Bès, B., "Latest Generation of Al-Li Alloys Developed in Alcan Aerospace," *First European Conference on Materials and Structure in Aerospace*, Berlin, Germany, May 26–27, 2008.

[4] Hills, D. A. and Nowell, D., *Mechanics of Fretting Fatigue* (*Solid Mechanics and Its Apllications*), Kluwer Academics Publishers, Dordrecht, The Netherlands, 1994.

[5] Laz, P. J. and Hillberry, B. M., "Fatigue Life Prediction from Inclusion Initiated Cracks," *Int. J. Fatigue*, Vol. 20, No. 4, 1998, pp. 263–270.

[6] Murakami, Y. and Endo, M., "Effects of Defects, Inclusions and Inhomogeneities on Fatigue Strength," *Int. J. Fatigue*, Vol. 16, 1994, pp. 163–182.

[7] Miyasato, S. M., Magnusen, P. E., and Hinkle, A. J., "Constituent Particles Distributions in 7050 Thick Plate," ONR Contract No. N00014-91-C-0128, ALCOA Technical Center, 1993.

[8] Proudhon, H., Buffière, J.-Y., and Fouvry, S., "Three-Dimensional Study of a Fretting Crack Using Synchrotron X-Ray Micro-Tomography," *Eng. Fract. Mech.*, Vol. 74, No. 5, 2007, pp. 782–793.

[9] Giummarra, C., Bray, G. H., and Duquette, D. J., "Fretting Fatigue in 2xxx Series Aerospace Aluminium Alloys," *Tribol. Int.*, Vol. 39, No. 10, 2006, pp. 1206–1212.

[10] Proudhon, H., Buffière, J.-Y., and Fouvry, S., "Characterisation of Fretting Fatigue Damage Using Synchrotron X-Ray Micro-Tomography, ISFF4: International Symposium on Fretting Fatigue No. 4, FRANCE (2004)," *Tribol. Int.*, Vol. 39, No. 10, 2006, pp. 1106–1113.

Reprinted from JAI, Vol. 7, No. 6
doi:10.1520/JAI102558
Available online at www.astm.org/JAI

Gregory Dvorak,[1] *Marcellin Zahui,*[2] *and Bryce Mitton*[3]

Development of a Sliding-Rolling Contact Fatigue Tester

ABSTRACT: Contact fatigue failure is a common problem experienced in many applications such as bearings, gears, and railway tracks. In recent years, research companies have developed finishing processes that aim to improve components' contact fatigue life. Preliminary rolling contact fatigue tests have shown that superfinishing processes could potentially improve a component's contact fatigue life by 300 %. However, before these technologies can move from the laboratories to industrial platforms, more tests are needed to verify the claim. The objective of the work herein is to discuss the completion and verification of a sliding-rolling contact fatigue (S-RCF) test rig. This project is funded by the U.S. Army to assess the real benefit of superfinishing on the contact fatigue life of gears used in helicopter transmission boxes. The proposed tester design uses three rollers around a specimen, a hydraulic loading mechanism, and two servo motors. This configuration of the S-RCF tester allows for shorter testing time, more flexible testing parameters such as any combination of slide-roll ratio between the surfaces, any operating speed, and dry or lubricated testing conditions. Failure is detected with a state-of-the-art eddy current crack detection system, which can also be used to monitor and investigate crack growth for different materials, levels of superfinish, and operating conditions. Preliminary tests on a common gear material (AISI 8620 steel) were performed to assess the mechanical limits as well as the control software performance. This paper

Manuscript received May 27, 2009; accepted for publication April 28, 2010; published online June 2010.

[1] Energy and Environmental Research Center, Univ. of North Dakota, 15 North 23rd St., Stop 9018, Grand Forks, ND 58202-9018, e-mail: gdvorak@undeerc.org
[2] Ph.D., Mechanical Engineering, Univ. of North Dakota, 243 Centennial Dr., Stop 8359, Grand Forks, ND 58202-8359, e-mail: Marcellin.Zahui@und.edu
[3] Ph.D., Engineering Surfaces Center, Univ. of North Dakota, 4201 James Ray Dr., Suite 1100, Grand Forks, ND 58202, e-mail: brycemitton@mail.und.edu

Cite as: Dvorak, G., Zahui, M. and Mitton, B., "Development of a Sliding-Rolling Contact Fatigue Tester," *J. ASTM Intl.*, Vol. 7, No. 6. doi:10.1520/JAI102558.

presents the detailed development and validation of the tester. It discusses issues involved with servo controllers, electronic gear ratio, and their ability to provide precise speed and slip ratios.

KEYWORDS: rolling contact fatigue, fatigue tester

Introduction

Failure eventually happens in any mechanical system [1]. Depending on the mechanics of the failure mode, it can occur suddenly or gradually over a short or long period of time. If unexpected, the results could be significant financial losses, damage to the machine, and/or severe injuries. Rolling contact fatigue (RCF) failure is one of many fatigue failures that can have unintended consequences especially in helicopter transmission boxes. The power density of these transmission boxes creates excessive loading of the gears, resulting in high probability of contact fatigue failure due to high Hertzian stresses, friction, and wear. To alleviate this type of premature failure, some manufacturers turn to superfinishing not only to reduce friction and wear but also to increase the fatigue life of the gears. One such technique was developed as part of the Power Transfer Systems Manufacturing Program sponsored by the U.S. Army and Missile Command [2]. Preliminary tests conducted on sample of superfinished coupons show an improvement in the fatigue life of 300 % over samples fabricated using conventional processing methods [3]. The proposed work is to develop a new sliding-RCF (S-RCF) test device to provide additional data points on the real benefit of superfinishing on contact fatigue. Brief discussion of contact fatigue is presented in this section along with the review of existing RCF testers.

Contact fatigue issues can be traced back to the railway industry in the 1840s. Other than the railways, gears, and bearings are other components subjected to contact fatigue failure. These parts affect many major industries, including automotive, manufacturing, and aerospace. Contact fatigue is the gradual wear that results from two surfaces directly contacting each other; thus, a material's contact fatigue strength is affected by numerous factors from operational and environmental to process-induced conditions. The environmental factors are contacting force, sliding or slip ratio between the two surfaces, lubrication type, lubrication regime, and surface temperature. The most obvious environmental factors affecting a material's contact fatigue life are the contact force and the slip ratio. The magnitude of the force and the slip ratio determine the intensity and nature of the stress field at the point of contact. The slip ratio is defined as the ratio of the relative velocities of the contacting surfaces. All conditions being the same, this ratio will control the amount of the tangential force between the two contacting surfaces. The process-induced factors include the surface roughness, microstructure purity, heat treatment, and the residual stresses in the material. Consequently, a design of contact fatigue investigation equipment must incorporate careful monitoring of these various factors.

Due to the lack of knowledge and information about the basic mechanisms of contact fatigue failures, different industries use different terminologies to

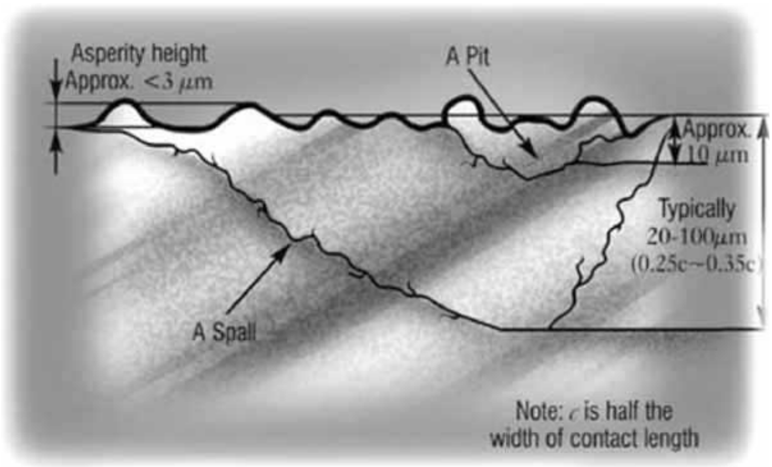

FIG. 1—*Pitting and spalling.*

describe this failure mode. In the present paper, the definitions and terminology used are those of American Society for Metals (ASM) International. ASM International states that the various terminologies can be categorized into two failure types and two contact fatigue failure modes [4]. The two failure types [5], shown in Fig. 1, for contact fatigue are macropits (large pits) and micropits (small pits). The failure modes for contact fatigue are subsurface-origin (SS-O) failure and surface-origin (S-O) failure. SS-O failure modes form macropits and can be separated into two classes. The two classes are inclusion originated (IO) and subcase fatigue. IO macropits develop in random locations where a defect in the bulk material is present, such as an inclusion or microstructure alteration. Subcase fatigue macropits originate at the interface of the case/core where the case hardness and core strength are lower than the Hertzian shear stress field. S-O pits result from asperity (surface roughness changes) and tractive (pulling) forces acting on defects or surface discontinuities on the surface or in the immediate subsurface. The three classes of S-O failure modes are point-surface origin (PSO), geometric stress concentration (GSC), and micropitting. PSO failure forms random macropits like IO macropits; however, the PSO macropits originate on the surface and have no inclusion as an initiation site. GSC macropits result from misalignments, deflections under loading, and contact geometries, which increase the Hertzian shear stress field at the surface. Micropitting occurs at low operating speeds when a low viscosity lubricant is used and a thin elasto-hydrodynamic lubrication (EHL) layer is present. The onset of micropitting is a glazed surface due to plastic deformation that contains microscopic cracks. If severe enough, micropitting can lead to macropitting.

The failure modes occur when the Hertzian stress field is greater than the material's strength. Since the significant stress in contact fatigue is the alternating shear stress, the shear strength of the material is important (Fig. 2). In a pure rolling condition, the plane of maximum shear stress is slightly below the

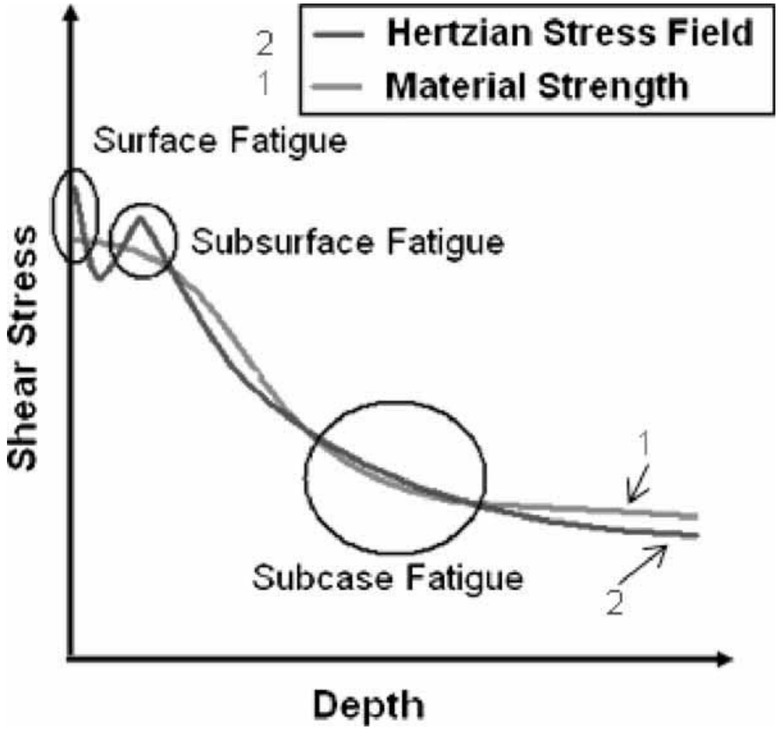

FIG. 2—*Hertzian stress distribution for different contact fatigue failure modes.*

surface, but with a sliding condition, the frictional forces and temperature change increase the magnitude and distribution of the shear stress field.

The contact fatigue failures described above have been somewhat investigated using experimental methods. Several contact fatigue testing devices are available in the world today. However, no standard method exists for designing a contact fatigue test machine; each tester is often developed for a specific application. Therefore, the parameters controlled and investigated vary for each machine. A summary of the many different types of RCF testing methods and a brief description of their capabilities can be found in literature. A few of the available testers are presented here in more detail.

Figure 3 is the picture of the gear test apparatus located at the Glenn Research Center [6]. The NASA tester uses a gear as the test specimen. The test gears are offset to allow four sets of fatigue tests to be performed on each set of gears. Since gears are being used, the sliding ratio cannot be varied or controlled. Loading is applied gradually and controlled by adjusting the hydraulic pressure, which applies a breaking torque to one of the shafts of the meshing gears. Lubricated or dry friction testing can be performed at speed around 10 000 r/min. Crack detection is accomplished visually and/or by using a vibration monitoring system.

The R-SCF tester [7] at Penn State University uses a round cylinder speci-

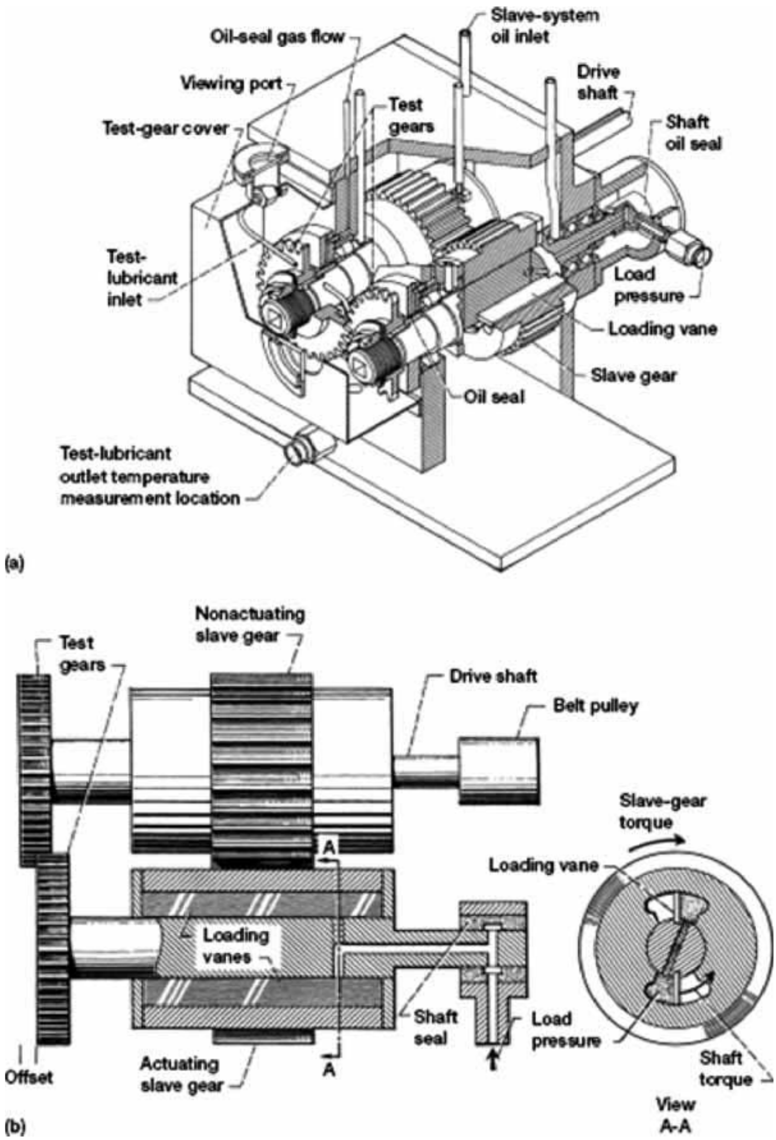

FIG. 3—*NASA Glenn Research Center's gear test apparatus.*

men at a speed of 1330 r/min with the load applied hydraulically on the roller, as shown in Fig. 4. The slide ratio between the roller and the specimen is varied by changing the gears on each of the shafts. No information in the literature was found as to how failure is defined or detected on this test rig.

The high pressure twin disk (HPTD) test device in Fig. 5 is used to determine friction coefficients at different slip ratios. Loading is applied by pushing on one disk, while the other is held in place with a maximum load and speed

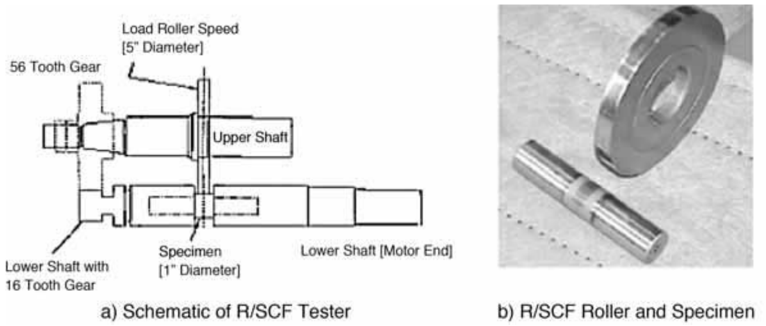

FIG. 4—*Penn State's Gear Research Institute rolling/sliding contact fatigue tester.*

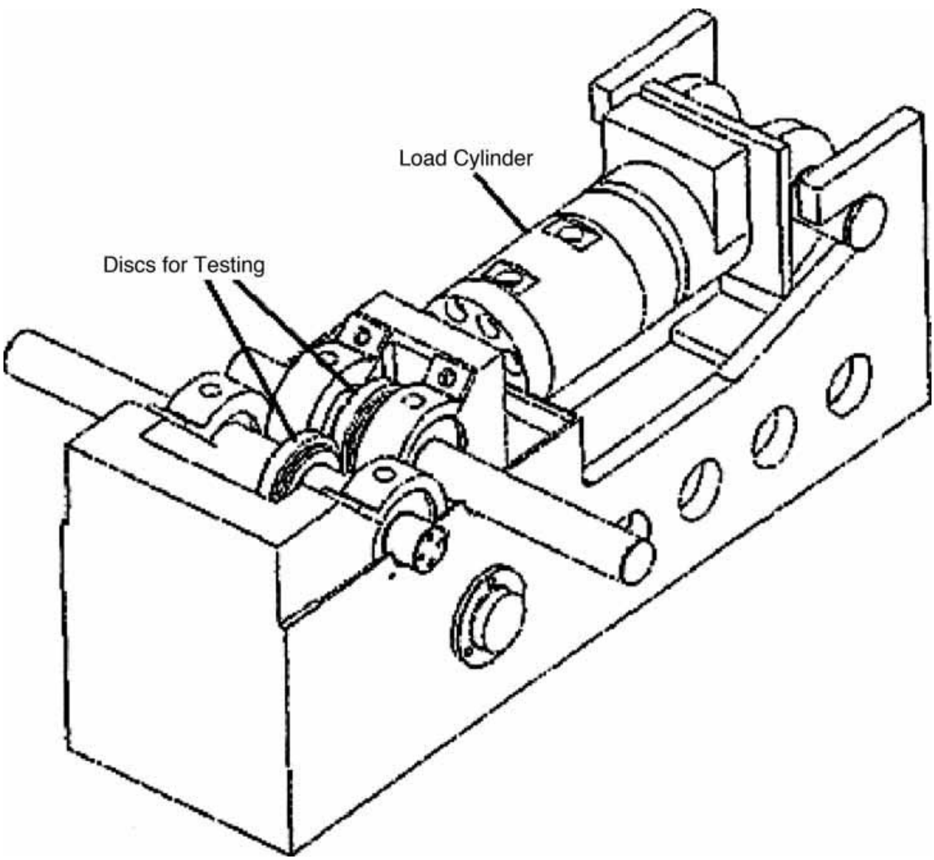

FIG. 5—*HPTD test device loading frame.*

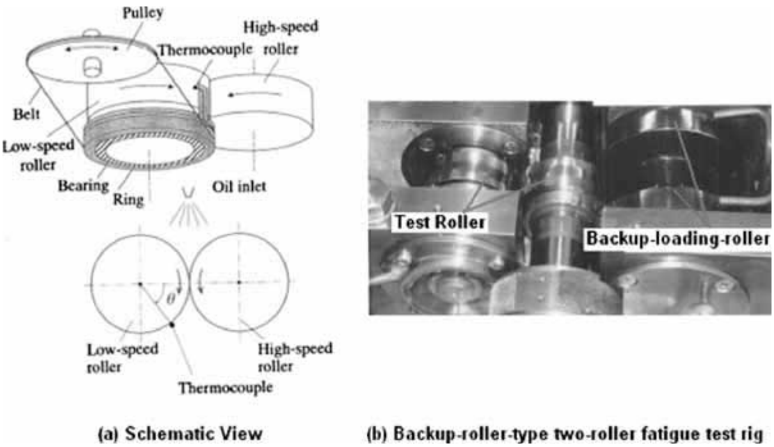

FIG. 6—*BRT2R fatigue test rig.*

capacity of 11 000 N and 6000 r/min, respectively [8]. Also lubrication temperature can be controlled using a heater and cooler.

The backup-roller-type two-roller [9] (BRT2R) fatigue test rig in Fig. 6 was used to study the effect of surface temperature on a material's fatigue strength. The BRT2R tester uses two disks of similar material, one as the roller and the other as a specimen. The shafts are turned using a belt and pulley system at a speed of 2000 r/min. It is unclear as to how the load is applied.

The ZF-RCF [10] tester shown in Fig. 7 uses three rollers to contact one

FIG. 7—*ZF-RCF tester.*

specimen. Each revolution of the specimen results in three load cycles, thereby decreasing testing time. The ZF-RCF can turn the specimen at a maximum speed of 3600 r/min. Loading is applied by pressurizing the oil, meaning the specimen is submerged in oil and the compartment must be sealed tight. The oil pressure is controlled by a servo-hydraulic valve, allowing variable loading to be applied during a test. Since gears are used to turn the roller shafts, different gearings will create different slip ratios between the rollers and specimen. The detection method used for the ZF-RCF is a non-destructive eddy current method.

Several other contact fatigue testers and test methods are available, which have not been mentioned in this paper. The machines discussed were primarily designed for the purpose of simulating gear contact. Other testing devices exist to simulate bearing and railway conditions. Some testers are designed to simulate contact fatigue in the most general conditions.

S-RCF Design

The section above described a few of the many RCF testers around the world or in literature. However, there is no detailed description at a level that will allow other researchers to build on the experience of these test rigs. Thus the objective of this paper is to provide as much as possible development details for the present S-RCF tester. Three major components are described herein in terms of (1) mechanical systems, (2) control systems, and (3) data acquisition systems. The key requirements for the new tester are as follows: First, each specimen must be tested in a fairly reasonable time; second, the tester must perform tests from dry to submerged lubrication conditions; and third, the Hertzian stresses in the most popular gear steel must reach at least 2.5 GPa, and finally continuous slip ratio values must be achievable.

Mechanical System

Several known factors affecting a material's contact fatigue strength were previously discussed. The quality of a contact fatigue tester depends upon its ability to accurately control and monitor the operational conditions. The mechanical system involves some of these factors. It is composed of the main structure, the power train, the lubrication system, and the loading mechanism. The first requirement of short test time is related to the rotational speed of the specimen and the number of contact points as stated by the expected failure time E_{ft} in hours of Eq 1 and Fig. 8

$$E_{\mathrm{ft}} = \frac{C_f}{\omega_s N_{\mathrm{cp}} \times 60} \tag{1}$$

where:

N_{cp} = number of contact points,
C_f = cycle to failure set to a maximum of 30×10^6 load cycles, and
ω_s = specimen speed in r/min.

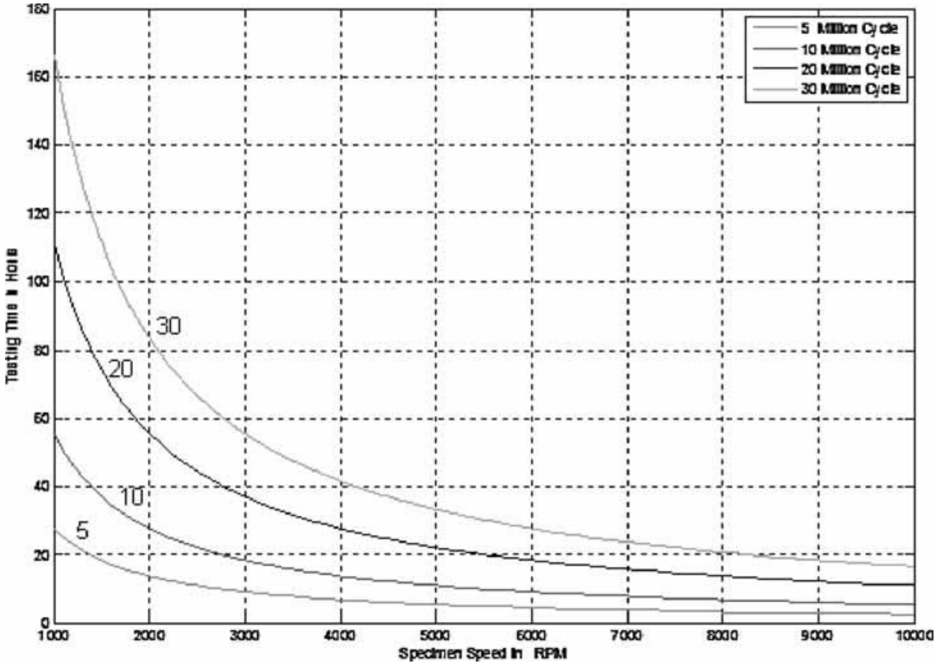

FIG. 8—*Testing time required for a number of load cycles using a three-contact point.*

From the figure, a testing time of about 24 h corresponding to a specimen speed of 3000 r/min is selected. Borrowing the configuration from the ZF-RCF, three contacts points are used, and the specimen and roller sizes are selected (see Sliding-Rolling Contact Fatigue Development Data Summary section).

To ensure that the 2.5 GPa Hertzian stress requirement is met without straining the machine to its limit, 3.0 GPa Hertzian pressure and the dry lubrication requirements are used to determine the power train design parameters. First the required radial load is calculated from Eq 2

$$F_R = \frac{\pi R L \sigma^2}{E} \tag{2}$$

where:

L = contact length,

σ = Hertzian pressure between the specimen and the roller, and

R and E = mean radius and mean Young's modulus, respectively, given by Eq 3

$$\left| \begin{array}{l} \dfrac{1}{R} = \dfrac{1}{R_s} + \dfrac{1}{R_r} \\ \dfrac{1}{E} = \dfrac{1 - \upsilon_s^2}{E_s} + \dfrac{1 - \upsilon_r^2}{E_r} \end{array} \right. \tag{3}$$

where:

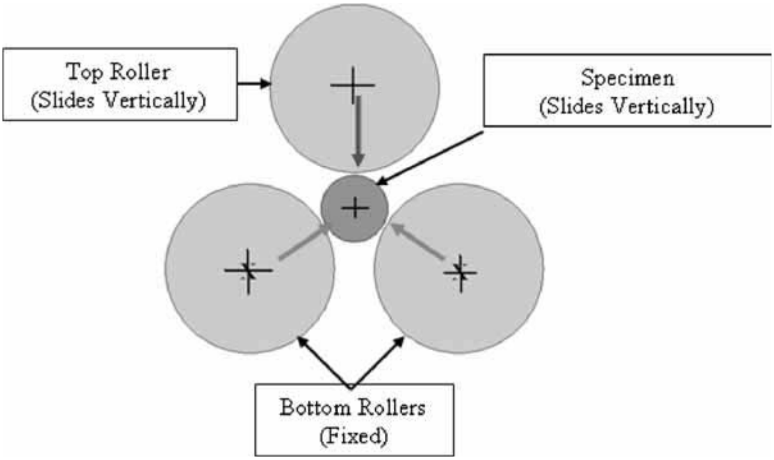

FIG. 9—*Diagram of symmetrical spacing (120° apart) of the rollers around the specimen.*

ν = Poisson's ratio and
subscripts stand for specimen and roller.
Using Fig. 9, the speed relationship is given by Eq 4

$$\omega_r = \frac{R_s}{R_r}\omega_s \tag{4}$$

where:
ω_r = speed of the rollers and
ω_s = speed of the specimen.

The tangential force F_T due to rolling friction and sliding friction can be approximated by Eq 5. From this equation, the required power at the roller and specimen shafts is calculated. The power at the specimen shaft for a single drive motor is evenly divided between the two electric motors as shown in Eq 6 for pure rolling and Eq 7 for slip plus rolling

$$F_T = \left(\mu + \frac{\bar{\mu}}{R_s}\right)F_R \tag{5}$$

where:
$\bar{\mu}$ = rolling friction and
μ = slip friction

$$P = \frac{3}{2}\frac{\bar{\mu}}{R_s}F_R\omega_s \tag{6}$$

$$P = \frac{3}{2}\left(\mu + \frac{\mu}{R_s}\right)\left(\frac{R_s}{R_r}\mathrm{SR} + 1\right)F_r\omega_s \tag{7}$$

where:

TABLE 1—*S-RCF components summary.*

Sub-System	Component	Description	Manuf./Vender
Mechanical system	Specimen motor	RL & URL2158Z	Reliance Electric
	Roller motor	RL & URL2158Z	Reliance Electric
	Roller gears	Y412	Browning
	Specimen shaft coupler	6408K19/6408K81	McMaster-Carr
	Rollers	117×12.7 mm	Machine shop
	Specimen	$6-35 \times 75$ mm	Machine shop
	Roller shaft	25.4 mm	In house
	Specimen shaft	25.4 mm	In house
	Bearings	FSHR206-18	Peer Chain
	Cylinders	6491KAC	McMaster-Carr
Control systems	Specimen drive	PowerFlex 70-10	Allen-Bradley
	Roller drive	PowerFlex700S-10	Allen-Bradley
	Encoders	SRS660/1024	Stegmann, Inc.
	Temperature sensor	THX-400-NPT-72	Omega
	Pressure sensor	PX209-200G5V	Omega
Fault detection and data acquisition	Data acquisition	TEAC LX-10	TEAC America
	Eddy current monitor	Defactomat EZ 2.828	Foerster
	Eddy current probe	5 mm probe	Foerster

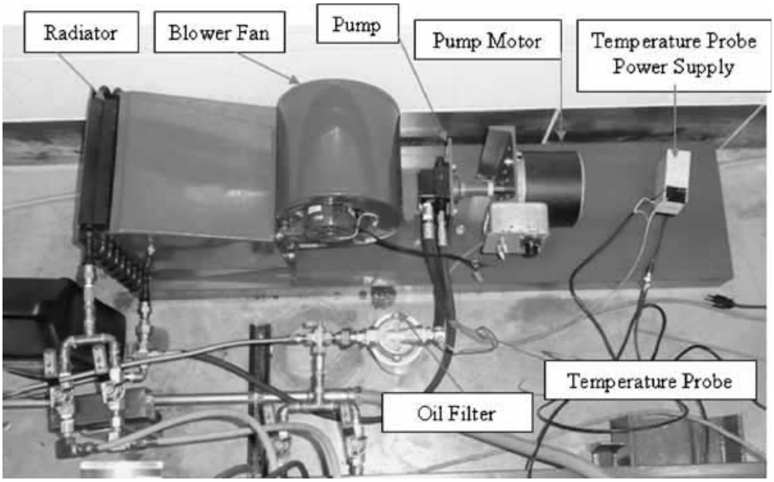

FIG. 10—*Lubrication system for S-RCF tester.*

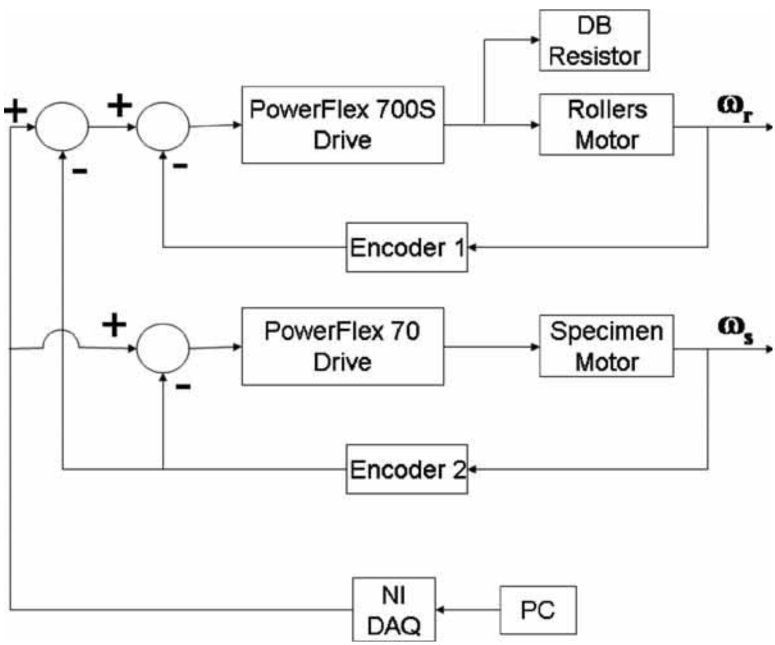

FIG. 11—*Speed control system.*

TABLE 2—*Basic characteristics of common NDI methods.*

	Inexpensive	Portable	Training Skill Level		Part Preparation Required		In Situ Monitoring	Accessible to Probe	Safety Hazard	Sensitivity		Ability to Detect Subsurface
			High	Low	High	Low				High	Low	
Visual inspection	x	x		x		x					x	
Dye penetrant	x	x		x	x						x	
Magnetic particle	x	x			x					x		x
Eddy current		x	x			x	x	x		x		x
Ultrasonic	x	x	x			x	x	x		x		x
X-ray radiography			x			x			x			
Isotope radiography			x			x			x			
Vibration monitoring	x	x		x		x					x	

FIG. 12—*Foerster® Defectomat EZ 2.828 eddy current detection device.*

SR = slip ratio defined in Eq 8 as

$$SR = \frac{R_s \omega_s - R_r \omega_r}{R_s \omega_s} \tag{8}$$

From the above analysis, nominal 20 hp motors and drives would have been ideal for this design in order to account for other type of frictions and inherent errors in material properties. However, for budgetary reasons, a 10 hp system is selected as shown in Table 1, Sliding-Rolling Contact Fatigue Development Data Summary section.

The lubrication system shown in Fig. 10 has two major components: The cooling and the lubrication regime control systems. For the latter, dry and film testing is accomplished by controlling with a valve the flow of lubricant through the nozzles. The oil cooling system uses a fan cooled heat exchanger to control the oil temperature. Finally a pneumatic loading mechanism is selected for the project over a hydraulic system because our facility has readily available compressed air line at about 700 KPa. The summary of the mechanical system can be found in Table 1, Sliding-Rolling Contact Fatigue Development Data Summary section.

TABLE 3—*TEAC channels and test parameters setting.*

TEAC Channel	Channel Description	Monitoring Unit	Voltage Range	Conversion Factor	Units
1	*Y*-component	Defetomat EZ	0–1	1	V
2	*X*-component	Defetomat EZ	0–1	1	V
3	*V*	Defetomat EZ	0–1	1	V
4	Y^2	Defetomat EZ	0–1	1	V
5	Cylinder pressure	Pressure sensor	0–5	277	kPa
6	Oil temperature	Thermistor	0–10	21.091	°C
7	Specimen speed	PowerFlex 700S	−10–10	416.5	r/min
8	Roller speed	PowerFlex 70	−10–10	416.5	r/min

Control System

To deliver accurate speed and slip ratio, the closed loop control system in Fig. 11 is used. The monitor PC runs a central MATLAB/SIMULINK® program that communicates with LABVIEW® and LX-NAVI® to ensure real time monitoring of the test. The operator issues a specimen test speed and slip ratio that is sent to the Allen Bradley PowerFlex controllers via the National Instrument Data Acquisition board. The controllers will execute whatever control scheme such as Proportional-Integral-Derivative, Proportional-Integral, or Proportional-Derivative that has been previously programmed and starts the test. The speed and slip ratio are monitored by the PowerFlex controllers using slave/master [11] relationship to provide electronic gear ratio (EGR). In essence the Power-

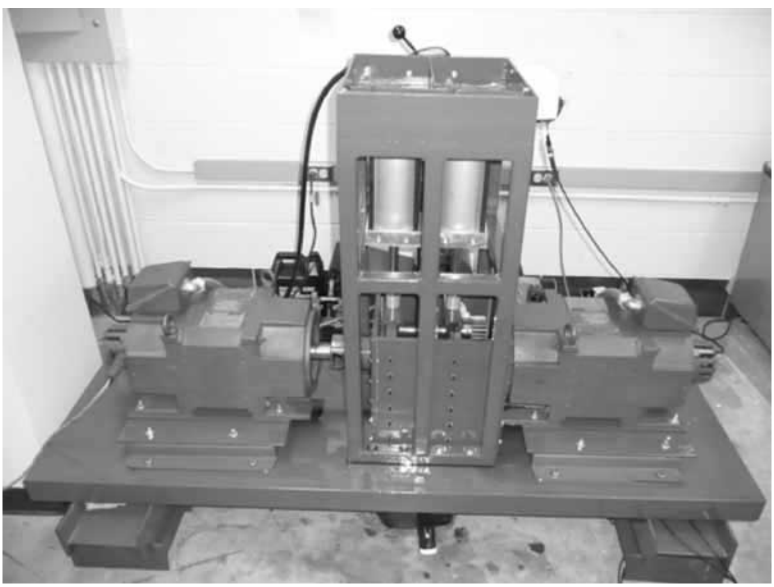

FIG. 13—*S-RCF main structure.*

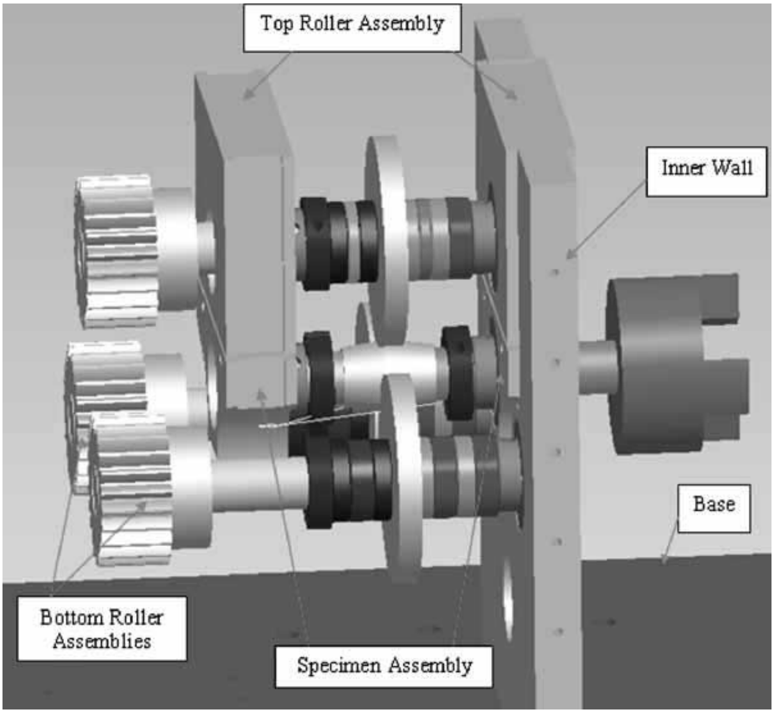

FIG. 14—*Roller and specimen assembly.*

Flex 700s controller has two feedback encoders that receive encoder signal from the specimen and rollers motors, respectively. It uses these two signals to control the speed of the specimen that can be accelerated or decelerated regardless of the original speed command to maintain the prescribed slip ratio, which has priority over the speed. In general a drive controls an electric motor's speed by monitoring the level of the frequency and voltage or current that it is delivering to the motor. However, in this application, the two motors are mechanically connected through the specimen and rollers; therefore, there is a tendency of the fast motor to entrain the slow motor or vice versa. When this happens, the slip ratio or the EGR will not be maintained. This problem is addressed by providing continuous dynamic braking. When the motor shaft is accelerated by mechanical means, for example, fast specimen, it generates energy that is sent back to the drive, which will normally cause a fault if the drive has no dynamic brake capability. The PowerFlex 700s has a small light duty internal dynamic braking resistor for quick stopping or intermittent deceleration. In this application, because continuous braking is required for a nonzero slip ratio; the internal resistor is replaced with an external continuous duty dynamic braking resistor.

Fault Detection and Data Acquisition

The main issue with any RCF test rig is the detection of the first crack. One could stop the tester after a certain number of load cycles, inspect the samples

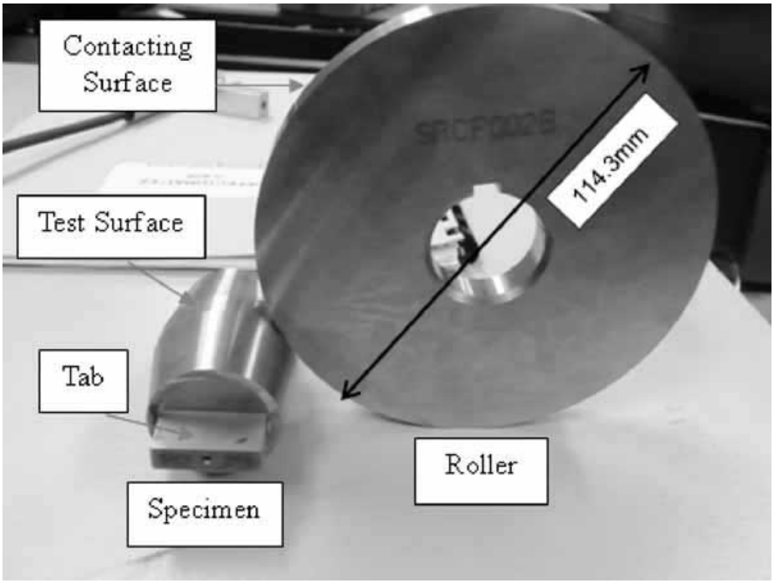

FIG. 15—*Specimen and roller for S-RCF tester.*

for cracks, and restart the machine if no failure or crack is observed. This method would be impractical given the fact that it is impossible to predict the occurrence of the first crack or surface damages due to the stochastic nature of fatigue failure. Fortunately, there are many techniques available for monitoring test specimens, such as vibration sensors, microphones, ultrasound, Barkhausen effect, eddy currents, etc. Table 2 describes basic characteristics of common Non-Destructive-Inspection (NDI) methods. Vibrations monitoring is the cheapest and most widely used technique; however, we decided to use eddy

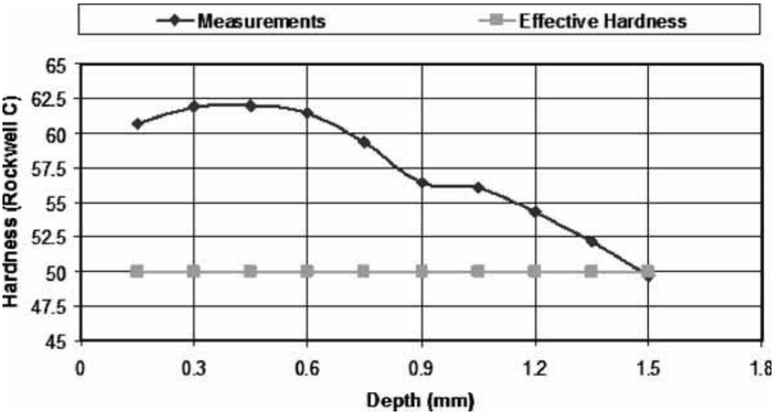

FIG. 16—*Hardness measurements for verifying the case depth.*

TABLE 4—*Heat treatment and surface finish specifications for AISI 8620.*

Property	Value
Hardness	58–62 HRC
Effective hardness	50 HRC
Case depth	0.940–1.40 mm
Surface carbon	0.85 ± 0.05
Average roughness	0.4–0.5 μm
Microstructure	Martensite + austenite (retained austenite: 10 %; other: 5 %)

current in this application because it can detect small cracks that do not necessarily create measurable vibrations especially when the samples are superfinished [12]. The eddy current detection system used by the S-RCF is the Foerster Defectomat® EZ 2.828 along with the differential probe, as shown in Fig. 12. This inspection system allows for eight different inspection frequencies. Material to be inspected can pass beneath the probe at a maximum speed of 120 m/s at 3000 r/min; the S-RCF specimen is only traveling at approximately 6 m/s.

As mentioned in the introduction, many factors are involved in contact failures; therefore, a careful monitoring of these factors requires a reliable multi channels data acquisition system. A TEAC LX-10 recording unit is used for the S-RCF (see Table 3 for recorded parameters and settings) to record data directly to the PC for real time processing as described in Testing and Results section.

Sliding-Rolling Contact Fatigue Development Data Summary

The three major subsystems of the S-RCF, i.e., the mechanical system, the control system, and the fault detection and data acquisition system, are summarized at the components level. It is the authors hope that the provided details are sufficient enough for the reconstruction or upgrading of the present S-RCF. The fully assembled mechanical system is shown in Fig. 13 with the specimen motor on the left. The details of Fig. 14 are provided to show the internal layout of the rollers and specimen. Finally Fig. 15 provides a view of the actual specimen and roller along with their contacting surfaces. The specimen is attached to the drive shaft with the tab and secured by a ring. Table 1 contains all the major components that have been used including dimensions and manufacturers name and part numbers.

Testing and Results

The stochastic character of fatigue failure makes relative the results obtained with any fatigue test rig including the S-RCF. Thus a rigorous test procedure [12] must be performed to establish bench mark data before making relative measurement intended to establish design tools such as stress-life curves. The results presented here are simply intended to establish the performance of the

TABLE 5—*Roughness measurements of randomly chosen specimens and rollers.*

			Specimen/Roller Number					
			13	4	3	4A	4B	4C
Axial Ra	Individual	Average (μm)	0.388	0.347	0.342	0.288	0.180	0.238
		95 % confidence interval (μm)	±0.058	±0.046	±0.085	±0.016	±0.027	±0.018
	Group	Average (μm)		0.359			0.235	
		95 % confidence interval (μm)		±0.063			±0.135	
Circumferential Ra	Individual	Average (μm)	0.276	0.264	0.272	0.152	0.117	0.146
		95 % confidence interval (μm)	±0.039	±0.062	±0.123	±0.054	±0.014	±0.042
	Group	Average (μm)		0.271			0.138	
		95 % confidence interval (μm)		±0.014			±0.047	

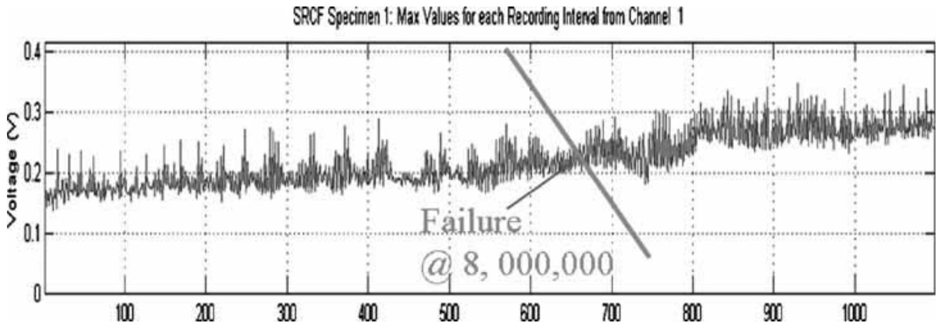

FIG. 17—*Screening plot.*

tester as an electromechanical device. Therefore, the S-RCF was tested for mechanical, instrumentation, and software integrity. A typical test starts with the verification of the properties and quality of the rollers and specimen samples. The physical dimensions are checked for tolerance specifications and the roughness of the surfaces is recorded using a Surfcom 480A profilometer. The test samples are manufactured along with a test bar (flat sample with the same machining, heat treatment, and surface quality as the specimen and rollers), which is used to determine case depth and microstructure of the parts. The case depth is determined by making several hardness measurements in a line starting near the edge of the cross-section of the test bar and moving incrementally toward the center. The measurements stop when the effective hardness (the hardness of the non-carburized core) is reached as shown in Fig. 16. The microstructure is checked by polishing and etching the surface with different etchants. The treated surface is then placed under a scanning electron microscope with the capability to do electron dispersion spectroscopy (EDS) analysis. The EDS determines the microstructure of the surface. Tables 4 and 5 show typical testing data for a AISI 8620 specimen. Once all the parts are checked, the machine is assembled and the test is started. The control system monitors the test and stops the machine at a crack initiation. Figure 17 shows the screening data at failure. The test rig stopped after the voltage was out of specifications. The failed specimen is shown in Fig. 18.

Conclusion

A three disk S-RCF has been developed and tested. The device uses two servo motors to respectively spin the specimen and the rollers. Two drives are used in close loop control with slave master setup to provide effective EGR and thus continuous slip ratio between the specimen and the rollers. A nonzero slip ratio results in the generation of "negative energy" that is absorbed by the dynamic brake resistor connected to one of the drives. One drawback of the EGR is the extra power required for the braking and the waste of that power in heat. Failure detection and monitoring of the specimen are achieved by an eddy current sensor, the output of which is continuously compared to a preset threshold. A specimen failure signal is issued when this threshold is reached or

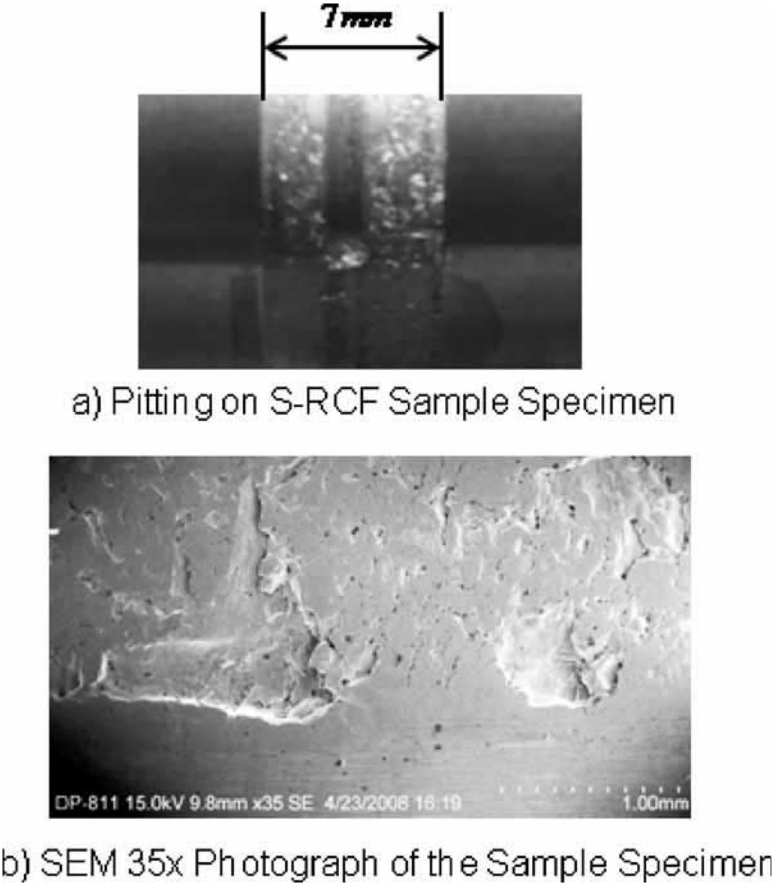

FIG. 18—*Failed specimen.*

exceeded. Two pneumatic cylinders are used to load the specimen by pressing on the shaft of the top roller, which transfers the load to the specimen and the bottom rollers. A pump circulates the lubricant from the test enclosure to an external fan cooled heat exchanger to ensure proper test temperature. Finally the whole operation is supervised by a MATLAB program to ensure proper test speed, oil temperature, specimen load, and data collection.

A mechanical integrity and software performance test was performed on the most common gear steel specimen AISI 8620. The results indicate that the tester design is robust; however, the tester can be improved to include pressurized lubricant or full EHL testing and also the possibility of reusing the regenerative energy from the motors when nonzero slip ratio is present.

Acknowledgments

Requesting Agency Representatives: Bob Dillon and Maira Senick U.S. Army Benét aboratories, Watervliet. The Engineered Surfaces for Weapons System

Life Extension Program is sponsored by the Defense Technical Information Center DTIC-AI John J. Kingman Road, Ste 0944, Fort Belvoir, VA.

References

[1] Stephens, R. I., Fatemi, A., Stephens, R. R., and Fuchs, H. O., *Metal Fatigue in Engineering*, 2nd ed., John Wiley & Sons, Inc., New York, 2001.

[2] Power Transfer Systems Manufacturing Program, U.S. Army Aviation and Missile Command Arsenal, Contract No. DAAH23-00-C-R232.

[3] Paul, N. and Ali, M., *AMOTIAC Q.*, Vol. 7, No. 1, 2003.

[4] ASM International Handbook Committee, "Failure Analysis and Prevention," *ASM Handbook*, ASM International, Materials Park, OH, 2002, Vol. 11.

[5] Kuhnell, B. T., "Wear in Rolling Element Bearings and Gears–How Age and Contamination Affect Them," *Machinery Lubrication*, September/October 2004, from Machinery Lubrication Magazine Online, http://www.machinerylubrication.com/article_detail.asp?articleid=664&relatedbookgroup=Lubrication (Last accessed Mar. 10, 2008).

[6] Krantz, T. L., Alanou, M. P., Evans, H. P., and Snidle, R. W., "Surface Fatigue Lives of Case-Carburized Gears with an Improved Surface Finish," *Trans. ASME, J. Tribol.*, Vol. 123, 2001, pp. 709–716.

[7] Niskanen, P., Manesh, A., and Morgan, R., "Reducing Wear with Superfinish Technology," *AMPTIAC Q.*, Vol. 7(1), 2003, pp. 3–9.

[8] Kleemola, J. and Aara, A. L., "Development of a High Pressure Twin Disc Test Device for the Simulation of Gear Contact," *Finn. J. Tribol.*, Vol. 25, 2006, pp. 8–17.

[9] Deng, G., Nakanishi, T., and Kato, M., "Surface Temperature Calculation and its Application to Surface Fatigue Strength Evaluation," *J. Mech. Des.*, Vol. 124, 2002, pp. 805–812.

[10] Hoffman, G. and Rice, J. A., "Initiation and Propagation of Cracks in Wrought and Sintered Steels During Rolling Contact Fatigue," *Adv. Powder Metall. Part. Mater.*, Vol. 3(3), 2005, pp. 176–200.0002-7820

[11] Rockwell Automation, "PowerFlex® 700S High Performance AC Drive—Phase II Control," *Publication* 20D-UM006F-EN-P, January 2007.

[12] Baldev, R., Jayakumar, T., and Thavasimuthu, M., *Practical Non-Destructive Testing*, 2nd ed., Woodhead Publishing Limited, Cambridge, 2002.

FATIGUE CRACK GROWTH

Reprinted from JAI, Vol. 6, No. 9
doi:10.1520/JAI102617
Available online at www.astm.org/JAI

M. Carboni,[1] *L. Patriarca,*[2] *and D. Regazzi*[2]

Determination of ΔK_{th} by Compression Pre-Cracking in a Structural Steel

ABSTRACT: The traditional experimental procedures used to generate thresholds (known as "ΔK-decreasing" and "constant K_{max}") have been challenged because it seems they affect the experimental results, sometimes in a non conservative way. In order to fix this problem, different experimental procedures ("compression pre-cracking constant amplitude" and "compression pre-cracking load reduction" (CPLR)) based on a compression-compression pre-cracking of fracture mechanics specimens have been proposed. Up till now, such procedures are not yet wide-spread between fracture mechanics experimentalists. In particular, due to the recent introduction, CPLR has been applied only to few cases: Al alloys, Ti alloys, and high strength steels (ultimate tensile strength>1300 MPa), all in the shape of *M(T)* or *C(T)* specimens subjected to positive stress ratios. The present paper deals with the application of these novel "compression pre-cracking" procedures, with particular attention to CPLR, to the unexplored and technically very important case of the structurally mild A1N steel grade (very commonly used to produce European railway axles) in the shape of SE(*B*) specimens subjected to stress ratios varying between −2 and 0.85.

KEYWORDS: threshold stress intensity factor range, compression pre-cracking, A1N steel grade

Introduction

From a "damage tolerant" point of view [1], the reliable characterization of crack propagation behavior of materials is one of the most critical points, together with the performance of the adopted non-destructive testing technique

---

Manuscript received June 15, 2009; accepted for publication August 4, 2009; published online September 2009.

[1] Dept. of Mechanical Engineering, Politecnico di Milano, Via La Masa 34, I-20156 Milano, Italy (Corresponding author), e-mail: michele.carboni@polimi.it

[2] Dept. of Mechanical Engineering, Politecnico di Milano, Via La Masa 34, I-20156 Milano, Italy.

Cite as: Carboni, M., Patriarca, L. and Regazzi, D., "Determination of ΔK_{th} by Compression Pre-Cracking in a Structural Steel," *J. ASTM Intl.*, Vol. 6, No. 9. doi:10.1520/JAI102617.

and the knowledge of service loads [2,3], for the estimation and the maintenance of the structural integrity of mechanical components during service. Moreover, since it is licit to assume that the largest part of the fatigue life of a mechanical component is spent in the near-threshold region, the reliable generation of threshold stress intensity factor (SIF) ranges is particularly critical.

The traditional experimental procedures used to generate thresholds are reported in ASTM E647-05, "Standard Test Method for Measurement of Fatigue Crack Growth Rates" [4] and are known as "ΔK-decreasing" and "constant $K_{\max}$." Such procedures have been challenged [5–8] because it seems they influence the experimental results they generate. One of the most popular evidence of this fact is the observation that small cracks propagate at SIF levels below the long crack thresholds [9] derived by means of these traditional procedures. In particular, the ΔK-decreasing has shown, for some materials, a sensibility to the growth rate reached by the crack at the beginning of the load reduction procedure: ASTM E647-05 [4] suggests to begin such a procedure at a 10^{-8} m/cycle, but Refs 6–8 have shown that such growth rate happens usually at a SIF level high enough to introduce significant load interaction effects (mainly due to plasticity-induced crack closure [10]) and, consequently, to arrest growth too early, so generating high and non conservative threshold values. In the case of constant $K_{\max}$, the sensibility seems to be related to the maximum applied SIF: In this case, depending on the considered material, the higher is the applied constant $K_{\max}$, the lower is the generated threshold.

In order to fix these problems related to the application of a load reduction technique, a different experimental procedure [5] is being more and more adopted based on a pre-cracking stage of fracture mechanics specimens, obtained by the growth of short cracks under cyclic compression [11], followed by a stabilization step of crack growth and then proper load programs able to generate threshold values in a condition where load interaction effects are absent or minimal. Such proper load programs are (i) "compression pre-cracking constant amplitude" (CPCA) and (ii) "compression pre-cracking load reduction" (CPLR), where the load reduction technique is carried out so as to minimize the interaction effects. Figure 1 shows a schematic of the compression-compression pre-cracking methods for experimentally generating thresholds. More details about the procedures are given in the following, and it should be remarked that the CPCA procedure is being (rarely) applied since the mid 1990s [5], while the CPLR one has been introduced much more recently [12].

First, compression-compression pre-cracking in order to generate a pre-crack at the V-notch of the fracture mechanics specimen. In particular, the first load cycle causes the material to yield in compression in the region of the notch, resulting then in a tensile notch-tip residual stress field when the specimen is unloaded [13]. Subsequent compression-compression fatigue loading nucleates the pre-crack that propagates, making the tensile residual stresses to gradually relax until the local driving force diminishes below the crack growth threshold and the pre-crack finally arrests. In this way, a closure-free and naturally non-propagating crack is generated at the notch-tip of the specimen.

The pre-crack must then be grown several compressive plastic-zone sizes in order to stabilize crack propagation by eliminating the influence of both the stress concentration of the notch and the tensile residual stresses [8]. As dis-

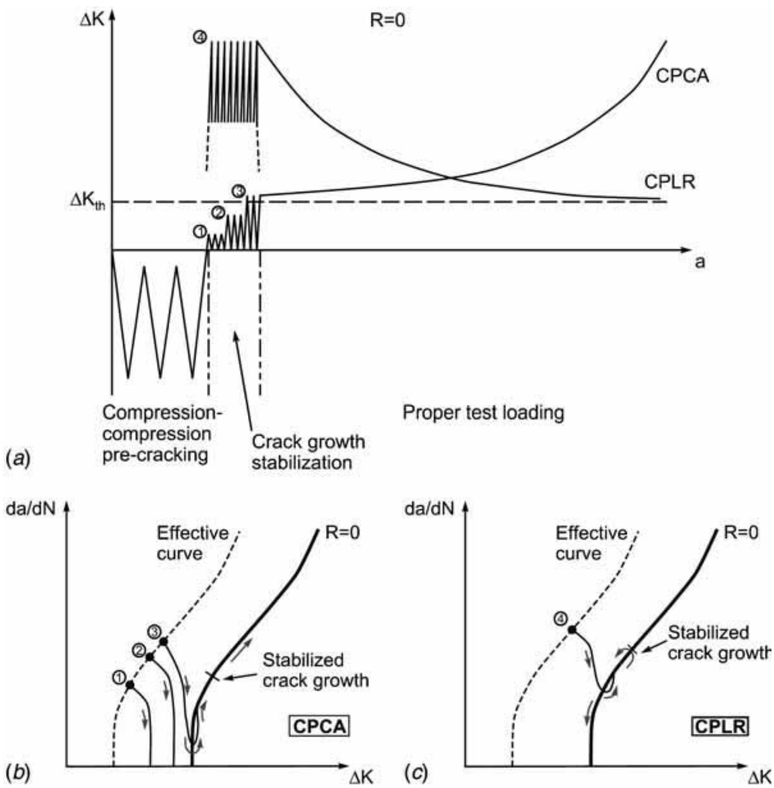

FIG. 1—*Compression-compression pre-cracking methods to experimentally generate thresholds:* (*a*) *Schematic of the experimental procedures at R=0;* (*b*) *CPCA; and* (*c*) *CPLR.*

cussed above, the obtained pre-crack is closure-free, so crack growth stabilization is related to the crack extension to be achieved in order to naturally develop the proper closure mechanisms and to move from the effective crack growth curve to the one of the considered stress ratios (Fig. 1(*b*) and 1(*c*)). Considering the case of CPCA testing, the stabilization is carried out applying small amplitude tensile load cycles: If this amplitude defines a SIF lower than the threshold, the crack becomes non-propagating after some cycles (cases 1 and 2 in Fig. 1(*a*) and 1(*b*)) and the load must be slightly increased (a suggested value is 5 % [6]). When the load is high enough, the crack starts growing (case 3 in Fig. 1(*a*) and 1(*b*)) in steady-state conditions corresponding to the applied stress ratio. Results can then be considered "valid" only when crack growth is stabilized and the crack tip is far enough from the notch-tip. In the case of CPLR, the tensile applied load cycles are characterized by an amplitude higher than the threshold (case 4 in Fig. 1(*a*) and 1(*c*)): When the crack tip is far enough from the notch-tip and the crack growth is stabilized, a ΔK-decreasing procedure is applied in order to generate the threshold. Such load reduction can so be applied from growth rates significantly lower (10^{-9} m/cycle or lower) than those suggested in ASTM E647-05, thus minimizing load interaction effects.

Theoretically, CPCA is the best procedure and should be preferred because load interaction effects are completely neglected during the whole experimental test. Unfortunately, some disadvantages make CPLR competitive, too: (i) The crack growth curve in the near-threshold region is quite steep, so it can be easily missed, increasing the load amplitude from a step to the subsequent one during a CPCA test; and (ii) it is reported [7] that a CPCA test can be as long as three times (of the order of 3×10^7 cycles for Al alloys) the corresponding CPLR test.

Up till now, compression pre-cracking techniques are not yet wide-spread between fracture mechanics experimentalists. In particular, due to the recent introduction, CPLR has been applied only to few cases: Al alloys, Ti alloys, and high strength steels (ultimate tensile strength (UTS) > 1300 MPa) in the shape of $M(T)$ and $C(T)$ specimens subjected only to positive stress ratios between 0 and 0.7. The present paper deals with the application of compression pre-cracking procedures (particularly CPLR) to the unexplored but technically very important case of the structural mild A1N steel grade ($R_{p0.2} = 365$ MPa and UTS $= 600$ MPa; very commonly used to produce European railway axles [14]), in the shape of SE(B) specimens subjected to a wide range of stress ratios between -2 and 0.85.

Previous Experimental Discrepancies from A1N Steel

The interest of the present authors in CPCA and CPLR is due to the observation of some discrepancies found in the threshold values for long cracks of A1N steel grade at $R = -1$ (the typical service stress ratio of railway axles). The ΔK-decreasing procedure was applied to a series of SE(B) specimens, made in A1N, in order to achieve the threshold values at different stress ratios. Figure 2(a) summarizes the results obtained from the seven tests carried out at $R = -1$; more details can be found in Ref 15. As can be seen, the mean threshold value for long cracks at $R = -1$ could be estimated to be about $\Delta K_{\text{th,LC}} = 13.5$ MPa$\sqrt{\text{m}}$. Moreover, a very high scatter, quantified in 1.6 MPa$\sqrt{\text{m}}$, could be observed and could be expected since wide limits about the chemical composition of A1N steel are provided in relevant standards. It is then worth noting that, for generality, crack growth tests were carried out onto specimens coming from three different batches of A1N steel grade.

A second experimental approach permitted to determine the threshold for long cracks as the asymptotic value of the thresholds obtained from small cracks. In particular, the relationship between the threshold and the dimension of the small defect was experimentally derived defining the so-called Kitagawa–Takahashi diagram [16] shown in Fig. 2(b) (where the defect dimension is given in terms of Murakami's $\sqrt{\text{area}}$ parameter, i.e., the square root of the area of the defects projected on a plane perpendicular to the applied load [17]). More details about this experimental campaign can be found in Ref 18. Results were then fit to the El-Haddad model [19] modified [20] in terms of the $\sqrt{\text{area}}$ param-

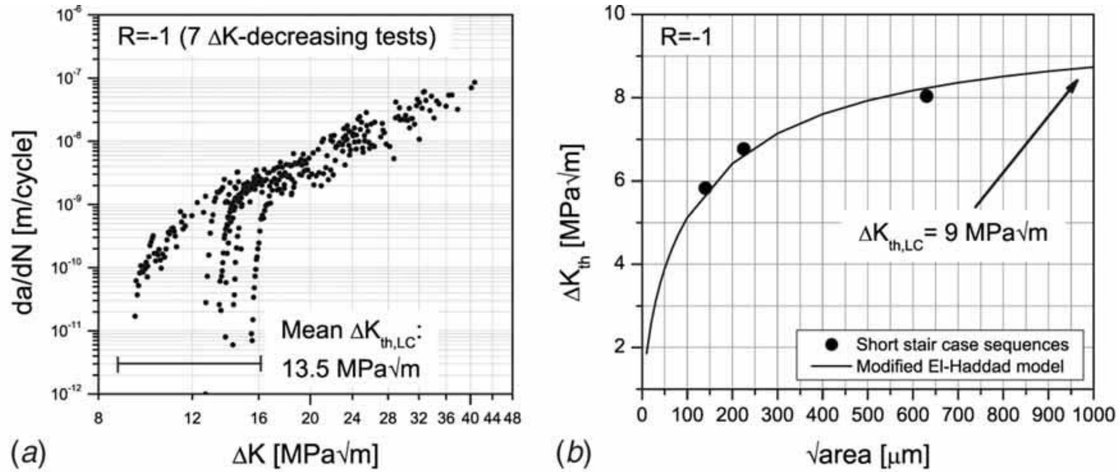

FIG. 2—*Discrepancies in the threshold values of A1N steel grade at R=−1:* (*a*) *Long crack threshold as obtained from ΔK-decreasing tests and* (*b*) *long crack threshold as asymptotic value of the Kitagawa–Takahashi diagram.*

eter. As can be seen, the extrapolation of this model to long cracks (i.e., considering a crack depth of 1000 μm or higher) seems to suggest an asymptotic threshold equal to $\Delta K_{th,LC} = 9$ MPa$\sqrt{}$m. This implies an error, in the application of the traditional procedure and the mean results determined above, equal to about 30 % towards the non conservative side. It should also be noted that the similarity between this asymptotic value and the lowest one of the ΔK-decreasing experimental results can be considered a statistical casualty not to be confused with the mean behavior of the material.

Considering the shape of the crack propagation curves obtained at different stress ratios, it was also possible to observe the so-called "fanning" phenomenon [12], i.e., a varying distance between the points of the curves at different R in the near-threshold and the linear regions. A theoretical explanation of this phenomenon is not available, it should not be present, and it is attributed to the different closure conditions due to the applied experimental procedure present in the near-threshold region with respect to the linear one. This conclusion was also supported by the present authors for A1N [21] by closure measurements and empirical calculations of Schijve's U factor ($U = \Delta K_{eff}/\Delta K$ [22]).

Finally, it is important to add that the "knee" of the sigmoidal propagation curve was also erroneously found to be at different growth rates varying the stress ratio.

Compression Pre-Cracking

Crack propagation tests were carried out on SE(B) specimens characterized by a 12×24 mm^2 section and a notch length equal to 8 mm. Using a dedicated optical device, the average notch radius was estimated to be about 0.12 mm.

Compression pre-cracking was applied to specimens by a four point bending configuration using a servo-hydraulic uniaxial facility with a 100 kN load cell and a dedicated device. The applied load was chosen in order to generate a 130 Nm bending moment at stress ratio $R = 10$ and at a frequency of 30 Hz. This bending value was set in order to generate the naturally arrested pre-crack in 10^6 cycles. This number of cycles was defined by regularly checking the pre-crack growth during the first tests by an optical microscope till its natural arrest. Figure 3 shows an example of pre-crack obtained by the compression procedure. The average surface length of the pre-cracks obtained from all the tested specimens was about 0.3 mm.

At the end of CPCA or CPLR test, all the specimens were broken in liquid nitrogen in order to investigate the fracture surface by the scanning electron microscope (SEM); an example is shown in Fig. 4(a). As expected, pre-cracks showed an average length at the center zone (Fig. 4(b); plane strain condition) shorter than the one observed on the surface (Fig. 4(c); plane stress condition). This perfectly agrees with the traditional theories concerning the plastic-zone extension in plane strain or plain stress conditions.

Finite Element Analysis of Compression Pre-Cracking on SE(B) Specimens

Three-dimensional finite element (FE) analyses of the SE(B) specimen were carried out in order to estimate the plastic-zone size and the tensile residual

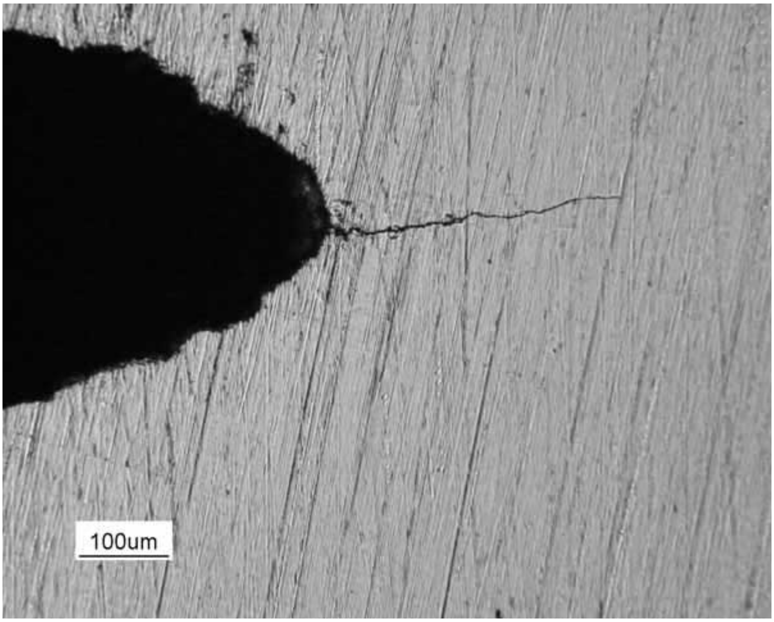

FIG. 3—*Compression pre-cracking of SE(B) specimens by a four point bending test: Example of a closure-free and naturally non-propagating compression pre-crack.*

stresses in proximity to the notch-tip during the first compressive cycle, i.e., at the first maximum and minimum bending moments. The subsequent cycles were not simulated and analyzed since it is demonstrated in literature [23] that the pre-crack driving force is related to the magnitude of the residual stress field established during the first compressive cycle.

The analyses were carried out by means of ABAQUS version 6.7-1 [24]. Figure 5(*a*) shows the numerical set-up in terms of boundary conditions and applied load. The latter was chosen in order to generate a bending moment at the notch equal to $M_{f,\min} = -144.4$ Nm and $M_{f,\max} = -14.4$ Nm, corresponding exactly to the experimental values. Moreover, the modeled geometry took advantage of all the possible symmetries.

The model was subdivided into two regions (Fig. 5(*b*)). The external one, where load and boundary conditions are applied, was discretized using quadratic hexahedral elements of C3D20R type [24]. The notch region, where the material is subjected to plasticization, was discretized using linear hexahedral elements of C3D8R type [24] and was characterized by a refined mesh with an average element dimension equal to $h = 0.015$ mm at the notch-tip.

The plastic behavior of the material was introduced adopting two different hypotheses (Fig. 5(*c*)). The first one consisted of the elastic–perfectly plastic behavior, while the second (here named "FfS") applied an approach proposed in Ref 25, where the stress-strain curve is evaluated by means of the monotonic yield and ultimate stresses of the material in the following way:

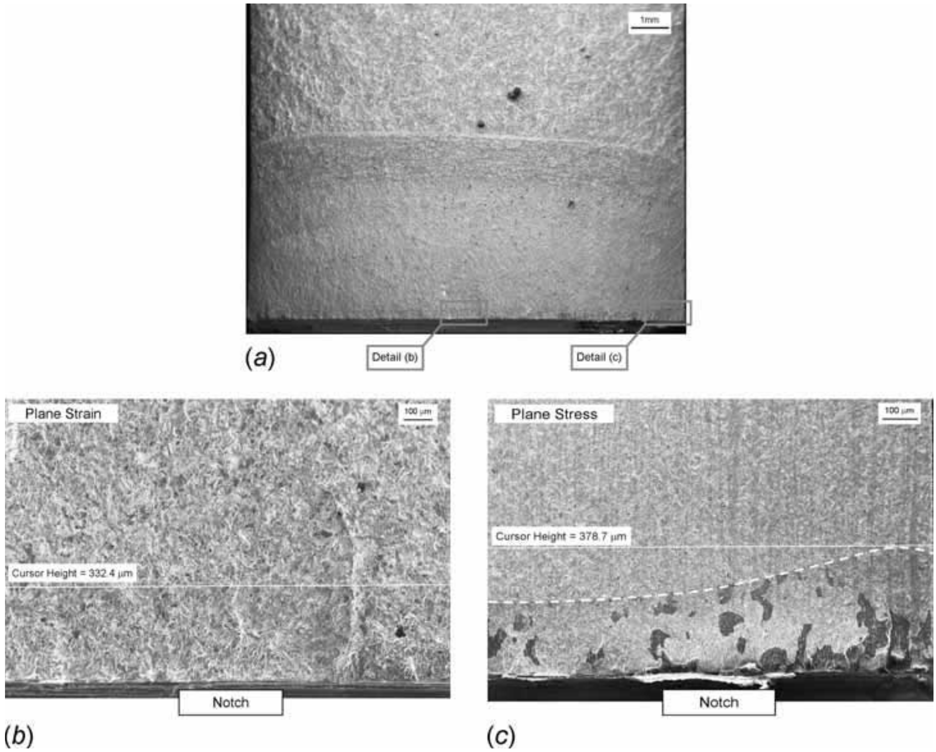

FIG. 4—*SEM observation of a pre-crack:* (*a*) *Global fracture surface;* (*b*) *center specimen* (*plain strain condition*)*; and* (*c*) *surface* (*plain stress condition*).

$$\sigma = R_{p0.2} \cdot \left(\frac{\varepsilon}{\varepsilon_{p0.2}} \right) \cdot N \tag{1}$$

where:

N (strain hardening coefficient) can be determined by the following expression:

$$N = 0.3 \cdot \left(1 - \frac{R_{p0.2}}{R_m} \right) \tag{2}$$

The considered constitutive stress-strain curves were provided to the simulations in terms of true values. The material behaviors so defined are appropriate for modeling the first cycle of an untested material when the monotonic characteristics are considered.

The results are here shown as the nodal average at the integration points and in regard to the Von Mises stress pattern at the maximum bending moment (Fig. 6(*a*)) and the bending stress distribution at the minimum bending moment (Fig. 6(*b*) and 6(*c*)), as typically suggested in the literature [26]. As can be seen from Fig. 6(*c*), the extension of the tensile residual stresses is slightly influenced

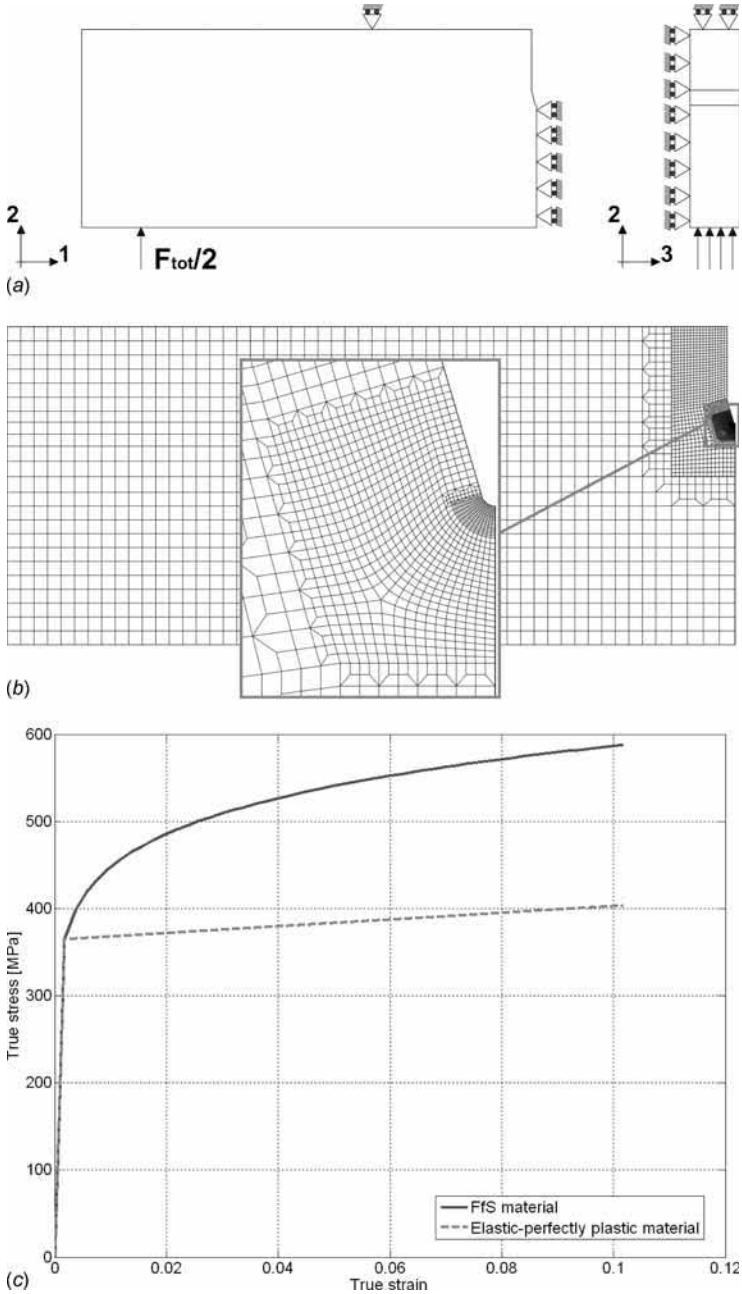

FIG. 5—*FE analysis of a SE*(*B*) *specimen during compression pre-cracking:* (*a*) *Geometry;* (*b*) *adopted mesh; and* (*c*) *modeling of the material.*

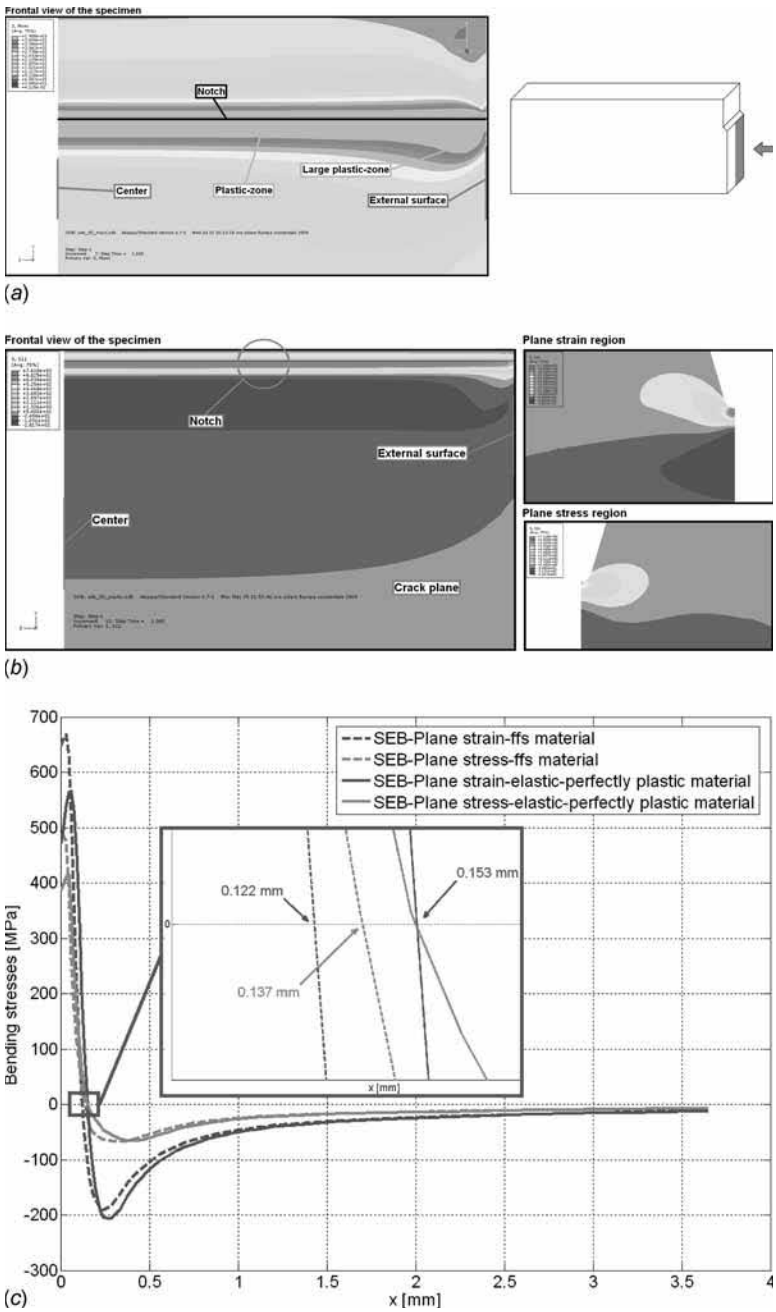

FIG. 6—*FE results:* (*a*) *Von Mises stress pattern in the crack plane at the maximum bending moment;* (*b*) *bending stresses in the crack plane at the minimum bending moment; and* (*c*) *trend of bending stresses at the minimum bending moment.*

TABLE 1—*Comparison between pre-cracks obtained from FE analyses and experiments.*

	Ffs	Elastic–Perfectly Plastic	Experimental Mean Value
Plane strain [μm]	256	285	306
Plane stress [μm]	324	320	319

by the material hypothesis; Ffs material denotes a larger extension in the case of plane stress despite the plane strain region presents a higher stress value at the notch-tip.

An important aspect to underline concerns the extension of the plastic zone in correspondence to the maximum bending moment. As reported in Ref 13, the first cycle determines the extension of the monotonic compressive plastic zone and so the maximum possible extension of the pre-crack. The extent of plasticity has then been estimated by applying the Von Mises yield criterion [26]. Results (Table 1) are in good agreement with the crack length obtained after the experimental compression pre-cracking for both plane strain and plane stress regions. It is worth noting that numerical plane stress values reported in Table 1 were derived from FE analyses as the mean values between the surface plastic-zone dimension and the maximum internal one: This was made in order to consider the average behavior of the plane stress region itself.

From a practical point of view, the implementation of a more refined tensile model for the monotonic behavior of the material (Ffs hypothesis) is not justified; indeed the simplified elastic–perfectly plastic material is sufficiently consistent with the experimental evidence.

Crack Growth Stabilization

As reported before, after compression pre-cracking, it is necessary to propagate the pre-crack from the notch-tip in order to eliminate the influence of both the notch stress concentration and the tensile residual stresses and to generate the correct steady-state closure mechanisms.

In order to check the influence of the notch on the stress field at the crack tip, the FE model already described was enriched introducing a crack at the notch by means of the Zencrack version 7.6 dedicated software [27]. A linear-elastic simulation was then carried out, letting the crack advance and calculating the SIF during propagation. Figure 7(*a*) shows an example of the computed stress field at the crack tip, while Fig. 7(*b*) shows a comparison between the simulated SIF trend and a literature solution [28]. As observed, the influence of the notch seems to last until a crack depth equal to about 8.2 mm (0.2 mm from the notch-tip), considering a tolerance between numerical results and literature suggestion of about ± 0.5 %.

The evaluation of the influence of the tensile residual stresses was instead determined by an empirical approach available in the literature [8]. In particular, the crack propagation Δa from the notch (so including the length of pre-crack) needed for crack growth stabilization can be determined by the expression

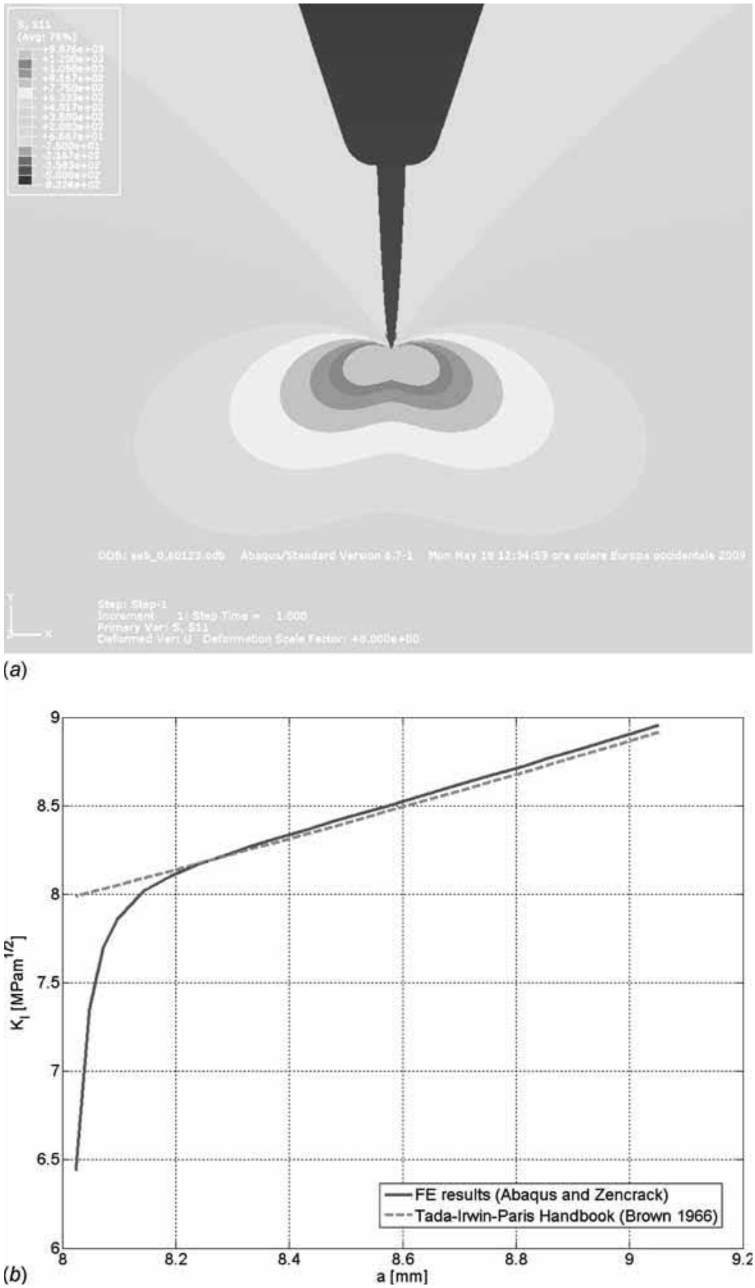

FIG. 7—*Determination of the influence of the notch stress concentration on the crack tip stress field:* (a) *Example of stress field determination and* (b) *comparison between FE results and a literature solution.*

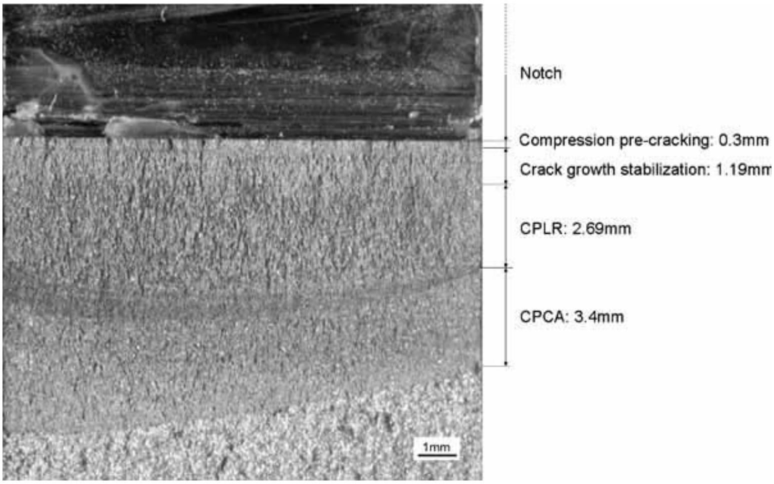

FIG. 8—*SEM analysis of a specimen subjected to CPLR and CPCA.*

$$\Delta a = \beta \cdot (1 - R) \cdot \rho_c \tag{3}$$

where:

R = pre-cracking stress ratio calculated using the absolute values of stress,

β = multiplying factor implicitly or explicitly reported in different references [6–8,12,13,29] and varying between two and four, and

ρ_c = classical cyclic plastic-zone dimension in the case of plane stress

$$\rho_c = \frac{\pi}{8} \cdot \left(\frac{|K_{cp}|}{R_{p0.2}}\right)^2 \tag{4}$$

where:

$|K_{cp}|$ = minimum SIF applied during the pre-cracking procedure.

The application of Eqs 3 and 4 for the present case yields $\rho_c = 790\ \mu$m and, considering some values for the β parameter, $\Delta a_{\beta=2} = 1422\ \mu$m, $\Delta a_{\beta=3} = 2133\ \mu$m, and $\Delta a_{\beta=4} = 2844\ \mu$m. From an experimental point of view, it is worth noting that the average Δa at which the propagation curve seemed to be stabilized was determined (by the application of special krak-gages) to be equal to about 1.7 mm, while SEM observations of the fracture surfaces of all the specimens permitted to determine an average $\Delta a = 1.5$ mm (Fig. 8). It can then be concluded that for A1N steel, the more appropriate β value is about two, and since the influence of tensile residual stresses lasts longer than that of notch stress concentration, it is necessary to propagate the pre-crack for about 1.5 mm from the notch before considering the experimental results to be valid.

Characterization of Crack Growth Behavior of A1N Steel

After compression pre-cracking, specimens were instrumented using two RMF-A10 krak-gages (one for each side and having a measuring base length equal to

10 mm) connected to a Fractomat control unit in order to monitor crack growth in real-time by means of a potential drop technique. The four point bending crack propagation test was carried out by a resonant bending machine having a 160 Nm maximum load and vibrating at approximately 130 Hz.

Ten SE(*B*) specimens were tested at different stress ratios in order to characterize both the linear part of the crack growth diagram (CPCA test) and the threshold region (CPLR test). In the second case, the typical parameters of the applied loading reduction procedure were set within the limits suggested by ASTM E647-05 [4]: The growth rate at which loading reduction was always started was about 10^{-9} m/cycle, and the loading reduction coefficient was set to $C=-0.08$ mm^{-1}. Figure 9(*a*) shows a selection of the most significant results compared to those previously obtained by the traditional procedures. Some interesting observations can be drawn. From the methodological point of view, the CPCA curve at $R=0.7$ shows all the trials-and-errors required to find the right SIF value needed to make the crack grow. Particularly, Fig. 9(*b*) shows three attempts ended with a non-propagating crack and where it was necessary to slightly increase the load before the test really started. This behavior was observed at the beginning of each test, but only this case is shown here in order to avoid a confused diagram.

Concerning experimental results, the shape of crack growth curves became more repeatable with the stress ratio: Both the fanning phenomenon and the different heights of the knees disappeared considering CPCA and CPLR tests. It is also worth noting that the linear regions of the curves were not influenced by the pre-cracking procedure, while the threshold regions were significant. In particular, a detailed analysis of the trend of thresholds with *R* is shown in Fig. 9(*c*) for both compression pre-cracking and traditional procedures. This diagram allows, first of all, to notice that the difference between the results generated by the procedures increased significantly at lower stress ratios, while it was not important at high *R* values. This can be explained in terms of the closure phenomenon, which assumes more influence as long as *R* gets lower, making load interaction effects stronger. Considering the case of $R=-2$, the difference between the procedures was about 25 %: This can have a significant (and frightening) influence on maintenance of railway axles at least in terms of the length of inspection intervals. In the case of $R=-1$, the average threshold value determined through CPLR was about 9.5–10 MPa$\sqrt{\text{m}}$, a value very close to the one extrapolated from small cracks and the Kitagawa diagram (see Fig. 2(*b*)). Finally, it is also interesting to observe that the scatter in experimental threshold values became much lower, considering compression pre-cracking.

Figure 9(*c*) shows also the experimental data interpolations obtained by the maximum likelihood method and the NASGRO equation for thresholds [30]

$$\Delta K_{\text{th}} = \Delta K_o \cdot \sqrt{\frac{a}{a+a_o}} / \left[\frac{1-f}{(1-A_o)(1-R)}\right]^{(1+C_{\text{th}}R)} \tag{5}$$

where:

R = stress ratio,

f = "Newman's closure function" [31] describing the closure phenomenon,

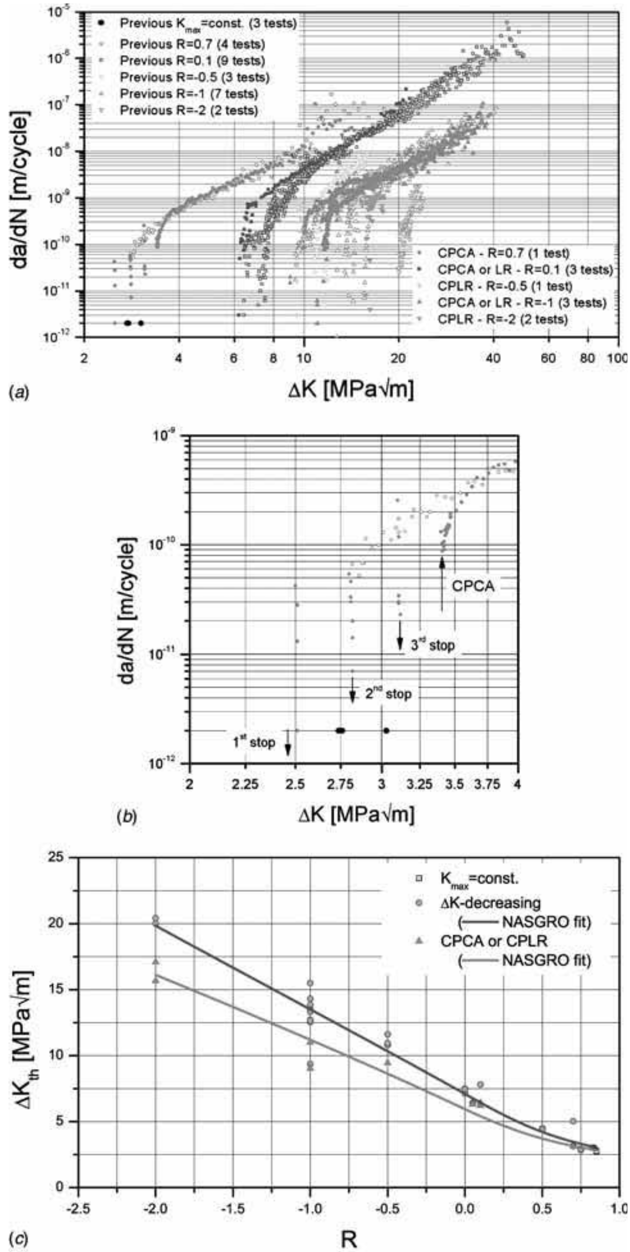

FIG. 9—*Experimental crack growth results for A1N steel grade:* (*a*) *Crack growth curves;* (*b*) *detail of the test at R=0.7; and* (*c*) *threshold trend with stress ratio.*

TABLE 2—*Fitting parameters for the NASGRO equation of thresholds.*

	ΔK-Decreasing	CPCA or CPLR
ΔK_0	7.11 MPa$\sqrt{}$m	5.96 MPa$\sqrt{}$m
C_{th+}	1.52	1.17
C_{th-}	−0.04	−0.02

A_o = constant in the formulation of f,
ΔK_0 = threshold value at $R=0$,
C_{th} = experimental constant,
a = crack length, and
a_o = El-Haddad parameter [19].

The dependence of ΔK_{th} with R is controlled through the C_{th} parameter: Different values of C_{th} (named C_{th+} and C_{th-}) have to be considered for positives and negatives R values. It should be noted that Eq 5 is generally valid in the range of $-2 \leq R \leq 0.7$: Outside these limits, thresholds tend to be constant. The empirical parameters determined fitting experimental data were then ΔK_0, C_{th+}, and C_{th-}: Table 2 compares the obtained fitting parameters. As can be seen, the differences are significant, suggesting the need for a review of the traditional choices about "safe life" inspection intervals made for the maintenance of railway axles.

Concluding Remarks

The application of alternative experimental procedures, based on a compression-compression pre-cracking and suitable constant amplitude or load reduction programs, for determining the threshold SIF range to a mild structural steel for railway axles in terms of SE(B) specimens subjected to stress ratios ranging from −2 to 0.85 permitted to draw the following conclusions:

- Compression pre-cracking seems to be a reliable procedure not influencing the experimental results it generates, unlike the traditional approaches proposed by relevant standards.
- FE analyses have been carried out adopting two different monotonic behaviors for the material in order to predict the final length of the pre-crack. Results show that both hypotheses give a good estimation of the plastic-zone size after the first compressive cycle, suggesting the possibility to apply a simple elastic–perfectly plastic material.
- Crack growth curves derived by means of CPCA or CPLR do not show the typical experimental discrepancies (such as the "fanning phenomenon" and a different height of the knee of the curve with R) observed using ΔK-decreasing and K_{max} = const.
- Considering the threshold region, the traditional approaches yield non conservative thresholds with respect to the novel methodology: The differences increase, decreasing the stress ratio (a difference equal to 25 % could be observed at $R=-2$).

- At $R = -1$, the threshold generated by CPLR is consistent with the one extrapolated for long cracks from experiments carried out on small cracks, while an error equal to 30 % on the non conservative side was observed considering the threshold generated by the traditional method.
- The scatter of thresholds obtained by CPCA or CPLR is much lower than the one generated by traditional approaches.

Acknowledgments

The authors gratefully thank RUMUL-Russenberger Prüfmaschinen AG (Neuhausen am Rheinfall, Swiss) for the financial support to the research and the provision of krag-gages.

References

[1] Grandt, A. F., Jr., *Fundamentals of Structural Integrity*, John Wiley & Sons, Inc., Hoboken, NJ, 2004.

[2] Cantini, S., Beretta, S., and Carboni, M., "POD and Inspection Intervals of High Speed Railway Axles," *15th International Wheelset Congress*, Prague, Czech Republic, 2007.

[3] Beretta, S. and Carboni, M., "Inspection Intervals of Railway Axles: Influence of Stress Spectrum," *Eighth International Conference on Engineering Structural Integrity Assessment* (*ESIA8*), Manchester, United Kigndom, 2006.

[4] ASTM E647-05, 2007, "Standard Test Method for Measurement of Fatigue Crack Growth Rates," *Annual Book of ASTM Standards*, Vol. 3(1), ASTM International, West Conshohocken, PA.

[5] Pippan, R., Stüwe, H. P., and Golos, K., "A Comparison of Different Methods to Determine the Threshold of Fatigue Crack Propagation," *Fatigue*, Vol. 16, 1994, pp. 579–582.

[6] Forth, S. C., Newman, J., Jr., and Forman, R. G., "On Generating Fatigue Crack Growth Thresholds," *Int. J. Fatigue*, Vol. 25, 2003, pp. 9–15.

[7] Forth, S. C., Newman, J., Jr., and Forman, R. G., "Evaluation of Fatigue Crack Thresholds Using Various Experimental Methods," *J. ASTM Int.*, Vol. 2, 2005, Paper ID JAI12847.

[8] Newman, J., Jr., Schneider, J., Daniel, A., and McKnight, D., "Compression Pre-Cracking to Generate Near Threshold Fatigue-Crack-Growth Rates in Two Aluminum Alloys," *Int. J. Fatigue*, Vol. 27, 2005, pp. 1432–1440.

[9] Pearson, S., "Initiation of Fatigue Cracks in Commercial Aluminum Alloys and the Subsequent Propagation of Very Short Cracks," *Eng. Fract. Mech.*, Vol. 7, 1975, pp. 235–247.

[10] Elber, W., "The Significance of Fatigue Crack Closure," *Damage Tolerance in Aircraft Structure, ASTM STP 486*, ASTM International, West Conshohocken, PA, 1971, pp. 230–242.

[11] Pippan, R., "The Growth of Short Cracks Under Cyclic Compression," *Fatigue Fract. Eng. Mater. Struct.*, Vol. 9, 1987, pp. 319–328.

[12] Newman, J., Jr. and Yamada, Y., "Compression Pre-Cracking Methods to Generate Near-Threshold Fatigue-Crack-Growth-Rate Data," *17th European Conference on Fracture* (*ECF17*), Brno, Czech Republic, 2008.

[13] James, M. A., Forth, S. C., and Newman, J. A., "Load History Effects Resulting

from Compression Pre-Cracking," *J. ASTM Int.*, Vol. 2, 2005, Paper ID JAI12025.
[14] BS EN13261, 2003, "Railway Applications—Wheelsets and Bogies—Axles—Product Requirements," European Committee for Standardization.
[15] Beretta, S., Carboni, M., Cantini, S., and Ghidini, A., "Application of Fatigue Crack Growth Algorithms to Railway Axles and Comparison of Two Steel Grades," *Proc. Inst. Mech. Eng., F J. Rail Rapid Transit*, Vol. 218, 2004, pp. 317–326.
[16] Kitagawa, H. and Takahashi, S., "Applicability of Fracture Mechanics to Very Small Cracks or the Cracks in the Early Stages," *Second International Conference on Mechanical Behavior of Materials*, Metals Park, OH, 1976, American Society for Metals, Metals Park, OH, pp. 627–631.
[17] Murakami, Y. and Endo, M., "Effects of Hardness and Crack Geometries on ΔK_{th} of Small Cracks Emanating from Small Defects," *The Behaviour of Short Fatigue Cracks*, K. J. Miller and E. R. De Los Rios, Eds., MEP, London, 1986, pp. 275–293.
[18] Beretta, S., Carboni, M., and Madia, M., "Modeling of Short Cracks Fatigue Thresholds by a Strip-Yield Model," *Ninth International Fatigue Congress* (*Fatigue2006*), Atlanta, GA, 2006.
[19] El-Haddad, M. H., Smith, K. N., and Topper, T. H., "Fatigue Crack Propagation of Short Cracks," *J. Eng. Mater. Technol.*, Vol. 101, 1979, pp. 42–46.
[20] Beretta, S., "Propagation of Short Cracks in a High Strength Steel for Railway Axles," *Proceedings of the 14th European Conference on Fracture*, Krakow, Poland, 2002.
[21] Beretta, S., Carboni, M., and Martinelli, E., "Variable Amplitude Crack Growth in Railway Axles: Influence on Inspection Intervals," *Second International Conference on Material and Component Performance Under Variable Amplitude Loading*, Darmstadt, Germany, 2009.
[22] Schijve, J., *Fatigue of Structures and Materials*, Kluwer Academic Publishers, New York, 2004.
[23] Aswath, P. B., Suresh, S., Holm, D. K., and Blom, A. F., "Load Interaction Effects on Compression Fatigue Crack Growth in Ductile Solids," *J. Eng. Mater. Technol.*, Vol. 110, 1988, pp. 278–285.
[24] *ABAQUS 6.7-1, User's Manual* (2008), Simulia, Providence, RI.
[25] Zerbst, U., Schődel, M., Webster, S., and Ainsworth, R. A., *Fitness-for-Service Fracture Assessment of Structures Containing Cracks*, Elsevier, Oxford, UK, 2007.
[26] Anderson, T. L., *Fracture Mechanics. Fundamentals and Applications*, 3rd ed., CRC Press, Boca Raton, FL, 2005, pp. 66–67.
[27] *Zencrack 7.6, User's Manual* (2009), Zentech, London, UK.
[28] Tada, H., Paris, P. C., and Irwin, G. R., *The Stress Analysis of Cracks Handbook*, 3rd ed., John Wiley and Sons, Ltd., London, UK, 2000.
[29] Newman, J., Jr. and Yamada, Y., "Crack Closure Behavior of Two Aluminium Alloys Near-Threshold Conditions for High Load Ratio and Constant Kmax Tests," *Ninth International ASTM/ESIS Symposium on Fatigue and Fracture Mechanics*, Vancouver, Canada, May 20–22, 2009, ASTM International, West Conshohocken, PA.
[30] *NASGRO 3.0.21, User's Manual* (2000), SwRI, San Antonio, Texas.
[31] Newman, J., Jr., "A Crack Opening Stress Equation for Fatigue Crack Growth," *Int. J. Fract.*, Vol. 24, 1984, pp. R131–R135.

Reprinted from JAI, Vol. 7, No. 4
doi:10.1520/JAI102490
Available online at www.astm.org/JAI

J. C. Newman, Jr.,[1] *Y. Yamada,*[2] *and J. A. Newman*[3]

Crack-Closure Behavior of 7050 Aluminum Alloy near Threshold Conditions for Wide Range in Load Ratios and Constant K_{max} Tests

ABSTRACT: Fatigue-crack-growth rate tests were conducted on compact specimens made of a 7050-T7451 aluminum alloy to study the behavior over a range in load ratios ($0.1 \le R \le 0.9$) and constant K_{max} test conditions. Previous research had suggested that differences in the threshold regime at high load ratios were attributed to K_{max} effects. But recent measurements of crack-closure behavior under high R and constant K_{max} test conditions near threshold conditions on a variety of materials have indicated that these tests may not be crack-closure free as suspected. Strain gages were placed near and ahead of the crack tip to measure crack-opening loads from local strain records. In addition, a back-face strain (BFS) gage was used to monitor crack sizes and to measure crack-opening loads from remote strain records during the same tests. The 7050 alloy produced very rough crack-surface profiles. For $R=0.1$, the BFS and local gages indicated very similar high crack-opening loads. For $R \ge 0.7$ and K_{max} test results in the threshold regime, the BFS gages indicated lower crack-opening loads than the local gages. Based on local measurements, crack-closure-free fatigue-crack-growth data (ΔK_{eff} against rate) were calculated. These results indicated that the ΔK_{eff} against rate relation is nearly a unique function over a wide range of R values even in the threshold regime, if crack-opening loads were measured from local strain gages. At low R, all three major shielding mechanisms (plasticity,

Manuscript received May 8, 2009; accepted for publication March 22, 2010; published online April 2010.
[1] Dept. of Aerospace Engineering, Mississippi State Univ., Mississippi State, MS 39762 (Corresponding author), e-mail: j.c.newman.jr@ae.msstate.edu
[2] Dept. of Aerospace Engineering, Mississippi State Univ., Mississippi State, MS 39762.
[3] NASA Langley Research Center, Hampton, VA 23681.

Cite as: Newman, J. C.Yamada, Y. and Newman, J. A., "Crack-Closure Behavior of 7050 Aluminum Alloy near Threshold Conditions for Wide Range in Load Ratios and Constant K_{max} Tests," *J. ASTM Intl.*, Vol. 7, No. 4. doi:10.1520/JAI102490.

roughness, and fretting debris) are suspected to cause crack closure. But for high R and K_{max} tests, roughness and fretting debris are suspected to cause crack closure above the minimum load. A strip-yield model was also used to correlate the data over a wide range in load ratios and rates, but required a very low constraint factor (α=1.3), due to the high crack-opening loads.

KEYWORDS: fatigue-crack growth, crack closure, K_{max}effect, threshold, compression precracking, load ratio

Nomenclature

a = crack size, mm
B = thickness, mm
da/dN = crack growth rate, m/cycle
K_{cp} = compressive stress-intensity factor during precracking, MPa m$^{1/2}$
K_{Ie} = maximum stress-intensity factor at failure, MPa m$^{1/2}$
K_{max} = maximum stress-intensity factor, MPa m$^{1/2}$
P_{max} = maximum applied load, N
P_{min} = minimum applied load, N
P_o = crack opening load, N
R = load (P_{min}/P_{max}) ratio
U = crack-opening function, $(1-P_o/P_{max})/(1-R)$
W = specimen width, mm
ΔK = stress-intensity factor range, MPa m$^{1/2}$
ΔK_c = critical stress-intensity-factor range at failure, MPa m$^{1/2}$
ΔK_{eff} = effective stress-intensity factor range ($U\Delta K$), MPa m$^{1/2}$
ΔK_i = initial stress-intensity factor range before load reduction, MPa m$^{1/2}$
BFS = back-face strain gage
CMOD = crack-mouth-opening displacement
CPCA = compression precracking and constant-amplitude test method
CPLR = compression precracking and load-reduction test method
C(T) = compact specimen
DICC = debris-induced crack closure
FCG = fatigue-crack growth
LaRC = Langley Research Center
NASA = National Aeronautics and Space Administration
OPn = crack-opening load (P_o/P_{max}) ratio at n% compliance offset
PICC = plasticity-induced crack closure
RICC = roughness-induced crack closure

Introduction

Cracks in high-cycle fatigue components spend a large portion of their fatigue life near threshold conditions. In order to characterize the evolution of damage and crack propagation during these conditions, fatigue-crack-growth (FCG) rate data at threshold and near-threshold conditions are essential in predicting service life and in determining the proper inspection intervals. Based on linear elastic fracture mechanics, FCG rate (da/dN) data are quantified in terms of the stress-intensity factor range, ΔK, at a given load ratio (R = minimum to maximum load ratio) [1]. The relation between ΔK and da/dN was shown to be nearly linear on a $\log(\Delta K) - \log(da/dN)$ scale. The relationship becomes non-linear when the crack approaches fracture [2] or when the FCG rate is very slow [3]. One of the significant mechanisms that influence crack-growth behavior is crack closure, which is partly caused by residual plastic deformations remaining in the wake of an advancing crack [4,5], roughness of the crack surfaces [6], and debris created along the crack surfaces [7]. The discovery of the crack-closure mechanism and development of the crack-closure concept led to a better understanding of FCG behavior, like the load-ratio (R) effect on crack growth. The crack-closure concept has been used to correlate crack-growth-rate data under constant-amplitude (CA) loading over a wide range in rates from threshold to fracture over a wide range in load ratios and load levels [8]. Difficulties have occurred in the threshold and near-threshold regimes using only plasticity-induced crack-closure modeling [9]. The load range where the crack tip is fully open is considered to be the effective range controlling crack growth. To calculate the effective stress-intensity factor range, ΔK_{eff}, the crack-opening load, P_o, was initially determined from load-displacement records using a local displacement gage placed near the crack tip [4,5]. For convenience, however, standard measurement methods have used either remote crack-mouth-opening-displacement (CMOD) gages or back-face strain (BFS) gages. These remote measurement methods have indicated that cracks are fully open under high load-ratio conditions for a variety of materials. Thus, high load ratio ($R \geq 0.7$) data have been considered to crack-closure free, even in the threshold regime, and load-ratio effects have been attributed to K_{max} effects. In the low rate regime, at or near threshold conditions, roughness-induced crack closure (RICC) [6,10] and debris-induced crack closure (DICC) [7,11], have been considered to be more relevant. However, plasticity-induced crack closure (PICC) [8,9] is still relevant under all load-ratio conditions. For high R conditions, where crack-opening loads from plasticity are nearly equal to the minimum load ($\Delta K_{eff} = \Delta K$, no PICC), the residual-plastic deformations along the crack surfaces are much larger than fretting-debris thicknesses [9,11] and, possibly, asperity influences. And, thus, plasticity contributes greatly to crack-opening loads that are higher than the minimum load. If the large amount of residual-plastic deformations had not been present in the wake of the crack in high R tests, then the small amount of fretting-debris would not have caused crack closure above the minimum load.

Until recently, the crack-closure concept was not always able to correlate data in the threshold regime, either from load-reduction (LR) tests at constant

R or constant K_{max} tests. Variations in the threshold and near-threshold behavior with load ratio could not be explained from PICC alone [9], but RICC and DICC mechanisms may be needed to correlate these data. The constant K_{max} test procedure [12] also produces what has been referred to as the "K_{max} effect," in that, lower thresholds are obtained using higher K_{max} values [13,14]. Compared with the constant R test method, constant K_{max} tests gradually decrease P_{max} and increase P_{min} to obtain a reduction in ΔK as the crack grows. One advantage of this test method is that it was commonly considered to produce crack-closure-free data ($R \geq 0.7$) using remote crack-opening load measurement methods (CMOD and BFS). But constant K_{max} testing also produces data at variable load ratios (R) and FCG thresholds at high load ratios (>0.8). For aluminum alloys and high K_{max} values, more dimpling and tunneling on the fatigue surfaces were observed [14], as the threshold was approached. This behavior indicated a change in the damage mechanism from classical FCG to more of a tensile fracture mode due to the K_{max} levels approaching the elastic fracture toughness. But extensive literature data reviewed by Vasudevan et al. [15] on a wide variety of materials do not show the so-called K_{max} effect. These mixed results suggest that something is different in the test procedure, test specimens, or crack-growth process that exhibits different behavior in the near-threshold regime. Recently, Yamada and Newman [16,17] have measured high-R closure (constant R and K_{max} tests) and used the results to establish a nearly unique ΔK_{eff} against rate relation for both Inconel-718 and 2324-T39 aluminum alloy in the threshold and near-threshold regimes.

To generate constant load-ratio data in the threshold and near-threshold regimes, ASTM E647 [18] uses the LR test method. But the LR test method has been shown to produce higher thresholds and lower rates in the near-threshold regime than steady-state CA data on a number of materials (two aluminum alloys, two titanium alloys and a superalloy), especially those that develop rough and tortuous crack surfaces [19–23]. On the other hand, some materials, such as 7075-T651 aluminum alloy and 4340 steel, have shown very little differences. In addition, the LR test method produces fanning with the load ratio in the threshold regime for some materials (fanning gives more spread in the ΔK-rate data with the load ratio in the threshold regime than in the mid-rate regime). It has also been shown that the test method induces a load-history effect, which may be caused by remote closure [9,19,24]. Thus, the LR test method does not, in general, produce CA FCG data, as was originally intended in ASTM E647. In order to produce steady-state CA data, compression-compression precracking methods have been proposed [25–27]. A prenotched specimen is cycled under compression-compression loading to produce an initial crack, which naturally stops growing (a threshold is reached under compression-compression loading). Then the specimen is subjected to the desired CA loading. If the crack had not grown after a million or so cycles, then the load is slightly increased (few percent). This process is repeated until the crack has begun to grow. Then the CA loading is held constant and FCG rate data is generated at the desired load ratio. The crack must be grown a small amount to eliminate the crack-starter notch and tensile residual-stress effects, and to stabilize the crack-closure behavior [21,28]. This method is called compression precracking CA (CPCA) loading threshold testing. Another method is

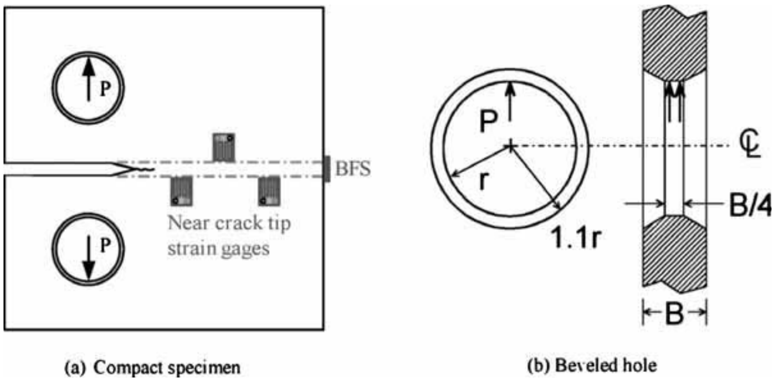

FIG. 1—*Compact specimen with local and remote (BFS) strain gages with beveled holes.*

to grow the crack at a low ΔK value, after compression precracking (CP), and then use the standard LR test method. CP allows the initial ΔK value or rate, before LR, to be much lower than would be needed or allowed in the ASTM standard LR test method. This method is called the compression precracking LR (CPLR) threshold test method. Both the CPCA and CPLR methods are used herein.

In this paper, FCG tests were conducted on compact specimens made of a 7050-T7451 (LT) aluminum alloy to study the behavior over a wide range in load ratios ($0.1 \leq R \leq 0.9$) and constant K_{max} test conditions from threshold to near fracture conditions. During the tests, strain gages were placed near and ahead of the crack tip to measure crack-opening loads from local load-strain records during crack growth, as shown in Fig. 1(*a*). In addition, a BFS gage was also used to monitor crack sizes and to measure remote load-strain records during the same test. Based on load-strain measurements (BFS and local), crack-opening loads were determined and crack-closure-free FCG data, ΔK_{eff}, were calculated and compared over a wide range in load ratios and K_{max} test conditions.

Material, Specimen and Test Procedures

Compact, C(T), specimens ($B = 6.35$ mm) were used to generate FCG rate data on 7050-T7451 aluminum alloy (LT-orientation). The specimens were obtained from the NASA Langley Research Center (LaRC) and some of these specimens had also been previously tested at LaRC under ASTM standard LR and CPCA loading procedures [29]. The yield stress was 470 MPa, the ultimate tensile strength was 525 MPa, and the modulus of elasticity was 76 GPa. Specimens had a width (W) of 50.8 mm. The specimens did not have the standard V-notch, but had an EDM (electrical-discharge machine) rectangular notch 10 mm long, measured from the pin-hole centerline, with a total notch height of 0.25 mm. In addition, the edges of the pin holes in the specimens were beveled to avoid or minimize undesired out-of-plane bending moments (pins forced to contact near mid-thickness of specimen), see Fig. 1(*b*).

The load sequences applied to the C(T) specimens are shown in Fig. 2. All specimens were fatigue precracked under compression-compression loading to initiate a crack at the EDM notch. Small aluminum alloy blocks were bonded on the top and bottom edges of the specimens along the pin-hole centerline, so that the blocks would contact with the loading clevis under compressive loading [21]. (Smaller pins were inserted in the standard pin holes as a safety measure to prevent loose specimens.) To minimize the development of multiple cracks at the notch, a sequence of CP loads were applied. The maximum load was −0.45 kN and the minimum loads were −2.7 kN for 10 kcycles, −3.6 kN for 10 kcycles and −4.8 kN for 30 kcycles (final $|K_{cp}|/E \approx 0.0002\ \mathrm{m}^{1/2}$). FCG rate tests were then conducted using constant K_{max} testing (shed rate of $-0.4\ \mathrm{mm}^{-1}$), CA (CPCA) loading, or LR (CPLR) at constant R after a small amount of crack extension under CA (CPCA) loading. LR tests were conducted when the FCG rate was 1×10^{-9} to 3×10^{-9} m/cycle, which is nearly an order of magnitude lower than the maximum rate allowed in the ASTM E647 standard [18]. FCG tests were performed under computer control on servo hydraulic testing machines (5 kN capacity) in laboratory air at room temperature and humidity (30 % RH). The loads were applied in sinusoidal waveform at 18 Hz in the low-rate regime and about 1–3 Hz in the high-rate regime. Crack sizes were monitored by using a BFS gage and occasionally calibrated with measurements made from a traveling optical microscope.

To measure load-strain records near the crack tip, strain gages were mounted close to the crack path for all test conditions. The location of the first strain gage was chosen to be slightly off the anticipated crack path by about 2 mm and about 5 mm away from the crack tip after compression-compression precracking. A number of strain gages were mounted along the anticipated crack path to record load-strain records as the crack approached these gages. The optimum signals were obtained when the crack tip was about 2–3 mm away from the strain gage during threshold testing. Approximately 20 load-strain records were recorded when the target FCG rates were achieved. During measurements, the frequency of cyclic loadings was reduced to 0.5 Hz to minimize external noise. The BFS and crack-monitoring software recorded various compliance-offset values using Elber's load-reduced-displacement (strain) approach [30]. In general, the results from the BFS showed the tail-swing associated with crack closure and the compliance-offset values from 1 % to 16 % [31]. The standard recommends the 2 % (OP2) value, but the 1 % (OP1) values were used herein.

Fatigue-Crack-Growth Results

FCG tests were conducted over a wide range in constant load-ratio conditions (R = 0.1, 0.7, and 0.9), and these results are shown in Fig. 3, which generally ranged from threshold to near fracture. At high rates, the asymptote to fracture, as expected, was a function of the load ratio, R. In this regime, the critical stress-intensity-factor range at failure, ΔK_c, is given by $K_{Ie}\ (1 - R)$, where K_{Ie} is

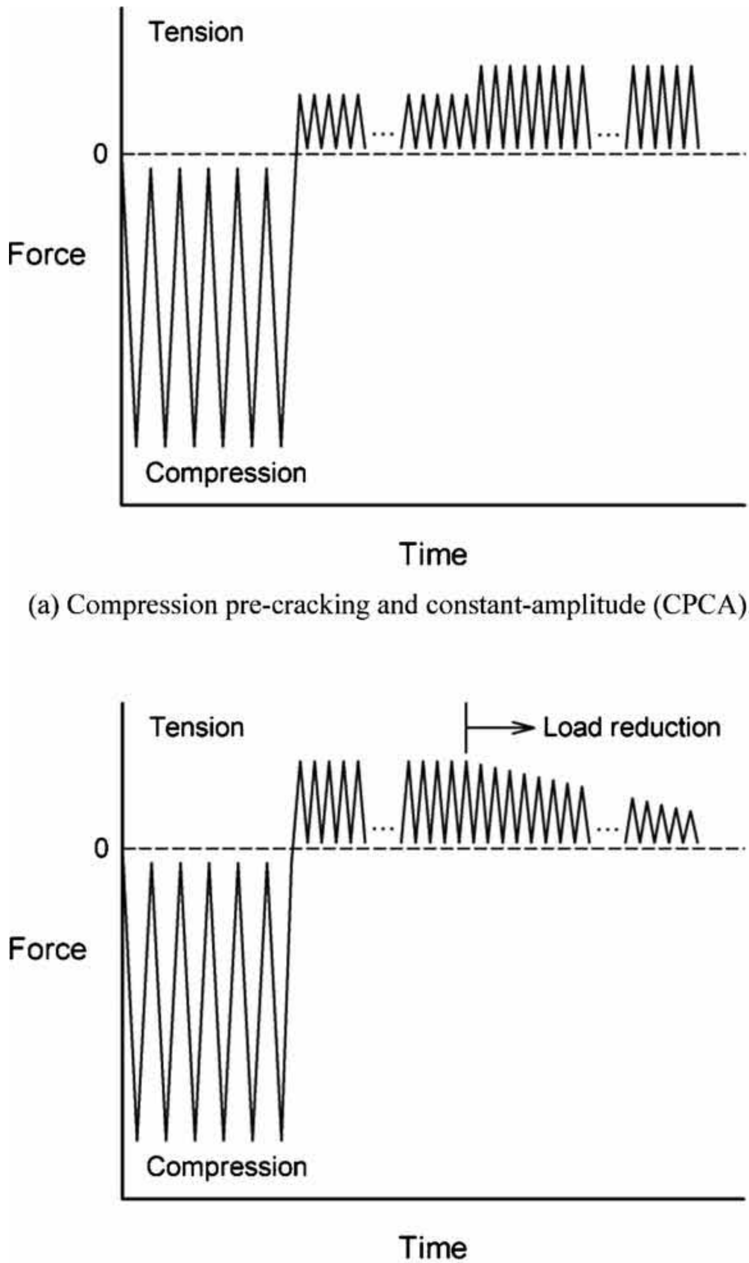

(a) Compression pre-cracking and constant-amplitude (CPCA).

(b) Compression pre-cracking and load-reduction (CPLR)

FIG. 2—*Load sequences for threshold and CA testing.*

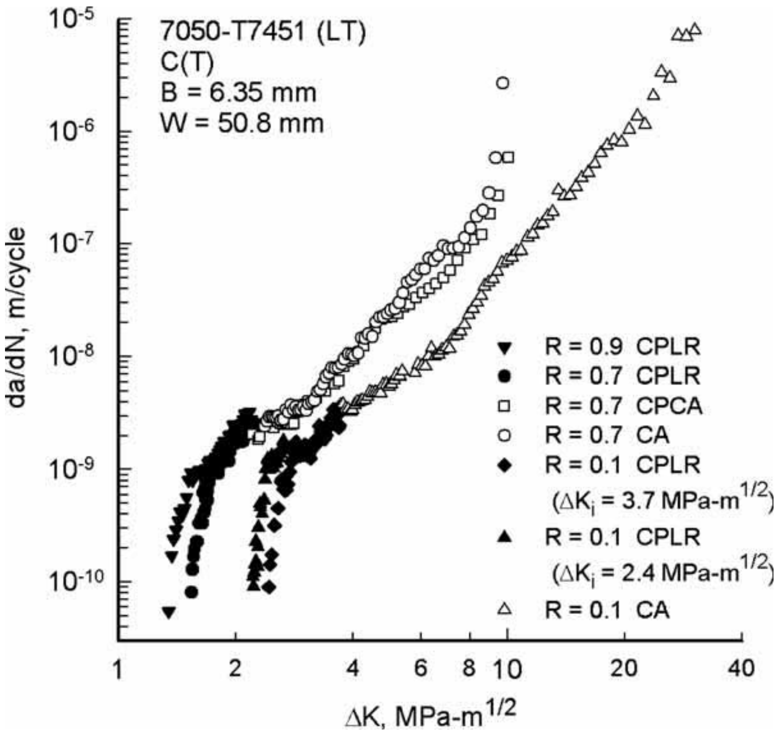

FIG. 3—*Fatigue-crack-growth-rate data for CPCA, CPLR, and CA tests at constant load ratio.*

the elastic fracture toughness or maximum stress-intensity factor at failure. Thus, at higher R-values, a crack will grow to failure at lower values of ΔK_c. In the near-threshold regime, the $R=0.9$ rates were higher than the $R=0.7$ rates at the same ΔK value, and the $R=0.9$ test produced a lower threshold than the $R=0.7$ test. The solid symbols show the CPLR test results. After CP, cracks were grown several compressive plastic-zone sizes before LR. The open symbols show CPCA or CA test data. Again, the CPCA test data is after the crack had grown beyond the crack-extension criterion, $\Delta c \geq 2\ (1-R)\ \rho_c$, where ρ_c is the Dugdale plane-stress plastic-zone size, $\rho_c=(\pi/8)\ (|K_{\text{cp}}|/\sigma_o)^2$ [28,32]. (Note that if Irwin's plastic-zone-size equation is used, then $\Delta c \geq 2.5\ (1-R)\ (2r_y)$, where $2r_y=(1/\pi)\ (|K_{\text{cp}}|/\sigma_o)^2$.)

Figure 4 shows a comparison of test data generated at $R=0.1$ using the ASTM LR test method [29] and those from the current study. The ASTM LR tests were conducted by Newman et al. (LaRC) on specimens machined from the same plate of material used in the current study. These results show that the LR test method produced higher thresholds (ΔK_{th} at 1×10^{-10} m/cycle) and lower rates than the CPLR test method. But the $R=0.1$ results from LaRC also showed some variations for different test specimens in the near threshold regime. This may have been due to the possible influence of residual-stress varia-

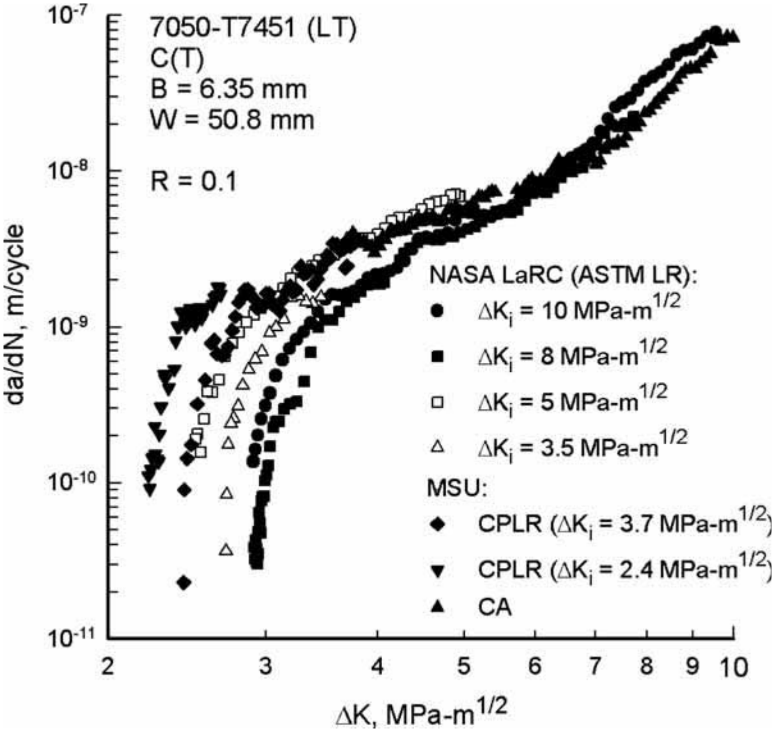

FIG. 4—*Comparison of FCG data generated from ASTM LR and CPLR/CA threshold testing.*

tions in the forging material and/or partially from load-history effects. Four tests were conducted with four different initial ΔK_i values to start the LR tests. The two test results shown by the solid symbols violated the ASTM LR standard (initial rate greater than 1×10^{-8} m/cycle). While the two tests at the lowest ΔK_i values satisfied the standard, they produced slightly lower thresholds than the two tests with highest ΔK_i values.

Two specimens were also tested at $R = 0.1$ using the CPLR test procedures. After CP loading, one test had a starting ΔK_i level near the lowest value from the LaRC tests. These results are shown as the solid diamond symbols in Fig. 4. After reaching a very low rate in the CPLR test, a CA test was conducted to generate the upper portion of the curve. These data fell at slightly lower ΔK values than the LaRC tests at the same rate. A second CPLR test had a ΔK_i level of 2.7 $\text{MPa}\sqrt{\text{m}}$ and these results are shown as solid triangles. These results fell at even lower ΔK values than the previous CPLR test. It was very surprising that the very low starting ΔK_i levels would still have an effect on the near-threshold results during LR. (Newman et al. [29] conducted two CPCA tests at $R = 0.1$ and these results are shown later.)

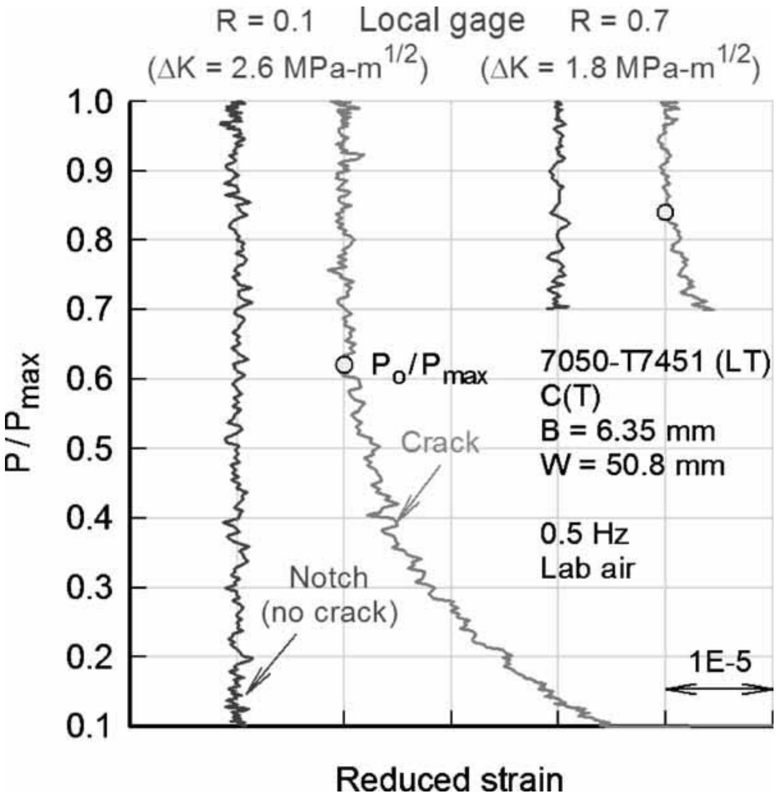

FIG. 5—*Linearity verification of load-reduced-strain records measured from local gages at low- and high-load ratio testing.*

Crack-Closure Measurements

Recently, Yamada and Newman [16,17] have used local strain gages mounted on one side of C(T) specimens to measure crack-opening loads. In measuring load-strain records, either from BFS or local strain gages, it is very important that nonlinearities, such as that due to out-of-plane bending or other causes, are not present in the measured data. Thus, a notch C(T) specimen was tested without a fatigue crack to verify the linearity of the local load-strain records. Figure 5 shows load-against-reduced strain records for a notched and cracked specimen at low and high R ratios. The records with only a notch were very linear, while the records with a fatigue crack show the typical crack-closure behavior. Where the nonlinear curve meets the upper linear portion is assumed to be the crack-opening load [30]. For all load ratios, the three major shielding mechanisms (plasticity, roughness, and debris) are expected to contribute to the crack-opening load. Under CA loading, is any remote closure involved in the crack-growth and closure process, like that suspected in the ASTM LR test due to residual-plastic deformations? For cracks that exhibit remote closure, the determination of the correct crack-opening load from a load-strain record to characterize crack-tip damage may be difficult [33]. In addition, crack-closure measurements using remote compliance methods are poor indicators of crack-tip events [34]. Changes in compliance are sensitive to remote closure or when a large portion of the crack closes. Because FCG behavior is determined by crack-tip events, near-tip measurement methods are better suited to describe their behavior [34]. For CA loading and plasticity modeling, crack opening is a local crack-tip event [33], and for roughness modeling [34,35] the first asperity from the crack tip controls the crack-opening load. Also, in threshold testing [11], the accumulation of fretting debris along the crack surface occurs in the interior, and near the crack-front location. Thus, it is assumed that under CA loading, crack-opening loads can be determined from the load-reduced-strain records using Elber's method [30].

Another issue is crack-opening loads in the interior (near plane-strain behavior) versus those measured at the free surface (plane stress). How three-dimensional crack-opening loads are used in a two-dimensional FCG analysis is still unclear [36]. Crack-opening loads at the free surface should affect the near crack-front-strain ranges in the interior, but at the small ΔK values near threshold, plane-strain behavior should be dominant and plane-stress behavior would be over a very small zone. In addition, PICC models (see, for example Ref 37) predict that above $R \geq 0.7$, the cracks should be fully open under plane-stress conditions, so PICC may not be the reason for high-R closure.

Initially, Elber [4,5] used a local displacement gage to measure crack-opening loads. But this method was more complicated than using a remote CMOD or BFS gage. Thus, the remote method has been standardized in ASTM E647. However, recent local crack-opening load measurements indicate that the remote method may not be sensitive enough or reliable for high-R test conditions. A comparison of remote and local crack-opening load measurements is shown in Figs. 6 and 7, respectively. For $R = 0.1$, both methods produced very high crack-opening-load ($P_o/P_{\max}$) ratios. The OP1 and OP2 values from the remote gage were extremely high, as the threshold conditions were approached. The $P_o/P_{\max}$ values from the local gage were only slightly lower than the remote gage at threshold conditions, but were still very high. But for $R = 0.7$ (Fig. 8) and $K_{\max}$ (Fig. 9) test conditions, the local gage produced slightly higher opening-load ratios than the remote gage. Crack-closure behavior was observed on the $K_{\max}$ tests at very high load ratios, as high as 0.94, as the threshold is approached.

Using these measured crack-opening-load ratios, the ΔK_{eff} values were determined and compared with the ΔK-rate data generated on constant R and two $K_{\max}$ tests in Fig. 10. Because of the very high crack-opening-load ratios, the ΔK_{eff} data fell at very low stress-intensity values in the near-threshold regime, but fell slightly to the upper bound of the $R = 0.7$ results in the mid- and upper-rate regions. This implies that in the mid- to upper-rate regions, only a slight amount of crack closure is occurring at $R = 0.7$, like expected from previous research. The solid lines with open circles show the selected ΔK_{eff}-rate baseline curve. The baseline curve fell fairly close to the ΔK_{eff} values determined from an $R = 0.1$ test (OP1 values from remote gage) over a very wide range in rates.

The crack-closure model FASTRAN [37–39] was then used to find a con-

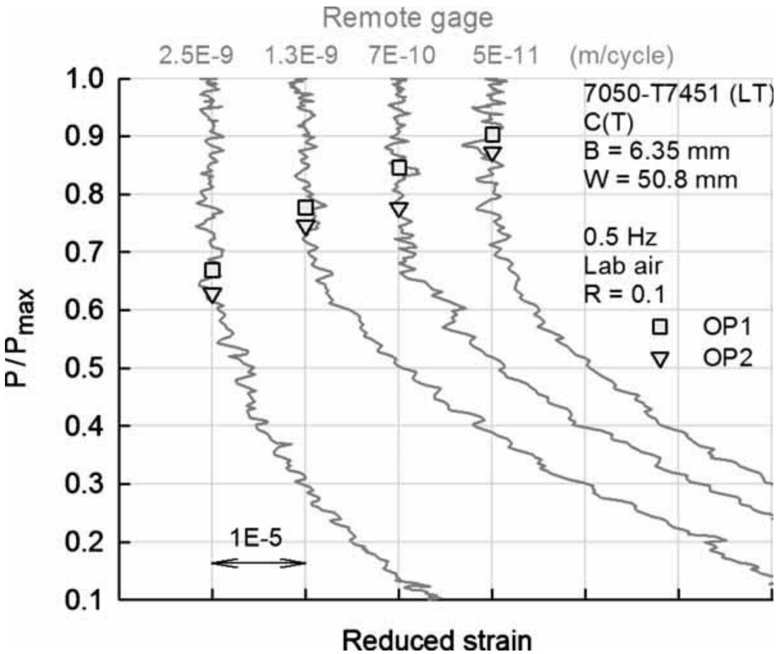

FIG. 6—*Crack-closure measurements from remote strain gage for R=0.1.*

straint factor (α) that would correlate the ΔK-rate data into a tight band on the ΔK_{eff} plot, as shown in Fig. 11. Surprisingly, a very low constraint factor ($\alpha = 1.3$) was required. The data correlated very well and even collapsed onto a unique curve in the near-threshold regime, but the data was very different from the measured ΔK_{eff} values. The discrepancy is due to the fact that FASTRAN is currently a PICC model and roughness- and/or fretting-debris play a dominant role in the threshold regime. At the high rates, the results show the usual R dependency on the approach to fracture. (Herein, the crack-closure model was able to collapse the CA FCG data into a fairly tight band over a wide range in R and rates, but caution should be exercised for variable-amplitude and spectrum loading. Having a plasticity parameter, such as α, correct for roughness and/or debris effects could lead to inaccurate life predictions. However, these effects are beyond the scope of the present paper. Combined plasticity, roughness and/or debris-induced crack-closure modeling, such as that by Newman et al. [34,35] and Kim and Lee [40], may be required to produce accurate life predictions.)

Crack-Growth Modeling

The crack-growth relation used in the crack-closure model, FASTRAN [37–39], is

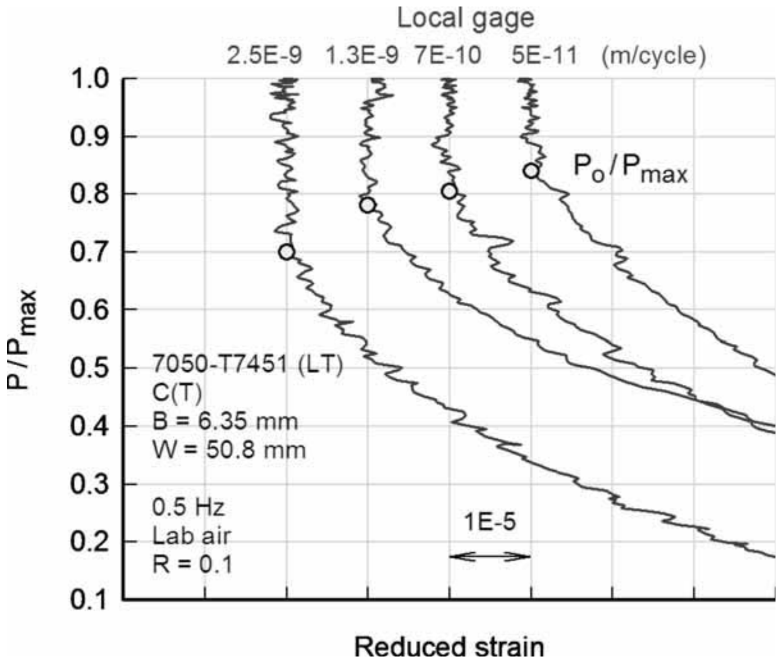

FIG. 7—*Crack-closure measurements from local strain gages for R=0.1.*

$$da/dN = C_{1i}(\Delta K_{eff})^{C_{2i}}[1 - (\Delta K_o/\Delta K_{eff})^p]/[1 - (K_{max}/C_5)^q] \tag{1}$$

where:

C_{1i} and C_{2i} = the coefficient and power for each linear segment,

ΔK_{eff} is the effective stress-intensity factor,

ΔK_o is the effective stress-intensity factor at threshold,

K_{max} is the maximum stress-intensity factor,

C_5 is the cyclic elastic fracture toughness (usually C_5 is set equal to K_{Ie}, which is generally a function of crack size, specimen width, and specimen type), and

p and q = constants selected to fit test data in either the threshold or fracture regimes.

Whenever the applied K_{max} value reached or exceeded C_5 (or K_{Ie}), then the specimen or component would fail (see Eq 1). The effective threshold stress-intensity-factor range, ΔK_o, is expressed as a function of load ratio and is

$$\Delta K_o = C_3(1 + C_4 R) \text{ for negative } C_4 \tag{2}$$

or

$$\Delta K_o = C_3(1 - R)^{C_4} \text{ for positive } C_4 \tag{3}$$

The values of p and q have ranged from 2 to 10 depending upon the material. A table-lookup form is used for the power-law term because many materials, especially aluminum alloys, show sharp changes in the crack-growth-rate curves

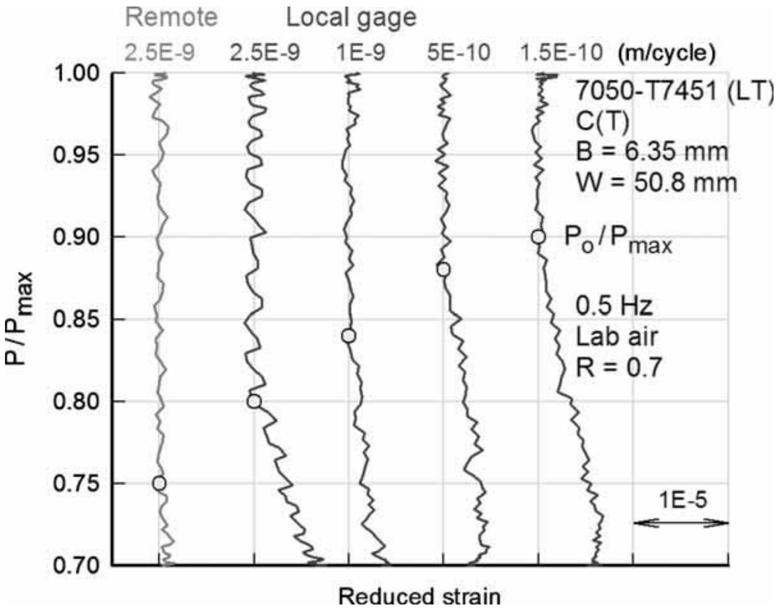

FIG. 8—*Load-reduced-strain records for several FCG rates near threshold conditions for R=0.7.*

at unique values of rates. These sharp changes have been associated with monotonic and cyclic plastic-zone sizes, grain sizes, and environments [41,42].

A very low constraint factor, $\alpha = 1.3$, was found to correlate the FCG test data fairly well, as shown in Fig. 11. The solid curve with open symbols shows the ΔK_{eff}-rate baseline curve (see Table 1). These results also show the classic plateau that occurs on most aluminum alloys in the (1×10^{-9} to 1×10^{-8} m/cycle) rate regime.

The coefficients in the threshold term of Eq 1 were evaluated from test data presented in Fig. 10. The ΔK_o values were nearly independent of R; thus, $C_3 = 1.3$ MPa$\sqrt{}$m and $C_4 = 0$. The power term, $p = 5$, was selected to best match the shape of the ΔK-rate curve from the previous CPLR test ($R = 0.1$) as the threshold conditions were approached, as shown in Fig. 10.

Coefficients in the fracture term were also estimated from test results in Fig. 10. Several C(T) specimens were cycled to failure at both low-R and high-R. From these results, the cyclic fracture toughness, C_5, was estimated at 40 MPa$\sqrt{}$m with $q = 5$. It is, however, suspected that the K_{Ie} values are not constant, but vary with crack size and specimen width. However, insufficient test data was available to conduct a two-parameter fracture criterion analysis [43].

A comparison of measured and calculated crack-growth (ΔK-rate) behavior from the crack-closure model at low-R and high-R is shown in Fig. 12. The solid curves show the calculated behavior from Eq 1 with the baseline data in

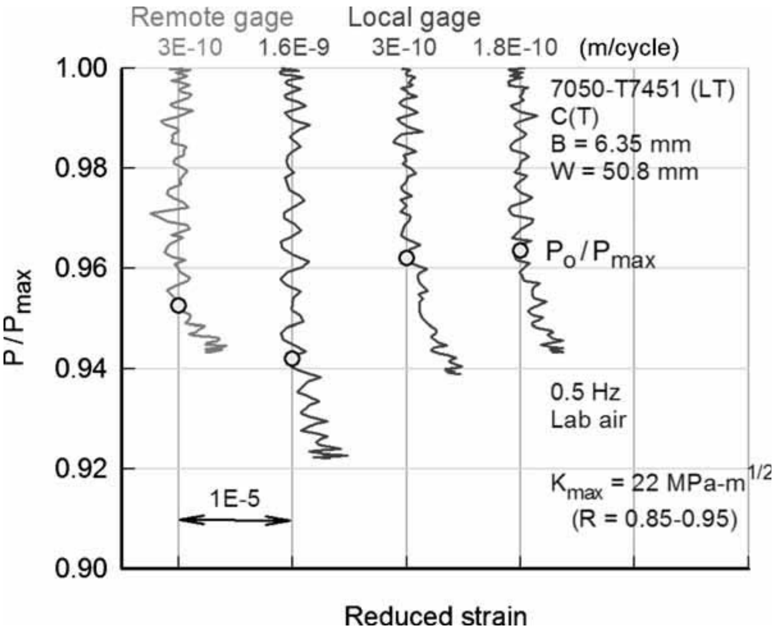

FIG. 9—*Load-reduced-strain records for several FCG rates near threshold conditions for* K_{max} *test.*

Table 1. The calculated curves agreed fairly well with the test data from threshold to fracture.

Further comparisons at $R = 0.1$ are shown in Fig. 13. NASA LaRC had also conducted two CPCA tests at $R = 0.1$ on specimens machined from the same block [29]. Both tests had nearly the same starting location and agreed very well with each other, as shown by solid symbols. The CPCA test results started on the high-R curve because the crack was fully open ($\Delta K = \Delta K_{\text{eff}}$), but as the cracks grew the crack-opening-load level rose and the data approached the $R = 0.1$ data. The solid diamond symbol shows where the crack extension in one of the CPCA tests had reached the crack-growth criterion. Here it is expected that the influence of the compression precracking tensile residual stresses would have diminished and the crack-opening loads would have stabilized [28]. The open diamond symbols show the results of the CPLR test that had the lowest ΔK_i level (2.7 $\text{MPa}\sqrt{\text{m}}$). The CPLR results matched well with the valid data from the CPCA tests. The dashed curve shows the results for a thin-sheet 7075-T6 aluminum alloy also tested at LaRC [44], which had a very similar shape at $R = 0.1$.

Discussion of Results

Testing on 7050-T7451 aluminum alloy has shown that near-threshold events, like threshold fanning with the R ratio and K_{max} effects, may be explained by

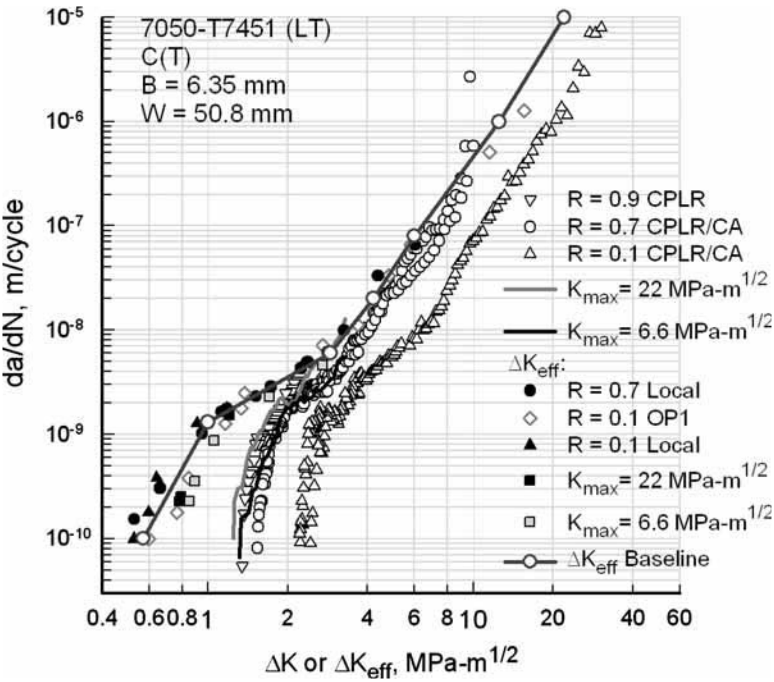

FIG. 10—*Effective stress-intensity-factor ranges for low R, high R, and K_{max} test results in near threshold regime.*

the crack-closure concept. Crack-opening loads measured with the local strain gages consistently showed a rise in the $P_o/P_{\max}$ ratio as the threshold conditions was approached. Figure 14 summaries the crack-opening-load ratios measured with the local strain gages over a wide range in R-values and $K_{\max}$ tests. The differences between the dashed lines and the measured values indicate the amount of crack closure for each R. Most of these tests were CPLR tests, but load-history effects due to LR are not likely due to the very low initial ΔK_i values used, especially at high R. But what has caused the rise in crack-closure behavior in the near-threshold regime?

In the literature, plasticity effects have been dismissed because the plastic-zone sizes are very small near threshold conditions, but crack-surface displacements are also very small. PICC is due to the interference between the residual-plastic deformations and crack-surface displacements. Thus, in the threshold regime, PICC is still a very dominant shielding mechanism at any R-value. Measurement of crack-opening loads at the free surface may also record plane-stress behavior instead of interior plane-strain or average through-the-thickness behavior. How three-dimensional crack-opening loads are used in a two-dimensional analysis is still unclear [36]. Crack-opening loads at the free surface should affect the near crack-front-strain ranges in the interior, but at the small ΔK values, plane-strain behavior should be dominant and plane-stress behavior would be over a very small zone. In addition, PICC models (see

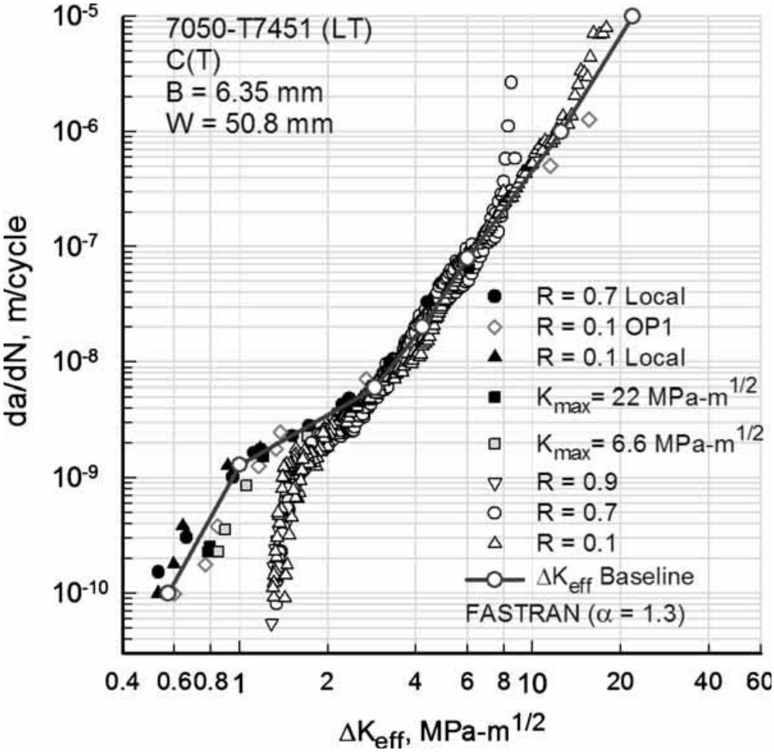

FIG. 11—*Effective stress-intensity-factor range against rate for all tests.*

TABLE 1—*Effective stress-intensity factor range against rate relation for 7050-T7451 (B =6.35 mm).*

ΔK_{eff} (MPa$\sqrt{}$m)	da/dN (m/cycle)
0.57	1.0×10^{-10}
1.00	1.3×10^{-9}
2.90	6.0×10^{-9}
4.20	2.0×10^{-8}
6.00	8.0×10^{-8}
12.5	1.0×10^{-6}
22.0	1.0×10^{-5}
$\alpha = 1.3$	All rates
$C_3 = 1.3$ MPa$\sqrt{}$m	$C_4 = 0$
$p = 5$	···
$C_5 = 40$ MPa$\sqrt{}$m	$q = 5$

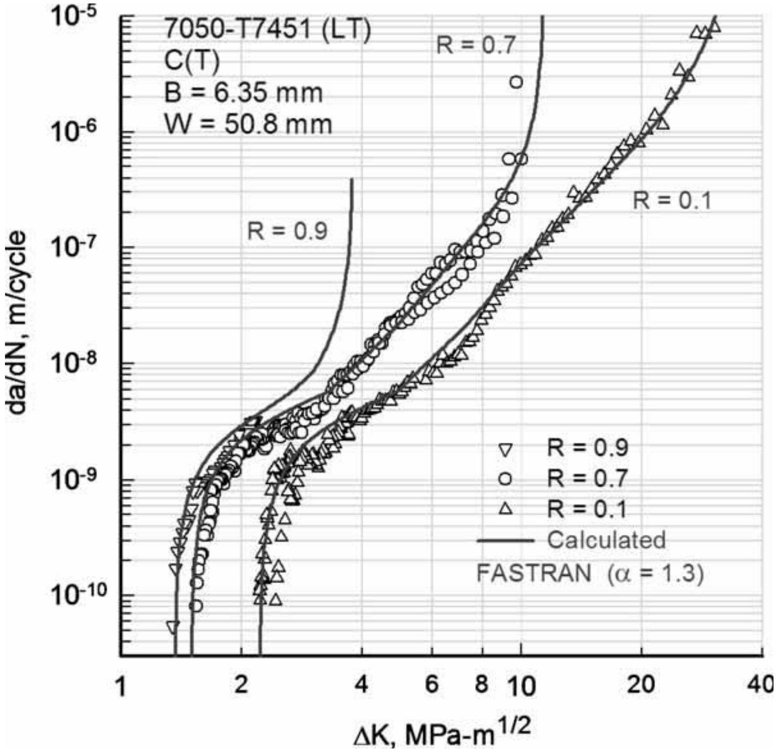

FIG. 12—*Measured and predicted FCG behavior over wide range in load ratios from threshold to fracture.*

for example Ref 37) predict that above $R \geq 0.7$, the cracks should be fully open under plane-stress conditions, so PICC may not be the reason for high-R closure.

Since the near crack-tip strain gages are located 2–3 mm away from the crack front ($B = 6.35$ mm), the crack-opening values measured at any R may be more of an average value through-the-thickness. The 7050-T7451 alloy creates a very rough and tortuous fatigue-crack surface, compared to 2024-T3 or 7075-T6. Thus, for high-R conditions, RICC is suspected to be a major contributor to the rise in the crack-opening-ratio level as the threshold is approached. Very rough crack surfaces with contacting asperities may also create debris along the crack surfaces, so DICC is also suspected to be a major contributor to the rise in the crack-opening-ratio levels in the threshold regime for high R [16,17].

Concluding Remarks

FCG rate tests were conducted on compact specimens made of a 7050-T7451 aluminum alloy (LT orientation) to study the behavior over a wide range in load ratios (0.1–0.9) and constant K_{max} test conditions. During FCG tests, strain

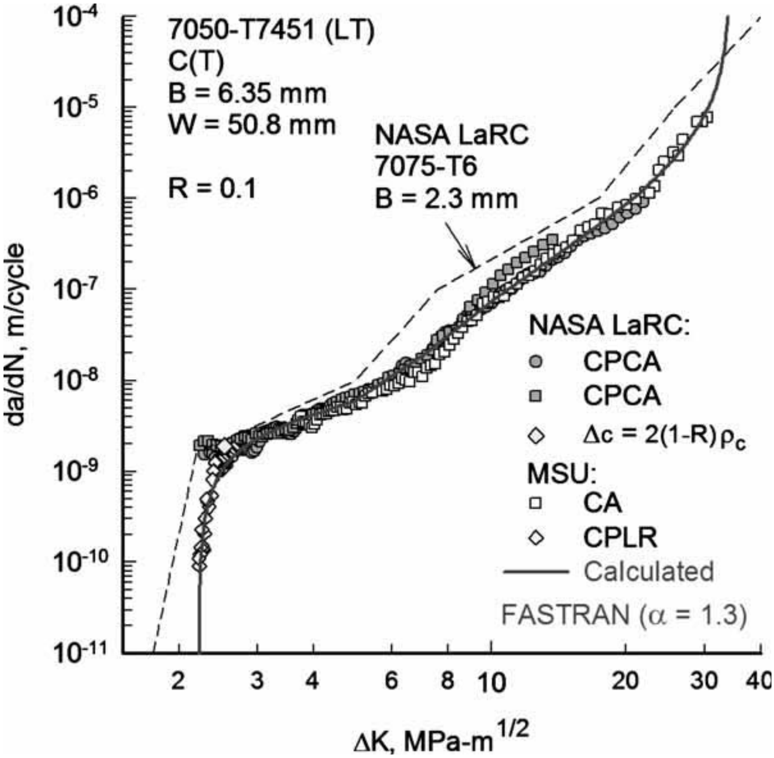

FIG. 13—*Comparison of measured and predicted FCG behavior at R=0.1 for CPCA, CPLR and CA testing.*

gages were placed near and ahead of the crack tip to measure crack-opening loads from local strain records. In addition, a BFS gage was also used to monitor crack sizes and to measure crack-opening loads from remote strain records during the same tests. The 7050 alloy produced very rough crack-surface profiles, which greatly contributed to the high crack-opening loads. For $R = 0.1$, the BFS and local gages indicated very similar high crack-opening loads. For $R \geq 0.7$ and K_{max} test results in the threshold regime, the BFS gages indicated lower crack-opening loads than the local gages. Also, the local gages were more sensitive to nonlinearities in the load-against-reduced-strain records than the remote gages. Based on these local measurements, crack-closure-free FCG data (ΔK_{eff} against rate) were calculated. These results indicated that the ΔK_{eff} against rate relation is nearly a unique function over a wide range of R values even in the threshold regime, if crack-opening loads were measured from local strain gages. At low R, all three major shielding mechanisms (plasticity, roughness, and fretting debris) are suspected to cause crack closure. But for high R and K_{max} tests, roughness and fretting debris are suspected to cause crack closure above the minimum load. A strip-yield model was also used to correlate

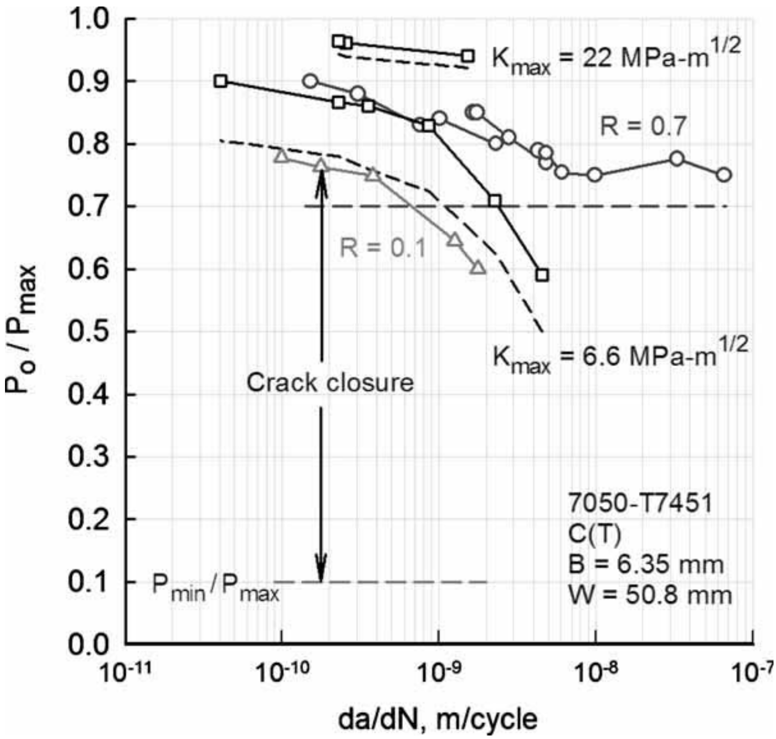

FIG. 14—*Crack-opening-load ratios for low R, high R, and K_{max} test results in threshold regime.*

the data over a wide range in load ratios and rates, but required a very low constraint factor ($\alpha = 1.3$), due to the high crack-opening loads.

Acknowledgments

The authors thank Dr. Dy Le and Dr. John Bakuckas, Federal Aviation Administration, and Dr. A. Vasudevan, Office of Naval Research (N00014-05-1-0871), for supporting development of the compression precracking test procedures at MSU; and to Dr. Keith Donald, Fracture Technology Associates, for his valuable advice on the use of his crack-monitoring software.

[1] Paris, P. C. and Erdogan, F., "A Critical Analysis of Crack Propagation Laws," *J. Basic Eng.*, Vol. 85, 1963, pp. 528–534.

[2] Barsom, J. M., "Fatigue-Crack Propagation in Steels of Various Yield Strengths," *J. Eng. Ind.*, Vol. 93, 1971, pp. 1190–1196.

[3] McEvily, A. J., Jr. and Illg, W. "The Rate of Fatigue-Crack Propagation in Two Aluminum Alloys," *NACA TN* 4394, National Advisory Committee for Aeronautics, Washington, DC, 1958.

[4] Elber, W., "Fatigue Crack Closure Under Cyclic Tension," *Eng. Fract. Mech.*, Vol. 2,

1970, pp. 37–45.
[5] Wolf, E., "The Significance of Fatigue Crack Closure," *ASTM STP 486*, American Society for Testing and Materials, West Conshohocken, PA, 1971, pp. 230–242.
[6] Walker, N. and Beevers, C. J., "A Fatigue Crack Closure Mechanism in Titanium," *Fatigue Fract. Eng. Mater. Struct.*, Vol. 1, 1979, pp. 135–148.
[7] Paris, P. C., Bucci, R. J., Wessel, E. T., Clark, W. G., and Mager, T. R., "Extensive study of low fatigue crack growth rates in A533 and A508 steels," *ASTM STP-513*, American Society for Testing and Materials, West Conshohocken, PA, 1972, pp. 141–176.
[8] Newman, J. C., Jr., "Effects of Constraint on Crack Growth Under Aircraft Spectrum Loading," *Fatigue of Aircraft Materials*, Delft University Press, Delft, The Netherlands, 1992, pp. 83–109.
[9] Newman, J. C., Jr., "Analysis of Fatigue Crack Growth and Closure near Threshold Conditions," *ASTM STP-1372*, American Society for Testing and Materials, West Conshohocken, PA, 2000, pp. 227–251.
[10] Kirby, B. R. and Beevers, C. J., "Slow Fatigue Crack Growth and Threshold Behaviour in Air and Vacuum of Commercial Aluminium Alloys," *Fatigue Fract. Eng. Mater. Struct.*, Vol. 1, 1979, pp. 203–215.
[11] Suresh, S., Zaminski, G. F., and Ritchie, R. O., "Oxide Induced Crack Closure: An Explanation for Near-Threshold Corrosion Fatigue Crack Growth Behavior," *Metall. Trans. A*, Vol. 12, 1981, pp. 1435–1443.
[12] Herman, W., Hertzberg, R., and Jaccard, R., "A Simplified Laboratory Approach for the Prediction of Short Crack Behavior in Engineering Structures," *Fatigue Fract. Eng. Mater. Struct.*, Vol. 11, 1988, pp. 303–320.
[13] Marci, G., "Fatigue Crack Growth Threshold Concept and Test Results for Al- and Ti-Alloys," *ASTM STP-1372*, American Society for Testing and Materials, West Conshohocken, PA, 2000, pp. 81–95.
[14] Newman, J. A., Riddell, W. T., and Piascik, R. S., "Effects of K_{max} on Fatigue Crack Growth Threshold in Aluminum Alloys," *ASTM STP-1372*, American Society for Testing and Materials, West Conshohocken, PA, 2000, pp. 63–77.
[15] Vasudevan, A. K., Sadananda, K., and Louat, N., "A Review of Crack Closure, Fatigue Crack Threshold and Related Phenomena," *Mater. Sci. Eng., A*, Vol. 188, 1994, pp. 1–22.
[16] Yamada, Y. and Newman, J. C., Jr., "Crack Closure Under High Load-Ratio Conditions for Inconel-718 Near Threshold Conditions," *Eng. Fract. Mech.*, Vol. 76, 2009, pp. 209-220.
[17] Yamada, Y. and Newman, J. C., Jr., "Crack-Closure Behavior of 2324-T39 Aluminum Alloy Near Threshold Conditions for High Load Ratio and constant K_{max} Tests," *Int. J. Fatigue*, Vol. 31, 2009, pp. 1780-1787.
[18] ASTM E-647, 2008, "Standard Test Method for Measurement of Fatigue Crack Growth Rates," *Annual Book of ASTM Standards*, Vol. 03.01, ASTM International, West Conshohocken, PA, pp. 1-44.
[19] Newman, J. C., Jr. "A Nonlinear Fracture Mechanics Approach to the Growth of Small Cracks," *Behavior of Short Cracks in Airframe Components*, AGARD CP-328, Specialised Printing Services Limited, UK, 1983, pp. 6.1–6.27.
[20] Forth, S. C., Newman, J. C., Jr., and Forman, R. G., "On Generating Fatigue Crack Growth Thresholds," *Int. J. Fatigue*, Vol. 25, 2003, pp. 9–15.
[21] Newman, J. C., Jr., Schneider, J., Daniel, A., and McKnight, D., "Compression Pre-Cracking to Generate Near Threshold Fatigue-Crack-Growth Rates in Two Aluminum Alloys," *Int. J. Fatigue*, Vol. 27, 2005, pp. 1432–1440.
[22] Ruschau, J. and Newman, J. C., Jr., "Compression Precracking to Generate Near

Threshold Fatigue Crack Growth Rates in an Aluminum and Titanium Alloy," *J. ASTM Intl.*, Vol. 5, 2008, paper ID JAI101623.

[23] Ruschau, J. and Newman, J. C., Jr., "Improved Test Methods for Very Low Fatigue-Crack-Growth-Rate Data," *American Helicopter Society International 64th Annual Forum & Technology Display*, American Helicopter Society, Montréal, Canada, April 29-May 1, 2008.

[24] McClung, R. C., "Analysis of Fatigue Crack Closure During Simulated Threshold Testing," *ASTM STP-1372*, American Society for Testing and Materials, West Conshohocken, PA, 2000, pp. 209–226.

[25] Pippan, R., "The Growth of Short Cracks Under Cyclic Compression," *Fatigue Fract. Eng. Mater. Struct.*, Vol. 9, 1987, pp. 319–328.

[26] Pippan, R., Plöchl, L., Klanner, F., and Stüwe, H. P., "The Use of Fatigue Specimens Precracked in Compression for Measuring Threshold Values and Crack Growth," *J. Test. Eval.*, Vol. 22, 1994, pp. 98.

[27] Topper, T. H. and Au, P., "Fatigue Test Methodology," *AGARD Lecture Series 118*, The Technical University of Denmark, Copenhagen, Denmark, 1981.

[28] Yamada, Y., Newman, J. C. III, and Newman, J. C., Jr., "Elastic-plastic finite-element analyses of compression precracking and its influence on subsequent fatigue-crack growth," *J. ASTM Intl.*, Vol. 5, 2008, paper ID JAI101617 .

[29] Newman, J. A., James, M. A., Johnston, W. M., and Le, D. D., "Fatigue Crack Growth Threshold Testing of Metallic Rotorcraft Materials," *NASA/TM* 2008–215331, ARL-TR-4472, National Aeronautics and Space Administration, Washington, DC, July 2008.

[30] Elber, W., "Crack-Closure and Crack-Growth Measurements in Surface-Flawed Titanium Alloy Ti-6Al-4V," *NASA TN* D-8010, National Aeronautics and Space Administration, Washington, DC, September 1975.

[31] Donald, J. K., "A Procedure for Standardizing Crack Closure Levels," in *ASTM STP 982*, American Society for Testing and Materials, West Conshohocken, PA, 1988, pp. 222–229.

[32] Newman, J. C., Jr., Vizzini, A., and Yamada, Y., "Fatigue-Crack-Growth Databases and Analyses for Threshold Behavior in Rotorcraft Materials," *DOT/FAA/AR-10/3, Federal Aviation Administration*, Washington, DC, March 2010.

[33] Newman, J. C., Jr., "Analysis of Fatigue Crack Growth and Closure Near Threshold Conditions," in *ASTM STP-1372*, American Society for Testing and Materials, West Conshohocken, PA, 2000, pp. 227–251.

[34] Newman, J. A. "The Effects of Load Ratio on Threshold Fatigue Crack Growth of Aluminum Alloys," Ph.D. thesis, Virginia Polytechnic Institute and State University, Blacksburg, VA, October 2000.

[35] Newman, J. A., Riddell, W. T., and Piascik, R. S., "A Threshold Fatigue Crack Closure Model: Part I—Model Development," *Fatigue Fract. Eng. Mater. Struct.*, Vol. 26, 2003, pp. 603–614.

[36] Dawicke, D., Shivakumar, K., Newman, J., and Grandt, A., "An Inverse Method for the Calculation of Through-Thickness Fatigue Crack Closure Behavior," *ASTM STP 1131*, American Society for Testing and Materials, West Conshohocken, PA, 1992, pp. 46–57.

[37] Newman, J. C., Jr., "A Crack-Closure Model for Predicting Fatigue Crack Growth Under Aircraft Spectrum Loading," in *ASTM STP 748*, American Society for Testing and Materials, West Conshohocken, PA, 1981, pp. 53–84.

[38] Newman, J. C., Jr., "A Crack-Opening Stress Equation for Fatigue Crack Growth," *Int. J. Fract.*, Vol. 24, 1984, pp. R131–R135.

[39] Newman, J. C., Jr., "FASTRAN II—A Fatigue Crack Growth Structural Analysis

Program," *NASA TM* 104159, National Aeronautics and Space Administration, Washington, DC, 1992.

[40] Kim, J. H. and Lee, S. B., "Behavior of Plasticity-Induced Crack Closure and Roughness-Induced Crack Closure in Aluminum Alloy," *Int. J. Fatigue*, Vol. 23, 2001, pp. 247–251.

[41] Yoder, G. R., Cooley, L., and Crooker, T. W., "On microstructural control on near-threshold fatigue crack growth in 7000-series aluminum alloys," *Scr. Metall.*, Vol. 16, 1982, pp. 1021–1025.

[42] Piascik, R. S., and Gangloff, R. P., "Environmental Fatigue of an Al-Li-Cu alloy: Part II. Microscopic Hydrogen Cracking Processes," *Metall. Trans. A*, Vol. 24, 1993, pp. 2751–2762.

[43] Newman, J. C., Jr., 1976, "Fracture Analysis of Various Cracked Configurations in Sheet and Plate Materials," *ASTM STP 605*, American Society for Testing and Materials, West Conshohocken, PA, pp. 104–123.

[44] Newman, J. C., Jr., Wu, X. R., Venneri, S. L., and Li, C. G., "Small-Crack Effects in High-Strength Aluminum Alloys—A NASA/CAE Cooperative Program," *NASA Report No.* 1309, National Aeronautics and Space Administration, Washington, DC, May 1994.

Reprinted from JAI, Vol. 6, No. 10
doi:10.1520/JAI102541
Available online at www.astm.org/JAI

C. Oberwinkler,[1] *H. Leitner,*[1] *and W. Eichlseder*[1]

Definition of the Influence of Pore Size on the Fatigue Limit Using Short Crack Propagation Experiments

ABSTRACT: Aluminium high pressure die casting is used to reduce costs and weight of various components in the automotive industry. The main problem of components made by pressure die casting is connected with inherent flaws (porosity, oxide skins, etc.), which can hardly be avoided. Today the fatigue calculation of aluminium high pressure die cast parts is usually performed using two S/N curves—one account for the flawed basic material and one for the pore-free surface layer. This does not provide an accurate estimate for the computation of the lifetime or safety against failure of the component. In a cast component the number and size of pores increases towards the center. As a consequence the fatigue strength decreases. This inhomogeneous distribution throughout the component has to be taken into account for a realistic estimation of the fatigue strength. To do so, two models are required—one to compute the pore size distribution in the component [Oberwinkler, C., Leitner, H., and Eichlseder, W. "Improvement of an Existing Model to Estimate the Pore Distribution for A Fatigue Proof Design of Al HPDC Components," *TMS 2009*, Shape Casting: 3rd Int. Symposium, 2009] and a material model [Oberwinkler, C., Leitner, H., and Eichlseder, W. "Computation of Fatigue Safety Factors for High-Pressure Die Cast (HPDC) Aluminium Components Taking into Account the Pore Size Distribution," *SAE World Congress 2009*], which describes the influence of the defect size on the fatigue strength. This paper focuses on the definition of the correlation between the fatigue strength and the pore size. The lifetime of a component is defined by the crack growth if the crack initiation period can be neglected. Casting defects usually show high stress concentration factors due to their irregular shapes where cracks initiate. In this case the defect size is a part of the total crack length. Pores can be considered as physically short cracks because of their size of approximately 10–500 μm. The El-Haddad equation

Manuscript received May 19, 2009; accepted for publication August 19, 2009; published online September 2009.

[1] Institute of Mechanical Engineering, Univ. of Leoben, 8700 Leoben, Austria.

Cite as: Oberwinkler, C., Leitner, H. and Eichlseder, W., "Definition of the Influence of Pore Size on the Fatigue Limit Using Short Crack Propagation Experiments," *J. ASTM Intl.*, Vol. 6, No. 10. doi:10.1520/JAI102541.

[El Haddad, M. H., Smith, K. N., and Topper, T. H., “Fatigue Crack Propagation of Short Cracks,” *ASME Transactions*, Vol. 101, 1979, pp. 42–46] has been used to describe the influence of the defect size on the fatigue strength. Short crack experiments have been performed to show that due to the shorter cracks the threshold stress intensity factor decreases below the threshold stress intensity factor of long cracks.

KEYWORDS: high-pressure die casting, fatigue, fracture mechanics, pores, El-Haddad

Introduction

Cast components exhibit pores, which influence the fatigue strength. There are two kinds of porosity—gas pores and shrinkage porosity. This paper focuses on the first one. Gas pores are formed by two mechanisms: Either by the entrapped air or by the dissolved gas. The size and shape of the gas pores depend mainly on the hydrogen content of the melt and the cooling rate [1,2]. A higher cooling rate produces smaller and sharp edged pores because the growing dendrites limit the extension of the gas pores. At lower cooling rates the gas pores have more time to expand and they are typically globular. Some typical pore geometries are shown in Fig. 1.

Various studies on the influence of pores on fatigue behavior have been published. Ting and Lawrence [3], Ammar et al. [4], and Couper et al. [5] identified a linear relationship between defect size and load cycles to failure in a double-logarithmic representation of data for cast aluminum specimens.

The Kitagawa-Takahashi diagram [6] is a criterion for the design of infinite-life components taking into account two thresholds, one given by the classical stress-based fatigue limit and the other by the threshold stress intensity factor derived from fracture tests. The Kitagawa diagram identifies the border between crack arrest (non-propagating cracks) and specimen failure in relation to defect size.

In the present research work fatigue and crack growth experiments are performed to investigate the influence of the casting defects on the fatigue strength. The crack growth behavior of high pressure die cast Al-9Si-3Cu is analyzed for long and physically short cracks. The results are reported as follows.

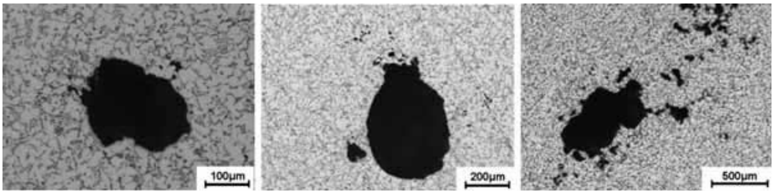

FIG. 1—*Typical pore geometries from a HPDC component.*

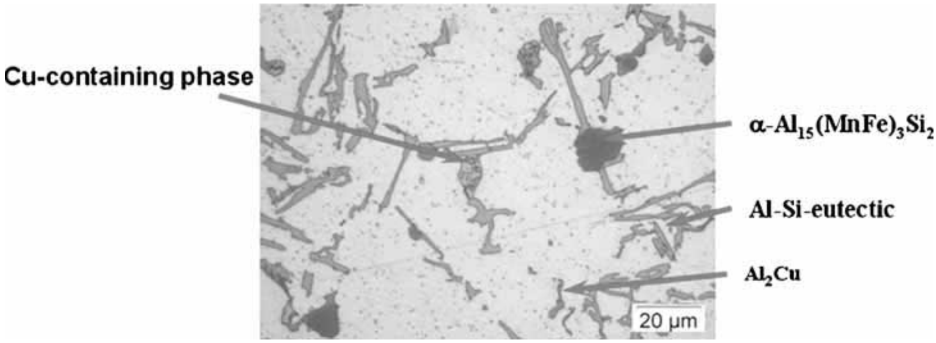

FIG. 2—*Microstructure of the cast aluminium alloy Al-9Si-3Cu.*

Material and Experimental

Material

The aluminum alloy used for the present research work is Al-9Si-3Cu. This hypoeutectic Al-Si alloy represents the most widely used alloy for high pressure die casting (HPDC). The microstructure with the α-Al dendrites, plate-like eutectic silicon and intermetallic phases is shown in Fig. 2.

Table 1 shows the chemical composition of the alloy.

Block-shaped components have been cast to investigate the pore distribution and the mechanical properties with dimensions of $140 \times 115 \times 20$ mm. The components were produced by HPDC at different solidification pressures and piston velocities. The casting parameters for the specimens are shown in Table 2. The three different casting qualities are referred to as Quality 1–3, where 1 is the highest quality and 3 is expected to have the highest porosity.

The casting system is visualized in Fig. 3. It shows the gating system, the component (plate) and the cooling.

The resulting pore distribution in the plates for the three different qualities is shown in Fig. 4. Quality 1 exhibits almost no pores in a distance of approxi-

TABLE 1—*Chemical composition of the material used in wt % (Al-9Si-3Cu).*

Si	Fe	Cu	Mn	Mg	Cr	Ni	Zn	Al
9.2	0.79	2.96	0.21	0.27	0.05	0.06	0.96	Balance

TABLE 2—*Casting parameters.*

Quality	Piston Velocity	Pressure
1	Low	High
2	Medium	Medium
3	High	Low

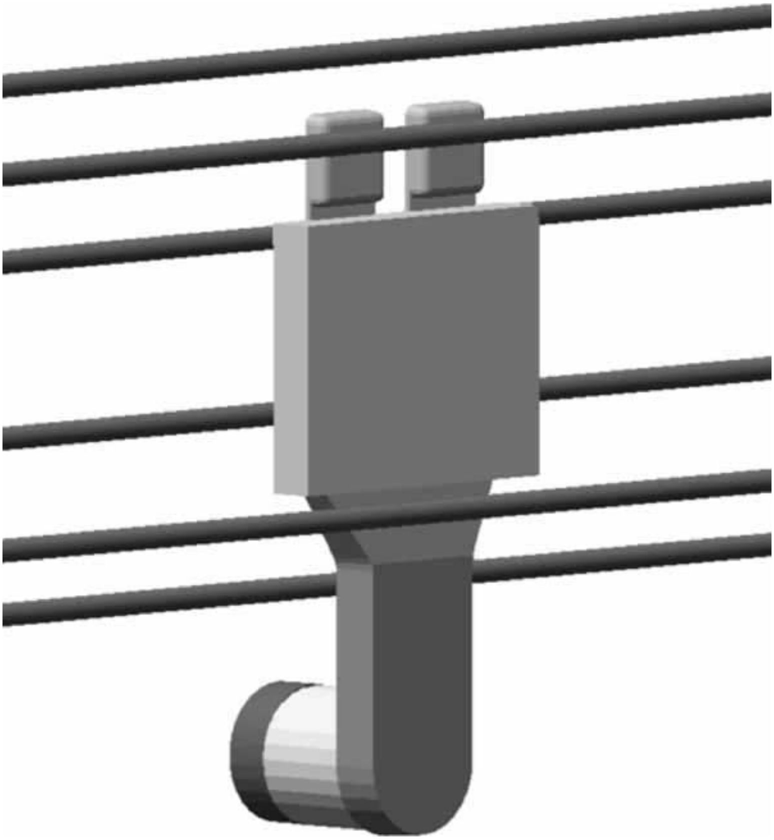

FIG. 3—*Cast component including the gating system and cooling system.*

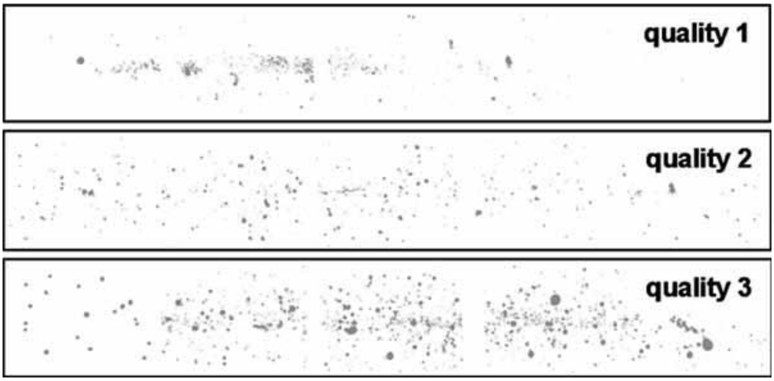

FIG. 4—*Pore distribution in a cut through the plate for all qualities.*

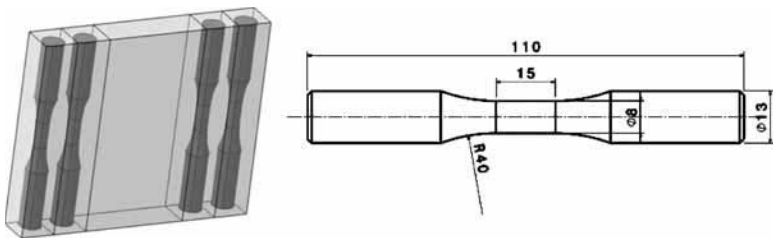

FIG. 5—*Location (left) and geometry of the pore-containing fatigue specimens (all the dimensions are in millimeters).*

mately 5 mm from the surface but a clear solidification porosity developed in the middle. On the opposite end, Quality 3 has a high porosity steadily increasing towards the middle of the plate.

Specimens

Different kinds of specimens have been produced from the cast plates—pore-containing specimens to test for the influence of the defects on the fatigue life time and pore-free specimens to get the fatigue limit of the homogeneous material.

Pore-Containing Specimens—The location of the specimens in the HPDC plate together with the geometry is displayed in Fig. 5. The cylindrical specimens are taken from the middle of the plate. This means the pore-free surface layer is removed. The critical zone of the specimens is a cylindrical volume with a homogeneous stress field. This assures that the specimen will fail at the most

FIG. 6—*Three-dimensional pore distribution in the critical volume.*

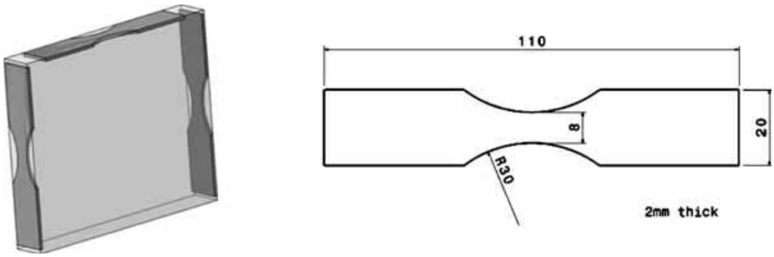

FIG. 7—*Location* (*left*) *and geometry of the pore-free fatigue specimens* (*all the dimensions are in millimeters*).

critical pore within the 15 mm long and 8 mm diameter gauge length.

A pore distribution in the critical volume for two specimens is shown in Fig. 6. This pore distribution had been measured by computer tomography. The different degree of porosity is due to the varying process parameters. The left specimen is from a plate of Quality 2; the right of Quality 3.

Pore-Free Specimens—The flat specimens were used to test the pore-free surface layer. They are manufactured from three sides of the plate (Fig. 7). The fourth side is where the gating system was connected. This led to an increase of porosity in this area. To assure pore-free specimens only plates from Quality 1 are used to manufacture the specimens.

The specimens for the fatigue crack growth experiments are depicted in Fig. 8. Both are manufactured from the locations shown in Fig. 7 and plates of Quality 1 are used only to avoid pores, which would influence the crack growth.

Testing

All tests were conducted in laboratory air at room temperature (21 °C) and relative humidity of 40–50 %.

Tension-compression ($R = -1$) and zero-tension ($R = 0$) fatigue tests have

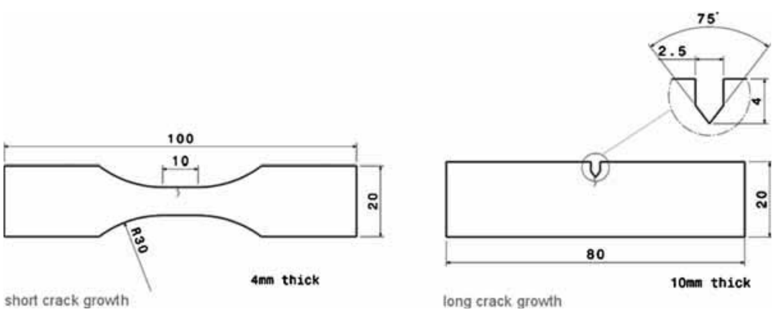

FIG. 8—*Specimens for the fatigue crack growth experiments—short crack growth* (*left*); *long crack growth* (*right*) (*all the dimensions are in millimeters*).

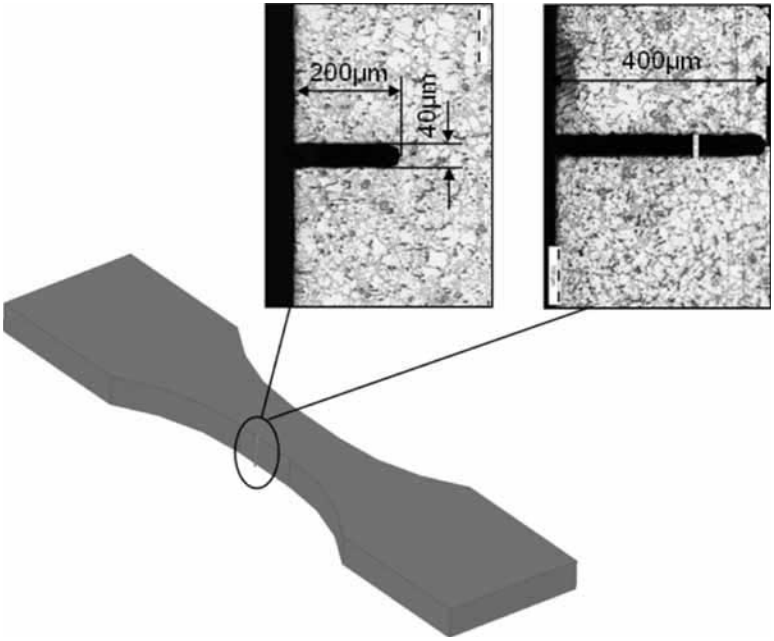

FIG. 9—*Geometry of the short cracks.*

been performed in a servo-hydraulic test rig with a test frequency of 30 Hz. The specimens were run for maximum 1e7 load cycles and specimens that did not fail before this limit were considered run-outs.

Two specimen geometries were used for the fatigue crack growth experiments. The long crack growth experiments were performed on single-edge bending (SEB) specimens ($80 \times 20 \times 10$). Threshold data were generated under decreasing K, while data for Regions II and III were produced under constant bending moment. To monitor the crack advance, a reversing DC potential difference method was used. The pre-cracking was performed at a stress ratio of $R = -1$ with a constant K until a crack length of 6.0 mm was reached.

The short crack growth experiments were conducted on notched (linear-elastic stress concentration factor $K_t = 9$) rectangular specimens with two different initial crack lengths of 200 and 400 μm (Fig. 9). The initial notches with a width of 40 μm were produced by wire-cut electrical discharge machining. The notch length has been chosen according to typical pore sizes. The notch is produced along the whole specimen thickness. This produces a more severe notch than a real pore would present, which has been accounted by the geometry factor.

The tension-compression ($R = -1$) and zero-tension ($R = 0$) fatigue tests have been conducted at constant stress amplitudes. All specimens were ground and polished to monitor the crack propagation using a digital camera system. The camera system consists of a digital charge-coupled device monochrome area scan camera with objective lens (eightfold magnification) and a dark field

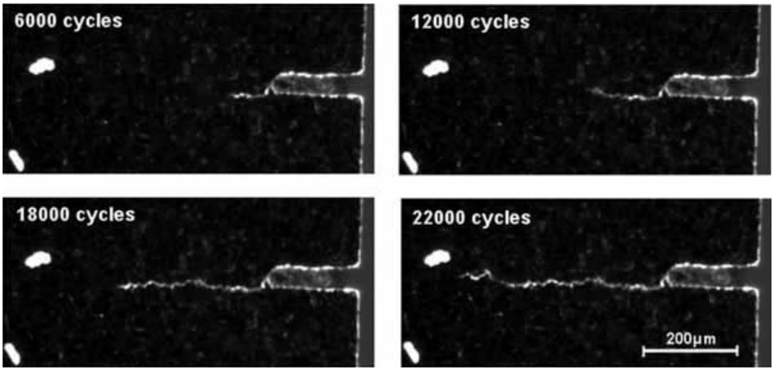

FIG. 10—*Crack lengths for different load cycles from the camera system.*

illumination [7]. In the dark field illumination technique the light which illuminates the sample is not collected by the objective lens; only diffusion on irregular surface texture leads to reflection of a small portion of light. Therefore dark field illumination produces a dark, almost black, background where cracks appear bright. For a better visibility of the cracks the specimens were polished and ultrasonic-cleaned before testing. To monitor crack growth the tests were interrupted after a defined number of cycles and a picture was taken by the camera system (Fig. 10).

Crack length was measured from the picture and the crack growth rate and the corresponding stress intensity range were calculated.

The procedure was repeated several times until failure. Each interruption produced a data point of the crack growth diagram. The measurement of the crack growth rate in the high-cycle fatigue (HCF) region was performed using an optical microscope (Fig. 11). The crack growth rate did not produce long enough cracks to measure it with the camera system. The crack tips are highlighted by the red arrows.

Fractography

The fracture surfaces of the failed pore-containing fatigue specimens were examined using an optical microscope and a scanning electron microscope (SEM) to identify the origin of the crack initiation. Image analysis was used to measure the area of the crack initiating defect (Fig. 12). The area equivalent defect diameter was calculated from the area of the crack initiating defect using Eq 1

FIG. 11—*Crack lengths for different load cycles from the optical microscope.*

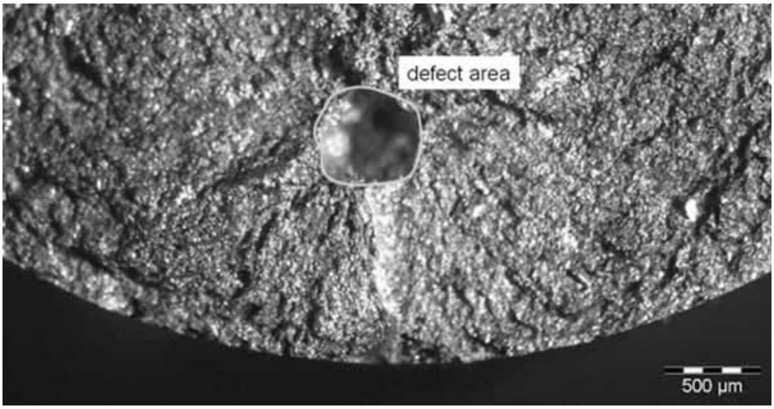

FIG. 12—*Crack initiating pore and corresponding defect area.*

$$d_{\text{equ}} = \sqrt{\frac{4A_{\text{defect}}}{\pi}} \tag{1}$$

The location of the crack in the fracture surface is defined as either at the surface or inside. If the distance from the surface is greater than the pore diameter the defect is regarded as inside. The equivalent diameter of pores inside the specimen is divided by 2, because the crack grows in all directions across the diameter. The problem is shown in Fig. 13.

Run-out specimens are tested at higher stress amplitudes until failure to obtain the size of the crack initiating defect.

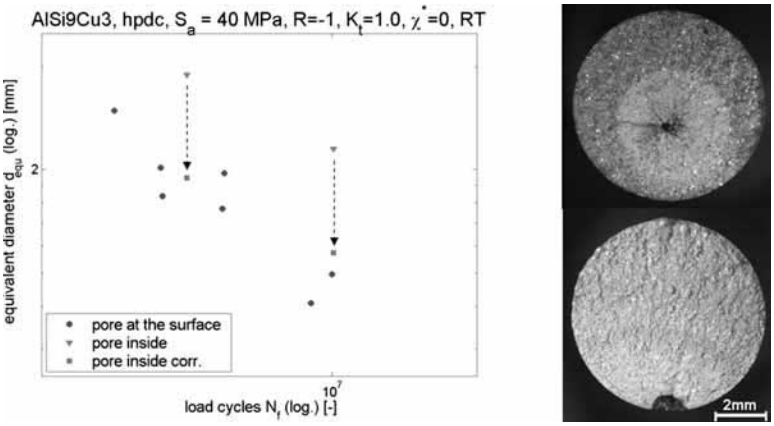

FIG. 13—*Correction of the defect size for pores inside the specimen* (*left*)*; fracture surfaces of crack initiating pores inside and at the surface* (*right*).

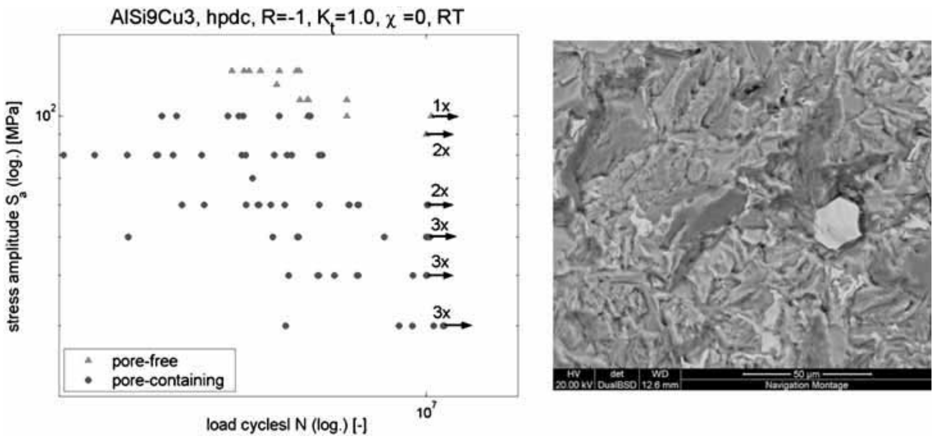

FIG. 14—*Cyclic test results for R=−1* (*left*)*; fracture surface from one specimen* (*right*).

Results and Discussion

Fatigue Tests

The test results for the two specimen geometries (round pore-containing specimens and flat pore-free specimens) for a stress ratio of $R = -1$ are shown in Fig. 14. The diagram shows the nominal stress versus cycles to failure. The data of the pore-containing specimens show an obvious scatter in the test data. This is because the specimens are produced from plates with different degrees of porosity. The pore-free data show a much lower scatter. Furthermore the fatigue strength at 1e7 load cycles is significantly higher than for the pore-containing specimens.

It is clear from Fig. 14 that it is not possible to derive a S/N curve from this data. The scatter is induced by the different degrees of porosity in the specimens. A parameter is needed to describe the influence of the casting defects on the fatigue life time at the different stress amplitudes.

A SEM picture of the fracture surface in the area of stable crack growth is shown in Fig. 14, right. The intermetallic brittle phases are shown as plate-like regions. In-between are the α-Al-dendrites which show striations from the crack propagation.

The size of the defect is the limiting factor to the number of load cycles as shown in Refs [3–5,8,9]. Figure 15 correlates fatigue life with defect size described by the equivalent diameter d_{equ}. Each stress amplitude is represented with a different shape of the data points. The data follow very well a linear trend. The slope of the four regression lines is in the range of 0.31–0.33. This trend highlights that the load cycles until failure depend strongly on the most critical defect size in the homogeneously stressed region of the specimen.

A bigger pore in a specimen leads consequently to a shorter fatigue life time. This points to the fracture mechanics approach, a larger initial crack size with a constant stress amplitude results in a higher initial stress intensity factor

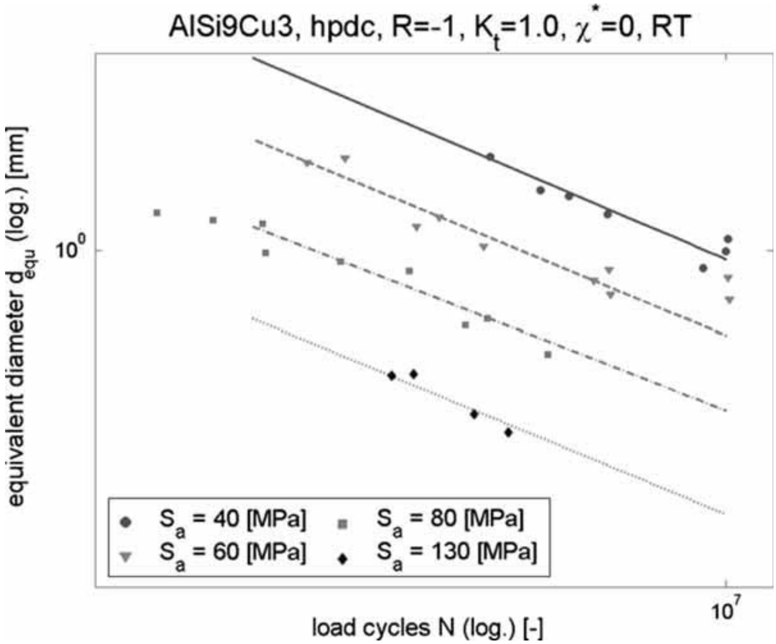

FIG. 15—*Influence of the equivalent diameter on the load cycles until failure.*

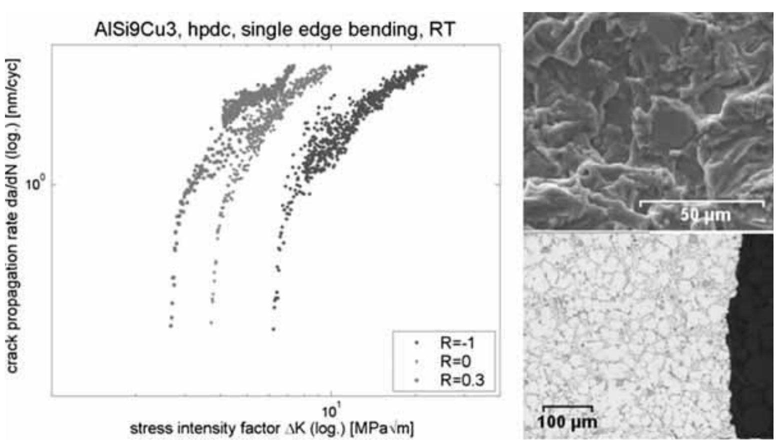

FIG. 16—*Long crack growth curves for different stress ratios R* (*left*)*; fracture surface* (*right*).

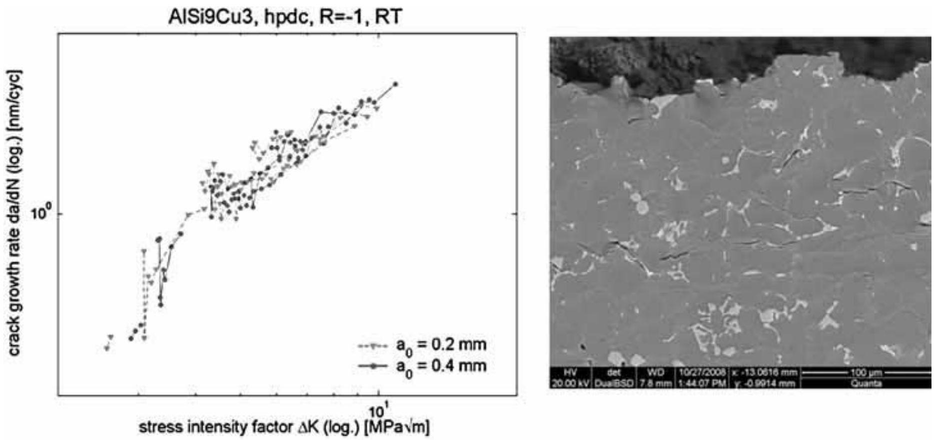

FIG. 17—*Short crack growth curve* (*left*)*; surface of the tested specimen below the crack path* (*right*).

ΔK_i. Due to the higher stress intensity factor the crack propagates faster through the material and leads to an earlier failure as compared to the case of a smaller pore. This means that the crack initiates immediately at the pore and the fatigue life time is only defined by the crack growth rate through the material. This will be looked at in more detail in the subsequent sections.

Fatigue Crack Growth and Threshold Data

Long Crack Growth—Experimentally measured long crack threshold values, ΔK_{th}, for different stress ratios R are shown in Fig. 16.

Figure 16 (right) depicts the crack surface (SEM) and transverse section (light optical microscopy) from the middle of the SEB specimens (plane strain state) resulting from a stress ratio of 0 and a loading in the Paris region (growth direction from top to bottom). The crack propagation seems to be intercrystalline for Al-9Si-3Cu.

Short Crack Growth—Crack length was measured from the pictures and the crack growth rate and the corresponding stress intensity range (Eq 2) were calculated. The procedure was repeated several times until failure of the specimen. Each interruption produced a data point of the crack growth diagram. Figure 17 (left) shows the test results for a stress ratio of −1. It can be observed that the small cracks propagate at lower stress intensity factors than long cracks and they propagate faster

$$\Delta K = 2S_a\sqrt{\pi a}F_I \tag{2}$$

where:

ΔK = stress intensity factor,

S_a = stress amplitude,

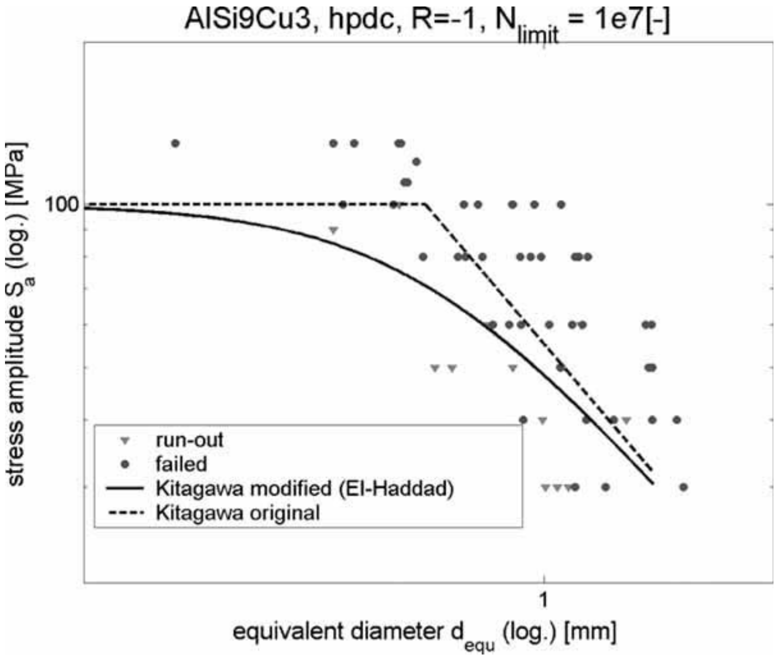

FIG. 18—*Kitagawa diagram for a stress ratio of R=−1.*

a = crack length, and
F_I = geometry factor.

Figure 17 (right) depicts the surface of a specimen tested at a stress amplitude of 80 MPa. The main crack path is on top of the picture. The small cracks below the main crack are induced by the plastic zone. The backscatter mode of the SEM highlights the different intermetallic phases at the surface. Due to the plastic zone at the crack tip some of these brittle phases either detach from the matrix or fail. A trend as observed in Ref [10] that the intermetallic phases fracture above an orientation of 45° and detach below this angle could not be found for Al-9Si-3Cu.

Discussion

In fracture mechanics, the stress state at crack tip of a crack is described by the stress intensity factor ΔK (Eq 2). In this formulation S_a is the stress amplitude applied on the specimen far away from the crack tip, a is the crack length and F_I is a function of geometry and type of loading.

If the stress intensity factor ΔK is below the threshold value ΔK_{th} no crack propagation occurs. Aluminium alloys do not have a distinct fatigue limit [11]. Therefore the fatigue limit for this computation was set to 1e7 load cycles. Kitagawa [6] used Eq 2 and reformulated it together with the threshold stress intensity ΔK_{th} factor to compute the fatigue limit (Eq 3)

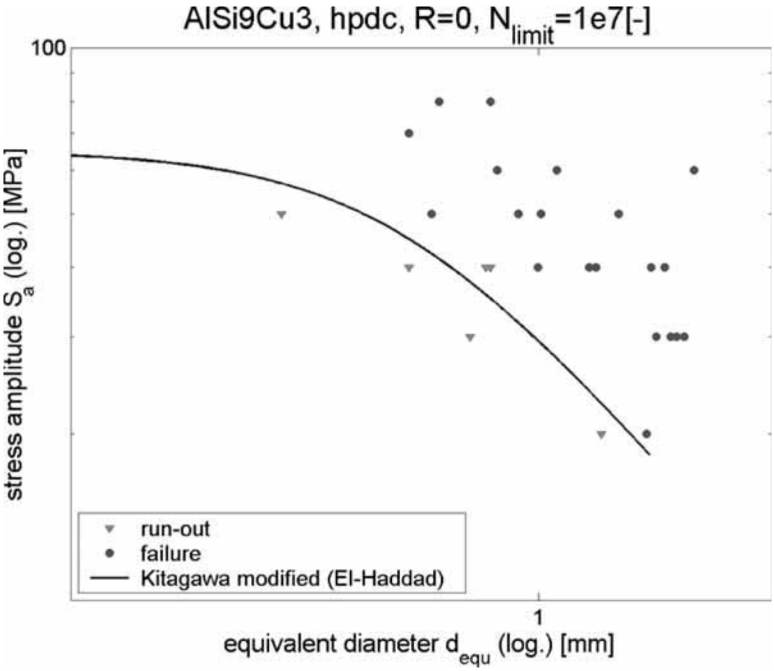

FIG. 19—*Kitagawa diagram for a stress ratio of R=0.*

$$S_a = \frac{\Delta K_{\text{th}}}{2\sqrt{\pi a}} \tag{3}$$

The resulting truncation line between run out and failed specimens, shown in Fig. 18 as a dashed line shows the result using the threshold stress intensity factor ΔK_{th} of the long crack experiments. The horizontal line is the fatigue limit S_{fat} of the defect free material (Fig. 14). The results from the fatigue specimen tests are visualized in the same plot by the circles (failed specimens) and triangles (run out specimens). Comparing the original Kitagawa line (Fig. 18, dashed line) with the results from the fatigue test shows that the Kitagawa approach overestimates the fatigue limit. This is particularly the case for small defect diameters where, as shown by the experiments, short cracks have a lower threshold stress intensity factor as compared to long cracks. This is due to the missing crack closure effects [12].

It is known that when a is very small, S_a approaches an asymptotic fatigue limit S_{fat}. To characterize this behavior El-Haddad [13,14] proposed the existence of an intrinsic crack length a_0 (Eq 4)

$$S_a = \frac{\Delta K_{\text{th}}}{2\sqrt{\pi(a_0 + a)}} \tag{4}$$

The intrinsic crack length a_0 is defined as following:

$$a_0 = \frac{1}{\pi}\left(\frac{\Delta K_{\mathrm{th}}}{2S_{\mathrm{fat}}}\right)^2 \tag{5}$$

The calculated line using El-Haddad's modified equation is shown in Fig. 18. The result shows a good agreement with the results from the fatigue tests. The computed line separates the run-outs from the failed specimens.

The resulting Kitagawa diagram using Eq 4 for a stress ratio of $R=0$ is shown in Fig. 19. The computed line separates the failed from the run-out specimens well.

Conclusions

Fatigue and fatigue crack growth experiments have been conducted for high pressure die cast components of Al-9Si-3Cu. The results can be summarized as follows:

- The fatigue strength of the pore-free material at 1e7 load cycles and a stress ratio of -1 was found to be 100 MPa;
- The pore-containing specimens show a huge scatter of the load cycles until failure at the different stress amplitudes;
- The fatigue strength decreases sharply in the HCF region from the pore-free to the pore-containing specimens;
- The load cycles till failure correlate well with the crack initiating defect size in the fracture surface. The slope of the regression lines in a double-logarithmic diagram is almost constant;
- The short crack growth experiments with two different initial crack lengths show a lower threshold stress intensity factor than for the long cracks; and
- The modified Kitagawa diagram (El-Haddad) shows a good agreement to the results of the fatigue tests.

The modified Kitagawa diagram is used to describe the influence of the defects size on the fatigue strength. A second model [15] allows estimating the pore size distribution in a HPDC-component. Combining the two models makes it possible to compute the local fatigue strength in the component [16].

Acknowledgments

Financial support by MAN Nutzfahrzeuge AG, Nürnberg and the Austrian Federal Government (in particular from Austrian Federal Ministry for Transport, Innovation and Technology and the Austrian Federal Ministry of Economics and Labour) and the Styrian Provincial Government, represented by Austrian Research Promotion Agency and by Steirische Wirtschaftsförderungsgesellschaft mbH, within the research activities of the K2 Competence Centre on "Integrated Research in Materials, Processing and Product Engineering," operated by the Materials Center Leoben Forschung GmbH in the framework of the Austrian COMET Competence Centre Programme, is gratefully acknowledged.

References

[1] Roy, N., Samuel, A. M., and Samuel, F. H., "Porosity Formation in Al-9 Wt Pct Si-3 Wt Pct Cu Alloy Systems: Metallographic Observations," *Metall. Mater. Trans. A*, Vol. 27A, 1996, pp. 415–429.

[2] Roy, N., Zhang, L., Louchez, P. R., and Samuel, F. H., "Porosity Formation in Al-9 wt % Si-3 wt % Cu-X Alloy Systems: Measurement of Porosity," *J. Mater. Sci.*, Vol. 31, 1996, pp. 1243–1254.

[3] Ting, J. C. and Lawrence, F. V., "Modeling the Long-Life Fatigue Behavior of a Cast Aluminium Alloy," *Fatigue Fract. Eng. Mater. Struct.*, Vol. 16, 1993, pp. 631–647.

[4] Ammar, H. R., Samuel, A. M., and Samuel, F. H., "Porosity and the Fatigue Behavior of Hypoeutectic and Hypereutectic Aluminium-Silicon Casting Alloys," *Int. J. Fatigue*, Vol. 30, 2008, pp. 1024–1035.

[5] Couper, M. J., Neeson, A. E., and Griffiths, J. R., "Casting Defects and the Fatigue Behavior of an Aluminium Casting Alloy," *Fatigue Fract. Eng. Mater. Struct.*, Vol. 13, 1990, pp. 213–227.

[6] Kitagawa, H. and Takahashi, S., "Applicability of Fracture Mechanics to Very Small Cracks or the Cracks in the Early Stage," *Proceedings of the Second International Conference on Mechanical Behavior of Materials*, ASM, Metals Park, 1976, pp. 627–631.

[7] Oberwinkler, B., Oberwinkler, C., Redik, S., and Leitner, H., "Analysis of Short Crack Growth for Two Representative Light Metals," *12th International Conference on Fracture*, Proceesings of the ICF, Ottawa, 2009.

[8] Wang Q. G., Davidson C. J., Griffiths J. R., Crepeau P. N., "Oxide Films, Pores and the Fatigue Lives of Cast Aluminium Alloys," *Metall. Mater. Trans. B*, Vol. 37B, 2006, pp. 887–895.

[9] Davidson, C. J., Griffiths, J. R., and Machin, A. S., "The Effect of Solution Heat-Treatment Time on the Fatigue Properties of an Al-Si-Mg Casting Alloy," *Fatigue Fract. Eng. Mater. Struct.*, Vol. 25, 2002, pp. 223–230.

[10] Lados, D. A. and Apelian, D., "Relationships Between Microstructure and Fatigue Crack Propagation Paths in Al-Si-Mg Cast Alloys," *Eng. Fract. Mech.*, Vol. 75, 2008, pp. 821–832.

[11] Leitner, H., 2001, "Simulation des Ermüdungsverhaltens von Aluminiumgusslegierungen," Ph.D Dissertation, University of Leoben, Austria.

[12] Tabernig, B., 2000, "Das Ermüdungsverhalten teilchenverstärkter Aluminiumlegierungen," Ph.D Dissertation, University of Leoben, Austria.

[13] El Haddad, M. H., Smith, K. N., and Topper, T. H., "Fatigue Crack Propagation of Short Cracks," *ASME Transactions*, Vol. 101, 1979, pp. 42–46.0002-7820

[14] El Haddad, M. H., Topper, T. H., and Smith, K. N., "Prediction of Non Propagating Cracks," *Eng. Fract. Mech.*, Vol. 11, 1979, pp. 573–584.

[15] Oberwinkler, C., Leitner, H., and Eichlseder, W., "Improvement of an Existing Model to Estimate the Pore Distribution for A Fatigue Proof Design of Al HPDC Components," *TMS 2009, Shape Casting: 3rd Int. Symposium*, 2009, pp. 45–52.

[16] Oberwinkler, C., Leitner, H., and Eichlseder, W., "Computation of Fatigue Safety Factors for High-Pressure Die Cast (HPDC) Aluminium Components Taking into Account the Pore Size Distribution," *SAE World Congress 2009*, 2009, Paper No. 2009-01-0082.

Reprinted from JAI, Vol. 7, No. 6
doi:10.1520/JAI102710
Available online at www.astm.org/JAI

Y. Pardhi,[1] *C. Dungey,*[2] *G. Baxter,*[2] *P. Bowen,*[1] *and T. P. Halford*[1]

Fatigue Crack Propagation Behavior of an Inertia Friction Welded α/β Titanium Alloy

ABSTRACT: The inertia friction welding process is being extensively investigated for the joining of high strength titanium alloys for aerospace applications. Although it offers solid state joining, the thermal cycle and deformation involved results in microstructural inhomogeneity across the weld interface. In this paper, the fatigue crack propagation behavior in an inertia welded microstructure in a high strength, high temperature α/β titanium alloy is considered. The fatigue crack propagation behavior in corner notched weld specimens at varying stress ratios is studied at room and elevated temperatures and compared with that of the parent material. Fatigue crack growth rates at lower stress intensity ranges are comparable with those in the parent material. However, in weld specimens tested at room temperature, unstable crack growth occurs at lower stress intensity range values compared to that at high temperature. Fracture surface observations show that this difference is related to a change in fracture mode from transgranular to intergranular/mixed mode during room temperature tests. This change in fatigue crack growth mechanism is deduced to be due to low ductility intergranular failure of grain boundary α in the refined transformed beta microstructure across the weld interface.

KEYWORDS: inertia friction welding, α/β titanium alloy, microstructure, fatigue crack propagation, stress intensity factor

---

Manuscript received August 27, 2009; accepted for publication May 14, 2010; published online June 2010.
[1] School of Metallurgy and Materials, Univ. of Birmingham, Birmingham B15 2TT, United Kingdom.
[2] Rolls-Royce Plc., Derby DE24 8BJ, United Kingdom.

Cite as: Pardhi, Y., Dungey, C., Baxter, G., Bowen, P. and Halford, T. P., "Fatigue Crack Propagation Behavior of an Inertia Friction Welded *α/β* Titanium Alloy," *J. ASTM Intl.*, Vol. 7, No. 6. doi:10.1520/JAI102710.

Introduction

In general, friction welding is becoming a more popular technique to join many aerospace components due to the evolution of advanced welding techniques such as friction stir welding, linear friction welding, and inertia welding [1]. These techniques are particularly desirable for the joining of dissimilar titanium alloys as well as titanium to other materials due to their ability to avoid embrittlement through air contamination experienced in fusion welds [1–3].

Inertia welding has been previously investigated to join titanium alloys by various researchers [4–8]. The microstructure of an optimized inertia welded titanium alloy usually consists of the refined transformed β microstructure in the weld zone, resulting in a hardness increase in this region [5,7]. Hardening is promoted principally due to the fine transformed β microstructure. The extremely high temperatures (possibly approaching the alloy solidus) experienced in the weld region combined with the severe local deformation result in the refined microstructure [7]. The thermomechanically affected zone (TMAZ) consists of a heavily deformed and partially dissolved parent metal microstructure. The postweld heat treatment (PWHT) leads to the formation of new α_{sec} platelets in the weld zone [8].

Axial force, surface speed, and the flywheel inertia are the main controlling parameters used in inertia welding. Although surface speed and joint area are critical in deciding the upset (change in axial dimension of the welded parts compared to their original length), a minimum upset value must be reached before the optimum mechanical properties are achieved [4]. The refined microstructure in the weld zone and the PWHT (at 640°C or 595°C) were shown to lead to tensile (room temperature and 300°C) and fatigue properties (300°C, $R=0.1$, in air) equivalent to the base material Ti-6Al-2Sn-4Zr-6Mo (Ti-6246) combined with slightly reduced creep resistance (450°C) [8,9]. Inertia welded assemblies of β forged Ti-6A1-2Sn-4Zr-2Mo-0.1Si (Ti-6242S) and Ti-17 (5Al-2Sn-2Zr-4Cr-4Mo) have been reported to have failed outside the weld zone in tension [6]. Thus inertia welds have good tensile strength, at least equivalent to the parent material. However, elongation and Charpy impact values have been shown to be less than that of the base material. The creep (at 450 and 500°C), low cycle fatigue (at 450°C, $R=0.05$) and high cycle fatigue (at 450°C, $R=0$) behavior of these welds has been found to be similar to that of the parent material.

The titanium alloy used in this study is a high strength, heat treatable α/β alloy used as intermediate pressure compressor disk material in Rolls-Royce Trent engines and has a potentially good hardening capability and high creep strength. Traditionally, this alloy is joined using electron beam welding for this application. Although currently acceptable, this welding technique does introduce an inherent porosity level in the weld joint resulting in non-optimized component life. Therefore, it is necessary to develop alternative ways of joining this alloy, and inertia welding is one of those techniques being investigated. In this paper the influence of the inertia welded microstructure on the fatigue crack propagation (FCP) behavior at various temperatures is investigated. The effect of varying stress ratio (a ratio of minimum applied stress, σ_{min} to maximum applied stress, σ_{max}) on crack growth rates in the weld microstructure is

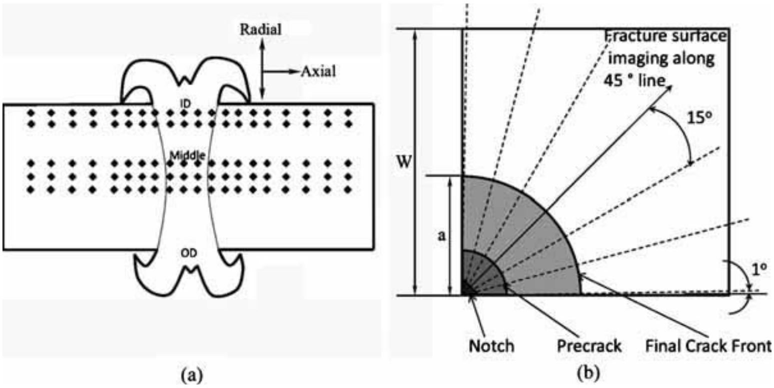

FIG. 2—*Schematics of* (*a*) *the arrangement of microhardness indentations with respect to the weld geometry and* (*b*) *the specimen cross section defining the measurement of crack length* (*a*) *and the specimen width* (*W*).

also evaluated. The resulting FCP behavior is compared with the response of the original β processed and fully heat treated microstructure of the parent metal. It is envisaged that the results of this investigation will help towards the understanding of the inertia welding process applied to titanium alloys and its influence on the mechanical properties.

Experimental Procedure

Materials and Specimens

β-forged and fully heat treated tubular rings with a wall thickness of 10 mm were inertia welded using parameters capable of producing reliable welds. A PWHT at 640 °C for 2 h [8,10] was carried out on these welds to re-establish the microstructure and relieve any residual stresses present. The welded assemblies were flash machined prior to the machining of mechanical test specimens. As shown in Fig. 1(*a*), cylindrical blanks were initially electrical discharge machining wire cut from the weld in the axial direction with the weld line located in the middle. For the purpose of FCP testing, corner notched (CN) specimens of dimensions shown in Fig. 1(*b*) were machined in such a way that the weld plane is located transversely across the middle of the gauge length. The notch was precisely positioned in the recrystallized CWZ in plane A-A, as shown in Fig. 1(*b*).

Microscopy

For microstructural observation, radial sections (as shown in Fig. 2(*a*)) were taken from each weld in the axial plane. Metallographic sections were mounted, polished, and then etched using a solution of 2 % HF and 10 % HNO_3 in water. High resolution secondary electron (using a field emission gun scanning electron microscope (SEM)) as well as optical images were taken from different parts of the weld region in order to understand the microstructure and precipitation behavior across the weld interface.

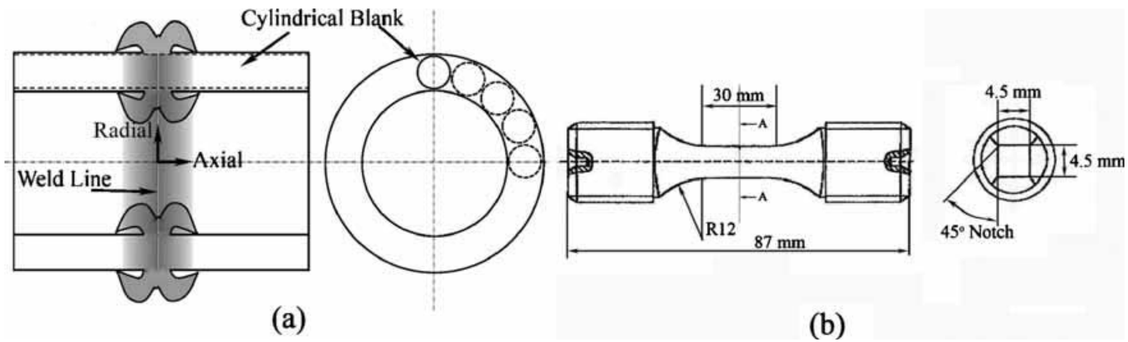

FIG. 1—*Schematic (not to scale) of (a) the orientation of cylindrical blank used for machining of FCP test specimens with respect to weld geometry and (b) FCP test specimen geometry with the notch positioned in plane A-A.*

Hardness Measurement

Microhardness measurements were carried out using a calibrated Vickers hardness indentation machine, with 1 kg load and a loading time of 10 s. The indentations were spaced greater than three to five times their width. Within the weld region, the indentations were spaced 300 μm apart, while further away from the weld centre, the distance between these indents was increased to 400 μm. Hardness profiles across the as welded and postweld heat treated specimens were generated based on the mean value of three profiles across the middle of the weld plane and two profiles across the inner diameter as shown in Fig. 2(*a*).

Fatigue Crack Propagation Testing

FCP testing was carried out on CN specimens of dimensions shown in Fig. 1(*b*). This specimen geometry was chosen because in the absence of minor (major-minor compound cycle) cycles, the FCP lives associated with flaws in aero-engine discs are believed to be more accurately predicted using crack growth data from CN specimens [11,12]. It also forms a quarter circular crack similar in shape and size to those typically found in aero-engine discs [13]. However, in these specimens, the crack front geometry can change during crack propagation, and in some cases of nickel base superalloys [14,15], elliptical ("tear drop") cracking has been observed. This has not been observed however in titanium alloys [12,13]. In this the study stress intensity solution for quarter circular corner cracks provided by Pickard [11] was used, with the ratio a/W (where *"a"* is crack length and *"W"* is the specimen width as defined in Fig. 2(*b*)) not exceeding 0.55 during the tests. FCP tests were carried out according to the Rolls-Royce standard test procedure [16] and the BS 6835-1:1998 [17] on postweld heat treated samples only. Initially, all specimens were precracked using suitable loads at room temperature. The tests were performed at stress ratios of 0.01, 0.4, and 0.8 using a trapezoidal loading waveform with a frequency of 0.25 Hz (1-1-1-1, i.e., 1 s dwell at maximum and minimum loads with ramping time of 1 s in between) and at room temperature, 400°C, and 450°C. After the completion of each test, the specimen was then fatigue opened at room temperature. For comparison, a limited number of tests were also performed on parent metal specimens at a stress ratio of 0.01.

During FCP tests, the crack length was monitored using a dc potential difference technique, a method based on the principle that the electrical resistance of a conductor increases with reduction in its cross sectional area [18]. The potential difference was then related to the actual crack length using an in-house calibration function for the specimen geometry used. The actual pre-crack length and final crack length were measured using a SEM at seven positions spaced 15° apart as shown in Fig. 2(*b*). The measured crack length was well in agreement with the calibrated crack length for all specimens tested. Figure 3 shows two examples of extreme cases where the largest difference between the final measured crack length and calibrated crack length is only about 0.06 mm. After testing, the fracture surfaces of the failed FCP specimens

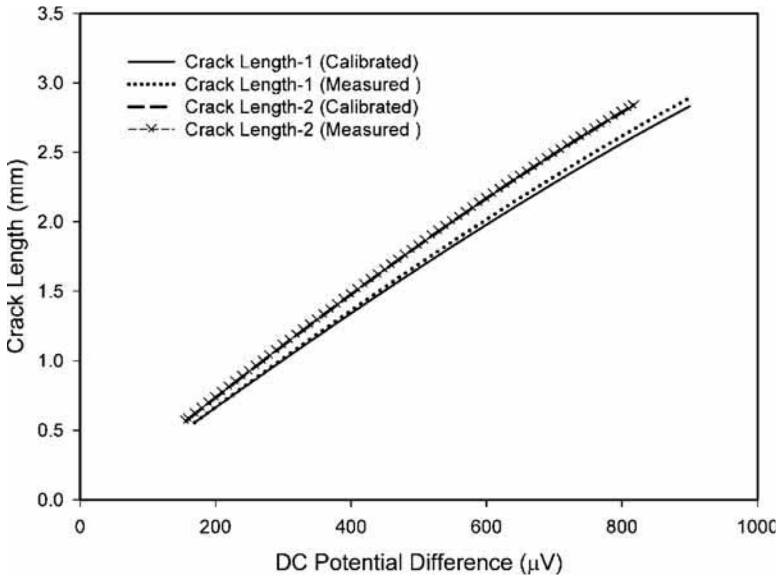

FIG. 3—*A comparison of calibrated crack length with measured crack length as a function of growing dc potential difference during FCP testing.*

were also examined by scanning electron microscopy in order to identify the failure mechanisms involved. The fracture surface images were taken along a line 45° to the specimen surface as indicated in Fig. 2(*b*).

Results and Discussion

Parent Metal Microstructure

A typical β processed microstructure of the disk material used in this investigation is shown in Fig. 4(*a*). It consists of colonies of coarse parallel α plates nucleated at β grain boundaries. The length and size of these plates are governed by the cooling rate from the forging temperature and increase if cooled slowly. Also, the coarse α plates assume a basket weave morphology within the grains. There are regions of both continuous and discontinuous α layers at the β grain boundaries. Within the matrix between the coarse α plates, a fine precipitation of secondary α platelets was observed as shown in Fig. 4(*b*). The formation of these fine secondary α platelets is known to have considerable influence on the yield strength of the material [19,20].

As Welded Microstructure

The inertia weld region of the alloy is characterized into three distinct zones starting from the weld centreline, viz., the central weld zone (CWZ), TMAZ, and heat affected zone (HAZ) followed by the parent metal as shown in Fig. 5.

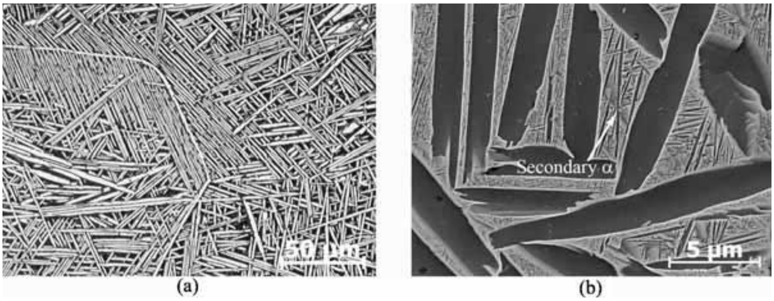

FIG. 4—*The microstructure of* β *forged parent material:* (*a*) *Showing coarse* α *grown in colonies of parallel plates at grain boundaries and as basket weave morphology within the grain and* (*b*) *showing secondary* α *precipitation within the matrix between coarse* α*. The darker phase in the SEM image* (*b*) *is* α*, whilst bright phase is* β*.*

Central Weld Zone—The CWZ consists of a dynamically recrystallized fine grain structure having needlelike martensitic α' as shown in Fig. 6(*a*), where continuous α forms at the grain boundaries. The α phase in these images is etched out and appears dark in contrast. The size of the α' needles is a function of cooling rate from the welding temperature, which can vary with the wall

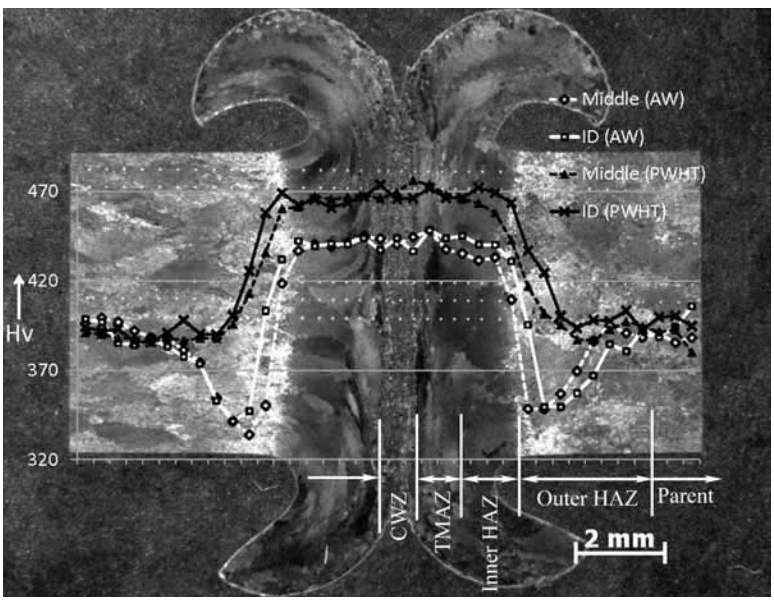

FIG. 5—*The macro image of a weld section and superimposed hardness profiles of as welded and postweld heat treated samples showing the variation of hardness within the different zones across the interface.*

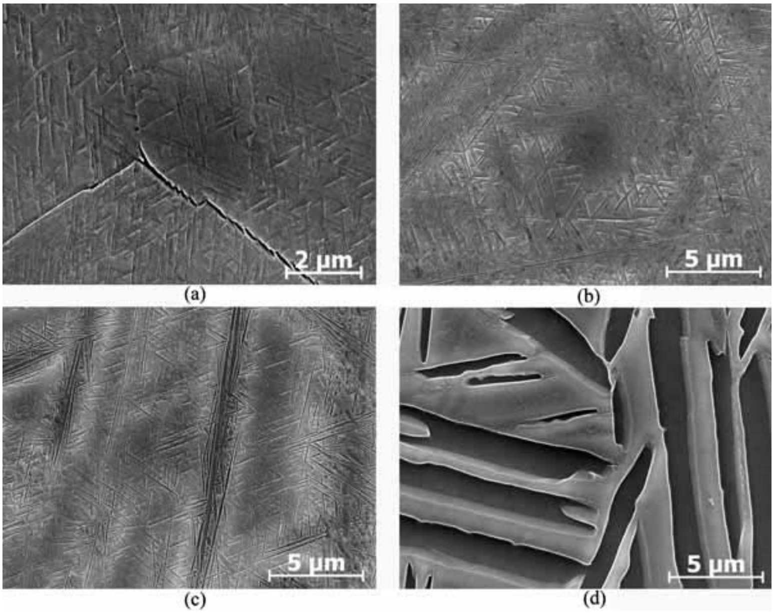

FIG. 6—*As welded microstructure:* (*a*) *The CWZ showing martensitic* α' *in* β *grains and grain boundary* α, (*b*) *the TMAZ showing martensitic* α' *and weakly defined phantom* α, (*c*) *the inner HAZ microstructure showing phantom* α *and martensitic* α', *and* (*d*) *the outer HAZ depleted in secondary* α.

thickness of the weld specimens. This microstructure is a result of transformation to the single phase β field during welding followed by rapid cooling. During welding, material at the interface is heated to very high temperatures above the β-transus of the material. Under the influence of the high strain rates involved, the CWZ is dynamically recrystallized into a fine grain structure of β, and subsequent rapid cooling results in the formation of basket weave α' along with retained metastable β. Similar characteristics of the weld zone have been reported previously for inertia welds of Ti-6246 [8], Ti-6Al-4V [5], Ti-6242S, and Ti-17 [6]. For the welding parameters used in this investigation, the average grain size of the CWZ was estimated to be ≈ 40 μm as opposed to ≈ 450 μm of the parent material. The fine grain size of the CWZ is a result of dynamic recovery or recrystallization due to thermomechanical processing above the β-transus, depending on strain rate and strain conditions resulting from the welding parameters.

Thermomechanically Affected Zone—A narrow region between the CWZ and the HAZ was observed to consist of highly deformed grains. The TMAZ microstructure consisted of martensitic α' along with some residual coarse α from the original microstructure (see Fig. 6(*b*)), hereafter referred to as phantom α. This phase is seen as darker regions of ~ 2 μm width and 10–15 μm in length. The presence of phantom α is attributed to incomplete homogenization due to the very short time at temperatures around the β-transus during welding. This region experiences peak temperatures near or above the β-transus temperature, at which homogenization of alloying elements originally partitioned to α and β phases remains incomplete. After cooling, the microstructure therefore contains a mixed proportion of unaffected parent metal and limited mechanical deformation [7].

Characteristics of Heat Affected Zone—The HAZ can be divided into two zones based on the extent of thermal effects in this region. The inner HAZ features undeformed grains of the original parent metal microstructure consisting of martensitic α' and phantom α, which is more clearly defined as shown in Fig. 6(*c*) due to the lower temperatures experienced. Further away towards the parent metal, the extent of coarse α dissolution reduces. Therefore the outer HAZ essentially consists of the parent microstructure depleted in secondary α and unaffected coarse α plates as shown in Fig. 6(*d*). The complete dissolution of secondary α occurs near the inner HAZ; however the extent of secondary α depletion reduces towards the parent metal. The secondary α platelets in this region, which form during low temperature ageing [19], dissolve due to exposure at high temperature, while subsequent rapid cooling restricts its reprecipitation. The transition between the HAZ and the parent metal microstructure is marked by the gradual reduction in the amount of dissolved secondary α as the temperature gradient drops near the unaffected parent metal.

Effect of Postweld Heat Treatment on Weld Microstructure

The division of different zones across the weld interface remains the same after PWHT. The martensitic α' in the CWZ is transformed into extremely fine secondary α having a basket weave morphology as shown in Fig. 7(*a*). Moreover, the retained metastable β is also decomposed into fine α, resulting in a further increase in density of reprecipitated α. The TMAZ and the inner HAZ also show an increased amount of fine α precipitation within and between phantom α phases. The microstructure of the TMAZ and the inner HAZ after PWHT is shown in Fig. 7(*b*) and 7(*c*), respectively. The outer HAZ, where secondary α was dissolved in the as welded condition, consisted of reprecipitated fine secondary α within the matrix between undissolved coarse α plates as shown in Fig. 7(*d*). In the transition region a mixture of retained secondary α and reprecipitated secondary α was observed, and the parent metal microstructure remained unaffected after PWHT.

Hardness Characteristics

The hardness characteristics across the weld interface are affected by the changes in microstructure. Figure 5 shows the microhardness profiles across the weld interface in the as welded and postweld heat treated conditions. The microhardness values and their relation to different zonal characteristics are shown in relation to the weld region. The hardness of the CWZ in the as welded condition is $\sim$440 Hv, an increase of $\approx$50 Hv above the parent metal hardness.

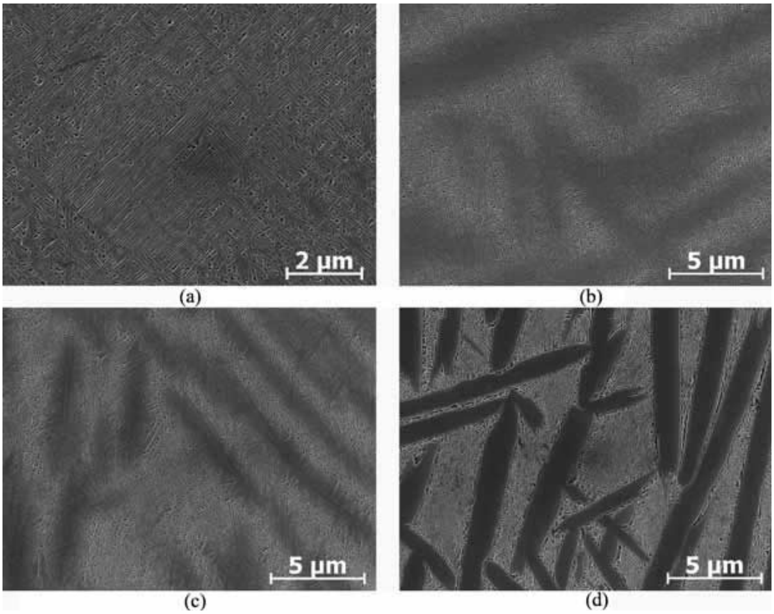

FIG. 7—*The postweld heat treated microstructure:* (*a*) *The CWZ features basket weave morphology of reprecipitated fine secondary* α, (*b*) *the TMAZ features traces of phantom* α *and reprecipitated* α *within the matrix,* (*c*) *the inner HAZ shows phantom* α *and reprecipitated* α, *and* (*d*) *the outer HAZ having reprecipitated fine* α *within the matrix between retained coarse* α *plates.*

The increase in hardness is usually attributed to the presence of martensitic α' and a refined grain size. However, the peak hardness value remains almost constant over the CWZ, TMAZ, and the inner HAZ, although there is a difference in grain sizes across these zones. This indicates that there is no effect of grain size (small in the CWZ and large in the TMAZ and inner HAZ) on the peak hardness value. Therefore, the increase in hardness is primarily governed by the presence of martensitic α'. At the transition between the inner HAZ and the outer HAZ, the hardness value drops to a minimum of $\approx$330 Hv. This drop in hardness is due to the dissolution of secondary α (shown in Fig. 6(*d*)) from the parent structure. As the amount of retained secondary α increases towards the parent metal, the hardness recovers to its original value of $\approx$390 Hv. There is no significant difference in the hardness profiles in the middle of the weld and near the inner diameter. The only difference observed is the increased width of the peak hardness region across the inner diameter which is due to the wider HAZ.

After PWHT the peak hardness values in the central part of the weld increase by $\approx$30 Hv. This is attributed to fine and dense precipitation of secondary α in this region. The PWHT also resulted in a recovery in hardness at the location where the minimum hardness was recorded in the as welded condition. The hardness values after PWHT in this region of recovery were above the

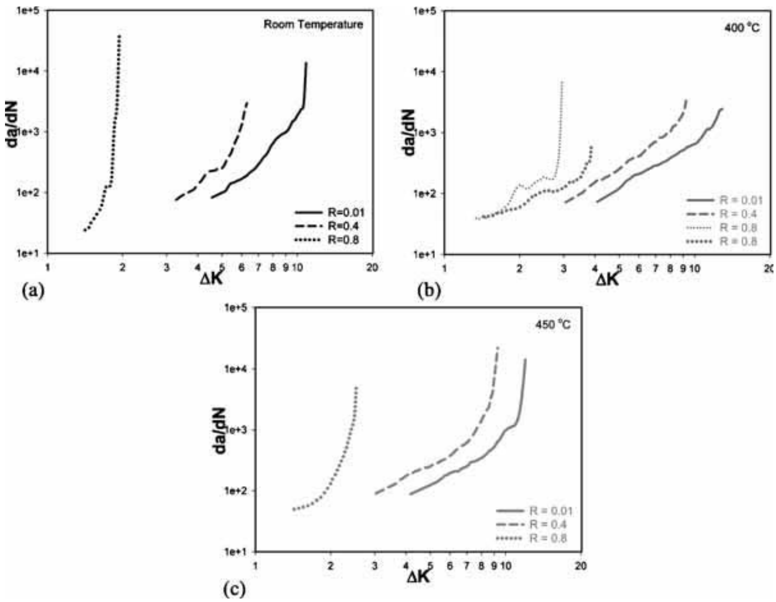

FIG. 8—*The effect of stress ratio on FCP behavior of inertia welds on an α/β titanium alloy at* (*a*) *room temperature,* (*b*) *400°C, and* (*c*) *450°C. Data in these graphs is normalized due to its commercial sensitivity.*

parent metal hardness. There is a smooth transition between the HAZ and parent metal hardness due to gradual decrease in the amount of reprecipitated secondary α towards the parent region.

The above observations show that the hardening capability of the alloy used is primarily affected by the presence of secondary α. In the as welded condition the depleted secondary α in the outer HAZ results in a hardness drop, while after PWHT its fine and dense form resulted in an increase in hardness above that of the parent metal.

Fatigue Crack Propagation Behavior

The results of FCP tests show that the fatigue crack growth rates for a given ΔK at the lower stress ratio of 0.01 are slower than those at higher stress ratios of 0.4 and 0.8. This is shown in Fig. 8(*a*), Fig. 8(*b*), and Fig. 8(*c*) for weld specimens tested at room temperature, 400°C, and 450°C, respectively. These curves include normalized scales on both axes due to commercial sensitivity of the data. The fatigue crack growth curves shown essentially consist of stage II (stable) and stage III (unstable) crack growth regimes. During stage III crack propagation, static failure modes dominate the fatigue failure leading to rapid increases in crack growth rates, a behavior common in most metallic materials [21,22]. It can be seen from the plots that the ΔK required to achieve the same crack growth rate decreases drastically as stress ratio is increased. At room temperature this decrease in ΔK is faster than that at high temperatures. This suggests that the fracture toughness of the weld material is low at room temperature, which results in early stage III crack growth. This is consistent with another study conducted by Miles [23], where fracture toughness at high temperature (400 and 450°C) has been found to be approximately two times that at room temperature. There is no significant difference in the trend at 400 and 450°C.

FCP tests were carried out twice for each test condition, and it was observed that the results are repeatable provided correct positioning of notch in the narrow CWZ is achieved. Hence, only one curve for each condition is shown. However, as shown in Fig. 8(*b*), at a stress ratio of 0.8 and 400°C, the two fatigue crack growth curves do not agree at higher ΔK values. This is believed to be the effect of inhomogeneity in the local microstructure. The reproducibility of results is heavily dependent on the path the fatigue crack follows in the narrow central weld region. Variations in microstructural features such as grain size and α platelet size can result in different behavior. During microstructure studies differences in the grain size within the CWZ have been observed. For the results at 400°C shown in Fig. 8(*b*), a slight difference in the local grain size was seen in the regions where fatigue crack growth took place.

Effects of Temperature—The effect of test temperature at stress ratios of 0.01, 0.4, and 0.8 on fatigue crack growth curves is shown in Fig. 9(*a*), Fig. 9(*b*), and Fig. 9(*c*), respectively. Figure 9(*a*) also includes fatigue crack growth plots of the parent material. The high temperature behavior of the parent metal and the weld material is similar; however, there is an obvious difference in the room temperature behavior. The weld metal, being harder (due to fine α) and having a fine grain microstructure, exhibits faster fatigue crack growth rates at room temperature. Also, the curves for the parent metal suggest that its fracture toughness is higher than that of the weld material at all temperatures. The curves of the parent metal are not complete in stage III because the ratio a/W exceeded the recommended maximum value of 0.55 [11] during testing. It can be seen from Fig. 9(*a*) that the crack growth behavior at 400 and 450°C for weld material is similar during stage II growth, but unstable crack growth appears to start at a lower ΔK in the latter case. The reasons behind this are not clear but creep deformation may have played role in early stage III crack growth at the higher temperature of 450°C. Although the alloy under investigation is believed to have good resistance to creep deformation at 450°C, the fine grain structure of the CWZ can reduce creep resistance as reported by Roder et al. [8] for Ti-6246 at this temperature.

At all stress ratios at room temperature, the fatigue crack grows relatively slowly compared to high temperatures in the low ΔK region but accelerates once a certain value is exceeded. Fracture surface observations reveal transgranular crack growth during all the high temperature tests. In comparison, in specimens tested at room temperature, the fatigue crack grew transgranularly at low ΔK but exhibits intergranular or mixed mode growth at high ΔK values. Figure 10(*a*) shows a low magnification image of the transition region from transgranular to intergranular fatigue crack growth. Figure 10(*b*) and Fig. 10(*c*) show high magnification SEM images of transgranular and intergranular

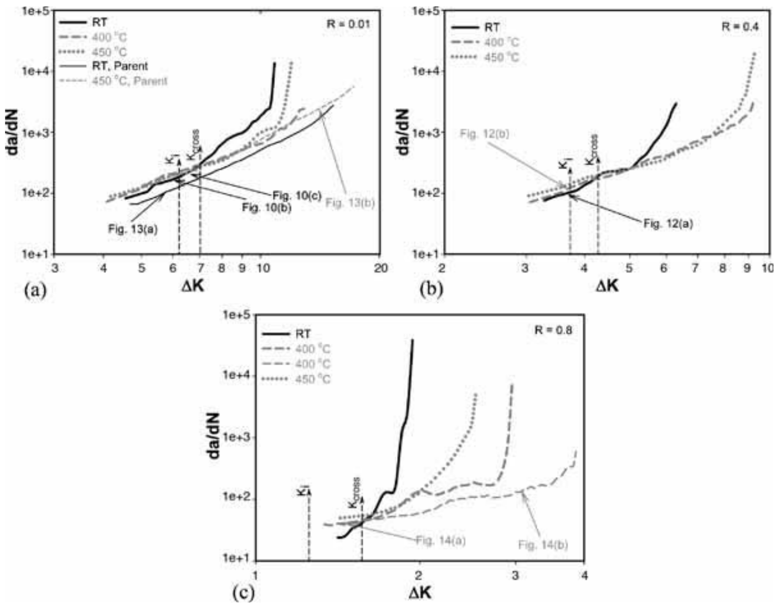

FIG. 9—*The effect of temperature on the FCP behavior of an inertia welded* α/β *titanium alloy at* (*a*) *R=0.01,* (*b*) *R=0.4, and* (*c*) *R=0.8. The room temperature and high temperature curves cross at a maximum stress intensity* (K_{cross}) *due to a change in the mode of fracture from transgranular to intergranular at a critical stress intensity equal to* K_i. *Data in these graphs is normalized due to its commercial sensitivity.*

growth of regions indicated in Fig. 10(*a*), respectively. The corresponding ΔK levels of these fractographs are indicated on the plots in Fig. 9(*a*). The transition from transgranular to intergranular crack growth can be identified as occurring when the maximum stress intensity factor approaches the crossover point of the two curves, suggesting accelerated crack growth to be related to a change in the crack growth mode.

The change in the mode of fatigue crack growth in the welds investigated in this study is believed to be due to the effect of the plastic zone size. The plastic zone size is determined by the maximum applied stress intensity factor. Therefore, at a certain maximum stress intensity, the plastic zone size must equal the local grain size of the weld material. According to Irwin's approximation [22], the plastic zone size (r_p) in plain strain conditions is given by

$$r_p = \frac{1}{3\pi}\left(\frac{K_I}{\sigma_y}\right)^2$$

where:

K_I = stress intensity and

σ_y = yield strength of the material.

When r_p is substituted for the local grain size in the weld material, the above equation gives a value, $K_i = 6.2$ (normalized), as indicated on the graphs

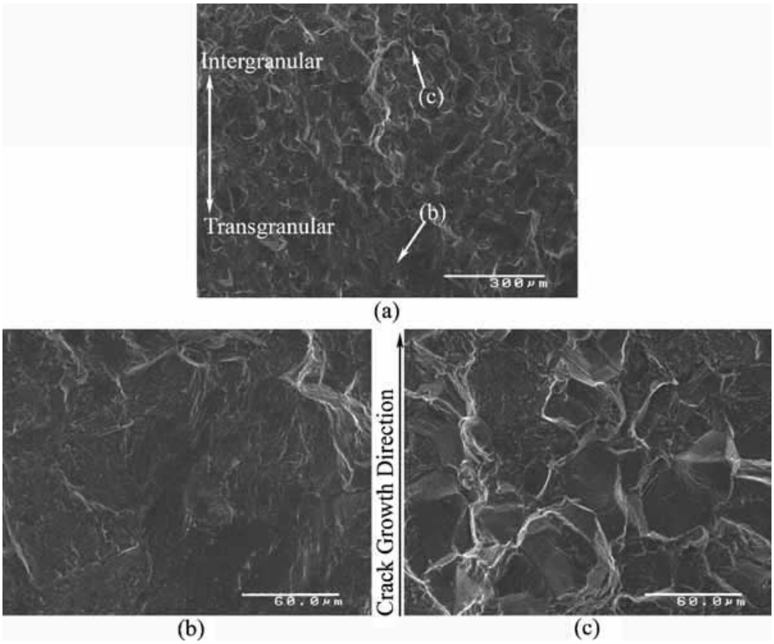

FIG. 10—*Fractographs of room temperature FCP tests:* (*a*) *A low magnification SEM image of the transition region where the fatigue crack growth mode changes from transgranular to intergranular,* (*b*) *a high magnification image of transgranular growth, and* (*c*) *a high magnification image of intergranular growth. The corresponding* ΔK *levels of* (*b*) *and* (*c*) *are indicated in Fig. 9*(*a*)*.*

in Fig. 9. This value of K_i is ~20 % lower than the maximum stress intensity (K_{cross}) at which room temperature and high temperature cross each other. Therefore, this stress intensity value, K_i, is deduced to mark the onset of intergranular fracture. This is confirmed by observations of fracture surfaces, whereby intergranular crack growth begins to appear at ΔK values corresponding to K_i (see Fig. 10(*b*)) and can be clearly seen at higher values in Fig. 10(*c*). Therefore, it can be concluded that the change in the mode of crack growth exhibited in these welds, which manifested for low ductility intergranular failure of grain boundaries occurs when the plastic zone size exceeds the grain size of the material. A previous study on Ti-6246 electron beam weldments indicated that grain boundary α formation can promote intergranular low ductility failure [24]. The welds used in this study were observed to have grain boundary α in the CWZ as shown in Fig. 6(*a*). The incompatibility of slip between the grain boundary α and transformed β may lead to the formation of dislocation clusters at the interface resulting in intergranular cracking [24].

Fractography—The macro images in Fig. 11(*a*) and Fig. 11(*b*) show the appearance of the fracture surface during the different stages of room temperature and elevated temperature tests, respectively. The fatigue precracked sur-

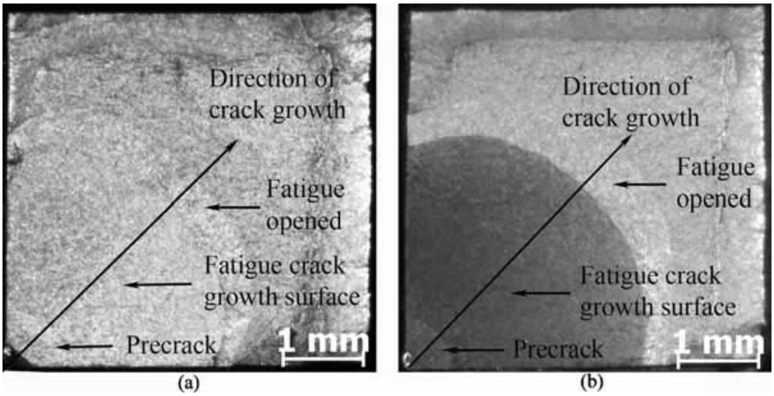

FIG. 11—*Macroscopic images of fracture surface of FCP specimens:* (*a*) *Room temperature and* (*b*) *high temperature.*

face is smooth and distinguished from the actual test surface due to the low loads (usually 40–50 % of testing loads) used during precracking. Similar loads were used when the specimens were fatigued open after the test. This assured a clear crack front and facilitated the measurement of the final crack length. During all FCP tests, the crack exhibited a quarter circular form, thus facilitating the use of a compliance function employed for stress intensity factor calculations [11].

At the beginning of the fatigue crack growth, transgranular crack growth was observed in room temperature as well as elevated temperature tests as shown in Fig. 12(*a*) and 12(*b*). At similar ΔK values, room temperature tests show less plastic deformation than at high temperature, and striations are not clearly defined (see Fig. 12(*a*), inset). This is attributed to the low ductility of the weld material at room temperature [22]. The microstructure of the material also plays an important role in the appearance of striations on the fracture surface under similar testing conditions. The fracture surface of the weld specimens at low ΔK is smooth and relatively featureless due to its transformed β

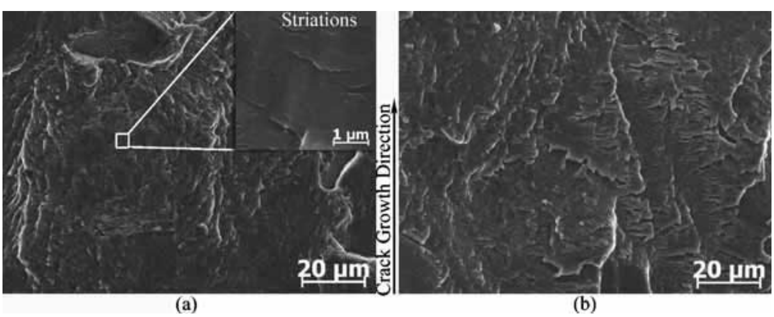

FIG. 12—*The fracture surface at low stress intensity range* (*as indicated in Fig. 9*(*b*)) *for samples tested at R=0.4:* (*a*) *Room temperature and* (*b*) *450°C.*

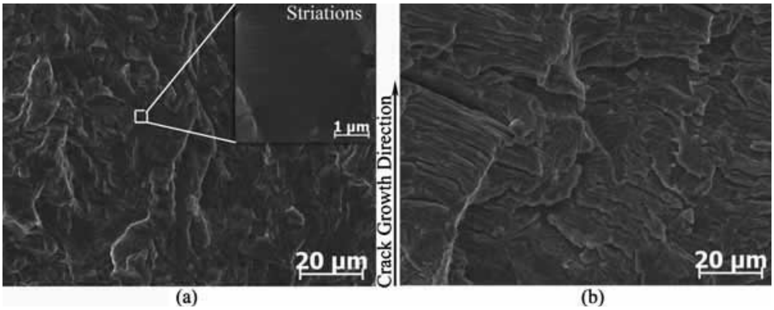

FIG. 13—*The fracture surface of parent Ti-6246 specimens at* (*a*) *room temperature and low* ΔK *exhibiting very fine striations and* (*b*) *450°C and high* ΔK *showing large deformation. The corresponding* ΔK *levels are indicated in Fig. 9*(*a*).

microstructure having fine α precipitation. On the fracture surface of parent material, which has a lamellar microstucture with coarse α, the direction of the striations growth is affected by the local microstructure. The fractographs of the parent material are shown in Fig. 13(*a*) and Fig. 13(*b*) for specimens tested at room temperature (low ΔK) and 450°C (high ΔK), respectively. The fracture surface of the parent specimens was rough and partly faceted at low ΔK values. At low ΔK, very fine striations were seen as shown in inset in Fig. 13(*a*). The spacing between striations increases in the direction of crack growth, while its density reduces, which is typical characteristic of growth by striation formation [25,26].

As ΔK increases during the test, the fracture surface appearance also changes. During room temperature tests, the fracture surfaces remained transgranular at low ΔK, as shown in Fig. 10(*b*). With further increases in ΔK, intergranular cracking became evident as seen in Fig. 10(*c*). There was also evidence of dimpled monotonic fracture at high ΔK on these fractographs, which correspond to stage III crack growth. Figure 14 shows fractographs of samples tested at high temperature and at a stress ratio of 0.8 for high and low ΔK values. For all stress ratios at high temperature, the fracture surface featured a transgranu-

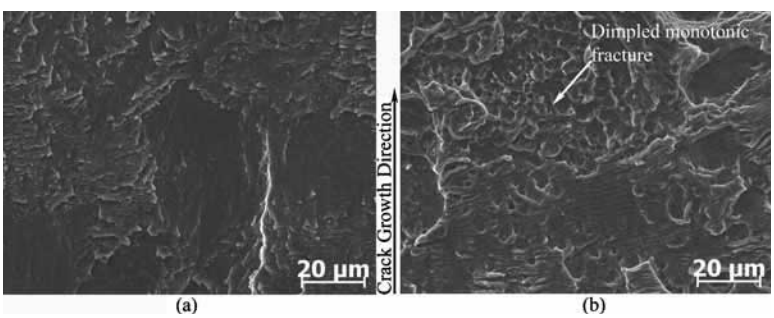

FIG. 14—*The fracture surface of high temperature FCP test piece:* (*a*) *at low* ΔK *and* (*b*) *at high* ΔK *as indicated in Fig. 9*(*c*).

lar mode. Due to increased plastic deformation at high ΔK, the fracture surface is rough and shows evidence of monotonic dimpled fracture (Fig. 14(*b*)). This type of fracture surface is typical to the stage III crack growth of ductile materials [22].

From the observations of fracture surfaces and the fatigue crack growth curves, some important conclusions can be made related to the effect of microstructure on the fatigue behavior of this material. Although fine, the transformed β microstructure of the weld resulted in comparable crack growth rates with that of the parent material at low ΔK; at higher values, it results in accelerated crack growth. This is mainly due to reduced fracture toughness of the fine α microstructure, which is hard (as seen from hardness profiles) and less ductile. Moreover, α grain boundaries of the weld microstructure are weak at room temperature, resulting in intergranular crack growth once the maximum plastic zone size exceeds the grain size of the material. In both cases of the parent and weld microstructure, the room temperature fracture toughness is lower due to reduced ductility compared to that at high temperature. Therefore, stage III crack growth was seen at lower ΔK levels at room temperature.

It has been reported previously [4,6,8,27] that the fatigue properties (low cycle fatigue and high cycle fatigue) of titanium alloy inertia welds are similar or better than the parent material. The results of this investigation show that this depends on the property being considered for the comparison. Although the FCP behavior of the weld microstructure is similar to that of the parent material at low ΔK, this is not the case at high ΔK values as it is inferior due to the reduced levels of fracture toughness, which is more noticeable at room temperature.

Conclusions

The following important conclusions are made from the study conducted on inertia welds of an α/β titanium alloy.

- The as welded microstructure consists of a dynamically recrystallized CWZ having a fine grained structure with martensitic α' and retained metastable β. The formation of martensitic α' in the zones across the interface results in an increase in hardness above the parent material by about 50 Hv.
- The PWHT at 640°C for 2 h results in the transformation of martensitic α' into fine secondary α, the density of which is further increased by decomposition of retained β. This resulted in further increases in hardness across the weld interface.
- The FCP behavior of the weld microstructure is similar to that of the parent material at low ΔK values, but stage III crack growth occurs much earlier in weld specimens due to reduced fracture toughness resulting from a fine α microstructure. The fatigue crack growth rate of the weld increases as the stress ratio is increased with the room temperature behavior being most affected.
- The room temperature FCP rates are slower at low ΔK values but increase rapidly once a critical maximum stress intensity is reached. At

high temperature, cracks grow faster but are stable for longer period.

- The early unstable (stage III) fatigue crack growth taking place at room temperature in these welds is due to a change in crack growth from transgranular to intergranular at a critical stress intensity value. This occurs when the maximum plastic zone size ahead of the crack tip exceeds the local grain size of the weld material. The change in fracture mode manifests itself as low ductility intergranular fracture of the grain boundary α.

Acknowledgments

The writer acknowledges Rolls-Royce Plc., Derby, UK, for supplying the necessary testing material and financial support for the project. The writer would also like to thank Universities UK (Award No. ORSAS-2006) for financial support of the project.

References

[1] Kallee, S. W., Nicholas, E. D., and Russell, M. J., "Friction Welding of Aero Engine Components," *Tenth World Conference on Titanium*, Hamburg, Germany, 13–18 July 2003, Gerd Luetjering and Joachim Albrecht, eds., Wiley VCH, Weinheim, Germany, pp. 2867–2874.

[2] Smith, L. S., Threadgill, P., and Gittos, M., *Welding Titanium: A Guide to Best Practice*, The Welding Institute, Cambridge, 1999, http://www.twi.co.uk/content/bpweldtis01.html (Last accessed 21 June 2009).

[3] Wang, K. K., "Friction Welding," *Weld. Res. Counc. Bull.*, Vol. 204, 1975, pp. 1–21.

[4] Nessler, C. G., Turz, D. A., Eng, R. D., and Vozzella, P. A., "Friction Welding of Titanium Alloys," *Weld. J. Res. Suppl.*, Vol. 50, 1971, pp. 379–385.

[5] English, C. L., "Inertia Welding of Jet Engine Components: Transitions from Electron Beam Welding to Inertia Welding of Titanium Alloy Fan Disk," *Proceedings of FABTECH International '95*, Rosemont, Chicago, IL, 1995, Vol. 2, pp. 1237–1250.

[6] Barussaud, A. and Prieur, A., "Structure and Properties of Inertia Welded Assemblies of Ti Based Alloy Disks," *Proceedings of the Eighth World Conference on Titanium*, Birmingham, United Kingdom, 22–26 October 1995, P. A. Blenkinsop, W. J. Evans, and H. M. Flower, eds., Institute of Materials, London, UK, pp. 798–804.

[7] Baeslack, W. A., Phillips, D., English, C., and Woodfield, A. P., "Inertia-Friction Welding of an Advanced Rapidly Solidified Titanium Alloy," *J. Mater. Sci. Lett.*, Vol. 10, 1991, pp. 1401–8.

[8] Roder, O., Helm, D., and Luetjering, G., "Microstructure and Mechanical Properties of Inertia and Electron Beam Welded Ti-6246," *Tenth World Conference on Titanium*, Hamburg, Germany, 13–18 July 2003, Gerd Luetjering and Joachim Albrecht, eds., Wiley VCH, Weinheim, Germany, pp. 2875–2882.

[9] Roder, O., Ferte, J. P., Gach, E., Mendez, J., Anglada, M., and Mateo, A., "Development and Validation of A Dual Titanium Alloy Dual Microstructure BLISK," *Fifth Aeronautic Days 2006*, MTU Aero Engines, Vienna, Austria, 2006.

[10] Attallah, M. A. and Preuss, M., 2009, *Metallurgical and Residual Stress Characterisation of Ti-6246 Inertia Friction Welds*, Rolls-Royce Plc., Derby, United Kingdom, p. 23.

[11] Pickard, A. C., *The Application of 3-Dimentional Finite Element Methods to Fracture Mechanics Life Prediction*, EMAS, Warley, United Kingdom, 1986, pp. 81–144.

[12] Powell, B. E., "Fatigue Crack Growth Behaviour of Two Contrasting Titanium Alloys," *Int. J. Fatigue*, Vol. 17, 1995, pp. 221–227.

[13] Hall, R. F. and Powell, B. E., "The Growth of Corner Cracks by Fatigue," *Int. J. Fatigue*, Vol. 19, 1997, pp. 429–35.

[14] Brooks, R. R. and Rainforth, W. M., "Effect of Microstructure on the Morphology of Fatigue Cracks in UDIMET 720," *Fatigue Fract. Eng. Mater. Struct.*, Vol. 23, 2000, pp. 725–736.

[15] Brooks, R. R. and Rainforth, W. M., "Fatigue Damage Mechanisms Associated with 'Tear-Drop' Cracking in UDIMET 720," *Fatigue Fract. Eng. Mater. Struct.*, Vol. 22, 1999, pp. 821–829.

[16] Rolls-Royce, 1995, "Crack Propagation in Corner Crack Test Pieces: Test Procedure, Rolls Royce Plc.," *Document MMM31002*, Derby, United Kingdom.

[17] BS 6835-1:1998, December 1998, "Method for the Determination of the Rate of Fatigue Crack Growth in Metallic Materials. Part 1: Fatigue Crack Growth Rates of Above 10^{-8} m per Cycle," BSI, London, UK, p. 30.

[18] Halliday, M. D. and Beevers, C. J., "The D. C. Electrical Potential Method for Crack Length Measurement," *The Measurement of Crack Length and Shape During Fracture and Fatigue*, C. J. Beevers, Ed., EMAS, Warley, United Kingdom, 1980, pp. 85–112.

[19] Sauer, C. and Luetjering, G., "Thermo-Mechanical Processing of High Strength β-Titanium Alloys and Effects on Microstructure and Properties," *J. Mater. Process. Technol.*, Vol. 117, 2001, pp. 311–317.

[20] Hall, J. A. and Pierce, C. M., "Property-Microstructure Relationships in the Ti-6AI-2Sn-4Zr-6Mo Alloy," *Mater. Sci. Eng.*, Vol. 9, 1972, pp. 197–210.

[21] Fine, M. E., Chung, Y.-W., and McCormick, R. R. "Fatigue Failures in Metals," *Fatigue and Fracture: ASM Handbook*, ASM International, Metals Park, OH, 1996, Vol. 19, pp. 63–72.

[22] Suresh, S., *Fatigue of Materials*, 2nd ed., Cambridge University Press, Cambridge, UK, 2004, pp. 331–382.

[23] Miles, C. J., personal communication, School of Metallurgy and Materials, University of Birmingham, United Kingdom, 2008.

[24] Baeslack, W. A. III, and Mahajan, Y., "Intergranular Fracture of Heat-Treated Weldments in a High-Strength Alpha-Beta Titanium Alloy," *Scr. Metall.*, Vol. 13, 1979, pp. 959–964.

[25] Shaniavski, A. A., Losey, A. I., and Banov, M. D., "Development of Fatigue Cracking in Aircraft Engine Compressor Disks of Titanium Alloy Ti-6Al-3Mo-2Cr," *Fatigue Fract. Eng. Mater. Struct.*, Vol. 21, 1998, pp. 297–313.

[26] Lloyd, G. J., "High Temperature Fatigue and Creep-Fatigue Crack Propagation: Mechanics, Mechanisms, and Observed Behaviour in Structural Materials," *Fatigue at High Temperature*, R. P. Skelton, Ed., Applied Science Publishers, London, 1983, pp. 187–258.

[27] Adam, P., "Schwungradreibschweiβen von Verdichter-Rotoren aus Titanlegierungen (Inertia Welding of Compressor Rotor Drums of Titanium-Alloys)," *DVS* (*Deutscher Verband fur Schweisstechnik*) *Berichte* (*Report*) *139*, 1991, DVS, Düsseldorf, Germany, pp. 36–39.

Reprinted from JAI, Vol. 7, No. 3
doi:10.1520/JAI102551
Available online at www.astm.org/JAI

D. Angeles Herrera,[1] *J. L. González Velázquez,*[2] *and*
A. de J. Morales Ramírez[3]

Fatigue Crack Propagation in SAW Seam Welds of API 5L X42 Steel Pipe in the Radial Short Direction

ABSTRACT: Fatigue crack propagation (FCP) rates in submerged arc welding (SAW) seam welds of 1524 steel (API 5L X42) pipe were measured by using an arc-shaped bend specimen with the same radius of curvature of the body of the pipe so the material did not have to be cold worked to get a flat shape nor extensively machined. The test direction was girth radial and the stress intensity factor (K) function was calibrated for this type of nonstandard specimen. The FCP tests were carried out in air at room temperature, testing the three zones: The base metal, the deposited metal, and the heat affected zone (HAZ). A fractographic analysis was done to analyze the role of the microstructure in the FCP in the three zones. It was found that the zone of greater resistance to FCP was the base metal, whereas the deposited metal showed the least resistance to crack propagation. FCP in the deposited metal and the HAZ behaved according to the Paris law, unlike the base metal, which showed a high data dispersion. The behavior in the base metal was attributed to the propagation of the crack in the transverse direction of the preferential alignment of the microstructure, while the deposited metal and the HAZ had a more homogeneous microstructure.

Manuscript received May 20, 2009; accepted for publication February 8, 2010; published online March 2010.

[1] Depto. De Ingeniería Metalúrgica—ESIQIE—Instituto Politécnico, National UPALM C.P. 07738, México D.F., Mexico, e-mail: dangelesh0600@ipn.mx
[2] Depto. De Ingeniería Metalúrgica—ESIQIE—Instituto Politécnico, National UPALM C.P. 07738, México D.F., e-mail: drjorgeluis@hotmail.com
[3] Centro de Investigación e Innovación Tecnológica CIITEC-IPN Cerrada de Cecato S/N, Col. Santa Catarina Azcapotzalco, C.P. 02250, México, D.F., Mexico, e-mail: amoralesra@ipn.mx

Cite as: Herrera, D. A., Velázquez, J. L. González and Ramírez, A. de J. Morales, "Fatigue Crack Propagation in SAW Seam Welds of API 5L X42 Steel Pipe in the Radial Short Direction," *J. ASTM Intl.*, Vol. 7, No. 3. doi:10.1520/JAI102551.

KEYWORDS: fatigue crack propagation (FCP), base metal (BM), deposited metal (DM), heat affected zone (HAZ), girth radial direction (CR), pipe steel

Introduction

The study of fatigue crack propagation (FCP) behavior in ASTM 1524 steel piping (or API 5L X42) with submerged arc welding (SAW) longitudinal seam, has been of growing interest in Mexico [1,2] since in recent years it has been observed that fatigue was the primary cause of several failures of hydrocarbon transport pipelines with SAW seam weld pipes. In the study of these failures it was observed that there was not sufficient information on the FCP behavior of these welds. One well known approach to determine the fatigue life span of fatigued structural elements is the Paris equation that relates the FCP rate (da/dN), with the range of the stress intensity factor (ΔK) [3]. The main advantage of this relationship is that, when it is mathematically integrated, the approach can predict the fatigue crack growth life [4].

In this work, FCP tests of 1524 steel pipe were carried out in nonstandard curved single edge notched (SEN) specimens, with the crack oriented at the short transverse direction (CR), according to the ASTM E399 nomenclature [5]. In order to avoid either machining or flattening to get straight standard test specimens, the specimens were cut directly from the pipe to contain the SAW weld without altering the pipe radius. Also, the crack initiating notch was aligned, so the FCP tests occur at the base metal (BM), the deposited metal (DM), and the heat affected zone (HAZ), so the FCP rates for each one of these zones could be measured accurately.

Nowadays there are published works about FCP rates in steel welds [6–10]; however most of these studies were done in the conventional long directions using compact $C(T)$, specimens, whereas, in order to assess the FCP in seam welds, it is necessary to test in the short transverse directions.

Experimental Methods

Nonstandard curved SEN samples with the fracture plane in the CR orientation were obtained from a 1524 steel pipe (API 5L X42) [11] of 0.91 m in diameter and 0.03 m in thickness. As shown in Fig. 1(*a*), the specimens were machined such that the crack initiating notch was aligned with the BM, DM, and the HAZ. The dimensions of the nonstandard curved SEN samples were: Width of 0.0254 m, thickness of 0.0254 m, and span of 0.096 m. The serration crack initiator was machined in the central part beginning on the internal diameter of the pipe and with a depth of 0.006 35 m, as shown in Fig. 1(*b*).

The stress intensity factor (K) function was calibrated for nonstandard curved SEN obtaining this equation

$$K_Q = \frac{\mathrm{PS}}{\mathrm{BW}^{3/2}} \times f\left(\frac{a}{W}\right) \tag{1}$$

where

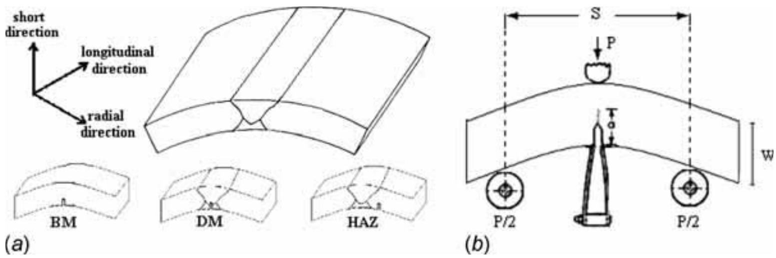

FIG. 1—(*a*) *Extracted specimens from pipe section with SAW seam and crack initiating location in each zone;* (*b*) *loading fixture for nonstandard curved SEN sample.*

$$f\left(\frac{a}{W}\right) = [13.914(a/W)^2 - 6.057(a/W) + 0.938] \quad (2)$$

Table 1 shows the chemical composition of the material, corresponding to a typical 1524 steel. The mechanical properties of the material are listed in Table 2, and were determined from tensile testing according to standard ASTM E8M [12]. The samples were oriented in the longitudinal direction of the pipe. The hardness values were obtained according to standard ASTM E18 [13] for each of the zones. The reported values are the average of three samples for the case of the tensile testing and five measurements for the hardness testing.

A typical sample used for a FCP test is shown in Fig. 2. FCP testing in the nonstandard curved SEN samples was done in three points bending following the specification ASTM E647 [14] for increasing ΔK. A servohydraulic machine under load control, a sinusoidal wave at a frequency of 15 Hz was used, as shown in Fig. 3, with the relation minimum to maximum load $\underline{R}=0.1$. The range of stress intensity factor for pre-cracking was $\Delta K=20\ \text{MPa}\sqrt{m}$. A stereomicroscope mounted on a mobile base connected to a micrometer displacement measurement device was used to observe and measure the advance of the crack. The FCP tests were performed in triplicate for each of the three zones of evaluation.

TABLE 1—*Chemical composition of the material used for FCP tests.*

C, %W	Mn, %W	P, %W	S, %W	Si, %W	Fe, %W
0.25	1.2	0.03	0.01	0.15	97.6

TABLE 2—*Mechanical properties at different zones.*

Zone	$\sigma_{0.2}$, MPa	Ultimate Tensile Strength, MPa	Area Reduction, %	Elongation, %	Hardness, Hardness Rockwell B
BM	271	411	62	35.5	89.8
DM	345	551	···	···	92.8
HAZ	277	362	···	···	84.4

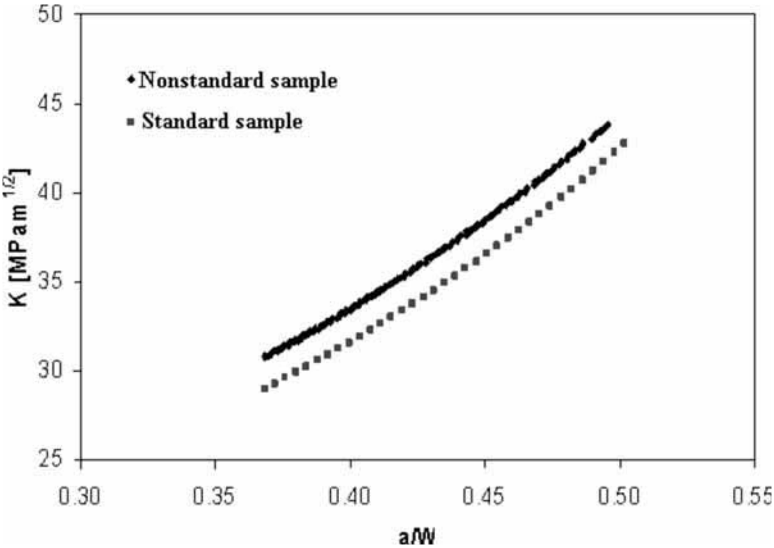

FIG. 2—*Stress intensity factor versus crack-length-to-width* (a/W) *ratio for two different SEN samples.*

Results and Discussion

The stress intensity factor (K) function for the nonstandard curved SEN bend specimen, calibrated by the compliance method, is shown in the Fig. 4, along with the values of K for the standard SEN bend specimen. The values of K for the nonstandard curved SEN bend specimen are higher than those of the standard SEN bend specimen. This behavior can be attributed to the curved geometry of the nonstandard specimen, which creates a higher bending moment in comparison to a standard SEN bend specimen, thus resulting in higher stresses at the crack tip and therefore higher K values.

FCP rates for BM, DM, and HAZ are shown in Figs. 5–7, respectively. As shown, the BM zone did not present a behavior according to the Paris relation, showing a high data dispersion, especially for low values of ΔK. The DM and

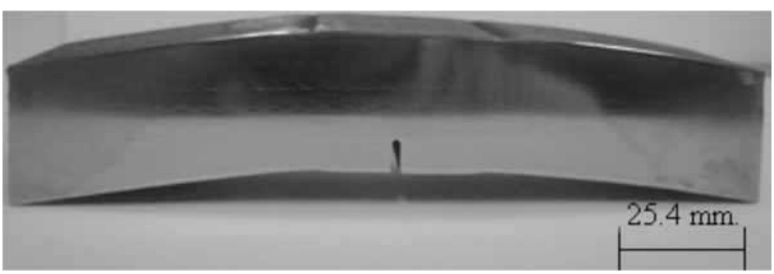

FIG. 3—*Nonstandard curved SEN sample.*

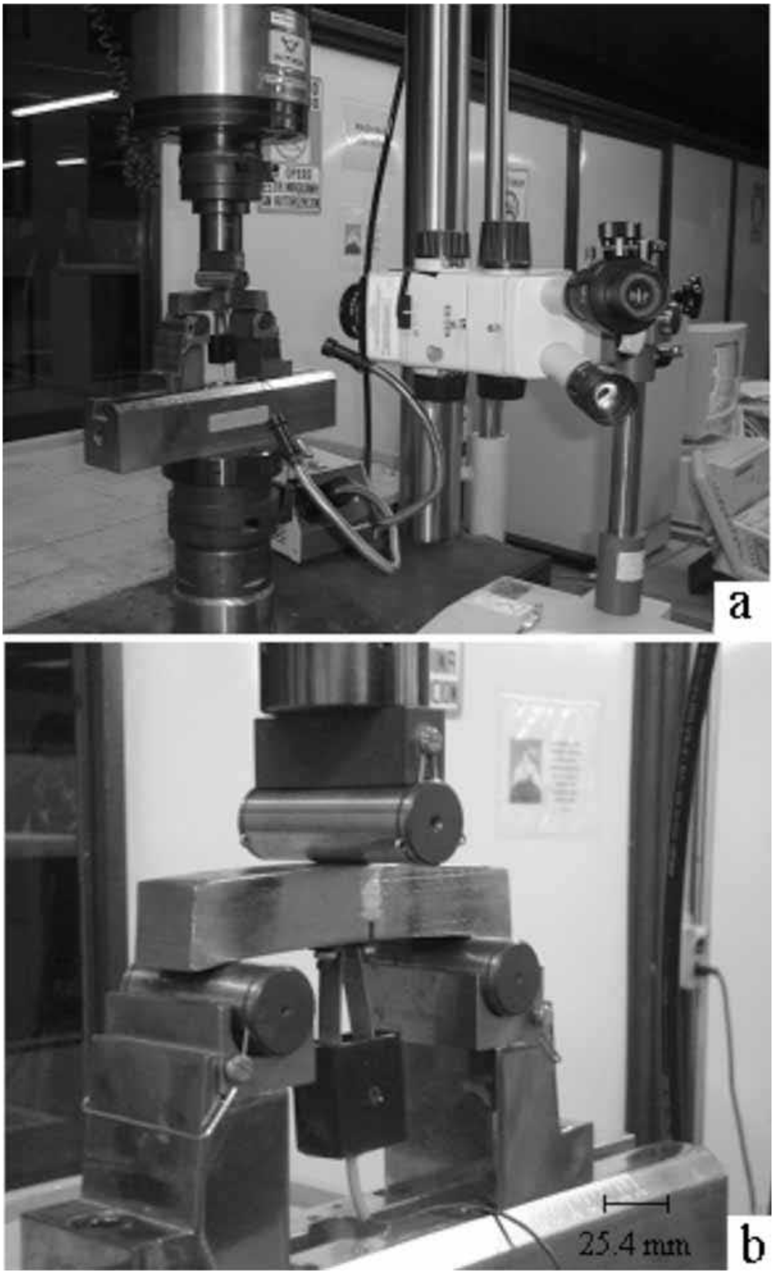

FIG. 4—*Test setup for FCP of curved SEN samples with three point flexion.*

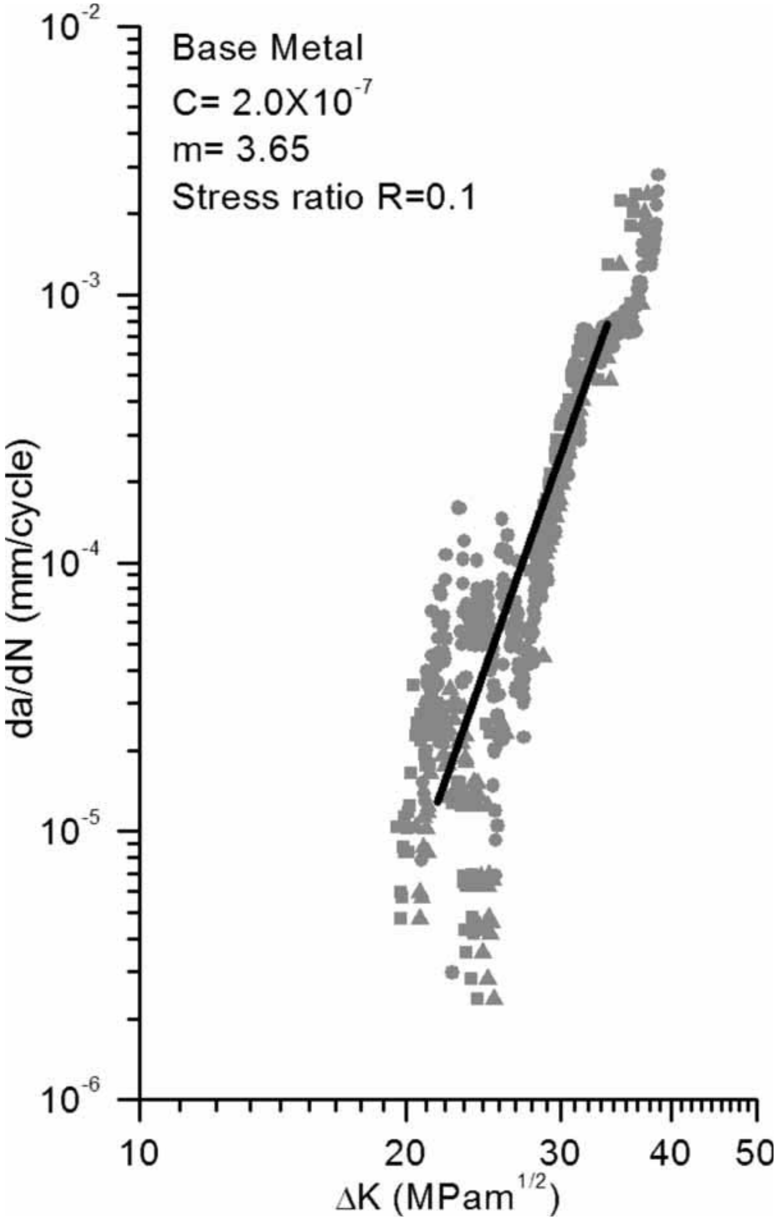

FIG. 5—*FCP rates versus* Δ*K for BM zone.*

the HAZ behavior showed minimal dispersion of data but exhibited a sigmoidal shape for low to high values of ΔK. Table 3 presents the constants in the Paris relation for each zone: BM, DM, and HAZ. The Paris relation (solid line) is shown for each zone on the respective figure.

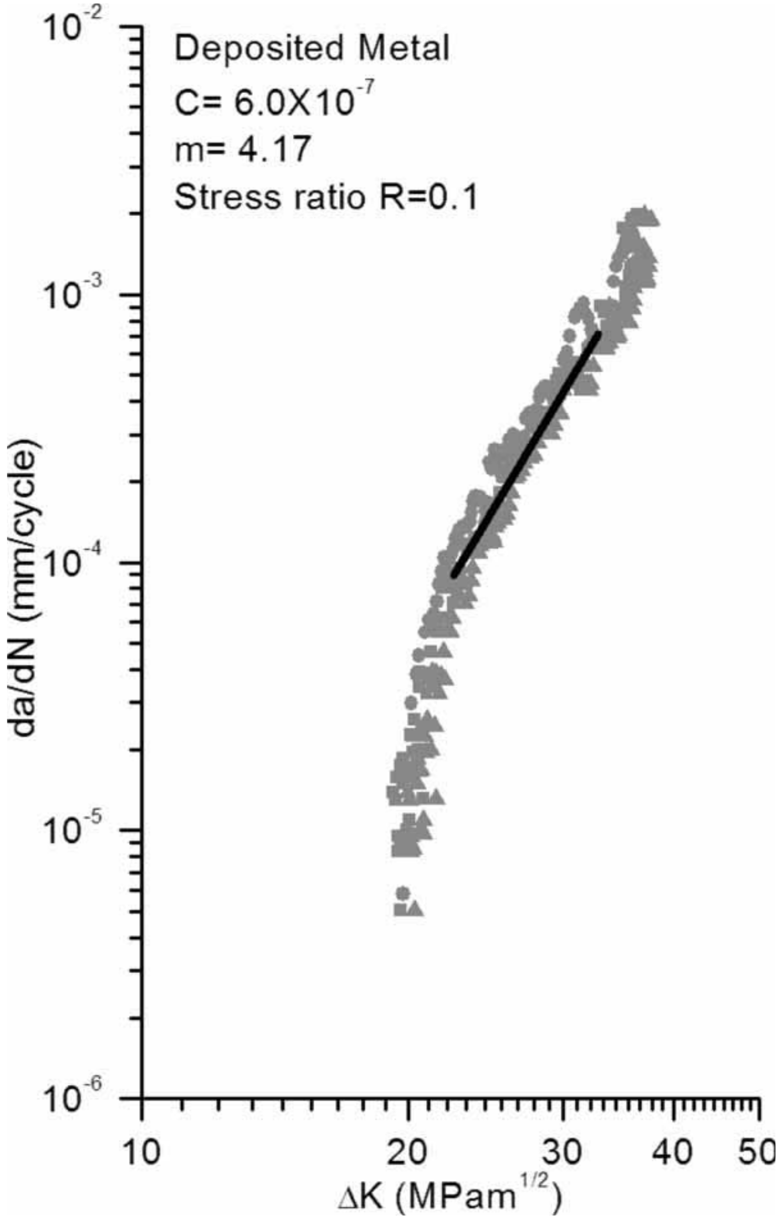

FIG. 6—*FCP rates versus* Δ*K for DM zone.*

Since the FCP tests were conducted until final fracture under increasing ΔK conditions at constant load amplitude, it is reasonable to suppose that the crack size just before final fracture is the critical size; by using these data along with the maximum load values in the applied load cycle [15], fracture tough-

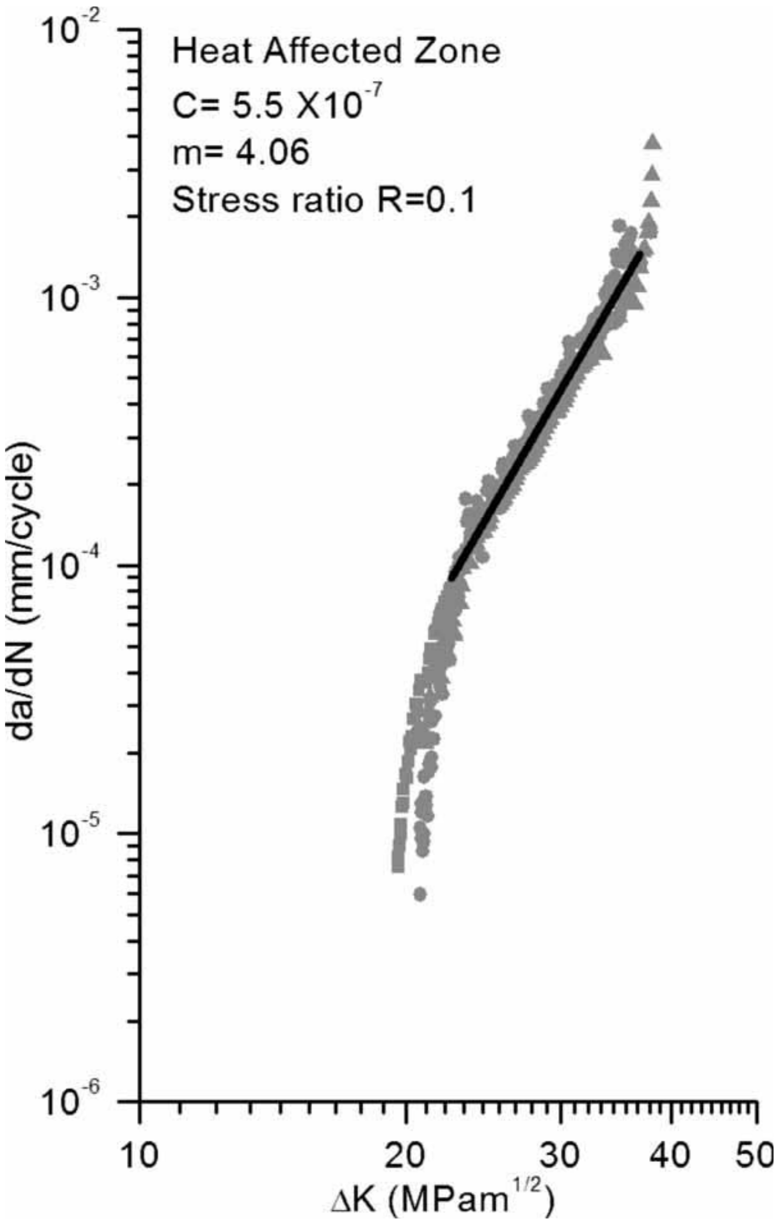

FIG. 7—*FCP rates versus ΔK for HAZ zone.*

ness values (K_C) of three zones of study were estimated and these results are shown in Table 4.

The microstructure of the transversal section of the BM is composed of a ferrite matrix with pearlite colonies in a banded configuration, as shown in Fig.

TABLE 3—*Paris' constants for different zones* (*R=0.1*).

Study Zone (Radial Short Direction)	Paris' constants C (10^{-7})	m
BM	2	3.65
DM	6	4.17
HAZ	5.5	4.06

TABLE 4—*Fracture toughness estimation for the three zones.*

Zone	Critical Size of Crack, mm	Maximum Load, kN	K_C, MPa$\sqrt{m}$
BM	16.35	15.5	79.17
DM	14.55	15.5	64.49
HAZ	14.35	15.5	62.91

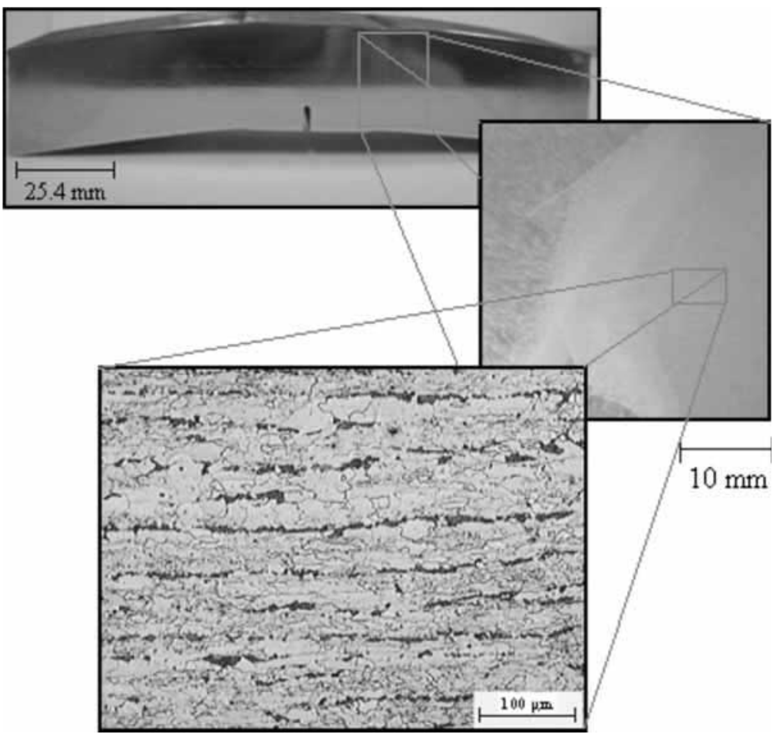

FIG. 8—*BM microstructure.*

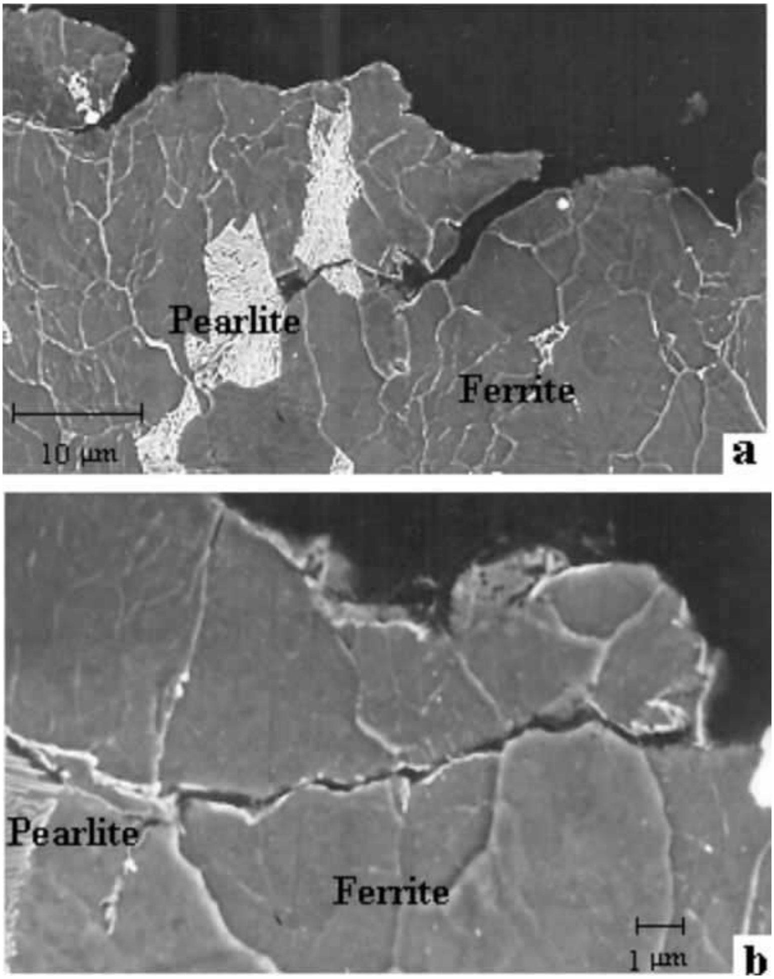

FIG. 9—*Microstructure at crack edge in BM zone.*

8. This microstructure is formed by the hot rolling passes applied during the fabrication of the plates that were formed into the pipe shape.

Greater FCP resistance was observed in the BM zone, however, the rates in this zone showed a significant dispersion, especially at ΔK values less than 30 $\mathrm{MPa}\sqrt{m}$, which means that the material did not behave according to the Paris relation. This behavior could be related to banded microstructure of the BM zone and to the crack propagation path. In Fig. 9, it is shown that the crack path through the microstructure of the BM was transgranular and changed its direction as it crossed the pearlite and ferrite bands, making a tortuous path with plenty of secondary cracking. These deviations in the crack path not only require more energy but also can slow down the FCP rate by roughness inducing crack closure [15,16]; leading to the overall effect of increasing the FCP

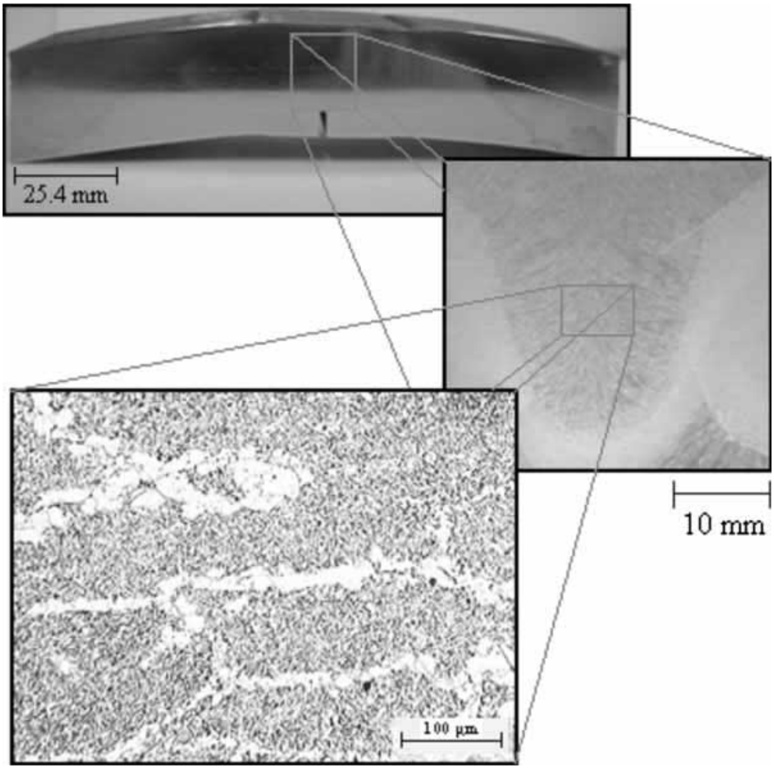

FIG. 10—*DM microstructure.*

resistance. This higher energy required to the crack propagation in the CR direction of the BM is confirmed by the greater calculated fracture toughness in this case, as compared with the other two zones of study.

The DM microstructure is shown in Fig. 10, which is the typical solidification microstructure of a SAW weld, consisting of columnar grains and fine dendrites, with ferrite zones in the form of thin plates. The least FCP resistance in this zone, as compared to the BM and the HAZ, can be attributed to the fine and homogeneous microstructure, since it is known that fine grain materials tend to show lower roughness induced crack closure than materials with coarser microstructures, therefore the effective range of the stress intensity factor is higher, leading to higher crack propagation rates [15,16].

The microstructure at the edge of the crack in the DM is shown in Fig. 11, it can be observed that it is very homogeneous and the crack path is relatively straight with little secondary cracking, as compared with that observed in the BM zone. Furthermore, the estimated fracture toughness of this zone had a lower value than that for the BM. These observations are congruent with the lower fatigue resistance in comparison with the BM, as discussed earlier. With regard to the fracture toughness, this zone showed an intermediate value, its behavior is congruent with the results obtained in the other zones.

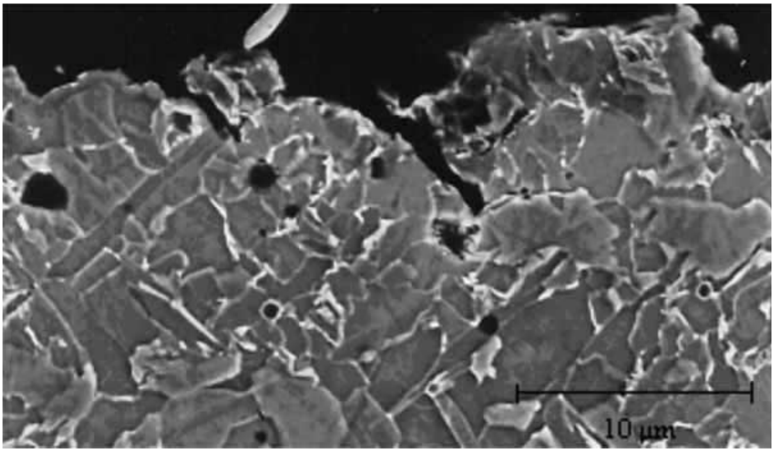

FIG. 11—*Crack edge microstructure in DM zone.*

Figure 12 shows the microstructure of the HAZ, which is composed a grain refinement zone, Fig. 12(*a*), away from the fusion line and promoted by the brief exposure to the thermal cycles introduced by the welding process, which is surrounded by a grain growth region and coarse perlite, Fig. 12(*b*), adjacent to the fusion line produced by a greater heat input during the welding process.

It is important to clarify that the HAZ does not have a regular geometry and, therefore, the crack path during the FCP tests was across different microstructures across this zone. However, as shown in Fig. 12(*b*), since the fine grain zone was located away from the initiating notch, the crack propagation occurred mainly across the grain growth zone with a tortuous crack path, which resulted in an increased roughness which consequently led to slower FCP rates due to the roughness induced crack closure and crack branching.

Finally, an example of the crack path through the microstructure in the HAZ is shown in Fig. 12(*b*). It is evident that the crack path is transgranular and more tortuous than the one in the DM but less than in the BM. Due to the fact that the coarse grain material produced a tortuous crack path, and then experienced roughness induced crack closure, the crack growth rate in the HAZ was reduced with respect to the DM, but not enough to have a behavior similar to the BM.

Conclusions

(1) The Paris' constants for the three regions tested at $R=0.1$ for FCP in SAW seam welds in API 5L X42 pipes are: BM, $C=2\times10^{-7}$ and $m=3.65$; DM, $C=6\times10^{-7}$ and $m=4.17$; and HAZ, $C=5.5\times10^{-7}$ and $m=4.06$;

(2) The greater resistance to FCP was observed in the BM, in comparison with the HAZ, which had an intermediate resistance and DM showed the least fatigue resistance of the three zones;

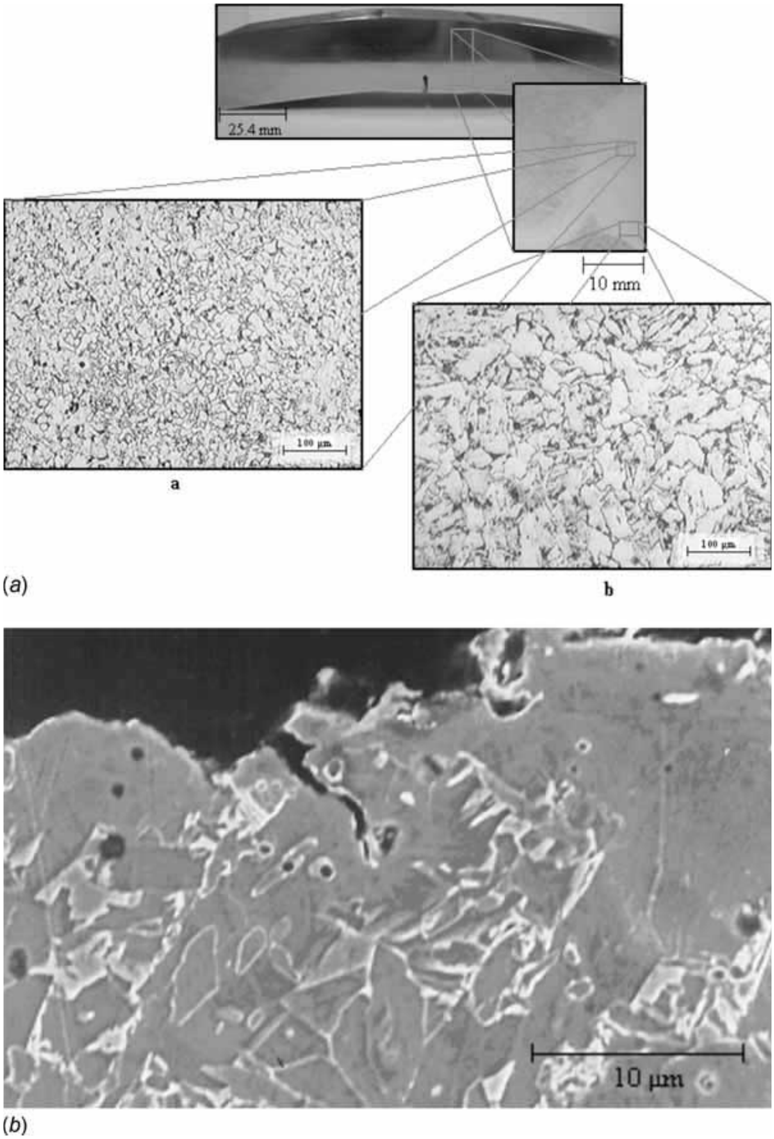

FIG. 12—(*a*) *HAZ microstructure;* (*b*) *crack edge microstructure in HAZ zone.*

(3) The DM and HAZ zones behaved according to the Paris relation in the mid-rate region but produced sigmoidal shaped results in the low and high applied stress intensity factor range; and
(4) The differences of the FCP rates among each zone of study were attributed to the differences in the crack propagation paths and the resulting roughness induced crack closure and crack branching, along with the differences in the apparent fracture toughness.

Acknowledgments

The writers thank "Instituto Politécnico Nacional," "Pemex Exploración y Producción," and the "Grupo de Análisis de Integridad de Ductos ESIQIE IPN" for the financial and material support to carry out this work.

References

[1] González, J. L., "Reportes de análisis de integridad de ductos," *Grupo de Análisis de Integridad de Ductos* (*GAID*), Instituto Politécnico Nacional, México, 2002–2005.

[2] González, J. L., "Integridad Mecánica para Equipos de Refinería de Petróleo," *Modulo V Grupo de Análisis de Integridad de Ductos* (*GAID*), Instituto Politécnico Nacional, México, 2005.

[3] Paris, P. C. and Erdogan, F., "A Critical Analysis of Crack Propagation Laws," *J. Basic Eng., Trans. ASME, 85* (*Series D*), Vol. 85, 1963, pp. 528–534.

[4] Anderson, T. L., *Fracture Mechanics. Fundamentals and Applications*, Taylor and Francis Publishers, USA, 2005, pp. 466–470.

[5] ASTM E399-05, 2001, "Standard Test Method for Linear-Elastic Plane-Strain Fracture Toughness *KIc* of Metallic Materials," *Annual Book of ASTM Standards*, Vol. 03.01, ASTM International, West Conshohocken, PA, pp. 5–13.

[6] Bussiba, A., "Fatigue Crack Growth Rates in Six Pipeline Steels," *Proceedings of the IPC, 6th International Pipeline Conference*, Calgary, Canada, September 25–29, 2006, ASME International, USA, pp. 1–10.

[7] Choi, D. H. and Choi, H. Y., "Fatigue Life Prediction of Out-of-Plane Guesset Welded Joints Using Strain Energy Density Factor Approach," *Theor. Appl. Fract. Mech.*, Vol. 44, 2005, pp. 16–26.

[8] Sriharsha, H. K., Pandey, R. K., and Chatterjee, S., "Towards Standardizing a Sub-Size Specimen for Fatigue Crack Propagation Behaviour of Nuclear Pressure Vessel," *Eng. Fract. Mech.*, Vol. 64, 1999, pp. 607–624.

[9] Broek, D., *Elementary Engineering Fracture Mechanics*, Martinus Nijhoff Publishers, The Netherlands, 1982, pp. 304–309.

[10] Saxena, A. and Hudak, S. J., "Review and Extension of Compliance Information for Common Crack Growth Specimens," *Int. J. Fract.*, Vol. 14, 1978, pp. 453–468.

[11] API Specification 5L 2000, American Petroleum Institute Publishing Services, Washington, D.C. USA, 2000.

[12] ASTM E8M-04, 2001, "Standard Test Methods for Tension Testing of Metallic Materials," *Annual Book of ASTM Standards*, Vol. 03.01, ASTM International, West Conshohocken, PA, pp. 40–46.

[13] ASTM E18-05, 2001, "Standard Test Methods for Rockwell Hardness and Rockwell Superficial Hardness of Metallic Materials," *Annual Book of ASTM Standards*, Vol. 03.01, ASTM International, West Conshohocken, PA, pp. 56–74.

[14] ASTM E647-00, 2001, "Standard Test Method for Measurement of Fatigue Crack Growth Rates Materials," *Annual Book of ASTM Standards*, Vol. 03.01, ASTM International, West Conshohocken, PA, pp. 5–13.

[15] González, J. L., "Mecánica de fractura," *Colección de textos politécnicos*, 2nd ed., Noriega-Limusa, México, 2004, pp. 47–54, 137–145.

[16] Janssen, M., Zuidema, J., and Wanhill, R., *Fracture Mechanics*, Delft University Press, The Netherlands, 2002, pp. 5–10.

MULTIAXIAL FATIGUE AND FRACTURE

Reprinted from JAI, Vol. 7, No. 4
doi:10.1520/JAI102643
Available online at www.astm.org/JAI

Gaëlle Leopold[1] *and Yves Nadot*[1]

Fatigue from an Induced Defect: Experiments and Application of Different Multiaxial Fatigue Approaches

ABSTRACT: An experimental database containing multiaxial fatigue results for C35 steel with induced defects has been previously published [Billaudeau, T., Nadot, Y., and Bezine, G., "Multiaxial Fatigue Limit for Defective Materials: Mechanisms and Experiments," Acta Mater., Vol. 52, 2004, pp. 3911–3920; Nadot, Y., and Billaudeau, T., "Multiaxial Fatigue Limit Criterion for Defective Materials," Eng. Fract. Mech., Vol. 73, 2006, pp. 112–133; Gadouini, H., Nadot, Y., and Rebours, C., "Influence of Mean Stress on the Multiaxial Fatigue Behaviour of Defective Materials," Int. J. Fatigue, Vol. 30, 2008, pp. 1623–1633]. Artificial defects, in a range of 100–900 μm, are introduced at the surface of fatigue samples. The database contains experimental fatigue results for different defect size and geometry, and multiaxial loading cases with different load ratios. In the present study, five models predicting the fatigue limit of materials with defects are compared. Each model is carefully presented, predictions are compared, and input data are discussed. It is shown that it is necessary to take account for the stress distribution around the defect in order to have a good prediction for a multiaxial case.

KEYWORDS: high cycle fatigue, defect, multiaxial fatigue, small notch, mean stress effect

Manuscript received August 20, 2009; accepted for publication March 22, 2010; published online April 2010.

[1] LMPM, UMR CNRS 6617, ENSMA Téléport 2, Avenue Clément Ader, BP 40 109, 86961 FUTUROSCOPE, France, e-mail: gaelle.leopold@lmpm.ensma.fr and e-mail: yves.nadot@lmpm.ensma.fr

Cite as: Leopold, G. and Nadot, Y., "Fatigue from an Induced Defect: Experiments and Application of Different Multiaxial Fatigue Approaches," *J. ASTM Intl.*, Vol. 7, No. 4. doi:10.1520/JAI102643.

Nomenclature

a = length of the semimajor axis for a semielliptical crack in Murakami's equation
a_0 = critical distance defined by El Haddad
a_v = crack length in Vallellano's model
b = length of the semiminor axis for a semielliptical crack in Murakami's equation
b_G = material parameter in Gadouini model's
f = fitting exponent in Vallellano's model
i = number of half grains in Vallellano's model
m_p = Paris's law parameter
A = elongation
C = material parameter in Chaboche's model
C_p = Paris's law parameter
D = grain size
E = Young's modulus
$F(b/a)$ = function of the aspect ratio (b/a) in Murakami's equation
G = stress gradient in Gadouini's model
H_v = Vickers hardness
J_1 = first invariant of the stress tensor
$J_{1,\max}$ = maximum of the first invariant of the stress tensor over a load cycle
J_2 = second invariant of the stress tensor
$J_{2,a}$ = amplitude of the second invariant of the stress tensor over a load cycle
K_t = elastic stress concentration factor
$L/2$ = critical distance for Susmel-Taylor's model
R = load ratio $(R = \sigma_{\min}/\sigma_{\max})$
R_d = spherical defect radius
R_m = tensile strength
$R_{p0,2}$ = conventional yield strength
$R_{p0,2cy}$ = cyclic yield strength
α = parameter in Murakami's equation
α_{Cr} = parameter in Crossland's model
α_v = notch depth in Vallellano's model
β_{Cr} = parameter in Crossland's model
γ = material parameter in Chaboche's model
ρ = initiation plane stress ratio $(\rho = \sigma_{n,\max}/\tau_a)$
ρ_v = notch radius in Vallellano's model
σ_a = amplitude of the principal maximal stress in loading direction

σ_{Cr} = Crossland equivalent stress
$\sigma_{n,\max}$ = maximum stress normal to the critical plane
σ_w = fatigue limit for a specimen with defect under tension loading
$\sigma_{w,\mathrm{defect}}$ = alternated tension fatigue limit for a given defect which allows identifying Susmel–Taylor model and Gadouini's approach
$\sigma_{w,i}$ = fatigue crack growth threshold stress for a defect-free specimen in Vallellano's model
σ_{w0} = alternated tension fatigue limit for a defect-free specimen
$\sigma_{w,i}^N$ = fatigue crack growth threshold stress for a notched specimen in Vallellano's model
σ_Y' = initial yield stress for Chaboche's model
τ_a = maximum shear stress amplitude
τ_w = fatigue limit for a material with defect under torsion loading
τ_{w0} = alternated torsion fatigue limit for a defect-free specimen
ΔK_{th} = nominal stress intensity factor threshold
$\Delta K_{\mathrm{th,eff}}$ = effective stress intensity factor threshold
$\Delta\sigma_c$ = positive stress amplitude of the crack modeling
$\sqrt{\mathrm{area}}$ = square root of the area of the defect projected on the plane perpendicular to the direction of the maximum principal stress

Introduction

Cast materials usually contain defects such as [1–3] shrinkages, pores, inclusions, or oxides. Fatigue tests show that the behavior of cast materials mainly depends on defect population. Several approaches have been developed to take into account the influence of defects on fatigue behavior [4,5]. Regarding these approaches, it can be observed that different geometrical and mechanical parameters are used to take account of defects. Murakami [6] proposed an empirical criterion based on Vickers hardness H_v and the famous size parameter $\sqrt{\mathrm{area}}$. Gadouini et al. [7] suggested a multiaxial criterion introducing an equivalent local stress gradient around the defect. Susmel and Taylor [8] extended two previously developed methods to multiaxial notch fatigue situations: The Susmel–Lazzarin modified Wöhler curves method (MCWM) [9] and the Taylor's critical distance method (CDM) [10]. The last approach analyzed in this paper was developed by Vallellano et al. [11]. They proposed a micromechanical model that describes the growth of a short crack across the steep stress gradient generated at the root of a notch.

The aim of this paper is to compare these approaches developed to predict influence of defects on fatigue limit. These models will be tested for C35 steel containing defects [7,12,13]. Influence of defect size will be discussed for tension and torsion. Multiaxiality and mean stress effect will also be analyzed. This work will allow capturing relevant parameters necessary to describe the impact

TABLE 1—*C35 chemical composition* (*weight percent*).

C	Mn	Si	Cr	Ni	Cu
0.36	0.6	0.27	0.14	0.07	0.07

of defects on fatigue properties for multiaxial case and for a given material containing an induced defect.

Experimental Database

Material: C35 Steel

The material tested is a low carbon steel C35. Table 1 shows its chemical composition. C35 steel is composed of two phases: Ferrite and pearlite. The average grain sizes are 22 and 16 μm, respectively. C35 steel microstructure contains pearlite bands, which are oriented in the rolling direction. This direction is the longitudinal axis for all of our specimens.

The previous work of Gadouini et al. [7] presented elastic-plastic behavior of the C35 steel. Smooth cylindrical specimens were used to quantify monotonic and cyclic elastic-plastic properties. This material presents a smooth softening and kinematic hardening. Experimental tests and numerical calculations performed have shown that nonlinear kinematic hardening can be identified with the stabilized cyclic hardening curve. Monotonic and cyclic properties are given in Table 2.

Crack growth reference data on this material are collected by Billaudeau et al. [12] thanks to crack growth test performed out of closure in a previous study conducted in our laboratory. A standard R variable test is conducted on a CT specimen in order to reach threshold for high load ratio, therefore, out of closure effect. The crack closure level has been measured and is shown to be negligible at the threshold due to high load ratio. Crack growth rate da/dN is described through Paris's law and the effective crack growth threshold $\Delta K_{\text{th,eff}}$ is determined. Crack propagation rate is given by the following equation:

TABLE 2—*C35 mechanical properties.*

Young modulus E, GPa	195
Monotonic yield strength $R_{p0.2}$, MPa	359
Tensile strength R_m, MPa	594
Elongation A, %	47
Cyclic yield strength $R_{p_{0.02cy}}$, MPa	250
Vickers hardness $H_v(30)$	163
Fatigue limit, defect free, $R=-1$, tension σ_{w0}, MPa	240
Fatigue limit, defect free, $R=-1$, torsion τ_{w0}, MPa	169

TABLE 3—*C35 experimental database.*

Case	Loading	Defect	$\sqrt{\text{area}}$ (μm)	Fatigue limit (MPa)
Case 1	Tension $R=-1$	Spherical	100	235
Case 2	Tension $R=-1$	Spherical	170	195
Case 3	Tension $R=-1$	Spherical	400	150
Case 4	Tension $R=-1$	Spherical	900	135
Case 5	Torsion $R=-1$	Spherical	150	160
Case 6	Torsion $R=-1$	Spherical	400	145
Case 7	Torsion $R=-1$	Spherical	900	125
Case 8	Tension $R=0$	Spherical	400	125
Case 9	Tension $R=-5$	Spherical	400	230
Case 10	Torsion $R=0$	Spherical	400	145
Case 11	Torsion $R=-0,5$	Spherical	400	140

$$\frac{da}{dN} = 1.88 \times 10^{-12} \Delta K^{3,69} \tag{1}$$

We have used effective long crack data because natural crack propagates without closure in the beginning of the crack propagation [14,15]. For the C35 steel, $\Delta K_{\text{th,eff}} = 3\ \text{MPa}\sqrt{\text{m}}$.

In order to study the influence of defects on fatigue strength, artificial defects are introduced at the surface of tension and torsion fatigue smooth specimens. Electric discharge machining is used to introduce these defects [12]. This method reproduces defects of different sizes and shapes. In order to anneal residual stresses due to machining, tempering is done at 500°C, 1H under high vacuum. Every sample, including defect free samples, has been tempered. In this paper, we will focus on spherical defects in a range of 100–900 μm. Defect size will be precisely described for each method in the following paragraphs.

Fatigue Loading Effects

Billaudeau and co-workers [12,13] and Gadouni et al. [7] performed fatigue experiments on C35 steel under alternated tension and torsion loadings, and under nonzero mean stress loading. The purpose of these experiments was to study effects of multiaxial loadings and effects of mean stress. Table 3 describes loading cases for each given defect. Throughout this paper, defect size corresponds to $\sqrt{\text{area}}$ parameter: It is defined by Murakami [6] as the projection of the defect on the plane perpendicular to the direction of the maximal principal stress. But, for each method, geometrical parameters defining the defect are directly linked to $\sqrt{\text{area}}$ by a simple relation. In this previous work, conducted in our laboratory, the fatigue limit is determined using a "step by step" method clearly detailed in Ref 12, this method uses two or three samples to estimate the fatigue limit. This method has been compared to a standard stair case method and is shown to be a very good way to estimate the fatigue limit for this material (2 % and 4 % difference between the two methods). This comparison has been performed under tension and torsion.

The aim of the present paper is to compare multiaxial fatigue criteria for materials with defects. In order to take into account defect impact on fatigue limit, this analysis will be focused on the three following parameters:

- *Defect size*: Defects can be characterized through four parameters: Type (pore, shrinkage, inclusion, or oxide), position from the surface, morphology, and size. Fatigue behavior sensitivity to each parameter has to be quantified. In our case, defects are surface type-spherical. Research is focused here on surface defect size effect.
- *Multiaxial effect*: Multiaxial fatigue approaches distinguish themselves through mechanical parameters used to represent stress distribution. This effect is mainly linked to loading and "geometrical" defect description. In this paper, artificial defects are spherical with various sizes. Tension and torsion fatigue loadings introduce different stress distributions around the defect.
- *Mean stress*: Influence of mean stress in defect free steel is well known. In the case of material with defect, very few studies are carried out, especially under torsion. Gadouini et al. [7] explained that to describe local stress evolution and mean stress relaxation in a material with defect, an elastic-plastic behavior law has to be used. The defect acts as a stress concentrator: There is a local redistribution of stresses introduced by the defect. In fact, at the tip of the defect, the material responds as if it was subjected to an imposed strain. Fatigue tests have been performed under nonzero mean stress loading to determine the fatigue limit [7].

The above-mentioned experimental data allow us to analyze each of these effects. It has been shown in a previous work that defect orientation has to be taken into account. In fact, tests have been performed on C35 steel containing artificial elliptical defects. These defects are longitudinal, transverse, and on a 45° direction, see Ref 12 for more details. In the present paper, we will focus on spherical defect.

Multiaxial Fatigue Approaches for Flawed Material

In the following section, the five approaches are presented. Each method is used to predict the evolution of fatigue limit with defect size and characterized by a different way to take account of the defect.

Murakami [*6*]

Murakami proposes to represent the defect as a surface entity and introduces the $\sqrt{\text{area}}$ parameter to describe defect size. He justifies this choice using fracture mechanics concepts. Murakami observes nonpropagating cracks in a small stressed zone around the defect. So, he considers that endurance threshold corresponds to crack growth threshold. He shows the fact that the maximum stress intensity factor $K_{I\,\max}$ is linearly related to $\sqrt{\text{area}}$ parameter for different

TABLE 4—*Material parameters and input data of Murakami's criterion.*

H_v	163
b, μm	Input data
a, μm	Input data
$\sqrt{\text{area}}$, μm	Input data

crack geometries. Then, he links the endurance threshold and this size parameter. He shows that for a given Vickers hardness, fatigue crack growth threshold depends mainly on $\sqrt{\text{area}}$ parameter. So Murakami has proposed an empirical equation based on the defect size ($\sqrt{\text{area}}$) and the material hardness to predict the fatigue limit of materials containing small defects. Under uniaxial loading, Murakami proposed empirical relations for tension loading:

$$\sigma_W = \frac{A(H_v + 120)}{(\sqrt{\text{area}})^{1/6}}\left[\frac{1-R}{2}\right]^{\alpha} \tag{2}$$

with $A = 1.43$ for surface defects and $A = 1.56$ for internal defects and

$$\alpha = 0.226 + H_v^{*}10^{-4} \tag{3}$$

For torsion loading, the fatigue limit is given by the following equation for surface defects:

$$\tau_W = \frac{1.43(H_V + 120)}{F(b/a)(\sqrt{\text{area}})^{1/6}}\left[\frac{1-R}{2}\right]^{\alpha} \tag{4}$$

with

$$F(b/a) = 0.995 + 2.11(b/a) - 2.26(b/a)^2 + 1.09(b/a)^3 - 0.196(b/a)^4 \tag{5}$$

Following an example of Murakami's equation applied to a 400 μm spherical defect under alternated torsion loading:

$$\sqrt{\text{area}} = 400\ \ \mu\text{m}; \quad R = -1; \quad H_v = 163; \quad b/a = 1$$

Murakami predicts $\tau_w = 115$ MPa. The experimental result is $\tau_w = 140$ MPa. The error prediction is 17.5 %.

Murakami developed an empirical approach to predict the fatigue limit for a given defect. The material is described by hardness. The defect is geometrically taken into account through $\sqrt{\text{area}}$. The loading case is described through the load ratio R. Table 4 summarizes input and material data necessary to apply this criterion. Figure 1 illustrates this criterion application steps.

A Defect is Equivalent to a Crack (*Fracture Mechanics Models*)

Linear elastic fracture mechanics (LEFM) describes crack propagation threshold with the amplitude of the stress intensity factor ΔK, a function of crack length a_c and stress amplitude $\Delta\sigma_c$. Table 5 summarizes input data and material parameters.

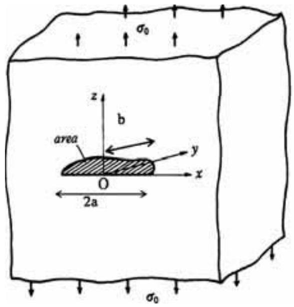

$$\sigma_W = \frac{A(H_v + 120)}{(\sqrt{area})^{1/6}}\left[\frac{1-R}{2}\right]^{\alpha}$$

$$\tau_W = \frac{A(H_V + 120)}{F(b/a)(\sqrt{area})^{1/6}}\left[\frac{1-R}{2}\right]^{\alpha}$$

FIG. 1—*Murakami's model application.*

This paper deals with spherical defect. So, crack depth is radius defect R_d. In order to illustrate this model's validity about influence of spherical defect with different sizes and under different loadings, the following relation is used:

$$\Delta\sigma_c = \frac{\Delta K_{\text{th,eff}}}{Y\sqrt{\pi^* R_d}} \tag{6}$$

where:

Y = the crack shape factor and

$\Delta K_{\text{th,eff}}$ is the effective stress intensity factor threshold.

This value is a material intrinsic parameter much more appropriate for natural cracks than the nominal one because plastic wake does not exist yet for a natural very small crack. Figure 2 illustrates this model's application steps.

This is an example for a 400 μm spherical defect under repeated tension:

$$Y = 0{,}64; \quad R_d = \sqrt{\frac{2}{\pi}}\sqrt{\text{area}}; \quad \Delta K_{\text{th,eff}} = 3 \ \text{MPa}\sqrt{\text{m}}$$

Applying Eq 5, $\Delta\sigma_c = 148$ MPa and the experimental value is $\Delta\sigma_c = 250$ MPa. The prediction error is 41 %.

Considering defects such as cracks is based on LEFM concepts. The crack shape factor and the defect radius describe geometrically the defect. $\Delta K_{\text{th,eff}}$ characterizes natural crack propagation. This approach predicts the stress amplitude $\Delta\sigma_c$ necessary to propagate crack initiated at the tip of the defect.

TABLE 5—*Material parameters and input data of the fracture mechanics model.*

$\Delta K_{\text{th,eff}}$, MPa$\sqrt{\text{m}}$	3
Y	0.64
R_d, μm	Input data

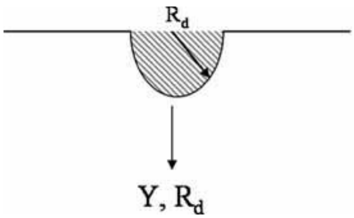

$$\Delta\sigma_W = \frac{\Delta K_{th,eff}}{Y\sqrt{\pi * R_d}}$$

FIG. 2—*Fracture mechanics model application.*

Nadot, Billaudeau, and Gadouini [*7,12,13*]

Billaudeau et al. [12] proposed a multiaxial fatigue criterion for material with defects using the hypothesis of Papadopoulos and Papadopoulos [5] on the influence of hydrostatic stress gradient. In order to take into account torsion effects, Gadouini et al. [7] proposed to calculate an equivalent stress gradient. The criterion can be written as follows:

$$\sigma^*_{\text{eq}} = \sigma_{\text{eq}}\left[1 - b_G\left(\frac{G(\sigma_{\text{eq}})}{\sigma_{\text{eq}}}\right)\right] \le \beta \tag{7}$$

with

$$G(\sigma_{\text{eq}}) = \frac{\sigma_{\text{eq}}(A) - \sigma_{\text{eq}}(\text{nom})}{R_d} \tag{8}$$

Nadot and Gadouini define defect size with the $\sqrt{\text{area}}$ parameter. Defect radius R_d is equal to $\sqrt{2/\pi}\times\sqrt{\text{area}}$. Authors have decided to measure the gradient $G(\sigma_{\text{eq}})$ over a physical length equal to the defect radius because stress distribution around the defect is affected over this length in the vicinity of the defect. This measure is done from the tip of the defect to the bulk: $\sigma_{\text{eq}}(A)$ and $\sigma_{\text{eq}}(\text{nom})$ are calculated at the tip of the defect and far from the defect, respectively. The application of Gadouini's criterion is independent of the equivalent stress. In this paper, Crossland equivalent stress σ_{Cr} is used [4]:

$$\sigma_{\text{Cr}} = \sqrt{J_{2,a}} + \alpha_{\text{Cr}} J_{1\,\max} \le \beta_{\text{Cr}} \tag{9}$$

Crossland's fatigue criterion (Eq 9) is based on a combination of the two invariants of the stress tensor. He supposes that the amplitude of the shear stress ($J_{2,a}$) and the maximum value of the hydrostatic stress ($J_{1\,\max}$) are the governing parameters in the case of proportional loadings and constant amplitude.

$$J_{1,\max} = \max_T\left(\frac{tr(\underline{\underline{\Sigma}}(t))}{3}\right) \tag{10}$$

TABLE 6—*Chaboche model parameter for C35* (*needed for Gadouini's model*).

C, MPa	45 000
γ	200
σ'_Y, MPa	278

$$\sqrt{J_{2,a}} = \sqrt{\frac{1}{6}((\Sigma_{xx,a} - \Sigma_{yy,a})^2 + (\Sigma_{yy,a} - \Sigma_{zz,a})^2 + (\Sigma_{zz,a} - \Sigma_{xx,a})^2 + 6(\Sigma_{xy,a}^2 + \Sigma_{yz,a}^2 + \Sigma_{xz,a}^2))} \tag{11}$$

To use Gadouini's criterion, three parameters have to be identified: α_{Cr}, β_{Cr}, and b_G. The first two parameters are calculated with two alternated fatigue limits of the defect free material: Tension and torsion. Gadouini introduces the material parameter b_G, which has the dimension of a length. This parameter allows accounting for the defect geometry and is calculated using fatigue limit of material containing a known artificial defect (size and shape). Identification is performed on a 170 μm spherical defect. Finite element calculations allow to measure stress distribution around defect.

$$\alpha_{Cr} = \frac{\beta_{Cr} - \frac{\sigma_{w0}}{3}}{\frac{\sigma_{w0}}{3}} \tag{12}$$

$$\beta_{Cr} = \tau_{w0} \tag{13}$$

$$b_G = \left(1 - \frac{\beta_{Cr}}{\sigma_{Cr}}\right)\left(\frac{\sigma_{Cr}}{G(\sigma_{Cr})}\right) \tag{14}$$

Material behavior is described by an elastic-plastic model using a nonlinear kinematic hardening [16]. Table 6 presents model's parameters. Figure 3 illustrates principal steps necessary to apply this criterion. Identification of input data and material parameters required to apply this criterion are in Table 7. The following example is for a 400 μm surface spherical defect under alternated tension

$$\underline{\underline{\Sigma}}_{max}(A) = \begin{pmatrix} 7.8 & 6.3 & 0.6 \\ & 283.2 & 2.3 \\ & & 4.3 \end{pmatrix} \quad \text{and} \quad \underline{\underline{\Sigma}}_{max}(\text{nom}) = \begin{pmatrix} 0 & 0 & 0 \\ & 150 & 0 \\ & & 0 \end{pmatrix}$$

$$\sigma_{Cr}(A) = 196 \text{ MPa}; \quad \sigma_{Cr}(\text{nom}) = 105 \text{ MPa}; \quad G(\sigma_{Cr}) = 0{,}285 \quad \text{and} \quad \sigma^*_{eq} = 174 \text{ MPa}$$

Criterion validity is quantified through an error calculation:

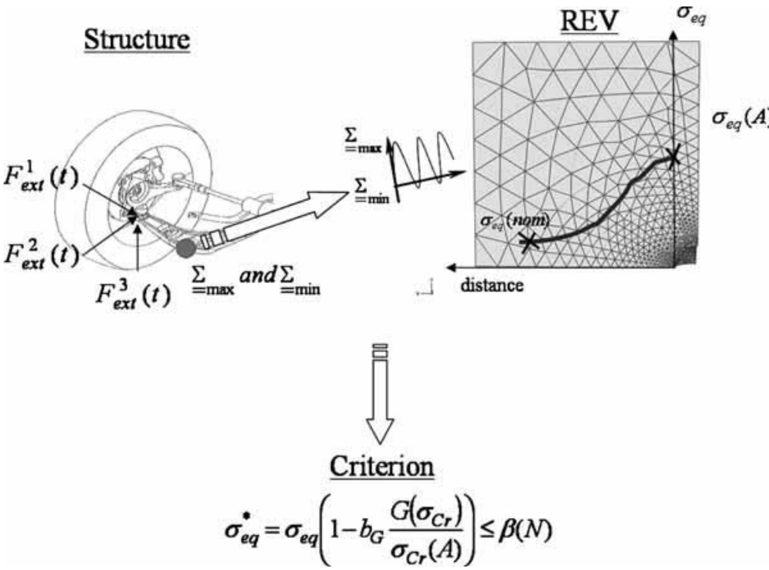

FIG. 3—*Gadouini's model application.*

$$E\% = \frac{\beta_{\mathrm{Cr}} - \sigma^*_{\mathrm{eq}}}{\beta_{\mathrm{Cr}}} \times 100 \tag{15}$$

For this defect, the assessment gives an error of about −3 %.

The relevant mechanical parameter of Gadouini's criterion is the equivalent stress gradient. The latter is calculated over the characteristic length equal to defect radius. The material parameter b_G takes into account defect while R_d defines defect size.

Susmel and Taylor: The MWCM Applied in Conjunction with the CDM [8]

Susmel and Taylor approach is a linear-elastic model used to describe notch influence on fatigue limit. Authors combined two previously developed approaches: The MWCM and the CDM. CDM is based on LEFM while MWCM is mainly based on two assumptions: (a) Crack initiation occurs on the plane which experiences the maximum shear stress amplitude, τ_a; (b) crack initiation and growth are influenced by the maximum stress normal to this plane, $\sigma_{n,\max}$.

TABLE 7—*Material parameters and input data of Gadouini's criterion.*

b_G, μm	99
$\sqrt{\text{area}}$, μm	Input data
R_d, μm	Input data
α_{Cr}	0.38
β_{Cr}, MPa	169

So, the CDM is essentially a criterion for nonpropagating cracks, whereas the MWCM is a critical plane approach and is essentially a fatigue crack initiation criterion.

To apply this approach, the MWCM expression is calculated at the critical distance $L/2$ defined in the CDM, more particularly the point method. The MWCM relation can be written as follows:

$$\sigma_{\text{eq}}^{ST} = \tau_a + \left(\tau_{w0} - \frac{\sigma_{w0}}{2}\right)\frac{\sigma_{n,\max}}{\tau_a} \leq \tau_{w0} \tag{16}$$

Finite elements calculations are used to calculate stress tensor and the stress Mohr's circle is used to calculate the two mechanical quantities τ_a and $\sigma_{n,\max}$. Susmel and Lazzarin [9] set up a parameter to simultaneously take into account the two stress components. This parameter, ρ, is defined as the ratio of the normal stress component to the amplitude of the shear stress component

$$\rho = \frac{\sigma_{n,\max}}{\tau_a} \tag{17}$$

Considering a notched specimen subjected to uniaxial load, the point method can be expressed by the following relation:

$$\sigma_a(r = a_0/2, \theta = 0) = \sigma_{w0} \tag{18}$$

σ_a is the amplitude of the maximum principal stress.

For this approach, we have decided to represent defect size with Murakami's parameter $\sqrt{\text{area}}$. In order to identify the critical distance $L/2$, linear-elastic finite element calculations are performed. Local stress components are picked up over a line from the tip of the defect to the bulk. For a spherical defect, the line is perpendicular to the tip of the defect. The identification of this distance is based on the fact that MWCM and CDM are equivalent in terms of multiaxial stresses near the notch tip even if they are based on different theoretical backgrounds.

Finite element (FE) calculations on a 170 μm defect allow the identification of the critical length: $L/2 = 70$ μm. At this distance, the maximum stress tensor for the 400 μm defect under alternated tension is

$$\underline{\underline{\Sigma}}_{\max} = \begin{pmatrix} 28.8 & 0.7 & 0.3 \\ & 184.6 & 0 \\ & & 0 \end{pmatrix}$$

Using the stress Mohr's circle

$$\tau_a = \frac{\Sigma_{22} - \Sigma_{33}}{2} \tag{19}$$

and

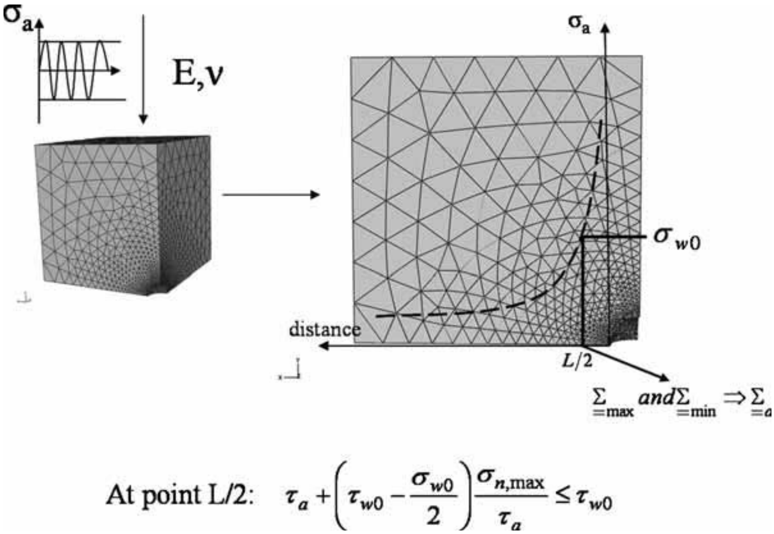

FIG. 4—*Susmel–Taylor approach application.*

$$\sigma_{n;\max} = \frac{\Sigma_{22} + \Sigma_{33}}{2} \tag{20}$$

$\tau_a = \sigma_{n,\max} = 92.3$ MPa; $\sigma_{eq}^{ST} = 141.3$ MPa. For this approach, the error calculation is

$$E\% = \frac{\tau_{w0} - \sigma_{eq}^{ST}}{\tau_{w0}} \times 100 \tag{21}$$

The prediction error is 19.6 %. Figure 4 presents the way to identify and validate Susmel and Taylor approach, while Table 8 summarizes input parameter.

Vallellano Model [*11*]

This micromechanical model based on microstructural fracture mechanics concepts has been developed to study fatigue crack growth in notches and predict fatigue limit of materials containing small notches. Vallellano's model can be applied for defects such as corrosion pits, inclusions, or pores.

TABLE 8—*Material parameters of Susmel-Taylor approach.*

σ_{w0}, MPa	240
τ_{w0}, MPa	169
$\sigma_{w0,\text{defect}}$, MPa	195
$L/2$, μm	70

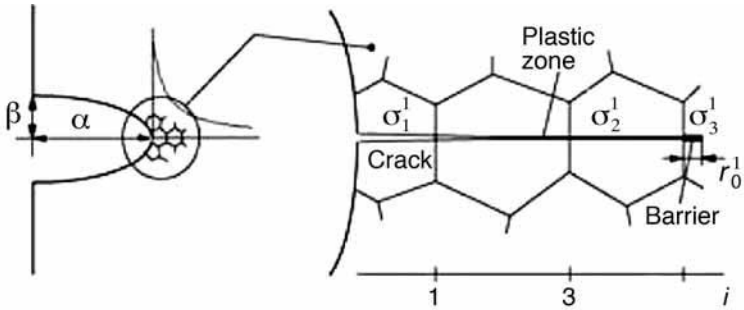

$$\underbrace{\alpha, \rho, Y, K_t, D}$$

$$\underbrace{a_0, \lambda_{i\,(i=1,3,5\,\ldots)}}$$

$$i = 1, 3, 5, \ldots \quad \sigma_w = \max_i \sigma^N_{w,i}$$

$$\frac{\sigma^N_{w,i}}{\sigma_{w0}} = \frac{\sigma_{w,i}}{\sigma_{w0}} \frac{\sqrt{iD/2}}{K_t} \left[\frac{1}{\lambda_i \sqrt{\alpha_v \rho_v}} + \frac{(K_t - 1)^2}{\alpha_v \sqrt{1 + \lambda_i^2}} \right]^{1/2}$$

FIG. 5—*Vallellano's model application.*

Vallellano set up an approach based on the theory of distributed dislocations. This model takes into account the interaction between short cracks and material barriers such as grain boundaries. In fact, Vallellano analyzes crack growth from the tip of the notch: A crack grows overcoming successive barriers of the plastic zone. So, in order to characterize fatigue failure in a notched component, the specific threshold conditions needed for a crack to overcome each successive barrier in the material have to been identified. Figure 5 illustrates Vallellano's model application. This figure presents the main parameters necessary to apply this criterion. Note that i is an odd integer representing the number of half grains from the notch root up to the barrier, where the plastic zone is stopped. As it can be seen in Fig. 5, Vallellano's model predicts fatigue limit of a notched component σ_w. Vallellano proposed the following expression to calculate the stress $\sigma^N_{w,i}$ required for a crack to overcome a generic barrier in the root of notch:

$$\frac{\sigma_{w,i}^{N}}{\sigma_{w0}} = \frac{\sigma_{w,i}}{\sigma_{w0}} \frac{\sqrt{iD/2}}{K_t} \left[\frac{1}{\lambda_i \sqrt{\alpha_v \rho_v}} + \frac{(K_t - 1)^2}{\alpha_v \sqrt{1 + \lambda_i^2}} \right]^{1/2} \tag{22}$$

with

$$\lambda_i = \frac{\sqrt{\alpha_v \rho_v}}{\alpha_v - \rho_v} \left[\sqrt{1 + \frac{iD/2}{\rho_v}\left(2 + \frac{iD/2}{\alpha_v}\right)} - \left(1 + \frac{iD/2}{\alpha_v}\right) \right] \tag{23}$$

This expression (Eq 22) is adapted to any defect. In fact, the stress concentration factor K_t, the notch radius ρ_v, and the notch depth α_v describe defect geometry. The stress $\sigma_{w,i}$ is the lowest stress required for a crack of length $a_v = iD/2$ to propagate up to fracture in a plain specimen. The crack length depends on the characteristic grain diameter D. In the absence of the experimental Kitagawa–Takahashi diagram, a common practice is to use the following expression to calculate $\sigma_{w,i}$

$$\sigma_{w,i} = \sigma_{w0} \frac{\sqrt{a_0}}{((iD/2)^f + a_0^f + l_0^f)} \tag{24}$$

with

$$a_0 = \frac{1}{\pi} \left(\frac{\Delta K_{\text{th}}}{\sigma_{w0}} \right)^2 \tag{25}$$

l_0 is the mean distance from the crack nucleation site to the first microstructural barrier in the material: l_0 is assumed to be one half of the grain size. ΔK_{th} is the crack growth threshold. The exponent f governs the transition speed between short crack regime and long crack regime: This is the transition between the two straight lines of Kitagawa–Takahashi diagram. In this paper, value of f is 2.5. This value is used because Vallellano took the same value for S10C steel which is similar to C35 steel in terms of composition and mechanical properties.

The present paragraph explains the methodology to apply Vallellano's approach for a 400 μm spherical defect under fully reversed tension loading.

- Geometrical parameters
- $\alpha_v = \sqrt{2/\pi} \times \sqrt{\text{area}} = 320\ \mu\text{m}$
- $\rho_v = 0.9999 \times \alpha_v$ and $\lambda_i = \sqrt{\alpha_v \rho_v / \alpha_v - \rho_v} \times f(i)$
  To calculate λ_i, it is necessary to have a nonzero denominator. Or, for a spherical defect $\alpha_v \cong \rho_v$.
- $K_t = 1.95$.
  This value has been calculated from a linear-elastic finite element simulation. The maximum principal local stress at the front of the defect has been measured and divided by the applied stress.
- $Y = 0.64$.This value is the crack shape factor for a semicircular crack.
- C35 steel material properties
- $D = 22\ \mu\text{m}$; $\sigma_{w0} = 240$ MPa; $\Delta K_{\text{th,eff}} = 3\ \text{MPa}\sqrt{\text{m}}$
- Calculation of the stress required to overcome microstructural barriers in the plain material, $\sigma_{w,i}$
- $l_0 = D/2 = 11\ \mu\text{m}$; $a_0 = 50\ \mu\text{m}$; $f = 2,5$.

TABLE 9—*Material parameters and input data of Vallellano's model.*

D, μm	22
$\Delta K_{th,eff}$, MPa$\sqrt{m}$	3
$K_{t(torsion)}$	2.25
$K_{t(tension)}$	1.95
α_v, μm	Input data
ρ_v, μm	Input data
f	2.5

- Calculation of the notch fatigue limit σ_w

$\sigma_w = \max\limits_i(\sigma^N_{w,i})$ and $i = 1, 3, 5, \ldots$ The prediction is $\sigma_w = 133$ MPa and the experimental result is 150 MPa. This result is quite good because the prediction error is about 11.5 %. Table 9 summarizes input data and material parameters needed to apply this micromechanical approach.

Vallellano's approach has been developed to account for the microstructure's influence on crack growth for a notched specimen. It predicts fatigue limit for a given notch making use of the stress intensity factor, the characteristic grain size, and defect size.

Comparison of the Different Approaches

Results are validated using a prediction error calculation. Murakami, fracture mechanics, and Vallellano model predictions can be directly compared to experimental results. Gadouini and Susmel–Taylor predictions are compared to the identified parameter β_{Cr} and the plain alternated torsion fatigue limit, respectively. The prediction error, used to validate all approaches, is expressed as follows:

$$E\% = \frac{\text{experiment} - \text{prediction}}{\text{experiment}} \times 100 \tag{26}$$

A positive error means that results are conservative.

Influence of Defect Size

Figures 6 and 7 present model's prediction for each case describing size effect for alternated tension and torsion loading. Defect size, defined on graphs as $\sqrt{\text{area}}$, is in a range of 100–900 μm. Results will be first discussed in terms of curve trend.

Fully Reversed Tension Loading—Figure 6 globally shows a good trend for each method, compared to experimental results, to predict defect size effect on fatigue limit of C35 containing artificial surface spherical defects. Fracture mechanics and Susmel–Taylor model tend to overestimate fatigue limit for the smallest defect, $\sqrt{\text{area}} = 100$ μm. In fact, predicted limits are higher than the

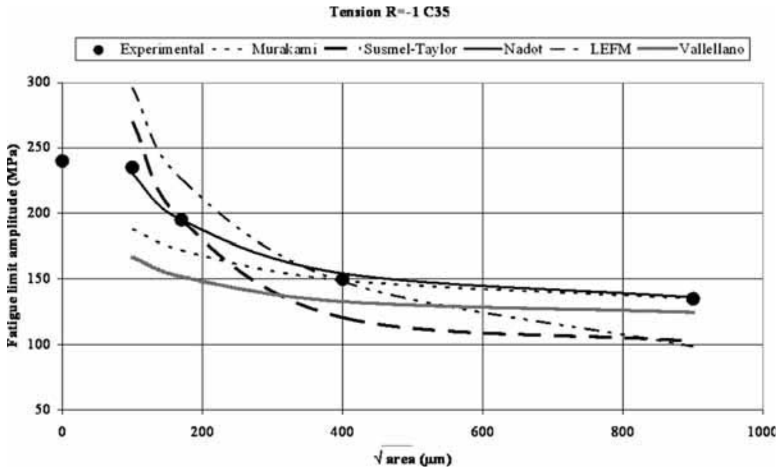

FIG. 6—*Defect size effect under alternated tension.*

smooth bar fatigue strength: Defects do not improve a material's fatigue properties. Murakami and Vallellano models underestimate fatigue limit for the two smallest defects, while they give quite good predictions for the defect sizes: 400 and 900 μm. The medium size is well treated by all approaches.

Fully Reversed Torsion Loading—Figure 7 illustrates results under torsion loading for three defect sizes: 150, 400, and 900 μm. Stress distribution around a defect under torsion loading is different than stress distribution under tension loading. Results show good trends for Murakami, Susmel–Taylor, Nadot, and Vallellano's models. Prediction evolution is in relatively good agree-

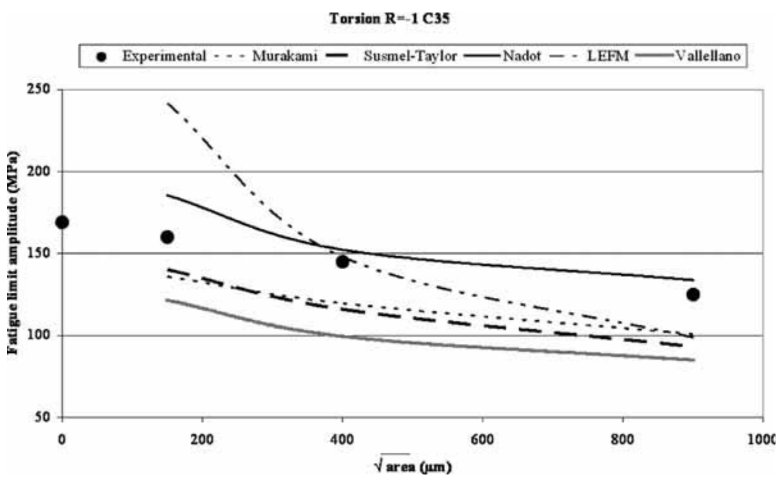

FIG. 7—*Defect size effect under alternated torsion.*

ment with experimental results (between 10 % and 30 %).

Fracture mechanics model gives poor predictions for small and big defects. So, we can wonder about the description of stress the distribution around defect. In fact, mechanical parameters used in this approach are based on LEFM concept. Can a defect really be assumed to behave like a crack using maximum principal stress? Results are quite good for the four other results. However, Vallellano's predictions seem to be under other criteria predictions even if the curve trend is good.

Multiaxial Effect

The previous results show each approach's ability to predict fatigue limit of materials with spherical defects with different sizes. In the present paper, defect shape effects are not analyzed. So, multiaxiality is introduced through the type of loading. The question is: what are the relevant mechanical parameters necessary to capture and represent mechanisms at the tip of the defect? In order to predict the defect's influence:

- Murakami uses hardness and $\sqrt{\text{area}}$ parameter.
- When defects are assumed to be cracks, the stress intensity factor represents stresses at the tip of the defect.
- Gadouini proposes an elastic-plastic FE analysis to describe stress distribution around defect in a multiaxial initiation criterion.
- Susmel–Taylor initiation criterion calculates an equivalent stress at a critical distance from the tip of the defect.
- Vallellano's model results are mainly influenced by the characteristic grain size and the maximum principal stress necessary to propagate cracks.

Mean Stress Effect

Figures 8 and 9 present model predictions for nonzero mean stress under tension and torsion loadings respectively. For tension, load ratios are -1, 0, and -5. For torsion, load ratios tested are -1, -0.5, and 0. The defect size is constant and equal to 400 μm.

Under tension loading, all approaches have difficulties for the high negative mean stress ($R=-5$). Figure 8 globally shows that Nadot and Susmel–Taylor predictions are quite good. It is due to the fact that a multiaxial criterion is able to capture the effect of compressive stress for steels. Under torsion loading, fracture mechanics model and Vallellano do not follow the experimental curves trends: Mean stress effect is not described. In fact, the effective stress intensity factor threshold is independent of load ratio, and the mean shear stress has no influence on the plain fatigue limit. In Vallellano's model, mean shear or normal stress can only be taken account through σ_w. This is one major limitation of such approach.

Good predictions are given for Susmel–Taylor approach. It seems that measuring the normal maximum stress $\sigma_{n,\max}$ and the amplitude of the maximum

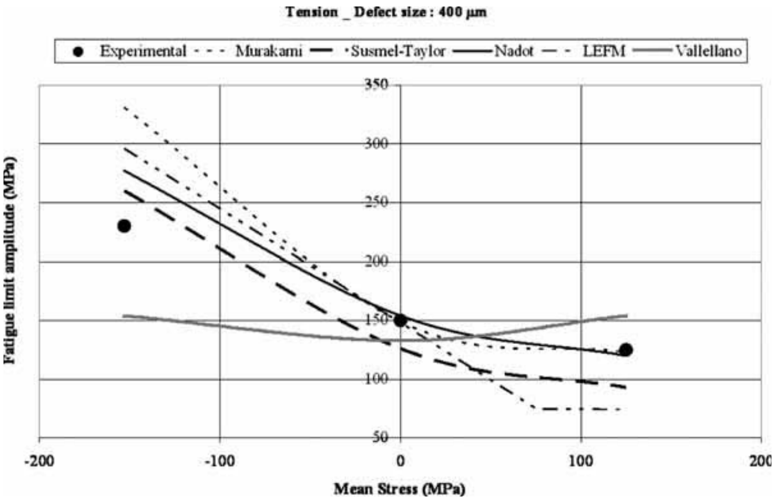

FIG. 8—*Mean stress effect for a 400 μm spherical defect under tension loading.*

shear stress at the critical distance $L/2$ partly takes into account mean stress effect. Note that this approach is different from Gadouini's model in not describing elastic-plastic behavior.

Figure 10 summarizes error prediction calculations for all cases. Absolute mean error predictions in order of presented approaches on Fig. 10 are 17 %, 7 %, 17 %, 25 %, and 26 %. These results show that the three first approaches generally give better predictions than the approaches considering defects like cracks. This observation can be supported by the measure of dispersion for each model's predictions. The standard deviations are about 20 for Murakami,

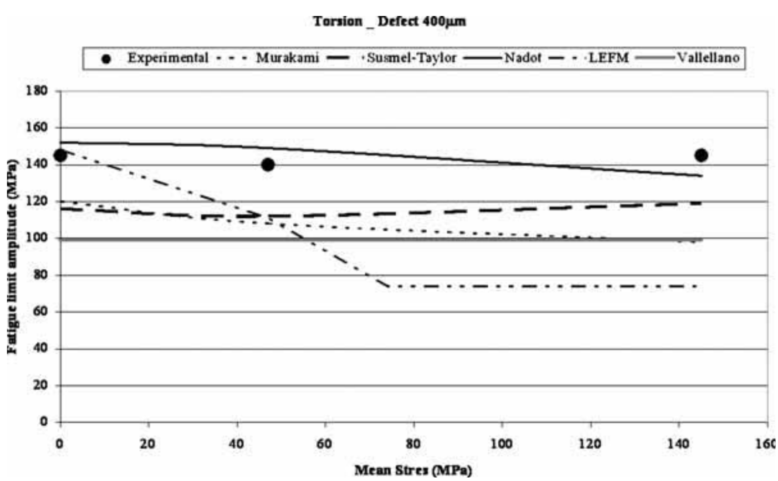

FIG. 9—*Mean stress effect for a 400 μm spherical defect under torsion loading.*

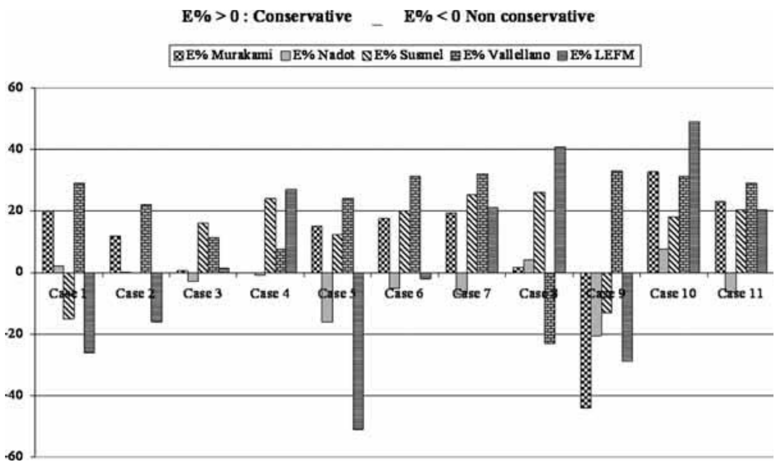

FIG. 10—*Model prediction error for spherical defects.*

8 for Nadot, 15 for Susmel, 17 for Vallellano, and 31 for LEFM (Table 10). Looking at Fig. 10 and Table 10, it can be seen that Nadot's approach is less conservative than the other approaches and the fracture mechanics model is not a conservative method as it could be expected, but neutral one.

Discussion

Shape and Size Defect Description

The previous section presented results regarding defect size, loading, and mean stress. Defects are artificial and spherical. Defects size is always linked to $\sqrt{\text{area}}$, which is proportional to R_d for spherical defect. Quite good results are obtained for each method studying the influence of size on fatigue limit. But, we can wonder about validity of this parameter to describe natural defects with irregular shape such as microshrinkages. De Kacinczy [17] and Murakami [6] proposed different definitions. De Kacinczy [17] deals with shrinkages in a hard

TABLE 10—*Comparison between number of experimental and input data to identify and result quality.*

	Experimental Data Needed	Input Data to Describe the Defect	Mean Absolute Error (%) ± Standard Variation	Mean Error (%)
Murakami	H_v	$\sqrt{\text{area}}$	17 ± 20	9
Nadot	σ_{w0}, τ_{w0}, $\sigma_{w0,\text{defect}}\gamma$, σ'_Y, C	$\sqrt{\text{area}}$	7 ± 8	-4
Susmel	σ_{w0}, τ_{w0}, $\sigma_{w0,\text{defect}}$	$\sqrt{\text{area}}$	17 ± 15	13
Vallellano	σ_{w0}, τ_{w0}, $\Delta K_{\text{th,eff}}$	α_v, ρ_v	25 ± 17	21
LEFM	$\Delta K_{\text{th,eff}}$	R_d, Y	26 ± 31	3

steel and defines defect size as the diameter of the smallest circle enclosing the defect. Murakami [6] defines size of shrinkage as the real surface, $\sqrt{\text{area}}$, described by the smoothing curve around the defect. This latter proposition seems to be closest to the real defect size influencing fatigue limit.

Comparison of approaches shows their limitations: Multiaxial models show good results for a large size range. In fact, all approaches generally give bad predictions for very small defects, about 100 μm. So, the application domain of each method needs to be defined in order to get relevant predictions.

Governing Mechanical Parameters

Approaches presented in this paper sweep the main mechanical quantities widely used to represent stress distribution around defect: material properties, stress intensity factor, linear elastic stress, and nonlocal stress. It is interesting to observe that using hardness and $\sqrt{\text{area}}$, Murakami's model gives good results for all cases. In fact, Murakami [6] validates this criterion on different steel containing a notch, a hole, a crack, and a Vickers indentation. We can wonder about the application to materials and natural defects with complex shape because most of the validations are performed on steels.

Numerical results show that the stress intensity factor threshold is not sufficient to capture mean stress effect. In fact, fracture mechanics model and Vallellano's criterion do not give good predictions for mean stress. Vallellano validates his model on results from literature. He considered the nominal crack growth threshold ΔK_{th} and not the effective one, as we have done in this paper. ΔK_{th} is the parameter taking into account loading ratio in Vallellano's approach. So, using the effective value, mean stress effect cannot be demonstrated, especially for torsion loading.

Susmel–Taylor and Gadouini approaches are similar: An equivalent initiation stress is measured at a critical distance and compared to an identified parameter in a multiaxial criterion. Gadouini and Nadot describe the elastic-plastic behavior to take into account mean stress relaxation and to measure a stress gradient: Predictions are good for all cases. To apply Susmel–Taylor approach finite element calculations are performed with linear elasticity: Predictions are quite good. So we can wonder if measuring an elastic equivalent stress at a critical distance is enough to describe defect's influence on fatigue limit. This result is also interesting because calculation time can be reduced and we can also compute elastic stresses using analytical solution for a given geometrical case.

After all, these models can be compared regarding to their ease of use. To apply these approaches, parameters have to be identified and experimental tests have to be performed. Table 10 can be used to classify approaches regarding to the experimental cost of identification and prediction quality. The first category concerns Murakami. To apply these equations only one experimental data and one input data are required. The fracture mechanics model and Vallellano's approach form another category for which the numbers of experimental and input data are not too important but predictions are bad. The last category concerns Nadot and Susmel approaches. These methods require a large number of parameters to be identified and give the better predictions.

Good results, obtained for Nadot's method, are illustrated by a small mean absolute error combined to a small standard deviation. But we have to take care of these predictions which seem to be in the unsafe domain regarding to the negative sign of the mean error. Looking at this parameter, it can be observed that the fracture mechanics model seems to be in the safe domain predictions. However, Fig. 10 shows that this model's predictions can be overestimated (−45 %) or underestimated (+45 %). It can be concluded that the fracture mechanics model is not a conservative method for all loading case. So in order to evaluate a fatigue criterion quality to take into account defects, it is necessary to consider the experimental identification cost, the conservative nature of the criterion, the standard deviation and the sign of the mean error.

Conclusion

Different artificial spherical defects are introduced at the surface of fatigue samples in C35 steel. Tension and torsion fatigue tests have been conducted in order to determine fatigue limit of defect free material and material containing defects for different load ratios. A comparative study of five approaches is carried out to capture the relevant quantities necessary to predict fatigue limit of materials with defect for multiaxial loadings. Each approach distinguishes itself from the other by the way it takes into account the defect and the way to represent stress distribution around the defect.

All approaches are able to capture the main shape of the evolution of the fatigue limit with defect size for tension and torsion loading. It is shown that approaches based on a multiaxial criterion are preferable for torsion loading. In fact, the choice of mechanical parameters describing stress distribution around defect is very important. Results show that the stress intensity factor is not adapted to take into account mean stress effect. So, approaches using fracture mechanics should be improved to describe experimental influence of load ratio. Gadouini demonstrated that a nonlinear kinematic model is necessary to describe stress relaxation and Susmel's approach shows that the way to calculate the equivalent stress can be important: measurements of an elastic equivalent stress at a critical distance give good results.

References

[1] Ammar, H. R., Samuel, A. M., and Samuel, F. H., "Effect of Casting Imperfections on the Fatigue Life of 319-F and A356-T6 Al-Si Casting Alloys," *Mater. Sci. Eng., A*, Vol. 473, 2008, pp. 65–75.

[2] Nadot, Y., Mendez, J., and Ranganathan, N., "Influence of Casting Defects on the Fatigue Limit of Nodular Cast Iron," *Int. J. Fatigue*, Vol. 26, 2004, pp. 311–319.

[3] Couper, M. J., Neeson, A. E., and Griffiths, J. R., "Casting Defects and the Fatigue Behavior of an Aluminum Casting Alloy," *Fatigue Fract. Eng. Mater. Struct.*, Vol. 13, 1990, pp. 213–227.

[4] Crossland, B. "Effect of Large Hydrostatic Pressures on the Torsional Fatigue Strength of Fan Alloy Steel," *Proceedings of the International Conference on Fatigue of Metals*, 1956, Institution of Mechanical Engineers, London, pp. 138–149.

[5] Papadopoulos, O. V. and Papadopoulos, V. P., "An Invariant Formulation of a Gradient Dependent Multiaxial High-Cycle Fatigue Criterion," *Eng. Fract. Mech.*, Vol. 55, 1996, pp. 513–528.

[6] Murakami, Y., *Metal Fatigue: Effects of Small Defects and Nonmetallic Inclusions*, Elsevier, Oxford, 2002, p. 16.

[7] Gadouini, H., Nadot, Y., and Rebours, C., "Influence of Mean Stress on the Multiaxial Fatigue Behaviour of Defective Materials," *Int. J. Fatigue*, Vol. 30, 2008, pp. 1623–1633.

[8] Susmel, L. and Taylor, D., "Two Methods for Predicting the Multiaxial Fatigue Limits of Sharp Notches," *Fatigue Fract. Eng. Mater. Struct.*, Vol. 26, 2003, pp. 821–833.

[9] Susmel, L. and Lazzarin, P., "A Bi-Parametric Modified Wöhler Curve for High Cycle Multiaxial Fatigue Assessment," *Fatigue Fract. Eng. Mater. Struct.*, Vol. 25, 2002, pp. 63–78.

[10] Taylor, D., "Geometrical Effects in Fatigue: A Unifying Theoretical Model," *Int. J. Fatigue*, Vol. 21, 1999, pp. 413–420.

[11] Vallellano, C., Mariscal, M. R., Navarro, A., and Dominguez, J., "A Micromechanical Approach to Fatigue in Small Notches," *Fatigue Fract. Eng. Mater. Struct.*, Vol. 28, 2005, pp. 1035–1045.

[12] Billaudeau, T., Nadot, Y., and Bezine, G., "Multiaxial Fatigue Limit for Defective Materials: Mechanisms and Experiments," *Acta Mater.*, Vol. 52, 2004, pp. 3911–3920.

[13] Nadot, Y. and Billaudeau, T., "Multiaxial Fatigue Limit Criterion for Defective Materials," *Eng. Fract. Mech.*, Vol. 73, 2006, pp. 112–133.

[14] Nadot, Y., Ranganathan, N., Mendez, J., and Beranger, A. S., "A Study of Natural Cracks Initiated on Casting Defects by Crack Front Marking," *Scr. Mater.*, Vol. 37, 1997, pp. 549–553.

[15] Verreman Y. and Espinosa, G., "Mechanically Short Crack Growth Form Notches in a Mild Steel," *Fatigue Fract. Eng. Mater. Struct.*, Vol. 20, 1997, pp. 129–142.

[16] Chaboche, J. L. and Lemaitre, J., *Mécanique des Matériaux Solides*, Dunod, Paris, 1996, p. 229.

[17] De Kacinczy, F., "Effect of Small Defects on the Fatigue Properties of Medium Strength Cast Steel," *J. Iron Steel Inst., London*, Vol. September, 1970, pp. 851–855.

Reprinted from JAI, Vol. 7, No. 4
doi:10.1520/JAI102544
Available online at www.astm.org/JAI

M. Scibetta,[1] *E. Lucon,*[1] *and T. Houben*[1]

Effect of Cladding on Biaxially Loaded Underclad Part-Through Cracks

ABSTRACT: Fracture toughness testing on standard specimens in the ductile to brittle transition regime is well established and standardized by the ASTM since 1997. However, its applicability to structural components and its potential conservatism remain a subject of concern. In structural integrity assessment of reactor pressure vessels submitted to an accidental loading condition called pressurized thermal shock, the cladding is generally considered not to play any role and is neglected. However, cladding has the ability to restrain the crack from opening due to its good ductility. To investigate the potential safety margin, a semielliptical crack introduced by fatigue is covered by a stainless steel cladding and specimens are tested under biaxial conditions in the ductile to brittle transition regime. Test results shows that cladding plays a significant role and contributes to an additional safety margin. In addition, cladding increases the potential for crack arrest.

KEYWORDS: fracture toughness, master curve, pressurized thermal shock, transferability, cladding, reactor pressure vessel, biaxial loading

Introduction

The inner surface of a reactor pressure vessel (RPV) is covered with a stainless steel cladding to protect the ferritic steel of the vessel against corrosion and pitting in a borated reactor coolant and to avoid polluting the coolant with activated corrosion products. The cladding also plays an important role in the heat transfer damping and in the structural integrity for small size defects close to the base material-cladding interface. It should also be noted that other heavy components of nuclear reactors such as nozzles, vessel piping, or steam generator plate are cladded for the same reasons.

Defects in the clad area have been observed in steam generator tube plates and in reactor vessel nozzles of French and American [1–4] power plants as well as in the core forgings of some French plants [5]. A detailed review of the

Manuscript received May 21, 2009; accepted for publication March 22, 2010; published online April 2010.
[1] SCK•CEN, Boeretang 200, 2400 Mol, Belgium.

Cite as: Scibetta, M., Lucon, E. and Houben, T., "Effect of Cladding on Biaxially Loaded Underclad Part-Through Cracks," *J. ASTM Intl.*, Vol. 7, No. 4. doi:10.1520/JAI102544.

fabrication procedures of the Belgian units, whose RPVs also consist of forged rings, shows that the presence of such underclad defects cannot be totally excluded. Therefore, detailed elastic-plastic fracture mechanics analyses were performed in order to evaluate the impact of postulated underclad defects on the integrity of the vessel. An input for integrity assessment is the mechanical properties of the cladding. Unfortunately, representative cladding material has not been found in Belgium. Therefore, Tractebel purchased a section of the RPV of the Lemoniz 1 unit whose construction has been cancelled. It is a Spanish 900 MW pressurized water reactor of Westinghouse design similar to the North Anna unit in the United States. This cladding has been thoroughly characterized in the nonirradiated condition and after an accelerated irradiation program in the BR2 reactor [6–9].

When safety integrity studies are performed, the presence of the cladding is generally neglected. A lot of studies are available in the literature for evaluating the potential benefit of cladding on the structural integrity. Most of them conclude that cladding has rather limited impact on the structural integrity of the vessel [10–22]; such effect could be slightly detrimental or beneficial.

The arguments to justify that cladding can be neglected are as follows

- The cladding thickness is quite limited as compared to the vessel thickness (~6 mm compared to ~200 mm).
- The yield stress of the cladding is much lower than for that of the ferritic material.
- The ductile tearing toughness of the cladding is not particularly high.

The factors that contribute to a slight beneficial effect are as follows.

- The cladding acts as a thermal buffer and tends to reduce the thermal gradient in the base material.
- There is a small beneficial compressive residual stress in the base metal.

The factors that contribute to a slight detrimental effect are as follows.

- The detrimental effect of tensile residual stress is limited to twice the cladding thickness.
- The dissimilar coefficients of thermal expansion can induce additional stresses in the base metal during a transient.

In a limited number of cases, cladding has been demonstrated to have a marked beneficial effect. For small underclad cracks, the cladding restrains cracks from opening and can reduce the stress intensity factor of the cracks [23–30]. This effect is however negligible for through-clad cracks. In Refs 28 and 29, it is found that the failure probability of an unclad surface crack was 100 times higher than an underclad crack. However, the crack length should be smaller than the clad thickness and the cladding should have a sufficient toughness to reach this conclusion. In another experimental study [31], it was demonstrated that the integrity of the cladding loaded above the general yield in presence of an underclad crack was assured. It was also demonstrated that in a number of loading conditions, the cladding toughness is sufficient to prevent an underclad crack to become a through-clad crack [26]. Both studies [26,31] conclude that cladding has a shielding effect.

An experimental study [32,33] also demonstrated that cladding enhances crack arrest initiated by an underclad defect. This effect is due to the fact that cladding is ductile and absorbs energy during crack opening. However, another

TABLE 1—*Chemical analyses* (*wt %*).

Material	C	Mn	Si	S	P	Cr	Ni	Mo	V	Cu	Co
Lemoniz	0.21	0.62	0.26	0.007	0.008	0.35	0.66	0.58	0.01	0.05	0.015
Soudokay layer 1	0.044	0.88	1	<0.005	0.014	19.2	10.2	0.09	0.03	0.08	0.05
Soudokay layer 2	0.034	0.78	1	<0.005	0.02	19.6	10.3	0.07	0.04	0.09	0.05

study [12] concludes the opposite, arguing that the cause of crack arrest was the high toughness of the heat affected zone (HAZ) and not the toughness of the cladding.

Finally, it should also be noted that the studies [34,35] strongly recommended performing the analysis using an elastic-plastic approach as they find out that an elastic approach used to determine the stress intensity factor can lead to a large unconservatism.

The objective of this work is to validate experimentally the potential benefit of cladding for small underclad cracks in loading condition representative of a pressurized thermal shock. The selected geometry is the pressurized thermal shock-disk (PTS-D) specimen described in Ref 36. The specimen is a 50 mm thick disk with 200 mm diameter. This geometry is able to reproduce biaxial loading representative of pressurized thermal shock and is relatively cheap compared to the cruciform specimen developed within the heavy-section steel technology program at ORNL [37]. As no underclad cracks were identified in the Lemoniz section, the feasibility of representative cladding deposition on a specimen was investigated in Ref 38. The mechanical properties of the obtained Soudokay cladding were compared to those of the original Lemoniz cladding and to literature data and were found to be representative.

In this work, semielliptical cracks are introduced by fatigue on 16 PTS-D specimens. The specimens are subsequently cladded and loaded to fracture in order to evaluate the effect of cladding.

Material

The Lemoniz material from the beltline region was not used due to the limited size of the block available after previous investigations. Therefore, the base material extracted at the outlet location of the Lemoniz vessel was used. Twenty specimens were extracted according to the cutting scheme given in Ref 38. It should be noted that the weld for the outlet bus was identified. However, the PTS-D specimens were fully within the base material.

The chemical and mechanical properties of the Lemoniz material at beltline location were thoroughly investigated in Refs 36 and 39 and are summarized in Tables 1 and 2.

The cladding is deposited by Soudokay by Submerged Arc Welding using 60 mm width strip. The first layer is 309 L and the second layer is 308 L. The welding procedure and post weld heat treatment are described in Ref 38. This

TABLE 2—*Mechanical properties of investigated materials. Note: σ_{YS} is the yield strength, σ_{TS} is the tensile strength, RA is the reduction of area, ε_t is the total elongation, T_{41J} is the 41 J transition temperature, USE is the upper shelf energy, NDT is the nil-ductility transition temperature, and T_0 is the master curve reference temperature.*

	Tensile at Room Temperature				Charpy		Drop Weight	Toughness
Material	σ_{YS} (MPa)	σ_{TS} (MPa)	RA (%)	ε_t (%)	T_{41J} (°C)	USE (J)	NDT (°C)	T_0 (°C)
Lemoniz	459	607	70	27	−19	204	−18	−99
Soud. 1	300	544	67	53	−93	96	n.a.	n.a.
Soud. 2	302	540	66	55	−93	96	n.a.	n.a.

procedure is selected to reproduce a cladding similar to Tihange II/Doel III. The main properties are also summarized in Tables 1 and 2.

Additional Material Characterization

After fracture toughness testing of the cladded PTS-D, it appears that the crack tip was located within the HAZ introduced by the cladding process. Therefore, 12 Charpy size specimens were extracted from the unbroken PTS-D specimen L20. Precracking was performed so that the crack tip was located within the HAZ. The crack propagates by fatigue from the cladding side toward the base material.

Specimens are precracked and tested according to the ASTM E1921–08 standard [40] in order to measure the reference temperature T_0. Precracking is done on a piezoelectrical testing machine. Crack propagation is monitored using specimen compliance. The cyclic loading has a frequency of 100 Hz and the amplitude is such that the applied stress intensity factor during final sharpening is less than 18 $\mathrm{MPa}\sqrt{\mathrm{m}}$. To promote a straight crack front, precracked Charpy v-notch (PCCv) specimens are 20 % side grooved after precracking. Testing is performed on the same machine at a constant crosshead displacement of 0.2 mm/min. Displacement is measured using the linear variable differential transformer (LVDT) of the machine. The analysis takes into account the compliance of the machine. After testing, specimens are broken open at nitrogen liquid temperature. Crack length is measured using the nine points average technique from a digital picture of the fracture surface. Fracture toughness results are summarized in Table 3. Results analyzed using the master curve are presented in Fig. 1 and summarized in Table 4. Figure 1 shows that the results follow the master curve shape, as all data are included within the 5 and 95 percentile. It should be noted that tests performed at −130°C are just outside the validity window. Including those tests in the analysis does not substantially change the reference temperature. The reference temperature of the HAZ is only 20°C above the one from the base metal. This difference is considered significant considering the combined uncertainty.

Testing of cladded PTS-D specimens led in some circumstances to fracture of the cladding. Therefore fracture toughness tests were performed on the clad-

TABLE 3—*Summary of PCCv test results on the HAZ. Note: No ductile crack growth was measured on the fracture surface. All specimens fulfill the validity criteria. Specimen L20_05 was tested but not recorded. a_0 is the specimen crack size, W is the specimen width, B is the specimen thickness, and K_{Jc} is the measured fracture toughness.*

Specimen ID	Test Temperature (°C)	a_0 (mm)	W (mm)	B (mm)	K_{Jc} (MPa $\sqrt{m}$)
L20_06	−130	5.09	9.96	9.90	41.2
L20_10	−130	4.99	10.00	9.94	45.8
L20_09	−90	5.09	9.97	9.91	63.2
L20_02	−130	5.12	9.96	9.95	72.3
L20_07	−100	5.12	9.96	9.91	83.5
L20_01	−90	5.32	9.97	9.92	84.9
L20_03	−130	5.10	9.99	9.95	85.9
L20_08	−90	5.01	9.98	9.90	94.7
L20_04	−90	5.13	9.98	9.90	97.4
L20_11	−90	5.08	10.00	9.94	129.8
L20_12	−90	4.97	9.93	9.91	141.8

ding material. As the cladding displays a brittle to ductile transition region due to the presence of ferrite in the austenitic matrix, it was initially assumed that fracture toughness of cladding below −130°C would display a brittle behavior. Testing at −130 and −170°C did not show any brittle fracture. Therefore, three additional fracture toughness tests at ductile crack initiation were performed according to the ASTM E1820–08 standard.

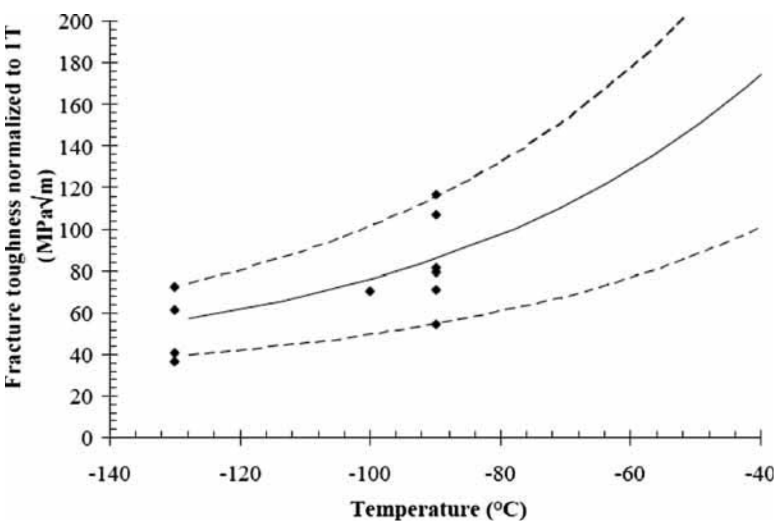

FIG. 1—*Fracture toughness test results of the HAZ material and associated 5, 50, and 95 percentile master curves.*

TABLE 4—*Master curve analysis of the HAZ material. Note: Four tests were just outside the validity window. N is the number of tested specimen, r is the number of valid data, n_i is a value that should be larger than 1 to obtain a valid reference temperature, T_0 is the reference temperature, and σ is the standard deviation.*

	N	r	n_i	$T_0 \pm 2\sigma$ (°C)
HAZ	11	7	1.14	−77.8 ± 13.6

For each test performed, three single-specimen methodologies are applied to derive J_{Ic} and the J-R curve: unloading compliance (UC), potential drop (PD) and normalization data reduction (NDR). Using these three methods together allows to better assess the material properties and the associated uncertainties. Each technique aims at monitoring crack extension during the test. UC is the primary method recommended by the standard. The compliance is measured during partial unloading and can be correlated with the crack size. PD used for these experiments consists in monitoring the potential across the specimen subjected to a pulsed current of 10 A. Current pulses are preferred to continuous dc current to avoid specimen temperature increase due to Joule effect. The potential increase is correlated with crack size. NDR has been included in the 2001 revision of the ASTM E1820 standard [41]. This method has the advantage that it does not use any instrumentation to monitor crack extension. Crack extension is inferred from the initial and final crack size measured on the sample and from the force displacement curve.

Specimens are precracked using the same parameters as for the HAZ PCCv specimens. Specimens are 20 % side grooved to avoid shear lips formation. Fracture toughness at test termination and initiation values at 0.2 mm offset from the blunting line are summarized in Tables 5 and 6, respectively. No brittle fracture occurred; initiation fracture toughness and tearing modulus are moderate but remain much higher than the fracture toughness of the HAZ in the lower transition region.

Precracking PTS-D Specimens

Except for specimen L14, which was used for the qualification of the Soudokay cladding, all specimens were precracked using the procedure described in Ref 36. The cutting scheme of specimen L14 is documented in Ref 38. The initial

TABLE 5—*Fracture toughness test result on the cladding at low temperature using PCCv specimens. Note: J_{end} is the J value when the test was interrupted and the specimen unloaded.*

Specimen ID	Test Temperature (°C)	a_0 (mm)	Δa (mm)	J_{end} (kJ/m^2)
L06_07	−130	5.33	2.06	233.9
L06_08	−170	5.03	1.81	160.5

TABLE 6—*Fracture toughness test result on the cladding at −130°C using PCCv specimens. Note:* J_Q *and T are the initiation fracture toughness and tearing resistance at an offset of 0.2 mm from the blunting line, respectively.*

			UC		PD		NDR		Average	
Specimen ID	a_0 (mm)	Δa (mm)	J_Q (kJ/m^2)	T (MPa)	J_Q (kJ/m^2)	T (MPa)	J_Q (kJ/m^2)	T (MPa)	J_Q (kJ/m^2)	T (MPa)
L06_05	5.2	1.20	127	129	125	144	130	129	127	134
L06_06	4.86	1.22	174	174	171	189	172	183	172	182
L06_10	5.28	1.47	169	105	140	166	161	133	156	135
Average			157	136	145	166	154	148	**152**	**150**
St. Dev.			26	35	24	22	21	30	23	28

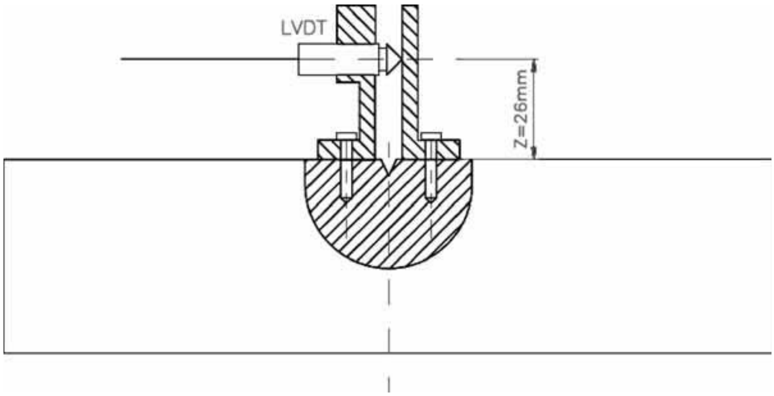

FIG. 2—*Schematic of the monitoring of the CMOD using an LVDT.*

and final precracking forces are 382 and 320 kN, which correspond to stress intensity factor values of 19.9 and 17.8 $\text{MPa}\sqrt{\text{m}}$, respectively. Precracking was performed at about 7 Hz. As the clip gauge detached from the specimen during precracking of specimens L8 and L9, a LVDT is used to monitor the crack mouth opening displacement (CMOD) for the remaining specimens. The LVDT is placed 26 mm above the specimen surface resulting in a Z distance of 26 mm (see schematic in Fig. 2). Due to the Z distance, the compliance is 2.35 times larger than that measured with the clip gauge.

The precracking results are summarized in Table 7. The reproducibility is similar to the one reported in Ref 36.

Cladding of PTS-D and Residual Stresses

A 4 mm deep notch is machined on the 50 mm thick PTS-D specimen prior to precracking in order to introduce a sharp defect able to initiate a crack by fatigue. This notch has to be removed before cladding. This was obtained by removing 5 mm of the specimen thickness. The PTS-D specimen thickness before cladding is therefore 45 mm.

Cladding is performed by welding two layers with a total thickness of about 9 mm [38]. After welding and post weld heat treatment, PTS-D specimen dimensions were controlled and clearly indicate that cladding introduces tensile residual stresses in the cladding and compressive residual stresses in the base metal underneath the cladding (see Fig. 3).

As the as welded surface is not flat especially at the junction of two strips, the cladded surface of the PTS-D specimen is machined and the final PTS-D specimen thickness is reduced to 50 mm.

Actual residual stress measurement is outside the scope of the study. However to have some idea of the magnitude of those stresses, a small literature study was performed. A lot of theoretical and experimental studies were performed to evaluate residual stresses [11–13,42–48]. All these studies conclude that tensile residual stresses are present in the cladding in both axial and cir-

TABLE 7—*Summary of precracking results.*

Specimen ID	Initial Compliance (mm/kN)	Final Compliance (mm/kN)	Number of Cycles
L1	1.14×10^{-04}	2.13×10^{-04}	947 000
L2	1.17×10^{-04}	2.13×10^{-04}	878 000
L3	1.15×10^{-04}	2.16×10^{-04}	828 000
L4	1.18×10^{-04}	2.22×10^{-04}	973 000
L5	1.45×10^{-04}	2.04×10^{-04}	4 979 000
L6	1.20×10^{-04}	2.24×10^{-04}	1 146 000
L7	1.15×10^{-04}	2.16×10^{-04}	990 000
L8[a]	4.85×10^{-05}	7.44×10^{-05}	4 577 500
L9[a]	5.12×10^{-05}	9.83×10^{-05}	850 000
L10	1.17×10^{-04}	2.19×10^{-04}	1 315 000
L11	1.21×10^{-04}	2.42×10^{-04}	1 208 000
L12	1.14×10^{-04}	2.14×10^{-04}	1 116 000
L13	1.14×10^{-04}	2.18×10^{-04}	1 004 000
L14	n.a.	n.a.	n.a.
L15	1.09×10^{-04}	2.02×10^{-04}	924 000
L16	1.16×10^{-04}	2.13×10^{-04}	1 049 000
L17	1.12×10^{-04}	2.17×10^{-04}	918 000
L18	1.16×10^{-04}	2.18×10^{-04}	2 990 000
L19	1.10×10^{-04}	2.04×10^{-04}	1 083 000
L20	1.20×10^{-04}	2.22×10^{-04}	1 023 000
Average	1.17×10^{-04}	2.16×10^{-04}	1 374 764
St. Dev.	7 %	4 %	76 %

[a]Specimen precracked with a clip gauge (values not taken into account for the average and St. Dev. calculations).

cumferential directions. According to Refs 11–13 and 42–48, the stress magnitude at room temperature is about 200 MPa and decreases with increasing temperature. In the base metal, the residual stresses due to cladding deposition are much more limited in magnitude. Near the cladding, stresses are in tension and change to compression 25 mm away from the cladding. It should be noted that the calculation of residual stresses is rather complex. Residual stresses are

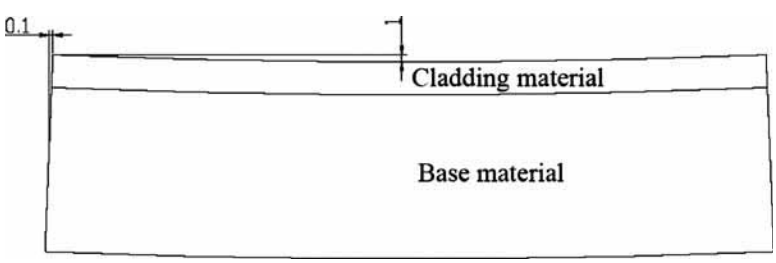

FIG. 3—*Schematic of the deformed specimen due to residual stresses after cladding.*

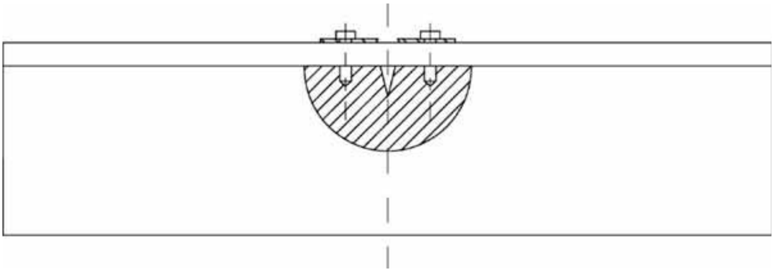

FIG. 4—*Schematic of the monitoring of the CMOD using a clip gauge attached to the two razor blades.*

initiated during cladding deposition and are partially relaxed during heat treatment due to creep. Due to hydrostatic loading, the yield stress of the cladding is reached which modifies again the residual stresses. The residual stresses in the vessel are also due to the initial forging process. When performing transient analysis, thermal stresses should also be taken into account.

The impact of these initial residual stresses on the safety analysis depends largely on the loading conditions, thermal transient, and on the crack size considered in the study. Note that compressive residual stresses are beneficial as they tend to close the crack and reduce the stress intensity factor.

Testing and Results

Testing is performed on a computer-controlled servo-hydraulic 3 MN compression testing machine YAW-3000A from TIME GROUP INC. It is a two column machine with a rigidity of 0.68 mm/MN measured with the crosshead 1000 mm above the working table. 1 mm thick razor blades are screwed on the cladding in order to monitor the CMOD (see Fig. 4). It should be noted that actual monitoring of the CMOD is not possible as the crack mouth is not accessible since it is located under the cladding.

Tests are performed at a constant crosshead speed of 0.5 mm/min up to failure. A dedicated environmental chamber is used to avoid thermal gradients and to guarantee a stable temperature during testing. Pictures of the test setup are given in Fig. 5. Due to the thermal mass, the time needed to stabilize the temperature starting from room temperature is about 2 h. An additional 30 min is used as a soaking period. During this period, the temperature is kept within $\pm 2^\circ$C of the nominal temperature.

A typical test record of force versus CMOD is shown in Fig. 6. At fracture, the force does not significantly decrease but CMOD increases. The specimen is unloaded after the pop-in event is detected. Force versus crosshead displacement was also recorded but due to the large compliance of the test setup (1.89 mm/MN), elastic displacements are much larger than plastic displacements and consequently those records are not reliable for evaluating fracture toughness.

After fracture the specimen is heated up to room temperature. In most cases, the cladding remains unbroken and no crack is visible on the outer sur-

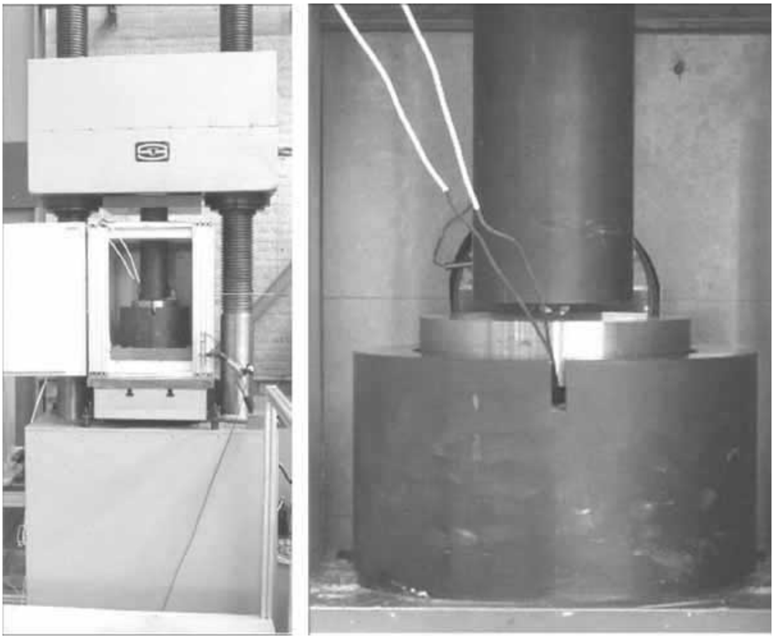

FIG. 5—*Pictures of the test setup.*

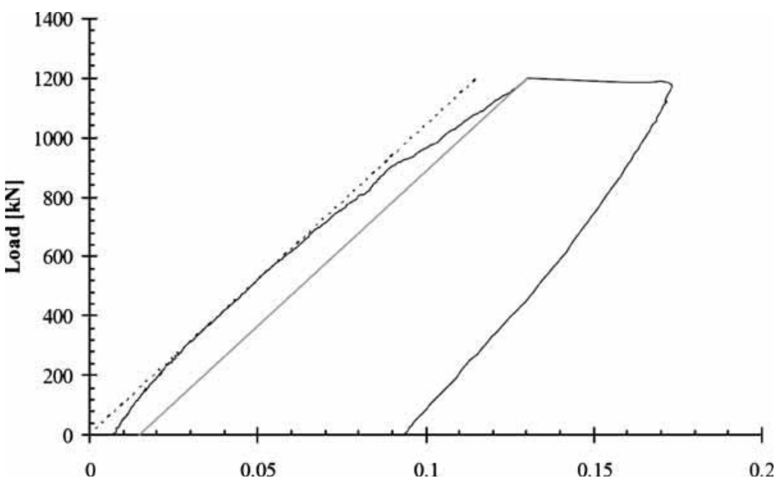

FIG. 6—*Typical test record of force versus CMOD. Unloading is performed after a pop-in is detected.*

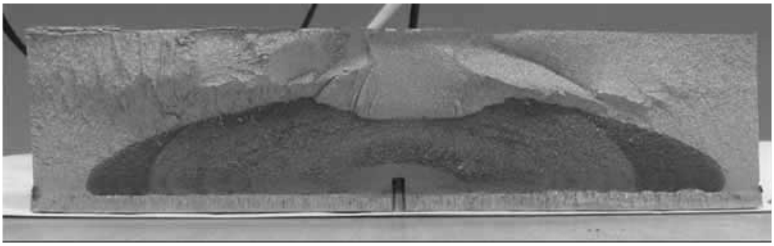

FIG. 7—*Picture of a typical fracture surface. Specimen diameter is 200 mm and specimen height is 50 mm.*

face. Heat tinting at 290°C for 30 min is the conventional method to mark crack advance. However, since the crack is fully embedded in the material and not in contact with air, oxidation cannot occur. The solution is to drill a small 2 mm diameter hole of 6 mm depth at the crack location before heat tinting. This allows air to enter the crack for successful heat tinting.

After heat tinting, specimens are cooled down to liquid nitrogen temperature and broken using the 3 MN testing machine. A typical picture is given in Fig. 7. Cladding, fatigue crack, hole for heat tinting and crack propagation can easily be identified. It should be noted that for specimens L12 and L16 the hole was not drilled deep enough and the crack arrest size could not be identified from the picture.

Using those pictures, the cladding thickness, crack shape, and crack size is measured for the fatigue crack and arrest crack respectively. Cladding thickness varies between 6 and 7.8 mm. As the initial base metal was 45 mm, it can be concluded that about 1–1.8 mm of the base metal was diluted during the first layer cladding deposition. From the picture, it is found that the HAZ width varies from 6 to 9 mm. The HAZ is found to be much larger than the original Lemoniz cladding as confirmed by the microstructure study documented in Ref 49. Since the fatigue crack tips are in the HAZ, the fracture toughness of the HAZ was characterized in the paragraph Additional Material Characterization.

Detailed observations of the fracture surface show that for some specimens the welding of the cladding has penetrated inside the fatigue crack resulting in partial closure. This phenomenon is illustrated in Fig. 8. Traces of crack closure were found on five specimens (see Table 8 for details). For specimen L2, the fatigue crack was completely closed. For this reason, no cleavage crack initiated during testing and the test resulted in just plastic deformation of the specimen. We therefore believed that crack closure is not plasticity-induced but due to back-filling with cladding.

Test results are summarized in Table 8. Specimen L20 was not tested and is used to extract PCCv specimens from the HAZ. Specimens L8, L11, and L15 were not cladded and were left untested. No test data were recorded for specimen L10 and L13 because the testing machine went out of control during cooling or during specimen handling.

During testing, pop-in events could be identified by the characteristic noise produced and sudden clip gauge opening. For the very first test on specimen L1, the noise was interpreted as ice breaking and the test was not immediately

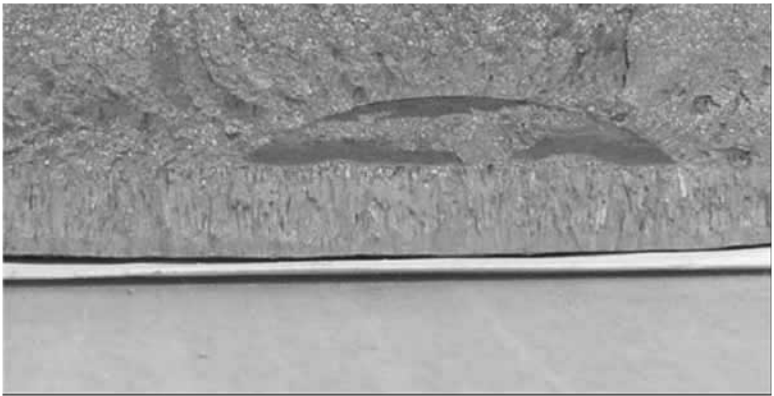

FIG. 8—*Partial crack closure due to the welding of the cladding. On this picture, the crack depth, a, is 4 mm and crack width, 2c, is 30 mm.*

stopped after this event. The test on specimen L1 was stopped after the specimen was completely broken including the cladding. For specimen L3, the fracture load was quite high and crack initiation resulted in the fracture of the cladding. For specimen L9, the fracture load was also very high which can be attributed to the large portion of crack closure observed on the fatigue crack surface. The specimen L9 also results in a complete fracture including the cladding. The fracture toughness of the cladding was only investigated above room temperature in the upper shelf using a ductile crack growth technique. The cladding contains a limited content of ferrite and shows a ductile to brittle transition. Therefore some tests at $-130^{\circ}C$ are recommended to support failure of the cladding in some limited cases.

For all specimens except L1, L3, and L9, pop-in's were identified during testing and specimen unloaded. The cladding remained unbroken and the crack was embedded below the cladding.

Analysis of Test Results

The cladded PTS-D specimen is not a standard geometry. Therefore no analytical equation exists that allows deriving the fracture toughness from the force versus crack mouth opening displacement. To develop those equations, three-dimensional finite element calculations were performed using the mesh and boundary conditions in Fig. 10. Displacement is shown imposed on the top surface (red arrows). Calculations were performed using an average cladding thickness of 6.6 mm, and an average crack size of 4.4 and 16.7 mm for the crack depth and half width respectively. Taking advantage of the symmetry planes, only one quarter of the geometry is calculated.

Fracture toughness along the crack front is evaluated using the following equation:

TABLE 8—*Summary of test results. Dimensions are presented schematically in Fig. 9.*

Specimen ID	Test Temperature (°C)	Cladding Thickness, t (mm)	Fatigue Crack Depth, a (mm)	Fatigue Crack Width, $2c$ (mm)	Arrest Crack Depth, a_a (mm)	Arrest Crack Width, $2c_a$ (mm)	Partial Welding of the Crack	Cladding Broken
L01	−130	6.02	5.13	33.00	n.a.	n.a.	Yes	Yes
L02	−130	n.a.	n.a.	n.a.	n.a.	n.a.	Full	No
L03	−130	7.16	3.84	34.50	n.a.	n.a.	No	Yes
L04	−130	7.79	4.76	36.60	15.52	115.05	No	No
L05	−130	6.63	2.93	36.40	12.55	65.50	No	No
L06	−130	7.92	3.95	30.00	17.17	126.00	Yes	No
L07	−130	6.78	4.20	39.00	29.05	200.00	No	No
L09	−130	6.28	3.34	29.50	n.a.	n.a.	Yes	Yes
L12	−130	5.90	5.76	33.45	n.a.	n.a.	Yes	No
L16	−130	6.12	5.76	24.50	n.a.	n.a.	Yes	No
L17	−130	4.82	5.88	39.60	19.97	173.50	No	No
L18	−130	6.19	4.53	36.20	11.99	50.25	No	No
L19	−130	7.65	3.17	28.00	16.34	136.25	No	No

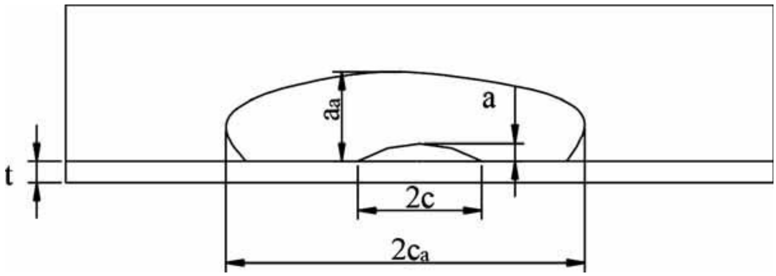

FIG. 9—*Schematic for the dimensions used in Table 8.*

$$J = \frac{(1-\nu^2)}{E}K^2 + J_{\text{pl}} \tag{1}$$

where:

ν = the is the Poisson ratio,
E = the Young's modulus,
K = the the stress intensity factor, and
J_{pl} = the the plastic component of the J-integral.

The equivalent plastic stress intensity factor is conventionally defined as

$$K_J = \sqrt{\frac{EJ}{1-\nu^2}} \tag{2}$$

The fracture toughness normalized to one inch thickness is obtained from

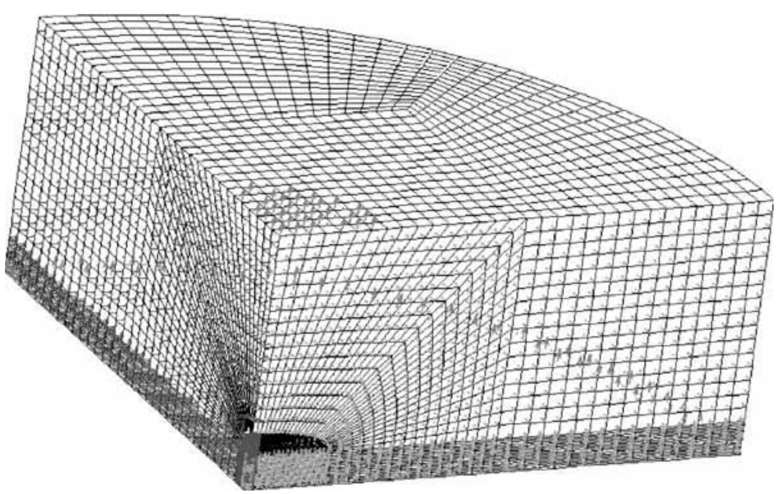

FIG. 10—*Mesh and boundary conditions. Blue, green, and red and small arrows indicate constrains in the three major orientations.*

$$K_{J,1T} = K_{\min} + \left(\int (K_J - K_{\min})^4 \frac{ds}{B_{1T}} \right)^{0.25} \tag{3}$$

where:

$K_{\min}$ = the is the minimum fracture toughness equal to 20 MPa$\sqrt{\text{m}}$,

$B_{1\mathrm{T}}$ = the the reference length of one inch, and

s = the the curvilinear abscissa along the crack front.

The stress intensity factor along the crack front is given by

$$K(s) = \frac{F}{(W - t)^{1.5}} f(s/s_0) \tag{4}$$

where:

s = the is the curvilinear position along the crack tip starting from the deepest point, s_0 = the is half the crack front length,

F = the the applied force,

W = the the specimen thickness, and

t = the the cladding thickness.

Using the linear elastic finite element results, K is evaluated along the crack front using the asymptotical crack opening displacement field.

From a practical point of view J_{pl} can be correlated with the dissipated energy

$$J_{\mathrm{pl}} = \eta \frac{U_{\mathrm{pl}}}{W^2} \tag{5}$$

where:

U_{pl} = the is the plastic energy under the force versus CMOD record and

η(eta factor) = a constant that needs to be identified for the considered geometry.

The average η-factor along the crack front has been evaluated using finite element calculations with crack size and material properties representative of the performed experiments. The CMOD is evaluated at a location identical to the location of the clip gauge as the actual crack mouth cannot be accessed due to the cladding.

The computation of J was performed using the equivalence with the energy release rate

$$J = - \left. \frac{\partial U}{\partial A} \right|_{\Delta} \tag{6}$$

where:

∂A is the increase in crack area.

In practice, the central difference approximation of the derivative was used.

The f function is evaluated with and without cladding using shallow crack and a specimen of 50 and 43.4 mm thickness, respectively. Figure 11 shows that the value of the f function is relatively constant for 80 % of the crack front. The

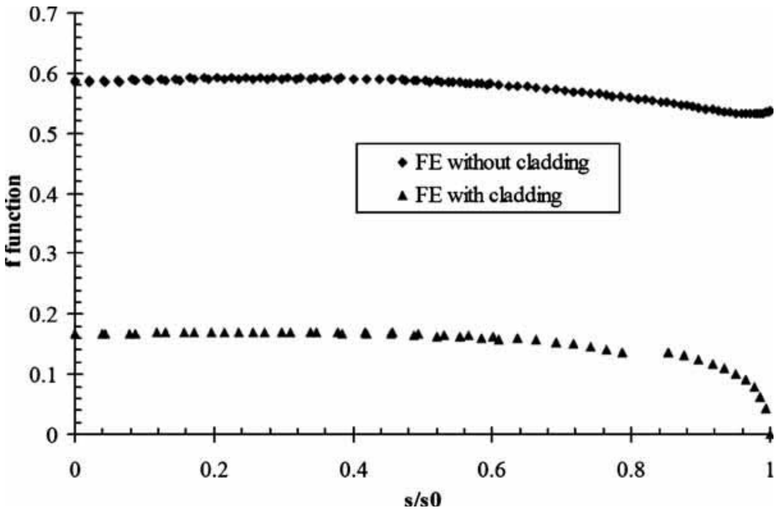

FIG. 11—*Dimensionless function, f, used for the stress intensity factor evaluation along the curvilinear abscissa.*

cladding has two effects, it reduces the stress intensity factor by a factor of about 3.5 and reduces the stress intensity factor down to zero at the junction of the crack with the cladding.

The eta factor for the specimen without and with cladding is evaluated as 0.91 and 1.5, respectively. The reason for having a larger eta factor for the geometry with cladding is due to the fact that the CMOD is measured at a location identical to the location of the clip gauge. For a given plastic deformation, the actual CMOD under the cladding turn out to be larger than on the outer surface. Therefore the actual driving force is larger resulting in a larger eta factor.

Results obtained neglecting the cladding and taking the cladding into account are summarized in Table 9. When the cladding is neglected and the contribution of plastic energy is small, the driving force is clearly overestimated.

Results can be analyzed using the ASTM E1921–08ae1 standard [40] to derive the reference temperature. Results are summarized in Table 10 and presented graphically in Figs. 12 and 13. Assuming all data to be valid, the calculated reference temperature is −180°C. This value is 102°C lower than for the HAZ material.

As demonstrated in Ref 36, there is also a possible effect of loss of constraint as three data points give a toughness value that is much larger than the median value. For a semielliptical crack depth of 12.5 mm, loss of constraint occurs at $M = b\sigma_{YS}/J = 140$ that correspond to a censoring limit of 140 MPa$\sqrt{m}$. It should be also noted that the cracks considered here are shallower than in Ref 36. Therefore a lower censoring limit should be used. The analysis has been performed using a censoring limit just above the largest fracture toughness (excluding the three invalid data). Additional finite element calculation should

TABLE 9—*Summary of test results obtained by neglecting the effect of the cladding and by taking it into account. Note:* $K_{Jc,1T}$ *is the average fracture toughness along the crack front normalized to 1 in. thickness.*

Specimen ID	Test Temperature (°C)	Crack Front Length (mm)	Cladding Neglected, $K_{Jc,1T}$ (MPa$\sqrt{m}$)	With Cladding, $K_{Jc,1T}$ (MPa$\sqrt{m}$)
L01	−130	42.27	97.7	65.7
L02	−130	n.a.	n.a.	n.a.
L03	−130	43.20	319.8	327.3
L04	−130	47.17	103.3	61.4
L05	−130	42.76	59.5	16.4
L06	−130	41.27	108.7	59.3
L07	−130	46.78	309.1	319.3
L09	−130	37.26	290.8	283.7
L12	−130	43.41	75.2	28.8
L16	−130	37.75	80.3	33.6
L17	−130	46.92	75.3	33.6
L18	−130	44.15	77.7	34.5
L19	−130	38.08	118.0	79.8

TABLE 10—*Master Curve analysis of the fracture toughness data.*

	N	r	n_i	$T_0 \pm 2\sigma$ (°C)
Without cladding; no censoring	12	12	2.0	-178 ± 10
Without cladding; censoring at 120 MPa$\sqrt{}$m	12	9	1.5	-131 ± 12
With cladding; no censoring	12	12	2.0	-179 ± 10
With cladding; censoring at 80 MPa$\sqrt{}$m	12	9	1.3	-96 ± 13

ideally be performed to evaluate the loss of constraint for this particular geometry.

Performing a master curve analysis with this censoring limit results in a reference temperature of −130°C when neglecting the cladding and −94°C when cladding is taken into account. When the cladding is taken into account, the reference temperature is in relatively good agreement with the one measured on the HAZ using PCCv specimens (−78°C).

In Fig. 13, several data points were found below the 5 % limit. Specimens L12, L16, and L17 have a longer crack length than the average value of 4.4 mm. This could explain the underestimation of the fracture toughness. A more in-depth study would require simulation of each test and not the average geometry. Specimen L05 has a particularly low toughness. The fracture surface indicates a HAZ size larger than the average. The HAZ of specimen L20 that was used to extract PCCv samples might not be representative of all specimens. In addition, residual stresses that are likely to be in tension below the cladding were not quantified and could also play an important role.

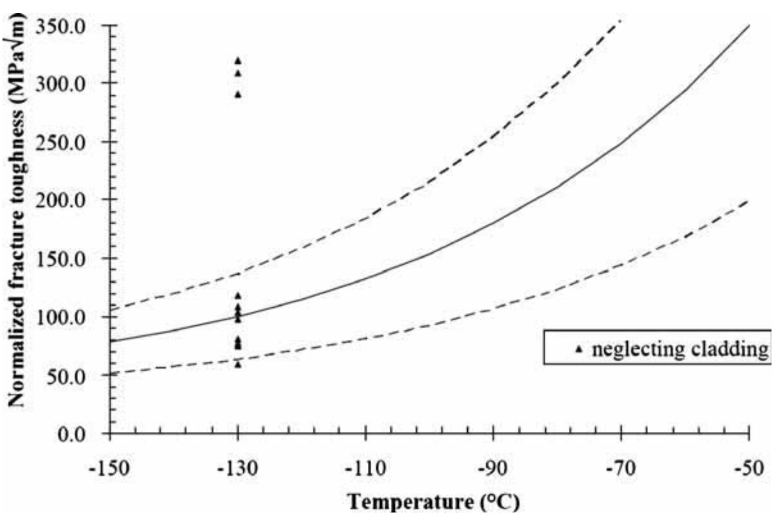

FIG. 12—*Master curve analysis of the fracture toughness data with 5, 50, and 95 percentile and assuming a censoring limit of 120 MPa$\sqrt{}$m.*

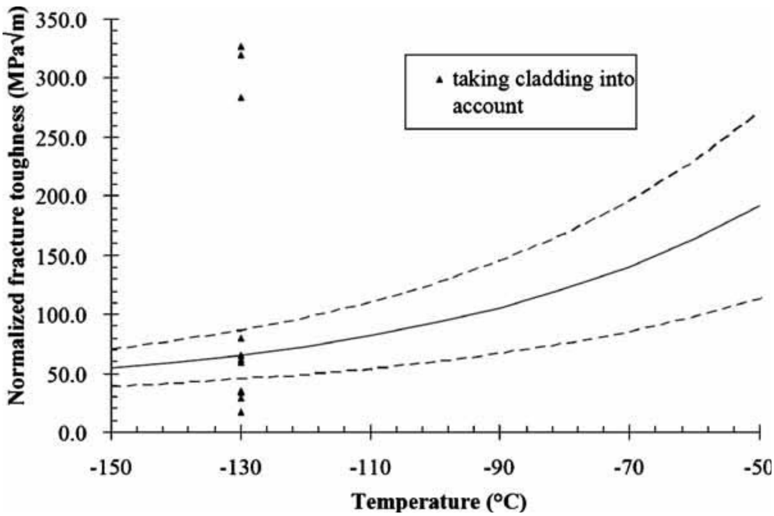

FIG. 13—*Master curve analysis of the fracture toughness data with 5, 50, and 95 percentile and assuming a censoring limit of 80 MPa√m.*

Analysis of Crack Arrest Event

Tests on cladded PTS-D specimens can also provide useful information on crack arrest fracture toughness. Indeed, in most cases the crack did arrest which was never the case for tests performed without cladding [36]. The cladding plays a very important role: It restrains the crack from opening and reduces the driving force during propagation. Detailed finite element calculations are needed to evaluate the driving force at arrest. Such finite element calculations with a dynamic growing crack were performed in Ref 50 but are outside the scope of this paper. Experimental data can be analyzed to develop some understanding on crack arrest. Due to the relatively high compliance of the test set-up (1.89 mm/MN), some energy is stored in the test set up. For a typical fracture load of 1200 kN, the stored energy is 1361 J. During crack propagation, this energy is partially released to stretch the cladding and to propagate the crack. Due to the high compliance of the test set-up, the load after a pop-in event is practically constant which is typical of high compliance systems and also explains the very low probability of observing arrest on non-cladded specimens. In all cases except on specimen L05, the clip gauge remains attached to the knife edges after the arrest event. This allows measuring the opening of the CMOD due to the crack jump. Data are summarized in Table 11 and presented graphically in Figs. 14 and 15. It is found that initiation force and CMOD jump are correlated with the crack jump length. The specimen with the largest crack jump or the largest CMOD jump is not necessarily the specimen with the lowest crack arrest toughness as the initiation force can be larger and the stored energy in the system is also generally larger.

Figure 16 shows that the half crack width to depth ratio increases with crack propagation depth. This observation can be explained as follows. The

TABLE 11—*Summary of useful crack arrest information.*

Specimen ID	Initial Crack Depth(mm)	Initial Crack Width(mm)	Arrest Crack Depth(mm)	Arrest Crack Width(mm)	Crack Jump (mm)	Force at Initiation(kN)	CMOD Jump (mm)
L04	12.55	36.60	22.88	115.05	10.33	1201	0.08
L05	9.56	36.40	19.22	65.50	9.66	833	n.a.
L06	11.87	30	24.44	126	12.57	1322	0.17
L07	10.98	39	35.77	200	24.79	2227	0.65
L17	10.71	39.6	24.89	173.5	14.18	1044	0.98
L18	10.72	36.20	18.21	50.25	7.49	1040	0.05
L19	10.82	28	23.27	136.25	12.45	1370	0.18

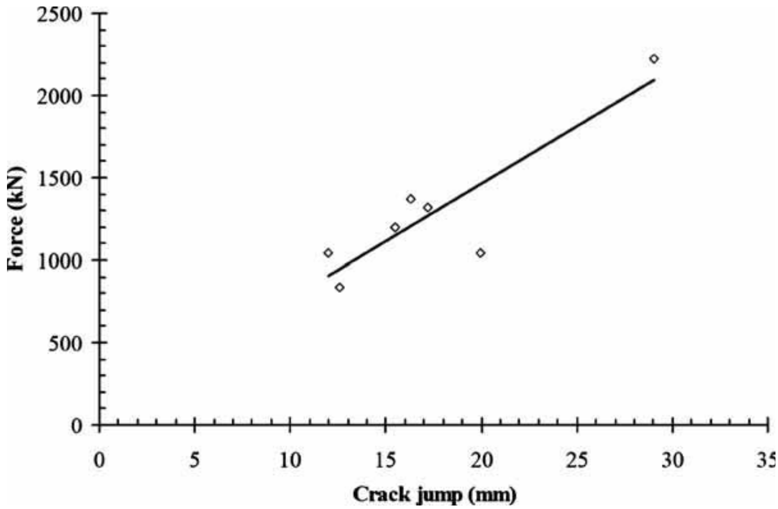

FIG. 14—*Force at crack initiation as a function of crack jump.*

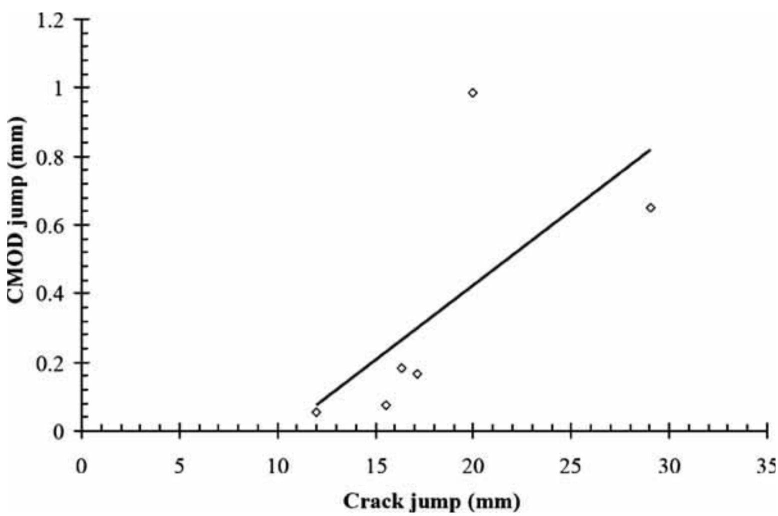

FIG. 15—*CMOD between initiation and arrest as a function of crack jump. The crack arrest event is very dynamic and in some case the clip gauge or razor blades can move from its location during this event therefore one data as been indicated as possible outlier.*

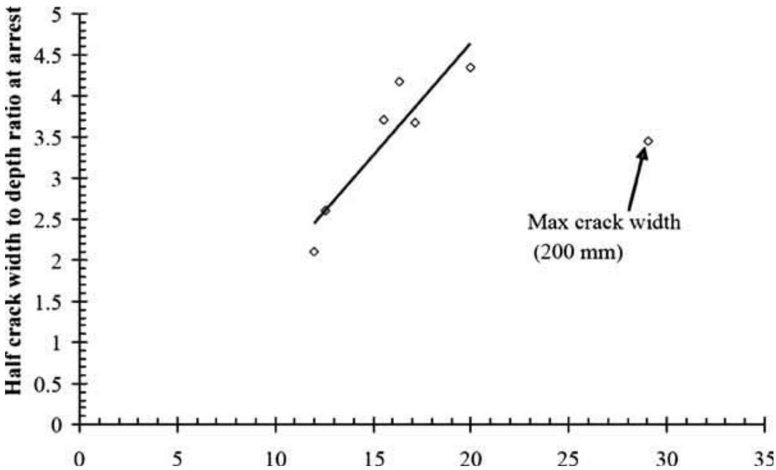

FIG. 16—*Half crack width to crack depth ratio at arrest as a function of crack propagation depth.*

crack shape will tend to follow a constant K value along its front. As the loading mode is mainly bending, increasing crack depth reaches a region of increasing compressive stresses.

Conclusions

This work demonstrates the feasibility of investigating the fracture toughness of biaxially loaded underclad cracks which are representative of actual PTS loading conditions. It is found that:

- The HAZ is larger than expected. The crack tip of the PTS-D specimen is located in the HAZ.
- The fracture toughness of the HAZ investigated using PCCv specimens is found to be lower than the base material.
- Residual stresses are identified but not quantified. The presence of residual stresses could explain some relatively low toughness values.
- The cladding reduces the driving force by restraining the crack to open. Performing the study by neglecting the cladding largely overestimates the driving force.
- Some PTS-D specimens display much larger fracture toughness. This was clearly identified to be due to loss of constraint. The loss of constraint was taken into account by setting a specimen maximum measuring capacity. Detailed quantification of loss of constraint using a Weibull model is outside the scope of this study.
- The reference temperature of cladded PTS-D specimens is in relatively good agreement with the toughness measured on the HAZ using conventional PCCv specimens.
- Finite element modeling of each tested specimen would yield more ac-

curate toughness evaluations. However, it is believed that the conclusion will not be affected.

- Pop-in's are almost systematically observed on cladded PTS-D specimens, which was never the case on noncladded specimens.
- Pop-in's are interpreted as crack arrest events. The cladding is playing a key role in reducing the driving force for propagating cracks. Evaluation of the crack arrest toughness from those tests would require additional work and validation.

Acknowledgments

This work has been financed by EDF-Suez; their support is kindly appreciated. The authors would also like to acknowledge the professional assistance of L. Van Houdt and R. Mertens.

References

[1] Gonnet, B. and Menjon, G., "Under-Cladding Cracking—La Fissuration sous Revetement, IAEA-CN-39/14, Current Nuclear Power Plant Safety Issues," *Proceedings of an International Conference on Current Nuclear Power Plant Safety Issues*, Stockholm, Sweden, October 20–24, 1980, IAEA, Vienna, Austria, Vol. 3, pp. 65–76 (in French).

[2] Sermadiras, P. H., Berger, J. Cl., and Samman, J., "Summary of the Actions Developed by EDF in Order to Dimension Underclad Defects in PWR Reactor Vessel Nozzles," *Sixth International Conference on NDE in the Nuclear Industry*, Zurich, Switzerland, 28 Nov.–2 Dec., 1984, ASM, Metals Park, OH, pp. 751–761.

[3] Bethmont, M., Soulat, P., and Houssin, B., "Toughness Properties of End of Life—Cladding," *Proceedings of a IAEA Specialists Meeting*, Espoo, Finland October 23–26, 1995, International Working Group on Life Management of Nuclear Power Plants, Vienna, Austria, pp. 155–168.

[4] US NRC, "Cladding Crack Found in Original RVH Cavity," *Davis Besse Condition Report No.* 02–05705, US NRC, Washington, DC, 2002.

[5] IRSN Agency, "Underclad Cracks in Tricastin 1 Reactor Pressure Vessel" *IRS Report No.* 0007368, Fontenay-aux-Roses, France, 2000.

[6] Scibetta, M., Bens, L., Puzzolante, J.-L., Van Houdt, L., "Characterization of the Lemoniz Reactor Pressure Vessel Cladding," *Report No.* SCK-CEN-R-4121, SCK-CEN, Mol, Belgium, March, 2005.

[7] Vandermeulen, W., Scibetta, M., Leenaers, A., Schuurmans, J., and Gérard, R., ""Measurement of the Young Modulus Anisotropy of a Reactor Pressure Vessel Cladding," *J. Nucl. Mater.*, Vol. 372, 2008, pp. 249–255.

[8] Scibetta, M., Lucon, E., and van Walle, E., "BR2 Irradiation of the Cladding of the Lemoniz Reactor Pressure Vessel," *Report No.* SCK·CEN-R-4333, SCK-CEN, Mol, Belgium, April 2006.

[9] Scibetta, M. and Lucon, E., "Tensile and Fracture Toughness Properties of the Cladding of the Lemoniz Reactor Pressure Vessel Irradiated in the BR2 Reactor," Report No. SCK·CEN-R-4456, SCK-CEN, Mol, Belgium, 2007.

[10] Wimunc, E. A., "How Serious Are Vessel Cladding Failure?," *Power React. Technol.*, Vol. 9, 1966, pp. 101–109.

[11] Baumjohann, F., "Calculation of Thermaplastic Stresses of a Reactor Pressure Vessel with Cladding from Stress-Relief Annealing up to a Thermal Shock," *Nucl. Eng. Des.*, Vol. 96, 1986, pp. 323–335.
[12] McCabe, D. E., "Fracture Evaluation of Surface Cracks Embedded in Reactor Vessel Cladding," *NUREG/CR-5207*, US NRC, Washington, DC, 1988.
[13] Sattari-Far, I., "Three-Dimensional Elastic-Plastic Fe-Analyses of Cladded Reactor Pressure Vessels Containing Surface Flaws," *Pressure Vessels and Piping Conference*, San Diego, CA, June 1991, ASME, New York, pp. 105–110.
[14] Griesbach, T. J., "Effect of Cladding on Stress Intensity Factors During Normal Plant Operation," *Proceedings of the 1994 Pressure Vessels and Piping Conference*, Minneapolis, MN, June 1994, Codes and Standards for Quality Engineering, American Society of Mechanical Engineers, Pressure Vessels and Piping Division, PVP, ASME, New York, Vol. 285, pp. 145–148.
[15] Gamble, R. M., "A Probabilistic Assessment of Reactor Vessel Integrity During Pressuring Thermal Transients," *Proceedings of the Third International Seminar on Assuring Structural Integrity of Steel Reactor Pressure Boundary Components*, Montery, CA 29-30 August, 1984, Elsevier Applied Science, London, pp. 369–379.
[16] Kim, J.-S., Choi, J.-B., Kim, Y.-J., and Park, Y.-W., "Investigation on Constraint Effect of Reactor Pressure Vessel Under Pressurized Thermal Shock," *Nucl. Eng. Des.*, Vol. 219, 2003, pp. 197–206.
[17] Kikuchi, M., Miyamoto, H., and Sugawara, S., "Evaluation of the J integral and the cladding effect of a crack in the reactor pressure vessel," *Bull. JSME*, Vol. 29, 1986, pp. 4026–4030.
[18] Kikuchi, M., Miyamoto, H., and Shindo, T., "Evaluation of the J Integral of a Crack in the Pressure Vessel Under Thermal Transient Loading," *J. Pressure Vessel Technol., Trans. Am. Soc. Mech. Eng., Pressure Vessels Piping Div.*, Vol. 108, 1986, pp. 312–319.
[19] Lee, T.-J., Choi, J. B., Kim, Y. J., and Park, Y. W., "A Parametric Study on Pressure-Temperature Limit Curve Using 3-D Finite Element Analyses," *Nucl. Eng. Des.*, Vol. 214, 2002, pp. 73–81.
[20] Iskander, S. K., Sauter, A. W., and Foehl, J., "Reactor Pressure Vessel Structural Implications of Embrittlement to the Pressurized-Thermal-Shock Scenario," *ASTM Spec. Tech. Publ.*, Vol. 909, 1986, pp. 163–176.
[21] Sauter, A., "Influence of Cladding on Linear Elastic RPV-Analysis During Loss of Coolant Accident," *Nucl. Eng. Des.*, Vol. 76, 1983, pp. 347–358.
[22] Smith, E., "The Restraining Effect of Austenitic Cladding on the Extension of a Three-Dimensional Crack into the Wall of a Water-Cooled Nuclear Reactor Pressure Vessel During a Hypothetical Overcooling Accident," *Nucl. Eng. Des.*, Vol. 78, 1984, pp. 79–84.
[23] Miyamoto, H., Kikuchi, M., Okazaki, T., and Kubo, M., "The J Integral Evaluation of a Corner Crack Under Thermal Transient Loading Condition," *Nucl. Eng. Des.*, Vol. 75(2), 1983, pp. 213–222.
[24] Moinereau, D., Rousselier, G., and Bethmong, M., "Behavior of Underclad Cracks in Reactor Pressure Vessels: Evaluation of Mechanical Analyses used in French PRV Integrity Assessment by Cleavage Fracture Tests on Large Scale Plates," *Am. Soc. Mech. Eng., Pressure Vessels Piping Div., PVP*, Vol. 250, 1993, pp. 47–59.
[25] Moinereau, D., Rousselier, G., and Bethmont, M., "Evaluation of Mechanical Analyses used in French RPV Integrity Assessment by Cleavage Fracture Tests on Large Scale Cladded Plates," *Conference: SISSI 94: International Seminar on Structural Integrity*, Saclay, France, 28–29 Apr. 1995, CEA, Paris, pp. 279–290.
[26] Blauel, J. G., Hodulak, L., Nagel, G., Schmitt, W., and Siegele, D., "Effect of Clad-

ding on the Initiation Behaviour of Finite Length Cracks in an RPV Under Thermal Shock," *Nucl. Eng. Des.*, Vol. 171, 1997, pp. 179–188.
[27] Choi, S. N., Jang, K. S., Kim, J. S., Choi, J. B., and Kim, Y. J., "Effect of Cladding on the Stress Intensity Factors in the Reactor Pressure Vessel," *Nucl. Eng. Des.*, Vol. 199, 2000, pp. 101–111.
[28] Simonen, F. A. and Johnson, K. I., "Effects of Residual Stresses and Underclad Flaws on the Reliability of Reactor Pressure Vessels," *Pressure Vessels and Piping Conference*, Denver, CO, June 1993, ASME, New York, NY, Vol. 251, pp. 101–113.
[29] Simonen, F. A., "Clad Failure Models for Underclad Flaws in Reactor Pressure Vessels," *Pressure Vessels and Piping Conference*, Minneapolis, MN, June 1994, ASME, New York, NY, Vol. 280, pp. 101–113.
[30] Sherry, A. H., Richardson, T., Sillitoe, B., and Trusty, F., "Analysis of benchmark PTS problem: Comparison of R6 and 3D-finite element results," *Am. Soc. Mech. Eng., Pressure Vessels Piping Div., PVP*, Vol. 392, 1999, pp. 239–249.
[31] Schmitt, W., Hodulak, L., and Sun, D. Z., "Toughness of the Austenitic Cladding and Its Influence on the Safety of a Reactor Pressure Vessels," *Transactions of the 13th International Conference on Structural Mechanics in Reactor Technology*, Port Alegre, 13–18 Aug. 1995, IASMIRT, Raleigh, NC, Vol. 2, pp. 379–384.
[32] Haggag, F. M. and Iskander, S. K., "Results of Irradiated Cladding Tests and Clad Plate Experiments," *Nucl. Eng. Des.*, Vol. 118, 1990, pp. 297–304.
[33] Iskander, S. K., Nanstad, R. K., Robinson, G. C., and Oland, C. B., ""Experimental Study of the Effect of Stainless Steel Cladding on the Structural Integrity of Flawed Steel Plates in Bending," *Advances in Fracture and Fatigue for the 1990's–Volume II: Non-Linear Analysis and Applications*, American Society of Mechanical Engineers, Pressure Vessels and Piping Division, PVP, New York, 1989, pp. 87–92.
[34] Fayolle, P., Churier-Bossennec, H., and Faidy, C., "J estimation scheme for cracks near the cladding of a reactor pressure vessel," in *Pressure Vessel Fracture, Fatigue, and Life Management*, S. Bhandari, P. P. Milella, and W. E. Pennell, Eds., American Society of Mechanical Engineers, Pressure Vessels and Piping Division, PVP, New York, 1992, Vol. 233, pp. 27–34.
[35] Moinereau, D., Messelier-Gouze, C., Bezdikian, G., Ternon-Morin, F., Meziere, Y., Faidy, C., Pellissier-Tanon, A., Vagner, J., and Guichard, D., "Some Recent Developments in French Reactor Pressure Vessel Structural Integrity Assessment," *Proceedings of the 1998 ASME/JSME Joint Pressure Vessels and Piping Conference*, San Diego, CA, July 26–30, 1998, American Society of Mechanical Engineers, Pressure Vessels and Piping Division, PVP, New York, Vol. 365, pp. 45–58.
[36] Scibetta, M., Schuurmans, J., and Lucon, E., "Experimental Study of the Fracture Toughness Transferability to Pressurized Thermal Shock Representative Loading Conditions," *J. ASTM Int.*, Vol. 5, 2008, paper ID JAI101561.
[37] Bass, B. R., McAfee, W. J., Williams, P. T., and Pennell, W. E., "Fracture Assessment of Shallow-Flaw Cruciform Beams Tested Under Uniaxial and Biaxial Loading Conditions," *Nucl. Eng. Des.*, Vol. 188, 1999, pp. 259–288.
[38] Scibetta, M., and Lucon, E. "Feasibility of Representative Cladding Deposition," *Report No.* SCK·CEN-R-4558, SCK-CEN, Mol, Belgium, 2007.
[39] Lucon, E., Leenaers, A., and Scibetta, M. "Study of the Fracture Toughness Variation within the Thickness of RPV Forgings—Part 2: Lemoniz," *Report No.* SCK·CEN-R-4607, SCK-CEN, Mol, Belgium, 2008.
[40] ASTM E1921, 2008ae1, 2008, "Standard Test Method for Determination of Reference Temperature, To, for Ferritic Steels in the Transition Range," *Annual Book of ASTM Standards*, Vol. 03.01, ASTM International, West Conshohocken, PA.
[41] ASTM E1820, 2008, "Standard Test Method for Measurement of Fracture Tough-

ness" *Annual Book of ASTM Standards*, Vol. 03.01, ASTM International, West Conshohocken, PA.

[42] Ganta, B. R., Ayres, D. J., and Hijeck, P. J., "Cladding Stresses in a Pressurized Water Reactor Vessel Following Application of the Stainless Steel Cladding, Heat Treatment and Initial Service," *Am. Soc. Mech. Eng., Pressure Vessels Piping Div., PVP*, Vol. 213, 1991, pp. 245–252.

[43] Bertram, W., "Residual Stresses in Weld-Clad Reactor Pressure Vessel Steel," *Structural Mechanics in Reactor Technology*, 1–5 September 1975, IASMIRT, Raleigh, NC.

[44] Kostylev, V. I. and Margolin, B. Z., "Determination of residual stress and strain fields caused by cladding and tempering of reactor pressure vessels," *Int. J. Pressure Vessels Piping*, Vol. 77, 2000, pp. 723–735.

[45] McCabe, D. E., "Fracture Evaluation of Surface Cracks Embedded in Reactor Vessel Cladding," *Technical Report No.* NUREG/CR-5207; MEA-2285, Division of Engineering, Materials Engineering Associates, Inc., Lanham, MD, 1988.

[46] Moinereau, D., Bethmont, M., Chas, G., and Rousselier, G., "Cleavage Fracture of Plates with Small Underclad Crack: Elements Presentation and Interpretation by Fracture Mechanics," *Am. Soc. Mech. Eng., Pressure Vessels Piping Div., PVP*, Vol. 213, 1991, pp. 53–60.

[47] Roos, E., "Analysis of Fracture Mechanics of the Reactor Pressure Vessel (RPV) by Taking into Account Residual Stresses Part 2: Stress Analysis, Assessment of Integrity and Experimental Investigation," *VGB PowerTech*, Vol. 81, 2001, pp. 91–99 (in German).

[48] Schimmoeller, H. A. and Ruge, J. L., "Estimation of Residual Stresses in Reactor Pressure Vessel Steel Specimens Clad by Stainless Steel Strip Electrodes," *International Conference on Residual Stresses in Welded Construction and Their Effects*, November 1977, Welding Institute, London, Vol. 1, pp. 251–258.

[49] Van Renterghem, W. and Kaers, K., "Characterisation of the Soudokay Cladding Deposition," *Report No.* SCK·CEN-R-4700, Mol, Belgium, 2008.

[50] Scibetta, M., Link, R., Schuurmans, J., and Lucon, E., "Towards Crack Arrest Testing Using Miniature Specimens," *J. ASTM Intl.*, Vol. 5, 2008, paper ID JAI101002.

Reprinted from JAI, Vol. 7, No. 4
doi:10.1520/JAI102717
Available online at www.astm.org/JAI

Sreeramesh Kalluri[1] *and Peter J. Bonacuse*[2]

An Assessment of Cumulative Axial and Torsional Fatigue in a Cobalt-Base Superalloy

ABSTRACT: Cumulative fatigue under axial and torsional loading conditions can include both load-order (high/low and low/high) as well as load-type sequence (axial/torsional and torsional/axial) effects. Previously reported experimental studies on a cobalt-base superalloy, Haynes 188 at 538°C, addressed these effects. These studies characterized the cumulative axial and torsional fatigue behavior under high amplitude followed by low amplitude (Kalluri, S. and Bonacuse, P. J., "Cumulative Axial and Torsional Fatigue: An Investigation of Load-Type Sequence Effects," in Multiaxial Fatigue and Deformation: Testing and Prediction, ASTM STP 1387, S. Kalluri, and P. J. Bonacuse, Eds., American Society for Testing and Materials, West Conshohocken, PA, 2000, pp. 281–301) and low amplitude followed by high amplitude (Bonacuse, P. and Kalluri, S. "Sequenced Axial and Torsional Cumulative Fatigue: Low Amplitude Followed by High Amplitude Loading," Biaxial/Multiaxial Fatigue and Fracture, ESIS Publication 31, A. Carpinteri, M. De Freitas, and A. Spagnoli, Eds., Elsevier, New York, 2003, pp. 165–182) conditions. In both studies, experiments with the following four load-type sequences were performed: (a) axial/axial, (b) torsional/torsional, (c) axial/torsional, and (d) torsional/axial. In this paper, the cumulative axial and torsional fatigue data generated in the two previous studies are combined to generate a comprehensive cumulative fatigue database on both the load-order and load-type sequence effects. This comprehensive database is used to examine applicability of the Palmgren–Langer–Miner linear damage rule and a nonlinear damage curve approach for Haynes 188 subjected to the load-order and load-type sequencing described above. Summations of life fractions from the experiments are compared to the predictions from both the

Manuscript received September 4, 2009; accepted for publication March 22, 2010; published online April 2010.
[1] Ohio Aerospace Institute, NASA Glenn Research Center, Brook Park, OH 44135.
[2] US Army Research Laboratory, NASA Glenn Research Center, Brook Park, OH 44135.

Cite as: Kalluri, S. and Bonacuse, P. J., "An Assessment of Cumulative Axial and Torsional Fatigue in a Cobalt-Base Superalloy," *J. ASTM Intl.*, Vol. 7, No. 4. doi:10.1520/JAI102717.

linear and nonlinear cumulative fatigue damage approaches. The significance of load-order versus load-type sequence effects for axial and torsional loading conditions is discussed. Possible reasons for the observed differences between the computed and observed summations of cycle fractions are rationalized in terms of the observed evolutions of cyclic axial and shear stress ranges in the cumulative fatigue tests.

KEYWORDS: axial fatigue, torsional fatigue, cumulative fatigue, cobalt-base superalloy

Introduction

Accumulation of fatigue damage under different amplitudes of loading has been investigated by numerous researchers on various materials [1–12]. Historically, in these cumulative fatigue investigations, load-order effects (high amplitude followed by low amplitude or low amplitude followed by high amplitude) within a given load-type were explored. Some of these load-types include axial tension/compression [3,12], torsion [4,7,8], and rotating bending [5]. Cumulative fatigue under dissimilar load-types can lead to a different cyclic life due to the potential of damage interaction between the different load-types. Such an interaction can either be beneficial (tends to increase overall cyclic life) or detrimental (tends to reduce the total number of cycles). More recently, several researchers studied cumulative fatigue behavior under dissimilar load-types on various materials [13–22]. The dissimilar load-types investigated for cumulative fatigue include the following: (1) Axial tension/compression, torsion, and proportional and nonproportional combined axial-torsional loads [13–21] and (2) bending and torsion [22].

Fatigue life prediction under cumulative loading conditions can be estimated by either linear or nonlinear damage rules. The linear damage rule (LDR) is simple, easily implementable in engineering design, and has been used extensively in cumulative fatigue life prediction [1–3]. However, for some materials and loading conditions, the load-order effects within a given load-type are not properly estimated by the LDR. For a given load-type, LDR can overestimate fatigue lives under high amplitude followed by low amplitude loading conditions and can underestimate fatigue lives under low amplitude followed by high amplitude loading conditions [5–12]. To remedy the shortcomings of the LDR with load-order effects, several nonlinear damage rules were developed to estimate fatigue lives under cumulative fatigue loading conditions [5–11]. Cumulative fatigue life estimation under different load-types such as axial and torsional loadings can be complicated due to the separate damage modes associated with each type of loading and the potential for interaction between these damage modes [13–19,21]. Frequently, in cumulative axial and torsional fatigue studies, damage equivalency is established in terms of cyclic life, equivalent strain range, or some form of damage parameter to separate the load-order effects from load-type sequencing effects. Investigations that include both load-order and load-type sequencing effects under cumulative axial and torisonal loadings are limited [14,20,23,24]. In particular, a comprehensive database, which contains both load-order (high amplitude followed by low amplitude and vice versa) and load-type (sequencing under axial and torsional loading conditions) variations, is necessary to properly evaluate the load-order and load-type sequencing effects for a material under cumulative fatigue loading conditions.

Two separate investigations on a cobalt-base superalloy, Haynes 188 were conducted previously at 538°C [23,24] to determine cumulative fatigue behavior under axial and torsional loading conditions. Cumulative fatigue data with axial and torsional load-type sequencing and high amplitude followed by low amplitude load ordering were reported in Ref 23. A complementing set of cumulative fatigue data with axial and torsional load-type sequencing and low amplitude followed by high amplitude load ordering was reported in Ref 24. In this study, the axial and torsional cumulative fatigue data generated in the two referenced investigations are combined to generate a comprehensive database on both load-order and load-type sequencing effects for the cobalt-base superalloy, Haynes 188. Applicability of two cumulative fatigue life prediction models, the LDR [1–3] and the nonlinear damage curve approach (DCA) [6,9] to the comprehensive Haynes 188 database is evaluated by comparing the summations of cyclic life fractions. The influences of load-order versus load-type sequencing were discerned by comparing the predicted and observed remaining cyclic life fractions and summations of cyclic life fractions. Some of the noticed differences are explained in terms of the cyclic deformation behavior in cumulative axial and torsional fatigue tests.

Material, Specimens, and Test System

Wrought, high-temperature annealed, cobalt-base superalloy, Haynes 188 was supplied in the form of cylindrical bars (50.8 mm diameter) by the manufacturer. The composition of the superalloy in weight percent was as follows: <0.002 S, 0.003 B, <0.005 P, 0.09 C, 0.35 Si, 0.052 La, 0.8 Mn, 1.17 Fe, 14.06 W, 22.11 Cr, 22.66 Ni, and balance Co. Thin-walled tubular specimens with the following gage section dimensions were machined from the cylindrical bars: Inner diameter, 22 mm; outer diameter, 26 mm; and gage length, 25 mm. The straight section and overall specimen lengths of the machined tubular specimen were 41 and 229 mm, respectively. The external surface of the gage section was polished in the longitudinal direction, whereas the internal surface (bore) of the specimen was honed. Additional details on the fabrication of the tubular specimen are available in Ref 25.

All axial and torsional fatigue tests on the thin-walled tubular specimens were conducted under strain control in air at 538°C within a servo-hydraulic fatigue rig equipped with hydro-collet grips and a personal computer (for test control and data acquisition). In all fatigue tests, failure was defined as a 10 % load-drop from a previously recorded cycle (see for example, Figs. 3(*a*) and 3(*b*), which are shown later). Average values of the elastic modulus, shear modulus, and Poisson's ratio for Haynes 188 at 538°C were 190 GPa, 73 GPa, and 0.3, respectively. Axial displacement and twist in the gage section of each tubular specimen was measured with a water-cooled, axial-torsional extensometer. Two indentations (25 mm apart and 80 μm deep) were pressed with a fixture in the middle of the straight section of the tubular specimen to mount the extensometer's probes. Thin-walled tubular specimens were heated to the test temperature in a three-coil induction heating fixture [26]. Temperature in the gage section of the specimen was monitored with a non-contacting temperature measurement system and the specimen temperature was controlled with thermocouples welded in the shoulder region of the thin-walled tubular specimen. Fatigue test control and data acquisition was accomplished with a data acquisition system and software written in the C programming language. Additional details on the fatigue test system and testing techniques are available in Ref 23.

Fatigue Database

Initially, fully reversed, strain-controlled axial and torsional fatigue tests were performed on thin-walled tubular specimens to establish baseline axial and torsional fatigue lives [23]. For all of the high strain range ($\Delta\varepsilon = 0.01$ and higher and $\Delta\gamma = 0.02$ and higher) fatigue tests a frequency of 0.1 Hz was used, whereas for all of the low strain range ($\Delta\varepsilon < 0.01$ and $\Delta\gamma < 0.02$) fatigue tests a higher frequency of 0.5 Hz was employed. If a specimen did not fail after 250 000 cycles, then that test was declared a runout. The axial and torisonal fatigue data (excluding the runout tests) were used to determine Manson–Coffin–Basquin type, total strain range (elastic and inelastic or plastic) versus cyclic life, relationships for axial and torsional loading conditions (Fig. 1). Data points with arrows represent runout tests in this figure. The axial and torsional fatigue life relationships determined with the baseline fatigue data for Haynes 188 at 538°C are as follows [23]:

$$\Delta\varepsilon = 0.0113(N_f)^{-0.08} + 0.501(N_f)^{-0.544} \tag{1}$$

$$\Delta\gamma = 0.0187(N_f)^{-0.082} + 1.24(N_f)^{-0.534} \tag{2}$$

In baseline axial fatigue tests, orientation of the fatigue crack(s) (Fig. 2) was predominantly perpendicular to the maximum principal stress direction ($\theta = 0°$ to $10°$), whereas in torsional fatigue tests their orientation was parallel mainly to one of the two possible maximum shear stress directions ($\theta = 90°$). Two nominal strain ranges for axial ($\Delta\varepsilon_{\text{high}} = 0.02$ and $\Delta\varepsilon_{\text{low}} = 0.0067$) and two for torsional ($\Delta\gamma_{\text{high}} = 0.035$ and $\Delta\gamma_{\text{low}} = 0.012$) loading conditions, were selected for the subsequent cumulative fatigue tests. For each test condition, duplicate tests were conducted to evaluate repeatability of the cyclic deformation behavior and to provide an accurate estimation of the baseline fatigue life. The evolution of cyclic axial and shear stresses in these baseline axial and torsional tests is shown in Fig. 3. Haynes 188 cyclically hardened for a majority of the life with a slight softening towards the end in all of these tests. Cyclic hardening behaviors of the duplicate axial and torsional tests at a given nominal strain range were nearly identical. Since fatigue lives tend to follow a log-normal distribution, geometric-mean fatigue lives computed from the cyclic lives of the duplicate baseline axial and torsional fatigue tests [23] were used for the subsequent cumulative axial and torsional fatigue data analysis. These geometric-mean fatigue lives are as follows: (a) $N_{\text{LCF,A}} = 825$ cycles (for $\Delta\varepsilon_{\text{high}} = 0.02$); (b)

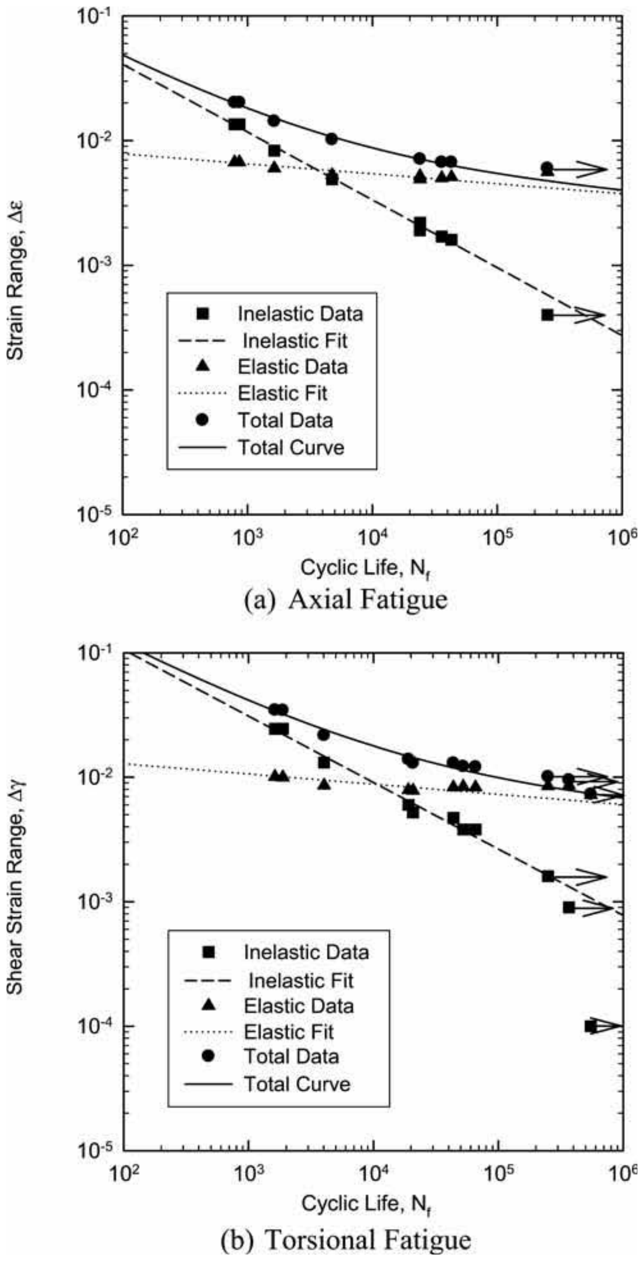

FIG. 1—*Axial and torsional fatigue life relationships for Haynes 188 at* 538°C (*from Ref 23*) (*a*) *Axial fatigue and* (*b*) *torsional fatigue.*

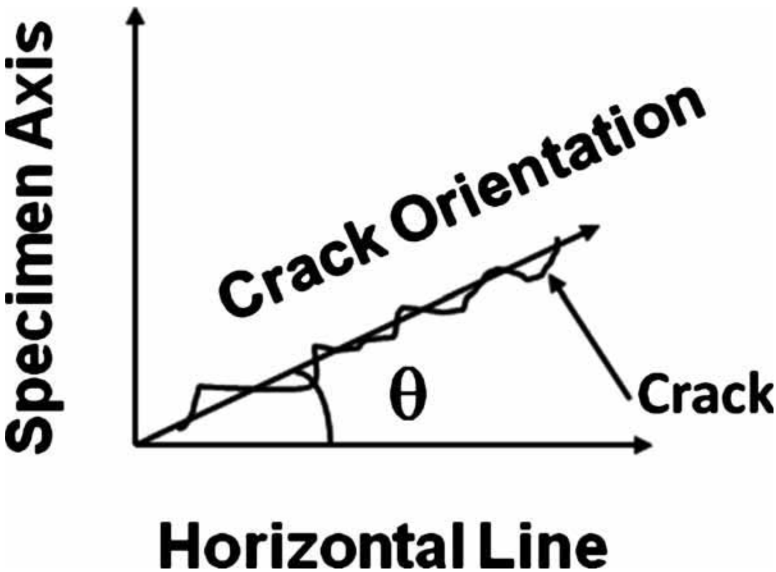

FIG. 2—*Schematic orientation of a fatigue crack in an axial or a torsional test (for an axial fatigue test, if crack is perpendicular to the maximum principal stress direction, θ=0°; for a torsional fatigue test, if crack is parallel to either maximum shear stress direction, θ=0° or 90°).*

$N_{HCF,A}=39,255$ cycles (for $\Delta\varepsilon_{low}=0.0067$); (c) $N_{LCF,T}=1,751$ cycles (for $\Delta\gamma_{high}=0.035$); and (d) $N_{HCF,T}=58,568$ cycles (for $\Delta\gamma_{low}=0.012$) where subscripts LCF and HCF are low- and high-cycle fatigue, respectively, and "A" and "T" are axial and torsional loading conditions, respectively.

Cumulative axial and torsional fatigue tests conducted previously on Haynes 188 at 538°C included both load-order and load-type sequencing tests [23,24]. Schematics of two load-level, high amplitude followed by low amplitude (LCF/HCF) and low amplitude followed by high amplitude (HCF/LCF) cyclic loadings are shown in Fig. 4. In these figures, n_1 and n_2 are the applied and remaining cycles and N_1 and N_2 are the baseline fatigue lives at the first and second load-levels, respectively. The applied and remaining cycle fractions at the first and second load-levels are n_1/N_1 and n_2/N_2, respectively. Load-order effects without load-type sequencing were investigated with axial ($\Delta\varepsilon_{high}=0.02$)/axial ($\Delta\varepsilon_{low}=0.0067$) and torsional ($\Delta\gamma_{high}=0.035$)/torsional ($\Delta\gamma_{low}=0.012$) fatigue tests, whereas load-order effects with load-type sequencing were investigated with axial ($\Delta\varepsilon_{high}=0.02$)/torsional ($\Delta\gamma_{low}=0.012$) and torsional ($\Delta\gamma_{high}=0.035$)/axial ($\Delta\varepsilon_{low}0.0067$) fatigue tests. In the initial portion of each of the two load-level cumulative fatigue tests, the first load-level life fraction ($n_1/N_1=0.1$, 0.2, 0.4, or 0.6) was applied. For the remainder, each of the tests was performed at the second load-level until failure of the specimen. Additional details on cumulative fatigue testing are available in Ref 23 and all

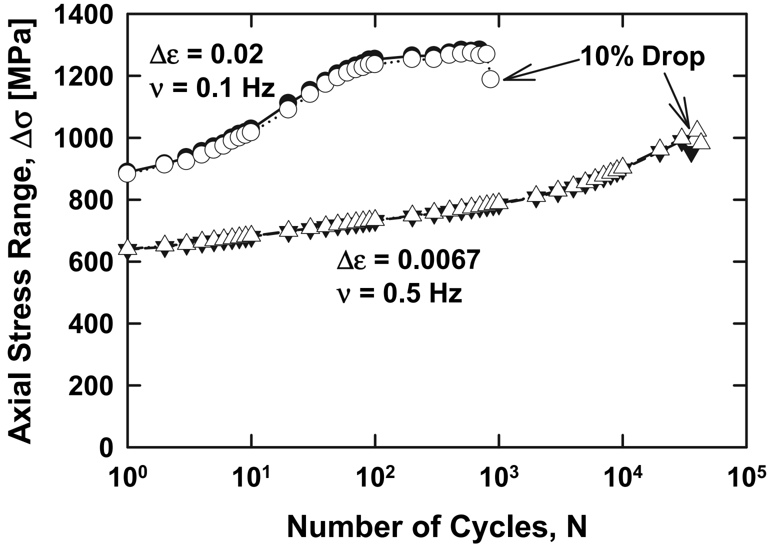

(a) Axial Fatigue

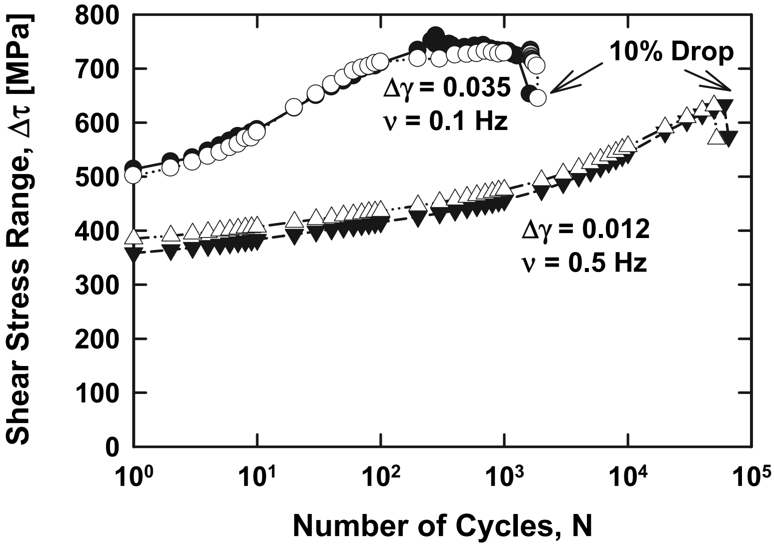

(b) Torsional Fatigue

FIG. 3—*Evolution of axial and shear stresses in fatigue tests on Haynes 188 at 538°C (from Ref 23) (a) Axial fatigue and (b) torsional fatigue.*

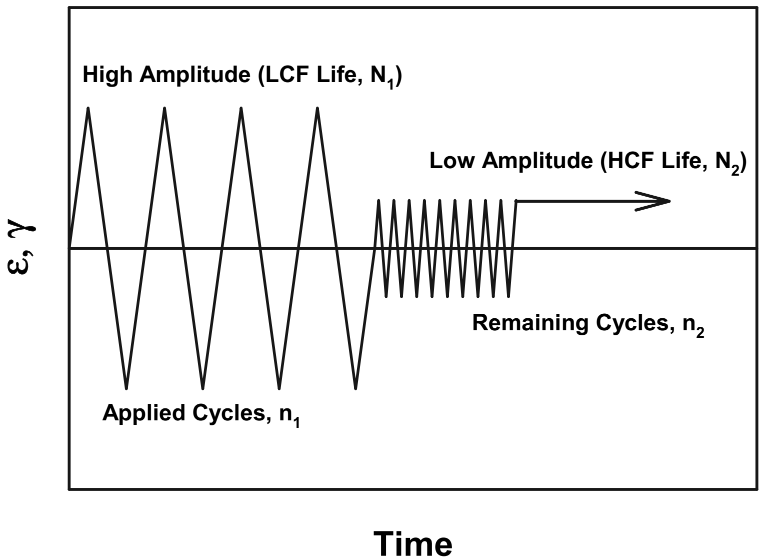

(a) High Amplitude Followed by Low Amplitude (LCF/HCF)

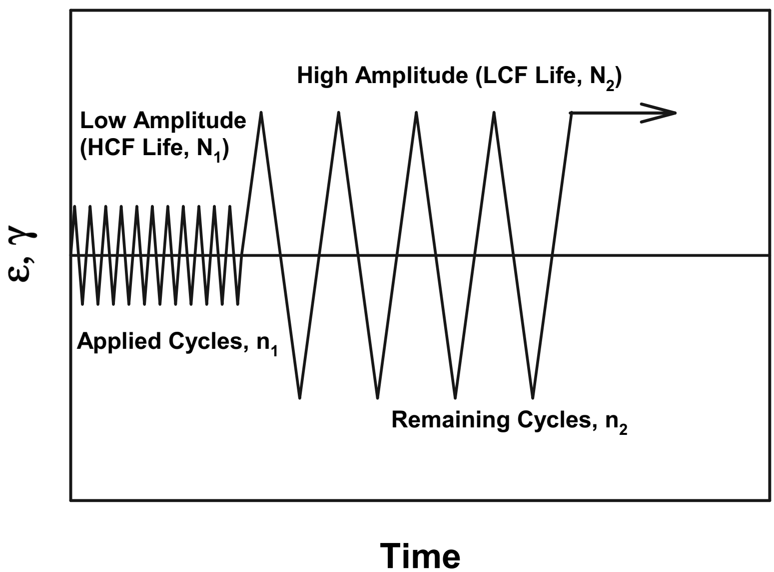

(b) Low Amplitude Followed by High Amplitude (HCF/LCF)

FIG. 4—*Schematics of axial and torsional cumulative fatigue loadings.* (*a*) *High amplitude followed by low amplitude* (*LCF/HCF*) *and* (*b*) *Low amplitude followed by high amplitude* (*HCF/LCF*).

of the axial and torsional cumulative fatigue data analyzed in this study are available in Refs 23 and 24.

Cumulative Axial and Torsional Fatigue Behavior

Remaining life fractions (n_2/N_2) at the second load-level in all of the cumulative axial and torsional fatigue tests were calculated with the LDR (Eq 3) and the DCA (Eq 4):

$$\left(\frac{n_2}{N_2}\right) = 1 - \left(\frac{n_1}{N_1}\right) \tag{3}$$

$$\left(\frac{n_2}{N_2}\right) = 1 - \left(\frac{n_1}{N_1}\right)^{(N_1/N_2)^{0.4}} \tag{4}$$

Estimated remaining life fractions (n_2/N_2) versus the applied life fractions (n_1/N_1) for all the axial and torsional tests analyzed in this study are shown in Figs. 5 and 6. The baseline axial and torsional fatigue lives used in estimating the remaining life fractions are also indicated. Geometric-mean fatigue lives computed from the baseline tests at the nominal axial and engineering shear strain ranges were used for most cumulative fatigue tests. For the torsional/axial cumulative fatigue tests, the geometric-mean axial strain range of all the LCF/HCF and HCF/LCF tests was slightly higher than the nominal value of $\Delta\varepsilon_{\text{low}} = 0.0067$. The corresponding baseline axial fatigue life was calculated from the axial fatigue life relation (Eq 1).

For the Haynes 188 testing at 538°C in cumulative axial and torsional fatigue, load-order effects without and with load-type sequencing are shown in Figs. 5 and 6, respectively. In the axial/axial cumulative fatigue tests, orientation of fatigue cracks was nearly perpendicular to the maximum principal stress direction ($\theta = 0°$ to 10°) and for all the LCF/HCF tests and for the HCF/LCF tests with applied life fractions, $n_1/N_1 > 0.4$, predictions by the DCA were better than those obtained using the LDR (Fig. 5(*a*)). Fatigue cracks were oriented along both maximum shear planes ($\theta = 0°$, 5°, and 90°) in the torsional/torsional cumulative fatigue tests and remaining life fraction predictions by the DCA were better than the LDR predictions for both LCF/HCF and HCF/LCF tests, when $n_1/N_1 > 0.4$ (Fig. 5(*b*)). Duplicate HCF/LCF torsional/torsional tests performed with $n_1/N_1 = 0.4$ resulted in a noticeable variation in the remaining life fraction, n_2/N_2.

In the case of axial/torsional cumulative fatigue tests, fatigue cracks were oriented along $\theta = 0°$ to 15° (mainly perpendicular to the maximum principal stress direction for axial loading and parallel to one of the two maximum shear stress directions for the torsional loading), except in one LCF/HCF test in which the fatigue crack was parallel to the other maximum shear stress direction ($\theta = 90°$). The remaining life fraction predictions determined by DCA were better than those obtained using LDR for LCF/HCF tests; however, the opposite was true for the HCF/LCF tests (Fig. 6(*a*)). Fatigue cracks occurred predominantly perpendicular to the maximum principal stress direction ($\theta = 0°$ to 15°) in the

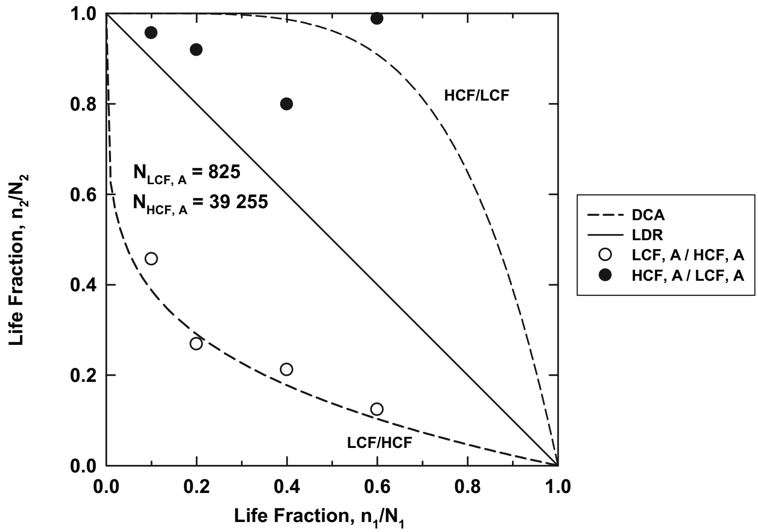

(a) Axial/Axial Tests

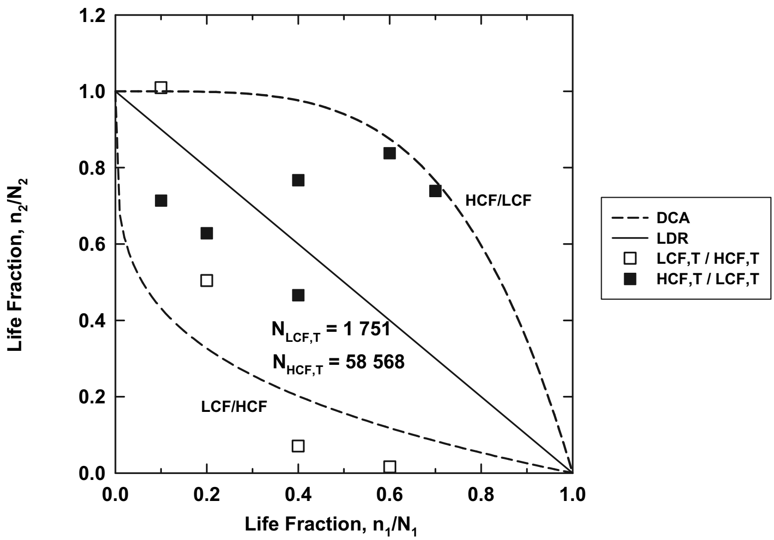

(b) Torsional/Torsional Tests

FIG. 5—*Load-order effects without load-type sequencing in cumulative axial and torsional fatigue of Haynes 188 at 538°C. (a) Axial/axial tests and (b) torsional/torsional tests.*

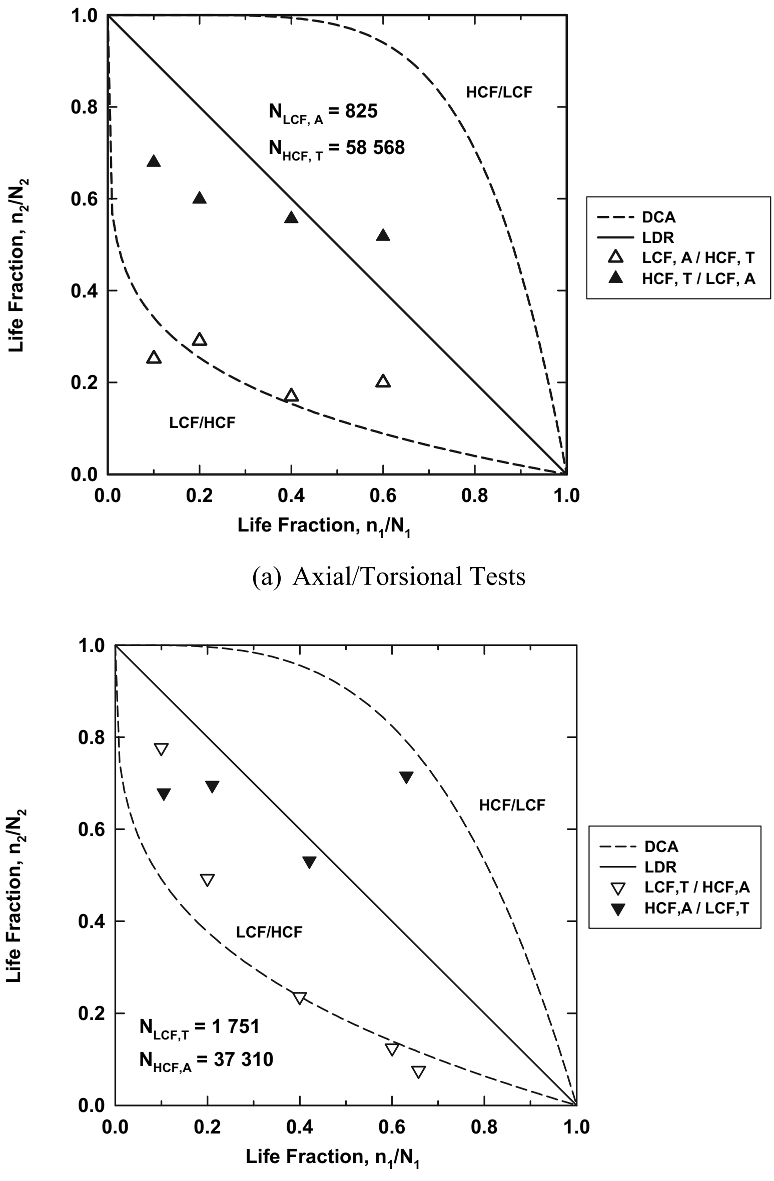

(a) Axial/Torsional Tests

(b) Torsional/Axial Tests

FIG. 6—*Load-order effects with load-type sequencing in cumulative axial and torsional fatigue of Haynes 188 at 538°C.* (*a*) *Axial/torsional tests and* (*b*) *torsional/axial tests.*

torsional/axial LCF/HCF tests, whereas the fatigue cracks were nearly parallel to one of the maximum shear stress directions ($\theta = 85°$ and $90°$) in the HCF/LCF tests. Predictions of the remaining life fractions by the DCA were better than the LDR predictions for both LCF/HCF and HCF/LCF tests, when $n_1/N_1 > 0.4$ (Fig. 6(*b*)). In cumulative axial/axial and torsional/torsional fatigue tests without load-type sequencing, fatigue crack initiation was similar to the respective baseline fatigue tests. However, with load-type sequencing (axial/torsional and torsional/axial) fatigue cracks initiated both perpendicular to the maximum normal stress and parallel to the maximum shear stress.

For all the cumulative axial and torsional fatigue tests, experimentally observed sum of life fractions ($n_1/N_1 + n_2/N_2$) versus applied life fractions (n_1/N_1) and the predictions by the LDR and the DCA are compared in Figs. 7 and 8. The sum of life fractions predicted by the LDR is unity for both LCF/HCF and HCF/LCF tests, whereas predictions by the DCA are less than unity for LCF/HCF tests and greater than unity for HCF/LCF tests due to the nonlinear interaction. Load-order effects were more clearly evident in axial/axial cumulative fatigue tests (Fig. 7(*a*)) than in torsional/torsional cumulative fatigue tests (Fig. 7(*b*)). Even in load-type sequencing cumulative fatigue tests (axial/torsional and torsional/axial) load-order effects were present, however, the beneficial effect of HCF/LCF interaction was somewhat diminished (Fig. 8).

Discussion

In this study, an attempt was made to systematically understand both the load-order and load-type sequencing effects in cumulative axial and torsional fatigue with a comprehensive database compiled for Haynes 188 at 538°C. The observed variation in the fatigue lives, both in the baseline and the cumulative axial and torsional fatigue tests, can make it difficult to characterize these load-order and load-type sequencing effects. In the comprehensive cumulative axial and torsional fatigue database, duplicate tests were conducted for baseline axial and torsional fatigue tests. At least three specimens might be necessary to capture variation in cyclic lives at high strain ranges, whereas at least five specimens would be required at low strain ranges. In cumulative axial and torsional fatigue tests, at least two tests should be performed at each initial life fraction (n_1/N_1) to capture variability in cyclic life at second load-level (see the scatter exhibited in the remaining LCF life fraction, n_2/N_2 for example in Fig. 5(*b*), where two HCF/LCF, torsional/torsional cumulative fatigue tests were conducted with an initial HCF life fraction, $n_1/N_1 = 0.4$).

In two load-level cumulative fatigue tests, cyclic deformation behavior at the second load-level can be influenced significantly by the first load-level. For example, in baseline torsional fatigue tests cyclic hardening was observed predominantly at both strain ranges (Fig. 3(*b*)). However, at the second load-level, in both torsional/torsional (Fig. 9(*a*)) and axial/torsional (Fig. 9(*b*)) cumulative LCF/HCF tests, cyclic softening was observed at the second load-level, which indicated that during the initially applied axial or torsional life fraction, the material had hardened significantly. Even in the case of HCF/LCF tests, the influence of cyclic hardening and associated reduction in the equivalent plastic

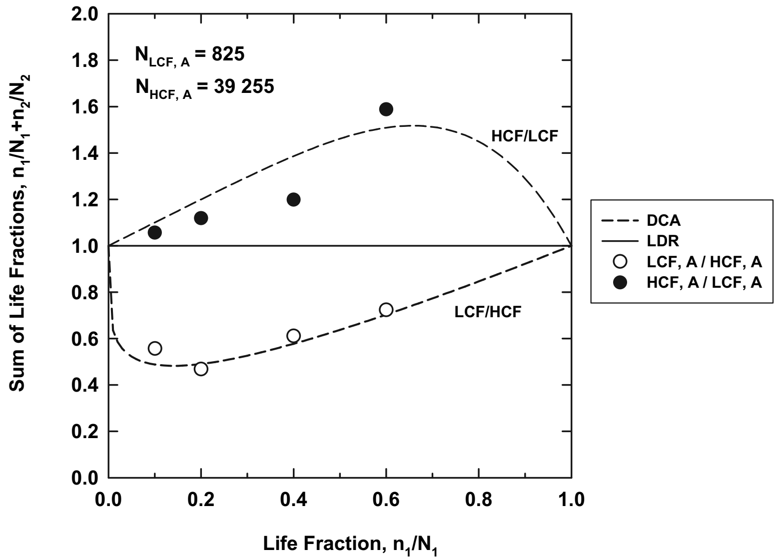

(a) Axial/Axial Tests

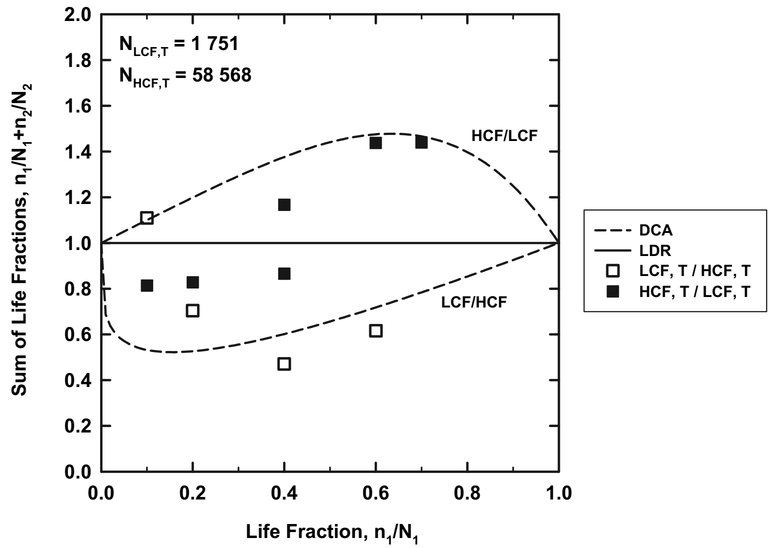

(b) Torsional/Torsional Tests

FIG. 7—*Comparison of the summation of life fractions in cumulative axial and torsional fatigue of Haynes 188 at 538°C: Load-order effects without load-type sequencing.* (*a*) *Axial/axial tests and* (*b*) *torsional/torsional tests.*

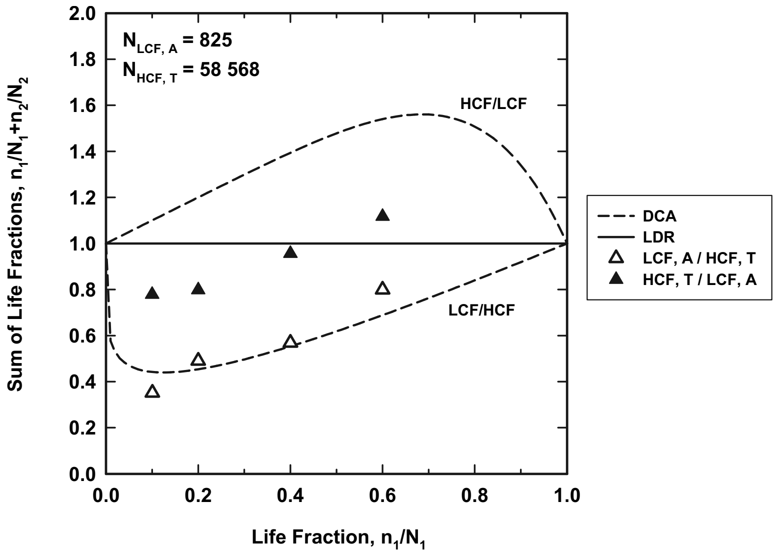

(a) Axial/Torsional Tests

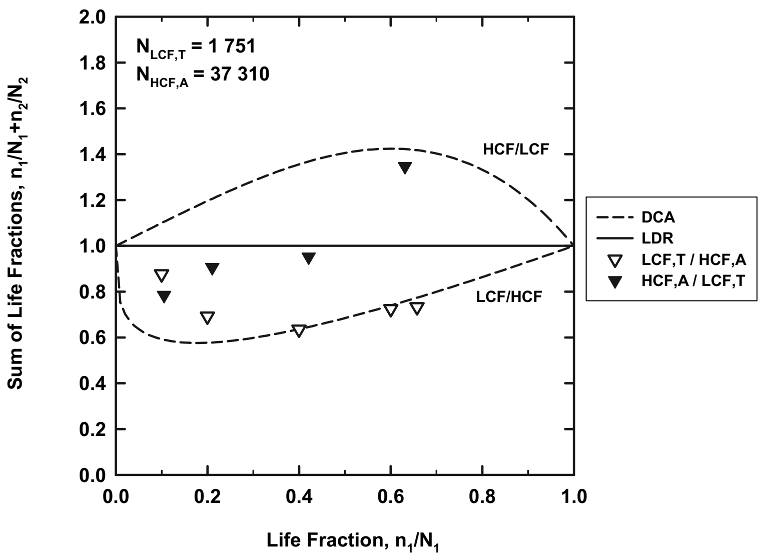

(b) Torsional/Axial Tests

FIG. 8—*Comparison of the summation of life fractions in cumulative axial and torsional fatigue of Haynes 188 at 538°C: Load-order effects with load-type sequencing.* (*a*) *Axial/torsional tests and* (*b*) *torsional/axial tests.*

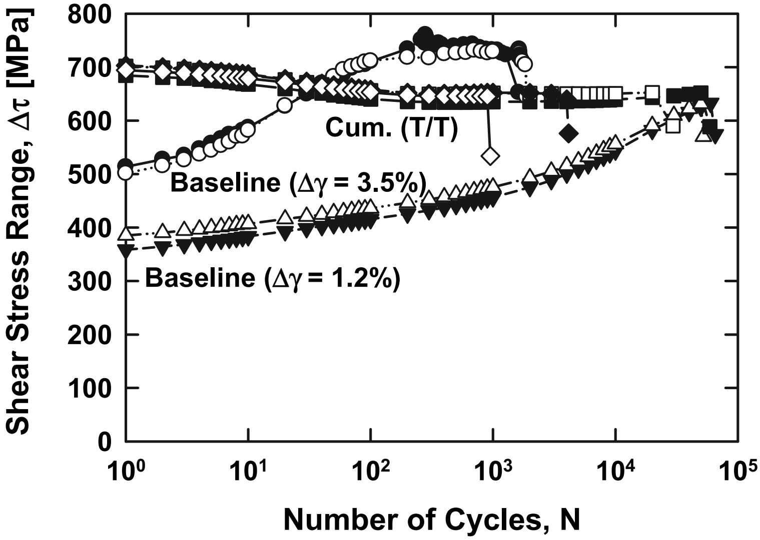

(a) Torsional/Torsional Tests

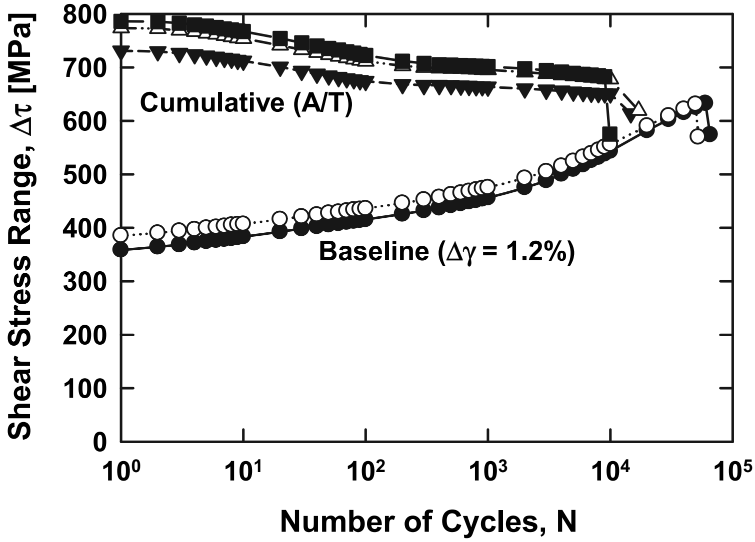

(b) Axial/Torsional Tests

FIG. 9—*Cyclic softening at second load-level after initial loading in axial and torsional fatigue (LCF/HCF). (a) Torsional/torsional tests and (b) axial/torsional tests.*

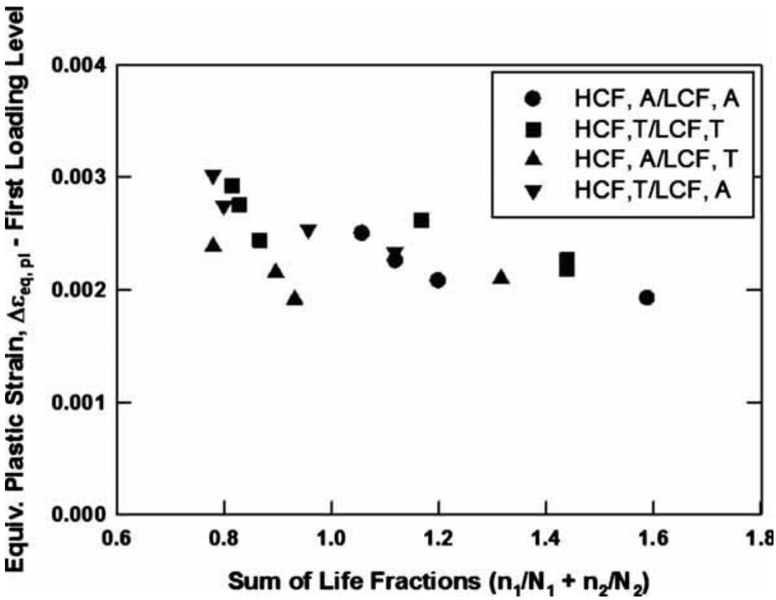

FIG. 10—*Equivalent plastic strain range at the end of first load-level versus sum of life fractions in HCF/LCF axial and torsional fatigue tests (from Ref 24).*

strain range was noticed on the sum of life fractions (Fig. 10). Sum of life fractions in all of the HCF/LCF axial and torsional fatigue tests exhibited an increase with a reduction in the equivalent plastic strain range at the end of first load-level [24]. Thus, either cyclic hardening at the first load-level or associated reduction in equivalent plastic strain range at the end of that level can be useful parameters in estimating remaining fatigue lives at the second load-level in cumulative axial and torsional fatigue tests.

Remaining cyclic life predictions, by either the LDR or the DCA at the second load-level, were not uniformly closer to the experimentally observed cyclic lives for all of the axial and torsional cumulative fatigue tests (Fig. 11). For the LCF/HCF tests, predictions by the LDR were higher than the observed cyclic lives, whereas predictions by the DCA in a majority of the cases were within factors of two of the observed cyclic lives. For most of the tests, predictions by both the LDR and the DCA methods were within factors of two of the observed cyclic lives for the HCF/LCF testing. However, most of the predictions by the DCA were higher than the experimentally observed cyclic lives.

Load-order effects within a given load-type were more clearly evident in Haynes 188 at 538°C under axial/axial fatigue (sum of life fractions is less than unity for all LCF/HCF tests and greater than unity for all HCF/LCF tests; see Figs. 5(*a*) and 7(*a*)) than in torsional/torsional fatigue (sum of life fractions is not less than unity for all LCF/HCF tests and is not greater than unity for all HCF/LCF tests; see Figs. 5(*b*) and 7(*b*)). The load-order effects were more pronounced in LCF/HCF tests than in HCF/LCF tests when load-type sequencing was present, as in the case of axial/torsional or torsional/axial tests (Fig. 6(*a*)

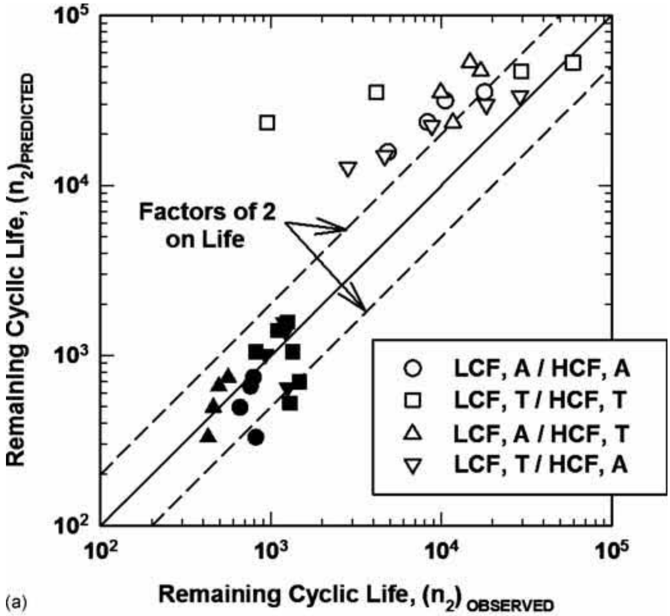

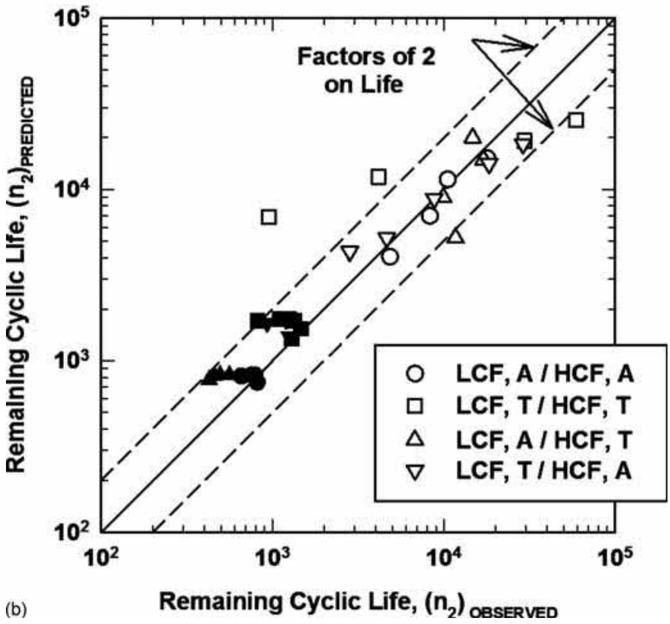

FIG. 11—*Comparison of remaining cyclic lives in the axial and torsional cumulative fatigue tests (open symbols: LCF/HCF and filled symbols: HCF/LCF). (a) LDR and (b) DCA.*

and 6(*b*)). Higher inelastic strain range values at the end of the first load-level in the LCF/HCF tests might have contributed to the pronounced load-order effects in these tests. The diminished beneficial effect observed during the HCF/LCF tests could be due to detrimental interaction among different damage modes in load-type sequencing tests. To delineate the different damage mechanisms, interrupted cumulative axial and torsional fatigue tests are required at different initial applied life fractions. Fractography and metallography can be used to identify the precise damage mechanisms.

Summary

Analysis of the comprehensive cumulative axial and torsional fatigue database on Haynes 188 at 538°C indicated that both load-order (axial/axial and torsional/torsional) and load-type sequencing (axial/torsional and torsional/axial) influenced cyclic lives. The following items provide the Haynes 188 study overview:

(1) Crack initiation in baseline axial fatigue tests occurred nearly perpendicular to the maximum normal stress direction, whereas in baseline torsional fatigue tests crack initiation occurred primarily parallel to one of the two possible maximum shear stress directions. In cumulative axial and torsional fatigue tests without load-type sequencing (axial/axial and torsional/torsional), crack initiation is essentially similar to baseline fatigue tests; however, with load-type sequencing (axial/torsional and torsional/axial) cracks initiated both perpendicular to the maximum normal stress direction and parallel to the two possible maximum shear stress directions, which is expected due to load-type mixing.

(2) Load-order effects dominated the load-type sequencing effects in LCF/HCF tests. Even though load-order effects were present in HCF/LCF tests, expected beneficial interaction in these types of tests was diminished by load-type sequencing effects indicating possible interaction between the cracking modes.

(3) For LCF/HCF tests with and without load sequencing, the remaining fatigue life predictions by LDR were higher (unconservative) and those by DCA were closer to the experimentally observed values in three out of four cases.

(4) In the HCF/LCF testing, the LDR more closely estimated remaining fatigue lives in lower initially applied life fractions ($n_1/N_1 \leq 0.4$) and the DCA estimates were better with higher ($n_1/N_1 > 0.4$) initially applied life fractions.

(5) In the case of the HCF/LCF tests, the amount of hardening in first load-level and associated reduction in equivalent plastic strain range appeared to influence the sum of life fractions. These two quantities can be important parameters in estimating remaining fatigue lives in cumulative axial and torsional fatigue tests.

References

[1] Palmgren, A. “Die Lebensdauer von Kugellagern,” *Z. Ver. Dtsch. Ing.*, Vol. 68, 1924, pp. 339–341.

[2] Langer, B. F., “Fatigue Failure from Stress Cycles of Varying Amplitude,” *J. Appl. Mech.*, Vol. 4, 1937, pp. A160–A162.

[3] Miner, M. A., “Cumulative Damage in Fatigue,” *J. Appl. Mech.*, Vol. 12, 1945, pp. A159–A164.

[4] Wood, W. A. and Reimann, W. H., “Observations on Fatigue Damage Produced by Combinations of Amplitudes in Copper and Brass,” *J. Inst. Met.*, Vol. 94, 1966, pp. 66–70.

[5] Manson, S. S., Nachtigall, A. J., Ensign, C. R., and Freche, J. C., “Further Investigation of a Relation for Cumulative Fatigue Damage in Bending,” *J. Eng. Ind.*, Vol. 87, 1965, pp. 25–35.

[6] Manson, S. S. and Halford, G. R., “Practical Implementation of the Double Linear Damage Rule and Damage Curve Approach for Treating Cumulative Fatigue Damage,” *Int. J. Fract.*, Vol. 17, 1981, pp. 169–192.

[7] Bui-Quoc, T., “Cumulative Damage with Interaction Effect due to Fatigue Under Torsion Loading,” *Exp. Mech.*, Vol. 22, 1982, pp. 180–187.

[8] Miller, K. J. and Ibrahim, M. F. E., “Damage Accumulation During Initiation and Short Crack Growth Regimes,” *Fatigue Fract. Eng. Mater. Struct.*, Vol. 4, 1981, pp. 263–277.

[9] Manson, S. S. and Halford, G. R., “Re-examination of Cumulative Fatigue Damage Analysis–An Engineering Perspective,” *Eng. Fract. Mech.*, Vol. 25, 1986, pp. 539–571.

[10] Golos, K. and Ellyin, F., “Generalization of Cumulative Damage Criterion to Multilevel Cyclic Loading,” *Theor. Appl. Fract. Mech.*, Vol. 7, 1987, pp. 169–176.

[11] Chaboche, J. L. and Lesne, P. M., “A Non-Linear Continuous Fatigue Damage Model,” *Fatigue Fract. Eng. Mater. Struct.*, Vol. 11, 1988, pp. 1–17.

[12] McGaw, M. A., Kalluri, S., Moore, D., and Heine, J., “The Cumulative Fatigue Damage Behavior of Mar-M 247 in Air and High Pressure Hydrogen,” in *Advances in Fatigue Lifetime Predictive Techniques: Second Volume, ASTM STP 1211*, M. R. Mitchell and R. W. Landgraf, Eds., American Society for Testing and Materials, West Conshohocken, PA, 1993, pp. 117–131.

[13] Miller, K. J., and Brown, M. W. “Multiaxial Fatigue: A Brief Review,” *Fracture 84, Proceedings of the Sixth International Conference on Fracture*, Pergamon Press, New Delhi, India, 1984, pp. 31–56.

[14] Hua, C. T., and Socie, D. F., “Fatigue Damage in 1045 Steel Under Variable Amplitude Biaxial Loading,” *Fatigue Fract. Eng. Mater. Struct.*, Vol. 8, 1985, pp. 101–114.

[15] Miller, K. J., “Metal Fatigue—Past, Current, and Future,” *Proc. Inst. Mech. Eng.*, Vol. 205, 1991, pp. 1–14.

[16] Robillard, M. and Cailletaud, G., “Directionally Defined Damage in Multiaxial Low-Cycle Fatigue: Experimental Evidence and Tentative Modelling,” *Fatigue Under Biaxial and Multiaxial Loading, ESIS10*, K. Kussmaul, D. McDiarmid, and D. Socie, Eds., Mechanical Engineering Publications, London, 1991, pp. 103–130.

[17] Weiss, J. and Pineau, A., “Continuous and Sequential Multiaxial Low-Cycle Fatigue Damage in 316 Stainless Steel,” in *Advances in Multiaxial Fatigue, ASTM STP 1191*, D. L. McDowell and R. Ellis, Eds.,American Society for Testing and Materials, West Conshohocken, PA, 1993, pp. 183–203.

[18] Weiss, J. and Pineau, A., “Fatigue and Creep-Fatigue Damage of Austenitic Stain-

less Steels under Multiaxial Loading," *Metall. Trans. A*, Vol. 24, 1993, pp. 2247–2261.

[19] Lin, H., Nayeb-Hashemi, H., and Berg, C. A., "Cumulative Damage Behavior of Anisotropic Al-6061-T6 as a Function of Axial-Torsional Loading Mode Sequence," *ASME J. Eng. Mater. Technol.*, Vol. 116, 1994, pp. 27–34.

[20] Hua, G. and Fernando, U. S., "Effect of Non-Proportional Overloading on Fatigue Life," *Fatigue Fract. Eng. Mater. Struct.*, Vol. 19, 1996, pp. 1197–1206.

[21] Morel, F. and Bastard, M., "A Multiaxial Life Prediction Method Applied to a Sequence of Non Similar Loading in High Cycle Fatigue," *Int. J. Fatigue*, Vol. 25, 2003, pp. 1007–1012.

[22] Harada, S. and Endo, T., "On the Validity of Miner's Rule under Sequential Loading of Rotating Bending and Cyclic Torsion," in *Fatigue Under Biaxial and Multiaxial Loading, ESIS10*, K. Kussmaul, D. McDiarmid, and D. Socie, Eds., Mechanical Engineering Publications, London, 1991, pp. 161–178.

[23] Kalluri, S. and Bonacuse, P. J., "Cumulative Axial and Torsional Fatigue: An Investigation of Load-Type Sequence Effects," in *Multiaxial Fatigue and Deformation: Testing and Prediction, ASTM STP 1387*, S. Kalluri, and P. J. Bonacuse, Eds., American Society for Testing and Materials, West Conshohocken, PA, 2000, pp. 281–301.

[24] Bonacuse, P. and Kalluri, S. "Sequenced Axial and Torsional Cumulative Fatigue: Low Amplitude Followed by High Amplitude Loading," *Biaxial/Multiaxial Fatigue and Fracture, ESIS Publication 31*, A. Carpinteri, M. De Freitas, and A. Spagnoli, Eds., Elsevier, New York, 2003, pp. 165–182.

[25] Bonacuse, P. J., and Kalluri, S., "Axial-Torsional Fatigue: A Study of Tubular Specimen Thickness Effects," *J. Test. Eval.*, Vol. 21(3), 1993, pp. 160–167.

[26] Ellis, J. R. and Bartolotta, P. A., "Adjustable Work Coil Fixture Facilitating the Use of Induction Heating in Mechanical Testing," in *Multiaxial Fatigue and Deformation Testing Techniques, ASTM STP 1280*, S. Kalluri, and P. J. Bonacuse, Eds., American Society for Testing and Materials, West Conshohocken, PA, 1997, pp. 43–62.

Reprinted from JAI, Vol. 7, No. 3
doi:10.1520/JAI102526
Available online at www.astm.org/JAI

R. Amargier,[1] S. Fouvry,[2] C. Poupon,[3] and L. Chambon[4]

A Non Local Multiaxial Fatigue Approach to Account for Stress Gradient Effect Applied to Crack Initiation in Fretting

ABSTRACT: Although fatigue limits of smooth specimens under various complex loadings have been determined, few models have been proposed to predict well-known experimental results such as size effects and stress gradient effects. This paper addresses the stress gradient effect issue. A new non local multiaxial fatigue approach is proposed and applied to rotating bending and fretting experiments. The proposal takes as a starting point the rotating bending results and stress gradient analysis of a cylinder-plane contact in partial slip sliding regime. Both weight function and "process volume," used to compute the mean value of the weight function, are introduced in a phenomenological way. The weight function reflects the experimental trend of fatigue limit under rotating bending whereas the connected process volume allows dealing with special stress gradient induced by cylinder-plane contact under partial slip. The proposal shows good capabilities to predict four-point rotating bending fatigue limit and crack initiation of a similar Inconel 718 cylinder/plane contact under partial slip regime.

KEYWORDS: multiaxial fatigue, fretting, stress gradient, Inconel 718

Manuscript received May 17, 2009; accepted for publication December 22, 2009; published online February 2010.

[1] Airbus, D41, rue Marius Terce, 31300 Toulouse, France and LTDS, Ecole Centrale de Lyon, bât. D4, 36 avenue Guy de Collongue, 69134 Ecully, France.
[2] LTDS, Ecole Centrale de Lyon, bât. D4, 36 avenue Guy de Collongue, 69134 Ecully, France.
[3] Airbus, D41, rue Marius Terce, 31300 Toulouse, France.
[4] EADS IW-Computational Structural Mechanics, BP13050, 18 rue Marius Terce, 31025 Toulouse Cedex 03, France.

Cite as: Amargier, R., Fouvry, S., Poupon, C. and Chambon, L., "A Non Local Multiaxial Fatigue Approach to Account for Stress Gradient Effect Applied to Crack Initiation in Fretting," *J. ASTM Intl.*, Vol. 7, No. 3. doi:10.1520/JAI102526.

Nomenclature

a = demi contact width
C = material parameter introduced to define the volume used to compute $\bar{w}$
c = demi sticking zone width
c' = additional stick zone width
E = Young's modulus
$J_{2,a}$ = amplitude of the second invariant of the stress tensor deviator
k = parameter of the weight function
L = contact width
M = geometrical point defined by its coordinates x,z for stress field computation
M_C = the maximally loaded point in terms of the Papadopoulos criterion
n = parameter of the weight function
P = normal load
p = surface pressure
p_0 = maximum pressure
$p_{0,\mathrm{ref}}$ = maximum pressure used as a reference for results normalization
Q = tangential load amplitude
Q_0 = maximum tangential load
Q' = secondary tangential amplitude
q = surface shear traction
$q_{\max}$ = surface shear traction for Q_0
$q_{0,\max}$ = maximum value of the surface shear traction for Q_0
R = cylinder radius
R_S = radius of fatigue test specimen
s = variable used for substresses integration
UTS = ultimate tensile strength
w = weight function
w_S = parameter of the weight function
$\bar{w}$ = mean value of the weight function
Ys = yield strength
α = parameter of local multiaxial fatigue criterion
β = parameter of local multiaxial fatigue criterion
δ = relative displacement
μ = coefficient of friction (COF)
ν = Poisson's ratio
σ_{b-1} = rotating bending fatigue limit
σ_{ij} = stress tensor component

σ_{-1} = tension-compression fatigue limit ($R=-1$)
$\bar{\bar{\sigma}}$ = stress tensor
τ_a = resolved shear stress amplitude
$\tau_{a,\max}$ = maximum resolved shear stress amplitude
τ_{-1} = torsion fatigue limit ($R=-1$)
$\sqrt{\langle T_a \rangle^2}$ = root mean square of the resolved shear stress amplitude: $\sqrt{\langle T_a \rangle^2}=\sqrt{\frac{5}{8\pi^2}\int_{\varphi=0}^{2\pi}\int_{\theta=0}^{\pi}\int_{\chi=0}^{2\pi}(\tau_a(\varphi,\theta,\chi))^2\cdot d\chi \sin\theta d\theta d\varphi}$

Introduction

Fatigue limit estimation of industrial components is a major problem for mechanical design. Many multiaxial fatigue criteria have been proposed to quantify high cycle fatigue limit. One can quote the Crossland criterion for the invariant approach whereas for instance the Dang Van criterion is based on the critical plane approach and on mesoscopic considerations. Papadopoulos in Ref 1 proposed a new criterion derived from the mesoscopic Dang Van's approach. The error in fatigue limits predictions with this formulation falls below 10 %. The criterion has been validated using varied multiaxial fatigue data in Refs 1 and 2. Morel, Palin Luc, and Froustey proposed an energy-based approach and showed that there are strong connections between the Papadopoulos' approach and their energy-based approach [3]. Whatever the approach, the most reliable multiaxial fatigue criteria predict fatigue limit within a 10 % range [1–3].

However, although these criteria provide accurate fatigue limits of smooth specimens under in-phase and out-of-phase multiaxial loadings, they quickly exhibit their weaknesses when addressing specimens featuring stress gradient. Fatigue limits predicted using these local criteria applied to notched specimens, smooth specimens under rotating bending, or to fretting problems are always largely conservative. This is a well-known fact when applying local criteria to predict fatigue limit of specimens featuring stress gradient.

Analysis of rotating bending data is an interesting way to address the stress gradient effect. Interesting data on the effect of stress gradient on fatigue limit have been published by authors studying fatigue limit under rotating bending. One can quote the four-point rotating bending tests performed by Pogoretskii and Karpenko [4], and by Pavan [5] who studied the evolution of the fatigue limit as a function of specimen radius and length. These results exhibit the larger effect of stress gradient compared to the size effect. Further details are available in Ref 6. By analyzing these data, Papadopoulos and Panoskaltsis proposed a modified Crossland criterion including a weight function depending on hydrostatic pressure gradient to predict the evolution of the fatigue limit under rotating bending. Recently, this criterion was successfully applied by Morel and Nadot in Ref 7 to micro-notched specimens.

The problem of stress gradient effect was also addressed by authors studying crack initiation under fretting. Fretting problem features non proportional loading and high stress gradient. This complex stress state led the authors to employ non local approach to overcome the weakness of local criteria to account for the experimentally observed crack initiation thresholds. First, simple approaches were applied which consist of computing the mean value of a multiaxial fatigue criterion over an elementary volume. This elementary volume is assumed to be a material parameter representing the necessary amount of material to produce a micro-crack [8]. Later, an advanced approach was proposed in Ref 9. A variable process volume is proposed to compute the mean value of a multiaxial fatigue criterion. The process volume is connected indirectly to the stress gradient by using a proportional relation between the sliding zone width and the process volume size.

Other methods have been proposed that are not described here. One can quote the theory of critical distance [10,11], the critical layer [12] or the effective distance [13]. A review is proposed in Ref 14. These methods give reasonable results when dealing with simple geometry. However, most of these methods cannot be easily or directly applied to a different geometry or a more complex one.

Recently, an original formulation was proposed by Schwob [15] who studied the fatigue limit of plates with holes. Different plate width and hole diameter are studied which enable to capture stress gradient effect on fatigue limit. Using the Papadopoulos' approach, a non local multiaxial fatigue criterion is proposed which depends on stress state and stress gradient. Next, the mean value of the Papadopoulos' criterion is computed over this volume. This formulation predicts accurately the evolution of fatigue limit of plates with holes for different ratios of diameter/plate width. Moreover, the general formulation proposed by the authors enables to apply directly their formulation to other industrial problems.

This paper focuses on fatigue limit estimation of specimens featuring stress gradient. In particular, a special interest is given to partial slip fretting problem. A detailed numerical analysis of stress gradient for an Inconel 718 cylinder/plane contact under partial slip regime is first discussed. Next, a non local multiaxial fatigue criterion is proposed. The proposed criterion, which is purely phenomenological at this stage, was designed with great care to account for rotating bending trend and for dealing with constraints due to special fretting stress fields.

Experimental Crack Analysis of an Inconel 718/Inconel 718 Contact under Partial Slip Fretting Loading

Introduction to Fretting

Fretting is a damaging process occurring in the contact area between two parts. Fretting damage comes from small oscillatory displacements between these parts and it results in wear or cracks depending on the displacement amplitude. A usual fretting experimental set-up is introduced on Fig. 1(*a*).

In this study, we focused only on crack initiation, which occurs for small displacement amplitude. In the case of small oscillatory displacement, the contact is in a partial slip sliding regime: the contact area is split between a sticking

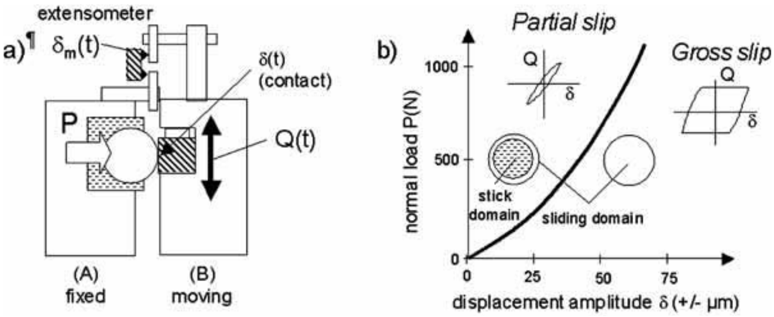

FIG. 1—(*a*) *Experimental fretting set-up;* (*b*) *fretting sliding regime as a function of displacement amplitude* δ *for a sphere/plane contact* [*16*].

area surrounded by a sliding area at the border of the contact area. On the contrary, in the case of large oscillatory displacement amplitude, the whole contact area is sliding and it results in wear (Fig. 1(*b*)). Wear does not appear during tests introduced in this study since all tests were performed in partial slip regime.

Usual tests of fretting consist of performing simple contact configurations such as cylinder/plane, sphere/plane or flat/plane contact. A normal load is usually kept constant to maintain contact and a tangential load is applied to generate the oscillatory motion. A detailed study of fretting damage process is described in Ref 16, including both wear and crack initiation analysis.

Material, Specimens, and Experimental Details

Fretting tests are performed with specimens made of Inconel 718, a Nickel base superalloy. The main mechanical properties are shown in Table 1. The two main properties are fatigue strength under tension-compression σ_{-1} and under alternated torsion τ_{-1}. The value of σ_{-1} is available in Ref 17. The alternated torsion fatigue strength was determined using the four fatigue strengths available in Ref 17 for the four load ratios ($R=-1$; $R=0.1$; $R=0.2$; $R=0.5$). The Papadopoulos multiaxial fatigue criterion is fitted on these values in order to find the fatigue limit under alternated torsion τ_{-1}.

The Papadopoulos multiaxial fatigue criterion is defined by

$$\sqrt{\langle T_a \rangle^2} + \alpha \cdot \sigma_{H,\max} < \beta \qquad (1)$$

where:

α and β=material parameters identified using for instance a tension-compression fatigue test and an alternated torsion fatigue test.

TABLE 1—*Inconel 718 mechanical properties* [*17*].

E (GPa)	ν	Ys (MPa)	UTS (MPa)	σ_{-1} (MPa)	τ_{-1} (MPa)
203	0.29	1034	1276	472	350

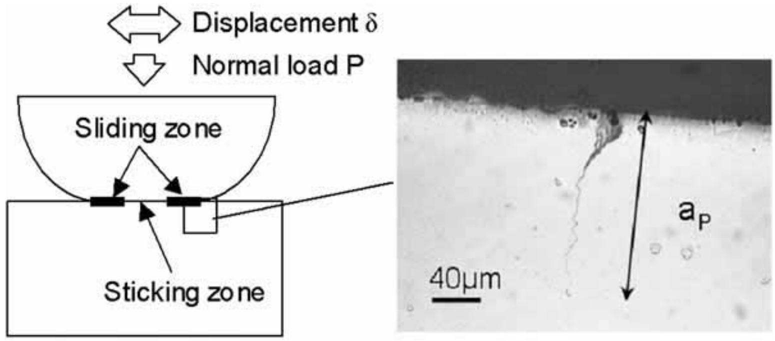

FIG. 2—*A crack in the Inconel 718 plane sample.*

Then, α and β are defined by

$$\alpha = 3 \cdot \tau_{-1}/\sigma_{-1} - \sqrt{3} \tag{2}$$

$$\beta = \tau_{-1} \tag{3}$$

The best set of parameters α and β fitting the data available in Ref 17 are introduced in Table 1.

The tests are performed using an 80 mm radius Inconel 718 cylinder pressed on Inconel 718 cubic specimens. Both surfaces were ground to achieve low shape defects and low roughness. Flatness and cylindricality defects are lower than 2 μm and roughness is characterized by Ra lower than 0.4 μm. These geometrical and roughness tolerances allow to reduce dispersion in crack initiation.

The normal forces have been adjusted to cover a large range of maximum pressure p_0. The ratio between the highest value of pressure p_0 and the lowest value is 2.3. The loading conditions are significantly lower than the yield stress of the Inconel 718 (Table 1). This ensures a consistent approach with the elastic assumption of the analytical model detailed later.

Moreover, the ratio $L/2a$ is kept higher than 5 to ensure a plane strain state in the middle of the contact. This also ensures a consistent approach with the analytical model.

All tests are interrupted at 10^5 cycles. It is supposed that high cycle fatigue criteria can be modified from infinite lifetime prediction to finite lifetime prediction simply by introducing instead of usual fatigue limits σ_{-1} and τ_{-1}, the fatigue strengths corresponding to the number of cycles to failure studied.

Crack initiation thresholds are identified for four normal loads. For each studied normal load, an iterative approach is applied consisting of adjusting the tangential force amplitude to bracket the crack initiation threshold. After the test, the plane is cut in the transversal direction, polished, and observed to check if cracks are initiated. The procedure is identical to those described in Ref 9. An optical microscopic analysis of the transversal section of a specimen is presented in Fig. 2.

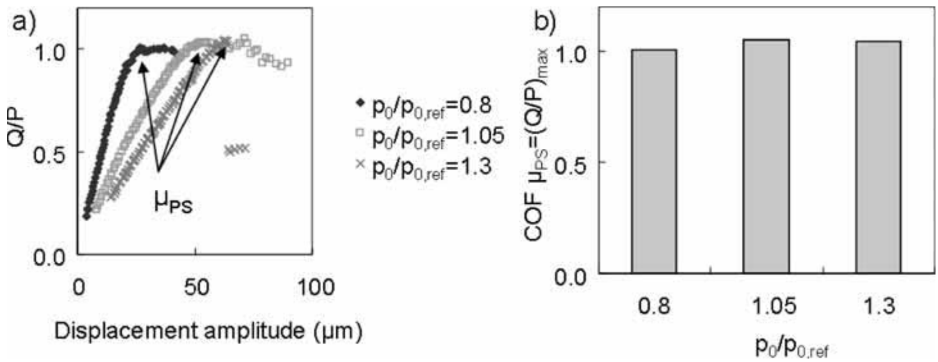

FIG. 3—(*a*) *Q/P ratio as recorded during variable amplitude tests performed on similar Inconel 718 cylinder/plane contact at 3 different maximum pressures p_0*; (*b*) *COF measured at the transition between partial slip and gross slip regime $\mu_{PS}=(Q/P)_{max}$.*

Results

Before studying crack initiation, the knowledge of the coefficient of friction (COF) of similar Inconel 718 contact is required. Variable displacement amplitude method is applied to identify the transition amplitude from partial to gross slip. The method consists of increasing step by step the displacement amplitude δ and to measure simultaneously the ratio Q/P. Proudhon et al. [18] demonstrated that the COF defined at the sliding transition (μ_t) is well representative of the friction operating in partial slip contacts (i.e., $\mu_{\mathrm{PS}}=\mu_t$). This latter variable is therefore applied to compute the stress fields under partial slip. The COF was measured at three different maximum pressures p_0 and the results (Fig. 3) show a very stable coefficient of friction at the transition partial slip/gross slip μ_{PS} close to 1.

Presently, the experimental results of cracking under partial slip are summed up in Fig. 4. The crack initiation threshold is plotted in a diagram $p_0/p_{0,\mathrm{ref}}$ versus $q_{0,\max}/p_{0,\mathrm{ref}}$. A sample is considered as cracked when the crack tip reaches a depth higher than 10 μm, $a_P=10$ μm. This threshold length was optimized in order to be small enough to characterize the incipient cracking process but long enough to avoid any misunderstanding with surface roughness discontinuities usually observed next to the sliding zone of the partial slip contact. These results give special fatigue limit since they correspond to fatigue limit of a specimen loaded with a non proportional tri-axial fatigue loading with high stress gradient. It is interesting to point that the crack initiation threshold is not very sensitive to the normal load since the border between the safe and unsafe region is nearly vertical.

Stress Gradient Analysis of Cylinder/Plane Contact under Partial Slip Regime

Stress Field Description

The pressure and shear distribution for a cylinder/plane contact under partial regime are illustrated in Fig. 5.

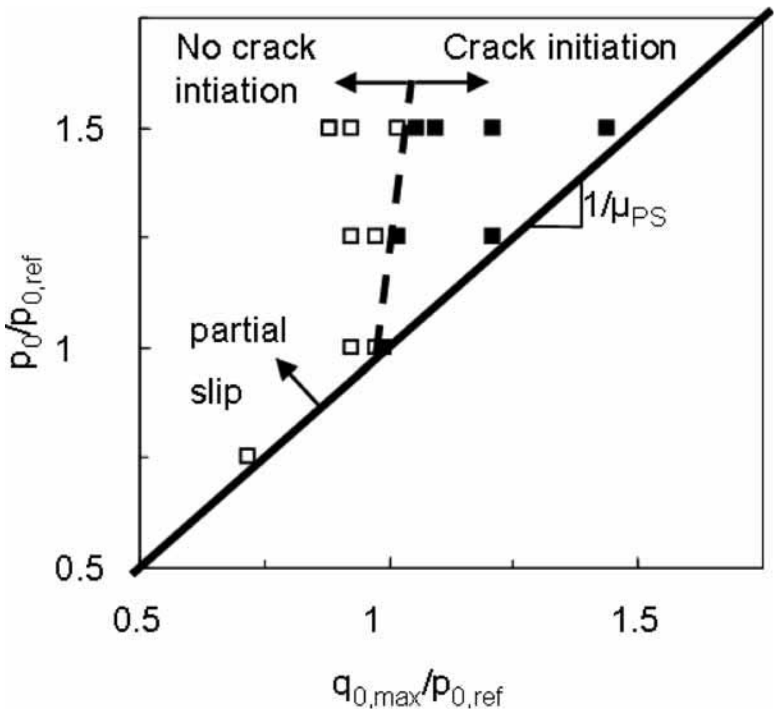

FIG. 4—*Experimental crack initiation thresholds plotted in a P-Q diagram.* □*: uncracked;* ■*: cracked.*

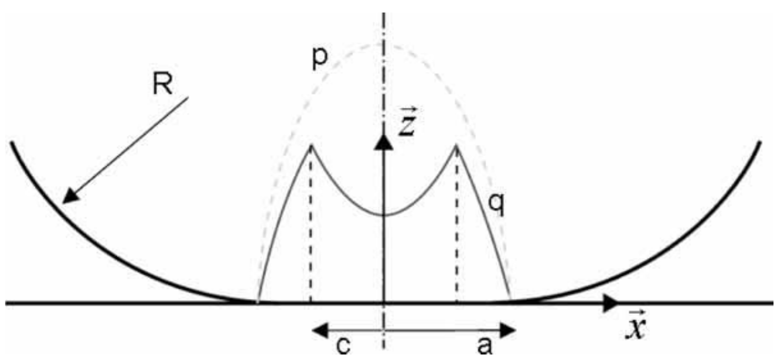

FIG. 5—*Pressure and shear surface tractions* (*a: contact width, c: stick zone width*).

The equations describing surface shear traction q under partial slip are known as the Mindlin-Cattaneo [19,20] solutions, whereas the surface pressure distribution p follows the Hertz theory

$$p(x) = -p_0\sqrt{1-\left(\frac{x}{a}\right)^2} \tag{4}$$

The maximum surface shear traction is defined by

$$\frac{q_{\max}(x)}{\mu p_0} = \begin{cases} \sqrt{1-\left(\frac{x}{a}\right)^2} - \frac{c}{a}\sqrt{1-\left(\frac{x}{c}\right)^2} & \left|\frac{x}{c}\right| < 1 \\ -\sqrt{1-\left(\frac{x}{a}\right)^2} & \text{else} \end{cases} \tag{5}$$

$$c = a\cdot\sqrt{1-\left|\frac{Q}{\mu\cdot P}\right|} \tag{6}$$

The time evolution of the surface shear traction is defined by

$$\frac{q(x)}{\mu p_0} = \begin{cases} -\sqrt{1-\left(\frac{x}{a}\right)^2} & c' < |x| < a \\ -\sqrt{1-\left(\frac{x}{a}\right)^2} + 2\frac{c'}{a}\sqrt{1-\left(\frac{x}{c'}\right)^2} & c < |x| < c' \\ -\sqrt{1-\left(\frac{x}{a}\right)^2} + 2\frac{c'}{a}\sqrt{1-\left(\frac{x}{c'}\right)^2} - \frac{c}{a}\sqrt{1-\left(\frac{x}{c}\right)^2} & |x| < c \end{cases} \tag{7}$$

$$c' = a\sqrt{1-\frac{Q_0-Q'}{2\mu P}} \tag{8}$$

and

$$Q' = Q_0\cdot\cos(\omega\cdot t) \tag{9}$$

The pressure distribution p is kept constant during a fretting test. On the contrary, the surface shear traction is a time dependent data since it depends on the tangential load Q. The time evolution of surface shear traction is described by Eqs 3 and 4 and is illustrated in Fig. 6.

These equations are of great relevance since the knowledge of the surface traction distributions allows computing the subsurface stress fields using elastic hypothesis. These results are presented in Ref 21. The subsurface stress field is defined by

$$\sigma_{xx}(x,z) = -\frac{2z}{\pi}\int_{-a}^{a}\frac{p(s)(x-s)^2ds}{((x-s)^2+z^2)^2} - \frac{2}{\pi}\int_{-a}^{a}\frac{q(s)(x-s)^3ds}{((x-s)^2+z^2)^2}$$

$$\sigma_{zz}(x,z) = -\frac{2z^3}{\pi}\int_{-a}^{a}\frac{p(s)ds}{((x-s)^2+z^2)^2} - \frac{2z^2}{\pi}\int_{-a}^{a}\frac{q(s)(x-s)ds}{((x-s)^2+z^2)^2}$$

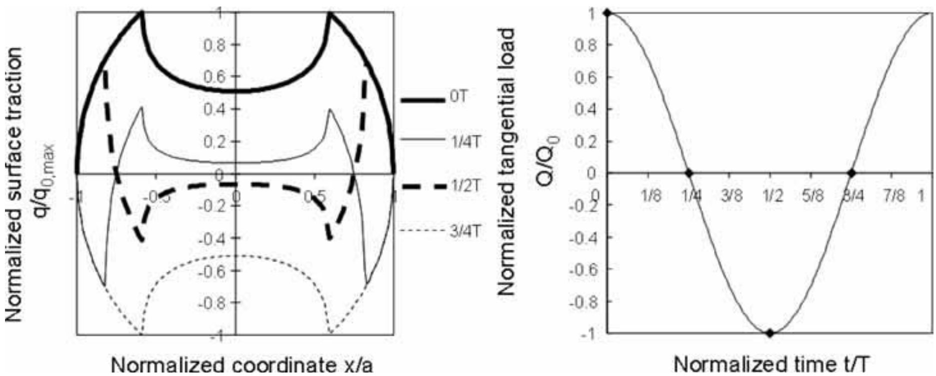

FIG. 6—*Normalized shear surface traction evolution over a period T.*

$$\sigma_{xz}(x,z) = -\frac{2z^2}{\pi}\int_{-a}^{a}\frac{p(s)(x-s)ds}{((x-s)^2+z^2)^2} - \frac{2z}{\pi}\int_{-a}^{a}\frac{q(s)(x-s)^2ds}{((x-s)^2+z^2)^2} \tag{10}$$

Figure 7 defines the parameters introduced in the Eq 9.

The analytical solution for a cylinder/plane contact under partial slip is implemented using the C++ programming language. The plane strain hypotheses are adopted to compute the full stress tensor

$$\bar{\bar{\sigma}} = \begin{pmatrix} \sigma_{xx} & 0 & \sigma_{xz} \\ 0 & \sigma_{yy} & 0 \\ \sigma_{xz} & 0 & \sigma_{zz} \end{pmatrix}$$

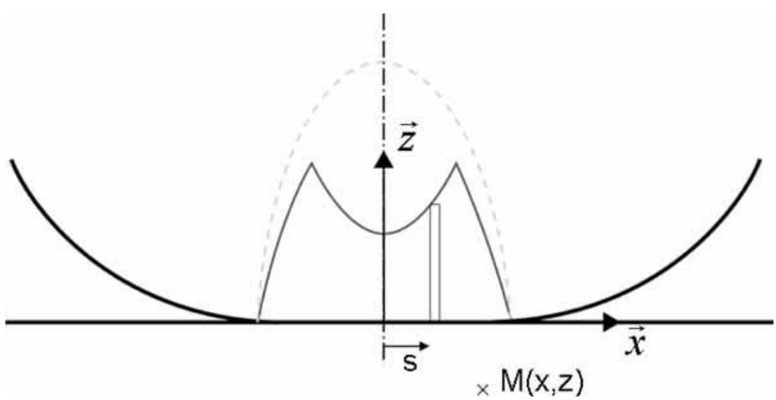

FIG. 7—*Description of parameters for integration of subsurface stress field computation.*

Stress Gradient Description

The analytical solution of a plane/cylinder contact under partial slip is used to study stress gradients. These results are presented in this section. The stress gradient analysis is carried out using the modulus of the gradient vector of:

- The maximum hydrostatic pressure over a period, $\sigma_{H,\max}$; and
- The maximum amplitude over a period (fretting cycle, Fig. 6) of the resolved shear stress (RSS), $\tau_{a,\max}$.

The gradient of these data is defined by

$$\|\nabla\sigma_{H,\max}(x,y,z)\| = \sqrt{\left(\frac{\partial\sigma_{H,\max}}{\partial x}\right)^2 + \left(\frac{\partial\sigma_{H,\max}}{\partial y}\right)^2 + \left(\frac{\partial\sigma_{H,\max}}{\partial z}\right)^2} \tag{11}$$

$$\|\nabla\tau_{a,\max}(x,y,z)\| = \sqrt{\left(\frac{\partial\tau_{a,\max}}{\partial x}\right)^2 + \left(\frac{\partial\tau_{a,\max}}{\partial y}\right)^2 + \left(\frac{\partial\tau_{a,\max}}{\partial z}\right)^2} \tag{12}$$

The RSS is the shear stress acting on a plane defined by its normal $\vec{n}$ and along a line defined by the vector $\vec{m}$ which belongs to the plane defined by $\vec{n}$

$$\tau = \vec{n} \cdot \bar{\bar{\sigma}} \cdot \vec{m} \tag{13}$$

The RSS is therefore a spatial function but also a time function in the case of variable loadings. For each plane defined by the normal vector $\vec{n}$, one can compute the amplitude of the RSS τ_a which is defined as the radius of the minimum circumscribed circle to the load path defined by the tip of the vector

$$\vec{\tau} = \bar{\bar{\sigma}} \cdot \vec{n} - (\vec{n} \cdot \bar{\bar{\sigma}} \cdot \vec{m}) \cdot \vec{n} \tag{14}$$

By computing the RSS amplitude τ_a for each plane, one defines the maximum value of the RSS amplitude $\tau_{a,\max}$. Details on the computation of the shear stress amplitude are available in Ref 22.

The analysis of the RSS gradient and the hydrostatic pressure gradient confirms the trends suggested by the derivative of the pressure and shear distribution. The derivatives of the pressure and shear distribution show two discontinuities at the point $x=c$ and $x=a$ with an infinite limit around these two points. The expressions of the partial derivative of the pressure and shear distribution are

$$\frac{1}{p_0}\frac{dp}{dx} = \frac{x}{a^2\sqrt{1-\left(\frac{x}{a}\right)^2}} \tag{15}$$

$$\frac{1}{\mu p_0}\frac{dq_{\max}}{dx}=\begin{cases}-\dfrac{x}{a^2\sqrt{1-\left(\dfrac{x}{a}\right)^2}}+\dfrac{x}{ac\sqrt{1-\left(\dfrac{x}{c}\right)^2}} & \left|\dfrac{x}{c}\right|<1\\ -\dfrac{x}{a^2\sqrt{1-\left(\dfrac{x}{a}\right)^2}} & \left|\dfrac{x}{c}\right|\geq 1\end{cases} \tag{16}$$

Therefore it appears clearly that

$$\lim_{x\to a}\frac{dp}{dx}=\infty \tag{17}$$

and

$$\begin{cases}\lim\limits_{x\to a}\dfrac{dq_{\max}}{dx}=\infty\\ \lim\limits_{x\to c}\dfrac{dq_{\max}}{dx}=\infty\end{cases} \tag{18}$$

In order to confirm this point, the gradients of the subsurface stress fields, especially $\sigma_{H,\max}$ and $\tau_{a,\max}$, are studied. The results are illustrated in Fig. 8. The gradients of $\sigma_{H,\max}$ and $\tau_{a,\max}$, i.e., G_σ and $G_{\tau a}$, also exhibit a divergent trend at the transition between the sticking and the sliding areas as well as at the contact border. Although that there is still no proof of the divergent behavior of stress gradients, both the surface traction analysis and the substress field analysis exhibit clear divergent trends.

In order to illustrate the stress gradient effect, the Dang Van and the Papadopoulos criteria are applied to the cylinder/plane problem under partial slip regime. The Dang Van criterion is defined by

$$\tau_a+\alpha'\cdot\sigma_H<\beta' \tag{19}$$

where:

α' and β' = two materials parameters specific to this criterion.

The Papadopoulos criterion is defined in Eq 1.

The Papadopoulos/Panoskaltsis proposal for bending tests is also applied. Due to high stress gradient close to surface, this proposal reduces to the inequality

$$\sqrt{J_{2,a}}<\tau_{-1} \tag{20}$$

Since fretting results in non proportional loading, the Papadopoulos/Panoskaltsis is modified to take advantage of the Papadopoulos criterion introducing the root mean square of the RSS amplitude noted $\sqrt{\langle T_a\rangle^2}$. Details on the computation of $\sqrt{\langle T_a\rangle^2}$ are available in Ref 2. Therefore, in case of high stress gradient, the modified Papadopoulos/Panoskaltsis reduces to

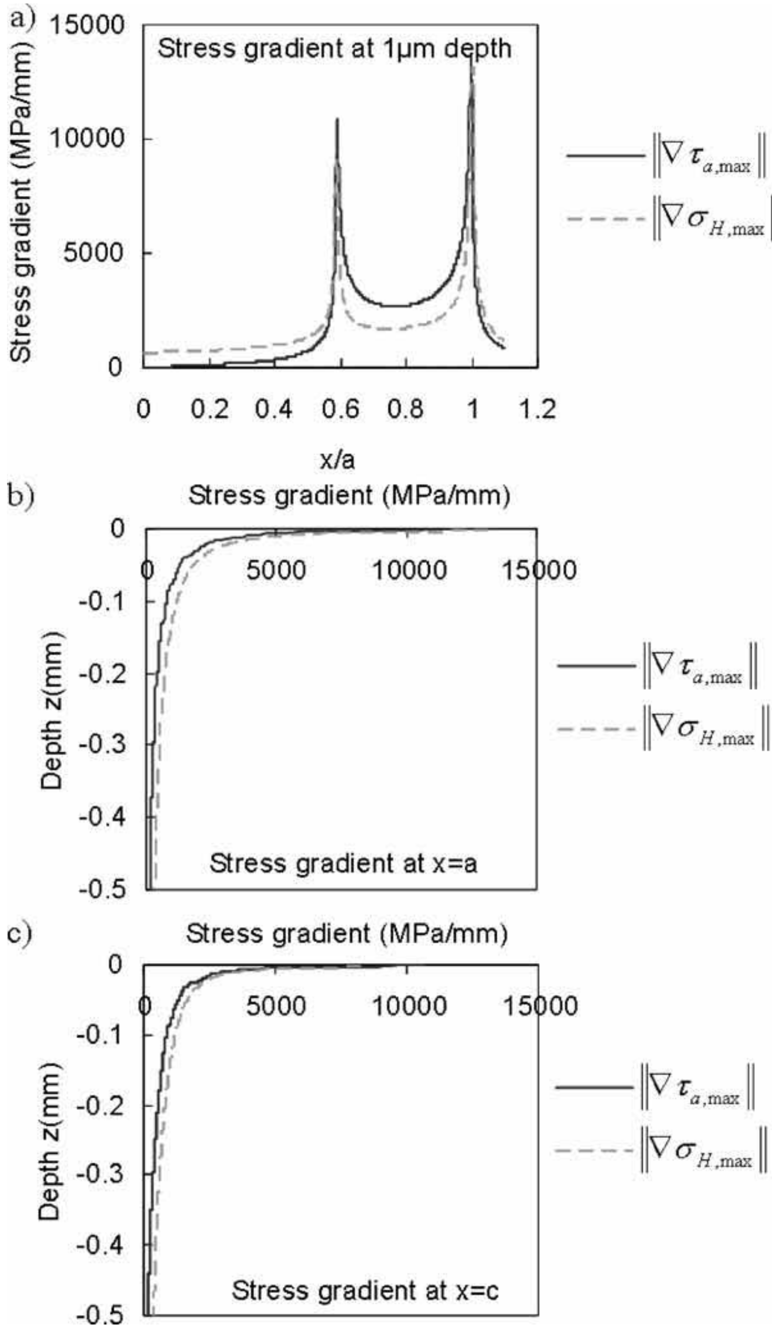

FIG. 8—(*a*) *Stress gradients* 1 μm *depth;* (*b*) *stress gradients at* $x = a$; *and* (*c*) *stress gradients at* $x = c$.

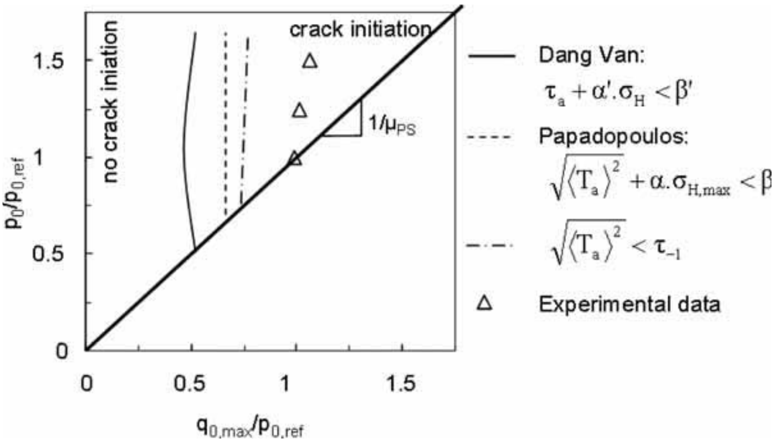

FIG. 9—*Crack initiation thresholds predicted using local multiaxial fatigue criterion.*

$$\sqrt{\langle T_a \rangle^2} < \tau_{-1} \tag{21}$$

The application of local multiaxial fatigue criteria confirms that a stress gradient superposed on a local stress state increases the fatigue limit. This fact results in largely conservative estimates of fatigue limit when local criteria are applied to components featuring stress gradients. This experimental result is confirmed in Fig. 9. None of these formulations are able to predict the experimental crack initiation boundary.

A second interesting fact results in the very conservative fatigue limit predicted by the root mean square of the amplitude of the RSS $\sqrt{\langle T_a \rangle^2}$. The result shows that the Papadopoulos/Panoskaltsis approach developed for rotating bending tests cannot predict reliable fatigue limit when applied to fretting. Therefore, in the case of a similar approach, a weight function should also be applied to the deviatoric component of the stress tensor. This fact is interesting since it is opposed to a rather well-established idea based which is that stress gradient does not affect the shear strength. The hypothesis is based on the comparison of fatigue limit based on torsion tests with and without mean shear stress. These results quoted by Papadopoulos in Ref 6 show that a mean value of shear stress does not affect the fatigue limit. However, the mean value of shear stress impacts directly on the shear stress gradient. Then, the hypothesis is that shear stress gradient does not affect the fatigue limit. This explanation is at the origin of the Papadopoulos/Panoskaltsis formulation with a weight function depending on the gradient of the hydrostatic pressure applied only to the maximum value of the hydrostatic pressure.

Although the results presented previously do not allow a definite conclusion, they suggest that both hydrostatic pressure stress gradient and shear stress gradient should be considered. The results published by Bertolino in Ref 23 support this idea.

Introduction of an Alternative Weight Function for Multiaxial Fatigue Criteria

Several interesting facts were pointed out in the previous sections. These points are summarized at the beginning of this section and are at the root of an alternative phenomenological proposal for a multiaxial fatigue criterion.

Important Facts

- Rotating bending—the rotating bending test is interesting since it results in a constant stress gradient all over the specimen section. Experimental results show that specimens with large radius have lower fatigue limit. Besides, large radius results in low gradient. On the contrary, specimens with small radius have high fatigue limit. Besides, small radius results in high gradient. These results suggest that, for an equivalent pointwise maximum stress, the higher the stress gradient the higher the fatigue limit; and
- Stress gradient in partial slip—the analysis of the stress gradient for a cylinder/plane under partial slip shows that stress gradients have divergent trends close to the surface. This results in the fact that the Papadopoulos/Panoskaltsis proposal predicts largely conservative fatigue limit. This suggests that the weight function should also be applied to the deviatoric part of the stress tensor.

It is worth noting that due to infinite stress gradient close to surface, a local multiaxial fatigue criterion such as the one proposed by Papadopoulos/Panoskaltsis would not predict differences between contact configurations (such as cylinder/plane contact with different radius).

Non Local Multiaxial Fatigue Criterion Proposal

The proposal is developed using the following structure

$$\text{crit} \times \bar{w} < \beta \tag{22}$$

where:

crit = local multiaxial fatigue criterion (Crossland, Dang-Van for instance),
$\bar{w}$ = mean value of the weight function w, and
β = material parameter.

The local multiaxial fatigue criterion chosen is the Papadopoulos criterion

$$\sqrt{\langle T_a \rangle^2} + \alpha \cdot \sigma_{H,\max} < \beta \tag{23}$$

The weight function w applied to the criterion must verify the following points:

- w must be a decreasing function of the stress gradient (since the fatigue limit is lower for specimen with bigger radius); and
- w must be equal to 1 when the stress gradient is 0.

The formulation proposed is (Fig. 10)

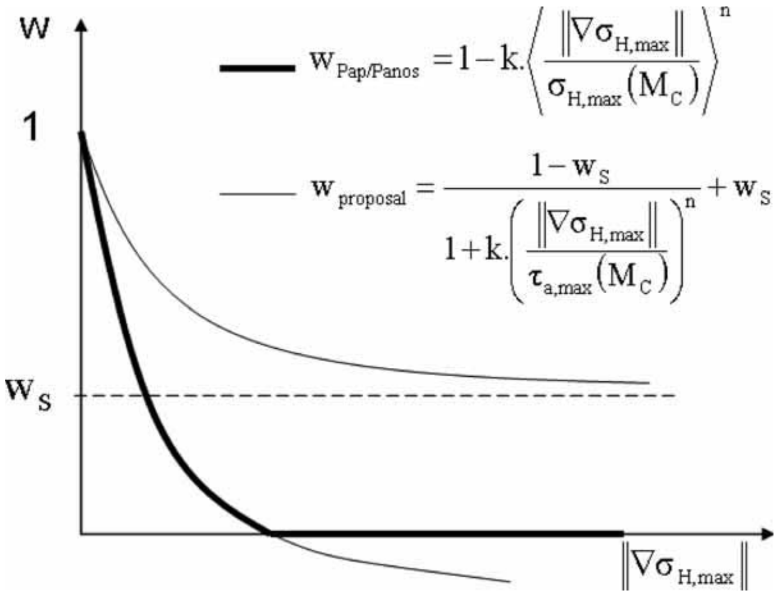

FIG. 10—*Comparison of the weight functions. Thin line: proposal. Bold line: Papadopoulos/Panoskaltsis proposal* [*6*].

$$w = \frac{1 - w_S}{1 + k \cdot \left(\frac{\|\nabla \sigma_{H,\max}\|}{\tau_{a,\max}(M_C)} \right)^n} + w_S \tag{24}$$

where:

$\|\nabla \sigma_{H,\max}\|$ = gradient of the maximum value of the hydrostatic pressure over a period, and

$\tau_{a,\max}(M_C)$ = maximum value over a period of the RSS amplitude at the maximum loaded point M_C in terms of the Papadopoulos criterion.

The local multiaxial fatigue criterion chosen is the Papadopoulos criterion

$$\sqrt{\langle T_a \rangle^2} + \alpha \cdot \sigma_{H,\max} < \beta \tag{25}$$

The proposition is based on the following assumptions:

- The hydrostatic stress gradient delayed the crack initiation: Introduction of $\|\nabla \sigma_{H,\max}\|$;
- There exists a threshold below which the stress gradient does not delay crack initiation anymore: w_S (i.e., the crack initiation risk cannot be suppressed by very high stress gradient); and
- The introduction of $\tau_{a,\max}$ allows to avoid division by 0 in the case of pure torsion test (Fig. 10).

The benefits of the formulation are:

- The derivative of the weight function is continuous. There is no need to use the McCauley brackets to keep the weight function positive; and

- The weight function introduces a threshold value w_S which illustrates that stress gradient cannot anneal the crack initiation resulting from stress state.

Since the weight function converges to w_S and the stress gradient under partial slip exhibits infinite values close to surface, the maximum value of the stress gradient cannot be used in the weight function. Then a volume V is defined to compute the mean value of the weight function over this volume. This volume is associated to the volume participating in the damage and it is defined by

$$V = \{M, \tau_{a,\max}(M) > C\} \tag{26}$$

where:

M = point of the structure, and

C = new parameter.

Since, the shear stress is well-known for driving initiation process at micro-scale, the damaged volume is defined as the volume over which the amplitude of the RSS is higher than a constant value C which is supposed to be a material parameter.

Finally, the formulation of the proposal is

$$\begin{cases} \left(\sqrt{\langle T_a \rangle^2} + \alpha \cdot \sigma_{H,\max}\right) \cdot \dfrac{1}{V} \displaystyle\int\int\int_V \left(\dfrac{1 - w_S}{1 + k\left(\dfrac{\|\nabla \sigma_{H,\max}\|}{\tau_{a,\max}(M_C)}\right)^n} + w_S \right) \cdot dV < \beta \\ V = \{M, \tau_{a,\max} > C\} \end{cases} \tag{27}$$

Application to Basic Fatigue Loadings

Tension-Compression—In the case of plain tension-compression fatigue test characterized by a zero mean stress and a stress amplitude σ_a, the stress gradient is zero, thus

$$\|\nabla \sigma_{H,\max}\| = 0 \tag{28}$$

and

$$\tau_a(M_C) = \frac{\sigma_a}{2} \tag{29}$$

The weight function is therefore

$$w = \frac{1 - w_S}{1 + 0} + w_S = 1 \tag{30}$$

The proposed criterion reduces to the usual Papadopoulos criterion

$$\frac{\sigma_a}{\sqrt{3}} + \alpha \cdot \frac{\sigma_a}{3} < \beta \tag{31}$$

Alternated Torsion—For a uniaxial alternated torsion test, $\tau_m = 0$ and the

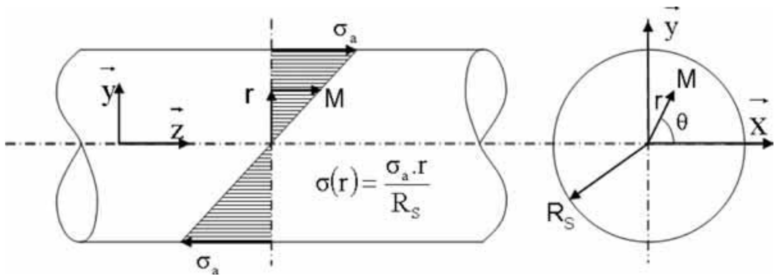

FIG. 11—*Four-point rotating bending stress field description.*

shear stress amplitude is τ_a.

Since the hydrostatic pressure is zero, it leads to

$$\|\nabla \sigma_{H,\max}\| = 0 \tag{32}$$

and

$$\tau_a(M_C) = \tau_a \tag{33}$$

The weight function in pure alternated torsion is the same as in tension-compression

$$w = \frac{1 - w_S}{1 + 0} + w_S = 1 \tag{34}$$

The criterion reduces to

$$\tau_a < \beta \tag{35}$$

Tension-compression and alternated torsion tests allow to identify the α and β parameters

$$\alpha = 3\frac{\tau_{-1}}{\sigma_{-1}} - \sqrt{3}$$

$$\beta = \tau_{-1} \tag{36}$$

It is worth noting that the formulation is such that the proposal reverts to the usual Papadopoulos criterion for these loads.

Rotating Bending—As mentioned previously, the stress gradient induced by a four-point rotating bending is constant over the whole specimen section (Fig. 11). The maximum normal stress amplitude in bending is at the surface of the specimen and is named σ_a and the stress in the section is defined by

$$\sigma(r) = \frac{\sigma_a \cdot r}{R_S} \tag{37}$$

It results in

$$\|\nabla \sigma_{H,\max}\| = \frac{\sigma_a}{3R_S} \tag{38}$$

and

$$\tau_a(M_C) = \frac{\sigma_a}{2} \tag{39}$$

The weight function is constant in the whole specimen section. Therefore the criterion does not depend on the definition of the volume V

$$\left(\frac{\sigma_a}{\sqrt{3}} + \alpha \cdot \frac{\sigma_a}{3}\right)\left(\frac{1 - w_S}{1 + k \cdot \left(\frac{2}{3R_S}\right)^n} + w_S\right) < \beta \tag{40}$$

The resolution of the previous equation gives the fatigue limit in four-point rotating bending

$$\sigma_{b-1} = \frac{\sigma_{-1}\left(1 + k \cdot \left(\frac{2}{3R_S}\right)^n\right)}{1 + w_S \cdot k \cdot \left(\frac{2}{3R_S}\right)^n} \tag{41}$$

The rotating bending fatigue limit is a function of specimen radius which means that the proposal is able to account for a kind of stress gradient effect.

Comparison with the Papadopoulos/Panoskaltsis Criterion

It is interesting to point out differences with the Papadopoulos/Panoskaltsis proposal. The latter proposal is defined by

$$\sqrt{J_{2,a}} + \alpha \cdot \sigma_{H,\max} \cdot \left(1 - k \cdot \left\langle \frac{\|\nabla \sigma_{H,\max}\|}{\sigma_{H,\max}} \right\rangle^n\right) < \beta \tag{42}$$

The resulting fatigue limit under four-point rotating bending is

$$\sigma_{b-1} = \frac{\sigma_{-1}}{1 - \left(1 - \frac{\sigma_{-1}}{\tau_{-1} \cdot \sqrt{3}}\right)\frac{k}{R_S^n}} \tag{43}$$

Figure 12 illustrates the two proposals. The two formulations have in common:

- To predict a decreasing fatigue limit with increasing specimen radius; and
- To converge to the tension-compression fatigue limit σ_{-1}.

However, the formulations do not predict the same trend for small radius specimens. In the case of $n > 0$, the Papadopoulos/Panoskaltsis criterion shows a discontinuity for $R_S = R_S^*$. At this point $R_S = R_S^*$ the fatigue limit reaches positive infinity for $R_S > R_S^*$

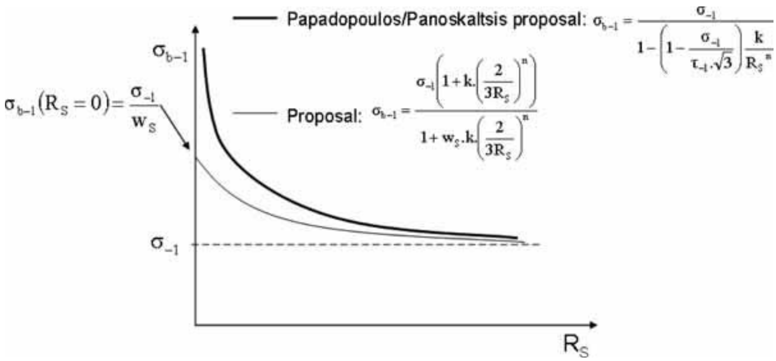

FIG. 12—*Comparison of four-point rotating bending fatigue limit between Papadopoulos/Panoskaltsis proposal and the new proposal.*

$$\lim_{R_S \to R_S^{*+}} \sigma_{b-1,\text{Pap/Pan}} = +\infty \tag{44}$$

On the contrary, the current proposal is continuous for $R_S > 0$ and it predicts a fatigue limit converging to a finite value

$$\lim_{R \to 0} \sigma_{b-1} = \frac{\sigma_{-1}}{w_S} \tag{45}$$

This point is a significant difference, but insufficient data are available to validate one or another trend. Rotating bending tests with specimen with small diameter may help to assess this difference.

Application to Fretting

Identification of Model Parameters—The previous analysis concludes that fatigue parameters (i.e., α and β) can be addressed combining tension-compression and torsion fatigue tests, whereas the other parameters implied by the "stress gradient weight function" approach (i.e., w_S, k, n, and C) require a specific fatigue analysis involving several rotating bending fatigue data obtained on different specimen diameters.

The studied Inconel 718 alloy displays all the conventional fatigue properties so both α and β can be computed. Using the fatigue data compiled in Table 1, one gets $\alpha = 0.49$ and $\beta = 350$ MPa.

Unfortunately, no rotating bending data obtained for various cylinder radii have been found for this specific alloy. This prevents us from a direct calibration of the stress gradient function. To alleviate this difficulty, the following strategy was applied: An analysis of rotating bending data published by various authors show that the mean fatigue limit variation in a radius range from 5 to 15 mm is about 10 % of the tension-compression fatigue limit σ_{-1}. Therefore, it is supposed that Inconel 718 has a behavior close to the mean behavior analyzed in the literature and the weight function parameters are identified to

TABLE 2—*Data from Pavan et al.* [5] *of rotating bending tests on a 35 % carbon steel.*

R (mm)	4	8	16	22
σ_{b-1} (MPa)	260	247	224	230

produce a similar trend.

The w_S, k, and n parameters of the weight function are identified and the same values are used for Inconel 718.

The data used to calibrate the model parameters are in the Table 2. A good fitting to the Pavan et al. data is reached with the following values (Fig. 13(*a*)):

$$w_S = 0.6$$

$$k = 3$$

$$n = 1$$

Since no data of rotating bending are available for Inconel 718, the weight function parameters are identified to produce a meaningful trend (Fig. 13(*b*)).

It appears that the exponent n does not seem to be necessary, which reduces the number of parameters to two instead of three. The total number of parameters is then five:

- α and β, the local multiaxial fatigue criterion parameters identified with a tension-compression and an alternated torsion test;
- k and w_S, the weight function parameters identified using at least two bending tests; and
- C, the volume parameter identified using one fretting test.

Application to Crack Initiation Prediction in Fretting—The experimental crack initiation thresholds identified are compared to the model prediction. To estimate the stability of the approach, the gap between prediction and experimental results is defined by an error E

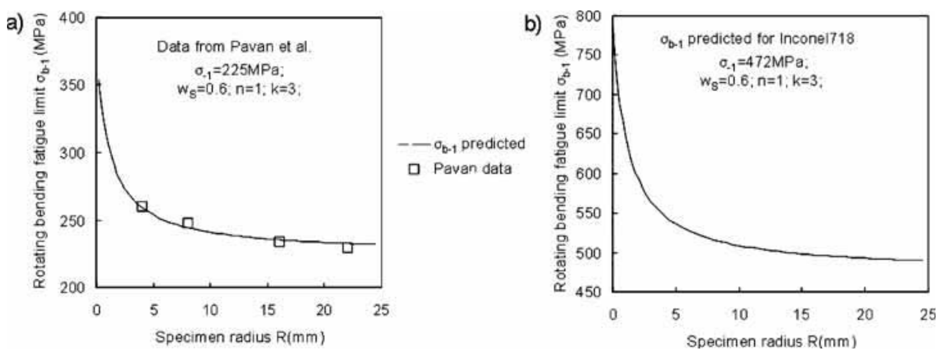

FIG. 13—(*a*) *Identification of weight function parameters using Pavan et al. data* [5]*;* (*b*) *prediction of rotating bending fatigue limit on Inconel 718.*

$$E = \frac{|\mathrm{NLC} - \beta|}{\beta} \tag{46}$$

where:

NLC = non local criterion computed using experimental crack initiation threshold

$$\mathrm{NL}C = \left(\sqrt{\langle T_a \rangle^2} + \alpha \cdot \sigma_{H,\max}\right) \cdot \frac{1}{V} \int\int\int_V \left(\frac{1 - w_S}{1 + k\left(\frac{\|\nabla \sigma_{H,\max}\|}{\tau_a(M_C)}\right)^n} + w_S \right) \cdot dV \tag{47}$$

The last parameter C, which is supposed to be a material constant, requires an experimental result featuring a non constant stress gradient to be calibrated. One solution consists of calibrating this parameter using a fretting crack initiation condition identified previously. Hence this value is determined from the crack initiation threshold found at $P = 4535N$ and $Q = 3000N$. Due to confidentiality reasons, the value of the parameter C is not mentioned.

The calibration procedure needs to be revised in the future, by using a simple experiment and not a fretting test, to demonstrate that the approach is robust with respect to the calibration tests. Numerous approaches would indeed work well if calibrated on the same type of experiments as the ones selected for prediction, and the transfer from one type of test to another is ultimately the appropriate target.

Presently, all the five variables required for the non local multiaxial fatigue description are identified. Therefore, the experimental fretting crack initiation thresholds obtained for various pressure conditions and consequently in various stress gradient states are compared to numerical boundary predicted by the model. Figure 14 confirms a good correlation. Although the studied pressure range is large, the theoretical prediction provides a good fitting with experimental results.

Because the parameter C is defined for the intermediate pressure situation $P = 4535N$, the error associated to this normal load is obviously zero. However for the other pressure situation the error is systematically lower than 5 % which confirms the stability of the approach.

Discussion

The proposal, which is purely phenomenological, is built analyzing macro-scale data. It does not bring any physical explanations about the stress gradient effect but it is devised to be in accordance with various experimental data of fatigue tests featuring stress gradient: rotating bending tests and fretting tests. The approach adopted consists of analyzing data such as crack initiation thresholds close to the grain scale, and to interpret them in the general framework of continuum mechanics and isotropy.

On the contrary, a micro-scale approach which aims to describe true physical mechanisms at the grain scale is adopted by Bertolino in Ref 23. The author models a material at the grain scale using electron backscattered diffraction data. A crystal anisotropic elastoplastic constitutive law with a linear kinematic

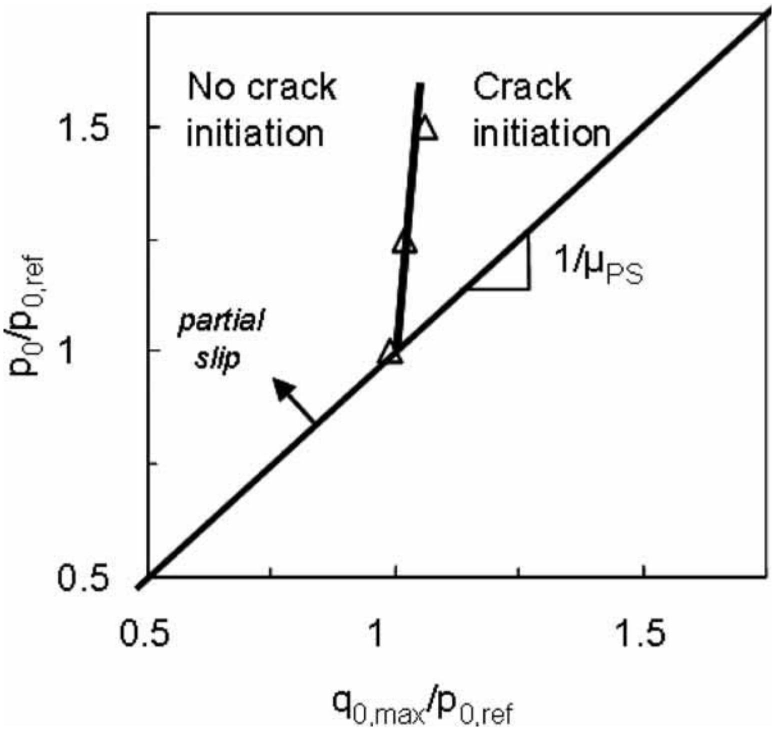

FIG. 14—*Comparison between numerical and experimental crack initiation boundary of the Inconel 718 submitted to partial slip fretting loadings plotted in a P-Q_0 diagram; △: experimental crack initiation threshold (Table 2); —: theoretical boundary based on the Papadopoulos criterion and the proposed weight function (α=0.49, β=350 MPa, n=1, w_S=0.6, k=3).*

hardening is attributed to each grain which accounts for grain orientation. The author imposed on the structure a linear load distribution to simulate a bending test. The author shows that the increase of stress gradient for a given maximum stress state reduces the stress of the hot spot i.e., the maximally loaded grain, and also the statistical occurrence of high stress state in unfavorably oriented grains. This means that the higher the stress gradient, the larger the gap between the homogeneous solution and the grain scale stresses. The increase of stress gradient also reduces the number of grains in elastic shakedown. As a consequence, the number of grains remaining in elastic condition increases.

Considering the macro-scale approach introduced in this paper, the interesting point of the Bertolino study is the decrease of the maximum stress in the maximally loaded grain. The gap regarding the stress state between the classical homogenization approach and the stress state at the grain scale (which accounts for grain lattice orientation) is larger when the stress gradient increases. The homogenization approach connected to the weight function introduced in this paper aims to describe this gap evolution by applying a weight factor to the stress state. This weight factor accounts in a phenomenological way for the surrounding stress gradient state around the maximally loaded point (the hotspot).

By analyzing the micro-scale modeling of Bertolino, the proposed approach seems relevant as a macro-scale approach. Presently, the goal is to propose an efficient weight function to deal with specific stress state (such very high stress gradient as discussed previously) for various applications such as notched specimens, fretting loadings or plates with holes.

A detailed analysis of stress gradient for a cylinder/plane contact in partial slip regime shows that the fretting stress field is highly demanding in terms of multiaxial fatigue criterion. Therefore, fretting appears as a good test for both multiaxial fatigue criteria. Fretting tests can be introduced as a complementary test to bending test. Bending tests produce low and constant stress gradient whereas fretting tests produce high and varied stress gradient.

Conclusions

This paper introduces a new non local multiaxial fatigue approach. The formulation is derived empirically by analyzing experimental data of rotating bending tests and cylinder/plane contact under partial slip regime.

Using various local multiaxial fatigue criteria to analyze fretting experiments, it is obvious that accurate fretting predictions based on independent experiments are difficult to obtain. Due to divergent stress gradient of cylinder/plane, the Papadopoulos/Panoskaltsis proposal which can be seen as a "semilocal" criterion, gives very conservative results.

From these observations, the proposed formulation is designed to account for the trends observed on rotating bending and fretting stress fields. The criterion is built as the product between a local value of multiaxial fatigue criterion and the mean value of a weight function. Although the parameters have not been independently calibrated yet, the weight function allows realistic prediction of fatigue limit under rotating bending, and the volume introduced to compute the mean value of weight function allows to account for complex stress gradients since accurate predictions of crack initiation thresholds for a cylinder/plane contact under partial slip are obtained. Further experimental work is needed to assess the robustness of the formulation with respect to the calibration tests.

References

[1] Papadopoulos, I. V., "A New Criterion of Fatigue Strength for Out-of-Phase Bending and Torsion of Hard Metals," *Fatigue*, Vol. 16, 1994, pp. 337–384.

[2] Papadopoulos, I. V., "A High-Cycle Fatigue Criterion Applied in Biaxial and Triaxial Out-of-Phase Stress Conditions," *Fatigue Fract. Eng. Mater. Struct.*, Vol. 18, 1995, pp. 79–91.

[3] Morel, F., Palin-Luc, T., and Froutey, C., "Comparative Study and Link Between Mesoscopic and Energetic Approaches in High Cycle Multiaxial Fatigue," *Int. J.*

Fatigue, Vol. 23, 2001, pp. 317–327.
[4] Pogoretskii, R. G. and Karpenko, G. V., "Effect of Test Piece Length on the Fatigue Limit of Steel in Air," *Fiziko-Khimicheskaya Mekhanika Materialov*, Vol. 1, 1965, pp. 90–94.
[5] Pavan, A., 1979, "Contribution to the Computation of the Fatigue Limits of Mechanical Components. Explanation of Main Reasons," Ph.D thesis, Université de Reims, Reims, France (in French).
[6] Papadopoulos, I. V., "Invariant Formulation of a Gradient Dependant Multiaxial High-Cycle Fatigue Criterion," *Eng. Fract. Mech.*, Vol. 55, 1996, pp. 513–528.
[7] Morel, F., Morel, A., and Nadot, Y., "Comparison Between Defects and Micro-Notches in Multiaxial Fatigue—The Size Effect and the Gradient Effect," *Int. J. Fatigue*, Vol. 31, 2009, pp. 263–275.
[8] Fouvry, S., Kapsa, P., Sidoroff, F., and Vincent, L., "Identification of the Characteristic Length Scale for Fatigue Cracking in Fretting Contacts," *J Phys IV France*, Vol. 8, 1998, pp. 159–166.
[9] Proudhon, H., Fouvry, S., and Yantio, G. R., "Determination and Prediction of the Fretting Crack Initiation: Introduction of the (P,Q,N) Representation and Definition of a Variable Process Volume," *Int. J. Fatigue*, Vol. 28, 2006, pp. 707–713.
[10] Taylor, D., "The Theory of Critical Distances," *Eng. Fract. Mech.*, Vol. 75, 2008, pp. 1696–1705.
[11] Susmel, L., "The Theory of Critical Distances: A Review of Its Applications in Fatigue," *Eng. Fract. Mech.*, Vol. 75, 2008, pp. 1706–1724.
[12] Flavenot, J.-F. and Skalli, N., "The Critical Layer Thickness or a New Approach for Fatigue Computation of Structures Under Multiaxial," *Revue Mécanique Matériaux Electricité*, Vol. 397, 1993, pp. 15–25 (in French).
[13] Qylafku, G., Azari, Z., Kadi, N., Gjonaj, M., and Pluvinage, G., "Application of a New Model Proposal for Fatigue Life Prediction on Notches and Key-Seats," *Int. J. Fatigue*, Vol. 21, 1999, pp. 753–760.
[14] Morel, F. and Palin-Luc, T., "A Non-Local Theory Applied to High Cycle Multiaxial Fatigue," *Fatigue Fract. Eng. Mater. Struct.*, Vol. 25, 2002, pp. 649–665.
[15] Schwob, C., 2007, "Non Local Probability Approach for the Fatigue Analysis of Areas Under Stress Gradients," Ph.D thesis, Université Paul Sabatier (Toulouse France) (in French).
[16] Fouvry, S., Kapsa, P., and Vincent, L., "Quantification of Fretting Damage," *Wear*, Vol. 200, 1996, pp. 186–205.
[17] USA Department of Defense, Federal Aviation Agency (FAA), *MIL-Handbook-5J: Metallic Materials and Elements for Aerospace Vehicle Structures*, FAA, 2003.
[18] Proudhon, H., Fouvry, S., and Buffière, J.-Y., "A Fretting Crack Initiation Prediction Taking into Account the Surface Roughness and the Crack Nucleation Process Volume," *Int. J. Fatigue*, Vol. 27, 2005, pp. 569–579.
[19] Mindlin, R. D. and Deresiewicz, H., "Elastic Spheres in Contact Under Varying Oblique Forces," *ASME Trans. J. Appl. Mech.*, Vol. 20, 1953, pp. 327–344.
[20] Cattaneo, C., "Get in Contact of Two Elastic Bodies: Local Distribution of Loads," *Rend. Accad. Naz. Lincei*, Vol. 6, 1938, pp. 343–348, 434–436, 474–478.
[21] Johnson, K. L., *Contact Mechanics*, Cambridge University Press, Cambridge, 1985.
[22] Papadopoulos, I. V., "Long Life Fatigue Under Multiaxial Loading," *Int. J. Fatigue*, Vol. 23, 2001, pp. 839–849.
[23] Bertolino, G., Constantinescu, A., Ferjani, M., and Treiber, P., "A Multiscale Approach of Fatigue and Shakedown for Notched Structures," *Theor. Appl. Fract. Mech.*, Vol. 48, 2007, pp. 141–151.

Reprinted from JAI, Vol. 7, No. 4
doi:10.1520/JAI102535
Available online at www.astm.org/JAI

C. Erny,[1] *D. Thévenet,*[2] *J. Y. Cognard,*[2] *and M. Korner*[3]

Experimental and Numerical Analyses of Fatigue Behavior of Welded Cruciform Joints

---

ABSTRACT: Ship structures are commonly assembled by using welding process. Due to the swell, all ships are submitted to some variable and complex loadings. The welding process creates specific geometries at the weld toe where local stress concentrations are generated and also creates various mechanical properties in the heat affected zone. Accordingly, welded joints could be a critical area for fatigue damage. In a previous work, a methodology to predict fatigue life has been developed and tested on butt-welded joints. To go further, the present work focuses on more complex assemblies in order to validate this strategy and be able to estimate the fatigue life of representative naval structures. First, the methodology consists of the elastic shakedown study and then of a post-treatment which predicts the fatigue crack initiation. A comparison between experimental and numerical results is proposed in order to present the accuracy of the proposed strategy to predict fatigue life time of welded assemblies typical of shipbuilding applications.

KEYWORDS: fatigue, welded joint, two-scale model, damage, crack initiation

---

Manuscript received May 19, 2009; accepted for publication March 2, 2010; published online April 2010.

[1] Laboratoire Brestois de Mécanique et des Systèmes (LBMS), EA 4325 ENSIETA, 2 rue François Verny, 29806 Brest Cedex 9, France and DCNS Ingénierie Navires Armés, rue Choiseul, 56311 Lorient Cedex, France.
[2] Laboratoire Brestois de Mécanique et des Systèmes, EA 4325 ENSIETA, 2 rue François Verny, 29806 Brest Cedex 9, France.
[3] DCNS Ingénierie Navires Armés, rue Choiseul, 56311 Lorient Cedex, France.

Cite as: Erny, C., Thévenet, D., Cognard, J. Y. and Korner, M., "Experimental and Numerical Analyses of Fatigue Behavior of Welded Cruciform Joints," *J. ASTM Intl.*, Vol. 7, No. 4. doi:10.1520/JAI102535.

Nomenclature

C, C_1, C_2 = kinematic hardening parameters
D = isotropic damage
D_c = critical damage
D_{1c} = critical damage (monotonic uniaxial tension)
E = Young modulus
f = yield function
H_v = Vickers hardness
h = micro-default closure parameter
$\underline{\underline{I}}$ = second-order identity tensor
J_2 = second invariant of stress tensor
m = non-linear exponent
N_i = fatigue crack initiation life
p = accumulated plastic strain
p_D = damage threshold
Q, b = isotropic hardening parameters
R = stress ratio
R_1 = isotropic hardening
S = damage strength
s = damage exponent
$\underline{\underline{X}}_1, \underline{\underline{X}}_2$ = kinematic hardening tensors
Y = strain elasticity energy density release rate
γ_1, γ_2 = kinematic hardening parameters
$\underline{\underline{\varepsilon}}$ = total strain tensor
$\underline{\underline{\varepsilon}}^e$ = elastic strain tensor
$\underline{\underline{\varepsilon}}^m$ = strain tensor in matrix
$\underline{\underline{\varepsilon}}^p$ = plastic strain tensor
ε_{pD} = damage threshold (monotonic uniaxial tension)
θ = weld toe angle
ν = Poisson coefficient
ρ = weld toe radius
$\sigma_{a\ \mathrm{nom}}$ = nominal stress amplitude
σ_f = fatigue limit (amplitude)
σ_u = ultimate strength
σ_y = yield strength
$\underline{\underline{\sigma}}$ = stress tensor
$\underline{\underline{\sigma}}^d$ = deviatoric part of $\underline{\underline{\sigma}}$
$\tilde{\underline{\underline{\sigma}}}$ = effective stress tensor
$\psi, \varphi_\infty, \omega$ = kinematic hardening parameter (Marquis model)

Introduction

In shipbuilding, welding is one of the most used assembly processes. The variations of geometry near the weld toe create some local stress concentrations and welding strongly affects the material by the process of heating and subsequent cooling. Moreover, all these assemblies are submitted to cyclic variable loading. Thus, fatigue failure appears in welded structures mostly at the weld rather than in other parts of the structure. In most cases, experimental observations point out that fatigue cracks initiate in weld toe. So, fatigue analyses are of high practical interest for all cyclically loaded welded structures and many authors [1–4] have already developed various models to predict fatigue life. Most of them take only into account the base metal (BM) but do not consider all the characteristics that appear due to the weld, i.e., the weld toe geometry, the material heterogeneity, and the residual stresses created due to the welding process itself. The global aim of this study is to propose a methodology which predicts fatigue life of welded assemblies and which could consider these specificities of welded assemblies.

In a previous study [5], a methodology has been developed and applied to butt-welded joints. A good correlation has been established between experimental fatigue life span and numerical fatigue life span. It seems fair to apply this strategy to other kind of assemblies more representative of shipbuilding applications. Thus, the aim of this current work is to adapt and improve this approach to more complex structures. First, some cruciform joints are considered and then this method will be applied on stiffened panels.

Strategy

The proposed strategy contains two stages: The structure shakedown study and the fatigue crack initiation study. The shakedown analysis is based on a finite element analysis (FEA) that takes constant or variable amplitude loading into account. This approach is based on the cyclic behavior of constitutive materials of the joint: BM, heat affected zone (HAZ), and melt metal (MM). In order to estimate and locate these different metals, some micro-hardness measurements have been done. These measurements have also been used to take into account the heterogeneity of mechanical properties through the joint. To have a better description of the weld, some monotonic and cyclic tests have been carried out on a simulated HAZ. The identified material parameters of the BM and the simulated HAZ are used to establish a relation which depends on the microhardness. To estimate the weld profile, some laser measurements have been done. If the structure shakedown occurs, i.e., that the behavior becomes elastic after a quite low time, a post-treatment can predict the period needed to initiate a fatigue crack. This calculation is based on a two-scale damage model initially developed by Lemaitre et al. [6]. A precise prediction of the life time requires an accurate numerical prediction of the elastic stabilized local loading at each point of the studied structure. Moreover, an accurate post-treatment is required. A comparison between experimental and numerical results is presented in order to underline the quality of the developed numerical strategy to predict fatigue life time of welded assemblies typical for shipbuilding applications.

Material Characterizations and Models

Both calculations (i.e., FEA and post-treatment), used in the proposed strategy, need an accurate knowledge of material parameters. Experimental tests have been done to identify these parameters.

Experiments

All welded samples used in this study were prepared with DH36 steel (DH36/BM). To characterize the material monotonic, cyclic, and fatigue behaviors, some tension-compression tests and some self-heating tests [7] have been performed on a servo-hydraulic testing machine with a capacity of 100 kN. All these tests were conducted using cylindrical specimens with a diameter of 8 mm and effective length of 12 mm.

Self-heating test is a method which allows a fast estimation of the high cycle fatigue properties: *S-N* curve and fatigue limit. It consists of applying successive series of cycles with different increasing stress amplitudes; at each step, the change of the temperature variation is measured and a significant increase is observed close to the fatigue limit. Thanks to this fatigue limit and fatigue life obtained for the last stress amplitude, the experimental *S-N* curve is obtained by using the Stromeyer's law.

Regarding the cyclic tests and self-heating tests, the applied stress ratios were $R=0.1$ and $R=-1$. In order to take into account the heterogeneity of the weld, all these tests were also performed on simulated HAZ (DH36/HAZ) in order to characterize this specific area of the weld. To obtain this simulated HAZ, a DH36 panel was heated at $1000\ ^\circ\mathrm{C}$ for 24 min and then it was cooled in oil. Unfortunately, the MM has not been characterized due to the difficulties to obtain specimens. Indeed, MM consists of a mix between the BM and the consumable electrode with a specific micro-structure due to the heating. Thereby, it seems quite difficult to reproduce this specific chemical composition and micro-structure in enough quantity to create some cylindrical specimens.

Constitutive Laws

For both metals, DH36/BM and DH36/HAZ, the monotonic and cyclic tests point out that there is a different yield strength depending if we consider the monotonic or the cyclic behavior, in particular, the cyclic yield strength is lower than the monotonic one (Figs. 1–4). Thus, the elastic-plastic model developed by Lemaitre and Chaboche [8,9] has been used to describe the monotonic and cyclic behavior of both metals. It consists of a combination of isotropic (R_1) and kinematic ($\underline{\underline{X}}_1, \underline{\underline{X}}_2$) hardenings. A classical Hooke's law is used to relate the elastic strain tensor $\underline{\underline{\varepsilon}}^e$ to the stress tensor $\underline{\underline{\sigma}}$

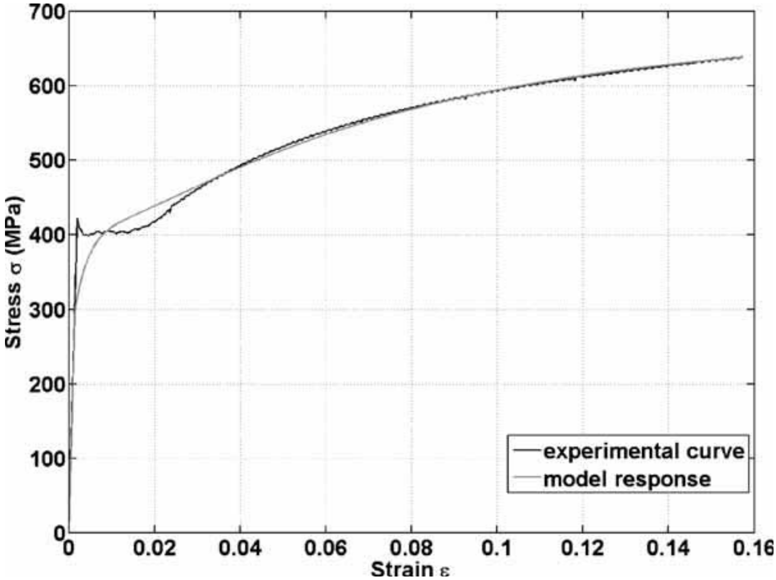

FIG. 1—*Comparison between experimental curve and model response: Monotonic tensile test (DH36/BM).*

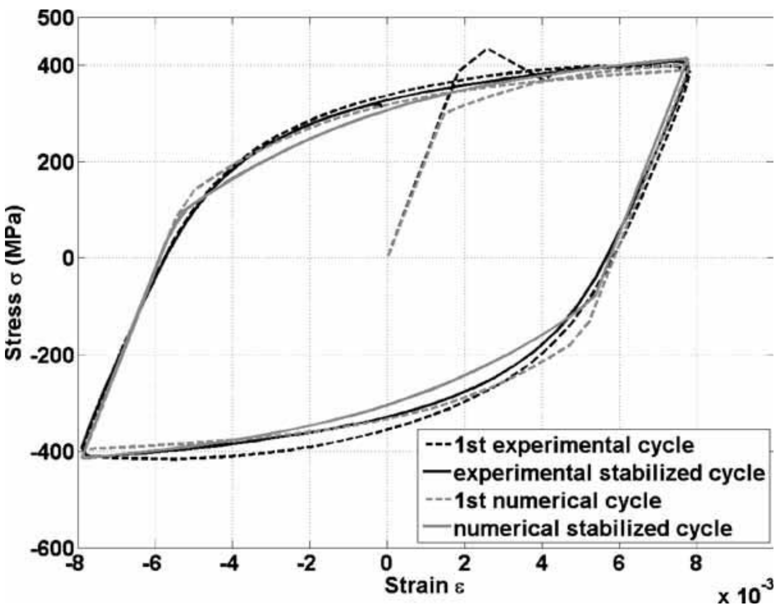

FIG. 2—*Comparison between experimental curve and model response: Cyclic tension-compression test* $\Delta\varepsilon$*=1.6 % (DH36/BM).*

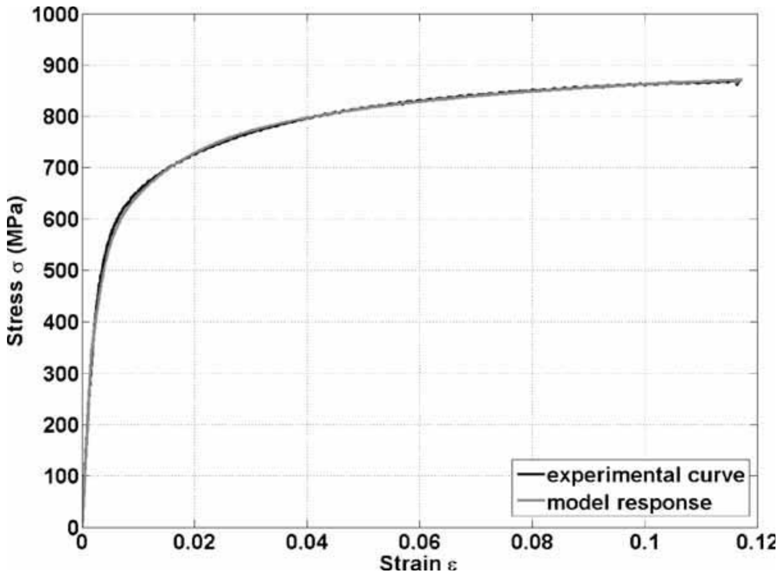

FIG. 3—*Comparison between experimental curve and model response: Monotonic tensile test (DH36/HAZ).*

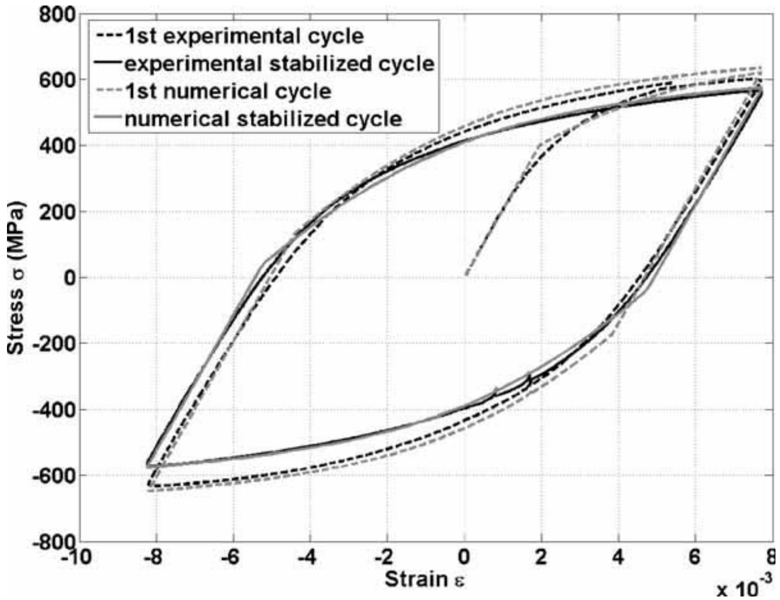

FIG. 4—*Comparison between experimental curve and model response: Cyclic tension-compression test Δε=1.6 % (DH36/HAZ).*

$$\underline{\underline{\varepsilon}}^e = \frac{1+\nu}{E}\underline{\underline{\sigma}} - \frac{\nu}{E}(\text{Tr } \underline{\underline{\sigma}})\underline{\underline{I}} \tag{1}$$

where:

E = elasticity modulus,

ν = Poisson's ratio, and

$\underline{\underline{I}}$ = second-order identity tensor.

The elastic domain is described by the yield criterion ($f \leq 0$)

$$f = J_2(\underline{\underline{\sigma}} - \underline{\underline{X}}_1 - \underline{\underline{X}}_2) - R - \sigma_y \leq 0 \tag{2}$$

where:

J_2 = second invariant of stress tensor, and

σ_y = yield strength.

The isotropic hardening is needed to allow the variation between the monotonic and the cyclic yield strength and its evolution law is defined by

$$\dot{R}_1 = b(Q - R_1)\dot{p} \tag{3}$$

where:

b and Q = material dependent parameters.

Two kinematic hardenings are useful to well describe the curvature of the loop. Moreover, the experimental cyclic tension-compression curves point out a softening, especially for DH36/HAZ (Fig. 4). To be able to model this phenomenon, the equations of the kinematic hardening $\underline{\underline{X}}_2$ are those developed by Marquis [10]. In this specific formulation, the parameter γ_2 takes into account the variation of the accumulated plastic strain p. The asymptotical value of kinematic hardening (C/γ) could change depending on the plastic strain evolution; i.e., at each loop the maximum value could be different from the previous cycle. Thus, the softening or the material hardening can be taken into account. The evolution laws can then be written such that

$$\dot{\underline{\underline{X}}}_1 = \frac{2}{3}C_1\dot{\underline{\underline{\varepsilon}}}^p - \gamma_1\dot{\underline{\underline{X}}}_1\dot{p} \tag{4}$$

$$\dot{\underline{\underline{X}}}_2 = \frac{2}{3}C_2\dot{\underline{\underline{\varepsilon}}}^p - \gamma_2(p)\dot{\underline{\underline{X}}}_2\dot{p} \tag{5}$$

$$\gamma_2(p) = \varphi_\infty + \psi e^{-wp} \tag{6}$$

where:

C_1, γ_1, C_2, ψ, and φ_∞ = some scalar material parameters.

The experimental curves have been used to identify all these parameters for DH36/BM (Figs. 1 and 2) and DH36/HAZ (Figs. 3 and 4). The method consists in researching the optimum parameters which minimize the difference between the experimental results and the model response. The obtained parameters are summarized in Table 1. Experimental and numerical results are presented in Figs. 1–4 and underline the accuracy of the proposed model.

TABLE 1—*Parameters of the elastic-plastic model.*

DH36	E	ν	σ_y (MPa)	b	Q (MPa)	C_1 (MPa)	γ_1	C_2 (MPa)	ω	φ_∞	ψ
/BM	205000	0.3	300	89	−50	4260	15.6	38300	10	252	106
/HAZ	205000	0.3	400	15	−100	8890	27.7	101300	10	418	19

Heterogeneity of Mechanical Properties

Due to the welding process, there is heterogeneity of mechanical properties through the joint (Fig. 5). In order to estimate this variation, some micro-hardness measurements (H_v) have been done on the welded profile by using a micro-hardness tester with a Vickers tip. The applied load is 1 N with a loading rate of 2 N/min. These measurements provide the two-dimensional (2D) hardness cartography and could be used to implement the micro-hardness field in the finite element calculation software. The identification process based on the experimental curves provides all the parameters of two specific areas of the joint where the micro-hardness is well-known: The BM ($H_v = 200$) and a simulated HAZ ($H_v = 275$). In this way a linear law was chosen to link the hardening parameters to the micro-hardness. Thus, each specific micro-hardness value is linked to a unique set of hardening parameters which defines the mechanical properties of a welded area. The knowledge of the micro-hardness field through the joint allows the introduction of variation of the mechanical properties in the finite element calculation (Fig. 6). Therefore, this methodology takes into account the fact that there are different metals in the welded joint.

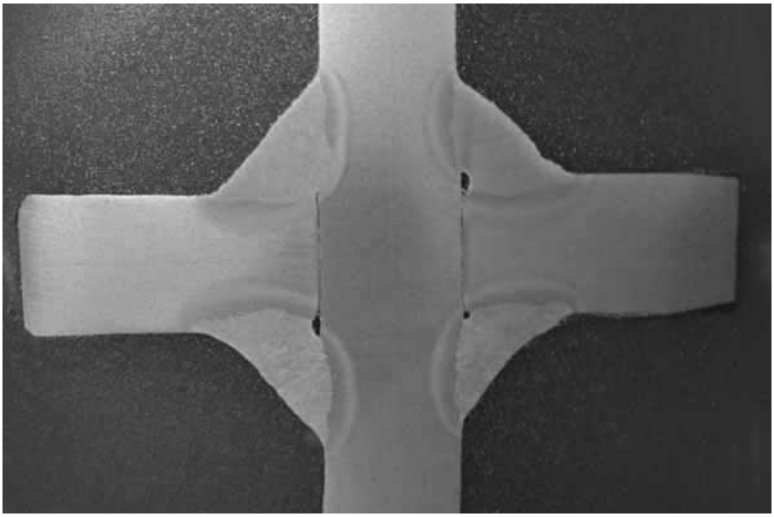

FIG. 5—*Cruciform joint profile* (t=*8 mm*).

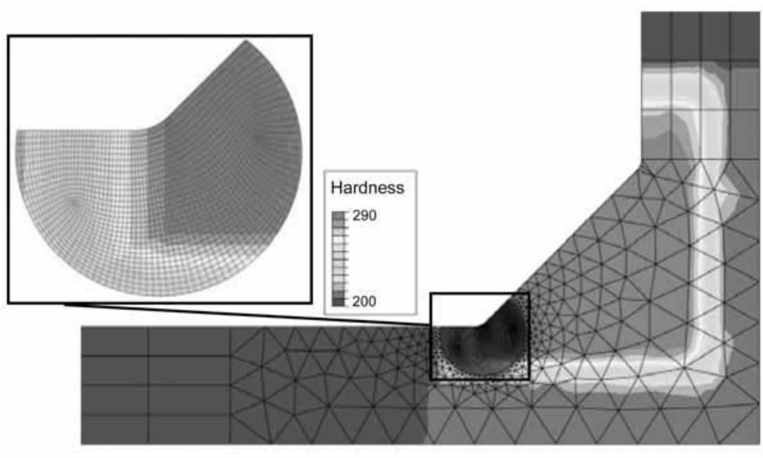

FIG. 6—*Mesh and micro-hardness field of a cruciform joint (1/4 sample).*

Two-Scale Damage Model

This study focuses on high cycle fatigue life. In this domain, the macroscopic behavior of the structure is elastic. The fatigue damage is due to micro-plasticity. Thus, to estimate the fatigue life span, a two-scale damage model is used. This model is based on the work developed by Lemaitre et al. [11]. To apply this model, the structure should have macroscopic elastic behavior. As a result, only the structure with an elastic shakedown behavior could be considered in the post-treatment. Indeed, a structure shakedown occurs when the plastic deformation takes place only during the first loading cycles and then due to residual stresses and hardening the behavior becomes perfectly elastic.

The elastic shakedown state is used at a macroscopic scale and the damaging elastic-plastic behavior is used at a microscopic scale. The model considers a representative volume element (RVE) made of an elastic matrix and an elastic-plastic inclusion which can suffer damage (Fig. 7). The inclusion considered in this two-scale model is a mechanical inclusion without physical size. The elastic matrix is used to describe the macroscopic elastic behavior of the structure. A Hooke's elasticity law (1) is used to describe this behavior.

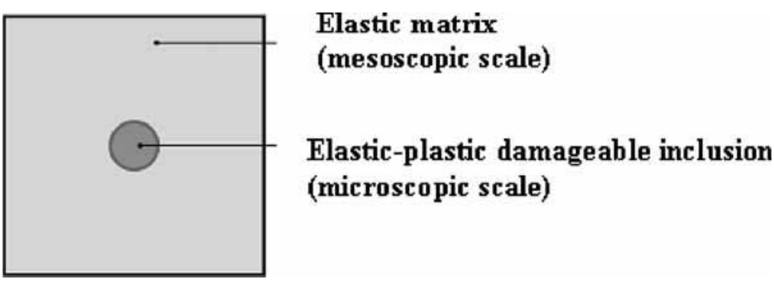

FIG. 7—*Scheme of the RVE.*

To link the elastic strain of the matrix to the elastic-plastic strain of the inclusion, a localization law is used

$$\underline{\underline{\varepsilon}} - \beta\underline{\underline{\varepsilon}}^p = \underline{\underline{\varepsilon}}^e + (1-\beta)\underline{\underline{\varepsilon}}^p = \underline{\underline{\varepsilon^m}} \tag{7}$$

$$\beta = \frac{2}{15}\frac{(4-5\nu)}{(1-\nu)} \tag{8}$$

where:

$\underline{\underline{\varepsilon}}^e$ and $\underline{\underline{\varepsilon}}^p$ = elastic and plastic strain of the inclusion, and

β = parameter from the Eshelby analysis [12] developed for a spherical inclusion.

The effective stress is used to take into account the damage. In this way, the elastic law can be written as

$$\underline{\underline{\varepsilon}}^e = \frac{1+\nu}{E}\frac{\underline{\underline{\sigma}}}{1-D} - \frac{\nu}{E}\left(\mathrm{Tr}\frac{\underline{\underline{\sigma}}}{1-D}\right)I \tag{9}$$

The yield strength of the inclusion is taken equal to the fatigue limit σ_f. As a result, fatigue damage and fatigue crack initiation can only occur if the loading is higher than this limit. Over the elastic domain, there is an accumulation of the damage in the inclusion. When the damage reaches a critical value, the crack of the inclusion occurs and we consider that there is fatigue crack initiation in the RVE. In order to model the elastic-plastic behavior of the inclusion, only a linear kinematic hardening has been used. Then the yield criterion is

$$f = J_2(\underline{\underline{\tilde{\sigma}}} - \underline{\underline{X}}) - \sigma_f \tag{10}$$

where:

$\underline{\underline{\tilde{\sigma}}}$ = effective stress which considers the damage

$$\underline{\underline{\tilde{\sigma}}} = \frac{\underline{\underline{\sigma}}}{1-D} \tag{11}$$

The evolution of the plastic strain and of the deviatoric effective stress are defined by

$$\underline{\underline{\dot{\varepsilon}}}^p = \frac{3}{2}\frac{\underline{\underline{\tilde{\sigma}}}^d - \underline{\underline{X}}}{J_2(\underline{\underline{\tilde{\sigma}}} - \underline{\underline{X}})}\dot{p} \tag{12}$$

$$\underline{\underline{\tilde{\sigma}}}^d = \underline{\underline{\tilde{\sigma}}} - \frac{1}{3}\mathrm{Tr}\,\underline{\underline{\tilde{\sigma}}}\mathrm{I} \tag{13}$$

The evolution of the kinematic hardening is assumed to be linear and takes also into account the damage evolution which depends on the loading history

$$\underline{\underline{\dot{X}}} = \frac{2}{3}C(1-D)\underline{\underline{\dot{\varepsilon}}}^p \tag{14}$$

$$\dot{D} = \left(\frac{Y}{S}\right)^s \dot{p} \tag{15}$$

where:

The parameter S = damage strength,

s = non-linear exponent,

p = accumulated plastic strain, and

Y = strain elasticity energy density release rate which could be written as

$$Y = \frac{1+\nu}{2E}\left[\frac{\mathrm{Tr}(\langle \underline{\underline{\sigma}} \rangle_+^2)}{(1-D)^2} + h\frac{\mathrm{Tr}(\langle \underline{\underline{\sigma}} \rangle_-^2)}{(1-hD)^2}\right] - \frac{\nu}{2E}\left[\frac{\langle \mathrm{Tr}\ \underline{\underline{\sigma}} \rangle_+^2}{(1-D)^2} - h\frac{\langle -\mathrm{Tr}\ \underline{\underline{\sigma}} \rangle_-^2}{(1-hD)^2}\right] \tag{16}$$

where:

$\langle . \rangle_+$ = scalar positive part ($\langle x \rangle_+ = x$ if $x \geq 0$ and $\langle x \rangle_+ = 0$ if $x < 0$), and

h = micro-default closure parameter.

The damage occurs only if the accumulated plastic strain p reaches a threshold value p_D. A fatigue crack appears when the damage reaches a critical value D_c which depends on the loading

$$D_c = D_{1c}\frac{(\sigma_u)^2}{2EY} \tag{17}$$

where:

D_{1c} = critical damage reached in a monotonic tensile test, and

σ_u = ultimate strength.

The calculation of the stored energy is a good indicator to determine the damage threshold. We suggest calculating this energy at the end of each cycle with the higher stress value $\sigma_{\mathrm{eq}} = \mathrm{cste} = \sigma_{\mathrm{eq}}^{\max}$, moreover we also consider that there is a perfect plasticity. Thus, the damage threshold p_D can be calculated using the monotonic tensile damage threshold e_{pD}, the fatigue limit σ_f, the ultimate strength σ_u, and a non-linear exponent m

$$p_D = \varepsilon_{pD}\left[\frac{\sigma_u - \sigma_f}{\sigma_{\mathrm{eq}}^{\max} - \sigma_f}\right]^m \tag{18}$$

This two-scale model is used to describe fatigue behavior of materials and all parameters of this model can be identified using the monotonic stress-strain curve and two S-N curves established for two different stress ratios ($R = -1$ and $R = 0.1$). The mesoscale parameters (E, ν, C, and σ_u) were easily identified on the monotonic stress-strain curve. The fatigue limit σ_f is obtained from an experimental S-N curve as the asymptote at very high number of cycles. Constant values were chosen for the h and D_{1c} parameters [11]: $h = 0.2$ and $D_{1c} = 0.3$. All the other parameters were numerically identified by minimization of difference between model response and the two experimental S-N curves. The obtained parameters identified for DH36/BM and DH36/HAZ are summarized in Table 2.

In order to obtain a first set of parameters, a pre-identification was carried out. This pre-identification points out that, for both metals, the value obtained for the parameters S, m, and ε_{pD} are very close. It seems that the heat treatment

TABLE 2—*Parameters of the two-scale damage model.*

DH36	C (MPa)	σ_u (MPa)	m	ε_{pD}	σ_f (MPa)	S (MPa)	s
/BM	2500	630	1.85	0.02	180	200	0.53
/HAZ	2500	870	1.85	0.02	230	200	0.84

does not modify these three parameters. Thus, constant values were chosen for these parameters: $S = 200$ MPa, $m = 1.85$, and $\varepsilon_{pD} = 0.02$. To obtain the final set of parameters, only one parameter (the damage exponent s) has to be determined during the last identification. In order to take into account the heterogeneity of fatigue properties, as previously, a linear law was used to establish a relationship between parameters and the micro-hardness and finally, only three parameters (s, σ_f, σ_u) depend on micro-hardness measurements.

The experimental *S-N* curves are compared to the model response for DH36/HAZ in Fig. 8. These experimental *S-N* curves are provided by self-heating tests made on cylindrical specimens. We notice that the predicted values and the experimental values are close, especially for $R = 0.1$. Moreover, the model takes into account the influence of the mean stress which is important when there is an elastic shakedown. This mean stress effect, largely established by researchers [13–15], in case of local plasticity due to a stress concentration area, reduces the fatigue life span. Indeed, the local stress ratio could be different than the applied ratio due to the plastic strains which modified the local

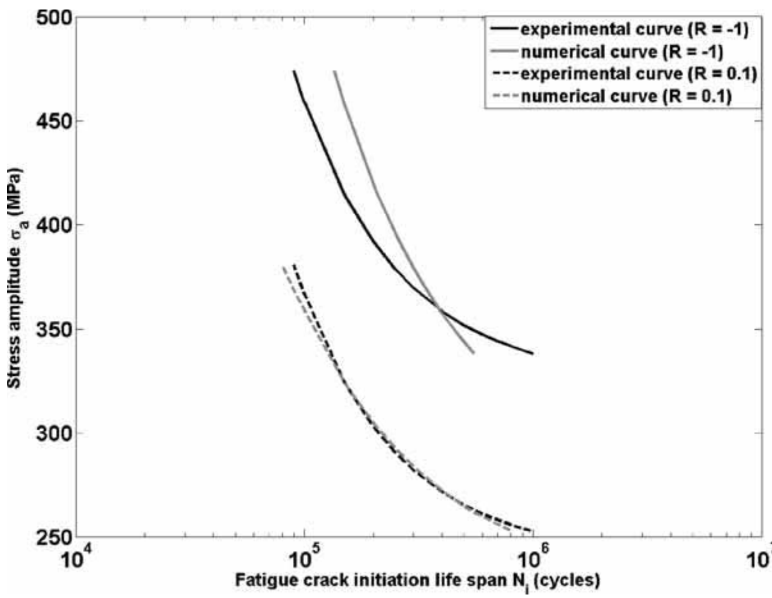

FIG. 8—*Experimental S-N curves and fatigue model responses* (*DH36/HAZ*).

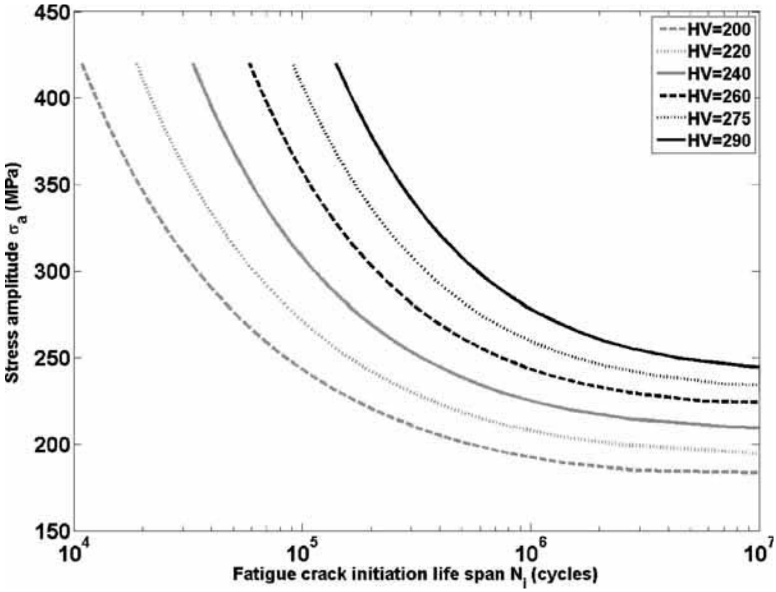

FIG. 9—*Variation of fatigue properties* (*R*=–0.2).

mean stress. By the way, at each point of the sample, the described model can establish a specific *S*-*N* curve depending on the local micro-hardness and the local stress ratio (Fig. 9).

Application to Cruciform Joints

All the presented methodologies were applied to cruciform joints. In order to be able to validate these numerical fatigue lives, some experimental fatigue tests were performed on welded cruciform joints provided by DCNS group. The BM used to create these samples is DH36.

Fatigue Tests

A semi-automatic metal active gas process was used to weld panels. The thickness of samples and their stiffeners is 8 mm; the width of each sample is about 56 mm (Fig. 10). All fatigue tests were carried out using a servo-hydraulic tension-compression machine with a capacity of 250 kN (Fig. 11). Moreover, in order to reduce the influence of residual stresses, welded specimens were systematically submitted to a stress relieving by heat treatment at 600 °C for 30 min. Fatigue tests were carried out under force control and the stop criterion is based on the alternating current potential drop (ACPD) signal. This system is used to measure the voltage variation in different areas of the sample. If a crack appears, there is locally a variation of electrical resistance and then a voltage variation is observed. Generally, fatigue cracks appear near the surface: Thus, a low intensity current (0.5 A) with high frequency were used (25 kHz). Moreover,

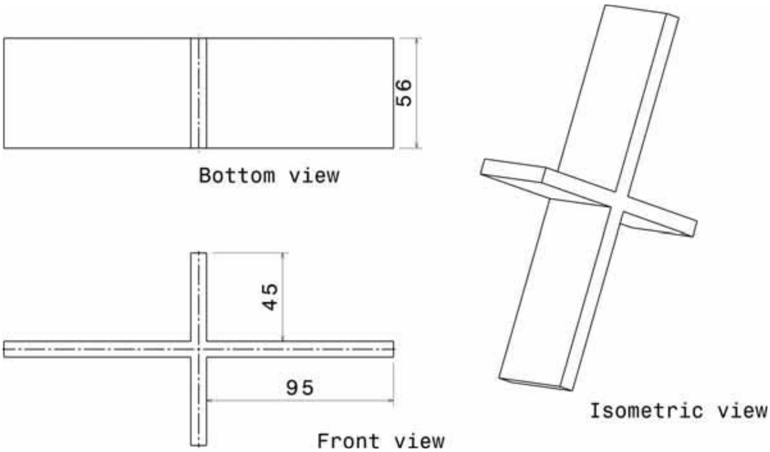

FIG. 10—*Drawing of cruciform joint specimens* (*lengths in millimeters* (*mm*)).

the crack initiates at the weld toe so the potential measurements are made really near this weld toe (Fig. 12). Fatigue tests were performed on two sets of welded specimens for two different stress ratios: $R = 0.1$ (set No. 1) and $R = -1$ (set No. 2).

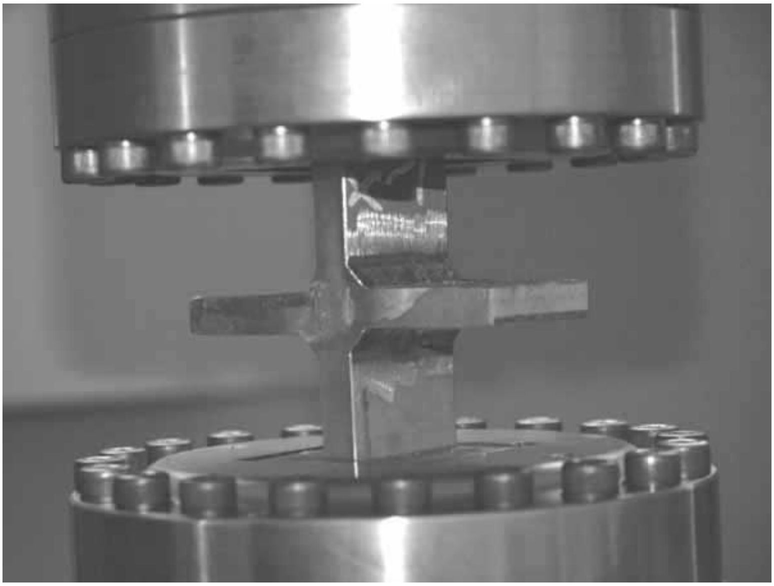

FIG. 11—*Sample in the tension-compression fatigue machine.*

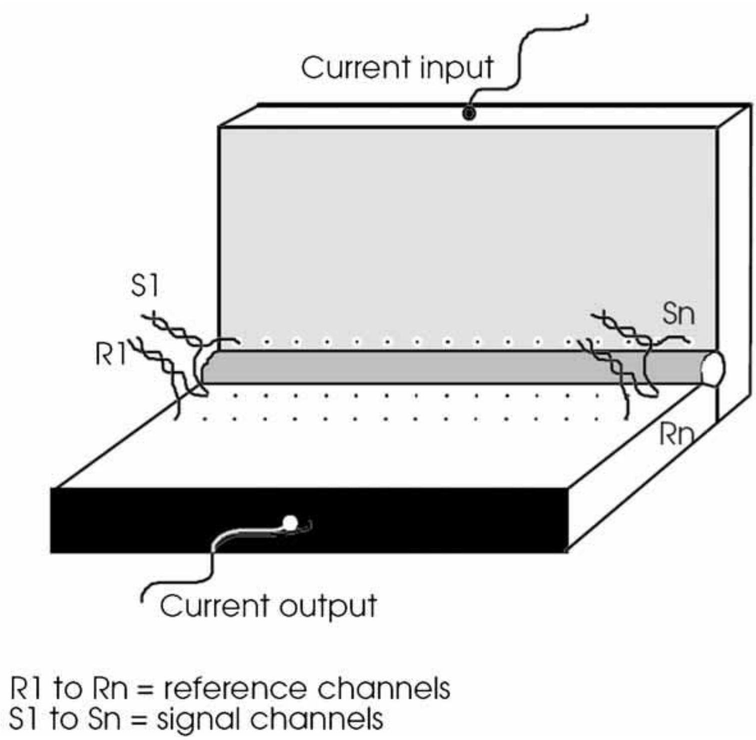

FIG. 12—*Scheme of ACPD connections on a cruciform joint* [*18*].

Finite Element Calculation

Due to the sample symmetry, only a 2D-quarter of the sample was modeled using Abaqus software with the plane stress hypothesis (CPS elements). Some laser measurements were made on a set of welded joints (set No. 1) in order to evaluate geometrical parameters. Finite element calculations were carried out using two different geometries: A first geometry inspired from the fictitious notch rounding approach [16,17] and a second geometry close to the laser measurements established from tested samples. The first geometry consists of a weld toe radius $\rho = 1$ mm, a weld toe angle $\theta = 45°$, and an effective throat thickness of 3.5 mm.

The proposed method is deterministic so, the second geometry, based on laser measurements, was chosen as one which introduces the highest stress concentration, i.e., which provides the shortest numerical life span. The second geometry was identified from the set of samples No. 1 ($R = 0.1$), but all the samples were not scanning with the laser equipment: It was characterized by a radius toe $\rho = 0.7$ mm, an angle toe $\theta = 45°$, and an effective throat thickness of 4 mm: This geometrical configuration creates a higher stress concentration than the first geometry.

Unfortunately, the second geometry was not measured for the set of samples No. 2 ($R=-1$) but this one seems to be more regular (compared to set No. 1).

It is important to note that finite element calculations are largely influenced by the weld toe radius ρ, the other parameters have a low influence on the results.

The welding process creates heterogeneity of the mechanical properties through the joint. To take this variation into account, a user subroutine (UFIELD) is created to introduce the micro-hardness field into calculations. These inputs are also required by another user subroutine (UMAT) which allows appropriate evolution laws depending on the micro-hardness (Fig. 13).

The finite element calculations were made for different loads on both geometries. The results provide the cyclic behavior of the structure and the loading domain where an elastic shakedown occurs.

Results

The post-treatment, based on a two-scale damage model, can only be applied on shakedown calculations in order to estimate the time needed to initiate a fatigue crack. The results point out some great differences between the two geometries (Fig. 14). First, because of the high stress concentration induced by a small radius ($\rho=0.7$ mm), the number of cycles in which plastic strain occurs, increases with respect to a large radius ($\rho=1.0$ mm). Thus, calculations made for high nominal stress amplitude $\sigma_{a\ \mathrm{nom}}$ do not lead to an elastic shakedown behavior and could not be submitted to the post-treatment.

For $R=0.1$ (set No. 1), the comparisons between numerical calculations and a large part of experimental results point out a good correlation for fatigue lives obtained with the second geometry ($\rho=0.7$ mm). However, some experimental results do not seem to follow this general tendency and the first geometry ($\rho=1$ mm) seems to be more representative. Indeed, it is important to note that only a part of the samples were submitted to laser measurements.

For $R=-1$ (set No. 2), a comparison between the experimental results and the numerical calculations points out a very good correlation for fatigue lives obtained with the first geometry ($\rho=1$ mm): The general tendency of these predictions is quite good and it seems to represent an average curve. On the opposite, the geometry ($\rho=0.7$ mm) established from set No. 1, seems to provide some safety factor because all the fatigue lives are shorter than those experimentally obtained.

This trend can easily be understood due to the way the laser measurement geometry was chosen. Even if only few cruciform joints were submitted to laser measurements, a lot of geometrical configurations (ρ, θ) were obtained along the specimens and the presented results ($\rho=0.7$ mm) are based on a critical configuration with a small radius. It seems fair to note that geometry has a great importance in the fatigue crack life estimation. Consequently, a critical configuration should be modeled in order to be sure to provide some safety estimation. Moreover, this methodology could also be used to certificate the quality of specific weld toe. Indeed, if a problem occurs during the welding process, the recommendation for fatigue design of welded joint, classically

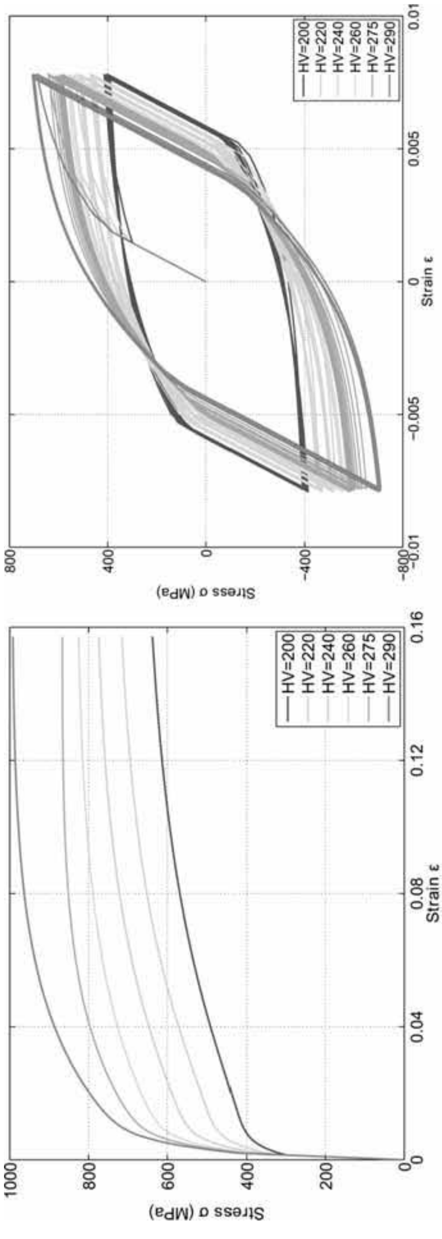

FIG. 13—*Evolution of the monotonic and cyclic behaviors with micro-hardness.*

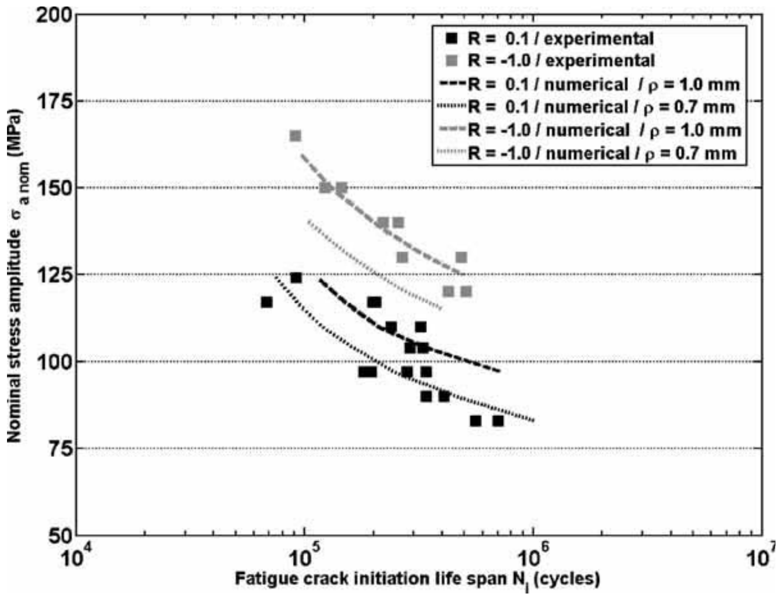

FIG. 14—*Comparison between experimental and numerical fatigue life of cruciform joint (R=0.1 and R=−1).*

based on FAT curves [3] (Fig. 15), could not qualify the use of such structures; whereas the presented method could take into account the geometrical default and predict if the joint could be used or not.

Moreover, all experimental tests point out, as expected, that fatigue cracks really initiated in the HAZ and grow perpendicularly to the loading direction (mode I). Due to the "small" thickness of the panel, the middle of the welded

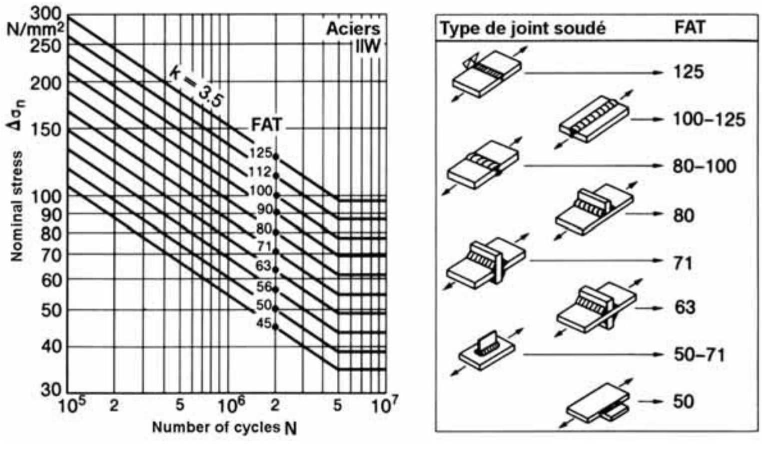

FIG. 15—*S-N curves established for different steel welded joint types [3].*

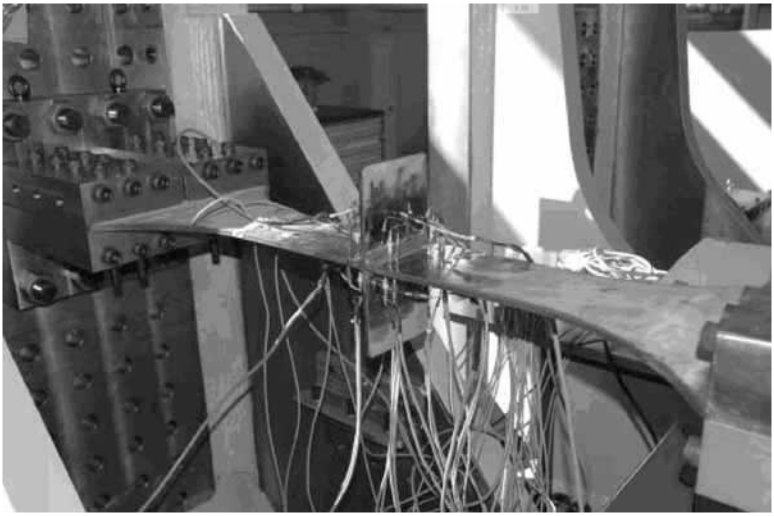

FIG. 16—*Tests conducted on the multi-axial fatigue machine* (*LBMS*).

area was submitted to a heat transformation. However, in this numerical study, the crack propagation is not studied and the fatigue crack initiation is only taken into account.

Prospects

The main purpose of this study is to be able to apply this strategy to representative ship welded structures (scale 1). Thanks to this work on cruciform joints,

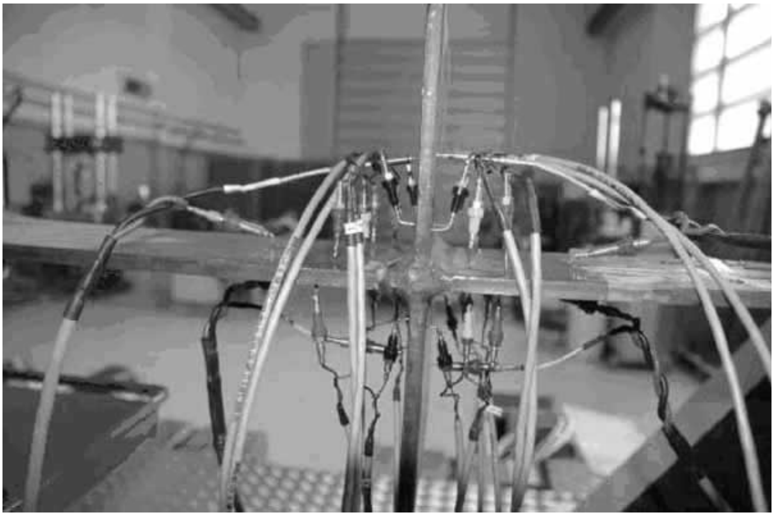

FIG. 17—*Tests conducted on the multi-axial fatigue machine* (*LBMS*).

it seems possible to go further. One difficulty will be to adapt experimental tests to larger specimens. These experimental tests will be conducted on a multiaxial fatigue testing machine using 400 kN actuators in order to apply a cyclic axial tension loading ($R = 0.1$). Currently, before testing such stiffened panels, an intermediate step has to be done. It consists of testing some cruciform joints with larger scale in order to validate all the measurement systems on representative parts of naval welded structures (Figs. 16 and 17). Two tests have already been done with the same stress loading that has been used for smaller cruciform joints. Their fatigue life spans were shorter than those from small specimens.

Conclusions

In this study, a methodology to determine fatigue life is presented and applied to cruciform joints. First, a FEA is done in order to establish the elastic cyclic behavior of the structure. In this stage, the elastic-plastic behavior of each metal (BM, HAZ, and MM) is taken into account by introducing the microhardness field. Moreover, the geometry is also considered to introduce some stress concentrations. If there is an elastic shakedown of the structure, a post-treatment could be applied to estimate the fatigue life span. This second step is based on a two-scale damage model. This method was already used for different welded joints [5] and especially for cruciform joints. The comparison between experimental and numerical fatigue life is hopeful. With the appropriate geometry and micro-hardness field, the calculation seems to well estimate the initiation of fatigue crack by providing safety estimation which are not so far from the experimental results. So it is possible to go further by considering some more complex assemblies such as a representative stiffened panel typical of shipbuilding applications (Scale 1).

Acknowledgments

The writers thank DCNS group for financing this work and supplying welded specimens. The authors are grateful to P. Martinat and B. Mecucci from ENSIETA/DTN/CMA for their collaboration in the design and the manufacturing of grips and fixtures.

References

[1] Radaj, D., Sonsino, C. M., and Fricke, W., *Fatigue Assessment of Welded Joints by Local Approaches*, 2nd ed., Woodhead Publishing, Cambridge, 2006.
[2] Radaj, D., "Review of Fatigue-Strength Assessment of Non-Welded and Welded Structures Based on Local Parameters," *Int. J. Fatigue*, Vol. 18, 1996, pp. 153–170.
[3] Hobbacher, A, "Recommendations for Fatigue Design of Welded Joints and Components," *IIW doc. XIII-1965-03/XV-1127-03*, Abington, Cambridge, U.K., 2006.
[4] Taylor, D., Barrett, N., and Lucano, G., "Some New Methods for Predicting Fatigue in Welded Joints," *Int. J. Fatigue*, Vol. 24, 2002, pp. 509–518.

[5] Lautrou, N., Thevenet, D., and Cognard, J. Y., "Fatigue Crack Initiation Life Estimation in a Steel Welded Joint by the Use of a Two-Scale Damage Model," *Fatigue Fract. Eng. Mater. Struct.*, Vol. 32, 2009, pp. 403–417.

[6] Lemaitre, J., Sermage, J. P., and Desmorat, R., "A Two-Scale Damage Concept Applied to Fatigue," *Int. J. Fatigue*, Vol. 97, 1999, pp. 67–81.

[7] Doudard, C., Calloch, S., Hild, F., Cugy, P., and Galtier, A., "A Probabilistic Two-Scale Model for High Cycle Fatigue Life Predictions," *Fatigue Fract. Eng. Mater. Struct.*, Vol. 28, 2005, pp. 279–288.

[8] Chaboche, J.-L., "Viscoplastic Constitutive Equations for the Description of Cyclic and Anisotropic Behavior of Metals," *Bull. Acad. Pol. Sci., Ser. Sci. Tech.*, Vol. 25, 1975, pp. 33–42.

[9] Lemaitre, J. and Chaboche, J.-L., *Mechanics of Solid Materials*, Cambridge University Press, Cambridge, 1994.

[10] Calloch, S. and Marquis, D., "Triaxial Tension-Compression Tests for Multiaxial Cyclic Plasticity," *Int. J. Plast.*, Vol. 15, 1999, pp. 521–549.

[11] Lemaitre, J. and Desmorat, R., *Engineering Damage Mechanics, Ductile, Creep, Fatigue and Brittle Failures*, Springer Verlag, Berlin, 2005.

[12] Eshelby, J. D., "The Determination of the Elastic Field of an Ellipsoidal Inclusion, Related Problems," *Proc. Roy. Soc.*, Vol. A241, 1957, pp. 376–396.

[13] Goodman, J., *Mechanics Applied to Engineering*, Longmans, Green and Co., London, 1919, pp. 631–636.

[14] Susmel, L., Tovo, R., and Lazzarin, P., "The Mean Stress Effect on the High-Cycle Fatigue Strength from a Multiaxial Fatigue Point of View," *Int. J. Fatigue*, Vol. 27, 2005, pp. 928–943.

[15] Zhang, Y. H. and Maddox, S. J., "Fatigue Life Prediction for Toe Ground Welded Joints," *Int. J. Fatigue*, Vol. 31, 2009, pp. 1124–1136.

[16] Radaj, D., "Fatigue Notch Factor of Gaps in Welded Joint Reconsidered," *Eng. Fract. Mech.*, Vol. 57, 1997, pp. 14–148.

[17] Lieurade, H. P., Huther, I., and Lebaillif, D., "Weld Quality Assessment with Regard to Fatigue Strength," *Méc. & Ind*, Vol. 6, 2005, pp. 133–143.

[18] Matelect LTD., "Practical Aspects of the ACPD Technique," *User Manual*.

RESIDUAL STRESS EFFECTS ON FATIGUE AND FRACTURE

Reprinted from JAI, Vol. 7, No. 2
doi:10.1520/JAI102534
Available online at www.astm.org/JAI

B. Oberwinkler,[1] *M. Riedler,*[2] *and W. Eichlseder*[1]

Importance of Residual Stresses and Surface Roughness regarding Fatigue of Titanium Forgings

ABSTRACT: This paper presents the results of a long-term research program aimed at developing qualitative and quantitative design guidelines for the use of mechanical surface treatments designed to improve the fatigue life of structural components. High cycle fatigue tests were performed on planar four-point bending specimens derived from Ti-6Al-4V pancake forgings with a mill-annealed microstructure. The high cycle fatigue behavior of specimens with different surface conditions (as-forged and machined) in both an unpeened and a shot peened state was compared. In order to assess the fatigue failure mechanisms, detailed investigations of the surface layers were carried out. The as-forged surface state exhibits a stress distribution with significant compressive stresses near the surface, resulting in equilibrium tensile stresses in the depth. When the tensile stresses were exposed by machining a bordering surface, a distinct decrease in the fatigue strength was observed. In such cases, a shot peening treatment was shown to improve the fatigue strength. Square edges lead to a decrease in the fatigue strength, which could be aggravated by shot peening.

KEYWORDS: titanium alloys, as-forged, fatigue, residual stresses, edges

Introduction

In the aerospace industry, the realization of lightweight structural components is a top priority. Reducing the weight of structural components increases the potential payload of the aircraft and decreases the fuel consumption. Titanium alloys have become very important materials in the aircraft industry due to

Manuscript received May 19, 2009; accepted for publication October 20, 2009; published online December 2009.

[1] Institute of Mechanical Engineering, Univ. of Leoben, 8700 Leoben, Austria.
[2] Böhler Schmiedetechnik GmbH & Co. KG, 8605 Kapfenberg, Austria.

Cite as: Oberwinkler, B., Riedler, M. and Eichlseder, W., “Importance of Residual Stresses and Surface Roughness regarding Fatigue of Titanium Forgings,” *J. ASTM Intl.*, Vol. 7, No. 2. doi:10.1520/JAI102534.

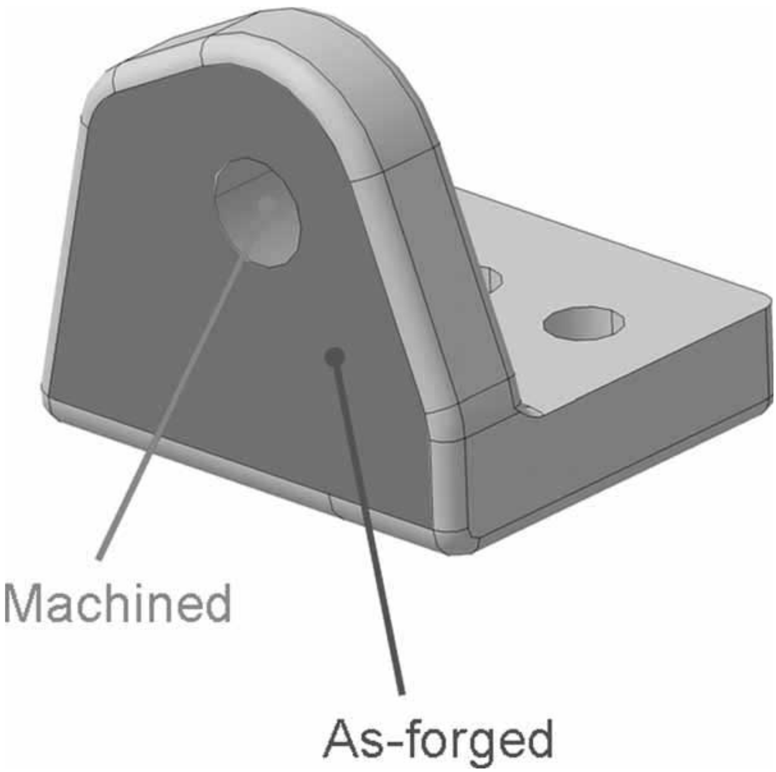

FIG. 1—*Different surface states on a forged component.*

their excellent properties (such as high fatigue strength and good corrosion resistance) and low density. Titanium components (particularly Ti-6Al-4V) are used in place of heavy steel components, especially for airfoils, undercarriage components, and other structural parts.

Manufacturing parts according to customer specifications by using forming techniques has both cost and quality advantages, compared to cutting and machining parts out of feedstock plates or bars. Because of this, components are increasingly manufactured by forging. Forging results in better utilization of material through near net shape manufacturing and also reduces manufacturing costs and provides better mechanical properties, such as high fatigue strengths. Some surfaces of forged components remain in the as-forged condition, whereas functional surfaces are subjected to additional machining (Fig. 1). Subsequent surface treatments (e.g., shot peening) serve to increase the fatigue strength.

In general, the fatigue behavior of Ti-6Al-4V is affected by many different parameters, such as microstructure, residual stress state, roughness, loading state, and geometry, all of which result in an enormous variation of fatigue strength. Such influences have been documented in numerous reports in the literature [1–15], although a holistic optimization of the entire product devel-

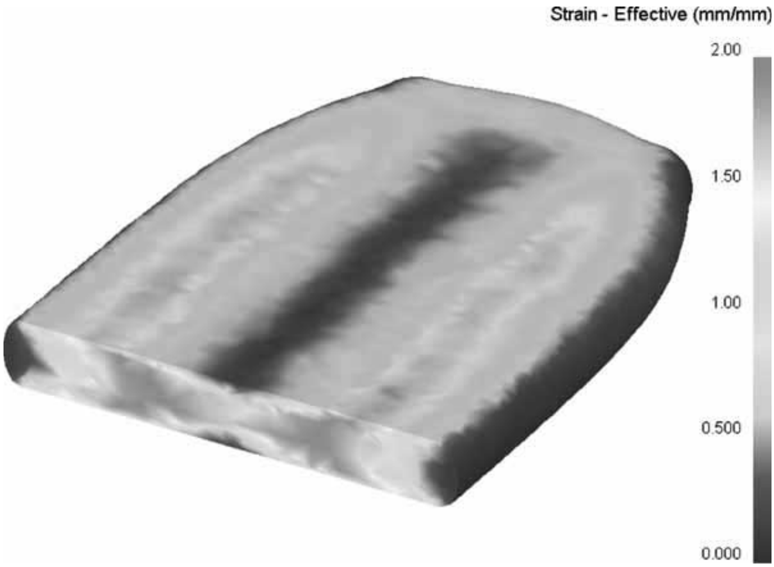

FIG. 2—*Effective strain distribution in a pancake forging.*

opment sequence (including design, processing, machining, and surface treatment) is still lacking. There is a shortage of documented fatigue tests, and the fatigue behavior in the as-forged surface condition has very rarely been reported. Gessinger and Corti [16] showed that the fatigue strength of isothermally forged Ti-6Al-4V specimens is much lower when the surface is in the as-forged condition, as opposed to the machined condition. They suggested that this is not due to a forging skin effect but rather an effect of mechanically working the surface during milling, which causes an improvement in the fatigue strength.

As mentioned above, some of the surfaces of forged components will remain in the as-forged condition, whereas functional surfaces are subject to additional machining (e.g., drilling holes; Fig. 1). To analyze the fatigue behavior of such components, plane specimens were designed such that an as-forged surface borders a machined one. The effect of a shot peening treatment on the fatigue strength of specimens with as-forged and machined surfaces was also determined.

Material Characterization

The material used in this study was provided by Böhler Schmiedetechnik GmbH & Co. KG, Kapfenberg (Austria), in the form of Ti-6Al-4V side pressed pancake forgings. The forging of the pancakes was simulated via finite element analysis using the software tool Deform™ (Scientific Forming Technologies Corporation). The effective strain distribution is shown in Fig. 2. The lateral cut clearly exhibits the typical crosswise distribution.

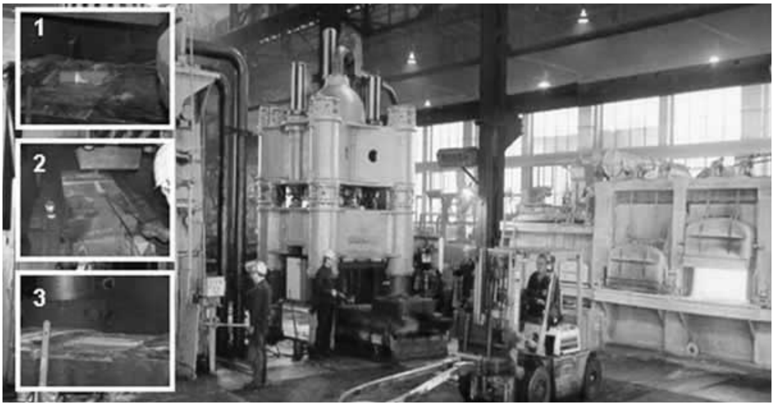

FIG. 3—*Forging of pancakes on a hydraulic press.*

The diameter of the feedstock was 45 mm and the pancakes were forged with a hydraulic press (Fig. 3). The forging process was done in one heating cycle (furnace temperature of 930°C) with a single pressing operation and an average ram speed of 15 mm/s. The samples were then subject to a mill-annealing treatment (720°C for 2 h, followed by an air cool). One-half of the pancakes were forged with a thickness of 13.5 mm (serving as the as-forged specimens) and the other half with a thickness of 15 mm (serving as the starting point for the machined specimens). Finally, sand blasting and pickling were carried out for descaling and removal of the α-case.

As a result of the heat treatment, the pancakes had a mill-annealed microstructure (Fig. 4). The average primary α-grain size was found to be 7.3 μm, measured using the line cut method. The primary α-phase content was 69 %. Mill-annealing does not cause complete recrystallization and therefore leads to a distinct texture of the primary α-grain shapes, representative of the forging process. Due to the forming temperature (between 900 and 930°C), no crystallographic texture occurs in the microstructures [4], which is confirmed by X-ray diffraction (XRD) measurements.

Test Procedure

To analyze the fatigue behavior of a typical surface state configuration, plane specimens were designed with an as-forged surface bordering a machined surface (Fig. 5). For the purpose of comparison, plane specimens with a machined surface bordering another machined surface were also tested. Additional shot peening was performed on as-forged and machined specimens.

Two planar four-point bending test specimens 200 mm long were extracted from each pancake in the longitudinal direction (Fig. 6). Regarding the quality of the top surface, two different types of specimens were produced: As-forged (from pancakes with a thickness of 13.5 mm) and machined (from pancakes with a thickness of 15 mm) (Fig. 7). All square edges were consistently deburred. According to finite element simulation, the stress concentration factor

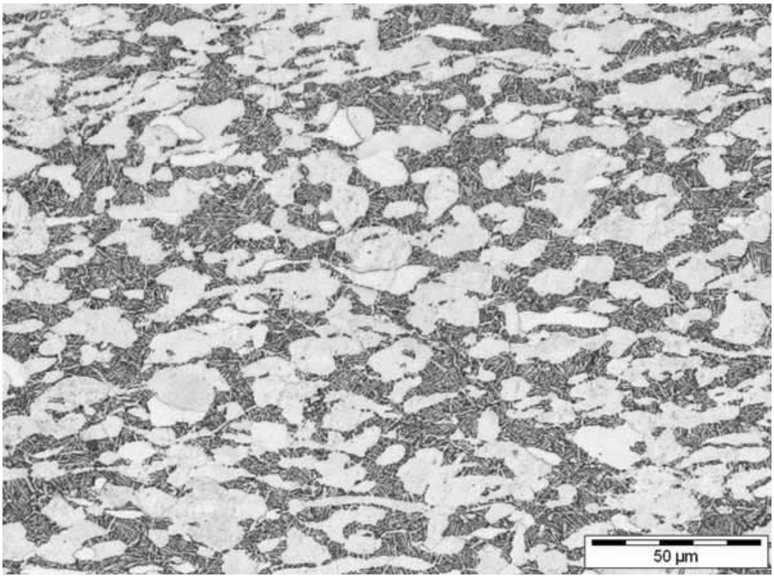

FIG. 4—*Micrograph of the mill-annealed microstructure.*

K_t of the specimen geometry was 1.07. The relative stress gradient, χ^*, is defined as the slope of the stress distribution at the point of maximum stress and is related to the maximum stress. Four-point bending loading of the plane fatigue test specimens resulted in a relative stress gradient of $0.15\ \text{mm}^{-1}$.

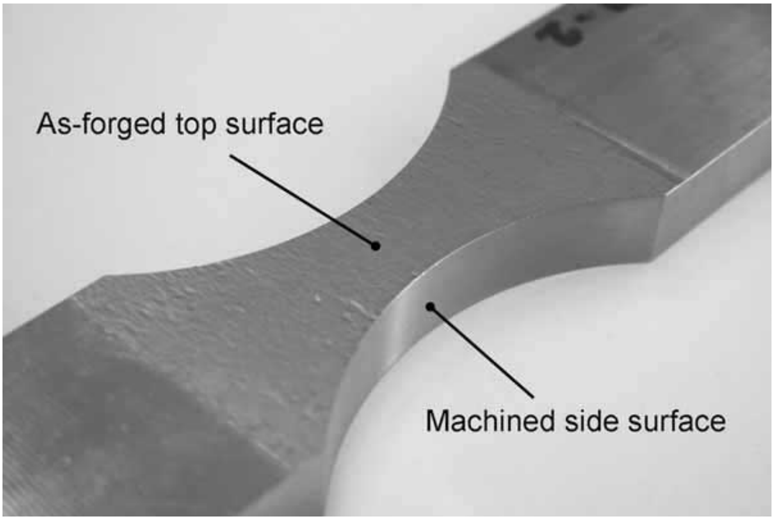

FIG. 5—*As-forged four-point bending fatigue test specimen.*

FIG. 6—*Sampling of four-point bending fatigue test specimens.*

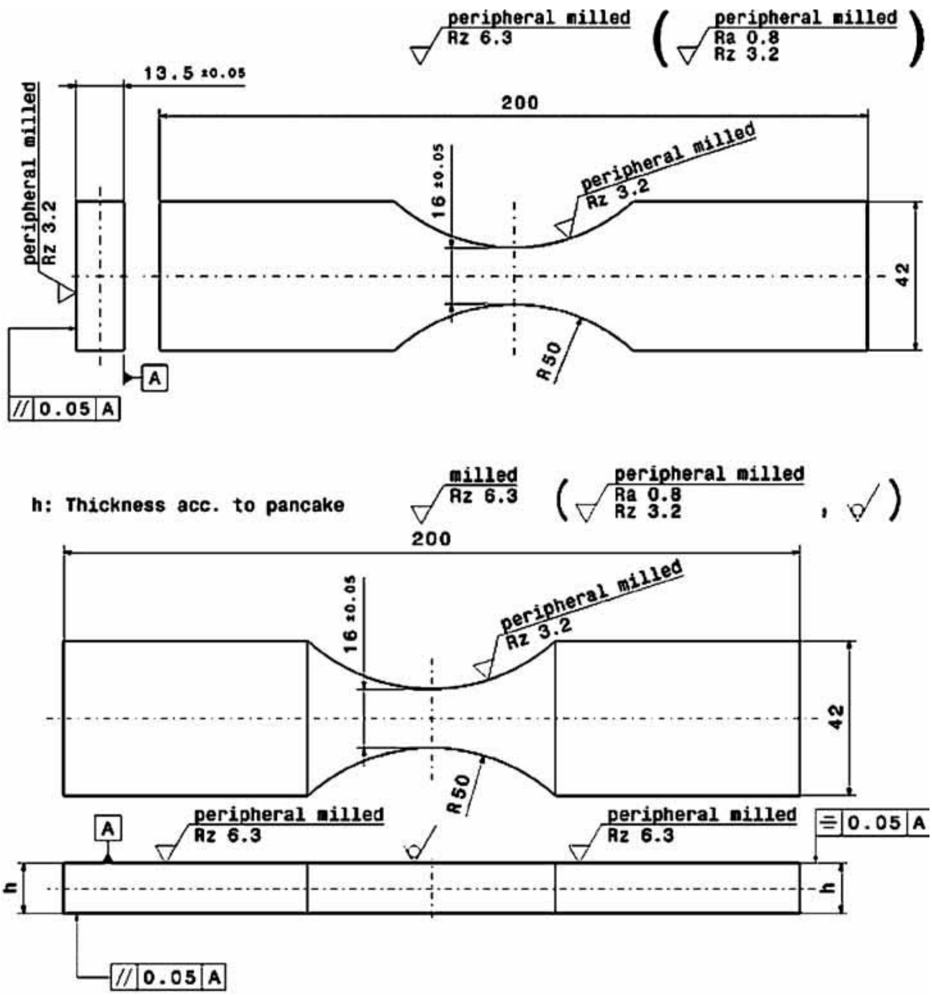

FIG. 7—*Drawings of the machined (left) and as-forged (right) plane fatigue test specimens.*

FIG. 8—*Four-point bending test rig with applied plane specimen.*

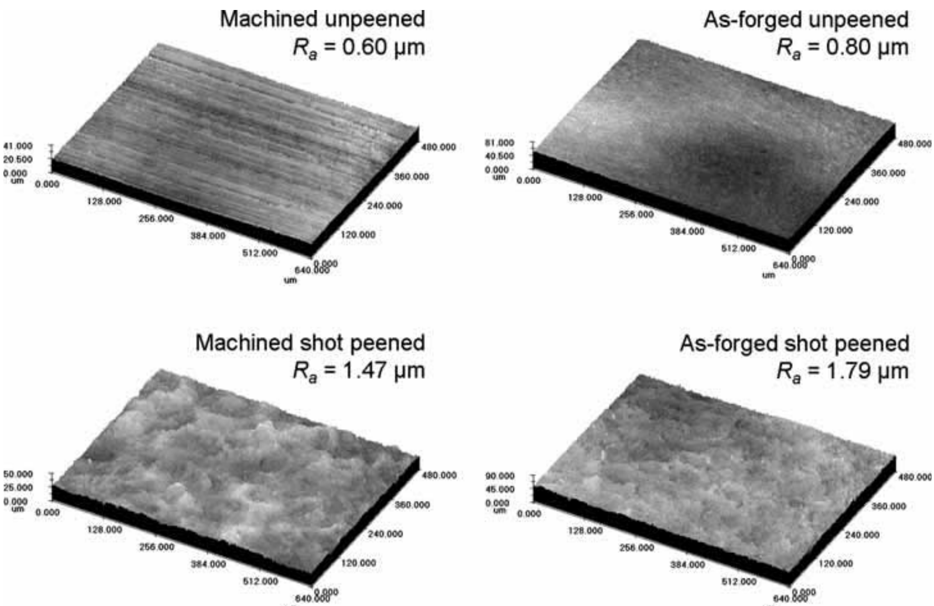

FIG. 9—*Roughness analyses of machined and as-forged surface in the unpeened and shot peened conditions, respectively (note different height scales).*

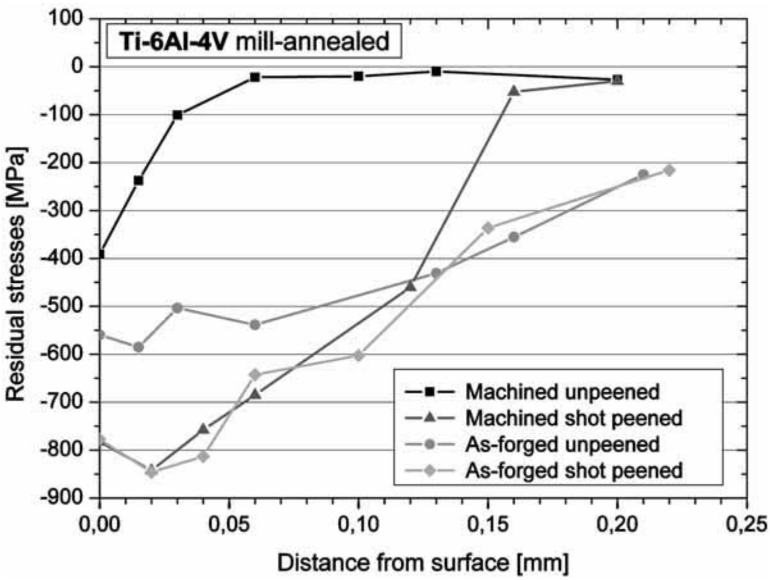

FIG. 10—*Residual stress distribution for different surface states.*

The shot peening was performed on both as-forged and machined specimens. First, the top surfaces were peened, followed by the side surfaces. The peening intensity of 0.18 A(mm) was chosen in accordance with MIL-S-13165C and MIL-P-81985 [17,18]. A coverage of 200 % was used for all experiments. A steel ball shot was used, StD-G3-0.35-HV640, with size classification of 0.35 mm and hardness of HV640.

To execute the testing of Ti-6Al-4V hourglass shaped plane specimens using a resonant testing machine, an existing four-point bending test rig was redesigned in cooperation with Russenberger Prüfmaschinen AG, Switzerland (cf. [19]). The tension/compression load on the rods of the test rig (Fig. 8) was converted via bending springs into a bending load for the specimen. The bending mode was considered as the most feasible since the highest stresses occur in the surface layer. All fatigue tests were carried out at room temperature and in ambient air, up to 10^7 load cycles, with a stress ratio of $R = -1$ and a frequency of 66 Hz. It is well known that Ti-6Al-4V is sensitive to fretting fatigue. Therefore, brass sheets were used to avoid fretting damage at the points of specimen restraint (see Fig. 8).

Characterization of the Surface Layer

Crack initiation typically takes place at the surface or close to the surface. For a better understanding of the initiation mechanism, the roughness, hardness, residual stresses, and microstructure of the surface layer were analyzed.

The roughness was measured with a confocal laser scanning microscope (Fig. 9). Analysis revealed that the as-forged surfaces have a slightly higher

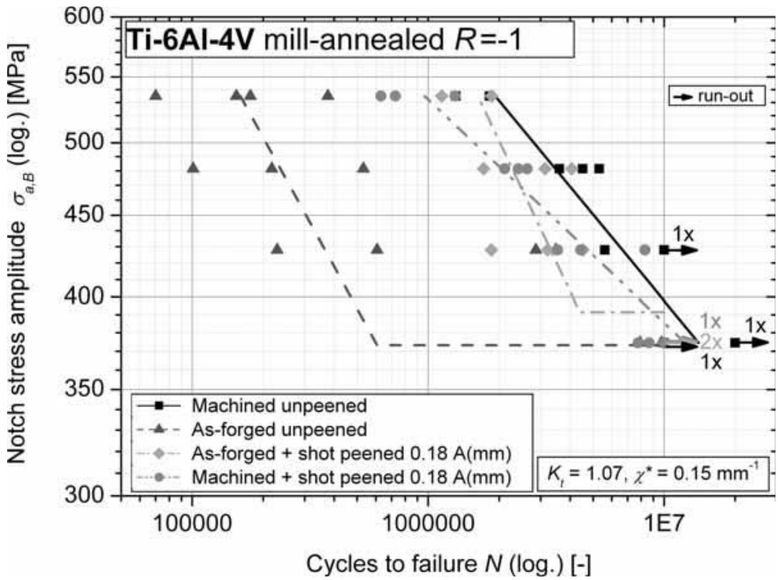

FIG. 11—*Four-point bending fatigue test results.*

center-line average roughness R_a compared to the machined surfaces. The shot peening treatment significantly increases the roughness in both the as-forged and machined cases, with the final as-forged surfaces still rougher than the machined and shot peened surfaces.

Vickers hardness measurements were performed on the as-forged and machined surfaces. The as-forged surfaces had an average hardness of 361HV1. In contrast, the average hardness of the machined surfaces was 343HV1. This slight difference of approximately 5 % suggests differences in the residual stress states.

All residual stress measurements were performed using XRD in combination with the $\sin^2 \psi$ method. Figure 10 shows the residual stress distributions for four different surface states. Graphs of residual stresses are comprised of measured data points (calculated by the average of data in the longitudinal and transversal direction, assuming a homogenous plane stress state) with no smoothing. Machining leads to residual compressive stresses in the first hundredths of a millimeter beneath the surface. In contrast, the as-forged surface exhibits distinct residual compressive stresses, reaching a depth of 0.25 mm beneath the surface. The peak value of the residual stress distribution for machined and as-forged surface state differs by a factor of 1.5.

Shot peening of the machined initial surface leads to a marked increase in the residual compressive stresses in the surface layer. The peak value of the residual compressive stresses increases from −400 MPa for an unpeened machined surface to −850 MPa for a shot peened machined surface, a difference of
100 %. The shot peening treatment of the as-forged initial surface leads to the

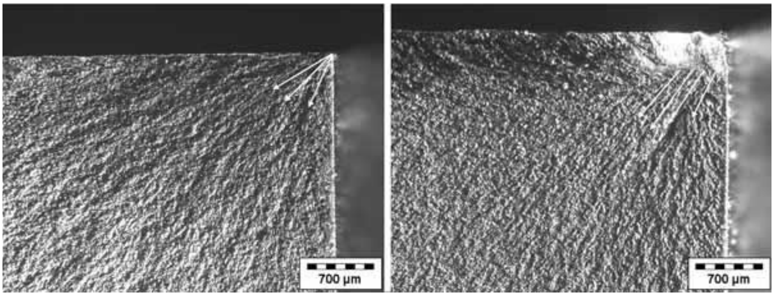

FIG. 12—*Fracture surface of machined (left) and as-forged (right) plane specimens.*

same peak value as the peening of the machined surface. However, the extent of the residual compressive stresses at depths greater than 0.13 mm is different and the residual stress profile for the as-forged shot peened sample merges with the as-forged unpeened profile.

Fatigue Test Results

Figure 11 shows the results of the four-point bending fatigue tests. All S/N curves correspond to a survival probability of 50 %. It can be seen from the data points that the as-forged surface condition leads to a significantly higher scatter (range of scatter $T_N = 1/6.6$) than the machined condition ($T_N = 1/2.8$). It has to be mentioned that the fatigue limit for the as-forged surface state is an approximation and not statistically confirmed. In the finite life region, the as-forged specimens exhibit a lower fatigue strength compared to the machined specimens, resulting in a difference in lifetime of a factor of 10.

The shot peening treatment of the machined specimens leads to a decrease in fatigue strength within the finite life region. The range of scatter of the shot peened surfaces ($T_N = 1/2.5$) is only slightly lower than that of the unpeened surfaces ($T_N = 1/2.8$). The shot peening of the as-forged specimens results in a significant increase in the fatigue strength within the finite life region, compa-

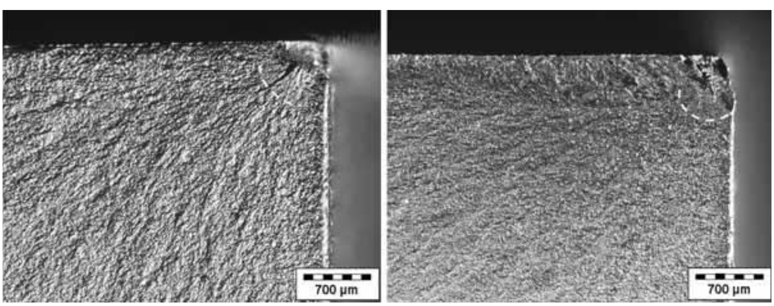

FIG. 13—*The fracture surfaces of the machined shot peened (left) and as-forged shot peened (right) plane specimens.*

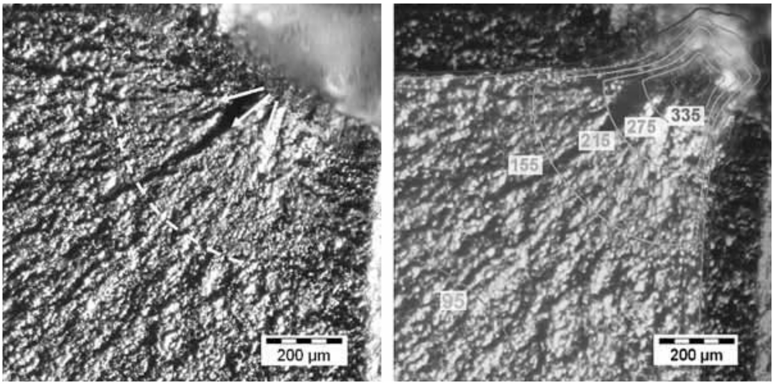

FIG. 14—*The crack initiation site at the edge of a machined shot peened plane specimen.*

rable with the fatigue strength of the machined shot peened specimens. The high scatter of the as-forged specimens ($T_N = 1/6.6$) is significantly reduced by the shot peening treatment ($T_N = 1/2.9$).

Fracture Analysis

The analysis of the fracture surfaces showed that for the machined surface condition, the crack emanated from the edge of the four-point bending test specimen (Fig. 12, left). In contrast, the crack initiation for the specimens with the as-forged top surface (Fig. 12, right) occurred near the machined side surface, approximately 340 μm beneath the as-forged surface. However, there is no observable region of different fracture characteristics near the crack initiation site. This means that the fraction of subsurface fatigue crack growth without contact to the ambient air is insignificant. The crack grows beneath the as-forged top surface, within the compressive residual stresses. If the fatigue crack is of a certain length, the edge region fails due to forced rupture at 45°.

For the shot peened surfaces, subsurface crack initiation beneath the edge was present (Fig. 13). Furthermore, a region of subsurface fatigue crack growth without contact to the ambient air (and therefore in vacuum) can be identified in the fracture surfaces, resulting in finer fracture characteristics (see Fig. 14, left). The transition between crack growth in vacuum and crack growth in air is marked with a dashed line. If the fatigue crack is of a certain length, the edge region fails due to forced rupture at 45°.

A finite element simulation was done to determine the equilibrium residual stress distribution for the edge region of the machined shot peened surface state. The measured residual stresses were thereby applied as initial conditions. The result of the finite element analysis, mapped on the fracture surface, is shown in Fig. 14 (right). The coloring indicates the maximum principal stresses: Red represents 400 MPa and blue represents −25 MPa. Iso-stress lines are additionally plotted for black-and-white depiction. It was observed that the

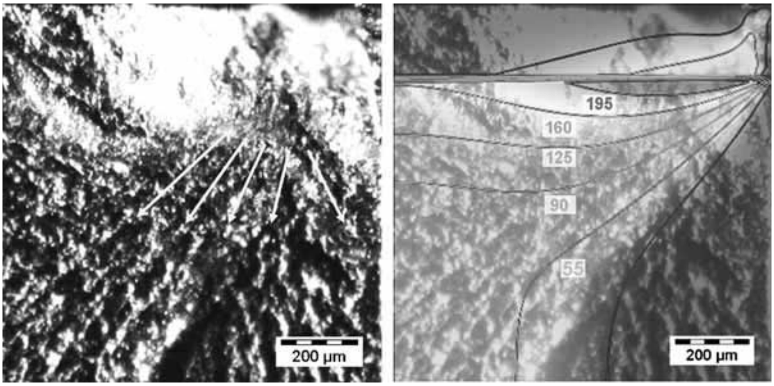

FIG. 15—*Crack initiation site at the edge of an as-forged plane specimen.*

fatigue crack initiates at the region with the highest maximum principal residual stress.

Discussion

The measured fatigue strength for mill-annealed Ti-6Al-4V in the high cycle fatigue region is very low compared to results found in the literature [1] and from previous work [5] done on round specimens under a rotating bending load. One possible reason for the low values is the rectangular shape of the cross section with the deburred edges. The influence of edges on fatigue behavior has rarely been reported in literature. Cohen et al. [20] analyzed the effects of specimen geometry on the fatigue behavior of carburized steel. They used cantilever bend specimens with square or round edges. Cohen et al. [20] suggested that the 13 % lower fatigue limit of the specimens with the square edges was due to the presence of a higher volume fraction of retained austenite in the sample corners and lower residual surface compressive stress. Differences in the residual stress state of the edge regions in combination with the complexity of the stress state (multiaxial stress) at the edge may be the reason for the low fatigue strength of Ti-6Al-4V measured under a four-point bending load. Future research will focus on analyzing this behavior in more detail.

For the machined plane specimens, crack initiation took place at the edge. This can be explained by the condition introduced by the four-point bending load, where the highest stresses occur in the top surface and the presence of the stress concentration is due to the sample edges.

The samples where the as-forged top surface bordered the machined side surface had significantly lower fatigue strengths, especially within the finite life region. Furthermore, the cracks did not initiate from the edge, at the location of maximum nominal stresses, but beneath the as-forged top surface, near the machined side surface. This can be attributed to the residual stress state in the as-forged surface layer, illustrated in Fig. 15. The residual compressive stresses in the as-forged surface layer involved a maximum principal stress distribution as shown, mapped on the fracture surface, in Fig. 15 (right). The coloring indicates the maximum principal stresses: Red represents 230 MPa and blue represents −20 MPa. Iso-stress lines are additionally plotted for black-and-white depiction. This stress distribution ties in well with the crack initiation mechanism suggested with respect to the fracture surface. However, there is a slight deviation between the depth of the maximum stress and the real crack initiation site. At this point, it has to be mentioned that the residual stresses in the as-forged surface layer are believed to vary with the position on the pancake. The residual stress distribution shown in Fig. 10 was measured in the middle of the specimen. Therefore, it can be assumed that the deviation between fracture surface and finite element simulation may be caused by variations of the residual stresses in the as-forged surface. Furthermore, the high scatter of the as-forged specimens compared with the machined ones can contribute to such variations.

The shot peening of the as-forged surface leads to a significantly higher roughness, but the residual stress state is just slightly modified. From a design point of view, to be conservative, it can be assumed that shot peening treatment of an as-forged surface (without any machining in safety critical regions) results in higher manufacturing costs and a lower fatigue strength due to the increased roughness.

Shot peening of square edges leads to high residual tensile stresses beneath the surface, which promotes early crack initiation. The fatigue strength in the finite life region of machined specimens is slightly decreased. This means that the negative effect of premature subsurface crack initiation caused by the residual tensile stresses prevails over the positive effect of decelerated crack growth in vacuum.

The shot peening of the as-forged specimens leads to a significant increase in the fatigue strength in the finite life region, comparable with the fatigue strength of the machined shot peened specimens. This can be explained by the shift in the residual tensile stresses near the machined side surface into deeper regions, resulting in subsurface crack initiation and propagation. The difference in the fatigue strengths of machined shot peened and as-forged shot peened surface states arises from variations in the residual stress distributions; the failure mechanism is the same for both.

Conclusion

- Machined square edges result in decreased fatigue strengths, as compared to round specimens. This may arise due to the residual stress state in the edge regions (lower compressive or multiaxial residual tensile stresses). For this reason, chamfered edges are recommended.
- Shot peening of square edges leads to a decrease in fatigue strength if both adjacent surfaces have been machined. If just one of the adjacent surfaces is shot peened, the sample will behave as the as-forged specimens due to residual tensile stresses at or near a surface, resulting in a significant decrease in fatigue strength. Therefore, shot peening is not recommended for square edges.

- The as-forged surface of mill-annealed Ti-6Al-4V exhibits high residual compressive stresses in the surface layer. A shot peening treatment leads to a significantly higher roughness and a slight modification in the residual stress distribution. For safety critical regions of shot peened as-forged surfaces, when no machining is performed, in order to be conservative it can be assumed that the fatigue strength is lowered due to the increased roughness at concomitant higher manufacturing costs owing to the shot peening process.
- If an as-forged surface borders a machined surface, tensile residual stresses are exposed. This leads to significantly lower fatigue strength. Such transition regions should be shot peened, causing the residual tensile stresses to shift beneath the surface, allowing for increased fatigue strength.

Acknowledgments

The writers would like to thank the Austrian Federal Ministry for Transport, Innovation, and Technology, the Austrian Federal Ministry of Economics and Labor, the federal governments of Vienna, Styria, Tyrol, Upper Austria, and Lower Austria, and the Austrian Research Promotion Agency for the funding of this work in the framework of the Austrian Aeronautics Research Program and FFG's BRIDGE program.

References

[1] Boyer, R., Welsch, G., and Collings, E. W., *Materials Properties Handbook: Titanium Alloys*, ASM International, Materials Park, OH, 1994, pp. 483–547, ISBN 0-871-70481-1.

[2] Leitner, H., Oberwinkler, B., Gaenser, H.-P., and Stoschka, M., "Influence of the Peening Intensity on the Fatigue Behavior of Shot Peened Titanium Components," *J. ASTM Int*, Vol. 5, No. 9, 2008, Paper ID JAI101537

[3] Nalla, R. K., Boyce, B. L., Campbell, J. P., Peters, J. O., and Ritchie, R. O., "Influence of Microstructure on High-Cycle Fatigue of Ti-6Al-4V: Bimodal Versus Lamellar Structures," *Metall. Mater. Trans. A*, Vol. 33A, 2002, pp. 899–918.

[4] Lütjering, G., "Influence of Processing on Microstructure and Mechanical Properties of ($\alpha+\beta$) Titanium Alloys," *Mater. Sci. Eng., A*, Vol. 243, 1998, pp. 32–45.

[5] Oberwinkler, B., Leitner, H., and Riedler, M., "Combination of Safe Life and Fail Safe Concepts to Assess the Lifetime of Ti-6Al-4V Forgings," *TMS 2009 Annual Meeting Supplemental Proceedings, Volume 1: Materials Processing and Properties*, San Francisco, 2009, TMS, Warrenale, PA, pp. 77–84.

[6] Zuo, J. H., Wang, Z. G., and Han, E. H., "Effect of Microstructure on Ultra-High Cycle Fatigue Behaviour of Ti-6Al-4V," *Mater. Sci. Eng., A*, Vol. 473, 2008, pp. 147–152.

[7] Henry, S. D., Dragolich, K. S., DiMatteo, N. D., *Fatigue Data Book: Light Structural Alloys*, ASM International, Materials Park, OH, 1995, p. 277, ISBN 0-87170-507-9.

[8] Oberwinkler, B., Leitner, H., and Stoschka, M., "Influence of Shot Peening on the Fatigue Behaviour of Ti-6Al-4V in Respect of Multiaxial Loading," *Conference Pro-*

ceedings: Tenth International Conference on Shot Peening (*ICSP10*), Tokyo, Japan, 2008, International Scientific Committee for Shot Peening, Mishawaka, IN, pp. 388–393.

[9] Gray, H., Wagner, L., and Lütjering, G., "Influence of Surface Treatment on the Fatigue Behavior of Titanium-Alloys at Room and Elevated Temperatures," *Sixth World Conference on Titanium*, Cannes, France, 1988, Societe Française de Metallurgie, Les Editions de Physique, Les Ulis, France, pp. 1895–1900.

[10] Koster, W. P., Gatto, L. R., and Cammett, J. T., "Influence of Shot Peening on Surface Integrity of Some Machined Aerospace Materials," *ICSP-1*, Paris, 1981, pp. 287–293, International Scientific Committee for Shot Peening, Warrendale, PA, www.shotpeening.org/ICSP (Last accessed 18 November 2009).

[11] Franz, H. E. and Obricht, A., "Optimization of Shot Peening to Improve the Fatigue Strength of Ti-6Al-4V," *ICSP3, Shot Peening: Science, Technology, Application*, Vol. 2, Garmisch-Partenkirchen, Germany, 1987, International Scientific Committee for Shot Peening, Warrendale, PA, pp. 439–446, www.shotpeening.org/ICSP (Last accessed 18 November 2009).

[12] Wohlfahrt, H., "Kugelstrahlen und Dauerschwingverhalten [Shot Peening and Fatigue Behavior]," *ICSP-1*, Paris, 1981, International Scientific Committee for Shot Peening, Warrendale, PA, www.shotpeening.org/ICSP (Last accessed 18 November 2009).

[13] Bache, M. R., Evans, W. J., Suddell, B., and Herrouin, F. R. M., "The Effects of Texture in Titanium Alloys for Engineering Components Under Fatigue," *Int. J. Fatigue*, Vol. 23, 2001, pp. 153–159.

[14] Morrissey, R. J., McDowell, D. L., and Nicholas, T., "Frequency and Stress Ratio Effects in High Cycle Fatigue of Ti-6Al-4V," *Int. J. Fatigue*, Vol. 21, 1999, pp. 679–685.

[15] Oberwinkler, B., Javidi, A., and Leitner, H., "Schwingfestigkeit von Ti-6Al-4V—Betrachtung Mehrerer Einflussgrößen [Fatigue Behavior of Ti-6Al-4V-Consideration of Several Influencing Variables]," *DGM, Tagung Werkstoffprüfung 2007* [*Materials Testing Conference 2007*], Verlag Stahleisen GmbH, Düsseldorf, 2007, pp. 145–150, ISBN 978-3-514-00753-6.

[16] Gessinger, G. H., and Corti, C. W., "Influence of Surface Condition on the Fatigue Strength of Isothermally Forged Ti-6Al-4V," *Titanium '80, Science and Technology*, Kyoto, Japan, 1980, AIME, New York, Vol. 3, pp. 1787–1795.

[17] U.S. Army, "Military Specification—Shot Peening of Metal Parts, MIL-S-13165C," 1998.

[18] U.S. Army, "Military Specification—Peening of Metals, MIL-P-81985," 1974.

[19] Oberwinkler, B., Riedler, M., Leitner, H., and Javidi, A., "Four Point Bending Fatigue Tests of Forged Ti-6Al-4V," *MP Materials Testing*, Vol. 51, 2009, pp. 580–586.

[20] Cohen, R. E., Matlock, D. K., and Krauss, G., "Specimen Edge Effects on Bending Fatigue of Carburized Steel," *J. Mater. Eng. Perform.*, Vol. 1, No. 5, 1992, pp. 695–704.

Reprinted from JAI, Vol. 7, No. 3
doi:10.1520/JAI102515
Available online at www.astm.org/JAI

Hans-Jakob Schindler[1] *and Christian Leinenbach*[2]

Fatigue Assessment of Brazed T-Joints Based on Damage Tolerance Including Residual Stress Effects

ABSTRACT: The fatigue crack growth behavior of a brazed joint is characterized by a Paris-exponent that is much higher than the one of bulk metals, which means that brazed components have only a short residual fatigue life after the initiation of a fatigue crack. Therefore, the threshold of fatigue crack growth of brazed joints is of particular importance in the fatigue analysis of brazed components and needs to be understood well. Residual stresses have to be considered in crack growth analysis in the threshold regime. The corresponding effects are explored experimentally and theoretically. The stress intensity factors due to the residual stresses in a brazed T-joint of compressor impellers were measured by using the cut compliance method. It was found that residual stresses are present but relatively small. They do not affect the endurance stress significantly. A concept for an endurance analysis of a brazed T-joint that includes imperfections and residual stresses is suggested.

KEYWORDS: fatigue crack, endurance limit, residual stress, stress intensity factor, threshold, brazed joint, notch, T-joint

Introduction

In brazed joints pores and zones of reduced bonding strength are usually inevitable. Therefore, highly loaded brazed components such as compressor impellers need to be designed according to the principles of damage tolerance, which include a defect assessment based on fracture mechanics [1,2]. Under mechanical loading, complex triaxial stresses form in the thin brazing zone due to the

Manuscript received May 14, 2009; accepted for publication December 11, 2009; published online February 2010.

[1] Mat-Tec AG, Winterthur, Switzerland.
[2] EMPA—Swiss Federal Laboratories for Materials Testing and Research, Dübendorf, Switzerland.

Cite as: Schindler, H.-J. and Leinenbach, C., "Fatigue Assessment of Brazed T-Joints Based on Damage Tolerance Including Residual Stress Effects," *J. ASTM Intl.*, Vol. 7, No. 3. doi:10.1520/JAI102515.

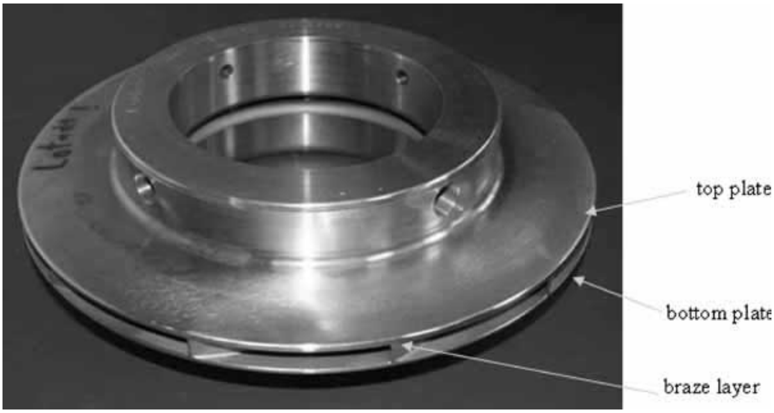

FIG. 1—*Example of a compressor impeller.*

different elastic-plastic properties of the filler metal and the base material and the constraining effect of the base material. As a result, the ultimate tensile strength of the bond can be several times higher than the strength of the unconstrained layer material [3,4]. This effect also influences the fatigue behavior, namely, the endurance limit of brazed components.

The characteristic feature of fatigue crack growth in brazed joints is its extremely steep slope of the da/dN-curve, which manifests in a very high exponent in a power law representation of the crack growth rate da/dN as a function of ΔK ("Paris' law") [5,6]. This means that a fatigue crack—once it is started—will accelerate rapidly and lead to a fracture. Thus, to guarantee safety with respect to fatigue, all cyclic load components, even those with relatively few numbers of cycles like the on/off load cycles, should stay well below the threshold of fatigue crack growth. However, little is known about the threshold behavior of brazed joints.

In the threshold regime of fatigue crack growth, the effect of residual stresses often plays an important role and should be considered principally in fatigue assessment. Little is known about residual stresses in brazed joints and their effects on fatigue. Gross residual stresses are rather unlikely to occur since the brazing process acts like a stress relief heat treatment. However, local residual stresses are likely to be generated during the final cooling due to the differences in thermal expansion between base and filler material and may affect the threshold behavior. In the present investigation they are measured and taken into account in the fatigue assessment. In order to perform a fatigue analysis based on fracture mechanics, particularly the stress intensity factor (SIF) caused by the residual stresses is required.

An example of a compressor impeller is shown in Fig. 1. The base material is martensitic stainless steel X3CrNiMo13-4 and the filler metal Au-18Ni. Brazing is used to connect the top plate of the impeller to the blades, which are part of the bottom plate in Fig. 1. Thus, the brazed joints are typically T-shaped, so there is a global stress concentration at the edge of the braze seam.

In a fatigue analysis of a brazed component such as the impeller, the spe-

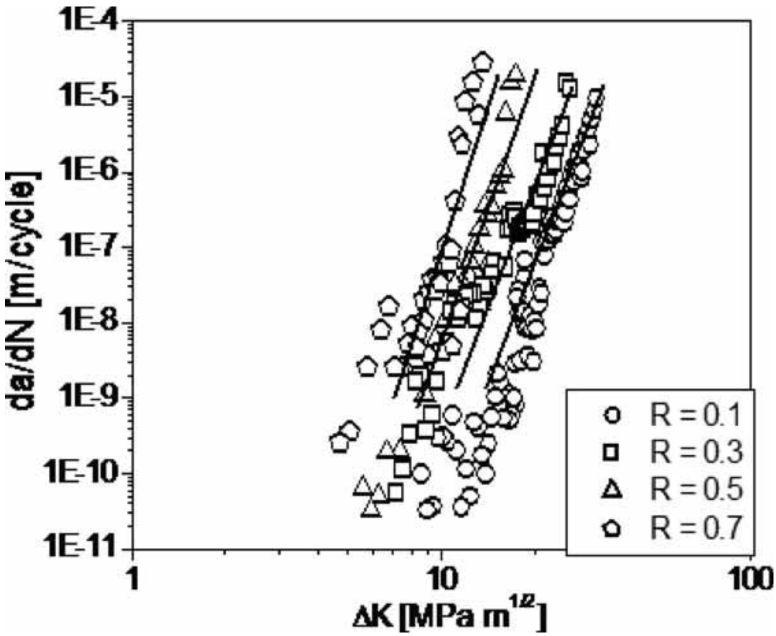

FIG. 2—*Fatigue crack propagation* ($da/dN-\Delta K$) *curves for R=0.1, 0.3, 0.5, and 0.7* (*from Ref 6*).

cial features mentioned above—including global stress concentration, local defects, steep da/dN-curves, and residual stresses—should be taken into account adequately. The aim of the present investigation was to explore a practical way of how to deal with these issues. In this paper, the fatigue behavior is reviewed, and the importance of the threshold of fatigue crack growth in endurance is emphasized. Near the threshold, residual stresses often play an important role in fatigue crack growth. It is shown how they can be measured and assessed. For the measurement the cut compliance (CC) method was adapted. In the present paper it is shown how the CC-method was adapted to measure the residual stress effects in an impeller. Furthermore a practical defect assessment procedure of a brazed T-joint is suggested.

Fatigue Behavior of Brazed Joints

The fatigue crack growth rates of brazed joints of X3CrNiMo13-4 steel with Au-18Ni filler material (as applied in the case of the compressor impeller shown in Fig. 1) were measured on double cantilever beam (DCB) specimens. The experimental data in terms of crack growth rate, da/dN, as a function of ΔK ("da/dN-curve") for several stress ratios are reported in Refs 5 and 6. Some da/dN-curves are shown in Fig. 2. The parameters C, n, and ΔK_{th} that correspond to an approximation of the da/dN-curve by

TABLE 1—*Threshold values ΔK_{th} and calculated C and n parameters at different R values* [6].

R	ΔK_{th} (MPa·m$^{0.5}$)	C	n
0.1	9	1.309×10^{-22}	11.17
0.3	7	4.071×10^{-23}	12.17
0.5	6	7.234×10^{-22}	12.64
0.7	4	8.489×10^{-21}	12.81

$$\frac{da}{dN} = C \cdot \log \Delta K_I^n, \quad \text{for } \Delta K_I > \Delta K_{\mathrm{th}} \tag{1a}$$

$$\frac{da}{dN} = 0, \quad \text{for } \Delta K_I < \Delta K_{\mathrm{th}} \tag{1b}$$

are given in Table 1 for some R-ratios. R denotes the stress ratio

$$R = K_{\mathrm{min}}/K_{\mathrm{max}} \tag{2}$$

with K_{min} and K_{max} being the minimum and maximum SIF, respectively, of a load cycle.

Compared with the fatigue crack growth rate in bulk metals, where the Paris-exponent n is typically in the range of $2.5 < n < 4$, the values of n shown in the Table 1 are extremely high. This unusually high slope of the da/dN-curves can be explained by the fact that the range of ΔK_I, in which fatigue crack growth is principally possible, i.e.

$$\Delta K_{\mathrm{th}}(R) < \Delta K < (1 - R) \cdot K_{\mathrm{cf}} \tag{3}$$

is relatively narrow since the threshold value ΔK_{th} of the brazing is—as discussed in the Fatigue Crack Growth Threshold section—of a similar level as the one of bulk steel, whereas the upper bound K_{cf} (which denotes the critical SIF in cyclic loading) is much lower than the corresponding value of bulk steel. Simply, the da/dN-curve has to be much steeper than the one of bulk material to fit in the narrow range of ΔK as given in Eq 3, which is less than one decade wide. Or in physical terms: The mechanisms that cause acceleration in the upper range and the ones that lead to retardation in threshold regime of the da/dN-curve interfere with the Paris-behavior nearly in the entire range of ΔK.

From a practical point of view the high n-values mean that crack growth accelerates rapidly as soon as the crack starts to grow. This behavior leaves only little space for a safe-life-design of a brazed component. Taking into account the relatively high natural scatter of threshold data on one hand and the uncertainties to calculate the applied stress range ΔK on the other, a defect-tolerant design based on a safe-life analysis appears to be too risky to be applied. Instead, it is appropriate to require endurance (i.e., infinite fatigue life) even for load cases that are applied in relatively small numbers, say, a few thousand times, like, e.g., the on-off load cycles of an impeller. In terms of fracture mechanics, endurance requires that no fatigue crack growth occurs for the crucial initial defect size a_0, i.e., that

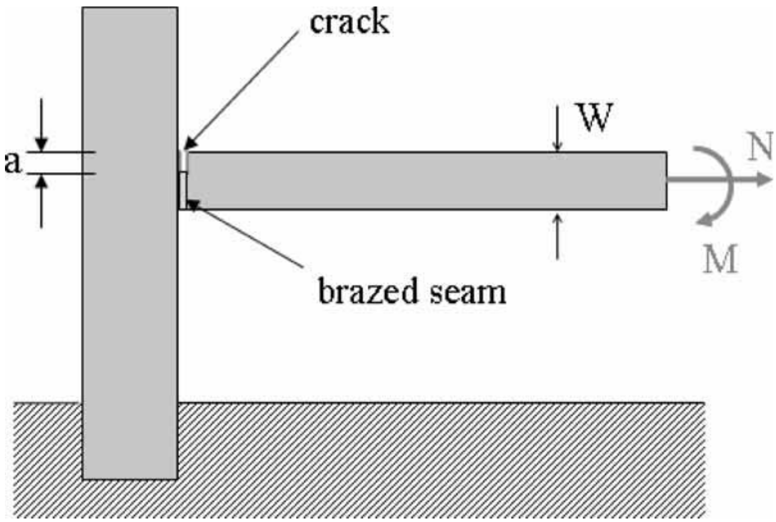

FIG. 3—*T-shaped brazed joint with crack of depth a loaded by a bending moment M and a normal force N.*

$$\Delta K(a_0) < \Delta K_{\mathrm{th}}(R) \tag{4}$$

In the following we take a closer look on both sides of Eq 4 for a brazed T-joint.

Stress Intensity Factor for a Crack in a T-Joint

As a representative simple plane geometry, we consider a T-shaped structural part of unit thickness loaded by a bending moment M and a normal tensile force N per unit thickness (Fig. 3). At the stress concentration in the corner, a crack of depth a is assumed to be present. Figure 4 shows the non-dimensional SIF k_{Ib} and k_{It}, which are defined as

$$k_{\mathrm{It}} = \frac{K_I \cdot W^{0.5}}{N}; \quad k_{\mathrm{Ib}} = \frac{K_I \cdot W^{1.5}}{M} \tag{5}$$

where the SIF K_I was calculated numerically by a boundary element analysis.

As it is typical for a crack emanating from a stress concentration, there is a steep rise of $K_I(a)$ with increasing crack length a in the short crack range, followed by a flatter part for larger crack depths [7,8].

Cracks in sharp corners like the one in a T-joint are difficult to be identified or measured by common methods of non-destructive testing, so their length is in general not known exactly. On the other hand—as it can be seen from Fig. 4—little differences in crack depth cause large differences in K_I in the initial state of crack growth. Therefore it is suggested in Refs 7 and 8 to cover the initial state of crack growth by extrapolating the subsequent flat part of $K_I(a)$ to $a = 0$. This is achieved by fitting the $K_I(a)$-curve to the form

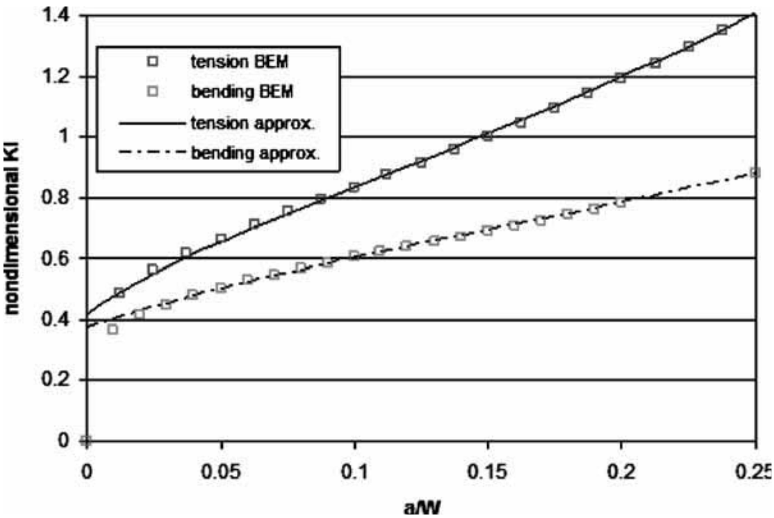

FIG. 4—*Non-dimensional SIF k_{It} and k_{Ib} as defined in Eq 5 for the system shown in Fig. 2.*

$$K_I(a) = 1.12 \cdot \sigma_N \cdot \sqrt{\pi(a + a_N)} \cdot Y(a/W) \tag{6}$$

where:

σ_N and a_N = fitting constants and

$Y(a/W)$ = character of the curve in the range of deeper cracks.

Equation 6 represents the upper bound of K_I for a short crack emanating from a notch or hot-spot of arbitrary shape regardless of the geometrical details of the corner such as its radius. For $a = 0$ approximation 6 delivers a theoretical SIF of

$$K_I(a = 0) = 1.12 \cdot \sigma_N \cdot \sqrt{\pi \cdot a_N} =: K_{IN} \tag{7}$$

where:

the sign =: means "defined as."

K_{IN} is called the notch SIF (NSIF). It can be interpreted as the "equivalent SIF" of a notch regardless of whether or not a real crack-like defect is present. Physically, a finite K_I at $a = 0$ cannot occur even at a very sharp notch, but it can occur in cases where a small crack-like defect disturbs the local geometry. However, K_{IN} represents the worst case of K_I of a short crack emanating from a sharp notch, including a small initial crack-like defect of unknown shape and depth.

Correspondingly, the endurance criterion 4 applied to a sharp notch or corner becomes

$$\Delta K_{IN} < \Delta K_{\text{th}}(R) \tag{8}$$

where:

ΔK_{IN} = range of K_{IN} in case of cyclic loading.

Criterion 8 is convenient for practical purposes since the initial crack size, which is poorly defined and difficult to be measured, does not appear explicitly in it. This concept has been successfully applied to predict the endurance limit of welded joints (Refs 7 and 8 and unpublished work).

In the present case of a T-joint as shown in Fig. 3, a curve fit in the sense of Eq 6 of the $K_I(a)$ data shown in Fig. 4 delivers

$$K_I = \frac{2.293 \cdot N}{\sqrt{W}} \cdot \sqrt{\frac{a}{W} + 0.0338} \cdot Y_N(a/W) \tag{9a}$$

with

$$Y_N(a/W) = 1 - 0.5454 \cdot \left(\frac{a}{W}\right) + 5.8863 \cdot \left(\frac{a}{W}\right)^2 - 8.9417 \cdot \left(\frac{a}{W}\right)^3 + 15.809 \cdot \left(\frac{a}{W}\right)^4 \tag{9b}$$

for a loading by a normal force N and

$$K_I = \frac{8.97 \cdot M}{W^{1.5}} \cdot \sqrt{\frac{a}{W} + 0.0625} \cdot Y_M(a/W) \tag{9c}$$

with

$$Y_M(a/W) = 1 - 0.0298 \cdot \left(\frac{a}{W}\right) - 0.2622 \cdot \left(\frac{a}{W}\right)^2 + 5.132 \cdot \left(\frac{a}{W}\right)^3 - 0.8777 \cdot \left(\frac{a}{W}\right)^4 \tag{9d}$$

for a bending moment M. These fitting curves are also shown in Fig. 4. From Eqs 9a–9d, K_{IN} as defined in Eq 7 turns out to be

$$K_{IN} = (0.374 \cdot \sigma_b + 0.422 \cdot \sigma_t) \cdot \sqrt{W} \tag{10a}$$

where:

$$\sigma_b = \frac{6M}{W^2} \quad \text{and} \quad \sigma_t = \frac{N}{W} \tag{10b}$$

denote the nominal bending and tensile stresses, respectively, that are introduced by M and N in the T-joint.

Fatigue Crack Growth Threshold

The threshold SIF ΔK_{th} of bulk metal is known to depend on the stress ratio R approximately in the following way [7,8]:

$$\Delta K_{th}(R) = \Delta K_{th0} \cdot (1 - R) \quad \text{for } R \leq 1 - \frac{\Delta K_{th/int}}{\Delta K_{th0}} \tag{11a}$$

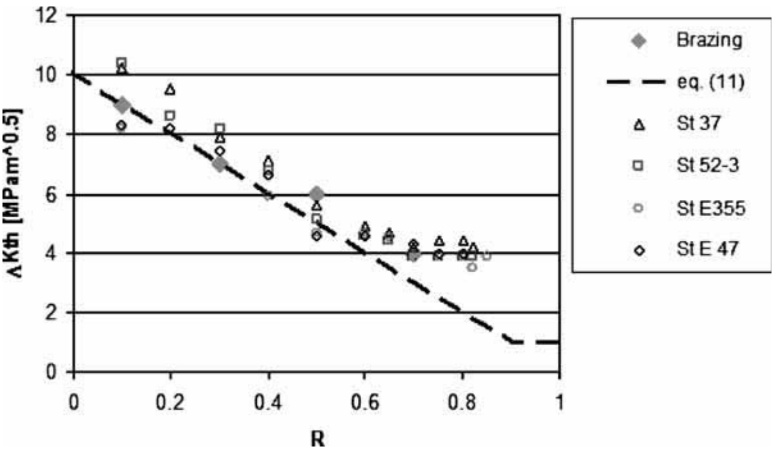

FIG. 5—*Fatigue threshold of a brazed joint* (*Table 1*) *as a function of R, in comparison to data of structural steels from Ref 14* (*cited in Ref 13*).

$$\Delta K_{th} = \Delta K_{th/int} \quad \text{for } R > 1 - \frac{\Delta K_{th/int}}{\Delta K_{th0}} \tag{11b}$$

where:

ΔK_{th0} = threshold SIF for $R=0$ and

$\Delta K_{th/int}$ = so-called intrinsic threshold.

The straight line described by Eq 11a can be physically explained by crack-closure effects that occur at relatively low R. $\Delta K_{th/int}$ forms a lower plateau that is reached for high R-values [9]. For bulk material the latter is known to be approximately proportional to Young's modulus E [10–12]. It can be estimated by

$$\Delta K_{th/int} \approx E \cdot d^{0.5} \tag{12}$$

where:

d = characteristic distance of about $d \approx 2.3 \times 10^{-10}$ (m).

The general behavior of the threshold of brazed joints is expected to be more complex. In Fig. 5 the values from Table 1 are compared with the threshold values of some typical structural steels. They are roughly in line with the latter, which means that the threshold of brazed joints seems to be similar as the one of bulk steel.

At present time there are no experimental data for $R > 0.7$ available, so it is unclear whether the curve of the $K_{th}(R)$ flattens out as R approaches 1 at the same plateau as bulk steel, or whether it further decreases to the plateau of bulk gold, which is obtained by Eq 12 with $E = 78$ MPa, to be about $\Delta K_{th/int/Au} = 1.1$ MPa$\cdot$m$^{0.5}$. From a theoretical point of view, the width of the braze layer is expected to play a certain role: If it is very narrow, then the threshold of bulk steel should apply. If it is wide enough to contain the active plastic zone caused by the cyclic load, the $\Delta K_{th/int}$ of bulk gold may apply. Anyway, in load cases of real components, the R-values are usually rather in the low and medium than in the very high range, so the question of the threshold at high R-values is not a very important one as far as practical applications are concerned. In the following, the dotted line shown in Fig. 5 is assumed to represent a lower bound, with $\Delta K_{th/int/Au}$ denoting the lower plateau. The curve parameters corresponding to the dotted line in Fig. 5 are $\Delta K_{th0} = 10\ \text{MPa}\cdot\text{m}^{0.5}$ and $\Delta K_{th/int} = 1.09\ \text{MPa}\cdot\text{m}^{0.5}$.

Residual Stress Effects on Crack Growth Threshold

It is well known that the fatigue threshold is affected by residual stresses by their effect on the R-ratio. Often the residual stresses in the specimen, by which the threshold is determined, differ from the ones in the component. In cases like the present one, where da/dN-curves are determined on DCB-specimens and applied to predict the behavior of a T-joint, the effect of the residual stresses on $\Delta K_{th}(R)$ should be considered.

To include the residual stress effect in the analysis, it is suitable to represent the lower-bound curve shown in Fig. 5 in the plane ΔK versus K_{max}, which is obtained by eliminating R from Eqs 11a and 11b by means of Eq 2. Therewith, the endurance criterion 4 becomes

$$K_{max} \le \Delta K_{th0} \quad \text{for } R \le 1 - \frac{\Delta K_{th/int}}{\Delta K_{th0}} \tag{13a}$$

$$\Delta K_I \le \Delta K_{th/int} \quad \text{for } R > 1 - \frac{\Delta K_{th/int}}{\Delta K_{th0}} \tag{13b}$$

The endurance criterion given by Eqs 13a and 13b is represented by the L-shaped line in Fig. 6. In the case of a crack emanating from a notch as considered here, K_{max} can be replaced by $K_{IN,max}$ and ΔK_I by ΔK_{IN}, which represent the maximum and the range of K_{IN}, respectively.

The SIF due to residual stresses should be either added to the left hand side of Eq 13a or subtracted from the right hand side. As mentioned in the Introduction, in brazed joints there are hardly any significant global residual stresses since the temperature history of the brazing process acts like a stress relief treatment. On the other hand, due to the mismatch of thermal expansion between the filler material and the bulk material, some local residual stresses are inevitable in the vicinity of the braze layer. Although the corresponding stress field acts only locally, they can give rise to a SIF $K_{Irs}(a)$, which can affect fatigue crack growth, particularly in the threshold region. This is an inherent effect of the considered brazed seam, so it is suitable to include it on the right hand side of Eq 13a, which leads to

$$K_{IN,max} \le \Delta K_{th0} - K_{Nrs} \quad \text{for } R \le 1 - \frac{\Delta K_{th/int}}{\Delta K_{th0}} \tag{14a}$$

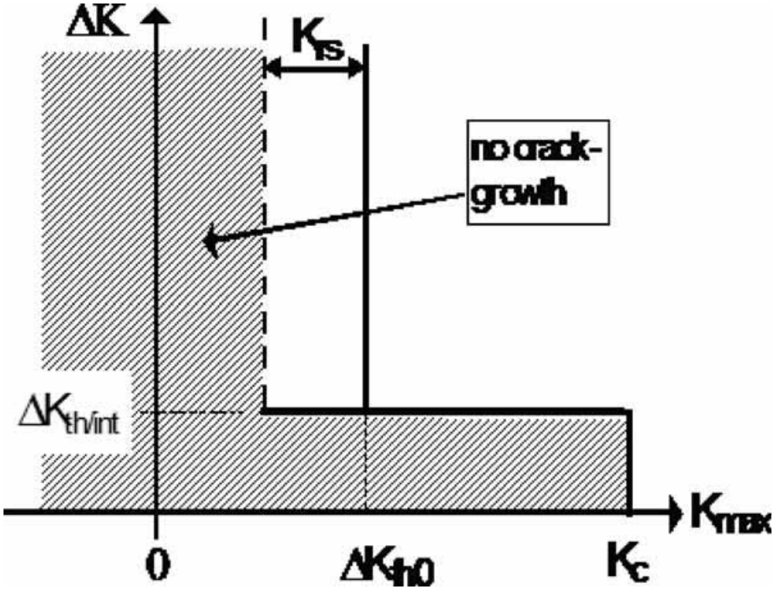

FIG. 6—*Fatigue crack growth threshold represented in the* ΔK *versus* K_{max} *diagram.*

$$\Delta K_{IN} \leq \Delta K_{\text{th/int}} \quad \text{for } R > 1 - \frac{\Delta K_{\text{th/int}}}{\Delta K_{\text{th0}}} \tag{14b}$$

In Eq 14a, K_{Nrs} denotes the local maximum of $K_{\text{Irs}}(a)$ in the vicinity of the surface, i.e., for short crack lengths. This value can be obtained from the measured curves $K_{\text{Irs}}(a)$ that are obtained by the CC-method as described in the next section.

Measurement of the Residual Stresses

An efficient method to determine SIF due to residual stresses is the CC technique [15,16]. It enables the residual stress distribution on a complete cross-section as well as the resulting SIF to be measured. However, the disadvantage of the method is that it works only for two-dimensional components. Thus, structures in three dimensions like the considered impellers have to be cut in such a way that approximately plane slices are obtained. The corresponding stress-redistribution on the cross-section in question has to be measured and taken into account.

The brazed turbo compressor impellers shown in Fig. 1 was use to measure the residual stresses. The impeller consists of the soft martensitic stainless steel X3CrNiMo13-4. Brazing was performed in an industrial shielding gas furnace (SOLO Profitherm 600) at a temperature of 1020°C for 20 min. Hydro-argon 7 (93 vol. % Ar and 7 vol. % H_2) was used as shielding gas. The addition of hydrogen to the argon allows removing the oxide film on the stainless steel surface, which is essential for filler metal wetting. After brazing, the specimens

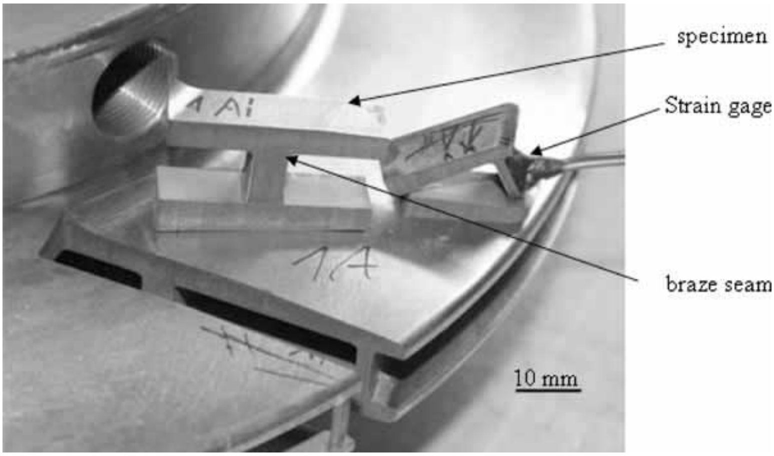

FIG. 7—*H-shaped specimen (denoted by 1Ai) removed from the impeller by EDM-cutting.*

were tempered at 520°C for 5.5 h in nitrogen atmosphere. A brazing zone width of approximately 100 μm is finally achieved. To obtain specimens at representative locations a cut was introduced by electric discharge machining (EDM) in the impeller such that H-shaped samples designated shown in Fig. 7 were obtained. The corresponding global stress release was measured by strain gage that can be seen on Fig. 7. As expected from the above discussion, no significant strains were measured by the strain gage due to cutting out the specimen. By a second cut, the H-shaped specimen shown in Fig. 7 was turned into a T-shaped one, on which the measurements described in the following were performed.

In order to apply the CC-method to a T-shaped specimen as small as the ones shown in Fig. 7, the procedure was modified such that the displacement v could be measured (Fig. 8) instead of the normally measured back-face strain (see example in Ref 7). As derived in Ref 17 for the case of a measured strain, the SIF due to the residual stresses can be obtained analogously from a measured displacement such as $v(a)$ by the general relation

$$K_{\mathrm{Irs}}(a) = \frac{E}{Z(a)} \cdot \frac{dv(a)}{da} \tag{15}$$

where:

E = Young's modulus and

$Z(a)$ = corresponding influence function [16,17].

Figure 9 shows the measured displacements. The $K_{\mathrm{Irs}}(a)$ resulting from applying Eq 15 to the measured displacements are shown in Fig. 10. From the distribution of $K_{\mathrm{Irs}}(a)$, one can see that there is a very sharp tensile peak near the surface, followed by region of predominant compression. The dimples in the $K_{\mathrm{Irs}}(a)$ curves are expected to reflect local inhomogeneities in the brazed

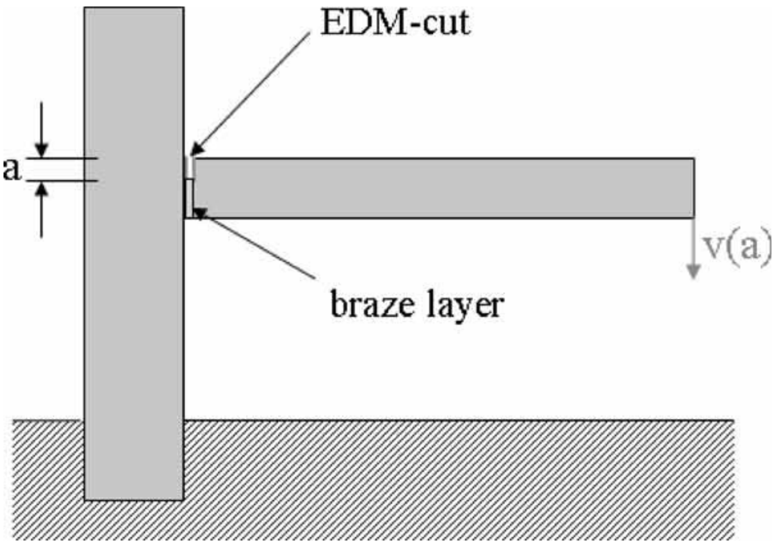

FIG. 8—*Displacement v at a T-shaped specimen due to cut of depth a along the brazed seam (schematically).*

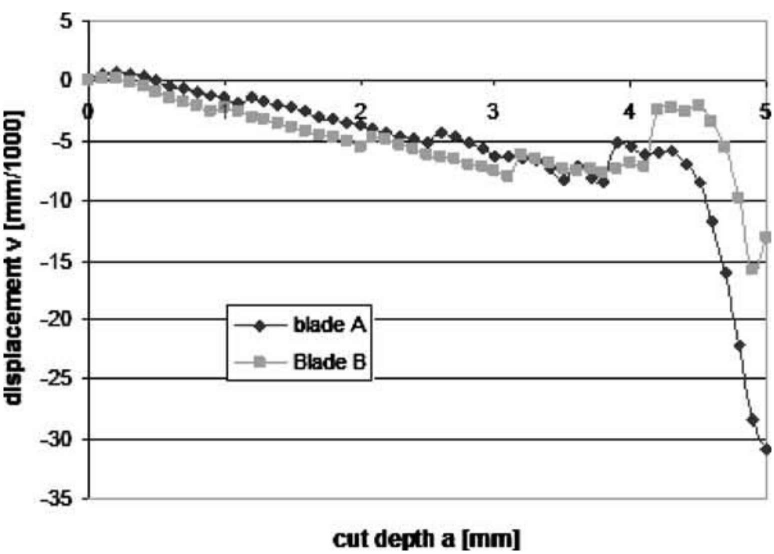

FIG. 9—*Measured displacements at two arbitrary blades A and B.*

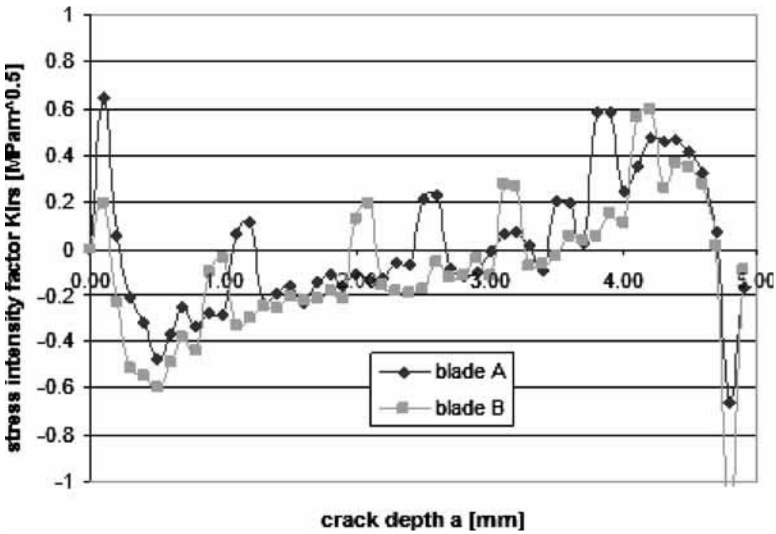

FIG. 10—*SIF as a function of cut depth a obtained by Eq 15 from displacements shown in Fig. 9.*

layer such as clusters of voids. The agreement between blades A and B, which are two arbitrary blades from the same impeller, is relatively good, indicating that the measurements were repeatable.

Fatigue Assessment of a T-Shaped Brazed Joint

For the sake of simplicity we ignore the relatively small difference between the weighting factors of the bending and tensile stresses, respectively, that appear in Eqs 9a–9d, which simplify the latter to

$$K_{IN} \cong 0.422 \cdot \sigma_{\text{app}} \cdot \sqrt{W} \tag{16}$$

where:

$$\sigma_{\text{app}} = \frac{6M}{W^2} + \frac{N}{W} \tag{17}$$

where:

σ_{app} is the total nominal stress of the T-joint near the braze seam.

In the case of an impeller, σ_{app} is the nominal stress perpendicular to the braze seam on the surface of a blade, which can be obtained by a finite element analysis.

By inserting Eqs 16 in 14a one obtains the following criterion for endurance:

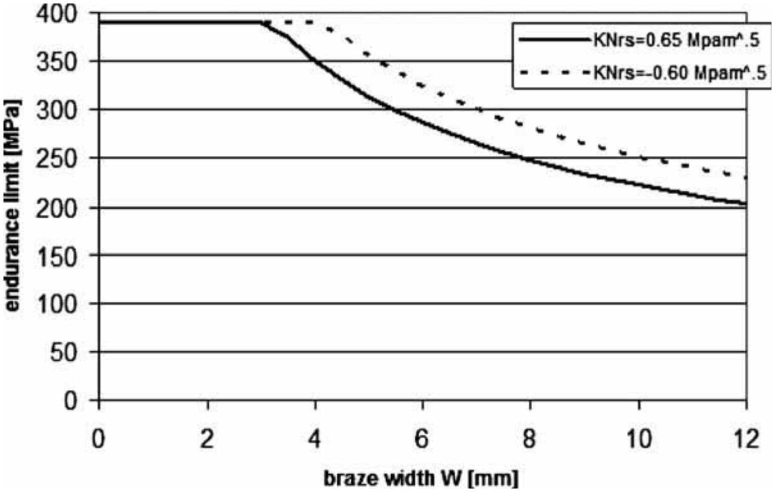

FIG. 11—*Endurance limit* (*right hand side of Eq 18*) *for two cases of residual stress.*

$$\sigma_{\text{app}} < \frac{\Delta K_{\text{th0}} - K_{\text{Nrs}}}{0.422 \cdot \sqrt{W}} \tag{18}$$

The value of ΔK_{th0} corresponding to the lower bound of the measured $\Delta K_{\text{th}}(R)$ (dotted line in Fig. 5) is $\Delta K_{\text{th0}} = 10.0\ \text{MPa}\cdot\text{m}^{0.5}$. K_{Nrs}, which is defined as the maximum K_{Irs} in the range of relatively small cut depths a, is found from the measured curves in Fig. 10 to be roughly $K_{\text{Nrs}} = 0.65\ \text{MPa}\cdot\text{m}^{0.5}$. However, the corresponding first peak is very narrow. After only a few tenths of a millimeter, K_{Irs} becomes about $K_{\text{Nrs}} = -0.60\ \text{MPa}\cdot\text{m}^{0.5}$ and stays negative for a large range of crack depth. This effect is discussed below.

With these numerical values, the right hand side of Eq 18, which represents the theoretical endurance limit, is shown graphically in Fig. 11 as a function of the width of the braze seam, i.e., the thickness of the blade in the case of an impeller. In order to show the effect of the residual stresses, the less conservative case of $K_{\text{Nrs}} = -0.60\ \text{MPa}\cdot\text{m}^{0.5}$ is included for comparison. As W approaches zero the endurance limit according to Eq 18 tends to infinity. Of course the curve is cut-off at the level of the endurance limit of the uniaxial tensile test, which is commonly assumed to be $\sim 0.4 \cdot R_m$ [13], with $R_m \approx 980\ \text{MPa}$ for the brazed joint considered here.

Discussion and Conclusions

The fatigue crack growth behavior of brazed joints is different from the one of bulk material. The threshold values are similar, but the subsequent da/dN-curve rises much steeper with increasing ΔK. Therefore it is not recommended to perform a crack growth calculation to show a safe-life behavior. There should be no growth at all of crack-like defects even for loads that occur only by relatively few cycles.

To show endurance for structures with stress concentrations and crack-like defects, an analysis based on fracture mechanics should be applied. A relatively simple method is suggested in this paper. Note that the initial crack size and shape do not appear explicitly in the corresponding equations. This is suitable since the defect size at the edge of a T-shaped braze seam is usually not known exactly. The endurance limit shown in Fig. 11 covers pre-existing cracks up to a few tenths of a millimeter. For known larger defect sizes, the full solution of $K_I(a)$ as given in Eqs 9a–9d should be used instead of the NSIF K_{IN}, but it is expected that the presented simple solution covers most of the pre-existing defects. Unpublished experiments performed by one of the authors have revealed that typical brazing defects like voids as a result of incomplete gap filling exhibit a significantly higher resistance to growth than an actual fatigue crack. This adds another component of safety.

Another interesting and important finding is that the derived endurance limit (Fig. 11) depends on the width W of the braze seam, i.e., the width of the impeller blade in the present case. This means that thinner blades can withstand higher fatigue stresses than thicker ones.

From the few residual stress measurements performed so far, one can conclude that there are some residual stresses in the impellers, but they do not play a crucial role in the endurance limit. It seems to be clear that they only contribute to the ΔK_{th} by less than about $1.0\ \text{MPa}\cdot\text{m}^{0.5}$ to the threshold, which means less than about 10 %. It is not quite clear yet whether they affect it in a positive or negative way: There is a very sharp positive peak of K_{Irs} at a cut depth of about 0.1 mm, followed by a large range of a, where K_{Irs} is negative. Physically, the latter is expected to be more relevant since it increases the threshold in the long and crucial phase where the defect or crack size is longer than 0.1 mm, whereas influencing factors in the initiation phase are less important. The effect of the residual stresses on the endurance limit is not very large anyway, as can be seen from the comparison of the two curves shown in Fig. 11. However, as long as this question is not resolved by further comparisons of experimental data, it is recommended to consider the more conservative value $K_{\text{Nrs}}=0.65\ \text{MPa}\cdot\text{m}^{0.5}$.

The procedure presented in this paper is a first attempt to establish a practical fatigue design concept for brazed structures. No considerations about adequate safety factors are made yet. The presented numbers and parameters have to be regarded as preliminary and informative. They need further justification by further experimental and theoretical data, particularly fatigue data from T-shaped brazed bonds, which are planned but not available yet.

Acknowledgments

The writers wish to thank MAN Turbo Switzerland, in particular Dr. Hans Gut, for enabling and supporting this work.

References

[1] Leinenbach, C., Schindler, H. J., Baser, T., Rüttimann, N., and Wegener, K., "Fracture Behaviour and Defect Assessment of Brazed Martensitic Stainless Steel Joints," *Eng. Failure Anal.*, in press.

[2] Leinenbach, C., Schindler, H. J., Baser, T. A., Rüttimann, N., and Wegener, K., "Fracture Behaviour and Defect Assessment of Brazed Steel Joints," *Proc. of the 17th European Conference on Fracture—ECF17*, Brno, Czech Republic, September 5–9, 2008, pp. 2121–2128.

[3] Kassner, M. E., Kennedy, T. C., and Schrems, K. K., "The Mechanism of Ductile Fracture in Constrained Thin Silver Films," *Acta Mater.*, Vol. 46, 1998, pp. 6445–6457.

[4] Tolle, M. C., Kassner, M. E., Cerri, E., and Rosen, R. S., "Mechanical Behaviour and Microstructure of Au–Ni Brazes," *Metall. Mater. Trans. A*, Vol. 26, 1995, pp. 941–8.

[5] Baser, T. A., Leinenbach, C., and Schindler, H. J., "Fracture Behaviour of Brazed Soft Martensitic Stainless Steel Joints Under Cyclic Loading," *Mater. Sci. Forum*, Vol. 636–637, 2010, pp. 1490–1495.

[6] Baser, T. A., Leinenbach, C., and Schindler, H. J., "Cyclic Fracture Behaviour of Brazed Steel Joints," *Proc. of the 12th International Conference on Fracture* (*ICF12*), Ottawa, July 12–17, 2009.

[7] Schindler, H. J., Sönnichsen, S., and Martens, H. J., "A Fracture Mechanics Approach to Estimate the Fatigue Endurance of Welded T-Joints Including Residual Stress Effects," *Fatigue Fract. Eng. Mater. Struct.*, Vol. 30, 2006, pp. 206–213.

[8] Schindler, H. J., "Endurance Assessment for Notched Structural Parts with Imperfections," *DVM-Bericht*, Vol. 234, 2002, pp. 67–76 (in German).

[9] Schindler, H. J., "On the Significance of Crack Tip Shielding in Fatigue Threshold—Theoretical Relations and Experimental Implications," *Fatigue Crack Growth Thresholds, Endurance Limits, and Design, ASTM STP 1372*, J. C. Newman and R. S. Piascik, Eds., ASTM International, West Conshohocken, PA, 2000.

[10] Hertzberg, R. W., "On the Calculation of Closure-Free Fatigue Crack Propagation Data in Monolithic Metal Alloys," *Mater. Sci. Eng., A*, Vol. 190, 1995, pp. 25–32.

[11] Sadananda, K. and Shahinian, P., "Prediction of Threshold Stress Intensity for Fatigue Crack Growth using a Dislocation Model," *Int. J. Fract.*, Vol. 13, 1977, pp. 585–594.

[12] Riemelmoser, F. O. and Pippan, R., *Fatigue Crack Growth Thresholds, Endurance Limits, and Design, ASTM STP 1372*, J. C. Newman and R. S. Piascik, Eds., ASTM International, West Conshohocken, PA, 2000.

[13] Forschungskuratorium Maschinenbau, *Stress Analysis Based on Fracture Mechanics*, VDMA Verlag GmbH, 2001, Frankfurt, Germany (in German).

[14] Han, S., *Crack Growth Behaviour of Structural Steels in the Threshold Regime*, Shaker Verlag, Aachen (Germany), 1996, Band 8/96 (in German).

[15] Prime, M. B., "Residual Stress Measurement by Successive Extension of a Slot: The Crack Compliance Method," *Appl. Mech. Rev.*, Vol. 52, No. 2, 1999, pp. 75–96.

[16] Schindler, H. J., "Effects of Residual Stresses on Crack Growth and Structural Safety," *Proceedings of the Ninth Int. Conf. on Mechanical Behaviour of Materials* (*ICM 9, Invited Sectional Lecture*), Geneva, 2003.

[17] Schindler, H. J., Cheng, W., and Finnie, I., "Experimental Determination of Stress Intensity Factors Due to Residual Stresses," *Exp. Mech.*, Vol. 37, No. 3, 1997, pp. 272–277.

Reprinted from JAI, Vol. 7, No. 6
doi:10.1520/JAI102698
Available online at www.astm.org/JAI

John T. Wang[1] *and Stephen W. Smith*[1]

Residual Strain Effects on Bridging Stress of Cracked and Delaminated Fiber Metal Laminates

ABSTRACT: An analytical model is developed that accounts for the effects of both residual thermal strain and residual post-cure stretching strain in the prediction of the bridging stress and the crack opening displacement (COD) of cracked and delaminated fiber metal laminates. Two GLARE® tensile specimen configurations with center cracks in the aluminum layers, one with elliptically shaped delaminations and the other with rhomboidally shaped delaminations, are analyzed with the governing solutions of the analytical model. The shear deformations at the delamination front of either the resin rich region at the metal-fiber layer interface or the fiber layer itself are modeled. Analytical results show that the presence of residual thermal strain reduces the bridging stress while residual post-cure stretching strain increases the bridging stress. A high post-cure stretching level, inducing a greater bridging stress for lowering the COD and also affecting crack closure at crack tips, can result in an increased fatigue life. The use of either of the two shear models has negligible effect on the calculated bridging stress and COD. The analytical results are correlated with available test data of CODs for validating the analytical model.

KEYWORDS: fiber metal laminate, GLARE®, bridging stress, crack opening displacement, fatigue crack growth, residual strain, post-cure stretching, delamination

---

Manuscript received August 21, 2009; accepted for publication May 4, 2010; published online June 2010.
[1] NASA Langley Research Center, Hampton, VA 23681.

Cite as: Wang, J. T. and Smith, S. W., "Residual Strain Effects on Bridging Stress of Cracked and Delaminated Fiber Metal Laminates," *J. ASTM Intl.*, Vol. 7, No. 6. doi:10.1520/JAI102698.

Nomenclature

$2a$ = total crack length
$2b$ = total delamination height at $x = 0$
$C(y_i)$ = shear correction factor for short delamination height y_i
E_{al}, E_{fm}, E_{la} = Young's moduli of the aluminum layers, the glass/epoxy layers, and the FML, respectively
E_T = tangent modulus of the aluminum layers beyond the yield point
F_{ad}, F_{al}, F_{fm}, F_{la} = stiffness parameters of the resin rich region, the aluminum layers, the glass/epoxy layers, and the FML, respectively
$G(x_i, x_j)$ = Green's function relating the bridging stress at location x_j to the COD at location x_i
G_{ad}, G_{fm} = shear modulus of the resin rich region, and the glass/epoxy layer, respectively
$L(x_j, y_j)$ = correction factor for COD at location x_j due to bridging stress applied at the delamination front y_j
N = number of bar elements
N_{test} = number of test data
t_{ad}, t_{al}, t_{fm}, t_{la} = thicknesses of the resin rich region, the aluminum layers, the glass/epoxy layers, and the FML, respectively
u_{ad}, u_{alrs}, u_{∞}, u_{br} = COD due to shear deformation of resin rich region or fiber layer, residual strain in aluminum layers, the applied remote stress, and the bridging stress, respectively
u_{fm} = fiber extension due to bridging stress
u_{fmrs} = fiber length change due to residual strain
w = specimen width
y_i = delamination height at x_i
δ_{ij} = Kronecker delta
ε_{alp} = plastic strain of stretched aluminum layers
ε_{altr}, ε_{fmtr} = residual thermal strains of aluminum and fiber layers, respectively
ε_{alsr}, ε_{fmsr} = residual strains after post-cure stretching of aluminum and fiber layers, respectively
ν = Poisson's ratio of FML
σ_o = applied remote uniform stress
σ_{br} = average bridging stress over the total thickness of FML
σ_{fm} = bridging stress of fiber layer

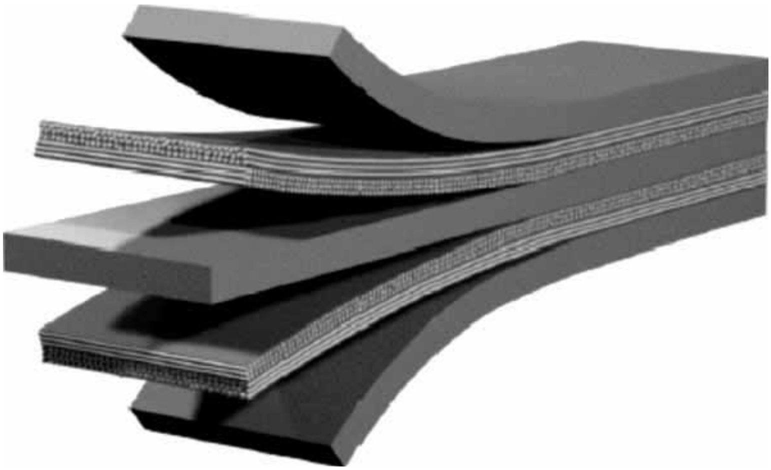

FIG. 1—*Illustration of Glare laminate consisting of two cross-ply prepreg layers* (*0°/90°*) *laminated between three metal layers* [*1*].

Introduction

Fiber metal laminates (FMLs) such as GLARE®, GLAss REinforced aluminum laminates, shown in Fig. 1 are increasingly being used in aircraft structures. GLARE® is a registered trademark of Structural Laminates Company, a joint venture of Aluminum Corporation of America (ALCOA) and Akzo Nobel. Although GLARE® is a registered trademark, the term Glare has been generically used for products manufactured with bonded thin aluminum sheets and glass fiber/epoxy layers. Glare has excellent fatigue capability due to the fact that the glass fiber layers can remain intact, carrying load even after the adjacent aluminum layers are damaged [1–3]. Under fatigue loading, cracks are nucleated and propagate in the aluminum layers. Delaminations are then produced at the metal-glass/epoxy interfaces as shown in Fig. 2. In the delaminated region, the axial loads are channeled through the intact fibers. This phenomenon is called fiber bridging and induces bridging stresses along the delamination boundary (see Fig. 2), restraining the crack opening of the metal layers. Greater bridging stresses will result in larger closure tractions to reduce crack opening displacement (COD) for the cracked aluminum layers, thus reducing the crack growth rates.

FMLs are fabricated by alternating layers of thin metallic sheet and fiber prepreg and curing the laminated layers in an autoclave at an elevated temperature (typically the process is performed at 120°C at a maximum pressure of 6 bar for Glare [1]). Upon cooling, a residual thermal strain is produced due to the coefficient of thermal expansion (CTE) for the metal layers being greater than the CTE of the glass/epoxy layers. A cured Glare has a residual tensile strain in the metal layers and a residual compressive strain in the glass/epoxy layers. The cured FML can be stretched at room temperature to create a small

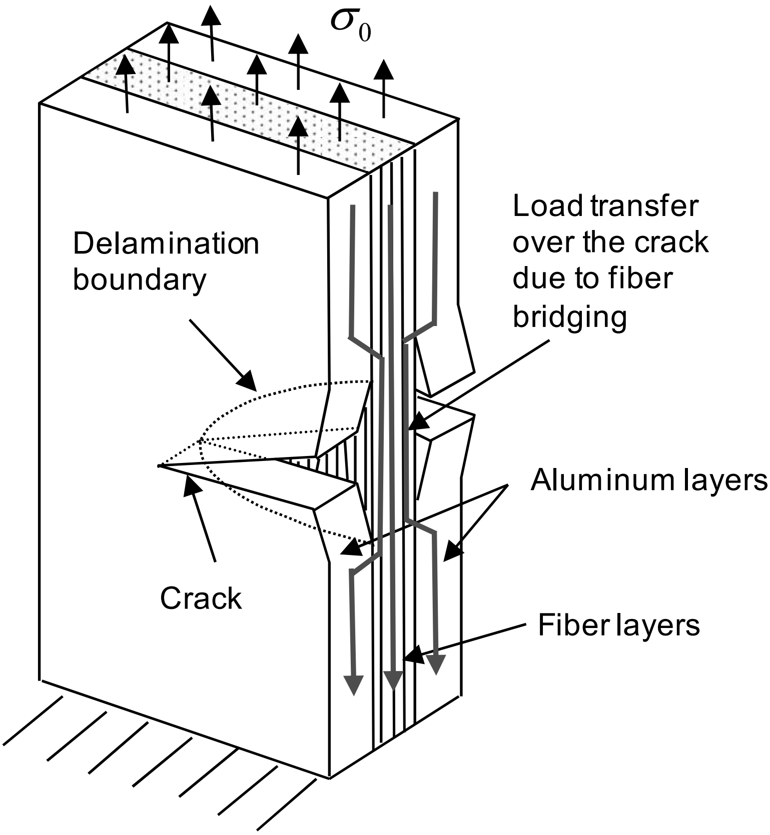

FIG. 2—*Fiber bridging and delamination affecting crack growth in metal layers* [3,5].

plastic strain in the metal layers, while the glass/epoxy layers are strained elastically. After stretching, the residual strain reverses from tension to compression in the metal layers and from compression to tension in the fiber layers. The compressive residual strain in the metal layers induced by the post-cure stretching process can be beneficial [2,4,5]. Tests have shown that the post-cure stretching process can further reduce the crack growth rate of the FMLs [2,4]. Since the crack growth rate is dependent upon the bridging stresses and the CODs [1,2], the reduction in crack growth rate indicates that the residual strain induced by the post-cure stretching process must be considered in predicting the bridging stresses and the CODs for a cracked FML under fatigue loading. It should be noted that a crack closure effect [6], due to the plastic deformation around the crack tip, will be heavily influenced by post-cure stretching, and should be considered for predicting crack growth rate [5]. The crack closure effect is not included in this study.

Analytical models for predicting the bridging stress distributions have been developed by many researchers, such as Marissen [2], Guo and Wu [3], and Alderliesten et al. [1,7]. Marissen's model assumes that fiber bridging stress over the entire crack length is constant, and thus the model may be only applicable for FMLs with near elliptical shape delamination. In Guo and Wu's model, the bridging stress is determined by equating the relations describing the crack opening in the aluminum layers and the relations describing the elongation and deformation of the fiber layers within the delaminated area. They derived the expressions for the CODs due to fiber elongation, adhesive shear deformation and the remote applied stress similar to Marissen [2]. Guo and Wu's model, which calculates the bridging stresses along the crack length based on the delamination shape, can be used for arbitrary delamination shapes. Their calculations and experiments show that the bridging stress for an elliptical shape delamination is approximately constant along the crack, while the bridging stress for a triangular shape delamination increases toward the crack tip. The adhesive shear model derived by Marissen [2] assumes an adhesive rich region along the aluminum interfaces, which is generally not the case for Glare [1,7]. Consequently, Alderliesten developed a prepreg shear model [1,7] to model the shear deformation of the prepreg layer without a resin rich region. Here, the bridging stress was computed following Guo and Wu's approach. The effects of residual strain are considered in Marissen's model, but they are not considered in Guo and Wu's and Alderliesten's models. To the author's knowledge, an analytical model that can systematically account for the effects of both residual thermal strain and residual post-cure stretching strain in the prediction of bridging stress distribution for cracked FMLs with arbitrary shape delamination has yet to be developed.

The objective of this paper is to develop and present an analytical method for investigating the effects of residual strains on the bridging stress and the COD of cracked FMLs with arbitrary shape delaminations to better understand the fatigue crack growth behavior of these materials. Governing equations developed by Guo and Wu [3] for predicting bridging stress and COD are modified to include the terms that reflect the residual strain effects. Residual strains include both residual thermal strains due to the cure process and residual stretch strains that can be induced if a post-cure stretching process is performed. Results of bridging stress distribution and COD for specimens with both residual thermal strain and residual post-cure stretching strain are calculated. These results are correlated with available test data for validating the analytical model.

Cracked and Delaminated Fiber Metal Laminate Models

Analytical methods developed in this paper were used to analyze two center-crack tension (CCT) configurations presented elsewhere [3] as depicted in Fig. 3. A remote uniform tensile stress of 150 MPa is applied in the analysis to be consistent with that applied to the specimens [3]. Both configurations are Glare 2/1 laminates (two aluminum layers and one glass/epoxy layer designated as 2/1) and have a width of 100 mm and a length of 300 mm. The fibers in the unidirectional glass/epoxy layer are along the loading direction. Two delamination configurations, elliptical or rhomboidal, as shown in Fig. 3 were examined. The two delamination configurations resemble typical delamination shapes ob-

TABLE 2—*Mechanical properties of S2 glass/epoxy tape.*

S2 Glass/Epoxy	Unit	
Young's modulus in fiber direction, E_{fm}	GPa	48.9
Shear modulus, G_{fm}	GPa	5.55
Poisson's ratio, ν_{12}/ν_{21}		0.33/0.0371
Thermal expansion coefficient in fiber direction, α_{fm}	$1/°C$	6.1×10^{-6}
Total fiber-layer thickness, t_{fm}	mm	0.25

served in the CCT specimens after fatigue tests [2,3]. The dimensions of both delamination configurations are the same, with the width of 40 mm and height of 20 mm. All aluminum layers have a center crack with length of 40 mm, while all glass fibers are intact. The side views of both specimen configurations are also shown in Fig. 3(*a*) and 3(*b*). The material properties for the aluminum layers, glass/epoxy tape layer (glass fibers in the longitudinal direction), and Glare FML laminate are listed in Tables 1–3, respectively. These properties were obtained from Refs 1, 3, and 8. Test data of CODs [3] for these two CCT specimens were used to compare with the analytical results to validate the analytical models developed in this paper.

Modeling Crack Opening Displacement and Bridging Stress

Under cyclic fatigue loading, cracks will nucleate and grow in the aluminum layers, and delaminations between the metal and glass/epoxy layers will propagate normal to the crack plane as shown in Fig. 2. Subsequently, the glass fibers are loaded, resulting in a bridging stress and a reduced stress at the crack tip. To be able to predict the crack growth rates of the aluminum layers, the bridging stress needs to be determined. The bridging stress is related to the tractions for the intact fibers in the crack wake. To be able to rapidly predict the bridging stress, governing equations for modeling the CODs for the aluminum layers and the extension and shear deformation of the glass/epoxy layers need to be derived.

The COD for the aluminum layers may be described by a simple superposition of the three displacement fields as shown in Fig. 4. Figure 4(*a*) shows a through-the-thickness saw cut of the same length as a crack of interest is assumed and a remote stress is applied. The displacement at any point, x_i, along the crack is labeled as $u_\infty(x_i)$. Figure 4(*b*) shows the displacement field, $u_{br}(x_i)$,

TABLE 3—*Material properties of Glare 2/1 laminate.*

Glare 2/1 Laminate Properties	Unit	
Young's modulus in fiber direction, E_{la}	GPa	62.2
Shear modulus of resin rich regions, G_{ad}	GPa	0.8
Fiber volume fraction	%	50
Total laminate thickness, t_{la}	mm	1.09

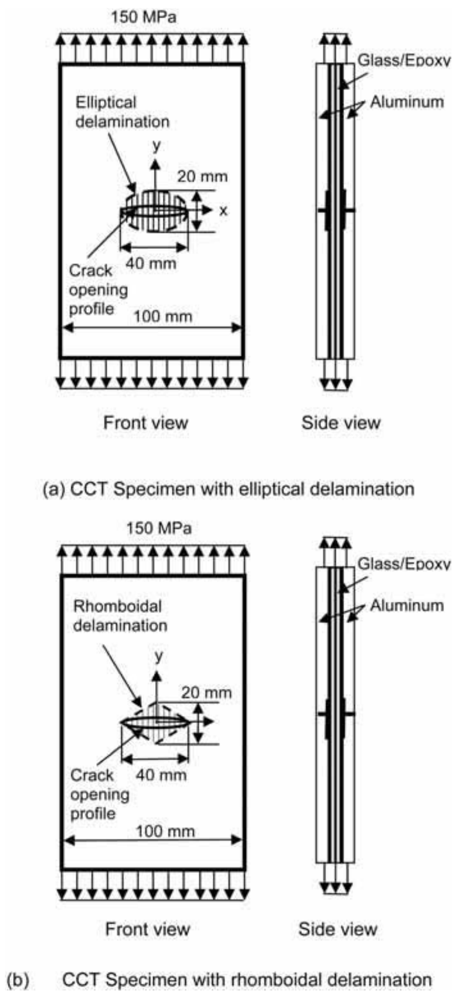

FIG. 3—*CCT specimens with elliptical or rhomboidal delaminations* [*3*].

TABLE 1—*Mechanical properties of aluminum 2024-T3.*

Aluminum 2024-T3	Unit	
Young's modulus, E_{al}	GPa	66.2
Tangent modulus, E_T	GPa	1.47
Tensile yield strain	%	0.524
Poisson's ratio, ν		0.33
Thermal expansion coefficient, α_{al}	1/°C	2.20×10^{-5}
Total aluminum layers thickness, t_{al}	mm	$2\times0.42=0.84$

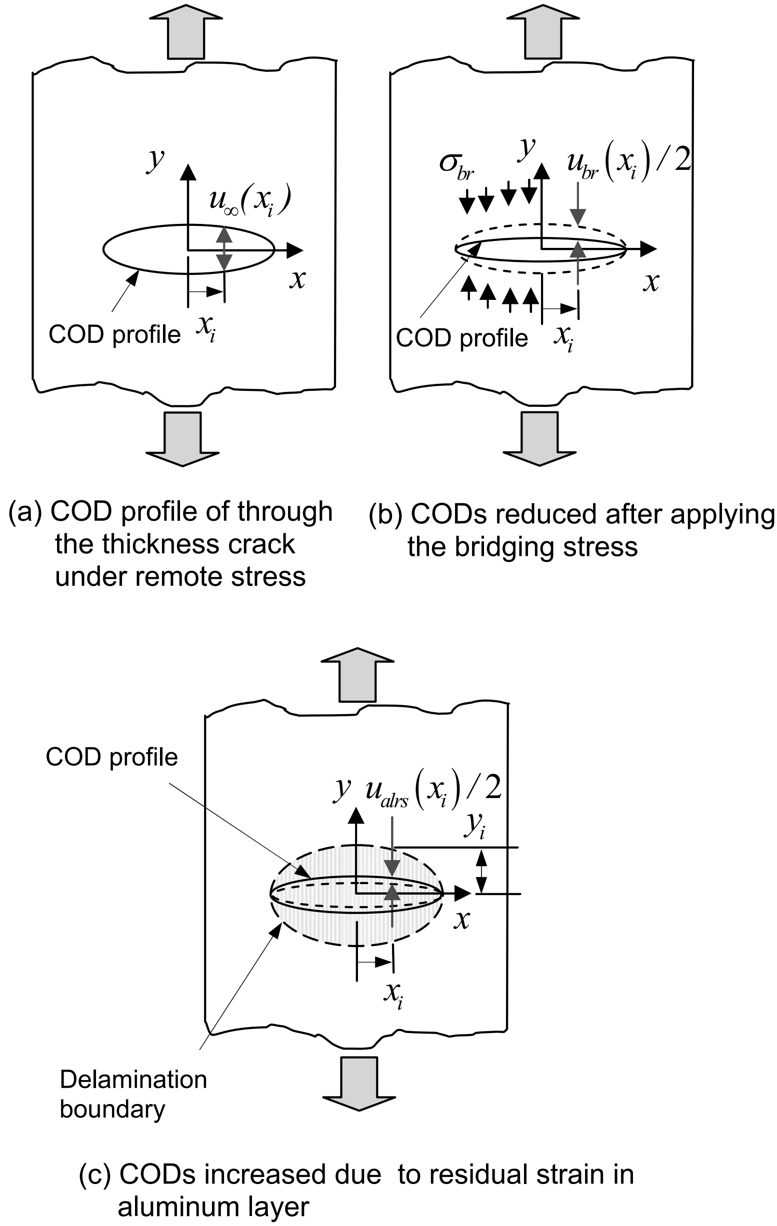

FIG. 4—*Influence of the superposition of different displacement fields on CODs.*

associated with the bridging stress for the fibers that are intact. Figure 4(*c*) shows the displacement field, $u_{alrs}(x_i)$, associated with the presence of residual strain in the aluminum layers. The summation of these displacements results in the determination of the COD

$$\mathrm{COD}(x_i) = u_\infty(x_i) - u_{br}(x_i) + u_{alrs}(x_i) \tag{1}$$

Note that a negative term is used for the bridging displacement since a bridging stress in the glass fiber will act to close the crack.

Assuming perfect bonding in the regions of the FML that are not delaminated (see Fig. 5), the delamination length between points A and B at any location, x_i, along the crack length can be related to the aluminum layer deformation and the fiber-layer deformation in the delaminated region. As shown in Fig. 5(*b*), these two deformations are equal and can be expressed as

$$\mathrm{COD}(x_i) - u_{alrs}(x_i) = u_{fm}(x_i) + u_{ad}(x_i) - u_{fmrs}(x_i) \tag{2}$$

where u_{fm} = fiber extension due to the bridging stress; u_{ad} = shear deformation of the resin rich region or the glass/epoxy layer; and u_{fmrs} = fiber length change due to residual strain. The residual strain can be computed with the classical lamination theory [5].

Substituting $\mathrm{COD}(x_i)$ in Eq 2 with Eq 1, Eq 2 can be expressed as

$$u_\infty(x_i) - u_{br}(x_i) = u_{fm}(x_i) + u_{ad}(x_i) - u_{fmrs}(x_i) \tag{3}$$

This equation will be used for computing the bridging stress (see Eq 21). The terms in Eq 3 and $u_{alrs}(x_i)$ in Eq 2 are defined in the following subsections.

Crack Opening Displacement due to Remote Uniform Stress

The first term, $u_\infty(x_i)$, on the left-hand-side of Eq 3 is the COD at a location x_i of a through-the-thickness crack (saw cut), assuming no intact fibers in the cracked region as shown in Fig. 4(*a*). The COD $u_\infty(x_i)$ under a remote uniform stress σ_o and plane stress condition is given as [3]

$$u_\infty(x_i) = \frac{4\sigma_o}{E_{la}}\sqrt{a^2 - x_i^2}\sqrt{\sec\left(\frac{\pi a}{w}\right)} \tag{4}$$

where:

w = specimen width,

a = half-length of the crack, and

E_{la} listed in Table 3=longitudinal modulus of the laminate.

The secant term in Eq 4 is a finite width correction factor [9] for correcting the Mode I stress intensity factor for CCT specimens. The secant term was compared with the correction factor derived by Tada et al. [10] for COD at the center of a crack in a finite width strip and found to be an appropriate approximation. Its accuracy is better than 1.30 % for $2a/w \leq 0.6$, 2.12 % for $2a/w \leq 0.7$, and 4.23 % for $2a/w \leq 0.8$.

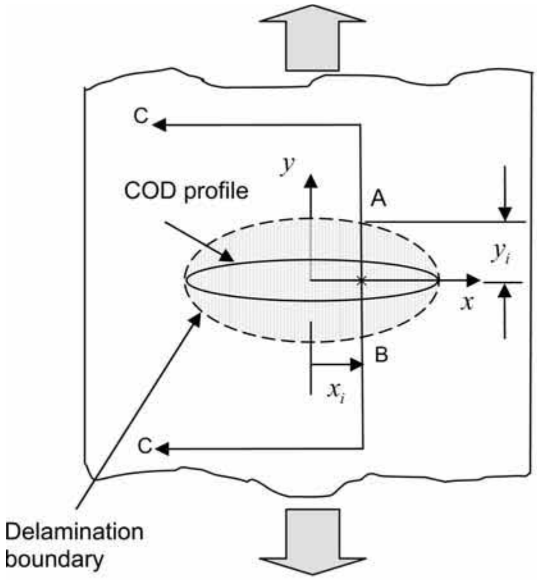

(a) COD profile of a delamination region

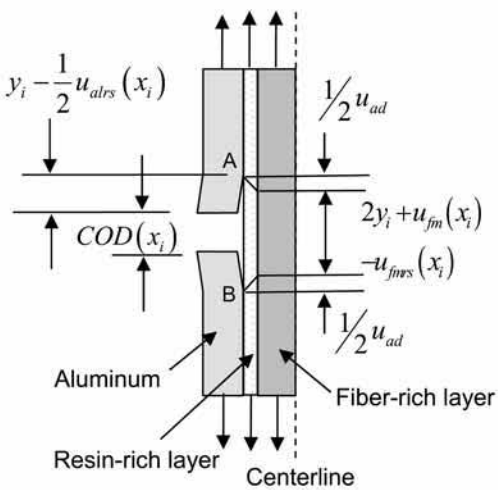

(b) Cross-section C-C view showing that COD is related to fiber extension and shear deformation of resin-rich layer

FIG. 5—*Relationship between COD and glass/epoxy layer deformation.*

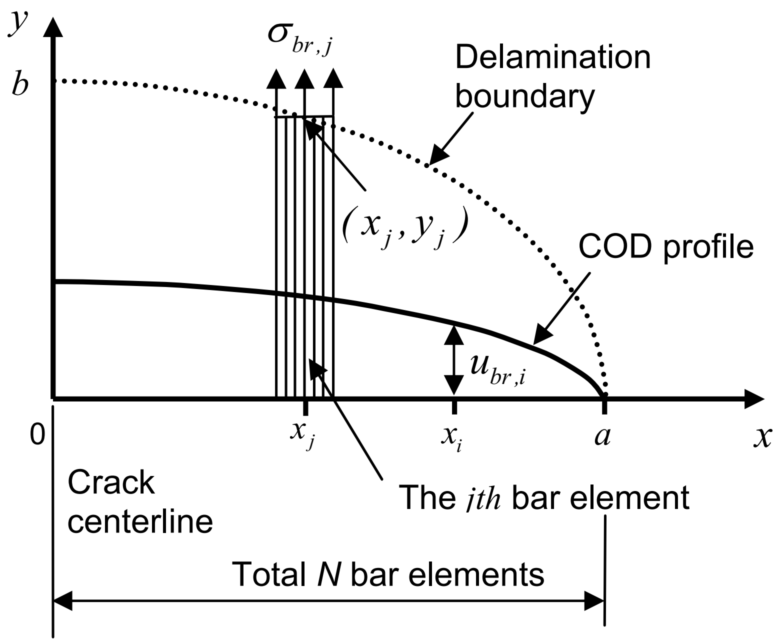

FIG. 6—*COD due to bridging stress* [3,6].

Crack Opening Displacement due to Bridging Stress

The second term, $u_{br}(x_i)$, on the left-hand-side of Eq 3 is the COD at location x_i due to the presence of a bridging stress as shown in Fig. 4(*b*). The COD can only be determined by numerical methods because there is no closed form solution for the COD induced by the bridging stress. Using a crack-closure model developed by Newman [6], the bridged area (from 0 to a) is divided into N bar elements as shown in Fig. 6. Following Ref 3, $N \geq 20$ was used for this study and the solutions obtained were found to be convergent. The width of each bar element is a/N. Note that the bridging area (from $-a$ to 0) is also divided into N bar elements. The COD at x_i can be determined as [3]

$$u_{br}(x_i) = 2\sum_{j=1}^{N} \sigma_{br,j} g(x_i, x_j) L(x_j, y_j) \tag{5}$$

where:

$\sigma_{br,j}$ = bridging stress at x_j, and
$g(x_i, x_j)$ is defined as

$$g(x_i, x_j) = G(-x_i, x_j) + G(x_i, x_j) \tag{6}$$

where:

$G(x_i, x_j)$ = Green's function to relate the bridging stress at location x_j to COD at location x_i, and

$L(x_j, y_j)$ = correction factor to account for the bridging stress applied at the delamination boundary instead of on the crack surface ($y = 0$).

As shown in Fig. 6, y_j is the height of the bar at x_j. For an elliptical delamination, y_j is defined as

$$y_j = b\sqrt{1 - (x_j/a)^2} \tag{7}$$

For a rhomboidal delamination, y_j is defined as

$$y_j = b(1 - x_j/a) \tag{8}$$

where:

b = one-half of the maximum height of the delamination.

Note that $a = 20$ mm and $b = 10$ mm for both delamination shapes as shown in Fig. 3. The bridging stress shown in Fig. 4(*b*) acts in the $-y$ direction to indicate that a positive bridging stress results in crack closure. For a finite width FML, the Green's function, $G(x_i, x_j)$, is expressed as [6]

$$G(x_i,x_j) = \frac{2(1-\eta^2)}{\pi E_{la}} \left\{ \begin{array}{l} \cosh^{-1}\left(\dfrac{a^2 - b_2 x_i}{a|b_2 - x_i|}\right)(b_2 - x_i) - \cosh^{-1}\left(\dfrac{a^2 - b_1 x_i}{a|b_1 - x_i|}\right)(b_1 - x_i) \\ + \sqrt{a^2 - x_i^2}\left[\sin^{-1}\left(\dfrac{b_2}{a}\right) - \sin^{-1}\left(\dfrac{b_1}{a}\right)\right] \end{array} \right\}$$
$$\times \left[\frac{\sin^{-1} B_2 - \sin^{-1} B_1}{\sin^{-1}(b_2/a) - \sin^{-1}(b_1/a)}\right]\sqrt{\sec(\pi a/w)} \tag{9}$$

where:

$\eta = 0$ for plane stress and $\eta = \nu$ for plane strain, and

ν = Poisson's ratio of the FML.

In this study, $\eta = 0$ is used

$$B_k = \frac{\sin\left(\dfrac{\pi b_k}{\mathrm{w}}\right)}{\sin\left(\dfrac{\pi a}{\mathrm{w}}\right)} \quad \text{for} \quad k = 1,2, \quad b_1 = x_j - \frac{a}{2N}, \quad \text{and} \quad b_2 = x_j + \frac{a}{2N}$$

The correction factor, $L(x_j, y_j)$, is expressed as [3,6]

$$L(x_j,y_j) = \sqrt{\frac{1}{2}(a^2 - x_j^2)}\left\{\frac{B}{\sqrt{A}} + y_j^2(1+\nu)\left(\frac{BC}{A^{3/2}} - \frac{\sqrt{A}+C}{2BA}\right)\right\} \tag{10}$$

where:

$A = (a^2 - x_j^2 + y_j^2)^2 + 4x_j^2 y_j^2$,

$B = \sqrt{a^2 - x_j^2 + y_j^2 + \sqrt{A}}$, and

$C = a^2 + x_j^2 + y_j^2$.

Crack Opening Displacement due to Residual Strain

The $u_{alrs}(x_i)$ term in Eq 2 is the COD at location x_i due to the presence of residual strain in the aluminum layers as shown in Fig. 4(*c*). $u_{alrs}(x_i)$ can be expressed as

$$u_{alrs}(x_i) = 2y_i\varepsilon_{alrs} \tag{11}$$

where:

y_i = delamination height at x_i, determined by Eqs 7 and 8 for elliptical and rhomboidal shape delaminations, respectively, and

ε_{alrs} = residual strain.

Explicit forms of ε_{alrs} are given in Eqs 30 and 35 for the residual thermal and residual post-cure stretching strains, respectively.

Extension of Fibers due to Bridging Stress

The first term, $u_{fm}(x_i)$, on the right-hand-side of Eq 3 is the extension of fibers as a result of bridging at a location x_i as shown in Fig. 5(*b*). The term $u_{fm}(x_i)$ can be expressed as

$$u_{fm}(x_i) = 2\frac{\sigma_{fm,i}}{E_{fm}}y_i = 2\frac{\sigma_{br,i}t_{la}}{E_{fm}t_{fm}}y_i \tag{12}$$

where:

$\sigma_{fm,i}$ = bridging stress at x_i of the glass/epoxy layer, and

$\sigma_{br,i}$ = bridging stress at x_i calculated over the total thickness of the FML.

The relationship between $\sigma_{br,i}$ and $\sigma_{fm,i}$ at location x_i can be expressed as

$$\sigma_{br,i} = \frac{\sigma_{fm,i}t_{fm}}{t_{la}} \tag{13}$$

where:

E_{fm} = Young's modulus of the glass/epoxy layer, and

t_{la} and t_{fm} = thickness of the FML and the total thickness of the glass/epoxy layer, respectively.

Shear Deformation

The second term, $u_{ad}(x_i)$, on the right-hand-side of Eq 3 is the total shear deformation of the delamination tips at x_i. Two shear modeling approaches were used to calculate $u_{ad}(x_i)$, one was derived by Marissen [2] and Guo and Wu [3] and the other one was derived by Alderliesten et al. [1,7]. The first approach is the adhesive shear model, which was developed for modeling the shear deformation of the resin rich region which can exist in the fiber layer at the interfaces with the metal, as shown in Fig. 7(*a*). The second approach is the prepreg shear model, which was developed for modeling the shear deformation of a fiber layer when no resin rich region exists between the metal and fiber layers as shown in Fig. 7(*b*). The micrographs shown in Fig. 7 were obtained from Refs 7 and 11.

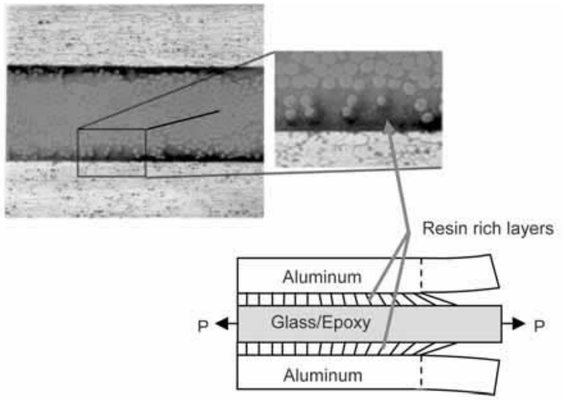

(a) Adhesive shear model [2] for resin rich layers (Note: no scale was provided for the original micrograph [7,11]).

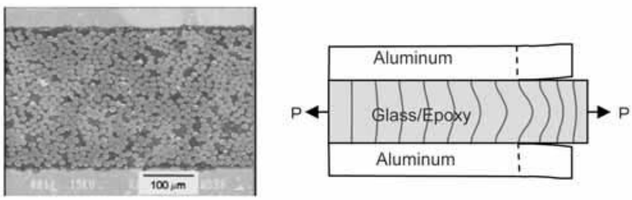

(b) Prepreg shear model [7] for no resin rich layers (Micrograph from Ref 7).

FIG. 7—*Two shear models for predicting the contribution of shear deformation to the COD:* (*a*) *Adhesive shear model* [2] *for resin rich layers* (*note: No scale was provided for the original micrograph* [7,11]); (*b*) *prepreg shear model* [7] *for no resin rich layers* (*micrograph from Ref* 7).

Adhesive Shear Model—For the adhesive shear model, the shear deformation occurs only within the resin rich regions shown in Fig. 7(*a*). This shear model was developed by Marissen [2] based on the approaches used by Hart-Smith [12] and Verbruggen [13]. The shear stress τ exponentially decays with distance from the delamination front. The equation for computing the shear stress at the delamination front is given as [2,3]

$$\tau(x_i) = \frac{\sigma_{br,i}}{E_{la}}\sqrt{\frac{F_{la}F_{al}F_{ad}}{2F_{fm}}} + F_{al}\varepsilon_{alrs}\sqrt{\frac{F_{ad}F_{la}}{2F_{al}F_{fm}}} \tag{14}$$

where:

E_{la} = Young's modulus of the FML, and

F_{la}, F_{al}, F_{fm}, and F_{ad} = stiffness parameters of the FML, the metal layers, the glass/epoxy layer, and the resin rich regions, respectively.

They are defined as

$$F_{la} = E_{la}t_{la}, \quad F_{al} = E_{al}t_{al}, \quad F_{fm} = E_{fm}t_{fm}, \quad F_{ad} = G_{ad}/t_{ad} \tag{15}$$

where:

E_{al} and E_{fm} = Young's modulus of the metal layer and the glass/epoxy layer, respectively,

t_{la}, t_{al}, and t_{fm} = total thicknesses of the FML, the aluminum layers, and the fiber layers, respectively,

G_{ad} = shear modulus of the resin rich region at the metal and fiber-layer interface, and

t_{ad} = thickness of the resin rich region in one interface and assumed to be 20 % of the thickness of a fiber-adhesive layer, t_{fm} [2,3].

At a distance x_i from the crack center, the total shear deformation at the delamination tips is

$$u_{ad}(x_i) = \frac{2\tau(x_i)t_{ad}}{G_{ad}} = \frac{2\sigma_{br,i}}{E_{la}}\sqrt{\frac{F_{la}F_{al}}{2F_{ad}F_{fm}}} + 2\varepsilon_{alrs}\sqrt{\frac{F_{al}F_{la}}{2F_{ad}F_{fm}}} \tag{16}$$

Prepreg Shear Model—The shear deformation model developed by Alderliesten et al. [1,7], assumes that no resin rich region is present at the interface with the aluminum layer as shown in Fig. 7(*b*). At the delamination tip, the shear stress in the glass/epoxy layer (prepreg) is expressed as

$$\tau(x_i) = C(y_i)\sigma_{br,i}\frac{F_{al}}{E_{la}}\sqrt{\frac{G_{fm}}{t_{fm}}\left(\frac{1}{F_{al}} + \frac{1}{F_{fm}}\right)} \tag{17}$$

where:

G_{fm} = shear modulus of the glass/epoxy layer, and

$C(y_i)$ = correction factor expressed as

$$C(y_i) = 1 - [\cosh(\sqrt{2\alpha_{UD}}y_i) - \tanh(\sqrt{2\alpha_{UD}}y_i)\sinh(\sqrt{2\alpha_{UD}}y_i)] \tag{18}$$

where:

$\alpha_{UD} = 16G_{fm}/t_{fm}F_{fm}$.

Note that $C(y_i) = 0$ when the delamination height is zero ($y_i = 0$), thus, the condition of no shear stresses at a symmetry plane is enforced. The displacement due to the shear deformations can be expressed as

$$u_{ad} = C(y_i)\sigma_{br,i}\frac{F_{al}}{E_{la}}\sqrt{\frac{t_{fm}}{G_{fm}}\left(\frac{1}{F_{al}} + \frac{1}{F_{fm}}\right)} \tag{19}$$

Fiber Extension due to Residual Strain

The third term, $u_{fmsr}(x_i)$, on the right-hand-side of Eq 3 is the fiber extension at location x_i due to the presence of residual strain in the fiber layer. $u_{fmrs}(x_i)$ can be expressed as

$$u_{fmrs}(x_i) = 2y_i\varepsilon_{fmrs} \tag{20}$$

where:

ε_{fmrs} = residual strain in the fiber layer.

An explicit form of ε_{fmrs} will be given in Eqs 30 and 32 for the residual thermal and residual post-cure stretching strains, respectively.

Bridging Stress Distribution Solution

The displacement balance expressed in Eq 3 can be rewritten by substituting the left-hand-side terms with Eqs 4 and 5 and the right-hand-side terms with Eqs 12, 16, 19, and 20 to yield the governing equation for the bridging stress distribution

$$2\sigma_{br,i}\left(\frac{t_{la}}{E_{fm}t_{fm}}y_i + D_i\right) + 2\sum_{j=1}^{N}\sigma_{br,j}g(x_i,x_j)L(x_j,y_j)$$
$$= \frac{4\sigma_0}{E_{la}}\sqrt{a^2 - x_i^2}\sqrt{\sec\left(\frac{\pi a}{w}\right)} + 2y_i\varepsilon_{fmrs}$$
$$+ \left(2\varepsilon_{alrs}\sqrt{\frac{F_{al}F_{la}}{2F_{ad}F_{fm}}}\right) \quad \text{(for the adhesive shear model)} \qquad (21a)$$

and

$$2\sigma_{br,i}\left(\frac{t_{la}}{E_{fm}t_{fm}}y_i + D_i\right) + 2\sum_{j=1}^{N}\sigma_{br,j}g(x_i,x_j)L(x_j,y_j) = \frac{4\sigma_0}{E_{la}}\sqrt{a^2 - x_i^2}\sqrt{\sec\left(\frac{\pi a}{w}\right)}$$
$$+ 2y_i\varepsilon_{fmrs} \quad \text{(for the prepreg shear model)} \qquad (21b)$$

where:

$D_i = (1/E_{la})\sqrt{F_{la}F_{al}/(2F_{ad}F_{fm})}$ for the adhesive shear model, and

$D_i = [(C(y_i)F_{al})/(2E_{la})]\sqrt{(t_{fm}/G_{fm})[(1/F_{al}) + (1/F_{fm})]}$ for the prepreg shear model.

Eq 21 can be expressed in matrix form as

$$H_{ij}\sigma_{br,j} = Q_i \quad (i = 1, N, j = 1, N) \qquad (22)$$

where:

$\sigma_{br,j}$ = bridging stress at a distance of x_j from the crack center.

H_{ij} is given by

$$H_{ij} = (P_i + D_i)\delta_{ij} + g_{ij}L_j \quad (i = 1, N, j = 1, N) \qquad (23)$$

where:

δ_{ij} = Kronecker delta ($\delta_{ij} = 1$ if $i = j$ and $\delta_{ij} = 0$ if $i \neq j$), and

$L_j = L(x_j, y_j)$ defined in Eq 10

$$P_i = \frac{t_{la}}{E_{fm}t_{fm}}y_i \qquad (24)$$

and Q_{ij} is given by

$$Q_i = \frac{2\sigma_0}{E_{la}}\sqrt{a^2 - x_i^2}\sqrt{\sec(\pi a/w)} + \varepsilon_{fmrs}y_i + \left(\varepsilon_{alrs}\sqrt{\frac{F_{al}F_{la}}{2F_{ad}F_{fm}}}\right) \quad \text{(for the adhesive shear model)} \tag{25a}$$

and

$$Q_i = \frac{2\sigma_0}{E_{la}}\sqrt{a^2 - x_i^2}\sqrt{\sec(\pi a/w)} + \varepsilon_{fmrs}y_i \quad \text{(for the prepreg shear model)} \tag{25b}$$

Note that the repeated index j in Eqs 22 and 23 does not imply a summation.

Deriving Bridging Stresses from COD Test Data

If CODs have been experimentally measured, either Eq 1 or Eq 2 can be used to determine the bridging stress. By substituting each term in these equations with the corresponding forms presented in the previous subsections, the bridging stress at any location can be determined.

If Eq 1 is used and the terms u_∞, u_{br}, and u_{alrs} are replaced with the solutions of Eqs 4, 5, and 11, respectively, the bridging stress at any location x_j can be expressed as

$$H_{ij}^{*}\sigma_{br,j} = Q_i^{*} - \mathrm{COD}(x_i) \tag{26}$$

where:

$H_{ij}^{*} = g_{ij}L_j$ ($i = 1$, Ntest, $j = 1$, Ntest).

Ntest is the total number of COD test data points. Q_i^{*} is given by

$$Q_i^{*} = \frac{2\sigma_0}{E_{la}}\sqrt{a^2 - x_i^2}\sqrt{\sec(\pi a/w)} + \varepsilon_{alrs}y_i + \varepsilon_{alrs}\sqrt{\frac{F_{al}F_{la}}{2F_{ad}F_{fm}}} \quad \text{(for the adhesive shear model)} \tag{27a}$$

and

$$Q_i^{*} = \frac{2\sigma_0}{E_{la}}\sqrt{a^2 - x_i^2}\sqrt{\sec(\pi a/w)} + \varepsilon_{alrs}y_i \quad \text{(for the prepreg shear model)} \tag{27b}$$

If Eq 2 is used and the terms u_{alrs}, u_{fm}, u_{ad}, and u_{fmrs} are replaced with the solutions of Eqs 4, 12, 16, and 20, respectively, the bridging stress for the adhesive shear model is expressed as

$$\sigma_{br,j} = \frac{\mathrm{COD}(x_j) + 2(\varepsilon_{fmrs} - \varepsilon_{alrs})y_j + \varepsilon_{alrs}\sqrt{\dfrac{F_{al}F_{la}}{2F_{ad}F_{fm}}}}{\dfrac{2t_{la}y_j}{F_{fm}} + \dfrac{2}{E_{la}}\sqrt{\dfrac{F_{la}F_{al}}{2F_{ad}F_{fm}}}} \tag{28}$$

If Eq 2 is used with the same substitutions with the exception of using Eq 19 for u_{ad}, the bridging stress for the prepreg shear model is expressed as

$$\sigma_{br,j} = \frac{\mathrm{COD}(x_j) + 2(\varepsilon_{fmrs} - \varepsilon_{alrs})y_j}{\dfrac{2t_{la}y_j}{F_{fm}} + \dfrac{C(y_j)F_{al}}{E_{la}}\sqrt{\dfrac{t_{fm}}{G_{fm}}\left(\dfrac{1}{F_{al}} + \dfrac{1}{F_{fm}}\right)}} \tag{29}$$

Note that for $y_j = 0$, the denominator is a constant greater than zero for Eq 28 and is reduced to zero for Eq 29. As a result, the bridging stress solution can become unbounded near the crack tip when the prepreg shear model is used.

Residual Thermal and Stretch Strains

Residual strains include both residual thermal strains due to the cure process and residual stretch strains that can be induced if a post-cure stretching process is performed. If the post-cure stretching strain level is sufficiently high to cause plastic deformation in the aluminum layers, the residual strain can be reversed from tension to compression in the aluminum layers and from compression to tension in the fiber layers. Researchers [2,4] have found that compressive residual strain in the aluminum layers can be beneficial for fatigue life of FMLs. Equations for predicting the residual thermal strains and the residual stretch strains are derived in the following subsections. This study assumes that the Glare laminate contains only unidirectional fibers along the loading direction, perpendicular to the crack surfaces, and the transverse residual strains have negligible effect on the COD and bridging stress. Only the residual strains along the loading direction are considered in the following derivations.

Residual Thermal Strain

Residual thermal strain is induced as a result of the differences in the coefficients of thermal expansion between the metal and fiber layers when the FML has cooled from the curing temperature. The nominal curing temperature, T_{cure}, is 120°C and the ambient temperature, T_{ambient}, is 20°C for this study. Using 120°C as the reference temperature, the residual thermal strains in the aluminum layers, ε_{altr}, and in the fiber layers, ε_{fmtr}, at the ambient temperature can be expressed as

$$\varepsilon_{altr} = \varepsilon_b - \alpha_{al}\Delta T, \quad \text{and} \quad \varepsilon_{fmtr} = \varepsilon_b - \alpha_{fm}\Delta T \tag{30}$$

where:

ε_b = equilibrium strain of the FML at 20°C computed by the following force balance equation:

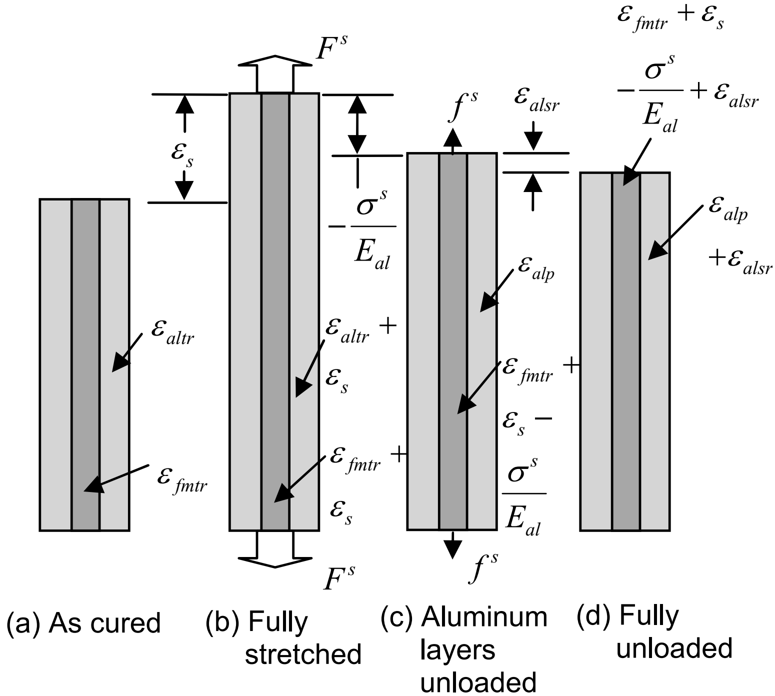

FIG. 8—*Post-cure stretching process steps with strains of the metal and fiber layers.*

$$\varepsilon_b = \frac{(E_{al}t_{al}\alpha_{al} + E_{fm}t_{fm}\alpha_{fm})}{E_{al}t_{al} + E_{fm}t_{fm}}\Delta T \tag{31}$$

where:

$\Delta T = T_{\text{ambient}} - T_{\text{cure}}$, assuming that the glass transition temperature is the same as T_{cure}.

Using the material properties supplied in Tables 1–3 and Eqs 30 and 31, the residual thermal strain in the aluminum layers, $\varepsilon_{altr} = 2.866 \times 10^{-4}$ mm/mm, the residual thermal strain in the fiber layers, $\varepsilon_{fmtr} = -1.303 \times 10^{-3}$ mm/mm, and the equilibrium strain, $\varepsilon_b = -1.913 \times 10^{-3}$ mm/mm. For as-cured FMLs, the residual thermal strains can be directly substituted for residual strains in Eqs 11 and 20 for determining the CODs and bridging stresses for a cracked FML material.

Residual Stretch Strain

Residual strains produced as a result of a stretching process will be evaluated to better understand how to improve the crack growth behavior of the Glare material presented in this study. If the FML is stretched following the cure process beyond the yield point of the aluminum material while still maintaining elastic behavior for the S2 glass fibers, it is possible to plastically deform the aluminum and modify the residual strains present in the aluminum and fiber layers. A series of schematics illustrating the post-cure stretching steps for a Glare 2/1 FML are shown in Fig. 8. The stretching process is performed at ambient temperature and the residual thermal strains in the aluminum and fiber layers are present prior to stretching, see Fig. 8(*a*). Fig. 8(*b*) represents the FML in its fully stretched state, where F^s is the maximum load and ε_s is the maximum stretching strain. Note that the maximum stress must be greater than the yield stress of the aluminum layers or there will be no change in the residual strains from those produced from the cure process. The force can be gradually reduced until the aluminum layers are fully unloaded, but the fibers are still under tensile force, f^s, as shown in Fig. 8(*c*). As the FML is fully unloaded, a compressive residual strain is produced in the aluminum layers, while a tensile residual strain is produced in the fiber layer, see Fig. 8(*d*). The residual strain in the fiber layer as a result of the post-cure stretching process can be expressed as

$$\varepsilon_{fmsr} = \varepsilon_s + \varepsilon_{fmtr} - \frac{\sigma_{al}^s}{E_{al}} + \varepsilon_{alsr} \tag{32}$$

where:

ε_s = stretching strain, and

σ_{al}^s = maximum stress of the aluminum layers during the stretching and can be expressed as

$$\sigma_{al}^s = E_{al}\varepsilon_y + E_T\varepsilon_{alp} \tag{33}$$

where:

$\varepsilon_{alp} = \varepsilon_s + \varepsilon_{altr} - \varepsilon_y$ = plastic strain of the stretched aluminum layers,

ε_y = strain at yield for the aluminum, and

E_T = past yield tangent modulus of aluminum given in Table 1.

Note that the aluminum is modeled as bilinear elastic-plastic material. The residual strain in the aluminum layers, ε_{alsr}, resulting from the post-cure stretching process can be determined from the following force balance equation:

$$E_{fm}t_{fm}\left(\varepsilon_s + \varepsilon_{fmtr} - \frac{\sigma_{al}^s}{E_{al}} + \varepsilon_{alsr}\right) + E_{al}t_{al}(\varepsilon_{alsr}) = 0 \tag{34}$$

from which the residual strain subsequent to post-cure stretching in the aluminum layers can be given by

$$\varepsilon_{alsr} = -\frac{E_{fm}t_{fm}\left(\varepsilon_s + \varepsilon_{fmtr} - \frac{\sigma_{al}^s}{E_{al}}\right)}{E_{fm}t_{fm} + E_{al}t_{al}} \tag{35}$$

Eqs 32 and 35 can be used to determine the residual strains in the aluminum and fiber layers for any strain level, ε_s, used for a post-cure stretching process. Note that if the aluminum layers are not stretched beyond the yield point, the residual stretch strains ε_{alsr} and ε_{fmsr} are equal to the residual thermal strains ε_{altr} and ε_{fmtr}, for the aluminum and fiber layers, respectively. These residual strains can be directly substituted for the residual strains presented in Eqs 11

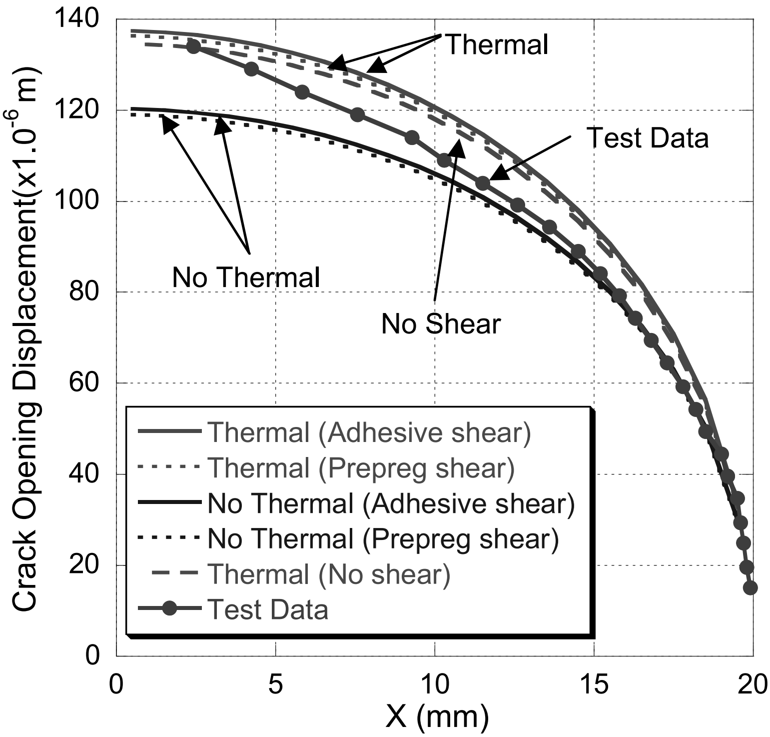

FIG. 9—*Correlating COD test data with predictions using two shear models with and without residual thermal strain for the specimen with elliptical delamination.*

and 20 for determining the CODs and bridging stresses for a cracked FML material that has been post-cure stretched.

Analytical Results

The governing equations derived in the prior section were used to analyze the two CCT specimens with elliptical and rhomboidal delaminations shown in Fig. 3. The CODs and bridging stresses were computed for both configurations with residual thermal strains and residual stretching strains produced for various stretching levels. Analytical results for both configurations were also compared with available test data for validating the analytical model.

Crack Opening Displacement

The CODs for the Glare CCT specimens were analyzed using the adhesive shear and prepreg shear models for both the elliptical and rhomboidal delamination configurations, and the results are presented in Figs. 9 and 10, respectively. Analyses for specimens with and without residual thermal strains were performed. The experimental COD data obtained by Guo and Wu [3] are also

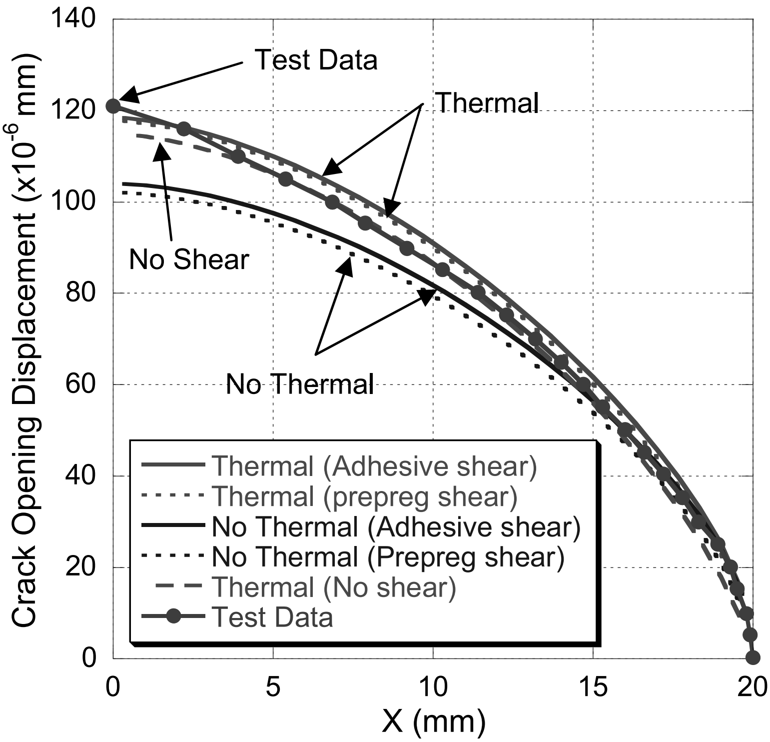

FIG. 10—*Correlating COD test data with predictions using two shear models with and without residual thermal strain for the specimen with rhomboidal delamination.*

presented for comparison. The experimental data were acquired at a remote uniform stress of 150 MPa, and this same stress was used for all analytical results. The adhesive shear model result and the prepreg shear model result are nearly identical for both specimen configurations. The test data for both delamination configurations are bounded by the analytical results for specimens with and without residual thermal strains. Comparison of the results in Figs. 9 and 10 indicates that the COD is greater over the entire crack length for the elliptical delamination than the COD for the rhomboidal delamination, suggesting that the rhomboidal delamination would result in a lower crack growth rate than the elliptical delamination.

A bridging stress analysis without considering the effects of the shear deformation in Eq 21 was performed for each specimen with residual thermal strains. COD results, based on the predicted bridging stresses, are plotted as the "No Shear" curve in Figs. 9 and 10. The closeness of the "No Shear" curve with the two "Thermal" curves, for the adhesive shear model and the prepreg shear model, indicates that COD is fairly insensitive to shear deformation. Note that "Thermal" and "No Thermal" in Figs. 9 and 10 and the subsequent figures identify results with and without residual thermal strains considered, respectively. Comparison of the "Thermal" and "No Thermal" curves in Figs. 9 and 10

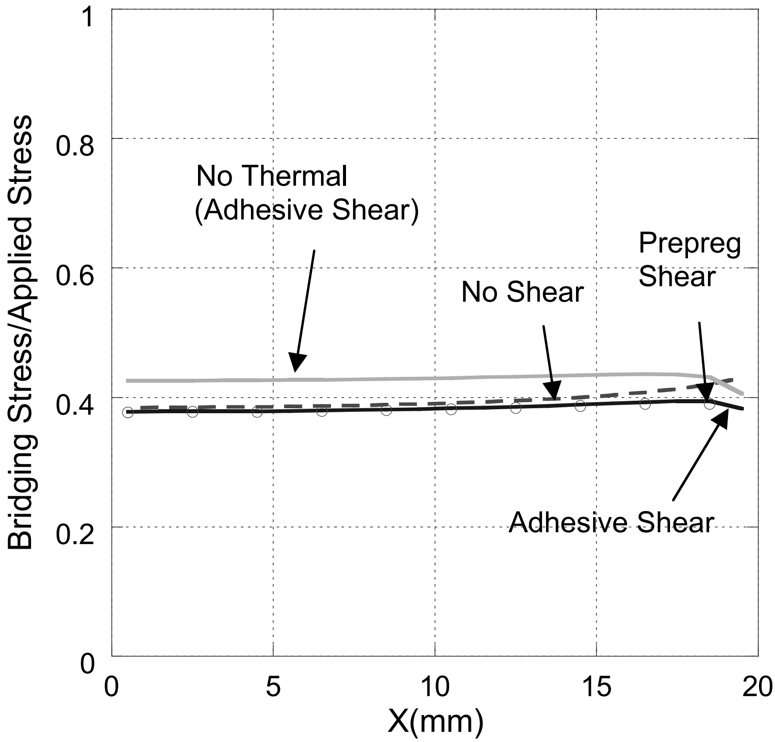

FIG. 11—*Bridging stress predicted using two shear models for the specimen with elliptical delamination.*

indicates that the predicted COD results with the residual thermal strain considered are greater than those with the residual thermal strain neglected for both specimens.

Bridging Stress Predictions

The bridging stress distributions for the Glare CCT specimens with residual thermal strains were analyzed using both the adhesive shear and prepreg shear models for the elliptical and rhomboidal delamination configurations, and the results are presented in Figs. 11 and 12, respectively. The bridging stress is normalized by the applied stress in both Figs. 11 and 12. For the elliptical delamination (Fig. 11), the results for the prepreg and adhesive shear models are nearly equal, with the general behavior being very consistent. For the rhomboidal delamination (Fig. 12), the results for the prepreg shear model are slightly higher than for the adhesive shear model and the bridging stress is observed to increase from the centerline to the crack tip over most of the crack length. However, as the crack tip is approached, the bridging stress determined for the prepreg shear model becomes unbounded. As the crack tip is approached, the delamination height, y_i, quickly approaches zero and the term

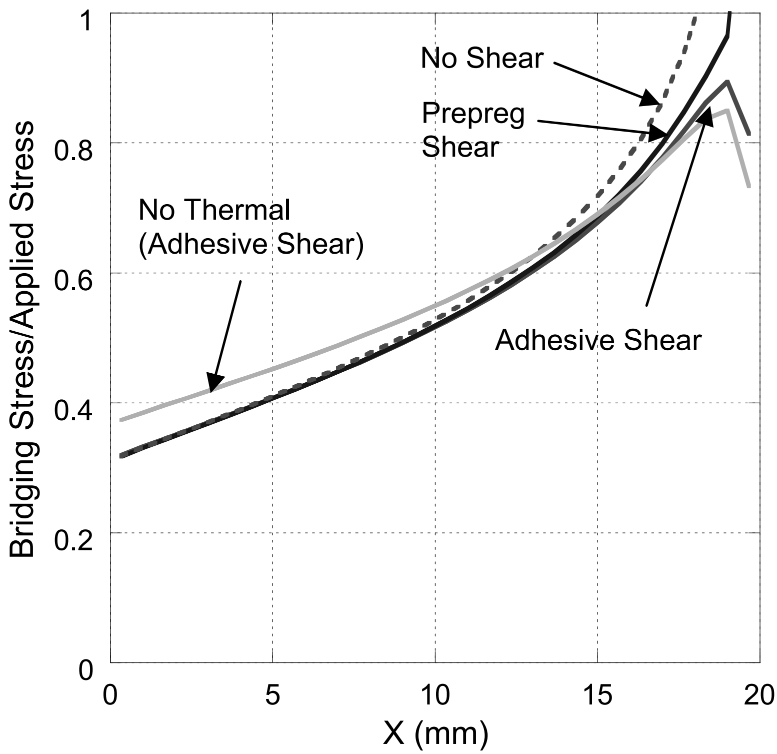

FIG. 12—*Bridging stress predicted using two shear models for the specimen with rhomboidal delamination.*

for the shear deformation, $u_{ad}(x_i)$, approaches zero for the rhomboidal delamination configuration using the prepreg shear model. To confirm that the unbounded bridging stress near the crack tip is indeed caused by the reduction of shear deformation, $u_{ad}(x_i)$, an analysis without considering the shear deformation for each delamination configuration was performed. The results are plotted as the "No Shear" curve in Figs. 11 and 12. The removal of the shear deformation can increase the bridging stress near the crack tip for the specimen with the elliptical delamination, but it can result in a rapidly increasing bridging stress near the crack tip for the specimen with rhomboidal delamination. This is due to the delamination height reducing faster near the crack tip for the rhomboidal shape delamination than for the elliptical shape delamination.

Since the high bridging stress predicted with the prepreg shear model exists very near the crack tip, it has little effect on the CODs along the crack length. The CODs predicted by the prepreg shear model are nearly the same as those predicted by the adhesive shear model as shown in Figs. 9 and 10 and are not affected by the unbounded bridging stresses near the crack tip. Near the crack tip, the bridging stress is greater for the rhomboidal delamination than

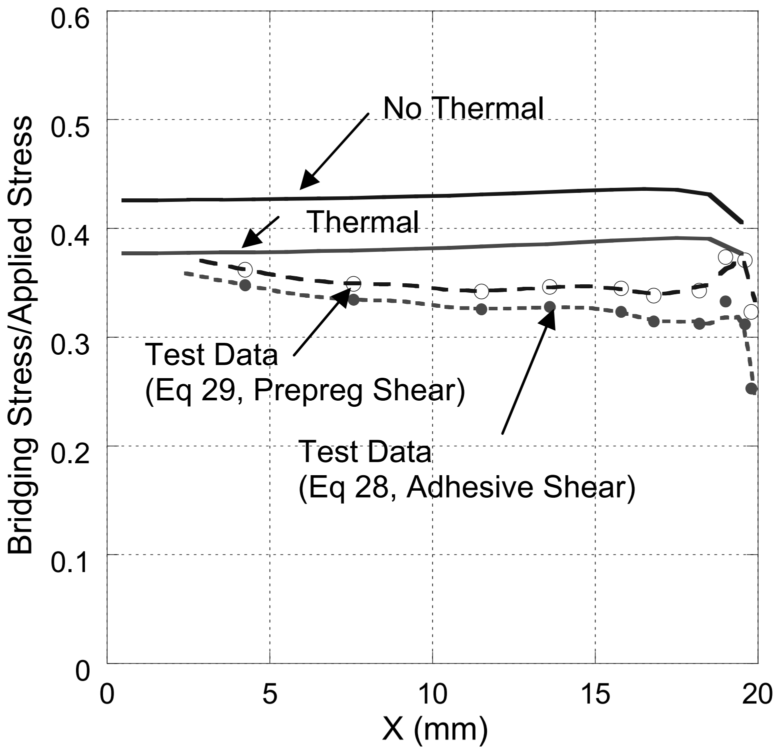

FIG. 13—*Bridging stress calculated with measured CODs for the specimen with elliptical delamination.*

for the elliptical delamination, suggesting that the rhomboidal delamination may grow at a lower loading level than the elliptical delamination around the crack tip.

To investigate the effect of residual thermal strain on the bridging stress, analyses for both specimens without residual thermal strains were also performed using the adhesive shear model. These analysis results are also plotted in Figs. 11 and 12 as the "No Thermal" curves. Comparing the "No Thermal" curve with the corresponding "Adhesive Shear" curve in each figure, we can conclude that the residual thermal strains do reduce the bridging stresses for both delamination configurations.

Bridging Stress Computed with Measured CODs

The bridging stresses for the Glare CCT specimens can be computed with the experimentally measured CODs using Eq 26, Eq 28, or Eq 29. The bridging stresses calculated with Eq 26 were found to be inconsistent with the "Thermal" and "No Thermal" curves that were obtained using the adhesive shear model. Since Eq 26 uses a Green's function to relate the bridging stress at location x_j to COD at location x_i, any COD data deviation at location x_i can

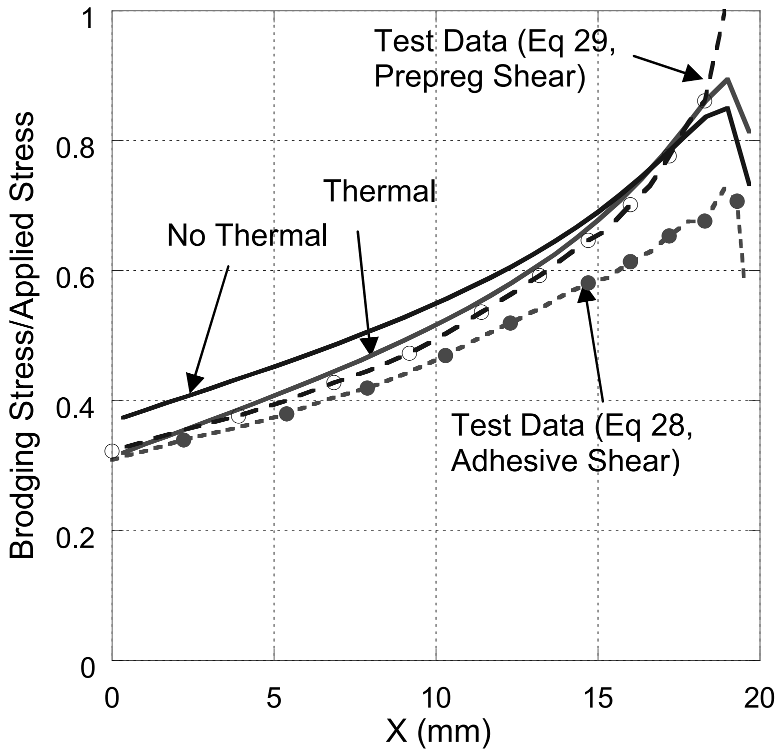

FIG. 14—*Bridging stress calculated with measured CODs for the specimen with rhomboidal delamination.*

affect the calculated bridging stress at all locations over the crack length. As a result, the bridging stresses calculated with Eq 26 and the measured COD data are not suitable for correlating with the analytical solutions. The issue of using the COD test data and Eq 26 for computing bridging stresses may be investigated in future studies.

The bridging stress calculated with Eqs 28 and 29 and the experimentally measured CODs are plotted in Figs. 13 and 14. Note that in these two equations, the bridging stress at location x_j is computed with the measured COD at x_j. The resulting bridging stresses determined with and without residual thermal strains are greater than those determined based on the experimentally measured CODs. For the residual thermal strain case with no post-cure stretching, the results for the elliptical delamination (Fig. 13) are in good agreement with the experimental data near the specimen center-line and the crack tip, but are observed to be approximately 10 % greater over most of the crack length. For the rhomboidal delamination (Fig. 14), the bridging stresses for the residual thermal strain case are higher than those determined based on the experimentally measured CODs. As with the case for the elliptical delamination geometry, the analysis results for the residual thermal strain case are in very

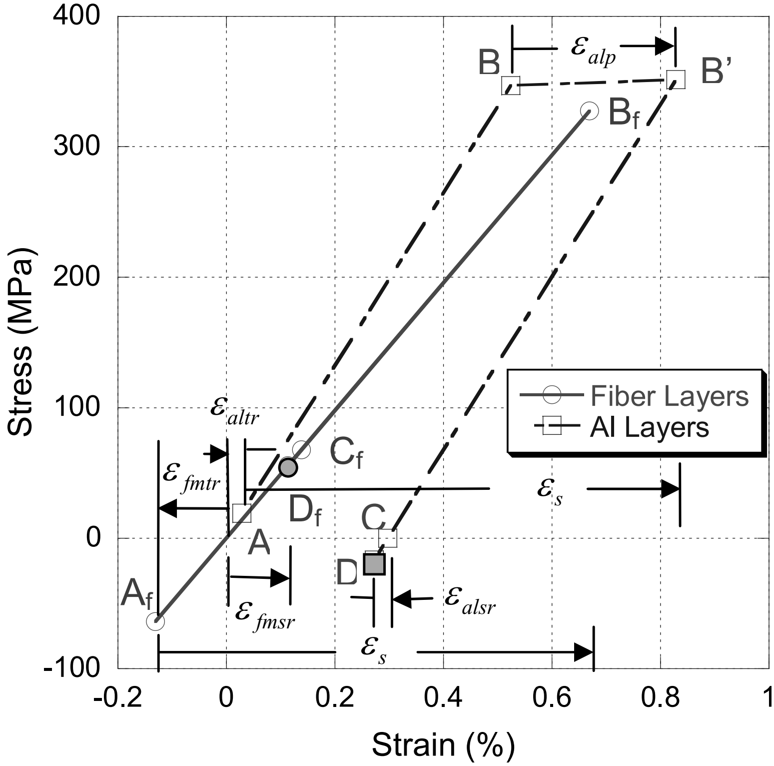

FIG. 15—*Stress strain relationship for post-cure stretching process.*

good agreement to that determined from the experimental COD data at the specimen centerline, but are slightly higher over most of the crack length.

Effects of Post-Cure Stretching

For the post-cure stretching process shown graphically in Fig. 8, residual strains were determined for post-cure stretching strains of 0.5, 0.8, 1.0, and 1.5 %. The stress strain results for the 0.8 % stretching level are presented in Fig. 15. Here, the stress and strain values for the aluminum and fiber layers for each configuration depicted in Fig. 8 are shown. Initially, the aluminum and fiber layers contain a residual thermal strain, Fig. 8(*a*) and points A and A_f in Fig. 15. As the FML is loaded, the stress and strain of each material are linearly related until the yield point of the aluminum layer is reached, point B in Fig. 15. Further straining to the desired stretching strain level, ε_s, results in plastic deformation of the aluminum, while the glass fibers remain elastic, Fig. 8(*b*) and points B' and B_f in Fig. 15. The FML is then unloaded until the aluminum layers are no longer carrying load, Fig. 8(*c*) and points C and C_f in Fig. 15. Here the fiber layers are still carrying a tensile load. As the FML is fully unloaded, a

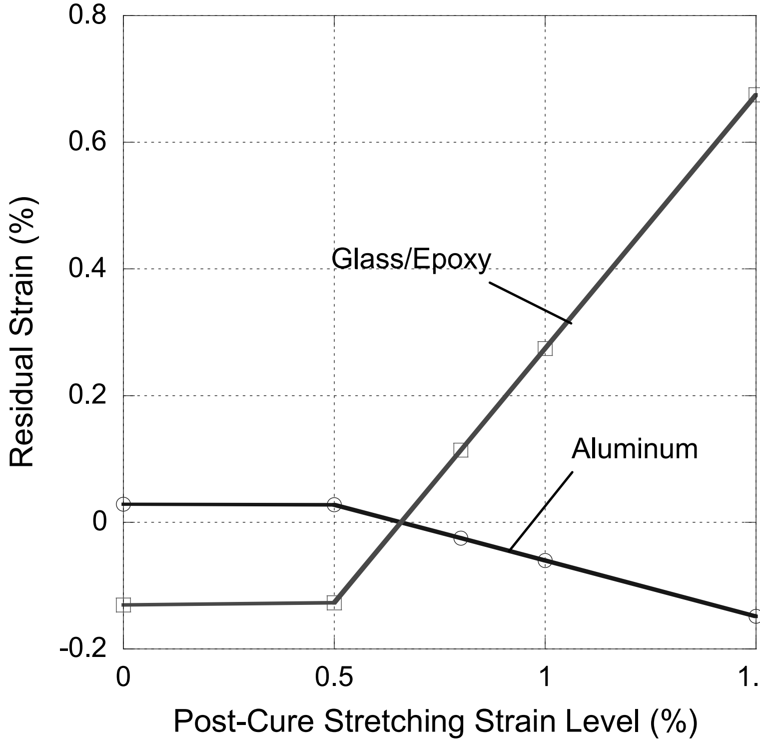

FIG. 16—*Final residual strains after post-cure stretching at various levels.*

compressive residual strain is produced for the aluminum layers and a tensile residual strain is produced for the fibers, Fig. 8(*d*) and points *D* and D_f in Fig. 15.

The residual stretching strains determined for the 0.5, 0.8, 1.0, and 1.5 % stretching strain levels are shown in Fig. 16. The residual thermal strains for an as-cured specimen are also represented as 0 % stretching strain level. Note that a 0.5 % post-cure stretching strain level will not yield the aluminum layers, so no residual strain change is observed. A stretch of approximately 0.66 % is required to compensate for the residual thermal strains (i.e. 0 % residual strain in the aluminum and fiber layers as shown in Fig. 16). Here, one can observe that the tensile residual thermal strain in the aluminum layers that was produced during the cure process has changed to a compressive residual strain as a result of the post-cure stretching procedures. Additionally, the compressive residual thermal strain of the fiber layer has been changed to a tensile residual strain due to the post-cure stretching process. The magnitudes of the residual strains are shown to increase with increasing stretching strain.

The bridging stress distributions for the CCT specimens subjected to residual thermal strain and post-cure stretching strains of 0.8, 1.0, and 1.5 % were analyzed using the adhesive shear model for both the elliptical and rhomboidal delamination configurations, and the results are presented in Figs. 17

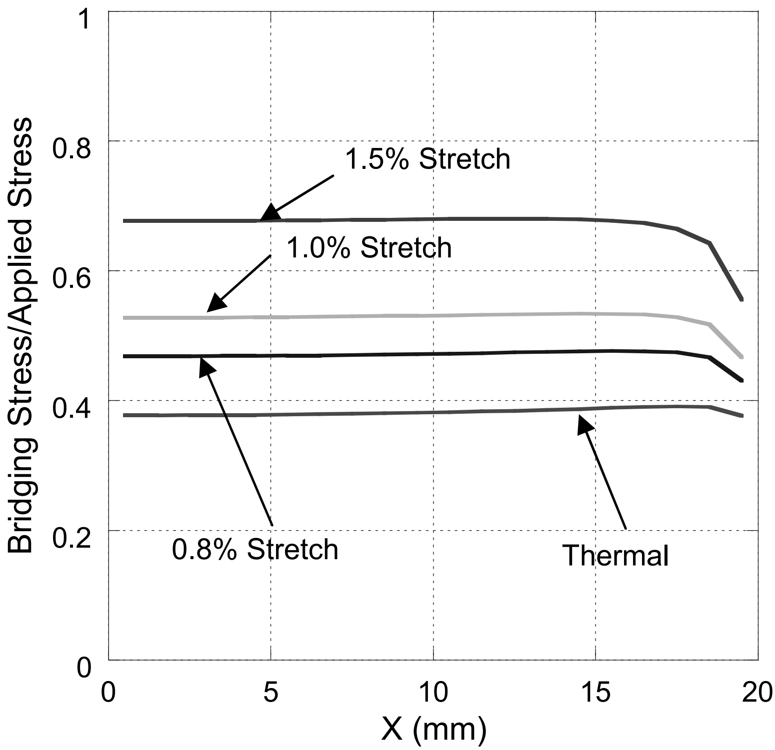

FIG. 17—*Bridging stress affected by residual thermal and post-cure stretching strains for the specimen with elliptical delamination.*

and 18, respectively. The bridging stress is normalized by the applied stress in both Figs. 17 and 18. The results in Figs. 17 and 18 were determined with the adhesive shear model, thus avoiding the unbounded solutions that can be produced for the rhomboidal delamination configuration (see Fig. 18). The bridging stresses determined for the elliptical delamination are shown to be fairly constant over most of the crack length, independent of stretching level, with a sharp decrease observed as the crack tip is approached. As the post-cure stretching level is increased, the bridging stress is increased to higher levels, with the 1.5 % stretching level resulting in a bridging stress that is approximately twice as high as those for the residual thermal strain without any stretching near the specimen centerline. The bridging stresses determined for the rhomboidal delamination specimen with various stretching strain levels are observed to increase from the specimen centerline toward the crack tip, converge near the crack tip, and then decrease sharply very near the crack tip. Near the crack tip, the bridging stresses are greater for the rhomboidal delamination than for the elliptical delamination, suggesting that glass fibers near the crack tip will carry more load, resulting in a reduced crack growth rate compared to the elliptical delamination.

CODs computed with Eq 1 based on the bridging stress distributions

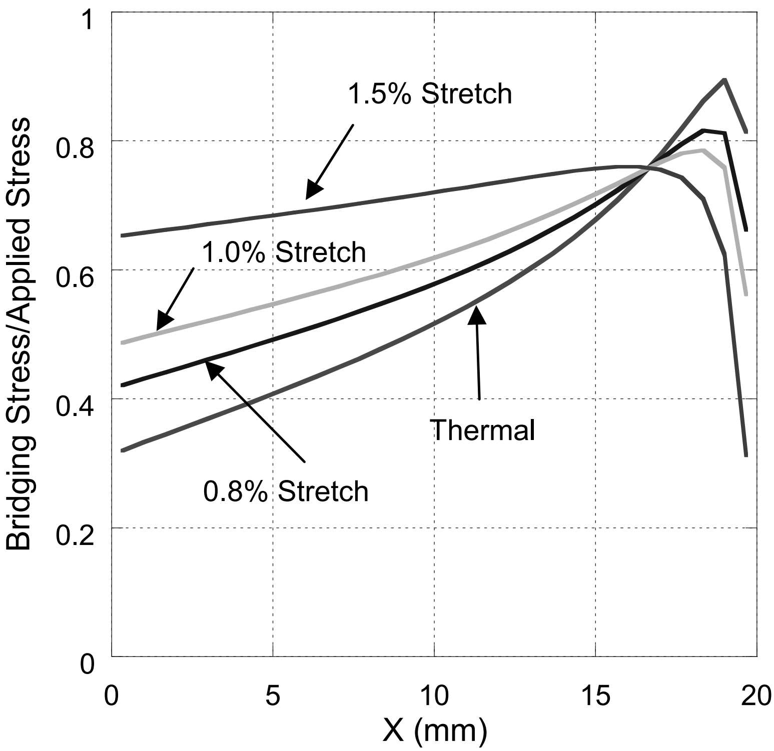

FIG. 18—*Bridging stress affected by residual thermal and post-stretching strains for the specimen with rhomboidal delamination.*

shown in Figs. 17 and 18 for the elliptical and the rhomboidal delamination configurations are presented in Figs. 19 and 20, respectively. As the post-cure stretching level is increased, the resulting COD profile is reduced. This would suggest that the driving force for fatigue crack growth can be reduced by utilizing a post-cure stretching procedure [2,4,5]. Comparison of the results in Figs. 19 and 20 indicates that the COD is greater over the entire crack length for all levels of post-cure stretching for the elliptical delamination than for the rhomboidal delamination, suggesting that the rhomboidal delamination would result in a lower crack growth rate than the elliptical delamination for the same post-cure stretching process. The COD for the case of a through-the-thickness saw cut of 40 mm is also shown in Figs. 19 and 20. The figures show that without fiber bridging, the CODs are much larger than those obtained with fiber bridging.

Concluding Remarks

Analytical models adopted from the open literature for determining COD and bridging stress were modified to create an analytical model that accounts for

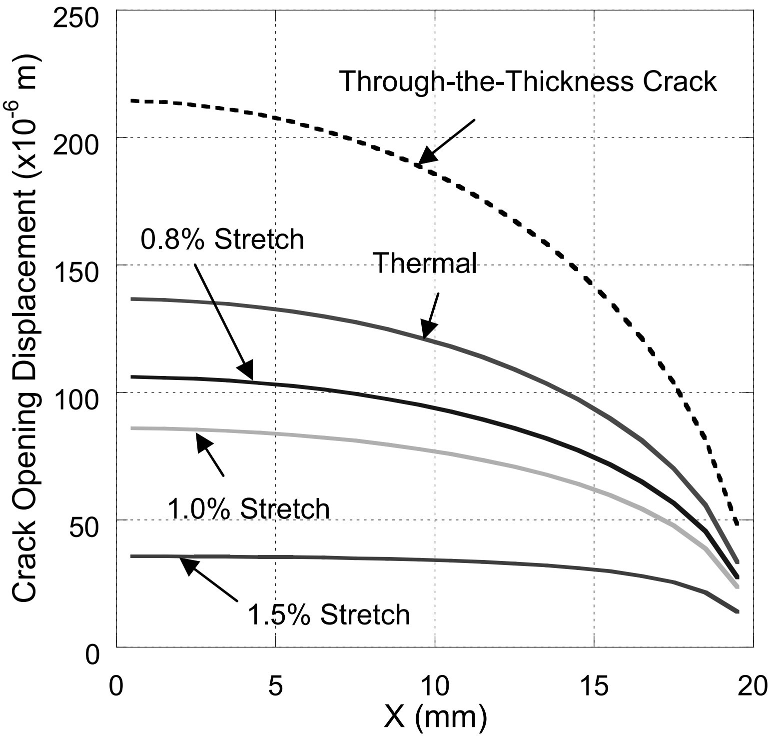

FIG. 19—*CODs affected by residual thermal and post-cure stretching strains for the specimen with elliptical delamination.*

the effects of residual thermal strains and residual post-cure stretching strains. The modified analytical model was used to analyze two Glare CCT specimens, one containing elliptical delaminations and the other containing rhomboidal delaminations. Note that the governing equations presented in this paper can also be used for other delamination configurations in FMLs other than Glare.

Analytical results for both specimens, with and without residual thermal strain, were obtained and compared with test data. The comparisons show that the COD test data are bounded by the residual thermal strain and the zero residual thermal strain curves. Near the specimen centerline, the COD test data compared well with the analytical results that included residual thermal strain. Furthermore, this study found that the difference in the predicted COD and the bridging stress distributions over the crack wake are negligible using either the adhesive shear model or the prepreg shear model; however, the bridging stresses predicted by the prepreg shear model are unbounded as the crack tip is approached. This is a result of the prepreg shear model not allowing shear deformation at the crack tip due to zero shear stress in this region. Since the high bridging stress predicted with the prepreg shear model exists only very near the crack tip, little effect is observed for the CODs predicted along the entire crack length.

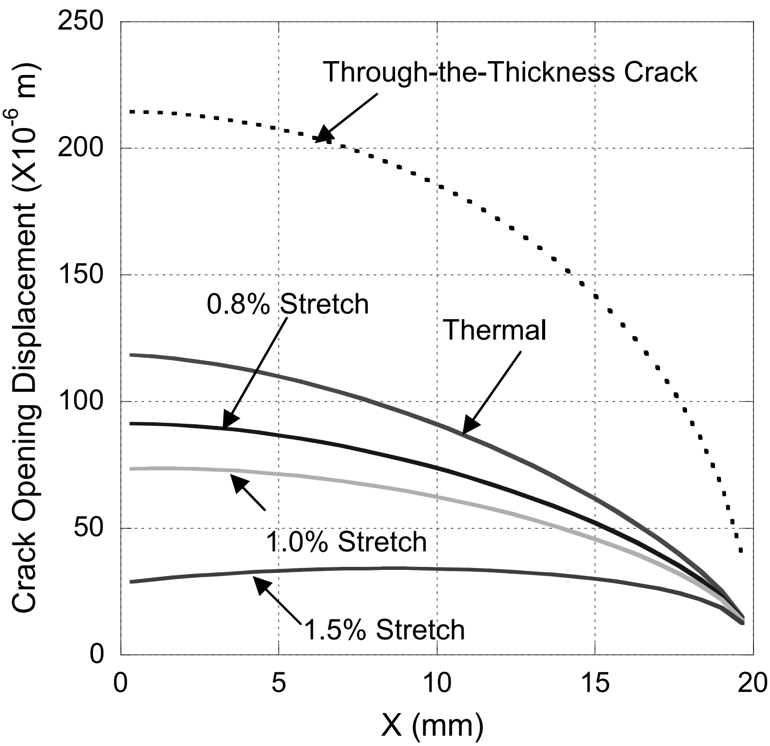

FIG. 20—*CODs affected by residual thermal and post-cure stretching strains for the specimen with rhomboidal delamination.*

Analytical results of both specimens indicate that the residual thermal strains reduce the bridging stress while the post-cure stretching residual strains can increase the bridging stresses. Note that the post-cure stretching can change the residual strain in aluminum layers from tension to compression and the residual strain in glass/epoxy layers from compression to tension. A higher post-cure stretching level results in a greater residual tensile strain in the glass/epoxy layers which in turn contributes to the increase of the bridging stress. Along with the increase in bridging stress, a decrease in COD is observed. This decrease in COD can result in a reduced crack-tip driving force, which should produce improved fatigue crack growth resistance for Glare specimens subjected to the post-cure stretching process.

References

[1] Alderliesten, R. C., 2005, "Fatigue Crack Propagation and Delamination Growth in Glare," Ph.D. thesis, Delft University of Technology, Delft, The Netherlands.

[2] Marissen, R., 1988, "Fatigue Crack Growth in ARALL, a Hybrid Aluminium-Aramid Composite Material, Crack Growth Mechanisms and Quantitative Predic-

tions of the Crack Growth Rate," Ph.D. thesis, Delft University of Technology, Delft, The Netherlands.

[3] Guo, Y. J. and Wu, X. R., "Bridging Stress Distribution in Center-Cracked Fiber Reinforced Metal Laminates: Modelling and Experiment," *Eng. Fract. Mech.*, Vol. 63, 1999, pp. 147–163.

[4] Pegels, C. S., 1995, "A Study on the Residual Stress of GLARE 1," M.S. thesis, Delft University of Technology, Delft, The Netherlands.

[5] Khan, S. U., Alderliesten, R. C., and Benedictus, R., "Post-Stretching Induced Stress Redistribution in Fibre Metal Laminates for Increased Fatigue Crack Growth Resistance," *Compos. Sci. Technol.*, Vol. 69, 2009, pp. 396–405.

[6] Newman, J. C., Jr., "A Crack-Closure Model for Predicting Fatigue Crack Growth Under Aircraft Spectrum Loading," *Methods and Models for Predicting Fatigue Crack Growth Under Random Loading, ASTM STP 748*, J. B. Chang and C. M. Hudson, Eds., ASTM International, West Conshohocken, PA, 1981, pp. 53–84.

[7] Alderliesten, R. C., Campoli, G., and Benedictus, R., "Modeling Cyclic Shear Deformation of Fiber/Epoxy Layers in Fiber Metal Laminate," *Compos. Sci. Technol.*, Vol. 67, 2007, pp. 2545–2555.

[8] U. S. Department of Defense, *Metallic Materials and Elements for Aerospace Vehicle Structures, Military Handbook, MIL-HDBK-5H*, 1998, Washington, DC, p. 3-94.

[9] Brown, W. F., Jr. and Srawley, J. E., *Plane Strain Crack Toughness Testing of High Strength Metallic Materials, ASTM STP 410*, ASTM International, West Conshohocken, PA, 1966, pp. 77–79.

[10] Tada, H., Paris, P. C., and Irwin, G. R., *The Stress Analysis of Cracks Handbook*, 3rd ed., ASME Press, New York, 2000, p. 43.

[11] Roebroeks, G. H. J. J., 1991, "Towards Glare, the Development of a Fatigue Insensitive and Damage Tolerant Aircraft Material," Ph.D. thesis, Delft University of Technology, Delft, The Netherlands.

[12] Hart-Smith, L. J., "Analysis and Design of Advanced Composite Bonded Joints," *Report No.* NASA CR-2218, Hampton, VA, August 1974.

[13] Verbruggen, M. L. C. E., 1987, "Aramid Reinforced Aluminum Laminates: ARALL Adhesion Problems and Environmental Effects," Ph.D. thesis, Delft University of Technology, Delft, The Netherlands.

Reprinted from JAI, Vol. 6, No. 10
doi:10.1520/JAI102503
Available online at www.astm.org/JAI

S. Ismonov,[1] *S. R. Daniewicz,*[1] *and J. C. Newman, Jr.*[2]

Elastic-Plastic Stress Analysis of Cold-Worked Pin-Loaded Holes

ABSTRACT: A detailed two-dimensional, elastic-plastic finite element analysis of a pin-loaded hole was conducted. A thin rectangular aluminum alloy sheet (7075-T6) with a circular hole was considered under plane stress conditions. The hole was loaded purely by a rigid pin to different load magnitudes. Appropriate contact elements were used at the pin-hole interface to transfer the traction loads from one surface to another. Material nonlinearities for the sheet and friction were included in the analyses. Radial and hoop stress solutions along the pin-hole interface were compared in elastically and plastically loaded holes. The influence of friction on the stress results was studied. The locations and magnitudes of the peak hoop stresses were determined. Lastly, an initial residual field was introduced around the hole by a cold expansion simulation before a subsequent pin-loading analysis. Because the cold expansion process involves some reverse yielding, both isotropic and kinematic material hardening models were considered.

KEYWORDS: finite element analysis, pin-loaded holes, friction, isotropic and kinematic hardening, contact stresses, residual stresses

Introduction and Background

Fastener joints, in which single or double lap sheets with circular holes are connected via cylindrical pins, have a broad range of applications in many engineering structures. These joints must also be considered a potential failure location due to the localized stress concentrations caused by the presence of the holes. Pin loading is a classical problem, which drew the attention of many researchers in the past. Numerous independent techniques have emerged to evaluate the stress state around a pin-loaded hole. Experimental methods include photoelasticity [1–3], moire interferometry [4,5], electronic speckle pattern interferometry [6], and strain gauges [2]. Analytical solutions have been

---

Manuscript received May 12, 2009; accepted for publication August 19, 2009; published online September 2009.
[1] Dept. of Mechanical Engineering, Mississippi State Univ., Starkville, MS 39759.
[2] Dept. of Aerospace Engineering, Mississippi State Univ., Starkville, MS 39759.

Cite as: Ismonov, S., Daniewicz, S. R. and Newman, J. C., "Elastic-Plastic Stress Analysis of Cold-Worked Pin-Loaded Holes," *J. ASTM Intl.*, Vol. 6, No. 10. doi:10.1520/JAI102503.

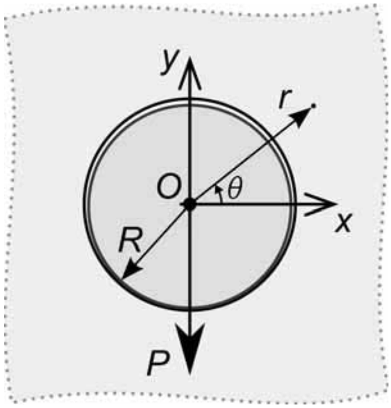

FIG. 1—*A sketch of an infinite sheet loaded by a resultant pin-load P.*

developed using linear elasticity with complex variable methods [7–10] and stress functions [11–16]. Noble and Hussain [7], for example, considered the problem of an infinite plate with a circular hole loaded by a pin under frictionless conditions. They formulated the problem in terms of dual series, which are then converted to an equivalent Cauchy-type or airfoil equation assuming the elastic constants of the pin and the plate satisfy the relationship $(1-2\nu_1)/G_1 = (1-2\nu_2)/G_2$ where G and ν denote the shear modulus and Poisson's ratio, respectively. Earlier theoretical solutions using stress functions include those by Night [11] and Theocaris [12] on the pin-loading problem of a finite width plate. Rao [13] employed an inverse method along with a collocation technique to solve for the unknown constants in an Airy stress function satisfying the prescribed boundary conditions. He considered both frictionless and nonzero friction, bonded interfaces, as well as clearance and interference fit pins. Mangalgiri et al. [14] extended the work of Rao for pin joints under combined pin and plate loads with frictionless contact. In Ref 8, a complex Fourier series, collocation procedure, and iteration technique were used to solve for stresses around pin-loaded orthotropic plates for different levels of friction as well as hole clearance. For the case of a rigid pin and zero friction, Muzushima and Hamada [15] also adopted a numerical approach to solve for the stress and displacement distributions around the loaded hole. Ho and Chau's work [16] regarding an infinite plate loaded by a pin is one of the recent closed form solutions that include friction, arbitrary stiffness for the pin material, as well as uniform and non-uniform shear loads distributed over the pin section. They solve the problem by partitioning it into two auxiliary sub-problems. The first sub-problem solves for the stress distribution in the plate loaded by a pin of a different material that is perfectly bonded to the plate. The second auxiliary problem seeks a solution so that the normal σ_{rr} and shear $\sigma_{r\theta}$ stress components cancel out at the top one-half of the circular boundary ($0° \leq \theta \leq 180°$, $r=R$), whereas the normal and shear contact stress distributions proportional to $\sin(\theta)$ and $\sin(2\theta)$ are produced at the bottom half of the hole ($-180° \leq \theta \leq 0°$, $r=R$, see Fig. 1). The sinusoidal radial pin-load distribution assumption is also used in Ref 10 in development of an analytical solution for pin-loaded elastic orthotropic plates via complex stress functions for frictionless conditions ($\mu = 0$).

The analytical solutions listed earlier are obtained for a linear elastic plate material. However, the problem becomes much more complicated if one considers the material non-linearity combined with friction and finite plate dimensions. Moreover, pinned connections rarely occur in isolation since most of the structures have multiple pinned connections with dissimilar configurations. This makes the finite element (FE) method a more desirable approach, because it can eliminate all of these concerns as long as the model size is kept at a reasonable level. Two dimensional (2D) finite element analysis (FEA) of the pin-loaded plates with an elastic plate, rigid pin, and a frictionless contact are previously reported in Refs 17 and 18. Local stress distributions from 2D and three-dimensional FE models with elastic pins and frictionless contact were presented in Ref 19. Iyer [20] and Lanza di Scalea [6] consider both pin elasticity, as well as, friction in their 2D plane strain [20] and plane stress [6] models. Iyer demonstrated that the stress solutions at the interface are largely independent of the material pair provided that the pin and the plate are metallic and friction is small. Yavari et al. [21] have performed a parametric study with respect to some design factors such as the plate width, edge distance, clearance, and friction at the pin-hole interface. Kumar [22] included material plasticity for the case of perfectly smooth pin-hole interface (i.e., $\mu = 0$), and obtained the stress distributions around the hole under constant amplitude cyclic loading.

The objective of the present paper is to continue the 2D FE modeling efforts of the pin-loaded hole problem with further sophistication, namely considering the material nonlinearity and friction as well as pre-existing residual stresses around the hole from cold-hole expansion. First, convergence studies were performed to validate the elastic and elastic-plastic model results. Furthermore, the FE model with linear elastic material properties was validated using: (a) A closed form solution by Ho and Chau [16]; (b) a FE solution by Yavari et al. [21]. Next, the linear elastic and elasto-plastic solutions were compared, and the influence of the friction was studied. Finally, a compressive residual stress field was introduced around the hole by cold expansion simulation. Cold expansion of a hole, initially developed by the Boeing Co. in 1960, is a life enhancement process used to mitigate the effect of the stress concentrations by creating a compressive circumferential residual stress field around the hole [23]. Because this process involves some reverse yielding, the effect of both isotropic and kinematic material hardening models is considered. The sheet was then pin-loaded and the subsequent changes in the stress state around the hole are presented.

Problem Description

Consider a rectangular finite sheet with a circular hole, as shown in Fig. 2. The size of the thin rectangular sheet is 65.0 mm (h) by 44.45 mm ($2w$) with a 7.07-mm diameter hole ($2R$) located at 22.23-mm distance (d) from the bottom edge. The sheet thickness is $t = 2.03$ mm. The hole is loaded purely by a neat-fit

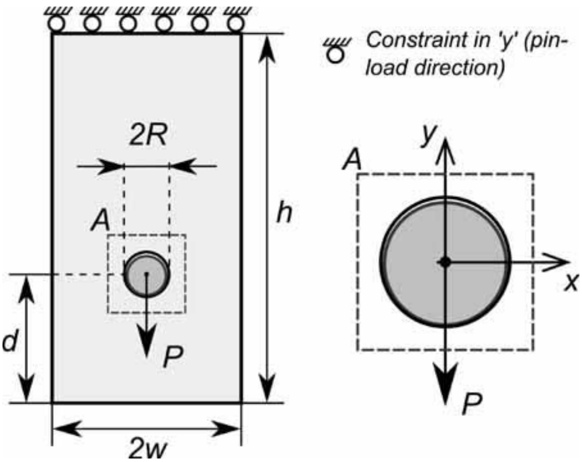

FIG. 2—*Model geometry.*

pin with a magnitude P. The sheet is constrained in the y direction at the top edge (Fig. 2). The diameter of the pin is same as the hole diameter since it is a neat-fit configuration. Out of plane bending effects for the sheet are ignored, which can be a reasonable approximation for the dual lap joints. This simplification may not be appropriate for a single lap pin joints.

The sheet material is 7075-T6 aluminum alloy with a yield strength of (Y) of $Y=483$ MPa. The Young's modulus and Poisson's ratio are $E=72.5$ GPa and $\nu=0.3$, respectively. Figure 3 gives the stress-strain curve used [24]. For the elastic case, only the elastic domain of the curve is used. Thus, the Young's modulus and Poisson's ratio are sufficient to describe the material behavior. For the elasto-plastic analysis, the stress-strain data in both elastic and plastic domains are used with the von Mises yield criterion. Two different work hardening material models were considered during the cold expansion simulation:

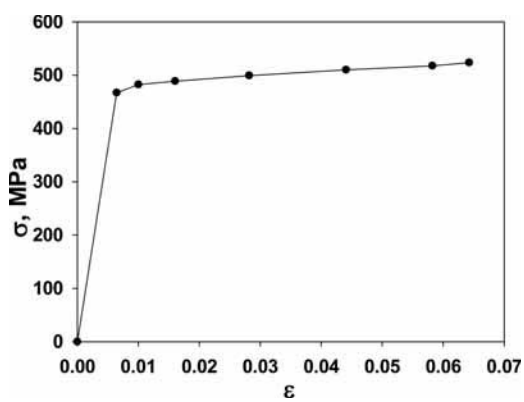

FIG. 3—*Elasto-plastic stress-strain curve of Aluminum AA7075-T6 sheet.*

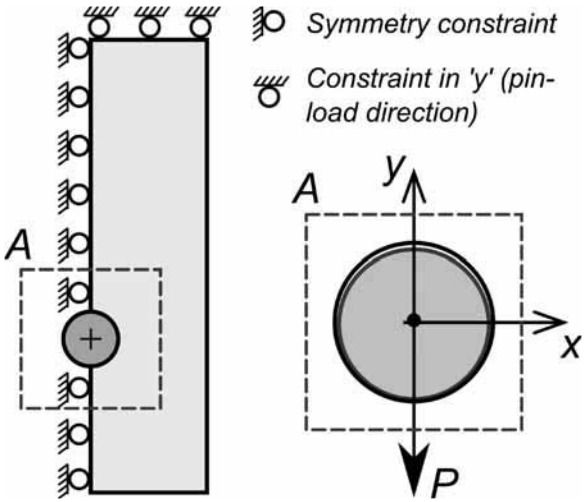

FIG. 4—*Prescribed boundary conditions of the FE model.*

Multilinear isotropic hardening and multilinear kinematic hardening. As will be shown, these two hardening models result in different residual stress fields from the cold expansion simulation due to Bauschinger's effect, which is incorporated in the kinematic hardening material model. For simplicity, the pin is assumed to be a rigid body.

Finite Element Model and Boundary Conditions

ANSYS 11.0 [25] was used to carry out the numerical simulations. Two-dimensional (2D) plane stress conditions were assumed because of the small sheet thickness. Due to symmetry, one-half of the specimen was modeled with appropriate symmetry boundary conditions, which are shown as vertical rollers in Fig. 4. These rollers are the constraints in the x direction, whereas the horizontal rollers applied at the sheet top edge indicate the constraints in the y direction.

The FE model was meshed using 2D four-noded linear structural elements with a highly refined mesh around the hole edge (Fig. 5). Rigid-to-deformable surface-to-surface contact elements with an augmented Lagrangian algorithm were used at the pin-hole interface so that the normal and shear traction loads can be transferred from the pin to the hole surface. Two different cases were studied regarding the friction. In the first case, the pin-hole interface was assumed to be perfectly smooth with zero friction. In the second case, a Coulomb friction model was used with an arbitrary friction coefficient $\mu = 0.2$.

Assuming that the pin-loading is a sufficiently slow process, it was simulated in a quasi-static manner without considering any dynamic or time dependent response of the material. The magnitude of the point load P, which is applied downward at the center of the pin (Fig. 4), was gradually increased in several load-steps up to the maximum level. Note that the point load is, in

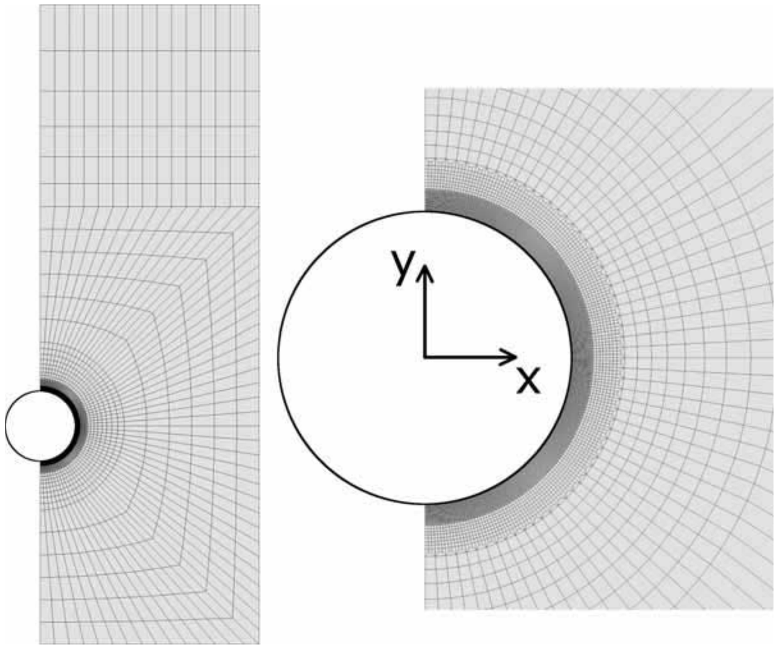

FIG. 5—*FE mesh.*

general not realistic, since the shear loads are distributed over the pin section in some fashion. However this will not have any significance in the present work because the pin was assumed to be rigid.

In the last stage of the study, a residual stress field was created around the hole by cold expansion simulation prior to subsequent pin-loading analyses. Cold expansion is a three dimensional process, in which a tapered mandrel is pulled through the hole of the structure, and the resulting residual stress field varies through the sheet thickness [26]. Although, it is not possible to realistically simulate the actual process in 2D, it can be performed in a rather simplistic way by following the two steps given next:

(1) *Hole expansion.* Uniform radial displacements, equal to the 2 % interference amount, are applied on the nodes of the hole edge. By this means the hole of the sheet is plastically expanded.
(2) *Hole recovery.* Pre-applied displacements are removed, which causes the partial but not full elastic recovery. This step creates the desired compressive residual stresses around the hole edge.

Model Validation

2D elastic and elastic-plastic FE models were first validated by performing convergence studies with respect to mesh density and loading increments (i.e., total number of load steps). Example convergence studies for the elastic-plastic model with friction coefficients $\mu = 0$ and 0.2 are given in Fig. 6. In each plot of

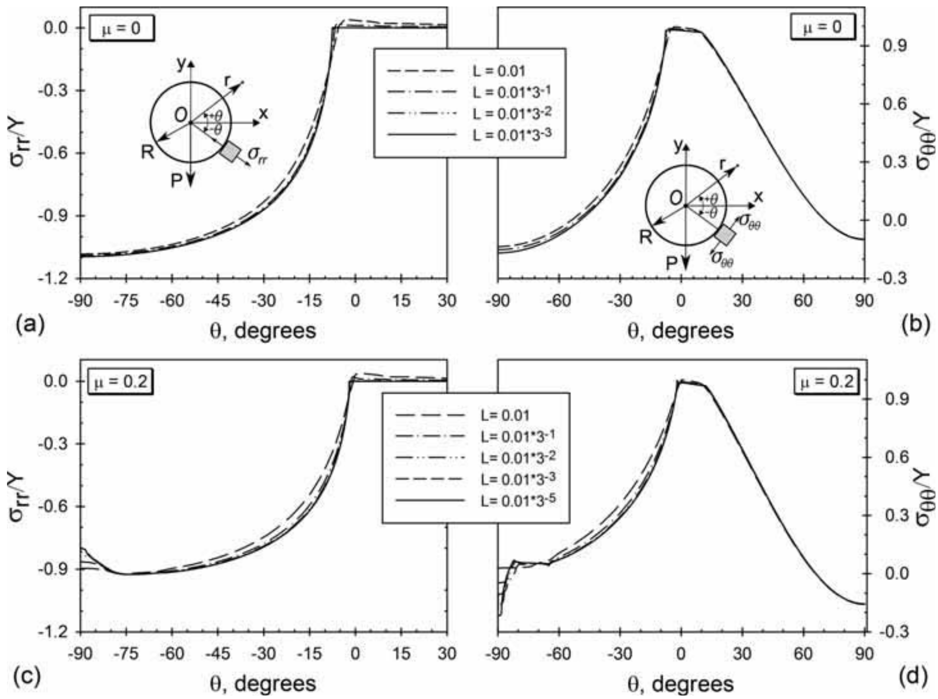

FIG. 6—*Convergence studies for radial, and hoop stress distributions at* $r = R$*,L—element size at the hole edge (normalized by* πR*).*

the figure, normalized stress values (σ_{ij}/Y) for progressively refined element sizes L are plotted versus the angular location θ along the hole circumference. The applied normalized pin-load magnitude is $S_b/Y = 1.0$, where S_b is the average bearing stress

$$S_b = \frac{P}{2Rt} \tag{1}$$

where:

P = pin-load magnitude,

R = hole radius, and

t = thickness of the sheet.

Note that L is the length of the elements at the hole edge normalized by πR. By default in ANSYS, L was reduced by a factor of 3 during each mesh refinement. As shown in Fig. 6(*a*) and 6(*b*), both radial and hoop stress distributions are easily converged in the frictionless case when L is reduced to $L = 0.01 \cdot 3^{-2}$. Including a friction coefficient $\mu = 0.2$ resulted in a slow local convergence in the vicinity of the angular location $\theta = -90°$. Although the radial stress magnitude (σ_{rr}/Y) near $\theta = -90°$ looks as if it may be converged with the smallest element size $L = 0.01 \cdot 3^{-5}$, the hoop stress values ($\sigma_{\theta\theta}/Y$) require further mesh refinement (Fig. 6(*c*) and 6(*d*)). Results away from this region are readily converged with the same level of mesh refinement as in the frictionless case (i.e., $L = 0.01 \cdot 3^{-2}$). Similar behavior was also observed when linear elastic material properties were used for the sheet, suggesting that the friction as well as the rigid pin assumption may be the source of the convergence difficulties. Because the smallest element size considered in this study ($L = 0.01 \cdot 3^{-5}$) lead to an impractically large model size with approximately 450K degrees of freedom, the second level of mesh refinement with $L = 0.01 \cdot 3^{-2}$ was chosen to be the final and optimum mesh density for all cases. In the results that follow for $\mu = 0.2$, attention is confined to the interval $-85° \leq \theta \leq 90°$, where the solutions are converged.

Further validations were done by solving two previously studied independent problems found in the literature: (a) A closed form solution by Ho and Chau [16] for an infinite sheet; (b) a numerical solution by Yavari et al. [21]. From the Ho and Chau solution, if the pin is assumed to be rigid ($E_{\text{pin}} \rightarrow \infty$), the contact stresses are

$$\sigma_{rr} = \begin{cases} \dfrac{P \cdot M_1 \cdot \sin(\theta)}{\pi \cdot R} & \text{for } -\pi \leq \theta \leq 0 \\ 0 & \text{for } 0 \leq \theta \leq \pi \end{cases}$$

$$\sigma_{r\theta} = \begin{cases} -\dfrac{P \cdot M_2 \cdot \sin(2\theta)}{\pi \cdot R} & \text{for } -\pi \leq \theta \leq 0 \\ 0 & \text{for } 0 \leq \theta \leq \pi \end{cases} \tag{2}$$

The parameters M_1 and M_2 are related to the friction coefficient μ by

$$M_1 = \frac{6\pi}{3\pi + 4\mu}$$

$$M_2 = \frac{3\pi \cdot \mu}{3\pi + 4\mu} \tag{3}$$

Note that the shapes of the normal and shear stress distributions at the pin-hole interface given in Eq 2 are presumed during the solution process. The stress components σ_{rr}, $\sigma_{r\theta}$, and $\sigma_{\theta\theta}$ are then determined in the sheet and in the pin. For the rigid pin, the hoop stress component $\sigma_{\theta\theta}$ along the hole circumference of the sheet under plane stress conditions is

$$\sigma_{\theta\theta} = \begin{cases} \dfrac{P}{\pi \cdot R}\left[\left(\dfrac{2}{\pi} + \sin(\theta)\right) \cdot M_1 + \left(\cos(2\theta) - \dfrac{4}{3\pi}\sin(\theta) + \dfrac{2}{\pi}\sin(2\theta) \cdot \tanh^{-1}(\cos(\theta))\right) \cdot M_2 - \left(\dfrac{\nu}{2} + \dfrac{1}{2}\right)\sin(\theta)\right] & \text{for } -\pi/2 \leq \theta < 0 \\ \dfrac{P}{\pi \cdot R}\left[\dfrac{2}{\pi} \cdot M_1 + \left(\cos(2\theta) - \dfrac{4}{3\pi}\sin(\theta) + \dfrac{2}{\pi}\sin(2\theta) \cdot \tanh^{-1}(\cos(\theta))\right) \cdot M_2 - \left(\dfrac{\nu}{2} + \dfrac{1}{2}\right)\sin(\theta)\right] & \text{for } 0 < \theta \leq \pi/2 \\ \dfrac{P \cdot (2M_1 + \pi M_2)}{\pi^2 \cdot R} & \text{for } \theta = 0 \end{cases} \tag{4}$$

where:

ν = Poisson's ratio of the sheet material.

For further details regarding this solution the reader may refer to Ref 16.

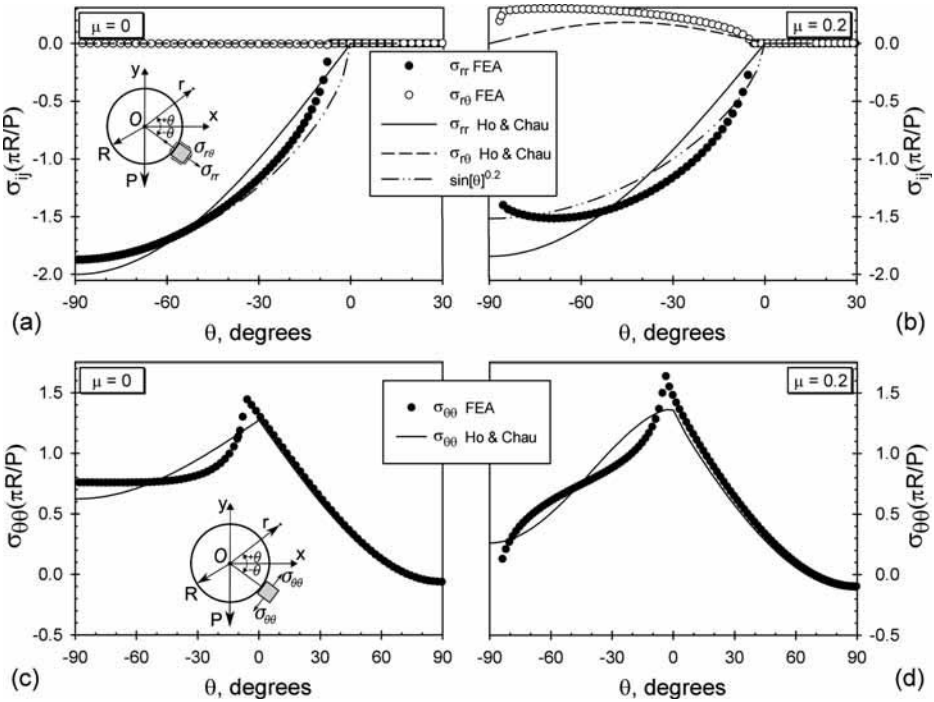

FIG. 7—*Comparison of the normal, shear and tangential stress distributions along the hole circumference* ($r=R$) *with Ref 14 for an infinite plate.*

To model an infinite sheet in ANSYS, a large finite square sheet with $w/R=100$ was created. A concentrated pin-load P per unit thickness was applied downward at the center of the rigid, neat-fit pin, while the top edge of the sheet was constrained in the pin-load direction. A modulus of elasticity of $E=72$ GPa, and a Poisson's ratio of $\nu=0.3$ were used for the sheet. Figure 7(*a*) and 7(*b*) gives the normal and shear stress distributions along the hole circumference for $\mu=0$ and $\mu=0.2$. In addition, a $[\sin(\theta)]^{0.2}$ function, as suggested in Ref 19, is included in the plots. All stress components are normalized as $\sigma_{ij}\cdot(\pi R/P)$. As shown in Fig. 7(*a*) and 7(*b*), differences are evident for both $\mu=0$ and $\mu=0.2$. It is observed from Fig. 7(*a*) that the $\sin[\theta]^{0.2}$ better approximates the shape of the normal contact stresses rather than the function used in Ref 16, which is proportional to $\sin(\theta)$ (see σ_{rr} in Eq 2). The numerical solution indicates that the edge of the downward slope corresponding to the boundary between the closed and open contact does not start at exactly $\theta=0°$. The shear stress values are zero everywhere on the hole surface as expected for $\mu=0$. Greater variations were observed in both shapes and magnitudes of the σ_{rr}, $\sigma_{r\theta}$ stress curves when a friction coefficient $\mu=0.2$ is considered. As shown in Fig. 7(*b*), normal contact stresses found from the Ho and Chau solution are lower in magnitude for $-50° \leq \theta \leq 0°$ and they are greater in the range $-85° \leq \theta \leq 50°$ with a maximum percentage difference of 27 % at $\theta=-85°$. Also, the $[\sin(\theta)]^{0.2}$

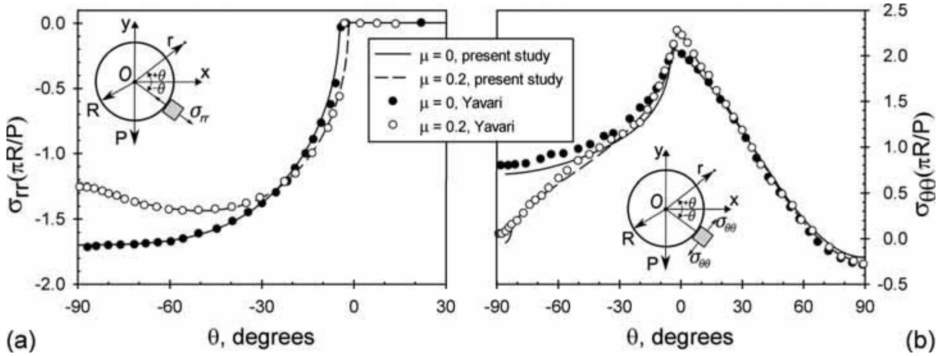

FIG. 8—*Comparison of the normal and tangential stress distributions along the hole circumference* ($r=R$) *with Ref 19 for a finite sheet with w/R=5.*

function fails to capture the accurate shape of the normal stress curve when friction is included. Shear stress values are significantly smaller than the FE solutions in the entire range, with a maximum percentage difference of 175 % at $\theta=-84°$. Moreover, it is observed that the distribution of the shear stress is not exactly proportional to $\sin(2\theta)$, which is used in Ref 16.

Comparisons between the hoop stress solutions of Ref 16 with the FE results along the hole circumference are given in Fig. 7(*c*) and 7(*d*) for $\mu=0$ and $\mu=0.2$. The variations in the stress magnitudes shown in the figure can be partially explained by the different contact stress distributions used as boundary conditions by Ho and Chau when compared to that predicted by the FE model. Percentage differences between the peak stress values are 11.5 % and 18.9 % for the cases with $\mu=0$ and $\mu=0.2$, respectively. However, it is observed that the analytical and numerical hoop stress curves follow a similar trend. In particular, increasing the friction coefficient raises the peak hoop stress value and lowers the stress magnitudes at the lower values of θ.

For further validation, Yavari et al.'s recent 2D numerical analysis [21] regarding the stress distribution around the elastically pin-loaded hole in a finite sheet was replicated. The geometry of the model is similar to the one considered in the present study (see Fig. 2). Dimensions of the sheet are: $d=15.3$ mm, $2R=6.12$ mm, $h=168.3$ mm, and $2w=30.6$ mm. The pin was modeled to be rigid, whereas $E=70$ GPa and $\nu=0.31$ were used for the aluminum alloy sheet. A pin-load P was applied downward at the pin center keeping the top edge of the sheet constrained in the y direction.

Figure 8 compares the normalized radial and hoop stress solutions along the hole circumference with the results given in Ref 21 for $\mu=0$ and 0.2. Stress components are normalized as $\sigma_{ij}\cdot(\pi R/P)$. As shown in Fig. 8(*a*), the radial stress distributions compare well for both friction levels. Hoop stress curves were also in good agreement, although slight variations are observed for $\theta<0°$ (Fig. 8(*b*)).

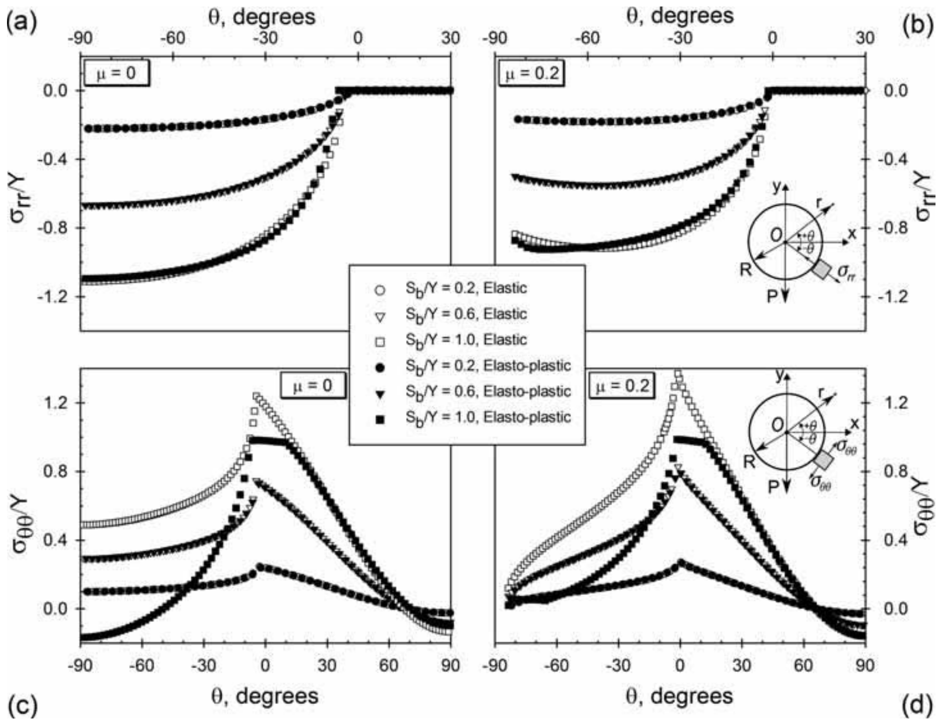

FIG. 9—*Hoop stress distributions along the hole circumference from elastic and elasto-plastic models.*

Results

Figures 9 presents the comparisons between the stress solutions from the linear elastic and elasto-plastic models with $\mu = 0$ and 0.2. In Fig. 9(*a*) and 9(*b*), normalized radial stress distributions σ_{rr}/Y are plotted along the hole circumference for the normalized pin-load magnitudes $S_b/Y = 0.2, 0.6, 1.0$. Results, in general, do not vary significantly, although a noticeable difference in the curve shapes are observed for the applied pin-load $S_b/Y = 1$ and a friction coefficient $\mu = 0.2$ (Fig. 9(*b*)). Figure 9(*c*) and 9(*d*) shows a significant influence of the material non-linearity on the hoop stress distributions when the applied load approaches its maximum level. For example, the peak hoop stress values for $S_b/Y = 1$ are reduced by as much as 19 % and 25 % in the cases with $\mu = 0$ and 0.2, respectively. Further variations are observed in the region $\theta < 0°$, particularly in the frictionless case with $S_b/Y = 1$, where the magnitudes of the hoop stresses from the elasto-plastic models are reduced by a significant amount. The stress solutions for the smaller applied loadings are in good agreement as expected since there is little plastic deformation.

The influence of friction can be studied by comparing the radial stress plots (a) with (b) and the hoop stress plots (c) with (d) in Fig. 9. The radial stress values are lower in the case with friction, which is more obvious for higher applied loadings (see Fig. 9(*a*) and 9(*b*)). For example, when the pin load is $S_b/Y=1$, the maximum percentage difference between $\mu=0$ and 0.2 is about 22.5 % at $\theta=-85°$. It is observed that the friction raises the peak hoop stresses for the elastic material models particularly when the applied loading is high (compare the open symbols in Fig. 9(*c*) and 9(*d*)). The percentage difference between the elastic peak hoop stress magnitudes with $\mu=0$ and 0.2 is approximately 13 % when $S_b/Y=1$. Furthermore, the elastic hoop stress solutions at the lower values of θ are larger with a maximum percentage difference of nearly 120 % at $\theta=-85°$ when $S_b/Y=1$. Note that similar observations were reported regarding friction in previous FE studies with the linear elastic material models in Refs 20 and 21. However, the influence of friction is not the same when the material nonlinearity is included. For the high applied loadings, the elastic-plastic hoop stress values reach the same highest levels which are approximately unity for both cases of friction (compare the closed symbols in Fig. 9(*c*) and 9(*d*)). This, of course, is a consequence of local material yielding. An additional difference with the elastic model solutions is that friction increased the hoop stress results at the lower values of θ when $S_b/Y=1$.

Of concern is the location of the maximum hoop stress, which is a susceptible region for crack initiation. For the elastic case, angles corresponding to the peak hoop stresses are approximately $\theta_{max}=-4.6°$ and $-1.5°$ for $\mu=0$ and 0.2, respectively. These values are approximately $\theta_{max}=-3.6°$ and $-1.0°$ for the elasto-plastic frictionless case and the case with $\mu=0.2$. However, when $S_b/Y=1$, the hoop stress values in the vicinity of these regions are approximately the same when material non-linearity is included, indicating that the cracks may initiate anywhere around $\theta=0°$ (Fig. 9(*c*) and 9(*d*)).

Graphical results of the pin-loaded hole in a finite width plate ($R/w=6.3$) with an initial compressive residual stress field created by the cold expansion simulation are presented in Figs. 10–12. In Fig. 10, the normalized radial stress distributions σ_{rr}/Y are plotted along the circumference of the cold expanded and pin-loaded hole with friction coefficients $\mu=0$ and 0.2. The radial stress solutions from kinematic and isotropic hardening material models were nearly identical. The stress and the influence of friction are very similar to that obtained from the elastic pin-loading analyses (see Fig. 9(*a*) and 9(*b*)). For example, including friction reduces the radial stress magnitude by as much as 29 % around $\theta=85°$, when the applied loading is $S_b/Y=1.0$.

Hoop stress distributions of the cold expanded pin-loaded hole for the isotropic and kinematic hardening material models are given in Fig. 11 for $\mu=0$ and 0.2. Results indicate that the hoop stress values are lower (in compression) throughout the pin-loading process when the kinematic hardening material model is used. That is because the compressive hoop stress magnitude produced from cold expansion simulation is lower. Lower residual stress values in kinematic hardening model result from Bauschinger's effect, in which the material more readily yields under reverse loading. It is observed that including friction raises the maximum hoop stress values in both hardening models and for all applied load levels up to $S_b/Y=1$. The locations of the maximum hoop stresses are approximately $\theta_{max}=-3.7°$ and $-1.3°$ for $\mu=0$ and 0.2, respectively.

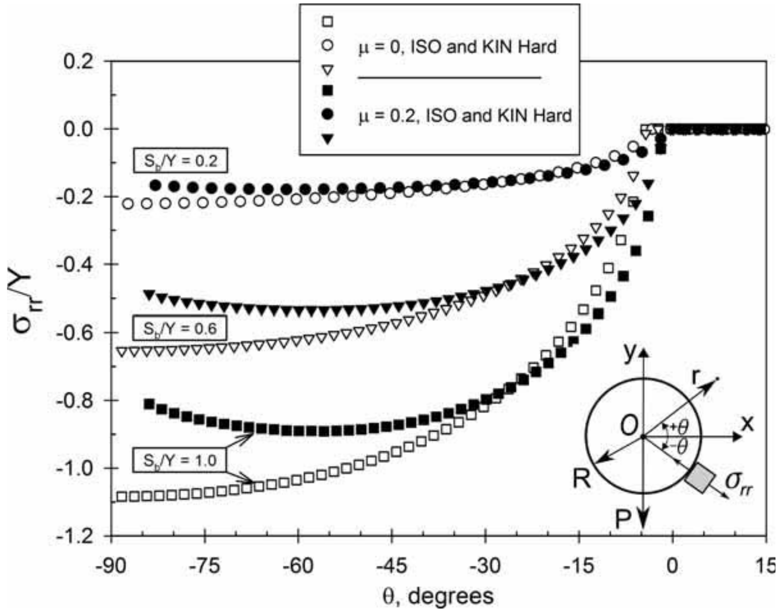

FIG. 10—*Radial stress distributions along the circumference of cold expanded and pin-loaded hole.*

These values are the same for both hardening models as shown in Fig. 11(*a*) and 11(*b*).

The hoop stress distributions along the line $y = 0$, as a function of the normalized distance x/R are given in Fig. 12. This figure demonstrates the variation of the residual stress field in the sheet material as the pin load is applied. It is observed that the location of the maximum hoop stress is not at the hole edge, but in the interior region of the sheet material. At the highest load level

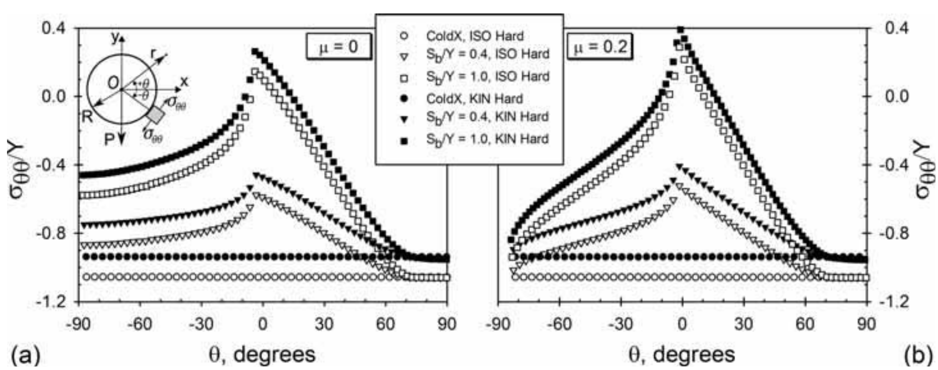

FIG. 11—*Hoop stress distributions along the circumference of the cold expanded and pin-loaded holes.*

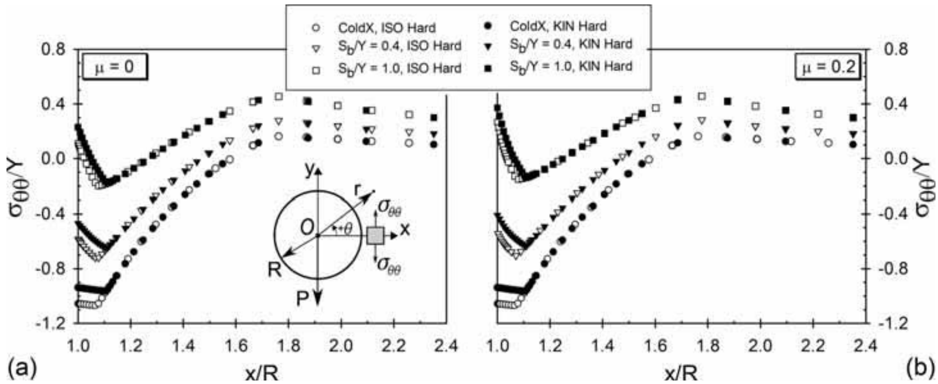

FIG. 12—*Hoop stress distributions along the line y=0 around the cold expanded and pin-loaded holes.*

(i.e., when $S_b/Y=1.0$), the hoop stress values for the kinematic hardening model at the hole edge (i.e., at $x/R=1$) are $\sigma_{\theta\theta}/Y=0.23$ and 0.37 for $\mu=0$ and 0.2. When the applied loading of $S_b/Y=1.0$ is removed, the residual stress curve returns to its original state with a negligible residual stress relaxation during the load cycle.

Finally, in Fig. 13, the stress distributions along the line $y=0$ for an isotropic hardening material (given in Fig. 12) are compared with the solutions obtained by superposing the elastic stress distribution due to the pin loading with the pre-determined residual stress curve. Results from both approaches compare well. Thus, once the residual stress field around the hole is known, the subsequent stress state for applied pin loadings $S_b/Y\leq 1.0$ on line $y=0$ can be computed by superposition.

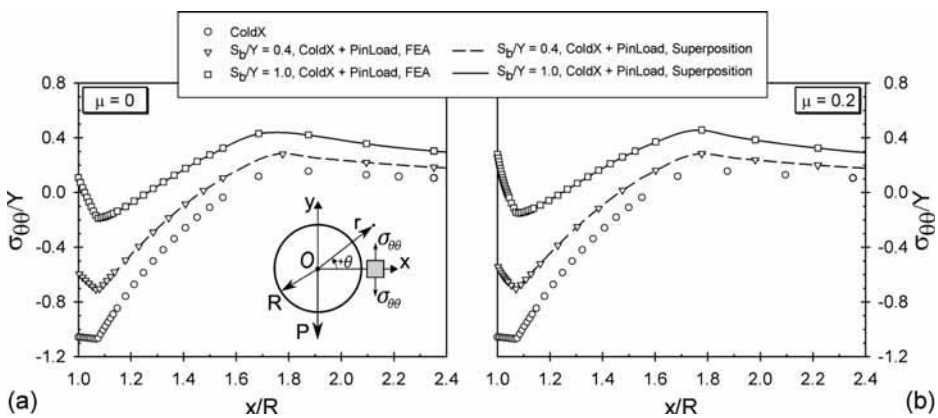

FIG. 13—*Hoop stress distributions along the line y=0 around the cold expanded and pin-loaded holes for isotropic hardening material model.*

Conclusions

A detailed 2D FEA of a pin-loaded hole in a rectangular aluminum alloy 7075-T6 sheet was performed. Plane stress conditions were assumed. The material of the sheet was modeled to be elastic and elastic-plastic with multilinear isotropic work hardening. A kinematic hardening material model was also considered during the cold hole expansion simulation to study Bauschinger's effect on the final stress results. The pin was assumed as rigid for simplicity. Convergence studies and comparison with other work were done to validate the FE model.

In the first phase of this work, the residual stress free hole was pin-loaded, and the influence of the material nonlinearity and friction on the stress distributions along the hole circumference was studied. Major variations in the hoop stress solutions from elastic and elasto-plastic models were observed in the region $\theta < 0°$. Also, the peak hoop stress values were reduced by a significant amount when material non-linearity was considered. Friction increased the peak hoop stress values for the elastically loaded holes and for small applied loadings with the elastic-plastic material model. However, as the applied load was increased to the maximum level in elastic-plastic model, the magnitudes of normalized σ_{max} approached unity for both friction cases.

The angles corresponding to the elastic peak hoop stresses were approximately $\theta_{max} = -4.6°$ and $-1.5°$ for $\mu = 0$ and 0.2, respectively. These values were nearly $\theta_{max} = -3.6°$ and $-1.0°$ in the elasto-plastic frictionless case and for the case with $\mu = 0.2$. The hoop stress values in the vicinity of these regions were approximately the same in the plastically loaded hole, indicating that the cracks may initiate anywhere around $\theta = 0°$.

In the next stage, a compressive residual stress field was introduced around the hole prior to the subsequent pin-loading analysis. The residual stress field was produced by a simplified cold expansion simulation, where the hole of the sheet was uniformly expanded beyond the elastic limit of the material. Radial stress distributions and the influence of friction were very similar to the ones obtained from previous elastic pin-loading analysis. Due to Bauschinger's effect, kinematic hardening produced compressive residual stresses with lower magnitudes around the hole. This resulted in higher hoop stress values along the hole circumference when using kinematic hardening throughout the subsequent pin-loading simulations. The locations of the maximum hoop stresses were same for both hardening material models with $\theta_{max} = -3.7°$ and $-1.3°$ for $\mu = 0$ and 0.2, respectively. As the applied pin-load was removed, the hole returned to its original residual stress state indicating that negligible residual stress relaxation occurred during this load cycle.

Acknowledgments

The present work is part of the FAA funded project *Analytical Tools for Residual Stress Enhancement of Rotorcraft Damage Tolerance* (FAA Contract No. DTFACT-06-C-00025).

References

[1] Coker, E. G., Filon, L. N. G., and Jessop, T. D., *A Treatise on Photo-Elasticity*, 2nd ed., Cambridge University Press, Cambridge, U.K., 1957, pp. 524–530.
[2] Frocht, M. M., *Photoelasticity*, 4th ed., Vol. II, Wiley, New York, 1948, pp. 179–193.
[3] Ahmad, I. and Stanley, P., "Deformations and Stresses in Pin-Loaded Tubes Under Axial Tension," *J. Strain Anal.*, Vol. 35(5), 2000, pp. 329–345.
[4] Cloud, G. L., *Optical Methods for Engineering Analysis*, 1st ed., Cambridge University Press, New York, NY, 1998, pp. 323–340.
[5] Herrera-Franco, P. J., Cloud, G. L., and Zimmerman, K., *Moire Study of 2 and 3–Hole Arrays of Composite Material Fasteners*, Applications of Advanced Measurement Techniques, British Society for Strain Measurement, Whittles London, U.K., 1987, pp. 25–35.
[6] Lanza di Scalea, F., Hong, S. S., and Cloud, G. L., "Whole-Field Measurement in a Pin-Loaded Plate by Electronic Speckle Pattern Interferometry and the Finite Element Method," *Exp. Mech.*, Vol. 38(1), 1998, pp. 55–60.
[7] Noble, B. and Hussain, M. A., "Exact Solutions of Certain Dual Series for Indentation and Inclusion Problems," *Int. J. Eng. Sci.*, Vol. 7, 1969, pp. 1149–1161.
[8] Hyer, M. W. and Klang, E. C., "Contact Stresses in Pin-Loaded Orthotropic Plates," *Int. J. Solids Struct.*, Vol. 21(9), 1985, pp. 957–975.
[9] Ho, K. C. and Chau, K. T., "A Finite Strip loaded by a Bonded-Rivet of a Different Material," *Comput. Struct.*, Vol. 70, 1999, pp. 203–218.
[10] Echavarria, C., Haller, P., and Salenikovich, A., "Analytical Study of a Pin-Loaded Hole in Elastic Orthotropic Plates," *Compos. Struct.*, Vol. 79, 2007, pp. 107–112.
[11] Knights, R. C. "The Action of a Rivet in a Plate of Finite Breadth," *Philos. Mag., Suppl. 7*, Vol. 19(127), 1935, pp. 517–540.
[12] Theocaris, P. S., "The Stress Distribution in a Strip Loaded in Tension by Means of a Central Pin," *Trans. ASME, J. Appl. Mech.*, Vol. 78, 1956, pp. 85–90.
[13] Rao, A. K., "Elastic Analysis of Pin Joints," *Comput. Struct.*, Vol. 9, 1978, pp. 125–144.
[14] Mangalgiri, P. D., Ramamurthy, T. S., Dattaguru, B., and Rao, A. K., "Elastic Analysis of Pin Joints in Plates Under Some Combined Pin and Plate Loads," *Int. J. Mech. Sci.*, Vol. 29(8), 1987, pp. 577–585.
[15] Mizushima, I. and Hamada, M., "Stress Analysis Around Circular Hole in Infinite Plate with Rigid Disk," *Bull. JSME*, Vol. 26(218), 1983, pp. 1296–1301.
[16] Ho, K. C. and Chau, K. T., "An Infinite Plane Loaded By a Rivet of a Different Material," *Int. J. Solids Struct.*, Vol. 34(19), 1997, pp. 2477–2496.
[17] Mangalgiri, P. D., Dattaguru, B., and Rao, A. K., "Finite Element Analysis of Moving Contact in Mechanically Fastened Joints," *Nucl. Eng. Des.*, Vol. 78, 1984, pp. 303–311.
[18] Solodovnikov, V. N., "Solution of the Contact Problem For a Pin-Loaded Plate," *J. Appl. Mech. Tech. Phys.*, Vol. 38(1), 1997, pp. 109–115.
[19] Newman, J. C., Harris, C. E., James, M. A., and Shivakumar, K. N. "Fatigue-Life Prediction of Riveted Lap-Splice Joints Using Small-Crack Theory," *Proceedings of the Fatigue in New and Ageing Aircraft Symposium*, 1997, pp. 523–552.
[20] Iyer, K., "Solutions for Contact in Pinned Connections," *Int. J. Solids Struct.*, Vol. 38, 2001, pp. 9133–9148.
[21] Yavari V., et al., "On the Stress Distributions Around the Hole in Mechanically Fastened Joints," *Mech. Res. Commun.*, Vol. 36, No. 3, 2009, pp. 373–380.
[22] Kumar, S. K., et al., "Elasto-Plastic Contact Stress Analysis of Joints Subjected to

Cyclic Loading," *Comput. Struct.*, Vol. 60(6), 1996, pp. 1067–1077.

[23] Restis, J. and Reid, L., *Cold Expansion of Holes Using the Standard Split Sleeve System and Countersink Cold Expansion* (*CsCx*), Fatigue Technology Inc., Seattle, WA, 2002, FTI Process Specification 8101D.

[24] Rice, R. C., Jackson, J. L., Bakuckas, J., and Thompson, S., "Metallic Materials Properties Development and Standardization," *Report No.* MMPDS-01 DOT/FAA, U.s Department of Transportation, Federal Aviation Administration, and Office of Aviation Research, Washington, D.C., 2003.

[25] ANSYS Inc., *ANSYS Release 11.0 Documentation*, Chap. 8, ANSYS, Inc., Canonsburg, PA, 2001, pp. 3–12.

[26] Ismonov, S., Daniewicz, S. R., Newman, J. C., Jr., Hill, M. R., and Urban, M. R., "Three Dimensional Finite Element Analysis of a Split-Sleeve Cold Expansion Process," *ASME J. Eng. Mater. Technol.*, Vol. 131, 2009 (in press).

Reprinted from JAI, Vol. 7, No. 10
doi:10.1520/JAI102703
Available online at www.astm.org/JAI

S. Hadidi-Moud[1] *and D. J. Smith*[2]

The Influence of Elastic Follow-Up on the Integrity of Structures

ABSTRACT: Based on the traditional definitions associated with creep strain accumulation in defect free components, a generalised definition for "elastic follow-up" factor, *Z*, is proposed that characterises the influence of a "nonlinear" event experienced locally within a structure, i.e., creep, plasticity, cracking, growth of an existing crack, or any combination of such events, on the response of the structure to the applied loading. A "crack affected zone" approach is then outlined for evaluation of this parameter in a defective component. The significance of quantifying elastic follow-up in relation to integrity assessment procedures and the challenges facing its practical implication to the codes is discussed. The approach is finally examined through its application to two example problems; a standard test geometry, centre cracked plate and an external circumferential cracked thick cylinder, i.e., a conventional structural component.

KEYWORDS: elastic follow-up, structural integrity, crack, stress classification

Introduction

Traditionally, the concept of elastic follow-up (EFU) has been deployed to describe the process of strain accumulation associated with stress relaxation due to creep. EFU has been characterised by defining a parameter that represents its significance and is incorporated into the evaluation of creep parameters such as C^*. Extensive evidence of such applications may be found in literature. The early work of Robinson [1,2] addressed the phenomenon of "follow-up elasticity" in several examples of engineering problems. A uni-axial description

Manuscript received September 5, 2009; accepted for publication September 9, 2010; published online October 2010.
[1] Mechanical Engineering Dept., Ferdowsi Univ. of Mashhad, Univ. Campus, Mashhad, Iran (Corresponding author), e-mail: Hadidi@ferdowsi.um.ac.ir; Saeid.Hadidi-Moud@Bristol.ac.uk
[2] Mechanical Engineering Dept., Queen's Building, Univ. of Bristol, Bristol BS8 1TR, United Kingdom.

Cite as: Hadidi-Moud, S. and Smith, D. J., "The Influence of Elastic Follow-Up on the Integrity of Structures," *J. ASTM Intl.*, Vol. 7, No. 10. doi:10.1520/JAI102703.

of EFU due to creep has been provided extensively by many authors. Boyle and Nakamura [3] used a simple two-bar in series model subjected to a fixed displacement and the creep power law to provide a description for quantifying EFU. Goodman and Booth [4] proposed an estimation method that used equivalent stress and strains and an effective elastic modulus. Goodman [5] also provided a worked example that used the proposed approach. An alternative simplified evaluation method for EFU was outlined by Seshadri [6] that uses a "modified" elastic modulus. The incorporation of EFU in high temperature assessment procedures R5 [7] is based on the above developments. Recent studies on creep related EFU were carried out by Nakamura et al. [8] and Kasahara et al. [9], who provided guidelines for fast reactor structural design standards.

Although the majority of research related to EFU is linked to creep-associated problems, a number of researchers have further investigated its influence on the overall response of structures in relation to the geometry of the component and the applied boundary conditions, as well as its dependence on the type of applied loading and the stress state. Part of this work is aimed at establishing recommendations for stress classification for use with integrity assessment codes like R6 [10] particularly in relation to the treatment of residual stresses. Although residual stresses are classed as secondary, it has come to the attention of many researchers that, depending on the geometry of the structure and the imposed boundary conditions, it may be necessary to treat these stresses as primary either partly or fully depending on the level of associated follow-up. Residual stresses that are self contained within the structure contribute to fracture by changing the driving force. The significance of their effect on fracture depends on the level and the extent ("local" or "global") of residual stress components. The distinction between primary and secondary stress was discussed by Roche [11]. Dhalla [12,13] outlined proposals for elastic and inelastic evaluation of EFU in piping systems based on which a method for classification of displacement controlled stresses into primary and secondary components was suggested [14]. A procedure for stress classification at structural discontinuities was further suggested by Dhalla [15,16]. Roche [11,17,18] outlined a procedure which would allow part of the secondary stress to be retained for classification purposes depending on the degree of follow-up.

Evaluation of EFU in defect free components is a rather established practice. For example, the route taken in R5 is based on the determination of a reference stress. Gamboni et al. [19] proposed a procedure to quantify EFU due to a generic structural discontinuity resulting in inelastic strain concentration in the presence of a deformation controlled loading.

The development of a reliable technique to quantify EFU due to the presence of cracks in structures may lead to important potential applications for the assessment of the integrity of structures. First, treatment of residual stresses in structural integrity assessment procedures remains ambiguous. It is generally agreed that residual stresses should be considered primary if the associated EFU is high whereas for low EFU, residual stress has to be considered as secondary stress. From earlier work [20,21] it has become evident that relaxation and redistribution of residual stresses is determined by EFU. Plastic straining accommodates and relaxes residual stresses and the relaxation depends on the relative stiffness of structural components that determines EFU. Second, a judgement on the integrity of real structures is based on experiments carried out using standard fracture test specimens tested under load controlled or displacement controlled conditions. The interaction between the locally nonlinear region and the rest of a structure depends on how the local region is embedded within the structure, with the surrounding structure imposing boundary conditions on the local region. Practical structures normally operate under "mixed boundary conditions," and as such, the standard fracture tests do not fully represent the practical structure. Therefore, quantifying EFU would help to address these two major concerns when performing integrity assessment of structures.

In earlier work [20], the concept of EFU was extended from its traditional creep related description to a general nonlinear event within a structure. Using benchmark model structures, a unified solution of EFU was provided, based on which it was suggested that EFU represents a measure for characterisation of the influence of a nonlinear responding element within a structure on its overall response to loading. Of particular interest is the problem of EFU associated with cracked structures. It was further demonstrated that the influence of residual stress on structural integrity depends on its interaction with the applied loading. When the load application is associated with plasticity, there is redistribution of residual stress and its subsequent relaxation on unloading. It was also shown, using benchmark model structures, that the relaxation of residual stresses depends on the relative stiffness within the structural components. The treatment of residual stresses in integrity assessment procedures is therefore related to the estimation of EFU through a factor, Z.

In the next section, the traditional definition of EFU is extended to a generalised concept. Then, it is used to derive closed form solutions for benchmark multi-bar structures. These are treated as simplified representatives of practical structures. A crack affected zone (CAZ) concept is then proposed to provide a practical method of examining cracked components.

Generalised Definition of EFU

In the R5 assessment procedure for the high temperature response of structures [7], the definition of EFU factor for general relaxation behaviour is based on the illustration shown in Fig. 1. The EFU factor, Z, is defined as

$$\frac{d\overline{\varepsilon_c}}{dt} + \frac{Z}{\bar{E}}\frac{d\bar{\sigma}}{dt} = 0$$

where:

$\bar{\sigma}$ = equivalent normal stress,

$\bar{\varepsilon}_c$ = equivalent creep strain,

$\bar{E}$ = equivalent elastic modulus, and

t = creep time.

In Appendix A.8 of R5, it is shown that for option 3 (refer to the code for details) the EFU factor may be estimated from

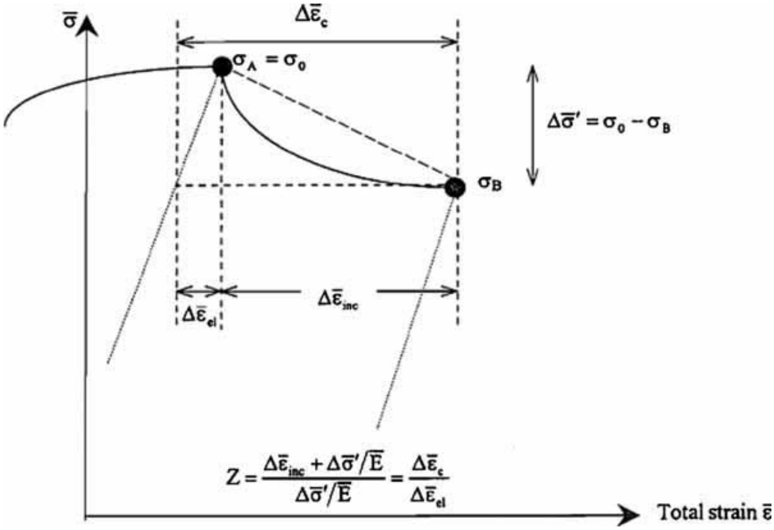

FIG. 1—*Graphical illustration of elastic follow-up factor definition in R5.* (*Reproduced from R5, issue 3, BEGL, United Kingdom.*)

$$Z = \frac{\Delta\bar{\varepsilon}_{\text{inc}} + \Delta\bar{\sigma}'/\bar{E}}{\Delta\bar{\sigma}'/\bar{E}} = \frac{\Delta\bar{\varepsilon}_c}{\Delta\bar{\varepsilon}_{\text{el}}}$$

where:

$\Delta\bar{\sigma}'$ = variation of equivalent normal stress.

The above equations are reproduced from R5 and the definitions for various terms in the above equation are graphically described in Fig. 1. As the figure suggests, the definition of EFU factor is associated with both strain accumulation and stress reduction. Stress reduction is normalised by the elastic modulus to provide a dimensionless parameter termed EFU factor, Z, that is effectively correlating the conditions "before" with "after" stress relaxation due to creep.

The alternative interpretation for Z factor is to view the terms $\Delta\bar{\varepsilon}_c$ and $\Delta\bar{\varepsilon}_{\text{el}}$ as the final and initial strain variations from a reference point on the "elastic" unloading line. Figure 2 demonstrates the generalised definition of EFU. Assuming that there was no prior nonlinear event (creep or plasticity) then the initial condition (A) would have been on the purely elastic linear response and the dotted line shown from A would have intersected the axes at the origin of stress strain diagram, i.e., point (0,0). It therefore follows that:

$$\Delta\varepsilon_c \equiv \varepsilon_B - \sigma_B/E \quad \text{and} \quad \Delta\varepsilon_{el} \equiv \varepsilon_A - \sigma_B/E$$

The EFU factor may be re-written as

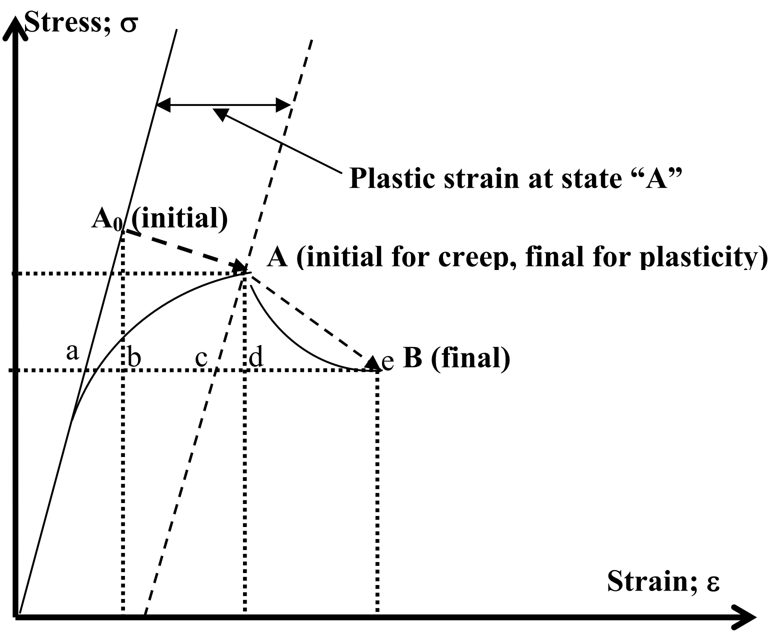

FIG. 2—*Graphical presentation of EFU for combined plasticity and creep EFU due to plasticity* (A_0A)*: ad/ab; EFU due to creep* (*AB*)*: ce/cd; combined overall EFU* (A_0B)*: ae/ab.*

$$Z \equiv \frac{\varepsilon_B - \sigma_B/E}{\varepsilon_A - \sigma_B/E}$$

Renaming the terms in the above equation by assigning "initial" and "final" to represent conditions "*A*" and "*B*," respectively, gives

$$Z \equiv \frac{\varepsilon^f - \sigma^f/E}{\varepsilon^i - \sigma^f/E} \quad \text{or} \quad Z = \frac{(\varepsilon)_{\text{final}} - (\varepsilon^{el}_{eq})_{\text{final}}}{(\varepsilon)_{\text{initial}} - (\varepsilon^{el}_{eq})_{\text{final}}} \quad \text{where} \quad (\varepsilon^{el}_{eq})_{\text{final}} = (\sigma)_{\text{final}}/E$$

The term $(\varepsilon^{\text{el}}_{\text{eq}})_{\text{final}}$ is the equivalent elastic strain at the final stress. If there was a nonlinear event prior to *A* (i.e., plastic deformation), then the above term should be replaced by

$$(\varepsilon^{\text{el}}_{\text{eq}})_{\text{final}} + (\varepsilon^{\text{pl}}_{\text{eq}})_{\text{final}}$$

The additional term $(\varepsilon^{\text{pl}}_{\text{eq}})_{\text{final}}$ is the plastic strain part of the strain corresponding to σ_B on the stress strain curve. It should also be noted that if this is the case, then the condition *A* itself is the final condition for the EFU due to plasticity. The initial condition would be the corresponding point on the purely linear elastic response of the component of interest. This is shown graphically in Fig. 2.

This definition may be viewed as a generalised description for quantifying EFU. Creep and plasticity are both nonlinear and non-recoverable processes

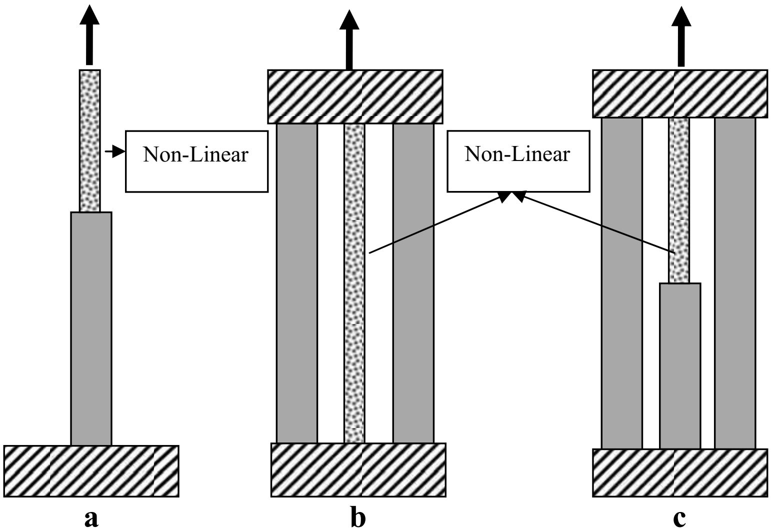

FIG. 3—(*a*) *Series bars formation subjected to displacement,* Δ*;* (*b*) *parallel bars system subjected to load, P; and* (*c*) *combined formation.*

and hence, the application of the generalised description to a localised plasticity problem would result in a similar description to that of creep stress relaxation.

Elastic Follow-Up for Simple Structures

The interaction between the locally nonlinear responding region of the structure and its surrounding elements may be characterised by idealising the structure as parallel bars, series bars, or a combined formation. In this section, the analytical solutions of the EFU factor for several benchmark model systems is briefly reviewed.

Series Formation

A two-bar structure subjected to a fixed end displacement, Δ is shown in Fig. 3(*a*). A practical example of such model is a pipe containing a hoop crack that is axially loaded.

For the case of perfect plasticity as shown in earlier work [20]

$$Z = \frac{\alpha + 1}{\alpha} \quad \text{where} \quad \alpha = \frac{K_B}{K_A}$$

where:

K_A and K_B indicate stiffness of bars.

The creep equations for each of the bars in the system are

$$\varepsilon_A = \frac{\sigma_A}{E_A} + b_A\sigma_A^m \quad \varepsilon_B = \frac{\sigma_B}{E_B} + b_B\sigma_B^m$$

where:

m, b_A, and b_B = creep constants for bars A and B.

It can be shown that (assuming bar B does not experience creep) the EFU factor due to creep for the series bars system is obtained from a similar expression, i.e.,

$$Z = \frac{\alpha + 1}{\alpha}$$

This result indicates that EFU is independent of the creep law and is a purely geometrical effect.

Parallel Formation

Shown in Fig. 3(b) is a parallel bar model that is subjected to an initial residual stress field introduced into the structure by imposing an initial misfit, δ_0. The structure is then loaded through a rigid block such that subsequent displacements in bars are essentially identical. The system is then unloaded. A practical example for this model is a pipe containing a central region with axial crack and subjected to internal pressure.

The expression for Z given for a series bar structure for the cases of plasticity and creep is also valid for a parallel bar structure subjected to a uniform far field load, Fig. 3(b).

Combined Parallel and Series Formation

The model shown in Fig. 3(c) (a centre cracked plate (CCP) subjected to far field tension normal to the crack plane) represents such structure.

For the combined series and parallel bar structure shown in Fig. 3(c) subjected to far field load, $\boldsymbol{P}$, the EFU factor due to plasticity in bar A is obtained as

$$Z = \left(\frac{\alpha + 1}{\alpha}\right)\left(\frac{\beta + 1}{\beta}\right) \quad \text{where} \quad \alpha = \frac{K_B}{K_A}, \quad \beta = \frac{K_C}{K_{AB}} \quad \text{and} \quad \frac{1}{K_{AB}} = \frac{1}{K_A} + \frac{1}{K_B}$$

A detailed derivation for these systems is given by Smith et al. [22]. Similarly, for the case of creep in bar A, the EFU factor for the combined system is obtained by multiplying the EFU descriptions of the series substructure by that of the parallel structure.

The expressions for EFU factor can be modified for plastic hardening as shown by Kasahara et al. [23].

Summary

Although the expressions for Z in series and parallel bar structures are the same, it should be noted that the series and parallel bars are very different in

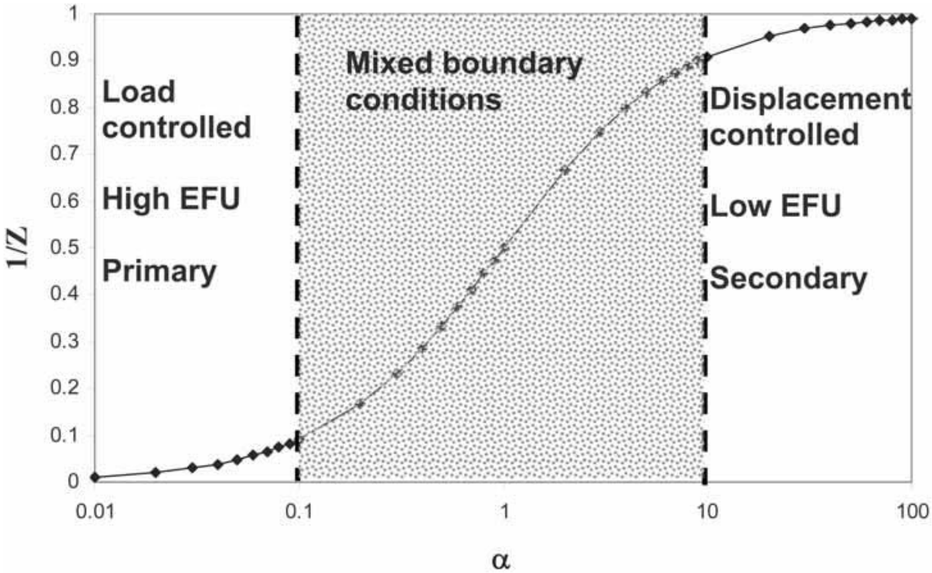

FIG. 4—*Variation of EFU with stiffness ratio in series and parallel bar structure.*

terms of the mechanism of load and displacement distribution between their structural components. The closed form description provided for EFU due to plasticity in series bars structure was based on the application of a fixed displacement to the structure. In a series formation, the load transfers through the components so that the same load is applied to both bars A and B. It is the applied displacement that distributes, and this distribution depends on the relative stiffness, α. EFU for this case is independent of the applied displacement as long as it is sufficient to introduce plasticity into bar A. Where the surrounding structure is stiffer than the "weak region" A, i.e., $\alpha > 1$, a bounding value $Z = 2.0$ limits the level of EFU. For large α, EFU tends to 1 and essentially represents displacement controlled conditions. Assuming a very low stiffness in the surrounding structure (e.g., a long bar B) the relative stiffness would be small ($\alpha \ll 1$), resulting in high estimates of EFU (EFU$\rightarrow\infty$ as $\alpha\rightarrow 0$). This represents load controlled conditions. The dependence of EFU on α is shown in Fig. 4.

The descriptions provided for EFU due to perfect plasticity and creep in series, parallel, and combined bar structures all resulted in similar expressions in terms of relative structural stiffness. Figure 4 suggests that $Z > 10$ and $Z < 1.1$ (equally, $\alpha < 0.1$ and $\alpha > 10$) may be considered as reasonable approximations for the extreme cases of load and displacement controlled conditions, respectively.

Previous work had highlighted the significant influence of EFU on the relaxation of residual stresses [21]. The study of multi-bar benchmark models provides an insight into the cause and source of the EFU effect in structures.

What introduces EFU is the fact that a region of the structure "softens" and the rest of structure responds to this "softening." It is the relative stiffness, α, that specifies EFU under the applied boundary conditions.

A New Approach to Estimating Elastic Follow-Up in Cracked Structures

Creep and plasticity are both processes that introduce permanent deformation, and the application of the generalised description to a localised plasticity problem will be similar to that of creep stress relaxation. The difficulty arises where discontinuities are present. The description given in "Generalised Definition of Elastic Follow-Up" results in a spatially dependent evaluation of EFU that is not helpful. A CAZ approach is therefore introduced to overcome this difficulty. The CAZ in a structure represents a nonlinear softening component of the structure whereas the remainder of the structure remains essentially elastic. The reference (initial) state is the un-cracked structure. Softening is due to the appearance of crack in the structure. For a fixed displacement input to the structure, as the crack grows the far field stress decreases, leading to an increase in strain in the CAZ.

The CAZ may be described as a region of the structure around the crack that contains the physical crack within which the stresses and strains are redistributed due to the presence of crack. To evaluate the extent of the CAZ, it is proposed to specify a boundary by comparing the local stress and strain fields in the region containing the crack with the same field variables corresponding to the un-cracked structure that is subjected to the same loading. Provisional finite element (FE) analyses of conventional cracked components such as plates and pipes suggests that the extent of the CAZ is essentially governed by the geometry of the component and the crack length, and also depends on the orientation of the crack with respect to the applied loading. Although the material response alters the levels of stresses and strains, it has a negligible influence on the extent of the affected zone. The CAZ approach utilised here is based on a series of FE analyses performed to identify the boundaries of the CAZ from the remaining structure.

Fig. 5 describes how the concept of CAZ is used to link the simplified multiple spring arrangement (for which closed form solutions of EFU were provided in "Elastic Follow-Up for Simple Structures") to a practical structure containing a crack. The structure depending on the crack orientation and loading type can be idealised by a two-dimensional (2D) description of regions representing the softened CAZ surrounded by the elastic material and subjected to a remotely applied load and/or displacement depending on the boundary conditions. The 2D representation of the structure can then in turn be replaced by a combination of "springs" representing various components of the structure that is in its most general form a combined multiple spring model for which closed form EFU solutions are available.

Two example problems, a CCP and a thick cylinder with an external fully circumferential crack (ECCC), have been used to examine the practicality of the CAZ approach in the estimation of EFU in cracked structures. A CCP is a conventional low constraint fracture specimen with well established solutions for

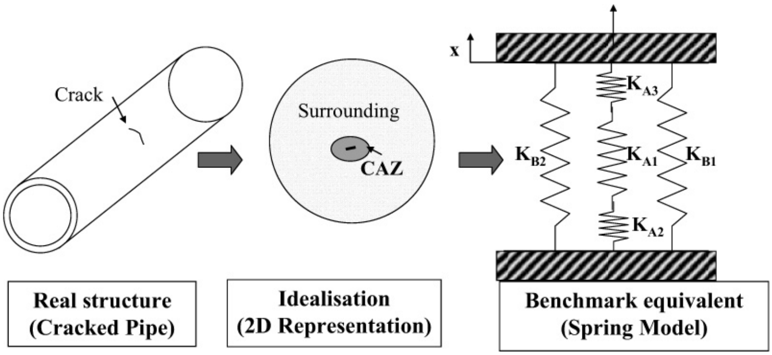

FIG. 5—*Idealisation of practical structure by multiple spring model based on CAZ approach for estimation of EFU associated with defects.*

fracture parameters that may be used with a range of crack sizes to explore the influence of component/crack geometry on the EFU response of the structure. The ECCC represents a practical example problem with direct industrial applications, and is used to explore the appropriate methodology for replacing the "real structure" by its equivalent simplified "multiple spring system."

CCP in Tension

A CCP, 80 mm wide and 240 mm long was used. A range of crack sizes were introduced in the FE analyses to explore the influence of crack size on the extent of the affected zone. Loading was applied as a uniform fixed displacement to the far ends of the plate in the plane parallel to the crack plane. A 2D plane strain analysis was performed. Due to the symmetry conditions, it was sufficient to model only 1/4 of the plate and a locally refined mesh was introduced at all crack tip regions to ensure that the corresponding stress strain distributions at the crack tip regions and hence the extent of the affected zone were not inconsistent for various cracks as a result of the FE procedure. Typical properties of steel, i.e., a Young modulus of 210 GPa and Poisson's ratio of 0.3, were used to describe the linear elastic response.

Exploration of CAZ Using Simplistic Finite Element Analyses—A series of preliminary FE analyses revealed that although the extent of plastic zone at the crack tip region would depend on the material response beyond the elastic limit, the overall zone within which stress and strain fields are affected due to the presence of crack did not vary with material behaviour and depended only on the geometrical aspects of the model, the crack orientation, and the far field boundary conditions. This was verified by performing FE analyses for a single crack geometry/loading configuration with typical elastic, elastic perfectly plastic and elastic hardening plastic material models subjected to identical load levels. It should be noted that the definition and the concept of CAZ is totally different from that of the crack tip "plastic zone" or "process zone" as traditionally defined in fracture mechanics. Comparison of displacement, stress, and

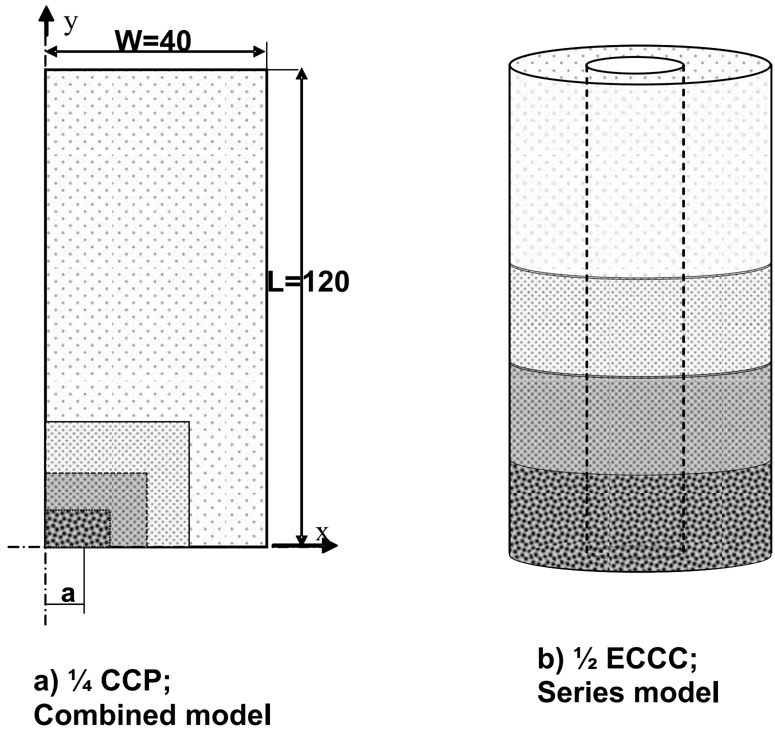

FIG. 6—*CCP and ECCC; CAZ boundaries examined in the trial analyses.*

strain distributions from elastic analyses with the inelastic solutions suggested that although at the vicinity of the crack tip region distributions were significantly different as expected, away from singular field, i.e., across the trial CAZ, boundaries approached similar values. It was therefore reasonable to base the estimation of Z factors on the elastic analysis data for all configurations in the subsequent analyses.

The CCP with various crack sizes was modelled using ABAQUS CAE and was subjected to a remote uniform fixed displacement of 0.2 mm.

Trial zone boundaries at x (parallel to the crack plane) and y (normal to crack from crack plane) directions shown in Fig. 6(*a*) were used to explore the extent of the affected zone. Stress, strain, and displacement profiles in normal to crack plane direction (y) across the width of the plate (x paths) at trial y-boundaries were obtained from FE analysis results and were plotted together with their corresponding distributions for the un-cracked plate under the same applied remote displacement to guide development of the CAZ for various crack sizes. Similarly, stress, strain, and displacement profiles along y-paths from trial x-boundaries were also extracted from FE analyses for various crack sizes.

In order to obtain the load corresponding to the applied displacement (note that the corresponding loads to the same applied displacement are different for

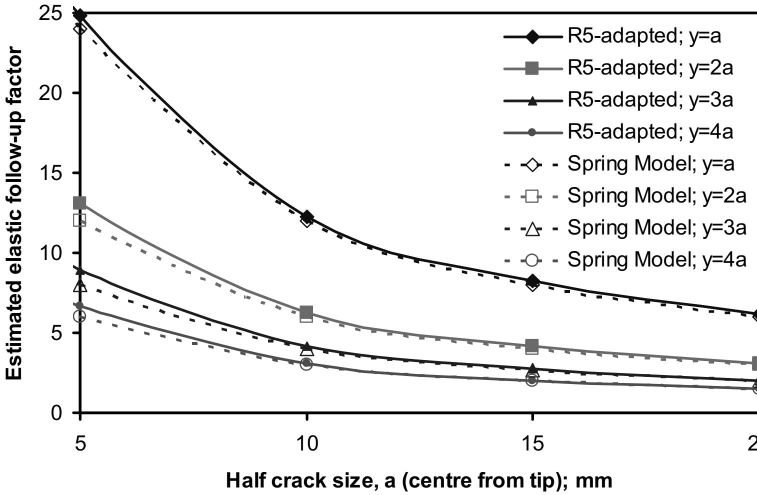

FIG. 7—*EFU estimates at assumed zone boundaries using the adapted R5 definition compared with those obtained using the spring equivalent model.*

various crack sizes and decrease with increasing crack size), the input displacement in ABAQUS was applied to one node on the far end of the plate and a simple function "EQUATION" was used in the ABAQUS input file to extend the applied displacement uniformly to all nodes across the top edge of the plate. The analysis then provided the corresponding equivalent load for each analysis. This is later required for estimation of EFU.

Using the geometry of the plate along with the trial zone boundaries and assuming a typical Young modulus for the plate material, spring stiffness values for the crack affected component of the structure as well as the remaining essentially linear elastic components surrounding the CAZ may be approximated. Two estimation approaches were examined and results were compared. First, using the closed form solutions provided for multi-bar benchmark models, it was possible to evaluate EFU factors corresponding to the assumed zone boundaries for each crack size. This was a rather straight forward procedure and used the basic calculations to calculate corresponding spring stiffness values to the decomposed components of the structure. Alternatively, the Z factor was evaluated from the generalised definition using the final, initial, and elastic equivalent to final strain values. These values in turn were extracted from displacement distributions across and along the assumed zone boundaries using simple averaging algorithms.

Results for a specific crack size are shown in Fig. 7.

Thick Cylinder with External Circumferential Hoop Crack in Tension

A 50 mm wall ECCC was used to determine EFU. It is also a common practical example where welding residual stresses and the presence of developing cracks around the locally stressed welded region are potentially expected. The cylinder was 700 mm long with internal and external diameters of 450 and 550 mm, respectively. Axi-symmetric modelling was used in development of the FE model in ABAQUS and crack plane symmetry was used to only model one half of the cylinder as shown in Fig. 6(*b*). Fully circumferential external cracks of 10, 20, 30, and 40 mm deep were introduced and axial, internal pressure, and combined loading schemes were used in a series of analyses. For this choice of geometry-crack-loading, a series bar formation consisted of a central spring representing the crack affected region and the two linear hollow bars representing the remaining length of the cylinder (one-half on each side of the CAZ) were used to define the equivalent spring system. Due to the presence of crack, application of similar far field displacements to the cracked and un-cracked geometries would result in higher local strain for the cracked cylinder in the crack affected region, suggesting that the creation of crack has introduced strain accumulation associated with stress relaxation (i.e., same far field displacement corresponds to a lower far field load for the cracked geometry when compared to the un-cracked cylinder). A similar approach to that explained for CCP geometry was used to evaluate EFU due to the presence of crack in ECCC. Similarly, the basis for decomposition of the structure into springs was the extent of violation of displacement, strain, and stress (in case of applying a similar load to the un-cracked and cracked models) due to the presence of crack. For the un-cracked cylinder, linearly increasing displacement and uniform stress profiles are expected. The required data were extracted from FE analyses where the applied far field displacement was 0.05 mm. As for the case of the plate, the cylinder geometry/crack configurations used in FE analyses assumed elastic material to estimate EFU. No plasticity or creep was considered, meaning that the analysis only examined the EFU associated with the presence of cracks. The boundary of CAZ was assumed at a range of normal distances from the crack plane equal to 1, 2, 3, and 4 times the crack depth. The main idea used in the CAZ approach is to set the zone boundary such that the zone represents the affected nonlinear behaving region whereas the remaining structure is mainly unaffected from the nonlinear event. However, at this stage, no specific rules have been applied and a range of "trial" zone boundaries were examined in EFU estimation. Similar procedures to that described for CCP in "CCP in Tension" were followed to evaluate strain components required for calculation of Z. The estimated EFU factors corresponding to trial zone boundaries for ECCC models are presented and compared in Fig. 8.

It should be noted that again, similar to the case of CCP, two approaches were used for EFU estimations in ECCC geometry. First, the definition suggested in R5 was applied to estimate EFU. In this approach, the average strain at the zone boundary was used and the corresponding strains to the initial and the equivalent elastic strains required in R5 formula were obtained from the analysis of the un-cracked elastic cylinder under similar displacement input. Second, the structure was idealised by replacing the structural components with equivalent springs. The stiffness of springs was estimated from analysis results and the analytical solution presented previously for the series multi-bar benchmark model was used for EFU estimation. The results obtained from the two estimation techniques were then compared.

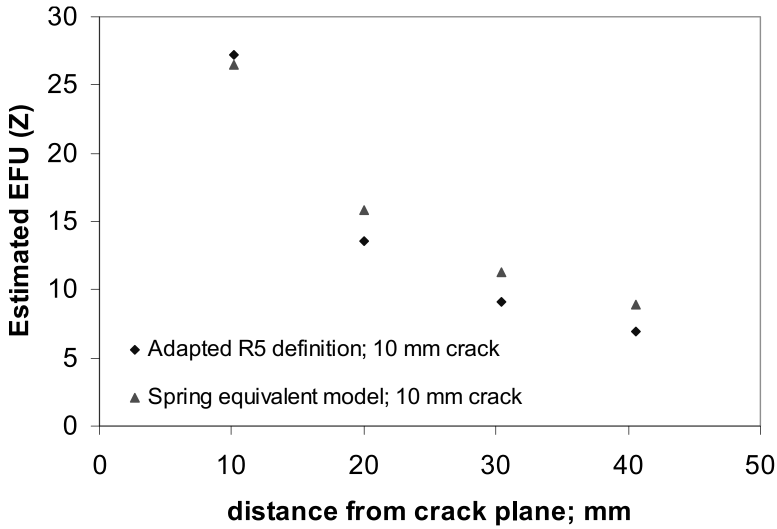

FIG. 8—*Estimated EFU using R5 definition and equivalent spring system based on assumed CAZ boundary at a, 2a, 3a, and 4a from crack plane; 1/2 ECCC FE model for 10 mm deep crack using series bar (spring) model.*

Concluding Remarks

R5 definition of EFU was analytically illustrated for benchmark series and parallel formations and closed form solutions were derived for cases of perfect plasticity, plastic hardening, and creep. It was shown that for parallel structures the stress equations were coupled and incremental analysis was required to achieve a solution. Furthermore, the analogy between plasticity and creep was demonstrated. The quantification approach for all cases was consistent with the extreme situations of pure displacement controlled and pure load controlled structures, showing the EFU limits of 1 and infinity, respectively. It was highlighted that the definition of EFU in R5 was accounting for both strain accumulation and its associated stress relaxation during the creep process.

This report provides a complete set of closed form solutions of EFU in series, parallel, and combined benchmark model structures. These results ideally represent a generalised solution for characterising the overall response of a structure containing a nonlinear element. The similarity of the influence of various local nonlinear events at the sub-structural level on the overall response of structures suggests that it may be possible to introduce a unified framework for quantification of EFU. Such approach would help to address the two major issues of integrity assessment; it would allow appropriate treatment of residual stresses in assessment procedures and would provide a means for proper interpretation of laboratory test data to real size structures through the concept of sub-modelling, i.e., exploring the imposed boundary conditions from the surrounding structure to the local nonlinear behaving component within the structure. It was argued that evaluation of EFU would be specifically useful and would have extensive practical applications if it could be achieved for structures containing defects. The traditional solution available for creep-associated EFU in defect free structures was extended and generalised to enable evaluation due to any local nonlinear event. Simple multiple bar structures forming series, parallel, and combined arrangements of bars subjected to uni-axial loading and/or displacement were used as benchmark models to provide closed form solutions for EFU associated with nonlinearity represented as creep, perfect plasticity, or hardening plasticity. Furthermore, it was suggested that a real continuum structure containing a defect could be idealised as a combination of bars (or springs) representing the local nonlinear event and the surrounding linear behaving components, generally in the form of a combined (series and parallel) multiple bar structure. Finally a CAZ approach was outlined for use in the characterisation of the local nonlinearity arising from the presence of defect. A region around the defect over which the stress/strain response of the structure to loading is affected due to the presence of defect was suggested to represent the nonlinear event with the remaining structure representing the linear behaving surrounding components.

The CAZ approach developed for evaluation of EFU in structures containing defects was examined through trial estimations of EFU in two example structures. Two geometries, a CCP representing a low constraint simple standard model structure as well as a thick pipe containing fully circumferential external part through cracks were used to explore CAZ and subsequently to estimate EFU using CAZ. Results were presented and the problem of how to identify the zone boundaries was discussed. A methodology to tackle the problem was suggested.

Validation of the estimated EFU based on CAZ approach remains to be further investigated. One possible route is to follow the procedures proposed in studies conducted by British Energy Generation, Ltd. that are based on the reference stress concept.

Acknowledgments

Hadidi-Moud was supported by a grant from the NPCT programme. Smith is grateful for the support of a Royal Society Merit Award.

References

[1] Robinson, E. L., "The Resistance to Relaxation of Materials at High Temperature," *Trans. ASME*, Vol. 61, 1939, pp. 543–554.

[2] Robinson, E. L., "Steam-Piping Design to Minimise Creep Concentrations," *Trans. ASME*, Vol. 77, 1955, pp. 1147–1162.

[3] Boyle, J. T. and Nakamura, K., "The Assessment of Elastic Follow-Up in High Temperature Piping Systems—Overall Survey and Theoretical Aspects," *Int. J. Pressure Vessels Piping*, Vol. 29, No. 3, 1987, pp. 167–194.

[4] Goodman, A. M. and Booth, P., "Approximate Methods for Estimating Elastic Follow-up in Creeping Structures," *Report No.* TD/SE/REP/0002, Nuclear Electric Plc, Barwood, UK, 1992.

[5] Goodman, A. M., "Simplified Methods of Structural Analysis for High Temperature

Integrity Assessment in Engineering Structural Integrity Assessment," *Structural Integrity Assessment*, P. Stanley, Ed., Taylor & Francis, Oxon, U.K., 1992, pp. 1–10.
[6] Seshadri, R., "The Effect of Multiaxiality and Follow-Up on Creep Damage," *J. Pressure Vessel Technol.*, Vol. 112, 1990, pp. 378–385.
[7] British Energy Generation, Ltd., *R5, Assessment Procedure for the High Temperature Response of Structures, Issue 3*, British Energy, Gloucester, UK, 2003,
[8] Nakamura, K., Kasahara, N., Morishita, M., Shibamoto, H., Inoue, K., and Nakayama, Y., "Development of Guidelines for Inelastic Analysis in Design of Fast Reactor Components," *Nucl. Eng. Des.*, Vol. 238, No. 2, 2008, pp. 380–388.
[9] Kasahara, N., Nakamura, K., Morishita, M., Shibamoto, H., and Inoue, K., "Main R&D Issues for Fast Reactor Structural Design Standard," *Nucl. Eng. Des.*, Vol. 238, No. 2, 2008, pp. 287–298.
[10] British Energy Generation, Ltd., *R6, Assessment of the Integrity of Structures Containing Defects, Revision 4, Amendments No. 1–6*, British Energy, Gloucester, UK, 2007.
[11] Roche, R. L., "Modes of Failure—Primary and Secondary Stresses," *J. Pressure Vessel Technol.*, Vol. 110(3), 1988, pp. 234–239.
[12] Dhalla, A. K., "Numerical Estimate of Elastic Follow-Up in Piping: Inelastic Evaluation," *J. Pressure Vessel Technol.*, Vol. 108, 1986, pp. 453–460.
[13] Dhalla, A. K., "Verification of an Elastic Procedure to Estimate Elastic Follow-Up," *J. Pressure Vessel Technol.*, Vol. 108, 1986, pp. 461–469.
[14] Dhalla, A. K. and Jones, G. L., "ASME Code Classification of Pipe Stresses: A Simplified Elastic Procedure," *Int. J. Pressure Vessels Piping*, Vol. 26, 1986, pp. 145–166.
[15] Dhalla, A. K., "Stress Classification for Elevated Temperature Service," *J. Pressure Vessel Technol.*, Vol. 113, No. 4, 1991, pp. 488–496.
[16] Dhalla, A. K., *A Simplified Procedure to Classify Stresses For Elevated Temperature Service, Design and Analysis of Piping, Pressure Vessels and Components*, W. E. Short et al., Eds., PVP Vol. 120, ASME, New York, 1987, pp. 177–188.
[17] Roche, R. L., "Estimation of Piping Elastic Follow-Up by Using Conventional Computations," *Int. J. Pressure Vessels Piping*, Vol. 26, 1986, pp. 53–78.
[18] Roche, R. L., "Appraisal of Elastic Follow-Up," *Transactions of the Sixth International Conference on Structural Mechanics in Reactor Technology*, Paris, France, August 17–21 1981, North Holland Pub. Co., Amsterdam, The Netherlands, 1981, paper E5/4.
[19] Gamboni, S., Ravera, C., Rebora, A., and Stretti, G., "Appraisal of Elastic Follow-Up for a Generic Mechanical Structure Through Two Simplified Methods," *Int. J. Pressure Vessels Piping*, Vol. 37, 1989, pp. 221–241.
[20] Hadidi-Moud, S. and Smith, D. J., "Use of Elastic Follow-Up in Integrity Assessment of Structures," *International Conference on Pressure Vessels and Piping* (*ASME-PVP2008-61754*), Chicago, IL, July 17–31, 2008.
[21] Arid, C. J., Hadidi-Moud, S., Truman, C. E., and Smith, D. J., "Impact of Residual Stress and Elastic Follow-Up on Fracture," *J. ASTM Int.*, Vol. 5(8), 2008, 14 p.
[22] Smith, D. J., McFadden, J., Hadidi-Moud, S., Smith, A. J., Stormonth-Darling, A. J., and Aziz, A. A., "Elastic Follow-Up and Relaxation of Residual Stresses, Proceedings of the Institution of Mechanical Engineers, Part C," *J. Mech. Eng. Sci.*, Vol. 224(4), 2010, pp. 777–787.
[23] Kasahara, N., Nagata, T., Iwata, K., and Negishi, H., "Advanced Creep-Fatigue Evaluation Rule for Fast Breeder Reactor Components: Generalization of Elastic Follow-Up Model," *Nucl. Eng. Des.*, Vol. 155, 1995, pp. 499–518.

FATIGUE AND FRACTURE UNDER THERMOMECHANICAL CONDITIONS

Reprinted from JAI, Vol. 8, No. 1
doi:10.1520/JAI102499
Available online at www.astm.org/JAI

H. Koeberl,[1] *G. Winter,*[1] *and W. Eichlseder*[1]

Lifetime Calculation of Thermo-Mechanically Loaded Materials (Al, Cu, Ni, and Fe Alloys) Based on Empirical Methods

ABSTRACT: Cyclic loading of metallic engineering components at constant elevated or fluctuating temperatures causes a complex evolution of damage, which cannot be described easily. In many engineering components, thermo-mechanical loading occurs, e.g., cooling components in metallurgy and metal forming, turbine blades, cylinder heads, exhaust systems, etc. At the same time, the thermal expansion is restricted in some regions due to the complex geometry of the components. Therefore, mechanical stresses take place, and the cyclic plastic deformation leads to thermo-mechanical fatigue of the material. A careful analysis and comparison of the experimental results, based on a systematic variation of the relevant influence factors, allow to develop empirical models for computing the fatigue life of thermo-mechanically loaded components made of AlSi cast alloys, Cu alloy, Ni alloy, and cast iron. Based on stress-strain loops from low cycle fatigue tests at different temperatures, a nonlinear combined material model was adopted to describe the cyclic deformation behavior. The simulated loading parameters of stress and strain were the basis for the subsequent lifetime simulation. Different lifetime approaches were tested and analyzed to fulfill the requirements for the fatigue analysis of components made of these alloys. In particular, strain based criteria, damage parameters as well as hysteresis energy criteria were investigated. Also, a new energy based parameter was developed to optimize the scatter band and standard deviation. In order to verify the simulation model for components, numerical results have to be compared, and—if necessary—it also has to be adapted to experimental results from component tests. In addition, the model parameters can be optimized by using these results.

Manuscript received May 26, 2009; accepted for publication September 23, 2010; published online November 2010.
[1] Chair of Mechanical Engineering, Univ. of Leoben, Leoben 8700, Austria.

Cite as: Koeberl, H., Winter, G. and Eichlseder, W., "Lifetime Calculation of Thermo-Mechanically Loaded Materials (Al, Cu, Ni, and Fe Alloys) Based on Empirical Methods," *J. ASTM Intl.*, Vol. 8, No. 1. doi:10.1520/JAI102499.

KEYWORDS: material modeling, plastic deformation, high temperature applications

Introduction

A wide range of metallic alloys is used for different applications at fluctuating temperatures. Due to the restriction of thermal expansion caused by complex geometry, thermo-mechanical loading occurs [1].

Thermo-mechanical fatigue (TMF) induced through cyclic loading by temperature variation along with simultaneous constrained elongation results in accompanied cyclic loads. This constraint leads to local plastic deformation, which thus results in the fatigue of the material. Due to the low number of bearable thermo-mechanical cycles and the macroscopic plastic deformation, TMF takes place in the low cycle fatigue (LCF) region of the classical S-N curve [1,2].

In practice, time- and cost-intensive TMF tests are often characterized by simple isothermal LCF tests to estimate the lifetime of components under thermo-mechanical loads. This characterization by LCF results in non-conservative lifetime calculations. This happens when, under TMF loading, the cyclic stress-strain behavior or the effective damage mechanism deviates explicitly from the material behavior observed under isothermal conditions. Therefore, special focus should be on the local and temporally unsteady temperature field acquired from the thermo-mechanical deformation behavior (stress and strain) to avoid incorrect interpretations. Fundamental investigations of the stress-strain behavior as well as the dominant damage mechanisms under TMF conditions are necessary for a correct lifetime assessment during thermo-mechanical loading [3,4].

During a TMF cycle, a wide temperature range is used, and thus, this can lead to a change in the materials' properties as well as to different material reactions. The central question of the comparability of LCF- with TMF-data is found in the microstructure, whose integral behavior is shown in the form of the stress-strain response.

Damage mechanisms that have occurred via a TMF process are affected by different temperature dependent mechanisms during every cycle. The damage mechanisms occur at elevated temperatures by an individual or a cumulative interaction.

The cyclic thermo-mechanical deformation behavior depends on thermally activated dislocation aspects at lower temperatures, cyclic aging processes at mid temperature ranges, and diffusion conveyed creep at higher temperatures. So, under both loading modes, IP-TMF (in-phase, i.e., temperature and stress are in-phase) as well as OP-TMF (out-of-phase, i.e., temperature and stress are opposite), the deformation and oxidation effects were predominantly formed in a range at the maximum temperature (see Fig. 1) [6,7].

Oxidation, for example, intensifies at high temperatures and can cause embrittlement or a reduction in strength. As a result, early crack initiation and accelerated crack propagation are enhanced during an OP-TMF cycle.

During out-of-phase testing conditions (Fig. 2), the mechanical strain works against the thermal strain, which results in compression at maximum

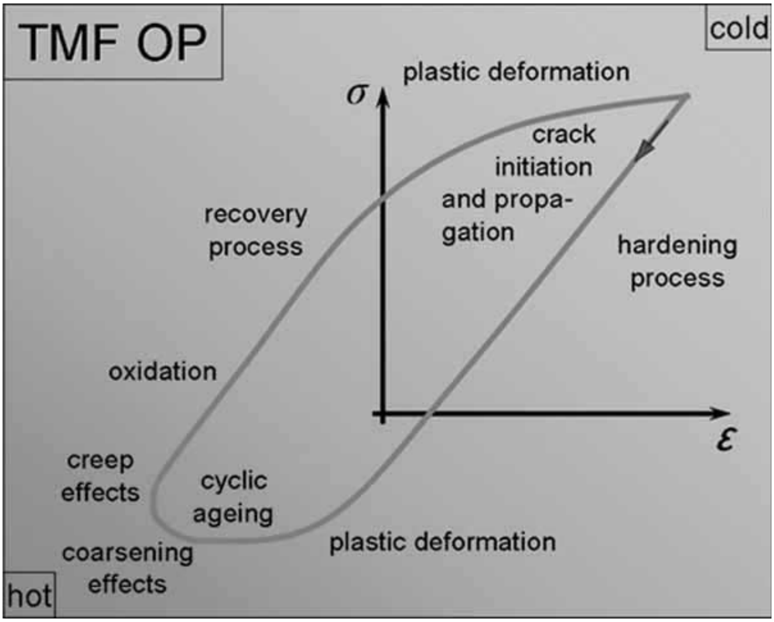

FIG. 1—*Active damage mechanisms during OP cycles* [*5*].

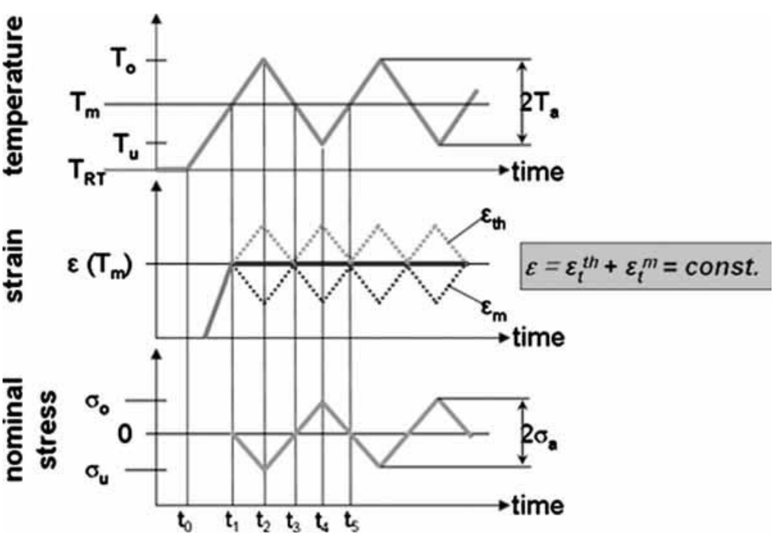

FIG. 2—*Temperature-strain-time characteristics with respect to OP-TMF* [*3*].

temperature. In comparison, during in-phase tests, the mechanical and thermal strains are cumulative and thus result in tension at maximum temperature

$$K_{\mathrm{TM}} = \frac{\Delta\varepsilon_t^{\mathrm{mech}}}{\Delta\varepsilon_t^{\mathrm{th}}} \tag{1}$$

The relationship between mechanical and thermal strain is defined by the degree of strain constraining [1,2] K_{TM} (Eq 1), where $\Delta\varepsilon_t^{\mathrm{mech}}$ is the total mechanical strain range and $\Delta\varepsilon_t^{\mathrm{th}}$ is the total thermal strain range. The strain constraint factor, K_{TM}, will be defined as negative for OP-TMF and positive for IP-TMF.

In order to work out a methodology for simulating the fatigue and lifetime behavior of thermo-mechanically loaded components, experiments like tensile or isothermal LCF tests were conducted to provide a basic understanding of the investigated alloys, which are standard materials in thermo-mechanically loaded components [8].

Based on stress-strain loops from LCF tests at different temperatures and aging conditions, a nonlinear combined material model was adopted to describe the cyclic deformation behavior. Simultaneous damage mechanisms were described by different models. Many of the empirical models used are strain based criteria like the Manson–Coffin [9,10] criterion with numerous modifications.

To find a correlation between the number of cycles of failure and loading parameters, different damage parameters are available as a function of life [2,8,11]. From the perspective of fracture mechanics, e.g., cyclic *J*-integrals, a description of the TMF lifetime can be obtained. Cumulative models, such as the Chaboche model [12], cumulate the damage for each cycle; therefore, these models need a lot of computing time for complex structures. Due to the interplay of strain and stress values under TMF loading, they are able to account for more specific influences as well as their interactions. It is shown in former works of Riedler [3,13] that energy based criteria are qualified for lifetime approaches. To estimate the lifetime, a damage parameter, which is based on the energy (elastic and plastic) of a hysteresis loop, has been developed.

Testing Conditions

The investigated materials for this research are three aluminum-silicon cast alloys with different amounts of silicon (5, 7, and 8) and different alloying components (Mg and Cu); two copper alloys, CuCoBe and CuCo2Be; two nickel alloys, pure nickel (Ni200/201) and IN718; and a cast iron with vermicular graphite GJV450 [2,6,7,14]. CuCoBe is a wrought alloy, CuCo2Be is a cold worked rod, Ni200/201 is an annealed cold worked rod, and IN718 is forged. Such materials can be strengthened by different heat treatments such as solution annealing and precipitation heat treatment.

To describe the influence of pre-aging (PA) on the yield strength of these materials, tensile test specimens were pre-aged at different temperatures with different PA times. Typical temperatures and time ranges for PA were up to 250°C and a maximum of 500 h for aluminum alloys, up to 425°C and a maximum of 1500 h for copper alloys, and up to 575°C and a maximum of 500 h for nickel alloys. Cast iron was not pre-aged because of the very low PA influence. LCF tests were also conducted at different temperatures (like the PA temperatures as explained before) and at variable PA conditions, on a servo-hydraulic test rig (nominal force 250 kN) with digital control. The clamping was controlled via hydraulic clamping grips. The specimens were tested under strain control with an extensometer using a gauge length of 12.5 mm and having a range of ±2.5 mm. The strain rate was 1 %/s, in accordance with DIN EN 3988 [15]. TMF tests were conducted for all investigated materials on a test rig developed in the Institute of Mechanical Engineering. With this test rig, it was possible to allow defined phase shifts between thermal and mechanical strains. The temperature ranges were up to 300°C for aluminum, up to 425°C for copper, up to 575°C for nickel, and up to 460°C for cast iron alloys, whereas the strain constraint values were between 0.5 and 2 for aluminum, 1.5 and 3 for copper, 0.75 and 2 for nickel, and 0.75 and 1 for cast iron alloys. Temperatures of LCF and TMF tests were controlled with an induction coil, operated by a radio frequency-generator [16].

Results

LCF and TMF tests were analyzed according to the Manson–Coffin–Basquin Model (Eq 2)

$$\varepsilon_{a,t} = \varepsilon_{a,p} + \varepsilon_{a,e} = \frac{\sigma_f'}{E} \cdot (2N_f)^b + \varepsilon_f' \cdot (2N_f)^c \tag{2}$$

where:

$\varepsilon_{a,t}$, $\varepsilon_{a,p}$, and $\varepsilon_{a,l}$ = total, plastic, and elastic strain amplitudes, respectively,

σ_f' = fatigue strength coefficient,

ε_f' = cyclic ductility coefficient,

b = fatigue strength exponent,

c = cyclic ductility exponent,

E = Young's modulus, and

N_f = number of cycles to failure.

For the copper alloys CuCoBe and CuCo2Be [8], under isothermal LCF, the influence of oxidation increases with a rise in the test temperature and with a decrease in strain rate. Figure 3 shows a comparison of strain lifetime curves (strain S-N curves) at different testing temperatures, strain rates, and PA conditions according to Manson–Coffin–Basquin. The influence of oxidation was also investigated, and therefore some tests were conducted under a protective argon (Ar) atmosphere.

There was no influence of test temperature on the fatigue behavior of CuCo2Be up to 125°C. The obtained strain-life curves at higher temperatures are displaced on the left, indicating a reduction in lifetime. At temperatures of 225°C, the lifetime reduced by ~40 % in comparison to that of 125°C. At 325°C, the reduction in lifetime was ~70 % when compared to the lifetime at room temperature. This reduction can be explained by the increase in the influence of oxidation (Fig. 3) during the testing period. CuCoBe demonstrated a

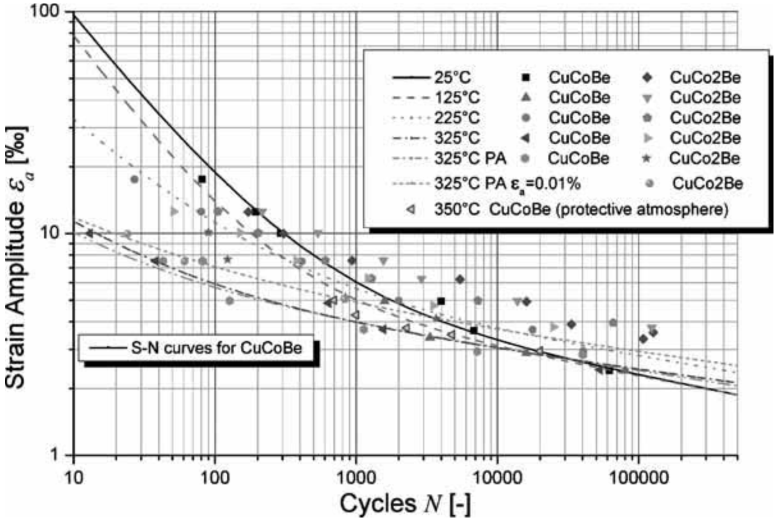

FIG. 3—*Comparison of LCF tests for CuCoBe and CuCo2Be according to the Manson–Coffin–Basquin.*

different lifetime behavior relative to CuCo2Be. The total strain amplitude tolerable is a factor of 1.5 lower than that for CuCo2Be, which is up to one decade in terms of lifetime. Typically, CuCo2Be shows very similar fatigue curves to CuCoBe and a collective intersection point at 40.000 cycles (see Fig. 3) [8].

The TMF behavior of Ni200/201 is shown in Fig. 4. The lifetime decreases with an increase in the maximum temperature. Due to the high mechanical

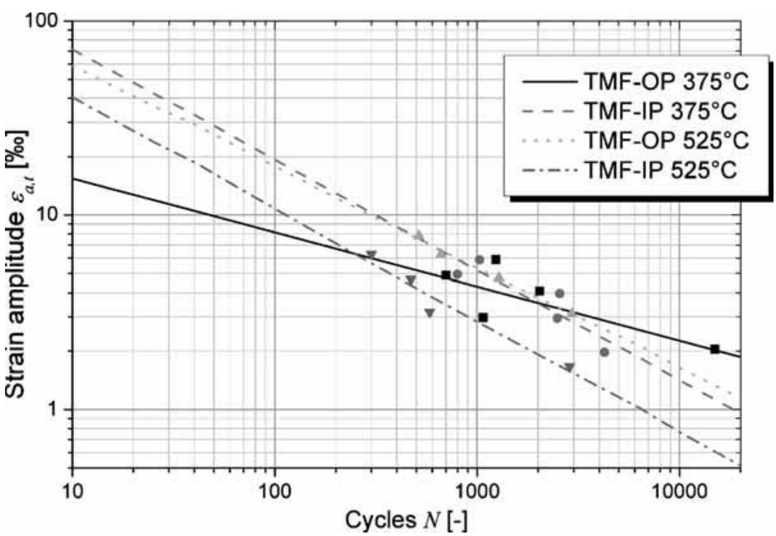

FIG. 4—*Comparison of all TMF tests of Ni200/201.*

strain resulting from the high thermal strain, the lifetime decreases due to a higher plastic deformation during one cycle. The main difference can be seen by IP and OP test conditions. At 375 °C, the OP test demonstrated creep damage, but at 575 °C, there was a balance between creep, pure fatigue, and oxidation damage [6].

Simulation of the Material Behavior

The description of the elastic-plastic cyclic deformation behavior for the investigated materials is the basis for lifetime assessment by using simulated loading parameters. Using the finite-element method and an appropriate material model, the local loading parameters can be calculated and used to estimate the lifetime. The elastic-plastic deformation behavior of the alloys was described by using a standard material model, that is, the combined hardening model implemented in the software package ABAQUS®. The combined hardening model describes the kinematic and isotropic deformation performance, which is dependent on the temperature

$$\dot{\boldsymbol{\alpha}} = C\frac{1}{\sigma^0 + k}(\boldsymbol{\sigma} - \boldsymbol{\alpha})\dot{\bar{\varepsilon}}_{\mathrm{pl}} - \gamma\boldsymbol{\alpha}\dot{\bar{\varepsilon}}_{\mathrm{pl}} \tag{3}$$

The evolution law of the kinematic hardening component, which describes the translation of the yield surface in stress space using the back stress tensor $\dot{\alpha}$, is given by Eq 3, which is effectual for the above mentioned case [17]. σ_0 is the first derivative of the elastic with respect to the plastic region; C is the initial kinematic hardening modulus; γ is the rate of decay of the kinematic hardening modulus; k is the isotropic hardening (which is change of size of yield surface); and $\dot{\bar{\varepsilon}}^{\mathrm{pl}}$ is the total plastic strain rate of the hysteresis.

The parameters of the material model were derived by using the stress-strain loops obtained from the LCF tests, near half the number of cycles of failure, $N_{f/2}$. A comparison of the hysteresis loops obtained from the experiments at $N_{f/2}$ to those simulated for different strain amplitudes of IN718 at 600 °C is given in Fig. 5. The hysteresis loops calculated with the adapted material model show a good correlation with those obtained from the experiments.

Using the investigated material model at different maximum temperatures and strain constraints to simulate the TMF hysteresis loops also reveals a good correlation with the experimental hysteresis loops (using the LCF data). Figure 6 shows a comparison of the hysteresis loops of Ni200/201 at different maximum temperatures and strain constraints for a dwell time of 6 s. These calculated TMF hysteresis loops are the basis for further lifetime assessments, which can be obtained by using the local loading parameters obtained from the hysteresis loop.

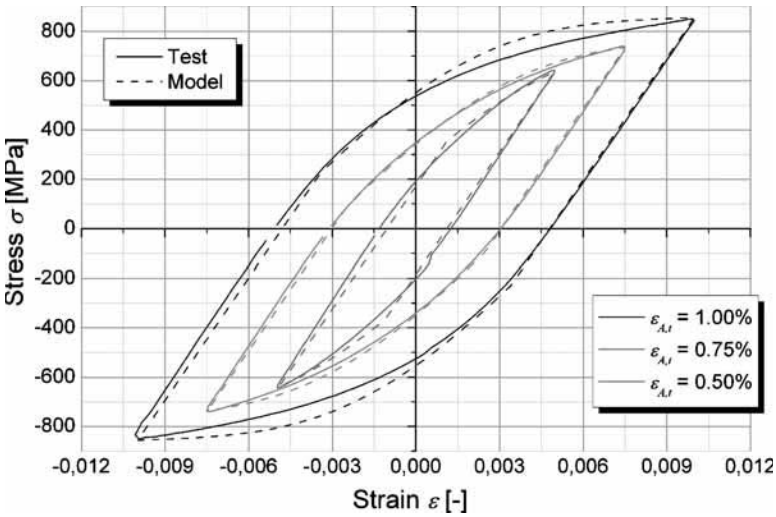

FIG. 5—*LCF simulation of IN718 at 600°C with different strain amplitudes.*

Simulation of the Lifetime

Many empirical models are strain-based, like the Manson–Coffin criterion [9,10] with numerous modifications. Criteria based on damage parameters are often used to find a correlation between the cycles of failure with respect to the loading parameters. The mechanical fracture view allows a description of the lifetime, mostly via cyclic *J*-integrals. Cumulative models, such as the Chabo-

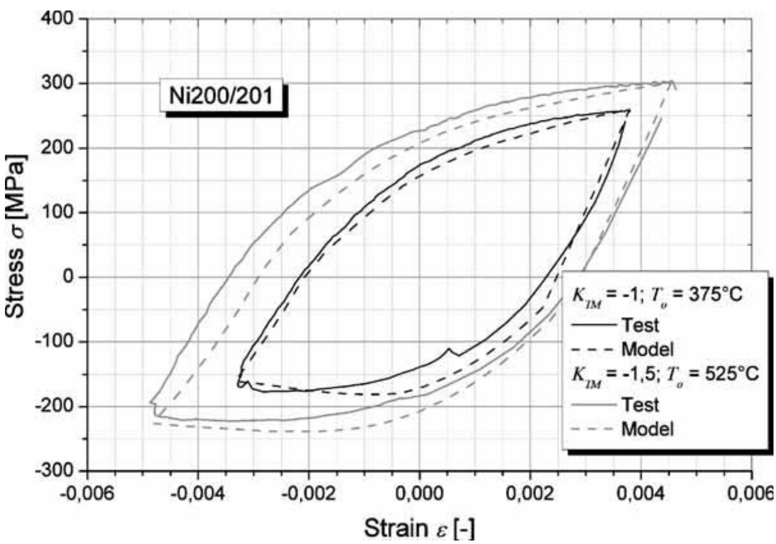

FIG. 6—*TMF simulation of Ni200/201 with different testing conditions.*

che model [12], try to accumulate damage for each cycle. Therefore, a lot of computing time is needed for complex structures. Other methods involve the accumulation of damage components (pure fatigue, oxidation, and creep), e.g., Miller et al. [18] and Neu–Sehitoglu [19].

The most common empirical model for lifetime estimation is the Manson–Coffin criterion, which exists with numerous modifications. Thereby, a lifetime can be calculated by the plastic strain (see Eq 4)

$$\Delta\varepsilon_{\mathrm{pl}} = \varepsilon_c' \cdot N_B^c \tag{4}$$

where:

$\Delta\varepsilon_{\mathrm{pl}}$ = plastic strain,

ε_c' = ductile coefficient,

N_B = fatigue lifetime, and

c = plastic exponent.

A comparison of the calculated lifetime with the observed test results enabled an evaluation of the quality of the lifetime prediction.

A classical description can be achieved by using the Smith–Watson–Topper [20] damage parameter (P_{SWT}) as given in Eq 5

$$P_{\mathrm{SWT}} = \sigma_{\max} \cdot \varepsilon_{a,t} \quad \text{with} \quad \sigma_{\max} = \sigma_a + \sigma_m \tag{5}$$

$$P_{\mathrm{SWT}} = a \cdot N_B^c \tag{6}$$

where:

$\sigma_{\max}$ = maximum stress (calculated via the stress amplitude and the mean stress) and

$\varepsilon_{a,t}$ = total mechanical strain amplitude.

The lifetime can be calculated using a power law as shown in Eq 6.

Ostergren [21] assumed a correlation between the lifetime of the material and the hysteresis energy, which is the area of the stress-strain-hysteresis in the tensile domain. Thereby, the hysteresis energy is established by calculating the product of the plastic strain range and the maximum stress level (see Eq 7)

$$P_{\mathrm{OST}} = \sigma_o \cdot \Delta\varepsilon_p \tag{7}$$

$$P_{\mathrm{OST}} = a \cdot N_B^c \tag{8}$$

The power law used to find the lifetime in Eq 6 can also be used to derive Eq 8.

Subsequent investigations of Riedler et al. [13] show the possibility of using a common energy criterion, which is the unified energy approach. Based on the consideration that the elastic loading part is affected by the maximum stress while the plastic part is affected by the stress amplitude, a combined approach is developed in order to simulate the lifetime of the OP-TMF loaded materials

$$\Delta W_u = c_u \cdot \Delta W_{u,e} + \Delta W_{u,p} = c_u(\sigma_{\max} \cdot \varepsilon_{a,e}) + (\sigma_a \cdot \varepsilon_{a,p}) \tag{9}$$

$$N_B = A_u \cdot \Delta W_u^{-B_u} \tag{10}$$

where:

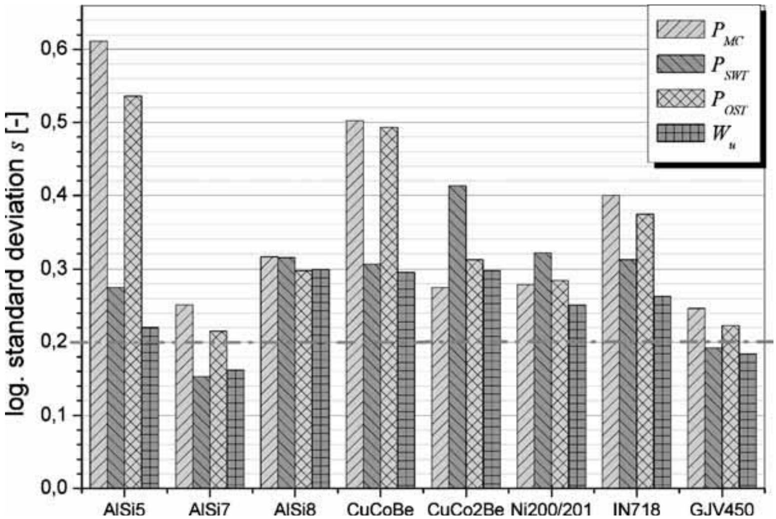

FIG. 7—*Comparison of the logarithmic standard deviation of all investigated materials with different lifetime calculation methods.*

ΔW_u = specific unified energy per cycle at a representative cycle (indexes e and p: Elastic and plastic),

c_u = specific unified energy parameter,

$\sigma_{\max}$ = maximum stress,

σ_a = stress amplitude,

$\varepsilon_{a,e}$ and $\varepsilon_{a,p}$ = elastic and plastic strain amplitudes, respectively,

N_B = number of cycles to failure, and

A_u and B_u = lifetime coefficient and exponent, respectively.

For all approaches, the representative values are the characteristic values taken at mid-life $N_B/2$, as explained in the former work [2,8,11].

The following overviews are based on both the logarithmic standard deviation s, which is a typical statistic index for Gaussian distribution, and on the 90 % scatter band, which means that the lifetime of 90 % of the calculated tests has to be in the range of ± 2.5 relative to the test results.

Figure 7 shows the comparison of the logarithmic standard deviation of all investigated materials to the different life prediction methods. It can be shown clearly in almost all cases that the methods due to Manson–Coffin and Ostergren exhibit the highest, while the methods due to Smith–Watson–Topper and the unified energy approach according to Riedler, respectively, gave the lowest logarithmic standard deviation. However, nearly all of the results exceed the defined limit of the logarithmic standard deviation of $s = 0.2$.

Figure 8 shows the 90 % scatter band of the different methods. Half of the investigated materials, regardless of the life prediction methods, exhibit a scatter band that is above the standard of $T = \pm 2.5$ [17]. A new approach was investigated for those results with the selected empirical lifetime prediction methods, which were not satisfied.

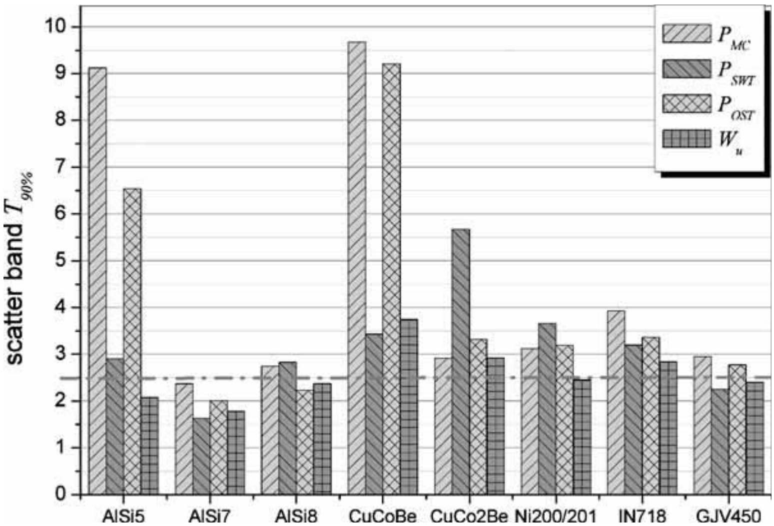

FIG. 8—*Comparison of the 90 % scatter band of all investigated materials with different lifetime calculation methods.*

In these cases, energy based damage parameters give the best ratio between applicability and effort because the former cases can describe the TMF lifetime using a few parameters only. In order to describe the lifetime according to cyclic loading parameters, a new lifetime criteria, the so-called *Separated Energy Approach*, $P_{W,\mathrm{foc}}$, was developed

$$P_{W,\mathrm{foc}} = (\Delta W_e + c_p \cdot \Delta W_p) \cdot (\xi_f + \xi_{\mathrm{ox}}) + (c_p \cdot \Delta W_p) \cdot \xi_c = (\varepsilon_{a,e} \cdot \sigma_o + c_p \cdot \varepsilon_{a,p} \cdot \sigma_a) \cdot (\xi_f + \xi_{\mathrm{ox}}) + (c_p \cdot \varepsilon_{a,p} \cdot \sigma_a) \cdot \xi_c \quad (11)$$

The objective of this damage parameter ($P_{W,\mathrm{foc}}$ (Eq 11)) is to separate the elastic from the plastic hysteresis energy components like Riedler (Eq 9) and the idea of Neu–Sehitoglu [19], which describe the lifetime using three parts (fatigue, creep, and oxidation). This damage parameter is defined as follows: $\varepsilon_{a,e}$ describes the elastic; $\varepsilon_{a,p}$ is the plastic strain amplitude; c_p is the specific plastic energy parameter ($0 \leq c_p \geq 5$); σ_o is maximum stress; σ_a is the stress amplitude; and ξ_f (Eq 12), ξ_{ox} (Eq 13), and ξ_c (Eq 14) are the weighted influence factors of fatigue, oxidation, and creep, respectively, at $N_B/2$

$$\xi_f = f(\sigma_m, \varepsilon_p) = \left(\frac{\sigma_o}{\sigma_a}\right)^{c_\sigma} \cdot \left(\frac{\varepsilon_{a,p}}{\varepsilon_{a,t}}\right)^{c_\varepsilon} \quad (12)$$

The above equation is showing the relationship of ξ_f, which is the influence of the mean stress, and the potential for plastic deformation, where, c_σ and c_ε are the exponents of the mean stress and the plastic deformation based on the total strain amplitude ($\varepsilon_{a,t}$). The weighted influence factors for oxidation and creep are not that simple to separate because both of them are mainly influenced by a function of dwell time, maximum temperature, and stress at maximum tem-

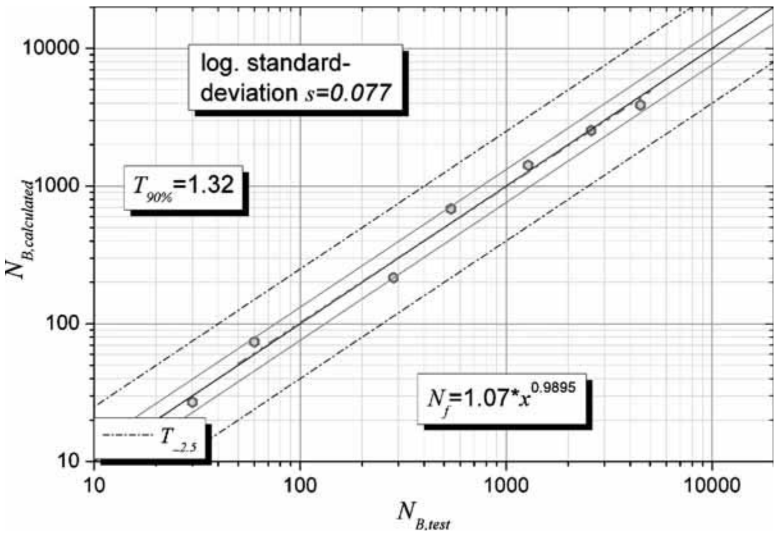

FIG. 9—*Calculated over the experimental lifetime of the LCF tests (CuCoBe).*

perature. Creep is simply weighted with c_c (Eq 5), and oxidation is weighted with c_{ox} additionally with a function of maximum stress (Eq 4). This additional weight function for the oxidation based on maximum stress varies from the former defined variation of the strain constraint (IP/OP). Both functions were defined as follows:

$$\xi_{\text{ox}} = f(T_o, t_d, \sigma_{T_o}, \sigma_o) = c_{\text{ox}} \cdot \left(\frac{\sigma_o}{\sigma_a}\right) \cdot e^{-t_d \cdot \sigma_{T_o}/T_o} \tag{13}$$

$$\xi_c = f(T_o, t_d, \sigma_{T_o}) = c_c \cdot e^{-t_d \cdot \sigma_{T_o}/T_o} \tag{14}$$

where:

t_d = absolute or normalized dwell time,

T_o = maximum temperature, and

σ_{T_o} = absolute stress at maximum temperature (IP inverse OP).

This damage parameter is described by a potential law for the lifetime (Eq 15)

$$W_{\text{foc}} = s \cdot (N_B)^{-t} \tag{15}$$

Lifetime Assessment with $P_{W,\text{foc}}$

In general, there is a clear dependency between $P_{W,\text{foc}}$ and the number of cycles to failure. Figure 9 shows the application of $P_{W,\text{foc}}$ for the TMF tests of CuCoBe. The comparison of the estimated lifetime, using the loading parameters from the simulation, with the lifetime according to the experimental tests, gives a

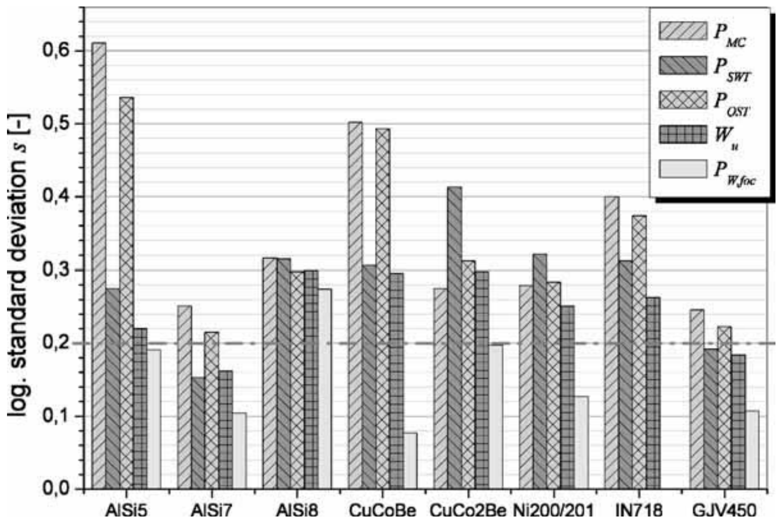

FIG. 10—*Comparison of the logarithmic standard deviation of all investigated materials with different lifetime calculation methods.*

good correlation agreement. The logarithmic standard deviation ($s = 0.077$) is low, and the scatter band for 90 % of all tests ($T_{90\ \%} = 1.32$) is excellent.

For the TMF tests of all investigated materials, the $P_{W,\text{foc}}$ results show a good correlation. This depends on the similarity of the deformation behavior of the hysteresis loops under LCF and TMF loading. Figure 9 shows the test results for all TMF tests. The exact specification of the cyclic deformation behavior and the created material model for the alloys is a reason for the accurate estimation, as well as for the precise lifetime assessment for TMF tests.

Figure 10 shows the comparison of the logarithmic standard deviation of all investigated materials with the different empirical lifetime simulation methods and the Separated Energy Approach, $P_{W,\text{foc}}$. This approach ($P_{W,\text{foc}}$) produced a logarithmic standard deviation of $s < 0.2$ for all materials (in the case of IN718, $s = 0.0$), excluding AlSi8.

The 90 % scatter bands of all investigated materials were reduced to $T_{90\ \%} < \pm 2.5$ (see Fig. 11). Both criteria, that is, $T_{90\ \%}$ less than ± 2.5 and s less than 0.2, can be achieved by using this approach.

Conclusion

An extensive test program was conducted to investigate the influences relevant to the cyclic deformation and lifetime behavior of the selected alloys under LCF and TMF loading conditions. Based on the stress-strain loops obtained from the LCF tests at different temperatures, a variety of material models was adopted to describe the cyclic deformation behavior in order to gain the stress and strain values for different loading conditions. This was the basis for a subsequent lifetime calculation. To describe the TMF lifetime behavior, a new

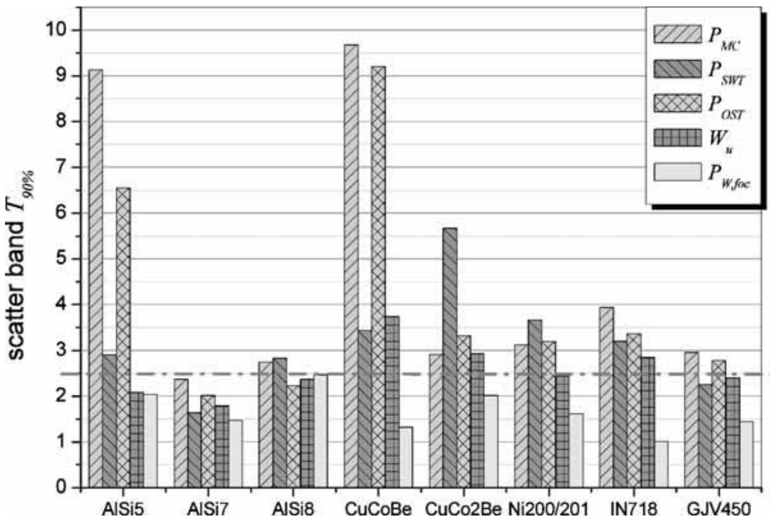

FIG. 11—*Comparison of the 90 % scatter band of all investigated materials with different lifetime calculation methods.*

damage parameter, the Separated Energy Approach, $P_{W,\text{foc}}$, was developed. This damage parameter delivers a good estimation for lifetime under TMF loading.

References

[1] Eichlseder, W., Winter, G., and Köberl, H., "Material and Fatigue Life Models for Thermomechanical Loaded Components," *Materialwiss. Werkstofftech.*, Vol. 39, No. 10, 2008, pp. 777–782.

[2] Köberl, H., 2009, "Development of a Model to Describe the Lifetime Behaviour of Non-Ferrous Alloys (Al, Cu, Ni) Under Thermomechanical Loading," Ph.D. thesis, University of Leoben, Leoben, Austria.

[3] Riedler, M., 2005, "Methodology for the Simulation of Thermo-Mechanically Loaded Components of Engines Made from Aluminium Alloys," Ph.D. thesis, University of Leoben, Leoben, Austria.

[4] Minichmayr, R., 2005, "Modelling and Simulation of Thermo-Mechanical-Fatigue Behaviour of Aluminium Components," Ph.D. thesis, University of Leoben, Leoben, Austria.

[5] Löhe, D., Beck, T., and Lang, K.-H., "Important Aspects of Cyclic Deformation, Damage and Lifetime Behaviour in Thermomechanical Fatigue of Engineering Alloys," *Fifth International Conference on Low Cycle Fatigue*, P. D. Portella, H. Sehitoglu, and K. Hatanaka, Eds., DVM, Berlin, 2005, pp. 161–175.

[6] Köberl, H., Winter, G., and Eichlseder, W., "Energy Based Lifetime Calculation for Ni-Alloys," *Mater. Test.*, Vol. 51, No. 5, 2009, pp. 276–285.

[7] Winter, G., 2008, "Thermomechanical Fatigue Behaviour of the Cast Iron GJV 450," Ph.D. thesis, University of Leoben, Leoben, Austria.

[8] Köberl, H., Winter, G., Leitner, H., and Eichlseder, W., "Comparison of the Teperature and Pre-Aging Influences on the Low Cycle Fatigue and Thermo-Mechanical Fatigue Behavior of Copper Alloys (CuCoBe/CuCo2Be)," *J. ASTM Int.*, Vol. 5(9), 2008, pp. 1–12.

[9] Manson, S. S., "Behaviour of Materials Under Conditions of Thermal Stress," *NACA Report No.* 1170, 1954.

[10] Coffin, L. F., "A Study of the Effects of Cyclic Thermal Stresses on a Ductile Metal," *Trans. ASME*, Vol. 76, 1954, pp. 931–950.

[11] Köberl, H., Winter, G., Riedler, M., and Eichlseder, W., "Failure Mechanism of Pure Nickel (Ni 200/201) Under Thermo-Mechanical Loading," *Key Eng. Mater.*, Vols. 348–349, 2007, pp. 793–796.

[12] Lemaitre, J. and Chaboche, J. L., *Mechanics of Solid Materials*, Cambridge Univ. Press, London, 1990.

[13] Riedler, M., Minichmayr, R., and Eichlseder, W., "Methods for the Thermo-Mechanical Fatigue Simulation Based on Energy Criteria," *Proceedings of the Sixth International Conference of Assessment of Reliability of Materials and Structures: Problems and Solutions, RELMAS 2005*, St. Petersburg, 2005, pp. 496–503.

[14] Winter, G., Köberl, H., and Eichlseder, W., "Methods for Lifetime Calculation of TMF Loaded CGI 450," *Gießerei-Rundschau* (*Giessereirundschau*), Vol. 55, No. 11/12, 2008, pp. 238–241.

[15] DIN EN 3988, 1998, "Test Methods for Metallic Materials, Constant Amplitude Strain-Controlled Low Cycle Fatigue Testing 1. Concept," *Deutsches Institute für Normung e.V.*, Aerospace series, Colonia, Germany.

[16] Basquin, O. H., "The Exponential Law of Endurance Tests," *Proceedings of the ASTMJ 10*, Luxembourgh, 1910, European Community in Brussles, Brussles, pp. 625–630.

[17] Hähner, P., Affeldt, E., Beck, T., Klingelhöffer, H., Loveday, M., and Rinaldi, C., "Validated Code-of-Practice for Strain-Controlled Thermo-Mechanical Fatigue Testing," *Report No.* EUR 22281 EN, DG JRC-Institute for Energy, Luxembourg, Office for Official Publications of the European Communities, Brussles, 2006, ISBN 92-79-02216-4.

[18] Miller, M. P., McDowell, D. L., Oehmke, R. L. T., and Antolovich, S. D., "A Life Prediction Model for Thermo-Mechanical Fatigue Based on Micro Crack Propagation," *Thermo-Mechanical Fatigue Behavior of Materials. Proceedings of the ASTM-STP-1186*, Philadelphia, 1993, H. Sehitoglu, Ed., ASTM International, West Conshohocken, PA, pp. 35–49.

[19] Neu, R. W. and Sehitoglu, H., "Thermo-Mechanical Fatigue, Oxidation and Creep, Part II: Life Prediction," *Metall. Trans. A*, Vol. 20A, 1989, pp. 1769–1783.

[20] Smith, K. N., Watson, P., and Topper, T. H., "A Stress-Strain Function for the Fatigue of Metals," *J. Mater.*, Vol. 5, No. 4, 1970, pp. 767–778.

[21] Ostergren, W. J., "A Damage Function and Associated Failure Equations for Predicting Hold Time and Frequency Effects in Elevated Temperature Low Cycle Fatigue," *J. Test. Eval.*, Vol. 4, No. 327, 1976, pp. 327–339.

Reprinted from JAI, Vol. 7, No. 5
doi:10.1520/JAI102517
Available online at www.astm.org/JAI

Mohit Pant,[1] *I. V. Singh,*[2] *B. K. Mishra,*[3] *Vivek Bhasin,*[4]
Kamal Sharma,[4] *and I. A. Khan*[4]

Mesh-Free Solution of Two-Dimensional Edge Crack Problems under Thermo-Mechanical Load

ABSTRACT: In this work, a mesh-free approach known as element free Galerkin method (EFGM) has been used to obtain the solution of two-dimensional edge crack problems in linear elastic fracture mechanics subjected to thermo-mechanical loads. The diffraction criterion has been modified with multiple crack weight technique to characterize the presence of all cracks in the domain of the influence of a node. The effect of crack orientation has been studied for two edge cracks lying on the same face as well as on opposite faces under plane stress conditions. The values of mode-I and mode-II stress intensity factors have been evaluated by domain based interaction integral approach. The results obtained by EFGM are compared with those obtained by finite element method.

KEYWORDS: EFGM, LEFM, edge cracks, thermal and mechanical loading, crack interaction

Introduction

Material selection and shape optimization are inherent part of engineering design. In spite of all scientific and technological advancements, engineering can-

Manuscript received May 29, 2009; accepted for publication April 20, 2010; published online May 2010.

[1] Research Scholar, Dept. of Mech. and Ind. Eng., IIT Roorkee, Roorkee, 247 667 UK, India.
[2] Assistant Professor, Dept. of Mech. and Ind. Eng., IIT Roorkee, Roorkee, 247 667 UK, India, e-mail: ivsingh@gmail.com; iv_singh@yahoo.com
[3] Professor, Dept. of Mech. and Ind. Eng., IIT Roorkee, Roorkee, 247 667 UK, India.
[4] Reactor Structures Section, Reactor Safety Division, Bhabha Atomic Research Centre, Mumbai, 400085 India.

Cite as: Pant, M., Singh, I. V., Mishra, B. K., Bhasin, V., Sharma, K. and Khan, I. A., "Mesh-Free Solution of Two-Dimensional Edge Crack Problems under Thermo-Mechanical Load," *J. ASTM Intl.*, Vol. 7, No. 5. doi:10.1520/JAI102517.

not claim perfection. Imperfections inherent in materials undermine engineering design and often result in catastrophic consequences.

Engineering components are often subjected to thermo-mechanical loads. Common examples of such components are the piston of an engine, where the variation of temperature takes place with the piston movement, and thermal barrier coatings applied over the blades of steam turbine to protect it from erosion and subjected to high temperature steam. In military applications, components are exposed to varying thermal loads, e.g., the gun chamber is subjected to very high temperature and pressure during the shell firing and cools down to nominal temperature soon afterwards. The walls of a nuclear reactor are subjected to extremely high temperatures. Hence, the failure of engineering components is not only due to mechanical loads but also due to thermal loads [1], for example, the integrated circuits formed by assemblage of dissimilar materials are having different mechanical and thermal properties. The mismatch of elastic constants and thermal expansion coefficients causes stress intensification at corners of interfaces and may lead to mechanical failure.

Defects that are unavoidable and characteristic for many structures decrease the life and strength of these structures. Thermo-mechanical loading may result in either the propagation of pre-existing cracks or may initiate new cracks in the structures. This may finally lead to catastrophic failure of the components, resulting in loss of property and lives. Under real working condition, multiple cracks are present in a component. They interact with each other, resulting in change of the stress distribution, stress intensity factor, and propagation direction of the main crack. As such, all important failure phenomena such as stress corrosion cracking, hydrogen embrittlement, and creep micro cracking are directly linked to crack interactions [2]. An accurate evaluation of stress intensity factor is quite essential for the prediction of failure and crack growth rate. Thus, the study of crack interactions under thermo-mechanical [3,4] loading is of great importance.

To evaluate the stress intensity factor of cracked component, a number of numerical tools such as finite element method (FEM), boundary element method, and finite difference method are available. Out of these numerical methods, FEM has been found to be the most successful and powerful numerical method for the simulation of fracture mechanics problems. However, FEM either is not suitable or often experiences difficulties in solving a class of problems, which requires re-meshing and adaptive simulation. The problems that fall in this category are large deformation with element distortion, moving crack simulation, crack growth with arbitrary and complex path, etc. Moreover, the accuracy of the solution depends upon the quality of the mesh in FEM. To handle these difficulties, a new class of methods, known as mesh-free methods [5,6], has been developed over the past 15 years. These methods do not require any kind of mesh for the discretization of the problem domain and only need a set of scattered nodes for the construction of an approximation function [7]. Although, some efforts have been made in the past to solve thermo-elastic fracture mechanics problems using mesh-free local Petrov–Galerkin approach [8–11], but very little effort has been made to study the effect of crack interactions using mesh-free element free Galerkin method (EFGM) [12]. Therefore, in the present analysis, EFGM has been opted to analyze the linear elastic fracture mechanics problems under thermo-mechanical loads. The diffraction criterion [13,14] has been modified with multiple crack weight approach to study the effect of crack interactions [12,15].

Review of Element Free Galerkin Method

In EFGM, the field variable u is approximated by moving least square approximation function $u^h(\mathbf{x})$ [5], which is given by

$$u^h(\mathbf{x}) = \sum_{j=1}^{m} p_j(\mathbf{x})a_j(\mathbf{x}) \equiv \mathbf{p}^T(\mathbf{x})\mathbf{a}(\mathbf{x}) \tag{1}$$

where:

$\mathbf{p}(\mathbf{x})$ = vector of basis functions,
$\mathbf{a}(\mathbf{x})$ = unknown coefficients, and
m = number of terms in the basis.

The unknown coefficients $\mathbf{a}(\mathbf{x})$ are obtained by minimizing a weighted least square sum of the difference between local approximation, $u^h(\mathbf{x})$, and field function nodal parameters u_I. The weighted least square sum $L(\mathbf{x})$ can be written in the following quadratic form:

$$L(\mathbf{x}) = \sum_{I=1}^{n} w(\mathbf{x} - \mathbf{x}_I)[\mathbf{p}^T(\mathbf{x})\mathbf{a}(\mathbf{x}) - u_I]^2 \tag{2}$$

where:

u_I = nodal parameter associated with node I at $\mathbf{x}_I$.

u_I are not the nodal values of $u^h(\mathbf{x}-\mathbf{x}_I)$ because $u^h(\mathbf{x})$ is used as an approximant and not an interpolant. $w(\mathbf{x}-\mathbf{x}_I)$ is the weight function having compact support associated with node I, and n is the number of nodes with domain of influence containing the point $\mathbf{x}$, $w(\mathbf{x}-\mathbf{x}_I) \neq 0$.

By setting $\partial L/\partial \mathbf{a} = 0$, following set of linear equation is obtained:

$$\mathbf{A}(\mathbf{x})\mathbf{a}(\mathbf{x}) = \mathbf{B}(\mathbf{x})\mathbf{u} \tag{3}$$

By substituting Eq 3 in Eq 1, the approximation function is obtained as

$$u^h(\mathbf{x}) = \sum_{I=1}^{n} \Phi_I(\mathbf{x})u_I \tag{4}$$

Problem Formulation

Consider a two-dimensional domain with small displacements on the domain Ω bounded by Γ. The governing equilibrium equations are given as

$$\nabla \cdot \boldsymbol{\sigma} + \mathbf{b} = 0 \text{ in } \Omega \tag{5}$$

with the following essential and natural boundary conditions:

$$\mathbf{u} = \bar{\mathbf{u}} \text{ on } \Gamma_u \tag{6}$$

$$\sigma \cdot \bar{\mathbf{n}} = \bar{\mathbf{t}} \text{ on } \Gamma_t \tag{7}$$

where:

$\boldsymbol{\sigma}$ = stress tensor, which is defined as $\boldsymbol{\sigma} = D(\boldsymbol{\varepsilon} - \boldsymbol{\varepsilon}_T)$,
D = linear elastic material property matrix,
ε = strain vector,
$\boldsymbol{\varepsilon}_T$ = thermal strain vector,
$\mathbf{b}$ = body force vector,
$\mathbf{u}$ = displacement vector,
$\bar{\mathbf{t}}$ = traction force, and
$\bar{\mathbf{n}}$ = unit normal.

For the case of plane stress in an isotropic material with coefficient of thermal expansion β subjected to a temperature change ΔT, the thermal strain matrix is given by

$$\varepsilon_T = \begin{Bmatrix} \beta\Delta T \\ \beta\Delta T \\ 0 \end{Bmatrix} \tag{8}$$

Enforcing essential boundary conditions [16] using Lagrange multiplier approach [17] and applying variational principle, the following discrete equations are obtained from Eq 4:

$$\begin{bmatrix} \mathbf{K} & \mathbf{G} \\ \mathbf{G}^T & 0 \end{bmatrix} \begin{Bmatrix} \mathbf{u} \\ \boldsymbol{\lambda} \end{Bmatrix} = \begin{Bmatrix} \mathbf{f} \\ \mathbf{q} \end{Bmatrix} \tag{9}$$

where:

$K_{IJ} = \int_\Omega \mathbf{B}_I^T \mathbf{D} \mathbf{B}_J d\Omega$,
$f_I = (f_I)_{\text{mech}} + (f_I)_{\text{thermal}}$

$$(f_I)_{\text{mech}} = \int_{\Gamma_t} \bar{\mathbf{t}} \Phi_I d\Gamma_t, \quad (f_I)_{\text{thermal}} = \int_\Omega \mathbf{B}_I^T \mathbf{D} \boldsymbol{\varepsilon}_T \Phi_I d\Omega, \quad G_{IK} = -\int_{\Gamma_u} \Phi_I \mathbf{N}_K d\Gamma_u, \quad q_K = -\int_{\Gamma_u} \mathbf{N}_K \bar{u} d\Gamma_u,$$

$$\mathbf{B}_I = \begin{bmatrix} \Phi_{I,x} & 0 \\ 0 & \Phi_{I,y} \\ \Phi_{I,y} & \Phi_{I,x} \end{bmatrix}, \quad \mathbf{N}_K = \begin{bmatrix} N_K & 0 \\ 0 & N_K \end{bmatrix}, \quad \mathbf{D} = \frac{E}{1-\nu^2} \begin{bmatrix} 1 & \nu & 0 \\ \nu & 1 & 0 \\ 0 & 0 & (1-\nu)/2 \end{bmatrix} \text{ (for plane stress)}$$

where:

E = modulus of elasticity and

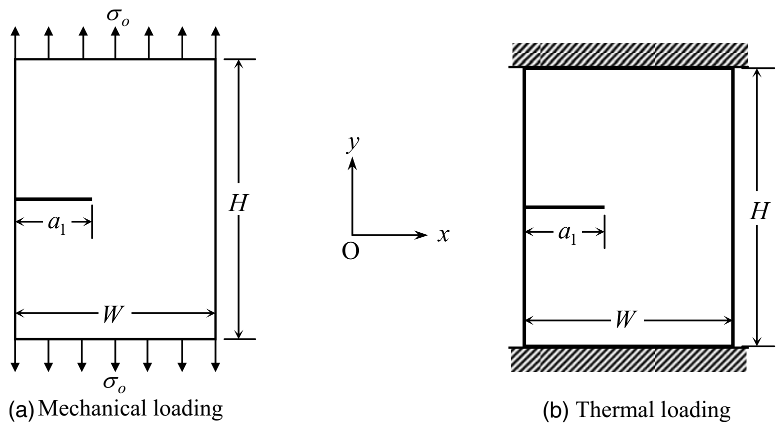

FIG. 1—*Problem geometries and their dimensions along with boundary conditions.*

ν = Poisson's ratio.

The diffraction criterion is modified by multiple crack weight method [12] for handling interaction of multiple cracks. This algorithm modifies the weight function so that it can characterize simultaneously all the crack tips located in the nodal domain of influence.

Results and Discussions

The dimensions of the cracked plate used in the present study are taken as $H = 200$ mm and $W = 100$ mm, as shown in Fig. 1. The material used in study is ASTM A36 [18] steel [19] with modulus of elasticity $(E) = 200$ GPa, coefficient of thermal expansion $(\beta) = 11.7 \times 10^{-6}/{}^\circ\mathrm{C}$, and Poisson's ratio $(\nu) = 0.3$. The far field stress (σ_o) is assumed to be 100 MPa.

Few cases of edge crack problems have been solved to study the effect of crack interactions. The first crack has been taken at a distance of $H/2$, i.e., 100 mm from the bottom with an orientation of $\alpha = 0°$ ($\alpha = 0°$ implies that the crack is parallel to the x-axis; Fig. 1), whereas the second edge crack (if present) has been placed at different locations and inclinations to study and analyze the effect of crack interactions. One edge crack with its geometry and boundary conditions is shown in Fig. 1. In case of mechanical loading, the bottom edge of the plate is constrained along the y-direction, and an external far field stress is applied at the top edge, as shown in Fig. 1(*a*), whereas in case of thermal loading, both top and bottom edges are constrained along the y-direction, as shown in Fig. 1(*b*), and thermal stresses are developed due to the change in temperature. The problem domain has been discretized using 800 regular nodes with additional nodes at the crack surface and crack tip. Six point Gauss quadrature [20] has been used for the numerical integration [17] of the Galerkin weak form. A plane stress condition has been assumed. The values of mode-I and mode-II stress intensity factors, i.e., K_{I} and K_{II}, have been calculated using the domain based interaction integral [20,21] approach. In me-

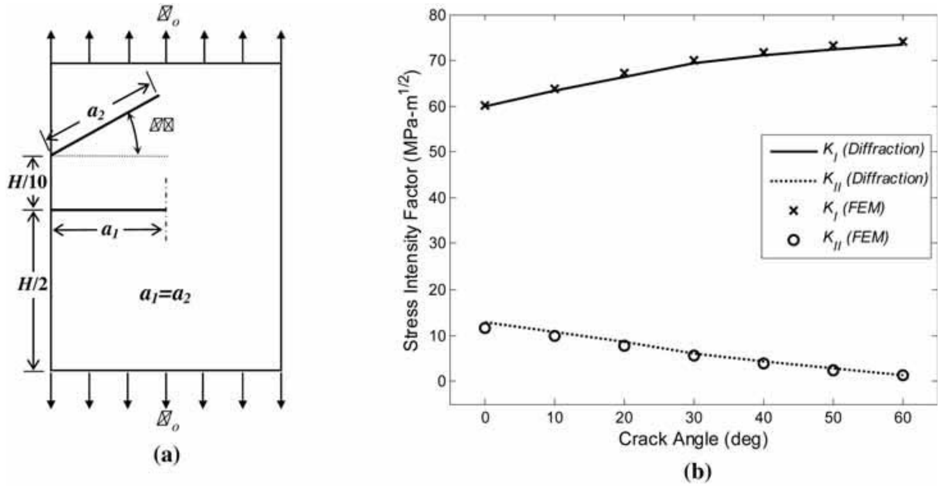

FIG. 2—*Effect of the second crack inclination* (α) *on* K_I *and* K_{II} *of the first crack.*

chanical loading, the results obtained by EFGM are compared with those obtained by FEM (ANSYS 11), whereas in thermal loading, the results are compared with intrinsic enriched EFGM.

Mechanical Loading

Various spatial and angular crack configurations have been used to analyze plane crack problems. Figure 2(*a*) shows two cracks on the same edge of the plate. The first crack is placed at a fixed orientation, i.e., $\alpha=0°$ with the horizontal, while the orientation of second crack is changed. Both cracks are equal in length, i.e., $a_1=a_2=40$ mm. K_{I} and K_{II} are evaluated at the tip of the first crack. Figure 2(*b*) presents the variation of the stress intensity factors of the first crack for different orientations of the second crack. From Fig. 2(*b*), it can be seen that K_{I} shows an increasing trend with the increase of α, while K_{II} decreases continuously with an increase of α. A comparison of EFGM results with FEM shows a similar trend for both values of K_{I} and K_{II}.

Two parallel cracks of equal length, i.e., $a_1=a_2=40$ mm, lying on the same edge with varying offset have been shown in Fig. 3(*a*). Figure 3(*b*) shows the effect of offset on the stress intensity factors of the first crack (lower crack). Figure 3(*b*) also shows that the presence of an equal length second crack lowers the value of K_{I} of the first crack, while K_{II} becomes nonzero. With the increase of offset, K_{I} increases continuously and approaches to K_{I} of a single edge crack. From Fig. 3(*b*), it can be seen that the FEM results are in good agreement with those obtained by EFGM.

Figure 4(*a*) shows two parallel cracks configuration lying on the same edge. The length of the first crack (a_1), i.e., the lower crack, is taken as 40 mm, while the length of the second crack (a_2), i.e., upper crack, is varied. The offset distance between two cracks is taken to be equal to the length of lower crack, i.e.,

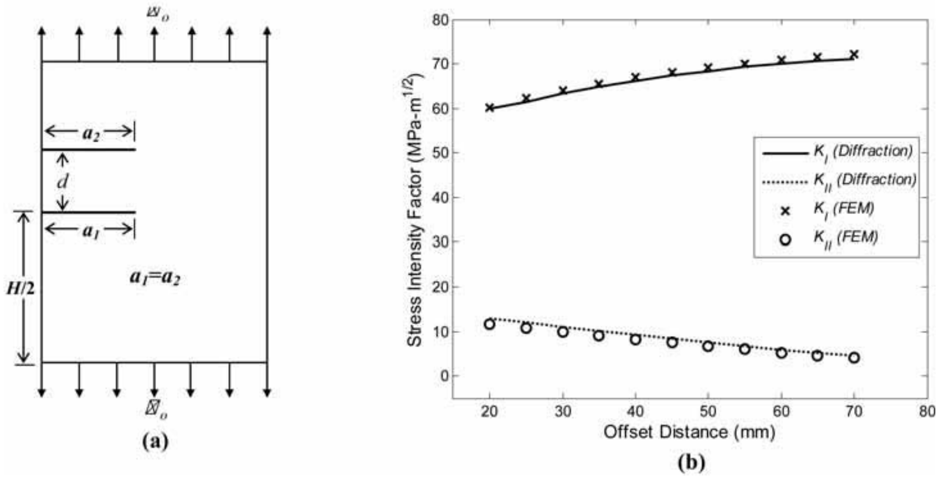

FIG. 3—*Effect of offset* (d) *on* K_I *and* K_{II} *of the first crack.*

a_1. The stress intensity factors have been evaluated at the tip of first crack. From Fig. 4(*b*), it is clear that the value of K_{I} decreases with the increase of the second crack length, while K_{II} shows an increasing trend. The decrease in the value of K_{I} for the first crack is due to the tendency of upper crack to become the major crack, thereby reducing the stresses near the lower crack tip. A comparison of EFGM results with those obtained by FEM can also be seen in Fig. 4(*b*).

A specimen with one crack on each of two opposite edges is considered as shown in Fig. 5(*a*). The crack on the left edge is kept at $\alpha = 0°$ with the horizon-

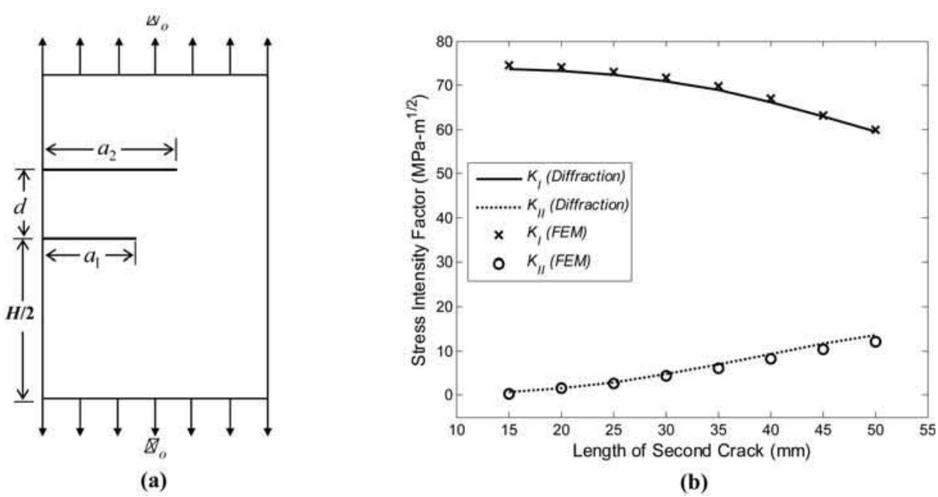

FIG. 4—*The effect of the second crack length* ($\boldsymbol{a}_2$) *on* K_I *and* K_{II} *of the first crack.*

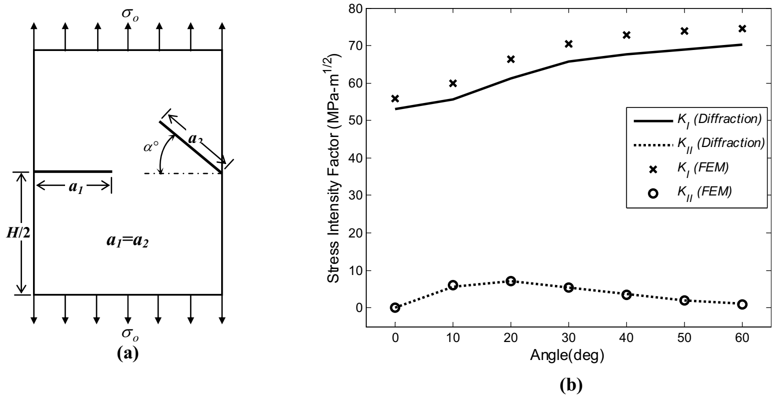

FIG. 5—*Effect of the second crack inclination* (α) *on* K_I *and* K_{II} *of the first crack.*

tal, while the crack on the right edge has a variable orientation (α). Both cracks have equal lengths, i.e., $a_1=a_2=40$ mm. The values of stress intensity factors have been evaluated at the tip of the left edge crack. Analysis shows an increasing trend of $K_{\rm I}$ with the increase in α, while $K_{\rm II}$ reaches its peak value around $\alpha=20°$ and thereafter approaches to zero at $\alpha=60°$, as shown in Fig. 5(*b*).

The effect of offset (d) between two same length (40 mm) parallel cracks (Fig. 6(*a*)) lying on the opposite edges is analyzed in this sub-section. $K_{\rm I}$ and $K_{\rm II}$ have been evaluated at the tip of left edge crack (first crack) for various values of d. The effect of d on $K_{\rm I}$ and $K_{\rm II}$ is shown in Fig. 6(*b*). In this case, the trend of results obtained by both EFGM and FEM is similar, but the values of $K_{\rm I}$ obtained by the diffraction criterion are on the lower side as compared to FEM. From the results shown in Fig. 6(*b*), it is observed that the value of $K_{\rm I}$ increases with the increase in the distance between two cracks, while $K_{\rm II}$ gains its maximum value at $d=20$ mm and thereafter reduces with the increase in offset.

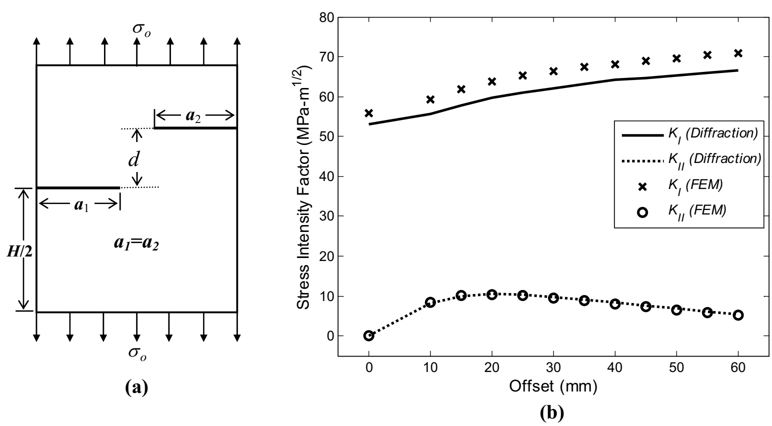

FIG. 6—*Effect of offset* (d) *on* K_I *and* K_{II} *of the first crack SIFs.*

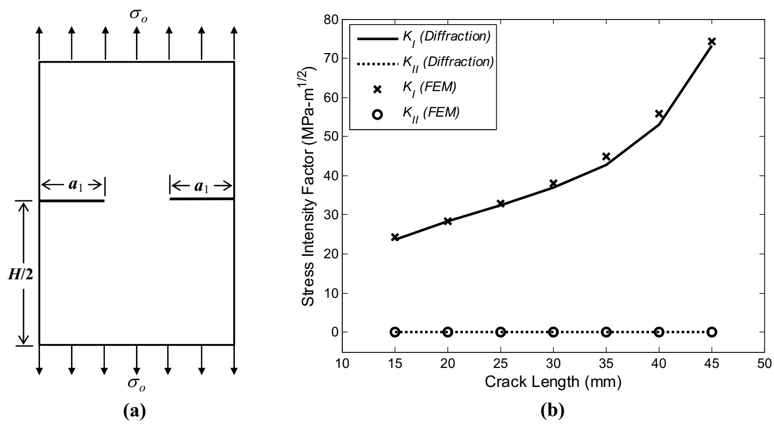

FIG. 7—*Effect of the collinear crack length* ($\boldsymbol{a_1}$) K_I *and* K_{II} *of the first crack.*

Next, three different cases of collinear cracks are chosen and analyzed. The values of stress intensity factors have been calculated at the tip of the left edge crack in all the cases. The first case considers two collinear edge crack of equal length, i.e., $a_1 = a_2$, as shown in Fig. 7(*a*). The values of $K_{\rm I}$ and $K_{\rm II}$ are calculated for different values of crack length and compared with FEM results as shown in Fig. 7(*b*). In the second case, the length of the left edge crack (a_1), i.e., the first crack, is kept fixed, and the second one is changed as shown in Fig. 8(*a*). The values of $K_{\rm I}$ and $K_{\rm II}$ are calculated for different values of a_2. The values of $K_{\rm I}$ and $K_{\rm II}$ obtained by EFGM are compared with FEM, as shown in Fig. 8(*b*). It is found that the value of $K_{\rm I}$ decreases continuously with the increase of a_2, while $K_{\rm II}$ nearly remains zero. The third case is similar to the previous one; the only small difference is that the length of the right edge crack is kept constant, while the length of the left one is varied, as shown in Fig. 9(*a*). The stress intensity factors are again evaluated at the tip of the left edge crack only. Both EFGM

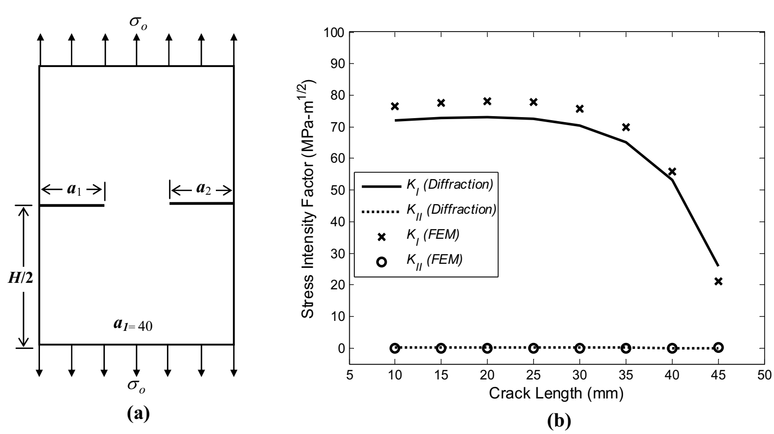

FIG. 8—*Effect of the crack length* ($\boldsymbol{a_1}$) *on* K_I *and* K_{II} *of the first crack.*

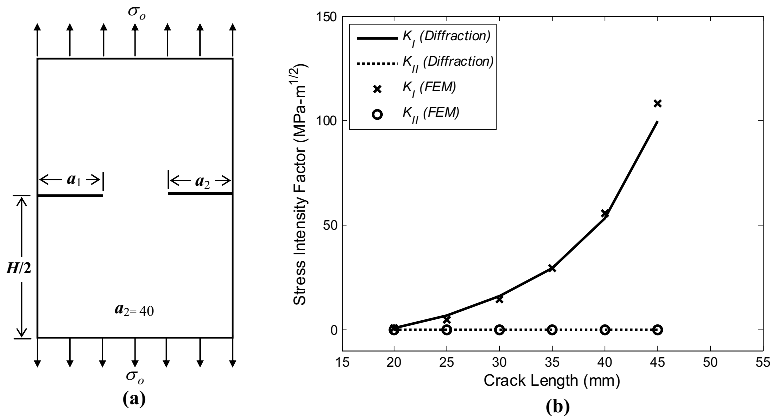

FIG. 9—*Effect of the crack length* ($\boldsymbol{a}_1$) *on* K_I *and* K_{II}.

and FEM results predict that with increase of crack length a_1, there is a monotonic increase in the value of K_{I}, while the value of K_{II} nearly remains zero. In all cases of collinear cracks, the results obtained by EFGM are found to be quite close to FEM results.

Thermal Loading

The crack configurations for studying the effect of thermal loading are the same as those presented earlier for mechanical loading. A uniform temperature change, $\Delta T = -43.7\,^\circ\mathrm{C}$, has been assumed such that it produces an equivalent mechanical stress $E\beta\Delta T = 200 \times 10^3 \times 11.7 \times 10^{-6} \times 43.7 = 99.9 \approx 100\ \ \mathrm{MPa}$.

Figure 10(*a*) shows two cracks lying on the same edge in a specimen. The first crack lying on the left edge has a fixed orientation along the width, while the orientation of the second crack is varied. Both K_{I} and K_{II} are calculated at

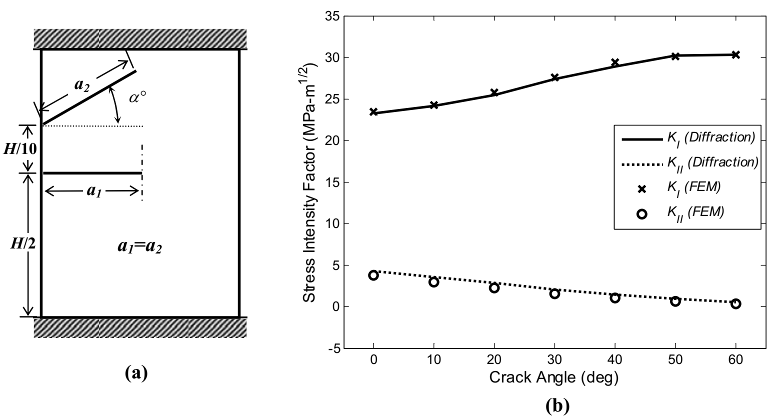

FIG. 10—*Effect of the second crack inclination* (α) *on* K_I *and* K_{II} *of the first crack.*

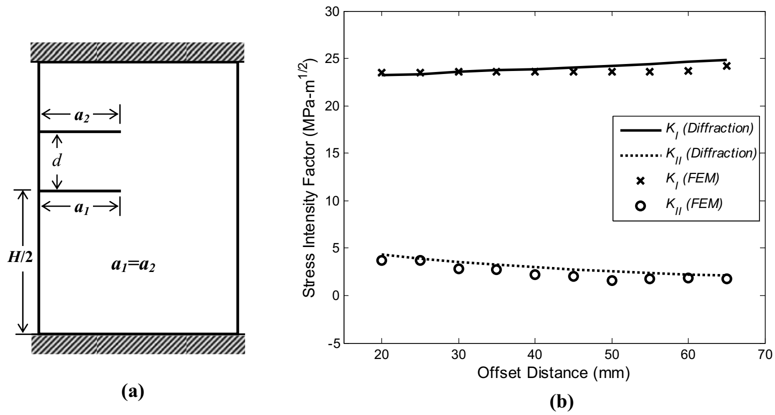

FIG. 11—*Effect of offset* (d) *on* K_I *and* K_{II} *of the first crack.*

the tip of the first crack. Figure 10(b) presents the variation of the stress intensity factors of the first crack with the angular orientation (α) of the second crack. From the results presented in Fig. 10(b), it can be noticed that the values of K_I increases with the increase of α, whereas K_II decreases with the increase of α. At $\alpha = 0°$, K_I and K_II are found to be minimum and maximum, respectively. A good agreement between the results obtained by the diffraction criterion and FEM can be clearly seen from Fig. 10(b).

The effect of offset distance, i.e., d (as shown in Fig. 11(a)), between two parallel cracks of equal length (40 mm) lying on the same edge has been analyzed in this sub-section. Figure 11(b) shows the effect of d on the stress intensity factors of the lower crack/first crack. From the results presented in Fig. 11(b), it can be noticed that the presence of the equal length upper crack lowers the value of K_I to 23.25 $\mathrm{MPa}\sqrt{\mathrm{m}}$, whereas K_II becomes nonzero due to the change in applied stress field for the lower crack. With the increase in offset distance, K_I increases continuously, while K_II shows a decreasing trend. From Fig. 11(b) it is clear that the results obtained by the diffraction criterion and FEM are in good agreement with each other.

Figure 12(a) shows two parallel crack configurations both lying on the same edge. The length (a_1) of the first crack, i.e., the lower crack, is taken as 40 mm, while the length (a_2) of the second crack, i.e., upper crack, is varied. The distance between two parallel cracks (d) is taken as 40 mm. The stress intensity factors have been evaluated at the tip of first crack. From the results presented in Fig. 12(b), it is found that with the increase in the length of the second crack, the value of K_I decreases, and K_II increases. The decrease in the value of K_I for the first crack with the increase in the length of the upper crack is due to the tendency of the upper crack to become the major crack. Moreover, the results presented by the diffraction criterion and FEM are quite close to each other.

A specimen with two cracks lying on the opposite edges is considered, as shown in Fig. 13(a). The crack on the left edge is kept at $\alpha = 0°$ with the horizontal, while the orientation (α) of the crack on the right edge has been varied from 0° to 60°. The values of stress intensity factors have been calculated at the

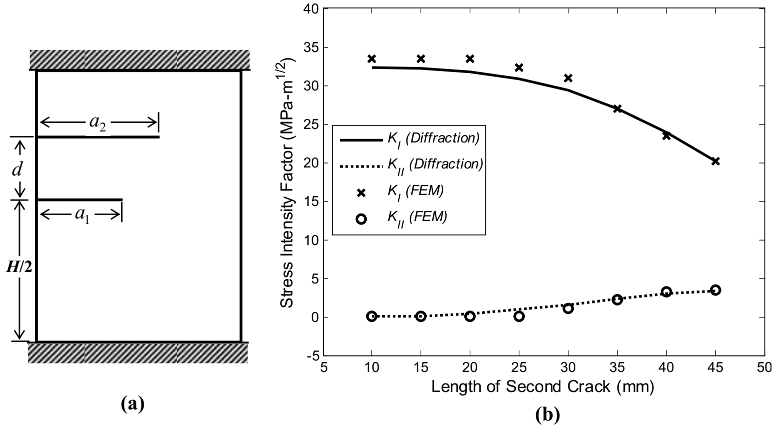

FIG. 12—*The effect of the second crack length (*$\boldsymbol{a}_2$*) on* K_I *and* K_{II} *of the first crack.*

tip of the left edge crack. From the results presented in Fig. 13(*b*), it has been found that with the increase of α, $K_{\rm I}$ keeps on increasing, whereas $K_{\rm II}$ initially increases up to $\alpha = 20°$ and decreases after that. The variation in the value of $K_{\rm I}$ for a 60° change in inclination is less as compared to mechanical loading. From the results presented in Fig. 13(*b*), it can be seen that the results obtained by the diffraction criterion are slightly on the lower side as compared to FEM; however, the trend is similar in both techniques.

Two parallel cracks of the same length, i.e., $a_1 = a_2$, lying on opposite edges (Fig. 14(*a*)) have been analyzed by varying the offset (d) between them. $K_{\rm I}$ and $K_{\rm II}$ have been evaluated at the tip of the left edge crack for various values of d. The effect of d on $K_{\rm I}$ and $K_{\rm II}$ is presented in Fig. 14(*b*), evaluated by the diffrac-

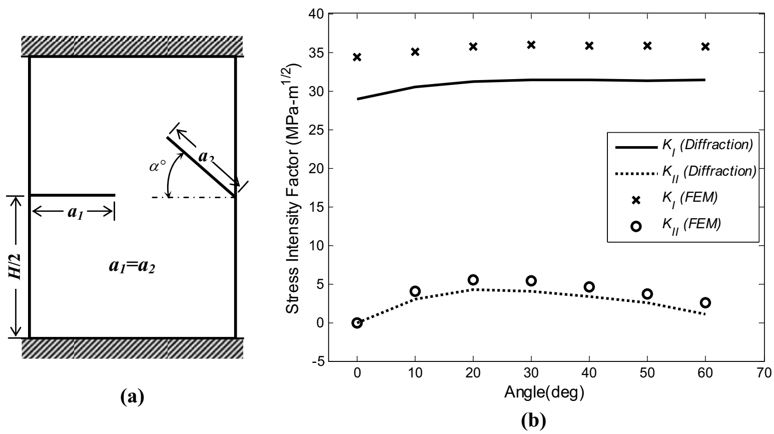

FIG. 13—*Effect of the second crack inclination (*α*) on* K_I *and* K_{II} *of the first crack.*

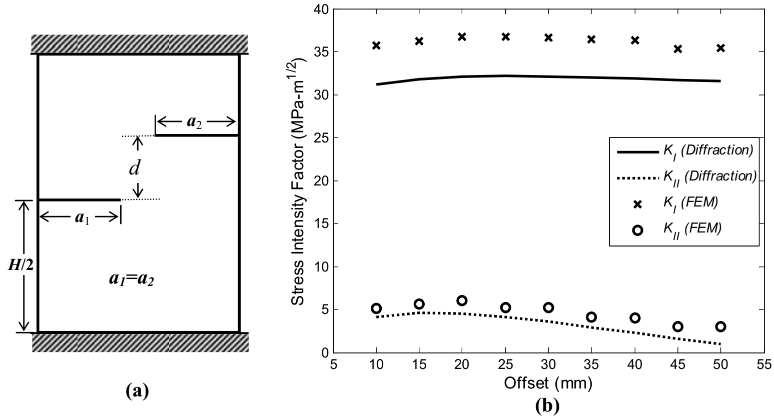

FIG. 14—*Effect of offset* (***d***) *on* K_I *and* K_{II} *of the first crack.*

tion criterion and FEM. The minimum value of K_{I} is obtained at $d=0$; then K_{I} increases continuously with the increase of d. The maximum value of K_{II} is found at $d=20$ mm.

Next, three different cases of collinear edge cracks have been considered. Figure 15(*a*) shows the configuration where the length of both collinear cracks is increased by equal amount. The values of K_{I} and K_{II} are evaluated at the tip of the left edge crack. A comparison of results obtained by the diffraction criterion and FEM suggests that the values are quite close for crack length $a_1 > 25$ mm, as can be seen from Fig. 15(*b*). For all values of the crack length, K_{I} values obtained by the diffraction criterion are smaller in comparison to FEM, whereas K_{II} nearly remains zero for all values of crack length.

For the second case of collinear cracks, the length of left edge crack a_1 has been taken as constant, i.e., 40 mm, while the length of the right edge crack a_2

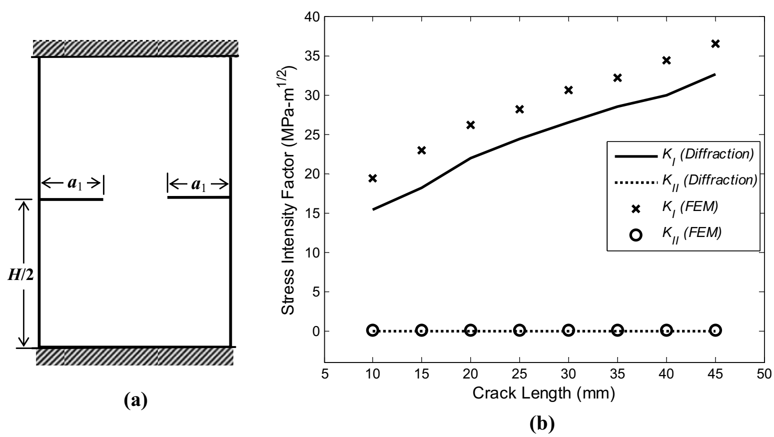

FIG. 15—*Effect of the collinear crack length* ($\boldsymbol{a}_1$) *on* K_I *and* K_{II} *of the first crack.*

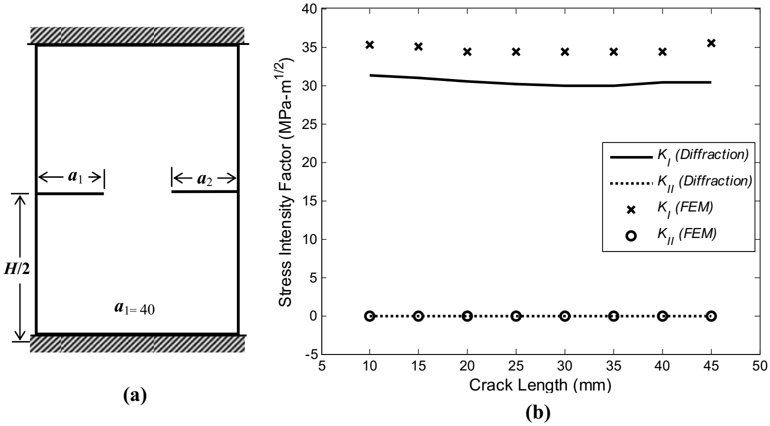

FIG. 16—*Effect of the crack length* ($\boldsymbol{a}_1$) *on* K_I *and* K_{II} *of the first crack.*

has been changed, as shown in Fig. 16(*a*). The values of K_I and K_II have been evaluated at the tip of the left edge crack. From the results presented in Fig. 16(*b*), it can be seen that the values of K_I remains nearly constant with the variation of crack length a_2 and K_II remains almost zero. From the results presented in Fig. 16(*b*), it is also noticed that the results obtained from the diffraction criterion are lower in comparison to FEM solution.

In the third case, the length of the right edge crack, i.e., a_2, is kept constant, i.e., 40 mm, while the length of the left edge crack has been varied, as shown in Fig. 17(*a*). The values of K_I and K_II have been evaluated at the tip of the left edge crack only. The results obtained by the diffraction criterion are again on the lower side as compared to FEM results, as can be seen from Fig. 17(*b*).

From the analysis above, it is also noticed that the results obtained by both the diffraction criterion and FEM are almost similar if both edge crack cracks

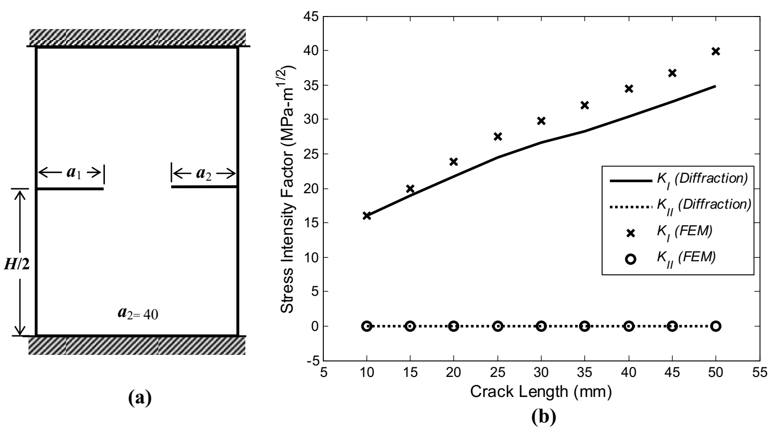

FIG. 17—*Effect of the crack length* ($\boldsymbol{a}_1$) *on* K_I *and* K_{II}.

are lying on the same edge, whereas the results predicted by the diffraction criterion are found to be on the lower side as compared to the FEM solution if cracks are lying on the opposite faces.

Conclusions

In the present work, few edge crack problems were studied and analyzed using EFGM under thermal and mechanical loadings. The results were obtained by the diffraction criterion and were compared with the FEM solution. In the case of mechanical loading, the results obtained by the diffraction criterion were found to be in good agreement with the FEM solution, whereas in thermal loading, the results obtained by the diffraction criterion were found quite similar to those by the FEM solution if all cracks were lying on the same edge of geometry, and the results obtained by diffraction were found on the lower side if cracks were lying on opposite faces. On the basis of these simulations, it was observed that the presence of the second edge crack may have either a magnifying or a shielding effect over the stress field of the first crack. Stress field interaction between cracks depends on the spatial and angular orientation of cracks over the specimen geometry. Moreover, the presence of the second crack creates mixed mode loading condition; hence mode-II stress intensity factor for the first crack becomes nonzero. The thermal loads have qualitatively the same effect as the mechanical load, but the severity of the stress field near the crack tip due to crack interaction effect is different.

References

[1] Lansinger, J., Hansson, T., and Clevfors, O., "Fatigue Crack Growth Under Combined Thermal Cycling and Mechanical Loading," *Int. J. Fatigue*, Vol. 29, 2007, pp. 1383–1390.

[2] Muravin, B. and Turkel, E., "Multiple Crack Weight for Solution of Multiple Interacting Cracks by Meshless Numerical Methods," *Int. J. Numer. Methods Eng.*, Vol. 67, 2006, pp. 1146–1159.

[3] Simkins, D. C. and Li, S., "Meshfree Simulations of Thermo-Mechanical Ductile Fracture," *Comput. Mech.*, Vol. 38, 2006, pp. 235–249.

[4] Dai, K. Y., Liu, G. R., Han, X., and Lim, K. M., "Thermo-Mechanical Analysis of Functionally Graded Material (FGM) Plates Using Element-Free Galerkin Method," *Comput. Struct.*, Vol. 83, 2005, pp. 1487–1502.

[5] Belytschko, T., Krongauz, Y., Organ, D. J., Fleming, M., and Krysl, P., "Meshless Methods: An Overview and Recent Developments," *Comput. Methods Appl. Mech. Eng.*, Vol. 139, 1996, pp. 3–47.

[6] Yagawa, G. and Furukawa, T., "Recent Developments of Free Mesh Method," *Int. J. Numer. Methods Eng.*, Vol. 47, 2000, pp. 1419–1443.

[7] Nguyen, P., Rabczuk, T., Bordas, S., and Duflot, M., "Meshless Methods: A Review and Computer Implementation Aspects," *Math. Comput. Simul.*, Vol. 79, 2008, pp. 763–813.

[8] Sladek, J., Sladek, V., Zhang, Ch., and Tan, C. L., "Meshless Local Petrov–Galerkin Method for Linear Coupled Thermoelastic Analysis," *Comput. Model. Eng. Sci.*,

Vol. 16, 2006, pp. 57–68.

[9] Sladek, J., Sladek, V., and Zhang, Ch., "Evaluation of the Stress Intensity Factors for Cracks in Continuously Nonhomogeneous Solids, Part I: Interaction Integral," *Mechanics of Advanced Materials and Structures*, Vol. 15, 2008, pp. 438–443.

[10] Sladek, J., Sladek, V., and Zhang, Ch., "Evaluation of the Stress Intensity Factors for Cracks in Continuously Nonhomogeneous Solids, Part II: Meshless Method," *Mechanics of Advanced Materials and Structures*, Vol. 15, 2008, pp. 444–452.

[11] Sladek, J., Sladek, V., Solek, P., Zhang, Ch., and Tan, C. L., "Two- and Three-Dimensional Transient Thermoelastic Analysis by the MLPG Method," *Comput. Model. Eng. Sci.*, Vol. 47, 2009, pp. 61–95.

[12] Muravin, B., 2003, "The Application of Element Free Galerkin Method in the Investigation of Crack Interaction," Ph.D. thesis, Tel-Aviv University, Israel.

[13] Belytschko, T. and Fleming, M., "Smoothing, Enrichment and Contact in the Element-Free Galerkin Method," *Comput. Struct.*, Vol. 71, 1999, pp. 173–195.

[14] Organ, D. J., Fleming, M., and Belytschko, T., "Continuous Meshless Approximation for Non-Convex Bodies by Diffraction and Transparency," *Comput. Mech.*, Vol. 18, 1996, pp. 225–235.

[15] Loehnert, S. and Belytschko, T., "Crack Shielding and Amplification Due to Multiple Micro-Cracks Interacting with a Macrocrack," *Int. J. Fract.*, Vol. 145, 2007, pp. 1–8.

[16] Krongauz, Y. and Belytschko, T., "Enforcement of Essential Boundary Conditions in Meshless Approximations Using Finite Elements," *Comput. Methods Appl. Mech. Eng.*, Vol. 131, 1996, pp. 133–145.

[17] Dolbow, J. and Belytschko, T., "An Introduction to Programming the Meshless Element Free Galerkin Method," *Arch. Comput. Methods Eng.*, Vol. 5, 1998, pp. 207–241.

[18] ASTM A36, 1978, "Standard Specification for Structural Steel," *Annual Book of ASTM Standards*, Vol. 4, ASTM International, West Conshohocken, PA, pp. 137-138.

[19] Beer, P., Johnston, E., and DeWolf, T., *Mechanics of Materials*, McGraw-Hill International Edition, Singapore, 2002, p. 747.

[20] Dolbow, J. and Belytschko, T., "Numerical Integration of Galerkin Weak Form in Meshfree Methods," *Comput. Mech.*, Vol. 23, 1999, pp. 219–230.

[21] Dag, S., "Thermal Fracture Analysis of Orthotropic Functionally Graded Materials Using an Equivalent Domain Integral Approach," *Eng. Fract. Mech.*, Vol. 73, 2006, pp. 2802–2828.

Reprinted from JAI, Vol. 7, No. 5
doi:10.1520/JAI102692
Available online at www.astm.org/JAI

David C. Dudzinski,[1] *Wieslaw Beres,*[2] *and Raymond K. Kersey*[3]

Temperature Calibration Techniques for TMF Testing

ABSTRACT: One of the methods to control the rapid temperature changes during a thermomechanical fatigue (TMF) test involves the use of an infrared pyrometer for temperature measurement. The infrared pyrometer relies on the emissivity of the test coupon. One way to determine this emissivity is to use a disappearing filament pyrometer. This paper presents two emissivity calibration techniques: Strain measurement and application of non-permanent thermocouples. Both techniques were applied for TMF testing, and the advantages and disadvantages of these techniques are described. The results show that the temperature indicated by these methods can significantly differ when compared to the actual temperature of the test specimen measured by thermocouples. However, these variances can be mitigated by calibration.

KEYWORDS: thermomechanical fatigue, TMF, disappearing filament pyrometer (DFP), emissivity

Introduction

Many machine components are subjected to simultaneous cyclic thermal and mechanical loads. This loading condition can be found in numerous engineering components ranging from hot sections of gas turbines engines to vehicle brakes. The thermomechanical fatigue (TMF) test is typically used during the design and development stage of these components to qualify them for particular operating conditions and to predict their service life. During a TMF test the temperature of the component is varied cyclically with respect to the specimen strain or applied load, and it is therefore imperative that an accurate temperature can be determined throughout the test. In fact, ASTM E2368 [1] stipulates

Manuscript received August 17, 2009; accepted for publication March 23, 2010; published online April 2010.

[1] National Research Council Canada, Ottawa, ON K1A 0R6, Canada, e-mail: david.dudzinski@nrc-cnrc.gc.ca
[2] National Research Council Canada, Ottawa, ON K1A 0R6, Canada.
[3] Pratt & Whitney, East Hartford, CT 06108.

Cite as: Dudzinski, D. C., Beres, W. and Kersey, R. K., "Temperature Calibration Techniques for TMF Testing," *J. ASTM Intl.*, Vol. 7, No. 5. doi:10.1520/JAI102692.

that the temperature indicated by the control sensor shall not vary by more than ±2 K from the corresponding values of the initial temperature cycle. Although there are many different methods to measure temperature [2,3], infrared pyrometry [4] and thermocouples (TC) [5] are the techniques primarily used for dynamic temperature measurements during TMF tests.

While it is not the authors' intent to debate the methods of temperature measurement during a TMF test, one must be aware of the limitations associated with the choice. For instance, the response time for a TC is dependent upon the thermal conductivity of the materials used in the junction, which is typically in the range of 0.5–4 s, with some specially designed TCs capable of responding to step changes in a fraction of a second [6]. In comparison pyrometers are capable of microsecond or even nanosecond responses. Other areas of concern, which can be an issue for TC usage, include errors introduced by conduction, radiation, and electrical noise [6] as well as time dependent oxide formation and material aging of the TC, particularly in Chromel-Alumel TCs [7]. While pyrometry does not exhibit as many drawbacks as TCs, it also has some limitations. For instance, changes in the surface condition of a measured component, such as oxide growth at high temperatures, will affect the emissivity [8] and therefore the accuracy of temperature readings. This is the most important limitation of pyrometry. Since the pyrometer is more suited as a method of temperature measurement during rapid temperature changes, which are associated with a TMF test, the impetus for this study was the pyrometer.

The measurement of temperature using pyrometry depends on the ability of a material to radiate absorbed energy. This is often referred to as the emissivity of the material, which is a dimensionless ratio of the electromagnetic radiation emitted by the material to that of a black body at the same temperature. For an ideal black body, the emissivity is 1, whereas it is less than 1 for real materials. Emissivity for various materials in various conditions can be found in literature [2,3].

The temperature of an unknown surface may be determined through the relation of its emissivity to emissivity of the same material at a known temperature. One correlation method is through the use of a disappearing filament pyrometer (DFP). In this method the brightness of a filament is adjusted by an operator until the filament visually disappears against the background of the measured material. Since the visibility threshold of the human eye is ~700°C (1292°F) [2], this limits the minimum temperature that can be validated using the DFP. However, the accuracy of this method is quite high, in the range of ±1°C (1.8°F) at 775°C (1427°F) [3]. Prior to conducting a TMF test at a lower temperature, the relationship between the emissivity and the temperature must be established at temperatures above 775°C. Unfortunately many superalloys used in gas turbines are subjected to an aging treatment below 775°C [9], and therefore they cannot be subjected to this emissivity correlation method without incurring the risk of the material property being changed.

In this paper two different methods are examined to determine the relation between emissivity of TMF test specimens, namely, strain and temperature based methods. A nickel-based superalloy, IN718, was used to validate both methods experimentally, and the results of these evaluations are discussed.

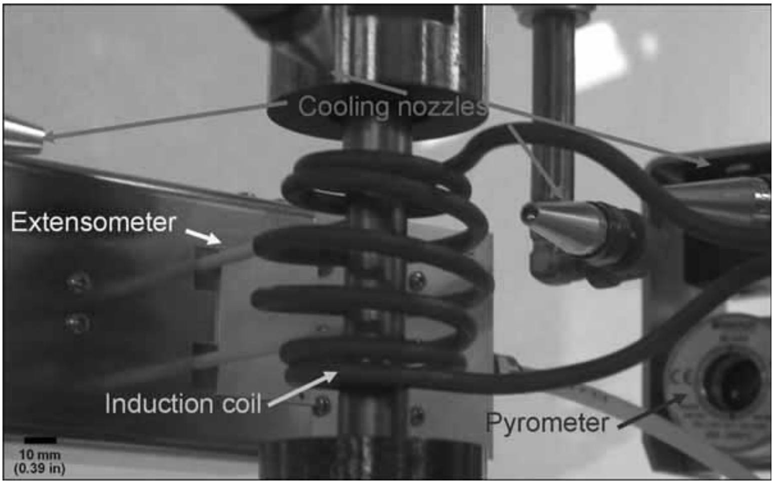

FIG. 1—*Experimental setup.*

Experimental Equipment

The equipment used for this investigation included a TMF servo-hydraulic test machine that consisted of a 100 kN load frame, a digital controller, a 5 kW induction heating system, a 25 mm gauge length extensometer for strain measurements, and a 0.14 mm spot size pyrometer for temperature signal. A water-cooled five-turn copper induction coil combined with internal and external cooling air jets was used to apply the thermal cycling. An image of the setup is shown in Fig. 1. Another handheld pyrometer with a 0.4 mm spot size was used for periodic temperature measurements.

Experimental Methods

Strain Relation

The first method to determine the emissivity will be referred to as the strain relation method. In this method a relation is developed between the strain measured via an extensometer and the temperature measured via a pyrometer that was previously calibrated using the DFP technique. In our experiments, this was done using eight calibration specimens taken from the same batch of material as the tested specimens. A graph of the average strain versus the control pyrometer setpoint temperature is presented in Fig. 2. As indicated in this figure, the standard deviation of strain at each temperature setpoint was within ± 0.015 %, and this translates into a temperature accuracy of $\sim\pm 14°C$ (20°F). Using this relation, a specimen can be heated until the strain indicated by the extensometer corresponds to the desired temperature, as shown in Fig. 2, and adjustments to the control pyrometer emissivity can then be made. The curve shown in Fig. 2 slightly deviates from a straight line because the coefficient of

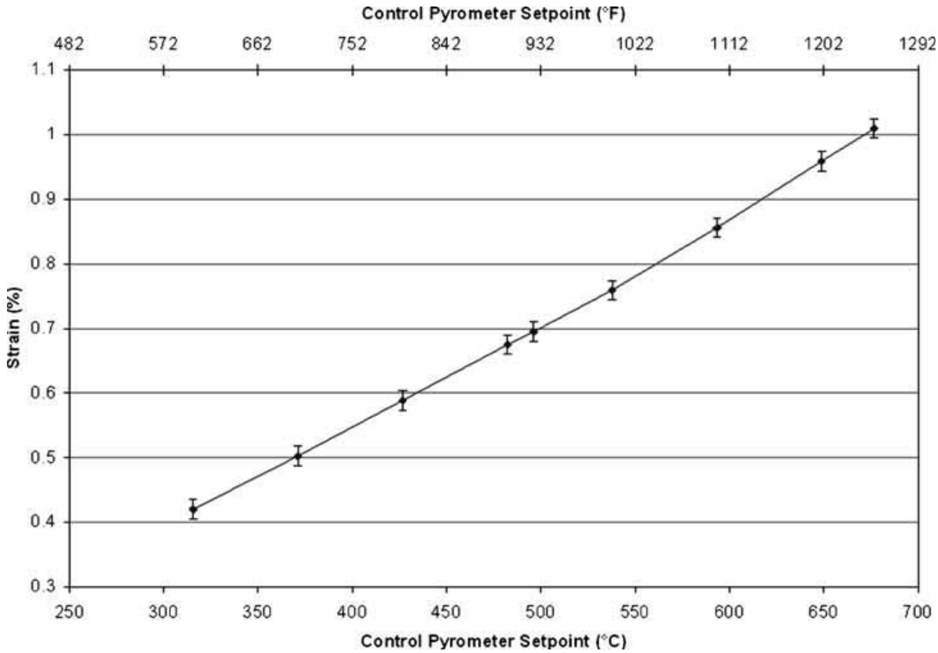

FIG. 2—*Pyrometer setpoint temperature versus average strain.*

thermal expansion for the alloy studied varies with temperature. It can be inferred from the data in Fig. 2 that the coefficient of thermal expansion at 677°C (1250°F) was 1.54×10^{-5}/°C (8.6×10^{-6}/°F), which differs by less than 2 % from the value of 1.57×10^{-5}/°C (8.7×10^{-6}/°F) extracted from the figure published in Ref 10.

Temperature Correlation

The second method to determine emissivity will be referred to as the temperature correlation method. In this method, a comparison is developed between an indicated temperature measured by a TC and the actual temperature as indicated by a pyrometer calibrated using the DFP technique.

Six non-permanent physical contact techniques of TC attachment presented schematically in Fig. 3 were initially examined at a single temperature of 621°C (1150°F). These techniques were examined so that the TC could be removed during the TMF test without permanently affecting the specimen surface such as in a welding procedure. For these experiments either a type S sheathed TC with an external diameter of 1.0 mm (0.040 in.) or a type S exposed TC with a wire diameter of 0.5 mm (0.020 in.) was used.

(a) The first technique examined was a sheathed TC placed longitudinally to the specimen and attached with two strips of nickel foil circumferentially around the specimen. For this attachment method, the difference between the pyrometer and TC was 36°C (64°F).

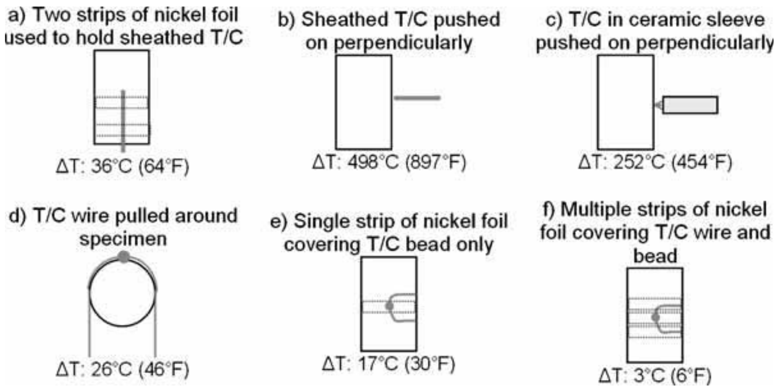

FIG. 3—*Schematic of temperature correlation methods examined and the temperature difference at 621°C (1150°F).*

(b) The second technique involved the sheathed TC pushed on perpendicularly onto the specimen, and this appeared to generate the most significant temperature difference at 498 °C (897 °F). The exposed TC was used for the remaining four attachment techniques.
(c) The third technique involved a ceramic sleeve that was used as a vessel to both hold and push the exposed TC perpendicularly onto the specimen. Using the ceramic sleeve, a temperature difference of 252 °C (454 °F) was observed.
(d) For the fourth technique, the exposed TC wire was pulled around the specimen, and the temperature difference between the pyrometer and TC was 26 °C (46 °F).
(e) The fifth technique involved a piece of nickel foil that covered only the exposed TC bead, and the wire was wrapped 180° around the specimen, which resulted in a temperature difference of 17 °C (30 °F).
(f) For the sixth and final technique, three strips of nickel foil covered the TC wire and the bead, which provided the smallest temperature difference of 3 °C (6 °F).

Finally, the TC in a ceramic sleeve technique (Fig. 1(*c*)) was chosen as the TC probe (TCP) despite having the second largest temperature difference of 252 °C (454 °F) between the TC and the pyrometer. This was due to the potential for repeatability of results as well as the minimal impact this method had on the TMF specimen since the TCP could be easily removed prior to starting the TMF test and then reattached for verification at the end of the test.

To ensure repeatability of temperature measurements, a fixture was designed that consistently positioned the TCP within a radius of 0.64 mm (0.025 in.) on the specimen (see Fig. 4). This fixture was spring loaded so that the pressure applied at the contact point of the TCP and the TMF specimen during temperature measurements was repeatable. The temperature indicated by the TCP was measured and recorded at various pyrometer setpoint temperatures so that a correlation could be made. This was done using a trial coupon manufactured from the same alloy and a pyrometer that had been calibrated using the

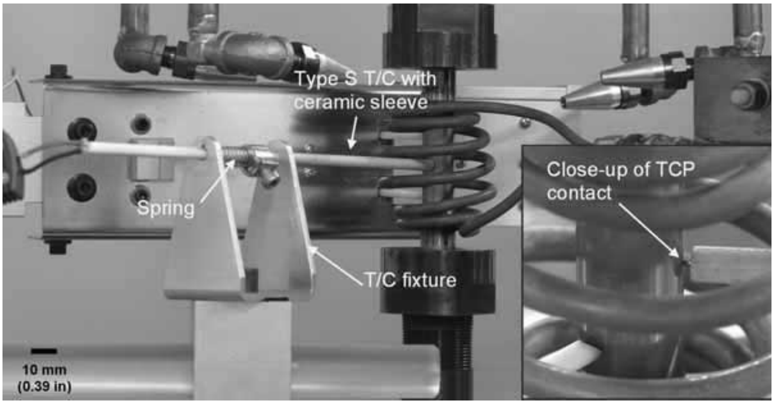

FIG. 4—*TC fixture.*

DFP technique at 788°C (1450°F). A graph of the pyrometer setpoint temperature versus the average TCP temperature for a TC in a ceramic sleeve (Fig. 1(*c*)) is presented in Fig. 5. From this figure and by examining the error bars, it can be concluded that a temperature accuracy of ~±6°C (11°F) was achieved using this temperature correlation method.

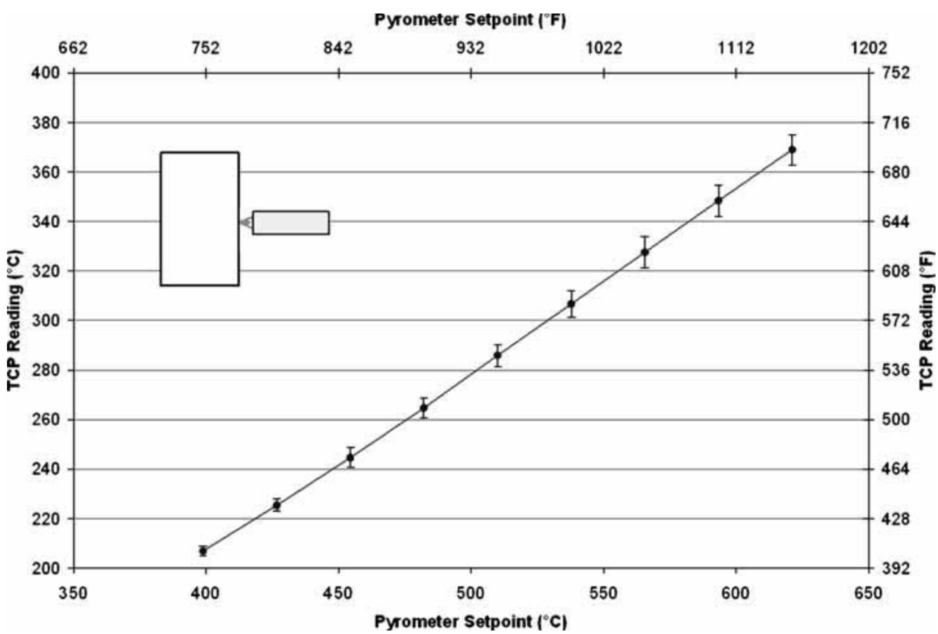

FIG. 5—*Pyrometer setpoint temperature versus the average TCP temperature reading.*

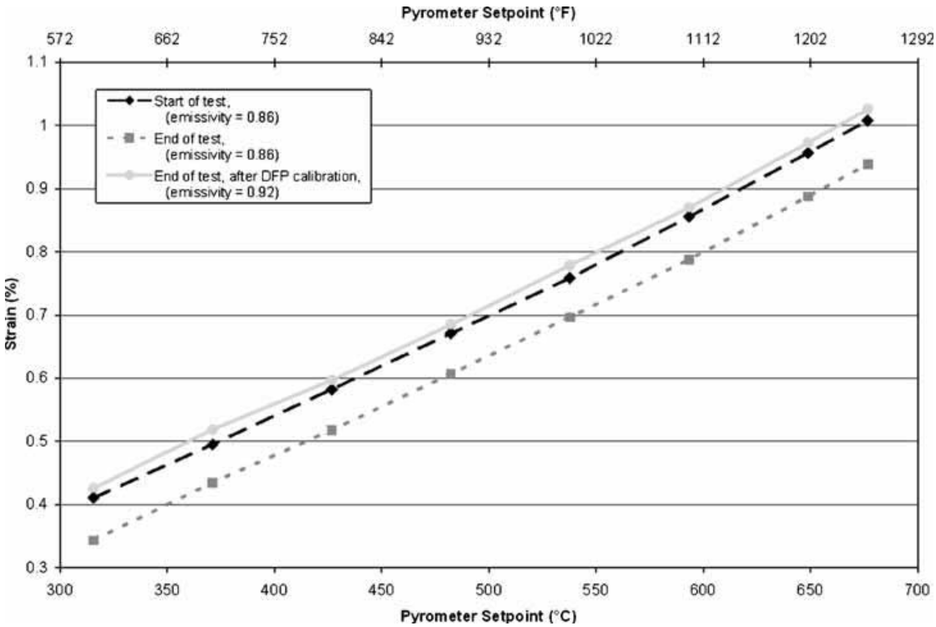

FIG. 6—*Strain correlation at the start of the test, at the end of the test, and after the DFP correlation.*

Results and Discussion

Two TMF tests were conducted. For the first test, the strain relation method was used to calibrate the emissivity and to achieve a peak temperature of 677°C (1250°F). No adjustments were made to the emissivity during this test. When the test was completed, the strains corresponding to different temperatures were measured. The DFP method was then used to calibrate the emissivity, after which the strains correlating to different temperatures were again measured. The results are shown in Fig. 6. It is evident from this figure that there was a change in emissivity between the start and the end of test, which affected the actual temperature by ~46°C (83°F). In comparison, the difference between the start and the end of test after DFP calibration temperature was ~10°C (18°F), which is in agreement with the strain data in Fig. 2. Although the records from the periodic temperature measurements during the TMF test using a handheld pyrometer indicated a potential change in the emissivity, the TMF test was not stopped to make adjustments. In hindsight, this test should have been interrupted so that a correction could be made to the emissivity, which would reduce the 46°C temperature difference found at the end of the TMF test.

For the second TMF test, the temperature correlation method was used with a TCP temperature of 369°C (696°F) to calibrate the emissivity and to achieve a peak specimen temperature of 621°C (1150°F). Prior to starting the test, the TCP was removed so that it was not in contact with the specimen. A

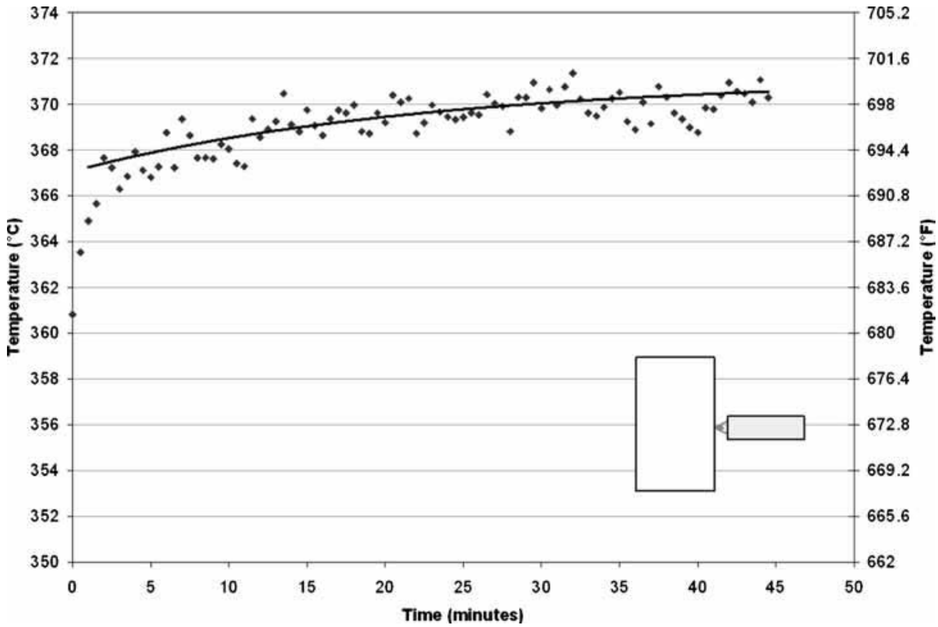

FIG. 7—*TCP temperature response over time.*

single adjustment to the emissivity was required during the test due to an indication from a handheld pyrometer. This was done by stopping the TMF test, re-applying the TCP, and then adjusting the emissivity until the pyrometer temperature matched the TCP calibration temperature of 369°C (696°F). The TCP was subsequently removed, and the test was continued. After the test was completed, the emissivity of the pyrometer was evaluated using the DFP method, and it was determined that the correct emissivity was used during the TMF test as verified by comparison of the pyrometer temperature to the temperature indicated by the DFP. The observed TCP temperature at the end of the TMF test was 365°C (689°F), which was 4°C (7°F) below the target correlation temperature shown in Fig. 5. This was within ±6°C (11°F) accuracy of the temperature correlation method. This difference might be a result of the TCP temperature settling time, an example of which is plotted in Fig. 7 where readings were taken every 30 s over a 45 min time period. From this figure, it can be observed that ~10 min was required for the TCP to reach a steady-state temperature of 370.5°C (699°F) within 2°C (3.6°F).

Conclusion

Both the strain relation and the temperature correlation methods were used to calibrate the emissivity for a pyrometer used to provide the temperature feedback during a TMF test. The strain relation method had an accuracy of ±14°C (20°F), while the temperature correlation method using a TC in a ceramic sleeve had a higher accuracy of ±6°C (11°F). The results at the end of each

TMF test showed that both methods can be used to calibrate the emissivity of a pyrometer, but changes in emissivity during a TMF test must be evaluated and corrected throughout the test.

Acknowledgments

The hard work and dedication to this project by Luc Lafleur are greatly appreciated.

[1] ASTM E2368-04, 2009, "Standard Practice for Strain Controlled Thermomechanical Fatigue Testing," *Annual Book of ASTM Standards*, Vol. 03.01, ASTM International, West Conshohocken, PA, pp. 1367-1374.
[2] Michalski, L., Eckersdorf, K., Kucharski, J., and McGhee, J., *Temperature Measurement*, 2nd ed., John Wiley & Sons, Ltd., England, 1991, p. 163.
[3] Childs, P. R. N., *Practical Temperature Measurement*, Butterworth-Heinemann, Oxford, 2001, p. 269.
[4] Evans, W. J., Screech, J. E., and Williams, S. J., "Thermo-Mechanical Fatigue and Fracture of INCO718," *Int. J. Fatigue*, Vol. 30(2), 2008, pp. 257–267.
[5] Jung, A. and Schnell, A., "Crack Growth in a Coated Gas Turbine Superalloy Under Thermo-Mechanical Fatigue," *Int. J. Fatigue*, Vol. 30(2), 2008, pp. 286–291.
[6] Rudnev, V., Loveless, D., Cook, R., and Black, M., *Handbook of Induction Heating*, Marcel Dekker Inc., New York, 2003, pp. 189–190.
[7] Sibley, F. S., Spooner, N. F., and Hall, B. F., "Aging in Type K Couples," *Instrum. Technol.*, Vol. 15, 1968, pp. 53-55.
[8] Iuchi, T., Furukawa, T., and Wada, S., "Emissivity Modeling of Metals During the Growth of Oxide Film and Comparison of the Model with Experimental Results," *Appl. Opt.*, Vol. 42(13), 2003, pp. 2317–2326.
[9] David, J. R., *Metals Handbook, Desk Edition*, 2nd ed., ASM International, Metals Park, OH, 1998.
[10] Klopp, W. D., "Inconel Alloy 718," *Aerospace Structural Metals Handbook*, 38th ed., CINDAS/USAF CRDA Handbooks Operation, Purdue University, West Lafayette, IN, 1999, Vol. 5, Code 4103.

APPLICATION OF FRACTURE MECHANICS AND COHESIVE ZONE MODELS

Reprinted from JAI, Vol. 6, No. 9
doi:10.1520/JAI102542
Available online at www.astm.org/JAI

M. Shirani[1] *and G. Härkegård*[2]

Fatigue Crack Growth Simulation in Components with Random Defects

ABSTRACT: The three dimensional distribution of defects within a fatigue specimen cut from a large spheroidal graphite cast iron component has been obtained by X-ray computed tomography. This distribution has been used as input for a fatigue assessment postprocessor for the calculation of fatigue life distribution in cast components.

KEYWORDS: spheroidal graphite cast iron, fatigue, casting defects, X-ray computed tomography, fatigue assessment postprocessor

Introduction

In cast materials, the fatigue life is often controlled by the growth of cracks initiated from inclusions, nodules, or other metallurgical defects such as shrinkage cavities [1–5]. It is therefore of primary importance to consider such defect features as input parameters in fatigue life assessment.

Most fatigue evaluation approaches for defect containing materials [6–8] consider that crack initiation stage to be negligible. Therefore fatigue life and fatigue limit are assumed to be controlled by the crack propagation law and by the threshold stress intensity factor, respectively. The effect of inclusions on fatigue strength has been successfully studied from the viewpoint of fracture mechanics by treating the defects as small cracks and by describing the relationship between fatigue thresholds and crack size [9]. It is well known that fatigue test results are scattered. It is therefore important to consider the defect as an input parameter for fatigue life estimation and to partially explain the scatter.

Manuscript received May 19, 2009; accepted for publication August 5, 2009; published online September 2009.

[1] Dept. of Engineering Design and Materials, Norwegian Univ. of Science and Technology, Richard Birkelandsvei 2B, NO-7491 Trondheim, Norway, e-mail: mehdi.shirani@ntnu.no

[2] Dept. of Engineering Design and Materials, Norwegian Univ. of Science and Technology, Richard Birkelandsvei 2B, NO-7491 Trondheim, Norway.

Cite as: Shirani, M. and Härkegård, G., "Fatigue Crack Growth Simulation in Components with Random Defects," *J. ASTM Intl.*, Vol. 6, No. 9. doi:10.1520/JAI102542.

Hence, every effort in order to try to predict fatigue lives of cast materials requires a sound characterization of the defect distribution in the material. Classically, such a distribution can be obtained from serial two dimensional metallographic observations. However, the amount of material that can be studied by such a tedious method is generally very low. Predictions of the three dimensional maximum defect size from the two dimensional method sometimes involve errors [10]. For instance, parameters like the statistical size or shape distribution of the pores are rather difficult to obtain precisely. Sometimes material includes a mixture of two different types of defects. The character of this mixed distribution is that as the number of inspections and the size of the inspection area increases, it is more likely to pick out the presence of the second particle type, which rarely occurs and leads to final fatigue failure. In these cases, most times the limited volume of material inspected by conventional methods does not catch the second type of particles, which have a large size but a rare population [11]. Conventional approaches only provide two dimensional information of defects, such as pores, which may not adequately describe their tortuous three dimensional morphology [12].

High resolution X-ray tomography is a technique that can be used to visualize the internal structure of materials. Recent developments in high resolution X-ray tomography allowed three dimensional characterization of porosity [13–15]. Most efforts in characterization of defect distribution in cast parts using X-ray tomography are limited to miniature parts with maximum size of about 3 mm. In large cast components some areas include defects of the order of 1 mm. To obtain the correct distribution of defects in large cast parts, it is essential to evaluate a large volume of these parts.

This paper shows how X-ray tomography can be used to obtain defect distribution in large parts. It also shows how such statistical results can be used to predict the fatigue behavior of large cast components parts.

The material used in this study is a ferritic ductile cast iron EN-GJS-400-18-LT. A large cast component was cut to smaller billets with $55 \times 65 \times 500$ mm^3 dimensions. These smaller parts were then machined to a final shape for fatigue tests. Figure 1(*a*) shows fatigue specimens machined from these billets. The dimensions of fatigue specimens are shown in Fig. 1(*b*). In large cast components some areas contain high density of large defects. Figure 2 shows that casting defects appear on a specimen surface after machining. X-ray computed tomography (CT) was used to obtain the distribution of defects in fatigue specimens. The obtained defect distribution parameters were imported to in-house developed finite element (FE) post-processor P•FAT in order to predict fatigue life distribution of these specimens. Detailed explanation of P•FAT will come in following sections.

X-Ray Computed Tomography

CT is a powerful nondestructive evaluation technique for producing two dimensional and three dimensional cross sectional images of an object. Characteristics of the internal structure of an object, such as dimensions, shape, inter-

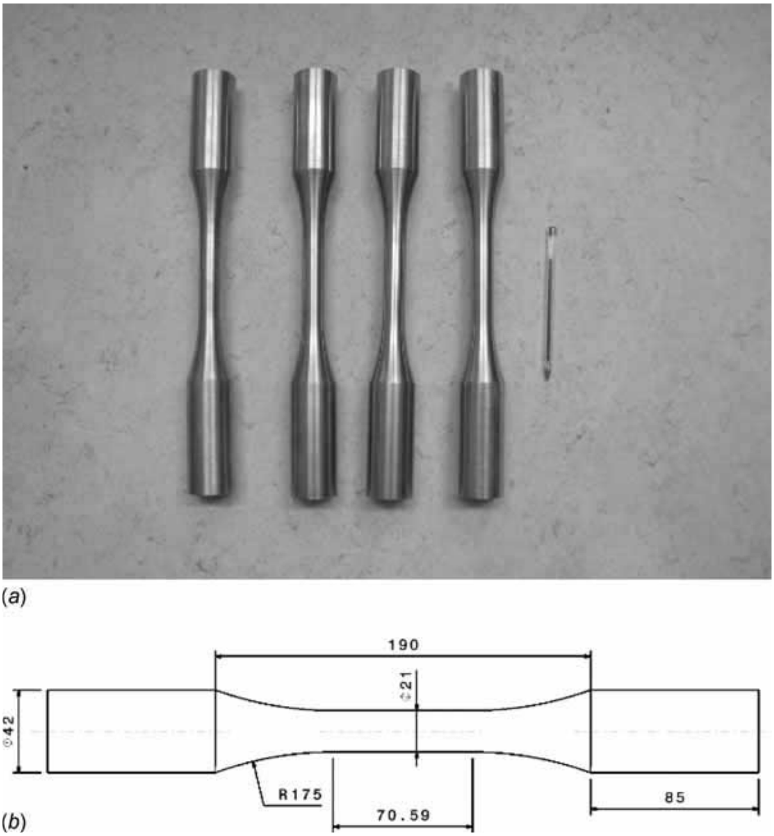

FIG. 1—(*a*) *Fatigue specimens.* (*b*) *Specimen's dimensions* (*all dimensions are in millimeters*).

nal defects, and density, are readily available from CT images. Figure 3 [16] shows a schematic of a CT system.

The test component is placed on a turntable stage that is between a radiation source and a detector system. In the simplest approach, planar X-rays pass through a slice of specimen and detector registers a CT image. Turntable stage rotates the specimen, and the process of registering CT images repeats for several different directions and produces the set of CT images. The intensity of the X-rays is measured before they enter the specimen and after they pass through it. Scanning of a slice is complete after collecting the intensity measurements for a full rotation of the specimen. The specimen is then shifted vertically by a fixed amount, and the entire procedure is repeated to generate additional slices.

The turntable and the imaging system are connected to a computer so that X-ray images collected can be correlated with the position of the test component. Specialized computer software makes it possible to produce three dimensional cross sectional images of the test component using CT images.

In this research X-ray CT has been used to obtain the three dimensional

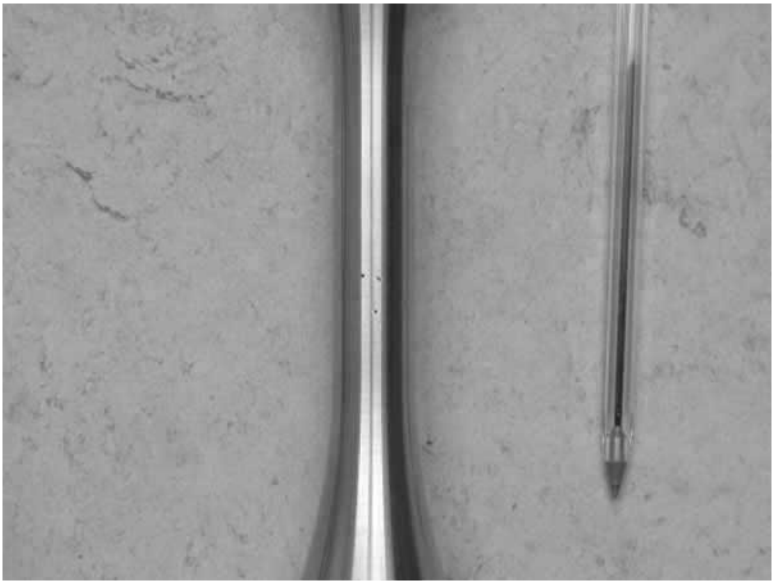

FIG. 2—*Casting defects appear on a specimen surface.*

distribution of defects in a fatigue specimen shown in Fig. 1. CT has been done for specimen gage section plus transition area. The chosen energy was 320 keV. The parameters were set so that it was possible to detect defects with dimensions larger than 0.1 mm. The volume of material investigated with this technique was about 100 000 mm^3. The results shown here, to the authors' knowledge, are the first published data on the use of X-ray CT to obtain the defect distribution in large specimens. Almost all published data are limited to miniature specimens with maximum 3 mm dimensions.

The VGStudio Max software was used for three dimensional visualization of the data. Using post-processing CT software, it is possible to obtain center position of defects, sizes of bounding box encapsulating defects, defect volume,

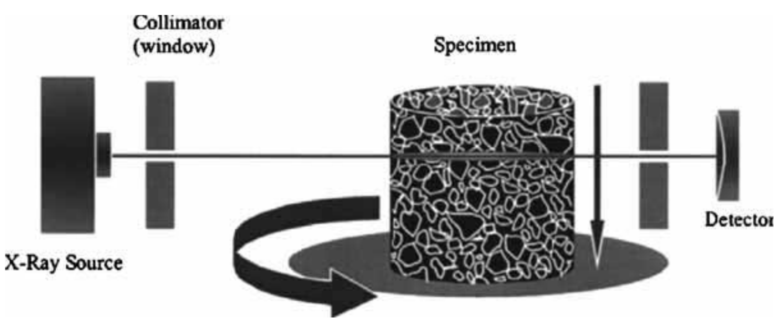

FIG. 3—*Schematic of a CT system.*

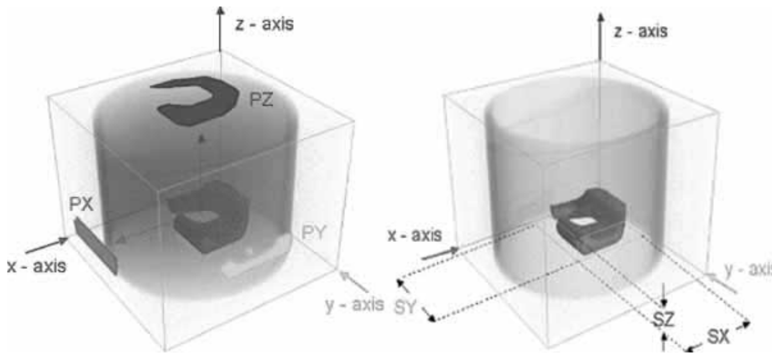

FIG. 4—*Some of the parameters that can be obtained by post processing CT data.*

surface of the defect, and the surface area of the defect projected along each of the axes of the selected coordinate system. Figure 4 [17] shows these parameters.

Defect Characterization

Figure 5(*a*) shows a view of defects detected by CT in a fatigue specimen. Figure 5(*b*) shows a three dimensional view of the classified defects in the centre region of the specimen.

In order to characterize defects, two parameters have been calculated from the measured volumes and surface areas of defects: An equivalent size (diameter of a sphere of same volume) and a sphericity parameter (the sphericity of a particle is the ratio of the surface area of a sphere with the same volume as the given particle to the surface area of the particle; one for a perfect sphere and close to zero for very tortuous shapes). The evolution of both parameters is shown in Fig. 6. From this figure, it can be seen that the sphericity diminishes as the size grows. This result can be explained with regard to the geometrical environment during the pore formation. This material was cut from a large cast component. In these types of components, shrinkage pores are dominant defects. Shrinkage pores appear at the end of solidification and have to grow between the dendrite arms network. Thus the growth of large pores is hindered by the dendrites, and the resulting shape is tortuous (low sphericity).

Figures 5(*b*) and 6 show that two or more populations of pores co-exist in the material. "Group A" exhibits a weak correlation between size and sphericity. Those pores correspond very probably to micro-shrinkages, which appear at the end of the solidification. "Group B" shows a strong correlation between size and sphericity: The larger the size, the lower the sphericity.

They correspond to pores appearing during the whole solidification process. Their growth is geometrically hindered by the solidifying dendrites, and these results, for the larger ones, in a very tortuous shape (low sphericity).

Figure 6 shows that there may be the third population of defects. It is difficult to judge it by the current information. In future works the density of defects will be available, and it will be easier to characterize defects.

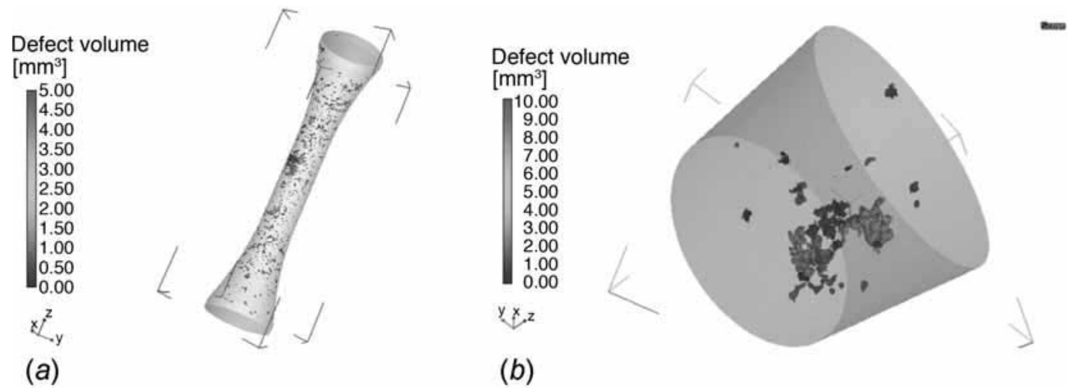

FIG. 5—(*a*) *Defects detected by CT in fatigue specimen.* (*b*) *Three dimensional view of the classified defects in the centre region of the specimen.*

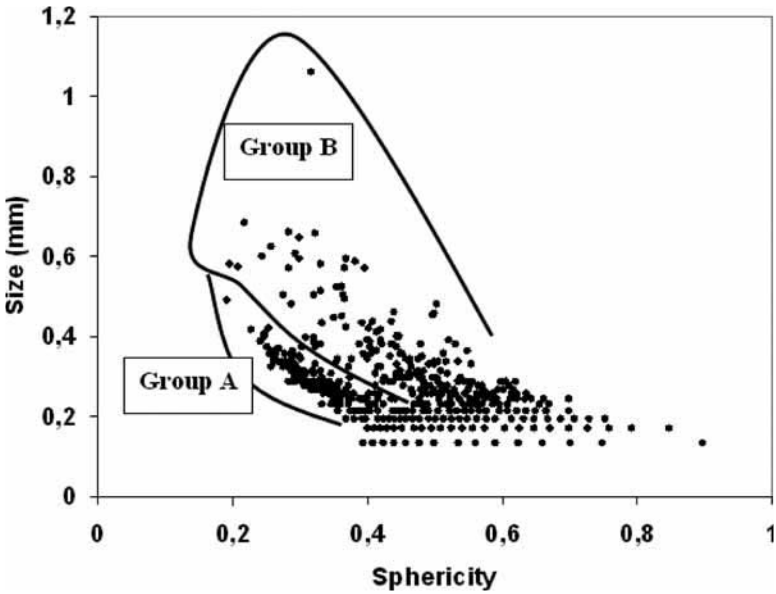

FIG. 6—*Size sphericity diagram.*

Determination of defect size distributions and the number of defects per unit volume is a prerequisite for modeling the fatigue behavior. In this research for post-processing the CT results, defects are considered to have spherical shape. To draw the defects distribution, the defect's diameter is required. Murakami [9] showed that the fatigue limit is correlated with the morphology of the defects. After his studies, he showed that the most relevant parameter is the square root of the area of defect. So the square root of the defect area perpendicular to the maximum principal stress axis is used to characterize defect diameter. It was found that size distribution of defects was well described by generalized extreme value distribution. It can be expressed by following equation:

$$f(x;\mu,\sigma,\xi) = \frac{1}{\sigma}\left[1+\xi\left(\frac{x-\mu}{\sigma}\right)\right]^{(-1/\xi)-1}\exp\left\{-\left[1+\xi\left(\frac{x-\mu}{\sigma}\right)\right]^{-1/\xi}\right\} \qquad (1)$$

where:

ξ, σ, and μ = shape parameter, scale parameter, and location parameter, respectively.

Figure 7 shows distribution of the square root of the defect area perpendicular to the specimen axis. ξ, σ and μ were determined by fitting the above equation to the square root of the defect's area perpendicular to the specimen axis. The inspected volume V_0 by X-ray CT is about 100 000 mm^3, and the number of defects larger than 0.1 mm detected by X-ray CT is about 1000, so the expected number of defects per unit volume is $V/V_0 = 0.01$. Table 1 shows these parameters.

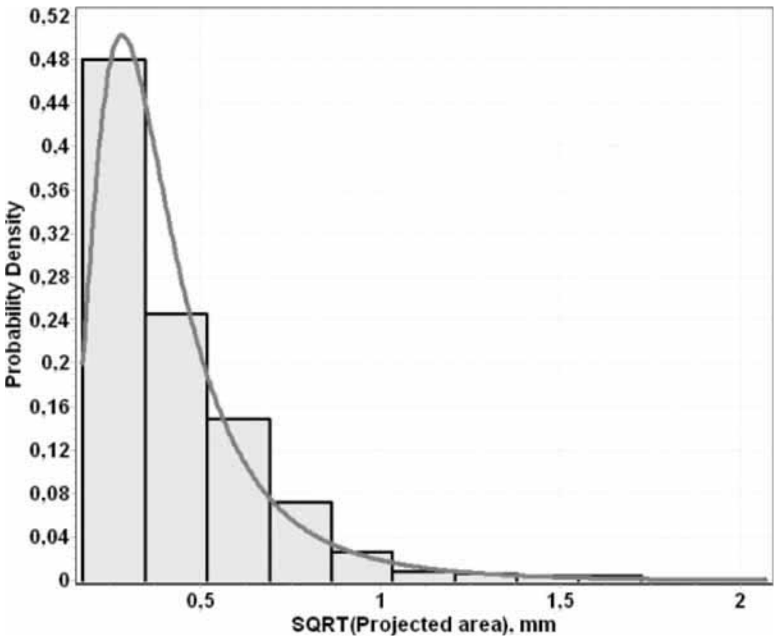

FIG. 7—*Distribution of square root of defect area perpendicular to specimen axis.*

The obtained distribution parameters were given to in-house developed FE post processor P•FAT in order to predict fatigue life distribution.

P•FAT **Finite Element Post Processor**

P•FAT is designed as a stand alone FE post processor with the component geometry and stresses given by a standard FE program. Data needed for the

TABLE 1—*Material properties used in simulations, EN-GJS-400-18-LT.*

Defect size shape parameter ξ	0.25961
Defect size scale parameter σ (mm)	0.13019
Defect size location parameter μ (mm)	0.31091
Expected number of defects per unit volume of material, $1/mm^3$	0.01
Crack growth exponent m	4.64
Crack growth constant C (MPa, m)	6.36×10^{-14}
Threshold stress intensity factor range ΔK_{th} (MPa$\sqrt{m}$)	8.5
Stress ratio for the threshold stress intensity factor range and crack growth constant, R	0.1
Walker exponent γ	0.44

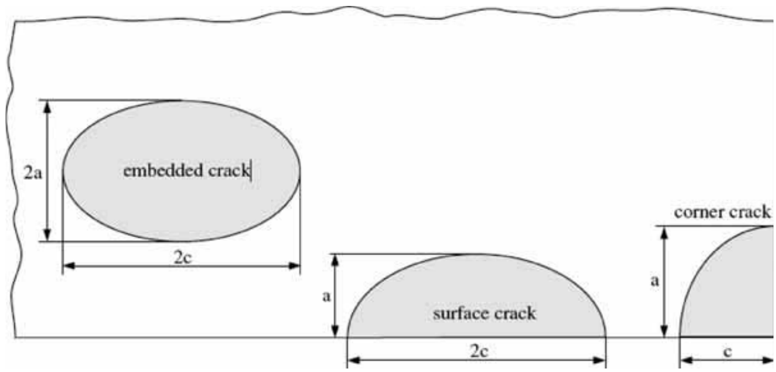

FIG. 8—*Crack configurations implemented in the finite element post processor.*

computation are nodal coordinates, element topology, and stresses. It has been developed to perform predictions of crack growth in arbitrary three dimensional components. It supports the simulation of both a single crack like defect that can be inserted into the component at a desired location (single defect module) and randomly inserted crack like defects (random defect module). The FE post processor uses a short crack model to determine the crack growth rate. The reader is referred to Ref 18 for the numerical aspects of the crack growth modules.

The defects are considered to be crack like, and the number of cycles required for a given defect to become critical is determined. The crack like defects are assumed to grow on the plane of maximum principal stress.

Weight functions [19], together with the stress field of the crack free component, are used to compute the required stress intensity factors. Generally, the direction of maximum principal stress in the uncracked component changes as the crack grows on a specific plane. In current version of P•FAT, the change in the crack growth direction is neglected. Generally, this is a good approximation as long as the crack is small compared with the dimensions of the component, i.e., for a large fraction of the fatigue life.

The crack surface is automatically meshed with plane elements. Subsequently, numerical integration (Gauss quadrature) is performed for determining the stress intensity factor at several locations at the crack front. For each incremental step, this process repeats itself: The crack surface is re-meshed, and updated stress intensity factors for the current crack are obtained. The program also updates the location of the crack front relative to the free surfaces. Hence, if the crack grows through the component surface, the crack is regarded as a surface crack or a corner crack (see Fig. 8). Failure of a component occurs when the crack has reached a predefined size, or if the stress intensity factor K has reached the fracture toughness K_{1c}.

In single defect module of P•FAT, it is possible to insert a single crack in component and compute the fatigue life. Also it is possible to import the center and dimension of defects into P•FAT, find the worst case defect, and compute fatigue life.

Due to the limited volume of material that can be examined by inspection methods, the number and size of defects in a large cast part have to be estimated by statistical analysis. P•FAT uses different approaches based on statistics of extremes for estimating the sizes of large defects in a large volume from those of a small volume [20–22]. This gives the capability to predict the fatigue life of large cast components, which may weigh 25 tons or more, based on defect distributions obtained for small parts of them.

A reference volume, V_0, is inspected for defects. From the inspection the number of defects and the sizes of these are obtained. A statistical distribution is fitted to the defect size data. This distribution is used for performing an extrapolation outside the observed defect size range. One of the three extreme value distributions, i.e., Gumbel, Frechet, or reversed Weibull, are often used since they are the limiting distributions for the largest defect. It can be shown that the probability of having a larger defect than found in the inspected volume will increase as a power function. The exponent of the power function is the fraction of the considered volume V to the reference volume V_0. The basic reason for this is that the expected number of defects will increase with the volume fraction V/V_0.

The considered component has a volume of V and is discretized into a sufficiently fine mesh to obtain convergence in the stress field. For each of the elements, the number of defects is found by drawing from a Poisson distribution. The Poisson distribution is formulated to depend on the element volume. The expected number of defects in the whole component is V/V_0 times that in the reference volume. The location of a defect within an element is obtained by drawing from a uniform distribution. The size of each defect is obtained by drawing from a statistical distribution with parameters obtained from the inspection of the reference specimen. It should be noted that the above procedure assumes statistical independence. This means that the number of defects in a given element is independent of the number of defects in any other element. Also, the location and size are assumed to be independent. All drawn defects are assumed to be penny-shaped cracks with a radius equal to the drawn defect size.

The main steps for obtaining the fatigue life distribution of a component can be summarized as follows:

(1) Develop a three dimensional FE model and perform a stress analysis of a component using a standard FE program, such as ABAQUS, ANSYS, or NASTRAN.
(2) Drawing defects inside the part.
(3) Calculate the maximum principal stress for all defects.
(4) Perform fatigue crack growth calculations.
(5) Repeat steps (2)–(4) for a large number of nominally equal components to obtain the fatigue life distribution of the component.

By repeating the foregoing analysis for a large number of nominally equal components (Monte Carlo simulation), the fatigue life distribution of the component is obtained. Thus, the designer will be able to find the probability of fatigue failure.

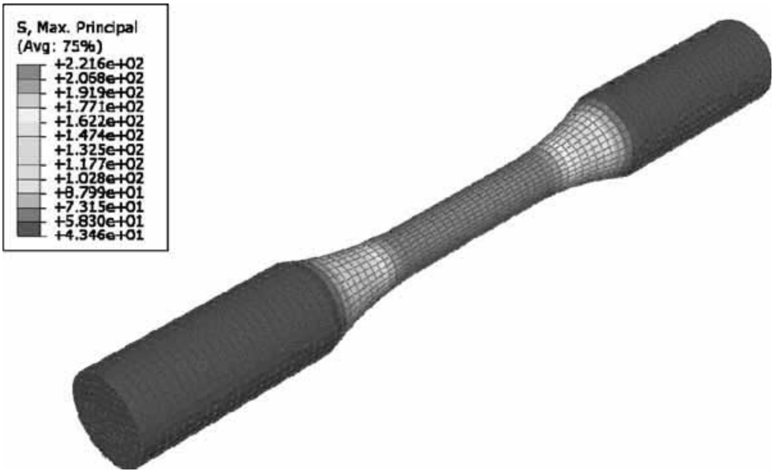

FIG. 9—*Stress distribution in fatigue specimen.*

Fatigue Life Prediction

When performing a Monte Carlo simulation for obtaining the fatigue life distribution of a component, one must generally perform a crack growth analysis of all defects located in each one of the nominally equal components. Since a fatigue crack growth calculation is a computer intensive task, it would be of interest to see whether it is possible to directly identify the life-controlling defect from the stress field and the initial crack growth rate. If this is possible, one could greatly reduce the simulation time. A crude simplified defect selection procedure has been implemented in the FE post processor.

Non-propagating defects are removed from the component by means of the Kitagawa–Takahashi diagram [23]. The remaining defects are sorted based on their initial crack growth rate. In order to determine the life-controlling defect, the stress field in the proximity of the defect must be taken into account. This is

FIG. 10—*Example of generated defect distribution.*

TABLE 2—*Defect-life data.*

Specimen Number	Number of Critical Defects	Initial Diameter of Life-Controlling Defect (mm)	Predicted Life
1	180	1.594 806	270 460
2	182	1.640 984	142 046
3	187	2.563 34	178 659
4	187	2.459 08	123 846
5	162	1.896 266	201 772
6	184	1.737 056	238 788
7	190	1.612 636	212 910
8	181	1.386 972	277 737
9	174	2.084 86	229 723
10	165	2.781 24	103 432
11	151	2.008 22	194 922
12	198	2.2003	190 326
13	198	2.424 86	136 669
14	174	1.851 154	271 178
15	169	1.743 486	137 868
16	200	1.553 418	321 125
17	176	2.067 32	241 429
18	176	1.422 64	208 702
19	179	1.257 162	320 214
20	201	2.372 04	148 779

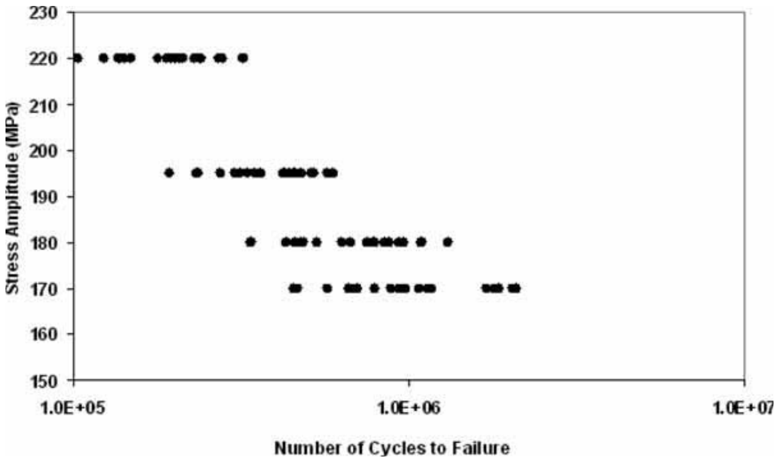

FIG. 11—*Predicted fatigue life distribution.*

done by using a crude correction of the initial crack growth rate with respect to the stress gradient acting on the crack surface. The method is described in Ref 24.

The fatigue specimen was modeled in ABAQUS. A reference axial load was applied to fatigue specimen. Table 1 shows material properties used in simulations. Figure 9 shows stress distribution in fatigue specimen. FE model was imported in P•FAT. Based on defect distribution parameters obtained in the above sections, P•FAT generates defect distribution in the specimen (Fig. 10). In order to obtain full distribution of fatigue life for this kind of specimen, four stress levels were used. For each stress level, P•FAT drew defect distribution for 20 specimens and calculated fatigue life.

Table 2 shows "number of critical defects," "diameter of life-controlling defect," and the "predicted life" for each of these 20 specimens at 220 MPa stress amplitude.

The obtained fatigue life distribution is shown in Fig. 11. The fatigue limit for EN-GJS-400-18 is about 195 MPa [25]. Figure 11 shows the effect of defects on decreasing fatigue life of this material.

Conclusion

High resolution X-ray CT was used to characterize defect distribution in a large EN-GJS-400-18-LT specimen. This specimen has been cut from a large cast component. The FE model of the specimen was prepared by ABAQUS and imported in FE post-processor P•FAT. Based on the defect distribution obtained by X-ray CT, the fatigue life distribution for modeled fatigue specimen was predicted by P•FAT at different stress levels. The effect of defect distribution on fatigue limit of EN-GJS-400-18-LT was obtained.

Acknowledgments

The writers would like to acknowledge financial and technical support by Fe-VIND, a project under the auspices of the Research Council of Norway. In particular, thanks are due to Siemens Wind Power AS, Denmark, for making available test material from rejected wind turbine components. The writers would also like to thank Dr. A. Wormsen for enhancing the P•FAT Random Defect module. The X-ray CT investigations were carried out by Mr. M. Mathes, ACCESS, Aachen.

References

[1] Clement, P., Angeli, J. P., and Pineau, A., "Short Crack Behavior in Nodular Cast Iron," *Fatigue Fract. Eng. Mater. Struct.*, Vol. 7, 1984, pp. 251–265.
[2] Palin-Luc, T. A., Lasserre, S. A., and Berard, J.-Y. B., "Experimental Investigation on the Significance of the Conventional Endurance Limit of a Spheroidal Graphite Cast Iron," *Fatigue Fract. Eng. Mater. Struct.*, Vol. 21, 1998, pp. 191–200.
[3] Nadot, Y., Mendez, J., and Ranganathian, N., "Fatigue Life Assessment of Nodular Cast Iron Containing Casting Defects," *Fatigue Fract. Eng. Mater. Struct.*, Vol. 22, 1999, pp. 289–300.
[4] Tokaji, K. and Ogawa, T., "Fatigue Life Distribution and Its Simulation in Spheroidal Graphite Cast Irons," *Mater. Sci. Res. Int.*, Vol. 2, 1996, pp. 39–45.
[5] Yaacoub Agha, H., Agha, A., Béranger, S., Billardon, R., and Hild, F., "High-Cycle Fatigue Behavior of Spheroidal Graphite Cast Iron," *Fatigue Fract. Eng. Mater. Struct.*, Vol. 21, 1998, pp. 287–296.
[6] Ting, J. C. and Lawrence, F. V., Jr., "Modelling the Long Life Fatigue Behavior of Cast Aluminium Alloy," *Fatigue Fract. Eng. Mater. Struct.*, Vol. 16, 1993, pp. 631–647.
[7] Skallerud, B., Iveland, T., and Härkegård, G., "Fatigue Life Assessment of Aluminium Alloys with Casting Defects," *Eng. Fract. Mech.*, Vol. 44, 1993, pp. 857–874.
[8] Couper, M. J., Neeson, A. E., and Griffiths, J. R., "Casting Defects and the Fatigue Behavior of an Aluminium Casting Alloy," *Fatigue Fract. Eng. Mater. Struct.*, Vol. 13, 1990, pp. 213–227.
[9] Murakami, Y., *Metal Fatigue: Effects of Small Defects and Nonmetallic Inclusions*, Yokendo, Tokyo, 1993.
[10] Shi, G., Atkinson, H. V., Sellars, C. M., and Anderson, C. W., "Application of the Generalized Pareto Distribution to the Estimation of the Size of the Maximum Inclusion in Clean Steels," *Acta Mater.*, Vol. 47, 1999, pp. 1455–1468.
[11] Zhou, S., Murakami, Y., Beretta, S., and Fukushima, Y., "Experimental Investigation on Statistics of Extremes for Three-Dimensional Distribution of Non-Metallic Inclusions," *Mater. Sci. Technol.*, Vol. 18, 2002, pp. 1535–1543.
[12] Lee, P. D., Chirazi, A., Atwood, R. C., and Wang, W., "Multiscale Modelling of Solidification Microstructures, Including Microsegregation and Microporosity, in an Al–Si–Cu Alloy," *Mater. Sci. Eng., A*, Vol. 365, 2004, pp. 57–65.
[13] Buffière, J.-Y., Savelli, S., Jouneau, P. H., Maire, E., and Fougères, R., "Experimental Study of Porosity and Its Relation to Fatigue Mechanisms of Model Al–Si7–Mg0.3 Cast Al Alloys," *Mater. Sci. Eng., A*, Vol. 316, 2001, pp. 115–126.
[14] Marrow, T. J., Buffiere, J.-Y., Withers, P. J., Johnson, G., and Engelberg, D., "High

Resolution X-ray Tomography of Short Fatigue Crack Nucleation in Austempered Ductile Cast Iron," *Int. J. Fatigue*, Vol. 26, 2004, pp. 717–725.

[15] Verdu, C., Adrien, J., and Buffiere, J. Y., "Three-Dimensional Shape of the Early Stages of Fatigue Cracks Nucleated in Nodular Cast Iron," *Mater. Sci. Eng., A*, Vol. 483–484, 2008, pp. 402–405.

[16] Masad, E., Jandhyala, V. K., Dasgupta, N., Somadevan, N., and Shashidhar, N., "Characterization of Air Void Distribution in Asphalt Mixes Using X-ray Computed Tomography," *J. Mater. Civ. Eng.*, Vol. 14, 2002, pp. 122–129.

[17] *VGStudio MAX 1.2* (2004), Volume Graphics GmbH, D-69123 Heidelberg, Germany, http://www.volumegraphics.com last accessed Sept. 1, 2009.

[18] Wormsen, A., Fjeldstad, A., and Härkegård, G., "A Post-Processor for Fatigue Crack Growth Analysis Based a Finite Element Stress Field," *Comput. Methods Appl. Mech. Eng.*, Vol. 197, 2008, pp. 834–845.

[19] Fett, T. and Munz, D., "Stress Intensity Factors and Weight Functions," *International Series on Advances in Fracture*, Computational Mechanics Publications, Southampton, 1997.

[20] Coles, S., *An Introduction to Statistical Modeling of Extreme Values*, 3rd ed., Springer Series in Statistics, London, 2001.

[21] Anderson, C. W. and Coles, S. G., "The Largest Inclusions in a Piece of Steel," *Extremes*, Vol. 5, 2002, pp. 237–252.

[22] Anderson, C. W., de Mare´, J., and Rootzen, H., "Methods for Estimating the Sizes of Large Inclusions in Clean Steels," *Acta Mater.*, Vol. 53, 2005, pp. 2295–2304.

[23] Kitagawa, H. and Takahashi, S., "Applicability of Fracture Mechanics to Very Small Cracks or the Cracks in Early Stage," *Proceedings of the Second International Conference on the Mechanical Behavior of Materials*, Boston, MA, 1976, ASM, Metals Park, OH, pp. 627–631.

[24] Fjeldstad, A., Härkegård, G., and Wormsen, A., "The Influence of a Stress Gradient on the Growth of a Fatigue Crack," *9th International Fatigue Congress*, Atlanta, GA, 2006.

[25] EN1563:1997, 1997, "Founding—Spheroidal Graphite Cast Irons," European Committee for Standardization.

Reprinted from JAI, Vol. 8, No. 1
doi:10.1520/JAI102525
Available online at www.astm.org/JAI

Anssi Laukkanen,[1] *Kenneth Homberg,*[1] *Helena Ronkainen,*[1] *and Kim Wallin*[2]

Cohesive Zone Modeling of Initiation and Propagation of Multiple Cracks in Hard Thin Surface Coatings

ABSTRACT: Surface coatings are increasingly used to improve the tribological performance of advanced products. The novel coating deposition techniques offer numerous possibilities for tailoring surfaces with different materials and structures. The tribological contact of loaded surfaces is, however, a complicated system itself, and further complexity is introduced when functionally graded coating structures are considered or improvement of specific micro- and nanostructural features is pursued. Furthermore, the mechanisms of damage in such a system are from a modeling standpoint highly complex and to great extent remain an active and open field of study. The focus of the current work is in the numerical modeling of graded thin hard coatings on a plastically deforming metallic substrate when loaded by contact that is typically exhibited during a scratch test. A finite element approach is implemented wherein a coating crack initiation and propagation are modeled using cohesive zone formalism. The cracks are considered to initiate and propagate within the coating and also within the coating to substrate interface. The results demonstrate how an optimization of the coating structure can enhance and exceed the performance of simplistic traditional coated systems. The material parameters of the problem and their significance in terms of fracture and failure behavior are discussed. The results are compared to fracture mechanical analyses and experimental information regarding the problem under study.

KEYWORDS: coatings, cohesive zone modeling, finite element method, fracture toughness

Manuscript received June 1, 2009; accepted for publication October 21, 2010; published online November 2010.

[1] VTT Technical Research Centre of Finland, Espoo 02044, Finland.
[2] Academy of Finland, Espoo 02044, Finland.

Cite as: Laukkanen, A., Homberg, K., Ronkainen, H. and Wallin, K., "Cohesive Zone Modeling of Initiation and Propagation of Multiple Cracks in Hard Thin Surface Coatings," *J. ASTM Intl.*, Vol. 8, No. 1. doi:10.1520/JAI102525.

Introduction

Thin hard coatings are nowadays being increasingly utilized to improve the tribological performance of advanced products. Manufacturing of coatings has evolved due to the introduction of new coating deposition techniques, which enable tailoring of surfaces with differing materials and underlying structures. By introducing a very thin coating layer, the coefficient of friction and wear rate can be decreased by orders of magnitude.

The work on fracture toughness forms the baseline experimental understanding concerning the behavior of the coated system as well as all modeling efforts. A typical failure mechanism, or a precursor to a wear event, is fracture containing stages of crack initiation, propagation, and often interaction of multiple cracks forming crack fields of differing density. Thus, the development of wear models has, in addition to traditional continuum and meso-mechanics approaches, relied extensively on fracture mechanics. The fundamental problems then lie in the estimation of fracture toughness of the coupled coating-substrate system and in introducing a mechanistic description of the process of wear utilizing the fracture mechanical framework. The fracture toughness and the characteristics of thin hard coatings have been studied for example by Diao et al. [1] for TiN and Al_2O_3 coatings on a cemented carbide substrate and by Li et al. [2], Li and Bhushan [3], and Nastani et al. [4] to evaluate the fracture toughness of diamond-like carbon (DLC) coatings on a silicon substrate. Studies have been conducted while developing the characterization means for fracture toughness testing, as has been done, for example, by Ollivier et al. [5] by performing tensile tests and by Wiklund et al. [6] by four-point bending of TiN and CrN coatings on a steel substrate. Sriram et al. [7] carried out a finite element analysis (FEA) to assess the inter-dependencies between the characteristic problem parameters such as coating thickness and applied loading in a two-body contact while determining the crack driving force solutions represented by the J-integral. Chai [8] determined the stress intensity factor (SIF) solutions by using FEA for thin hard coating systems on a soft glass and polycarbonate substrate. The detailed FEA based fracture evaluation has been performed by Souza et al. [9] where a hard elastic film on an elastic-plastic substrate was studied with respect to coating and interface (adhesion) cracks. The results of this work emphasize the importance of treating the problem in a system-wide sense, the behavior of the coating not being comprehensible by focusing solely on properties of the coating, but rather on the strong coupling between the coating and the substrate to understand the resulting fracture process. The SIF based work has been performed by Malzbender et al. [10] to yield methods for fracture toughness determination on the basis of normal and tangential loading.

During the last ten or so years, the cohesive zone modeling (CZM) has gained significant ground in the modeling of crack initiation and propagation as a result of various highly differing micromechanisms of material damage. The CZM has its origins in the work of Barenblatt [11] and Dugdale [12], which by enabling the implementation of the ideas set forth by Griffith [13] to an elastic-plastic realm make it a widely applicable methodology. The CZM can be easily implemented irrespective of the methodology utilized in the numerical solution of the boundary value problem ranging from the finite element method (FEM) to methods better suited for moving boundaries, such as the extended FEM (XFEM) and mesh free methods. The traction-separation laws (TSLs) have been developed to suit the characteristic damage rates of various failure processes and work to further enhance and introduce new features to TSLs is ongoing. As most means related to the solution of the problem of a growing crack, the FEM implementations of CZM have and in many respects continue to suffer from numerous drawbacks. The problems of the FEM in handling the movement of a discontinuity are presented by de Borst in Ref 14, where a detailed dissection of issues with mesh bias, both with respect to initial mesh design as well as the inability to pose the decohesion process consistently, are discussed with respect to the means of eliminating the sources of error. In Ref 14 and in de Borst et al. [15], the ability of enriched methods, such as XFEM, to handle strong discontinuities in conjunction with CZM is emphasized. While the use of CZM has spread and the analyses have become ever more quantitative in their goals, the formulation of TSLs and their parameters gain ground. This is presented in Chen and Kolednik [16], where differing crack-tip constraint is shown to couple with TSL parameters for the ductile failure micromechanism of void initiation, growth, and coalescence. The linkage between damage mechanics models and TSLs can be viewed to tackle this aspect of TSL formulation as well, as presented by Tvergaard in Ref 17 for ductile crack propagation and fracture resistance behavior. Steps are taken in Ref 18 by Tijssens et al. for the assessment of fracture of concrete, describing both the applicability of FEM with embedded cohesive surfaces and application of TSLs suited for the brittle-like fracture behavior.

The CZM of strong discontinuities in the presence of weak discontinuities, such as various interface problems, is one of the strong application areas of CZM due to the existence of a weak discontinuity for prescribing the movement of the strong discontinuity, thus in many cases eliminating one of the problem areas in the determination of the crack path. The works in this field have focused to great extent in tackling the problem of adhesion (or delamination) or crack growth at an interface, and fewer works have dealt with cracking taking place also within the coating during a specific type of contact loading. Bosch et al. [19] worked with the coating and substrate delamination problem by deriving the cohesive zone (CZ) means that are able to include the mixed-mode fracture mechanical aspects of the problem. Their findings stated that an exponential TSL was able to capture the features of the mixed-mode decohesion process. The need for an experimental mixed-mode determination of fracture parameters was found apparent. The mixed-mode nature of the problem has also been identified by Freed et al. [20]. By focusing on the mixed-mode dependency of the interfacial fracture toughness, they were able to attain consistent results for ceramic clays. Hu et al. [21] worked with the delamination problems of diamond-coated cutting tools by using a CZM approach in an effort to resolve issues with poor adhesion performance and in doing so were able to deduce some of the characteristic dependencies between various problem parameters. Yan et al. [22] performed the CZ analyses of interfacial delamination of lead-zirconate-titanate (PZT) films and were able to identify the interface of a multilayer coating critical for adequate adhesive properties. The adhesive properties of thermal barrier coatings were investigated by Yuan et al. [23]. The crack propagation process and its dependencies were captured by the CZM modeling approach and enabled the study of specific interface fracture energies. Jansson et al. [24] carried out an extensive study for the determination of adhesive and cohesive fracture parameters of a thin hard coating on a polymer substrate. Their work focused on the evolution of cracking with applied loading and the development of the crack field and its density, and they were able to deduce the energy dissipation characteristics of the problem under study. Segmentation cracking has been studied by Bialas et al. [25], where detailed experimental in situ observations were combined to a CZM approach for a thermal barrier coating system. Their work focused as well on the interplay between segmentation cracking and delamination behavior, indicating how lower segmentation cracking fracture toughness couples with the adhesive behavior, particularly by alleviating the conditions driving interfacial crack initiation and propagation. Chandra et al. [26] assessed the problem of push-out in silicon carbide fiber reinforced titanium matrix composites. Their work rightly suggests that while most studies so far utilize solely the cohesive fracture energy and strength as the significant parameters in determining the characteristics of the fracture process, the description of damage rate can have a marketable impact whenever truly quantitative assessments are being made. The functionally graded aspect, which is ever present in real life coatings, has been studied by way of CZM by Jin et al. [27]. Their investigation of elastic-plastic crack growth in a ceramic-metal functionally graded material display how the material property gradients, both with respect to elastic-plastic and cohesive properties, affect the development of system fracture properties.

The current work addresses the failure processes of a coating-substrate system by performing the CZ analyses of a thin hard 2 μm thick TiN coating on a high speed steel substrate. The analyses are carried out when the coating-substrate system is undergoing a so called scratch test, where a diamond tip is slid on the surface with a progressively increasing applied load. Cracking is assessed both with respect to through coating as well as interface adhesive cracking utilizing a CZ approach. The numerical results are compared to the experimental findings and the results discussed, and the computations are found to be consistent with observed crack paths and behavior both with respect to coating cracking and interface adhesive failure. The problem of optimizing the coating characteristics with respect to crack initiation and propagation that caused failure is addressed by carrying out analyses where different gradient and multilayer structures are investigated. These results indicate how, by an appropriate tailoring of property gradients, an efficient and fracture resistant component can be attained by minimizing the interfacial mismatch and enhancing the interplay of the contact geometry induced loading and material property distributions.

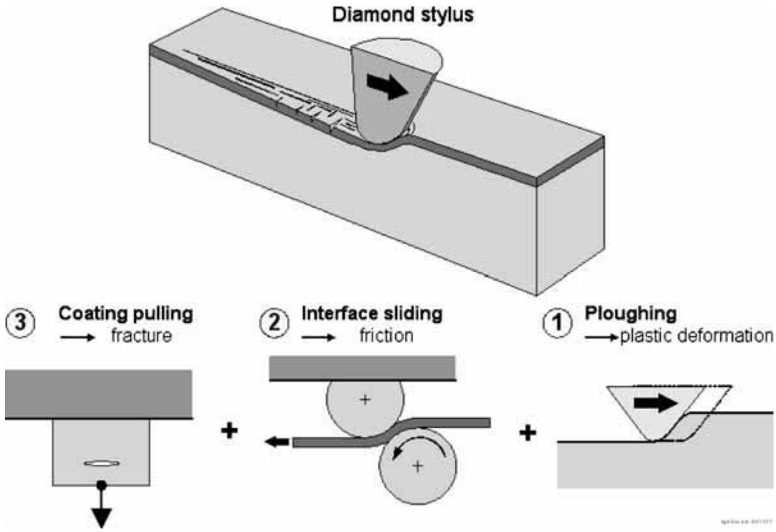

FIG. 1—*The schematic representation of scratch tester stylus drawn along a coated sample. The material loading and response can be divided into three stages: Ploughing, interface sliding, and pulling of the coating.*

Tribosystem and Cracking in Thin Hard Tin Coatings

Scratch Testing

The tribological system studied in the current work is that of a coated flat surface under contact by a sphere under an increasing normal load [28]. The scratch test configuration has been found suitable for coatings with thickness ranging all the way from 0.1 to 20 μm. The diamond tip usually possesses a Rockwell C geometry. A schematic representation of the scratch test is provided in Fig. 1, along with distinct phases when classified by deformation and fracture as commonly observed in such an experiment.

The failure of the coating occurs progressively by the increase of the normal load during the sliding of the stylus, and several distinct stages of cracking can be observed. These stages are presented schematically in Fig. 2. The lower loading range of the test is populated by cracking within the coating and typically through the coating itself, where the magnitude of the loading affecting the types of cracks are found. For lower loads, cracking at the edges of the contact groove is often found, while at a certain point of loading, the dominating form of cracking changes to parallel cracking within the scratch itself. While the previous stages are related primarily to cracking of the coating, interface failure such as coating chipping and spalling can be seen at higher loads, which eventually for a progressively increasing load lead to a complete interface adhesive failure and an exposed substrate. The loading in a scratch test is specified such that an initial preload of 5 N is used and a maximum load

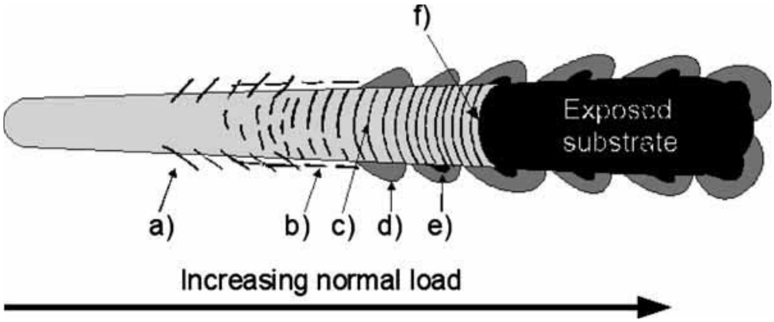

FIG. 2—*The surface cracking generated during a scratch test in a thin hard coating:* (*a*) *Angular cracks,* (*b*) *parallel cracks,* (*c*) *transverse* (*angled*) *cracks,* (*d*) *coating chipping,* (*e*) *coating spalling, and* (*f*) *coating breakthrough.*

of 50 N is specified with a loading rate of 100 N/min and speed of 10 mm/min, the final scratch length being 10 mm. For current materials, the test speed has not been witnessed to have an effect in the results.

Crack Fields and Experimental Results for 2 μm *Thick TiN Coating*

The scanning electron microscope (SEM) figures presenting the cracking of a 2 μm thick TiN coating with an elastic modulus of 300 GPa are presented in Figs. 3 and 4. Figure 3 pertains to 2 mm of sliding and Fig. 4 to 3 mm of sliding. In Fig. 3, the cracking occurs from the edge of the groove towards the symmetry plane of the problem, while in Fig. 4, the crack field extends over the entire groove width, the direction of sliding being from left to right. The crack densities for an array of different types of cracks have been attained by careful examination of figures such as Figs. 3 and 4. The scratch depth and width have been measured after testing by using surface profilometry to act as references for the FEA in order to verify that the numerical model captures the features of the contact problem accurately.

Fracture Toughness Evaluation

Previously, a methodology for calculation of fracture toughness out of scratch test experiments has been presented in Ref 29, where it is treated in more detail and compared to other solutions of similar application domain. This method is applicable for thin hard coatings on top of an elastic-plastic, softer, substrate as in current study as is utilized in the determination of fracture toughness.

In order to accurately capture the features of the problem in terms of estimation of the SIFs, as in the core of the methodology given in Ref 29, a weight function approach is utilized. This enables one to account for local variations of stress as a result of the solution of the contact problem and differing loading modes, as well as the densities of the crack fields. According to Ref 30, we can present the SIF by using a reference case in a two-dimensional domain as

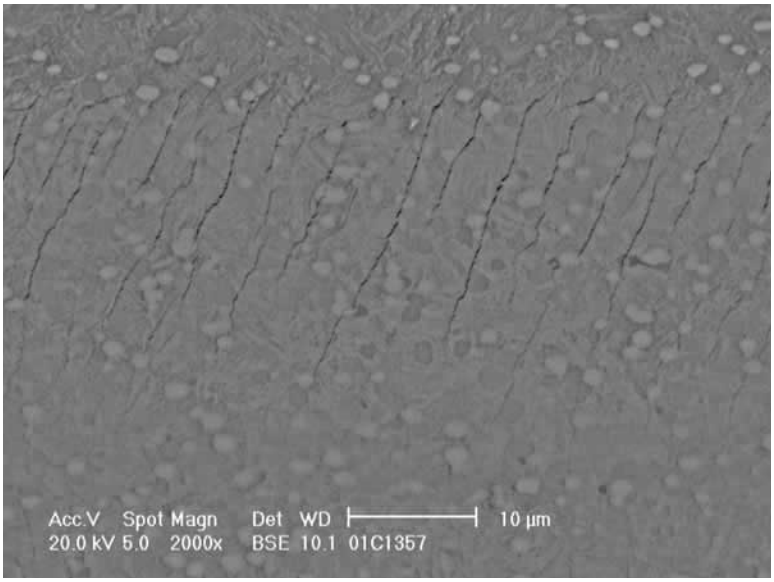

FIG. 3—*The SEM image of a crack field in a 2 μm thick TiN coating with a sliding distance of 2 mm, sliding direction from left to right. Scratch edge given by the white marker.*

$$K^{(2)} = \frac{E'}{2K^{(1)}}\left[\int_{\Gamma} \mathrm{t}^{(2)} \frac{\partial u^{(1)}}{\partial a} d\Gamma + \int_{\Omega} f^{(2)} \frac{\partial u^{(1)}}{\partial a} d\Omega\right] \tag{1}$$

where:

E' = stress field dependent elastic modulus,
(1) = denotes the reference solution,
u = displacement field,
t = traction vector,
f = body force vector,
Ω = solution domain, and
$\Gamma = \partial\Omega$.

The weight function is defined as

$$h = \frac{E'}{2K^{(1)}} \frac{\partial u^{(1)}}{\partial a}, \tag{2}$$

and by substituting Eq 2 to Eq 1, it can be written as

$$K^{(2)} = \int_{\Gamma} t^{(2)} h d\Gamma + \int_{\Omega} f^{(2)} h d\Omega. \tag{3}$$

Equation 3 can be generalized for mixed-mode loading and a three-dimensional (3D) solution domain. In Ref 29, the weight functions were determined for mixed-mode loading by using boundary element analysis and a dis-

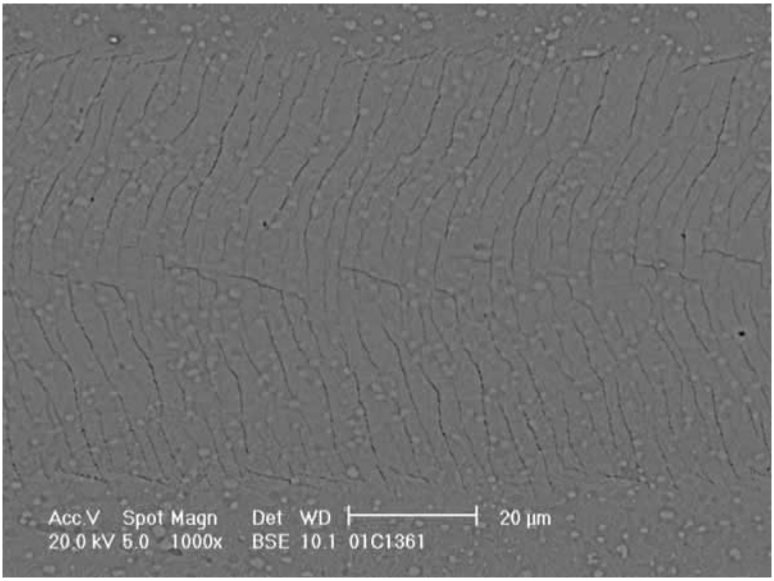

FIG. 4—*The SEM image of a crack field in a 2 µm thick TiN coating with a sliding distance of 3 mm, sliding direction from left to right. Scratch edge given by the white marker.*

placement correlation method was utilized in the computation of the SIFs. The analyses were carried out for straight through coating cracks (Fig. 4, center of scratch), crack oblique within the groove with respect to the scratching path (Fig. 4, angular cracks within the scratch), cracks oblique at the edge of the contact groove (all cracks of Fig. 3), and cracks parallel to direction of scratching at the edge of the contact groove. The crack orientation, density of crack field, crack location within crack field, load biaxiality, and loading mode effects on the SIF solution were considered. The weight functions were interpolated over the crack face in a numerical fashion to permit feasible computation of the crack driving force on the basis of FEA results by using a finite element interpolation function based scheme.

The crack densities for the through coating cracks were measured and along with the scratch test FEA results of Refs 29 and 31, the fracture toughness of the coating can be evaluated. The results for a 2 µm thick TiN with an elastic modulus of 300 GPa are presented in Fig. 5 and are used in the calibration of CZM parameters.

Numerical Analyses

Finite Element Scheme

The Abaqus 6.9-2 FEA software [32] with various user coded constitutive and numerical routines and other research software are used in carrying out the

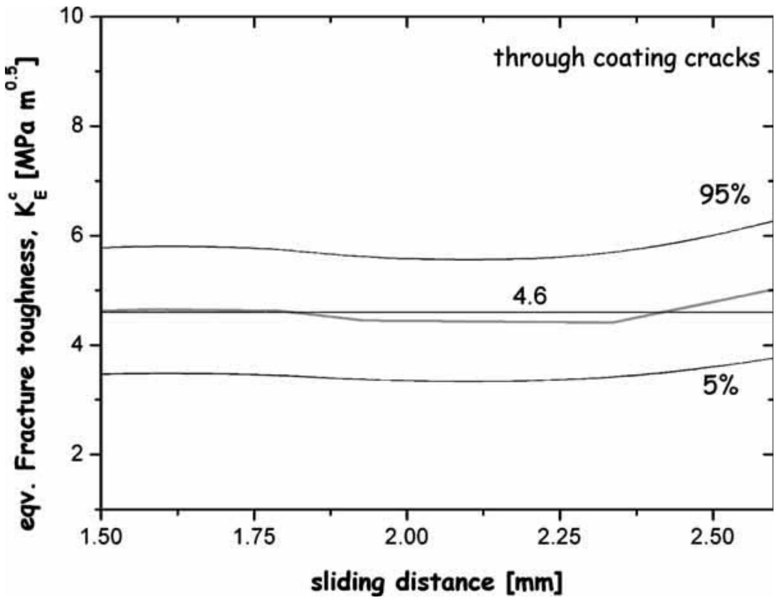

FIG. 5—*The fracture toughness of through coating cracks for 2 μm thick TiN coating on the basis of scratch test results.*

computations. The analyses are carried out by using a finite deformation measure of strain, Green's strain, and the Jaumann objective stress rate is applied. Full Newton's scheme is used in solving the finite element equation system, and tangential stiffness is updated during each iteration. Direct sparse solver is applied in the solution of the resulting linear system. In all analyses, the isoparametric eight-node 3D brick elements are utilized with reduced integration and hourglass stabilization. The substrate elastoplasticity is modeled by using a bilinear formulation of incremental plasticity utilizing isotropic hardening. The substrate material in the current study is of very low hardening type, and thus a bilinear model is adequate. Contact is enforced by a surface geometry based routine by using a finite sliding tracking approach. A penalty approach is used to control the enforcement process and a "hard" contact approach is adopted, i.e., no penetration with a finite contact stiffness is permitted. Frictional contribution is specified according to a Coulombian approach.

In order to improve the convergence of the finite deformation and sliding contact problem, with a mesh refinement needed for accurate CZM, an arbitrary Lagrangian Eulerian (ALE) approach was adopted. By constraining the mesh topology throughout the analysis but allowing the mesh move independent of the material contrary to a typical Lagrangian analysis, the mesh distortion can be reduced and the convergent results can be attained for exceedingly large contact deformations. An ALE technique is utilized in modeling the solution space ranging from the coating surface up to two times the coating thickness in the substrate.

Finite Element Contact Models

As a precursor to the CZM, a 3D contact model of the scratch test is build following the specifications of the previous chapter. The model comprises of an indenter, which is modeled as a linear-elastic material region, with the isotropic elastic modulus of diamond, 1.1 TPa. The tip radius is 200 μm. The underlying domain comprises of a coating layer of 2 μm and is followed by the steel substrate. The coating has a nominal elastic modulus of 300 GPa, the steel substrate has an elastic modulus of 200 GPa. The yield strength of the substrate material is 3500 MPa and its strain hardening coefficient is 20. These are modified accordingly when gradient structures and their impact is considered. The symmetry plane of the problem is exploited. The geometry model has dimensions of $10\,000 \times 150 \times 50$ μm^3 (length, width, and thickness). The end surfaces are fixed following the rigid posture of the scratch test.

The finite element mesh is constructed of bilinear eight-node brick element with hourglass control and reduced integration. Discretization is done in a problem dependent manner (differing CZ meshes are used depending on analysis variant). The mesh seed of the coating material domain is nearly constant and of the order of 0.2 μm, the underlying substrate layer has a linear gradient seed which in the end is meshed by using a sweep routine for faster coarsening. The surfaces are assumed ideal with respect to smoothness. The Coulombian coefficient of friction is given a constant value of 0.08 on the basis of scratch test measurements. Contact searches are carried out between the tip outer surface and the surface of the coating material domain.

Cohesive Zone Models

The nominal strains of a CZ element are computed as follows:

$$\epsilon_i^{CZ} = \frac{\delta_i}{t_{CZ}} \tag{4}$$

where:

δ_i = cohesive separation and

t_{CZ} = cohesive element initial thickness.

The initial thickness of CZ elements is given a finite value to aid convergence, and a value of 1 nm is used without physical basis. The elastic tractions are given by

$$t_i = k_i \cdot \epsilon_i^{CZ} \tag{5}$$

where:

k_i = elastic stiffness.

The elastic tractions are presented in a non-coupled manner, i.e., the shear tractions are decoupled from the normal traction of a cohesive element. The damage is considered to be a scalar type variable. The initiation of damage is modeled by using a simple quadratic criterion

$$\left(\frac{\langle t_n \rangle}{t_n^0}\right)^2 + \left(\frac{t_s}{t_s^0}\right)^2 + \left(\frac{t_t}{t_t^0}\right)^2 = 1 \tag{6}$$

where:

t_s = shear traction,

t_t = out of plane shear traction, and

t_i^0 = initiation value of traction i.

In the softening region when the criterion specified by Eq 6 is met, the tractions are computed according to

$$t_i = (1 - d)t_i|^{d=0} \tag{7}$$

where:

d = scalar damage.

Compressive loading leads to a linear response without damage. An effective displacement is defined as

$$\delta_m = \sqrt{\langle \delta_n \rangle^2 + \delta_s^2 + \delta_t^2}, \tag{8}$$

which is used under mixed-mode loading to describe the damage evolution, the initiation, and failure displacement are specified according to the effective measure of Eq 8. The mode-mixity is defined in terms of work done by the respective tractions

$$m_i = \frac{G_i}{G_k}, \tag{9}$$

where:

G_i = mode specific energy.

Damage evolution is modeled by using an exponential TSL

$$d = 1 - \frac{\delta_m^0}{\delta_m^f} \cdot \left(1 - \frac{1 - \exp\left(-\alpha \frac{\delta_m^f - \delta_m^0}{\delta_m^f - \delta_m^0}\right)}{1 - \exp(\alpha)}\right) \tag{10}$$

where:

α = failure rate parameter and

δ_m^f = cohesive element separation at failure, $d = 1$.

Four CZ parameters, elastic stiffness, initiation separation, failure separation, and damage rate parameter, need to be specified. As presented previously, the information available with respect to fracture mechanical behavior is the fracture toughness of the coating when through coating cracks are considered. The fracture energy can be expressed as

$$G_f = \int_{\delta_m^0}^{\delta_m^f} (1 - d)t_i|^{d=0} d\delta \tag{11}$$

which is utilized through its equivalence to the coating cracking fracture toughness. The initial linear stiffness of the CZ elements should in principle be infinite, but since this is numerically unattainable, a finite value three times the coating elastic moduli is used. The initiation of cohesive damage is specified to

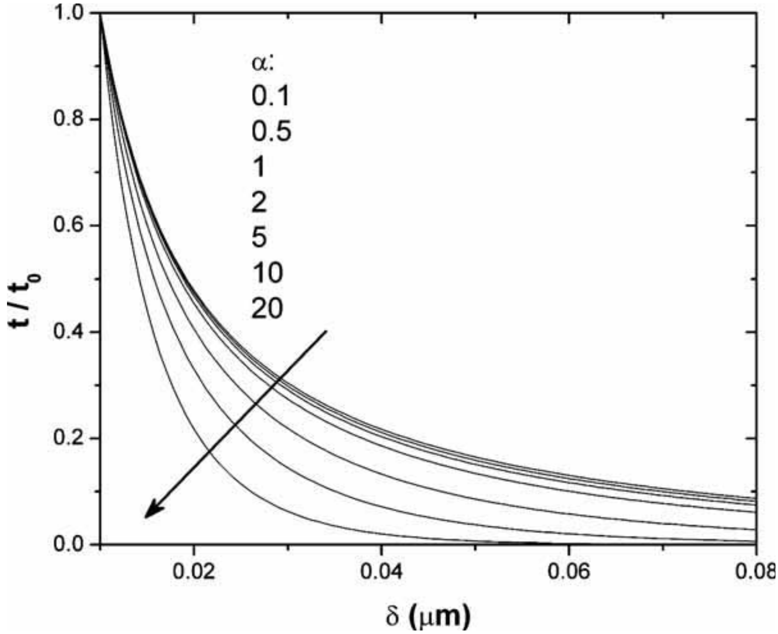

FIG. 6—*Exponential TSL for different values of the damage rate parameter.*

occur at the instance of substrate plasticity. By using Eq 11, the two remaining parameters are the rate term and the equivalent separation at failure. The rate term is specified such that it is feasible for a material to be failing essentially in a brittle manner. The exponential TSL for different rate is presented in Fig. 6. It is noted that for a brittle-like material, a high rate of damage would be preferable, and this information is utilized in fixing the value of the rate parameter, which on this basis is given a constant value of two. The exponential TSL in this respect appears a feasible tool in providing a high rate of damage and fairly quick softening. The separation at fracture is given a value which fulfills Eq 11. These values form the nominal set of TSL parameters; in order to reflect on their effects, further analyses with different parameter sets are carried out as well. This parameter set is calibrated on the basis of fracture toughness results for through coating cracks, and no other fracture toughness data is used. Thus, interface adhesive behavior is considered to be up to par with the parent coating material.

Three CZ model types are generated, all with bilinear brick like CZ elements the material oriented orthogonal to expected fracture path. The CZ elements are generated through the coating thickness and at the coating to substrate interface, motivated by the experimental observations that the crack initiation and propagation processes follow these two orientations quite meticulously. This alleviates some concerns with respect to solution sensitivity to mesh alignment, although a FEM solution has a number of issues in this respect no matter what. The number of CZ elements ranges from 7500 (CZ elements at coating to substrate interface) to 132 500 (CZ elements at both coating to substrate interface and through coating). The analyses focus on initiation and propagation of cracks through the coating and within the interface, and no material removal is considered. Since the contact problem does not lead to progressive cohesive element distortion in the same degree as, for example, typical fracture mechanical applications, the drawbacks related to accuracy in the modeling of the softening process may be somewhat alleviated. In the three CZM meshes, the CZ elements are positioned at the coating-substrate interface, through the coating, or both.

The analyses are carried out with a 3D model, but the results in the following are presented on the plane of symmetry. No mesh tie or related means were used in embedding the CZ elements to the continuum contact analysis, but in order not to decrease the rate of convergence the mesh topology was adjusted appropriately and the CZ elements were housed between standard continuum elements. Sensitivity analyses were carried out also modifying the TSL parameters and the structure of the coating. Since it is possible to tailor the coating structure, and often the manufacturing processes themselves by default lead to property gradients, a number of variants were analyzed in order to find structures able to withstand higher contact loads than solely homogeneous coatings. This was performed by specifying nodal material properties, which were interpolated to element integration points on the basis of element shape functions. Analyses were performed for a transition bond layer (softer layer between the coating and substrate at the interface), linear and nonlinear functional property gradient structures, and composite layered structures. Since only one set of TSL values can be calibrated out of the fracture toughness data, the sensitivity analyses were carried out by focusing on the constitutive properties of the coating, which again can be influenced by manufacturing means.

Numerical Results

Scratch Test Contact of a Coated Sample

The contours of the first principal and von Mises stress for scratch test contact without CZM are presented in Fig. 7(*a*) and 7(*b*). The figures display several features typical to contact when a thin hard coated layer is present. It is seen that within the coating there are essentially two maximum locations of the largest tensile stress, one local maximum in front of the contact, while a global maximum can be found behind the actual area under contact. The presence of these peaks can be understood by considering the contact geometry and the resulting bending in front and trailing the contact, as well as the tensile stress state imposed by the movement of the stylus. The existence of a typical area under the contact under compression is acknowledged.

Fracture Characteristics and Cohesive Zone Damage

Interface Cracking—First, the effects of failure of the interface layer are considered, i.e., the CZ elements are placed only at the coating-substrate interface. The first principal stress distribution for the experimented TiN coating is

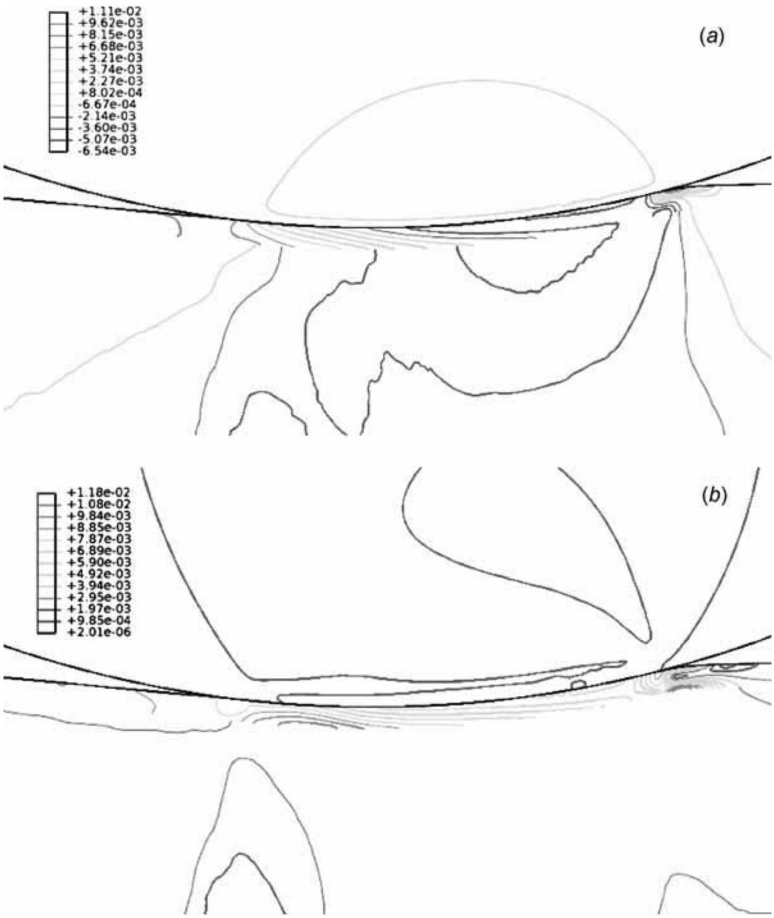

FIG. 7—*The contours of* (*a*) *first principal and* (*b*) *von Mises stress in scratch test contact without CZ elements* (*units: N and* μm).

presented in Fig. 8. The first variant is one with higher coating elastic modulus, 500 GPa. The second is one with lower, 100 GPa. The third variant deals with a fairly typical practical scenario, where a bond layer (transition layer) is placed between the coating and the substrate to decrease the material property mismatch and improve the adhesive properties. The bond layer thickness is 10 % of coating thickness, and it has an elastic modulus of 100 GPa. All situations correspond to an equal state of loading where the interface adhesion has been completely lost in the most severe of cases (the case with elastic modulus of 500 GPa has lost interface adhesion all around the contact tip). This is further depicted in Fig. 9, where the values of damage at the interface are presented. The evolution of damage during the contact process is presented in Fig. 10, the scalar damage initiating out of two locations and increasing in value during tip movement, ultimately leading to complete interface failure and spanning

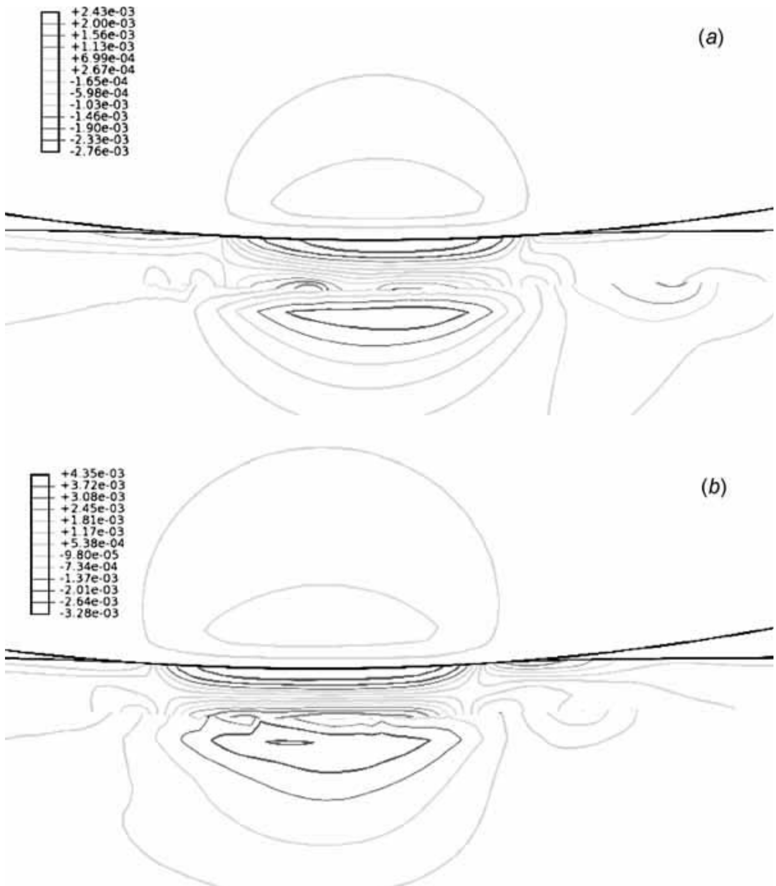

FIG. 8—*The contours of first principal stress in scratch test contact with CZ elements at* (*a*) *the coating-substrate interface with E=300 GPa,* (*b*) *the coating-substrate interface with E=500 GPa,* (*c*) *the coating-substrate interface with E=100 GPa, and* (*d*) *the coating-substrate interface with E=300 GPa and a bond layer with E=100 GPa and thickness of 10 % of the coating* (*units: N and μm*).

nearly the whole studied path. The increase in coating elastic moduli is seen to increase, as expected, the tensile stress state within the coating, while a decrease in coating elastic moduli does the opposite and alters the characteristics of damage in the system, such as its distribution (under displacement control loading as in our scratch test). These changes, however, do not produce an improvement in terms of interface fracture properties due to the resulting adhesive failure. Increasing the stiffness of the coating itself leads to high rates of damage, while the bond layer results are nearly identical to the reference analysis with an elastic modulus of 300 GPa. The softer layer, as expected, decreases the rate of damage significantly, and actually the adhesive failure initiates at a different location for a compliant coating, but it is then likely that a coating

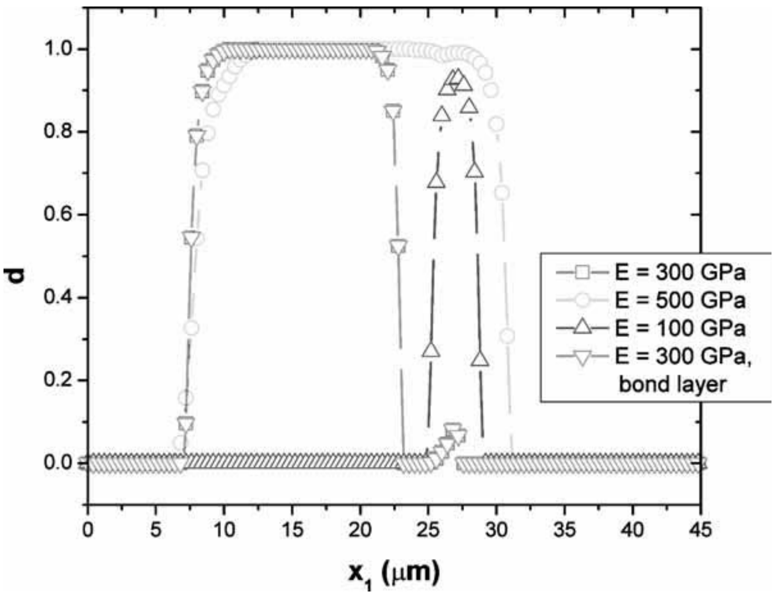

FIG. 9—*The values of scalar damage at different interface CZ analyses with an identical state of loading. The analyses for coatings with differing elastic modulus and one with a thin transition bond layer between coating and substrate.*

such as this one may not be adequate in terms of tribological performance. The bond layer, when being in thickness of typical order (10 %), is not seen to drastically change the CZ response. Thus, it seems likely that the bond layer needs to alter the TSL properties in order to be a factor in the softening process. The initiation of adhesive damage is shown to occur such that there are two separate crack-tips, both ahead and trailing the actual contact. The cracks link up as the contact process progresses leading to a macroscopic crack with dimensions about 20 times the coating thickness. It is noted that bridges may remain within the crack as a combination of stress relaxation and progressive movement of the stylus, i.e., the segmentation like nature often observed in the experiments appears plausible.

Through Coating Cracking—Second, through coating cracking is considered for two cases, one with a constant through coating material property profile and second with a gradient structure. Both have the basic identical set of TSL parameters deduced on the basis of coating fracture toughness information. The contour plots of the first principal stress are presented in Figs. 11 and 12, and the distribution of damage over the coating thickness of the first through coating crack is presented in Fig. 13. It is noted that the initiation of damage occurs when the coating is slightly ahead of the contact, and this is attributed to the prevailing tensile stress state within the coating at this region of contact. As seen in Fig. 13 however, the scale of damage done by this process near the coating-substrate interface is fairly minor, and only limited softening is com-

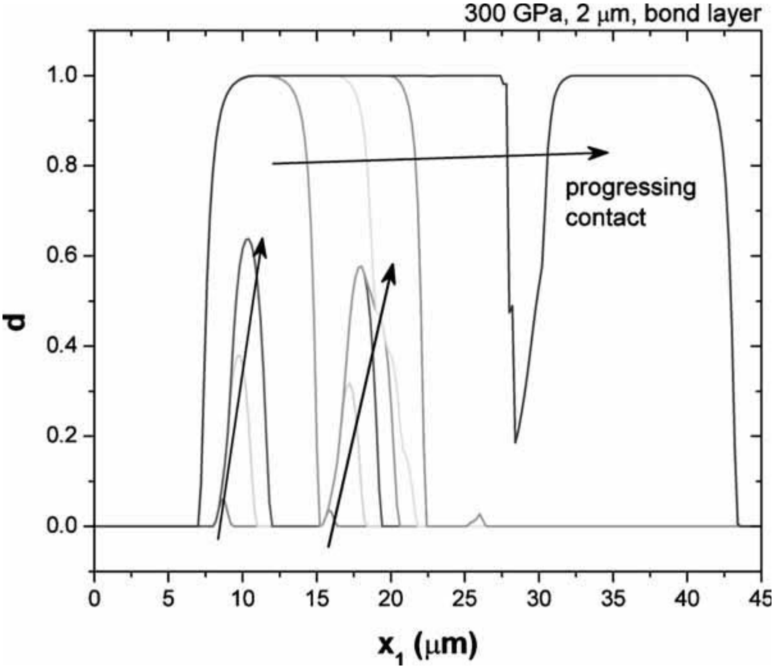

FIG. 10—*The evolution of damage for an interface crack during the scratch test from initiation of damage to ultimate interface failure for the model including a bond layer. As the tip moves, the contact process progresses, with the damage increasing and spreading at the interface.*

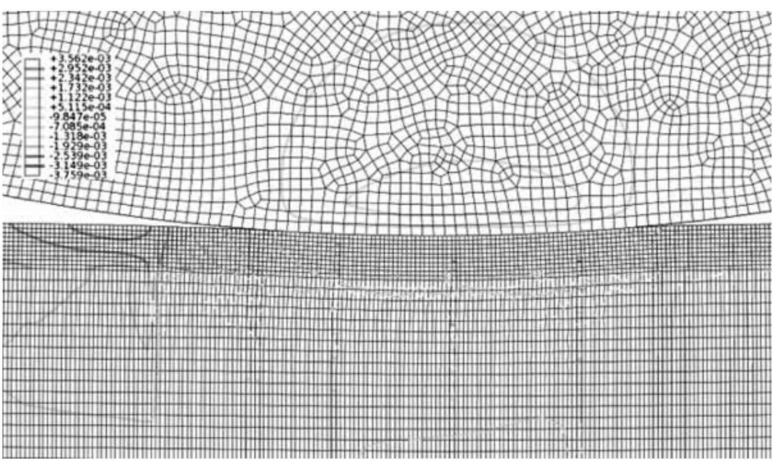

FIG. 11—*The contours of first principal stress in scratch test contact with CZ elements through coating (units: N and μm).*

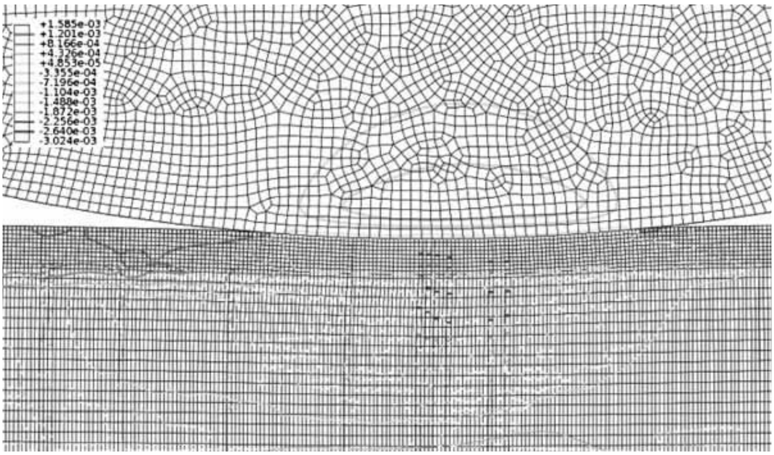

FIG. 12—*The contours of first principal stress in scratch test contact with CZ elements through coating and gradient material property distribution over coating (units: N and μm).*

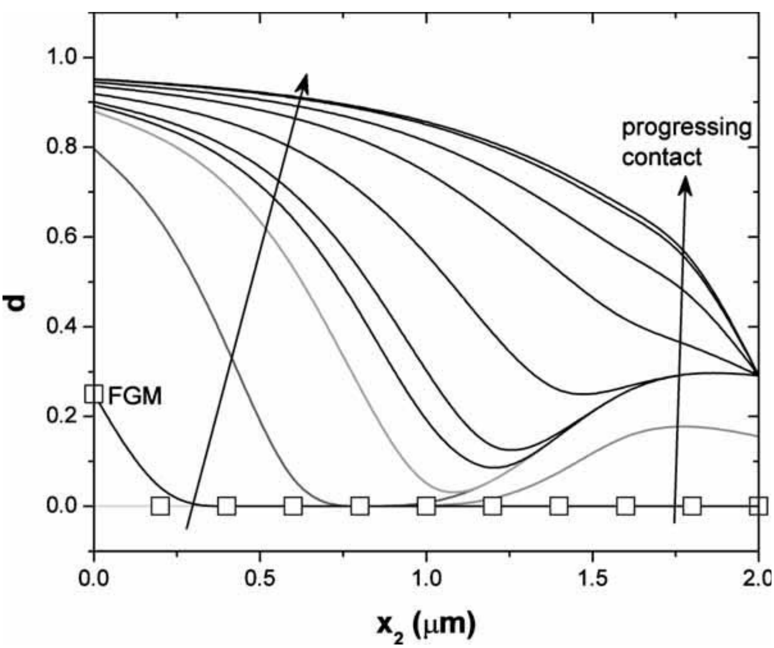

FIG. 13—*The evolution of scalar damage for a through coating crack during the scratch test from initiation of damage to through coating failure. Distribution of damage in gradient structure coating at the instance of failure in the traditional coating is also presented.*

puted. It does have an influence on the through coating stress distribution as seen in both Figs. 11 and 12. The final through coating fracture is seen to occur initiating at the surface of the coating when the contact has traveled over the point where crack initiation has occurred and is followed by its subsequent propagation. The surface tensile stress state, having both membrane and bending contributions biaxially, initiates the crack and in a swift manner propagates it through the entire coating.

In order to investigate the behavior of a graded coating and consider the "optimized" distribution of material properties within the coating, a gradient structure was analyzed. This structure was generated by affecting the properties, which can be tailored fairly easily by manufacturing means, i.e., the elastic modulus of the coating. The property distribution was given a range of 100–500 GPa, and TSL properties were not modified. The shape of the distribution was specified by following the results in Figs. 10 and 11 to redistribute the tensile stress in a more homogeneous manner through the coating thickness, essentially by trying to generate a coating with a "constant through thickness strain energy density." As such, softer surface and interface layers were generated with a stiffer center section, and the transitions between these layers were made as continuous as possible, the distribution of elastic modulus following in shape stress distribution (with the property range given above, which is obtainable via manufacturing processes). The results of this numerical experiment are shown in Fig. 13 where the damage in the gradient structure is compared to that of the single layer coating at the moment of failure in the latter one. It is seen that the gradient structure is able to avoid initiation of damage ahead of the contact, and the layer-like structure is able to homogenize the state of stress and deformation over the coating thickness, resulting in an improvement in performance.

Simultaneous Cracking—Third, the analysis case with both through and interface cohesive elements is considered. These analyses are a natural continuation since their interaction in the ultimate failure process appears quite evident on the basis of experimental findings. First, the effects of TSL parameters on crack formation are addressed via Figs. 14 and 15. These are the results of analyses where in Fig. 15, the TSL initiation parameters have been decreased by 67 % to yield easier crack initiation compared to Fig. 14, which houses the standard calibrated TSL parameters. The initiation criterion has been alleviated to one third, while the cohesive properties otherwise are retained (fracture energy is still preserved). The result is a crack growth through coating at a different stage compared to the analysis in Fig. 14, and the crack growth occurs already ahead of contact within the previously noted tensile stress peak. Since the initiation leads swiftly to through coating growth, the significance of crack initiation is emphasized in determining the integrity of the system since the fracture energy does not appear to be able to generate a crack arrest event in itself. The issue indicating how much the placement of CZ elements on both through coating and at the interface affects the outcome is addressed in Fig. 16, where damage values are presented with and without the adjoining elements. The results are presented such that they are comparable to results of Fig. 13, i.e., the highest damage values over coating thickness are from a state of iden-

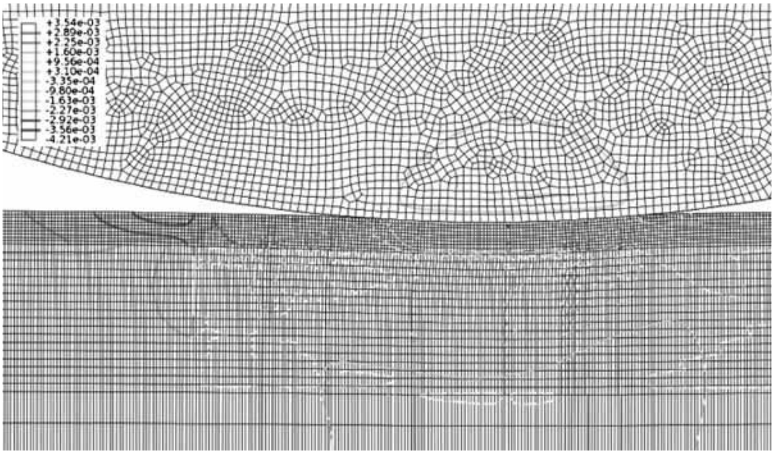

FIG. 14—*The contours of first principal stress in scratch test contact with CZ elements through coating and at the material interface* (*units: N and* μm).

tical loading. The results demonstrate that the introduction of the interface elements does affect the through coating crack growth, although not fundamentally but rather by decreasing the rate of damage slightly. These findings are further refined by Fig. 17 where the initiation is presented for a situation where a through coating crack has nearly grown through the coating. It is seen that the through coating cracks affect the interface behavior by adding to the loading exhibited by the interface CZ elements. However, it is seen that the

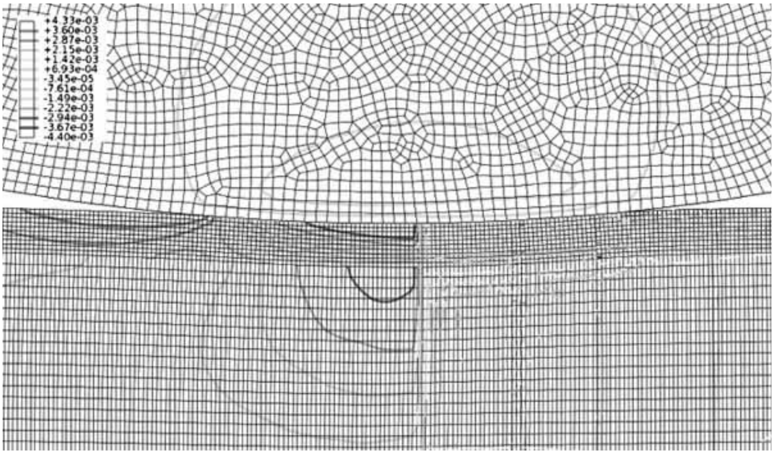

FIG. 15—*The contours of first principal stress in scratch test contact with CZ elements through coating and at the material interface with initiation resistance decreased to one third* (*units: N and* μm).

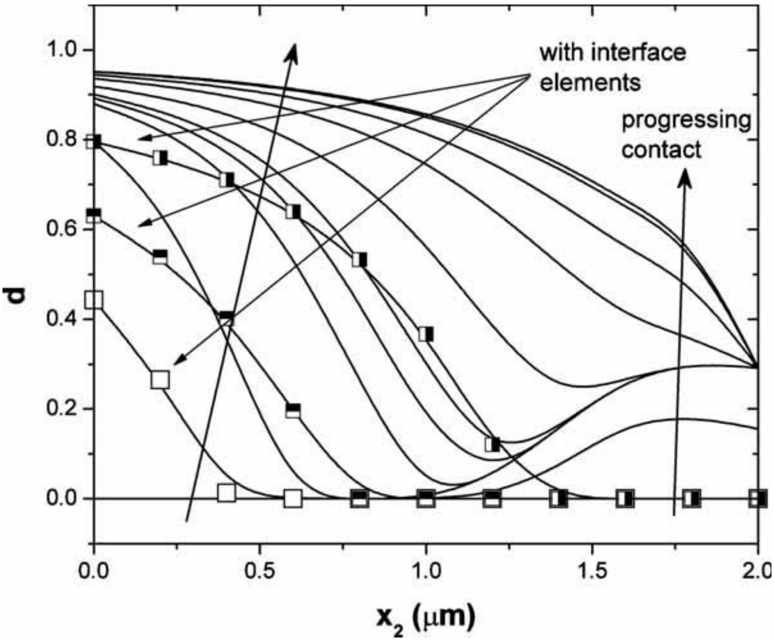

FIG. 16—*The effect of interface elements on through coating fracture behavior.*

through coating cracks at this stage of cracking do not lead to adhesive failure of the interface, but for that higher loading, such as in the interface analyses, is required.

The analyses with further gradient structures, retaining TSL properties, are presented in Fig. 18. The results are presented for a situation where a through coating crack has nearly grown through the whole coating. The results for the three different bond layer configurations and a linear gradient one are presented. It is found that by selecting either a discontinuous softer layer within the coating or near the interface, the rate of damage can be lessened. However, if this yields a decrease in TSL properties, as seen for the case labeled soft bond layer where an order of two decrease in initiation traction and fracture toughness were introduced, the changes in the stress and deformation states cannot be effectively exploited. Thus, cohesive properties need to be retained, but otherwise the other layer configurations appear promising. A soft functionally graded materials (FGM) layer with a low elastic modulus top was assessed as well, but the resulting compliant behavior prevented crack initiation altogether and the merits of this configuration are discussed as follows.

Discussion

Compliance with Experimental Findings

Fracture mechanical assessment of experimental data with respect to crack fields as well as their initiation has been performed for example in Refs 28, 29,

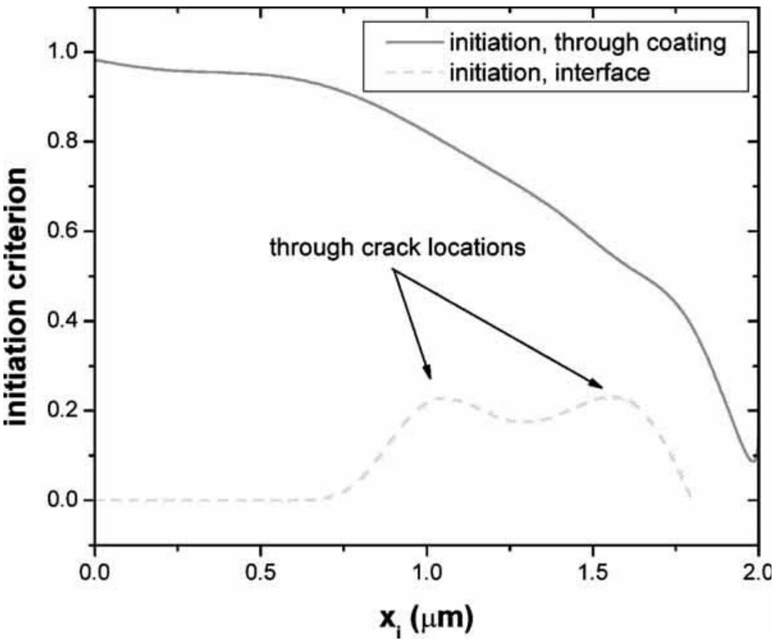

FIG. 17—*The coupling between through coating and interface cohesive elements when cracks have penetrated the coating.*

and 31. Although the micromechanical interpretations of the failure processes are in many respects still under study, some features can be identified with fair certainty. For thin hard coatings according to current understanding, the crack initiation process takes place at the tail region of the contact and immediately after the material has resurfaced from under the scratch test stylus. The experimental information, such as those presented in current study, suggest that through coating cracking is the first mechanism of failure, and loss of adhesion at the coating-substrate interface is not an active mechanism at this point. The CZM results support this statement, since with the TSL parameter sets compliant with experimental fracture toughness the results indicated that while an adequately high loading state has been generated as a result of the contact, the crack initiation and propagation occur in a swift manner through the coating thickness. The numerical results indicated some other possible avenues of failure. It was indicated that brittle coatings can go through the whole crack growth process already when subjected to the loading by an approaching stylus. This may also have a link to various observed chipping and spalling mechanisms of failure. Also, a detailed examination of initiation and damage profiles at different stages of stylus movement over a material point suggested, that the initiation process (and sometimes also the crack initiates) can and most likely occurs during the stage when the material is within the contacting region. The ultimate through coating failure occurs then when the location in question is subjected to the biaxial membrane and bending stresses at the contact trail.

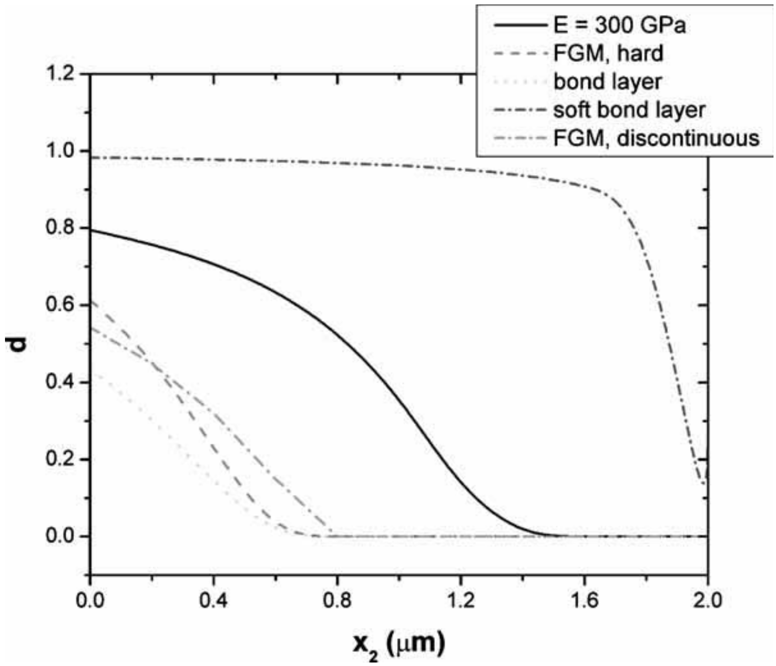

FIG. 18—*Comparison of damage distributions over coating thickness for different gradient structures.*

The CZM results indicated that the through cracking mechanism can occur fairly independently of the other noted process and appears to be the primary controlling mechanism, immediately leading to coating failure (when defined such that it refers to the existence of several through coating cracks) and during this process the interface exhibits damage, but not enough to result in complete interface failure. This most likely has to do with the contribution of the substrate material (available mechanisms of plastic deformation) and stress relaxation due to crack propagation within the coating, as well as the contact geometry. It is also worth noting the selected modeling scheme, since although different types of bond layers and gradient structures were introduced, further investigation of interface properties and material structures is needed. However, the results in terms of interface failure appeared to be in the right direction, since the order in which the fracture mechanisms appear is captured by the CZ approach, and through cracking is the first form of failure, which later in the scratch test turns into adhesive failure of the interface.

The comparison between the crack densities of experimental and CZM results is presented in Fig. 19. The CZM results have been extracted for the first through coating cracks out of different analyzed models with the 2 μm TiN with a 300 GPa modulus of elasticity. The comparison to experimental results is made difficult by the fact that "real" cracks tend to have a slight curvature and there are numerous crack types, which are difficult to handle with traditional FEMs. However, acknowledging these differences Fig. 19 does suggest that the

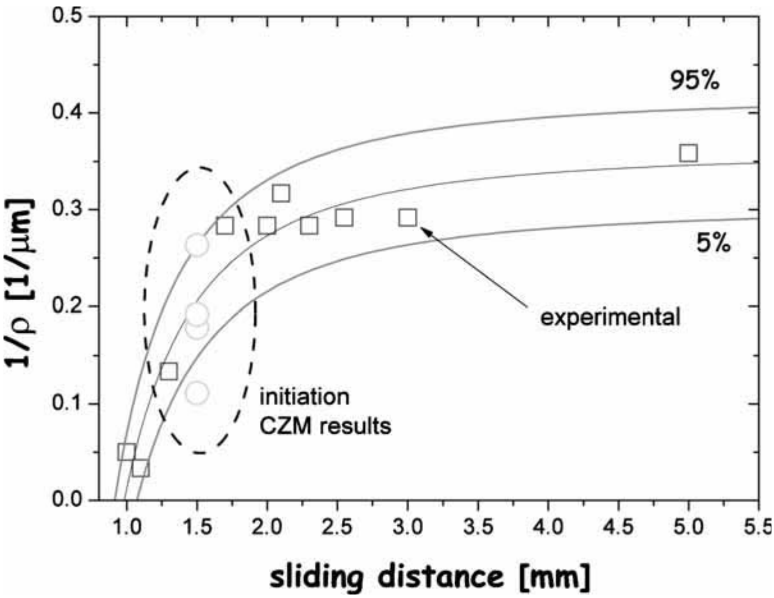

FIG. 19—*Comparison of experimental and CZM crack density results.*

analyses yield results which are of the right order, and imply that the CZ approach has potential in capturing the features of the cracking process including stress relaxation (i.e., every CZ element column does not fail).

Coating-Substrate System Optimization

The purpose of a coating is to carry as much of the tribological loading as possible without subjecting the substrate to any sort of a failure mechanism. Typically, this function can be achieved by making sure that the coating is intact at service conditions. Thus, a criterion describing both damages to the coating with respect to loading experienced by the coating-substrate system will suffice. Such a comparison can be made by comparing a contact problem related parameter, such as contact pressure, to damage in the coating. To generate a measure of the latter, a normalized integral of damage over all cohesive elements is utilized. After assessing the different CZM analysis cases this way, the results can be presented for the three CZM types, as is done in Fig. 20. The results are presented at such a stage of loading where the model-case, coating with 300 GPa elastic modulus over the coating thickness, has developed the first through coating cracks. The results are provided for different property sets and FGM structures which were attempted within the study. Also present are some TiN coating results with differing fracture toughness to indicate how the behavior is altered. In Fig. 20(*a*) the results are presented for the interface cracking CZM analyses. By comparing the interface analysis results, it is noted that both the soft and hard coatings (in terms of elastic modulus) are in some way unfavorable. A rigid-like coating can essentially take on higher contact

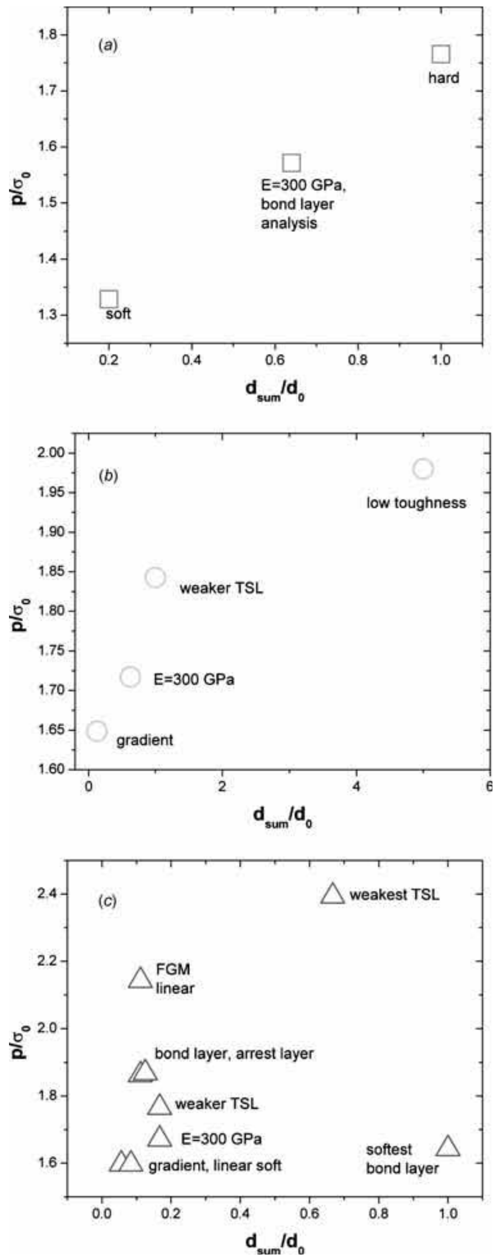

FIG. 20—*The quantification of coating performance in terms of contact pressure and resulting damage:* (*a*) *Interface CZM,* (*b*) *through crack CZM, and* (*c*) *interface and through crack CZM.*

pressures, but this resulted in a far more damage to the adhesion of the interface. The soft compliant coating avoids damage but the surface pressures remain at a fairly low value as a result. The model-case and bond layer ones yield a result in between these two extremes. The results of Fig. 20(*b*) apply for the through coating cracking analyses. The analyses with lower toughness properties and modified TSL behavior are seen to yield more coating damage, although the coating damage itself does permit higher contact pressures for example in the weakened TSL case, albeit this damage does with a high probability lead to imminent coating failure. The gradient structure is seen to significantly decrease damage to the coating, while the property gradient does not significantly alter the behavior in terms of contact pressure. The remainder of the results is presented in Fig. 20(*c*) for cracking, both through coating and at interface. Some of the failed trials with bond layers and TSL parameters stand out of the data, as well as softer gradient structures as in Fig. 20(*b*). Compared to the 300 GPa coating reference case, it is seen that two other variants can contain higher contact pressures with the same degree of damage. The first case is one where a discontinuous material layer, a bond layer-like region at mid-coating thickness, is added to the system. The second and the one producing the best result is a graded system with a linear through thickness gradient, such where the immediate surface has an elastic modulus of 500 GPa, which over coating thickness has a linear variation to a value of 100 GPa. Overall, the results indicate that the behavior of the coating-substrate system can be influenced by tailoring of available properties, in current study primarily the distribution of modulus of elasticity over the thickness of the coating. Irrespective of the interpretation of what is the "best" coating, the results demonstrate that tailoring a coating for a specific application can have great benefits. This way, a suitable structure can be selected to be able to withstand the contact induced loading with minimal damage to the coating-substrate system.

Further work is required so that the TSL and gradient properties can be tied tighter to actual material properties, which will aid in bringing an additional degree of accuracy to current analyses. This can be attained by introducing smaller-scale damage and meso-scale models, as well as the means of multiscale modeling in conjunction with appropriate experimental work. Similarly, the use of other solution methods, such as XFEM will be a benefit in improving the quality of the numerical solution.

Conclusions

The CZM of adhesive interface and through coating cracking was carried out in order to better comprehend the experimentally observed cracking behavior. The results of the work can be concluded as follows.

- The CZM approach was found suitable for analyzing the experimentally observed cracking behavior and the characteristics of failure were reproduced numerically.
- Numerical analyses indicated that in the studied coating-substrate system, 2 μm TiN with an elastic modulus of 300 GPa, the primary mechanism of failure in the system is crack initiation and propagation imme-

diately after the coating resurfaces from under the contacting stylus. Interface failure results only after subsequent substantial increase in applied loading. Predicted crack density values near the formation of first through coating cracks are of the right order.
- The approach of choosing TSL parameters on the basis of fracture toughness data was found successful.
- Gradient coating structures can be used to significantly improve the coating-substrate system performance and tailor optimal application specific structures. The results indicate that linear and more complex property gradients, as well as bond layers, can be used to reduce the rate of damage in the coating.

Acknowledgments

The writers want to acknowledge the following colleagues for interesting and valuable discussions in relation to the work: Ali Erdemir, Argonne National Laboratory, United States; Sture Hogmark, Uppsala University, Sweden; Philippe Kapsa, Ecole Central de Lyon, France; Henry Haefke and Imad Ahmed, CSEM, Switzerland; Koij Kato, Tohoku University, Japan; and Kaj Pischow and Rosa Aimo, Savcor Coatings, Finland.

The financial support of TEKES the Finnish Technology Agency; Taiho Kogyo Tribology Research Foundation, Japan; Savcor Coatings, Finland; and the VTT Technical Research Centre of Finland is gratefully acknowledged.

References

[1] Diao, D., Kato, K., and Hayashi, K., "The Maximum Tensile Stress on a Hard Coating Under Sliding Friction," *Tribol. Int.*, Vol. 27, 1994, pp. 267–272.

[2] Li, K., Diao, D., and Bhushan, B., "Fracture Mechanics of Thin Amorphous Carbon Films in Nanoindentation," *Acta Mater.*, Vol. 45, 1997, pp. 4453–4461.

[3] Li, K. and Bhushan, B., "Measurement of Fracture Toughness of Ultra-Thin Amorphous Carbon Films," *Thin Solid Films*, Vol. 315, 1998, pp. 214–221.

[4] Nastani, M., Kodali, P., Walter, K., Embury, R., and Raj, Y., "Fracture Toughness of Diamondlike Carbon Coatings," *J. Mater. Res.*, Vol. 14, 1999, pp. 2173–2180.

[5] Ollivier, B., Dowey, S., Young, S., and Matthews, A., "Adhesion Assessment of DLC Films on PET Using a Simple Tensile Tester: Comparison of Different Theories," *J. Adhes. Sci. Technol.*, Vol. 9, 1995, pp. 769–784.

[6] Wiklund, U., Bromark, M., Larsson, M., Hedenquist, P., and Hogmark, S., "Cracking Resistance of Thin Hard Coatings Estimated by Four-Point Bending," *Surf. Coat. Technol.*, Vol. 91, 1997, pp. 57–63.

[7] Sriram, K., Narasimhan, R., and Biswas, S. K., "A Numerical Aanalysis of Indentation Into Thin Hard Films on Soft Substrates," *Eng. Fract. Mech.*, Vol. 70, 2003, pp. 1323–1338.

[8] Chai, H., "Fracture Mechanics Analysis of Thin Coatings Under Plane-Strain Indentation," *Int. J. Solids Struct.*, Vol. 40, 2003, pp. 591–610.

[9] Souza, R., Mustoe, G., and Moore, J., "Finite Element Modeling of the Stresses, Fracture and Delamination During the Indentation of Hard Elastic Films on

Elastic-Plastic Soft Substrates," *Thin Solid Films*, Vol. 392, 2001, pp. 65–74.
[10] Malzbender, J. and de With, G., "Modeling of the Fracture of a Coating Under Sliding Indentation," *Wear*, Vol. 239, 2000, pp. 21–26.
[11] Barenblatt, G., "The Mathematical Theory of Equilibrium Cracks in Brittle Fracture," *Adv. Appl. Mech.*, Vol. 7, 1962, pp. 55–129.
[12] Dugdale, D., "Yielding of Steel Sheets Containing Slits," *J. Mech. Phys. Solids*, Vol. 8, 1960, pp. 100–104.
[13] Griffith, A., "The Phenomena of Rupture and Flow in Solids," *Philos. Trans. R. Soc. London, Ser. A*, Vol. 221, 1921, pp. 163–198.
[14] de Borst, R., "Numerical Aspects of Cohesive-Zone Models," *Eng. Fract. Mech.*, Vol. 70, 2003, pp. 1743–1757.
[15] de Borst, R., Wells, G. N., and Sluys, L. J., "Some Observations on Embedded Discontinuity Models," *Eng. Comput.*, Vol. 18, 2001, pp. 241–254.
[16] Chen, C. R. and Kolednik, O., "Comparison of Cohesive Zone Parameters and Crack Tip Stress States Between Two Different Specimen Types," *Int. J. Fract.*, Vol. 132, 2005, pp. 135–152.
[17] Tvergaard, T., "Crack Growth Predictions by Cohesive Zone Model for Ductile Fracture," *J. Mech. Phys. Solids*, Vol. 49, 2001, pp. 2191–2207.
[18] Tijssens, M., Sluys, B., and Giessen, E., "Numerical Simulation of Quasi-Brittle Fracture Using Damaging Cohesive Surfaces," *Eur. J. Mech. A/Solids*, Vol. 19, 2000, pp. 761–779.
[19] van den Bosch, M. J., Schreurs, P. J. G., and Geers, M. G. D., "An Improved Description of the Exponential Xu and Needleman Cohesive Zone Law for Mixed-Mode Decohesion," *Eng. Fract. Mech.*, Vol. 73, 2006, pp. 1220–1234.
[20] Freed, Y. and Banks-Sills, L., "A New Cohesive Zone Model for Mixed Mode Interface Fracture in Bimaterials," *Eng. Fract. Mech.*, Vol. 75, 2008, pp. 4583–4593.
[21] Hu, J., Chou, Y. K., and Thompson, R. G., "Cohesive Zone Effects on Coating Failure Evaluations of Diamond-Coated Tools," *Surf. Coat. Technol.*, Vol. 203, 2008, pp. 730–735.
[22] Yan, Y. and Shang, F., "Cohesive Zone Modeling of Interfacial Delamination in PZT Thin Films," *Int. J. Solids Struct.*, Vol. 46, 2009, pp. 2739–2749.
[23] Yuan, H. and Chen, J., "Computational Analysis of Thin Coating Layer Failure Using a Cohesive Model and Gradient Plasticity," *Eng. Fract. Mech.*, Vol. 70, 2003, pp. 1929–1942.
[24] Jansson, N. E., Leterrier, Y., Medico, L., and Månson, J.-A. E., "Calculation of Adhesive and Cohesive Fracture Toughness of a Thin Brittle Coating on a Polymer Substrate," *Thin Solid Films*, Vol. 515, 2006, pp. 2097–2105.
[25] Bialas, M., Majerus, P., Herzog, R., and Mróz, Z., "Numerical Simulation of Segmentation Cracking in Thermal Barrier Coatings by Means of Cohesive Zone Elements," *Mater. Sci. Eng., A*, Vol. 412, 2005, pp. 241–251.
[26] Chandra, N., Li, H., Shet, C., and Ghonem, H., "Some Issues in the Application of Cohesive Zone Models for Metal-Ceramic Interfaces," *Int. J. Solids Struct.*, Vol. 39, 2002, pp. 2827–2855.
[27] Jin, Z.-H., Paulino, G. H., and Dodds, R. H., Jr., "Cohesive Fracture Modeling of Elastic-Plastic Crack Growth in Functionally Graded Materials," *Eng. Fract. Mech.*, Vol. 70, 2003, pp. 1885–1912.
[28] Holmberg, K. and Matthews, A., *Coatings Tribology*, Elsevier Science, New York, 2009.
[29] Laukkanen, A., Holmberg, K., Koskinen, J., Ronkainen, H., Wallin, K., and Varjus, S., "Tribological Contact Analysis of a Ball Sliding on a Flat Coated Surface, Part III: Fracture Toughness Calculation and Influence of Residual Stresses," *Surf.*

Coat. Technol., Vol. 200, 2006, pp. 3824–844.

[30] Bruckner, H. F., "A Novel Principle for the Computation of Stress Intensity Factors," *Z. Angew. Math. Mech.*, Vol. 50, 1970, pp. 529–546.

[31] Holmberg, K., Laukkanen, A., Ronkainen, H., and Wallin, K., "Surface Stresses in Coated Steel Surfaces–Influence of a Bond Layer on Surface Fracture," *Tribol. Int.*, Vol. 42, 2009, pp. 137–148.

[32] *Abaqus 6.9-2 FEA*. (2009), Simulia, Providence, RI.

Reprinted from JAI, Vol. 7, No. 5
doi:10.1520/JAI102531
Available online at www.astm.org/JAI

Cédric Lequesne,[1] *André Plumier,*[2] *Laurent Duchêne,*[3] *and Anne Marie Habraken*[4]

Modeling of Crack Propagation in Weld Beam-to-Column Connections Submitted to Cyclic Loading with a Cohesive Zone Model

ABSTRACT: During the earthquakes in Japan and California in the 1990s, cracks appeared in some weld beam-to-column connections of heavy rigid frame steel buildings. This prompted the necessary assessment of the performance of weld connections in terms of rotation capacity and crack propagation. In the present study, experimental tests were performed where weld connections were submitted to cyclic loadings with increasing amplitude until a macrocrack event was reached. However the crack phenomenon depends on many parameters: The geometry, the material, the welding process…. For this reason, it was interesting to develop a finite element modeling of these connections in order to complete these experiments and perform a parametric study. This paper describes the finite element model development, its material parameter identification, and its comparison with experimental results. The weld connections were modeled by using three-dimensional mixed solid elements. The constitutive laws applied were elastoplastic with isotropic hardening identified for the base metal and the weld metal. Crack propagation was modeled by a cohesive zone model. The parameters of this cohe-

Manuscript received May 18, 2009; accepted for publication April 20, 2010; published online May 2010.
[1] Dept. of ArGEnCo, Univ. of Liège, Chemins des Chevreuils, 1, B-4000 Liège, Belgium, e-mail: Cedric.Lequesne@ulg.ac.be
[2] Dept. of ArGEnCo, Univ. of Liège, Chemins des Chevreuils, 1, B-4000 Liège, Belgium, e-mail: A.Plumier@ulg.ac.be
[3] Dept. of ArGEnCo, Univ. of Liège, Chemins des Chevreuils, 1, B-4000 Liège, Belgium, e-mail: L.Duchene@ulg.ac.be
[4] Dept. of ArGEnCo, Univ. of Liège, Chemins des Chevreuils, 1, B-4000 Liège, Belgium, e-mail: Anne.Habraken@ulg.ac.be

Cite as: Lequesne, C., Plumier, A., Duchêne, L. and Habraken, A. M., "Modeling of Crack Propagation in Weld Beam-to-Column Connections Submitted to Cyclic Loading with a Cohesive Zone Model," *J. ASTM Intl.*, Vol. 7, No. 5. doi:10.1520/JAI102531.

sive zone model were identified by an inverse method with the modeling of three-point bending tests of pre-cracked samples performed on the base and weld metals. The fatigue damage generated by the cyclic loading was computed by the fatigue continuum damage model of Lemaitre and Chaboche, which was coupled with the cohesive zone model.

KEYWORDS: cohesive zone, fatigue, finite element, beam-to-column connection, welding

Introduction

In seismic zones, steel moment-resisting frame buildings contain heavy welded beam-to-column connections. By means of energy dissipation due to plastic strain, the ductility of steel makes it possible to avoid the appearance of cracks in the connections. However, earthquakes in the 1990s in the United States and Japan resulted in widespread and unpredicted damage in welded beam-to-column connections in rigid steel frame buildings. These failures explain why the engineering community decided to investigate the reasons for this unexpected behavior and to explore alternative connection types. Research in many countries resulted in a number of changes to building design codes and specifications. However, performance is affected by many factors such as dimensions of beam-to-column components, connection design, manufacturing quality, and the mechanical properties of the different regions of the joint. A procedure for analyzing these factors, called the Risk Assessment Procedure (RAP), was recently published under the auspices of the International Institute of Welding [1]. This procedure determines the risk of fracture in seismically affected moment connections. It covers design, material, fabrication, and loading issues.

European steelmakers produce heavy sections used in multi-storey buildings in seismic zones. In order to maintain the competitiveness of the European Union in this market, methods need to be available for steel users to verify the specification of steel sections, to define connections, and to assess safety in service.

The Validation and Enhancement of Risk Assessment Procedure for Seismic Connections (VERAPS) project [2] aimed to validate and enhance the RAP for connections in seismic areas. Fabrication, testing, modeling methods, and reliability analyses were combined to achieve this aim. A series of full-scale tests on connections with different parent material strength and weld metal toughness was carried out by the University of Karlsruhe. The variables covered included moment capacity ratios, welding methods, weld metal toughness, and joint design details. However these tests were expensive and required significant installation.

An objective of the VERAPS project was to model the crack propagation in heavy welded beam-to-column connections submitted to cyclic quasi-static loading by finite elements. The objective of the simulation is the assessment of the cyclic plastic rotation capacity of heavy welded beam-to-column connections as a function of the mechanical properties of the beams, columns, and weld materials and of the type of joint preparation. This modeling approach was compared with tests performed by the University of Karlsruhe, and a validated model made it possible to predict the behavior of non-tested connections and to explore a larger field of possibilities. This paper focuses on the description and the comparison on these finite element models.

The finite element code used was the Lagrangian non-linear finite element code LAGAMINE, developed at the University of Liège since the 1980s. The damage in the connections was due to a high level of deformation and to cyclic loading. The monotonic damage and the crack process were modeled by a cohesive zone model (CZM), which was used to simulate initiation and propagation. This model required few parameters and was easy to implement. The classical fatigue damage due to cyclic loading was evaluated by the fatigue continuum damage model (CDM) of Lemaitre and Chaboche [3]. The computation was performed in two steps. A first simulation evaluated the fatigue damage without the CZM. The crack path was identified with the zone where the damage was significant. Then a second simulation was performed with cohesive zone elements to model the crack propagation. After the Karlsruhe's tests, some samples were machined to perform some material tests, such as tensile tests, Charpy tests, and three-point bending tests. These tests allowed the authors to identify the material parameters of their model.

This paper first presents the weld beam-to-column connections and the test characteristics. Second, it explains the model of crack propagation. Third, it sets out the modeling of the connection tests. Finally the results from the numerical model and the experiments are compared.

Connection Tests

Eight large-scale tests were performed with a 6300 kN alternating load test frame at the University of Karlsruhe [2]. All beams, columns, and plates were 355 J0 and J2 grade steel. Varying their dimensions made it possible to test different ratios between joint plastic moment and beam plastic moment.

In all specimens, the beam flanges were welded to the column flanges with butt welds. The flange butt welds transmitted the full plastic moment of the section area of the beam flange. The beam web was bolted to a shear tab, which was welded to the column flange. For some specimens, the shear tab was welded and bolted to the beam web. The shear tab was welded to the column flange for all specimens (see Fig. 1). The shear tab transmitted the plastic moment of the beam web and the corresponding shear.

Regarding the welding, the VERAPS connections were manufactured using a range of consumables to cover the full toughness range together with three different types of process: Manual metal arc welding, tubular cored metal arc welding with active gas shield, or metal arc welding without gas shield. Due to the significant thickness of the flange, the number of passes was ranging from 10 to 30. The dimensions of the weld access holes complied with FEMA [4] requirements. Some characteristic flaws, such as a lack of fusion, were artificially added during the welding process. During the welding process of the beam flange to the column flange, a backing bar in steel or ceramic was installed below the butt weld to support the welding at the beginning. This was removed at the end of the welding process.

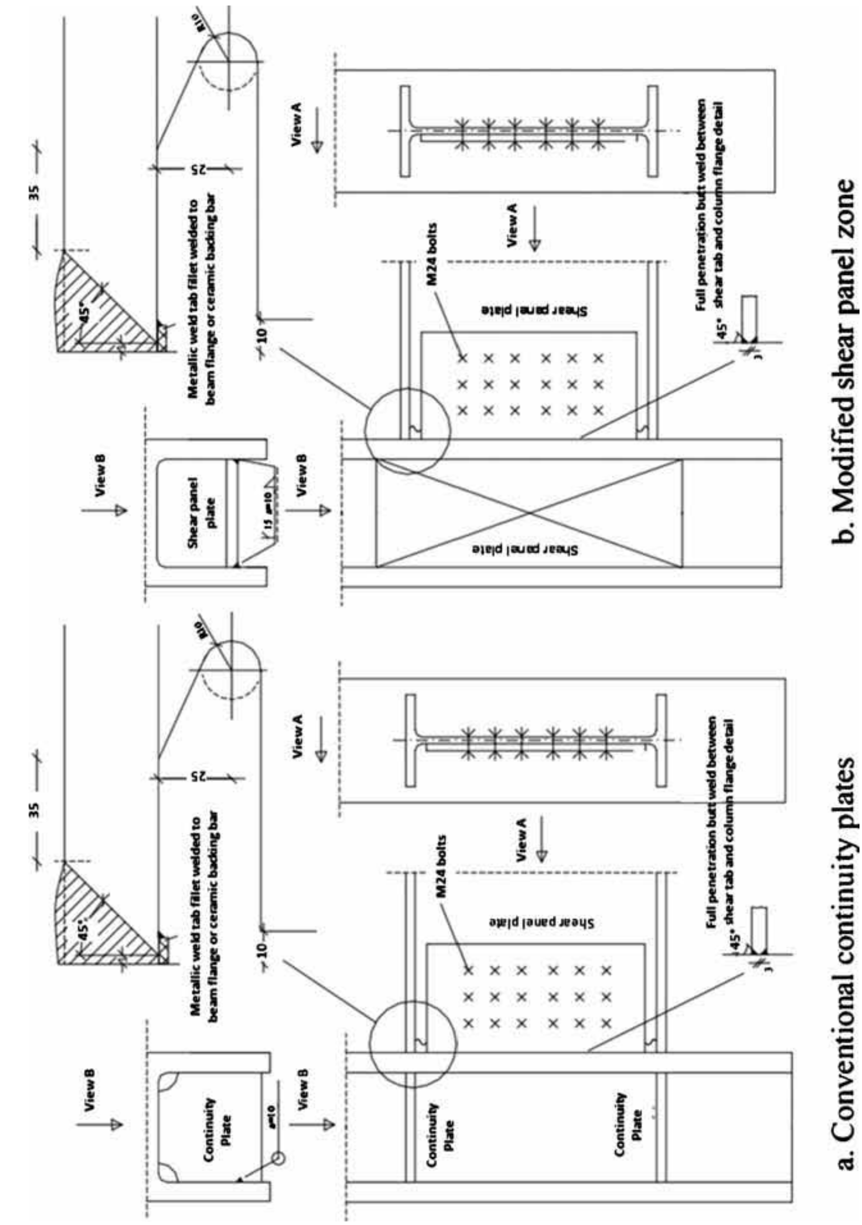

FIG. 1—*Details of the connections from Ref 2.*

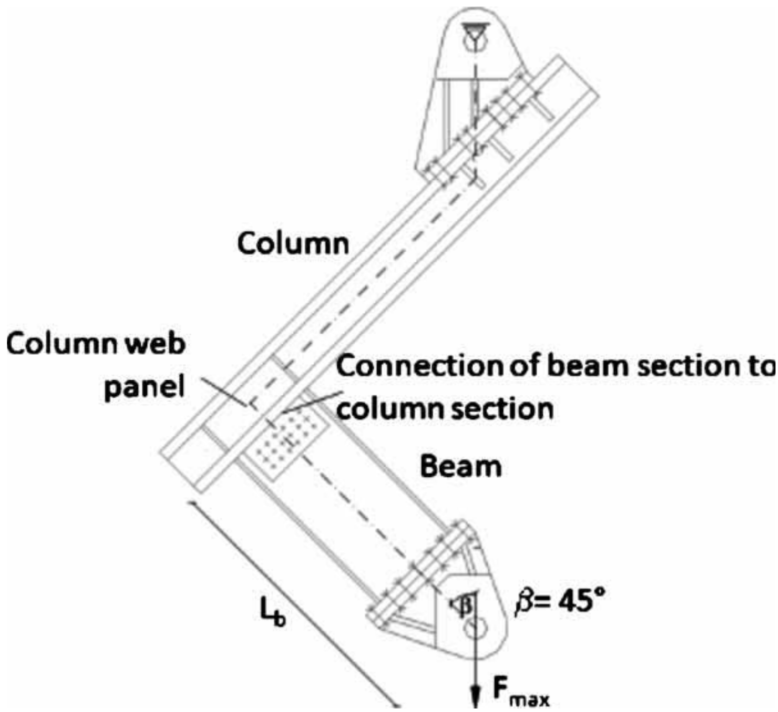

FIG. 2—*Test specimen* (*from Ref 2*).

Two types of stiffener were also manufactured for the column panel (see Fig. 1), listed as follows:

- 30-mm-thick transverse stiffeners acting as continuity plates for the beam flanges but bringing no increase in the shear resistance of the panel zone and
- 40-mm-thick extended doubler plates placed parallel to the column web; these acted as stiffeners and as continuity plates and significantly increased the shear resistance of the panel zone.

The frame was oriented for a classic compression-tension test, which resulted in the specimen geometry presented in Fig. 2. Each test sample was subjected to cyclic loading with step-wise deformation cycles increasing up to failure according to the loading procedure of FEMA 350. The protocol imposes the number and the amplitude of cyclic rotations defined in Table 1 until macrocracks are observed. If no macrocrack appears after the total number of cycles, the rotation amplitude is incremented by 0.01 rad, with two cycles of loading at each rotation level. During the test, the displacement was imposed and the force of the machine was measured. For this purpose, some actuators and strain gauges were installed on the connection. The rotation is obtained from the imposed displacement and the beam length. The beam end moment comes from the measured force and the beam length. The results of the tests are available in Refs 2 and 5.

TABLE 1—*Cyclic rotation imposed on the connection according to FEMA 350.*

Step	Number of Cycles	Rotation Amplitude (rad)
1	6	0.00375
2	6	0.00500
3	6	0.00750
4	4	0.010
5	2	0.015
6	2	0.020
7	2	0.03

TABLE 2—*Loading record of the experimental test reference.*

Step	Cycle	Imposed Displacement (mm)	Crack Control Is Indicated with Gray
1	1	17.6	
	2		
	3		
	4		
	5		
	6		No crack detected
2	1	24	
	2		
	3		
	4		
	5		
	6		No crack detected
3	1	35	No crack detected
	2		
	3		
	4		
	5		
	6		No crack detected
4	1	47	No crack detected
	2		No crack detected
	3		No crack detected
	4		No crack detected
5	1	70.6	Abrupt failure of the weld of the beam bottom flange

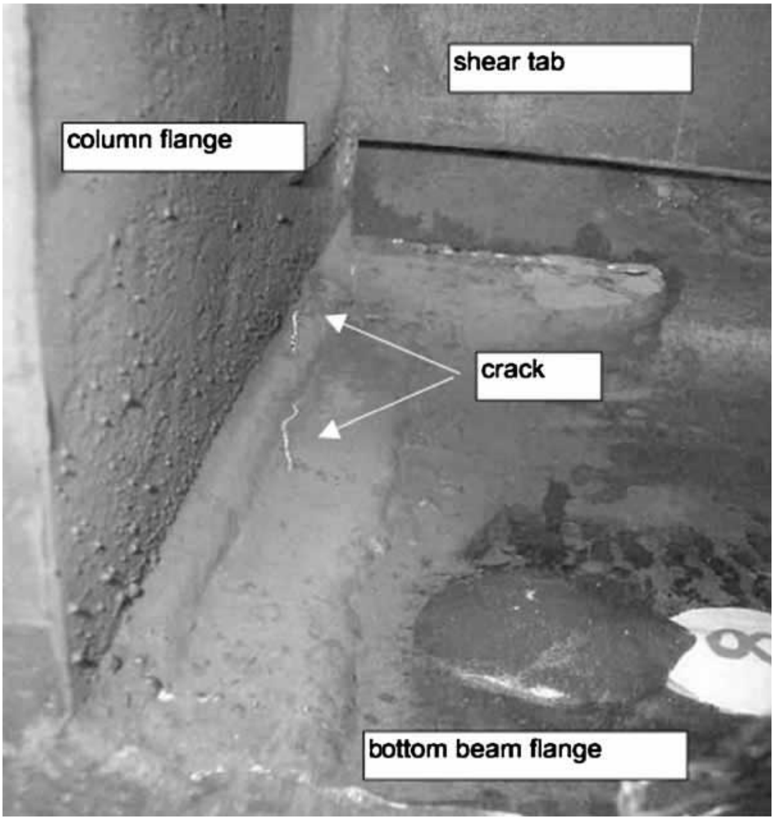

FIG. 3—*Experimental crack observations.*

For this paper, only one connection test was modeled. The time of the crack observation is described in Table 2. The operator observed the connection at different cycles of the loading in order to check if a macrocrack event occurred. An abrupt failure appeared at the first cycle of step 5 at the beam bottom flange (see Fig. 3). Perhaps some microcracks initiated through the thickness during step 4, which were not observed.

Crack Propagation Modeling

The Fatigue Continuum Damage Model

In multiaxial state, the fatigue stress limit is defined by a fatigue surface. The criterion of fatigue limit depends on the amplitude and the mean values per cycle. As observed experimentally, the mean shear does not affect the fatigue limit, as opposed to the mean tension [3]. Therefore it was defined as follows:

- The second invariant of the amplitude of the deviator of the stress tensor, $\underline{\underline{\sigma}}$

$$A_{\mathrm{II}} = \frac{1}{2}\sqrt{\frac{3}{2}(\hat{\sigma}_{ij,\max} - \hat{\sigma}_{ij,\min})(\hat{\sigma}_{ij,\max} - \hat{\sigma}_{ij,\min})} \tag{1}$$

where: $\hat{\sigma}_{ij} = \sigma_{ij} - \Sigma_k \frac{1}{3}\sigma_{kk}$, $\hat{\sigma}_{ij,\max}$, and $\hat{\sigma}_{ij,\min}$ = maximum and minimum components of the deviatoric stress tensor during one cycle;

- The mean hydrostatic stress, σ_{Hm}

$$\sigma_{\mathrm{Hm}} = \frac{1}{T}\int_T \sum_k \frac{\sigma_{kk}}{3} dt \tag{2}$$

The multiaxial fatigue criterion is defined by a damage yield locus, noted f_D, as in plasticity

$$f_D = A_{\mathrm{II}} - A_{\mathrm{II}}^{*} \tag{3}$$

where A_{II}^{*} represents the fatigue limit.

Therefore if the loading, A_{II}, is smaller than the threshold value, the structure does not undergo any damage. Although different criteria exist, the Sines criterion [6] was chosen because of its simplicity. No test was available to evaluate the performance of other criteria. The fatigue limit of the Sines criterion is

$$A_{\mathrm{II}}^{*} = \sigma_{l0}(1 - 3b\sigma_{\mathrm{Hm}}) \tag{4}$$

where:

σ_{l0} = fatigue stress limit.

For multiaxial loading, Lemaître and Chaboche [3] stated that the evolution law for the fatigue damage variable, D_f, during the Nth cycle, is as follows:

$$\frac{\partial D_f}{\partial N} = \begin{cases} 0 & \text{if } f_D < 0 \\ [1 - (1 - D_f)^{\beta+1}]^{\alpha}\left(\frac{\tilde{A}_{\mathrm{II}}}{M}\right)^{\beta} & \text{if } f_D \geq 0 \end{cases}$$

$$\tilde{A}_{\mathrm{II}} = \frac{A_{\mathrm{II}}}{1 - D_f}; \quad M = M_0(1 - 3b\sigma_{\mathrm{Hm}}); \quad \alpha = 1 - a\left\langle \frac{A_{\mathrm{II}} - A_{\mathrm{II}}^{*}}{\sigma_u - \sigma_{\mathrm{eq\,max}}} \right\rangle \tag{5}$$

This damage evolution law depends on the maximum von Mises's stress per cycle, $\sigma_{\mathrm{eq\,max}}$. σ_u is the ultimate tensile stress of the material. M_0, b, a, and β are other material parameters. The symbol $\langle x \rangle$ corresponds to the following definition: If x is negative, then its value is null, and if x is positive, then its value is x. The fatigue CDM makes it possible to compute the non-linear evolution of the damage with different levels of loading amplitude.

The parameters of this model were identified from Wohler's curves, which were determined by cyclic tensile tests for the base and weld metal samples extracted from different locations of the connection (see Table 3). The procedure is described in Ref 7.

TABLE 3—*Parameters of the identified constitutive law.*

	Fatigue Continuum Damage Parameters						Cohesive Zone Parameters		
	σ_l (MPa)	σ_u (MPa)	β	a	b	M_0 (MPa)	σ_{max} (MPa)	δ_0 (mm)	δ_n (mm)
Base metal	275	585	7.38	0.15	0.00171	1069	1700	1.70×10^{-4}	1.89×10^{-1}
Weld metal	228	650	4.08	0.15	0.00155	2255	1650	1.65×10^{-4}	6.06×10^{-2}

The Cohesive Zone Model

In the early 1960s, Dugdale [8] and Barenblatt [9] introduced the concept of the CZM. This model has been used for monolithic and composite materials. During crack propagation, there is a fracture process occurring behind the crack tip, where microcracks and microvoids nucleate, grow, and then coalesce. Thus the behavior of this zone is different from the sound bulk material due to its progressive degradation. The CZM describes this behavior. The potential crack is modeled by two interface areas connected by cohesive stresses (see Fig. 4). The degradation process is described by the constitutive law linking the cohesive stress, T, and the separation, Δu. According to a literature review, there are different forms of this law, but they all have common features. Cohesive stress, during the increase in separation, begins to increase until it reaches a maximum stress value σ_{max}; it then decreases and vanishes after full rupture.

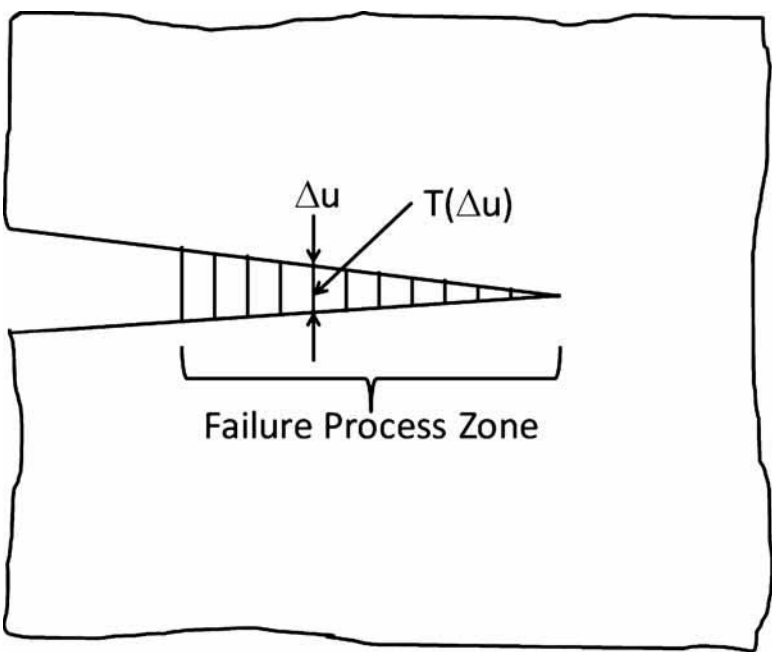

FIG. 4—*CZM description.*

In mixed mode fracture, stress and separation components are defined by (Δu_n, Δu_p, and Δu_s) and (T_n, T_p, and T_s), where n, p, and s correspond to crack modes I, II, and III, respectively. Mode I is a normal opening of the interface, while modes II and III are shear slipping of the crack interfaces.

The Crisfield's model [10] was chosen here. The initial stiffness can be regulated so that the global stiffness of the structure does not interfere with the presence of the cohesive zone in the model [11]. Crisfield's model has a bilinear shape and is used to define the initial stiffness $\underline{\underline{E}}_{\mathrm{co}}$

$$\underline{\underline{E}}_{\mathrm{co}} = \begin{bmatrix} \dfrac{\sigma_{\max}}{\delta_{n0}} & 0 & 0 \\ 0 & \dfrac{\tau_{\max}}{\delta_{t0}} & 0 \\ 0 & 0 & \dfrac{\tau_{\max}}{\delta_{t0}} \end{bmatrix} \tag{6}$$

where:

$\sigma_{\max}$ and $\tau_{\max}$ = maximum normal and shear stresses and

δ_{n0} and δ_{t0} = normal and shear separations when the normal and shear stresses reach their maximum values, $\sigma_{\max}$ and $\tau_{\max}$.

A cohesive damage tensor, $\underline{\underline{D}}_c$, is defined as a function of the separation, $\Delta \underline{u}$. At the beginning of the loading phase, the damage is equal to zero. If one separation component, Δu_i, is beyond the separation, δ_{i0}, where the stress is equal to the maximum stress, then the damage begins to grow until the separation is equal to a critical displacement, δ_{ic}, when the damage is equal to 1. In unloading, the damage stops growing. Then, in reloading, the damage grows again when the separation reaches the value when the unloading began.

For the mixed fracture mode, the cohesive damage tensor is defined by

$$\underline{\underline{D}}_c = \frac{\langle \omega_0 \rangle}{1 + \langle \omega_0 \rangle} \underline{\underline{F}} \quad \text{with} \begin{cases} \omega = \left[\left(\dfrac{\langle \Delta u_n \rangle}{\delta_{n0}} \right)^{\alpha} + \left(\dfrac{|\Delta u_p|}{\delta_{p0}} \right)^{\alpha} + \left(\dfrac{|\Delta u_s|}{\delta_{s0}} \right)^{\alpha} \right]^{1/\alpha} - 1 \\ \omega_0 = \max\limits_{t}(\omega) \\ \underline{\underline{F}} = \begin{bmatrix} \dfrac{\delta_{\mathrm{nc}}}{\delta_{\mathrm{nc}} - \delta_{n0}} & 0 & 0 \\ 0 & \dfrac{\delta_{\mathrm{tc}}}{\delta_{\mathrm{tc}} - \delta_{t0}} & 0 \\ 0 & 0 & \dfrac{\delta_{\mathrm{tc}}}{\delta_{\mathrm{tc}} - \delta_{t0}} \end{bmatrix} \end{cases} \tag{7}$$

where:

δ_{nc} and δ_{tc} = separations when the normal and the shear stresses are null,

α = material parameter, and

t = time.

The condition when the monotone damage rate is positive is

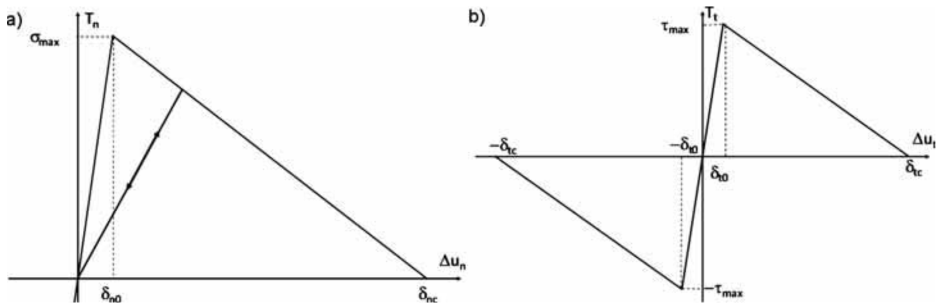

FIG. 5—*Crisfield's CZM* (*a*) *for mode I and* (*b*) *for mode II or mode III.*

$$\text{if } (\omega - \omega_0 > 0), \text{ then} \begin{cases} \dot{\underline{\underline{D}}}_c > 0 \\ \omega_0 = \omega \end{cases} \tag{8}$$

Otherwise, $\dot{\underline{\underline{D}}}_c$ is zero since no decrease in damage is possible.

Thus, the constitutive law of the CZM is (see Fig. 5)

$$\underline{T} = [\underline{\underline{I}} - \underline{\underline{D}}_c]\underline{\underline{E}}_{co}\Delta\underline{u} \tag{9}$$

where:

$\underline{\underline{I}}$ = unity matrix.

In compression ($\Delta u_n < 0$), the damage tensor becomes null to model penalty contact. As a result, the cohesive stiffness matrix is

$$\underline{\underline{C}} = \begin{cases} [\underline{\underline{I}} - \underline{\underline{D}}_c]\underline{\underline{E}}_{co} \text{ if } \dot{\underline{\underline{D}}}_c = \underline{\underline{0}} \\ [\underline{\underline{I}} - \underline{\underline{D}}_c]\underline{\underline{E}}_{co} - \dfrac{1}{(1+\omega)^{\alpha+1}}\underline{\underline{F}}\underline{\underline{E}}_{co}\begin{bmatrix} \Delta u_n^{\alpha} & \Delta u_n \Delta u_p^{\alpha-1} & \Delta u_n \Delta u_s^{\alpha-1} \\ \Delta u_p \Delta u_n^{\alpha-1} & \Delta u_p^{\alpha} & \Delta u_p \Delta u_s^{\alpha-1} \\ \Delta u_s \Delta u_n^{\alpha-1} & \Delta u_s \Delta u_p^{\alpha-1} & \Delta u_s^{\alpha} \end{bmatrix}\begin{bmatrix} \dfrac{1}{\delta_{n0}^{\alpha}} & 0 & 0 \\ 0 & \dfrac{1}{\delta_{t0}^{\alpha}} & 0 \\ 0 & 0 & \dfrac{1}{\delta_{t0}^{\alpha}} \end{bmatrix} \text{ if } \dot{\underline{\underline{D}}}_c > \underline{\underline{0}} \end{cases} \tag{10}$$

During the project, the project's partner Corus carried out three-point bending tests on fatigue pre-cracked base metal samples extracted from the connection in the base location. They plotted the crack growth by function of the *J*-integral. For the weld metal, the Charpy energy was measured, and the *J*-integral/crack growth curve was plotted by power-law description. This curve was correlated with the Charpy V-notch energy [12]. The parameters of the CZM were identified by inverse method in modeling the three-point bending tests (see Table 3). Different parameters of the CZM were tested until they reached the equivalent of the *J*-integral/crack growth curve [13].

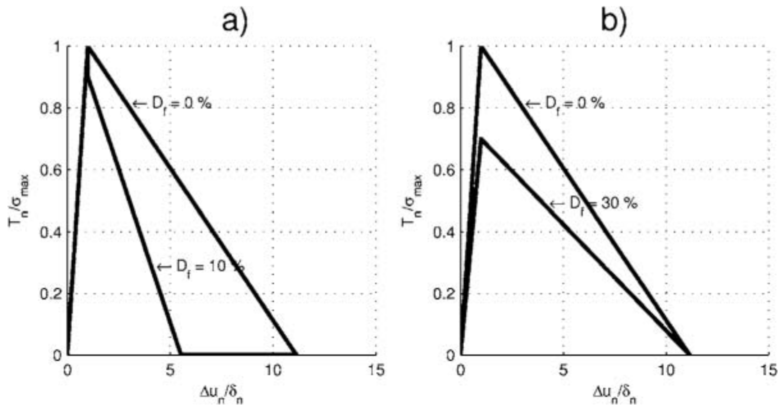

FIG. 6—*Coupling between the CZM and fatigue damage suggested in* (*a*) *Ref 11 and* (*b*) *Ref 14.*

Coupling between the Cohesive Zone and Fatigue Damage

Fatigue damage can be taken into account using the same method as in Ref 11. By adding the fatigue damage parameter, D_f, computed by Eq 5 to the cohesive damage tensor, $\underset{=}{D}_c$ (see Fig. 6)

$$\underset{-}{T} = [\underset{=}{I} - \underset{=}{D}]\underset{=}{E}_{co}\underline{\Delta u}, \quad \text{where} \quad \underset{=}{D} = \underset{=}{D}_c + D_f \underset{=}{I} \tag{11}$$

However, in this way the fatigue damage reduces the separation when the material is totally debonding (see Fig. 6(*a*)). Therefore, the stiffness of the cohesive law, which is negative when the cohesive stress decreases, strongly decreases, and this can affect the convergence of the computation. Roe and Sigmund [14]

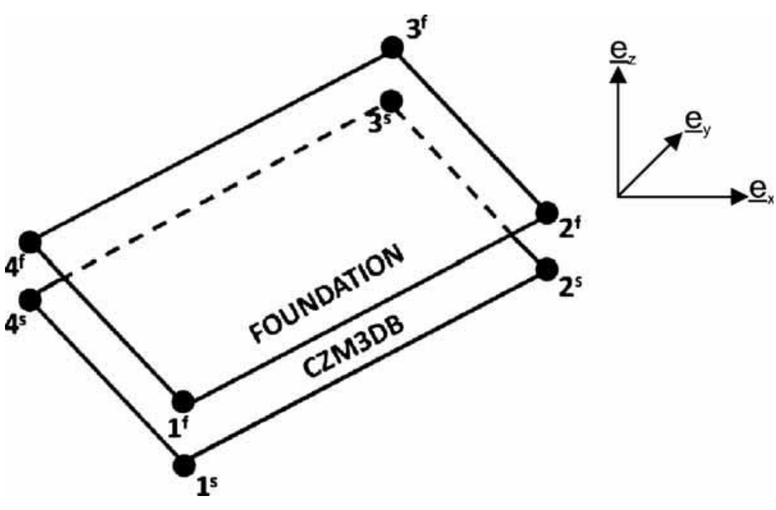

FIG. 7—*Description of CZM3D.*

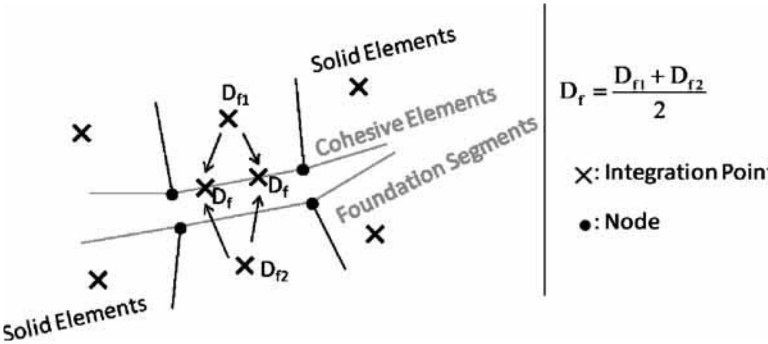

FIG. 8—*Transfer of fatigue damage from solid elements to cohesive elements.*

suggested taking the fatigue damage into account by affecting the stiffness by the following relationship (see Fig. 3(*b*))

$$\underline{T} = [\underline{\underline{I}} - \underline{\underline{D}}_c]\underline{\underline{\tilde{E}}}_{co}\underline{\Delta u}, \text{ where } \underline{\underline{\tilde{E}}}_{co} = (1 - D_f)\underline{\underline{E}}_{co} \tag{12}$$

Finite Element Modeling

A three-dimensional cohesive element was developed in the LAGAMINE code. In this element, the interface side of each crack is modeled by four nodes (see Fig. 7). They are called respectively

- CZM3D and
- Foundation segment.

CZM3D and the foundation segment are four-node plane elements. As a result, they can be computed with one, four, or nine integration points.

The fatigue damage was computed according to the fatigue CDM of Lemaître and Chaboche [3] from the stress tensor components in the solid elements. The method of transferring the fatigue damage from the solid elements to the cohesive elements is illustrated in Fig. 8. The fatigue damage transferred to the integration points of the cohesive element was the mean of the occurrences of fatigue damage computed in the integration points of the

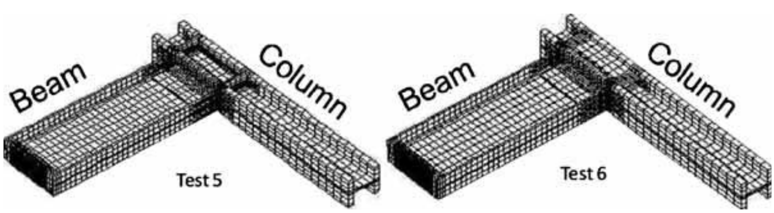

FIG. 9—*Mesh of two beam-to-column connections tested by the University of Karlsruhe.*

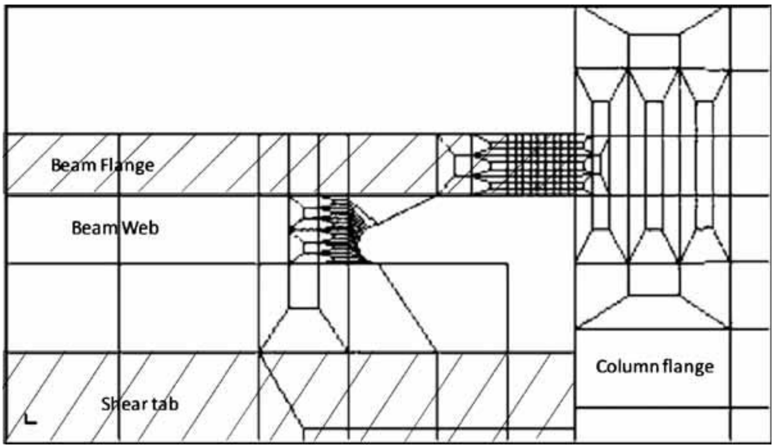

FIG. 10—*Mesh of the connection around the welding.*

solid elements linked to the cohesive element and to the foundation segment. In the studied cases, the solid elements contained only one integration point for two-dimensional and three-dimensional simulations.

Connection Modeling

A special mesh generator was developed for this test modeling. The input of this module was the beam and the column dimensions and the type of rein-

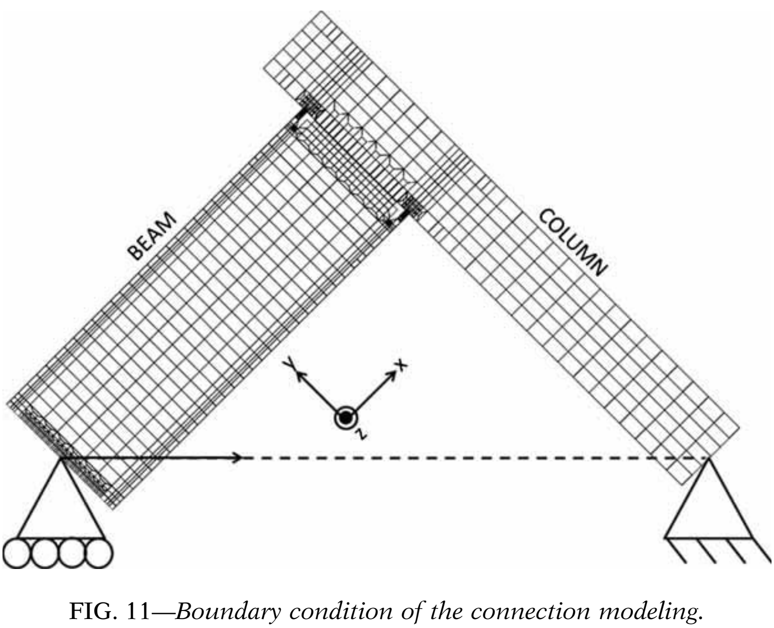

FIG. 11—*Boundary condition of the connection modeling.*

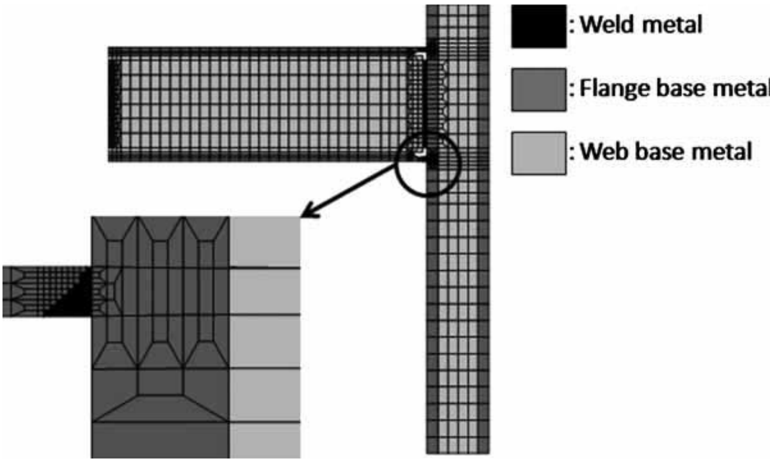

FIG. 12—*Position of the different sets of hardening coefficient.*

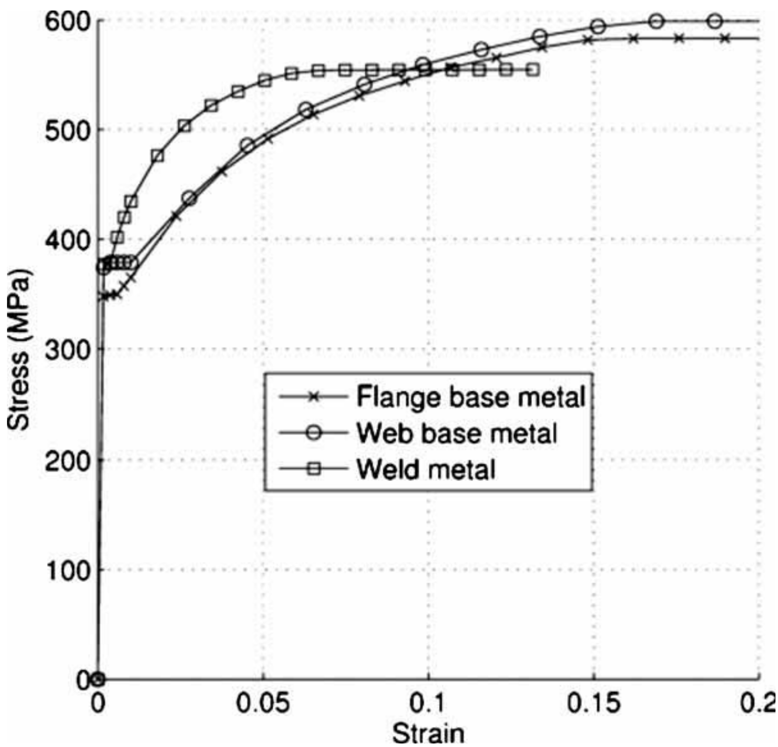

FIG. 13—*Strain-stress curves for the different materials.*

TABLE 4—*Simulation characteristics.*

Number	Model	Goal
1	Connection + CDM	Identify location of fatigue damage defining where to put CZM elements
2	Connection + CZM + CDM	Model crack propagation with fatigue effect
3	Connection + CZM	Model the crack propagation if fatigue damage is neglected

forcement. In this study, the meshes generated were composed of ~13 000 nodes and 8500 elements. The elements are mechanical solid eight-node BWD3D [15] of mixed type available in the LAGAMINE code. Figures 9 and 10 present the meshes of a test with transverse stiffeners and a test with an improved doubler.

A plate was added to the end of the beam in order to stiffen it and to avoid yielding due to the imposed displacement. The beam support was equivalent to a rolling bearing, whereas the column support was equivalent to a hinge. Displacements were imposed on node lines at the centre of the web at the end of the beam. Therefore, the rotation was, free and no physical plasticity was allowed at this point. The boundary conditions are described in Fig. 11.

The constitutive laws for each material are elastoplastic with isotropic hardening. These were calibrated from tensile tests on specimens extracted at different locations of the connection. As a result, the constitutive laws used were different for the flanges, the web, and the welding (see Fig. 12). The strain-stress curves are described in Fig. 13.

The mesh did not model the bolts of the shear tab. Instead, the connection between the shear tab and the beam web was complete because the nodes were merged at the interface between the two components. The weld metal material of the shear tab-to-column flange and the beam flange-to-column flange connections were modeled.

This paper presents the results for the connection shown in Fig. 1(*a*). Three simulations were performed and their characteristics are summarized in Table 4. A first computation (simulation 1) was performed without the CZM but with the fatigue damage model. The latter being a decoupled approach did not affect the mechanical behavior of the structure. It was just used to find the damage evolution and localization defined by the fatigue damage, D_f. The first aim of this simulation was to compare the beam end moment versus rotation curve with the experimental measurement. The second was to identify the potential crack path to add cohesive zone elements in the simulation.

As the crack location was identified by the first simulation, the second simulation contained cohesive elements coupled with the fatigue damage. The aim of the simulation was to model the propagation of the crack at the connection and to observe its impact on the moment rotation curve. This modeling was compared with the experimental results. Finally, a third simulation was performed with cohesive elements where the fatigue was neglected. The aim was to quantify its effect on the crack initiation.

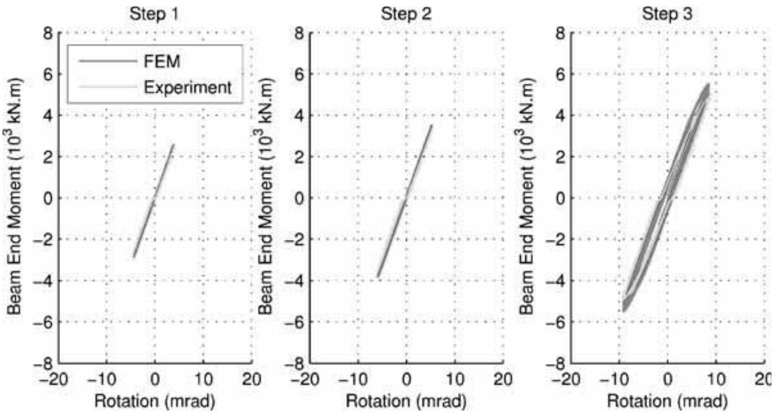

FIG. 14—*Beam end moment versus rotation curves for FE and experimental results.*

Results and Discussion

Identification of the Crack Path (*Simulation 1*)

Figure 14 shows the comparison of the beam end moment versus rotation curves between the finite element simulation 1 results and the experimental measurement for the first three steps. The elastic stiffness of the connection curve was equivalent for the two results curves (see steps 1 and 2). For positive rotation angles, which correspond to a tensile state in the studied specimen, the numerical and experimental values are similar. A small difference is observed for negative rotation angles. The experimental curves show a slight shift towards negative rotation angles due to the sliding of the connection around the bolts, which was not modeled. Moreover the numerical curves present a cyclic hardening in contrast to the experimental ones for step 3.

Regarding the beam flange end (see Fig. 15), the damage variable was different from zero and was concentrated at the interface between the weld metal and the column flange. In fact, damage grew when the moment was at its highest, as the longitudinal stress. In addition, an experimental macrocrack observed at this location validated the model prediction. In the weld flange, the damage increased in the beam flange near the interface between the base metal and the weld metal (see Fig. 15). Figure 3 presents the location of the macrocrack at the end of the experiments in accordance with the numerical simulation. The cracks appeared at the beam bottom flange weld.

Simulation with the Cohesive Zone Model (*Simulation 2 and 3*)

The simulation 2 (see Table 4) took into account both the fatigue damage model and the CZM. The cohesive zone elements were defined at the interface between the weld metal and the base metal in the beam flange end.

During the computation, a crack initiated at the root of the welding on the beam bottom flange end and propagated along the column flange. Figure 16

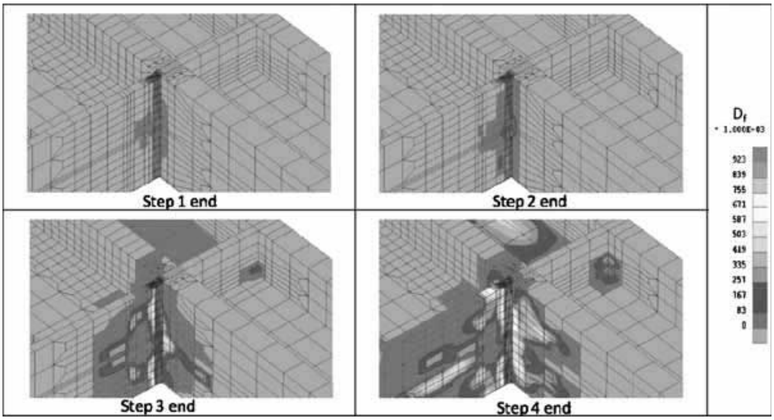

FIG. 15—*Evolution of the fatigue damage near the lower weld flange.*

gives the crack propagation: It happened at cycle 2 of step 3 and quickly propagated during the first part of the loading cycle. The crack is the zone where the longitudinal stresses are released. Figure 17(*a*) is a contour plot of the fatigue damage, and Fig. 17(*b*) gives the longitudinal stress on a cross section at the mid width close to the beam bottom flange. During this second simulation, the fatigue damage is significant at the crack initiation location, but it did not develop during the short propagation time.

Figure 18 shows the evolution of the beam end moment versus the rotation for the finite element computation and the experimental test. The curves of the first two steps are similar to the curves of the previous analysis. However, the

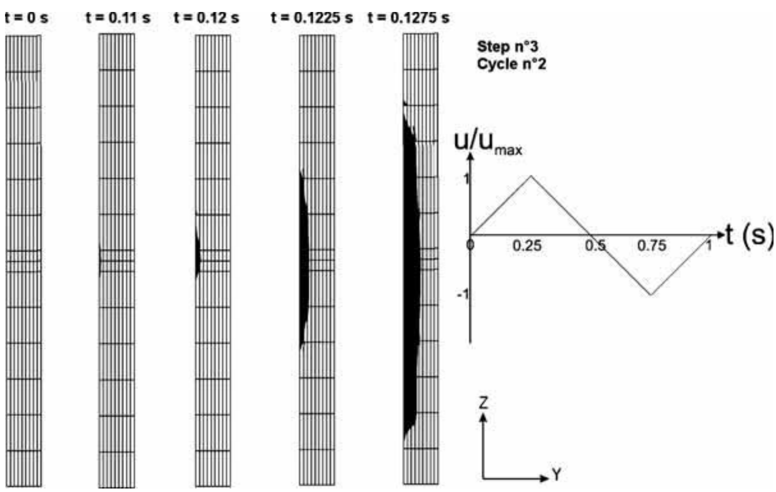

FIG. 16—*Cohesive elements* (*black if cracked*) *during the second cycle of the step 3.*

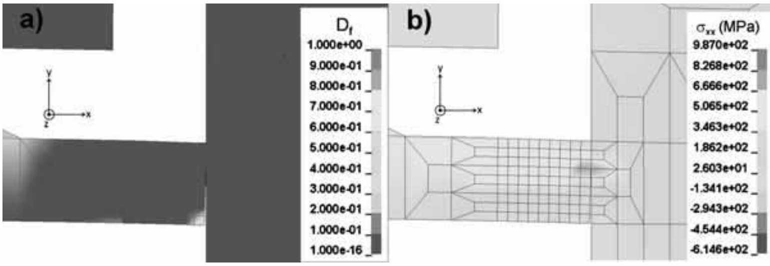

FIG. 17—*Fatigue damage (a) and longitudinal stress (b) at the mid width on the beam bottom flange in the middle of step 3.*

cyclic hardening of the finite element simulation for step 3 is less significant than for the simulation without the cohesive element so that the numerical results are closer to the experimental measurements.

The experimental crack event was observed at cycle 1 of step 5 (see Table 2). Its exact propagation was not recorded. The operator just reported an abrupt failure. This abrupt event can follow a less visible crack not detected by the operator eye. However it seems clear that the model is too conservative and predicts a crack event earlier than in the experiment.

Simulation 3 where only cohesive zone elements were present without coupling with the fatigue damage modeling did not predict any crack. It proves the significant effect of the decrease of the maximum cohesive stress due to fatigue damage (see Fig. 3).

Conclusions

The objective of this study was the modeling of welded steel beam-to-column connection cracking submitted to cyclic loading by the finite element method.

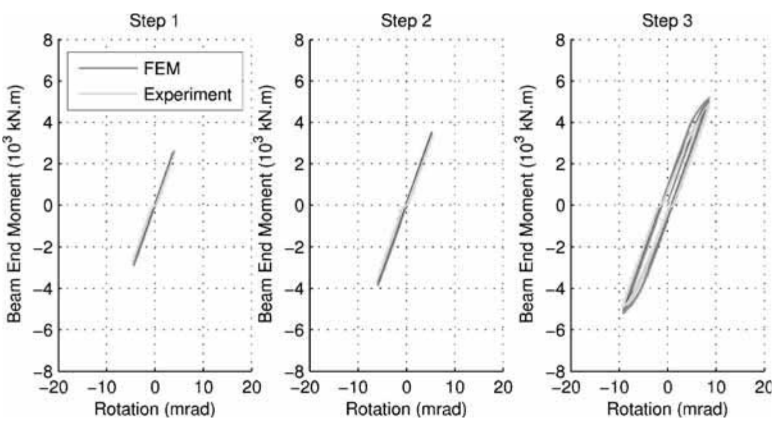

FIG. 18—*Beam end moment versus rotation curves for FE with CZM and experimental results.*

The CZM is a practical model due to its ease of implementation and its small number of parameters. It makes it possible to model crack initiation and propagation. The fatigue damage was calculated by the classical Lemaitre and Chaboche's model [3]. The addition of these two models improved the results by enabling the numerical analysis to get close to the experiments. It was observed in simulation 2 that the crack initiation was driven by the fatigue damage, D_f, while the propagation was driven by the cohesive damage, tensor $\underline{\underline{D}}_c$, generated by the high level of deformations.

Moreover the drawback of the CZM is that the crack path must be known during the meshing. An initial idea was to perform a first analysis without cohesive elements because the fatigue damage field gave an idea of the crack location. However as the fatigue damage drove only the crack initiation, this model gave only the root of the crack without validating the crack path. Future studies are needed in order to perform a finite element analysis with a remeshing step where some cohesive elements are added as a function of a crack bifurcation criterion.

Finally it should be noted that due to welding, the connection contains some residual stresses, which can affect the crack propagation. In the present study, these residual stresses were not taken into account. Another study has evaluated such residual stresses, and the results are presented in Ref 7. It would be interesting to implement the residual stresses in the present simulation in order to observe their impact on predicted results.

Acknowledgments

This study was carried out thanks to the supply of the European Community (VERAPS Project No. RFS-CR-03035) and the assistance of the project partners (Corus, ISQ, The University of Karlsruhe). The writers of this article would like to thank the Belgian Federal Science Policy Office (Contract No. IAP P6-24) for its financial support. A.M.H. and L.D. acknowledge the Fund for Scientific Research (FRS-FNRS, Belgium).

References

[1] International Institute of Welding, "IIW Recommendations for Assessment of Risk of Fracture in Seismically Affected Moment Connections," *Report Nos.* IIW-X-1504-02, IIW-XV-1102-02, IIW-XV-SCG-103-02, IIW Annual Assembly, Bucarest, Roumania, 2002.

[2] Bannister, A., "VERAPS: Validation and Enhancement of Risk Assessment Procedure for Seismic Connection," *Report No.* RFS-CT-2003-00035, Report EUR, Publication Office, Publications, Europa.eu, Luxembourg, 2007.

[3] Lemaitre, J. and Chaboche, J. L., *Mécanique des Matériaux Solides*, Dunod, Paris, France, 1996.

[4] FEMA 350, 2000, "Recommended Seismic Design Criteria for New Steel Moment-Frame Buildings," FEMA, Washington, DC.

[5] Plumier, A., Lequesne, C., Degee, H., Bannister, A., and Hoebling, W., "Behaviour

of Heavy Sections Welded Moment Connections," *STESSA09*, Philadelphia, 2009, University of Lehigh, Bethlehem, USA.

[6] Sines, G., "Behavior of Metals Under Complex Static and Alternating Stresses," *Metal Fatigue*, G. Sines and J. L. Waisman, Eds., McGraw-Hill, New York, 1959.

[7] Lequesne, C., 2009, "Modeling of Fracture in Heavy Steel Welded Beam-to-Column Connection Submitted to Cyclic Loading by Finite Elements," Ph.D. thesis, University of Liege, Liege, Belgium, available from http://bictel.ulg.ac.be/ETD-db/collection/available/ULgetd-07062009-125347/.

[8] Dugdale, D. S., "Yielding of Steel Sheets Containing Slits," *J. Mech. Phys. Solids*, Vol. 8, 1960, pp. 100–104.

[9] Barenblatt, G. I., "Mathematical Theory of Equilibrium Cracks in Brittle Fracture," *Adv. Appl. Mech.*, Vol. 7, 1962, pp. 55–129.

[10] Mi, Y., Crisfield, M. A., Davies, G. A. O., and Hellweg, H.-B., "Progressive Delamination Using Interface Elements," *J. Compos. Mater.*, Vol. 32(14), 1998, pp. 1246–1272.

[11] Bouvard, J. L., 2006, "Modélisation de la Propagation de Fissure dans les Aubes de Turbines Monocristalline [Crack Growth Modelling in Single-Crystal Turbine Blades]," Ph.D. thesis, Ecole Nationale Supérieur des Mines, Paris, France.

[12] Wallin, K., "Low-Cost J-R Curve Estimation Based on CVN Upper Shelf Energy," *Fatigue Fract. Eng. Mater. Struct.*, Vol. 24(8), 2001, pp. 537–549.

[13] Lequesne, C., Plumier, A., Degee, H., and Habraken, A. M., "Numerical Study of the Fatigue Crack in Welded Beam-to-Column Connection Using Cohesive Zone Model," *Fracture and Damage Mechanics V*, M. H. Aliabadi, F. G. Buchholz, J. Alfaiate, J. Planas, B. Abersek, and S.-i. Nishida, Trans Tech Publications, Key Engineering Materials, Harbin, China, 2006.

[14] Roe, K. L. and Siegmund, T., "An Irreversible Cohesive Zone Model for Interface Fatigue Crack Growth Simulation," *Eng. Fract. Mech.*, Vol. 70(2), 2003, pp. 209–232.

[15] Li, X. K. and Cescotto, S., "A Mixed Element Method in Gradient Plasticity for Pressure Dependent Materials and Modelling of Strain Localization," *Comput. Methods Appl. Mech. Eng.*, Vol. 144(3–4), 1997, pp. 287–305.

Author Index

A

B

C

D

E

F

G

H

I

J

K

L

M

Subject Index

Cover image courtesy of Andrzej Neimitz

www.astm.org

ISBN: 978-0-8031-7512-9
Stock #: STP1526